Mineral Resource Reviews

Mohammed Bouabdellah
John F. Slack *Editors*

Mineral Deposits of North Africa

EXTRAS ONLINE

Springer

Mineral Resource Reviews

Series editor

John Slack, Reston, VA, USA

More information about this series at http://www.springer.com/series/11683

Mohammed Bouabdellah
John F. Slack
Editors

Mineral Deposits of North Africa

Springer

Editors
Mohammed Bouabdellah
Department of Earth Sciences
Mohammed Ist University
Oujda
Morocco

John F. Slack
U.S. Geological Survey
Farmington, ME
USA

ISSN 2365-0559 ISSN 2365-0567 (electronic)
Mineral Resource Reviews
ISBN 978-3-319-31731-1 ISBN 978-3-319-31733-5 (eBook)
DOI 10.1007/978-3-319-31733-5

Library of Congress Control Number: 2016936575

Printed on acid-free paper

This Springer imprint is published by Springer Nature
The registered company is Springer International Publishing AG Switzerland

Preface

This book is the first assembly of modern scientific papers on mineral deposits of North Africa. In total, 22 papers report new field and laboratory data on diverse types of metallic deposits in Morocco, Algeria, Tunisia, Mali, Mauritania, Egypt, Sudan, and Eritrea. Originally our goal was to include papers on deposits in Niger, Libya, and Chad, but political and other issues prevented this from being realized. Most of the deposits described herein are economically important—including several of world-class stature in terms of amount of contained metal, but others are relatively small or at present are only exploration prospects, yet are important in terms of regional metallogeny and potential future mining activity.

The lead paper, by M. Bouabdellah and J.F. Slack, provides a comprehensive overview of the geology and metallogeny of North Africa. This contribution synthesizes geological, geochemical, isotopic, and radiometric data bearing on the setting and origin of major deposits in the region, together with information on tonnages and grades, where available. All types of economically important metallic and non-metallic deposits are described, divided among the following categories: (1) orthomagmatic chromium-nickel-platinum group elements, (2) rare metal (tantalum, niobium, tin, rare-earth element [REE]) granites and related rare-metal pegmatites, (3) volcanic-hosted massive sulphide (VHMS) copper-zinc-gold-silver, (4) sedimentary-exhalative (SEDEX) zinc-lead-silver, (5) orogenic and intrusion-related gold, (6) iron oxide-copper-gold (IOCG), (7) banded iron formation (BIF), (8) Mississippi Valley-type (MVT) zinc-lead, (9) sediment-hosted stratiform copper, (10) sediment-hosted lead, uranium, manganese, and phosphate, (11) five-element veins containing nickel-cobalt-arsenic-silver-bismuth(-uranium), (12) epithermal gold-silver, (13) skarn and replacement tungsten, tin, and/or base-metals, (14) residual manganese, phosphate, salt, potash, bentonite, etc., and (15) mechanically concentrated deposits (e.g., paleoplacer gold).

Papers on specific deposits or districts are divided among commonly defined major types or classes of deposits. Within the category of porphyry, skarn, and epithermal deposits, the first paper by G. Levresse, M. Bouabdellah, A. Cheilletz, D. Gasquet, L. Maacha, J. Tritlla, D. Banks, and A. Samir describes the giant Imiter silver-mercury vein deposit and suggests that degassing was the main ore-forming process. The next contribution, by M. Rossi, L. Tarrieu, A. Cheilletz, D. Gasquet, E. Deloule, J.-L. Paquette, H. Bounajma, T. Mantoy, L. Ouazzani, and L. Ouchtouban, reports ages of

magmatic and hydrothermal events in the polymetallic tungsten-gold and lead-zinc-silver deposits of the Tighza district of Morocco, proposing links to granite-related porphyry and epithermal processes. M. Bouabdellah and G. Levresse follow with a description of the Bou Madine gold-silver-lead-zinc (±copper) deposit in a Neoproterozoic caldera setting, and summarize evidence for an epithermal origin. The next paper, by E. Pelleter, A. Cheilletz, D. Gasquet, A. Mouttaqi, M. Annich, Q. Camus, E. Deloule, L. Ouazzanni, H. Bounajma, and L. Ouchtouban, reports new U/Pb ages of magmatism in the Zgounder epithermal silver-mercury deposit of Morocco, providing evidence for a genetic tie to Neoproterozoic felsic magmatism. The following contribution by C. Marignac, D.E. Aïssa, A. Cheilletz, and D. Gasquet describes the metallogenic evolution of tungsten skarn and polymetallic vein deposits of the Edough-Cap de Fer district of Algeria, including fluid inclusion data that support a model for tectonically controlled mineralization during the formation of a late Miocene metamorphic core complex. M. Bouabdellah, R. Jabrane, D. Margoum, and M. Sadequi conclude this part with a study of the skarn to porphyry–epithermal transition recorded in the Ouixane iron district of Morocco, using new geochronological and fluid inclusion data to suggest a genetic link to Neogene high-K calc-alkaline to shoshonitic magmatism.

Hydrothermal vein-type deposits are described in the next group of papers. The first, by M. Bouabdellah, L. Maacha, G. Levresse, and O. Saddiqi, summarizes information on the vein-type cobalt-nickel-iron-arsenic (±gold ±silver) deposits of the famous Bou Azzer district in Morocco, and proposes a long-lived, magmatic-hydrothermal to low-sulphidation epithermal system of late Hercynian to Triassic age. The next paper, by C. Marignac, D.E. Aïssa, A. Cheilletz, and D. Gasquet, reports on copper-zinc-lead vein mineralization of the Aïn Barbar deposit in the Edough-Cap de Fer polymetallic district of Algeria, suggesting links to a late Miocene paleogeothermal system. Following is a contribution by M. Bouabdellah, L. Maacha, M. Jébrak, and M. Zouhair on Re/Os geochronological and isotopic (lead and sulphur) constraints on the origin of the Bouskour copper-lead-zinc vein-type deposit in Morocco and its relationship to Neoproterozoic granitic magmatism. The next paper by M. Bouabdellah and D. Margoum describes the Aouli sulphide ± barite ± REE-rich fluorite vein systems of the upper Moulouya district in Morocco, attributing this mineralization to Pangean rifting and opening of the Tethys and Central Atlantic oceans. The last paper in this group, by M. Bouabdellah, O. Zemri, M. Jébrak, A. Klügel, G. Levresse, L. Maacha, A. Gaouzi, and M. Souiah, reports on the geology and mineralogy of the El Hammam REE-rich fluorite deposit in Morocco, suggesting a link to transtensional Pangean and Central Atlantic rifting.

The next category comprises orogenic and granitoid-hosted gold and/or rare-metal deposits. In the first paper, D.M. Lawrence, J.S. Lambert-Smith, and P.J. Treloar review orogenic and reduced granitoid-hosted gold mineralization in Mali, and present fluid inclusion and stable isotope data for major deposits in districts such as Loulo-Gounkoto and Morila. This is followed by I.K. Khalil, A.M. Moghazi, and A.M. El Makky on mineralogical and geochemical constraints bearing on the origin and geodynamic setting of

Neoproterozoic vein-type gold mineralization in the Eastern Desert of Egypt. The following contribution, by C. Marignac, D.E. Aïssa, L. Bouabsa, M. Kesraoui, and S. Nedjari, describes the Hoggar gold and rare metals metallogenic province of the Pan-African Tuareg Shield in Algeria, proposing an early Cambrian rift-related origin for this mineralization. The final paper in this part is by M. Bouabdellah, F. Chekroun, A. Alansari, and D. Margoum, on the granitoid-related Tiouit gold deposit in Morocco, including a model involving a polyphase, late magmatic to hydrothermal system of Neoproterozoic age.

Two papers are included in the category of VHMS deposits. The first, by C.T. Barrie, M. Abu Fatima, and R.D. Hamer, reports on VHMS and oxide gold mineralization in the Neoproterozoic Nubian Shield of Northeast Africa, with a focus on deposits in Eritrea, Sudan, and Egypt. The second paper is by M. Bouabdellah, M. Hibti, L. Maacha, M. Zouhair, and F. Velasco, who describe geologic, hydrothermal, and geochemical relationships between bimodal magmatism and massive sulphide mineralization in the Hercynian central Jebilet-Guemassa province of Morocco.

MVT and Sedex deposits are represented by two contributions. The first by M. Bouabdellah and D.F. Sangster reviews the geology, geochemistry, and current genetic models for major MVT lead-zinc deposits of Morocco, and based on orebody geometries and lead isotope constraints proposes a link to the closing stage of the Alpine orogeny. The second paper, by S. Decrée, C. Marignac, R. Abidi, N. Jemmali, E. Deloule, and F. Souissi, describes Sedex lead-zinc and polymetallic deposits in northern Tunisia and draws comparisons and contrasts with MVT deposits in the region.

The last part is focused on sediment-hosted iron and manganese deposits. The first contribution, by C.D. Taylor, C.A. Finn, E.D. Anderson, D.C. Bradley, M.Y. Joud, M.A. Taleb, and J.D. Horton, summarizes information on the giant Mesoarchean and Paleoproterozoic BIF deposits of the F'derik-Zouérate iron district in Mauritania, and presents the results of new airborne geophysical surveys and detrital zircon geochronology. The last paper by A. Dekoninck, R. Leprêtre, O. Saddiqi, J. Barbarand, and J. Yans describes the giant, high-grade, karst-hosted Imini manganese deposit in Morocco, and proposes a model in which Mn precipitation occurred with increasing pH and Eh, linked to dolomite dissolution and the influx of oxygenated meteoric waters.

Mohammed Bouabdellah
John F. Slack

Contents

Part I
Regional Overview

Geologic and Metallogenic Framework of North Africa

Mohammed Bouabdellah and John F. Slack

Abstract

North Africa is noteworthy for having a great diversity of geology and mineral resources. Geologically, the region contains numerous terranes that contain rocks ranging in age from Archean to Quaternary, including diverse igneous, sedimentary, and metamorphic lithologies. Major geological features were built during the main phases of Proterozoic and subsequent Phanerozoic orogenies, the break-up of the supercontinents Rodinia, Gondwana, and Pangea, and during the opening and closing of major ocean basins such as the Iapatus, Atlantic, Pacific, and Tethys. Three major tectono-stratigraphic domains are recognized (1) the Precambrian province that includes the African-Nubian Shield (ANS) to the east and the West African Craton (WAC) to the west, and the intervening Tuareg Shield and "Saharan Metacraton"; (2) the Variscan (Paleozoic) fold belt; and (3) the Atlas-Alpine (Mesozoic-Cenozoic) system. Mineral deposits of North Africa formed in a variety of geologic settings at different time periods from Archean to Quaternary. Mineral commodities including gold, silver, cobalt, nickel, chromium, arsenic, copper, lead, zinc, iron, and many other elements. Major deposit types present in the region are (1) orthomagmatic Cr-Ni-platinum group elements (PGE); (2) rare-metal granites and related rare-element pegmatites; (3) volcanic-hosted massive sulphide (VHMS); (4) sedimentary-exhalative (SEDEX); (5) orogenic and intrusion-related gold; (6) iron oxide-copper-gold (IOCG); (7) banded iron formation (BIF); (8) Mississippi Valley-type (MVT) lead-zinc; (9) sediment-hosted stratiform copper;

Electronic supplementary material The online version of this chapter (doi:10.1007/978-3-319-31733-5_1) contains supplementary material, which is available to authorized users.

M. Bouabdellah (✉)
Laboratoire des Gîtes Minéraux, Hydrogéologie & Environnement, Faculté des Sciences, Université Mohammed Premier, 60000 Oujda, Morocco
e-mail: mbouabdellah2002@yahoo.fr

J.F. Slack
U.S. Geological Survey, National Center, Mail Stop 954, Reston, VA 20192, USA

M. Bouabdellah and J.F. Slack (eds.), *Mineral Deposits of North Africa*, Mineral Resource Reviews, DOI 10.1007/978-3-319-31733-5_1

(10) sediment-hosted U, Mn, and phosphate; (11) five-element veins containing nickel-cobalt-arsenic-silver-bismuth(-uranium); (12) epithermal gold-silver veins; (13) skarn and replacement tungsten, tin, and/or base-metals; (14) residual manganese, phosphate, salt, potash, bentonite, etc.); and (15) mechanically concentrated deposits (e.g., paleoplacer gold). Some deposits are world class in terms of size, grade, and ore production, including phosphate deposits and the Imiter silver deposit in Morocco, Precambrian BIF deposits in Mauritania, orogenic gold deposits in Mali and Mauritania, uranium deposits in Niger, and MVT lead-zinc deposits in the High Atlas system of Morocco and Tunisia. Resources and exploration potential are also known for gold, diamonds, strategic metals, and other commodities within the Precambrian cratonic terranes of most North African countries. Based on absolute ages for mineralization, or alternatively for ages of the host rocks (where radiometric age determinations are lacking), seven major time periods of mineralization defining distinct metallogenetic epochs are recognized. Each has different metal associations, mineralogical and geochemical features, spatial distributions, and geodynamic environments that collectively discriminate time periods and related metallogenic provinces. These are: (1) Archean (>2500 Ma), (2) Paleoproterozoic (2500–1600 Ma), (3) Neoproterozoic (630–542 Ma), (4) Hercynian (540–290 Ma), (5) Permian-Triassic (~300–200 Ma), (6) Late Cretaceous-Paleogene (100–23 Ma), and (7) Late Miocene-present (<16 Ma).

1 Introduction

The goal of this introductory chapter is to provide a geologic and metallogenic synthesis of North Africa. Focus is on the importance and diversity of various mineral deposits, their temporal and spatial distributions, and especially relationships between the geological evolution of North Africa and the Archean to Quaternary mineralization that occurred in the region.

2 Regional Geology

The northernmost part of the African continent has experienced a long-lived and complex geological history dating back to the Archean. Resulting geological features (Fig. 1) were built during the main phases of Proterozoic and subsequent Phanerozoic orogenies, the break-up of the supercontinents Rodinia, Gondwana, and Pangea, and during the opening and closing of major ocean basins such as the Iapatus, Atlantic, Pacific, and Tethys (Tawadros 2011).

North African geology has been extensively studied over the last few decades resulting in a wealth of geological, mineralogical, geochemical, and geochronological data, reported in hundreds of research papers, and in geological maps published at a variety of scales (e.g., Stern 1994, 2002; Walsh et al. 2002; Ennih and Liégeois 2001; Johnson and Woldehaimanot 2003; Liégeois et al. 2003, 2005, 2013; Inglis et al. 2004, 2005; Key et al. 2004, Thomas et al. 2004; Gasquet et al. 2005; Schofield et al. 2006; Bendaoud et al. 2008; Fezaa et al. 2010; Johnson et al. 2011; Fritz et al. 2013; and references therein). Therefore, only a summary of major conclusions relevant to the present synthesis is given below.

Overall, the geology of North Africa is subdivided broadly into three major tectono-stratigraphic domains (1) the Precambrian province that includes the African-Nubian Shield (ANS) to the east and the West African Craton

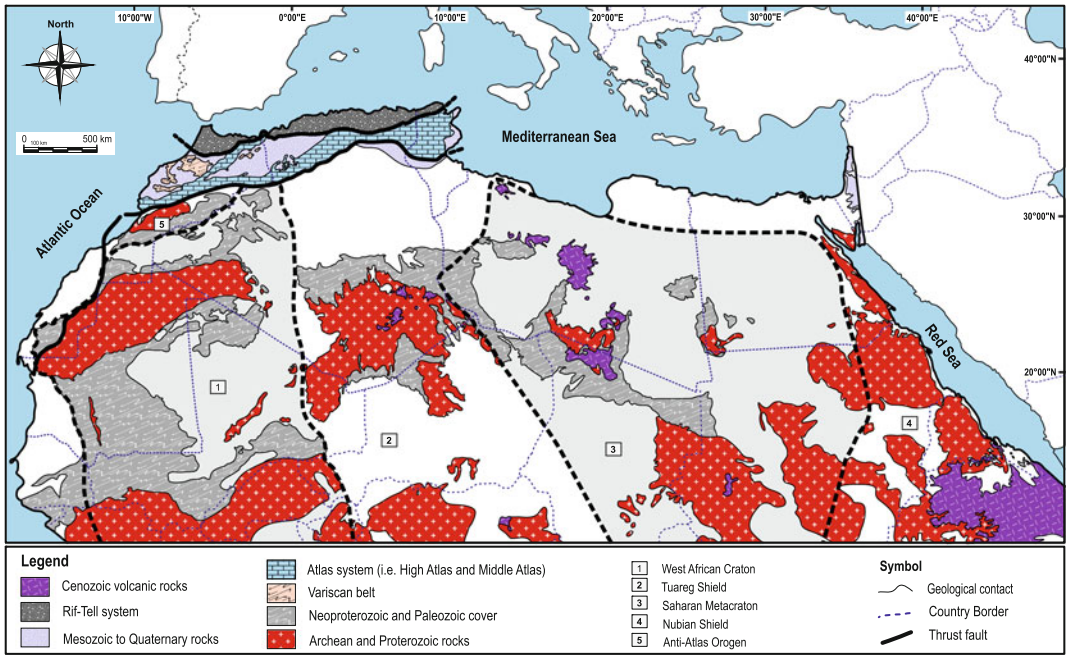

Fig. 1 Regional geological map of North Africa showing main lithotectonic domains (modified after geological map of Africa at scale of 1:1,000,000; Milési et al. 2004). *Thick dashed lines* are inferred margins of Precambrian cratons and shields

(WAC) to the west, and the intervening Tuareg Shield and "Saharan Metacraton"; (2) the Variscan (Paleozoic) fold belt; and (3) the Atlas-Alpine (Mesozoic-Cenozoic) system (Fig. 1).

3 Precambrian Evolution

The Precambrian of North Africa evolved through two main geodynamic cycles, including the Archean (>2.5 Ga) and Proterozoic (2.5–0.57 Ga). Precambrian terranes are exposed in cratons that cover a large region in the southern part of North Africa (Fig. 2). Major cratons include the ANS, WAC, Tuareg Shield, and Saharan Metacraton. Additional Precambrian outcrops exist along the northern edge of the WAC within the Anti-Atlas Range of Morocco (Fig. 1). From a historical metallogenic standpoint, the Precambrian province has provided a source of gold in Egypt since Pharaonic times, and recently has become an important frontier for gold exploration; discoveries of >45 Moz of gold equivalent have been made in the last two decades alone (i.e., Arabian-Nubian Shield; Trench and Groves 2015). Potential also exists for the discovery of new deposits containing a variety of other commodities such as silver, copper, zinc, tin, tungsten, tantalum, and uranium. Accordingly, there is now a resurgence of mining and exploration activity in much of North Africa, especially in those countries where Precambrian outcrops are widely distributed such as Mauritania, Algeria, Mali, Niger, Sudan, Eritrea, Egypt, and Morocco. Geological aspects of the major cratons, and of younger orogens and cover sequences, are considered below.

4 Arabian-Nubian Shield

The Arabian-Nubian Shield (ANS; Figs. 1 and 2) constitutes the northern part of the Neoproterozoic to early Paleozoic East African orogen (Stern 1994). This shield is a Neoproterozoic accretion-type orogen comprising a stack of thin-skinned nappes that record the oblique convergence of bounding plates (Fritz et al. 2013). Geochronological and isotopic constraints (e.g., Liégeois and Stern 2010; Johnson et al. 2011) indicate that the ANS consists mainly of

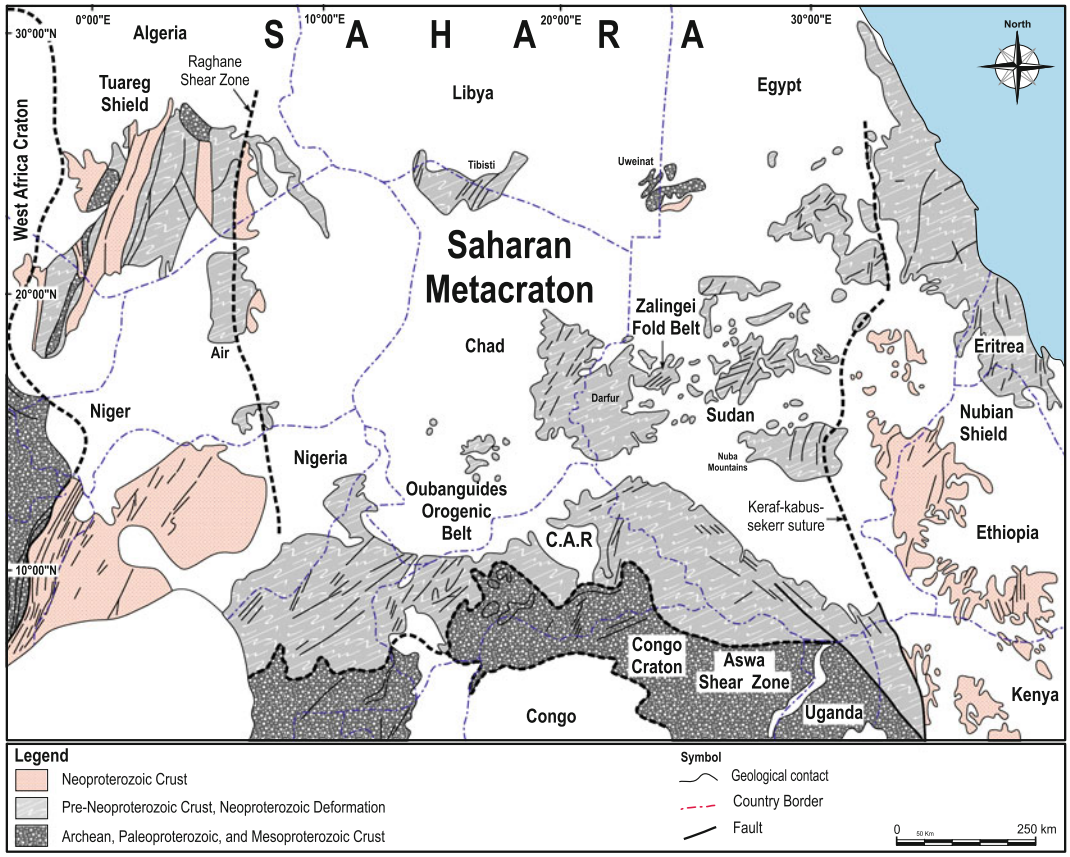

Fig. 2 Geological map showing main lithotectonic units of Saharan Metacraton and relationships to adjacent Tuareg Shield and Arabian-Nubian Shield (modified after Unrug 1997; Abdelsalam et al. 2002). *Thick dashed lines* represent limits of the major cratons

accreted Neoproterozoic greenstone terranes (Fig. 3). These terranes subsequently collided and amalgamated during a protracted period that included intra-oceanic subduction, arc and back-arc magmatism (>700 Ma), through collisional events and terrane amalgamation (700–620 Ma), to tectonic escape, strike-slip faulting, and extension (620–550 Ma) of newly formed continental crust (Stern 1994; Johnson and Woldehaimanot 2003).

Major lithologies (Fig. 3) consist of metamorphosed (greenschist-facies) volcanosedimentary sequences of mafic to felsic island arc lavas, volcaniclastic rocks, and related sedimentary rocks, segmented by dismembered ophiolitic complexes (Johnson and Woldehaimanot 2003; Blasband 2006). Diverse pre-, syn-, and postkinematic intrusions cut these sequences. The volcanosedimentary sequences are essentially Neoproterozoic (ca. 800–700 Ma) although older protoliths dated at 1025 Ma have been identified (Be'eri-Shlevin et al. 2011). During the late Cryogenian–Ediacaran (650–542 Ma), the ANS underwent final assembly and accretion to the Saharan Metacraton concurrent with assembly of eastern and western Gondwana (Johnson et al. 2011; Fritz et al. 2013). At ca. 620–530 Ma, a major period of felsic magmatism generated post-accretionary to postorogenic, rare-metal granites and rare-element granitic pegmatites (Küster 2009; Melcher et al. 2015) that intrude all of the Neoproterozoic terranes.

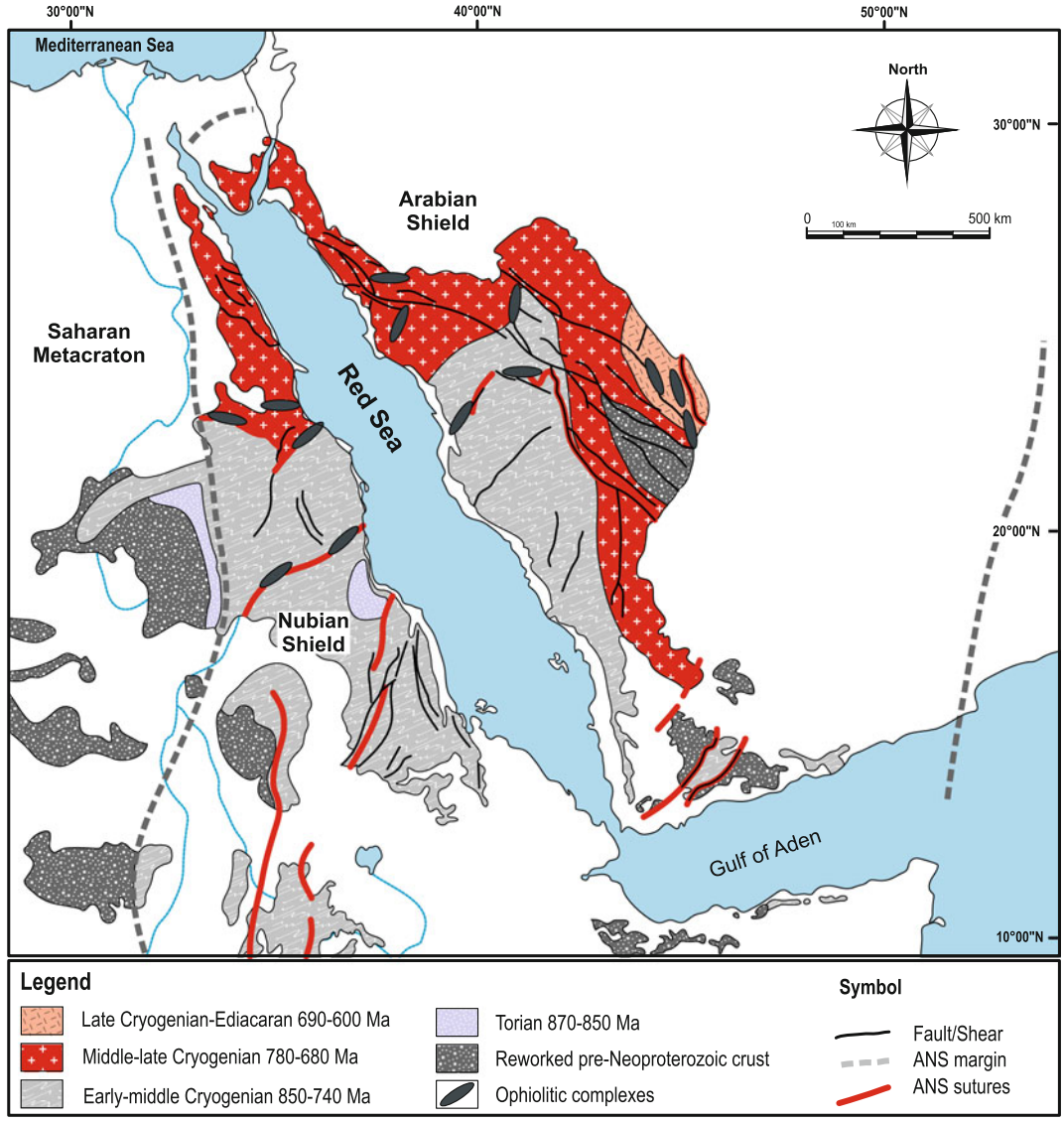

Fig. 3 Regional geological map of Arabian-Nubian Shield (ANS) showing main tectonostratigraphic terranes, suture zones, spatial distribution of major ophiolitic complexes, boundary between eastern and western arc terranes, and boundaries between ANS and flanking older crustal blocks (modified after Berhe 1990; Stoeser and Frost 2006; Fritz et al. 2013; Johnson 2014)

5 West African Craton

The West African Craton (WAC) contains the Reguibat Shield and the extreme northern termination of the Anti-Atlas Range in southern Morocco (Figs. 1 and 4). This craton records a protracted history of crustal evolution beginning with the formation of Mesoarchean and Paleoproterozoic basement, which was affected by the Eburnean orogeny at ca. 2 Ga. The Mesoproterozoic (1.7–1.0 Ga) corresponds to a quiescent period during which the WAC was unaffected by major geological events, thus promoting its acquisition of a thick lithospheric base (Black and Liégeois 1993).

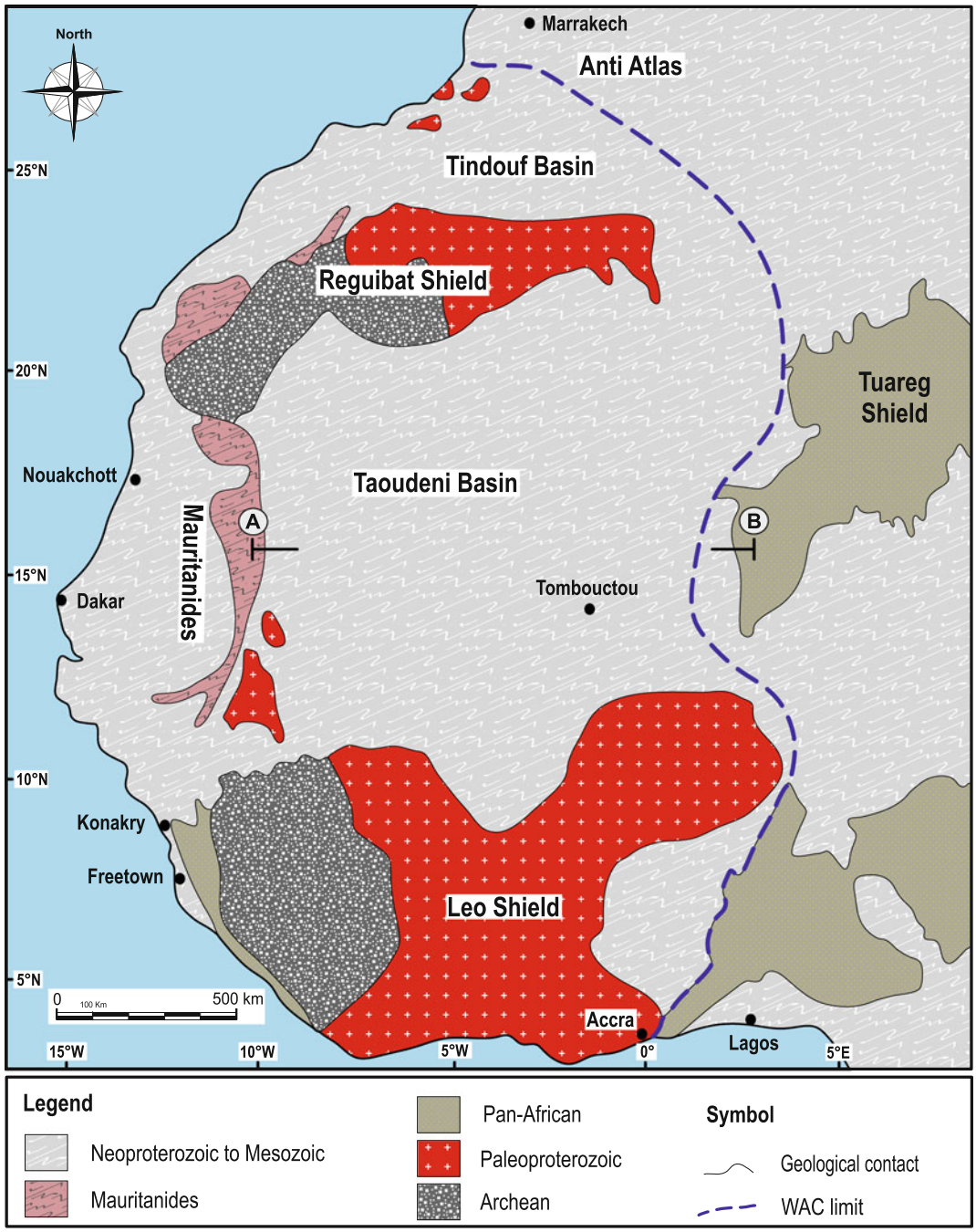

Fig. 4 Regional geological map showing main lithostructural domains of West African Craton (WAC) (modified after Villeneuve, 1984). Section line *A–B* indicates cross-section shown in Fig. 8

Since the Paleoproterozoic (ca. 1700 Ma) the craton has been largely stable with respect to magmatic and major tectonic events. The only exceptions are extensional tectonics and emplacement of intrusions related to opening of the North Atlantic during the Late Triassic (Clauer et al.

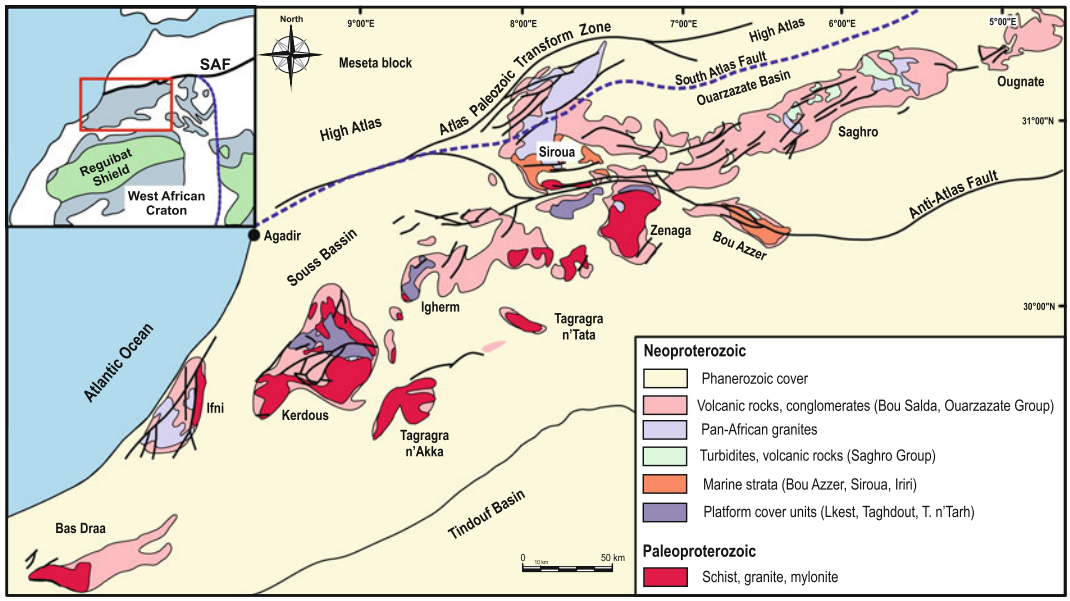

Fig. 5 Structral map of Anti-Atlas orogen of central Morocco showing Precambrian inliers and relationships to West African Craton (WAC) to the south and to High Atlas Mountains to the north (modified after Thomas et al. 2004; Gasquet et al. 2005). *Inset* shows location of Anti-Atlas within WAC. Abbreviation: *SAF* South Atlas Fault

1982; Villeneuve and Cornée 1994; Verati et al. 2005; Rooney et al. 2010). At the beginning of the Neoproterozoic, the WAC experienced several extensional events associated with continental breakup. By the end of the Neoproterozoic at 760–660 Ma, this craton was subjected to island arc accretion on its northern and eastern sides in the present-day Anti-Atlas of Morocco (Thomas et al. 2002; Samson et al. 2004; D'Lemos et al. 2006; Bousquet et al. 2008; Ennih and Liégeois 2008, and references therein), and in the Tilemsi of Mali (Caby et al. 1989). During the main Pan-African orogeny, the WAC was subjected to convergence on all margins from the north in the Anti-Atlas (Ennih and Liégeois 2001; Walsh et al. 2002; Inglis et al. 2004, 2005; Gasquet et al. 2005; El Hadi et al. 2010), to the east along the Trans-Sahara belt (Black et al. 1994; Affaton et al. 1991; Attoh and Nude 2008), to the south within the Rockelides and Bassarides belts and to the east within the Mauritanides belt (Villeneuve 2008). Several thrust sheets are also preserved on the craton itself, such as in Mali (Caby et al. 1989).

6 Anti-Atlas Orogen

The Anti-Atlas orogen of southern Morocco (Fig. 5) is among the most important segments of the major Pan-African (0.5 Ga) system of North Africa. This orogen extends over a distance of 700 km at the northwestern rifted margin of the WAC to the south of, and parallel to, the High Atlas Range (Figs. 1 and 5). Precambrian terranes are exposed in a series of dispersed, SW-NE-trending inliers termed "boutonnières" (Bas Draa, Ifni, Kerdous, Tagrara n'Akka, Igherm, Siroua, Bou Azzer, Saghro, and Ougnat), which record at least two Precambrian orogenic events—the Paleoproterozoic Eburnean and the Neoproterozoic Pan-African (e.g., Walsh et al. 2002; Thomas et al. 2004). Scattered outcrops of related rocks in northwestern Algeria show that, from southeastern Morocco, the belt continues southeastwards with a NW–SE trend.

Structurally, the Anti-Atlas is subdivided into western, central, and eastern domains.

Paleoproterozoic rocks of the western Anti-Atlas are assigned to the northwest border of the WAC, which is thought to have formed as the result of extensive Eburnean magmatism and metamorphism at ca. 2.1–2.0 Ga (e.g., Ennih and Liégeois 2008), whereas the central and eastern domains are parts of the Pan-African mobile belt. More interestingly, the central Anti-Atlas domain is considered a suture zone because of the presence of ophiolitic remnants, amongst which the most impressive is Bou Azzer (Leblanc and Lancelot 1980; Hefferan et al. 2000; El Hadi et al. 2010). In this regard, Ennih and Liégeois (2001) proposed that the actual northern boundary of the WAC is expressed by the South Atlas fault (Fig. 5), instead of the major Anti-Atlas Fault as proposed by previous workers (e.g., Hefferan et al. 2000).

Over the last past two decades, an impressive number of geological, geochemical, and geochronological studies have been carried out by the World Bank-funded PNCG program (Programme National de Cartographie Géologique). At the time of its release in 1994, results of this program were supervised by the Moroccan Ministry of Energy and Mines. The PNCG produced a series of excellent syntheses that describe comparable models for the evolution of the orogen belt (e.g., Hefferan et al. 1992; Saquaque et al. 1992; Fekkak et al. 2000; Ennih and Liégeois 2001; Thomas et al. 2002, 2004; Walsh et al. 2002). Recent reviews of the geology of the Anti-Atlas can be found in Walsh et al. (2002), Thomas et al. (2002, 2004), and Gasquet et al. (2005), to which the interested reader is referred for details. Therefore, only a brief synopsis of the complex geological history of the Anti-Atlas system is given below.

The oldest rocks of the Anti-Atlas consist of Paleoproterozoic (2.0–2.1 Ga), medium- to high-grade, amphibolite-facies grey gneiss, biotite-rich schist, garnet ± sillimanite paragneiss, calc-silicate rocks, migmatite, and granitoids (Thomas et al. 2002; Walsh et al. 2002; Ennih and Liégeois 2008). These rocks are unconformably overlain either by Neoproterozoic (800–550 Ma) strata or the Cambrian Tata Group (Ennih and Liégeois 2008), all of which were intruded by Pan-African granitoids between 625 and 550 Ma (Walsh et al. 2002; Thomas et al. 2004; Gasquet et al. 2005). Together, these rocks represent a complex accretionary mélange that was sutured to the northern edge of the Eburnean (~2 Ga) WAC during the amalgamation of Gondwana in the Neoproterozoic, from ca. 700 to 600 Ma (e.g., Hefferan et al. 2002; Thomas et al. 2002). After a major stratigraphic gap (hiatus) that encompasses all of the Mesoproterozoic, a thick Neoproterozoic (800–550 Ma) volcanosedimentary sucession was deposited unconformably on the Paleoproterozoic rocks of the cratonic basement, before initial basin closure during the Pan-African orogeny that formed the Anti-Atlas Supergroup (Thomas et al. 2004). Lithologically, the Neoproterozoic consists of a siliciclastic package made of turbidites, shale, diamictite, quartzite, greywacke, sandstone, and coarse clastic rocks with interbedded mafic lava flows and related peridotitic intrusions, all of which are intruded by high-K, calc-alkaline granitoids and mafic plutons. Prolonged convergence gave rise to a sinistral transpressional regime during which volcanosedimentary rocks of the Ouarzazate Supergroup were deposited (615–550 Ma; Thomas et al. 2004). Late Ediacaran volcanism produced pyroclastic ash-flow tuffs (ignimbrites) and related epiclastic rocks. Shallow-marine carbonate and clastic rocks (Adoudounian Formation) that span the Cambrian-Precambrian boundary overlie the Neoproterozoic sequence, and were intruded by Pan-African, post-kinematic, high-K calc-alkaline granitoids between 625 and 550 Ma (e.g., Thomas et al. 2002; Walsh et al. 2002).

Structurally, the ca. 2.0 Ga Eburnian deformation was oriented N-S to NE-SW and is linked to high-grade metamorphism, whereas the mostly NW-SE-oriented Pan-African deformation occurred under greenschist-facies conditions (Ennih et al. 2001). During the Neoproterozoic Pan-African orogeny, the northwestern rifted margin of the WAC underwent repeated tectonic cycles, including collision, accretion, and dismemberment of oceanic crust and island arcs (D'Lemos et al. 2006). The earliest Pan-African deformation, at ca. 660 Ma, resulted from closure of the ocean basin, SW-directed thrusting, and accretion of island-arc remnants. Most workers agree that the development of the Pan-African orogen occurred during three stages (1) rifting and break-up of the WAC

during the period 800–690 Ma; (2) basin closure at ca. 690–605 Ma, accompanied by southward directed, arc-continent collision, ophiolite obduction, deformation, metamorphism, and calc-alkaline magmatism; and (3) post-collision extension at 605–530 Ma (Gasquet al. 2005).

Younger Variscan deformation at ca. 359–298 Ma reactivated the older Pan-African structures and produced Precambrian-cored domes, major décollements between Paleoproterozoic basement and Neoproterozoic/Phanerozoic cover, and disharmonic folds and listric extensional faults (Faik et al. 2001; Caritg et al. 2004; Soulaimani et al. 2004; Burkhard et al. 2006). The resulting structures were reactivated again by the Alpine orogeny during the Late Permian to Late Triassic, coincident with Central Atlantic opening and Tethyan rifting (El Arabi et al. 2006; Knight et al. 2004). Malusa et al. (2007) and Sebti et al. (2009) suggested a polyphase exhumation history for the Anti-Atlas orogen, contemporaneously with the break-up of Pangea and the convergence of Africa and Europe.

7 Reguibat Shield

The Reguibat Shield or "Dorsale des Reguibat" (Figs. 1 and 4) is an uplifted, NE-trending crustal block that represents the exposed northern part of the WAC that has been stable since ca. 1700 Ma. This shield extends from northern Mauritania into southern Morocco and the northwestern part of Algeria. It is bounded by the Paleozoic Tindouf Basin in the north, the Neoproterozoic to Paleozoic Taoudeni Basin in the southeast, and the Pan-African, Caledonian, and Variscan fold–thrust belt of the Mauritanide belt in the southwest and west-northwest. The following summary of major geological attributes of this region is inspired from the recent papers of Schofield et al. (2003, 2006), and Key et al. (2004), as these reports constitute the most exhaustive and comprehensive descriptions published on this shield.

Geologically, the Reguibat Shield consists of two major contrasting domains (Fig. 4) separated by a crustal shear zone that represents a major accretionary boundary (Lahondère et al. 2003; Pitifield et al. 2004; Schofield et al. 2012). Included in this context are the southwestern Mesoarchean to Paleoproterozoic (~3.1–2.9 Ga) domain, and the northeastern Paleoproterozoic (~2.6 Ga) to Neoproterozoic domain, both of which were amalgamated during the ca. 2.0 Eburnean orogeny. The southwestern domain comprises high-grade, ca. 3.5–2.5 Ga TTG-type migmatitic orthogneisses (Tiris and Amsaga Complexes) and greenstone assemblages (Tasiast-Tijirit terranes), together with ferrugineous quartzite, marble, ultramafic rocks, and interlayered amphibolite, greywacke, and pelite, all intruded by 2.99–2.83 Ga charnockitic gneisses (Berger et al. 2013). Together, these Mesoarchean metasedimentary and meta-igneous rocks host the Tasiast gold deposit and most of the BIF deposits (Taylor et al. 2012; Taylor et al. this volume). In contrast, the northeastern part of the shield consists of younger Paleoproterozoic (Birimian) to Neoproterozoic volcanosedimentary successions and associated batholitic-scale granitic intrusive suites of different ages, which cut the major shear zones (Taylor et al. 2012) that host many orogenic gold deposits in the WAC (i.e., Tasiast gold field of Mauritania).

The host rocks experienced at 3.42 Ga the effects of polyphase folding and high-grade metamorphism followed by the emplacement of late-tectonic granites at 2.73–2.72 Ga. Retrograde amphibolite-facies mineral assemblages occur near the main shear zones (Attoh and Ekwueme 1997; Potrel et al. 1998). Metamorphic grade within the shield generally increases from mid-greenschist facies in the southwest to granulite facies in the northeast. Numerous N-S elongate greenstone belts consisting of metasedimentary rocks and metavolcanic to meta-plutonic rocks ranging in composition from ultramafic to felsic occur over a broad area in the western part of the shield, each marking major crustal discontinuities. From a metallogenic standpoint, both domains host major mineralization (i.e., Tasiast gold deposit in the Archean domain; Heron et al. 2015) and BIF (Kediat Ijil deposit in the Eburnean domain; Taylor et al. this volume). Considered together, the presence of these two major ore deposits demonstrates the high mineral potential of the two lithotectonic domains. The importance of Archean terranes as the host for gold

producers in Africa is further highlighted by productivity of the Zimbabwe and Kaapvaal cratons in southern Africa (e.g., Foster and Piper 1993), and more importantly by the recent discoveries of orogenic and related granitoid-hosted gold deposits in Neoproterozoic terranes of North Africa (i.e., ANS-hosted Um Egat and Dungash deposits in southeastern Egypt; Klemm et al. 2001; Zoheir et al. 2008; Khalil et al. this volume) and the world-class Amesmessa-Tirek gold field in the Hoggar Shield in Algeria (Ferkous and Monie 2002; Marignac et al. this volume).

8 Tuareg Shield

The Tuareg Shield of the central Sahara consists of 500,000 km^2 of Archean to Paleoproterozoic and Neoproterozoic terranes situated between the WAC to the west and the Saharan Metacraton to the east (Fig. 2). The shield is composed of the three distinct lithotectonic domains (1) the Hoggar massif of southern Algeria, (2) the Adrar Iforas massif of northern Mali, and (3) the Aïr massif of northern Niger (Fig. 6). Collectively, these domains were amalgamated during the Pan-African orogeny at the end of the Neoproterozoic, in response to collision between the Tuareg terranes and the WAC (Black et al. 1994). Among these, the Hoggar massif is the largest and best studied in terms of geological, geochemical, and geochronological evolution (Ouzegane et al. 2003; Peucat et al. 2003; Abdallah et al. 2007; Bendaoud et al. 2008; Liégeois et al. 2003, 2005, 2013; Henry et al. 2009; Fezaa et al. 2010; Nouar et al. 2011; Liégeois et al. 2013).

Geologically, the Hoggar massif consists of a complex sequence of fault-bound segments apparently assembled by dextral transpression

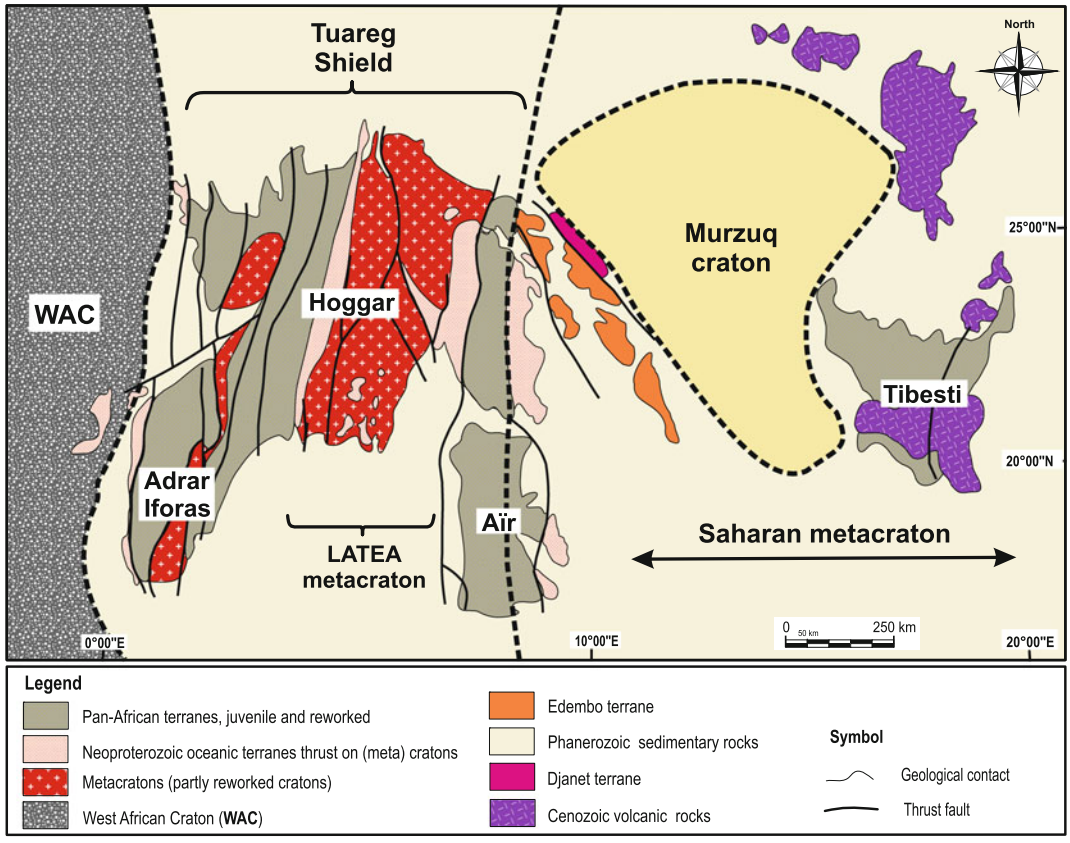

Fig. 6 Simplified geological map of Tuareg Shield showing main lithotectonic domains and spatial relationships to adjacent West African Craton (WAC) and Saharan Metacraton (adapted and modified from Liégeois et al. 2005; Fezaa et al. 2010). LATEA, Laouini-Azrou-n-Fad-Tefedest-Egere-Aleksod

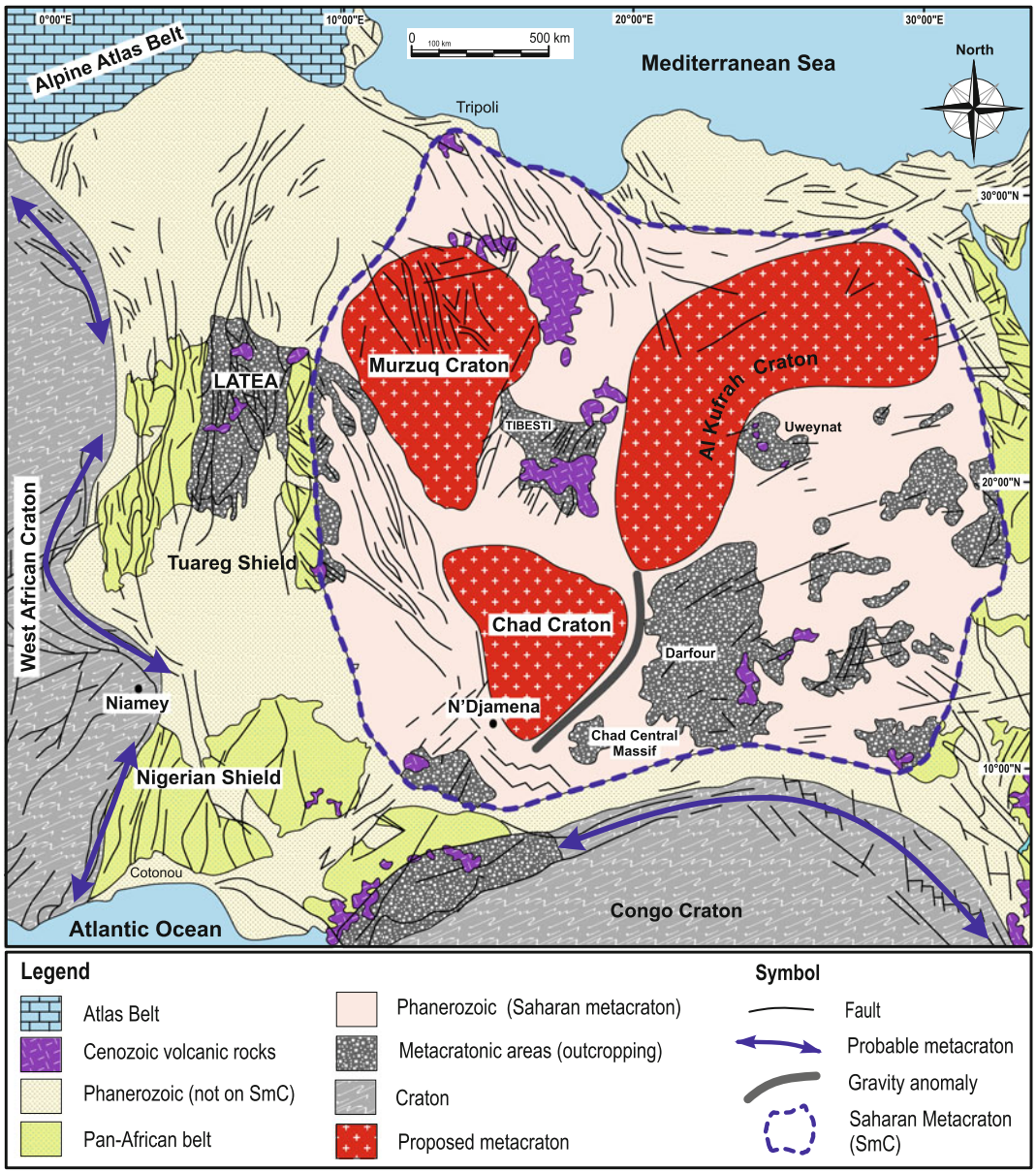

Fig. 7 Geological map showing main lithotectonic domains of Saharan Metacraton and relationships to surrounding Tuareg and Arabian-Nubian shields to the west and east, respectively, and to Congo Craton to the south (modified from Fezaa et al. 2010; Liégeois et al. 2013). Major subdivisions and structural and gravity data are from Cratcheley et al. (1984), Küster et al. (2008), and Milési et al. (2010)

during late Neoproterozoic time (e.g., Black et al. 1994). The massif can be subdivided into western, central, and eastern lithotectonic domains. The western domain (i.e., within Ouzzal metacraton) comprises well-preserved, 2-Ga ultra-high-temperature, granulite-facies metamorphic rocks (up to 1050 °C for 11 kbar; Ouzegane et al. 2003) and related igneous terranes that formed during island arc and continental arc subduction at 730–630 Ma, followed

by Ediacaran collisional and post-collisional events at 630–580 Ma (Caby 2003; Liégeois et al. 2013). Effects of the Pan-African orogeny are limited to movement on major shear zones and associated faults, along which a few granitic plutons were intruded (Ouzegane et al. 2003).

The central Hoggar domain is characterized by an Archean-Paleoproterozoic basement variably affected by the Pan-African orogeny (Fig. 6; Abdelsalam et al. 2002; Liégeois et al. 2003). This domain, referred to by the acronym LATEA (Laouini-Azrou-n-Fad-Tefedest-Egere-Aleksod), is composed of four distinct blocks (Black et al. 1994) that originally were part of a single, pre-Pan African passive margin (Liégeois et al. 2003). The distinguished blocks consist predominantly of Archean and Paleoproterozoic metamorphic rocks, accompanied by emplacement of intrusive rocks at ca. 2.1 Ga in the southeast (Bendaoud et al. 2008) and ca. 1.9 Ga in the northwest (Peucat et al. 2003). Neoproterozoic events correspond to collisions with Neoproterozoic oceanic terranes at several times including ca. 685 Ma (Liégeois et al. 2003). Pan-African overprints are represented by reactivation of shear zones along which granitic bodies were intruded, accompanied by greenschist- to amphibolite-facies metamorphism at 630–580 Ma (Bertrand et al. 1986; Liégeois et al. 2003; Abdallah et al. 2007; Bendaoud et al. 2008; Fezaa et al. 2010). According to Liégeois et al. (2003), the Archean and Eburnean LATEA microcontinent was dismembered by mega-shear zones and intruded by granitic batholiths during the main episode of the Pan-African orogeny (640–580 Ma). The high-grade metamorphism that affected the Precambrian metasedimentary rocks and associated granitoids occurred in three main stages (M_1, M_2, M_3; Benouda et al. 2008). No Neoproterozoic events older that 630 Ma are known in the LATEA basement (Fig. 7), a time span that coincides with the beginning of the collisions of the Tuareg Shield and WAC (Liégeois et al. 2013). In response to this collision, the LATEA lithosphere was segmented into several terranes and intruded by Paleoproterozoic/Archean-derived (Liégeois et al. 2003; Abdallah et al. 2007), high-K, calc-alkaline granitoids at ca. 580 Ma (Abdallah et al. 2007). This granitoid magmatism marked the end of the metacratonization within the LATEA.

The eastern Hoggar domain is structurally linked to the Saharan Metacraton (Fig. 7). Fezaa et al. (2010) showed that this part of the Tuareg Shield was subjected to a late Ediacaran tectono-magmatic episode at ca. 575–555 Ma, distinct from and unrelated to the Pan-African orogeny, which they named the Murzukian intracontinental episode. These age constraints led Fezaa et al. (2010) and Liégeois et al. (2013) to propose that the eastern Hoggar domain was a stable cratonic lowland at ca. 600 Ma. This eastern domain also contains Paleoproterozoic (1.9 Ga) Eburnean basement rocks, as documented by U–Pb LA-ICP-MS dating of zircon from the Arokam orthogneiss (Nouar et al. 2011).

The Air massif constitutes the southern extension of the eastern Hoggar domain (Fig. 6). Crystalline parts of this massif comprise an assemblage of arc-type terranes that were mostly cratonized at ca. 700 Ma. Radiometric ages for granites range from 700 to 500 Ma (U–Pb on zircon), with some ages showing Paleoproterozoic inheritance (Liégeois et al. 1994). Conversely, in the Adrar Iforas massif there is evidence of units that formed during Pan-African time in the Pharusian ocean basin that bordered the WAC. This ocean closed at 600 Ma, when subduction of oceanic lithosphere formed the Trans-Saharan orogenic belt (Boullier 1991; Caby and Monie 2003) that includes the Iforas orogen (Dostal et al. 1994).

9 Saharan Metacraton

The Saharan Metacraton (Abdelsalam et al. 2002) comprises medium- to high-grade gneissic and migmatitic pre-Neoproterozoic and/or remobilized Neoproterozoic continental crust that underlies most of the Saharan Desert in Egypt, Libya, Sudan, Chad, and Niger (Fig. 7). This metacraton corresponds to the vast arid region (5,000,000 km^2) that extends from the ANS in the east to the Tuareg Shield in the west, and from the Congo Craton in the south to the shallow-water Phanerozoic sedimentary rocks of

the northern margin of the African continent in southern Egypt and Libya. From a geological perspective, the Saharan Metacraton remains probably one of the world's least known areas. Published geochronological and isotopic data indicate that the metacraton is heterogeneous, and contrasts with the Neoproterozoic juvenile crust of the ANS to the east and the Archean continental crust of the Congo Craton to the south (e.g., Abdelsalam et al. 2002; Liégeois et al. 2013, and references therein). More than half of the Precambrian terrane of the Saharan Metacraton is buried under Cretaceous and younger flat-lying and unmetamorphosed sedimentary sequences, or covered by sands.

The oldest rocks of the metacraton consist of Archean (3.0 Ga SHRIMP U–Pb zircon, Uweinat massif; Bea et al. 2011a, b) to Proterozoic, medium- to high-grade gneiss, metasedimentary rocks, migmatite, and granulite together with low-grade volcanosedimentary rocks, all of which are intruded by ca. 750–550 Ma Neoproterozoic granitoids (Fig. 7). These Precambrian rocks are preferentially exposed in favor of uplifted Cenozoic massifs, of which the most prominent and best documented are those of Tibesti and Uweinat. Two structural trends are recognized (e.g., Abdelsalam et al. 2002), including (1) an older ENE-WSW trend, and (2) a younger N-S trend that offsets the older trend. Four models have been proposed to explain remobilization of the Saharan Metacraton during Neoproterozoic time (1) collision (Stern et al. 1994), (2) delamination of the sub-continental mantle lithosphere at ~700 Ma (Black and Liégeois 1993; Ashwal and Burke 1989), (3) extension of the lithosphere (Schandelmeier et al. 1994; Stern et al. 1994; Abdelsalam et al. 1995; Küster and Liégeois 2001), and (4) amalgamation of the metacraton from exotic terranes (Rogers et al. 1978).

10 Tibesti Massif

The Tibesti massif of southern Libya and northern Chad (Fig. 7) consists of two greenschist- to amphibolite-facies metamorphosed supracrustal units locally known as the lower and upper Tibestian units. These units are made of metasedimentary and metavolcanic rocks unconformably overlain by sandstone, shale, and carbonate rocks (Suayah et al. 2006). The only available radiometric data for these metamorphic rocks is an age of ca. 900 Ma determined on the lower Tibestian unit (whole-rock Rb-Sr; El-Makhrouf 1988). The metamorphosed supracrustal rocks were intruded by calc-alkaline, subduction-related igneous suites between ca. 600 and 550 Ma (Pegram et al. 1976; El-Makhrouf 1988). Neoproterozoic crust of the Tibesti massif was stabilized by magmatism that included subduction-generated batholithic suites and post-orogenic granite plutons. All of the magmatism occurred in a period of about 20 m.y., centered on ~550 Ma (Suayah et al. 2006). In contrast to both the Arabian–Nubian and Tuareg shields, the exposed part of the Tibesti massif lacks evidence for separate terranes assembled during the Neoproterozoic along faults, shear zones, or zones of oceanic closure (Suayah et al. 2006).

11 Uweinat-Kamil Inlier

The Uweinat-Kamil inlier is exposed along the triple-point border of Libya, Egypt, and Sudan (Fig. 7). Undeformed Paleozoic to Mesozoic strata and volcano-plutonic rocks unconformably overlie the Precambrian basement. Within the basement, Klerkx (1980) and more recently Bea et al. (2011a, b), described the occurrence of ca. 3.16–0.59 Ga rocks that consist of (1) a variably metamorphosed metaigneous complex composed dominantly of tonalitic, trondhjemitic, and granitic (TTG) gneisses with subordinate gabbroic-dioritic gneisses; (2) an anatectic complex formed of strongly migmatized metasedimentary rocks and orthogneiss with abundant Ediacaran (~590 Ma) granitoids; and (3) a Neoproterozoic unit composed of siliciclastic sedimentary rocks and iron formations (i.e., BIFs) dated at ~600 Ma (Bea et al. 2011a, b).

The oldest rocks of the Uweinat-Kamil inlier are migmatitic charnockitic gneisses with intercalated amphibolite, marble, and calc-silicate rocks. The charnockites have a Rb–Sr age of

~2.6 Ga (Klerkx 1980) and Nd model ages (T_{DM}) of 3.2–3.0 Ga (Harris et al. 1984). This time span is supported by recently SHRIMP U–Pb zircon ages as old as 3.0 Ga (Bea et al. 2011a, b). An even older age (3.16 ± 0.16 Ga) has been reported on TTG samples from east of the Gebel Kamil area. These ages are interpreted to represent the intrusion of arc magmas between 3.3 and 3.1 Ga. No new additions of juvenile material occurred until the Neoproterozoic, when Pan-African granitoids having a juvenile component were emplaced 0.75–0.6 Ga (Bea et al. 2011a, b). The migmatitic gneisses are intruded by small bodies of syntectonic S-type granites and late-tectonic diorite, granodiorite, and biotite granite. Dikes and volcanic plugs of various ages are also common (Schandelmeier et al. 1987). Precambrian to Pan-African polyphase deformation (D_1, D_2; D_3) of variable intensity affected all of the stratigraphic units, resulting in the development of shear zones, folds, and thrust faults.

12 Phanerozoic Evolution

12.1 Variscan Orogeny

By 550 Ma, the Gondwana Supercontinent had formed. For the next 350 m.y., African domains experienced only sedimentation along the Gondwanan margin or within intracontinental rift-sag basins. Subsequent orogenic activity affected only the northwestern and western parts of the continent (Trouw and de Wit 1998). Paleozoic terranes are represented throughout North Africa, occurring as mappable borders to Precambrian inliers; however, it is in Morocco and Mauritania where the largest Variscan outcrops are best known and documented. In both countries, the Paleozoic terranes occur preferentially within uplifted inliers distributed along the Atlantic coast (i.e., Meseta domain, Morocco; Fig. 1) and the northwest termination of the WAC (i.e., Adrar Settouf, Mauritanides; Fig. 4). These terranes were built during the late Paleozoic in response to the oblique collision between Gondwana and Laurussia (Matte 2001; Hoepffner et al. 2005). The lack of oceanic remnants (i.e., ophiolites) and subsequent high-pressure, low-temperature metamorphism (Piqué 2001) suggests that the North African Variscan belt is an intracontinental part of the Variscan orogen, having evolved near the margin of the WAC as a continental prism moderately thinned during early Paleozoic extensional events, and subsequently shortened during the Laurentia-Gondwana collision (Hopeffner et al. 2005).

13 Moroccan Hercynides or Variscides

The Moroccan Variscan belt is interpreted as the southwestern extension of the European Carboniferous orogen of the northwestern Gondwana margin. Paleozoic basins within this belt were deformed by folds and thrust faults, with the major collision dated as Late Devonian to late Carboniferous (Hopeffner et al. 2005). Among all Paleozoic basins that form the Moroccan Hercynides, the Meseta domain is by far the largest.

Structurally, the Meseta domain corresponds to a collage of moderately displaced, thinned crustal blocks derived from the distal Gondwanan paleomargin. Variscan orogenesis there is recorded by NW-verging thrust faults, greenschist- to amphibolite-facies metamorphism, and widespread syn- to late orogenic magmatism. Tectonic polarity is predominantly oriented WNW (Michard et al. 2010). Crustal extension occurred repeatedly during the Cambrian, Ordovician, Devonian, and early Carboniferous. The resultant blocks were shortened mainly during the early (eastern Meseta) and late Carboniferous, and were intruded by ca. 330–290 Ma calc-alkaline granitoids (El Hadi et al. 2003; 2006). The dispersed Paleozoic inliers consist mainly of Cambrian carbonate rocks, siliciclastic phyllite, and greywacke with intercalated tuffs and tholeiitic basalt flows (Ouali et al. 2003); followed by shallow marine Acritarch-dated Ordovician micaceous shale with interlayered sandstone and quartzite (Cailleux 1994), which in turn are overlain by Silurian graptolitic black shale and intercalated quartzite and carbonate and intraplate, anorogenic alkaline basalt (Cornée et al. 1985; El Kamel et al. 1998).

Younger strata include Devonian conglomerate, shale, argillite, greywacke, and reefal carbonates that grade laterally to distal argillite and sandstone. Above these strata are Carbonifeous turbiditic and siliciclastic sedimentary sequences accompanied by bimodal tholeiitic to calc-alkaline volcanic rocks with locally associated volcanogenic massive sulphide deposits (Bouabdellah et al. this volume).

All of these stratified rocks were affected by intense folding, thrusting, and strike-slip faulting accompanied by low-grade to greenschist-facies metamorphism and subsequent intrusion by late Hercynian calc-alkaline granitoids. For more details on the stratigraphy and tectonic evolution of the Moroccan Hercynides or Variscides, the reader is referred to Guiraud et al. (2005), Hoepffener et al. (2005, 2006), and Michard et al. (2010).

In the Anti-Atlas Mountains, the Variscan orogeny produced basement-controlled structures that formed basement uplifts together with inversion and folding of the Paleozoic sedimentary strata at the edge the WAC. Deformation is greatest near the borders of, and between closely spaced, basement uplifts. Regionally, deformation intensity decreases, either abruptly or progressively, towards the southeast and is absent within the undeformed Tindouf basin (Soulaimani and Burkhard 2008).

14 Taoudeni Basin

The Taoudeni intracratonic basin is a huge depression that extends ENE from Mauritania to Mali (Fig. 3) over a total area of 2,000,000 km^2. This geometry led Villeneuve and Cornée (1994) and Lottaroli et al. (2009) to describe the Taoudeni Basin, one of the largest sedimentary basins in the world, as a "super basin" segmented into a number of sub-basins. The basin is surrounded by the Reguibat Shield to the north, the Leo Shield to the south, the Hoggar Shield to the east, and the Mauritanide belt to the west (Fig. 3). The Taoudeni basin records a discontinuous sedimentation history from the Mesoproterozoic to the Carboniferous, containing strata with a total thickness of 2000–4000 m, averaging 1250 m (Deynoux et al. 2006; Rooney et al. 2010). Recent Re–Os ages (1107 ± 12 Ma, 1109 ± 22 Ma, and 1105 ± 37 Ma; Rooney et al. 2010) indicate that the older rocks of the Taoudeni Basin are Mesoproterozoic (Stenian 1000–1200 Ma; Ogg et al. 2008). The relatively thick strata of the basin (Fig. 7) are of potential interest for hydrocarbon exploration. Indeed, the Neoproterozoic and the Silurian black shales within this basin could constitute potential targets for petroleum production, as many oil wells have been sited in the area by international petroleum companies. Thin Mesozoic to Cenozoic cover rocks, together with large areas of Quaternary sand dunes, occur in the basin center and along the eastern margin adjacent to the Adrar des Iforas massif.

Overall, the stratigraphy of the Taoudeni Basin (Trompette 1973; Makhous et al. 1997; Villeneuve 2005; Villeneuve et al. 2006) is a succession of marine clastic sedimentary rocks and subordinate dolomitic limestones and thickly bedded stromatolitic limestones (Zhilong et al. 2008). In the Adrar region of the Mauritanian section of the basin, where outcrops and the stratigraphic database are optimum, four tectono-sedimentary supergroups have been recognized (Trompette 1973). The first supergroup consists of stromatolitic carbonates interbedded with siliciclastic units that were deposited in a marine setting; these strata were defined as Proterozoic based on classification of the stromatolites as Riphean; the second, third, and fourth supergroups are latest Proterozoic, Late Ordovician and Silurian, and Devonian, respectively (Fig. 7; Trompette 1973; Bertrand-Sarfati and Moussine-Pouchkine 1988; Deynoux et al. 2006; Rooney et al. 2010). Lithologically, the third and the fourth supergroups consist of rhythmically interlayered graptolitic shale and sandstone with subordinate limestone. The base of the third supergroup comprises the triad of diamictite, dolomite, and bedded chert. The Eocambrian glacial deposits have long been used as stratigraphic markers (Zimmermann 1960) that can be correlated across West Africa. Because the cratonic platform remained emergent since the Carboniferous, only a thin sequence of Mesozoic-Cenozoic continental sediments (including Quaternary dunes and lacustrine deposits) covered the platform (Villeneuve 2005).

15 Tindouf Basin

The Tindouf Basin, located north of the Taoudeni Basin, is an asymmetric, E-W-trending, Paleozoic depocenter 200–300 km wide and more than 700 km along strike from southern Morocco into northwestern Algeria, and covers a total area of 100,000 km^2 (Fig. 3). The basin is part of the large Saharan epicontinental platform that developed on the northern margin of Gondwana (Guiraud et al. 2005). Basin stratigraphy consists of >4,000 m of strongly folded and metamorphosed (greenschist-facies), Cambro-Ordovician to Carboniferous marine strata buried beneath a blanket of continental Cretaceous and Pliocene sedimentary rocks. The epicontinental character of the Saharan platform (Guiraud et al. 2005) prevented the formation of deep- and shallow-water carbonate facies; interbedded shale and sandstone within the basin have been attributed to the deepest-water facies that were deposited on an open marine ramp (Sebbar et al. 2000). Multiple sets of interlayered strata composed of organic-rich Silurian, Devonian (Frasnian), and Carboniferous (Visean) shales may have been buried to mature to overmature depths in the central part of the basin. In this regard, a number of well-placed hydrocarbon exploration wells have been drilled in the basin, but as yet unsuccessfully, probably owing to late Hercynian and subsequent Alpine tectonic and thermal overprints that affected the host rocks. This conclusion led Boote et al. (1998) to describe the Tindouf Basin as an extinct Paleozoic petroleum system.

16 Mauritanides Belt

The NW-trending Mauritanide fold-and-thrust belt is located along the western margin of the WAC extending over more than 2500 km from Morocco to Guinea Bissau (Fig. 3). This is a poly-orogenic, Pan-African to Variscan belt that was dismembered by Atlantic rifting (e.g., Haworth 1983; Dallmeyer 1991; Keppie et al. 1991). The belt developed between 350 and 290 Ma as a result of subduction and accretion of volcanic arcs and microcontinents, in response to collision involving Gondwana, Laurasia, and microcontinental blocks (Avalonia, Armorica) to form the Supercontinent Pangea (Dirks et al. 2010). The collision resulted in uplift and erosion of the North African platform between 300 and 280 Ma (Dallmeyer and Villeneuve 1987).

Pioneering descriptions on regional geology of the Mauritanides belt include those by Sougy (1962), Sougy and Lécorché (1963), Dia et al. (1969, 1979), Lécorché and Sougy (1978), Bronner et al. (1980), Lécorché (1980), and Lécorché et al. (1983). Extensive field mapping and geochemical and geochronological studies were carried out over the last two decades by the French Bureau de Recherches Géologiques et Minières (BRGM), the British Geological Survey (BGS), and the U.S. Geological Survey (USGS), as part of research programs funded by the World Bank, Islamic Development Bank, and European Union. Work by these organizations in Mauritania has greatly improved our geological understanding of this country including the Mauritanides belt (Schofield et al. 2003; Key et al. 2004; Villeneuve 2005; Taylor et al. 2012, and references therein). The geological descriptions presented below are drawn extensively from these papers.

The Mauritanides belt is subdivided into three main lithotectonic domains (Villeneuve 2005). From north to south, these are (1) the northern Mauritanides of which the Adrar Souttouf section is the most prominent, (2) the central Mauritanides, and (3) the southern Mauritanides that extend in their southern termination to Guinea Bissau and thus are not considered further because this domain lies outside the coverage of our book.

Structurally, the Mauritanides belt is generally interpreted as consisting of allochtonous terranes that were thrust eastward onto the WAC (e.g., Villeneuve 2005). K–Ar and Ar–Ar muscovite age dating indicates that final thrusting occurred at ca. 315–305 Ma, accompanied by folding of Devonian molass within the Taoudeni Basin (Dallmeyer and Lécorché 1989; Clauer et al. 1991; Martyn and Strickland 2004). Geochronological constraints suggest that the geodynamic evolution of the Mauritanides belt involved three main stages (Sougy 1962; Villeneuve et al. 1990; Dallmeyer

and Lécorché 1989; Villeneuve 2005), including (1) the period 680–620 Ma referred to as the Pan-African I orogeny, (2) 600–550 Ma that represents the second stage of the Pan-African orogeny, and (3) 330–270 Ma that corresponds to the Variscan orogeny. From a metallogenic standpoint, the Mauritanides belt is considered a fertile orogenic belt because it hosts in its southern termination the Guelb Moghrein IOCG deposit, and also has potential for volcanogenic massive (VMS), orogenic Au, and magmatic Ni–Cu deposits (Taylor et al. 2012).

17 Adrar Souttouf Massif

The Adrar Souttouf massif (ASM) extends in an ENE-WSW direction for more than 240 km along strike and is 120 km wide straddling the boundary between southern Morocco and northern Mauritania (Fig. 8). This massif has seen a recent surge of mineral exploration culminating in discovery of the Glibat Lafhouda and Twihinate carbonatites and associated REE–Ta–Nb–U mineralization (ONHYM 2015).

The ASM consists of allochtonous Precambrian and lower Paleozoic stacked nappes that were thrust eastward onto the WAC during the Mauritanide orogeny. These nappes lie either directly on the basement in the south and southwest, or on a thin sequence of Upper Ordovician to Devonian foreland rocks in the southeast (Lécorché 1980; Lécorché et al. 1991). Metamorphic grade of the nappes ranges from lower greenschist facies to granulite facies (Sougy and Bronner 1969; Lécorché et al. 1991). Contained strata vary from metasedimentary and metavolcanic rocks to high-grade migmatite, mica schist, and gneiss. The structure and stratigraphy of the ASM remain poorly known due to scarcity of reliable geochronological data. Sm–Nd and U–Pb whole-rock and single-mineral ages reported by Le Goff et al. (2001) and K–Ar ages presented by Villeneuve et al. (2006) show that the various lithostratigraphic units of the massif experienced a complex polyphase tectonothermal evolution. This evolution involves several Neoproterozoic to Early Cambrian events and a late Paleozoic overprint (i.e., Grenvillian ca. 1.1–1.0 Ga, Neoproterozoic ca. 730–660 Ma, early Paleozoic ca. 500 Ma, and Hercynian ca. 300 Ma; Lécroché et al. 1991; Villeneuve et al. 2006). Two main episodes of deformation have been recognized. The first, related to the Pan-African orogeny (680–520 Ma), caused large-scale compression with south-vergent thrusting and amphibolite-facies metamorphism.

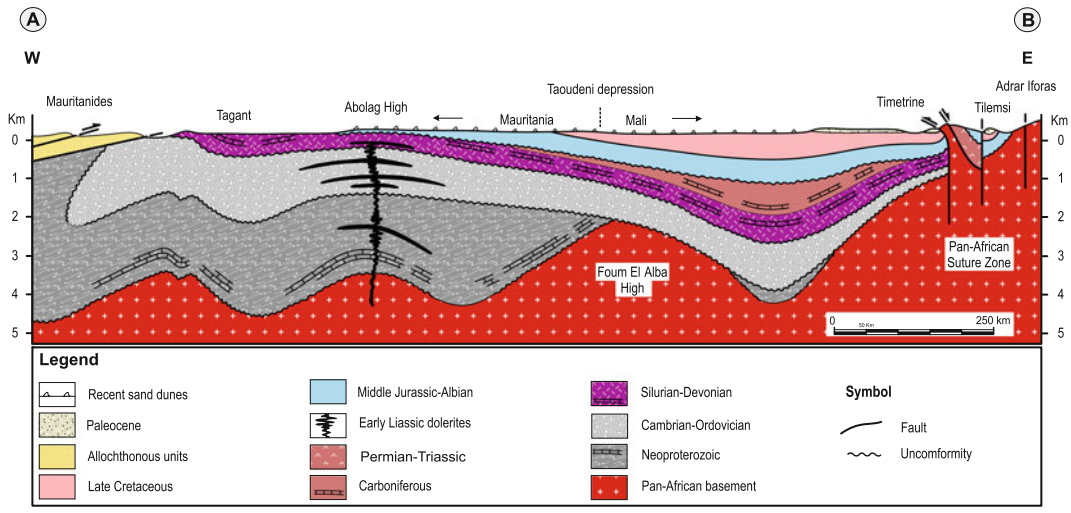

Fig. 8 Schematic E-W geological cross section through Taoudeni Basin (modified after Guiraud et al. 2005). See Fig. 4 for line of section

The younger Hercynian event (325–300 Ma) produced strong folding, faulting, and thrusting along the southern, western, and eastern margins of the massif (Lécorché et al. 1991).

18 Central Mauritanides Belt

The central Mauritanides belt (i.e., Akjoujt section of Villeneuve 2005) is probably the best-studied segment of the Mauritanide belt due mainly to its mineral potential based on occurrence of the Guelb Moghrein IOCG deposit and large BIF deposits plus a variety of other commodities (Taylor et al. 2012, this volume). The central Mauritanides belt consists of several internally imbricated, polydeformed, and variably metamorphosed supracrustal nappes that were thrust eastward and northeastward onto the Archean Tasiast-Tijirit terrane (Maurin et al. 1997; Pitfield et al. 2004). In the Akjoujet area that hosts the Guelb Moghrein deposit, the supracrustal rocks consist of two basal metabasalts overlain by BIF and schistose pelite of the Eizzene Group, which are unconformably overlain by quartzite, siliciclastic rocks, mafic tuffaceous siltstone, and BIF of the Oumachoueïma Group (Martyn and Strickland 2004; Meyer et al. 2006). Elsewhere in the belt, the outcropping host rocks consist of metamorphosed sedimentary lithologies, calc-alkaline mafic volcanic and volcaniclastic rocks related to a dismembered ophiolite, and a granite-gneiss complex containing large amounts of rhyolitic or dacitic tuffs (Villeneuve 2008).

19 Alpine Orogeny

The Mesozoic and Cenozoic geological evolution of North Africa involved the interplay of two major events: (1) opening of the North Atlantic and Neotethys oceans in the early Mesozoic, and (2) continental collision between the African-Arabian and Eurasian plates in the middle Cenozoic. These events resulted in development of the Alpine Maghrebian belts along the northern African-Arabian shelf margin (Michard 1976; Mattauer et al. 1977; Piqué et al. 1987; Jacobshagen et al. 1988a, b; Westaway 1990; Gomez et al. 2000). Effects were concentrated mainly along the Maghrebian Alpine belts, shaping the present architecture of the three major structural domains of Northwest Africa: the Rif-Tell fold-and-thrust belt in the north, the Atlas, and the Anti-Atlas Mountains in the south (Fig. 1). Elsewhere in the northern margin of the African plate, effects of the Alpine tectonic overprints were less intense, resulting in local preservation of large petroliferous basins such the Sirt Basin of Libya, western Egypt, and offshore Libya-Tunisia (Echikh 1998; Macgregor and Moddy 1998).

Late Carboniferous to Early Permian time coincides with the first stage of Pangean rifting and subsequent opening of the Permo-Tethyan seaway and formation of the east Mediterranean basins (Stampfli et al. 1991). Rifting and crustal stretching propagated westwards during the Triassic, associated with diffuse crustal extension (Andrieux et al. 1989; Favre and Stampfli 1992). This event was followed by more localized rifting in the High, Middle, and Saharan Atlas Mountains, and along the western margin of the platform during the Early Jurassic. Crustal separation followed in Middle Jurassic time with the opening of the Alpine Tethys and Central Atlantic oceans (Boote et al. 1998).

During early to middle Tertiary time, the western Tethys Ocean began to close in conjunction with inversion of the Atlas Basin in the early Eocene (Courbouleix et al. 1981; Laville 1981; Vially et al. 1994). This inversion was coeval with the early collision of the African and European plates (i.e., Kabylie Block; Macgregor 1998). Convergence with Eurasia accelerated during late Oligocene-Miocene time, culminating in folding and nappe emplacement in the Maghrebian belts of northern Morocco, Algeria, and Tunisia (Caire et al. 1953; Wildi 1983). Further reactivation and uplift of the inverted Atlas Rift basins occurred during the late Pliocene-Pleistocene, in response to dextral movement along the South Atlas Fault (Boote et al. 1998). The Mesozoic-Cenozoic sedimentary sequences consist of eustatically and tectonically controlled depositional cycles. Through time, progressive southwards shifts of the basin margins occurred in response to opening of the

Neotethys Ocean and to marine transgressions that resulted from global warming and associated sea level rise (Guiraud et al. 2005).

20 Alpine Maghrebian Domain

The Alpine Maghrebian domain comprises two contrasting belts: the Rif-Tell to the north and the Atlas System to the south (Fig. 1). The Rif-Tell belt is fundamentally different, being an asymmetric, Alpine-type, fold-and-thrust belt with numerous, well-mapped thrust faults and complex nappe structures (Loomis 1975; Leblanc and Olivier 1984; Morley 1987; Doblas and Oyarzun 1989; Ait Brahim and Chotin 1990; Leblanc 1990; Miranda et al. 1991). In contrast, the Atlas System is an intracontinental, largely symmetrical mountain belt that predominantly has brittle structures characterized by vertical movement (Beauchamp et al. 1996).

21 Atlas System

The Atlas System includes branches in the High and Middle Atlas Mountains in Morocco, the Saharan Atlas and Aurès Mountains in Algeria, and the Tunisian Atlas Mountains in Tunisia (Fig. 1). This system is an intracontinental fold-and-thrust belt that formed during the Cenozoic from moderate tectonic shortening of 15–24 % (Gomez et al. 1998; Teixell et al. 2003) by inversion of a previous transtensional Mesozoic rift system in the interior of the African plate (e.g., Beauchamp 1998; Piqué et al. 2002). The geodynamic evolution of the Atlas System involves the interplay of two major events (1) Triassic to Late Cretaceous pre-orogenic rifting of the Variscan crust, and subsequent filling of Mesozoic basins; and (2) Late Cretaceous to Holocene basin inversion, followed by shortening of the basement and cover units, and formation of syn-orogenic basins (Frizon de Lamotte et al. 2008). It should be stressed, however, that despite a high elevation culminating at 4165 m (Toubkal, Morocco), the lithosphere beneath the Atlas System is relatively thin (30–50 km) and abnormally hot (Seber et al. 1996; Ramdani 1998). Such features have been interpreted as the product of thermal erosion resulting from internal mantle dynamics (Teixell et al. 2005). The alkaline igneous rocks that occur throughout the Atlas System consitute the surface expression of this lithospheric thinning and subsequent buoyant upwelling of the mantle.

In the High and Middle Atlas Mountains, Triassic–Jurassic pull-apart basins (Laville and Piqué 1991) formed in conjunction with Pangean rifting and subsequent opening of the Central Atlantic Ocean. These basins contain red-bed clastics (conglomerate, sandstone, siltstone, mudstone) and widespread evaporites, tholeiitic basaltic flows related to the Central Atlantic Magmatic Province (CAMP), and carbonate strata up to 7 km thick. Paleogeographic reconstructions suggest the presence of a sinistral transform zone (Gibraltar-Newfoundland fault zone) that connected the Central Atlantic and western Tethys oceans during Jurassic to Early Cretaceous time (Michard et al. 2014). Sedimentation rates accelerated through the Jurassic as rifting continued with the breakup of Pangea, and with opening of the neo-Tethys and North Atlantic Ocean (Ziegler 1982). Rifting in the Atlas continued into Middle Jurassic time, followed by subsidence of the rift systems during the Late Jurassic–Early Cretaceous, a time span when a thick Cretaceous sedimentary sequence was deposited in sedimentary troughs. By the end of the Cretaceous, inversion and dextral shear of the Mesozoic rifts and formation of the Atlas system occurred in response to convergence of the African and European plates (Morabet et al. 1998). Resulting tectonic structures consist of thrust faults, strike-slip faults, and block uplifts (e.g., Schaer and Rodgers 1987; du Dresnay 1988; Fraissinet et al. 1988; Jacobshagen et al. 1988a, b; Medina 1988; Jacobshagen 1992; Giese and Jacobshagen 1992). The Paleogene-Neogene marine clastics and continental deposits, occurring above a regional unconformity, formed from syndeformational erosion of the existing mountain belt (Miocene-Pliocene molass deposits).

Two main magmatic episodes occurred during the Mesozoic evolution of the Atlas System. The

first of these formed during the Late Triassic to Early Liassic (200–195 Ma) coeval with opening of the Central Atlantic and Western Tethys oceans. Emplacement of the igneous bodies occurred during a relatively short interval straddling the Triassic-Jurassic boundary at 200 ± 1 Ma (Knight et al. 2004), and was temporally linked to a climatic and biotic crisis (Marzoli et al. 2004). During the second episode, alkaline basaltic lava flows and associated subvolcanic intrusive complexes were emplaced mostly in the Central High Atlas Mountains during two main periods at ca. 175–155 ± 5 Ma and 135–110 ± 5 Ma (e.g., Frizon de Lamotte 2008, and references therein). From a metallogenic standpoint, the Atlas System is a fertile reservoir because it is the exclusive host for all exploited Mississippi Valley-type Pb–Zn ± F ± Ba deposits of North Africa and for many other commodities.

22 Rif-Tell Belt

The roughly E-W-trending Rif-Tell belt constitutes the western segment of the Alpine Maghrebide belt (e.g., Durand-Delga and Fontboté 1980, and references therein). The Rif-Tell is a late Oligocene to Pleistocene Alpine belt that extends along the Mediterranean coast from Morocco in the west to Tunisia in the northeast (Fig. 1). Structurally, the Rif belt proper (i.e., Moroccan segment) consists of several nappes that are subdivided, from top to base, into three main domains (1) Alboran internal zones, (2) Maghrebian flysch nappes, and (3) external zones (Michard et al. 2005; Chalouane et al. 2008).

The Alboran internal zones comprise stacked, variably metamorphosed, Paleozoic to Triassic upper and lower nappes (Michard et al. 2006). The upper nappes (i.e., Ghomarides) consist of Paleozoic to Tertiary sedimentary rocks affected only by low-grade Variscan metamorphism (Chalouan and Michard 1990; Chalouane et al. 2008), whereas the lower nappes (i.e., Sebtides) experienced high-pressure/low-temperature metamorphism during the Oligocene-Miocene (Bouybaouène et al. 1995; Goffé et al. 1996; Agard et al. 1999), to low-pressure/high-temperature metamorphism during the Miocene (El Maz and Guiraud 2001; Negro et al. 2006; Gueydan et al. 2015). The most prominent metamorphosed rocks include highly foliated and metamorphosed Beni Bousera serpentinized garnet and spinel lherzolites (Kornprobst et al. 1990; Gueydan et al. 2015) and associated granulite, gneiss, and mica schist of the Lower Sebtides, together with metamorphic remnants of Permian-Triassic cover rocks. P-T reconstructions indicate that deformation of the lherzolites occurred during decompression from ca. 22 kbar and a temperature of 1050 °C to ca. 9–15 kbar at a temperature of ca. 800 °C (Afiri et al. 2011). Accordingly, exhumation of the Beni Bousera lherzolites would have occurred during the Oligo-Miocene. Uplift of these hot mantle rocks simultaneously induced high-temperature metamorphism in the overlying crustal units. The internal zones include also the so-called "Dorsale Calcaire" that originates from the Mesozoic-Cenozoic sedimentary cover of the Alboran Domain paleomargin (El Hatimi et al. 1991; El Kadiri et al. 1992).

The Maghrebian flysch nappes comprise remnants of Early Cretaceous to Early Miocene calcareous turbidites that grade upwards into arenaceous turbidites containing rare ophiolitic slivers (Durand-Delga et al. 2000). The resulting nappes root beneath the Alboran internal zones and overlie the external zones, excluding some back-thrusted units occurring in the western Betics, northern Rif, and Kabylias. The host basin opened during the Early Jurassic along a transcurrent boundary separating the African and European plates (Durand-Delga and Fontboté 1980; Bouillin et al. 1986; Puglisi 2009). Michard et al. (2007) interpreted the highly mylonitized contact at the base of the Alboran domain as representing the main suture zone of the Maghrebide orogen.

The external zones consist of a succession of Paleozoic to Paleogene, allochthonous, gravity-driven nappes that were thrust over para-autochthonous units. Subdivisions of these external zones include the intrarif, mesorif, and prerif zones (Suter 1980a, b), which are attributed to derivation from the North African paleomargin during Cenozoic collision of the internal

zones (Wildi 1983; Favre et al. 1991). More recently, Benzaggagh et al. (2013) and Michard et al. (2014) recognized within the external zones of the Central Rif the presence of Middle to Upper Jurassic ophiolite slivers, together with a tholeiitic gabbro basement and an oceanic-type cover sequence (ophicalcite, basalt-serpentinite breccias, marble, radiolarian chert). Collectively, these rocks define the 400-km-long Mesorif suture zone. Based on this finding, Michard et al. (2014) proposed that the Tethyan suture includes two branches, each being north and south of the intrarif continental allochthons. For more details on the paleogeographic evolution of the Rif belt, and specifically on each domain, the reader is referred to the syntheses of Michard et al. (2005, 2007) and Chelouan et al. (2008).

23 Cenozoic Basins and Related Tertiary to Quaternary Igneous Rocks

During the Cretaceous, Eocene, Oligocene, and Neogene, numerous basins of different style developed in different regions of North Africa. These basins reflect different stages of the opening of the Central, South, and Equatorial Atlantic Ocean coupled with evolution of the northern and southern Peri-Tethys platform areas, on both sides of the African/Arabian-Eurasian convergent plate boundary (Meulenkamp and Sissingh 2003). Many of these basins are of economic interest because of their high potential for hydrocarbons and metals.

In northwest Africa, the largest basins are developed along the central Atlantic continental margins of Morocco and Mauritania and include the Rharb and Pre-Rif basins, Doukkala Basin, Essaouira–Hana Basin, Tarfaya–Aaiun Basin, Dakhla–Laayoune–Tarfaya Basin, and the Mauritanian Basin that hosts the Chinguetti oil field (Davison 2005). Overall, basin infills consists of a Triassic red-bed rift sequence, followed by Early Jurassic salt, Jurassic to Early Cretaceous carbonate platform strata, and Cretaceous to Tertiary marine clastic successions (Davison 2005). In addition to these continental margin basins, two sets of Cretaceous-Tertiary plateaus are recognized in Morocco (Zouhri et al. 2008). The first encompasses the giant Late Cretaceous to early Eocene phosphorous Oulad Abdoun, Ganntour, Meskala, and Oued Eddahab-Bou Craa plateaus, whereas the second set comprises the Saharan cratonic 'Hamadas' and plateaus that consist of late Early Cretaceous to Neogene sediment. Similar basins of comparable age (i.e., Early Cretaceous-Tertiary) occur along the northern margin of the African plate in Algeria, Tunisia, Libya, and Egypt where some host significant resources of oil and natural gas. Examples include the Pelagian Basin in eastern Tunisia and northwestern Libya (Klett 2001), the giant Syrt Basin in north-central Libya with known reserves of 43.1 billion barrels of oil equivalent (36.7 billion barrels of oil, 37.7 trillion cubic feet of gas, 0.1 billion barrels of natural gas liquids), and the Nile Delta and Western Desert Basin in Egypt (Tawadros 2011). Elsewhere in North Africa, other petroliferous basins are the Chad and Niger Delta rift basins. Post-nappe Neogene sedimentary basins (Serravallian to Quaternary), some of which host significant mineral resources (Pb, Zn, Fe, and bentonite principally), occur in the Alpine Rif-Tell belt that extends from Morocco to Tunisia (Decrée et al. 2008a, b; Melki et al. 2011, and references therein).

During the Cenozoic to present (i.e., ≤ 30 Ma), most of the host rocks described above experienced widespread, anorogenic, bimodal, intra-plate igneous activity that formed distinct magmatic provinces (e.g., Maghrebian Africa, Hoggar-Tibesti, Al Haruj, Darfur, East African Rift, and Red Sea; Fig. 1) (Gourgaud and Vicent 2004; Duggen et al. 2005; Farahat et al. 2006; Lustrino and Wilson 2007; Cvetkovic et al. 2010; Keppie et al. 2011; Lucassen et al. 2013). The resulting volcanic rocks are part of the large Circum-Mediterranean Anorogenic Cenozoic Igneous province (CiMACI; Lustrino and Wilson 2007), whereas in northeast Africa the coeval igneous activity relates to formation of the East African Rift and the Red Sea (Chorowicz 2005; Lucassen et al. 2013). The igneous rocks are mostly effusive accompanied by minor pyroclastic deposits and high-level

intrusions. About 60 % are basic to intermediate in terms of SiO_2 content (SiO2 ~ 45–57 wt%), with the remainder represented by more differentiated (trachyte, phonolite, rhyolite) and ultrabasic (Lustrino and Wilson 2007) compositions. Very rare occurrences of carbonatite have been documented in Morocco (e.g., Ibhi et al. 2002; Wagner et al. 2003; Bouabdellah et al. 2010) and Libya (Conticelli et al. 1995). In Maghrebian Africa (i.e., Morocco, Algeria, Tunisia), there is a temporal magmatic evolution of two distinct types of igneous activity, characterized by different geochemical and petrographic signatures (El Bakkali et al. 1998; Coulon et al. 2002; Duggen et al. 2005). The first type is mainly Oligocene to Miocene in age, whereas the second is chiefly Pliocene to Recent. Conversely, intra-plate magmatism of northern Sudan and southern Egypt produced a diffuse spatial distribution (Lucassen et al. 2013), in which ages cluster in the Cretaceous–Tertiary, although older and younger volcanic rocks have been reported (Schandelmeier and Reynolds 1997; Wilson and Guiraud 1998).

Proposed geodynamic and petrological models have interpreted Cenozoic magmatism in northwest Africa as resulting from the collision between Africa and Europe that triggered linear delamination along pre-existing Pan-African mega-shears inducing rapid asthenospheric upwelling and partial melting (Liégeois et al. 2005, and references therein). Lustrino and Wilson (2007) invoked the involvement of recycled oceanic and continentally-derived crustal components into the ambient depleted sub-lithospheric mantle, which ultimately partially melted in response to (1) lithospheric extension; (2) continental collision and orogenic collapse; and (3) contemporaneous subduction, slab roll-back, and slab-window formation. More recently, Duggen et al. (2009) proposed that part of the western High Atlas Mountains was derived from the Canary Island plume with the magma migrating approximately 1500 km eastwards through a subcontinental lithosperic corridor, beneath the High Atlas to the western Mediterranean. Unlike the continental margin of northwest Africa, the genesis of the Cenozoic to Recent volcanism in northeast Africa is attributed to rifting centered on the Afar triple junction from which propagated the Red Sea, the Gulf of Aden, and the East African Rift System. Trace element geochemistry together with isotopic and geochronological constraints suggest that magmatism there resulted from interactions with lithospheric-derived melts and/or fluids triggered by thermal influence of one or more mantle plumes that played an active role in initiating the rifting process (Lin et al. 2005, and references therein).

24 Regional Metallogeny

24.1 Introduction

Lithotectonic terranes of North Africa are characterized by a diverse and complex metallogenic history reflecting polyphase geologic processes that operated through protracted periods due to the interaction of major tectonic plates since the Archean. The resulting mineral deposits, which formed in various geologic settings at different time periods from Archean to Quaternary, contain a variety of mineral commodities including gold, silver, cobalt, nickel, chromium, arsenic, copper, lead, zinc, iron, and many other elements.

Major deposit types present in North Africa are (1) orthomagmatic Cr–Ni-platinum group elements (PGE); (2) rare-metal granites and related rare-element pegmatites; (3) volcanic-hosted massive sulphide (VHMS); (4) sedimentary-exhalative (SEDEX); (5) orogenic and intrusion-related gold; (6) iron oxide–copper–gold (IOCG); (7) banded iron formation (BIF); (8) Mississippi Valley-type (MVT) lead–zinc; (9) sediment-hosted stratiform copper; (10) sediment-hosted U, Mn, and phosphate; (11) five-element veins containing nickel–cobalt–arsenic–silver–bismuth(–uranium); (12) epithermal gold–silver veins; (13) skarn and replacement tungsten, tin, and/or base-metals; (14) residual manganese, phosphate, salt, potash, bentonite, etc.); and (15) mechanically concentrated deposits (e.g., paleoplacer gold). The economically most

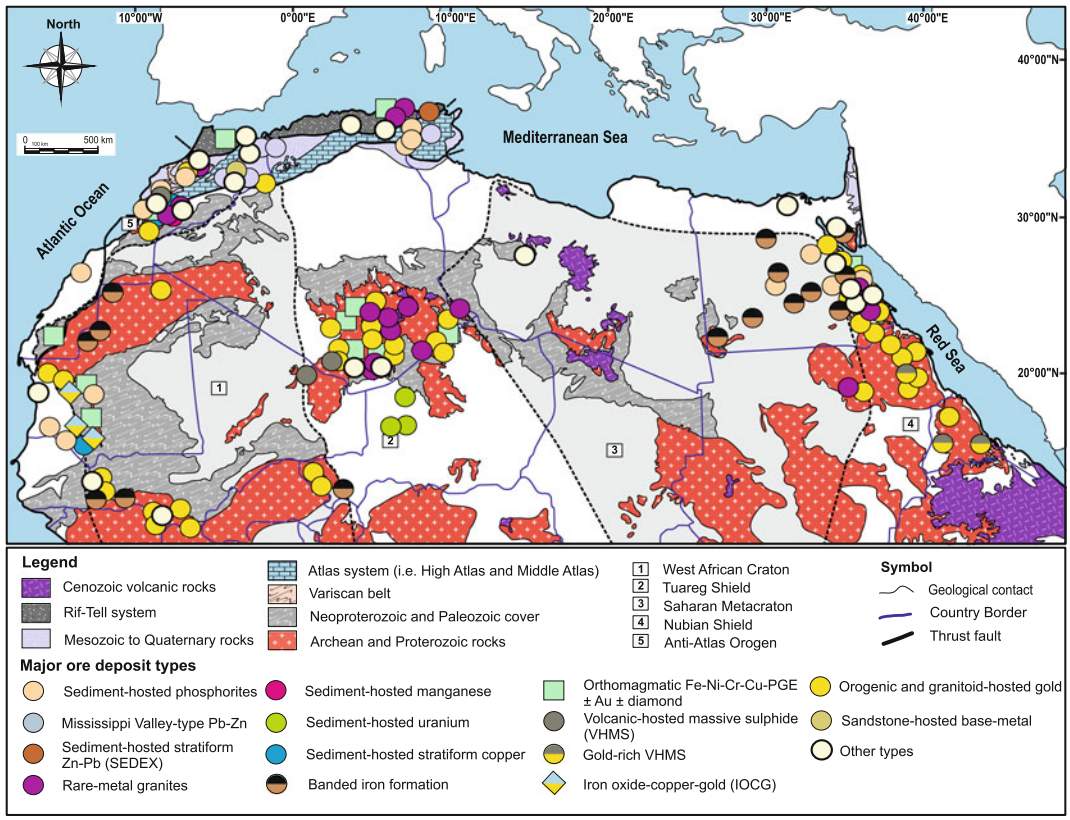

Fig. 9 Simplified metallogenic map showing spatial distributionof significant mineral deposits of North Africa with respect to host lithotectonic domain

significant North African ore deposits are shown in Figs. 9, 10 and 11 and listed in Table 1. For detailed information on the listed deposits and many others, the reader is referred to Tables 1A–1E given in the online appendix. Several of these are within the category of world-class deposits in terms of size, grade, and ore production. Noteworthy examples include the giant phosphate deposits and Imiter silver deposit of Morocco, Precambrian BIF deposits in Mauritania, orogenic gold deposits in Mali and Mauritania, uranium deposits in Niger, and MVT lead–zinc deposits in the High Atlas system of Morocco and Tunisia.

Resources and potential for gold, diamonds, strategic metals, and other commodities are significant within Precambrian cratonic terranes of most North African countries. The presence of these resources and potential also makes the entire region prospective for undiscovered deposits of precious metals, and major new discoveries in the future are likely. Indeed, the process of craton formation during the Birimian and Eburnean orogenies and subsequent later remobilization during Pan-African and Variscan time periods resulted in the formation of gold deposits related to granitic intrusions as well as to those related to shear zones developed within and/or adjacent to ultramafic intrusions (e.g., orogenic gold in suture zones). Significant orogenic gold deposits occur in Mali, Algeria, Mauritania, Morocco, and Egypt and a number of epithermal gold–silver deposits are in Morocco and other countries (Figs. 9 and 10). The amalgamated Neoproterozoic terranes of the ANS contain major VHMS deposits, some of which have significant gold concentrations. Such gold enrichment led Trench and Taylor (2015) to qualify the western ANS as a rapidly emerging,

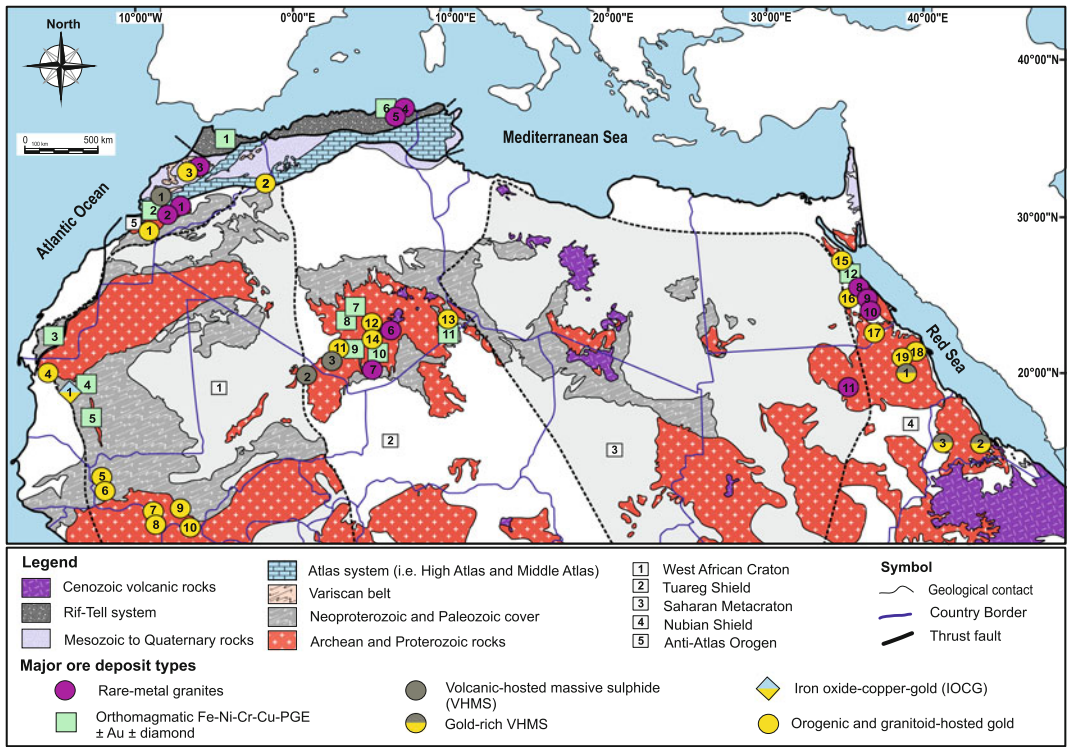

Fig. 10 Simplified metallogenic map of North Africa showing spatial distribution of major magmatic and hydrothermal ore deposits with respect to hostlithotectonic domain. Due to lack of geological and more importantly production data, only large documented deposits are labeled. Number deposit codes are as follows: Orthomagmatic Fe-Ni-Cr-Cu-PGE ± Au ± diamond deposits: *1*. Beni Bousera *2*. Bou Azzer *3*. Haraicha *4*. Guelb El Azib *5*. Gouerate i. Collo *7*. Tihailioune *8*. Aderniba *9*. In Tedeini *10*. Laouni *11*. Timoletine *12*. Fawakhir; Rare-metal granites: *1*. Tazenakht *2*. Angarf *3*. Zrari *4*. Edough *5*. Filfila *6*. Alemeda *7*. Tin-Amezi *8*. Abu Dabbab *9*. Nuweibi-Igla *10*. Um Desi *11*. Bayuda; VHMS deposits: *1*. Jebilt-Guemassa *2*. Tassalit *3*. Tilemsi; Gold-rich deposits: VHMS: *1*. Hassai *2*. Emba-Derho *3*. Bisha; Orogenic gold deposits: *1*. Tagragra-Akka *2*. Tamellalt *3*. Tighza *4*. Tasiast 5. Yatela-Sadiola *6*. Loulou-Yalea-Tabakotio-Segala-Gounkoto-Fekola *7*. Komana *8*. Kalama *9*. Morila *10*. Syama *11*. Amesmesa-Tirets *12*. Tin n'Felki *13*. Tirine *14*. Silet *15*. Fawakhir-Elsid *16*. Dungash *17*. Um Egat *18*. Gebeit *19*. Ekwan-Shigriyay-Abir Katib; IOCG deposits: *1*. Guelb Moghrein

high-impact frontier gold terrane, which in the last two decades has had discoveries of >45 Moz gold equivalent.

Periods of magmatic activity that followed peak phases of the main orogenies (i.e., Late Eburnean, Late Neoproterozoic, Late Variscan, and Late Neogene) produced large granitoid intrusions and related pegmatites to which many tin, tungsten, niobium, REE, columbite-group minerals, and Ta–Nb oxide deposits are associated. The illustrative example of this category is the Ta–Nb–Sn province of Egypt (Melcher et al. 2015).

Small- to medium-sized tin and tungsten lode and placer deposits are abundant in Algeria, Morocco, and Egypt. No economic orthomagmatic deposit is known in the region, although several prospects of chromium, nickel, and REE are documented. The Saharan platform that hosts the vast petroleum and natural gas resources of North Africa (i.e., giant Sirt Basin) together with the Mesozoic to Cenozoic basins extending from Morocco to Egypt are also well endowed with giant phosphate deposits that define the Tethyan phosphate province of North Africa (Lucas and Prévôt-Lucas 1995). Similarly,

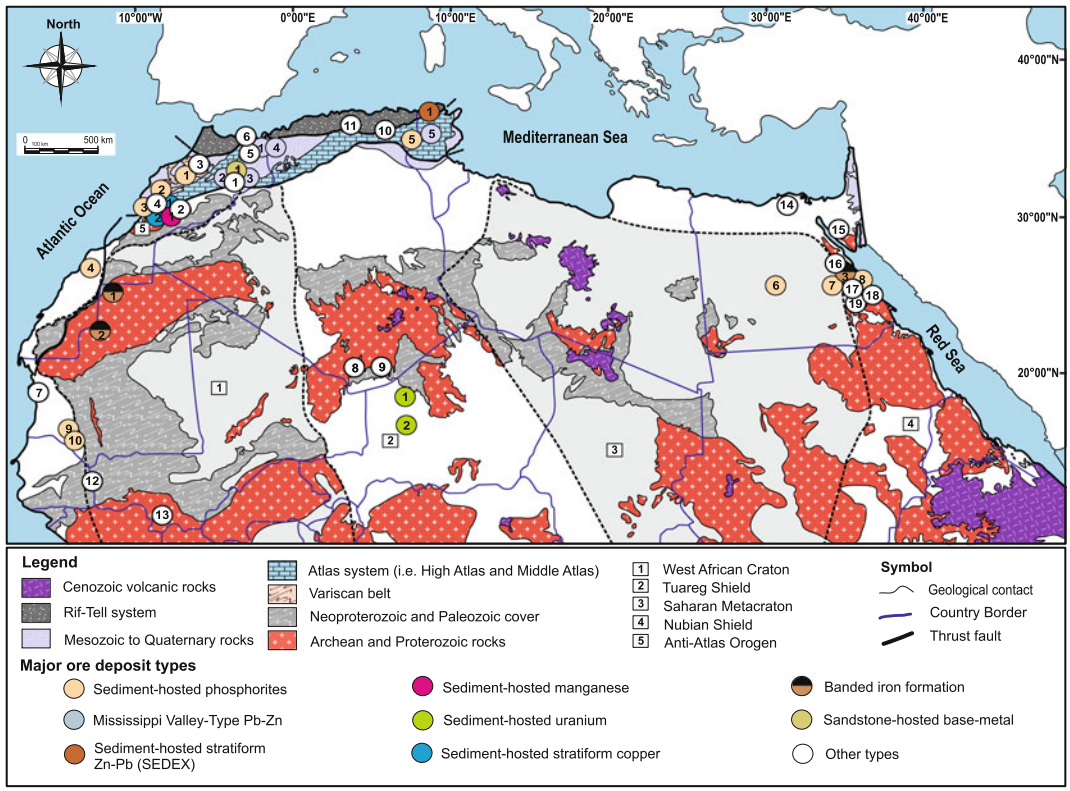

Fig. 11 Simplified metallogenic map of North Africa showing location of major sediment-hosted and miscellaneous deposits with respect to host lithotectonic domain. Sediment-hosted phosphorites: *1*. Oulad Abdoun *2*. Ganntour *3*. Meskala *4*. Bou Craa *5*. Gafsa *6*. Abu Tartur-Maghrabi-Liffiya *7*. Sibaiya *8*. Duwi *9*. Bofal *10*. Loubbroïra; Mississippi Valley-Type deposits: *1*. Touissit-Bou Beker *2*. Upper Moulouya *3*. Jebel Bou Dahar *4*. El Abed *5*. Bou Grine; Sediment-hosted stratiform Zn–Pb (SEDEX) deposits: *1*. Nefza; Sediment-hosted manganese deposits: *1*. Imini; Sediment-hosted uranium deposits: *1*. Akouta-Arlit-Imouraren *2*. Azelik; Sediment-hosted stratiform copper deposits: *1*. Jbel Laassel-Bleida-Tizert-Jebel N'Zourk-Amadouz *2*. Tazalaght; Banded iron formation deposits: *1*. Ijil *2*. Tiris *3*. Hadrabia-Abu Merwat-Gebel Semna-Diwan-Wadi Kareim-Wadi el Dabbah-Um Ghamis-Gebel el Hadid-El emra- Umum Nar-Wadi Hammama-Umm Anab; Sandstone-hosted lead deposits: *1*. Zeida; Other deposit types (see text): *1*. Aouli *2*. Bouskour-Bou Azzer *3*. El Hammam-El Karit-Achemmach *4*. Assif El Mal-Azegour *5*. Sidi Lahcen *6*. Gourougou-Tidiennit *7*. Jreida-Lemsid *8*. Amzi-Ebelekan *9*. Rechla-Nahda *10*. Guerioun *11*. Taourirt *12*. Kenieba *13*. Bougouni *14*. Nile Delta *15*. Sinai *16*. El Erediya-El Missikat *17*. Mueilha-Abu Dabbab *18*. Nuweibi *19*. Igla

these unmetamorphosed sedimentary terranes host the world-class MVT lead–zinc deposits of North Africa (i.e., Bouabdellah et al. this volume) and the world-class Imini manganese deposit in southern Morocco.

Many types of industrial mineral deposits are also present throughout much of the region including building stones, aggregates (sand and gravel), limestone, salt, barite, and a number of semi-precious gem deposits, as well as other industrial mineral deposits such as bentonite, perlite, andalusite, and mica. Marine and non-marine (lacustrine) salt and potash deposits are found throughout the length of the Red Sea coast of Egypt and Sudan, and also occur in parts of Morocco, Algeria, Tunisia, Mauritania, Libya, Niger, and Chad. These salt and potash deposits form thick bedded accumulations within Triassic, Cretaceous, and Messinian evaporite-bearing sedimentary successions. Libya also has relatively large deposits of gypsum. Heavy-mineral beach sand deposits rich in titanium, zirconium, and rare

Table 1 Major mineral deposits of North Africa*

Country	Deposit/orebody	Metal assemblage	Deposit type	Production ± reserves	Grade
Morocco	Zgounder	Ag–Hg	Epithermal	>500 kt Ag	300 g/t
	Bou Azzer	Co–Ni–Fe–As (±Au ±Ag)	Five-element vein	Annual production: 2,500 t Co, 10,000 t As, 300 t Ni, 250 kg Au	~1 % Co, 1 % Ni, 3–42 g/t Ag, and 3–4 g/t Au
	Imini	Mn	Sediment- and karst-hosted	>8 Mt	>72 % MnO_2
	Imiter	Ag–Hg	Epithermal? Five-element vein?	250 t Ag/year (2010)	300 g/t Ag
	Bouskour	Cu–Ag	Granitoid-related, epithermal?	>53 Mt	0.8 % Cu, 9 g/t Ag
	Kettara	Fe–Cu	Volcanogenic massive sulphide	>20 Mt	0.6 % Cu
	El Hammam	F	Granite-related, epithermal?	>10 Mt	98 % CaF_2
	Bou Beker	Pb–Zn ± Cu	Mississippi Valley-type	18 Mt	4 % Zn, 3.5 % Pb
	Ouixane	Fe	Skarn	>65 Mt	>50 % Fe
	Oulad Abdoun	Phosphate	Sedimentary	Resources 28 Gt	>35.7 % P_2O_5
	Ganntour	Phosphate	Sedimentary	Resources 15 Gt	>35.7 % P_2O_5
	Oued Eddahab-Bou Craa	Phosphate	Sedimentary	2 Mt/year. Resources: 1.6 Gt	> 35.7 % P_2O_5
	Glibat Lafhouda	Nb–Ta-REE-U	Magmatic-hydrothermal	49 Mt	0.4 % Nb_2O_5, 265 ppm Ta_2O_5, 508 ppm U_3O_8, 0.2 % REE, 35 % Fe
	Aghracha	Fe–U-REE	Magmatic-hydrothermal	50–70 Mt	57 % Fe, 13 % TiO_2, 0.6–0.8 % V, ~1000 ppm U_3O_8, 4.6–10.1 % LREEE
Mauritania	Guelb Moghrein	Cu–Au	Iron oxide-copper-gold	Reserves 31.3 Mt	0.92 % Cu, 0.69 g/t Au
	Tasiast	Au	Orogenic gold	Reserves 9.644 Moz, Resources 4.706 Moz , Inferred 0.664 Moz	Reserves 1.71 g/t Au , Resources (M & I) 0.84 g/t Au, Inferred 1.46 g/t Au
	Lebtheinia	Fe	Algoma-type	2.742 Gt total resources	30.7–32.4 % Fe
	Guelb El Aouj East	Fe	Algoma-type	755 Mt reserves, 1.87 Gt resources	35 % Fe, 36 % Fe
	Aquelt Assfaya	U	calcrete-type	68.7 Mt inferred	330 ppm U_3O_8
	A238	U	Granite-hosted vein/shear	42.8 Mt inferred	233 ppm U_3O_8

(continued)

Table 1 (continued)

Country	Deposit/orebody	Metal assemblage	Deposit type	Production ± reserves	Grade
Algeria	Tala Hamza	Pb–Zn	Volcanogenic massive sulphide	68.6 Mt	4.6 % Zn (cut-off 2.5%); 1.2 % Pb
	El Abed	Zn–Pb ± Cu	Mississippi Valley-type	>30 Mt	4.5 % Zn, 1% Pb
	Djebel Onk	Phosphate	Sedimentary	500 Mt	24.3–27.5 % P_2O_5
	Gara Djebilet	Fe	Oolitic ironstone	3.5 Gt	57 % Fe
	Amesmessa	Au	Orogenic gold	3.38 Mt	18 g/t Au
	In Abeggui	Au	Orogenic gold	8 Mt	3.59 g/t Au
Egypt	Abu Dabab	Ta–Sn	Magmatic	~48 Mt	243 g/t Ta_2O_5, 0.11 % SnO_2
	Nuweibi	Ta	Magmatic	98 Mt	146 g/t Ta_2O_5
	Sukari	Au	Hydrothermal	18.8 Mt	2.14 g/t
	Duwi-Abu Tartur	Phosphate	Sedimentary	Resources >3 Gt	20–28 % P_2O_5
Tunisia	Jebel Hallouf-Sidi Bou Aouan	Pb–Zn (–As–Sb)	Polymetallic Mississippi Valley-type	~565,000 t Pb-~82,000 t Zn	■
	Bou Grine	Pb–Zn	Mississippi Valley-type	87,000 t Pb-640,000 t Zn	■
	Sra Ouertane	Phosphate	Sedimentary	2.5–3.0 Gt	14 % P_2O_5
	Gafsa	Phosphate	Sedimentary	Resources 1.1–2.5 Gt	20–28 % P_2O_5
Niger	Arlit-Akouta	U	Sedimentary	2014 Production: 2331 t U	■

*Detailed information on the listed deposits and many others is available in online Tables 1A–1E
■Not available

earth elements occur along the Atlantic coast of Morocco, being recovered from modern eluvial and alluvial placer deposits.

25 Mineral Deposit Systems and Their Spatial Distribution

25.1 Orthomagmatic Fe–Ni–Cr–Cu–PGE ± Au ± Diamond and Ophiolite-Hosted Cr Deposits

Orthomagmatic Fe–Ni–Cu–Cr–PGE ore deposits that also may contain recoverable amounts of gold, diamond, titanium, and/or vanadium (e.g., U.S. Geological Survey 2013) are typically confined to large layered mafic-ultramafic intrusions or lava flows. Their genesis is related to (1) early crystallization of the host mafic-ultramafic rocks, resulting in massive layered and/or disseminated mineralization; (2) later crystallization of the host rock units giving rise to stratabound ore; and (3) fractional crystallization of thick flows and sills resulting in the development of relatively PGE-rich stratiform layers.

In North Africa, exploration and historical mining of this class of ore deposit has focused entirely on near-surface, chromite-bearing occurrences associated with (1) fragments of the Neoproterozoic Pan-African dismembered ophiolitic complexes of the Eastern Desert of Egypt and

northeast Sudan, and with those in the Bou Azzer district of the central Anti-Atlas orogen of Morocco; and (2) the Alpine Beni Bousera and Collo massifs of the internal zones of the Alpine Betic-Rif orogen of northern Morocco and adjacent Algeria (Fig. 10). Recently, several PGM-bearing chromitite occurrences were recognized in Mauritania, being associated either with the Archean ultramafic–mafic–anorthositic layered complex of Guelb el Azib (WAC; Berger et al. 2013) or the Pan-African serpentinites of the Agane and Gouérarate areas within the axial zone of the Mauritanides Belt (Ould Moctar et al. 2014) (Fig. 10). However, at the present time, none of these layered mafic-ultramafic igneous bodies and associated ophiolitic complexes hosts economic orthomagmatic sulphide or oxide occurrences.

The main Egyptian and Sudanese chromite-PGE deposits are concentrated in the central and southern parts of the Eastern Desert of Egypt and northeast Sudan (Fig. 10). These deposits have been extensively investigated by Amstutz et al. (1984), Khudeir et al. (1992), El Haddad (1996), Ahmed (2007, 2013), Ahmed et al. (2001, 2006, 2012a, b), Abd El-Rahman et al. (2009), El-Taher (2010), and Hamdy and Lebda (2011). Numerous irregularly distributed ophiolites and ophiolitic mélange units have been reported from these areas in both countries, with the most fertile occurrences being located mainly south of latitude 26° N (Ahmed 2007). Overall, the host rocks consist of a succession of Neoproterozoic, variably serpentinized, harzburgite-dunite-chromitite bodies (Ahmed 2013). Serpentinites and talc-carbonate rocks predominate in the mantle sections of the ophiolite and ophiolitic mélange, either as matrix or variably sized blocks, having been derived from harzburgite and subordinate dunite (Ahmed 2007). Geodynamic reconstructions indicate that these ophiolitic complexes, and by inference those of the northern part of the ANS, were generated in supra-subduction zone tectonic settings by forearc seafloor spreading, during subduction initiation associated with closing of the Neoproterozoic Mozambique Ocean.

Chromite mineralization produced either podiform bodies of variable dimensions or, to a lesser extent, veinlets and disseminations within the dismembered ophiolitic complexes. Podiform chromitites account for most of the high-grade orebodies and form irregularly shaped lenses, several centimeters to 50 m in diameter, confined to the serpentinized envelopes of harzburgite and dunite; pyroxenites are virtually devoid of chromite concentrations (El-Taher 2010). A few small chromitite lenses (up to 3 m × 5 m) have been reported within talc-carbonate zones of the serpentinized ultramafic rocks (Ahmed 2013). In addition to chromite, subordinate amounts of PGM, sulpharsenides and arsenides, and base-metal sulphides occur as fine inclusions either within or along cracks of chromian spinel, or as large aggregates within the interstitial silicate matrix among chromian spinel grains, as documented by El Haddad (1996) and Ahmed et al. (2006). Geochemically, the Egyptian chromitites show a wide compositional range from high-Al to high-Cr spinels (Ahmed et al. 2001, and references therein), with total PGE contents ranging from 80 to 320 ppb (Ahmed 2007, 2013). All of the chromitite pods show enrichment in the Ir-subgroup (IPGEs = Os, Ir, Ru) relative to the Pd-subgroup (PPGEs = Rh, Pt, Pd), and display steep, negatively-sloped, chondrite-normalized PGE patterns like those of most ophiolitic chromitites worldwide (e.g., Leblanc 1991; Zhou et al. 1998).

In Morocco, orthomagmatic Cr–Ni and associated PGE, sulpharsenide, and arsenide ± gold ± diamond orebodies are spatially and temporally related to ultramafic fragments of the Neoproterozoic Bou Azzer dismembered ophiolitic complex of the central Anti-Atlas orogen, and to the Alpine Beni Bousera high-temperature peridotite intrusion of the Rif-Tell orogenic belt (Fig. 10). Both of these mafic-ultramafic massifs have been extensively studied (Pearson et al. 1993; Pearson and Nowell 2004; Piña et al. 2013), not only due to their promising Ni–Cr and associated PGE mineralization but more importantly because of a high potential for gold and more intriguingly diamond occurrences, expressed as a graphite-sulphide overprint that is an atypical feature of these mafic-ultramafic intrusions (Crespo et al. 2006, and references therein).

Petrographically, the Beni Bousera zoned intrusion (~70 km^2) consists predominantly of

spinel lherzolite (up to 95 % by volume) and to a lesser extent garnet lherzolite, harzburgite, and minor dunite, with subordinate sheeted dikes of pyroxenite, all of which intrude Paleozoic to Triassic metasedimentary rocks of the Upper Sebtide Formation (Saddiqi et al. 1988). A swarm of ENE- to EW-trending, anatectic cordierite-andalusite leucogranite dikes cuts the main units of the Beni Bousera intrusion. Surrounding metamorphic host rocks, made mostly of high-grade, migmatitic, graphite-sillimanite-garnet gneiss (kinzigite) and schist, which are part of a lower crustal assemblage exposed with peridotite (Pearson and Nowell 2004), display a decreasing metamorphic grade outward from the contact with the intrusion. Proposed geodynamic and petrogenetic models suggest that the Beni Bousera intrusion represents a portion of old (Proterozoic) subcontinental lithospheric mantle that was emplaced tectonically, at high temperature, within the lower crust during the Alpine orogeny from 22 to 20 Ma (Zindler et al. 1983; Tubia and Cuevas 1986; Pearson and Nowell 2004). Lu–Hf geochronology indicates a mean age of emplacement at ca. 25.0 ± 0.9 Ma, consistent with a Sm–Nd age of 23.6 ± 4.3 Ma (Pearson and Nowell 2004). In contrast, K–Ar and $^{39}Ar/^{40}Ar$ ages are slightly younger, clustering around 21 Ma (Pearson et al. 1993). These age discrepancies have been attributed to emplacement of the Beni Bousera spinel lherzolite within a time span of 4 ± 2 m.y. Based on these age constraints, Blichert-Toft et al. (1999) estimated a fast decompression rate of the rising peridotite, on the order of 10 cm $year^{-1}$, consistent with a nearly adiabatic ascent. Moreover, the clinopyroxene-garnet assemblage locally contains graphitized diamonds (Pearson et al. 1989; Pearson and Nixon 1996; Ruiz Cruz et al. 2011), thus indicating high temperatures in the range of 1200–1350 °C and crystallization pressures of at least 20 Kb (Kornprobst et al. 1990), within the diamond stability field. It is noteworthy that the graphitized diamonds may represent 10 to as much as 15 vol% of the host rocks and reach up to 20 mm in size (Pearson et al. 1989; Pearson and Nixon 1996; Ruiz Cruz et al. 2011). The original diamonds may have crystallized from subducted, ^{13}C-depleted, crustally derived carbon at a crystallization pressure above 45 Kb (Pearson et al. 1993).

Field and textural relationships indicate that Cr–Ni and associated PGM, arsenide- sulpharsenide ± gold, and diamond mineralization formed during three main stages. The resulting mineralized structures consist of veins and stockworks, intergranular disseminations, and banded ores with alternating chromite-Ni arsenides and pyroxenite (Gervilla and Leblanc 1990; Gervilla et al. 2002; Crespo et al. 2006; and present study). Early stages I and II consist of an unusual chromite (60–90 vol%)-niccolite (5–40 vol%) assemblage composed of massive aggregates of polygonal to rounded chromite grains accompanied by intergranular and fracture-filling Ni-arsenides with lesser orthopyroxene, clinopyroxene, and/or cordierite. Later stage III consists mainly of a sulphide-graphite assemblage composed of Fe–Ni–Cu sulphides (i.e., pyrrhotite, pentlandite, chalcopyrite, cubanite) with variable amounts of Fe-chromite having high Zn and V contents, maucherite, violarite, niccolite, cobaltite–gersdorffite, westerveldite, and graphite (Gervilla and Leblanc 1990; Gervilla et al. 1996; Piña et al. 2013), accompanied by plagioclase and phlogopite. High contents of gold (3–35 ppm) and average PGE up to 2000 ppb, together with the presence of discrete inclusions of Au, Au–Cu, and Au–Bi–Te, are documented within the Cr–Ni ore.

Chromitite orebodies and associated PGE mineralization are also documented within the Neoproterozoic ultramafic section of the Bou Azzer ophiolitic complex (Leblanc 1981; El Ghorfi et al. 2008; Ahmed et al. 2005, 2009). Serpentinized harzburgite with subordinate dunite are the dominant host rocks accounting for about 40 vol% of the total exposed part of the complex (Bodinier et al. 1984). Wehrlite containing a notable amount of amphibole accompanied by olivine and clinopyroxene as primary phases occurs as late-stage intrusions (Ahmed et al. 2005). Geochemical data indicate that the chromitites formed either by high-degree partial melting of primitive mantle, or by melting of

previously depleted mantle peridotite (Ahmed et al. 2009). Thorough descriptions of the geological environment of the Bou Azzer ophiolite are available in many papers, including the following to which the reader is referred for more details: Leblanc (1981), Saquaque et al. (1989), and Bouabdellah et al. (this volume).

The chromitite orebodies and associated PGE mineralization occur throughout an area of $\sim 10 \times 4$ km from Aït Ahmane in the east to Ightem in the west (El Ghorfi et al. 2008). Overall, 100,000 t of podiform chromite ore at an average grade >45 % Cr_2O_3 was mined by "Compagnie de Tinfout-Tiranimine" (CTT) between 1990 and 1998. Recent exploration and reevaluation of the chromite resources in the district by Managemgroup, the owner of the Bou Azzer deposits, has delineated more than 50 significant new chromitite pods. The shape and size of the orebodies are variable, with lenses generally ranging from <1 up to 20 m long and as much as 5 m thick, paralleling the N110°E orientation of the magmatic layering. Locally present are serpentinized harburgite- and dunite-hosted disseminations of euhedral to subhedral chromite grains, locally amounting to 4 vol %, together with massive chromitite that contains 30–80 vol% chromite (Ahmed et al. 2005, 2009; El Ghorfi et al. 2008; Maacha et al. 2011a).

Mineralogical residence of the PGE within the chromitites is chiefly in fine inclusions of Rh-bearing laurite occurring within spinel or the silicate matrix. Bulk PGE contents are relatively uniform, ranging from 182 to 219 ppb, with predominance of IPGE (Os ± Ir ± Ru), variable Rh, and low Pt and Pd (El Ghorfi et al. 2008). These geochemical characteristics fit within the global diagnostic criteria of ophiolitic chromitites poor in sulphides (Ahmed 2013), and may be comparable to the Neoproterozoic ophiolitic complexes in the Eastern Desert of Egypt described above (Ahmed 2007, 2013). Moreover, Ni–Co–Fe sulphide, arsenide, and sulpharsenide orebodies devoid of PGE, which form the bulk of the economically exploited vein mineralization in the Bou Azzer district (Bouabdellah et al. this volume), are spatially associated with alterated chromite grains, hence their genesis is linked to a late hydrothermal event that overprinted podiform chromite mineralization. Uneconomic occurrences of podiform chromitite and associated PGM also have been documented within basement rocks of the Moroccan Western Sahara (Mauritanides Belt) in the form of small lenses occurring within undated serpentinites (Lehbib et al. 2008).

Orthomagmatic chromite and associated PGM, sulpharsenide, and arsenide mineralization occurs in Algeria within two contrasting domains (1) the Pan-African Hoggar massif of the Tuareg Shield to the south, which was recognized by the late 1950s as "a platinum province" (Meindre 1959); and (2) the Collo massif of the West Mediterranean Rif-Tell Alpine belt to the north (Fig. 10). Within the Hogger Pan-African mafic–ultramafic complexes, all in various stages of serpentinization, podiform and subordinate stratiform chromite mineralization (chromitite layers) are spatially and genetically related either to serpentinite occurrences at the Aderniba, Tihailioune, and Timoletine prospects, or more importantly to the zoned ultramafic intrusive complexes of In Tedeini and Laouni that were emplaced between 600 and 520 Ma (Cottin et al. 1998; Augé et al. 2012). Within the serpentinites, chromite and associated PGM and base-metal sulphide mineralization occur mainly as podiform bodies ca. 250 m long and 30–50 m wide, typical of ophiolite-type chromitites worldwide (Augé et al. 2012). Subordinate amounts of fine- to medium-grained disseminated chromite and layered chromitites are also present. The layered mafic-ultramafic intrusions of In Tedeini and Laouni, which comprise wehrlite, olivine gabbronorite, and troctolite units, also contain disseminated Ni–Cu sulphides of potential economic interest (Augé et al. 2012).

Further north in the internal zones of the Rif-Tell Alpine belt, within the Petite Kabylie of northern Algeria, is the Alpine Collo ultramafic massif (20 km^2) that contains about 25 podiform chromitite bodies (Temagoult 1989; Leblanc and Temagoult 1989) (Fig. 10). These ultramafic rocks consist of strongly sheared and serpentinized plagioclase lherzolite with minor harzburgite and dunite, together with thin (2–3 mm) layers of websterite and orthopyroxenite,

cut by subvertical gabbro dikes. High-P granulite-grade metamorphism resulted in the development of K-feldspar-garnet gneiss (i.e., kinzigite). From a geodynamic view, the Collo massif has been interpreted as an atypical, high-temperature lherzolite that represents a mantle intrusion emplaced in a transition zone from continental to oceanic rift (Leblanc and Temagoult 1989). The podiform chromitite bodies are elongate and aligned parallel to foliation and lineation of the plagioclase-lherzolite host rocks. Locally present are disseminated and layered (2–3 cm) chromite ores (Leblanc and Temagoult 1989). The chromite is massive with a cataclastic texture and contains diopside, olivine, pargasite, and Na-phlogopite. Geochemically, the Collo chromitites display high Ru, Os, and Ir contents and chondrite-normalized PGE patterns with a strong negative slope from Ru to Pt (Leblanc and Temagoult 1989) typical of chromitite pods found in ophiolite complexes worldwide (e.g., Ahmed et al. 2006).

In addition to Egypt, Morocco, and Tunisia, orthomagmatic chromite and associated PGM, arsenide, and sulpharsenide mineralization occurs in Mauritania within the WAC and along the axial zone of the Mauritanides Belt (Fig. 10). The most significant occurrences include the Archean PGM-bearing chromitites of the Guelb el Azib layered complex in WAC (Berger et al. 2013) and chromite-bearing serpentinites of the Agane and Gouérarate areas of the Mauritanides Belt (Ould Moctar et al. 2014).

The Archean Guelb el Azib ultramafic–mafic–anorthosite layered complex of the WAC consists of amphibolite- to granulite-facies serpentinized ultramafic rocks. These include ultramafic cumulates, chromitite, layered gabbro, leucogabbro, and anorthosite, all of which were emplaced within a 3.5–2.9 Ga TTG gneiss terranes. Chromite mineralization, predominantly of podiform type although locally in layered ore, occurs as NE-trending, massive to brecciated Fe-rich chromitite orebodies several meters wide and tens of meters long, hosted in serpentinite, ultramafic cumulates, mafic rocks (coarse- and fine-grained amphibolite), and anorthosite layers (Barrère 1967; Berger et al. 2013); these features are typical of Archean ultramafic–mafic–anorthosite complexes worldwide (e.g., Rollinson et al. 2010). PGM have only been observed in massive and layered chromitites where laurite (RuS_2), as the most abundant PGM, forms small (<5 mm, mostly 2–3 mm) euhedral inclusions within the cores and rims of chromite grains. In this regard, three phases of PGE mineralization have been recognized (Berger et al. 2013): (1) early igneous crystallization of laurite, (2) late magmatic IPGE sulpharsenides (irarsite–hollingworthite), and (3) hydrothermal Pt–Pd mineralization typified by sperrylite and rustenburgite.

Minor podiform chromite mineralization has also been documented within serpentinized parts of the ultramafic-mafic section of the Agane and Gouérarate ophiolites (Ould Moctar et al. 2014). These ophiolites are within the suture that characterizes the axial zone of the Pan-African Mauritanides Belt (Pitfield et al. 2004).

26 Rare-Metal Granites and Related Rare-Element Granitic Pegmatites

Granitoid plutons and related pegmatite-hosted Ta–Nb–Sn ± REE mineralization are widely distributed within lithotectonic terranes of North Africa. These intrusions occur as pre-, syn-, and post-kinematic bodies of Pan-African, late Hercynian, and late Neogene age (Melcher et al. 2015). However, it is in the Eastern Desert of Egypt within the ANS, and to a lesser extent in Algeria and Morocco (Fig. 10), where the largest and economic Ta–Nb–Sn ± REE deposits are known (Melcher et al. 2015; Marignac et al. this volume).

Examples in Egypt include the Abu Dabbab and Nuweibi deposits that contain resources of 44.5 Mt at 250 g/t Ta_2O_5 and 0.09 % Sn, and 98 Mt at 143 g/t Ta_2O_5 and 95 g/t Nb_2O_5, respectively (Gippsland Limited 2013; Melcher et al. 2015) (Fig. 10). Other deposits include Igla (Sn–W–Be) and Homr Akarem (Mo–Sn–Bi–F) (Sillitoe 1979). Collectively, these Pan-African, highly evolved, peraluminous rare-metal granites are the oldest known in orogenic belts (Tkachev

2011), having been emplaced along late-orogenic structures into juvenile Neoproterozoic rocks (Helba et al. 1997; Sharara 2000; El-Sharkawy 2001; Küster 2009; Ali et al. 2012). Recent geochronological determinations indicate that the Ta–Nb–Sn ± REE mineralization in the peraluminous rare-metal granites is associated with a post-accretionary magmatic phase that ranges in age from 610 Ma in the north to 530 Ma in the south (Küster 2009; Melcher et al. 2015, and references therein).

The Abu Dabbab and Nuweibi deposits occur either as fine-grained Ta–Nb–Sn ± REE-bearing disseminations within hydrothermally albitized and greisenized peraluminous granitic cupolas (Sharara 2000; El-Sharkawy 2001) and adjacent pegmatitic bodies, or as massive fillings of quartz veins and stockworks. U–Pb dating of tantalite from the Nuweibi deposit yields an isochron age of 550 Ma, suggesting Pan-African emplacement for the Ta–Nb–Sn ± REE mineralization. However, U–Pb age estimates on cassiterite from the Abu Dabbab, Nuweibi, and Igla granites are older, at 685–616 Ma (Ali et al. 2012; Melcher et al. 2015). These age constraints indicate that the mineralizing fluids are related to a late magmatic event. In addition to the economic Abu Dabbab and Nuweibi peraluminous granite-hosted deposits, numerous rare-metal pegmatite occurrences are known in the southern Eastern Desert of Egypt. The pegmatites are hosted by Neoproterozoic metasedimentary rocks, and form steeply dipping bodies from 50 to 750 m long and up to 150 m wide (Saleh 2007). Among these, the Bayuda and more importantly the Um Desi pegmatite occurrences seem to be the most prospective, being related to the post-orogenic phase of granitoid magmatism (Saleh 2007; Küster 2009). Tantalum-mineralized pegmatites from the ANS belong to the rare-element class (REL-Li subclass of Černý and Ercit 2005), and are classified as complex to albite–spodumene types (Küster 2009).

In the mobile belts of northwest Africa, rare-metal granites and related pegmatites of Pan-African and late Hercynian ages are found in the Anti-Atlas and Variscan inliers of Morocco (i.e., Tazennakht and Angarf, Schneiderhöhn 1961; Zrari, Belkasmi et al. 1999), and more importantly in the Hoggar Shield terranes of Algeria (i.e., Alemeda and Tin Amzi occurrences, Bouabsa 1987; Cheilletz et al. 1992; Chalal and Marignac 1997; Marignac et al. 2001; Kesraoui and Marignac 2010; Marignac et al. this volume). The latter contain subeconomic Ta–Nb–Sn ± REE concentrations and are spatially and genetically associated with geochemically specialized granitoids. Farther to the north, the youngest rare-metal granites are Neogene, occurring in the Alpine Edough massif (Aïssa et al. 1995) and Filfila granitic complex (Internal Maghrebides, Lesser Kabylia) of northeastern Algeria. In these areas, rare-metal mineralization forms fine-grained disseminations of cassiterite, ferberite, and very abundant Ta-rutile, and columbo-tantalite minerals, all of which overprint Langhian (Middle Miocene) topaz-bearing granites and rhyolites (Bouabsa et al. 2010; Marignac et al. this volume). Genetic models propose that rare-metal-rich magmas originated, together with other peraluminous magmas, by high-level partial melting induced by the intrusion of large meta-aluminous magmas, and subsequently mixed with this meta-aluminous melt to produce the observed rare-metal granites (Bouabsa et al. 2010; Marignac et al. this volume).

27 Volcanic-Hosted Massive Sulphide Deposits

Volcanic-hosted massive sulphide deposits (VHMS) developed in two contrasting geological terranes that were accreted during two main episodes of submarine-arc volcanism in the Neoproterozoic and Carboniferous.

The Neoproterozoic episode coincides with formation of the VHMS deposits of the ANS. These deposits occur along the length of the Red Sea coast from Egypt through Sudan to Eretria and Ethiopia (Barrie et al. this volume). The Carboniferous episode generated the Variscan deposits of the Central Jebilet and Guemassa Massifs in Morocco, which are related to the large Variscan VHMS province of Western Europe (Lescuyer et al. 1998) (Fig. 10). Indeed, the late Paleozoic is regarded as one of the most

productive periods in Earth history for massive sulphide mineralization (Eremin et al. 2002, 2004; Moreno et al. 2008; Huston et al. 2010). The western ANS is inferred to be particularly prospective for gold-rich VHMS deposits, owing to the primitive geochemical signature of the oceanic crust produced during the Neoproterozoic rifting. In particular, the VHMS deposits hosted in the western part of the ANS include a high gold potential that exceeds 15 % gold in terms of relative metal value in calculated total gold-equivalent resources (Trench and Groves 2015). Well-documented examples are the giant gold-rich VHMS deposits of the Hassai district in Sudan with resources of ca. 6.3 Moz Au and 1.3 Mt Cu (52 % Au by relative metal value; Trench and Groves 2015), and in Eretria the large but low-grade Emba Derho deposit totaling ca. 8 % Au by relative metal value within a 6.3-Moz gold-equivalent resource, and the Bisha deposit that contains >39 Mt of base and precious metal resources (Barrie et al. 2007, this volume). This region is an emerging new belt containing gold-rich, porphyry-related, high sulphidation, epithermal-VHMS deposits that share many geological characteristics with the newly recognized group of gold-rich VMS systems as defined by Dubé et al. (2014).

The Moroccan VHMS deposits of the central Jebilet and Guemassa massifs developed during Carboniferous rifting and formation of a restricted intracontinental rift basin. This basin was filled with shale and subordinate clastic and carbonate strata in a back-arc environment (Huvelin 1977; Aarab and Beauchamp 1987), contemporaneously with emplacement of Visean to late Hercynian tholeiitic to alkaline bimodal intrusive and extrusive igneous rocks (i.e., Bouabdellah et al. this volume). The Moroccan deposits have been correlated stratigraphically with VHMS deposits of the Iberian Pyrite Belt (Bordonaro et al. 1979) and integrated into a global genetic model that involves progressive migration of the mineralizing fluids along the western Hercynides, from Late Devonian time in France to early Carboniferous (Dinantian) time in Morocco, with a metalliferous "peak" occurring at ca. 350 Ma (Lescuyer et al. 1998; Essaifi and Hibti 2008). Overall, the Variscan VHMS deposits in Morocco includes four major orebodies (Kettara, Hajar, Dra Sfar, and Koudiat Aicha), which together produced more than 70 Mt of ore (Bouabdellah et al. this volume). Striking features of these deposits are the abundance of pyrrhotite (up to 90 vol%) relative to pyrite, and more importantly the intensely sheared and metamorphosed nature of the ores (Marcoux et al. 2008). The predominance of pyrrhotite has been interpreted as reflecting very low f_{O2} conditions that prevailed during mineralization, and neither high temperatures nor low a_{H2S} (below 10^{-3}) is required to explain this mineralogy (Marcoux et al. 2008).

VHMS deposits are also documented in the Pan-African Pharusian belt of Mali (Markwitz et al. 2015) where the Tessalit deposit is the most significant (up to 7 % Zn, 1–2 % Pb, <1 % Cu) (Fig. 10). Polymetallic orebodies there occur on the western edge of the Precambrian In Ouzzal inlier, within Upper Proterozoic submarine island arc volcanic rocks including porphyritic rhyolite domes and surrounding laminated felsic tuffs stratigraphically assigned to the Tilemsi Group. A distinctive mineral zoning is typified by a lower magnetite-rich zone to upper carbonate-copper sulphide and carbonate-sphalerite zones (Leblanc and Sauvage 1986).

28 Iron Oxide-Copper-Gold Deposits

The Mauritanian Guelb Moghrein iron oxide–Cu–Au–Co deposit is the sole representative of the IOCG class (Williams et al. 2005) yet documented in North Africa (Fig. 10). This deposit occurs within the allochtonous supracrustal terranes of the Mauritanides Belt along the western edge of the WAC. In 2004, First Quantum Minerals Ltd. acquired an 80 % interest in the property and in 2010 assumed 100 % ownership. Production commenced in 2006, and by the end of 2013 mineral reserves were estimated at 31.3 Mt grading 0.92 % Cu and 0.69 g/t Au

(http://www.first-quantum.com). Historic production of Au to 2013 was 690,155 oz (Kirschbaum and Hitzman 2016).

Early studies of the Guelb Moghrein deposit suggested either a syn-sedimentary origin based on the close association of the orebodies with widespread BIF and Fe-carbonate units (Pouclet et al. 1987), or a VHMS origin owing to the presence of volcanic rocks in the vicinity and similarities in metal contents to some VHMS deposits (Ba Gatta 1982). However, reinterpretation of the Fe-rich host rocks as products of metasomatic replacement instead of chemical sedimentation, the distinctive minor-element geochemical signature, alteration styles, and new geochronological data all point to an epigenetic hydrothermal origin and consequently a classification as an IOCG type of deposit (Martyn and Strickland 2004; Meyer et al. 2006; Sakellaris 2007; Kolb et al. 2008; Kirschbaum 2011; Kolb and Petrov 2015).

Host rocks to the ores are predominantly greenschist- to amphibolite-facies mafic schist and amphibolite stratigraphically assigned to the Akjoujt metabasalts of the Oumachoueïma Group. These mafic rocks overlie meta-rhyodacite to meta-dacite volcaniclastic rocks and schists of the St. Barbe volcanic unit (Martyn and Strickland 2004; Kolb et al. 2008). Regionally, the St. Barbe unit is overlain by a pyritic chert facies of BIF (a regional stratigraphic marker) referred to as the Lembeitih Formation (Strickland and Martyn 2002), which includes the iron carbonate host rock unit at Guelb Moghrein (Kolb et al. 2008). From a geodynamic view point, the local stratigraphic package was emplaced in a continental or island arc setting (Kolb et al. 2008). Recent radiometric dating (in situ U–Pb on monazite and xenotime; Meyer et al. 2006) indicates that the supracrustal host rocks of the Guelb Moghrein deposit (i.e., Eizzene and Oumachoueïma Groups; Meyer et al. 2006) are Archean (2492 ± 9 Ma), having formed marginal to the Reguibat Shield (Meyer et al. 2006; Kolb et al. 2008; Kolb and Petrov 2015).

The Guelb Moghrein deposit consists of two distinct, brecciated meta-carbonate-hosted orebodies referred to as Occidental and Oriental (Kirschbaum and Hitzman 2016), both of which are surrounded by Fe–Mg clinoamphibole-chlorite schist (Meyer et al. 2006). In detail, the mineralized structures form multiple coalescing tabular and coarse-grained lenses, ca. 30 m thick, that developed parallel to D_2 shear zones (Meyer et al. 2006; Kolb and Petrov 2015). The carbonate host rocks consist predominantly of Fe–Mg siderite (pistomesite) and ankerite, with subordinate amounts of ferroan dolomite and calcite (Sakellaris 2007; Kirschbaum 2011). Abundant magnetite (up to 40 vol%), as much as several percent graphite, fibrous amphibole (cummingtonite-grunerite), and locally coarse biotite and pyrosmalite have been documented (Kirschbaum 2011).

Historic mining has focused on the Occidental orebody that has higher gold and copper grades, and abundant secondary copper minerals, relative to the Oriental orebody. To date, no mining of the Oriental orebody has taken place (Kirschbaum and Hitzman 2016). The highest grades are encountered within carbonates in proximity to hangingwall and footwall faults, whereas lower-grade mineralization (1–3 % Cu) occurs within fractured to weakly brecciated carbonates as disseminated chalcopyrite and cubanite. Primary ore consists mainly of various proportions of magnetite, pyrrhotite, and chalcopyrite with subordinate Fe–Co–Ni arsenides, arsenopyrite, cobaltite, and Bi–Au–Ag–Te minerals (Kolb et al. 2006; Sakellaris 2007; Kirschbaum 2011). Supergene alteration and weathering of the orebody resulted in the formation of abundant iron and copper oxides (hematite, limonite, goethite, malachite, and chrysocolla) as well as native copper.

Fluid inclusion data together with isotopic constraints (Kolb et al. 2008; Kolb and Petrov 2015) indicate that the Guelb Moghrein IOCG mineralization formed during retrograde tectono-metamorphic processes in reponse to fluid mixing at 0.75–1.80 kbar and ~410 °C, with the mineralizing fluids having been focused into regional-scale shear zones. Gold was transported as an $AuCl^{2-}$complex in the ore fluids and was concentrated in coexisting Bi melt-droplets, resulting in the precipitation of an Au–Bi-assemblage during cooling (Kolb and Petrov 2015).

29 Orogenic and Intrusion-Related Gold Deposits

Orogenic gold deposits also referred to as mesothermal deposits (e.g., Groves et al. 1998) are widely recognized in both Phanerozoic mobile belts and older cratonic blocks. This class of gold deposit is characteristically associated with deformed and metamorphosed, mid-crustal blocks in close spatial association with major crustal structures (Goldfarb et al. 2001, 2005). Conversely, intrusion-related gold deposits typically occur in metaluminous subalkalic plutonic bodies of felsic to intermediate composition, mainly in a tectonic setting inboard of convergent plate boundaries (Lang and Baker 2001).

In North Africa, economically significant orogenic and intrusion-related gold deposits are both in Precambrian cratons and the Pan-African Anti-Atlas orogen of Morocco (Figs. 9 and 10). The mineralized structures occur as crustal-scale, multi-kilometer-long shear zones hosted by a variety of lithotectonic units. These units include deformed and variably metamorphosed, greenschist-facies (locally amphibolite-facies) supracrustal sedimentary sequences. World-class examples include the Tasiast deposit in Mauritania, deposits of the Loulo-Gounkoto and Sadiola-Yatela districts in Mali (Lawrence et al. this volume), the Tirek-Amesmessa deposits in Algeria related to the In Ouzzal mega-shear zone in the western Hoggar of the Tuareg Shield (Ferkous and Monie 2002; Marignac et al. this volume), and deposits in Egypt and Sudan fringing the Red Sea (El Boushi 1972; Almond et al. 1984; Klemm et al. 2001; Zoheir et al. 2008, 2014). In Morocco, intrusion-related gold occurrences are represented by the Iourirn-Akka and Tiouit deposits in the Anti-Atlas Mountains, and by the recently discovered Tamlalt–Menhouhou prospect (Pelleter et al. 2008) in the eastern High Atlas.

Radiometric ages have determined for gold mineralization by numerous workers (Ferkous and Monie 2002; Doebrich et al. 2004; Gasquet et al. 2004; Pelleter et al. 2008; McFarlane et al. 2011; Lawrence et al. this volume; Marignac et al. this volume). Based on these data, three age groupings are recognized, corresponding to three major peaks of orogenic gold mineralization in the intervals 2098 ± 4 to 2074 ± 14 Ma (McFarlane et al. 2011), 655.6 ± 2.7 to 525 ± 5 Ma (Ferkous and Monie 2002; Doebrich et al. 2004), and 301 ± 7 Ma to 293 ± 7 Ma (Gasquet et al. 2004; Pelleter et al. 2008). These intervals are within the Paleoproterozoic (2.5–1.6 Ga), Neoproterozoic (1.6–0.57 Ga), and Paleozoic (570–250 Ma) time spans considered by Goldfarb et al. (2001) as being favorable periods for the formation of orogenic gold deposits.

29.1 Egypt

Intracratonic orogenic gold deposits in Egypt (e.g., Um Egat, Dungash, and Fawakhir-El Sid districts in central Eastern Desert; Klemm et al. 2001; Zoheir et al. 2008, 2014; Khalil et al. this volume) and their equivalents in northern Sudan (i.e., Abirkatib, Ekwan, Shigriyay, and Gebeit deposits; EL Boushi 1972; Almond et al. 1984) (Fig. 10) occur within Neoproterozoic greenstone terranes of the ANS. The mineralized structures consist of an array of gold-bearing quartz veins confined within regional mega-shear structures. Host rocks are greenschist-facies ophiolitic sequences, island arc assemblages, and post-orogenic calc-alkalic and alkali granitoids (e.g., Zoheir et al. 2008, 2014; Khalil et al. this volume, and references therein). Gold mineralization is closely associated, in time and space, with the emplacement of late- to post-orogenic, intracrustal granitoid intrusions. This model is consistent with newly acquired Re–Os geochronological data for the Fawakhir–El Sid deposit that indicate an age for gold mineralization of 601 ± 17 Ma (Zoheir et al. 2014), which coincides within error of the U–Pb zircon age of 598 ± 3 Ma for the spatially associated monzogranite intrusion (Zoheir et al. 2014). These temporal relationships suggest a key role for granite-derived hydrothermal fluids in forming the quartz-vein system. However, structural constraints indicate that the gold-bearing quartz veins developed late in the orogenic cycle of the ANS (e.g., Klemm et al.

2001; Zoheir et al. 2008; Khalil et al. this volume). Indeed, Re–Os age dating of molybdenite from the neighboring Ad Duwayhi gold deposit in western Saudi Arabia has yielded ages of 655.6 ± 2.7 and 649.9 ± 2.3 Ma, recording a late Neoproterozoic timing for that gold mineraliszation (Doebrich et al. 2004). These contrasting radiometric ages suggest a polyphase history for the genesis of Egyptian gold mineralization, involving an early magmatic stage related to crystallization of local granitic magma followed by a later brittle-ductile stage during which gold mineralization was deposited within regional mega-shear structures.

29.2 Algeria

Algerian orogenic gold deposits include those of the world-class Amesmessa-Tirek (>5 Moz Au), Tiririne (1.7 Moz Au), and Silet-Tinfelki (~2.5 Moz Au) goldfields (Fig. 10). Among these, the currently exploited Amesmessa and Tirek deposits are the most productive. Both are spatially related to the East In Ouzzal shear zone of the western Hoggar Shield and its southward extensions into the Adrar Iforas (Mali) and Aïr (Niger) shields. The estimated gold resource of the 16 gold veins known within the Amesmessa deposit is 1.40 Moz, whereas that calculated for the Tirek deposit (mine closed in 2007) is much lower, at ca. 593,100 oz at an average grade of 25.1 g/t (www.enor.dz/documents/presentation-enor.pdf).

Host rocks of these deposits consist of regionally folded and amphibolite-facies, Paleoproterozoic para- and orthogneiss, marble, quartzite, amphibolite, schistose pelite, and metamorphosed intrusions. Archean basement is represented mainly by mafic and felsic granulites with subordinate marble and quartzite (Ferkous and Monie 2002, and references therein). The mineralized structures, which are confined to the dextral, lithospheric-scale East In Ouzzal shear zone (EIOSZ), comprise two sets of multi-kilometer, N-S-trending, gold-bearing quartz vein systems and extensional, E-W-trending, gold-poor quartz veins (Marignac et al. 1996; Ferkous and Monie 2002; Marignac et al. this volume). Genesis of the gold mineralization has been related to late Neoproterozoic reactivation of the ca. 626–575 Ma EIOSZ shear zone (Semiani et al. 1995; Marignac et al. 1996). In this regard, Ferkous and Monie (2002) reported a systematic increase of gold grades towards the tectonic front (WAC vs. Hoggar Shield), from 1.7 Moz at Tiririne in the east to more than 5 Moz at Amesmessa-Tirek in the west.

29.3 Morocco

In Morocco, most gold production is derived from the Iourirn-Akka and Tiouit deposits of the Pan-African Anti-Atlas system. Recently, a new promising gold prospect has been identified in Neoproterozoic rocks of the eastern High Atlas Mountains (Pelleter et al. 2008) (Fig. 10). Common features for all of these deposits and related prospects include host rocks of Neoproterozoic greenschist-facies successions, and an age of gold mineralization that coincides with late Carboniferous-Permian (300–270 Ma) tectonism (Gasquet et al. 2004). This time interval suggests, in accordance with the conclusions of Bellot et al. (2003), that gold mineralization in Morocco is linked to a large-scale thermal event during the early stages of post-thickening extension of the Variscan lithosphere. It appears, therefore, that Moroccan terranes contain the youngest orogenic and intrusion-related gold deposits of North Africa. Gold has also been reported as being associated with the polymetallic Jbel Tighza deposit in central Morocco (Fig. 10), where gold-bearing occurrences are related to late Hercynian calc-alkaline granitoid stocks (Marcoux et al. 2015; Rossi et al. this volume).

The Iourirn-Akka gold deposit occurs within the Precambrian Tagragra de Tata inlier of the western Anti-Atlas orogen. Mineralization is centered on the apex of a Paleoproterozoic basement-cored dome unconformably overlain by weakly deformed and metamorphosed Neoproterozoic clastic and volcanic rocks of the Anezi and Ouarzazate Series (Walsh et al. 2002; Thomas et al. 2004). Paleoproterozoic basement rocks consist of metasedimentary

and metavolcanic sequences comprising mica schist, tuffaceous schist, metasiltstone, and metasandstone with interbedded felsic metatuffs (2072 ± 8 Ma), all of which are intruded by post-Eburnean granites (i.e., Targant and Oudad granites, U–Pb zircon ages of 2046 ± 7 Ma and 2041 ± 6 Ma, respectively), metadolerites dated at 2040 ± 6 Ma, and microgranite dikes (Walsh et al. 2002). The unconformably overlying Anezi and Ouarzazate Series comprises clastic and volcanic rocks including breccias, rhyolitic ignimbrites dated at 565 ± 7 Ma (Walsh et al. 2002), andesite, siltstone, sandstone, and conglomerate.

The mined gold-bearing structures exposed underground are hosted nearly entirely within Paleoproterozoic schists cut by dense swarms of ENE- to NE-trending porphyritic rhyodacite and quartz diorite dikes. All of the surrounding rocks are dissected by a network of E-W-striking, dextral strike-slip shear zones within which the mineralized structures occur. Gold-bearing orebodies dominantly are multistage brecciated and ribbon-textured quartz veins, networks of quartz veinlets (i.e., stockworks), and en echelon tension-gash fillings. Ore veins are commonly 200–300 m long and 0.5 to as much as 5 m thick, and extend to more than 600 m depth, with the uppermost 50–100 m intensely oxidized. The geometry of these veins is very similar to those of fault-fill veins and extensional veins typically associated with strike-slip fault systems, as described by Pitfield and Campbell (1996) and Bellot et al. (2003). Native gold forms dendrites, veinlets, and films, and locally grains that are visible in hand specimen. Mineral assemblages consist of varying proportions of pyrite, arsenopyrite, pyrrhotite, chalcopyrite, sphalerite, and galena, with subordinate magnetite, hematite, covellite, malachite, and azurite. Arsenopyrite and chalcopyrite are the most important gold-bearing minerals. Three main stages of ore deposition are recognized: (1) an early arsenopyrite-pyrite-quartz-gold stage comprising massive fine-grained quartz; (2) a sulphide stage characterized by massive sulphide including pyrite, arsenopyrite, sphalerite, galena, chalcopyrite, and native gold; and (3) a late gold-bearing carbonate-tourmaline-oxide (magnetite-hematite) stage with abundant calcite, siderite, and ankerite. Hydrothermal alteration of wall rocks produced assemblages of quartz, sericite, muscovite-phengite, chlorite (Fe-ripidolite), carbonate (siderite, ankerite), leucoxene, and tourmaline.

The origin and age of the gold mineralization remain the subject of ongoing debate. Rb–Sr, $^{40}Ar/^{39}Ar$, and K–Ar dating of muscovite synchronous with the gold-bearing stage yields contrasting ages of 445 ± 34 Ma (Zverev et al. 2003), 301 ± 7 Ma (Gasquet et al. 2004), and 276 ± 4 Ma (Gasquet et al. 2001). These ages clearly postdate crystallization of the Paleoproterozoic and Neoproterozoic igneous rocks in the area. Rather, these ages indicate that gold mineralization at Iourirn-Akka is related to a late Variscan postcollisional event. Fluid inclusion data further suggest that this mineralization was associated with a pressure decrease from 5 Kb–200 bars and cooling from lithostatic to hydrostatic conditions as temperatures decreased from 400 to 200 °C. Early fluids were of metamorphic derivation and later mixed with low-salinity fluids probably of meteoric origin, triggering deposition at low temperatures (150–250 °C) of economic gold mineralization (Zouhair et al. 1991).

The Tamlalt-Menhouhou gold prospect occurs in upper Neoproterozoic bimodal volcanic and volcano-sedimentary sequences of the Neoproterozoic–Paleozoic Tamlalt inlier of the eastern High Atlas Mountains. Mineralization consists of arrays of gold-bearing quartz veins that display brittle-ductile deformation within E-W- to NE-SW-trending dextral shear faults associated with strong quartz-phyllic-argillic alteration. $^{40}Ar/^{39}Ar$ dating of muscovite intergrown with gold has yielded an age of 293 ± 7 Ma (Pelleter et al. 2008), which is similar within error to the 301 ± 7 Ma $^{40}Ar/^{39}Ar$ and 276 ± 4 Ma K–Ar ages determined for the Iourirn-Akka gold mineralization (Gasquet et al. 2001, 2004).

Further to the north, the Jbel Tighza polymetallic deposit in central Morocco contains recently discovered, uneconomic Au–W mineralization that is spatially closely related to a late Hercynian calc-alkaline intrusion (Cheilletz and Zimmermann 1982; Nerci 2006; Marcoux et al.

2015; Magali et al. this volume). The host rocks consist of a succession of greenschist-facies Ordovician micaceous schist with interlayered sandstone, quartzite, and micro-conglomerate; Silurian graptolite-bearing black shale and limestone; Devonian siliceous carbonates; and Tournaisian (360–350 Ma) sandstone, conglomerate, and greywacke. Overlying strata are Middle Visean (340 Ma) bioclastic limestone and marl, and a thick pile of Visean flysch, all of which are intruded by three small (1 km^2 each) late Hercynian stocks referred to as the "Kaolin," "Mispickel," and "Mine" granites (Cheilletz 1984; Ntarmouchant 1991). All of the enclosing host rocks are deformed into a succession of NE-trending anticlines and synclines, localized in a major E-W sinistral shear zone (Rossi et al. this volume).

Gold- and W-bearing veins are intimately related to the 286.0 ± 0.4 Ma Mine granite. These veins form an array of N90° E–N120° E-trending structures up to 2 m thick that can be followed more than 1400 m along strike; some have been intersected in drill cores at depths up to 220 m (Marcoux et al. 2015). Primary mineral assemblages consist of various generations of quartz, Bi-tellurides, sulphides (arsenopyrite, loellingite, pyrrhotite, chalcopyrite, and sphalerite), and native gold or electrum (84 % Au, 16 % Ag) accompanied by muscovite, biotite, and phlogopite. Gold grades reach a maximum close to the granite (up to 70 g/t) and decreases progressively from the granite contact, defining a typical peri-granitic zoning (Marcoux et al. 2015). Fluid inclusion studies (Nerci 2006; Marcoux et al. 2015) show the presence of: (1) low-salinity, aqueous-carbonic inclusions; and (2) high-salinity inclusions containing at least one solid phase (i.e., halite plus calcite, micas, or chalcopyrite). The second generation of fluid inclusions, which homogenize at temperatures of 257–284 °C and have salinities of ~34 to ~37 wt% NaCl equiv, is thought to be representative of fluids linked to the gold-bearing stage rich in Au–Te–Bi–Cu (Marcoux et al. 2015). Timing of the Au–W stage is well constrained by multiple Ar–Ar and K–Ar age determinations that collectively indicate a time span for this mineralization of 300–260 Ma (Cheilletz and Zimmermann 1982; Watanabe 2002; Nerci 2006), which is contemporaneous with the second magmatic event at 295–285 Ma (Magali et al. this volume). Recently published $^{40}Ar/^{39}Ar$ dating of muscovite yields a mean age of 285.3 ± 0.5 Ma (Marcoux et al. 2015) that is within error, coeval with emplacement of the Permian Mine granite. These temporal relationships suggest a genetic tie between Au–W mineralization that operated at the end of the magmatic stage and the spatially associated intrusion. It is therefore proposed that magmatic-hydrothermal fluids exsolved from the cooling Mine pluton, migrated along fractures in the metasedimentary country rocks, and reacted with these rocks resulting in precipitation of the Au–W vein ores.

29.4 Mali

Compared with North African countries, Paleoproterozoic Malian greenstone terranes and nearby sedimentary basins of Birimian age (ca. 2.2–2.0 Ga) host the largest and most productive orogenic and intrusion-related gold deposits of North Africa including some that contain significant resources (>1 Moz Au) (Fig. 10). Over the last two decades, and even at the present time where exploration is ongoing, the number of new findings has resulted in the discovery, delineation, and development of additional world-class gold deposits. In 2014, the discovery and rapid development by Papillion Resources of the Fekola deposit with resources estimated at 83.7 Mt at 1.90 g/t Au and contained measured + indicated reserves of 5.12 Moz above a cut-off grade of 0.6 g/t Au (www.pdac.ca/…/new-discoveries—brown.pdf; www.miningne.ws/tag/fekola-gold-project/), provides strong evidence of the outstanding prospectivity for gold in Mali. Indeed, with a total gold production in 2013 of over 64 t (Diarra and Holliday 2014), Mali currently ranks as Africa's third-largest gold producer after South Africa and Ghana. The main and most productive deposits include Morila (7.5 Moz Au; Randgold Resources 2009) and Syama (7 Moz Au) to the south, Sadiola-Yatela with current probable reserves of 3.8 Moz of Au at an average grade of 2.1 g/t (IAMGOLD Corporation 2014), the Loulo-Gounkoto district of Gara (current

reserves of 1.5 Moz at 4.15 g/t), Yalea (reserves of 2.9 Moz at 5.82 g/t), and Gounkoto (reserves of 2.8 Moz at 5.1 g/t) (Randgold Resources Ltd. 2014), and Tabakoto/Segala (Avion) to the southwest (e.g., McFarlane et al. 2011; Lawrence et al. 2013a, b; Salvi et al. 2015; Markwitz et al. 2015; Masurel et al. 2015, 2016); Lawrence et al. this volume) (Fig. 10).

Host rocks to these deposits consist predominantly of a succession of strongly deformed and metamorphosed (greenschist to amphibolite facies) Birimian volcanic, volcano-sedimentary, and siliciclastic and carbonate sedimentary strata of the Kofi and Mako Series. All of these rocks are intruded by plutons of different generations and sizes, emplaced between ca. 2100 and 1980 Ma (Masurel et al. 2015; Lawrence et al. this volume). The main lithologies are calc-alkaline volcaniclastic rocks, arenite, wacke, siltstone, argillite, and carbonates with varying proportions of tholeiitic basalt and andesite, together with calc-alkaline granitoid intrusions. All of the Birimian country rocks were deformed and metamorphosed during the Eburnean orogeny around 2.1–2.0 Ga.

Most of the gold deposits occur as sheeted vein arrays developed either proximal or distal to large regional shear zones, or surrounding and/or within intrusions. In this regard, it is noteworthy that the majority, if not all, of the productive deposits are aligned along two regional-scale lineaments referred to as the Main Transcurrent Zone (i.e., Fekola, Sadiola, and Yatela) and the Senegal-Mali Shear Zone (i.e., Petowal, Oromin, and Sabadola) (Lawrence et al. 2013a, b; Masurel et al. 2015, 2016; Lawrence et al. this volume). Gold deposits of the West Mali gold belt are confined to second- and higher-order structures on the eastern side of the Senegal-Mali Shear Zone, in which mineralization was synchronous with D_3 transtensional deformation that triggered hydrothermal fluid flow and displacement along the regional-scale shear zones and local N- and NNE-trending fault arrays (Lawrence et al. 2013a, b; Treloar et al. 2015; Masurel et al. 2015, 2016; Lawrence et al. this volume). Recently determined radiometric ages indicate that most of the major dated Malian gold deposits formed between 2090 and 2020 Ma (McFarlane et al. 2011; Lawrence et al. 2013a, b; Masurel et al. 2015, 2016), although some may have formed before the Eburnean during a period of back-arc extension (Markwitz et al. 2015).

For detailed geological descriptions and updated genetic models on these gold deposits in Mali, the reader is referred to the excellent synthesis provided by Lawrence et al. (this volume) and the newly released papers of Masurel et al. (2015, 2016) and Salvi et al. (2015).

29.5 Mauritania

The Tasiast goldfield constitutes the newest area of significant gold discoveries in the northwestern limit of the Mauritanian segment of the WAC (Fig. 10). This goldfield lies in the southwesternmost part of the Reguibat Shield and contains several gold orebodies owned by Tasiast Mauritanie Limited S.A., a subsidiary of Kinross Gold Corporation. Having an estimated gold resource of 12.8 Moz at an average grade of 1.5 g/t, the Tasiast orebody is considered one of the largest gold deposits in North Africa. Commercial production began in 2008 when the mine was owned and operated by Red Back Mining B. V. (Stuart 2010); as of December 31, 2011, approximately 0.7 Moz of gold has been produced from the Tasiast mine (Sedore and Masterman 2012). In 2013, production included 2.5 Mt of ore yielding 144,000 oz Au at a grade of 1.96 g/t, plus 104,000 oz derived from the reprocessing of mine dumps via heap-leaching (Sims 2014; Heron et al. 2015).

The Tasiast gold deposits are located along a N-S-trending shear system within the 70 × 15 km Precambrian Aouéouat greenstone belt. Three main prospective trends are recognized, in which all known deposits show spatial association with the Tasiast trend (Sedore and Masterman 2012). The orebodies occur within two parallel zones that continue for >10 km along strike (Sedore and Masterman 2012). U–Pb ages obtained from host gneiss, TTG, and granites fall between 2.97 and 2.91 Ga (Key et al. 2008; Schofield et al. 2012; Gärtner et al. 2013; Montero et al. 2014), although older ages

of 3.03 and 3.01 Ga have also been reported (Gärtner et al. 2013; Montero et al. 2014).

Stratigraphy of the host rocks consists of a succession of deformed and metamorphosed (upper greenschist- to lower amphibolite-facies) mafic to felsic igneous rocks. Some of these rocks have been dated at 2.97 Ga, which is currently considered the best age estimate for the host rocks at Tasiast (Key et al. 2008; Heron et al. 2015). The meta-igneous rocks are overlain by siliciclastic sedimentary strata composed of greywacke, siltstone, and turbidites together with BIF, all deposited during a rifting stage in a sinistral, transtensional tectonic regime (Kruse 2013). Structural constraints indicate that gold mineralization formed during an approximately E-W bulk shortening event that accompanied inversion of the Tasiast sedimentary basin (Heron et al. 2015). The Tasiast gold deposit consists of two distinct groups of orebodies referred to as Piment and West Branch, both being confined to the west-vergent Tasiast thrust fault but hosted in contrasting lithologic units. Piment orebodies are within metaturbidites and subordinate BIF, whereas the West Branch orebodies that account for the bulk of gold mineralization occur within meta-igneous rocks, predominantly diorite and quartz diorite (Sedore and Masterman 2012; Heron et al. 2015).

Gold mineralization has been defined over a strike length of more than 10 km and to vertical depths of at least 740 m. It occurs as sheeted quartz-carbonate-albite-tourmaline-pyrrhotite-pyrite veins, gold-bearing quartz-carbonate veinlets, and disseminated gold in adjacent wall rocks (Heron et al. 2015, and references therein). Coarse-grained visible gold, >100 μm in diameter (Sims 2014), is common within the quartz-carbonate-pyrite ± biotite-rich veinlets. Kinematic constraints led Heron et al. (2015) to interpret these veins as syn-orogenic, having formed in extensional or shear fractures that were subsequently folded, boudinaged, and locally transposed into the foliation plane. Multiple generations of quartz account for more than 80 vol% of the vein fillings, accompanied by subordinate carbonates (i.e., ankerite, dolomite, and calcite), together with trace amounts of muscovite, biotite, chlorite, amphibole, albite, and garnet. Minerals such as scheelite and tourmaline, typical of many orogenic gold deposits worldwide (e.g., Hagemann and Cassidy 2000), are present locally. Major metallic minerals are pyrite, pyrrhotite, and native gold. Accessories include sphalerite ± galena, chalcopyrite, tennantite ± tetrahedrite, arsenopyrite, electrum, wolframite, scheelite, magnetite, hematite, petzite, covellite, and pentlandite. The total sulphide content of the deposit is typically less than 5 vol%.

Recent U–Pb ages on determined on hydrothermal zircon overgrowths on igneous zircon separates indicate emplacement of the gold mineralization at 2839 ± 36 Ma (Heron et al. 2015), coincident with early stages of post-peak (retrograde) greenschist-facies metamorphism. This new age constraint contrasts with much younger K–Ar dates of 1.85 and 1.50 Ga on hydrothermal sericite separates (Higashihara et al. 2004; Marutani et al. 2005), the younger ages likely recording metamorphic resetting of the K–Ar isotope system.

29.6 BIF Deposits

Banded iron formations (BIF) are widely accepted as products of the diagenetic and metamorphic alteration of typically thin-bedded or laminated, Fe-rich, chemically precipitated marine sediments. BIF contains a minimum of 15 % Fe, commonly but not necessarily including layers of chert (James 1992; Klein and Beukes 1993). Most economic BIF is of Archean and Paleoproterozoic age (James 1983; Hofmann 2005; Alexander et al. 2008; Johnson et al. 2008; Bekker et al. 2010), although some deposits occur in younger terranes of Neoproterozoic age following a hiatus of over a billion years from ~1800 to ~800 Ma (e.g., Pelleter et al. 2006, Ali et al. 2010, Basta et al. 2011; Stern et al. 2013; Khalil et al. 2015).

In North Africa, significant BIF deposits occur in Egypt and more importantly in Mauritania where the largest deposits are documented (Bronner and Chauvel 1979; Taylor et al. this volume) (Figs. 9 and 10). Uneconomic prospects are in Morocco (Pelleter et al. 2006). In Egypt,

major BIF deposits occur in the central part of the country between latitudes 25°15′–26°40′ N and longitudes 33°22′–34°20′ E, within Neoproterozoic island-arc/ophiolitic sequences of the ANS (e.g., Basta et al. 2011; El-Shazly and Khalil 2014; Khalil et al. 2015). Overall, the host rocks consist of a succession of greenschist- to amphibolite-facies, tholeiitic to calc-alkaline metavolcanics comprising basaltic, andesitic, and dacitic lava flows interbedded with pyroclastic rocks, mainly lapilli and ash-flow tuffs, and fine-grained sedimentary rocks (e.g., Sims and James 1984; Takla et al. 1999; El Habaak 2005). All of these strata are cut by a suite of shallow intrusive dike swarms of diverse composition (i.e., granitoid to trachyte), overlain by molasse sediments, and display structural contacts against serpentinites (Maurice 2006). The BIF units can be followed up to 3 km along strike and consist mainly of rhythmically interlayered Fe-oxide-rich laminae and barren quartz–carbonate ± chlorite ± magnetite layers, which collectively reflect seasonal changes in the deposition of Fe versus Si in the model of Stern et al. (2013). Recent radiometric ages determined on host rocks indicate that the BIF of the ANS, including those of central Egypt, formed at ~750 Ma (Stern et al. 2013) or 717 ± 8 Ma (Khalil et al. 2015), and prior to the Sturtian (Cryogenian) glacial episode that began at ~716 Ma. These age constraints led many other workers to classify these iron deposits as Rapitan-type BIF (e.g., Khalil et al. 2015), although their size together with the prevalence of basaltic volcanic host rocks suggest a better fit within the Algoma-type category (Basta et al. 2011; Stern et al. 2013), having formed before the final collision between major fragments of East and West Gondwana (Khalil et al. 2015). The relationship of these BIF deposits to glacial events nonetheless remains the subject of ongoing debate. In this regard, Stern et al. (2006, 2013) and Ali et al. (2010) related the genesis of the BIF of the ANS to Neoproterozoic glaciation based on the presence of the glaciogenic "Atud diamicrite." Conversely, Basta et al. (2011) and Khalil et al. (2015) challenged this model by suggesting that the Neoproterozoic BIF in the Eastern Desert are of volcanic origin and therefore lack any direct genetic link to the Snowball Earth event (cf. Bekker et al. 2010, and references therein). A polyphase model has thus been proposed by Khalil et al. (2015), in which submarine diagenesis under suboxic conditions produced an early generation of magnetite, hematite, and quartz, followed by regional metamorphism that formed coarse-grained and porphyroblastic magnetite and quartz. Post-metamorphic oxidation led to martitization of magnetite, and to the formation of abundant hematite.

The largest and economically most productive BIF deposits occur in Mauritania where crude iron ore reserves are estimated at 1.1 Gt (Jorgenson 2012; Taib 2014). With annual production estimated at 11.2 Mt in 2012, Mauritania was the second-ranked exporter and producer of iron ore in Africa, after South Africa, and is expected to produce 18 Mt per year by 2016 (U.S. Geological Survey 2012). The main deposits are hosted in Mesoarchean to Paleoproterozoic metasedimentary sequences assigned to the Tiris and Ijil Complexes (Bronner and Chauvel 1979; Taylor et al. this volume) (Figs. 9 and 10).

BIF host rocks in the Tiris Complex include Mesoarchean granulite-facies (O'Connor et al. 2005; Schofield and Gillespie 2007), granite-migmatite assemblages and supracrustal rocks including paragneiss, calc-silicate rocks, metamafic igneous rocks, quartzite, and magnetite-chert BIF (Schofield et al. 2012; Taylor et al. this volume). All of these rocks underlie the northeastern portion of the western Reguibat Shield. In contrast, the allochthonous Paleoproterozoic sequences of the Kediat Ijil Complex, which overlies the Tiris Complex, consist of metamorphosed (low grade) magnetite-rich chert and barren clastic sedimentary rocks including conglomerate, sandstone, and mica schist with subordinate carbonates and very few volcanic rocks (Bronner and Chauvel 1979). Although not directly dated radiometrically, geological constraints suggest that the Ijil Complex is Paleoproterozoic (Taylor et al. this volume) and that the contained iron formations (i.e., Kediat Ijil and Guelb El Mhaoudat deposits) are Superior-type BIF that was deposited on the

northeastern passive margin of the Archean Rgueibat Shield. Mineralogically, the Ijil BIF consists principally of quartz and iron oxides (hematite ± magnetite) with silicates and carbonates being virtually absent. Iron deposits within the Tiris Complex have relatively low grades and are of Algoma type (i.e., Guelb el Rhein and Guelb El Aouj deposits), averaging ca. 34–37 wt% Fe, containing approximately equal proportions of coarse-grained (3–5 mm) quartz and magnetite, with subordinate amphibole and pyroxene, and rare sulphides. For more details on the geological environment, geochemistry, and mineralogy of Mauritanian BIF deposits, the reader is referred to the contribution of Taylor et al. (this volume).

29.7 Sediment-Hosted Deposits

Sediment-hosted deposits of Pb–Zn, Cu, U, Mn, and phosphate are by far the economically most important deposit types mined during historic times in North Africa. According to our estimates, inferred from published data, these types of deposits dominate North Africa's base-metal production and contain the greatest resources of phosphate, uranium, and manganese (Fig. 9). Based on the composition of the enclosing host rocks (carbonates vs. siliciclastics and metasedimentary rocks) and the nature of the exploited metals, sediment-hosted deposits in North Africa can be classified broadly into six major metallogenic groups: (1) Mississippi Valley-type (MVT) Pb–Zn ± Cu ± Ba ± F, (2) sandstone-hosted Pb and U, (3) stratiform Cu, (4) manganese, (5) phosphorite, and (6) sedimentary-exhalative (SEDEX) Zn–Pb.

29.8 Mississippi Valley-Type Pb–Zn Deposits

Sediment-hosted Pb–Zn ± Cu ± Ba ± F deposits of MVT affinity (Leach et al. 2005) represent a significant class of base-metal deposits that have contributed as much as 80 % of past Pb–Zn production in North Africa. Major districts are restricted to the intracontinental Mesozoic-Cenozoic basins of the Atlas system (Figs. 9 and 11). With a total estimated production that exceeds 20 Mt of combined Pb + Zn, the Atlas system extends 2000 km along strike from Morocco to Tunisia. Included is the world-class Pb–Zn Tethyan-Atlantic metallogenic province that hosts the highest concentration of MVT deposits and occurrences in Africa. From a metallogenic standpoint, the Atlas system is therefore a high-impact Pb–Zn frontier with ongoing exploration programs centered on historical Pb–Zn deposits and nearby exposed occurrences.

Major deposits are concentrated in six mining districts (Bouabdellah et al. this volume), including the world-class and historically important Touissit-Bou Beker district in Morocco (>100 Mt at 4 % Pb, 3.5 % Zn, <1 % Cu, 120 g/t Ag; Bouabdellah et al. 2012, 2015), the Upper Moulouya district in Morocco (>30 Mt at 4 % Pb), and the Jbel Bou Dahar district in Morocco (>30 Mt at 4 % Pb, 4 % Zn). Also important are the El Abed deposit in Algeria that constitutes the eastern end of the Moroccan Touissit-Bou Beker district and the Bou-Grine district, and related deposits of the diapir zone in Tunisia (Fig. 11). Economic orebodies are enclosed within unmetamorphosed, flat-lying Mesozoic to Cenozoic shallow-water carbonate platform strata that experienced multiple episodes of dolomitization, dissolution (i.e., karstification), and uplift during Mesozoic breakup of the Pangean continental shelf of West Africa. No Paleozoic or Precambrian examples of MVT deposits are known in North Africa.

Dolostone-hosted deposits are commonly the largest and contain high-grade orebodies owing to typically high permeability of dolostone compared to limestone. Sulphide mineralization is epigenetic and stratabound, and consists principally of open-space fillings and bedded replacements of carbonate rocks. The high-grade orebodies, accounting for most of the extracted Pb–Zn ore, form massive fillings of interconnected cavities (i.e., karsts, veins, veinlets, fractures, and vuggy pore spaces), and cements in solution-collapse breccias related to post-lithification dissolution of the host

carbonates. In contrast to the open-space fillings, the bedded replacement mineralization is restricted to more porous oolithic or fossiliferous limestones. Mineral paragenesis consists of different proportions of sphalerite and galena with subordinate pyrite, chalcopyrite, and/or tetrahedrite. Non-sulphide gangue minerals vary from one district to another, comprising saddle dolomite, calcite, and barite, with minor quartz. Most districts, if not all, are typically associated spatially with positive structures (i.e., basement highs), and are structurally controlled. The formation of ENE-WSW- and E-W-trending faults appears to have been a critical factor in ore genesis, providing favorable channels for metal-bearing brines into permeable host rocks and dissolution structures. The presence of overlying shale and shaley sandstone aquitards forced the ascending mineralizing fluids, centered mainly on the basement high structure and its flanks, to flow laterally into the more porous carbonates that were replaced, and alternatively filled open spaces where available. The age of mineralization has not been clearly determined, although field relationships and isotopic data constrain this timing to between Late Cretaceous and Messinian (Bouabdellah et al. 2015).

Fluid inclusion and halogen data together with stable and radiogenic isotopic constraints suggest that most MVT mineralization in the Atlas system is genetically related to the topographically driven flow of deep basinal brines triggered by the Alpine (Atlasic) orogeny during Late Miocene time (Bouabdellah et al. 2012, and references therein). More recently, Bouabdellah et al. (2015) challenged conventional MVT models for the Touissit- Bou Beker district and suggested an alternative model involving a genetic link among extensional tectonics, Neogene-Quaternary mafic magmatism, the Messinian salinity crisis, and the world-class Pb–Zn mineralization. Compared to Moroccan MVT deposits, less is known about those in Algeria and Tunisia, for which halogen and isotopic constraints are scarce or lacking. For these MVT deposits, limited microthermometric fluid inclusion and stable isotope data show the same signatures as recorded for the extensively studied Touissit-Bou Beker district.

29.9 Sandstone-Hosted Base-Metal Deposits

Sandstone-hosted base-metal deposits are known from a wide stratigraphic range of Neoproterozoic to Cretaceous, have a global distribution, and are characterized by large tonnages but low grades (Björlykke and Sangster 1981). In North Africa, the only documented example of this class of ore deposit is in the Zeida-Bou Mia Pb district (Caïa 1976; Björlykke and Sangster 1981, and references therein) of the eastern Moroccan Meseta (Fig. 11). From a metallogenic standpoint, the Zeida-Bou Mia district, referred to hereafter as the Zeida deposit, is one of the three major exploited Pb–(Zn–Ba–F) deposits of the Upper Moulouya district (Bouabdellah et al. this volume). The mineralized zone covers a total area of 70 km × 25 km (e.g., Amade 1965, and references therein), making this one the largest fertile Pb districts of North Africa. The Pb–(Ba) mineralization was discovered in 1958 and mined from 1972 to 1985, producing 16 Mt of ore at 3 % Pb, with Zn being virtually absent. Inferred reserves, estimated at the time of the closure of the mines in 1985, are 8 Mt at 3 % Pb (Wadjinny 1998).

The deposit comprises large-tonnage and low-grade disseminated ore (2–3 % Pb), and smaller but richer vein ore (5–6 % Pb) (Amade 1965; Dagallier 1993; Annich and Rahhali 2002). Enclosing strata are Permian-Triassic continental, terrigenous, fluvial to lagoonal-lacustrine, quartzose and arkosic sandstone, conglomerate, and siltstone with intercalated evaporite beds. The arkosic sandstone, which constitutes the sole host rocks for mineralization, is part of a transgressive siliciclastic sedimentary sequence that lies unconformably on the multiphase Aouli granitoid intrusion of late Hercynian (329–319 Ma) age (Oukemeni et al. 1995). Following a major stratigraphic gap

(hiatus) that spans all of Jurassic time, renewed sedimentation deposited Cretaceous and Miocene-Pliocene conglomerate, marl, clay, and carbonates (Amade 1965; Dagallier 1993).

The stratabound Pb–(Ba) mineralization is contained within a generally thin (0.5–2 m, locally up to 40 m) arkosic sandstone that lies conformably on Permian basal conglomerate. The arkosic sandstone is poorly to well sorted and fine to medium grained, and is interlayered with sandstone, red marl, and shale. Mineralogically, the arkose consists of quartz (50–80 vol%) and feldspar (<50 vol%). Pb–(Ba) mineralization forms variably-sized intergranular disseminations and clusters of galena and barite that replace former cement in the arkose. Discordant mineralization occurs locally as veinlets. The bulk of the disseminated ore partially occludes the original porosity. Primary mineral assemblages are dominated by galena and barite with lesser chalcopyrite and pyrite. Sphalerite is virtually absent as is the case for all other MVT deposits of the Upper Moulouya district (i.e., Aouli and Mibladen deposits; Bouabdellah et al. this volume). The common association of galena and barite, together with textural relationships, indicate penecontemporaneous precipitation of these two minerals. Post-ore supergene assemblages resulting from the oxidation of primary sulphides consist of cerussite, anglesite, malachite, and azurite. It is noteworthy that the Pb–(Ba) ore of the Zeida deposit is so oxidized that nearly 60 % of total lead production has been derived from the non-sulphide component (Amade 1965). Proposed genetic models for the Zeida-Bou Mia mineralization range from an epigenetic hydrothermal origin (Amade 1965) to pedogenetic concentration during the early stage of basin diagenesis, with subsequent remobilization having produced the structurally controlled vein-type ore (Dagallier 1993).

29.10 Sandstone-Hosted Uranium Deposits

Sandstone-hosted uranium deposits constitute a major contributor to global production of this metal accounting for about 18 % of world uranium resources, 41 % of known deposits, and 45 % of global uranium production in 2011 (Penney 2012). Major deposits occur in Kazakhstan, Uzbekistan, USA, and Niger.

In 2010, Niger was the world's fifth-ranked producer of uranium amounting to about 7.8 % of world production (U.S. Geological Survey 2010a) derived from several world-class deposits. In 2011, Niger produced 4351 t U; cumulative production from the country was 114,346 t U to the end of 2010, of which 62,000 t were exploited from underground mines and 52,000 t from open pits (World Nuclear Association 2015). At the end of 2010, Niger's defined and inferred resources were estimated by the International Atomic Energy Agency (IAEA) as 339,000 and 82,000 t U, respectively. Most of the uranium production has come from (1) the Akouta underground mine, which is operated by "la Compagnie minière d'Akouta" (COMINAK); (2) the Arlit open pit mine that began production in 1971 and is currently operated by "la Société des Mines de l'Aïr" (SOMAIR); (3) the Azelik mine operated by "la Société des Mines d'Azelik SA" (SOMINA) that came into production in 2010; and (4) the Imouraren mine where development began in 2008 by the French Areva Group (Fig. 11).

All of the exploited deposits owned by Paris-based Areva Group occur within continental (non-marine) sedimentary sequences of the Cambrian to Cretaceous Tim Mersoi sedimentary basin (140,000 km^2) in northern Niger, west of the Aïr Massif (Fig. 11). In addition to this giant basin, which is considered the largest U-bearing sedimentary basin in North Africa (having excellent prospectivity for other sandstone-hosted uranium deposits), the Paleozoic Djado and Emi Lulu basins show good uranium potential (El Hamet and Idde 2009). The major productive orebodies in the Tim Mersoi basin occur in a wide range of rocks ranging in age from Carboniferous to Cretaceous, including the Carboniferous Guezouman Formation that hosts the Akouta and Arlit deposits, and the Lower Cretaceous Tchirezrine and Assouas formations that enclose the Imouraren and Azelik deposits, respectively.

Uranium mineralization occurs in several organic- and pyrite-rich units along or near sandstone-shale boundaries (Bigotte and Obellianne 1968; Bowden et al. 1981). In the Arlit area, the host rocks are a succession of red clastic strata composed of interlayered conglomerate, sandstone, and siltstone with intercalated shale and volcano-sedimentary units (Cazoulat 1985), unconformably overlain by Permian-Triassic arkosic sandstone and conglomerate. Stratigraphic and sedimentological constraints indicate that these rocks were deposited in organic-rich fluviatile and fluoviodeltaic environments, in which westward paleocurrents carried detritus, minerals, and plant debris (Cazoulat 1985; Yahaya et al. 1986; Forbes et al. 1988). Tectonic uplift, anorogenic magmatism, and subsequent weathering and erosion of the volcanic cover, together with sedimentation in nearby continental basins, all contributed to the development of the uranium mineralization (Bowden et al. 1981).

Important uranium ore deposits such as Arlit, Imouraren, and Azelik occur along the eastern part of the Arlit-in Azawa regional lineament (Cazoulat 1985) close to the contact with oxidized rocks (Pagel et al. 2005). This major fault, which is interpreted as a polyphase Pan-African structure that was reactivated during the Visean, late Carboniferous, and Early to Late Cretaceous (Valsardieu 1971; Forbes et al. 1988), appears to have been a critical factor in ore genesis, providing a fluid channel for U-bearing fluids. In addition to faults or faulted rocks, main ore controls include stratigraphic contacts and lithology, paleogeography, availability of organic matter, movement of underground waters, and redox state (i.e., Eh vs. pH).

The uraniferous deposits are strongly controlled by sedimentary structures (Turpin et al. 1991) and form either massive stratiform to stratabound concentrations or intergranular matrix cements in bottomset layers and along basal fore-set layers (Sanguinetti et al. 1982). Roll-front-type structures have been reported in the Akouta deposit (e.g., Cazoulat 1985; Pagel et al. 2005, and references therein). Principal uranium minerals are pitchblende and coffinite (Bowie 1979) accompanied by varying proportions of sulphides (pyrite, marcasite, and sphalerite), and montroseite (VOOH) that is a highly oxidized vanadium hydroxide (Forbes et al. 1986, 1987, 1988). Gangue minerals include vanadiferous chlorite, corrensite, and jordisite (Turpin et al. 1991). Relatively high Nb and Zr concentrations have been reported in the ore (Forbes 1984; Turpin et al. 1991). Fluid inclusion studies indicate that the ore-forming fluids were evolved, basin-derived, hot (80–180 °C), saline brines (Forbes et al. 1987; Forbes 1989), consistent with vitrinite reflectance measurements, Rock-Eval pyrolysis data, and C, H, and O stable isotope values (Forbes et al. 1988). U–Pb and K–Ar data constrain the age of uranium mineralization to between ~260 and 130 Ma, with two distinct peaks occurring at ~190 and ~150 Ma (Turpin et al. 1991; Pagel et al. 2005). These geochronological results contrast with the Visean age (335 Ma) of the host Guezouman Formation, and seemingly rule out an early syndiagenetic origin for the U ore, as suggested by Cazoulat (1985). Rather, the recorded radiometric ages imply an epigenetic and polyphase emplacement for Niger's sediment-hosted uranium mineralization. Available geochemical data suggest an origin involving the mixing of reduced, U-bearing basement-derived brines with shallow oxidized ground waters along the Arlit-in Azawa regional lineament. Indeed, the presence of V-rich minerals (e.g., montroseite; Forbes et al. 1986) and U-bearing species provide further support for fluid mixing between V-bearing ground waters and U-bearing basinal brines. Pan-African metamorphic and alkaline to calc-alkaline crystalline basement rocks, together with the eroded volcanic cover of the Paleozoic ring complexes of the nearby Aïr massif, constitute the most viable source reservoir to have provided the required U and, by inference, associated metals for the sandstone-hosted U mineralization (Bigotte and Obellianne 1968; Bowie 1979; Bowden et al. 1981; Forbes et al. 1984; Cazoulat 1985; Turpin et al. 1991; Pagel et al. 2005).

29.11 Sediment-Hosted Stratiform Copper Deposits

Sediment-hosted stratiform copper deposits are common worldwide and account for approximately 23 % of global Cu production and known reserves (Hitzman et al. 2005). In North Africa, economically important deposits occur in the central and western Anti-Atlas system of Morocco, within two sedimentary successions of contrasting age, Neoproterozoic and terminal Neoproterozoic-Cambrian (Fig. 11). Major orebodies include the historically mined Bleïda deposit (2.5 Mt at 2 % Cu; Maacha et al. 2011b), and newly rediscovered and reevaluated deposits at Jbel Laassel (7.5 Mt at 1 % Cu; Maacha et al. 2011c; Bourque et al. 2015), Tizert (30 Mt at 1 % Cu and 20 g/t Ag with mineral potential over 100 Mt; ManagemGroup Confidential report), Jbel N'Zourk (4 Mt at 0.8 % Cu; Maacha et al. 2011d), Tazalaght (3 Mt at 1.5 % Cu; El Basbas et al. 2011), Agjgel (5 Mt at 1 % Cu; Maddi et al. 2011), and Amadouz (1–2.5 Mt at 1 % Cu) (Fig. 11). Collectively, these deposits and associated prospects and showings delineate a new Moroccan copper metallogenic province in the western and central Anti-Atlas, with mineral resources estimated at >100 Mt grading 1 % Cu (ManagemGroup unpublished data). These inferred resources are comparable to the production and reserves of some giant deposits of this type in the Zambian portion of the Central African Copperbelt (Hitzman et al. 2005), and as such, Morocco is positioned to become the top copper-producing country in North Africa.

At the Bleïda deposit, the host rocks are lower Neoproterozoic rift-fill metamorphosed volcanosedimentary strata assigned to the Tachdamt-Bleida Formation of the Taghdout-Lkest Group (Thomas et al. 2002). This sedimentary sequence, which forms the upper part of the Bou Azzer ophiolite complex, consists from base to top of: (1) a 300–400-m-thick succession of alternating siltstone and carbonate strata that grades upward to quartzite and stromatolitic limestone, all of which are interpreted as shallow-water shelf sediments deposited on a continental margin (Leblanc and Moussine Pouchkine 1994); (2) submarine tholeiitic basaltic flows that were emplaced at 762 ± 9 Ma (Rb/Sr; Clauer et al. 1976); (3) a tectonically overlying volcanosedimentary sequence 300–400 m thick composed of organic- and pyrite-rich black shale with intercalated pyroclastic units (i.e., ash and tuff) referred to hereafter as the Ore Shale; and (4) a 500-m-thick sequence of turbidite fans (Leblanc and Billaud 1978, 1990) that form the hanging wall of the deposits. Major orebodies occur along two main copper-bearing units referred to as the lower and upper horizons, both being spatially associated with synsedimentary faults and felsic igneous rocks (Leblanc and Billaud 1990), and are similar in terms of mineralization style, morphology, mineralogy, and alteration patterns. The lower mineralized horizon has af lower grade (i.e., southern mineralized zone with total production of 700,000 t at 3 % Cu; Maacha et al. 2011b) and occurs along the interface between the thick basaltic sequence and the lowermost part of the Ore Shale, whereas the upper mineralized horizon has a higher grade (i.e., northern mineralized zone with total production of 1.8 Mt at 9.3 % Cu; Maacha et al. 2011b) and is confined to the uppermost part of the Ore Shale, close to the contact with the overlying turbiditic unit. In both mineralized horizons, copper forms either massive, 5–15-m-thick lenses, fine- to medium-grained disseminations, finely laminated stratiform ore, and/or anastomosing veinlets and stockworks.

Sulphide minerals include variable proportions of bornite, chalcopyrite, and pyrite. Neither sphalerite nor galena has been documented in the deposit. Hydrothermal alteration assemblages consist of chlorite, sericite, and Ti-bearing species such as anatase, pseudobrookite, and leucoxene with accessory albite, quartz, calcite, and tourmaline (Leblanc and Billaud 1990). The spatial distribution of sulphide minerals shows a mineral zoning developed along major N70° E-trending synsedimetary faults, in which an inner core zone is dominated by bornite grading laterally to chalcopyrite and distally to pyrite (Leblanc and Billaud 1990; Mouttaqi and Sagon 1999). This mineral zoning, together with the

occurrence of ferrugineous jasper and inferred Na–Mg–Fe–Si exhalative chemical sediments, led Mouttaqi and Sagon (1999) to classify Bleïda as a sedimentary-exhalative (SEDEX) deposit; previously, Leblanc and Billaud (1978, 1990) invoked a synsedimentary hydrothermal origin related to felsic volcanism. A syngenetic plus overprinting epigenetic model was proposed by later workers including Leblanc and Arnold (1994) and Maacha et al. (2011b). In this regard, available sulphur isotope data suggest multiple sulphur sources including biogenic and magmatic-hydrothermal end members (Leblanc and Arnold 1994

Host rocks of the copper mineralization related to the newly delineated Moroccan copper belt of the western and central Anti-Atlas system are late Neoproterozoic to Cambrian arenite and carbonates, and minor shale. These strata, which unconformably overlie Neoproterozoic and older basement rocks, are stratigraphically assigned to the Taroudant and Tata Groups (Soulaimani et al. 2013) that comprise a lower section of red-bed arenite overlain by trangressive marine carbonates and/or shale having variable permeabilities and oxidation states (El Basbas et al. 2011; Maacha et al. 2011b, c, d; Maddi et al. 2011; Bourque et al. 2015; and present study). Major orebodies occur either at the boundary between late Neoproterozoic-Lower Cambrian units, or more importantly at the uppermost part of the clastic sequence or within the basal portion of the Cambrian marine transgressive sequence, particularly within dark, organic-rich dolostone (i.e., Tamjout dolostones). These dolomite-rich rocks, which constitute regional stratigraphic and lithologic metallotects, grade upwards into a predominantly siliciclastic sequence capped by black shale. Spatially associated igneous rocks consist of the Jbel Boho syenite and trachyandesitic volcanic rocks dated at 534 ± 10 Ma (Ducrot and Lancelot 1977), and a younger Jurassic dike swarm (Bourque et al. 2015).

In all deposits of the newly delineated copper metallogenic province, copper mineralization seems to be controlled by paleogeography (i.e., presence of basement highs) and tectonics with most orebodies confined to the apexes of anticlines and associated faults. Hypogene sulphides consist of varying proportions of chalcopyrite, bornite, and chalcocite; non-sulphide copper assemblages include malachite, covellite, digenite, chrysocolla, tenorite, native copper, and cuprite. Dominant gangue minerals are quartz and calcite. As discussed for sediment-hosted stratifrom copper deposits worldwide, debate continues over the timing of this copper mineralization. Proposed genetic models, in the absence of reliable geochemical data, range from syngenetic (Leblanc and Billaud 1990; Mouttaqi and Sagon 1999) to epigenetic (Bourque et al. 2015), the latter supported by the presence of multiple stages of Cu mineralization.

29.12 Sediment-Hosted Manganese Deposits

Manganese mineralization occurs globally in a wide range of deposit types including sediment-hosted, hydrothermal, and residual. Among these, sediment-hosted deposits occurring on the margins of reduced (anoxic) marine basins in response to transgressive-regressive events are by far the largest in term of tonnage and ore grade (Force and Maynard 1991; Maynard 2010). The formation of sediment-hosted Mn deposits peaked during three time periods (1) Paleoproterozoic, (2) Neoproterozoic, and (3) Cenozoic.

In North Africa, the largest deposits are stratigraphically assigned and temporally related to the youngest group. Of these, the most productive is the Imini deposit in southern Morocco (Force et al. 1986; Lalaoui et al. 1991; Rhalmi et al. 1997; Gutzmer et al. 2006; Dekoninck et al. 2015; Dekoninck et al. this volume), making this country one of the major global suppliers of non-metallurgical Mn ore (Harben 1999). The historically mined Imini deposit in the central Anti-Atlas orogen (Fig. 11) remains the largest high-grade manganese deposit in North Africa, with total cumulative production exceeding 10 Mt at 72 wt% MnO_2 (Lalaoui et al. 1991). Current annual production is approximately 50,000 t of high-grade concentrate (>92 wt% MnO_2).

Host rocks at the deposit are a succession of Cenomanian-Turonian (Cretaceous; 88.5–97.0 Ma) clastic and dolostone strata that record shallow-water, near-shore deposition (Thein 1990). High-grade ores are contained mainly in shallow-marine porous dolostone composed of bioturbated biomicrite and coarse-grained dolosparite with interlayered silty and marly intercalations. Mn-oxyhydroxide mineralization extends in a roughly E-W trend more than 40 km long and 1 km wide, and is confined to three laterally continuous dolostone beds referred to as C_1, C_2, and C_3; orebodies are stratiform (Force et al. 1986) to stratabound, the latter occurring as fillings of karstic caves (Gutzmer et al. 2006; Dekoninck et al. this volume). The resulting high-grade Mn accumulations are interpreted to be closely linked to Late Cretaceous paleogeographic evolution of the North Atlantic Ocean (Thein 1990). Ore mineralogy consists mainly of pyrolusite, cryptomelane, hollandite, coronadite, romanechite, and lithiophorite (Gutzmer et al. 2006; Dekoninck et al. 2015). The peculiarity of the Imini ore resides in unusually high Mn/Fe ratios and exceptional enrichment in barium and lead, reaching up to 7 wt% Pb in coronadite-rich samples and up to 5 wt% Ba in hollandite and psilomelane (Thein 1990; Gutzmer et al. 2006).

Analogous to models proposed for sediment-hosted manganese deposits worldwide, those for the Imini mineralization range from syngenetic (Thein 1990; Lalaoui et al. 1991; Rhalmi et al. 1997) to epigenetic (Pouit 1964, 1976; Gutzmer et al. 2006; Dekoninck et al. 2015), with metals being derived from underlying alkali feldspar-rich igneous basement rocks of the Anti-Atlas orogen. Alternative models invoke syngenetic processes plus overprinting epigenetic mineralization (Force et al. 1986) or lateritic weathering (Thein 1990; Dekoninck et al. 2015). The surficial environment provided supergene conditions suitable for the deposition of the Mn-oxyhydroxides (Dekoninck et al. 2015). However, regardless of the origin (i.e., syngenetic vs. epigenetic), all existing genetic models for the Imini deposit emphasize the importance of physicochemical factors and advocate manganese precipitation during periods of high sea-level stand, a warm climate, and global anoxic conditions in the ocean, including coastal zone mixing between metal-rich, reduced meteoric waters and oxygenated surface waters. Redox state also seems to have played a crucial role in Mn ore deposition (Dekoninck et al. this volume).

29.13 Sediment-Hosted Phosphorite Deposits

More than 75 % of the world's phosphate production derives from sediment-hosted marine phosphate rocks (i.e., phosphorite deposits). These deposits range in age from Paleoproterozoic to Cenozoic, although some eras appear more productive than others. In fact, several phosphogenic periods are of global extent, principally in the Precambrian and Cambrian of Central and Southeast Asia, the Permian of North America, the Jurassic and Early Cretaceous of Eastern Europe, the Late Cretaceous through Eocene of North Africa, and the Miocene of North America (e.g., Cook 1976). The formation of phosphorite deposits requires the interaction of favorable paleoceanographic, paleogeographic, and paleoclimatic ingredients (Sheldon 1980). Large sulphur bacteria may also play an important role based on studies of phosphate accumulations in modern shelf sediments of Namibia and Peru (Schulz and Schulz 2005; Cosmidis et al. 2013).

The largest high-grade sedimentary phosphorites form at low latitudes in areas of upwelling and high organic productivity, principally along the west coasts of continents or, in large Mediterranean seas, along equatorial side of the basin (Sheldon 1964). Many of the most extensive and commercially valuable phosphate basins in the world are in Upper Cretaceous to Lower Tertiary (Eocene) strata of North Africa, from Morocco to Egypt eastward (Fig. 9) within the so-called Mediterranean or Tethyan phosphogenic province (Notholt 1987; Lucas and Prévôt-Lucas 1995). Giant deposits occur in the Western Meseta domain of Morocco, and to a lesser extent in Tunisia, Egypt, and Mauritania.

Collectively, North Africa contains one of the three largest phosphorite provinces in the world, with identified phosphate resources of 62.75 Gt (Notholt et al. 1989). The U.S. Geological Survey (2010b) reported that the phosphate rock reserves of Morocco total 5.70 Gt and are 100 Mt for Tunisia, Egypt, and Mauritania combined. Morocco alone accounts for one third of international trade in phosphate rock with an annual output of 21 Mt, equivalent to about 15 % of total global production (Notholt et al. 1989). Moreover, Morocco hosts the world's largest high-grade phosphate deposits that together—including those in Moroccan Western Sahara—constitute three quarters of global land-based reserves of 67 Mt (U.S. Geological Survey 2014).

Tunisia is the second-largest phosphate producer in North Africa with a total annual average production of about 8 Mt of phosphatic rock in recent years. Algeria has been a major producer since the late 1800s (Savage 1987) with current production of about 2 Mt/year. In Egypt, annual phosphate rock production averages about 1.5 Mt (Zhang et al. 2006). In addition to these giant to world-class deposits, medium-sized phophorite deposits occur in Mauritania, Mali, and Niger that contain phosphate resources of 100, 12, and 100 Mt, respectively (Notholt et al. 1989).

In Morocco, phosphorite deposits occur in four major basins of Late Cretaceous to early Eocene age, including (1) Oulad Abdoun covering an area of 10,000 km^2, (2) Ganntour, (3) Meskala, and (4) Oued Eddahab-Bou Craa (Fig. 11), all of which are owned and explored by the "Office Cherifian des Phosphates" (OCP). At the end of 1986, Morocco's reserves were estimated at 64.45 Gt, of which 28.0 and 15.0 Gt are in the Oulad Abdoun and Ganntour basins, respectively. The Oued Eddahab-Bou Craa deposits of Moroccan Western Sahara were estimated to have ca. 1.6 Gt of phosphate with half of the ore reserve averaging 31 wt% P_2O_5 (Zhang et al. 2006). Host rocks there consist of a thick succession of alternating Maastrichtian to Lutetian shallow-marine mudstone, dolomitic limestone, clay, marl, sandstone, and chert that were deposited during transgressive-regressive cycles (Daafi et al. 2014; El Haddia et al. 2014; Kocsis et al. 2014). The contained phosphate-rich strata have a stratigraphic range of about 25 m.y. (Gheerbrant et al. 2003), which represents the greatest duration of phosphate deposition known in the Tethyan province. Overlying barren sediments consist of Lutetian dolomitic limestone or locally Neogene continental deposits. Carbon and oxygen isotope data suggest a sedimentary gap during the latest Thanetian and the Paleocene-Eocene thermal maximum (Kocsis et al. 2014). Geochemically, Moroccan phosphorites are characterized by relatively low contents of silica, iron, and aluminum and by exceptionally high phosphate concentrations that exceed 35.7 wt% P_2O_5 (78.0 % BPL [Bone Phosphate of Lime]; 1 % P_2O_5 = 2.185 % BPL).

Phosphate accumulations along the Algerian-Tunisian border occur predominantly in the Gafsa basin of western Tunisia and the Djebel Onk and Tebassa areas of adjacent Algeria (Notholt et al. 1989; Boulemia et al. 2015) (Fig. 11). Host rocks consist of a succession of Paleocene to Eocene, shallow-marine, interlayered dolomitic limestone, marl, clay, and chert of the Metlaoui Formation. More than 90 % of Tunisian phosphorites are currently mined from the Gafsa basin where approximately 500 Mt of phosphate rock is presently economic (Zhang et al. 2006). Estimates of total resources range from 2.5 to 1.10 Gt at 12–15 wt% P_2O_5 (Savage 1987). During the Maastrichtian–Paleogene, the intracratonic Gafsa basin was connected to the open sea westward, and periodically had a restricted water mass in the east (Zaïer et al. 1998). Sedimentation fluctuated from relatively deep marine to lagoonal environments. In Lower Maastrichtian time, marly phosphorite with interlayered dark marl was deposited. The phosphate strata locally reach 1 m in thickness (Ounis et al. 2008). REE contents range from 420 to 1700 ppm, and together with carbon and oxygen isotope constraints, indicate that the depositional environment during phosphatization shifted from early suboxic to later anoxic conditions under a consistently warm climate (Ounis et al. 2008). The higher REE contents—

especially for heavy REE—in some of these deposits may be economically recoverable using leaching technology (Emsbo et al. 2015, and references therein).

In Algeria, the most important phosphate deposit occurs along the western extension of the Tunisian Gafsa basin (Fig. 11) within which total phosphate resources are estimated at about 1.00 Gt (U.S. Geological Survey 2010c). Very few published geological data are available on these deposits, however.

In Egypt, major phosphorite deposits form part of the Middle Eastern to North African phosphogenic province of Late Cretaceous to Paleogene age. These deposits occur close to the Red Sea coast, in the Nile Valley, the Eastern Desert, and Western Desert in the Abu Tartur area, between latitudes 26°40′N and 29°30′N (Awadalla 2010) (Fig. 11). Phosphate resources have been estimated to exceed 3.00 Gt (Notholt 1985) at grades of 20–28 wt% P_2O_5. The U.S. Geological Survey (2010d) reported Egyptian reserves of 100 Mt. Host rocks to the deposits consist of alternating Upper Campanian to Early Maastrichian, shallow-marine shale, chert, porcellanite, glauconitic sandstone, and fine-grained bioclastic carbonate (Glenn and Arthur 1990); these strata are assigned to the Duwi Formation (Youssef 1957), the Sibaïya Phosphate Formation (EL-Nagger 1966), and the Phosphate Formation (Awad and Ghobrial 1965). Among these, the Maghrabi-Liffiya province contains the most important phosphorite deposits in the Abu Tartur area, based on large thicknesses and high grades of a lower phosphorite bed having ~20–30 wt% (avg ~ 25 wt%) P_2O_5. Geochemical data indicate low U contents of 15–34 ppm with an average of 22 ppm, but relatively high total REE contents from 519 to 1139 ppm with an average of about 879 ppm (Awadalla 2010). Sedimentary facies analysis suggests that the major phosphorite beds represent transgressive lag deposits that accumulated in an oxic, bioturbated, wave-dominated shelf environment (Baioumy and Tada 2005).

In southwestern Mauritania, close to its southern border with Senegal, the largest phosphorite deposits of this country are Bofal and Loubboïra (Fig. 11). Paleogeographically, these two deposits encompass a total area of 68 km^2 within the large Cretaceous to Tertiary Senegal-Mauritania-Guinea basin. The phosphatic succession consists of variably thick (>1 m up to 10 m), Middle Eocene (early Lutetian) phosphate-dolomite-claystone rocks (Prian 2014). Phosphorous mineralization is in one to five, 0.5–3 m-thick units composed of fine- to coarse-grained phosphatic rudite. Resources have been estimated at 115–118 Mt, of which only ~42 Mt at a minimum grade of ~20 wt% P_2O_5 would be exploitable (Prian 2014). This moderate grade has been interpreted as reflecting the absence of a well-defined trapping or concentration mechanism (e.g., reworking) and the action of long-shore currents that spread and disseminated phosphorus nutrients into other sediments (Prian 2014). In addition to these deposits, uneconomic sedimentary phosphate prospects of Neoproterozoic/Cambrian age are documented in northwestern Mauritanian, within the Taoudeni basin (Dallmeyer and Lécorché 1990; Markwitz et al. 2015).

29.14 Other Deposit Types

Besides the mineral deposit types described above, a wide variety of additional metallic and non-metallic deposits occurs throughout the diverse terranes of North Africa (Figs. 9 and 11). Of these, the most significant belong to categories of vein-type, skarn-hosted, sedimentary-exhalative (SEDEX), paleoplacer, oolitic ironstone/lateritite, and residual deposits.

Polymetallic veins are historically amongst the oldest exploited mineral deposits in North Africa with significant contained resources of Sn–W, Mo–Ag–Bi–U, Pb–Zn–Cu–Ag, F, Ba, and other commodities. These deposits are hosted in a wide range of rock types of different ages, including igneous, metamorphic, and clastic sedimentary lithologies. Major variations exist among deposits in terms of mineral assemblages, production, and ore grades.

The economically most attractive deposits are spatially associated with Pan-African, late

Hercynian, and Alpine granitoid intrusions. Genetic models for these deposits remain controversial, including purely magmatic through magmatic-hydrothermal to basinal sedimentary processes (e.g., Margoum et al. 2015). The largest and best documented examples—some extending over a strike length of 10 km—are the Pb–Zn–Cu ± Ba ± F vein deposits of Aouli, Bou Skour, El Hammam, Assif El Mal, and Sidi Lahcen in Morocco (Bouabdellah et al. 2009; Bouabdellah et al. this volume and Table 1), and the five-element (Ni–Co–As–Ag–Bi (± U) vein deposits of Bou Azzer, Morocco (Bouabdellah et al. this volume) and those in Algeria (Suzaki et al. 2013, Marignac et al. this volume), Tunisia (Bejaoui et al. 2011, 2014), Sudan (Ismail et al. 2015), and Egypt (Helmy et al. 2014).

A common feature shared by many of the base-metal deposits is high silver grades that in places reach more than 1000 g/t (Rossi et al. this volume). Recent geochemical and geochronological investigations indicate that these silver-rich Pb–Zn–Cu ± Ba ± F vein-type deposits were emplaced under an extensional setting from low-temperature, NaCl–$CaCl_2$ brines, with fluid mixing and wall-rock interactions being the main processes that triggered ore deposition (Bouabdellah et al. 2009; Margoum et al. 2015, and references therein).

Numerous U and W–Sn–Ta–Li–Be-bearing veins, greisens, are related placers are also associated with Pan-African to late Hercynian granitoid intrusions in Egypt, Algeria, Niger, Morocco, and elsewhere in North African (Figs. 9 and 11). Notable and well-documented examples include the El-Erediya and El-Missikat post-tectonic plutons in the Eastern Desert of Egypt, where rare-metal and associated vein-type uranium deposits occur within NE- to ENE-trending shear zones. Primary uranium mineralization consists of pitchblende accompanied by jasper and black silica (Hussein et al. 1986). The albite granite-hosted Sn–W Mueilha deposit is one of many other Sn–W ± F deposits (i.e., Igla, Nuweibi, and Abu Dabbab) scattered throughout the Eastern Desert of Egypt (Amine 1947) (Fig. 10). Cassiterite and/or wolframite, sheelite, and beryl are principal ore minerals, which occur in greisens and quartz veins. Fluid inclusion data suggest that Sn–W deposition formed in response to immiscibility at temperatures of 340–260 °C, and estimated pressures between 2.2 and 1.2 kb. In contrast, associated fluorite mineralization is attributed to mixing of at least two fluids at minimum temperatures of 140–180 °C and an estimated minimum pressure of 800 bars (Abdel-Moneim 2013).

In the Pan-African Hogger massif of the Tuareg Shield in southern Algeria, about 100 Sn–W–Ta–Li–Be–bearing occurrences have been delineated, ten of which are of potential economic interest (Marignac et al. this volume). Overall, the economic and sub-economic deposits and prospects have been subdivided into (1) Sn–W–quartz (± greisen) type (i.e., Taourirt deposit); (2) disseminated cupola type (i.e., Amzi, Ebelekan, and Rechla deposits); and (3) Be-pegmatite bodies, known at Guerioun (containing large euhedral beryl crystals up to 20 cm), Nahda, and Rechla (Marignac et al. 2001; Kesraoui 2005; Suzaki et al. 2013). Other polymetallic "mesothermal" vein-type occurrences are in the Edough-Cap de Fer polymetallic district of northeastern Algeria (i.e., Aïn Barnar, Mellaha, and Saf deposits; Marignac et al. this volume). In Niger, Be mineralization together with Cu–Pb–Zn–bearing quartz veins occur within the Taghouaji biotite granite of the Aïr massif (Perez et al. 1990).

Moroccan Sn ± W vein-type deposits are closely related to the magmatic and magmatic-hydrothermal evolution of late Hercynian granitic intrusions of the Paleozoic Central massif of the western Meseta domain. One example is at the abandoned El Kirat Sn–Be mine (33°25′05″ N, 6°06′09″ W) (Fig. 11). The newly reevaluated Sn–W Achammach deposit (33°32′31.15″ N, 5°46′6.80″ W) has updated mineral resources of 14.9 Mt grading 0.85 % Sn, amounting to ca. 127,300 t of contained tin (Kasbah Resources Ltd. 2015).

Host rocks at the Achammach deposit consist of a strongly deformed and weakly metamorphosed Lower Carboniferous flysch sequence of shale and sandstone. Tin mineralization occurs predominantly as veins, stockworks, and breccia fillings, and to a lesser extent as disseminations mostly within intense tourmaline-silica replacement zones referred to as "lodes." Resulting mineralized structures form a 500-m-wide array with individual lodes ranging in width from a meter up to 30 m. The tin assemblage consists exclusively of cassiterite without any tungsten-bearing minerals; quartz is the sole gangue mineral. The mineralized system has been defined by diamond drill holes to a vertical depth of approximately 600 m (www.pdac.ca/…/new-discoveries—chaponniere.pdf).

The El Karit Sn–Be vein-type deposit consists of five main orebodies referred to as Marsouin I, Marsouin II, Hirondelle I, El Karit, and Hirondelle II (Boushaba 2011). Tin mineralization occurs along the contact of the western margin of the late Hercynian (308–296 Ma) Oulmes peraluminous granite and adjacent contact metamorphosed Cambro-Orovician biotite schist. Semi-artisanal mining undertaken between 1925 and 1974 resulted in the production of about 750 t of tin concentrate at an average grade of ca. 65 % Sn (Anonymous 2011).

Skarn-hosted polymetallic deposits and related replacement bodies, commonly occurring as veins, hydrothermal breccias, and stratabound massive lenses, are widely distributed either within (endoskarn) or adjacent to granitic intrusive complexes within metasomatized carbonates (exoskarn). The most productive and significant deposits are associated with Pan-African (El Habaak 2004; Marignac et al. this volume) to late Hercynian granitoid intrusions, and to a lesser extent with Alpine plutons. Late Hercynian examples in Morocco include the Azegour Cu–Zn–Mo–W deposit of the western High Atlas Mountains (Berrada et al. 2011; Ibouh et al. 2011; El Khalile et al. 2014) and the Sn–W ± Pb–Zn–Ag province of the Paleozoic Central massif of the western Meseta (i.e., El Hammam-Achemmach district; Jébrak 1982, 1984; Cheilletz 1983, 1984; Sonnet and Verkaeren 1989; Boushaba and Qalbi 2011). Stratigraphically, the El Hammam-Achemmach Sn–W skarn district contains an intensely deformed and greenschist-facies Cambro-Ordovician flysch sequence composed of intelayered shale and carbonate with subordinate volcanic and volcaniclastic rocks, all of which are intruded by several exposed (i.e., Zaers, Ment, and Oulmes) and buried (i.e., El Hammam coupola; Bouabdellah et al. this volume) calc-alkaline granite stocks dated at ca. 290 Ma (Guiliani and Sonnet 1982). Tin-tungsten mineralization consists of cassiterite, wolframite, scheelite, or molybdenite in veins and scheelite-bearing skarns (Guiliani 1984; Cheilletz 1985; Sonnet and Verkaeren 1989). At the Azegour deposit (31°08′59″N, 8°18′14″W), the host rocks are Lower Cambrian folded and greenschist-facies pelite and interlayered limestone together with volcanic and volcaniclastic rocks, intruded by the Hercynian Azegour monzogranitic pluton dated at 273 ± 2 Ma (Berrada et al. 2011; Ibouh et al. 2011). Skarn orebodies occur within the metamorphic aureole surrounding the Azegour pluton. The dominant mineral assemblage consists of varying amounts of molybdenite, scheelite, and chalcopyrite ± cassiterite ± fluorite ± apatite-zircon-titanite. Also documented in the deposit are occurrences of Ni–Co–Ag–Be–U–bearing minerals (Permingeat 1957; Agard et al. 1966).

Skarn-hosted deposits are commonly associated spatially with deep-seated porphyry to epithermal mineralizing systems (Mamedov et al. 2012; Bouabdellah et al. this volume). To our knowledge, no major porphyry-type orebodies occur in North Africa. However, one possible candidate is described by Markwitz et al. (2015) who cited the Kourki Cu–Mo deposit in southwestern Niger as being of this type. In this regard, a limited diamond drill exploration program there by Orezone Resources Inc. has intersected significant Mo and Cu mineralization over long intervals, including typical Mo–Cu zoning in the tested area (http://www.orezone.com). Some porphyry-style occurrences are also documented in the Um Zerriq area of the Neoproterozoic Kid belt in the southeastern Sinai of Egypt (Mamedov et al. 2012).

Sedimentary-exhalative (SEDEX) deposits are poorly documented in North Africa. In the literature, the only described SEDEX deposits are Sidi Driss and Douahria of the Nefza mining district in northern Tunisia (Decrée et al. 2008a, b, this volume) (Fig. 11). Host rocks there consist of Upper Miocene carbonates overprinted by Fe and Mn during early diagenesis and later partially to totally replaced by barite and celestite. Zn–Pb–Fe mineralization occurs as open-space fillings and partial to massive replacements of dedolomitized limestone. The ore mineralogy is dominated by sulphides (i.e., sphalerite, galena, marcasite, and pyrite) together with barite and celestite, and, to a lesser extent, fluorite, siderite, and ankerite. At the Sidi Driss deposit, carbonate-hosted mineralization predominates, whereas at the Douahria deposit celestite-hosted mineralization is the most important (Decrée et al. 2008a, this volume).

In Morocco, the Bleida stratiform copper deposit of the central Anti-Atlas Mountains (Fig. 11) described above has been classified as SEDEX based on the occurrence of ferrugineous jasper and Na–Mg–Fe–Si chemical sedimentary rocks or exhalites (Mouttaqi and Sagon 1999). However, this classification has been challenged by several workers who emphasize the epigenetic character of the copper ores, instead classifying the Bleida mineralization as a sediment-hosted copper deposit (Leblanc and Arnold 1994; Maacha et al. 2011b; present study, and references therein).

Significant beach placer deposits of Cenozoic to Quaternary age occur along the Atlantic Ocean and Mediterranean coasts of Mauritania, Morocco, Algeria, Tunisia, and Egypt (Fig. 11). The most significant of these are the ilmenite ± zircon ± hematite ± vesuvianite ± monazite ± rutile ± corundum Jreida-Lemsid placer deposit of Mauritania (Markwitz et al. 2015), and the black sand deposits of the northern Mediterranean coastal plain of the Nile Delta and Sinai Peninsula in Egypt (Hedrick and Waked 1989; Dawood and Abd El-Naby 2007). It is noteworthy that the Egyptian black sand deposits constitute huge reserves of ilmenite, magnetite, garnet, zircon, rutile, and monazite (Mahmoud et al. 2013). Beside these coastal beach accumulations, eluvian and alluvial placer deposits in Egypt, Sudan, Niger, Mali, and Mauritania have been worked since Predynastic (ca. 3000 BC) times, and remain important sources of gold, diamonds, and precious stones including rubies, sapphires, and emeralds (Klemm et al. 2001). Most of these deposits are developed near primary and secondary gold deposits adjacent to major cratons, having been concentrated in ancient to modern stream channels. Indeed, alluvial diamonds have been found over very large parts of Mali along river drainages. Two promising tracts in terms of diamond potential have been delineated: (1) the Kenieba region in the western portion of Mali along its border with Senegal (Fig. 11), and (2) the Bougouni region south of Bamako near the border with Guinea and Côte d'Ivoire (Chirico et al. 2010). Some gossans developed on sulphide orebodies and their attendant eluvial deposits have been mined, or are being mined currently, for precious metals including gold. Residual deposits are widespread throughout terranes of North Africa, the most important being ferrugineous laterites of western Mali and Egypt (Aly 2015), low-grade bauxite deposits occurring along the Niger River, and large bentonite deposits of Morocco, Algeria, and Tunisia.

In Morocco, extensive bentonite deposits occur in the eastern termination of the Alpine Rif-Tell belt surrounding the Neogene Gourougou and Tidiennit stratovolcanoes (Fig. 11). Host rocks are thick beds of volcanic and volcaniclastic rocks within Miocene (Messinian) sediments. The deposits are spatially associated with Upper Miocene to Pleistocene (8.2–0.65 Ma), predominantly calc-alkaline volcanic rocks (El Bakkali et al. 1998; Duggen et al. 2005). The main orebbodies, which are owned and exploited as open pits by Spanish, Greek, German, and Moroccan mining companies, are Providencia, Trebia (inferred resources of 1.44 Mt), Azzouzet (inferred reserves of 430,000 t), Iboughardain (inferred reserves of 725,000 t), Afrah-Haïdoun (inferred reserves of 627,000 t), Ikesmiouen (inferred reserves of 500,000 t), Tizza, and Tighza. Collectively, these deposits

are currently producing more than 120,000 t of bentonite annually, with remaining reserves estimated at ~4 Mt (Eisenhour and Reisch 2006; and present study). The exploited bentonite deposits consist predominantly of smectite with subordinate zeolite and tridymite as neoformed minerals; plagioclase, K-feldspar, amphibole, and mica occur as detrital phases. Ores are magnesium-rich with extractable interlayer cations of magnesium and sodium. Average purity of the smectites is up to 98 %. The origin of the bentonite deposits is attributed to: (1) hydrothermal alteration of perlitic glass inside of the volcanoes, (2) hydrothermal alteration of pyroclastic flows in a shallow marine to lagoonal lacustrine environment, and/or (3) hydrothermally altered ash falls in marine or lacustrine settings. All of these deposits are interpreted as having formed from a parent rhyolitic magma at different stages of differentiation (Ddani et al. 2005). Similar bentonite deposits of the same age and geological environment occur in Algeria (Maghnia and Mostaghanem deposits; Abdelouahab et al. 1988) and northern Tunisia (Nefza region; Sghaier et al. 2014), on the eastern extension of the Moroccan volcanic province. Products of the hydrothermal alteration are closely related to the composition of the protolith and to physicochemical aspects of the geological environment, which in turn are controlled by climatic, tectonic, and geomorphological processes over time.

29.15 Time-Space Distribution of Major Mineral Deposit Types: Metallogenic Epochs and Provinces

As stressed above, North Africa is richly endowed with mineral deposits of different types that are widely distributed in space and time, occurring in all lithotectonic terranes and ranging in age from Pleistocene-Quaternary to Archean (Fig. 10). One of the critical and outstanding issues in North African metallogeny relates to the absolute age of mineralization needed to determine the time spans during which deposits formed. More important is the lack of reliable geochronological data on ages of mineralization in most deposits, owing to the generally absence of readily datable and robust ore-related minerals, together with the complex geologic history of the investigated deposits. As a result, delineation of temporal patterns for most types of mineral deposits in North Africa is limited, and consequently also the development of reliable genetic models. Accordingly, the temporal distribution scheme presented below should be regarded as a first attempt on North African deposits, stressing major mineralizing events and an overview of time-space distributions in terms of metallogenic provinces and epochs within evolving plate tectonics, formation and break-up of supercontinents, global heat flow (super plumes), and evolution of the atmosphere-hydrosphere-biosphere system (e.g., Groves et al. 2005). For those deposits where the timing of mineralization has not been clearly established, we use an empirical approach based on the age of the host rocks as a maximum limit.

Based on absolute ages for mineralization, or alternatively for ages of the host rocks (where radiometric age determinations are lacking), seven major time periods of mineralization defining distinct metallogenetic epochs are recognized. Each has different metal associations, mineralogical and geochemical features, spatial distributions, and geodynamic environments that collectively discriminate time periods and related metallogenic provinces. These are: (1) Archean (>2500 Ma), (2) Paleoproterozoic (2500–1600 Ma), (3) Neoproterozoic (630–542 Ma), (4) Hercynian (540–290 Ma), (5) Permian-Triassic (~300–200 Ma), (6) Late Cretaceous-Paleogene (100–23 Ma), and (7) Late Miocene-present (<16 Ma).

29.16 Archean-Paleoproterozoic (2500–1600 Ma)

During the Archean and Paleoproterozoic orogenic and intrusion-related gold, IOCG, and BIF mineralization formed thus defining the largest and economically one of the most fertile time periods

in North Africa. Significantly, the major exploited ore deposits are restricted to the northern part of the WAC. Recent geochronological age determinations (McFarlane et al. 2011; Lawrence et al. 2013a, b; Heron et al. 2015; Kolb and Petrov 2015; Masurel et al. 2015; Lawrence et al. this volume) reveal two different age groupings that cluster at ca. 2.8 and 2.0 Ga. These time periods coincide with major increased rates of crustal growth and subsequent supercontinent formation and breakup, all of which are associated with mantle plumes and the development of Archean-Paleoproterozoic cratons (e.g., Groves et al. 2005). Major and well-documented examples include in Mauritania the Guelb Moghrein IOCG deposit (Meyer et al. 2006; Kolb et al. 2008; Kirschbaum 2011; Kolb and Petrov 2015; Kirschbaum and Hitzman 2016) and associated Mesoarchean to Paleoproterozoic BIFs (Bronner and Chauvel 1979; Taylor et al. this volume), the numerous Birimian orogenic and intrusion-related gold deposits of Mali (McFarlane et al. 2011; Lawrence et al. 2013a, b, Salvi et al. 2015; Markwitz et al. 2015; Masurel et al. 2015, 2016; Lawrence et al. this volume), and the Tasiast orogenic goldfield of Mauritania (Heron et al. 2015).

29.17 Neoproterozoic (630–542 Ma)

From 630 to 542 Ma, Proterozoic terranes of North Africa were affected by widespread late-orogenic, bimodal, calc-alkaline and alkaline igneous activity. This magmatism developed in response to mantle lithospheric delamination, following significant crust-mantle thickening during the Pan-African orogeny (Avigad and Gvirtzman 2009). The resulting igneous activity produced large volumes of both intrusive and extrusive rocks such as granite-syenite-gabbro plutons in ring complexes and volcanic rocks including pyroclastics. Existence of an extensional regime (Avigad and Gvirtzman 2009) favored the escape of mantle volatiles to shallow crustal levels. In turn, this process resulted in high heat flow and consequently an increased geothermal gradient and fluid activity in the upper crust, ultimately leading to formation of a wide variety of mineral deposits. Similar to the Archean-Paleoproterozoic, the Neoproterozoic era represents an especially fertile time period during which major deposits formed within all Precambrian shields in this part of the African continent.

The best documented Neoproterozoic deposits include: (1) orthomagmatic Fe–Ni–Cu–Cr–PGE ores associated with fragments of Pan-African dismembered ophiolitic complexes in the Eastern Desert of Egypt and northeastern Sudan (Abd El-Rahman et al. 2009; El-Taher 2010; Hamdy and Lebda 2011; Ahmed et al. 2012a, b), in the Bou Azzer district in the central Anti-Atlas orogen of Morocco, and Pan-African serpentinites in the Amsaga, Agane, and Gouérarate areas of the Reguibat Shield and axial zone of the Mauritanides Belt (Ould Moctar et al. 2014; Markwitz et al. 2015); (2) VHMS deposits that occur along the length of the Red Sea coast from Egypt through Sudan to Eretria (Barrie et al. this volume), and in Mali (Markwitz et al. 2015); (3) granitoid- and related pegmatite-hosted Ta–Nb–Sn–W ± REE deposits in the Eastern Desert of Egypt (i.e., Abu Dabbab and Nuweibi) and Algeria (Melcher et al. 2015; Marignac et al. this volume); (4) BIF occurrences in the central part of Egypt (Basta et al. 2011; Stern et al. 2013; Khalil et al. 2015); and (5) orogenic and intrusion-related gold-bearing quartz veins in regional mega-shear structures, including Tirek-Amesmessa in Algeria (Ferkous and Monie 2002; Marignac et al. this volume), deposits in Egypt and Sudan that fringe the Red Sea (El Boushi 1972; Klemm et al. 2001; Zoheir et al. 2008, 2014), and the Iourirn-Akka and Tiouit deposits of the Anti-Atlas Mountains in Morocco (Maacha et al. 2011a, b, c, d; Bouabdellah et al. this volume). Some mineralization related to the Bou Azzer five-element (Co–Ni –Fe–As ± Au ± Ag) and Imiter Ag–Hg deposits also formed during this time span (Bouabdellah et al. this volume).

29.18 Paleozoic (540–290 Ma)

The Paleozoic lithotectonic domain in North Africa consists of monotonous successions of

intensely folded and weakly metamorphosed Early Cambrian to Early Permian continental and marine strata together with volcanic and volcaniclastic rocks. These successions contain several types of mineral deposits, some of which have significant resources. Most described deposits occur in Cambrian-Ordovician and more importantly Carboniferous rocks; the Silurian is virtually devoid of known deposits. The Hercynian terranes, which are preferentially exposed in large inliers within Mesozoic series, are intruded by large syn- to post-collisional granitoid intrusions of Westphalian to Early Permian age (330–260 Ma) having calc-alkaline to shoshonitic, peraluminous and metaluminous compositions (El Hadi et al. 2003, 2006). It is noteworthy that the largest Paleozoic inliers and associated mineralized structures occur in Morocco, and to a much lesser extent in Algeria. Overall, the Paleozoic metallogenic history can be subdivided into three mineralizing epochs referred to as Eo-Variscan (Cambrian to Silurian), Meso-Variscan (Devonian-early Carboniferous), and Neo-Variscan (late Carboniferous-Early Permian). This classification scheme is consistent with that proposed by Marignac and Cuney (1999) for ore deposits in the Massif Central of France.

The Eo-Variscan epoch coincided with Early Cambrian rifting and includes host rocks to the newly delineated sediment-hosted stratiform copper province in the western and central Anti-Atlas that contains estimated total resources of >100 Mt of ore. Major deposits within this province are Jbel Laassel, Tizert, Jbel N'Zourk, Tazalaght, Agjgel, Jbel N'Zourk, and Amadouz. These deposits occur within transgressive siliciclastic and carbonate sequences of late Neoproterozoic, Cambrian, and Ordovician age that were deposited on basement topographic highs. Owing to the absence of radiometric data on age (s) of mineralization, the genesis of these deposits remains controversial with proposed models ranging from syngenetic to epigenetic (Bourque et al. 2015, and references therein).

The Meso-Variscan epoch (Devonian-early Carboniferous) coincided with the main collision event related to the Variscan orogeny. This epoch apparently was not a period of major mineralization since no deposits are known to have formed during this time span. Accordingly, this epoch is classified as being metallogenically barren.

Conversely, the Neo-Variscan (late Carboniferous-Early Permian) was a fertile mineralizing epoch during which several significant deposit types formed including some that contain world-class resources. Most of the ore deposits are either linked to exhalative and/or magmatic-hydrothermal processes related to Visean bimodal volcanism and/or the emplacement of late Hercynian peraluminous to metaluminous granitoids. The main Hercynian crustal-scale metallogenic peak therefore correlates with the late stages of the Variscan orogen.

The late Paleozoic was especially notable for generation of the economically largest VHMS province in northern Africa. This is reflected by the Jebilet-Guemassa bimodal ultramafic and felsic-hosted province that contains Zn–Cu–Pb massive sulphide deposits having total resources of more than 80 Mt (Bouabdellah et al. this volume). In addition to VHMS mineralization, other deposit types are spatially associated with crustal-scale, strike-slip shear zones including late Variscan gold-bearing quartz veins (i.e., Iourirn-Akka and Tamlalt–Menhouhou deposits; Gasquet et al. 2004; Pelleter et al. 2008), rare-metal granite occurrences and related W–Sn–Ta–Li–Be(± U)-bearing veins, greisens, and associated pegmatites (Belkasmi et al. 1999, 2000; Marignac et al. this volume), and Pb–Zn ± fluorite ± barite deposits. Late Carboniferous ages determined for some of these deposits cluster around 300 Ma (Watanabe 2002; Gasquet et al. 2004; Marcoux et al. 2008, 2015; Pelleter et al. 2008; Oberthür et al. 2009; Magali et al. this volume, and references therein). As stressed by Bellot et al. (2003), such deposits formed during the early stages of post-thickening extension of the Variscan lithosphere, as a result of dextral shearing between central Europe, northern Africa, and the northern Appalachians, associated with opening of the paleo-Tethys Ocean and closing of the Theic Ocean during the late Paleozoic collision of Gondwana-Laurasia.

29.19 Permian-Triassic (~300–200 Ma)

The Permian-Triassic mineralizing epoch seems to be among the most fertile in North Africa because many major deposit types formed during this time span. Regionally, this period is when most of Western Europe's polymetallic ± F ± Ba vein-type deposits formed (Sizaret et al. 2009; Wolff et al. 2015, and references herein). In North Africa, the Permian-Triassic period coincides with two major geodynamic events: opening of the Central Atlantic Ocean to the west as a result of the breakup of Pangea, and incipient opening of the Tethys Ocean to the east. Subsequent crustal thinning, together with related increased geothermal gradients and fluid activity, would have developed regional-scale convective systems that acted as the driving mechanism to move mineralizing fluids toward shallow crustal depths where hydrothermal deposits formed. Indeed, the emplacement during Pangean rifting and opening of the Tethys and Central Atlantic oceans of Triassic tholeiitic basaltic dikes, sills, and lava flows over large areas in Morocco, Algeria, and Tunisia (Marzoli et al. 1999) was contemporaneous with the genesis of numerous significant ore deposits and districts including polymetallic Jbel Tighza (280.6–267.7 Ma, Ar–Ar; Watanabe 2002; Marcoux et al. 2015; Magali et al. this volume), Aouli Pb–Zn ± F ± Ba deposits (Margoum et al. 2015), and El Hammam REE-rich F (205 ± 1 Ma, $^{40}Ar/^{39}Ar$; Cheilletz et al. 2010). Some mineralization related to the giant Imiter (Ag–Hg) deposit (254.7 ± 3.2 Ma, $^{40}Ar/^{39}Ar$; Borisenko et al. 2013), and the Bou Azzer (Co–Ni–Fe–As ± Au ± Ag) deposit (240 ± 10 Ma, Re/Os, Lendent 1960; 218 ± 8 Ma, Ar–Ar, Levresse 2001; 308 ± 31–310 ± 5 Ma, U–Pb and Sm–Nd, Oberthür et al. 2009) also formed during this time span, coincident with Pangean rifting and opening of the Tethys and Central Atlantic oceans (Muttoni et al. 2003; Martins et al. 2008; Wolff et al. 2015).

29.20 Late Cretaceous-Paleogene (100–23 Ma)

The Late Cretaceous to Paleogene epochs coincide with development of the largest sediment-hosted phosphorite deposits of the world. Contained within the so-called Mediterranean or Tethyan phosphogenic province, these deposits have total resources exceeding 70 Gt (Notholt 1987). All exploited North African deposits are of shallow-water marine origin, and occur within sequences of limestone, chalk, marl, and chert. The largest and most extensive deposits are in Morocco; smaller deposits are in Tunisia and Egypt. Moroccan examples include deposits in the giant Late Cretaceous-early Eocene basins of Oulad Abdoun, Ganntour, Meskala, and Oued Eddahab-Bou Craa that collectively—including those in Moroccan Western Sahara—host the world's largest high-grade phosphate deposits, accounting for three quarters of global land-based reserves of 67.0 Mt (U.S. Geological Survey 2014).

Paleogeographic and geodynamic reconstructions indicate that all of the North African phosphorite deposits accumulated on the continental margin along the southern side of the Tethys Seaway and are genetically related to ancient upwelling currents (Baioumy and Tada 2005; Ounis et al. 2008; Awadalla 2010; Kocsis et al. 2014). Phosphogenesis was triggered by the interplay of multiple factors including warm climatic conditions, strong upwelling currents, high biological productivity and related plankton blooms, and the production of large amounts of organic matter and subsequent accumulation on the sea floor. Most phosphorite deposits formed when sea level was relatively high or during short-lived transgressions (Baioumy and Tada 2005; Ounis et al. 2008; Awadalla 2010; Kocsis et al. 2014).

29.21 Miocene-Present Day (<23 Ma)

The Neogene period constitutes the youngest mineralizing time period recorded in North Africa. Resulting mineral deposits have diverse sizes and commodities and are distributed throughout Jurassic to Miocene terranes of Morocco, Algeria, and Tunisia. Geodynamically, the mineralizing events were coincident with: (1) widespread Neogene to Quaternary, high-K, calc-alkaline to alkaline anorogenic basaltic magmatism (El Bakkali et al. 1998; Duggen et al. 2005; Lustrino and Wilson 2007; Decrée et al. 2014; Bouabdellahg et al. 2015); and (2) a drastic paleoclimatic event at 5.96–5.33 Ma referred to as the Messinian salinity crisis (Hsü et al. 1973, 1977; Krijgsman et al. 1999), both of which are linked to collision between the African and European plates (Bouabdellah et al. 2012, 2014, 2015). Two competing models have been proposed to explain the petrogenesis of North African Neogene-Quaternary basaltic magmas: (1) subduction, slab break-off, and/or lithospheric delamination (Coulon et al. 2002; Gutscher et al. 2002; Duggen et al. 2005); and (2) intraplate mantle processes (Comas et al. 1999; Platt et al. 2003). Both models are consistent with extensional tectonics, melting, and a subsequently increased geothermal gradient. The existence of an extensional regime favors mantle volatiles escaping to shallow crustal levels, which in turn results in high heat flow and consequently an increased geothermal gradient and fluid activity in the crust. This addition of heat to the upper crust also may have promoted regional-scale convective hydrothermal circulation, which ultimately resulted in formation of the various polymetallic hydrothermal deposits and geothermal fields within the Alpine lithotectonic domain of northwest Africa. Examples include deposits of the world-class MVT district of Touissit-Bou Beker in northeastern Morocco and adjacent Algeria (Bouabdellah et al. 2012, 2015), and the polymetallic epithermal to mesothermal, vein-type and SEDEX Pb–Zn ± F ± Ba deposits of northern Algeria (i.e., Edough-Cap de Fer polymetallic district; Marignac et al. this volume) and Tunisia (Decrée et al. 2008a, b, 2013, 2014; Jemmali et al. 2011; Souissi et al. 2013; Decrée et al. this volume). Metasomatic contact aureoles developed around Neogene intrusions gave rise to numerous mineralized skarn deposits including the Ouixane Fe and Karézas W skarns (Bouabdellah et al. this volume; Marignac et al. this volume). Finally, hydrothermal to supergene alteration of the Neogene volcanic and pyroclastic rocks in shallow marine waters and lagoonal to lacustrine environments formed the numerous bentonite deposits distributed throughout the Alpine Rif-Tell orogen.

References

Aarab EM, Beauchamp J (1987) Le magmatisme carbonifère pré-orogénique des Jebilet centrales (Maroc): précisions pétrographiques et sédimentaires. Implications géodynamiques. Comptes Rendus Acad Sci Paris 304:169–174

Abdallah N, Liégeois J-P, De Waele B, Fezaa N, Ouabadi A (2007) The Temaguessine Fe-cordierite orbicular granite (central Hoggar, Algeria): U-Pb SHRIMP age, petrology, origin and geodynamical consequences for the late Pan-African magmatism of the Tuareg Shield. J African Earth Sci 49:153–178

Abdel-Moneim MM (2013) Evolution of mineralizing fluids of cassiterite–wolframite and fluorite deposits from Mueilha tin mine area, Eastern Desert of Egypt: evidence from fluid inclusion. Arab J Geosci 6:775–782

Abd El-Rahman Y, Polat A, Dilek Y, Fryer BJ, El-Sharkawy M, Sakran S (2009) Geochemistry and tectonic evolution of the Neoproterozoic Wadi Ghadir ophiolite, Eastern Desert Egypt. Lithos 113:158–178

Abdelouahab C, Ait Amar H, Obretenov TZ, Gaid A (1988) Physicochemical and structural characteristics of some bentonitic clays for north-western Algeria. Analysis 16:292–299

Abdelsalam MG, Stern RJ, Schandelmeier H, Sultan M (1995) Deformation history of the Keraf Zone in NE Sudan, revealed by Shuttle Imaging Radar. J Geol 103:475–491

Abdelsalam MG, Liégeois J-P, Stern RJ (2002) The Saharan metacraton. J African Earth Sci 34:119–136

Affaton P, Rahaman MA, Trompette R, Sougy J (1991) The Dahomeyide orogen: tectonothermal evolution and relationships with the Volta basin. In: Dallmeyer RD, Lécorché J-P (eds) The West African orogens and circum-Atlantic correlatives. Springer, Berlin, pp 107–122

Afiri A, Gueydan F, Pitra P, Essaifi A, Précigout J (2011) Oligo-Miocene exhumation of the Beni-Bousera peridotite through a lithosphere-scale extensional shear zone. Geodinam Acta 24:49–60

Agard J, Chatenet R, Mazéas JP (1966) Prospection au bérylliumètre et découverte du beryllium dans les tactites en bordures du massif granitique d'Azegour (Haut Atlas). Mines Géologie Rabat 8:47–50

Agard P, Jullien M, Goffé B, Baronnet A, Bouybaouène M (1999) TEM evidence for high-temperature (300°C) smectite in multistage clay-mineral pseudomorphs in pelitic rocks (Rif, Morocco). Eur J Miner 11:655–668

Ahmed AH (2007) Diversity of platinum-group minerals in podiform chromitites of the Late Proterozoic ophiolite, Eastern Desert, Egypt: genetic implications. Ore Geol Rev 32:1–19

Ahmed AH (2013) Highly depleted harzburgite–dunite–chromitite complexes from the Neoproterozoic ophiolite, south Eastern Desert, Egypt: a possible recycled upper mantle lithosphere. Precam Res 233:173–192

Ahmed AH, Arai S, Attia AK (2001) Petrological characteristics of the Pan African podiform chromitites and associated peridotites of the Proterozoic ophiolite complexes, Egypt. Miner Deposita 36:72–84

Ahmed AH, Arai S, Abdel Aziz YM, Rahimi A (2005) Spinel composition as a petrogenetic indicator of the mantle section in the Neoproterozoic Bou Azzer ophiolite, Anti-Atlas, Morocco. Precamb Res 138:225–234

Ahmed AH, Hanghøj K, Kelemen PB, Hart SR, Arai S (2006) Osmium isotope systematics of the Proterozoic and Phanerozoic ophiolitic chromitites: in situ ion probe analysis of primary Os-rich PGM. Earth Planet Sci Lett 245:777–791

Ahmed AH, Arai S, Abdel-Aziz YM, Ikenne M, Rahimi A (2009) Platinum-group elements distribution and spinel composition in podiform chromitites and associated rocks from the upper mantle section of the Neoproterozoic Bou Azzer ophiolite, Anti-Atlas, Morocco. J African Earth Sci 55:92–104

Ahmed AH, Gharib M, Arai S (2012a) Characterization of the thermally metamorphosed mantle–crust transition zone of the Neoproterozoic ophiolite at Gebel Mudarjaj, south Eastern Desert, Egypt. Lithos 142–143:67–83

Ahmed AH, Harbi HM, Habtoor AM (2012b) Compositional variations and tectonic settings of podiform chromitites and associated ultramafic rocks of the Neoproterozoic ophiolite at Wadi Al Hwanet, northwestern Saudi Arabia. J Asian Earth Sci 56:118–134

Aïssa DE, Cheilletz A, Gasquet D, Marignac C (1995) Alpine metamorphic core complexes and metallogenesis: the Edough case (NE Algeria). In: Pašava J, Kříbek B, Žák K (eds) Mineral deposits: from their origin to their environmental impacts. Proceed 3rd Biennial SGA Meeting, Prague. A.A. Balkema, Rotterdam, pp 23–26

Ait-Brahim L, Chotin P (1990) Oriental Moroccan Neogene volcanism and strike-slip faulting. J African Earth Sci 11:273–280

Alexander BW, Bau M, Andersson P, Dulski P (2008) Continentally-derived solutes in shallow Archean seawater: rare earth element and Nd isotope evidence in iron formation from the 2.9 Ga Pongola Supergroup, South Africa. Geochim Cosmochim Acta 72:378–394

Ali KA, Stern RJ, Manton WI, Johnson PR, Mukherjee SK (2010) Neoproterozoic diamictite in the Eastern Desert of Egypt and northern Saudi Arabia: evidence of 750 Ma glaciation in the Arabian-Nubian Shield? Int J Earth Sci 99:705–726

Ali KA, Moghazi A-KM, Maurice AE, Omar SA, Wang Q, Wilde SA, Moussa EM, Manton WI, Stern RJ (2012) Composition, age, and origin of the 620 Ma Humr Akarim and Humrat Mukbid A-type granites: no evidence for pre-Neoproterozoic basement in the Eastern Desert, Egypt. Inter J Earth Sci 101:1705–1722

Almond DC, Ahmed F, Shaddad MZ (1984) Setting of gold mineralization in the northern Red Sea Hills of Sudan. Econ Geol 79:389–392

Aly GAM (2015) Mineralogical and geochemical aspects of Miocene laterite, Sharm Lollia area, south Eastern Desert, Egypt. Arabian J Geosci 8:10,399–10,418

Amade E (1965) Les gisements Pb-Zn de Zeida et de Bou Mia. Notes Mem Serv Géol Maroc, Rabat 180:175–184

Amine MS (1947) A tin-tungsten deposit in Egypt. Econ Geol 42:637–671

Amstutz G, El-Gaby S, Ahmed AA, Habib ME, Khudeir AA (1984) Podiform chromitite in the Rubshi ophiolite association, west of Quseir, Egypt. Bull Faculty Sci Assiut Univ 13:75–93

Andrieux J, Frizon de Lamotte D, Braud J (1989) A structural scheme for the western Mediterranean area in Jurassic and Early Cretaceous times. Geodinam Acta 3:5–15

Annich M, Rahhali M (2002) Gisement de plomb de Zeida. In: Barodi E-B, Watanabe Y, Mouttaqi A, Annich M (eds) Méthodes et techniques d'exploration minière et principaux gisements au Maroc. Projet JICA/BRPM, Bureau Recherche Participations Minières—BRPM, Rabat, pp 179–183

Anonymous (2011) El Karit project. Kasbah Resources. http://www.24hgold.com

Ashwal LD, Burke K (1989) African lithospheric structure, volcanism and topography. Earth Planet Sci Letters 96:8–14

Attoh K, Ekwueme BN (1997) The West African Shield. Oxford Monogr Geol Geophys 35:517–528

Attoh K, Nude PM (2008) Tectonic significance of carbonatite and ultrahigh–pressure rocks in the Pan-African Dahomeyide suture zone, southeastern Ghana. In: Ennih N, Leiégeois J-P (eds) The boundaries of the West African Craton. Geol Soc London Spec Publ 297, pp 217–231

Augé T, Joubert M, Bailly L (2012) Typology of mafic–ultramafic complexes in Hoggar, Algeria: implications for PGE, chromite and base-metal sulphide mineralization. J African Earth Sci 63:32–47

Avigad D, Gvirtzman Z (2009) Late Neoproterozoic rise and fall of the northern Arabian-Nubian shield: the role of lithospheric mantle delamination and subsequent thermal subsidence. Tectonophys 477:217–228

Awad GH, Ghobrial MG (1965) Zonal stratigraphy of the Kharga Oasis. Ministry of Industry, General Egyptian Organization for Geological Research and Mining, Geological Survey, Paper 34:1–77

Awadalla GS (2010) Geochemistry and microprobe investigations of Abu Tartur REE-bearing phosphorite, Western Desert, Egypt. J African Earth Sci 57:431–443

Ba Gatta A (1982) Contribution à l'étude géologique et minéralogique du gisement Dakjoujt (Mauritanie). Unpubl PhD Thesis, Université Orléans, Orléans, France, 172 pp

Baioumy H, Tada R (2005) Origin of Late Cretaceous phosphorites in Egypt. Cretaceous Res 26:261–275

Barrère J (1967) Le groupe précambrien de l'Amsaga entre Afar et Akjoujt (Mauritanie). Etude d'un métamorphisme profond et de ses relations avec la migmatisation. Unpublished Ph.D. Thesis, Université Clermont-Ferrand, France, 275 pp

Barrie CT, Nielsen FW, Aussant CH (2007) The Bisha volcanic-associated massive sulfide deposit, western Nakfa terrane, Eritrea. Econ Geol 102:717–738

Basta FF, Maurice AE, Fontboté L, Favarger PY (2011) Petrology and geochemistry of the banded iron formation (BIF) of Wadi Karim and Um Anab, Eastern Desert, Egypt: implications for the origin of Neoproterozoic BIF. Precamb Res 187:277–292

Bea F, Montero P, Abu Anbar M, Molina JF, Scarrow JH (2011a) The Bir Safsaf Precambrian inlier of south west Egypt revisited: a model for 1.5 Ga TDM late Pan-African granite generation by crustal reworking. Lithos 125:897–914

Bea F, Montero P, Abu Anbar M, Talavera C (2011b) SHRIMP dating and Nd isotope geology of the Archean terranes of the Uweinat-Kamil inlier, Egypt-Sudan-Libya. Precamb Res 189:328–346

Beauchamp WH (1998) Tectonic evolution of the Atlas Mountains, North Africa. Unpublished Ph.D. Thesis, Cornell University, Ithaca, New York, USA, 235 pp

Beauchamp W, Barazangi M, Demnati A, El Alji M (1996) Intracontinental rifting and inversion: Missour Basin and Atlas Mountains, Morocco. AAPG Bull 80:1459–1482

Be'eri-Shlevin Y, Gee D, Claesson S, Ladenberger A, Majka J, Kirkland C, Robinson P, Frei D (2011) Provenance of Neoproterozoic sediments in the Särv nappes (middle allochthon) of the Scandinavian Caledonides: LA-ICP-MS and SIMS U-Pb dating of detrital zircons. Precamb Res 187:181–200

Bejaoui J, Bouhlel S, Barca D, Braham A (2011) The vein-type Zn-(Pb, Cu, As, Hg) mineralization at Fedj Hassène orefield, north-western Tunisia: mineralogy, trace elements, sulfur isotopes and fluid inclusions. Estudios Geol 67:5–20

Bejaoui J, Bouhlel S, Sellami A, Braham A (2014) Geology, mineralogy and fluid inclusion study of Oued Jebs Pb–Zn–Sr deposit: comparison with the Bou Grine deposit (diapirs zone, Tunisian Atlas). Arabian J Geosci 7:2483–2497

Bekker A, Slack JF, Planvasky N, Krapež B, Hofmann A, Konhauser KO, Rouxel OJ (2010) Iron formation: the sedimentary product of a complex interplay among mantle, tectonic, oceanic, and biospheric processes. Econ Geol 105:467–508

Belkasmi M, Cuney M, Boushaba A, Marignac C, Bastoul A (1999) Are there any rare-metal granitoids in the Moroccan Massif Central? In: Stanley CJ et al (eds) Mineral deposits: processes to processing, vol 1. Balkema, Rotterdam, pp 305–308

Belkasmi M, Cuney M, Pollard PJ, Bastoul A (2000) Chemistry of the Ta–Nb–Sn–W oxide minerals from the Yichun rare metal granite (SE China): genetic implications and comparison with Moroccan and French Hercynian examples. Miner Mag 64:507–523

Bellot J-P, Lerouge C, Bailly L, Bouchot V (2003) The Biards Sb-Au–bearing shear zone (Massif Central, France): an indicator of crustal-scale transcurrent tectonics guiding late Variscan collapse. Econ Geol 98:1427–1447

Bendaoud A, Ouzegane K, Godard G, Liégeois J-P, Kienast JR, Bruguier O, Drareni A (2008) Geochronology and metamorphic P–T–X evolution of the Eburnean granulite-facies metapelites of Tidjenouine (central Hoggar, Algeria): witness of the LATEA metacratonic evolution. In: Ennih N, Liégeois J-P (eds) The boundaries of the West African craton. Geological Soc London Spec Publ 297, pp 111–146

Benzaggagh M, Mokhtari A, Rossi P, Michard A, EL Maz A, Chalouan A, Saddiqi O, Rjimati E (2013). Oceanic units in the core of the External Rif (Morocco): intramargin hiatus or south-Tethyan remnants? J Geodynam, http://dx.doi.org/10.1016/j.jog.2013.10.003

Berger J, Diot H, Loc K, Ohnenstetter D, Féméniase O, Pivina M, Demaiffe D, Bernard A, Charlier B (2013) Petrogenesis of Archean PGM-bearing chromitites and associated ultramafic–mafic–anorthositic rocks from the Guelb el Azib layered complex (West African craton, Mauritania). Precamb Res 224:612–628

Berhe SM (1990) Ophiolites in northeast and East Africa: implications for Proterozoic crustal growth. J Geol Soc 147:41–57

Berrada SH, Hajjaji M, Belkabir A (2011) Mineralogical and geochemical features of the wollastonite deposit of Azegour, Haut-Atlas (Morocco). J African Earth Sci 60:247–252

Bertrand JM, Michard A, Boullier AM, Dautel D (1986) Structure and U/Pb geochronology of central Hoggar (Algeria): a reappraisal of its Pan-African evolution. Tectonics 5:955–972

Bertrand-Sarfati J, Moussine-Pouchkine A (1988) Is cratonic sedimentation consistent with available models? An example from the Upper Proterozoic of the West African craton. Sedim Geol 58:255–276

Bigotte G, Obellianne JM (1968) Découverte de minéralisations uranifères au Niger. Miner Deposita 3:317–333

Björlykke A, Sangster DF (1981) An overview of sandstone lead deposits and their relation to red-bed copper and carbonate-hosted lead-zinc deposits. In: Skinner BJ (ed) Economic Geology Seventy-Fifth Anniversary Volume, 1905–1980. Lancaster Press Inc, Lancaster, Pennsylvania, USA, pp 178–213

Black R, Liégeois J-P (1993) Cratons, mobile belts, alkaline rocks and continental lithospheric mantle: the Pan-African testimony. J Geol Soc 150:89–98

Black R, Latouche L, Liégeois J-P, Caby R, Bertrand JM (1994) Pan-African displaced terranes in the Tuareg Shield (central Sahara). Geology 22:641–644

Blasband BB (2006) Neoproterozoic tectonics of the Arabian-Nubian Shield. Unpublished Ph.D. Thesis, Mededelingen van die Faculteit Geowetenschappen, Universiteit Utrecht No. 256, Utrecht University, Utrecht, The Netherlands, 213 pp

Blichert-Toft J, Albarede F, Kornprobst J (1999) Lu-Hf isotope systematics of garnet pyroxenites from Beni Bousera, Morocco: implications for basalt origin. Science 283(5406):1303–1306

Bodinier JL, Dupuy C, Dostal J (1984) Geochemistry of Precambrian ophiolites from Bou Azzer, Morocco. Contrib Miner Petrol 87:43–50

Boote DRD, Clark-Lowes DD, Traut MW (1998) Paleozoic petroleum systems of North Africa. In: Macgregor DS, Moody RTJ, Clark-Lowes DD (eds) Petroleum geology of North Africa. Geol Soc London Spec Publ 132, pp 7–68

Bordonaro M, Gaillet JL, Michard A (1979) Le géosynclinal carbonifère sud-mésétien dans les Jebilet (Maroc); une corrélation avec la province pyriteuse du sud de l'Espagne. Comptes Rendus Acad Sci Paris Sér D 288:1371–1374

Borisenko AS, Borovikov AA, Pavlova GG, Kalinin YuA, Nevolko PA, Lebedev VI, Maacha L, Kostin AV (2013) Formation conditions of Hg-silver deposition at the Imiter deposit (Anti-Atlas, Morocco). In: Johnsson E et al. (eds) Mineral deposit research for a high-tech world. Proceedings of 12th Biennial SGA Mtg, Uppsala, Sweden, vol 3, pp 1243–1246

Bouabdellah M, Beaudoin G, Leach D, Grandia F, Cardellach E (2009) Genesis of the Assif El Mal Zn-Pb (Cu, Ag) vein deposit, an extension-related Mesozoic vein system in the High Atlas of Morocco: structural, mineralogical and geochemical evidence. Mineral Deposita 44:689–704

Bouabdellah M, Hoernle K, Kchit A, Duggen S, Hauff F, Klügel A, Lowry D, Beaudoin G (2010) Petrogenesis of the Eocene Tamazert continental carbonatites (central High Atlas, Morocco): implications for a common source for the Tamazert and Canary and Cape Verde islands carbonatites. J Petrol 51:1655–1686

Bouabdellah M, Sangster DF, Leach DL, Brown AC, Johnson CA, Emsbo P (2012) Genesis of the Touissit-Bou Beker Mississippi Valley type district (Morocco-Algeria) and its relationships to the Africa-Europe collision. Econ Geol 107:117–146

Bouabdellah M, Castorina F, Bodnar RB, Jébrak K, Prochaska W, Lowry D, Klügel A, Hoernle K (2014) Petroleum migration, fluid mixing and halokinesis as the main ore-forming processes at the peridiapiric Jbel Tirremi fluorite-barite hydrothermal deposit (northeastern Morocco). Econ Geol 108:1223–1256

Bouabdellah M, Niedermann S, Velasco F (2015) The Touissit-Bou Beker Mississippi Valley-type district of northeastern Morocco: relationships to the Messinian salinity crisis, Late Neogene-Quaternary alkaline magmatism, and buoyancy-driven fluid convection. Econ Geol 110:1455–1484

Bouabsa L (1987) Intrusions granitiques à albite-topaze: minéralistions stanno-wolframifères et altérations hydrothermales associées, l'exemple du Hoggar central, Algérie. Unpubl Ph.D. Thesis, Université Nancy, Nancy, France, 113 pp

Bouabsa L, Marignac C, Chabbi R, Cuney M (2010) The Filfila (NE Algeria) topaz-bearing granites and their rare metal minerals: petrologic and metallogenic implications. J African Earth Sci 56:107–113

Bouillin JP, Durand-Delga M, Olivier P (1986) Betic-Rifian and Tyrrhenian arcs: distinctive features, genesis and development stages. In: Wezel FC (ed) The origin of arcs. Elsevier, Amsterdam, pp 281–304

Boulemia S, Hamimed M, Bouhlel S, Bejaoui J (2015) Petro-mineralogical analysis of sedimentary phosphate of marine origin, case of the locality of El Kouif (Algerian-Tunisian confines). Open J Geol 5:156–173

Boullier AM (1991) The Pan-African trans-Saharan belt in the Hoggar Shield (Algeria, Mali, Niger): a review. In: Dallmeyer RD, Lécorché JP (eds) The West African orogens and circum-Atlantic correlatives. Springer, Berlin-Heidelberg, pp 85–105

Bourque H, Barbanson L, Sizaret S, Branquet Y, Ramboz C, Ennaciri A, El Ghorfi M, Badra L (2015) A contribution to the synsedimentary versus epigenetic origin of the Cu mineralizations hosted by terminal Neoproterozoic to Cambrian formations of the Bou Azzer–El Graara inlier: new insights from the Jbel Laassel deposit (Anti Atlas, Morocco). J African Earth Sci 107:108–118

Boushaba A (2011) The El Karit cassiterite-beryl veins (Oulmes granite, central Massif): nouveaux guides géologiques miniers Maroc. In: Mouttaqi A,

Rjimati EC, Maacha L, Michard A, Soulaimani A, Ibouh H (eds) Les principales mines du Maroc. Notes Mémoires Service Géol Maroc 564, pp 255–259

Boushaba A, Qalbi A (2011) A complex mining district: the El Hammam fluorite and Achmmach cassiterite deposits (central Massif): nouveaux guides géologiques miniers Maroc. In: Mouttaqi A, Rjimati EC, Maacha L, Michard A, Soulaimani A, Ibouh H (eds) Les principales mines du Maroc. Notes Mémoires Service Géol Maroc 564, pp 247–253

Bousquet R, Mamoun R, Saddiqi O, Goffé B, Möller A, Madi A (2008) Mélanges and ophiolites during the Pan-African orogeny: the case of the Bou-Azzer ophiolite suite (Morocco). In: Ennih N, Liégeois J-P (eds) The boundaries of the West African craton. Geol Soc London Spec Publ 297, pp 233–247

Bouybaouène ML, Goffé B, Michard A (1995) High-pressure, low-temperature metamorphism in the Sebtides nappes, northern Rif, Morocco. Geogaceta 17:117–119

Bowden P, Bennett JN, Kinnaird JA, Whitley JE, Abaa SI, Hadzigeorgiou-Stavrakis PK (1981) Uranium in the Niger-Nigeria younger granite province. Mineral Magazine 44:379–389

Bowie SHU (1979) The mode of occurrence and distribution of uranium deposits. Phil Trans Royal Soc London A291:289–300

Bronner G, Chauvel JJ (1979) Precambrian banded iron-formations of the Ijil Group (Kediat Ijil, Reguibat Shield, Mauritania). Econ Geol 74:77–94

Bronner G, Roussel J, Trompette R, Clauer N (1980) Genesis and geodynamic evolution of the Taoudeni cratonic basin (Upper Precambrian and Paleozoic), western Africa. In: Bally AW, Bender PL, McGetchin TR, Walcott RT (eds) Dynamic of plate interiors. Amer Geophys Union, Washington, DC, USA, Geodynamics series 1, pp 81–90

Burkhard M, Caritg S, Helg U, Robert-Charrue C, Soulaimani A (2006) Tectonics of the Anti-Atlas of Morocco. Comptes Rendus Geosci 338:11–24

Caby R (2003) Terrane assembly and geodynamic evolution of central–western Hoggar: a synthesis. J African Earth Sci 37:133–159

Caby R, Monié P (2003) Neoproterozoic subductions and differential exhumation of western Hoggar (southwest Algeria): new structural, petrological and geochronological evidence. J African Earth Sci 37:269–293

Caby R, Andreopoulos-Renaud U, Pin C (1989) Late Proterozoic arc-continent and continent-continent collision in the Pan-African trans-Saharan belt of Mali. Canad J Earth Sci 26:1136–1146

Caïa J (1976) Paleogeographical and sedimentological of copper, lead and zinc mineralizations in the Lower Cretaceous sandstones of Africa. Econ Geol 71:409–422

Cailleux Y (1994) Le Cambrien et l'Ordovicien du Maroc central septentrional. Le Massif Central marocain et la Meseta orientale. Bull Inst Sci Rabat 18:10–31

Caire A, Glangeaud L, Mattauer M, Polvèche J (1953) Essai de coordination de l'autochtone et de l'allochtone dans l'Atlas tellien de l'Algérie centrale. Bull Soc Géol France 6:941–972

Caritg S, Burkhard M, Ducommun R, Helg U, Kopp L, Sue C (2004) Fold interference patterns in the late Palaeozoic Anti-Atlas belt of Morocco. Terra Nova 16:27–37

Cazoulat M (1985) Geologic environment of the uranium deposits in the Carboniferous and Jurassic sandstones of the western margin of the Air Mountains in the Republic of Niger. In: Geological Environments of Sandstone-type Uranium Deposits, I.A.E.A. (Inter Atomic Energy Agency), Vienna, TECDOC 328, pp 247–263

Černý P, Ercit TS (2005) The classification of granitic pegmatites revisited. Canad Mineral 43:2005–2026

Chalal Y, Marignac C (1997) Découverte de wolframoixiolite dans les microgranites à albite-topaze d'Aléméda (Hoggar central, Algérie): implications métallogéniques. Bull Serv Géol Algérie 8:71–79

Chalouan A, Michard A (1990) The Ghomarides nappes, Rif coastal range, Morocco: a Variscan chip in the Alpine belt. Tectonics 9:1565–1583

Chalouan A, Michard A, El Kadiri K, Negro F, Frizon de Lamotte D, Soto JI, Saddiqi O (2008) The Rif belt. In: Michard A, Saddiqi O, Chalouan A, Frizon de Lamotte (eds) The geology of Morocco. Springer, Berlin, pp 203–302

Cheilletz A (1983) Les lentilles rubanées stratiformes à scheelite-biotite du Jbel Aouam, Maroc central: première description et interprétation. Comptes Rendus Acad Sci Paris 297:581–584

Cheilletz A (1984) Caractéristiques géochimiques et thermobarométriques des fluides associés à la scheelite et au quartz des minéralisations de tungstène du Jbel Aouam (Maroc central). Bull Minéral 107:255–272

Cheilletz A (1985) Les minéralisations stratiformes à scheelite-biotite du Djebel Aouam (Maroc central): exemple de skarn d'infiltration développé par remplacement de séries sédimentaires gréso-pélitiques. Bull Minéral 108:367–376

Cheilletz A, Zimmermann JL (1982) Datations par la méthode K-Ar du complexe intrusif et des minéralisations en tungstène du Jbel Aouam (Maroc central). Comptes Rendus Acad Sci Paris Série II 295:255–258

Cheilletz A, Bertrand JM, Charoy B, Moulahoum O, Bouabsa L, Farrar E, Zimmermann JL, Dautel D, Archibald DA, Boullier AM (1992) Géochimie et géochronologie Rb-Sr, K-Ar et $^{40}Ar/^{39}Ar$ des complexes granitiques pan-africains de la région de Tamanrasset (Algérie): relations avec les minéralisations Sn–W associées et l'evolution tectonique du Hoggar central. Bull Soc Géol France 163:733–750

Cheilletz A, Gasquet D, Filali F, Archibald DA, Nespolo M (2010) A Late Triassic $^{40}Ar/^{39}Ar$ age for the El Hammam high-REE fluorite deposit (Morocco): mineralization related to the Central Atlantic Magmatic Province? Mineral Deposita 45:323–329

Chirico PG, Barthélémy F, Koné F (2010) Alluvial diamond resource potential and production capacity assessment of Mali. U.S. Geological Survey Scientific

Investigations Report 2010–5044, 23 pp (available only online at http://pubs.usgs.gov/sir/2010/5044/)
Chorowicz J (2005) The East African rift system. J African Earth Sci 43:379–410
Clauer N (1976) Géochimie isotopique du strontium des milieux sédimentaires. Applications à la géochronologie de la couverture du craton Ouest-Africain. Mém Sci Géol Strasbourg 45, 256 p
Clauer N, Caby R, Jeannette D, Trompette R (1982) Geochronology of sedimentary and metasedimentary Precambrian rocks of the West African craton. Precamb Res 18:53–71
Clauer N, Dallmeyer RD, Lécorché JP (1991) Age of the late Paleozoic tectonothermal activity in northcentral Mauritanide, West Africa. Precamb Res 49:97–105
Comas MC, Platt JP, Soto JI, Watts AB (1999) The origin and tectonic history of the Alboran Basin: insights from Leg 161 results. Proceed Ocean Drilling Pgm Sci Results 161:555–580
Conticelli S, Manetti P, Capaldi G, Poli G (1995) Petrology, mineralogy and isotopes in olivine mela-nephelinites, basanites and carbonatites from Uwaynat region, south east Libya: inferences on their genesis. African Geosci Rev 2:227–245
Cook PJ (1976) Sedimentary phosphate deposits. In: Wolf KH (ed) Handbook of strata-bound and stratiform ore deposits; II regional studies and specific deposits, vol 7., Au, U, Fe, Mn, Hg, Sb, W, and P depositsElsevier, New York, pp 505–535
Cornée JJ, Costagliola C, Leglise H, Willefert S, Destombes J (1985) Précisions stratigraphiques sur l'Ordovicien supérieur et le Silurien du synclinal d'Oulad Abbou (Meseta marocaine occidentale): manifestations volcaniques au Silurien. Annales Soc Géologique Nord 104:141–146
Cosmidis J, Benzerara K, Menguy N, Arning E (2013) Microscopy evidence of bacterial microfossils in phosphorite crusts of the Peruvian shelf: implications for phosphogenesis mechanisms. Chem Geol 359:10–22
Cottin JY, Lorand JP, Agrinier P, Bodinier JL, Liégeois JP (1998) Isotopic (O, Sr, Nd) and trace element geochemistry of the Laouni layered intrusions (Pan-African belt, Hoggar, Algeria): evidence for post-collisional continental tholeiitic magmas variably contaminated by continental crust. Lithos 45:197–222
Coulon C, Megartsi M, Fourcade S, Maury RC, Bellon H, Louni-Hacini A, Cotton J, Coutelle A, Hermitte D (2002) Post-collisional transition from calc-alkaline to alkaline volcanism during the Neogene in Oranie (Algeria): magmatic expression of a slab breakoff. Lithos 62:87–110
Courbouleix S, Delpont G, Destaucq C (1981) Un grand decrochement est-ouest au nord du Maroc, à l'origine des structures plissées atlasiques: arguments géologiques et experimentaux. Bull Soc Géol France 1:33–43
Crespo E, Luque FJ, Rodas M, Wada H, Gervilla F (2006) Graphite-sulfide deposits in Ronda and Beni Bousera peridotites (Spain and Morocco) and the origin of carbon in mantle-derived rocks. Gondwana Res 9:279–290
Cvetkovic V, Toljic M, Ammarb NA, Rundic L, Trish KB (2010) Petrogenesis of the eastern part of the Al Haruj basalts (Libya). J African Earth Sci 58:37–50
Daafi Y, Chakir A, Jourani E, Ouabba SM (2014) Geology and mine planning of phosphate deposits: Benguerir deposit Gantour basin–Morocco. Procedia Engineer 83:70–75
Dagallier G (1993) Les arkoses plombo-barytiques du Trias de la Haute-Moulouya (Maroc): piégeaige et concentration intrapédimentaires. Mines Géologie Energie Rabat 54:83–99
Dallmeyer RD (1991) Exotic terranes in the central-southern Appalachian orogen and correlations with West Africa. In: Dallmeyer RD, Lécorché JP (eds) The West African orogens and Circum-Atlantic correlatives. Springer, Berlin-Heidelberg, pp 335–371
Dallmeyer RD, Villeneuve M (1987) $^{40}Ar/^{39}Ar$ mineral age record of polyphase tectonothermal evolution in the southern Mauritanide orogen, southeastern Senegal. Geol Soc America Bull 98:602–611
Dallmeyer RD, Lécorché JP (1989) $^{40}Ar/^{39}Ar$ polyorogenic mineral age record within the central Mauritanide orogen, West Africa. Geol Soc America Bull 101:55–70
Dallmeyer RD, Lécorché JP (1990) $^{40}Ar/^{39}Ar$ polyorogenic mineral age record in the northern Mauritanide orogen, West Africa. Tectonopysics 177:81–107
Davison I (2005) Central Atlantic margin basins of north West Africa: geology and hydrocarbon potential (Morocco to Guinea). J African Earth Sci 43:254–274
Dawood YH, Abd El-Naby HH (2007) Mineral chemistry of monazite from the black sand deposits, northern Sinai, Egypt: a provenance perspective. Mineral Mag 71:389–406
Ddani M, Meunier A, Zahraoui M, Beaufort D, El Wartiti M, Fontaine C, Boukili B, El Mahi B (2005) Clay mineralogy and chemical composition of bentonites from the Gourougou volcanic massif (northeast Morocco). Clays Clay Min 53:250–267
Decrée S, Marignac C, De Putter T, Deloule E, Liégeois JP, Demaiffe D (2008a) Pb-Zn mineralization in a Miocene regional extensional context: the case of the Sidi Driss and the Douahria ore deposits (Nefza mining district, northern Tunisia). Ore Geol Rev 34:285–303
Decrée S, De Putter T, Yans J, Recourt P, Jamoussi F, Bruyère D, Dupuis C (2008b) Iron mineralization in Pliocene sediments of the Tamra iron mine (Nefza mining district, Tunisia): mixed influence of pedogenesis and hydrothermal alteration. Ore Geol Rev 33:397–410
Decrée S, Baele JM, De Putter T, Yans J, Clauer N, Dermech M, Aloui K, Marignac C (2013) The Oued Belif hematite-rich breccia (Nefza mining district, NW Tunisia): a potential candidate for a Miocene small-scale iron oxide copper gold (IOCG) deposit in northern Tunisia. Econ Geol 108:1425–1457

Decrée S, Marignac C, Liégeois JP, Yans J, Abdallah RB, Demaiffe D (2014) Miocene magmatic evolution in the Nefza district (northern Tunisia) and its relationship with the genesis of polymetallic mineralizations. Lithos 192:240–258

Dekoninck A, Bernard A, Barbarand J, Saint-Bezar B, Missenard Y, Leprêtre R, Saddiqi O, Yans J (2015) Detailed mineralogy and petrology of manganese oxyhydroxide deposits of the Imini district (Morocco). Miner Deposita doi:10.1007/s00126-015-0590-3

Deynoux M, Affaton P, Trompette R, Villeneuve M (2006) Pan-African tectonic evolution and glacial events registered in Neoproterozoic to Cambrian cratonic and foreland basins of West Africa. J African Earth Sci 46:397–426

Dia O, Sougy J, Trompette R (1969) Discordance de ravinement et discordance angulaire dans le "Cambro-Ordovicien" de la région de Méjéria (Taganet occidental, Mauritanie): Bull Société Géol France 7:207–221

Dia O, Lécorché JP, Le Page A (1979) Trois événements orogéniques dans les Mauritanides d'Afrique occidentale. Rev Géol Dynam Géogr Phys 21:403–409

Diarra H, Holliday J (2014) Deep potential starts to emerge: new projects in Mali highlight deeper potential of Birimian belt. Mining J Nov 2014:19–21

Dirks PHGM, Belnkinsop TG, Jelsma HA (2010) The geological evolution of Africa. Geology IV. UNESCO-EOLSS (http://www.eolss.net/Eolss-sampleAllChapter.aspx

D'Lemos RS, Inglis JD, Samson SD (2006) A newly discovered orogenic event in Morocco: Neoproterozoic ages for supposed Eburnean basement of the Bou Azzer inlier, Anti-Atlas Mountains. Precamb Res 147:65–76

Doblas M, Oyarzun R (1989) Neogene extensional collapse in the western Mediterranean (Betic-Rif Alpine orogenic belt): implications for the genesis of the Gilbraltar arc and magmatic activity. Geology 17:430–433

Doebrich JL, Zahony SG, Leavitt JD, Portacio JS Jr, Siddiqui AA, Wooden JL, Fleck RJ, Stein HJ (2004) Ad Duwayhi, Saudi Arabia: geology and geochronology of a Neoproterozoic intrusion-related gold system in the Arabian shield. Econ Geol 99:713–741

Dostal J, Dupuy C, Caby R (1994) Geochemistry of the Neoproterozoic Tilemsi belt of Iforas (Mali, Sahara): a crustal section of an oceanic island arc. Precamb Res 65:55–69

Dubé B, Mercier-Langevin P, Kjarsgaard I, Hannington M, Bécu V, Côté J, Moorhead J, Legault M, Bédard N (2014) The Bousquet 2-Dumagami world-class Archean Au-rich volcanogenic massive sulfide deposit, Abitibi, Quebec: metamorphosed submarine advanced argillic alteration footprint and genesis. Econ Geol 109:121–166

Ducrot J, Lancelot JR (1977) Problème de la limite Précambrien-Cambrien: étude radio chronologique par la méthode U-Pb sur zircons du volcan du Jbel Boho (Anti-Atlas Marocain). Canad J Earth Sci 14:2771–2777

Du Dresnay R (1988) Recent data on the geology of the Middle-Atlas (Morocco). In: Jacobshagen V (ed) The Atlas system of Morocco. Lecture Notes Earth Sci 15, pp 293–320

Duggen S, Hoernle K, Pvd Bogaard, Garbe-Schönberg D (2005) Postcollisional transition from subduction- to intraplate-type magmatism in the westernmost Mediterranean: evidence for continental-edge delamination of subcontinental lithosphere. J Petrol 46:1155–1201

Duggen S, Hoernle K, Hauff F, Kluegel A, Bouabdellah M, Thirlwall MF (2009) Flow of Canary mantle plume material through a subcontinental lithospheric corridor beneath Africa to the Mediterranean. Geology 37:283–286

Durand-Delga M, Fontboté JM (1980) Le cadre structural de la Méditerranée occidentale. 26th Int Geol Congr. Paris, Coll C5:67–85

Durand-Delga M, Rossi P, Olivier P, Puglisi D (2000) Structural setting and ophiolitic nature of Jurassic basic rocks associated with the Maghrebian flyschs in the Rif (Morocco) and Sicily (Italy). Comptes Rendus Acad Sci Paris 331:29–38

Echikh K (1998) Geology and hydrocarbon occurrences in the Ghadames basin, Algeria, Tunisia, Libya. Geol Soc London Spec Publ 132:109–129

Eisenhour DD, Reisch FJ (2006) Bentonite. In: Kogel JE, Trivedi N, Barker JM, Krukowski ST (eds) Industrial minerals and rocks, 7th edition.Society of Mining, Metallurgy and Exploration, Inc., pp 357–368

El Arabi EH, Hafid M, Ferrandini J, Essamoud R (2006) Interprétation de la série syn-rift haut-atlasique en termes de séquences tectonostratigraphiques, transversale de Telouet, Haut Atlas (Maroc). Notes Mém Serv Géol Maroc 541:93–101

El Bakkali S, Gourgaud A, Bourdier J-L, Bellon H, Gundogdu N (1998) Post-collision Neogene volcanism of the eastern Rif (Morocco): magmatic evolution through time. Lithos 45:523–543

El Basbas A, Aissa M, Ouguir H, Mahdoudi M, Maddi O, Baoutoul H, Zouhair M (2011) The Tazalarht copper mine (western Anti-Atlas). In: Mouttaqi A, Rjimati EC, Maacha L, Michard A, Soulaimani A, Ibouh H (eds) Les principales mines du Maroc. Notes Mémoires Service Géologique Maroc 564, pp 145–149

El Boushi IM (1972) Geology of the Gebeit gold mine, Democratic Republic of the Sudan. Econ Geol 67:481–486

El Ghorfi M, Melcher F, Oberthür T, Boukhari AE, Maacha L, Maddi A, Mhaili M (2008) Platinum group minerals in podiform chromitites of the Bou Azzer ophiolite, Anti Atlas, central Morocco. Mineral Petrol 92:59–80

El Habaak GH (2004) Pan-African skarn deposits related to banded iron formation, Um Nar area, central Eastern Desert, Egypt. J African Earth Sci 38:199–221

El Habaak GH (2005) Sedimentary facies and depositional environments of some Egyptian banded iron-formations. 4th International Conference on the Geology of Africa, Assiut University, Assiut, Egypt (Abstract)

El Haddad MA (1996) The first occurrence of platinum group minerals (PGM) in a chromitite deposit in the Eastern Desert, Egypt. Mineral Deposita 31:439–445

El Haddia H, Benbouziane A, Moufliha M, E-s Jouranib, Amaghzaz M (2014) Siliceous forms of phosphate deposits of Cretaceous age in Oulad Abdoun basin (central Morocco): mineralogy, geochemistry and diagenetic phenomena. Procedia Engineer 83:60–69

El Hadi H, Tahiri A, Reddad A (2003) Les granitoïdes hercyniens post-collisionnels du Maroc oriental: une province magmatique calco-alcaline à shoshonitique. Comptes Rendus Geosci 335:959–967

El Hadi H, Simancas JF, Tahiri A, González-Lodeiro F, Azor A, Martínez-Poyatos D (2006) Comparative review of the variscan granitoids of Morocco and Iberia: proposal of a broad zonation. Geodinam Acta 19:103–116

El Hadi H, Simancas JF, Martínez-Poyatos D, Azor A, Tahiri A, Montero P, Fanning CM, Bea F, González-Lodeiro F (2010) Structural and geochronological constraints on the evolution of the Bou Azzer Neoproterozoic ophiolite (Anti-Atlas, Morocco). Precamb Res 182:1–14

El Hamet MO, Idde Z (2009) Uranium resources of Niger. International symposium on uranium raw material for the nuclear fuel cycle: Exploration, mining, production, supply and demand, economics and environmental issues (URAM-2009). Abstracts, 109

El Hatimi N, Duee G, Hervouet Y (1991) La Dorsale calcaire du Haouz; ancienne marge continentale passive tethysienne (Rif, Maroc). Bull Société Géol France 162:79–90

El Kadiri K, Linares A, Oloriz F (1992) La Dorsale calcaire rifaine (Maroc septentrional): evolution stratigraphique et géodynamique durant le Jurassique-Crétacé. Notes Mém Service Géol Maroc 336:217–265

El Kamel F, Remmal T, Mohsine A (1998) Mise en évidence d'un magmatisme alcalin d'intraplaque post-calédonien dans le bassin silurien des Ouled Abbou (Meseta côtière, Maroc). Comptes Rendus Académie Sci Paris 327:309–314

El Khalile A, Touil A, Hibti M, Bilal E (2014) Metasomatic zoning, mineralizations and genesis of Cu, Zn, and Mo Azegour skarns (western High Atlas, Morocco). Carpath J Earth Environ Sci 9:21–32

El-Makhrouf AA (1988) Tectonic interpretation of Jebel Eghei area and its regional application to Tebisti orogenic belt, south central Libya (S.P.L.A.J). J African Earth Sci 7:645–967

El Maz A, Guiraud M (2001) Paragenèse à faible variance dans les métapelites de la série de Filali (Rif interne marocain): description, interpretation et conséquences géodynamiques. Bull Société Géol France 172:469–485

EL-Nagger ZR (1966) Stratigraphy and planktonic foraminifera of the Upper Cretaceous-Lower Tertiary succession in the Esna-Adfu region, Nile Vally, Egypt. Bull British Museum Natural Hist, Suppl 2:1–291

El-Sharkawy MF (2001) Nb-Ta bearing minerals in a metasomatized granite, Eastern Desert, Egypt. In: Piestrzynski et al (eds), Mineral deposits at the beginning of the 21st Century. Swets & Zeitlinger, Krakow, pp 485–487

El-Shazly AK, Khalil KI (2014) Banded iron formations of Um Nar, Eastern Desert of Egypt: P-T–X conditions of metamorphism and tectonic implications. Lithos 196–197:356–375

El-Taher A (2010) Determination of chromium and trace elements in El-Rubshi chromite from Eastern Desert, Egypt by neutron activation analysis. Appl Radiation Isotopes 68:1864–1868

Emsbo P, McLaughlin PI, Breit GN, du Bray EA, Koenig AE (2015) Rare earth elements in sedimentary phosphate deposits: solution to the global REE crisis? Gondwana Res 27:776–785

Ennih N, Liégeois J-P (2001) The Moroccan Anti-Atlas: the West African craton passive margin with limited Pan-African activity: implications for the northern limit of the craton. Precamb Res 112:291–304

Ennih N, Liégeois JP (2008) The boundaries of the West African craton, with a special reference to the basement of the Moroccan metacratonic Anti-Atlas belt. In: Ennih N, Liégeois J-P (eds.) The boundaries of the West African craton. Geol Soc London Spec Publ 297, pp 1–17

Ennih N, Laduron D, Greiling RO, Errami E, de Wall H, Boutaleb M (2001) Superposition de la tectonique éburnéenne et panafricaine dans les granitoïdes de la bordure nord du craton ouest africain, boutonnière de Zenaga, Anti-Atlas central, Maroc. J African Earth Sci 32:677–693

Eremin NI, Dergachev AL, Pozdnyakova NV, Sergeeva NE (2002) Epochs of volcanic-hosted massive sulfide ore formation in the Earth's history. Geologiia Rudnykh Mestorozhdenii 44:227–241

Eremin NI, Dergachev AL, Pozdnyakova NV, Sergeeva NE (2004) Large and super large volcanic-associated massive sulfide deposits. Geologiia Rudnykh Mestorozhdenii 46:91–107

Essaifi A, Hibti M (2008) The hydrothermal system of central Jebilet (Variscan belt, Morocco): a genetic association between bimodal plutonism and massive sulphide deposits? J African Earth Sci 50:188–203

Faik F, Belfoul MA, Bouabdelli M, Hassenforder B (2001) Les structures de la couverture Néoprotérozoïque terminal et Paléozoïque de la région de Tata, Anti-Atlas centre-occidental, Maroc: déformation polyphasée, ou interactions socle/couverture pendant l'orogenèse hercynienne? J African Earth Sci 32:765–776

Farahat ES, Abdel Ghani MS, Aboazom AS, Asran AMH (2006) Mineral chemistry of Al Haruj low-volcanicity rift basalts, Libya: implications for petrogenetic and geotectonic evolution. J African Earth Sci 45:198–212

Favre P, Stampfli GM (1992) From rifting to passive margin: the examples of the Red Sea, Central Atlantic and Alpine Tethys. Tectonophys 215:69–97

Favre P, Stampfli G, Wildi W (1991) Jurassic sedimentary record and tectonic evolution of the northwestern corner of Africa. Palaeogeogr Palaeoclimatol Palaeoecol 87:53–73

Fekkak A, Boualoul M, Badra L, Amenzou M, Saquaque A, El-Amrani IE (2000) Origine et contexte geotectonique des depots detritiques du groupe Neoproterozoïque inferieur de Kelaat Mgouna (Anti-Atlas Oriental, Maroc). J African Earth Sci 30:295–311

Ferkous K, Monie P (2002) Neoproterozoic shearing and auriferous hydrothermalism along the lithospheric N-S east in Ouzzal shear zone (western Hoggar, Algeria, North Africa). J African Earth Sci 35:399–415

Fezaa N, Liégeois J-P, Abdallah N, Cherfouh EH, De Waele B, Bruguier O, Ouabadi A (2010) Late Ediacaran geological evolution (575–555 Ma) of the Djanet terrane, eastern Hoggar, Algeria: evidence for a Murzukian intracontinental episode. Precamb Res 180:299–327

Forbes P (1989) Rôles des structures sédimentaires et tectoniques, du volcanisme alcalin régional et des fluides diagénétiques-hydrothermaux pour la formation des minéralisations à U-Zr-Zn-Mo d'Akouta (Niger). Mém Cent Recherche Géol Uranium, Nancy, France 378 pp

Forbes P, Pacquet A, Chantret F, Oumarou J, Pagel M (1984) Marqueurs du volcanisme dans le gisement d'uranium d'Akouta (République du Niger). Comptes Rendus Académie Sci Paris 298:647–650

Forbes P, Dubessy J, Kosztolanyi C (1986) Vibrational spectroscopy of the alteration of montroseite ((V, Fe) OOH): comparison with goethite and diaspore. Terra Cognita 7(1):16 (abstract)

Forbes P, Landais P, Pagel M, Meyer A (1987) Thermal evolution of the Guezouman Formation in the Akouta uranium deposit (Niger). Terra Cognita 7:343 (abstract)

Forbes P, Landais P, Bertrand P, Brosse E, Espitalie J, Yahaya M (1988) Chemical transformations of type-III organic matter associated with the Akouta uranium deposit (Niger): geological implications. Chem Geol 71:267–282

Force ER, Maynard JB (1991) Manganese: syngenetic deposits on the margins of anoxic basins. Rev Econ Geol 5:147–159

Force ER, Back W, Spiker EC, Knauth LP (1986) A ground-water mixing model for the origin of the Imini manganese deposit (Cretaceous) of Morocco. Econ Geol 81:65–79

Foster RP, Piper DP (1993) Archaean lode gold deposits in Africa: crustal setting, metallogenesis and cratonization. Ore Geol Rev 8:303–347

Fraissinet C, Zouine EM, Morel JL, Poisson A, Andrieux J, Faure-Muret A (1988) Structural evolution of the southern and northern central High Atlas in Paleogene and Mio-Pliocene times. In: Jacobshagen V (ed) The Atlas system of Morocco. Lecture Notes Earth Sci 15, pp 273–291

Fritz H, Abdelsalam M, Ali KA, Bingen B, Collins AS, Fowler AR, Ghebreab W, Hauzenberger CA, Johnson PR, Kusky TM, Macey P, Muhongo S, Stern RJ, Viola G (2013) Orogen styles in the East African orogen: a review of the Neoproterozoic to Cambrian tectonic evolution. J African Earth Sci 86:65–106

Frizon de Lamotte D, Zizi M, Missenard Y, Hafid M, El Azzouzi M, Maury RC, Charrière A, Taki Z, Benammi M, Michard A (2008) The Atlas System. In: Michard A et al (eds) Continental evolution: the geology of Morocco. Lecture Notes Earth Sci 116, pp 134–202

Gärtner A, Villeneuve M, Linnemann U, El Archi A, Bellon H (2013) An exotic terrane of Laurussian affinity in the Mauritanides and Souttoufides (Moroccan Sahara). Gondwana Res 24:687–699

Gasquet D, Roger J, Chalot-Prat F, Hassenforder B, Baudin T, Chevremont P, Razin P, Benlakhdim A, Mortaji A, Benssaou M (2001) Mémoire explicatif, carte géol. Maroc (1/50 000), Feuille Tamazrar, Notes Mem Serv Géol Maroc, Rabat, No 415 bis

Gasquet D, Chevremont P, Baudin T, Chalot-Prat F, Guerrot C, Cocherie A, Roger J, Hassenforder B, Cheilletz A (2004) Polycyclic magmatism in the Tagragra d'Akka and Kerdous-Tafeltast inliers (western Anti-Atlas, Morocco). J African Earth Sci 39:267–275

Gasquet D, Levresse G, Cheilletz A, Azizi-Samir MR, Mouttaqi A (2005) Contribution to a geodynamic reconstruction of the Anti-Atlas (Morocco) during Pan-African times with the emphasis on inversion tectonics and metallogenic activity at the Precambrian-Cambrian transition. Precamb Res 140:157–182

Gervilla F, Leblanc M (1990) Magmatic ores in high-temperature Alpine-type lherzolite massifs (Ronda, Spain, and Beni Bousera, Morocco). Econ Geol 85:112–132

Gervilla F, Leblanc M, Torres-Ruiz J, Hach-Ali PF (1996) Immiscibility between arsenide and sulfide melts; a mechanism for concentration of noble metals. Canadian Mineral 34:485–502

Gervilla F, Gutiérrez-Narbona R, Fenoll-Hach-Alí P (2002) The origin of different types of magmatic mineralizations from small-volume melts in the lherzolite massifs of the Serranía de Ronda. Bol Soc España Mineral 25:79–96

Gheerbrant E, Sudre J, Cappetta H, Mourer-Chauviré C, Bourdon E, Iarochène M, Amaghzaz M, Bouya B (2003) Les localités à mammifères des carrières de Grand Daoui, basin des Ouled Abdoun, Maroc, Yprésien: premier état des lieux. Bull Soc Géol France 174:279–293

Giese P, Jacobshagen V (1992) Inversion tectonics of intracontinental ranges: High and Middle Atlas, Morocco. Geol Rundschau 81:249–259

Gippsland Limited (2013) Abu Dabbab tantalum; Nuweibi tantalum, niobium, feldspar. http://www.gippslandltd.com

Glenn CR, Arthur MA (1990) Anatomy and origin of a Cretaceous phosphorite-greensand giant, Egypt. Sedimentol 37:123–154

Goffé B, Azañon JM, Bouybaouène ML, Jullien M (1996) Metamorphic cookeite in Alpine metapelites from Rif, northern Morocco, and the Betic Chain, southern Spain. Eur J Mineral 8:335–348

Goldfarb RJ, Groves DI, Gardoll S (2001) Orogenic gold and geologic time: a global synthesis. Ore Geol Rev 18:1–75

Goldfarb RJ, Baker T, Dubé B, Groves DI, Hart CJR, Gosselin P (2005) Distribution, character, and genesis of gold deposits in metamorphic terranes. In: Hedenquist JW, Thompson JFH, Goldfarb RJ, Richards JP (eds) Economic Geology 100th Anniversary Volume, 1905–2005. Society of Economic Geologists Inc, Littleton, Colorado, USA, pp 407–450

Gomez F, Allmendinger R, Barazangi M, Er-Raji A, Dahmani M (1998) Crustal shortening and vertical strain partitioning in the Middle Atlas Mountains of Morocco. Tectonics 17:520–533

Gomez F, Allmendinger R, Barazangi M, Beauchamp W (2000) Role of the Atlas Mountains (northwest Africa) within the African-Eurasian plate-boundary zone. Geology 28:769–864

Gourgaud A, Vincent PM (2004) Petrology of two continental alkaline intraplate series at Emi Koussi volcano, Tibesti, Chad. J Volcan Geotherm Res 129:261–290

Groves DI, Goldfarb RJ, Gebre-Mariam M, Hagemann SG, Robert F (1998) Orogenic gold deposits: a proposed classification in the context of their crustal distribution and relationship to other gold deposit types. Ore Geol Rev 13:7–27

Groves DI, Condie KC, Goldfarb RJ, Hronsky JMA, Vielreicher RM (2005) Secular changes in global tectonic processes and their influence on the temporal distribution of gold-bearing mineral deposits. Econ Geol 100:203–224

Gueydan F, Pitra P, Afiri A, Poujol M, Essaifi A, Paquette J-L (2015) Oligo-Miocene thinning of the Beni Bousera peridotites and their Variscan crustal host rocks, internal Rif, Morocco. Tectonics 34:1244–1268

Guiliani G (1984) Les concentrations filoniennes à tungstène-étain du massif granitique des Zaer (Maroc central): minéralisations et phases associées: Mineral Deposita 19:193– 201

Guiliani G, Sonnet J (1982) Contribution à l'étude géochronologique du massif granitique hercynien des Zaër (Massif central marocain). Comptes Rendus Acad Sci Paris 294:139–143

Guiraud R, Bosworth W, Thierry J, Delplanque A (2005) Phanerozoic geological evolution of northern and central Africa: an overview. J African Earth Sci 43:83–143

Gutscher MA, Malod J, Rehault JP, Contrucci I, Klingelhoefer F, Mendes-Victor L, Spakman W (2002) Evidence for active subduction beneath Gibraltar. Geology 30:1071–1074

Gutzmer J, Beukes NJ, Rhalmi M, Mukhopadhyay J (2006) Cretaceous karstic cave-fill manganese-lead-barium deposits of Imini, Morocco. Econ Geol 101:385–405

Hagemann SG, Cassidy KF (2000) Archean orogenic lode gold deposits. Reviews Econ Geol 13:9–68

Hamdy MM, Lebda EM (2011) Al-compositional variation in ophiolitic chromitites from the south Eastern Desert of Egypt: petrogenetic implications. J Geol Mining Res 3:232–250

Harben PW (1999) The industrial minerals handbook, 3rd edn. Industrial Minerals Information Ltd, London 296 pp

Harris NBW, Hawkesworth CJ, Ries AC (1984) Crustal evolution in north-east and east Africa from model Nd ages. Nature 309:773–776

Haworth RT (1983) Geophysics and geological correlation within the Appalachian-Caledonide-Hercynian-Mauritanide orogens—an introduction. In: Schenk PE (ed) Regional trends in the geology of the Appalachian-Caledonian-Hercynian-Mauritanide orogen. D. Reidel, Dordrecht, The Netherlands, pp 1–9

Hedrick JB, Waked L (1989) Heavy minerals, including monazite, in Egypt's black sand deposits. J Less Common Metals 148:79–84

Hefferan KP, Karson JA, Saquaque A (1992) Proterozoic collisional basins in a Pan-African suture zone, Anti-Atlas Mountains, Morocco. Precamb Res 54:295–319

Hefferan KP, Admou H, Karson JA, Saquaque A (2000) Anti-Atlas (Morocco) role in Neoproterozoic western Gondwana reconstruction. Precamb Res 103:89–96

Hefferan KP, Admou H, Hilal R, Karson JA, Saquaque A, Juteau T, Bohn MM, Samson SD, Kornprobst JM (2002) Proterozoic blueschist-bearing mélange in the Anti-Atlas Mountains, Morocco. Precamb Res 118:179–194

Helba H, Trumbull RB, Morteani G, Khalil SO, Arslan A (1997) Geochemical and petrographic studies of Ta mineralization in the Nuweibi albite granite complex, Eastern Desert, Egypt. Miner Deposita 32:164–179

Helmy HM, Kaindl R, Shibata T (2014) Genetically related Mo–Bi–Ag and U-F mineralization in A-type granite, Gabal Gattar, Eastern Desert, Egypt. Ore Geol Rev 62:181–190

Heron K, Jessell M, Benn K, Harris E, Crowley QG (2015) The Tasiast deposit. Ore Geol Rev, Mauritania. doi:10.1016/j.oregeorev.2015.08.020

Higashihara M, Marutani M, Bellal AO, Dioumassi B, Ousmane D, Emenetoullah L (2004) Plate-tectonic and metallogenic evolutions of western Reguibat shield—proposition of a hypothesis. Prog Abstr Intern Geol Correlation Prog Conf (UNESCO/IUGS) 485, Nouakchott, Mauritania, 5–13 Dec 2004, pp 10–13

Hitzman M, Kirkham R, Broughton D, Thorson J, Selley D (2005) The sediment-hosted stratiform copper ore system. In: Hedenquist JW, Thompson JFH, Goldfarb RJ, Richards JP (eds) Economic Geology 100th Anniversary Volume, 1905–2005.

Society Economic Geologists Inc, Littleton, Colorado, USA, pp 609–642
Hoepffner C, Soulaimani A, Piqué A (2005) The Moroccan Hercynides. J African Earth Sci 43:144–165
Hoepffner C, Houari MR, Bouabdelli M (2006) Tectonics of the North African Variscides (Morocco, western Algeria): an outline. Comptes Rendus Geosci 338:25–40
Hofmann A (2005) The geochemistry of sedimentary rocks from the Fig Tree Group, Barberton greenstone belt: implications for tectonic, hydrothermal and surface processes during mid-Archaean times. Precamb Res 143:23–49
Hsü KJ, Ryan WBF, Cita MB (1973) Late Miocene desiccation of the Mediterranean. Nature 242:240–244
Hsü KJ, Montadert L, Bernoulli D, Cita MB, Erickson A, Garrison RE, Kidd RB, Mèlierés F, Müller C, Wright R (1977) History of the Mediterranean salinity crisis. Nature 267:399–403
Hussein HA, Hassan MA, El-Tahir MA, Abou-Deif A (1986) Uranium-bearing siliceous veins in younger granites, Eastern desert/Egypt. In vein-type uranium deposits report of the working group on uranium geology. International Energy Agency, Vienna, IAEA-TECDOC-361
Huston DL, Pehrsson S, Eglington BM, Zaw K (2010) The geology and metallogeny of volcanic-hosted massive sulfide deposits: variations through geologic time and with tectonic setting. Econ Geol 105:571–591
Huvelin P (1977) Etude géologique et gîtologique du massif hercynien des Jebilet (Maroc occidental). Notes Mem Serv Géol Maroc 37:7–22
IAMGOLD Corp (2014) Mineral Reserves and Resources. IAMGOLD Corp http://www.iamgold.com/English/operations/reserves-and-resource-summary/default.aspx
Ibhi A, Nachit H, Abia EH, Hernandez J (2002) Intervention des ségrégats carbonatitiques dans la pétrogenèse des néphélinites à pyroxène de Jbel Saghro (Anti-Atlas, Maroc). Bull Soc Géol France 173:37–43
Ibouh H, Hibti M, Saidi A, Touil A (2011) Azegour Cu-Mo-W metasomatic desposit (western High Atlas): nouveaux guides géologiques miniers Maroc. In: Mouttaqi A, Rjimati EC, Maacha L, Michard A, Soulaimani A, Ibouh H (eds) Les principales mines du Maroc. Notes Mémoires Service Géologique Maroc 564:229–233
Inglis JD, MacLean JS, Samson SD, D'Lemos RS, Admou H, Hefferan K (2004) A precise U-Pb zircon age for the Bleïda granodiorite, Anti-Atlas, Morocco: implications for the timing of deformation and terrane assembly in the eastern Anti-Atlas. J African Earth Sci 39:277–283
Inglis JD, D'Lemos RS, Samson SD, Admou H (2005) Geochronological constraints on Late Precambrian intrusion, metamorphism, and tectonism in the Anti-Atlas Mountains. J Geol 113:439–450
Ismail I, Baioumy H, Ouyang H, Mossa H, Fouad Aly H (2015) Origin of fluorite mineralizations in the Nuba Mountains, Sudan and their rare earth element geochemistry. J African Earth Sci 112:276–286
Jacobshagen V (1992) Major fracture zones of Morocco: The south Atlas and the Transalboran fault systems. Geol Rundschau 81:185–197
Jacobshagen V, Görler K, Giese P (1988a) Geodynamic evolution of the Atlas System (Morocco) in post-Palaeozoic times. In: Jacobshagen V (ed) The Atlas system of Morocco. Lecture Notes Earth Sci 15, pp 481–499
Jacobshagen V, Brede R, Hauptmann M, Heinitz W, Zylka R (1988b) Structure and post-Palaeozoic evolution of the central High Atlas. In: Jacobshagen V (ed) The Atlas system of Morocco. Lecture Notes Earth Sci 15, pp 245–271
James HL (1983) Distribution of banded iron-formation in space and time. In: Trendall AF, Morris RC (eds) Iron-formation: facts and problems. Elsevier, Amsterdam, pp 471–490
James HL (1992) Precambrian iron-formation: nature, origin, and mineralogic evolution from sedimentary to metamorphism. In: Wolf KH, Chiligarian CV (eds), Develop Sedimentol 47, pp 543–589
Jébrak M (1982) Les districts à fluorine du Maroc central. Bur Recherches Geol Min Bull 2(II):211–221
Jébrak M (1984) Contribution à l'histoire naturelle des filons (F, Ba) du domaine Varisque. Unpublished PhD thesis, University Orléans, Orléans, France, 470 pp
Jemmali N, Souissi F, Villa IM, Vennemann TW (2011) Ore genesis of Pb–Zn deposits in the Nappe zone of northern Tunisia: constraints from Pb–S–C–O isotopic systems. Ore Geol Rev 40:41–53
Johnson PR (2014) An expanding Arabian-Nubian Shield geochronologic and isotopic dataset: defining limits and confirming the tectonic setting of a Neoproterozoic accretionary orogen. Open Geol J 8 (Suppl 1: M2):3–33
Johnson PR, Woldehaimanot B (2003) Development of the Arabian-Nubian Shield: perspectives on accretion and deformation in the northern East African orogen and the assembly of Gondwana. Geol Soc London Spec Publ 206:289–325
Johnson CM, Beard BL, Klein C, Beukes NJ, Roden EE (2008) Iron isotopes constrain biologic and abiologic processes in banded iron formation genesis. Geochim Cosmochim Acta 72:151–169
Johnson PR, Andresen A, Collins AS, Fowler AR, Fritz H, Ghebreab W, Kusky T, Stern RJ (2011) Late Cryogenian-Ediacaran history of the Arabian-Nubian Shield: a review of depositional, plutonic, structural, and tectonic events in the closing stages of the northern East African orogen. J African Earth Sci 61:167–232
Jorgenson JD (2012) Iron ore: U.S. Geological Survey, Mineral commodity summaries, January 2012, pp 84–85. http://minerals.usgs.gov/minerals/pubs/mcs/2012/mcs2012.pdf

Kasbah Resources Ltd (2015) Achmmach tin project. Kasbah Resources Ltd http://www.kasbahresources.com/index.php/projects/achmmach-tin-project

Keppie JD, Dostal J, Murphy JB (2011) Complex geometry of the Cenozoic magma plumbing system in the central Sahara, NW Africa. Intern Geology Rev 53:1576–1592

Kesraoui M (2005) Nature et évolutions comparées de granites à métaux rares dans le Hoggar central (Algérie) à travers la pétrographie, la cristallochimie des micas et des minéraux à Ta, Nb, Sn. Unpubl Doct Etat, USTHB-Alger, Algeria, W et la géochimie 257 pp

Kesraoui M, Marignac C (2010) Liquides résiduels et évolution magmatique-hydrothermale des granites à métaux rares: l'exemple des "pegmatites" à quartz-zinnwaldite de la coupole de Rechla (Hoggar, Algérie). 22ème Réun Sci Terre, Octobre 2010, Bordeaux, France, (Société Géologique de France, 77 rue Claude-bernard, 05 Paris)

Key RM, De Waele B, Liyungu AK (2004) A multi-element baseline geochemical database from the western extension of the Central Africa Copper belt in north-western Zambia. Institn Mining Metall Trans B (Appl Earth Sci) 113:205–226

Key RM, Loughlin SC, Horstwood MSA, Gillespie M, Pitfield PEJ, Henney PJ, Crowley QG, Del Rio M (2008) Two Mesoarchaean terranes in the Reguibat Shield of NW Mauritania. In: Ennih N, Liégeois J-P (eds), Boundaries of the West African craton. Geol Soc London Spec Publ 297, pp 33–52

Khalil KI, El-Shazly AE, Lehmann B (2015) Late Neoproterozoic banded iron formation (BIF) in the central Eastern Desert of Egypt: mineralogical and geochemical implications for the origin of the Gebel El Hadid iron ore deposit. Ore Geol Rev 69:380–399

Khudeir AA, EL Haddad MA, Leake BE (1992) Compositional variation in chromite from the Eastern Desert, Egypt. Mineral Magazine 56:567–574

Kirschbaum MJ (2011) Geology of the Guelb Moghrein iron oxide-copper-gold deposit. Unpubl MSc Thesis, Colorado School of Mines, Golden, Colorado, USA, 88 pp

Kirschbaum MJ, Hitzman MW (2016) Guelb Moghrein: an unusual carbonate-hosted iron oxide copper-gold deposit in Mauritania, northwest Africa. Econ Geol 111:763–770

Klein C, Beukes NJ (1993) Sedimentology and geochemistry of the glaciogenic Late Proterozoic Rapitan Iron-Formation in Canada. Econ Geol 88:542–565

Klemm D, Klemm R, Murr A (2001) Gold of the pharaohs—6000 years of gold mining in Egypt and Nubia. J African Earth Sci 33:643–659

Klerkx J (1980) Age and metamorphic evolution of the basement complex around Jabal al Awaynat. Geology of Libya 3:901–906

Knight KB, Nomade S, Renne PR, Marzoli A, Bertrand H, Youbi N (2004) The Central Atlantic Magmatic Province at the Triassic-Jurassic boundary: paleomagnetic and 40Ar/39Ar evidence from Morocco for brief, episodic volcanism. Earth Planet Sci Lett 228:143–160

Kocsis L, Gheerbrant E, Mouflih M, Cappetta H, Yans J, Amaghzaz M (2014) Comprehensive stable isotope investigation of marine biogenic apatite from the Late Cretaceous–early Eocene phosphate series of Morocco. Palaeogeogr Palaeoclimatol Palaeoecol 394:74–88

Kolb J, Petrov N (2015) The Guelb Moghrein Cu–Au deposit: Neoarchaean hydrothermal sulfide mineralization in carbonate-facies iron formation. Ore Geol Rev. doi:10.1016/j.oregeorev.2015.09.003

Kolb J, Sakellaris GA, Meyer FM (2006) Controls on hydrothermal Fe oxide–Cu–Au–Co mineralization at the Guelb Moghrein deposit, Akjoujt area, Mauritania. Miner Deposita 41(1):68–81

Kolb J, Meyer FM, Vennemann T, Hoffbauer R, Gerdes A, Sakellaris GA (2008) Geological setting of the Guelb Moghrein Fe oxide-Cu-AuCo mineralization, Akjoujt area, Mauritania. In: Ennih N, Liégeois J-P (eds), The boundaries of the West African craton. Geol Soc London Spec Publ 297, pp 53–75

Kornprobst J, Piboule M, Roden M, Tabit A (1990) Corundum-bearing garnet clinopyroxenites at Beni Bousera (Morocco): original plagioclase-rich gabbros recrystallized at depth within the mantle. J Petrol 31:717–745

Krijgsman W, Hilgen FJ, Raffi I, Sierro FJ, Wilson DS (1999) Chronology, causes and progression of the Messinian salinity crisis. Nature 400:652–655

Kruse S (2013) Regional geometry and tectonic evolution of the Aouéouat greenstone belt and Tasiast metallogenic district. Unpubl Internal Rept for Kinross Tasiast, Terrane Geoscience Inc

Küster D (2009) Granitoid-hosted Ta mineralization in the Arabian-Nubian Shield: ore deposit types, tectono-metallogenetic setting and petrogenetic framework. Ore Geol Rev 35:68–86

Küster D, Liégeois J-P (2001) Sr, Nd isotopes and geochemistry of the Bayuda Desert high-grade metamorphic basement (Sudan): an early Pan-African oceanic convergent margin, not the edge of the East Saharan ghost craton? Precamb Res 109:1–23

Küster D, Liégeois J-P, Matukov D, Sergeev S, Lucassen F (2008) Zircon geochronology and Sr, Nd, Pb isotope geochemistry of granitoids from Bayuda Desert and Sabaloka (Sudan): evidence for a Bayudian event (920–900 Ma) preceding the Pan-African orogenic cycle (860–590 Ma) at the eastern boundary of the Saharan metacraton. Precamb Res 164:16–39

Lahondère D, Thieblemont D, Goujou JC, Roger J, Moussine-Pouchkine A, Le Metour J, Cocherie A, Guerrot C (2003) Notice explicative des cartes géologiques et gîtologiques à 1/200,000 et 1/500,000

du Nord de la Mauritanie, vol 1. DMG, Ministère des Mines et de l'Industrie, Nouakchott, Mauritania

Lalaoui MD, Beauchamp J, Sagon JP (1991) Le gisement de manganèse de l'Imini (Maroc): un dépôt sur la ligne de rivage. Chroniques Recherche Minière 502:23–36

Lang JR, Baker T (2001) Intrusion-related gold systems: the present level of understanding. Miner Deposita 36:477–489

Laville E (1981) Rôle des décrochements dans le mécanisme de formation des bassins d'effondrement du Haut Atlas marocain au cours des temps triasique et liasique. Bull Soc Géol France 3:303–312

Laville E, Piqué A (1991) La distension crustale atlantique et atlasique au Maroc au début du Mésozoique; le rejeu des structures hercyniennes. Bull Soc Géol France 162:1161–1171

Lawrence DM, Treloar PJ, Rankin AH, Harbidge P, Holliday J (2013a) The geology and mineralogy of the Loulo mining district, Mali, West Africa: evidence for two distinct styles of orogenic gold mineralization. Econ Geol 108:199–227

Lawrence DM, Treloar PJ, Rankin AH, Boyce A, Harbidge P (2013b) A fluid inclusion and stable isotope study at the Loulo mining district, Mali, West Africa: implications for multifluid sources in the generation of orogenic gold deposits. Econ Geol 108:229–257

Leach DL, Sangster DF, Kelley KD, Large RR, Garven G, Allen CR, Gutzmer J, Walters S (2005) Sediment-hosted lead-zinc deposits: a global perspective. In: Hedenquist JW, Thompson JFH, Goldfarb RJ, Richards JP (eds) Economic Geology 100th Anniversary Volume, 1905–2005. Society of Economic Geologists Inc, Littleton, Colorado, USA, pp 561–607

Leblanc D, Olivier P (1984) Role of strike-slip faults in the Betic-Rifian orogeny. Tectonophys 101:345–355

Leblanc D (1990) Tectonic adaptation of the external zones around the curved core of an orogene: the Gibraltar arc. J Struct Geol 12:1013–1018

Leblanc M (1981) The Late Proterozoic ophiolites of Bou Azzer (Morocco): evidence for Pan African plate tectonics. In: Kroner A (ed) Precambrian plate tectonics. Elsevier, Amsterdam, pp 436–451

Leblanc M (1991) Platinum-group elements and gold in ophiolitic complexes: distribution and fractionation from mantle to oceanic floor. In: Peters Tj, Nicolas A, Coleman R (eds), Ophiolite genesis and evolution of the oceanic lithosphere, Oman. Kluwer, Dordrecht, The Netherlands, pp 231–260

Leblanc M, Billaud P (1978) A volcano-sedimentary copper deposit on a continental margin of Upper Proterozoic age: Bleida (Anti-Atlas, Morocco). Econ Geol 73:1101–1111

Leblanc M, Lancelot JR (1980) Interprétation géodynamique du domaine pan-africain (Précambrien terminal) de l'Anti-Atlas (Maroc) à partir de données géologiques et géochronologiques. Canad J Earth Sci 17:142–155

Leblanc M, Sauvage JF (1986) Un gisement polymétallique en milieu volcano-sédimentaire du Protérozoïque supérieur: Tissalit (Adrar des Iforas, Mali). J African Earth Sci 5:201–207

Leblanc M, Temagoult A (1989) Chromite pods in a lherzolite massif (Collo, Algeria): evidence of oceanic-type mantle rocks along the west Mediterranean Alpine belt. Lithos 23:153–162

Leblanc M, Billaud P (1990) Zoned and recurrent deposition of Na-Mg-Fe-Si exhalites and Cu-Fe sulfides along synsedimentary faults (Bleïda, Morocco). Econ Geol 85:1759–1769

Leblanc M, Arnold M (1994) Sulfur isotope evidence for the genesis of distinct mineralizations in the Bleida stratiform copper deposit (Morocco). Econ Geol 89:931–935

Leblanc M, Moussine Pouchkine A (1994) Sedimentary and volcanic evolution of a Neoproterozoic continental margin (Bleida, Anti-Atlas, Morocco). Precamb Res 70:25–44

Lécorché JP (1980) Les Mauritanides face au craton ouest-africain: structure d'un secteur-clé: la région d'Ijibiten (Est d'Akjoujt, R. I. de Mauritanie). Unpublished PhD Thesis, Université d'Aix-Marseille III, France, 446 pp

Lécorché JP, Sougy J (1978) Les Mauritanides, Afrique occidentale: essai de synthèse. In: Dallmeyer RD, Lécorché JP (eds), Caledonian-Appalachian orogen of the North-Atlantic region. Geological Survey Canada Paper 78–13:231–239

Lécorché JP, Roussel J, Sougy J, Guetat Z (1983). An interpretation of the geology of the Mauritanides orogenic belt (West Africa) in the light of geophysical data. In: Hatcher RD Jr, Williams H, Zietz I (eds) Contributions to the tectonics and geophysics of mountain chains. Geol Soc America Mem 158, pp 131–147

Lécorché J-P, Bronner G, Dallmeyer RD, Rocci G, Roussel J (1991) The Mauritanide orogen and its northern extensions (western Sahara and Zemmour), West Africa. In: Dallmeyer RD, Lécorché JP (eds) The West African orogens and Circum-Atlantic correlatives. Springer, Berlin, pp 187–227

Le Goff E, Guerrot C, Maurin G, Iohan V, Tegyey M, Ben Zarga M (2001) Découverte d'éclogites hercyniennes dans la chaîne septentrionale des Mauritanides (Afrique de l'Ouest). Comptes Rendus Acad Sci Paris 333:711–718

Lehbib S, Arribas A, Melgarejo JC, Proenza JA, Zaccarini F, Thalhammer O, Garuti G (2008) Chromite deposits from western Sahara: textures, composition and platinum group minerals. SEM/SEA Colloquium, Revista Soc Española Mineral 9:143–144

Lescuyer JL, Leistel JM, Marcoux E, Milési JP, Thiéblemont D (1998) Late Devonian–early Carboniferous peak sulphide mineralization in the western Hercynides. Miner Deposita 33:208–220

Levresse G (2001) Contribution à l'établissement d'un modèle génétique des gisements d'Imiter (Ag-Hg),

Bou Madine (Pb-Zn-Cu-Ag-Au) et Bou Azzer (Co-Ni-As-Ag-Au) dans l'Anti-Atlas marocain. Unpubl PhD Thesis, CRPG-CNRS, Nancy, France, 191 pp

Liégeois JP, Stern RJ (2010) Sr-Nd isotopes and geochemistry of granite-gneiss complexes from the Meatiq and Hafafit domes, Eastern Desert, Egypt: no evidence for pre-Neoproterozoic crust. J African Earth Sci 57:31–40

Liégeois J-P, Black R, Navez J, Latouche L (1994) Early and late Pan-African orogenies in the Air assembly of terranes (Tuareg Shield, Niger). Precamb Res 67:59–88

Liégeois J-P, Latouche L, Boughrara M, Navez J, Guiraud M (2003) The LATEA metacraton (central Hoggar, Tuareg Shield, Algeria): behaviour of an old passive margin during the Pan-African orogeny. J African Earth Sci 37:161–190

Liégeois J-P, Benhallou A, Azzouni-Sekkal A, Yahiaoui R, Bonin B (2005) The Hoggar swell and volcanism: reactivation of the Precambrian Tuareg Shield during Alpine convergence and West African Cenozoic volcanism. In: Foulger GR, Natland JH, Presnall DC, Anderson DL (eds) Plates, plumes and paradigms. Geol Soc America Spec Paper 388, pp 379–400

Liégeois J-P, Abdelsalam MG, Ennih N, Ouabadi A (2013) Metacraton: nature, genesis and behavior. Gondwana Res 23:220–237

Lin S-C, Kuo B-Y, Chiao L-Y, van Keken PE (2005) Thermal plume models and melt generation in East Africa: a dynamic modeling approach. Earth Planet Sci Letters 237:175–192

Loomis TP (1975) Tertiary mantle diapirism, orogeny, and plate tectonics east of the Strait of Gibraltar. Amer J Sci 275:1–30

Lottaroli F, Craig J, Thusu B (2009) Neoproterozoic-Early Cambrian (Infracambrian) hydrocarbon prospectivity of North Africa: a synthesis. Geol Soc London Special Publ 326:137–156

Lucas J, Prévôt-Lucas L (1995) Tethyan phosphates and bioproductites. In: Nairn AEM et al. (eds) The ocean basins and margins. Plenum Press, New York, vol 8 (The Tethys Ocean), pp 367–391

Lucassen F, Pudlo D, Franz G, Romer RL, Dulski P (2013) Cenozoic intra-plate magmatism in the Darfur volcanic province: mantle source, phonolite-trachyte genesis and relation to other volcanic provinces in NE Africa. Internat J Earth Sci 102:183–205

Lustrino M, Wilson M (2007) The circum-Mediterranean anorogenic Cenozoic igneous province. Earth-Sci Rev 81:1–65

Maacha L, El Ghorfi M, Ennaciri O, Alansari A, Saquaque A, Soulaimani A (2011a) Chromite and platinum group elements associated with the Bou Azzer ophiolites (central Anti-Atlas). In: Mouttaqi A, Rjimati EC, Maacha L, Michard A, Soulaimani A, Ibouh H (eds) Les principales mines du Maroc. Notes Mémoires Service Géologique Maroc 564, pp 99–104

Maacha L, Maamar B, Kersit M, Saquaque A, Soulaimani A (2011b) The Bleida copper deposit (Bou azzer-El Graara inlier). In: Mouttaqi A, Rjimati EC, Maacha L, Michard A, Soulaimani A, Ibouh H (eds) Les principales mines du Maroc. Notes Mémoires Service Géologique Maroc 564, pp 105–109

Maacha L, Ennaciri O, El Ghorfi M, Baoutoul H, Saquaque A, Soulaimani A (2011c) The Jbel La'sal oxidized copper deposit (El Graara inlier, central Anti-Atlas). In: Mouttaqi A, Rjimati EC, Maacha L, Michard A, Soulaimani A, Ibouh H (eds) Les principales mines du Maroc. Notes Mémoires Service Géologique Maroc 564, pp 117–121

Maacha L, Ennaciri O, Saquaque A, Soulaimani A (2011d) A promizing prospect: the Jbel N'Zourk deposit (central anti-Atlas). In: Mouttaqi A, Rjimati EC, Maacha L, Michard A, Soulaimani A, Ibouh H (eds) Les principales mines du Maroc. Notes Mémoires Service Géologique Maroc 564, pp 123–127

Macgregor DS (1998) Giant fields, petroleum systems and exploration maturity of Algeria. Geol Soc London Spec Publ 132:79–96

Macgregor DS, Moody RTJ (1998) Mesozoic and Cenozoic petroleum systems of North Africa. Geol Soc London Spec Publ 132:201–216

Maddi O, Baoutoul H, Maacha L, Ennaciri O, Soulaimani A (2011) The Agjgal mine of southern Kerdous: overview of the stratabound copper and silver deposits in the western and central Anti-Atlas. In: Mouttaqi A, Rjimati EC, Maacha L, Michard A, Soulaimani A, Ibouh H (eds) Les principales mines du Maroc. Notes Mémoires Service Géologique Maroc 564, pp 151–156

Mahmoud HH, Abdel-Lateef AM, Attiah AM (2013) Distribution of some elements in the Egyptian black sands from Abu Khashaba beach area. J Anal Sci Methods Instrum 3:62–66

Makhous M, Galushkin Y, Lopatin N (1997) Burial history and kinetic modeling for hydrocarbon generation, part II: applying the GALO model to Saharan basins. AAPG Bull 81:1679–1699

Malusa MG, Polino R, Cerrina Feroni A, Ellero A, Ottria G, Baidder L, Musumeci G (2007) Post-Variscan tectonics in eastern Anti-Atlas (Morocco). Terra Nova 19:481–489

Mamedov EA, Ahmed ES, Chiragov MI (2012) Mineralogy, types and genesis of the copper-gold sulphide ore mineralization of Um Zerriq area, metallogenic Kid belt in southeastern Sinai Egypt. Caspian J Appl Sci Res 1:42–53

Marcoux E, Belkabir A, Gibson HL, Lentz D, Ruffet G (2008) Draa Sfar, Morocco: AVisean (331 Ma) pyrrhotite-rich, polymetallic volcanogenic massive sulphide deposit in a Hercynian sediment-dominant terrane. Ore Geol Rev 33:307–328

Marcoux E, Nerci K, Branquet Y1 Ramboz C, Ruffet G, Peucat J-J, Stevenson R, Jebrak M (2015) Late-Hercynian Intrusion gold-related gold deposits:

an integrated model on the Tighza polymetallic district, central Morocco. J African Earth Sci 107:65–88

Margoum D, Bouabdellah M, Klügel A, Banks DA, Castorina F, Cuney M, Jébrak M, Bozkaya G (2015) Pangea rifting and onward pre-Central Atlantic opening as the main ore-forming processes for the genesis of the Aouli REE-rich fluorite–barite vein system, upper Moulouya district, Morocco. J African Earth Sci 108:22–39

Marignac C, Cuney M (1999) Ore deposits of the French Massif Central: insight into the metallogenesis of the Variscan collision belt. Miner Deposita 34:472–504

Marignac C, Semiani A, Fourcade S, Boiron MC, Joron JL, Kienast JR, Peucat JJ (1996) Metallogenesis of the late Pan-African gold-bearing East Ouzzal shear zone (Hoggar, Algeria). J Metamorphic Geol 14:783–801

Marignac C, Belkasmi M, Chalal Y, Kesraoui M (2001) W-Nb-Ta oxides as markers of the magmatic to hydrothermal transition condition in rare-metal granites. In: Piestrzynski A (ed) Mineral deposits at the beginning of the 21st century. Proceed IIIrd Biennial SGA Meeting, Krakow, Poland, Balkema, Rotterdam, pp 441–444

Markwitz V, Hein KAA, Miller J (2015) Compilation of West African mineral deposits: spatial distribution and mineral endowment. Precamb Res (in press)

Martins LT, Madeira J, Youbi N, Munhá J, Mata J, Kerrich R (2008) Rift-related magmatism of the central Atlantic magmatic province in Algarve, southern Portugal. Lithos 101:102–124

Martyn J, Strickland C (2004) Stratigraphy, structure and mineralisation of the Akjoujt area, Mauritania. J African Earth Sci 38:489–503

Marutani M, Higashihara M, Watanabe Y, Murakami H, Kojima G, Dioumassi B (2005) Metallic ore deposits in the Islamic Republic of Mauritania. Resource Geol 55:59–70

Marzoli A, Renne PR, Piccirillo EM, Ernesto M, Bellieni G, De Min A (1999) Extensive 200-million-year-old continental flood basalts of the Central Atlantic magmatic province. Science 284:616–618

Marzoli A, Bertrand H, Knight KB, Cirilli S, Buratti N, Vérati C, Nomade S, Renne PR, Youbi N, Martini R, Allenbach K, Neuwerth R, Rapaille C, Zaninetti L, Bellieni G (2004) Synchrony of the Central Atlantic magmatic province and the Triassic-Jurassic boundary climatic and biotic crisis. Geology 32:973–976

Masurel Q, Thébaud N, Miller J, Ulrich S, Hein KAA (2015) The Alamoutala carbonate-hosted gold deposit in Mali, West Africa. Ore Geol Rev 33. doi: 10.1016/j.oregeorev.2015.10.012

Masurel Q, Miller J, Hein KAA, Hanssen E, Thébaud N, Ulrich S, Kaisin J, Tessougue S (2016) The Yatela gold deposit in Mali, West Africa: The final product of a long-lived history of hydrothermal alteration and weathering. J African Earth Sci 113:73–87

Mattauer M, Tapponnier P, Proust F (1977) Sur les mécanismes de formation des chaînes intracontinentales; l'exemple des chaînes atlasiques du Maroc. Bull Société Géol France 3:521–526

Matte Ph (2001) The Variscan collage and orogeny (480–290 Ma) and the tectonic definition of the Armorica microplate: a review. Terra Nova 13:122–128

Maurice AE (2006) Petrology and geochemistry of the banded iron-formation of some localities in the Eastern and Western Deserts of Egypt. Unpubl PhD thesis, Cairo University, Egypt, 383 pp

Maurin G, Bronner G, Le Goff E, Chardon D (1997) Notice explicative de la carte géologique à 1/200 000 de la feuille Chami (Mauritanie)-Prospection aurifère dans le Tasiast-Tijirit. BRGM Rept 2459, 32 pp

Maynard JB (2010) The chemistry of manganese ores through time: a signal of increasing diversity of Earth-surface environments. Econ Geol 105:535–552

McFarlane C, Mavrogenes J, Lentz D, King K, Allibone A, Holcombe R (2011) Geology and intrusion-related affinity of the Morila gold mine, southeast Mali. Econ Geol 106:727–750

Medina F (1988) Tilted-blocks pattern, paleostress orientation and amount of extension, related to Triassic early rifting of the Central Atlantic in the Amzri area (Argana basin, Morocco). Tectonophys 148:229–233

Meindre M (1959) Principales minéralisations du Hoggar (Sahara algérien). Chronique Mines d'Outre-mer 271:9–22

Melcher F, Graupner T, Gäbler H-E, Sitnikova M, Henjes-Kunst F, Oberthür T, Gerdes A, Dewaele S (2015) Tantalum–(niobium–tin) mineralisation in African pegmatites and rare metal granites: constraints from Ta–Nb oxide mineralogy, geochemistry and U-Pb geochronology. Ore Geol Rev 64:667–719

Melki F, Zouaghi T, Harrab S, Casas Sainz A, Bédir M, Zargouni F (2011) Structuring and evolution of Neogene trascurrent basins in the Tellian foreland domain, north-eastern Tunisia. J Geodyn 52:57–69

Meulenkamp JE, Sissingh W (2003) Tertiary palaeogeography and tectonostratigraphic evolution of the Northern and Southern Peri-Tethys platforms and the intermediate domains of the African–Eurasian convergent plate boundary zone. Palaeogeog Palaeoclimatol Palaeoecol 196:209–228

Meyer FM, Kolb J, Sakellaris GA, Gerdes A (2006) New ages from the Mauritanides belt: recognition of Archean IOCG mineralization at Guelb Moghrein. Terra Nova 18:345–352

Michard A (1976) Eléments de géologie marocaine. Notes Mém Serv Géol Maroc 252, 408 pp

Michard A, Frizon de Lamotte D, Chalouan A (2005) Comment on "The ultimate arc: differential displacement, oroclinal bending, and vertical axis rotation in the external Betic-rif arc". Tectonics 24:1–3

Michard A, Negro F, Saddiqi O, Bouybaouene ML, Chalouan A, Montigny R, Goffé B (2006) Pressure-temperature-time constraints on the Maghrebide mountain building: evidence from the Rif-Betic transect (Morocco, Spain), Algerian correlations, and geodynamic implications. Comptes Rendus Geosci 338:92–114

Michard A, Frizon de Lamotte D, Negro F, Saddiqi O (2007) Serpentinite slivers and metamorphism in the external Maghrebides: arguments for an intracontinental suture in the African paleomargin (Morocco, Algeria). Rev Soc Geol España 20:173–185

Michard A, Soulaimani A, Hoepffner C, Ouanaimi H, Baidder L, Rjimati EC, Saddiqi O (2010) The south-western branch of the Variscan belt: evidence from Morocco. Tectonophys 492:1–24

Michard A, Mokhtari A, Chalouan A, Saddiqi O, Rossi Ph, Rjimati E (2014) New ophiolite slivers in the external Rif belt, and tentative restoration of a dual Tethyan suture in the western Maghrebides. Bull Soc Géol France 185:313–328

Milési JP, Feybesse JL, Pinna P, Deschamps Y, Kampunzu H, Muhongo H, Lescuyer JL, Le Goff E, Delor C, Billa M, Ralay F, Heinry C (2004) Geological map of Africa 1:10,000,000, SIG Afrique project. In 20th Conference of African Geology, BRGM, Orléans, France, 2–7 June, http://www.sigafrique.net

Milesi JP, Frizon de Lamotte D, de Kock G, Toteu F (2010) Tectonic map of Africa 1/10,000,000, (2nd Edition). Commission for the Geological map of the World

Miranda JM, Luis JF, Abreu I, Victor LA, Galdeano A, Rossignol JC (1991) Tectonic framework of the Azores triple junction. Geophys Res Letters 18:1421–1424

Moctar DO, Boushaba A, Dubois M (2014) Serpentinization of mantle formations in the Mauritanides belt: regions of Agane and Gouérarate (middle-western Mauritania). Arabian J Geosci 7:1985–1992

Montero P, Haissen F, Archi AE, Rjimati E, Bea F (2014) Timing of Archean crust formation and cratonisation in the Awsard-Tichla zone of the NW Reguibat Rise, West African Craton: a SHRIMP, Nd–Sr isotopes, and geochemical reconnaissance study. Precamb Res 242:112–137

Morabet AM, Bouchta R, Jabour H (1998) An overview of the petroleum systems of Morocco. Geol Soc London Spec Publ 132:283–296

Moreno C, Sáez R, González F, Almodóvar G, Tosano M, Playford G, Alansari A, Rziki S, Bajddi A (2008) Age and depositional environment of the Draa Sfar massive sulphide deposit, Morocco. Miner Deposita 43:891–911

Morley CK (1987) Origin of a major cross-element zone: Moroccan Rif. Geology 15:761–764

Mouttaqi A, Sagon JP (1999) Le gisement de cuivre de Bleida (Anti-Atlas central): une interférence entre les processus de remplacement et d'exhalaison dans un contexte de rift. Chron Rech Minière 536:5–21

Muttoni G, Kent DV, Garzanti E, Brack P, Abrahamsen N, Gaetani M (2003) Early Permian Pangea 'B'to Late Permian Pangea 'A'. Earth Planetary Sci Letters 215:379–394

Negro F, Beyssac O, Goffé B, Saddiqi O, Bouybaouène ML (2006) Thermal structure of the Alboran domain in the Rif (northern Morocco) and the western Betics (southern Spain): constraints from Raman spectroscopy of carbonaceous material. J Metamorphic Geol 24:309–327

Nerci K (2006) Les minéralisations aurifères du district polymétallique de Tighza (Maroc central): un exemple de mise en place périgranitique tardihercynienne. Unpublished PhD Thesis, Université d'Orléans-Université du Québec à Montréal, France-Canada, 302 pp

Northolt AJG (1987) Phosphate rock. Yorkshire Geol Soc, Hull University, Kingston upon Hull, UK, General meeting-phosphate rich sediments

Notholt AJG (1985) Phosphorite resources in the Mediterranean (Tethyan) phosphogenic province. A progress report. Sci Geol Mem 77:9–21

Notholt AJG, Sheldon RP, Davidson DF (1989) Phosphate deposits of the world, vol 2. Cambridge University Press, Cambridge, UK, Phosphate rock resources 566 pp

Nouar O, Henry B, Liégeois J-P, Derder MEM, Bayou B, Bruguier O, Ouabadi D, Amenna M, Hemmi A, Ayache M (2011) Eburnean and Pan-African granitoids and the Raghane mega-shear zone evolution: image analysis, U-Pb zircon age and AMS study in the Arokam Ténéré (Tuareg Shield, Algeria). J African Earth Sci 60:133–152

Ntarmouchant A (1991) Le magmatisme hercynien de la région de Mrirt. Unpub PhD thesis, Université Sidi Mohamed Ben Abdellah, Fès, Morocco, 169 pp

O'Connor EA, Pitfield PEJ, Schofield DI, Coats S, Waters C, Powell J, Ford J, Clarke S, Gillespie M (2005) Notice explicative des cartes géologiques et gîtologiques à 1/200 000 et 1/500 000 du nord-ouest de la Mauritanie. Ministere Mines l'Industrie, Nouakchott, Mauritania, DMG 398 pp

Oberthür T, Melcher F, Henjes-Kunst F, Gerdes A, Stein H, Zimmerman A, El Ghorfi M (2009) Hercynian age of the cobalt-nickel-arsenide-(gold) ores, Bou Azzer, Anti-Atlas, Morocco: Re-Os, Sm-Nd and U-Pb age determinations. Econ Geol 104:1065–1079

Ogg JG, Ogg G, Gradstein FM (2008) The concise geologic time scale. Cambridge University Press, Cambridge, UK

ONHYM (2015) Minéralisations d'uranium et terres rares dans le prospect d'Aghracha (Provinces du Sud, Maroc): Office National des Hydrocarbures et des Mines. Office National des Hydrocarbures et des Mines, Rabat, Morroco 5 pp

Ouali H, Briand B, Bouchardon JL, Capiez P (2003) Le volcanisme Cambrien du Maroc central: implications géodynamiques. Comptes Rendus Geosci 335:425–433

Ould Moctar D, Boushaba A. Dubois M (2014) Serpentinization of mantle formations in the Mauritanides Belt: regions of Agane and Gouérarate (middle-western Mauritania). Arabian J Geosci 7 (5):1985–1992

Ounis A, Kocsis L, Chaabani F, Pfeifer H-R (2008) Rare earth elements and stable isotope geochemistry ($\delta^{13}C$ and $\delta^{18}O$) of phosphorite deposits in the Gafsa basin, Tunisia. Palaeogeogr Palaeoclimatol Palaeoecol 268:1–18

Ouzegane K, Kienast JR, Bendaoud A, Drareni A (2003) A review of Archaean and Paleoproterozoic evolution of the In Ouzzal granulitic terrane (western Hoggar, Algeria). J African Earth Sci 37:207–227

Pagel M, Cavellec S, Frobes P, Gerbaud O, Vergely P, Wagani I, Mathieu R (2005) Uranium deposits in the Arlit area (Niger). In: Mao J, Bierlein MP (eds), Mineral deposit research, meeting the global challenge. Proceed 8th Biennial SGA Meeting, Beijing, China. Society for Geology Applied to Mineral Deposits, pp 303–305

Pearson DG, Nixon PH (1996) Diamonds in young orogenic belts: graphitized diamonds from Beni Bousera, N Morocco, a comparison with kimberlite-derived diamond occurrences and implications for diamond genesis and exploration. Africa Geosci Rev 3:295–316

Pearson DG, Nowell GM (2004) Re-Os and Lu-Hf isotope constraints on the origin and age of pyroxenites from the Beni Bousera peridotite massif: implications for mixed peridotite-pyroxenite mantle sources. J Petrol 45:439-455

Pearson DG, Davis GR, Nixon PH, Milledge HJ (1989) Graphitized diamonds from a peridotite massif in Morocco and implications for anomalous diamond occurrences. Nature 338:60–62

Pearson DG, Davies GR, Nixon PH (1993) Geochemical constraints on the petrogenesis of diamond facies pyroxenites from the Beni Bousera peridotite massif, north Morocco. J Petrol 34:125–172

Pegram WJ, Register JK, Fullagar PD, Ghuma MA, Rogers JJW (1976) Pan-African ages from a Tibesti massif batholith, southern Libya. Earth Planet Sci Letters 30:123–128

Pelleter E, Cheilletz A, Gasquet D, Moutaqqi A, Annich M, El Hakour A (2006) Discovery of Neoproterozoic Banded Iron Formation (BIF) in Morocco. Geophys Res Abstracts 8, 04635, SRef-ID: 1607-7962/gra/EGU06-A-04635

Pelleter E, Cheilletz A, Gasquet D, Mouttaqi A, Annich M, El Hakour A, Féraud G (2008) The Variscan Tamlalt-Menhouhou gold deposit, eastern High-Atlas, Morocco. J African Earth Sci 50:204–214

Penney R (2012) Australian sandstone-hosted uranium deposits. Inst Mining Metall Trans B 121:65–75

Perez JB, Dusausoy Y, Babkine J, Pagel M (1990) Mn zonation and fluid inclusions in genthelvite from the Taghouaji complex (Air Mountains, Niger). Amer Mineral 75:909–914

Permingeat F (1957) Le gisement de molybdène, tungstène et cuivre d'Azegour. Notes Mémoires Service Géologique Maroc 141, 284 pp

Peucat JJ, Drareni A, Latouche L, Deloule E, Vidal P (2003) U-Pb zircon (TIMS and SIMS) and Sm–Nd whole-rock geochronology of the Gour Oumelalen granulitic basement, Hoggar massif, Tuareg shield, Algeria. J African Earth Sci 37:229–239

Piña R, Gervilla F, Barnes S-J, Ortega L, Lunar R (2013) Partition coefficients of platinum group and chalcophile elements between arsenide and sulfide phases as determined in the Beni Bousera Cr-Ni mineralization (north Morocco). Econ Geol 108:935–951

Piqué A (2001) Geology of northwest Africa. Borntraeger, Berlin 310 pp

Piqué A, Dahmani M, Jeannette D, Bahi L (1987) Permanence of structural lines in Morocco from Precambrian to present. J African Earth Sci 6:247–256

Piqué A, Tricart P, Guiraud R, Laville E, Bouaziz S, Amrhar M, Ouali RA (2002) The Mesozoic-Cenozoic Atlas belt (North Africa): an overview. Geodinam Acta 15:185–208

Pitfield PEJ, Campbell SDG (1996) Significance for gold exploration of structural styles of auriferous deposits in the Archaen Bulawayo-Bubi greenstone belt of Zimbabwe. Inst Mining Metall Trans B 105:41–52

Pitfield PEJ, Key RM, Waters CN, Hawkins MPH, Schofield DI, Loughlin S, Barnes RP (2004) Notice explicative des cartes géologiques et gîtologiques à 1/200 000 et 1/500 000 du Sud de la Mauritanie, vol 1. Direction des Mines l'Industrie, Nouakchott, Mauritania 580 pp

Platt JP, Whitehouse MJ, Kelley SP, Carter A, Hollick L (2003) Simultaneous extensional exhumation across the Alboran basin: implications for the causes of late orogenic extension. Geology 31:251–254

Potrel A, Peucat JJ, Fanning CM (1998) Archean crustal evolution of the West African craton: example of the Amsaga area (Reguibat Rise): U-Pb and Sm-Nd evidence for crustal growth and recycling. Precamb Res 90:107–117

Pouclet A, Guillot PL, Gatta AB (1987) Nouvelles données lithostructurales, pétrographiques, minéralogiques et géochimiques sur le gisement de cuivre d'Akjoujt et son environment géologique (République Islamique de Mauritanie). J African Earth Sci 6:29–43

Pouit G (1964) Les gîtes de manganèse marocains encaissés dans les Formations carbonatées: éléments pour une synthèse. Chronique Mines Recherche Minière 337:371–380

Pouit G (1976) La concentration de manganèse de l'Imini (Maroc) peut-elle être d'origine karstique? Comptes Rendus Sommaire Soc Géol France 5:227–229

Prian J-P (2014) Phosphate deposits of the Senegal-Mauritania-Guinea basin (West Africa): a review. Procedia Engineer 83:27–36

Puglisi D (2009) Early Cretaceous flysch from Betic-Maghrebian and Europe Alpine chains (Gibraltar Strait to the Balkans): comparison and palaeotectonic implications. Balcanica 38:15–22

Ramdani F (1998) Geodynamic implications of the intermediate-depth earthquakes and volcanism in the intra-plate Atlas Mountains (Morocco). Phys Earth Planet Inter 108:245–260

Randgold Resources (2009) Annual Report 2009. Randgold Resources, 156 pp http://www.randgoldresources.com/file/4921/download?token=qaCpikly

Randgold Resources (2014) Annual Report. Randgold Resources, 248 pp http://reports.randgoldresources.com/sites/reports.randgoldresources.com/files/Annual%20Report%202014_0.pdf

Rhalmi M, Pascal A, Lang J (1997) Contrôle sédimentaire et diagénétique de la minéralisation manganésifère au cours du Crétacé Supérieur dans la région d'Imini (Haut-Atlas central, Maroc). Comptes Rendus Acad Sci 323:213–220

Rogers JW, Ghuma MA, Nagy RM, Greenburg JK, Fullagar PD (1978) Plutonism in Pan-African belts and the geologic evolution of northeastern Africa. Earth Planet Sci Letters 39:109–117

Rollinson H, Reid C, Windley B (2010) Chromitites from the Fiskenæsset anorthositic complex, West Greenland: clues to late Archaean mantle processes. Geol Soc London Spec Publ 338:197–212

Rooney AD, Selby D, Houzay JP, Renne PR (2010) Re–Os geochronology of a Mesoproterozoic sedimentary succession, Taoudeni basin, Mauritania: implications for basin-wide correlations and Re–Os organic-rich sediments systematics. Earth Planet Sci Letters 289:486–496

Ruiz Cruz MD, De Galdeano CS, Garrido C (2011) Electron backscatter diffraction-based identification and quantification of diamonds from the Rif gneisses (Spain and Morocco): economic implications. Econ Geol 106:1241–1249

Saddiqi O, Reuber I, Michard A (1988) Sur la tectonique de dénudation du manteau infracontinental dans les Beni Bousera, Rif septentrional, Maroc. Comptes Rendus Acad Sci Paris 307:657–662

Sakellaris GA (2007) Petrology, geochemistry, stable and radiogenic isotopy of the Guelb Moghrein iron oxide–copper–gold–cobalt deposit, Mauritania. Unpubl PhD Thesis, RWTH Aachen University, Aachen, Germany, 222 pp

Saleh GM (2007) Rare metal-bearing pegmatites from the southeastern desert of Egypt: geology, geochemical characteristics, and petrogenesis. Chinese J Geochem 26:8–22

Salvi S, Sangaré A, Driouch Y, Siebenaller L, Béziat D, Debat P, Femenias O (2015) The Kalana vein-hosted gold deposit, southern Mali. Ore Geol Rev (in press)

Samson SD, Inglis JD, D'Lemos RS, Admou H, Blichert-Toft J, Hefferan K (2004) Geochronological, geochemical, and Nd-Hf isotopic constraints on the origin of Neoproterozoic plagiogranites in the Tasriwine ophiolite, Anti-Atlas orogen, Morocco. Precamb Res 135:133–147

Sanguinetti H, Oumarou J, Chantret F (1982) Localisation de l'uranium dans les figures de sédimentation des grès hôtes du gisement d'Akouta, République du Niger. Comptes Rendus Acad Sci Paris Sér II:591–594

Saquaque A, Admou H, Karson J, Hefferan K, Reuber I (1989) Precambrian accretionary tectonics in the Bou Azzer-El Graara region, Anti-Atlas, Morocco. Geology 17:1107–1110

Saquaque A, Benharref M, Abia H, Mrini Z, Reuber I, Karson JA (1992) Evidence for a Panafrican volcanic arc and wrench fault tectonics in the Jbel Saghro, Anti-Atlas, Morocco. Geol Rundschau 81:1–13

Savage C (1987) World survey of phosphate deposits. British Sulphur Corporation Ltd., London, UK 274 pp

Schaer JP, Rodgers J (1987) The anatomy of mountain ranges. Princeton University Press, Princeton, New Jersey, USA 298 pp

Schandelmeier H, Reynolds PO (eds) (1997) Paleogeographic-paleotectonic atlas of north-eastern Africa, Arabia, and adjacent areas. Balkema, Rotterdam, pp 249–258

Schandelmeier H, Huth A, Harms U, Franz G, Bernau R (1987) The east Saharan craton in southern Egypt and northern Sudan: lithology, metamorphism, magmatism, geochronology and structural development. Berliner Geowissenschaft Abhandlungen A 75:25–48

Schandelmeier H, Wipfler E, Küster D, Sultan M, Becker R, Stern RJ, Abdelsalam MG (1994) Atmur-Delgo suture: a Neoproterozoic oceanic basin extending into the interior of northeast Africa. Geology 22:563–566

Schneiderhöhn H (1961) Die pegmatite. Die Erzlagerstätten der Erde, v II. Gustav Fischer Verlag, Stuttgart, Germany, p 720

Schofield DI, Gillespie MR (2007) A tectonic interpretation of "Eburnian terrane" outliers in the Reguibat shield, Mauritania. J African Earth Sci 49:179–186

Schofield DI, Pitfield PEJ, Jordan CJ, Wildman G, Bateson L (2003) Carte géologique de la région Oussat-Sfariat (nord Mauritanie) at 1:200,000. OMRG, Ministère Mines l'Industrie, Nouakchott, Mauritania

Schofield DI, Horstwood MSA, Pitfield PEJ, Crowley QG, Wilkinson AF, Sidaty HCO (2006) Timing and kinematics of Eburnean tectonics in the central Reguibat shield, Mauritania. J Geol Society 163:549–560

Schofield DI, Horstwood MSA, Pitfield PEJ, Gillespie MR, Darbyshire F, O'Connor EA, Abdouloye TB (2012) U-Pb dating and Sm-Nd isotopic analysis of granitic rocks from the Tiris complex: new constraints on key events in the evolution of the Reguibat shield, Mauritania. Precamb Res 204–205:1–11

Schulz HN, Schulz HD (2005) Large sulfur bacteria and the formation of phosphorite. Science 307:416–418

Sebbar A, Préat A, Mamet BL (2000) Microfaciès et biozonation de la rampe mixte carbonifère du basin de Tindouf, Algérie. Bull Centre Recherche Elf Exploration Prod 22:203–239

Seber D, Barazangi M, Ibenbrahim A, Demnati A (1996) Geophysical evidence for lithospheric delamination beneath the Alboran Sea and Rif-Betic Mountains. Nature 379:785–790

Sebti S, Saddiqi O, El Haimer FZ, Michard A, Ruiz G, Bousquet R, Baidder L, de Lamotte DF (2009) Vertical movements at the fringe of the West African craton: first zircon fission track datings from the Anti-Atlas Precambrian basement, Morocco. Comptes Rendus Geosci 341:71–77

Sedore M, Masterman G (2012) Tasiast mine Mauritania 43-101F1. Technical Report for Kinross Gold Corporation. Kinross Corp., 43-101F1 Technical Report, 162 p, http://www.br-kinrossconnected.kinross.com/media/165609/tasiast.pdf

Semiani A, Marignac C, Fourcade S, Peucat JJ, Boiron MC, Joron JL, Kienast JR (1995) Metallogenesis of the gold-bearing East-Ouzzal shear-zone (Hoggar, Algeria). Mineral Deposits, Rotterdam, pp 187–190

Sghaier D, Chaabani F, Proust D, Vieillard Ph (2014) Mineralogical and geochemical signatures of clays associated with rhyodacites in the Nefza area (northern Tunisia). J African Earth Sci 100:267–277

Sharara NAF (2000) Geochemistry and genesis of the specialized stanniferous granites of the central Eastern Desert of Egypt. Assiut Univ, Bull Faculty Science, Geology 29(1-F):1–2

Sheldon RP (1964) Paleolatitudinal and paleogeographic distribution of phosphorite. US Geol Survey Prof Paper 501-C:106–113

Sheldon RP (1980) Episodicity of phosphate deposition and deepocean circulation. An hypothesis. In: Bentor YK (ed), Marine phosphorites, geochemistry, occurrence, genesis. Soc Econ Paleont Mineral Spec Publ 29, pp 239–247

Sillitoe RH (1979) Metallogenic consequences of Late Precambrian suturing in Arabia, Egypt, Sudan, and Iran: evolution and mineralization of the Arabian–Nubian shield. Proceed Symposium Convened by Ahmad MS Al-Shanti 1979, Institute Applied Geology, King Abdulaziz University, Jeddah, Saudi Arabia. Elsevier, pp 109–120

Sims J (2014) Tasiast project, Mauritania National Instrument 43-101 Technical Report, Prepared for Kinross Gold Corporation, 253 pp

Sims PK, James HL (1984) Banded iron-formations of Late Proterozoic age in the central Eastern Desert, Egypt; geology and tectonic setting. Econ Geol 79:1777–1784

Sizaret S, Branquet Y, Gloaguen E, Chauvet A, Barbanson L, Arbaret L, Chen Y (2009) Estimating the local paleo-fluid flow velocity: new textural method and application to metasomatism. Earth Planetary Sci Letters 280:71–82

Sonnet PM, Verkaeren J (1989) Scheelite-, malayaite-, and axinite-bearing skarns from El Hammam, central Morocco. Econ Geol 84:575–590

Sougy J (1962) West African fold belt. Geol Soc America Bull 73:871–876

Sougy J, Lécorché JP (1963) Sur la nature glaciaire de la base de la série de Garat el Hamouéid (Zemmour, Mauritanie septentrionale). Comptes Rendus Acad Sci Paris 256:4471–4474

Sougy J, Bronner G (1969) Nappes hercyniennes au Sahara espagnol méridional (tronçon nord des Mauritanides). 5th Inter Coll African Géol Ann Faculty Sci. Université de Clermont-Ferrand 41:75–76

Souissi F, Jemmali N, Souissi R, Dandurand J-L (2013) REE and isotope (Sr, S, and Pb) geochemistry to constrain the genesis and timing of the F–(Ba–Pb–Zn) ores of the Zaghouan district (NE Tunisia). Ore Geol Rev 55:1–12

Soulaimani A, Burkhard M (2008) The Anti-Atlas chain (Morocco): the southern margin of the Variscan belt along the edge of the West African craton. Geol Soc London Spec Publ 297:433–452

Soulaimani A, Essaifi A, Youbi N, Hafid A (2004) Les marqueurs structuraux et magmatiques de l'extension crustale au Protérozoïque terminal–Cambrien basal autour du massif de Kerdous (Anti-Atlas occidental, Maroc). Comptes Rendus Geosci 336:1433–1441

Soulaimani A, Razin P, Youbi N, Barbanson L, Admou H, Blein O, Gasquet D, Bouabdelli M, Anzar C (2013) Notice explicative de la Carte géologiques du Maroc (1/50 000), feuille Al Gloa. Notes Mém Serv Géol Maroc (532 bis)

Stampfli G, Marcoux J, Baud A (1991) Tethyan margins in space and time. Palaeogeogr Palaeoclimatol Palaeoecol 87:373–409

Stern RJ (1994) Arc assembly and continental collision in the Neoproterozoic E African orogen: implication for the consolidation of Gondwanaland. Ann Rev Earth Planet Sci 22:319–351

Stern RJ (2002) Crustal evolution in the East African orogen: a neodymium isotopic perspective. J African Earth Sci 34:109–117

Stern RJ, Avigad D, Miller NR, Beyth M (2006) Evidence for the snowball Earth hypothesis in the Arabian-Nubian shield and the East African orogen. J African Earth Sci 44:1–20

Stern RJ, Mukherjee SK, Miller NR, Ali K, Johnson PR (2013) ~750 Ma banded iron formation from the Arabian-Nubian shield—implications for understanding Neoproterozoic tectonics, volcanism, and climate change. Precamb Res 239:79–94

Stoeser DB, Frost CD (2006) Nd, Pb, Sr, and O isotopic charcterization of Saudi Arabian shield terranes. Chem Geol 226:163–188

Strickland C, Martyn JE (2002) The Guelb Moghrein Fe-oxide copper-gold-cobalt deposit and associated mineral occurrences, Mauritania: a geological introduction. In: Porter TM (ed) Hydrothermal iron oxide copper-gold & related deposits: a global perspective. PGC Publishing, Adelaide, Australia, vol 2, pp 275–291

Stuart H (2010) Technical Report on the Tasiast Gold Mine Islamic Republic of Mauritania. Unpubl technical report, Red Back Mining Inc., 104 pp

Suayah IB, Miller JS, Miller BV, Bayer TM, Rogers JJ (2006) Tectonic significance of late Neoproterozoic granites from the Tibesti massif in southern Libya inferred from Sr and Nd isotopes and U-Pb zircon data. J African Earth Sci 44:561–570

Suter G (1980) Carte géologique de la chaine Rifaine, échelle 1:500,000. Ministère de l'Energie et des Mines du Maroc, Direction de la Géologie, Rabat. Notes Mém Serv Géol Maroc 245a

Suzaki R, Kolli O, Mokrane K, Boutaleb A, Taguchi S, YonezuK Watanabe K (2013) Granite related mineralization of tungsten in Hoggar, southern Algeria. 11th Inter Conf Mining, Materials and Petroleum Engineering, 7th Intern Conf Earth Resources Technology, ASEAN Forum on Clean Coal Technology, November 11–13, Chiang Mai, Thailand, Geology, Geophysics and Geotechnique 37. Paper ID 109:33–37

Taib M (2014) The mineral industry of Mauritania. U.S. Geological Survey 2012 Minerals Yearbook—Mauritania, 6 pp. http://minerals.usgs.gov/minerals/pubs/country/2012/myb3-2012-mr.pdf

Takla MA, Hamimi Z, Hassanein SM, Kaoud NN (1999) Characterization and genesis of the BIF associating arc metavolcanics, Umm Ghamis area, central Eastern Desert Egypt. Egyptian Mineral 11:157–185

Tawadros EE (2011) Geology of North Africa. CRC Press, Balkema, Leiden, The Netherlands 931 pp

Taylor CD (ed) (2015) Second projet de renforcement institutionnel du secteur minier de la République Islamique de Mauritanie (PRISM-II): U.S. Geological Survey Open-File Rept 2013–1280-H, 22 pp, http://dx.doi.org/10.3133/ofr20131280h/. [In English and French]

Taylor CD, Anderson ED, Bradley DC, Beaudoin G, Cosca MA, Eppinger RG, Gl Fernette, Finn CA, Friedel MJ, Giles SA, Goldfard RJ, Horton JD, Lee GK, Marsh EE, Mauk JL, Motts HA, Ould El Joud MY, Ould Soueidatt S, Ould Taleb Mohamed A, Rockwell BW (2012) Mairitania: a greenfields exploration opportunity in northwestern Africa. SEG Newsletter 91:10–17

Teixell A, Arboleya ML, Julivert M, Charroud M (2003) Tectonic shortening and topography in the central High Atlas (Morocco). Tectonics 22:1051–1064

Teixell T, Ayarza P, Zeyen H, Fernandez M, Arboleya ML (2005) Effects of mantle upwelling in a compressional setting: the Atlas Mountains of Morocco. Terra Nova 17:456–461

Temagoult A (1989) Prospection et étude des indices de chromite de l'oued Tamanart. Magister Thesis, Constantine University, Constantine, Algeria, 114 pp

Thein J (1990) Paleogeography and geochemistry of the "Cenomano-Turonian" formations in the manganese district of Imini (Morocco) and their relation to ore deposition. Ore Geol Rev 5:257–291

Thomas RJ, Chevallier LC, Gresse PG, Harmer RE, Eglington BM, Armstrong RA, de Beer CH, Martini JE, de Kock GS, Macey P, Ingram B (2002) Precambrian evolution of the Sirwa window, Anti-Atlas orogen, Morocco. Precamb Res 118:1–57

Thomas RJ, Fekkak A, Ennih N, Errami E, Loughlin SC, Gresse PG, Chevallier LP, Liégeois JP (2004) A new lithostratigraphic framework for the Anti-Atlas orogen, Morocco. J African Earth Sci 39:217–226

Tkachev AV (2011) Evolution of metallogeny of granitic pegmatites associated with orogens throughout geological time. In: Sial AN, Bettencourt JS, de Campos CP, Ferreira VP (eds) Granite-related ore deposits. Geol Soc London Spec Publ 350, pp 7–23

Treloar PJ, Lawrence DM, Senghor D, Boyce A, Harbidge P (2015) The Massawa gold deposit, eastern Senegal, West Africa: an orogenic gold deposit sourced from magmatically derived fluids? Geol Soc London Spec Publ 393:135–160

Trench A, Groves D (2015) The western Arabian-Nubian shield: a rapidly emerging gold province. SEG Newsletter 101:1–16

Trouw RAJ, De Wit M (1998) Intracontinental deformation of Gondwana: fundamental shear zones and Gondwanide fold belts: links with the onset of Gondwana fragmentation? J African Earth Sci 27:200–200

Tubia JM, Cuevas J (1986) High-temperature emplacements of Los Reales peridotite nappe (Betic Cordillera, Spain). J Struct Geol 8:473–482

Turpin L, Clauer N, Forbes P, Pagel M (1991) U-Pb, Sm-Nd and K-Ar systematics of the Akouta unranium deposit. Niger. Chem Geol 87:217–230

Unrug R (1997) Rodinia to Gondwana: the geodynamic map of Gondwana supercontinent assembly. GSA Today 7:1–6

U.S. Geological Survey (2010a) Minerals Yearbook: Mali and Niger. U.S. Geological Survey, 4 pp http://minerals.usgs.gov/minerals/pubs/country/2010/myb3-2010-ml-ng.pdf

U.S. Geological Survey (2010b) Minerals Yearbook: Morocco and Western Sahara. U.S. Geological Survey, 9 pp http://minerals.usgs.gov/minerals/pubs/country/2010/myb3-2010-mo-wi.pdf

U.S. Geological Survey (2010c) Minerals Yearbook: Algeria. U.S. Geological Survey, 11 pp http://minerals.usgs.gov/minerals/pubs/country/2010/myb3-2010-ag.pdf

U.S. Geological Survey (2010d) Minerals Yearbook: Egypt. U.S. Geological Survey, 13 pp http://minerals.usgs.gov/minerals/pubs/country/2010/myb3-2010-eg.pdf

U.S. Geological Survey (2012) Minerals Yearbook: Mauritania. U.S. Geological Survey, 6 pp http://minerals.usgs.gov/minerals/pubs/country/2012/myb3-2012-mr.pdf

U.S. Geological Survey (2013) Mineral commodity summaries 2013. U.S. Geological Survey, 198 pp http://minerals.usgs.gov/minerals/pubs/mcs/2013/mcs2013.pdf

U.S. Geological Survey (2014) Phosphate rock. In U.S. Geological Survey Mineral Commodity Summaries 2014, pp 118–119

Valsardieu C (1971) Étude géologique et paléogéographique du bassin du Tim Mersoï, région d'Agadès (République du Niger). Unpubl PhD Thesis, Université de Nice, Nice, France, 518 pp

Verati C, Bertrand H, Féraud G (2005) The farthest record of the Central Atlantic magmatic province into West Africa craton: precise 40Ar/39Ar dating and geochemistry of Taoudenni basin intrusives (northern Mali). Earth Planet Sci Letters 235:391–407

Vially R, Letouzey J, Benard F, Haddadi N, Desforges G, Askri H, Boudjema A (1994) Basin inversion along the North African margin. The Saharan atlas (Algeria). Peri-Tethyan platforms. Paris, Technip, pp 79–118

Villeneuve M (1984) Etude géologique de la bordure SW du craton ouest africain-la suture Panafricaine et l'evolution des bassins sédimentaires Protérozoïques et Paléozoïques de la marge NW du continent de Gondwana. Unpublished PhD thesis, Université Aix-Marseille III, France, 552 pp

Villeneuve M (2005) Paleozoic basins in West Africa and the Mauritanide thrust belt. J African Earth Sci 43:166–195

Villeneuve M (2008) Review of the orogenic belts on the western side of the West African craton: the Bassarides, Rokelides and Mauritanides. In: Ennih N, Liégeois J-P (eds) Boundaries of the West African craton. Geological Soc London Spec Publ 297, pp 169–201

Villeneuve M, Cornée JJ (1994) Structure, evolution and palaeogeography of the West African craton and bordering belts during the Neoproterozoic. Precamb Res 69:307–326

Villeneuve M, Bonvalot S, Albouy Y (1990) L'agencement des chaînes (Panafricaines et Hercynienne) de la bordure occidentale du craton ouest africain. Comptes Rendus Académie Sci 310:955–959

Villeneuve M, Bellon H, El Archi A, Sahabi M, Rehault J-P, Olivet J-L, Aghzer AM (2006) Événements panafricains dans l'Adrar Souttouf (Sahara marocain). Comptes Rendus Geosci 338:359–367

Wadjinny A (1998) Le plomb au Maroc: cas des districts de Touissit et de Jbel Aouam. Chronique Recherche Minière 531–532:9–28

Wagner C, Mokhtari A, Deloule E, Chabaux F (2003) Carbonatite and alkaline magmatism in Taourirt (Morocco): petrological, geochemical and Sr–Nd isotope characteristics. J Petrol 44:937–965

Walsh GJ, Aleinikoff JN, Benziane F, Yazidi A, Armstrong TR (2002) U-Pb zircon geochronology of the Paleoproterozic Tagragra de Tata inlier and its Neoproterozoic cover, western Anti-Atlas, Morocco. Precamb Res 117:1–20

Watanabe Y (2002) $^{40}Ar/^{39}Ar$ geochronologic constraints on the timing of massive sulfide and vein-type Pb-Zn mineralization in the western Meseta of Morocco. Econ Geol 97:145–157

Westaway R (1990) Present-day kinematics of the plate boundary zone between Africa and Europe, from the Azores to the Aegean. Earth Planet Sci Letters 96:393–406

Wildi W (1983) La chaîne tello-rifaine (Algérie, Maroc, Tunisie): structure, stratigraphie et evolution du Trias au Micène. Rev Géol Dyn Geogr Phys 24:201–297

Williams PJ, Barton MD, Johnson DA, Fontboté L, De Haller A, Mark G, Oliver NHS, Marschik R (2005) Iron oxide copper-gold deposits: geology, space-time distribution, and possible modes of origin. In: Hedenquist JW, Thompson JFH, Goldfarb RJ, Richards JP (eds) Economic Geology 100th Anniversary Volume, 1905–2005. Society of Economic Geologists Inc, Littleton, Colorado, USA, pp 371–405

Wilson M, Guiraud R (1998) Late Permian to Recent magmatic activity on the Africa-Arabian margin of Tethys. In: MacGregor SD, Moody JR, Clark-Lowes DD (eds) Petroleum geology of North Africa. Geol Soc London Spec Publ 132, pp 231–263

Wolff R, Dunkl I, Kempe U, von Eynatten H (2015) The age of the latest thermal overprint of tin and polymetallic deposits in the Erzgebirge, Germany: constraints from fluorite (U–Th–Sm)/He thermochronology. Econ Geol 110:2025–2040

World Nuclear Association (2015) Uranium in Niger: World Nuclear Association http://www.world-nuclear.org/info/country-profiles/countries-g-n/niger/

Yahaya M, Lang J, Cazoulat M, Crasquin S, Doubinger J, Forbes P, James O, Pagel M, Pascal A, de Rouvre I (1986) La formation viséenne Guezouman (Arlit-Niger)-Dynamique sédimentaire en milieu fluvio-deltaïque-Piégeage de l'uranium. Abstr Vol Meeting Working Group on African Continental Sediments, Jos. Geol Soc Afr Int Geol Correl Prog (IGCP) 210:66–67

Youssef MI (1957) Upper Cretaceous rocks in Kosseir area. Bull Inst Desert Egypt VII:35–53

Zaïer A, Beji-Sassi A, Sassi S, Moody RTJ (1998) Basin evolution and deposition during the Early Paleocene in Tunisia. In: Macgregor DS, Moody RTJ, Clark-Lowes DD (eds), Petroleum geology of North Africa. Geol Soc London Spec Publ 132, pp 375–393

Zhang P, Wiegel R, El-Shall H (2006) Phosphate rock. In: Kogel JE, Trivedi NC, Barker JM, Krukowski ST (eds) Industrial minerals and rocks: commodities, markets, and uses. 7th edn. Society for Mining, Metallurgy and Exploration, Inc. (SME) Littleton, Colorado, USA, 80127, pp 703–722

Zhou MF, Sun M, Keays R, Kerrich RW (1998) Control on platinum-group elemental distributions of podiform chromitites: A case study of high-Cr and high-Al chromitites from Chinese orogenic belts. Geochim Cosmochim Acta 62:667–688

Zindler A, Staudiel M, Hart SR, Enders R, Goldstein S (1983) Nd and Sr isotope study of a mafic layer from Ronda ultramafic complex. Nature 304:226–230

Zoheir BA, El-Shazly AK, Helba H, Khalil KI, Bodnar RJ (2008) Origin and evolution of the Um Egat and Dungash orogenic gold deposits, Egyptian Eastern

Desert: evidence from fluid inclusions in quartz. Econ Geol 103:405–424

Zoheir BA, Creaser RA, Lehmann B (2014) Re-Os geochronology of gold mineralization in the Fawakhir area. Inter Geology, Eastern Desert, Egypt. doi:10.1080/00206814.2014.935964

Zouhair M, Marignac C, Macaudière J, Boiron MC (1991) Gold deposition in the gold-bearing quartz veins of the Tagragra d'Akka (western Anti-Atlas, Morocco): P-T–X conditions and place in the evolution of metamorphic fluids. In: Pagel Leroy (ed) Source, transport and deposition of metals. Balkema, Rotterdam, pp 723–726

Zverev S, Novikov V, Tcheremisin A, Abramov, Lebedev V (2003) Rapport sur les études portant sur l'élaboration d'un modèle génétique sur le gisement d'Iourirn (boutonnière de Tagra d'Akka, Anti-Atlas, Maroc). Unpubl Report, Akka Gold MIning Company, 91 pp

Part II

Porphyry, Skarn, and Epithermal Deposits

Degassing as the Main Ore-Forming Process at the Giant Imiter Ag–Hg Vein Deposit in the Anti-Atlas Mountains, Morocco

Gilles Levresse, Mohammed Bouabdellah, Alain Cheilletz, Dominique Gasquet, Lhou Maacha, Jordi Tritlla, David Banks and Azizi Samir Moulay Rachid

Abstract

The giant Imiter epithermal Ag–Hg vein deposit in the Anti-Atlas Mountains of southern Morocco formed during a major episode of mineralization linked with Ediacaran volcanism at ca. 550 Ma. Silver was

G. Levresse (✉) · J. Tritlla
Programa de Geofluidos, Centro de Geociencias
UNAM-Campus Juriquilla, AP 1-253, CP 76230
Juriquilla, Querétaro, Mexico
e-mail: glevresse@geociencias.unam.mx

M. Bouabdellah
Laboratoire des Gîtes Minéraux, Hydrogéologie & Environnement, Faculté Des Sciences, Université Mohammed Premier, 60000 Oujda, Morocco

A. Cheilletz
ENSG, Géoressources, Université de Lorraine, 2 rue du Doyen Marcel Roubault, 54518
Vandoeuvre-les-Nancy, France

D. Gasquet
Université de Savoie Mont Blanc, SceM-EDYTEM, CNRS-UMR 5204, Campus Scientifique,
73376 Le Bourget du Lac Cedex, France

L. Maacha
Managem Group, Twin Center, Tour A, Angle Boulevards Zerktouni et al Massira al Khadra, B. P. 5199, 20000 Casablanca, Morocco

J. Tritlla
Repsol Exploración, Paseo de la Castellana 280, 28046 Madrid, Spain

D. Banks
School of Earth Sciences, University of Leeds, Leeds LS2 9JT, UK

A.S. Moulay Rachid
AXMINE Company, Yougoslavie Avenue, Immeuble106/6, Guéliz, 40000 Marrakech, Morocco

M. Bouabdellah and J.F. Slack (eds.), *Mineral Deposits of North Africa*,
Mineral Resource Reviews, DOI 10.1007/978-3-319-31733-5_2

deposited during two main epithermal mineralizing events referred to as epithermal-quartz (ESE-Qz) and epithermal-dolomite (ESE-Dol) stages under distinct stress fields (i.e., WNW-ESE and N-S shortening directions), and is confined to the late Neoproterozoic, N60-90° E-trending, transcrustal Imiter fault zone. Economic orebodies are aligned mainly along the interface between sedimentary and volcanic units of lower and upper Cryogenian age. The ore mineralogy consists principally of Ag–Hg amalgam, argentite, polybasite, pearceite, tetrahedrite-tennantite, proustite-pyrargyrite, imiterite, acanthite, arsenopyrite, pyrite, sphalerite, and galena. Gangue constituents are dominated by quartz (ESE-Qz stage) and dolomite (ESE-Dol stage). Wall-rock alteration is well developed and includes silicification and dolomitization, and minor propylitization and kaolinitization. Fluid inclusion data indicate that the mineralizing fluids evolved through time, from a mean temperature of ~180 °C and salinity of ~10 wt% NaCl during ESE-Qz stage I, to a mean temperature of ~165 °C and salinity of ~24 wt% NaCl equiv during ESE-Dol stage II. Calculated trapping pressures, in the range of 1.1–0.9 kbar, exclude fluid unmixing "effervescence" as a viable ore depositional mechanism. Conversely, halogen compositions suggest the involvement of magmatic brines and evolved seawater. Stable (C, O, S) and radiogenic (Pb, Re/Os) isotope data, together with noble gas isotope compositions, are consistent with various degrees of mixing between mantle and crustal sources along the fluid flow path. Collectively, these data suggest that degassing of CO_2 and SO_2 during epithermal mineralization and related fluid/rock interactions led to local redox-potential decreases and pH increases that resulted in preferential deposition of massive amounts of native Hg-rich silver instead of Ag and Hg sulphide minerals.

1 Introduction

The first mining activity documented in the world-class Imiter Ag–Hg district dates to the Almohad Dynasty in the 12th Century (Leistel and Qadrouci 1991). In more recent times, the deposit was rediscovered during a campaign of aerial prospection carried out in 1951 by the Office National des Hydrocarbures et des Mines (ONHYM; formerly BRPM). In 1969, Omnium Nord Africain Group (ONA) and ONHYM created the so-called "Société Métallurgique d'Imiter" (SMI) to re-process tailings by cyanidation (650,000 t at 300 ppm Ag). In parallel, continuing exploration delineated significant new proven reserves of silver. Underground mining began in 1978 and continues to the present. Production has increased exponentially from 40 to 250 Mt of Ag/yr since the creation of SMI in 1969. Continued intensive exploration over the past 10 years has outlined three additional orebodies referred to as Igoudrane, Puits IV, and Imiter South. As a result, silver reserves have grown to more than 10,000 t with mine life being extended an additional 15 years (Newman 2009). Average silver grades range from 300 to 1,000 g/t and locally can reach 5,000 g/t. Current annual production is about 200—300 t Ag; remaining mineral resources are estimated at 3,000 Mt Ag (Newman 2009).

Based on these production estimates, the Imiter deposit is considered one of the largest silver deposits in the world (Katrivanos 2015). To explain the origin of such a huge silver concentration, diverse genetic models have been proposed (Leistel and Qadrouci 1991; Baroudi et al. 1999; Levresse et al. 2004). These models range from syngenetic (Vargas 1983; Popov et al. 1986; Guillou et al. 1988; Popov 1995) to epigenetic (Leistel and Qadrouci 1991). From 2000 onward, most workers have advocated epithermal mineralizing processes (Levresse 2001; Cheilletz et al. 2002; Levresse et al. 2004). However, despite an impressive number of geochemical investigations, the genesis of the Imiter Ag deposit remains uncertain, particularly the origin(s) of the ore-forming fluids, sources of heat and metal components, mechanism(s) of ore deposition, and the age of mineralization. The objective of the present contribution is to update the geologic history, mineralization, and paragenesis of the Imiter deposit, and more importantly to contribute, with new data on fluid inclusions, halogens, and lead isotopes, constraints on the source (s) of sulphur and metals. Based on these newly acquired data, we provide important insights into the origin and evolution of the mineralizing system, together with implications for understanding ore-forming processes in the context of local Neoproterozoic magmatism.

2 District Geology

The Ag–Hg Imiter deposit (32° 43′ N Lat; 5° 36′ W Long) is located in the northern part of the Precambrian Saghro massif (Fig. 1). This massif forms part of the 680–580 Ma Pan African Anti-Atlas orogenic belt, north of the West African Craton margin (Ennih and Liégeois 2001). Regional and local geology of the district have been extensively investigated over the past several decades, resulting in a wealth of scientific information including geological maps at different scales, university theses, research papers, and unpublished mining company reports (Leistel and Qadrouci 1991; Pašava 1994; Ouguir et al 1996 ; Baroudi et al. 1999; Levresse 2001; Fekkak et al. 2001; Cheilletz et al. 2002; Levresse et al. 2004; Gasquet et al. 2005; Tuduri et al. 2005). Accordingly, only a summary relevant to the present synthesis is given below.

The oldest rocks assigned to the Saghro Group (Thomas et al. 2004) were deposited on the Neoproterozoic basement. Strata of the Saghro Group form a lower complex consisting of a strongly folded Cryogenian succession of greenschist-facies greywacke and organic-rich black shale, locally intruded by ca. 570–580 Ma granodioritic to dioritic intrusions (e.g., Taouzzakt and Igoudrane plutons). The black shales, which host the majority of Imiter silver mineralization, were deposited at the outer part of a passive continental margin that developed in an extensional back-arc environment (Marini and Ouguir 1990; Ouguir et al. 1996).

Unconformably overlying the clastic sedimentary rocks of the lower complex are Ediacaran volcanic and volcaniclastic rocks of the upper complex assigned to the Ouarzazate Supergroup (580–560 Ma; Mifdal and Peucat 1985). The main lithologies are immature conglomerate at the base grading upward into andesitic lava flows and felsic ignimbrites (572–550 ± 3 Ma; U/Pb zircon) and associated cogenetic granites (580–570 Ma, U/Pb zircon) (Cheilletz et al. 2002). At the end of the Neoproterozoic, a marine transgression invaded all of the Anti-Atlas and deposited the so-called "Adoudounian" (Lower Cambrian) succession. This succession is composed of interbedded carbonate, purple shale with minor siltstone, evaporites, greywacke (Piqué et al. 1999; Álvaro et al. 2014) and mafic sills dated at 529 ± 3 Ma (Ducrot and Lancelot 1977, recalculated) and 531 ± 5 Ma (Gasquet et al. 2005).

Silver mineralization occurs within the Cryogenian black shale and partly in the Ediacaran volcanic rocks. More importantly, this mineralization is localized along the Late Neoproterozoic, N60–90° E-trending transcrustal Imiter fault zone (Fig. 1), which straddles the boundary between the lower and upper complexes. The prominent Imiter fault zone consists of complex arrays of N90° E and N60–70° E faults that exhibit, at map scale, apparent sinistral pull-apart

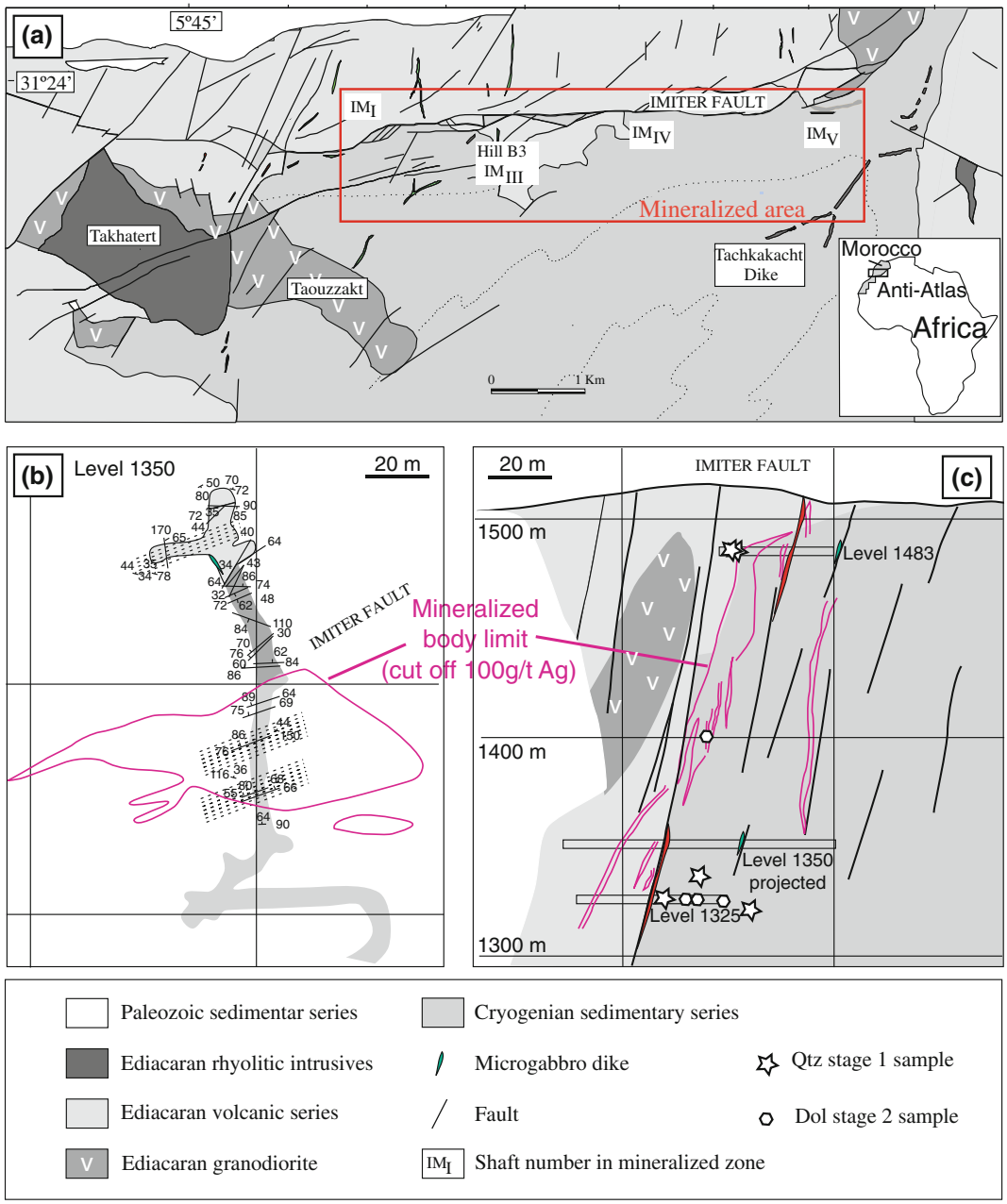

Fig. 1 **a** Geological map of Imiter Ag–Hg deposit area, Anti-Atlas, Morocco. Modified from Leistel and Qadrouci (1991). **b** Horizontal projection of silver ore body in B3 Hill workings (1350 m is altitude of this mining level); **c** N–S synthesized geological cross section drawn for B3 Hill (*white stars* indicate sampling locations within the mine)

structures (Ouguir et al., 1994; 1996; Tuduri et al. 2005). Reactivation of the Imiter fault system during the Hercynian orogeny facilitated the injection of variously aged dike swarms of diverse composition ranging from trachyandesite to high-K microsyenite and microgabbro. One microsyenite dike has been dated at ca. 200–204 Ma (^{40}Ar/^{39}Ar on biotite and K-feldspar;

Borisenko et al. 2013). The Takhatert rhyolite is characterized by a well-defined, domal structure (Fig. 1), suggesting that it is a hypabyssal body. The felsic dikes, including the Tachkakacht dike, are similar in composition and age to the Takhatert rhyolite (547 ± 8 Ma; U/Pb zircon; Levresse 2001). Pan-African regional metamorphism under greenschist-facies conditions resulted in the formation of chlorite-, muscovite-, and pyrophyllite-bearing mineral assemblages, with peak conditions reaching 350 °C and up to 3 kb (Thomas et al. 2004). Higher temperatures were attained locally in the aureoles of post-kinematic intrusions (547 ± 26 Ma; Thomas et al. 2004).

3 Mineralization

Silver mineralization is structurally controlled within a system of ENE-WSW- to E-W-trending, variously dipping, transpressive to transtensional structures. These structures include vein swarms, veinlets, cemented breccias within veins, and lensoidal or pocket-like masses and fillings of en echelon tension gashes. Most, if not all, of the exploited silver orebodies are confined to the prominent Imiter fault zone (Fig. 1), which is typically aligned along the interface between the lower and upper lithostratigraphic complexes. In addition to the Ag–Hg ores within the mineralized structures, Ag–Hg minerals also occur disseminated in the basal conglomerate and black shales. Overall, the veins are up 4 m wide and extend laterally from a few meters to more than 1 km, are spaced 50–100 m apart, strike N160° E, and dip steeply (70° to ~90°).

Where Ediacaran volcanic rocks of the upper complex are present (e.g., Hill B3; Fig. 1), the orebodies are largest within the basal conglomerate and are continuous through the fractured rock within the Imiter fault zone. Silver mineralization has never been found within the andesitic host rocks or the ca. 580–570 Ma granodiorite exposed at Hill B3. Both rock types seem to represent a "cap rock" for mineralization. The spatial distribution of the orebodies appears, therefore, to be linked directly to the rheology of the surrounding host rocks. In this regard, we suggest that the foliated nature of the host rocks facilitated later fracturing, fluid flow, and emplacement of the mineralized veins.

Two principal vein systems, referred to as "Imiter 1" and "Imiter 2" have been mined both from open pits and underground workings. The Imiter I vein system consists of three variably dipping structures (F_0, F_0 north, and F_0 south) that strike N90–N65° E. In contrast, Imiter 2 comprises three vein orebodies referred to as R_6, R_7, and B_3 that exhibit roughly the same geometric characteristics in terms of orientation and dip. Recent exploration in the district has delineated three new orebodies referred to as Igoudrane, Puits IV, and Imiter South (Fig. 1).

Textural relationships together with mineral assemblages indicate a complex history involving contemporaneity of replacement and open-space filling. The veins display comb, cockade, laminated, breccia, and crack-and-seal textures, suggesting that multiple mechanisms were important for trans-tensional vein formation. Early precipitated minerals are cut or brecciated, and subsequently cemented, by later phases. Collectively, these textural features indicate that mineralization took place in open spaces, and imply that the Imiter orebodies formed in a relatively shallow environment.

Spatial and temporal relationships between the silver mineralization and country rocks indicate four distinct and successive mineralizing events. From oldest to youngest, these events are: (1) recrystallization during Pan-African metamorphism of syngenetic-diagenetic pyrite hosted in Cryogenian black shale; (2) development of a discrete, base-metal mineral assemblage (BMS) adjacent to metamorphic aureoles induced by intrusion of the granodiorite (ca. 572 Ma); (3) formation of epithermal silver mineralization (i.e., ESE stage) dated at ca. 550 Ma (Cheilletz et al. 2002; Levresse et al. 2004), which constitutes the bulk of exploited mineralization in Imiter; and (4) Ag–Hg remobilization at 255 Ma (Borisenko et al. 2013). Cross-cutting relationships and mineral assemblages indicate that the epithermal silver mineralization occurred during two main stages referred to as epithermal-quartz (ESE-Qz) and

epithermal-dolomite (ESE-Dol) (Levresse 2001; Cheilletz et al. 2002; Levresse et al. 2004; Burniaux and Williams-Jones 2006; Tuduri et al. 2005; Borisenko et al. 2013; this study). Each stage is characterized by particular styles, ore and gangue mineral assemblages, and silver grades (Fig. 2).

The first silver mineralizing stage (ESE-Qz Stage I) formed during a dextral transpressive event under WNW-ESE shortening (Tuduri et al. 2005). Principal minerals are quartz (Qz-1), Ag–Hg amalgam, argentite, polybasite, pearceite, tetrahedrite-tennantite, proustite-pyrargyrite, imiterite, acanthite, arsenopyrite, pyrite, and galena. The following stage (ESE-Dol Stage II) resulted from reopening of the earlier veins in response to normal, sinistral regime (Tuduri et al. 2005). This stage comprises pink dolomitic alteration and an associated mineral assemblage dominated by Ag–Hg amalgam, acanthite, tetrahedrite-tennantite, galena, sphalerite, pyrite, chalcopyrite, and arsenopyrite. The type of gangue mineral (i.e., quartz vs. dolomite) appears to be strongly controlled by lithology of the host rocks (Ediacaran volcanics vs. Cryogenian black shale).

Within the Imiter deposit, the most highest grade impressive orebodies are developed along

Mineralogical stage	$\delta^{13}C$	$\delta^{18}O$	$\delta^{34}S$	$^{206}Pb/^{204}Pb$ $^{207}Pb/^{204}Pb$	$^{187}Os/^{188}Os$	^{4}He
Qtz stage 1						
quartz-1						1,05-1,84Ra
muscovite						
pyrite			-11,9 to -4,5			
arsenopyrite						
chalcopyrite			-2,4			
sphalerite			-10,9 to -8,0		0,199	
galena			-10,0 to -4,8		0,185	0,76Ra
tetrahedrite						
Ag-amalgam					0,183 to 0,195	
argentite						
polybasite						
pyargyrite					0,143	
proustite						
Dol stage 2						
dolomite	-10.5 to -8.1	-13.4 to -0.1				0,89Ra
pyrite			-8,0 to -4,1			
arsenopyrite			-22,6 to -1,8			
chalcopyrite			-3,2			
sphalerite			-9,3 to -5,0			
galena			-19,6 to -7,1	15,55 to 15,59 18,11 to 18,17		
Ag-amalgam						
argentite						
polybasite						
imiterite						
pyargyrite			-7,0		0,147	1,21Ra
proustite						
pearcite						
cinnabar			-27,7			

Fig. 2 Paragenetic succession for Imiter Ag–Hg deposit and ranges of isotopic values for C, O, S, Pb, Os, and He during epithermal silver mineralization (Pašava 1994; Levresse 2001; Levresse et al. 2004; this study)

extensive fault zones and related breccias that in places contain tens of kilograms of native silver (i.e., Ag–Hg and Ag). It is noteworthy that Hg contents of the Ag–Hg amalgam increase from quartz-dominant stage I to dolomite-dominant stage II, with Hg abundances ranging from 10 to 30 % and 20 to 40 %, respectively. Where observed, silver sulphosalts precipitated either with, or as replacements of, preexisting sulphides. Imiterite (Ag_2HgS_2) is the most common Hg-bearing sulphide and forms needles filling dolomitic geodes that are spatially associated with cinnabar and argentite (Guillou et al. 1985). Supergene oxidation is scarce and limited to upper levels of the deposit (Levresse et al. 2004). The oxidized mineral assemblage there includes milky quartz, rhodochrosite, kaolinite, erythrite, malachite, azurite, marcasite, lavendulan [$NaCaCu_5(AsO_4)_4Cl{\bullet}5H_2O$], cerussite, and the iron oxides hematite and goethite.

Wall-rock alteration is weakly developed. Major types include propylitization, silicification, dolomitization, and kaolinitization. Silicification and dolomitization are prominent around the mineralized structures, whereas kaolinitization is spatially limited and paragenetically late.

4 Age of Mineralization

Based on field relationships and $^{40}Ar/^{39}Ar$ ages of hydrothermal muscovite, Levresse (2001) and Cheilletz et al. (2002) concluded that the bulk of Imiter silver mineralization occurred between 563 ± 8 and 542 ± 0.2 Ma. More recently, Borisenko et al. (2013) reported a single-crystal $^{40}Ar/^{39}Ar$ age of 255 ± 3 Ma for adularia intergrown with Qz-1 from the ESE-Qz stage and proposed a Triassic age of mineralization, coincident with early opening of the Central Atlantic Province. This new age determination suggests that the Triassic rifting event could have remobilized the primary Cryogenian Ag–Hg mineralization at Imiter, as documented in other hydrothermal deposits of the Anti-Atlas system such as the Iourirn Au deposit (Gasquet et al. 2004), the Tamlalt-Menhouhou orogenic gold deposit (Pelleter et al. 2008, 2010), and the Bou-Azzer Co–Ni–As–Au deposit (Oberthur et al. 2007).

5 Analytical Methods

5.1 Fluid Inclusion Study

A Linkam stage was used to record ice-melting temperature (Tmi) and homogenization temperature (Th) of fluids in the ESE quartz- and dolomite-hosted inclusions. Calibrations were performed with appropriate chemicals from Merck. Measurement accuracy was about ±0.2 °C for freezing runs and ±1 °C for heating runs. Representative inclusions were further analyzed with a Labram-type (DilorR) Raman microprobe with a NotchR filter at the laboratory of " GeoRessources (Nancy, France); technical details are provided in Debussy et al. (2001).

Bulk crush-leach analyses were performed on quartz and dolomite separates from the ESE-Qz and ESE-Dol stages at the School of Earth Sciences, University of Leeds. The procedure has been described in detail by Banks et al. (2000). Samples were crushed to 1–2 mm size and cleaned in 18.2 MΩ water. Dry samples of 0.5–1 g were crushed to a fine powder in an agate pestle and mortar, transferred to a sample container, and the dried salts redissolved in 18.2 MΩ water. Anions (Cl^- and Br^-) were determined with a Dionex DX-500 ion chromatograph; cations (Na^+ and K^+) were determined on the same solution with an acidified $LaCl_3$ solution by flame emission spectroscopy. Analytical precision of these analyses was better than ±10 % (2σ).

6 Lead Isotope Study

Lead isotope analyses were performed at Sgiker Laboratories of the Basque Country University in Bilbao, Spain, on representative galena separates from the main ore stages. About 0.10 g of powdered material and an aliquot of about 0.02 g, respectively, were digested overnight in $HF–HNO_3$ and evaporated to dryness. The

resulting residue was taken in HBr; Pb was isolated by conventional ion-exchange chromatography (AG1-X8 resin in HBr and HCl media). Recovered lead was evaporated to dryness, dissolved in 0.32 N HNO_3, and diluted to a final concentration of 150–200 ppb. Lead isotope ratios were measured using a ThermoNEPTUNE multicollector inductively coupled plasma-mass spectrometer (ICP-MS), and the mass fractionation was internally corrected after the addition of thallium isotope reference material NBS-997. Analytical error, determined as a total uncertainty of the results and confirmed by more than 20 analyses of lead isotope reference material NBS-981, was about 0.04 % per mass unit (2σ), equivalent to 0.041, 0.040, and 0.039 %, respectively, for $^{206}Pb/^{204}Pb$, $^{207}Pb/^{204}Pb$, and $^{208}Pb/^{204}Pb$ ratios.

7 Fluid-Inclusion Microthermometry

New microthermometric measurements were performed on quartz (Qz-1) and dolomite (Dol-2) wafers from the ESE-Qz (I) and ESE-Dol (II) stages. Data are presented in Table 1 and plotted in Figs. 3 and 4. The fluid inclusions are classified as primary, pseudosecondary, or secondary according to the criteria of Roedder (1984). Based on the number of observable phases present at room temperature, four distinct fluid inclusion types (designated 1–4) are recognized: (1) liquid-vapor (L + V; Type 1); (2) liquid-vapor-one solid (L + V + S_1; Type 2); (3) liquid-vapor-two solids (L + V + $S_{1\text{-}2}$, Type 3); and (4) vapor (V; Type 4). All fluid inclusion types generally occur together within a trail or cluster. In Type 1 fluid inclusions, visually estimated liquid to vapor ratios are highly variable, ranging from 0.4 to 0.8. Vapor-rich inclusions (liquid/vapor <0.5) are rare, representing less than 10 % of the total.

Fluid inclusions hosted in Qz-1 are isolated and up to 50 μm in diameter, or are grouped in clusters that show a random distribution within a single grain or growth zone. The fluid inclusions in Qz-1 are spatially associated with silver blebs distributed along growth zones within the host quartz. Raman analyses indicate that the trapped solid phases correspond to muscovite (S_1) and sulphide (S_2). Chloride daughter minerals such as halite and sylvite have not been observed.

Fluid inclusions hosted in Dol-2 are isolated or form trails distributed along growth zones. Estimated liquid to vapor ratios are less than 0.8. Owing to the fluorescence of the dolomite, no reliable Raman data have been obtained on these fluid inclusions.

Overall, microthemometric data indicate that the mineralizing fluids evolved through time, from a mean temperature of ~180 °C and calculated salinity of ~10 wt% NaCl equiv in Qz-1, to a mean temperature of ~165 °C and calculated salinity of ~24 wt% NaCl equiv in Dol-2 (Table 1; Figs. 3 and 4).

In the $T_{h(LV)}$ versus T_{mi} plot shown in Fig. 3, data for Qz-1 and Dol-2 display a negative correlation. Primary and pseudosecondary fluid inclusions in both minerals exhibit roughly the same T_h range of ca. 217–126 °C but fluid inclusions hosted in Dol-2 have consistently higher salinities (~24 wt% NaCl equiv; Table 1). In addition, the type of host rock and fluid salinity are related. For example, data for Qz-1 samples hosted in Ediacaran volcanic rocks display a weakly isohaline-cooling path, whereas those for Qz-1 and Dol-2 samples in Cryogenian black shale exhibit a parallel negative correlation between $T_{h(LV)}$ and T_{mi} (Fig. 3).

Raman analyses of the vapor phase related to Qz-1 reveal the occurrence of mixtures of CH_4–CO_2 or CH_4–N_2. CH_4 is commonly the predominant component (up to 52 vol.%). CO_2 and N_2 have not been found together in the same fluid inclusion. With increasing depth, N_2 proportion decreases and CH_4 proportion increases up to 100 %.

P-T reconstruction of Qz-1 fluid evolution has been determined using the intersection coordinates of calculated fluid inclusion isochores together with results of chlorite geothermometry. Accordingly, the minimum trapping pressure estimates are in the range of 1.1–0.9 kbar for the mineralizing fluid that deposited the high-grade portion of the Imiter silver orebodies.

Table 1 Microthermometric data of typical fluid inclusions of silver epithermal stages from Imiter Ag–Hg deposit

Silver epithermal mineralizing event								
Quartz-1 in volcanite			Quartz-1 in black shale			Dolomite-2 in black shale		
Inclusions	T_h (°C)	T_{mi} (°C)	Inclusions	T_h (°C)	T_{mi}(°C)	Inclusions	T_h (°C)	T_{mi} (°C)
Inc. 1	189.95	−3.70	Inc. 1	184.56	−11.24	Inc. 1	125.74	−21.32
Inc. 2	185.18	−2.56	Inc. 2	180.01	−9.59	Inc. 2	137.25	−21.21
Inc. 3	176.23	−4.10	Inc. 3	178.37	−13.05	Inc. 3	137.66	−19.87
Inc. 4	217.82	−6.62	Inc. 4	172.87	−13.40	Inc. 4	139.85	−21.09
Inc. 5	214.77	−5.06	Inc. 5	167.91	−15.45	Inc. 5	147.14	−27.43
Inc. 6	206.03	−5.53	Inc. 6	167.91	−16.27	Inc. 6	151.89	−21.20
Inc. 7	199.19	−5.69	Inc. 7	174.00	−16.18	Inc. 7	196.22	−10.61
Inc. 8	196.53	−8.67	Inc. 8	166.59	−15.21	Inc. 8	206.60	−13.66
Inc. 9	193.95	−9.15	Inc. 9	162.58	−14.86	Inc. 9	208.59	−13.66
Inc. 10	189.99	−9.03	Inc. 10	159.96	−13.54	Inc. 10	208.46	−20.20
Inc. 11	191.55	−8.79	Inc. 11	161.70	−12.88	Inc. 11	190.99	−21.20
Inc. 12	185.60	−9.22	Inc. 12	163.90	−11.91	Inc. 12	194.08	−22.41
Inc. 13	185.60	−8.99	Inc. 13	161.30	−9.91	Inc. 13	186.44	−20.79
Inc. 14	187.65	−8.90	Inc. 14	168.51	−9.87	Inc. 14	193.02	−17.52
Inc. 15	187.65	−7.62	Inc. 15	172.71	−10.92	Inc. 15	207.81	−15.90
Inc. 16	183.18	−7.95	Inc. 16	170.71	−8.02	Inc. 16	194.37	−15.03
Inc. 17	178.78	−7.95	Inc. 17	184.55	−6.93	Inc. 17	190.54	−27.23
Inc. 18	176.40	−9.25	Inc. 18	147.52	−7.69	Inc. 18	170.50	−29.09
Inc. 19	176.18	−8.94	Inc. 19	148.23	−7.25	Inc. 19	163.10	−27.09
Inc. 20	173.84	−8.01	Inc. 20	146.69	−10.62	Inc. 20	159.90	−25.90
Inc. 21	168.36	−7.21	Inc. 21	157.71	−18.32	Inc. 21	165.47	−22.66
Inc. 22	175.99	−7.33	Inc. 22	151.59	−17.58	Inc. 22	161.97	−23.10
Inc. 23	176.32	−6.51	Inc. 23	155.35	−16.48	Inc. 23	161.97	−22.29
Inc. 24	179.94	−7.29	–	–	–	Inc. 24	162.43	−22.14
Inc. 25	180.88	−6.59	–	–	–	Inc. 25	166.23	−21.33
Inc. 26	178.97	−5.46	–	–	–	Inc. 26	169.41	−22.58
Inc. 27	179.64	−6.16	–	–	–	Inc. 27	169.70	−22.33
Inc. 28	181.24	−5.85	–	–	–	Inc. 28	173.08	−22.72
Inc. 29	183.22	−5.26	–	–	–	Inc. 29	170.75	−20.90
Inc. 30	189.94	−5.73	–	–	–	Inc. 30	173.54	−20.77
Inc. 31	188.29	−5.81	–	–	–	Inc. 31	167.69	−20.77
Inc. 32	188.06	−6.64	–	–	–	Inc. 32	177.60	−20.55
Inc. 33	189.89	−6.57	–	–	–	Inc. 33	178.23	−20.33
Inc. 34	192.33	−6.45	–	–	–	Inc. 34	178.12	−19.21
Inc. 35	193.70	−6.23	–	–	–	Inc. 35	174.76	−18.94
Inc. 36	194.75	−6.78	–	–	–	Inc. 36	174.36	−19.10
Inc. 37	196.97	−6.66	–	–	–	Inc. 37	181.37	−20.73

(continued)

Table 1 (continued)

Silver epithermal mineralizing event								
Quartz-1 in volcanite			Quartz-1 in black shale			Dolomite-2 in black shale		
Inclusions	T_h (°C)	T_{mi} (°C)	Inclusions	T_h (°C)	T_{mi}(°C)	Inclusions	T_h (°C)	T_{mi} (°C)
Inc. 38	196.28	−6.27	–	–	–	Inc. 38	179.50	−21.96
Inc. 39	185.46	−6.82	–	–	–	Inc. 39	159.11	−16.39
Inc. 40	185.10	−5.74	–	–	–	Inc. 40	166.53	−18.78
Inc. 41	183.87	−6.04	–	–	–	Inc. 41	155.39	−25.54
Inc. 42	192.35	−7.62	–	–	–	Inc. 42	154.94	−23.16
Inc. 43	159.10	−7.30	–	–	–	Inc. 43	169.36	−24.68
Inc. 44	158.72	−7.27	–	–	–	Inc. 44	183.31	−17.48
–	–	–	–	–	–	Inc. 45	181.03	−16.01
–	–	–	–	–	–	Inc. 46	175.55	−17.36

See text for the abbreviations

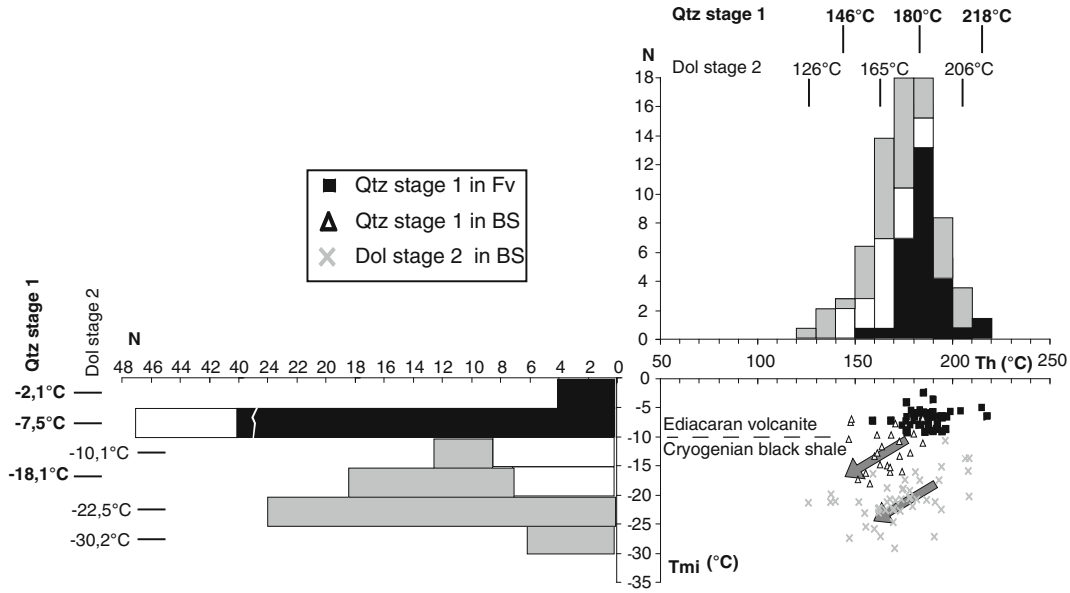

Fig. 3 Homogenization temperature (T_h) versus melting temperature (T_{mi}) diagram for fluid inclusions from the Imiter epithermal silver deposit. *Arrows* represent inferred fluid evolution and related degassification process

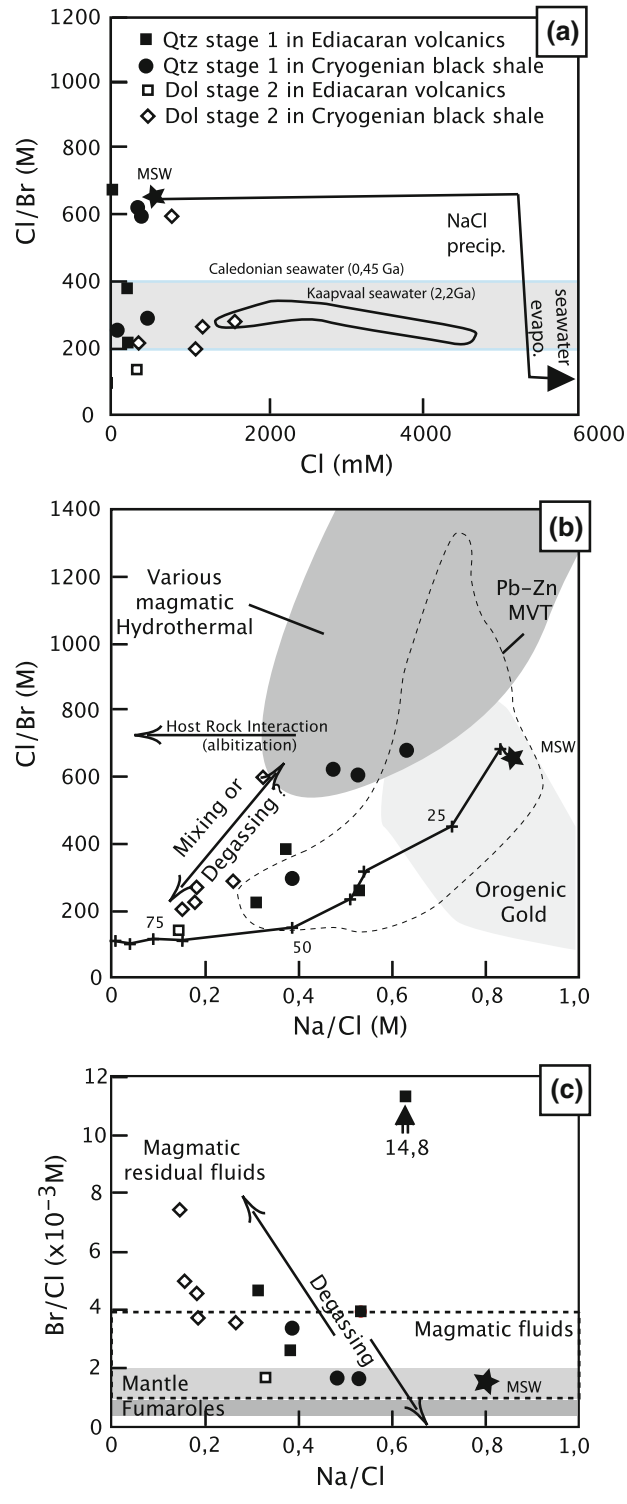

Fig. 4 Halogen ratios for fluid-inclusion leachates from the Imiter Ag–Hg deposit. **a** $(Cl/Br)_{mol}$ versus Cl_{mmol}. Data for Kaapvaal Proterozoic and Caledonian seawater are from Kendrick et al. (2005), Foriel et al. (2004), and Spear et al. (2014). *Black line* shows seawater evaporation trend; filled star is modern seawater composition (MSW) (Fontes and Matray 1993). **b** $(Cl/Br)_{mol}$ versus $(Na/Cl)_{mol}$. Various magmatic and hydrothermal fields and or ogenic gold fields are shown for comparison (modified from Hofstra and Landis 2012). In this plot, both mixing and degassing processes can explain the observed data distribution. **c** $(Br/Cl)_{mol}$ versus $(Na/Cl)_{mol}$. Fields for magmatic fluids, mantle, and fumaroles are from Kendrick et al. (2001, 2005). Distribution of data suggests predominance of degassing from primary magmatic fluids to magmatic-hydrothermal fluids

8 Fluid Inclusion Leachate Compositions

Na–K–Cl–Br–Li–F–SO_4 compositions of fluid inclusions hosted in Qz-1 and Dol-2 from both mineralized and barren veins were determined on the same mineral wafers as those used for microthermometric measurements. The recorded compositions are presented in Table 2 and plotted in Fig. 4.

Overall, the leachate compositions are dominated by Na, Cl, K, and $SO_4 \pm Br \pm Li \pm$ (Table 2; Fig. 4a–c). Concentrations of Cl, Br, Na, K, and SO_4 show relative enrichment from Qz-1 to Dol-2. Conversely, F and Li contents decrease gradually with paragenetic stage from early to late. It is noteworthy that the leachate composition of Qz-1 samples from veins hosted in the Cryogenian black shale display higher Na/Br and K/Br molar ratios than those samples hosted in Ediacaran volcanic rocks. This pattern is attributed to a host-rock chemical control and hence suggests the importance of water-rock interactions during silver mineralization.

In the Cl/Br versus Cl diagram, the halogen compositions of Qz-1and Dol-2 plot in two distinct fields (Fig. 4a). The field for Qz-1 fluid inclusions shows a vertical distribution in two groups, both having low Cl concentrations. The first group has a Cl/Br ratio comparable to those inferred for Archean and Devonian seawater (Foriel et al. 2004; Kendrick et al. 2005; Spear et al. 2014), whereas data for the second group are close to the Cl/Br ratio for modern seawater. Data for Dol-2 display a level distribution with a lower Cl/Br ratio and increasing chlorine concentration. Br/Cl ratios of fluids trapped both in Qz-1 and Dol-2 vary from 1 to 14, and are consistent with magmatic brine compositions (Fig. 4c; Déruelle et al. 1992; Johnson et al. 2000), bounded at lower limits by mantle values of 1–2 (Kendrick et al. 2001, 2005). In the Cl/Br versus Na/Cl diagram (Fig. 4c), the Qz-1 and Dol-2 halogen compositions show Na enrichment attributed to either water/rock interaction with clays, or leaching of sodic plagioclase from footwall rocks. Both processes produced a similar distribution connecting the magmatic fluid field and the mean sea water (MSW) evaporation line. Intersections with the MSW evaporation line and the epithermal silver event occur up to 50 % evaporation, which represents the maximum evaporation reported for evolved brines (as in MVT deposits; Kesle et al. 1996; Tritlla et al. 2001). Two main processes could explain these distributions (1) mixing between magmatic and evaporated meteoric water, and (2) a degassing process.

9 Mineral Assemblage Thermometry

Electron microprobe analyses of chlorite from the main veins indicate a wide spectrum of compositions from brunsvigite to picnochlorite (Baroudi 1992; Bajja 1998; Cheilletz et al. 2002; present study). Application of the chlorite geothermometer of Cathelineau (1988) suggests temperatures of equilibration of 266 ± 15–304 ± 15 °C (mean 278 ± 15 °C; Fig. 5). Moreover, the mineral assemblage pyrite-proustite-argentite-realgar indicates equilibrium temperatures in the range of 350–230 °C (pyrite/pyrrhotite and silver sulphides in coexisting domains; see paragenetic sequence in Fig. 2), corresponding to sulphur fugacities of 10^{-8}–10^{-15} (Fig. 6; see Barton and Skinner 1967). The identification of dodecahedral crystals of acanthite (Levresse 2001) establishes a lower temperature limit for crystallization of 173 °C for the silver in Dol-2 stage (Kracek 1946). For the temperature range of Qtz-1 (350–230 °C), the oxygen fugacity is estimated at 10^{-30}–10^{-39} (D'Amore and Panichi 1980), and together with the lack of abundant Ag sulphides suggests low oxygen and sulphur activities during the major silver mineralizing event (Levresse 2001).

Table 2 Chemical composition of typical fluid inclusions of silver epithermal stages from Imiter Ag–Hg deposit

Sample	Host rock	Level	Th_{LV} range	T_{mi} range	$CO_2/CH_4/N_2$	F	Cl	Br	SO_4	Na	K	Li	Na/Br	Cl/Br	K/Cl	Na/Cl
Shaft-number		masl	°C	°C	Mean mol%	mol%										
IMIII-9958	BS	1325	181/342	−7.3/−1.7	26/68/21	26	4396	14	99	1430	445	19	347.57	692.9	0.09	0.50
IMIV-9937	BS	1320	151/323	−13.5/−0.1	nd	23	3197	57	65	1000	453	11	609.78	1264	0.13	0.48
ESE-Qtz2																
IMIII-9959	VF	1483	156/211	−7.7/−2.5	nd	24	807	27	46	330	95	10	424.81	673.7	0.11	0.63
IMIII-9960	VF	1483	158/204	−6.7/−2.1	00/66/44	20	7134	75	167	1440	486	16	66.82	214.7	0.06	0.31
IMIII-9960	VF	1483	156/218	−9.2/−2.8	36/64/0	13	6832	40	12,201	1650	493	165	142.31	382.1	0.07	0.37
IMI-0501	BS	1400	148/162	−12.7/−7.1	00/72/28	0	12,835	48	536	4390	689	24	315.91	599	0.05	0.53
IMIII-9954	BS	1335	147/185	−8.1/−3.4	nd	13	15,263	119	92	3830	972	110	111.87	289.1	0.06	0.39
IMIII-0004	BS	1325	147/180	−18.1/−9.5	nd	31	11,634	42	402	3590	1410	67	294.99	619.9	0.11	0.48
IMIII-0022	BS	1320	154/185	−8.6/−4.2	nd	16	2323	21	534	800	369	21	134.33	253	0.14	0.53
ESE-Dol																
IMIII-9960	VF	1483	145/197	−18.8/−11.5	nd	0	11,239	187	270	1040	277	80	19.28	135.1	0.02	0.14
IMI-0501	BS	1400	126/182	−22.8/−13.7	nd	0	26,355	100	1099	5550	954	15	192.90	594	0.03	0.32
IMIII-0022	BS	1320	141/224	−13.1/−10.1	nd	0	11,523	119	300	1333	409	10	38.93	218.3	0.03	0.18
IMIII-9957	BS	1325	149/171	−30.2/−12.8	nd	0	37,796	429	429	3720	1654	59	30.14	198.6	0.04	0.15
IMIII-9958	BS	1325	145/206	−28.4/−18.6	nd	20	56,010	447	17,844	9480	2322	47	73.71	282.4	0.04	0.26
IMIII-0005	BS	1325	152/163	−23.7/−12.1	nd	0	41,261	354	1099	4890	1592	58	48.01	262.7	0.04	0.18

Abbreviations BS black shale; *nd* not determined; *VF* volcanic formation

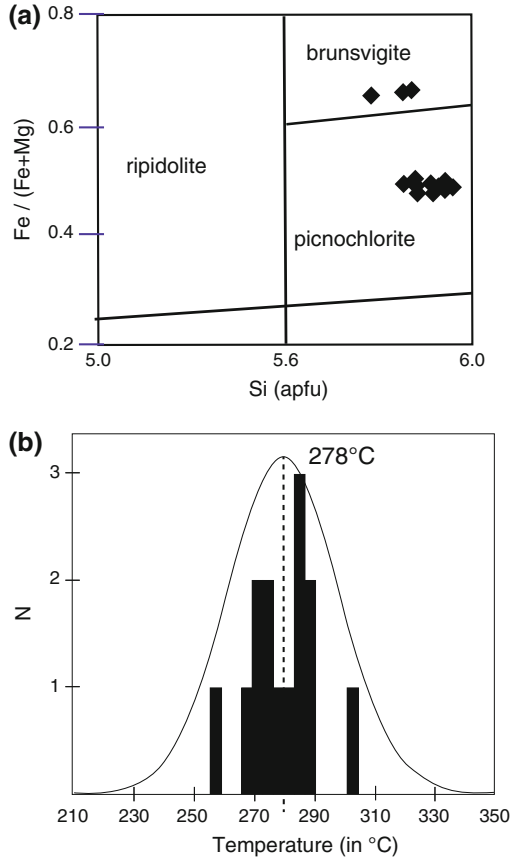

Fig. 5 **a** Plot of Fe/(Fe + Mg) ratio in chlorite versus number of Si atoms for samples from the base-metal-bearing quartz veins. Classification scheme after Bayliss (1985). **b** Calculated temperatures for chlorite crystallization, based on the chlorite geothermometer of Cathelineau (1988). N, number of analyses

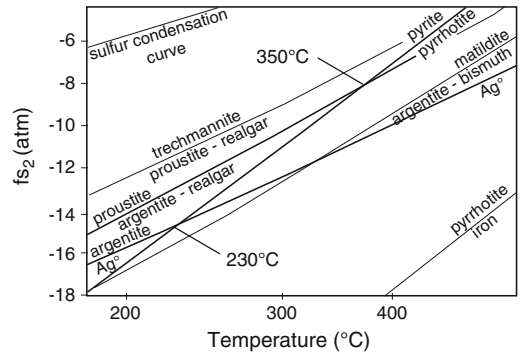

Fig. 6 Phase equilibria in Ag–Hg–Fe–Bi–S system as a function of temperature and sulphur fugacity during ESE-Qz—epithermal silver stage (modified from Barton and Skinner 1967). Noted are 230 and 350 °C isotherms that represent range of temperatures of Imiter epithermal system, where pyrite and silver sulphides coexist (see Fig. 2)

10 C–O–S Isotopic Compositions

Sulphides and gangue minerals from the early uneconomic, non-argentiferous, base-metal (BSM) stage and the following ESE-Qz and ESE-Dol stages related to the main epithermal silver mineralization, and pyrite from the Cryogenian black shales, have been analyzed for carbon, oxygen, and sulphur isotopic compositions by previous workers (Pašava 1994; Levresse et al. 2004).

Pyrite separates from the black shales have $\delta^{34}S_{CDT}$ values of -38.5 ± 2.0 to -37.4 ± 2.0 ‰. In contrast, pyrite separates from the BSM stage show $\delta^{34}S$ values that range from -7.4 ± 1.0 to -2.0 ± 0.8 ‰. Sulphide separates (i.e., pyrite, galena, sphalerite, chalcopyrite) from the ESE-Qz and ESE-Dol stages show a wide spread in sulphur isotopic compositions, with $\delta^{34}S_{CDT}$ ratios for the ESE-Qz stage ranging from -11.9 ± 0.8 to -2.4 ± 0.8 ‰ (avg -8.5 ± 2.5 ‰), whereas those determined for following ESE-Dol stage oscillate form -27.7 ± 0.4 to -1.8 ± 1.2 ‰ (avg -13 ± 8.1 ‰). The isotopically lowest value ($\delta^{34}S = -27.7 \pm 0.4$ ‰) was measured on cinnabar that is paragenetically the latest mineral phase (Levresse et al. 2004).

Carbon and oxygen isotopic compositions of dolomite separates (i.e., Dol-2) from both barren and mineralized orebodies display overlapping $\delta^{13}C$ and $\delta^{18}O$ values. Carbon isotope values ($\delta^{13}C_{PDB}$) range from −10.5 to −2.2 ‰, with most data between −11 to −8 ‰, whereas oxygen isotope values ($\delta^{18}O_{PDB}$) vary from −13.4 to −0.1 ‰ (Pašava 1994).

11 Os and He Isotopic Compositions

Initial age-corrected Os isotope ratios [$(^{187}Os/^{188}Os)_{550Ma}$] determined for the ESE-Qz and ESE-Dol stages range from 0.142 to 0.197 and record a predominant mantle source for osmium in the Imiter ores (Levresse et al. 2004). These ratios are slightly higher than the average mantle value of about 0.12 at ca. 550 Ma, which probably reflects a minor contribution (<10 vol. %) from a crustal component, possibly the Cryogenian black shales. $^{3}He/^{4}He$ ratios measured on quartz, dolomite, galena, and pyrargyrite from the ESE-Qz and ESE-Dol stages vary from 0.77 to 1.85. ^{20}Ne concentrations are indistinguishable from the blank, demonstrating an extremely low Ne content and lack of significant contribution from atmospheric gases. $^{3}He/^{4}He$ ratios show excesses of ^{3}He relative to typical crustal fluids, thus strongly suggesting a contribution of mantle volatiles to fluids that were trapped in the analyzed minerals (Levresse et al. 2004).

12 Lead Isotopic Compositions

New lead isotope measurements performed on six galena separates from the ESE-Qz and ESE-Dol stages are presented in Table 3 and plotted in Fig. 7. Lead isotope ratios for galena separates range from 17.995 to 18.523 for $^{206}Pb/^{204}Pb$, 15.532–15.673 for $^{207}Pb/^{204}Pb$, and 37.462–38.797 for $^{208}Pb/^{204}Pb$. These compositions, which overlap the values reported by Pašava (1994), plot between the upper crust and mantle growth curves and resemble the orogen reservoir of Zartman and Doe (1981). Good reproducibility of the data indicates that the observed scatter does not represent an artefact of analytical error and/or mass fractionation bias. Instead, we interpret the roughly linear array as a binary mixing line, suggestive of a mixing of

Table 3 Sulphur and lead isotopic compositions of galena separates from Imiter Ag–Hg deposit

Samples	Mineral	$\delta^{34}S_{CDT}$ (‰)	$^{206}Pb/^{204}Pb$	$^{207}Pb/^{204}Pb$	$^{208}Pb/^{204}Pb$
I 1.1	Galena	−7.8	18.112	15.559	37.810
I 1.2	Chalcopyrite	−7.3	–	–	–
I 2.2	Pyrite	−6.2	–	–	–
I 3.1	Pyrite	−5.7	–	–	–
I 4.2	Galena	–	17.995	15.536	37.661
I 7.1	Galena	−5.8	–	–	–
I 8.1	Galena	−6.2	–	–	–
I 8.1 QCD	Galena	−5.9	–	–	–
I10.2	Galena	–	18.136	15.553	37.826
I 11.2	Galena	−5.6	–	–	–
I12.1	Galena	–	18.123	15.565	37.840
I 13.1	Galena	−5.1	–	–	–
I 14.1	Galena	−8.3	–	–	–
L 1.2	Galena	−7.2	18.111	15.561	37.823
L1 5	Galena	–	18.244	15.636	38.462

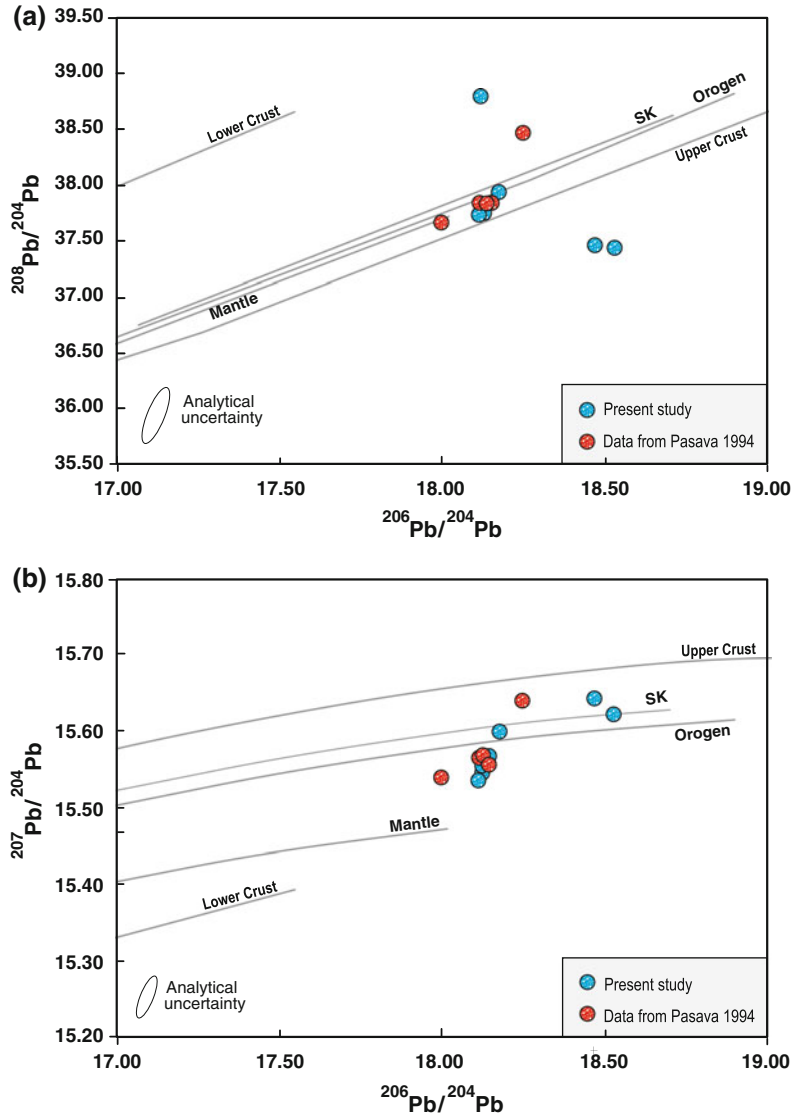

Fig. 7 Lead isotopic compositions of galena separates from Imiter Ag–Hg deposit, plotted on **a** $^{208}Pb/^{204}Pb$ versus $^{206}Pb/^{204}Pb$ and **b** $^{207}Pb/^{204}Pb$ versus $^{206}Pb/^{204}Pb$ diagrams. Evolution curves of Stacey and Kramers (1975) labeled SK and those for Upper Crust and Orogen (Zartman and Doe 1981) are shown for reference

lead from mantle and crustal reservoirs during leaching and fluid transport, consistent with the sulphur isotope and He isotope data described above.

13 Discussion

Mineralogical, textural, and geochemical attributes of the Imiter silver vein mineralization clearly point to an epithermal deposit type (Figs. 1 and 2). Diagnostic features in support of this classification include the presence of adularia (Borisenko et al. 2013), occurrence of large open structures filled by ore and gangue minerals, and widespread development of vuggy quartz, all of which are characteristic of a shallow and brittle environment. An epithermal model for Imiter has been proposed by previous workers (Levresse 2001; Cheilletz et al. 2002; Levresse et al. 2004; Burniaux and Williams-Jones 2006), and since then has been extended to most, if not all, of the Ag-rich deposits in the Anti-Atlas Mountains (Ennaciri et al. 1997; Essaraj et al. 1999, 2005; Marcoux and Wadjinny 2005).

Paragenetic studies indicate that the history of the Imiter mineralizing system involved two main contrasting hydrothermal events (Fig. 1) that occurred under two distinct mainly extensive tectonic events (Ouguir et al. 1994; Tuduri et al. 2005). These two stress fields are similar to those that gave rise to the late Neoproterozoic Bou Madine epithermal Au–Ag–Pb–Zn deposit described in this volume by Bouabdellah and Levresse. However, owing to the lack of robust absolute ages for each mineralizing event at Imiter, it is unclear whether these two hydrothermal events involved a single mineralizing fluid or two chronologically separate fluids. The confinement of silver mineralization to the transcrustal Imiter fault zone suggests that silver-bearing hydrothermal fluids were channeled through fractured rocks, en route to depositional sites in veins hosted by overlying black shales and along the contact between the upper and lower lithostratigraphic units of the Neoproterozoic succession.

Fluid inclusion data show the existence of two distinct fluid inclusion populations having similar temperature ranges but contrasting salinities (Table 1, Figs. 3 and 4). A consistent trend is apparent towards slightly lower temperatures but higher salinities with advancing paragenetic stage. The early mineralizing fluids related to the ESE-Qz stage had a mean temperature of ~180 °C and corresponding salinity of ~10 wt % NaCl equiv, whereas the subsequent ESE-Dol stage fluids had a lower mean temperature of ~165 °C but with a substantially higher mean salinity of ~24 wt% NaCl equiv. Similarly, the fluid compositions evolved by relative decreases in Na^+, K^+, and SO_4 and a concomitant increase in Ca^{2+} with time (i.e., from Qz-1 to Dol-2 stages).

Estimates of minimum trapping pressure are in the range of 1.1–0.9 kbar for the mineralizing fluid responsible for Imiter silver mineralization. Within this range of pressures, as well as temperatures (206–126 °C) and salinities (0–15 wt% NaCl equiv), thermodynamic restrictions preclude boiling of the fluid (Hass 1976). The absence of platy calcite (Simmons et al. 2005), and also of co-existing vapor-rich and liquid-rich inclusions that homogenize over the same temperature range (see Roedder 1984), indicate again that fluid boiling did not occur during trapping of these fluid inclusions.

Measured Br/Cl molar ratios of fluids related to the ESE-Qz and ESE-Dol stages are consistent with the involvement of magmatically derived fluid components (Fig. 4). Moreover, elements such F and Li that are considered reliable proxies of magmatic degassing (Deering et al. 2012; Vlastélic et al. 2013; Chen et al. 2015), have higher concentrations in Qz-1 than in Dol-2. We thus propose that degassing of CO_2 and SO_2 during epithermal mineralization (e.g., Bendezú et al. 2008 and references therein) led to a decrease of local redox potential and a pH increase, which together with other ore controls such as decreasing temperature and lowering of f_{O2} by fluid interaction with the organic-rich black shales, resulted in deposition of massive Hg–Ag amalgam instead of separate Ag and Hg sulphide minerals (Borisenko et al. 2013). The high water/rock ratios that prevailed during ore deposition would have developed a large hydrothermal alteration halo around and adjacent to the Imiter mineralized structures, and within the Cryogenian black shales as well.

It is noteworthy that halogen contents of fluids generated during open-system degassing can be highly variable (Villemant and Boudon 1999; Aiuppa et al. 2009) with concentrations being higher in the first extracted fluid fractions than in the last ones. Conversely, fluids produced during closed-system evolution commonly show nearly constant halogen contents but much lower Br abundances; Cl contents, in contrast, remain similar to those resulting from open-system degassing (Villeman and Boudon 1999). Involvement of ore-forming brines in which high salinities are derived either directly from seawater evaporation or from exchange reactions with sedimentary evaporite strata (i.e., halite dissolution) is precluded, because the expected increase in the abundances of salt (KCl_2, $CaCl_2$, $MgCl_2$) and sulphate in the residual fluids (Horita et al. 2002; Brennan et al. 2004; Foriel et al. 2004; Kendrick et al. 2005; Spear et al. 2014) are not observed in the Imiter fluid inclusions.

In contrast to this predicted trend, measured Na/Cl, K/Cl, and SO_4/Cl ratios for the fluid inclusions show a systematic decrease from early to late mineralizing stages. Moreover, the negative correlation between SO_4 abundances and Br/Cl ratios indicates that seawater is unlikely to be the predominant source of the ore-forming brine. In our model for the Imiter Ag–Hg deposit, the degassing process explains the physico-chemical evolution of the epithermal system without the necessity of invoking a mixing with basinal brines. More importantly, at the time of ore formation the closest basinal brine sources were 80 km from the mineralized area (Álvaro 2014). Also, the first sedimentary record known in the Imiter deposit area is from the Middle Cambrian (Piqué et al. 1999; Álvaro 2014), which is 30 m.y. later than the Neoproterozoic silver mineralizing event.

In conclusion, fluid inclusion data together with halogen compositions and sulphur and lead isotope data are consistent with the involvement of a magmatic component in the Imiter hydrothermal system. Indeed, the large spread in sulphur isotopic values for the ESE mineralizing event is interpreted as resulting from preferential degassing of SO_2 in ascending fluids and mixing between magmatic and country rock reservoirs. Moreover, the linearity displayed by lead isotopic compositions is suggestive of a mixing of lead from mantle and crustal reservoirs during leaching and fluid transport.

Continuous input of magmatically equilibrated fluids into the hydrothermal system is supported by the observed increases in Hg concentrations of the Hg–Ag amalgam from the Qz-1 to Dol-2 stages (10–30 vol.% and 20–40 vol.%; respectively). Calculated $\delta^{18}O_{H2O}$ values of the ore-forming fluid, using the dolomite-H_2O fractionation factor of Zheng (1999) and the average temperature of 165 °C inferred from fluid inclusion data, are in the range of 6.3–19.6 ‰ V-SMOW. These values are consistent with a mixture of magmatic and metamorphic fluids. Interaction of the mineralizing fluids with the enclosing Neoproterozoic organic-rich black shale host rocks could have produced a large volume of reduced and low-pH fluids that were capable of transporting and precipitating Ag and associated base metals, as well as providing a source of carbon for the late ore-bearing carbonate gangue.

The light carbon isotopic signatures of Dol-2 separates (Pašava 1994) and abundance of CH_4- and N_2-rich fluid inclusions provide further support for involvement of the black shales as reactive host rocks during the mineralizing process. Such water/rock interaction may have contributed to thermochemical reduction and associated precipitation of Ag-bearing sulphide minerals. Mass-balance calculations suggest, however, that the contribution of components from the black shales to the Imiter hydrothermal system was rather limited (i.e., <10 vol.%; Levresse et al. 2004). Moreover, $^{187}Os/^{188}Os$ and $^{3}He/^{4}He$ data, together with lead isotope data, are consistent with various degrees of mixing between mantle and crustal sources along the fluid flow path.

Integrated results from geological, structural, and geochemical studies (Fig. 8) indicate that hydrothermal fluids were channeled from a deep source to a shallow hydrothermal system by the crustal-scale Imiter fault zone. In our model, these magmatic-related fluids percolated though the Cryogenian black shales, and were progressively buffered and acquired a different geochemical signature compared to the initial magmatically derived fluids. This concept involves different pulses of epithermal mineralizing fluids and a wide range of water/rock ratios, in particular for CO_3, Ca, Mg, Pb, and S that were leached from the Cryogenian black shales and/or rocks in the lower basement. The proposed magmatic input during the epithermal silver mineralizing stages added to the fluid confinement within the Cryogenian black shales (favored by the Ediacaran volcanic seal), and is considered the principal reason for the richness of the Imiter deposit and its continuity at depth (at least 900 m at present).

It is also noteworthy that the He and Os isotope data are inconsistent with the supergene model for silver enrichment as initially proposed by Guillou et al. (1988), Leistel and Qadrouci (1991), and Baroudi et al. (1999).

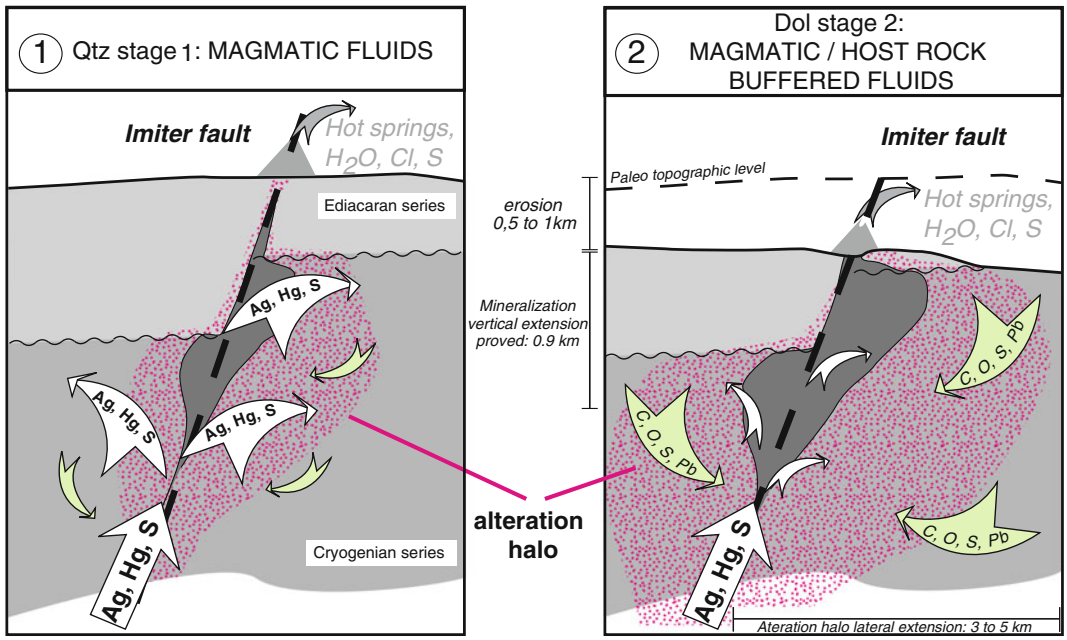

Fig. 8 Genetic model for Imiter Ag–Hg deposit. *1* ESE quartz stage 1 event. *2* ESE dolomite stage 2 event. Simplified geological cross sections are drawn from B3 Hill transect (modified from Levresse 2001). Model illustrates evolution of the silver epithermal system particularly the importance of magmatic fluid degassing, the Ediacaran volcanic seal, and increasing water-rock interaction from stage ESE Qz-1 to ESE Dol-2 stages

14 Conclusions

The giant Imiter deposit is a prime example of major Ag–Hg mineralization linked with Ediacaran volcanism dated at ca. 550 Ma. To build such a giant metal concentration, three essential ingredients should have been available together (Fig. 8), including: (1) a powerful and long-lasting magmatic source connected by major tectonic structures to one or more asthenosphere reservoirs; (2) reactive and highly permeable, metamorphosed and foliated organic-rich host rocks that facilitated the transmission of fluids and increased the surface area of fluid/rock interactions, in addition to generating the reducing conditions necessary for metal precipitation; and (3) overlying cap rocks that prevented escape of the hydrothermal fluids to the surface, instead forcing these fluids to an increased residence time and dissemination within the most receptive formation (lithological trap).

The striking feature of the Imiter Ag–Hg deposit is the duration and chemical evolution of the causative epithermal activity. With advancing paragenetic sequence, the epithermal system was self-regulating, whereas the interaction between magmatically derived fluids and host rocks became predominant. This inferred process may explain the transition from quartz-dominant to dolomite-dominant Ag–Hg mineralization through the paragenetic sequence. In such a low-sulphidation metallogenic model, the involvement of meteoric waters is not a prerequisite to explain metal precipitation, nor is supergene enrichment needed to obtain the very high volume and grade of the ores. Magmatic degassing into the hydrothermal system, coupled with fluid/rock interactions, ultimately led to development of a local decrease in redox potential and an increase in pH, which coupled with other ore controls (e.g., decreasing fluid temperature), triggered deposition of massive Hg–Ag amalgam instead of Hg and Ag sulphide minerals.

Acknowledgments Special thanks to Marina Vega and Teresa Soledad Medina Malagón for assistance at the CGEO laboratory. This study was financed by UNAM-PAPIIT project IN110912 and CONACYT projects 81584 and 80142. We also thank John Slack for his constructive review, which led to numerous improvements in the quality and clarity of the text.

References

Aiuppa A, Baker DR, Webster JD (2009) Halogens in volcanic systems. Chem Geol 263:1–18

Álvaro JJ (2014) Rift, pull-apart rift and continental drift crossword puzzles across the lower-middle Cambrian transition of Iberia and Morocco. GFF 136:2–5

Álvaro JJ, Beellido F, Gasquet D, Pereira MF, Quesada C, Sanchez-Garcia T (2014). Diachronism in the late Neoproterozoic–Cambrian arc-rift transition of North Gondwana: A comparison of Morocco and the Iberian Ossa-Morena Zone. J Afr Earth Sci 98:113–132

Bajja A (1998) Volcanisme syn à post orogénique du Néoprotérozoïque de l'Anti-Atlas: implications pétrogénétiques et géodynamique. Thèse d'Etat Es-sciences, Univer Chouaib Doukkali, El Jadida, Maroc, 215 pp

Banks DA, Giuliani G, Yardley BWD, Cheilletz A (2000) Emerald mineralisation in Colombia: fluid chemistry and the role of brine mixing, Mineralium Deposita 35:699–713

Baroudi Z (1992) Contribution à l'étude métallogénique des minéralisations mercuro-argentifères du district d'Imiter Saghro Oriental, Anti-Atlas, Maroc. Thèse, University of Marrakech, 188 pp

Baroudi Z, Beraouz H, Rahimi A, Saquaque A, Chouhaidi M (1999) Minéralisations polymétalliques argentifères d'Imiter Jbel Saghro, Anti-Atlas, Maroc: minéralogie, évolution des fluides minéralisateurs et mécanismes de dépôts. Chronique Recherche Minière 536–537:91–111

Barton PB Jr, Skinner BJ (1967) Sulfide mineral stabilities. In: Barnes HL (ed) Geochemistry of hydrothermal ore deposits. Holt, Reinhart & Winston Inc, New York, pp 236–333

Bayliss P (1985) Nomenclature of the trioctahedral chlorites. Can Mineral 13:178–180

Bendezú R, Page L, Spikings R, Pecskay Z, Fontboté L (2008) New $^{40}Ar/^{39}Ar$ alunite ages from the Colquijirca district, Peru: evidence of a long period of magmatic SO_2 degassing during formation of epithermal Au-Ag and Cordilleran polymetallic ores. Miner Deposita 43:777–789

Borisenko AS, Borovikov AA, Pavlova GG, Kalinin YuA, Nevolko PA, Lebedev VI, Maacha L, Kostin AV (2013) Formation conditions of Hg-silver deposition at the Imiter deposit (Anti-Atlas, Morocco). In: Johnsson E et al (eds) Mineral deposit research for a high-tech world. Proceedings of 12th biennial SGA meeting, Uppsala, Sweden 3:1243–1246

Brennan ST, Lowenstein TK, Horita J (2004) Seawater chemistry and the advent of biocalcification. Geology 32:473–476

Burniaux P, Williams-Jones AE (2006) Controls of silver-mercury mineralization at Imiter, Morocco. Geol Assoc Canada Pgm Abs 31:22

Cathelineau M (1988) Cation site occupancy in chlorites and illites as a function of temperature. Clay Miner 23:471–485

Cheilletz A, Levresse G, Gasquet D, Azizi Samir MR, Zyadi R, Archibald DA (2002) The Imiter epithermal deposit (Morocco): new petrographic, microtectonic and geochronological data. Importance of the Precambrian-Cambrian transition for major precious metals deposits in the Anti-Atlas. Miner Deposita 37:772–781

Chen Z, Xu Y, Zheng K (2015) Geochemistry of potential high temperature geothermal resources in Kangding, Sichuan, China. In: Proceedings of world geothermal congress, Melbourne, Australia, pp 1–7

D'Amore F, Panichi G (1980) Evaluation of deep temperatures of hydrothermal systems by a new gas geothermometer. Geochim Cosmochim Acta 44:549–556

Deering CD, Horton TW, Gravley DM, Cole JW (2012) Hornblende, cummingtonite, and biotite hydrogen isotopes: direct evidence of slab-derived fluid flux in silicic magmas of the Taupo volcanic zone, New Zealand. J Volcanol Geoth Res 233–234:27–36

Déruelle B, Dreibus G, Jambon A (1992) Iodine abundances in oceanic basalts: implications for Earth dynamics. Earth Planet Sci Lett 108:217–227

Dubessy J, Buschaert S, Lamb W, Pironon J, Thiery R (2001) Methane-bearing aqueous fluid inclusions: Raman analysis, thermodynamic modelling and application to petroleum basins Chem Geol 173:193–205

Ducrot J, Lancelot JR (1977) Problème de la limite Précambrien-Cambrien: étude radiochronologique par méthode U-Pb sur zircon du Jbel Bobo (Anti-Atlas marocain). Can J Earth Sci 14:2771–2777

Ennaciri A, Barbanson L, Touray JC (1997) Brine inclusions from the Co-As-(Au) Bou Azzer district, Anti-Atlas Mountains, Morocco. Econ Geol 92:360–367

Ennih N, Liégeois JP (2001) The Moroccan Anti-Atlas: the West African craton passive margin with limited Pan-African activity, implications for the northern limit of the craton. Precambr Res 112:289–302

Essaraj S (1999) Circulations de fluides associées aux minéralisations argentifères de l'Anti- Atlas central: exemples des gisements de Zgounder (Ag-Hg) et Bou-Azzer (Co-Ni-As-Au-Ag). Université Cadi-Ayyad, Marrakech, Maroc, Thèse d'État 358 pp

Essaraj S, Boiron MC, Cathelineau M, Banks DA, Benharref M (2005) Penetration of surface-evaporated brines into the Proterozoic basement and deposition of Co and Ag at Bou-Azzer (Morocco):

evidence from fluid inclusions. J Afr Earth Sci 41:25–39
Fekkak A, Pouclet A, Ouguir H, Ouazzani H, Badra L, Gasquet D (2001) Géochimie et signification géotectonique des volcanites du Cryogénien inférieur du Saghro (Anti-Atlas oriental, Maroc). Geodinam Acta 14:373–385
Fontes JC, Matray JM (1993) Geochemistry and origin of formation brines from the Paris Basin, France 1. Brines associated with Triassic salts. Chem Geol 109:149–175
Foriel J, Philippot P, Rey P, Somogyi A, Banks DA, Menez B (2004) Biological control of Cl/Br and low sulfate concentration in a 3.5-Gyr-old seawater from North Pole, Western Australia. Earth Planet Sci Lett 228:451–463
Gasquet D, Chevremont P, Baudin T, Chalot-Prat C, Guerrot C, Cocherie A, Roger J, Hassenforder B, Cheilletz A (2004) Polycyclic magmatism in the Tagragra and Kerdous-Tafeltast inliers (western Anti-Atlas, Morocco). J Afr Earth Sci 39:267–275
Gasquet D, Levresse G, Cheilletz A, Deloule E, Azizi Samir MR, Zyadi R (2005) Contribution to a geodynamic reconstruction of the Anti-Atlas (Morocco) during Pan African times with the emphasis on inversion tectonics and metallogenetic activity at the Precambrian-Cambrian transition. Precambr Res 140:157–182
Guillou J-J, Monthel J, Picot P, Pillard F, Protas J, Samama J-C (1985) L'imitérite, Ag2HgS2, nouvelle espèce minérale; propriétés et structure cristalline. Bulletin de Mineralogie 108:457–464
Guillou JJ, Monthel J, Samama JC, Tijani A (1988) Morphologie et chronologie relative des associations minérales du gisement mercuro-argentifère d'Imiter (Anti-Atlas, Maroc). Notes Mémoires Service Géologique Maroc 334:215–228
Haas JL (1971) The effect of salinity on the maximum thermal gradient of a hydrothermal system at hydrostatic pressure. Econ Geol 66:940–946
Hey MH (1954) A new review of the chlorites. Min Mag 30:227–292
Hofstra AH, Landis GP (2012) Ore genesis constraints on the Idaho cobalt belt from fluid inclusion gas, noble gas isotope, and ion ratio analyses. Econ Geol 107:1189–1205
Horita J, Zimmermann H, Holland HD (2002) Chemical evolution of seawater during the Phanerozoic: implications from the record of marine evaporates. Geochim Cosmochim Acta 66:3733–3756
Johnson L, Burgess R, Turner G, Milledge JH, Harris JW (2000) Noble gas and halogen geochemistry of mantle fluids: comparison of African and Canadian diamonds. Geochim Cosmochim Acta 64:717–732
Katrivanos FC (2015) Silver. U.S. Geological Survey 2012 Minerals Yearbook. http://minerals.usgs.gov/minerals/pubs/commodity/silver/myb1-2012-silve.pdf
Kendrick MA, Burgess R, Pattrick D, Turner G (2001) Fluid inclusion noble gas and halogen evidence on the origin of Cu-porphyry mineralising fluids. Geochim Cosmochim Acta 65:2651–2668
Kendrick MA, Burgess R, Harrison D, Bjorlykke A (2005) Noble gas and halogen evidence for the origin of Scandinavian sandstone-hosted Pb-Zn deposits. Geochim Cosmochim Acta 69:109–129
Kesle SE, Martini AM, Appold MS, Walter LM, Hston TJ, Furman FC (1996) Na-Cl-Br systematics of fluid inclusions from Mississippi Valley-type deposits, Appalachian basin: constraints on solute origin and migration paths. Geochim Cosmochim Acta 60:225–233
Kracek FC (1946) Phase relations in the system silver-sulfur and the transitions in silver sulfide. Trans Am Geophys Union 27:367–374
Leistel JM, Qadrouci A (1991) Le gisement argentifère d'Imiter (protérozoïque supérieur de l'Anti-Atlas, Maroc): contrôles des minéralisations, hypothèse génétique et perspectives pour l'exploration. Chroniques Recherche Minière 502:5–22
Levresse G (2001) Contribution à l'établissement d'un modèle génétique des gisements d'Imiter (Ag-Hg) Bou Madine (Pb-Zn-Cu-Au) et Bou Azzer (Co-Ni-As-Au-Ag) dans l'Anti-Atlas marocain. Unpublished Ph.D. thesis, Université INPL-Nancy, 191 pp
Levresse G, Cheilletz A, Gasquet D, Reisberg L, Deloule E, Marty B, Kyser K (2004) Osmium, sulphur, and helium isotopic results from the giant Neoproterozoic epithermal Imiter silver deposit, Morocco: evidence for a mantle source. Chem Geol 207:59–79
Marcoux E, Wadjinny A (2005) Le gisement Ag-Hg de Zgounder (Jebel Siroua, Anti-Atlas, Maroc): un épithermal néoprotérozoïque de type Imiter. Comptes Rendus Geosci 337:1439–1446
Marini F, Ouguir H (1990) Un nouveau jalon dans l'histoire de la distension pre-panafricaine au Maroc: le précambrien II des boutonnières du Jbel Saghro nord-oriental (Anti-Atlas, Maroc). Comptes Rendus Acad Sci Paris 310:577–582
Mifdal A, Peucat JJ (1985) Datations U/Pb et Rb/Sr du volcanisme acide de l'Anti-Atlas marocain et du socle sous-jacent dans la région de Ouarzazate. Apport au problème de la limite Précambrien-Cambrien. Sci. Géol. Bull., 38:185–200
Newman HR (2009) Morocco and Western Sahara. U.S. Geological Survey 2009 Minerals Yearbook. http://minerals.usgs.gov/minerals/pubs/country/2009/myb3-2009-mo-wi.pdf
Oberthür T, Melcher F, Henjes-Kunst F, Gerdes A, Stein H, Zimmerman A (2007) Hercynian age of the cobalt-nickel-arsenide-(gold) ores, Bou Azzer, Anti-Atlas, Morocco: Re-Os, Sm-Nd, and U-Pb age determinations. Econ Geol 104:1065–1079
Ouguir H, Macaudière J, Dagallier G (1996) Le protérozoïque supérieur d'Imiter, Saghro oriental, Maroc: un contexte géodynamique d'arrière-arc. J Afr Earth Sci 22:173–189

Ouguir H, Macaudiére J, Dagallier G, Qadrouci A, Leistel JM (1994) Cadre structural du gîte Ag–Hg d'Imiter (Anti-Atlas, Maroc): implications métallogéniques. Bull Soc Géol France 165:233–248

Pašava J (1994) Geochemistry and role of anoxic sediments in the origin of the Imiter silver deposit in Morocco. Czech Geol Surv Bull 69:1–11

Pelleter E, Cheilletz A, Gasquet D, Mouttaqi A, Annich M, El Hakour A, Feraud G (2008) The Variscan Tamlalt-Menhouhou gold deposit, eastern High-Atlas, Morocco. J Afr Earth Sci 50:204–214

Pelleter E, Cheilletz A, Gasquet D, Mottaqi A (2010) Alteration processes and impacts on regional-scale element mobility and geochronology, Tamlalt-Menhouhou deposit, Morocco. Geol Assoc Canada, Short Course Notes 20:177–185

Piqué A, Bouabdelli M, Soulaimani A, Youbi N, Iliani M (1999) Les conglomérats du P III (Néoprotérozoïque supérieur) de l'Anti Atlas (Sud du Maroc): molasses panafricaines, ou marqueurs d'un rifting fini-proterozoique? Comptes Rendus Acad Sci Paris 328:409–414

Popov AG (1995) Gisement argentifère d'Imiter: étude minéralogique, paragenèse et zonalité du gisement. Unpublished Report, Société Minière d'Imiter, Tinghir, Maroc, 115 pp

Popov AG, Belkasmi A, Qadrouci A (1986) Le gisement argentifère d'Imiter: synthèse géologique, résultats des recherches de 1985 et bilan des réserves au 31/12/1985. Unpublished Report, Société Minière Imiter, Tinghir, Maroc, 134 pp

Roedder E (1984) Fluid inclusions. Rev Mineral 12:1–644

Simmons SF, White NC, John DA (2005) Geological characteristics of epithermal precious and base metal deposits. In: Hedenquist JW, Thompson JFH, Goldfarb RJ, Richards JP (eds) Economic geology 100th anniversary volume, 1905–2005, pp 485–522

Spear N, Holland HD, Garcia-Veígas J, Lowenstein TK, Giegengack R, Peters H (2014) Analyses of fluid inclusions in Neoproterozoic marine halite provide oldest measurement of seawater chemistry. Geology 42:103–106

Stacey JS, Kramers JD (1975) Approximation of terrestrial lead isotope evolution by a two-stage model. Earth Planet Sci Lett 26:207–221

Thomas RJ, Fekkak A, Ennih N, Errami E, Loughlin ES, Gresse PG, Chevallier LP, Liégeois JP (2004) A new lithostratigraphic framework for the Anti-Atlas orogen, Morocco. J Afr Earth Sci 39:217–226

Tritlla J, Cardellach E, Sharp ZD (2001) Origin of vein hydrothermal carbonates in Triassic limestones of the Espadán Ranges (Iberian Chain, E Spain). Chem Geol 172:291–305

Tuduri J, Chauvet A, Ennaciri A, Barbanson L (2005) Model of formation of the Imiter silver deposit (eastern Anti-Atlas, Morocco): new structural and mineralogical constraints. Comptes Rendus Géosci 338:253–261

Vargas JM (1983) Etude métallographique des minéralisations mercuro-argentifere d'Imiter. Rapport Fondation Scientifique Géologie Applic, Nancy 358 pp

Villemant B, Boudon G (1999) H_2O and halogen (F, Cl, Br) behaviour during shallow magma degassing processes. Earth Planet Sci Lett 168:271–286

Vlastélic G, Menard A, Gannoun JL, Piro T, Staudacher V (2013) Magma degassing during the April 2007 collapse of Piton de la Fournaise: the record of semi-volatile trace elements (Li, B, Cu, In, Sn, Cd, Re, Tl, Bi). J Volcanol Geoth Res 254:94–107

Zartman RE, Doe BR (1981) Plumbotectonics—the model. Tectonophys 75:135–162

Zheng Y-F (1999) Oxygen isotope fractionation in carbonate and sulfate minerals. Geochem J 33:109–126

The Polymetallic (W–Au and Pb–Zn–Ag) Tighza District (Central Morocco): Ages of Magmatic and Hydrothermal Events

Magali Rossi, Leïla Tarrieu, Alain Cheilletz, Dominique Gasquet, Etienne Deloule, Jean-Louis Paquette, Hassan Bounajma, Tristan Mantoy, Lofti Ouazzani and Lahcen Ouchtouban

Abstract

The W–Au, Pb–Zn–Ag, and Sb–Ba deposits of the polymetallic Tighza-Jbel Aouam district (central Meseta, Morocco), hosted in Paleozoic rocks surrounding late Variscan granite stocks, have been considered of magmatic-hydrothermal origin. The spatial distribution of the mineralization was attributed in early studies to zoning around a supposed hidden batholith. New geophysical data (El Dursi 2009) and U/Pb geochronology on zircon and monazite grains (this study) allow revision of this model, giving insights of a more complex setting and history for the Tighza-Jbel Aouam district. The W–Au mineralization formed at 295–280 Ma and is related to a magmatic event visible only in a large hydrothermal biotitic alteration halo, thus suggesting the presence of a hidden batholith. This mineralization cuts the granitic stocks that are dated at 320–300 Ma. From the occurrence of large veins, stockworks, sheeted veins, and disseminations in skarns, the W–Au deposit is considered similar to a porphyry-type deposit. The currently mined Pb–Zn–Ag deposit, which is spatially separated from the W–Au deposit, developed

M. Rossi (✉) · L. Tarrieu · D. Gasquet
Laboratoire EDYTEM, Université Savoie Mont-Blanc, CNRS-UMR5204, Campus Scientifique, 73376 Le Bourget du Lac, France
e-mail: magali.rossi@univ-smb.fr

A. Cheilletz
Ecole Nationale Supérieure de Géologie, Laboratoire Géoressources, Université de Lorraine, rue du Doyen Marcel Roubault, BP 40, 54501 Vandoeuvre-lès-Nancy, France

E. Deloule
Centre de Recherches Pétrographiques et Géochimiques, Université de Lorraine, BP 20, 54501 Vandoeuvre-lès-Nancy, France

J.-L. Paquette
Laboratoire Magma et Volcans, Université Blaise Pascal, CNRS-UMR 6524, 63038 Clermont-Ferrand Cedex, France

H. Bounajma · T. Mantoy · L. Ouazzani · L. Ouchtouban
Compagnie Minière de Touissit (CMT), 5 rue Ibnou Tofail, Quartier Palmiers, 20340 Casablanca, Centre minier de Tighza, BP 114, M'rirt 54450, Province de Khénifra, Morocco

M. Bouabdellah and J.F. Slack (eds.), *Mineral Deposits of North Africa*, Mineral Resource Reviews, DOI 10.1007/978-3-319-31733-5_3

during an epithermal magmatic-hydrothermal episode dated at 254 ± 16 Ma. The polymetallic district of Tighza-Jbel Aouam thus appears to contain Cordilleran-style, porphyry-type mineralization (W–Au) followed by epithermal mineralization (Pb–Zn–Ag), both being related to pulses of calc-alkaline magmatism. Late Variscan and Permo-Triassic transpressive tectonics in the region localized magma emplacement and the generation of genetically associated hydrothermal fluids, with the magmas originating in the mantle and the continental crust.

1 Introduction

The polymetallic W–Au–Pb–Zn–Ag (Sb–Ba) district of Tighza (central Morocco), also referenced as the Jbel Aouam district, has been mined for centuries for Pb and Ag. The oldest reported mining is from the XIth Century, when Ag-rich lead was extracted from supergene alteration zones of mineralized veins, down to depths of 200 m. The Compagnie Royale Asturienne des Mines (CRAM) began exploration in 1924 and extraction in 1930 in the southern part of the district. From 1957 to 1993, CRAM in association with the BRPM (Bureau de Recherches et de Participations Minières) extracted more than 6 Mt of ore, averaging 8 % of Ag-bearing lead. In 1996, the Compagnie Minière de Touissit (CMT), a new owner of the Tighza district, released conservative estimates of reserves at 12 Mt of ore including 1 Mt of Pb and 1200 t of Ag (Wajdinny 1998; CMT pers. comm.). Since 1996, CMT has extracted 5.8 Mt of ore at 7 % Pb, 1 % Zn and 130 g/t Ag.

Underground mining, which started in the 1930s, gave access to the Pb–Zn–Ag mineralization and provided new information on different types of mineralization found in the district. In the 1950s, Agard et al. (1958) proposed the first metallogenic model for this district, suggesting that during upper Visean time, an early Sb–Ba mineralization stage formed in relation to a hidden felsic magma that was the source of the outcropping granitic stocks. The later W–Au stage was also genetically associated with these stocks, followed by the Pb–Zn–Ag mineralization stage. According to Agard et al. (1958), these three mineralization stages characterize the evolution over time of a protracted hydrothermal system related to a single magmatic event, which formed a concentrically zoned, polymetallic district. This model was revised in the 1970s based on tectonic studies (Desteucq 1974) and in the 1980s on detailed structural, geochemical, and metallogenic analysis of the W–Au and Pb–Zn–Ag deposits (Cheilletz and Zimmermann 1982; Cheilletz 1983a, b, 1984; Jébrak 1984, 1985; Giulani et al. 1987, 1989). A particular emphasis in these studies was on a large hydrothermal biotitic halo spatially related to the W–Au mineralization (Cheilletz and Isnard 1985).

Several lines of evidence, however, suggest that the accepted model of a single magmatic-hydrothermal system needs to be re-evaluated. First, isotopic data show that the Pb–Zn–Ag mineralization formed from hydrothermal fluids

that were derived from the Paleozoic basement (Castorina and Masi 2000, 2008). Unlike the W–Au mineralization, the Pb–Zn–Ag thus appears to be genetically disconnected from the granites, thus implying the involvement of two distinct hydrothermal episodes. Second, dating of the W–Au mineralization and magmatic rocks (granitic stocks and dikes) indicates a range of ages from 300 to 260 Ma (Cheilletz and Zimmermann 1982; Watanabe 2002; Nerci 2006). Furthermore, recent dating of the neighboring El Hammam fluorine deposit (Cheilletz et al. 2010) allows revision of the accepted model, showing this mineralization to be much younger (205 ± 1 Ma) than the Late Variscan age commonly accepted for mineralization in this area. In order to revise the metallogenic model for the Tighza polymetallic district, we performed detailed geochemical studies to decipher the source of the W–Au and Pb–Zn–Ag mineralization and related hydrothermal fluids, together with new geochronological studies of the mineralization and the intrusive rocks (Tarrieu 2014).

This paper only focuses on dating of the hydrothermal and magmatic events that were possible triggers for the mineralization. A relative chronology of all of the events will be presented first, using detailed observations of spatial relationships among the W–Au mineralization, the Pb–Zn–Ag mineralization, and the magmatic rocks (granitic stocks and dikes). Our new geochronological data (U/Pb on zircon and Th/Pb on monazite) help constrain the timing of different magmatic and hydrothermal events, as reported for other hydrothermal systems by Grove and Harrison (1999), Vielreicher et al. (2003), and Pelleter et al. (2007), for instance. These new data for the Tighza polymetallic district thus provide new insights into the metallogenic evolution of this district.

2 Geological Setting

The Moroccan Meseta domain corresponds to the southwesternmost segment of the Variscan belt of Europe (Michard et al. 2008). The Tighza district belongs to the eastern part of the Meseta domain, which is underlain by Paleozoic metasedimentary rocks cut by Variscan magmatic stocks and dikes (Fig. 1). These felsic intrusive rocks are spatially associated with W, Sn, F, Sb and Pb–Zn–Ag mineralization.

Mineral deposits of the Tighza district are hosted in Paleozoic metasedimentary and granitic rocks studied by Agard et al. (1958), Desteucq (1974), Cheilletz (1984), Jébrak (1984), and Nerci (2006). Upper Visean (Mississippian) limestone and schist unconformably overlie Ordovician siliceous schist and quartzite, Silurian graptolite-bearing black shale, and Devonian siliceous limestone. All of these strata are deformed into a succession of SW-NE-trending anticlines and synclines, localized in a major EW sinistral shear zone whose northern branch crosses Tighza village (Fig. 2). These formations are metamorphosed up to greenschist facies and are intruded by microgranite and micogranodiorite dikes, and by four monzogranite stocks termed Kaolin, Mine, Mispickel, and Izougarza. These intrusive bodies have high-K calc-alkaline affinities, like most Moroccan Variscan granites, testifying to a large enriched mantle component (Giulani et al. 1987; Ntarmouchant 1991; Gasquet et al. 1996; El Hadi et al. 2006). The three southernmost intrusives are surrounded by a large and well-delimited biotitic alteration halo, which records the development of a hydrothermal convective cell related to the W–Au mineralization (Cheilletz 1984; Cheilletz and Isnard 1985). The gravimetric study of El Dursi (2009), carried on the entire district, suggests that this hydrothermal alteration halo might be

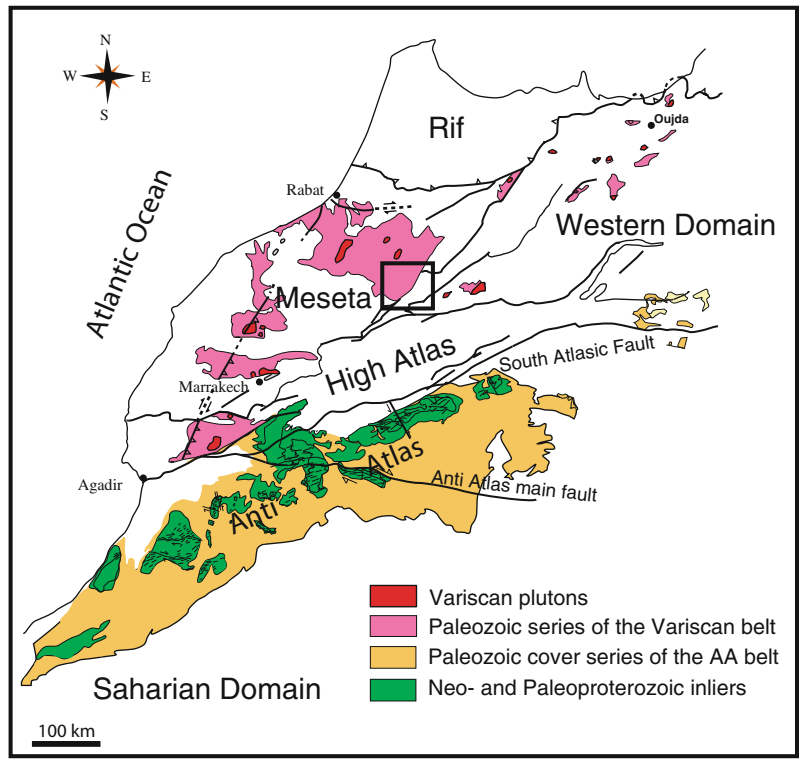

Fig. 1 Map showing main structural units of northern Morocco. AA stands for Anti Atlas. Box outlines area of Fig. 2

associated with a hidden shallow intrusive stock having a complex morphology (Fig. 3). El Dursi (2009) proposed that the outcropping granite stocks associated with the W–Au mineralization represent apexes developed at the top of this hidden pluton.

3 Mineralization

3.1 Mineralization and Paragenesis

Three main types of mineralization occur in the Tighza district: (1) W–Au, (2) Pb–Zn–Ag, and (3) Sb–Ba.

W–Au: This mineralization cuts or is located in the vicinity of the outcropping stocks (Fig. 2) suggesting that these deposits are genetically linked to this magmatic activity (e.g., Cheilletz 1984; Nerci 2006). Different types of W–Au mineralization have been identified by Nerci (2006) and Cheilletz (1984), including skarns, large veins, stockworks, sheeted veins, and disseminations.

The skarns developed either at the contacts between the Visean calcareous rocks and the Mispickel Monzogranite, or the Kaolin Monzogranite (to a lesser extent). Metasomatism formed pyroxene-rich skarns with clusters of scheelite, or replacements of discontinuous carbonate-rich layers within Lower Devonian pelitic schists. The latter replacements developed stratabound lenses having a characteristic banded structure defined by alternating layers rich in plagioclase and dark biotite and scheelite (Cheilletz 1983a; Cheilletz and Isnard 1985, and references therein). Skarn formation involved the infiltration into the Lower Devonian schists and the Visean carbonates by W-rich hydrothermal fluids under P-T conditions estimated by Cheilletz (1984) at 180 MPa and 580 °C.

According to Cheilletz (1984), the skarn formation was followed by brittle deformation that promoted opening of an abundant fracture network that was filled by W–Au veins that cut the skarns. This deformation is related to development of the dextral Anguelmous-Mrirt shear zone. Different

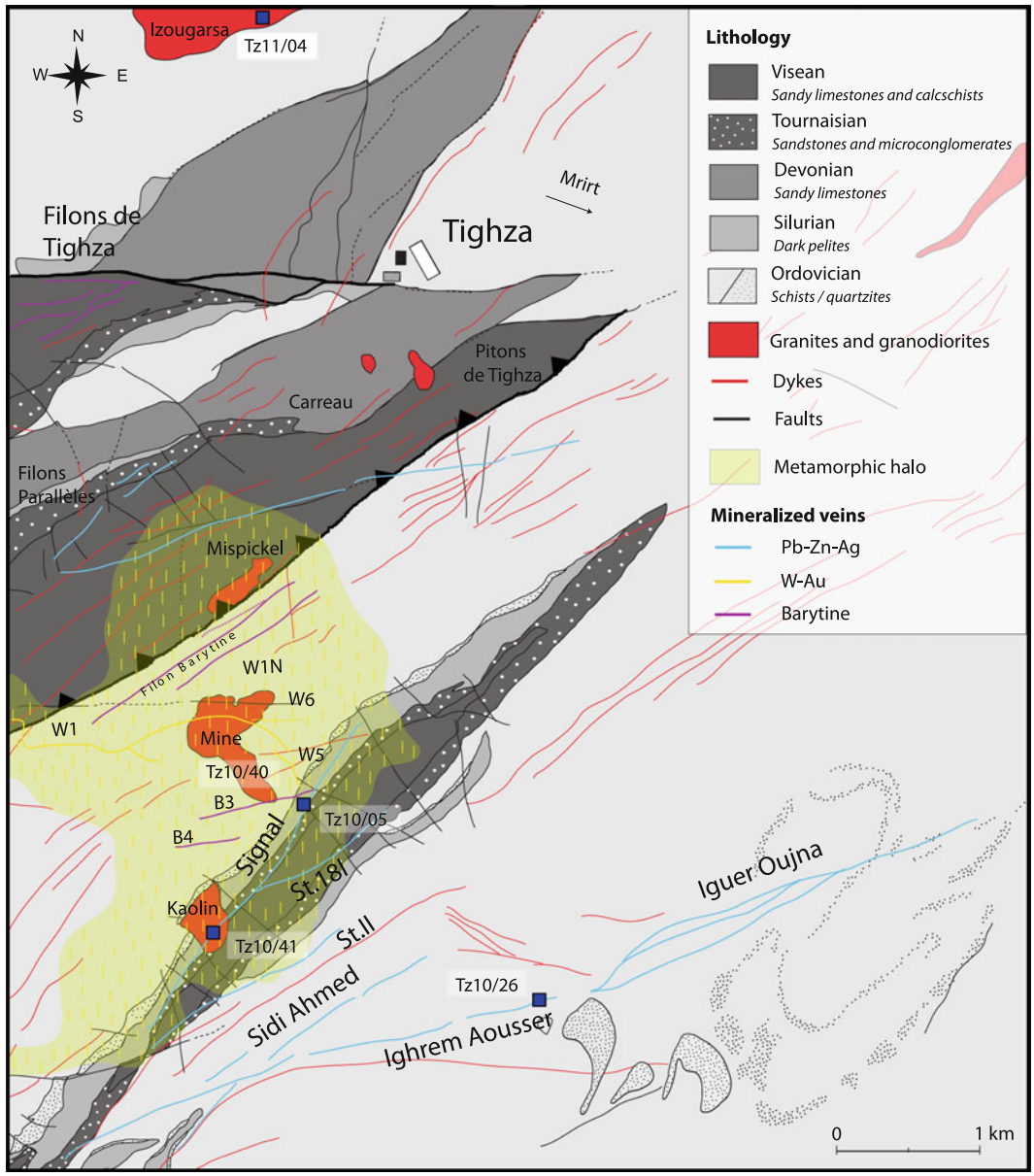

Fig. 2 Geological map of the polymetallic Tighza district in central Morocco. Modified from Agard et al. (1958), Cheilletz (1984), and CMT (pers. comm.). *Small blue squares* are locations of dated samples

types of W–Au veins have been identified by Cheilletz (1983b, 1984) and the geological staff of the mine in the biotite alteration halo: (1) large N70E-N110E veins that are located mainly within the vicinity of the Mine Monzogranite (W1, W1 N, WO3, W4, W5, W6 veins in Fig. 2); (2) stockworks, and (3) sheeted veins that display an "en echelon" geometry. Two main paragenetic assemblages have been recognized: scheelite + wolframite ± molybdenite, and scheelite + arsenopyrite + pyrrhotite + pyrite + arsenopyrite. Gold occurs in the latter paragenetic sequence

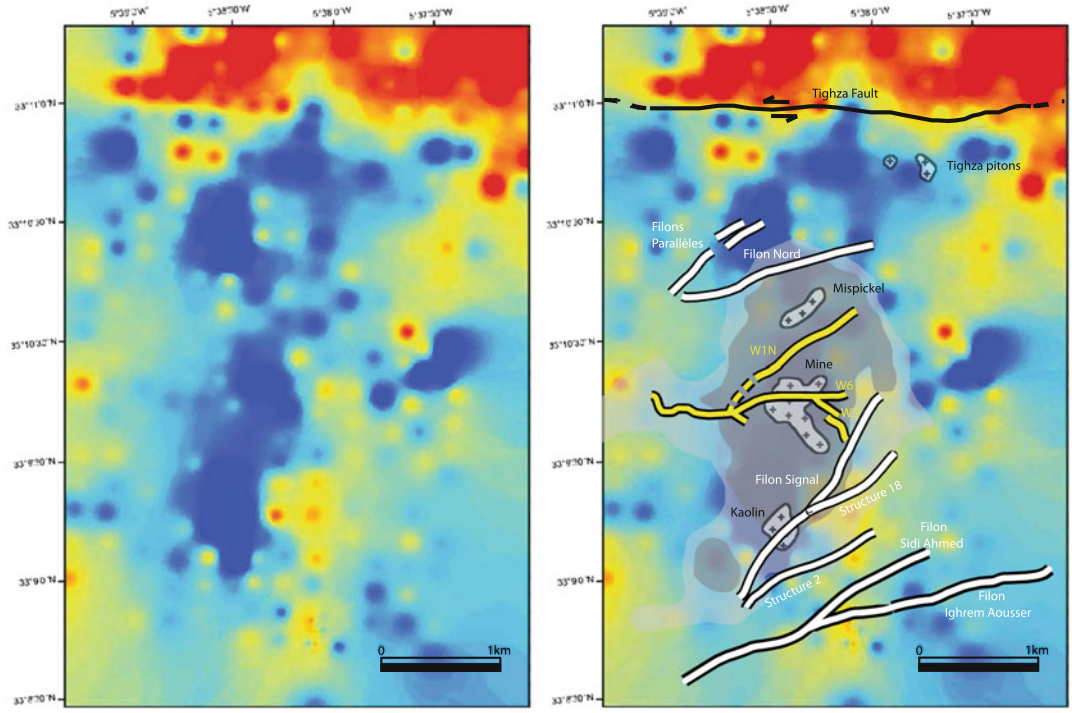

Fig. 3 Gravity map of the Tighza district showing raw data on the *left* (El Dursi 2009). Interpreted map, on the *right*, includes outcropping granitic stocks and main W–Au and Pb–Zn–Ag veins (*yellow* and *white* respectively); *gray shading* represents the hydrothermal biotitic alteration halo (see Fig. 2). Complete Bouguer anomalies, interpolated by the ordinary kriging method, range from 9.64 milligal (*red areas*) to −8.2 milligal (*blue areas*); standard deviation is 1.903. Map is georeferenced based on WGS 84 UTM Zone 30 N (El Dursi 2009)

(Nerci 2006). Formational temperatures of 400–450 °C and pressures of 100 MPa were estimated for the W–Au veins by Cheilletz (1984).

Disseminated mineralization composed of pyrrhotite and arsenopyrite is also found in calcareous layers of Visean rocks in the vicinity of Filon Nord and the Kaolin Monzogranite (Nerci 2006). The disseminated sulphide minerals impregnate porous layers adjacent to sulphide-rich veins, thus forming pseudo-stratabound disseminations.

Based on field observations and P-T estimates of the mineralizing fluids, it is thus possible to determine the following chronology of the W–Au mineralization (from oldest to youngest): skarns, veins, and disseminations. A peri-granitic zoning of the W–Au veins shows (1) an inner halo having a W–Mo assemblage (wolframite + scheelite, molybdenite), (2) a middle halo with a Bi–Te–Au–As assemblage (including löllingite), and (3) an external halo with a sulphide-rich assemblage (arsenopyrite-pyrrhotite) and lesser Au (Nerci 2006).

Pb–Zn–Ag: This mineralization has been mined since 1930 (Wajdinny 1998). Several large veins with N25° E to N75° E orientations have been identified (Fig. 2). In most cases, the veins display a "Y" shape in plan view, showing a connection between two veins that suggest fracture opening as part of a conjugate strike-slip fault system (see Cheilletz 1984 for details; Fig. 2). The main Pb–Zn–Ag veins are, from north to south: Filons Parallèles and Filon Nord, Filon Signal and Structure 18, Structure II, Sidi Ahmed, and Filons Sud (Ighrem Aousser and Iguer Oujna). Filon Signal, Structure 18, Sidi Ahmed and Ighrem Aousser are currently being mined, allowing extensive observations and sampling in three dimensions.

The Pb–Zn–Ag mineralization comprises sulphides (galena + sphalerite) in a gangue of

carbonates ± quartz. Carbonate alteration of the Paleozoic host rocks occurred during vein formation. Pressure and temperature conditions of this hydrothermal event have been estimated by Nerci (2006), from fluid inclusions trapped in secondary calcite, as $\leq$30 MPa and 230 °C (Filon Sidi Ahmed). The paragenetic sequences are slightly different among the different veins.

In Filon Signal and Structure 18, the mineralization is typically banded and rather symmetrical: vein minerals grew from the edge of the vein towards its center (Fig. 4). These large veins display a succession of four paragenetic assemblages (Figs. 4 and 5): (P1) quartz + siderite, (P2) galena + calcite ± sphalerite, (P3) galena + sphalerite + siderite, and (P4) calcite + quartz + pyrite. As shown in Fig. 4, the early barren P1 assemblage is not present everywhere. The Pb–Zn–Ag mineralization is associated with P2 and P3 assemblages (Figs. 4 and 5). The latest hydrothermal phase (P4) is barren (Figs. 5a and 6).

In Sidi Ahmed and Ighrem Aousser, a succession of four hydrothermal events has been identified, each being associated with a different paragenetic assemblage (Figs. 7 and 8): (P1) hydraulic fracturing and precipitation of siderite + quartz, (P2) banded galena + ankerite ± sphalerite, (P3) brecciation and precipitation of galena + sphalerite, and (P4) calcite + quartz + pyrite. In Fig. 7, the early stage of hydraulic fracturing is evidenced by a breccia made of blocks of Paleozoic host rocks cemented with siderite + quartz (assemblage P1). The beginning of the second stage may have remobilized elements of P1. Occurrence of banded structures in the P2 assemblage record pulses of the hydrothermal fluid in the vein. The following brecciation stage (P3) remobilized P1 and P2 assemblages, and cemented these with sulphides. The latest hydrothermal stage (P4) is barren and cuts the older assemblages.

As previously described by Jébrak (1984, 1985), the gangue carbonates of the Pb–Zn–Ag mineralization are REE-rich (Table 2). Based on recent SEM observations (Tarrieu 2014), REE are concentrated in micron-sized inclusions of monazite and xenotime that locally are strongly altered to synchysite.

Sb–Ba: This mineralization has been poorly documented. The best description is found in Agard et al. (1958). The Sb–Ba mineralization occurs along a vein network connected to the Tighza fault (Fig. 2), and in veins hosted within Visean rocks (not shown on Fig. 2). These veins are filled with a gold-free assemblage of

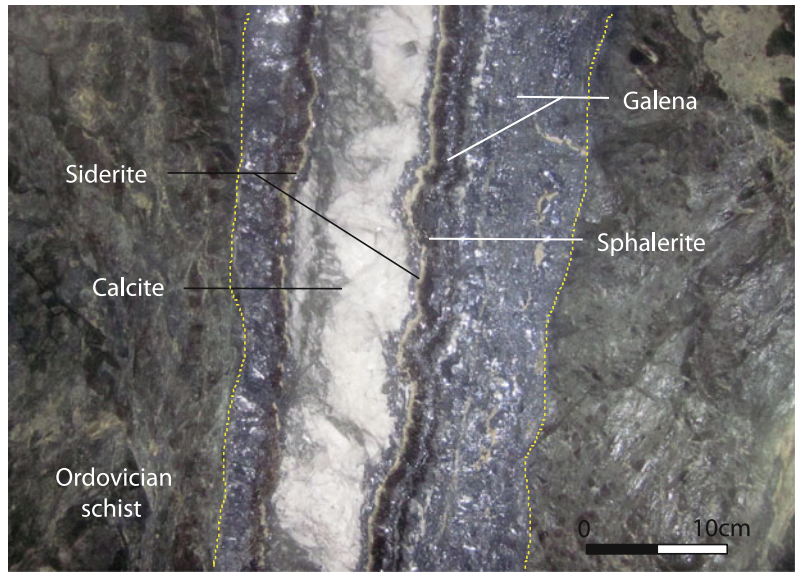

Fig. 4 Underground photograph showing banded mineralized vein from Filon Signal (sub-level 13)

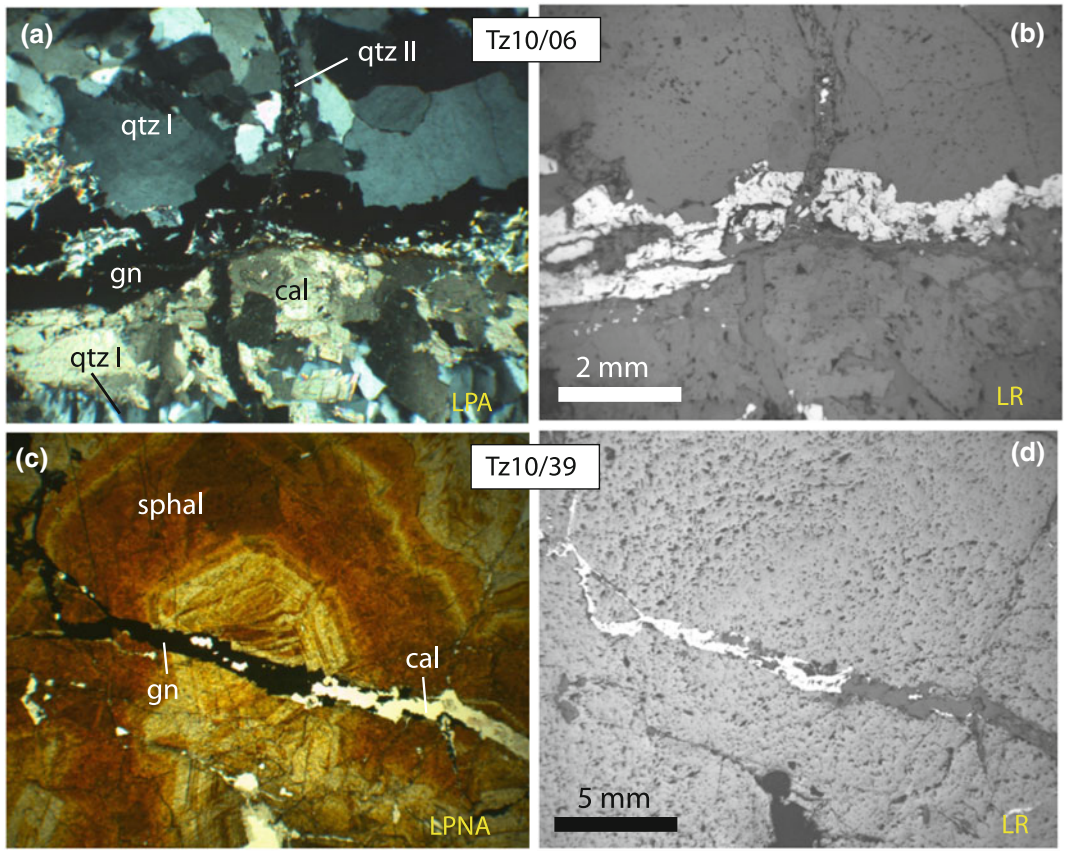

Fig. 5 Paired photomicrographs of Filon Signal veins. **a** and **b** from samples Tz10/06; **c** and **d** from sample Tz10/39. In **c** note growth zoning in sphalerite. *LPA* crossed polarized light; *LPNA* polarized light; *LR* reflected light. Mineral abbreviations from Kretz (1983)

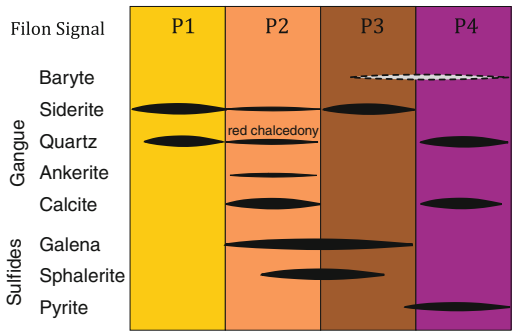

Fig. 6 Paragenetic sequences of Filon Signal and Structure 18 veins

stibnite ± pyrite ± chalcopyrite in a gangue of quartz having a comb-like or rosette-like texture. Late rosette-like pinkish barite occurs in voids. The stibnite is very discontinuous, forming local lenses in a continuous and large (meter-scale) quartz gangue.

3.2 Relative Chronology of Mineralization and Magmatism

As there are no spatial relationships between the Sb–Ba mineralization and the W–Au and Pb–Zn–Ag mineralizations, it is impossible to determine the relative chronology of this Sb–Ba event. However, based on comparison with other sites in Morocco, Agard et al. (1958) suggested that the Pb–Zn–Ag event might be younger than the Sb–Ba one.

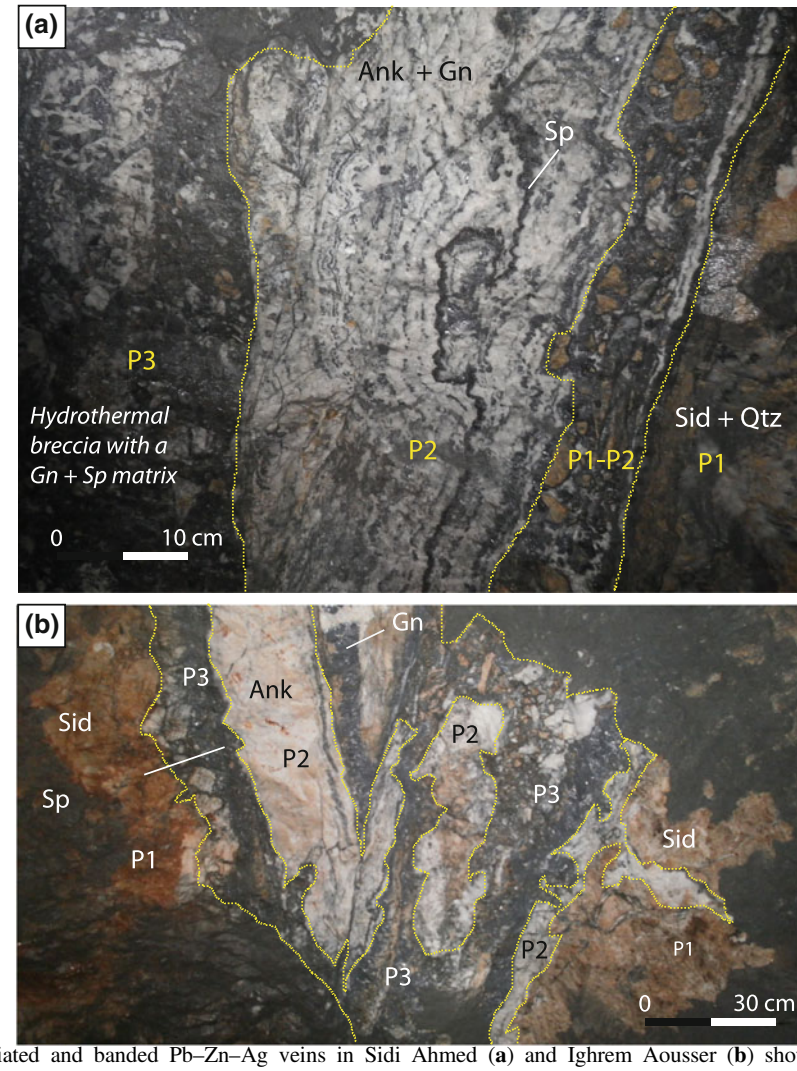

Fig. 7 Brecciated and banded Pb–Zn–Ag veins in Sidi Ahmed (**a**) and Ighrem Aousser (**b**) showing successive hydrothermal events (*P1–P3*; see text for explanation). Mineral abbreviations from Kretz (1983)

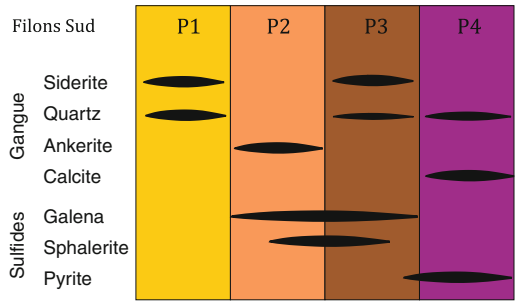

Fig. 8 Paragenetic sequence in Sidi Ahmed and Ighrem Aousser veins

The chronology of the W–Au and the Pb–Zn–Ag events is evidenced from field observations. Indeed, as shown in Fig. 9a, the Pb–Zn–Ag veins cut the W–Au veins, thus demonstrating that the Pb–Zn–Ag mineralization formed after the W–Au episode.

The skarns that formed in Visean calcareous rocks at the contact with the Mispickel and Kaolin Monzogranites are contemporaneous with any magmatic event. The stratabound replacement W skarns (scheelite bearing) have only been found in the hydrothermal halo in

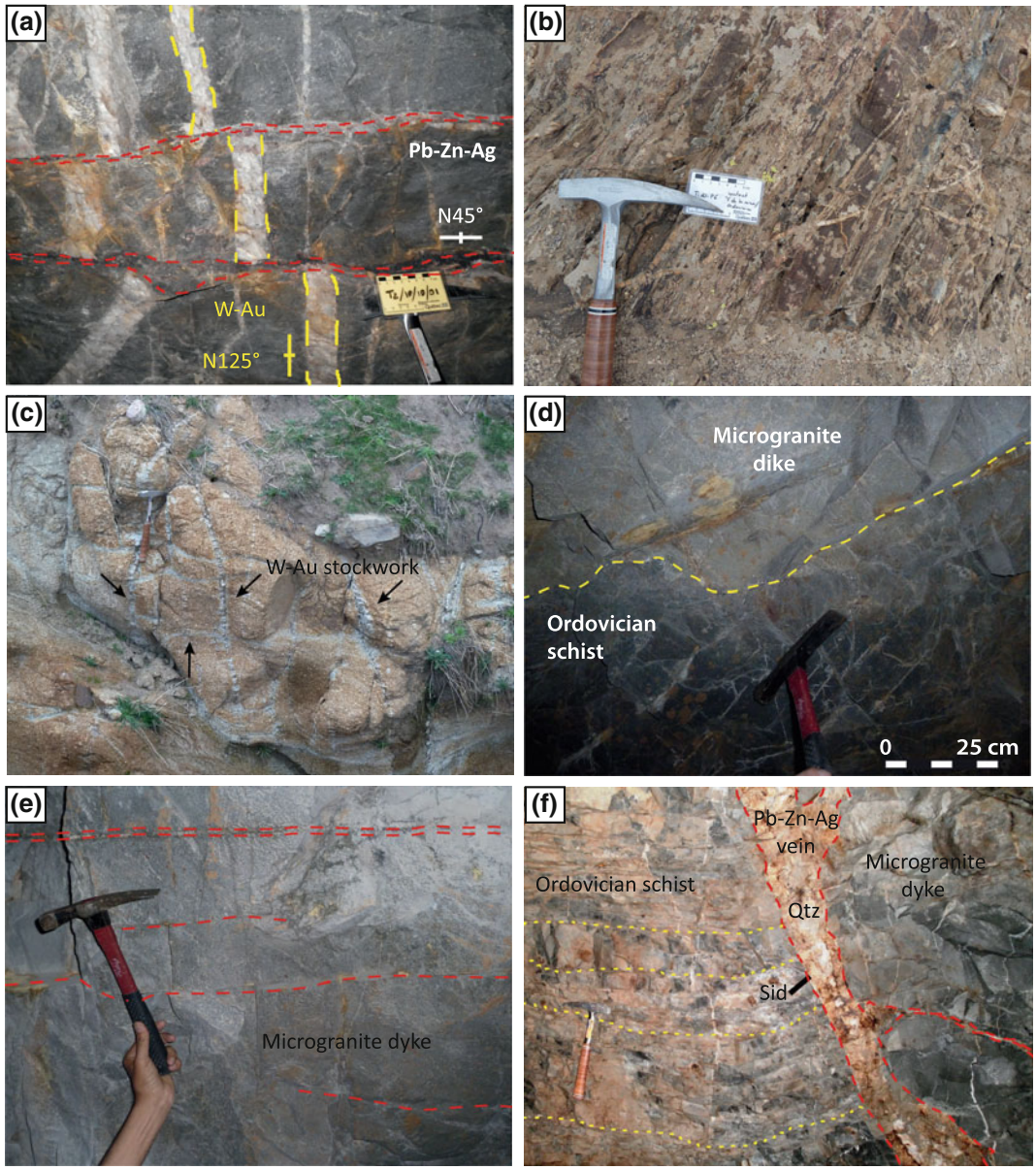

Fig. 9 **a** Relationships between Pb–Zn–Ag and W–Au mineralization: Pb–Zn–Ag veins cut W–Au veins at the roof of Structure 18. **b** W–Au-stockwork in the Mine Monzogranite. **c** Same stockwork cutting both Mine Monzogranite and Ordovician schist (*gray*). **d** W–Au stockwork (*arrows*) ending at dike contact in Filon Signal (sub-level 11, PK 6). **e** Pb–Zn–Ag veins (*red dashed lines*) cutting microgranite dike (Filon Signal, sub-level 11, PK 6). **f** Pb–Zn–Ag vein at contact between Ordovician schist and microgranite dike

underground mining developments, between outcrops of the Mine and Kaolin Monzogranites. This pattern suggests that the mineralizing fluid is genetically related to the hydrothermal halo, but gives no direct insights of any links with the granites. Furthermore, Cheilletz (1984) noted that some of the replacement skarns are cut by microgranite dikes, thus supporting a post-magmatic timing for this mineralization event.

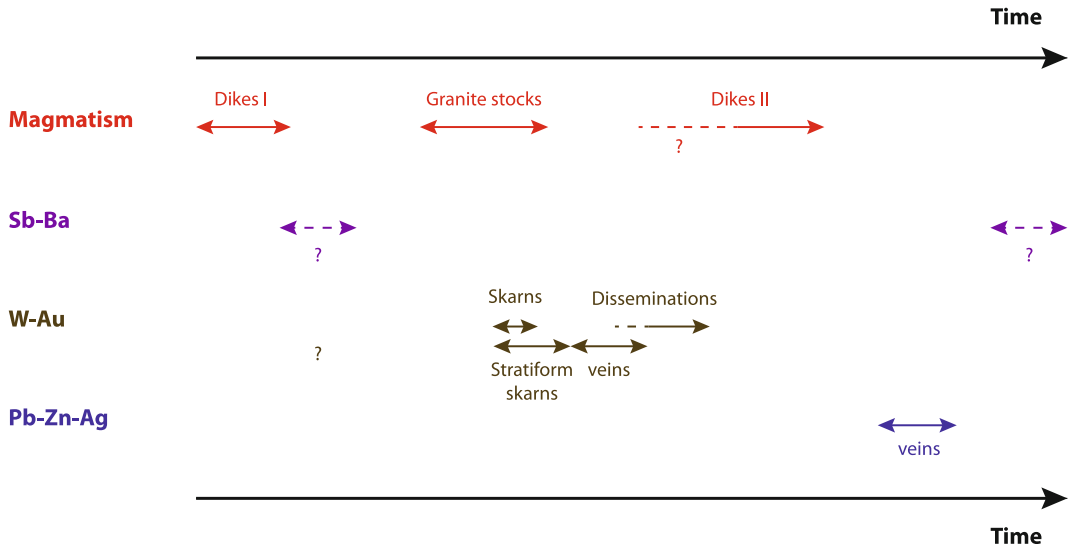

Fig. 10 Successive magmatic and hydrothermal events evidenced from field observations compiled from Agard et al. (1958), Cheilletz (1984), and this study

The W–Au veins are only found in the vicinity of the Mine Monzogranite, which they clearly cut (Fig. 9b, c), thus showing that the W–Au episode followed emplacement of this granite. However, as evidenced in Filon Signal, the W–Au stockwork developed in the Ordovician schists formed along the contact of a microgranite dike (Fig. 9d), suggesting that some magmatic dikes post-date the mineralization. Therefore, two magmatic episodes must be distinguished: firstly the outcropping granitic stocks, and secondly the dikes. The W–Au mineralization formed between these two magmatic events.

The Pb–Zn–Ag mineralization is not spatially related to the outcropping granites nor to the W–Au hydrothermal halo. As shown in Fig. 9e, f, all veins of this type cut and offset the granitic dikes, indicating that the related hydrothermal event occurred after these magmatic episodes.

According to Agard et al. (1958), the Sb–Ba veins cut several microgranite dikes. As these authors observed that some of the dikes are cut by the Mine Monzogranite, the Sb–Ba mineralization is assumed to predate the W–Au mineralization.

The field relationships among W–Au, Pb–Zn–Ag, and Sb–Ba mineralization and the magmatic rocks permit a relative chronology between the hydrothermal and magmatic events (Fig. 10). At least three episodes of magmatism are evidenced (dikes I, granitic stocks, and dikes II); the three mineralization events appear to be rather independent. Because the Sb–Au mineralization is spatially disconnected from the granitic stocks, and as the dikes formed both before and after the granitic stocks, it is therefore not possible to know if the Sb–Ba mineralization occurred before the granitic stocks, as suggested by Agard et al. (1958).

4 Analytical Procedures and Mineral Descriptions

4.1 U–Pb Geochronology of Zircon from Magmatic Rocks

U–Pb ages were obtained on single zircon grains from three samples of high-K calc-alkaline intrusions (Tz10/05, Tz10/41, Tz11/04) and two samples of dikes (Tz10/26, Tz10/40; Fig. 11). All of the zircon grains (50–200 μm) were studied and imaged using SEM before analysis by the CAMECA IMS 1270 ion microprobe at

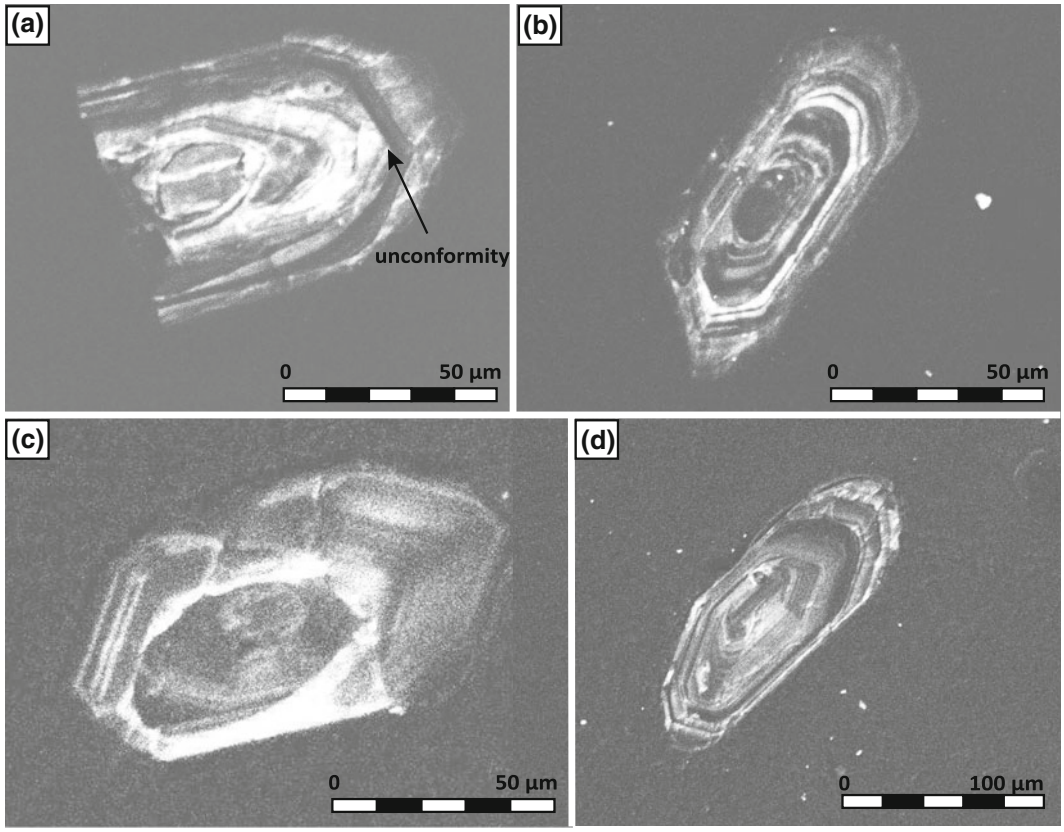

Fig. 11 Cathodoluminescence images of zircon grains from Mine Monzogranite (**a** and **b**), Kaolin Monzogranite (**c**), and microgranitic dike from Ighrem Aousser (**d**). Note presence of inherited cores in (**a**) and (**c**). Zoning observed in all zircons either has a magmatic or hydrothermal origin. Where present, hydrothermal zoning corresponds to outermost parts of zircon crystals, which are commonly discordant with magmatic zoning (*arrow* in **a**)

the CRPG-CNRS in Nancy (France). The zircon preparation procedure is given in Deloule et al. (2002).

Backscattered electron microscopy and cathodo-luminescence imaging reveal that most zircons are euhedral, showing a fine magmatic zonation and/or sector zoning. Some zircons have an inherited core (Fig. 11a, c). The zircons lack evidence of inclusions or mineral overgrowths, suggesting that no dissolution-precipitation process occurred. However, as stated by Geisler et al. (2003), some hydrothermal zircons are featureless, such that the possibility of a hydrothermal origin for some growth zones cannot be totally ruled out. Nonetheless, some zircon crystals from this study have a discordant outer rim suggesting multiple growth stages, the later most probably resulting from hydrothermal growth (Fig. 11a). Therefore, the zoning observed in our study might be related to magmatic growth, as well as to hydrothermal growth from a Zr-rich aqueous fluid, or to diffusion reactions following primary growth zones (Geisler et al. 2003; Hoskin 2005).

4.2 $^{232}Th/^{208}Pb$ Geochronology of Gangue Monazite

Monazites have been observed by SEM in carbonates from the "Filons parallèles" to the north of the Tighza district. Characteristic are 1–5 µm inclusions occuring within gangue carbonates of

the Pb–Zn mineralization. Two monazite crystals 10–15 µm in diameter were of sufficient size to allow in situ LA-ICPMS dating, which was done at Clermont-Ferrand University (UMR Magmas et Volcans) by J.L. Paquette using the technique reported in Hurai et al. (2010). 9 µm-wide spots were sampled using an Excimer 193 nm wavelength Resonetics M-50 laser system coupled to an Agilent 7500cs ICP-MS (Paquette et al. 2014). All fractionation effects were corrected simultaneously by use of a matrix-matched external standard (Jackson et al. 2004; Paquette and Tiepolo 2007), using the C83-32 (Corfu 1988) and Moacyr monazite standard (Gasquet et al. 2010).

5 Results

5.1 U–Pb Geochronology of Zircons from Magmatic Rocks

Concordant ages: U/Pb analytical data are reported in Table 1 for 56 zircon grains from five samples. Discordia lines and individual ages were determined using the Isoplot program of Ludwig (2003).

Two groups of zircon ages can be distinguished among grains analyzed from the Mine Monzogranite, Kaolin Monzogranite, and Izougarsa Monzogranite. In the Mine Monzogranite, the first group yields an intercept age of 309 ± 10 Ma using the Wetherhill-concordia diagram (Fig. 12a, 13 samples), whereas the second group has a younger intercept age of 270.4 ± 3.9 Ma (Fig. 12b, 6 samples). In the Kaolin Monzogranite, the first group of zircon gives a lower intercept age of 295 ± 9 Ma (Fig. 12c, 7 samples); the second has a lower intercept age of 268 ± 27 Ma (Fig. 12d, 3 samples). The age of this latter group is poorly constrained, however, due to large uncertainties. The Izougarsa Monzogranite yields ages similar to those obtained for the Mine and the Kaolin Monzogranites: the two groups of zircon have lower intercept ages of 295 ± 15 and 261 ± 13 Ma (Fig. 12e, f, 7 samples + 6 samples, respectively). Therefore, the intercept ages obtained for the older group, as well as for the younger one, are rather consistent. The microgranite dike from Ighrem Aousser (Tz10/26) contains a single zircon group that gives a lower intercept age of 273 ± 13 Ma (Fig. 12g, 4 samples), which is consistent with the younger age obtained for the granitic stocks.

5.2 $^{206}Pb/^{238}U$ Individual Ages

Figure 13 presents frequency distribution of the $^{206}Pb/^{238}U$ individual ages of all analyzed zircons. Three zircon grains from the Mine (n = 1) and Izougarsa (n = 2) Monzogranites have inherited cores with lower and middle Paleozoic ages (498 ± 11, 413 ± 13, and 369 ± 7 Ma), suggesting that the Carboniferous calc-alkaline magma originated from melting of Paleozoic crustal rocks. Apart from these older cores, most zircons display $^{206}Pb/^{238}U$ ages ranging from 320 to 240 Ma. A few zircons have younger ages between 200 and 100 Ma.

Within the 320–240 Ma time span, the $^{206}Pb/^{238}U$ zircon ages show a polymodal distribution, suggesting several magmatic and/or hydrothermal events. Three main periods can be distinguished: 320–305, 295–285, and 275–240 Ma. Comparison of these periods with published ages (Gasquet et al. 1996) indicates that (1) the 320–307 Ma period agrees with most U/Pb Concordia ages obtained for Moroccan Variscan plutons, (2) the time period of 295–285 Ma is consistent with late Variscan magmatic events (U/Pb ages), and (3) the young 275–240 Ma ages do not coincide with any known U/Pb ages, but are similar to whole-rock Rb–Sr ages. One microdiorite dike from the Jebilet Massif was dated at 241 ± 5 Ma, using the K/Ar method on kaersutite (Gasquet and Bouloton 1995). Furthermore, Permo-Triassic volcanic activity is known in Morocco that is related to the Central Atlantic Magmatic Province (Verati et al. 2007).

Table 1 Summary of IMS1270 U–Th–Pb zircon results for the intrusive stocks and dikes

Grain-spot	Pb (ppm)	U (ppm)	Th (ppm)	Th/U	Measured ratios		Radiogenic ratios				Ages (Ma)			
					$^{207}Pb/^{206}Pb$	$^{204}Pb/^{206}Pb$	$^{207}Pb/^{235}U$	±	$^{206}Pb/^{238}U$	±	206Pb/^{238U}	±	207Pb/^{235U}	±
Granodiorite de la Mine														
tz10-05@2	106	2852	1054	0.37	0.2289	0.0121	0.3054	0.0262	0.0434	0.0005	274	3	271	20
tz10-05@4	85	2239	729	0.33	0.0661	0.0023	0.1914	0.0159	0.0440	0.0006	277	4	178	13
tz10-05@16	73	2022	392	0.19	0.1184	0.0040	0.3612	0.0446	0.0422	0.0007	267	4	313	33
tz10-05@24	124	3361	1382	0.41	0.0677	0.0017	0.2524	0.0117	0.0429	0.0004	271	3	229	9
tz10-05@19	43	1135	355	0.31	0.1233	0.0075	0.0596	0.0687	0.0440	0.0011	278	7	59	64
tz10-05@9	97	2706	1039	0.38	0.0724	0.0025	0.2022	0.0195	0.0417	0.0015	263	9	187	16
tz10-05@10	88	2419	699	0.29	0.0940	0.0045	0.1544	0.0458	0.0426	0.0012	269	7	146	40
tz10-05@6	282	6643	1371	0.21	0.0558	0.0006	0.3216	0.0047	0.0493	0.0005	310	3	283	4
tz10-05@7	69	1746	434	0.25	0.0724	0.0023	0.2463	0.0279	0.0459	0.0007	290	4	224	22
tz10-05@8	226	5608	712	0.13	0.0651	0.0010	0.3285	0.0128	0.0469	0.0007	295	4	288	10
tz10-05@15	180	4320	1573	0.36	0.0678	0.0013	0.3261	0.0062	0.0486	0.0005	306	3	287	5
tz10-05@17	64	1536	215	0.14	0.1444	0.0059	0.3951	0.0688	0.0482	0.0010	303	6	338	49
tz10-05@20	33	773	209	0.27	0.1265	0.0052	0.3501	0.0347	0.0494	0.0007	311	4	305	26
tz10-05@21	123	2970	1028	0.35	0.0836	0.0030	0.2681	0.0225	0.0483	0.0006	304	4	241	18
tz10-05@22	37	928	264	0.28	0.0645	0.0018	0.2413	0.0127	0.0464	0.0005	293	3	220	10
tz10-05@26	350	8026	1127	0.14	0.0564	0.0005	0.3410	0.0047	0.0507	0.0006	319	4	298	4
tz10-05@27	122	2945	332	0.11	0.0686	0.0010	0.3571	0.0120	0.0483	0.0005	304	3	310	9
tz10-05@23	43	1058	182	0.17	0.1305	0.0072	0.1455	0.0786	0.0473	0.0011	298	7	138	67
tz10-05@18	24	592	135	0.23	0.1877	0.0100	0.2736	0.0902	0.0480	0.0018	302	11	246	70
tz10-05@11	50	1269	272	0.21	0.1036	0.0038	0.3069	0.0340	0.0458	0.0013	288	8	272	26
tz10-05@3	64	1873	653	0.35	0.1470	0.0052	0.3992	0.0443	0.0396	0.0006	250	4	341	32
tz10-05@12	46	805	168	0.21	0.1695	0.0064	0.7228	0.0445	0.0662	0.0008	413	5	552	26

(continued)

Table 1 (continued)

Grain-spot	Pb (ppm)	U (ppm)	Th (ppm)	Th/U	Measured ratios		Radiogenic ratios				Ages (Ma)			
					$^{207}Pb/^{206}Pb$	$^{204}Pb/^{206}Pb$	$^{207}Pb/^{235}U$	±	$^{206}Pb/^{238}U$	±	206Pb/^{238U}	±	207Pb/^{235U}	±
Granodiorite du Kaolin														
tz10-41@1	81	2223	347	0.16	0.0747	0.0017	0.2948	0.0435	0.0422	0.0045	267	28	262	34
tz10-41@3	65	1845	167	0.09	0.2393	0.0124	0.3371	0.1702	0.0408	0.0053	258	33	295	122
tz10-41@9	49	1418	145	0.10	0.1336	0.0058	0.2716	0.1115	0.0404	0.0016	255	10	244	85
tz10-41@2	50	1260	227	0.18	0.0669	0.0010	0.3330	0.0214	0.0463	0.0012	292	8	292	16
tz10-41@12	29	698	115	0.16	0.0814	0.0025	0.3025	0.0454	0.0476	0.0010	299	6	268	35
tz10-41@4	121	3045	1575	0.52	0.2471	0.0103	0.6804	0.2581	0.0461	0.0044	291	27	527	145
tz10-41@6	45	1136	117	0.10	0.2004	0.0094	0.4282	0.2437	0.0465	0.0064	293	39	362	160
tz10-41@10	75	1731	552	0.32	0.2152	0.0136	0.0334	0.2936	0.0504	0.0049	317	30	33	254
tz10-41@14	68	1808	320	0.18	0.2035	0.0114	0.1995	0.2026	0.0436	0.0032	275	20	185	158
tz10-41@17	43	1110	62	0.06	0.2572	0.0158	0.1023	0.2561	0.0447	0.0040	282	25	99	212
Granoriodite d'Izougarsa														
tz11-04@11	101	3062	567	0.19	0.0879	0.0034	0.2015	0.0258	0.0386	0.0007	244	4	186	22
tz11-04@15	63	1945	419	0.22	0.1150	0.0046	0.2518	0.0554	0.0377	0.0034	238	21	228	44
tz11-04@20	35	1131	241	0.21	0.1260	0.0060	0.1854	0.0516	0.0356	0.0017	225	11	173	43
tz11-04@24	35	978	227	0.23	0.0879	0.0024	0.2996	0.0302	0.0414	0.0006	262	4	266	23
tz11-04@25	42	1329	352	0.26	0.1620	0.0081	0.2134	0.0742	0.0371	0.0012	235	7	196	60
tz11-04@4	44	1230	247	0.20	0.0955	0.0030	0.2984	0.0240	0.0415	0.0005	262	3	265	19
tz11-04@8	54	1378	170	0.12	0.1240	0.0044	0.3830	0.0929	0.0454	0.0015	286	9	329	66
tz11-04@12	146	3345	749	0.22	0.0755	0.0021	0.3158	0.0175	0.0507	0.0008	319	5	279	13
tz11-04@16	31	825	199	0.24	0.0718	0.0012	0.3298	0.0163	0.0440	0.0007	278	4	289	12
tz11-04@26	35	902	171	0.19	0.0807	0.0031	0.2173	0.0292	0.0449	0.0006	283	3	200	24
tz11-04@2	41	1022	106	0.10	0.0721	0.0014	0.3340	0.0334	0.0472	0.0009	298	5	293	25

(continued)

Table 1 (continued)

Grain-spot	Pb (ppm)	U (ppm)	Th (ppm)	Th/U	Measured ratios		Radiogenic ratios				Ages (Ma)			
					$^{207}Pb/^{206}Pb$	$^{204}Pb/^{206}Pb$	$^{207}Pb/^{235}U$	±	$^{206}Pb/^{238}U$	±	$206Pb/^{238U}$	±	$207Pb/^{235U}$	±
tz11-04@5	49	1245	227	0.18	0.0740	0.0014	0.3393	0.0236	0.0460	0.0007	290	4	297	18
tz11-04@6	24	581	66	0.11	0.0977	0.0029	0.3685	0.0564	0.0473	0.0009	298	5	319	41
tz11-04@3	49	1751	347	0.20	0.1290	0.0041	0.3189	0.0545	0.0326	0.0011	207	7	281	41
tz11-04@13	27	384	147	0.38	0.0841	0.0016	0.6863	0.0866	0.0804	0.0019	498	11	531	51
tz11-04@10	90	1772	189	0.11	0.4290	0.0255	0.4810	0.0489	0.0589	0.0011	369	7	399	33
Microgranite (IA)														
tz10-26@4	114	3269	619	0.19	0.0560	0.0002	0.2959	0.0057	0.0406	0.0005	256	3	263	4
tz10-26@6	112	3316	1374	0.41	0.1770	0.0084	0.2940	0.0908	0.0392	0.0009	248	6	262	69
tz10-26@10	28	814	264	0.32	0.1060	0.0030	0.3496	0.0615	0.0398	0.0026	252	16	304	45
tz10-26@3	65	1746	404	0.23	0.0856	0.0022	0.3250	0.0100	0.0434	0.0004	274	3	286	8
tz10-26@5	30	805	150	0.19	0.1190	0.0046	0.3130	0.0379	0.0437	0.0006	276	4	276	29
tz10-26@11	30	810	295	0.36	0.0757	0.0015	0.3190	0.0388	0.0425	0.0023	268	14	281	29
tz10-26@17	81	2184	549	0.25	0.0591	0.0004	0.3190	0.0079	0.0434	0.0008	274	5	281	6
tz10-26@19	127	3023	751	0.25	0.1272	0.0047	0.3985	0.0477	0.0487	0.0014	307	8	341	34

Average age calculations are denoted at 2σ level

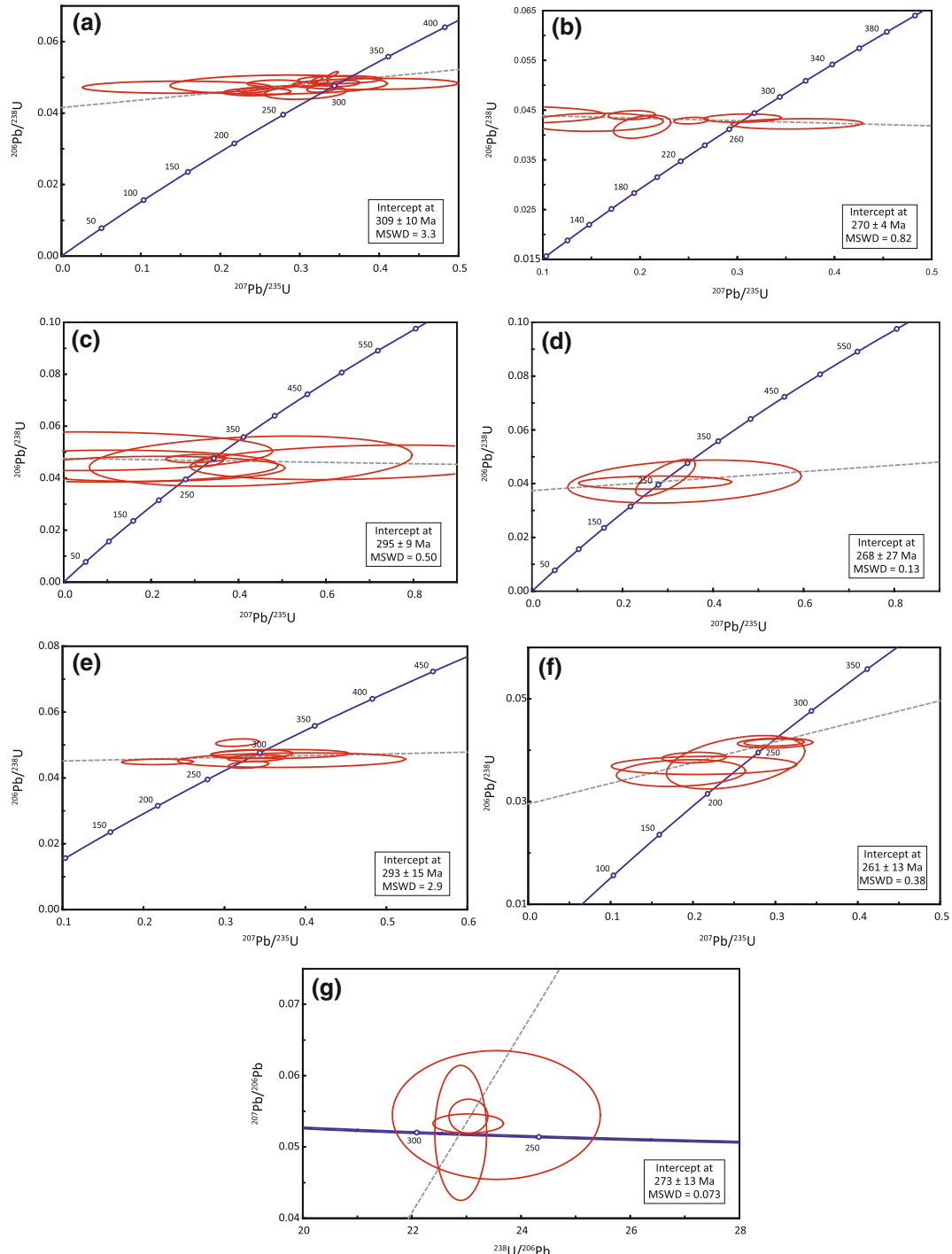

Fig. 12 Wetherhill-Concordia U–Pb plots for zircons from magmatic rocks of Tighza district: Mine Monzogranite (Tz10/05; **a** and **b**), Kaolin Monzogranite (Tz10/41; **c** and **d**), Izougarsa Monzogranite (Tz11/04; **e** and **f**). Tera-Wasserburg U–Pb diagram for microgranite dike from Ighrem Aousser (Tz10/26; **g**)

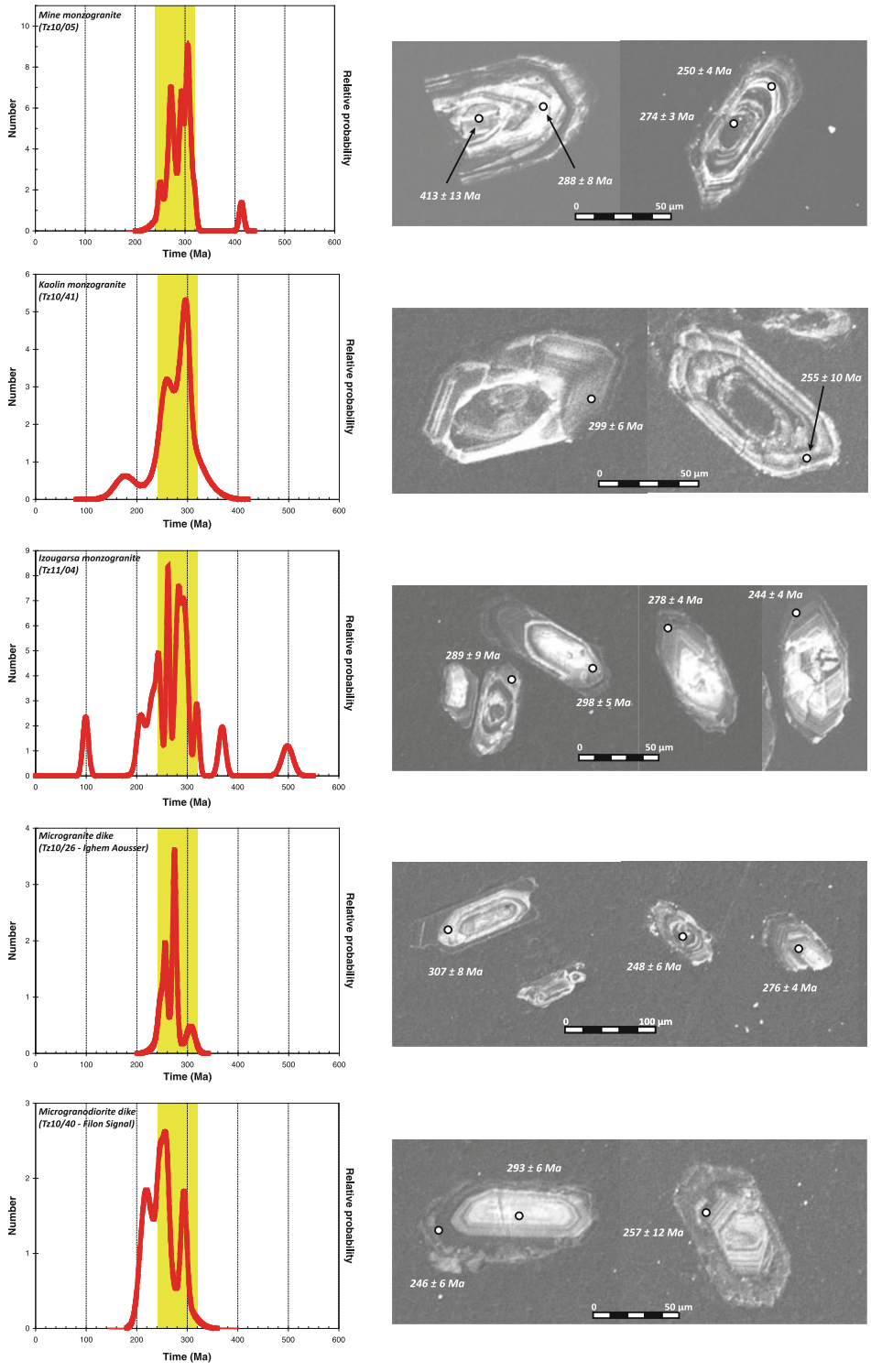

Fig. 13 Frequency distribution of all $^{206}Pb/^{238}U$ ages from Mine Monzogranite, Kaolin Monzogranite, Izougarsa Monzogranite, microgranite dike from Ighrem Aousser, and microgranodiorite dike from the Signal Pb–Zn vein. These ages confirm that youngest ages, which record hydrothermal events, occur in outermost zone of zircon crystals. Note also presence of some hydrothermal zircons and hydrothermal overgrowths (see Fig. 15 for explanation)

Table 2 REE contents (ppm) in the carbonates from the Tighza district

	Filon Signal	Filon Sidi Ahmed						Filon Ighrem Aousser									
	Tz11/47	Tz10/22	Tz10/17	Tz11/49	Tz11/48	Tz10/25	Tz11/53	Tz10/30.2	Tz10/33	Tz10/30.1	Tz10/28	Tz10/29	Tz10/31	Tz11/58	Tz10/32	Tz10/34	Tz10/32
	P1	P1	P2	P4	P4	P4	P4	P2	P3	P4	P4	P4	P4	P4	P4	P4	P4
	sid	sid	ank	cal	cal	cal	cal	ank	sid	cal	cal	cal	cal	cal	cal	cal	cal
La	95.94	32.52	14.75	105.20	47.60	107.50	36.23	665.60	5.22	140.10	61.47	127.60	132.30	38.27	448.40	133.20	322.80
Ce	174.60	65.15	59.83	138.60	83.85	218.10	61.61	1352.00	13.75	279.00	138.10	266.20	282.80	62.26	1020.00	275.90	727.00
Pr	20.42	7.97	9.70	15.29	9.59	28.24	7.19	174.00	1.92	34.41	18.74	33.40	36.43	6.84	132.40	35.02	92.76
Nd	87.39	34.63	45.42	65.08	45.58	132.80	34.24	742.70	9.95	147.60	91.33	142.40	159.50	33.74	538.80	151.90	372.60
Sm	22.50	9.63	19.31	16.01	13.97	35.53	9.71	262.10	3.31	44.79	27.39	41.76	54.37	9.17	158.60	50.46	112.00
Eu	7.98	5.13	6.47	6.66	5.98	4.76	4.22	152.80	1.89	23.94	3.01	21.17	29.74	5.18	55.98	27.57	42.85
Gd	21.30	9.07	19.39	20.77	15.17	41.16	10.42	306.70	3.20	48.24	34.70	43.15	60.42	11.55	162.40	55.69	113.50
Tb	2.96	1.20	2.63	2.40	2.25	6.65	1.48	41.91	0.48	7.11	6.54	6.11	8.41	1.57	22.01	8.09	15.29
Dy	15.69	5.88	11.89	11.11	11.33	41.06	7.30	196.60	2.41	37.19	46.54	30.01	40.39	7.76	99.44	40.57	66.53
Ho	2.87	0.96	1.64	1.84	1.87	8.49	1.22	29.08	0.38	6.27	11.21	4.87	6.14	1.28	13.96	6.57	9.08
Er	8.60	2.39	3.44	4.27	4.82	23.29	3.04	62.53	0.92	15.97	38.44	12.17	14.13	3.01	27.83	16.19	18.12
Tm	1.70	0.36	0.43	0.51	0.69	3.14	0.40	7.37	0.13	2.33	7.14	1.68	1.83	0.36	2.97	2.29	2.01
Yb	17.18	2.58	2.79	3.13	4.76	18.84	2.53	42.71	0.92	16.36	59.08	11.54	12.65	1.98	17.28	16.21	12.88
Lu	3.22	0.37	0.38	0.48	0.72	2.50	0.36	5.40	0.13	2.40	10.13	1.75	1.77	0.27	2.30	2.40	1.86
ΣREE	482.35	177.84	198.06	391.35	248.18	672.06	179.95	4041.50	44.61	805.71	553.82	743.81	840.89	183.25	2702.37	822.07	1909.27

Mineral abbreviations from Kretz (1983)

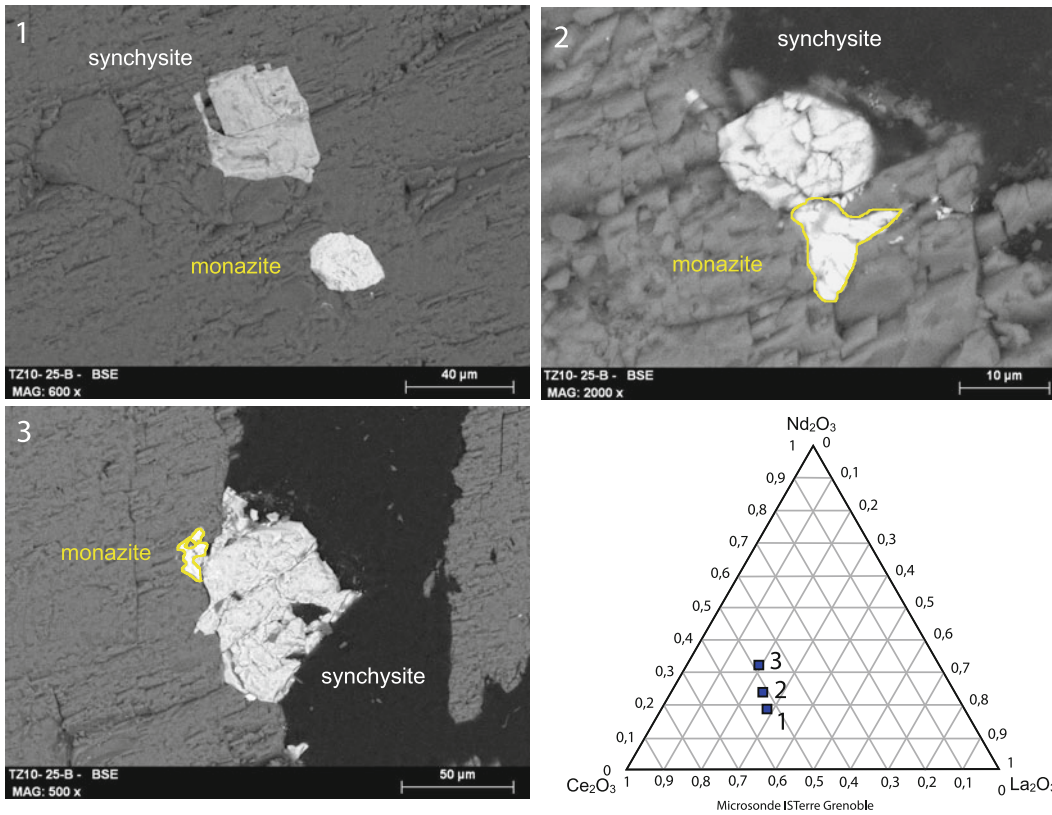

Fig. 14 *1–2–3* Monazite and synchysite inclusions in gangue calcite (sample Tz10/25 from Sidi Ahmed, sub-level 9, PK 6 W). Triangular diagram shows REE compositions of three analyzed monazite grains

5.3 $^{232}Th/^{208}Pb$ Geochronology of Monazite in Carbonate Gangue

In the Tighza district, gangue carbonates are 8× to 40× enriched in REE compared with barren carbonates (calcite III, recrystallized carbonates; Jébrak 1985). Our SEM observations have identified REE-rich carbonates (synchysite) forming 50–100 µm inclusions in calcite, ankerite, and siderite. Typically, the synchysite grains grew by dissolution of xenotime and monazite in the presence of a F- and CO_2-rich, and Ca-bearing, fluid (Fig. 14). U–Th–Pb dating of xenotime and monazite was attempted, but these minerals are very U- and Th-poor (Table 3), with the result that ages on xenotime could not be obtained. U–Th–Pb dating of monazite yields rather consistent ages, however, although with high 2σ values. The two dated

Table 3 U–Th–Pb composition of the dated monazite crystals, and apparent age

Sample	Pb (ppm)	Th (ppm)	U (ppm)	Th/U	$^{208}Pb/^{232}Th$ ±2σ error	$^{208}Pb/^{232}Th$ Age (Ma)
Tz10/25B/Mz1	1.3	106	0.5	193	0.0127 ± 0.0008	254 ± 16
Tz10/25B/Mz3	0.4	22	3.3	7	0.0128 ± 0.0024	257 ± 48

The monazite crystals are hosted in sample Tz10/25 from Sidi Ahmed (sub-level 9, PK 6 W)

monazite grains have ages of 254 ± 16 and 257 ± 48 Ma (Table 2). Despite the high uncertainties, the age of 254 ± 16 Ma is accepted for the Pb–Zn–Ag mineralization. This age is concordant with the youngest hydrothermal event evidenced from U/Pb ages on zircons hosted in the magmatic rocks (275–240 Ma).

6 Discussion

6.1 U/Pb Zircon Geochronology: A Tool to Date Magmatic and Hydrothermal Events

U/Pb geochronology of zircon is a powerful tool that permits identification of igneous, hydrothermal, and metamorphic events (e.g., Pelleter et al. 2007, and references therein). Our study shows that separate zircon crystals from a single igneous rock sample record several ages (e.g., the Izougarsa Monzogranite—sample Tz11/04—has individual ages ranging between 320 and 240 Ma) that can either be attributed to magmatic or to hydrothermal events (Table 1, Fig. 13). As shown in Fig. 15, all zircons display LREE depleted spectra. The most depleted spectra are attributed to magmatism whereas the less depleted ones are attributed to hydrothermal events (Pettke et al. 2005; Pelleter et al. 2007). Most zircons analyzed from magmatic rocks of the Tighza district show less depleted spectra from core to rim (Fig. 15a, b), thus suggesting a hydrothermal origin of the outer rims whereas the core are magmatic in origin. In some cases, the core of zircon crystals equilibrated with the hydrothermal fluid, thus displaying less depleted spectra, similar to those of the outer rim (Fig. 15c). These data are consistent with single zircon crystals recording several events (Fig. 15): the oldest ages, which are found in cores, are thus well attributed to magmatism, whereas the younger ages, which are found in outer rims, are assigned to hydrothermal activity. Comparison of all ages thus allows the delineation of several magmatic and hydrothermal events in the Tighza district (see discussion below).

6.2 Dating the Magmatic Stocks

Figure 16 summarizes the available geochronological data obtained in the Tighza district from this study and the literature (Cheilletz and Zimmermann 1982; Watanabe 2002; Nerci 2006). Excluding inherited zircon cores, most data (oldest U/Pb ages, biotite and whole-rocks K–Ar ages) converge towards a main magmatic episode between 325 and 285 Ma. The oldest U–Pb ages for zircons range from 320 to 305 Ma, suggesting that emplacement of the outcropping granitic stocks took place during this time interval. Such a late Variscan magmatic period has been documented throughout Morocco, and especially in the Meseta domains (Gasquet et al. 1996; El Hadi et al. 2006). The inherited zircon cores give Late Cambrian to Devonian ages (498 ± 11, 413 ± 5, and 369 ± 7 Ma). Even though no magmatic episode has been identified during this time period, inherited cores of Paleozoic age have been increasingly reported recently (e.g., Izart et al. 2001; Pelleter et al. 2007). The presence of these cores suggests that the Late Variscan magmatism is partly related to melting of the underlying Paleozoic crust.

6.3 Dating the W–Au Mineralization

Timing of the W–Au mineralization in the Tighza district is well constrained from Ar–Ar and K–Ar ages on biotite and muscovite hosted in W–Au veins and W-rich skarns (Cheilletz and Zimmermann 1982; Nerci 2006). All samples have ages from 295 to 280 Ma; the W–Au mineralization most likely formed during this time period (Fig. 16). This mineralization thus appears to be synchronous with the second magmatic event (295–285 Ma). This event, characterized at the present erosion level by the large biotitic hydrothermal halo that surrounds the mineralization (Cheilletz and Isnard 1985), could be related to the hidden pluton suggested by the gravity anomaly (Fig. 3; El Dursi 2009). Therefore, considering these new dating results, we suggest that the hidden pluton (1) is

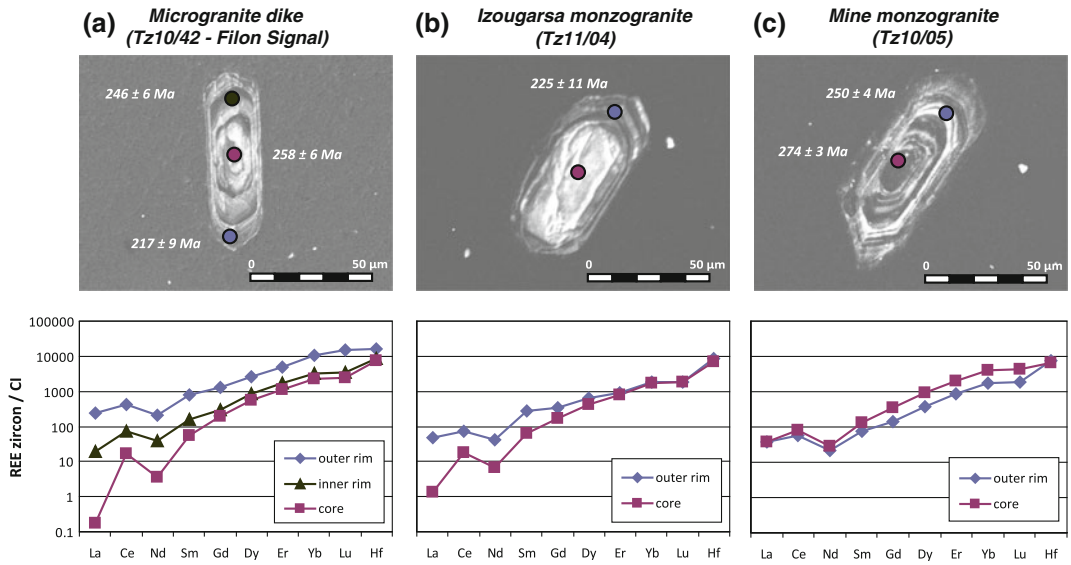

Fig. 15 REE contents of outer rim, inner rim and core of selected zircons. In most zircon crystals, outer rims are less depleted in LREE than inner rims and cores, suggesting late hydrothermal growth (**a**, **b**; Pettke et al. 2005). As shown in **a**, this trend is well correlated with the age recorded at each growing stage: the magmatic core (258 ± 6 Ma) is more depleted than the first hydrothermal rim (inner rim; 246 ± 6 Ma), and the last hydrothermal rim (outer rim; 217 ± 9 Ma) is the least depleted. In **b**, the outer rim is clearly discordant with the core suggesting late growth from a hydrothermal fluid around an homogeneous core, which most probably has a magmatic origin. Finally, in some zircon crystals, cores and outer rim display similar spectra, which are less depleted, suggesting equilibration of the core with a hydrothermal fluid (**c**). In such a case, the magmatic core rejuvenated due to a younger hydrothermal event, or the zircon has a hydrothermal origin

disconnected from the granitic stocks, (2) was emplaced at 295–280 Ma, and (3) is genetically related to the hydrothermal activity responsible for the potassic alteration halo and the W–Au mineralization.

6.4 Dating the Pb–Zn–Ag Mineralization

All granitic stocks and dikes record hydrothermal and or magmatic ages younger than 280 Ma (Fig. 16). These ages are well identified until about 240 Ma, suggesting that the two first magmatic-hydrothermal episodes were followed by a 40-m.y.-long period of hydrothermal activity and dike emplacement. Based on monazite ages (254 ± 16 Ma) and despite their large uncertainties, the Pb–Zn–Ag mineralization appears related to this later hydrothermal activity. In contrast to previous interpretations (e.g., Cheilletz 1984), the dating results presented here confirm that the Pb–Zn–Ag mineralization is unrelated to the W–Au mineralization, as also suggested by field evidence. Late Permian ages are already established in the Moroccan Meseta (Gasquet et al. 1996; El Hadi et al. 2006), mainly by the Rb–Sr method. Considering the mobility of Rb and Sr, and the fact that hydrothermal alteration will generally reset Rb–Sr ages, one can consider that the Permian and Early Triassic ages reported in the literature also reflect this important period of hydrothermal and magmatic activity, as evidenced in the Tighza district.

6.5 Dating the Dike Network

Geochronological data on the dike network clearly show multiple generations (Fig. 13), as already recorded from field observation (Fig. 9). The oldest ages (300-310 Ma) are similar to those of

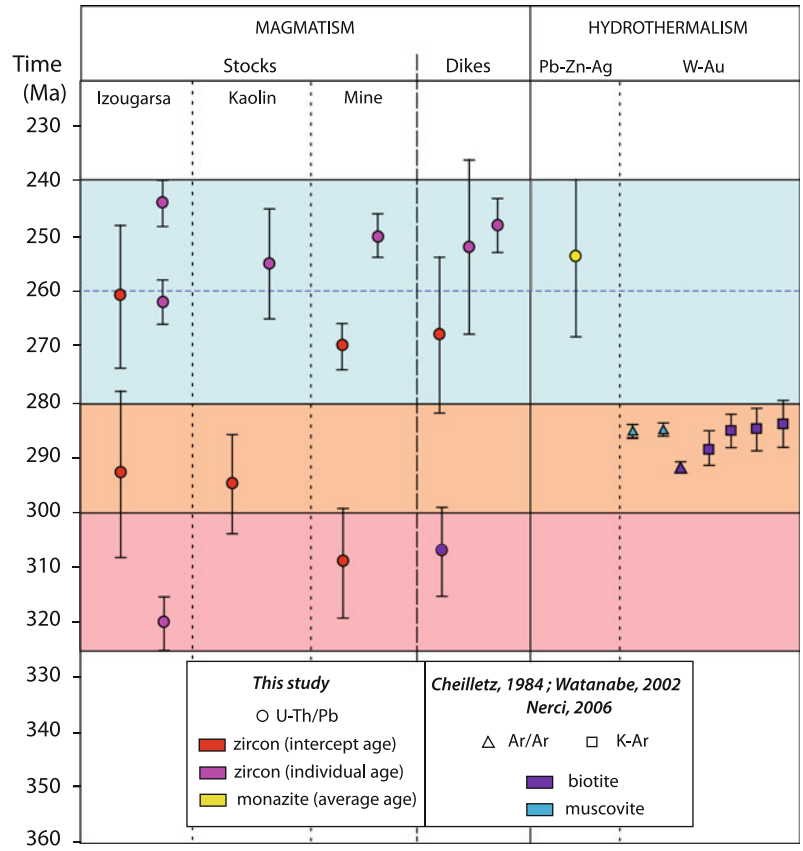

Fig. 16 Synthesis of ages obtained using U/Pb, Ar–Ar, and K–Ar methods in minerals and rocks from Tighza district. U/Pb data are from this study; Ar–Ar data from Watanabe (2002) and Nerci (2006); K–Ar data from Cheilletz and Zimmermann (1982). Three main stages are distinguished: I, emplacement of outcropping stocks; II, hidden magmatism and formation of hydrothermal biotitic alteration halo (W–Au mineralization); III, emplacement of dikes and late hydrothermal activity (Pb–Zn–Ag mineralization)

magmatic crystallization of the outcropping granitic stocks (Fig. 13). Most individual zircon ages range within 280 and 240 Ma. They are similar to the intercept age on Tz10/26 (Fig. 12g) and to whole-rock K-Ar ages from Watanabe (2002). Therefore, dike emplacement might be related either to the main period of late Variscan magmatism or to the post-Variscan hydrothermal event.

7 Conclusions

New U/Pb dating of zircon and monazite provides new constraints on the magmatic and hydrothermal history of the polymetallic Tighza district of central Morocco. The W–Au mineralization, which occurred at 295–280 Ma, is associated with a major magmatic period. However, new U–Pb data suggest that this mineralization is unrelated to the emplacement of the outcropping stocks (320–300 Ma), but instead to a hidden pluton that is inferred to be responsible for the potassic alteration halo and related W-rich mineralization.

For the first time, the Pb–Zn–Ag mineralization in the district has been dated (254 ± 16 Ma). This new age, together with field evidence, indicates that the Pb–Zn–Ag mineralization is not genetically connected with the W–Au mineralization, as suggested by previous workers. The polymetallic deposits of the district therefore record the superposition of two independent mineralizing events: a porphyry-style W–Au deposit followed by an epithermal Pb–Zn–Ag deposit. Because the age of the Sb–Ba mineralization is poorly constrained, its geochronological and genetic position relative to the two other mineralization styles is not considered herein.

In conclusion, the polymetallic Tighza district is spatially associated with multiple intrusions of Cordilleran-type calc-alkaline magmatism (cf. Sillitoe 2010; Catchpole 2011). Successive magmatic-hydrothermal pulses produced first a porphyry-style W–Au mineralization stage followed by an epithermal-style Pb–Zn–Ag stage. Fluid flow and related polymetallic mineralization were generated during a late Variscan to Permo-Triassic transpressional regime (Michard et al. 2008) that favored the development of mantle and crustally derived magmas.

Acknowledgments This study was supported by INSU-CNRS through the CESSUR programme, by Université Savoie Mont Blanc, and the Compagnie Minière de Touissit (CMT). It was part of L.T.'s Ph.D. project at Université Savoie Mont Blanc, supported by the French Ministry for Research and Higher Education. Thorough and constructive reviews by J.F. Slack and M. Bouabdellah significantly improved the manuscript. This paper is dedicated to the memory of Pete Burnard, recently passed away, who contributed to better understand the fluid sources of the W–Au and Pb–Zn–Ag deposits in the polymetallic district of Tighza.

References

Agard J, Balcon JM, Morin P (1958) Etude géologique de la région minéralisée du Jebel Aouam (Maroc central). Notes Mémoire Service Géol Maroc 132, 127 pp

Castorina F, Masi U (2000) Sr-isotopic composition of siderite for assessing the origin of mineralizing fluids: the case study from the Jebel Awam deposit (central Morocco). Ore Geol Rev 17:83–89

Castorina F, Masi U (2008) REE and Nd-isotope evidence for the origin of siderite from the Jebel Awam deposit (central Morocco). Ore Geol Rev 34:337–342

Catchpole HP (2011) Porphyry-related polymetallic mineralisation in the Morococha district, central Peru: mineralisation styles, timing and fluid evolution. Unpubl PhD Thesis, Univer Genève, Switzerland, 288 pp

Cheilletz A (1983a) Les lentilles rubanées stratiformes à scheelite-biotite du Jbel Aouam, Maroc central: première description et interprétation. Comptes Rendus Acad Sci Série II 297:581–584

Cheilletz A (1983b) Le contrôle structural des minéralisations filoniennes en tungstène du Jbel Aouam, Maroc central: application au système filonien plomb-zinc-argent. Comptes Rendus Acad Sci Série II 297:417–420

Cheilletz A (1984) Contribution à la gîtologie du district polymétallique (W-Mo-Cu-Pb-Zn-Ag) du Djebel Aouam (Maroc central): application à la prospection des gisements de tungstène. Unpubl PhD thesis, Inst National Polytech Lorraine, France, 273 pp

Cheilletz A, Isnard P (1985) Contribution à la prospection des gisements hydrothermaux de tungstène sur l'exemple du district polymétallique W-Pb-Zn-Ag du Jbel Aouam (Maroc central). Mineral Deposita 20:220–230

Cheilletz A, Zimmermann JL (1982) Datations par la méthode K-Ar du complexe intrusif et des minéralisations en tungstène du Jbel Aouam (Maroc central). Comptes Rendus Acad Sci Série II 295:255–258

Cheilletz A, Gasquet D, Filali F, Archibald DA, Nespolo M (2010) A Late Triassic $^{40}Ar/^{39}Ar$ age for the El Hamman high-REE fluorite deposit (Morocco): mineralization related to the Central Atlantic Magmatic Province? Mineral Deposita 45:323–329

Corfu F (1988) Differencial response of U-Pb systems in coexisting accessory minerals, Winnipeg River Subprovince, Canadian Shield: implications for Archean crustal growth and stabilization. Contrib Mineral Petrol 98:312–325

Deloule E, Alexandrov P, Cheilletz A, Laumonier B, Barbey P (2002) In situ U-Pb zircon ages for Early Ordovician magmatism in the eastern Pyrenees, France: the Canigou orthogneisses. Int J Earth Sci (Geolog Rundschau) 91:398–405

Desteucq C (1974) Le système filonien du Jbel Aouam (Maroc central); essai d'interprétation structurale. Unpubl PhD thesis, Univer Paul Sabatier, Toulouse, France, 93 pp

El Dursi K (2009) Minéralisations et circulations péri-granitiques: modélisation numérique couplée 2D/3D, applications au district minier de Tighza (Maroc central). Unpubl PhD Thesis, Univer Orléans, France, 218 pp

El Hadi H, Tahiri A, Simancas JF, Gonzalez Lodeiro F, Azor A, Martinez Poyatos DJ (2006) Un exemple de volcanisme calco-alcalin de type orogénique mis en place en contexte de rifting (Cambrien de l'oued Rhebar, Meseta occidentale, Maroc). Comptes Rendus Geosci 338:229–236

El Ouazzani A, Zheni A, Kido H (2002) Le district polymétallique du Jbel Aouam. In: Barodi EB, Watanabe Y, Mouttaqi A, Annich M (eds) Méthodes et techniques d'exploration minière et principaux gisements au Maroc. Report of Projet JICA/BRPM, Bureau Recherche Participations Minières – BRPM, Rabat, pp 185–187

Gasquet D, Bouloton J (1995) Les filons de microdiorite des Jebilet centrales (Meseta marocaine): pré-rifting permien? Abstract Réunion extraordinaire de la Société Géologique de France, Marrakech, Morocco, p 55

Gasquet D, Stussi JM, Nachit H (1996) Les granitoïdes hercyniens du Maroc dans le cadre de l'évolution géodynamique régionale. Bull Société Géol France 167:517–528

Gasquet D, Bertrand JM, Paquette JL, Lehmann J, Ratzov G, De Ascençao Guedes R, Tiepolo M, Boullier AM, Scaillet S, Nomade S (2010) Miocene to Messinian deformation and hydrothermal activity in

a pre-Alpine basement massif of the French western Alps: new U-Th-Pb and argon ages from the Lauzière massif. Bull Société Géol France 181:227–241

Geisler T, Schaltegger U, Tomasckek F (2003) Re-equilibration of zircon in aqueous fluids and melts. Elements 3:43–50

Giulani G, Cheilletz A, Mechiche M (1987) Behaviour of REE during thermal metamorphism and hydrothermal infiltration associated with skarn and vein-type tungsten ore bodies in central Morocco. Chem Geol 64:279–294

Giulani G, Cheilletz A, Zimmermann JL (1989) The emplacement, geochemistry and petrogenesis of two central Morocco Hercynian granites: geotectonic implications. J African Earth Sci 9:617–629

Grove M, Harrison TM (1999) Monazite Th-Pb age depth profiling. Geology 27:487–490

Hoskin PWO (2005) Trace-element composition of hydrothermal zircon and alteration of Hadean zircon from the Jack Hills, Australia. Geochim Comochim Acta 69:637–648

Hurai V, Paquette JL, Huraiová M, Konečný P (2010) Age of deep crustal magmatic chambers in the intra-Carpathian back-arc basin inferred from LA-ICPMS U-Th-Pb dating of zircon and monazite from igneous xenoliths in alkali basalts. Jour Volc Geo Res 198:275–287

Izart A, Tahiri A, El Boursoumi A, Chèvremont P (2001) Carte géologique Maroc (1/50 000), feuille Bouqachmir. Notice explicative par Izart A, Chèvremont P, Tahiri A, El Boursoumi A, Thiéblemont D. Notes Mémoir Service Géol Maroc n° 411bis, Rabat

Jackson SE, Pearson NJ, Griffin WL, Belousova EA (2004) The application of laser ablation-inductively coupled plasma mass spectrometry to in situ U-Pb zircon geochronology. Chem Geol 211:47–69

Jébrak M (1984) Contribution à l'histoire naturelle des filons (F, Ba) du domaine varisque français et marocain : essai de caractérisation structurale et géochimique des filons en extension et en décrochement. Doctorat d'Etat Thesis, Univer Orléans, France, BRGM Edition 99, 510 pp

Jébrak M (1985) Le district filonien à Pb-Zn-Ag et carbonates du Jebel Aouam (Maroc central). Bull Minéral 108:487–498

Kretz R (1983) Symbols for rock-forming minerals. Amer Mineral 68:277–279

Ludwig KR (2003) User's manual for Isoplot/Ex version 3.00: a geochronological toolkit for Microsoft Excel, v. 4. Geochronology Center, Univ California, Berkeley, pp 1–71

Michard A, Hoepffner C, Soulaimani A, Baidder L (2008) The Variscan belt. In: Michard A, Saddiqi O, Chalouan A, Frizon de Lamotte D (eds) Continental evolution: the geology of Morocco. Lecture notes earth science, vol 116. Springer, Berlin, pp 65–132

Nerci K (2006) Les minéralisations aurifères du district polymétallique de Tighza (Maroc central): un exemple de mise en place périgranitique tardi-hercynienne. Unpubl PhD Thesis, Université du Québec à Montréal, Canada, 302 pp

Ntarmouchant A (1991) Le magmatisme hercynien de la région de Mrirt (Est du Massif central marocain: cartographie, pétrographie, géochimie et contexte géodynamique. Unpubl PhD Thesis, Univer Fès, Morocco, 175 pp with annexes

Paquette JL, Tiepolo M (2007) High resolution (5 microns) U-Th-Pb isotope dating of monazite with excimer laser ablation (ELA)-ICPMS. Chem Geol 240:222–237

Paquette JL, Piro JL, Devidal JL, Bosse V, Didier A (2014) Sensitivity enhancement in LA-ICP-MS by N2 addition to carrier gas: application to radiometric dating of U-Th-bearing minerals. Agilent ICP-MS Jour 58:4–5

Pelleter E, Cheilletz A, Gasquet D, Mouttaqi A, Annich M, El Hakour A, Deloule E, Féraud G (2007) Hydrothermal zircons: a tool for ion microprobe U-Pb dating of gold mineralization (Tamlalt-Menhouhou gold deposit–Morocco). Chem Geol 245:135–161

Pettke T, Audetat A, Shaltegger U, Heinrich CA (2005) Magmatic-to-hydrothermal crystallization in the W-Sn mineralised Mole Granite (NSW, Autralia) Part II: Evolving zircon and thorite trace element chemistry. Chem Geol 222:191–213

Sillitoe RH (2010) Porphyry-copper systems. Econ Geol 105:3–41

Tarrieu L (2014) Nouvelles données minéralogiques, géochimiques et géochronologiques sur le gisement polymétallique de Tighza (Maroc Central) – Contribution à la métallogénie des géisements de métaux de base filoniens en contexte post-collisionnel. Unpubl PhD Thesis, Univer Savoie, France, 240 pp

Verati C, Rapaille C, Féraud G, Marzoli A, Bertrand H, Youbi N (2007) 40Ar/39Ar ages and duration of the Central Atlantic Magmatic Province volcanism in Morocco and Portugal and its relation to the Triassic-Jurassic boundary. Palaeogeogr Palaeoclimatol Palaeoecol 244:308–325

Vielreicher NM, Groves DI, Fletcher IR, McNaughton NJ, Rasmussen B (2003) Hydrothermal monazite and xenotime geochronology: a new direction for precise dating of orogenic gold mineralization. SEG Newslett 53:1–16

Wajdinny A (1998) Le plomb au Maroc: cas des districts de Touissit et de Jbel Aouam. Chronique Recherche Min 531–532:9–28

Watanabe Y (2002) $^{40}Ar/^{39}Ar$ Geochronologic constraints on the timing of massive sulfide and vein-type Pb-Zn mineralization in the WesternMeseta of Morocco. Econ Geol 97:145–157

The Bou Madine Polymetallic Ore Deposit, Eastern Anti-Atlas, Morocco: Evolution from Massive Fe–As–Sn to Epithermal Au–Ag–Pb–Zn ± Cu Mineralization in a Neoproterozoic Resurgent Caldera Environment

Mohammed Bouabdellah and Gilles Levresse

Abstract

The Bou Madine Au–Ag–Pb–Zn ± Cu epithermal deposit in the Ougnat Pan-African inlier of the eastern Anti-Atlas occurs within the lower unit of the late Neoproterozoic Tamerzaga-Timrachine Formation. Host rocks are a thick succession of alternating rhyolitic to dacitic ignimbrites locally interlayered with andesitic to dacitic lava flows. Mineralization is structurally controlled, consisting of zones of vuggy quartz and veins, veinlets, and tectonic-hydrothermal breccias. Alteration produced a predominantly strong phyllic-argillic assemblage (quartz, sericite, pyrite) that overprints earlier pervasively propylitized rocks. Overall, five mineralized vein systems, referred to as Imariren, Tizi, North zone, Central zone, and South zone are recognized. Higher grade orebodies tend to occur where NNE- and NNW-oriented veins intersect. Three successive and overlapping stages of mineralization are distinguished. Among these, stage II was coeval with dextral reactivation of the N160° E veins and is economically the most important for Au and Ag. Gold is foremost distributed in pyrite and arsenopyrite, and to a lesser extent in galena and sphalerite. Gangue minerals include quartz and minor calcite. Structural and textural data indicate that mineralization took place during the late Neoproterozoic as a result of open-space filling. These data further suggest that the Bou Madine deposit represents a relatively shallow mineralizing system that was open to the surface, and is similar to volcanic-hosted

M. Bouabdellah (✉)
Département de Géologie, Faculté des Sciences,
Université Mohammed Premier,
Avenue Mohammed VI, B.P. 717,
60000 Oujda, Morocco
e-mail: mbouabdellah2002@yahoo.fr

G. Levresse
Geofluidos, Centro de Geociencias,
Universidad Nacional Autónoma de México,
Blvd. Juriquilla no. 3001, 76230 Querétaro, Mexico

M. Bouabdellah and J.F. Slack (eds.), *Mineral Deposits of North Africa*,
Mineral Resource Reviews, DOI 10.1007/978-3-319-31733-5_4

epithermal veins developed in subaerial resurgent caldera environments. Fluid inclusion measurements indicate mean homogenization temperatures of 150 °C and salinities in the range of 1–5 wt% NaCl equiv. These data are interpreted as reflecting fluid mixing and fluid-rock interaction between two contrasting fluids: (1) an ascending, acidic, deep-seated fluid that equilibrated with Neoproterozoic crystalline basement rocks; and (2) formation and/or meteoric waters. Mixing between these two fluid end members would have triggered precipitation of precious- and associated base-metal mineralization.

1 Introduction

Bou Madine (longitude 4° 55′ 36″ West; latitude 31° 23′ 28″ North) is an Au-rich epithermal ore deposit in the Precambrian Ougnat inlier of the eastern Pan-African Anti-Atlas system of Morocco (Fig. 1). The deposit is situated about 100 km northeast of the giant epithermal Ag deposit of Imiter and is representative of the numerous Au–Ag epithermal deposits dispersed throughout the Anti-Atlas domain.

The Bou Madine deposit has been mined since the 15th Century, during which Portuguese miners exploited the outcropping limonitic gossans for silver, gold, and ochre. The deposit was re-discovered in the beginning of the 20th Century and operated intermittently during French colonial times. From 1957 to 1992, the so-called Moroccan "Office National des Hydrocarbures et des Mines" (ONHYM, formerly BRPM) conducted an extensive surface drilling program on the main mineralized veins that ultimately led, in

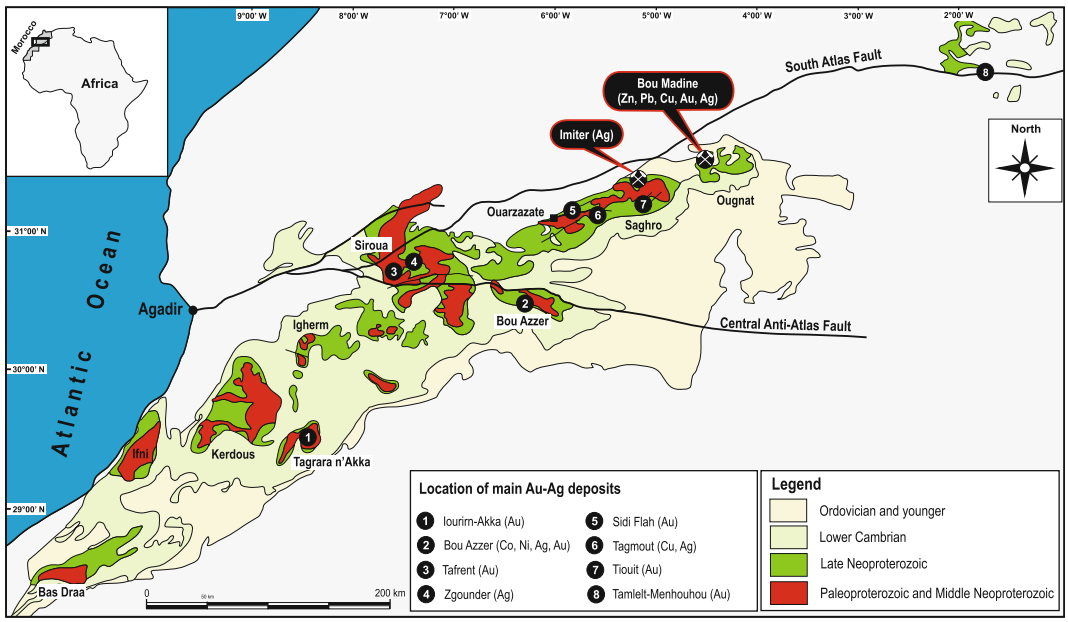

Fig. 1 Simplified geological map of the Anti-Atlas system showing location of the Bou Madine polymetallic Au–Ag–Pb–Zn–Cu district, regional-scale faults, and its relationship to the adjacent Au–Ag-bearing mining camps. *Inset* shows location of Bou Madine district with respect to the Anti-Atlas and Africa continent

1983, to an internal feasibility plan based on a 100-t-per day test pilot plant. The major period of base-metal mining ended with the closure of the mine in 1992 owing to depressed prices of zinc and to difficulty in recovering precious metals from the ore. At the end of mining, the ONHYM estimated historical mineral resources (past production + reserves + mineral resources) of ~3.5 Mt of ore grading 0.9 % Pb, 4 % Zn, 203 g/t Ag, and 3.6 g/t Au. Copper grades are uneconomic. In 2013, a joint venture between Canadian Maya Gold and Silver Inc (85 %) and ONHYM (15 %) was signed to explore and develop the Bou Madine deposit.

All of the economic orebodies are hosted by the lower ignimbrite-rhyolite portion of the late Neoproterozoic Tamerzaga-Timrachine Formation (TTF) (Fig. 2). Gold is the main commodity, but the polymetallic nature of the ore makes this economically attractive district atypical comparative to neighboring base-metal deposits in the Anti-Atlas System, both in style of mineralization and most importantly in type of associated host rocks. However, despite its economic importance, the genesis of the Bou Madine mineralization is still controversial (Paile 1983; Freton 1988; Abia 2001; Abia et al. 1999; Levresse 2001), and questions remain about the source of heat and metal components, origin of the ore fluids, mechanism(s) of ore deposition, and the age of mineralization.

The main objectives of the present contribution are to provide an updated geologic synthesis of the Bou Madine deposit, summarize its mineralogical and geochemical attributes, compare this information with that for equivalent deposits of the Anti-Atlas system, and review the current genetic models.

2 Geological Setting

The Bou Madine deposit is defined here as an area of some 3 km east-west by 4 km north-south within the Ougnat Pan-African inlier on the eastern margin of the Anti-Atlas system (Fig. 1). Stratigraphy of the Ougnat Precambrian inlier consists of a thick succession (>1200 m) of regionally deformed and metamorphosed, predominantly felsic and intermediate-composition volcanic and intrusive rocks of the Cryogenian to Ediacaran Saghro Group (Abia et al. 2003). The host rocks are grouped into three main Late Neoproterozoic (586 ± 20 to 563 ± 10 Ma; Mifdal and Peucat, 1985) supracrustal formations (Figs. 2 and 3) including the basal high-K, calc-alkaline volcaniclastic Tamerzaga-Timrachine Formation (TTF), the intermediate Isilf-Ouinou-Oufrouh Formation (IOF), and the upper Aoujane-Aïssa-Akchouf Formation (AAF).

The contact between the crystalline basement and overlying TTF is characterized by a breccia member that lies unconformably on the basement. The TTF is the exclusive host for the Au–Ag–Pb–Zn–Cu ores. This formation, together with the conformably overlying IOF and AAF, consist predominantly of a thick succession of alternating rhyolitic to dacitic ignimbrite units locally interlayered with andesitic to dacitic lava flows and hypabyssal volcanic bodies (andesite and rhyolite). Individual ignimbrites are up to 400 m thick and are represented by distinct units (Fig. 4). Fiamme, sparse lithic fragments, and abundant phenocrysts of feldspar, biotite, and quartz occur in a vitroclastic matrix. No age determination exists for these ignimbrites. The rhyolitic pyroclastic rocks, pyroclastic breccias, and welded rhyolite tuffs are interpreted to form a pyroclastic vent complex whose funnel-shaped geometry resulted from caldera collapse and compaction. Flanking the volcaniclastic rocks is a sequence of sedimentary rocks of the IOF that range from sandstone, conglomerate, fine-grained argillite (pelite), to limestone. The occurrence of sedimentary rocks between the main pyroclastic flows indicates both subaerial and subaqueous deposition.

A rhyolite dome dated at 553 ± 16 Ma (U–Pb on zircon; Levresse 2001; Gasquet et al. 2005) together with numerous felsic and doleritic dike swarms are the youngest rocks of the region as they intrude all lithologies of the TTF and AAF (Fig. 4). A Cambrian clastic sedimentary cover sequence composed of conglomerates and

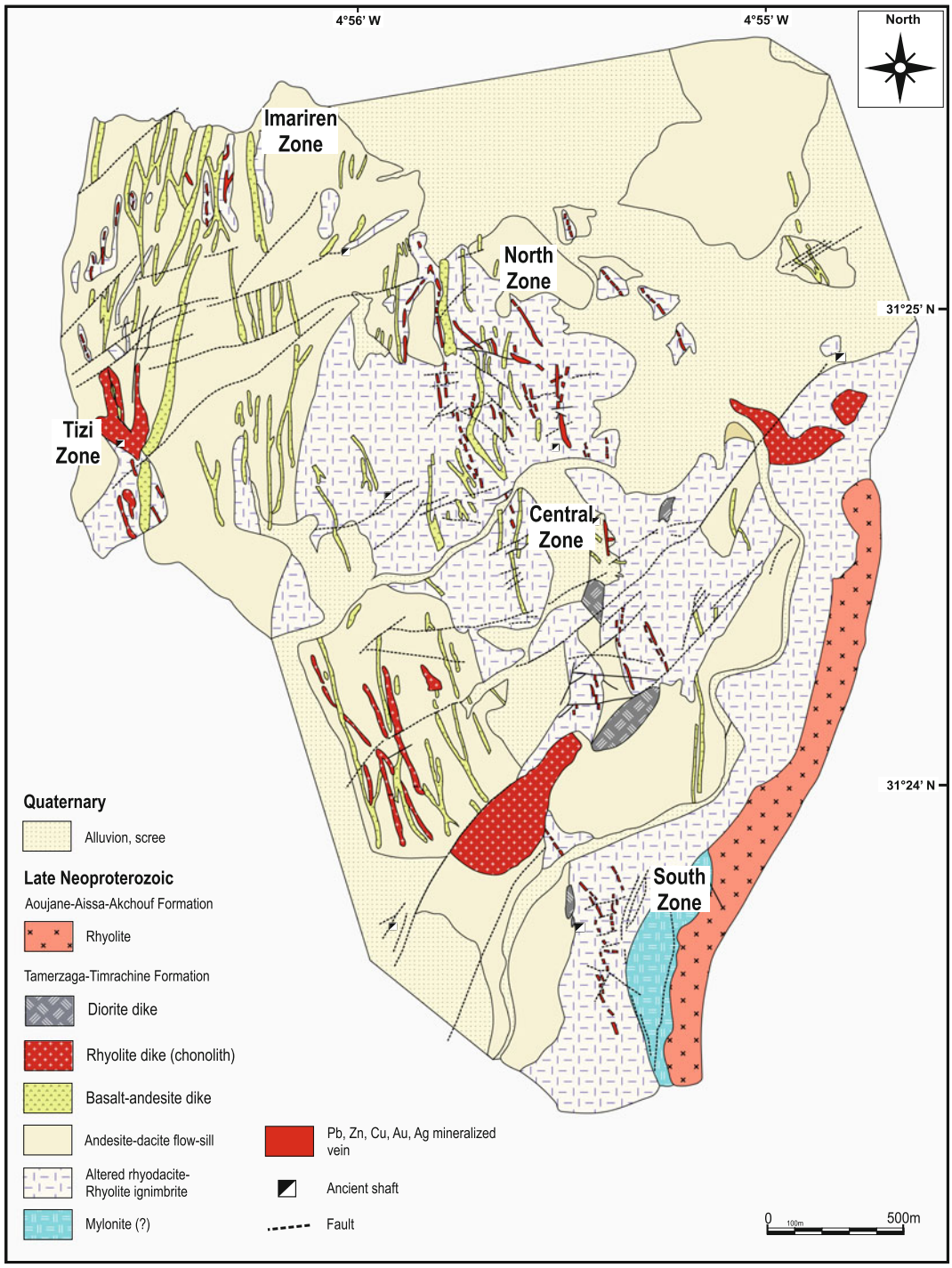

Fig. 2 Representative lithostratigraphic column for the Ougnat Precambrian inlier showing the main lithostratigraphic Formations and relative position of the Bou Madine vein-type mineralization

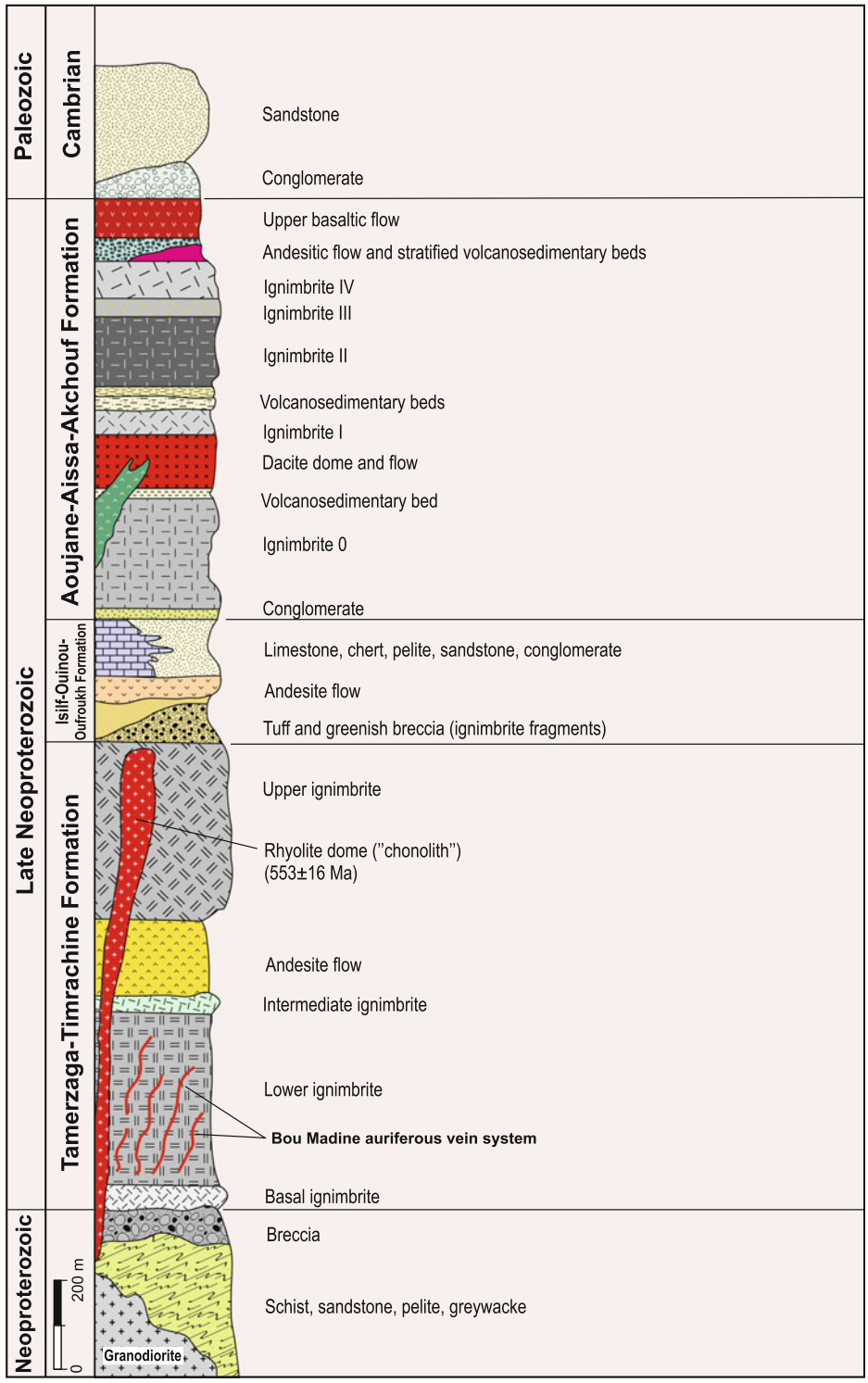

Fig. 3 Geological map of the Bou Madine polymetallic Au–Ag–Pb–Zn–Cu district (modified after Paile 1983) showing the main lithostratigraphic units, the extent of structural styles, and the relative position of known vein-type orebodies, and their relationships to the Late Neoproterozoic ignimbrites

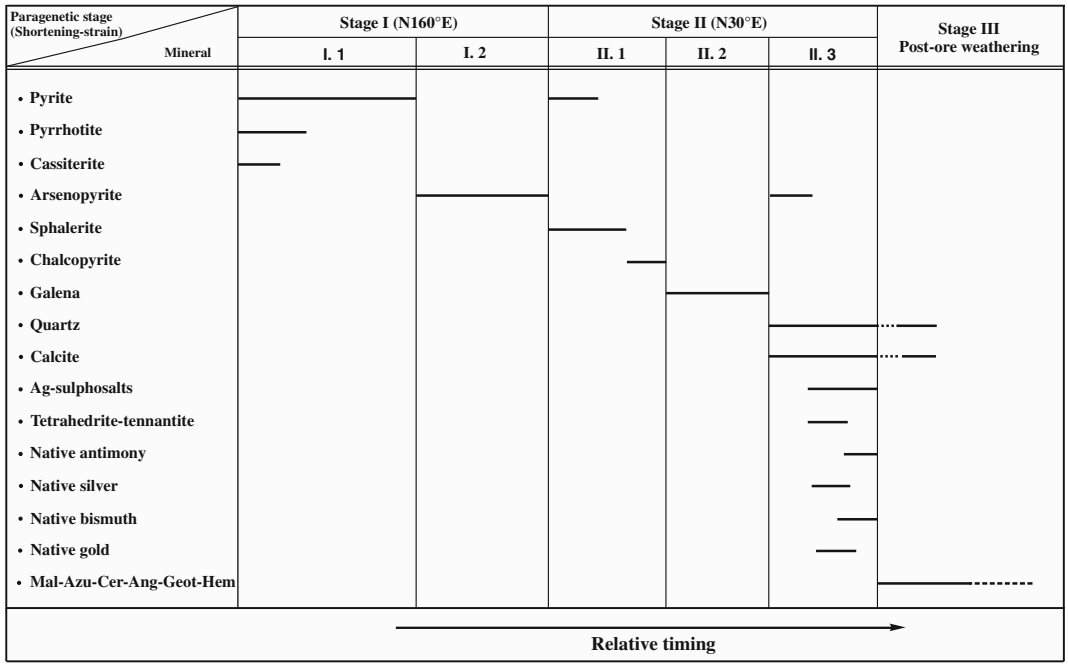

Fig. 4 Summary of the idealized paragenetic sequence of the Bou Madine polymetallic deposit (modified after Paile 1983; Abia et al. 2003). *Mal* malachite; *Azur* azurite; *Cer* cerussite; *Ang* anglesite; *Geot* goethite; *Mem* hematite

sandstones unconformably overlies the Neoproterozoic rocks. Paleogeographic reconstructions indicate that the Bou Madine mineralized structure corresponds to a resurgent caldera as evidence by the following diagnostic features (Lipman 1997; Kennedy et al. 2012): (1) lack of a single centralized vent; (2) structural uplift of the margins of the caldera, which occurred along regional and subsidence faults resulting in development of apical graben structures near the center of the collapsed structure; and (3) occurrence of recurrent shallow lava domes of dacitic and rhyolitic compositions along the fracture zones and related graben structures. Based on our estimates, the minimum structural relief caused by resurgence is >500 m as indicated by the elevation difference between the flat-lying tuff outside the caldera and the top of the tuffaceous lithologies within the caldera. These observations suggest that resurgence of the Bou Madine structure is temporally related to caldera subsidence, with the upward migration of dacitic-rhyolitic magma having been the driver of resurgence.

Regional metamorphism under greenschist-facies conditions resulted in the formation of chlorite, muscovite, and pyrophyllite-bearing mineral assemblages with peak conditions reaching 350 °C and <3 kb (Thomas et al. 2004). Higher temperatures were reached locally in the aureoles of post-kinematic (547 ± 26 Ma) intrusions. Ductile deformation created large recumbent folds that are believed to be coincident with metamorphism; later, post-metamorphic deformation is also associated with recumbent folding. Brittle structures are associated with regional uplift, including thrust faults.

3 Mineralogy, Alteration, Textures, and Paragenesis

The Bou Madine Au-Ag-rich mineralization is structurally controlled and comprises a system of transtensional, sub-vertical veins, veinlets, cemented breccias within veins, and lensoidal or

pocket-like masses and fillings of en echelon tension gashes (Fig. 3). Mineralized structures occur exclusively within the rhyolitic sequence of the TTF. On the surface, the vein swarm extends at least for 4 km; most mineralized structures have been mined from surface to a depth of about 500 m. Surface drilling and underground workings suggest an increase of vein thickness with depth. Most of the exploited veins that were mined initially for Pb–Zn sulphides are auriferous and silver-rich.

Four mineralized vein systems, referred to as Imariren, Tizi, North zone, Central zone and South zone, are recognized (Fig. 3). Higher grade orebodies tend to occur where NNE- and NNW-oriented veins intersect each other. The veins are up to 4 m wide and extend laterally from a few meters up to 600 m, spaced 50–100 m apart, strike N160° E, and dip steeply (70° to ~90°). Texturally, the veins display comb, cockade, laminated, breccia, and crack and seal features, suggesting that episodic, multiple mechanisms were important in vein formation. Overall, these textural features indicate that mineralization took place in open space, and suggest that the Bou Madine deposit represents a relatively shallow mineralizing system that was open to the surface, and is therefore similar to volcanic-hosted epithermal veins in subaerial caldera environments.

All of the mineralized vein structures display more or less similar mineral assemblages although the proportions of base-metal sulphides relative to other minerals vary from one system to another. The idealized sequence of mineral deposition, constructed on the basis of mineral assemblages, and textural and crosscutting relationships, shows three successive and overlapping stages of mineralization, two of which (i.e., stages I and II) are of economic interest (Levresse 2001, and reference therein) (Fig. 4). Several sub-stages are distinguished within both main stages (Abia et al. 2003). The earlier of these two stages, referred to as "Fe–As–(Sn) stage," was emplaced under N160° E shortening and has a mineral assemblage dominated by massive pyrite, pyrrhotite, cassiterite, and arsenopyrite. Based on the style of mineralization and textural features, the above mineral assemblage is interpreted to have resulted from massive replacement of carbonate strata intercalated within the Late Neoproterozoic stratigraphic package (i.e., IOF). Conversely, paragenetically later stage II, referred to as "precious metal-stage ore," is economically the most important for Au–Ag and comprises massive quartz veins, stockwork veins, and hydrothermal breccias containing variable amounts of sphalerite, galena, tetrahedrite argentopyrite, mixture of galena and matildite, pyrargyrite, polybasite, and native antimony-silver-bismuth that overprints stage I. Gangue minerals include quartz and minor calcite. Gold is foremost distributed in pyrite and arsenopyrite, and to a lesser extent in galena and sphalerite. Emplacement of the precious-metal mineralization was coeval with dextral reactivation of the N160° E veins coevally with a northeastward shift of the shortening direction (Abia et al. 2003). There is a systematic decrease in Pb concentrations with depth and correspondingly an increase in Au, Cu, and Sn contents. The postore supergene mineral assemblage (stage III) resulting from the oxidation of primary sulphides consists of minor amounts of goethite, and jarosite with traces of hematite.

The mineralized area is characterized by regional and pervasive propylitic alteration (quartz, albite, chlorite, epidote, rutile; Freton 1988) that affects the entire stratigraphic column. Conversely, wall-rock hydrothermal alteration spatially related to the Bou Madine mineralization is only present adjacent to the mineralized structures, forming distinctive overlapping halos and stringers of a strong phyllic-argillic assemblage (quartz, sericite, pyrite) that overprints the pervasively propylitized rocks. Late silicification typified by the development of millimeter- to meter-thick quartz veins cuts across both the phyllic and propylitic zones.

4 Discussion

Based on mineralogical observations and textural relationships, the paleohydrothermal history of the Bou Madine ore-forming system comprised two

main contrasting hydrothermal events that were emplaced under distinct stress fields (i.e., N160° E and N30° E shortening directions; Fig. 4). However, it is unclear whether these two hydrothermal events involved a single mineralizing fluid or two chronologically separated hydrothermal fluids. The regional distribution of host rock types, the thick volcanic succession (>1,200 m; Figs. 2 and 3), and the morphology of these rocks all provide strong evidence for the existence in the Bou Madine district of a caldera structure that, after formation, was deformed along N160° E and N30° E shortening axes (Fig. 5).

The shift in the tectonic regime from N160° E to N30° E shortening resulted in a drastic change in the nature of the hydrothermal system, namely from early Fe–As–(Sn) mineralization (i.e., stage I) to late epithermal precious metal stage II. Both types are intimately associated with the rhyolite porphyries and related ignimbrites. In the absence of radiometric age dating of mineralization, based on stratigraphic and structural constraints it appears that the Bou Madine mineralization took place between eruption of the rhyolite porphyries dated at ca. 553 ± 16 Ma (U–Pb on zircon; Levresse 2001; Gasquet et al. 2005) and the ignimbritic unit of the AAF that constitutes the hanging wall of mineralization, consistent with a late Neoproterozoic age. More interestingly, Abia et al. (2003) proposed a syn-TTF emplacement for the Bou Madine mineralization, whereas Lécolle and Derré (2005) argued that the two mineralizing events are unrelated to emplacement of the TTF ignimbrites (i.e., post-TTF age), instead being linked to late subvolcanic activity following resurgence of a caldera concealed first by the dacitic magmas then by rhyolitic intrusion.

Overall, a systematic trend exists of decreasing temperatures and f_{S2} along with P–T trapping

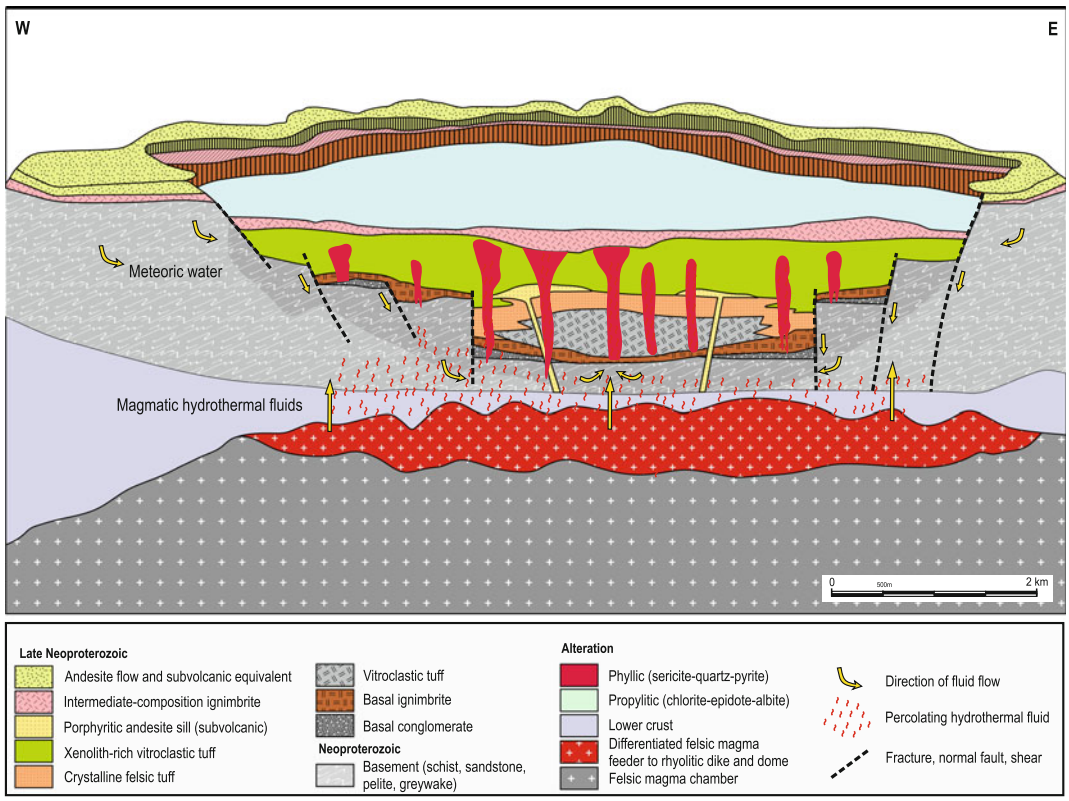

Fig. 5 A caldera hypothesis for the genesis of the Bou Madine polymetallic Au–Ag–Pb–Zn–Cu district (modified after Boily 2014)

conditions with advancing paragenetic sequence. Calculated temperatures determined from mineral pairs (i.e., pyrrhotite-arsenopyrite, pyrite-pyrrhotite) and phase relationships in the Fe–As–S system suggest that stage I mineralization occurred at temperatures of 310 °C at f_{S2} close 10^{-9} and $10^{-10.5}$ (Abia et al. 2003). Conversely, fluid inclusions in vein quartz from stage II. 3 have mean homogenization temperatures (T_h) of 150 °C and salinities in the range of 1–5 wt% NaCl equiv (Ait Saadi 1992; Abia et al. 1999). These salinity estimates are interpreted to indicate fluid mixing and fluid-rock interaction between two contrasting fluids (1) ascending, acidic, deep-seated fluid that has equilibrated with Neoproterozoic crystalline basement rocks; and (2) formation and/or meteoric waters. Mixing between these two fluid end members would have resulted in precipitation of the precious-metal mineralization. Based on bismuth-bismuthinite equilibrium, the f_{S2} associated with precious-metal deposition has been estimated at 10^{-9} (Abia et al. 2003). Moreover, the acidic character of the ore-forming fluids, together with their high sulphur content, may be related to degassing of a deep magmatic reservoir. Sulphur isotopic compositions determined on pyrite, sphalerite, and galena (Levresse 2001) are consistent with this interpretation. Indeed, the clustering of $\delta^{34}S_{sulphide}$ values near 0 ± 3 ‰ suggests magmatic and mantle sources for the sulphur, although $\delta^{34}S$ values as low as −6 ‰ could indicate the involvement of an additional sulphur source such as biogenic sulphur. Based on these fluid constraints, we suggest that the near-surface, silica-rich auriferous stage of mineralization resulted from low salinity gas condensates (<5 wt% NaCl equiv), an interpretation consistent with lead isotope ratios (Abia et al. 1999) that imply lead derivation from crustal sources.

All recent workers agree with the epithermal nature of the Bou Madine mineralization. The emplacement of caldera-forming eruptions resulted in development of a dense fracture and fault system suitable for hosting Au–Ag–Pb–Zn–Cu mineralization. Convection of large volumes of meteoric waters around the resurgent extrusions and along the margins of the caldera, and their mixing with magmatic-derived fluids, resulted in deposition of mineralization and associated alteration along extensional faults within the resurgent dome. The mineralized structures appear to have scavenged metals largely from intracaldera explosive ash-flow lithologies (i.e., tuffs and ignimbrites).

References

Abia EH, Nachit H, Baroudi Z, Ibhi A (1999) Les minéralisations filoniennes à Pb, Zn et Cu de la boutonnière de l'Ougnat. Relations avec les déformations et essai de calage chronologique. Chronique Recherche Minière 536:83–95

Abia EH (2001) Étude des formations magmatiques et crystallophylliennes néoprotérozoiques de l'Ougnat (Anti-Atlas Oriental, Maroc) et des minéralisations polymétalliques associées. Unpubl PhD Thesis, Ibn Zohr University, Agadir, Morocco, 150 pp

Abia EH, Nachit H, Marignac C, Ibhi A, Aït Saadi S (2003) The polymetallic Au–Ag-bearing veins of Bou Madine (Jbel Ougnat, eastern Anti-Atlas, Morocco): tectonic control and evolution of a Neoproterozoic epithermal deposit. J Afr Earth Sci 36:251–271

Ait Saadi S (1992) Contribution à l'étude de l'environnement paléovolcanqiue du Protérozoïque Supérieur (PIII) et du mode de genèse des concentrations polymétalliques de Bou-Madine (Ougnat, Anti-Atlas Oriental, Maroc). Unpubl PhD Thesis, Institut National Polytechnique de Lorraine, École Nationale de Géologie Appliquée et de Prospection Minière, Nancy, France, 123 pp

Boily M (2014) The Boumadine polymetallic (Au, Ag, Zn, Pb, Cu) Deposit Errachidia Province. Maya Gold and Silver Inc, reportKingdom of Morocco 207 pp

Dagallier G, Freton R, Aït Saadi S (1998) Étude préliminaire du gîte polymétallique épithermal à or-argent de Bou Madine (Anti-Atlas, Maroc). In: Johan Z, Ohnenstetter D (eds) Gisements métallifères dans leur contexte géologique. Document BRGM 158:729–751

Freton R (1988) Contribution à l'étude métallogénique du district de Bou Madine (Anti-Atlas, Maroc): Environnement tectonique et concentrations épithermales B.P. G.C à Ag et Au. Unpubl PhD Thesis, Institut National Polytechnique de Lorraine, École Nationale de Géologie Appliquée et de Prospection Minière, Nancy, France, 63 pp

Gasquet D, Levresse G, Cheilletz A, Azizi Samir MR, Mouttaqi A (2005) Contribution to a geodynamic reconstruction of the Anti-Atlas (Morocco) during

Pan-African times with the emphasis on inversion tectonics and metallogenic activity at the Precambrian-Cambrian transition. Precambr Res 140:157–182

Kennedy B, Wilcock J, Stix J (2012) Caldera resurgence during magma replenishment and rejuvenation at Valles and Lake City calderas. Bull Volcanol 74:1833–1847

Lécolle M, Derré C (2005) Discussion of "The polygenetic Au–Ag bearing veins of Bou Madine (Jbel Ougnat, Eastern Anti-Atlas, Morocco): tectonic control and evolution of a Neoproterozoic epithermal deposit. J Afr Earth Sci 41:151–154

Levresse G (2001) Contribution à l'établissement d'un modèle génétique des gisements d'Imiter (Ag-Hg), Bou Madine (Pb-Zn-Cu-Ag-Au) et Bou Azzer (Co-Ni-As-Au-Ag) dans l'Anti-Atlas marocain. Unpubl PhD Thesis, Institut National Polytechnique de Lorraine, École Nationale de Géologie Appliquée et de Prospection Minière, Nancy, France, 191 pp

Lipman PW (1997) Subsidence of ash-flow calderas: relation to caldera size and magma-chamber geometry. Bull Volcanol 59:198–218

Mifdal A, Peucat J-J (1985) Datations U–Pb et Rb-Sr du volcanisme acide de l'Anti-Atlas Marocain et du socle sous-jacent dans la région de Ouarzazate: apport au problème de la limite Précambrien-Cambrien. Sci Géol Bull 38(2):185–200

Paile Y (1983) Etude des séries volcaniques du Précambrien III de l'Ougnat (Anti-Atlas oriental, Maroc) et des minéralisations plombo-zincifères complexes associées (gîte de Bou Madine). Unpubl PhD Thesis, University of Paris XI, Orsay, France, 290 pp

Thomas RJ, Fekkak A, Ennih E, Errami E, Loughlin SC, Gresse PG, Chevallier LC, Liégeois JP (2004) A new lithostratigraphic framework for the Anti-Atlas Orogen, Morocco. J Afr Earth Sci 39:217–226

U/Pb Ages of Magmatism in the Zgounder Epithermal Ag–Hg Deposit, Sirwa Window, Anti-Atlas, Morocco

Ewan Pelleter, Alain Cheilletz, Dominique Gasquet, Abdellah Mouttaqi, Mohammed Annich, Quentin Camus, Etienne Deloule, Lofti Ouazzani, Hassan Bounajma and Lahcen Ouchtouban

Abstract

The Zgounder epithermal Ag–Hg deposit (Jbel Sirwa inlier, Anti-Atlas, Morocco) is hosted in Neoproterozoic volcanosedimentary and magmatic rocks in a Pan-African belt. Strongly altered U-rich zircons were analyzed for in situ SIMS U–Pb ages of multiple rhyolitic intrusions spatially associated with the Ag–Hg mineralization. Morphological features, internal microstructures, and chemical characteristics allow the discrimination of two types of zircon, magmatic and hydrothermal. U/Pb data

E. Pelleter · A. Cheilletz (✉) · Q. Camus
Ecole Nationale Supérieure de Géologie,
Laboratoire Géoressources, Université de Lorraine,
rue du Doyen Marcel Roubault, BP 40, 54501
Vandoeuvre-lès-Nancy, France
e-mail: alain.cheilletz@univ-lorraine.fr

D. Gasquet
Laboratoire EDYTEM, Université de Savoie
Mont Blanc, CNRS, Campus scientifique,
73376 Le Bourget du Lac, France

A. Mouttaqi · M. Annich
Office National des Hydrocarbures et des Mines,
5 Avenue Moulay Hassan, BP 99,
10000 Rabat, Morocco

E. Deloule
Centre de Recherches Pétrographiques et
Géochimiques, Université de Lorraine, BP 20,
54501 Vandoeuvre-lès-Nancy, France

L. Ouazzani · H. Bounajma · L. Ouchtouban
Compagnie Minière de Touissit (CMT),
5 rue Ibnou Tofail, Quartier Palmiers, 20340
Casablanca, Centre minier de Tighza, BP 114,
54450 M'rirt, Province de Khénifra, Morocco

E. Pelleter
Geosciences Marines, IFREMER—ZI de la Pointe
du Diable, CS 10070, 29280 Plouzané, France

M. Bouabdellah and J.F. Slack (eds.), *Mineral Deposits of North Africa*,
Mineral Resource Reviews, DOI 10.1007/978-3-319-31733-5_5

reveal four main geologic events: (1) ca. 815 Ma corresponding to inherited cores of zircons that reflect the reworking of Neoproterozoic crust during the Pan-African (~885–555 Ma) orogenic cycle; (2) 610 ± 7 Ma; (3) 578 ± 4 Ma corresponding to the emplacement-crystallization of multiple rhyolitic intrusions and the large magmatic input within the upper crust of the Pan-African chain during the late Neoproterozoic; and (4) 564 ± 15 Ma, a less-precise age obtained on hydrothermally altered domains that may be related to a dissolution-reprecipitation mechanism in U-rich magmatic zircons. Presently, this last age represents the best estimate for the timing of hydrothermal albitization/mineralization in the Zgounder epithermal Ag–Hg deposit.

1 Introduction

Silver mineralization in the Zgounder area was exploited intermittently from the 12th to 20th Centuries. Recent mining by the SOMIL Company began in 1982; the Zgounder mine closed in 1990 after producing 500 kt of Ag at an average grade of 300 g/t. The Zgounder deposit is located on the flanks of the Precambrian Sirwa massif. Surrounding geology of the district (Choubert et al. 1980; Demange 1977) includes weakly metamorphosed volcano-sedimentary rocks of the Sarhro Group (Cryogenian) striking E-W and overturned to the south, which are intruded by an Ediacaran (Thomas et al. 2002) polyphase plutonic and volcanic suite of the Tadmant Formation (Figs. 1 and 2). In the eastern part of the district, these formations are overlain by Ediacaran volcano-sedimentary rocks of the Ouarzazate Supergroup. The youngest strata are represented by Late Miocene to Pliocene tuffite and phonolite, and Quaternary cover. The silver mineralization is disseminated within lenticular veins of various size (10–25 m wide, and 20–60 m long), mainly hosted by the clastic Imghi Formation that forms part of the Sarhro Group (Fig. 1). The main strike of the mineralized veins is E-W. However, several Ag veins trend N-S; major silver ore bodies occur at the intersection of E-W and N-S fracture systems (Petruk 1975). Silver mineralization is accompanied by a strong chloritic alteration. Disseminated ores extends laterally over more than 1000 m and dips south; known vertical extent of ore is 300 m.

The paragenetic sequence of the Zgounder deposit has been studied by Essarraj et al. (1998) and Marcoux and Wadjinny (2005). It shows two successive stages belonging to the same main hydrothermal event (Fig. 3). The early stage (Fe–As) is characterized by pyrite with arsenopyrite and rare micropatches of native silver. The second, highly metalliferous stage (Ag–Zn–Pb–Cu–Hg), is composed of native Ag–Hg amalgam, acanthite, polybasite, pearceite, sphalerite, chalcopyrite, galena, and rare tennantite and tetrahedrite. Also present is a late uraniferous mineralization that may be related to Late Miocene-Pliocene volcanism (Smeykal 1972; Petruk 1975; Popov et al. 1989). Zgounder appears, therefore, to be an Ag–Hg ore deposit rich in silver (native Ag–Hg amalgams yield 70–95 wt% Ag) belonging, as the Imiter deposit (4 Mt grading 800 g/t; Cheilletz et al. 2002), to the class of epithermal deposits (Marcoux and Wadjinny 2005). Zgounder deposit formed along the Anti-Atlas domain during the Neoproterozoic and represents an additional example of this Ag-rich metallogenic belt (Gasquet et al. 2005). A major characteristic of these epithermal precious metal deposits is a spatial and genetic association with subvolcanic intrusions, as is the case for Imiter where bimodal calc-alkaline magmatic dikes control—together with major normal faults—the Ag

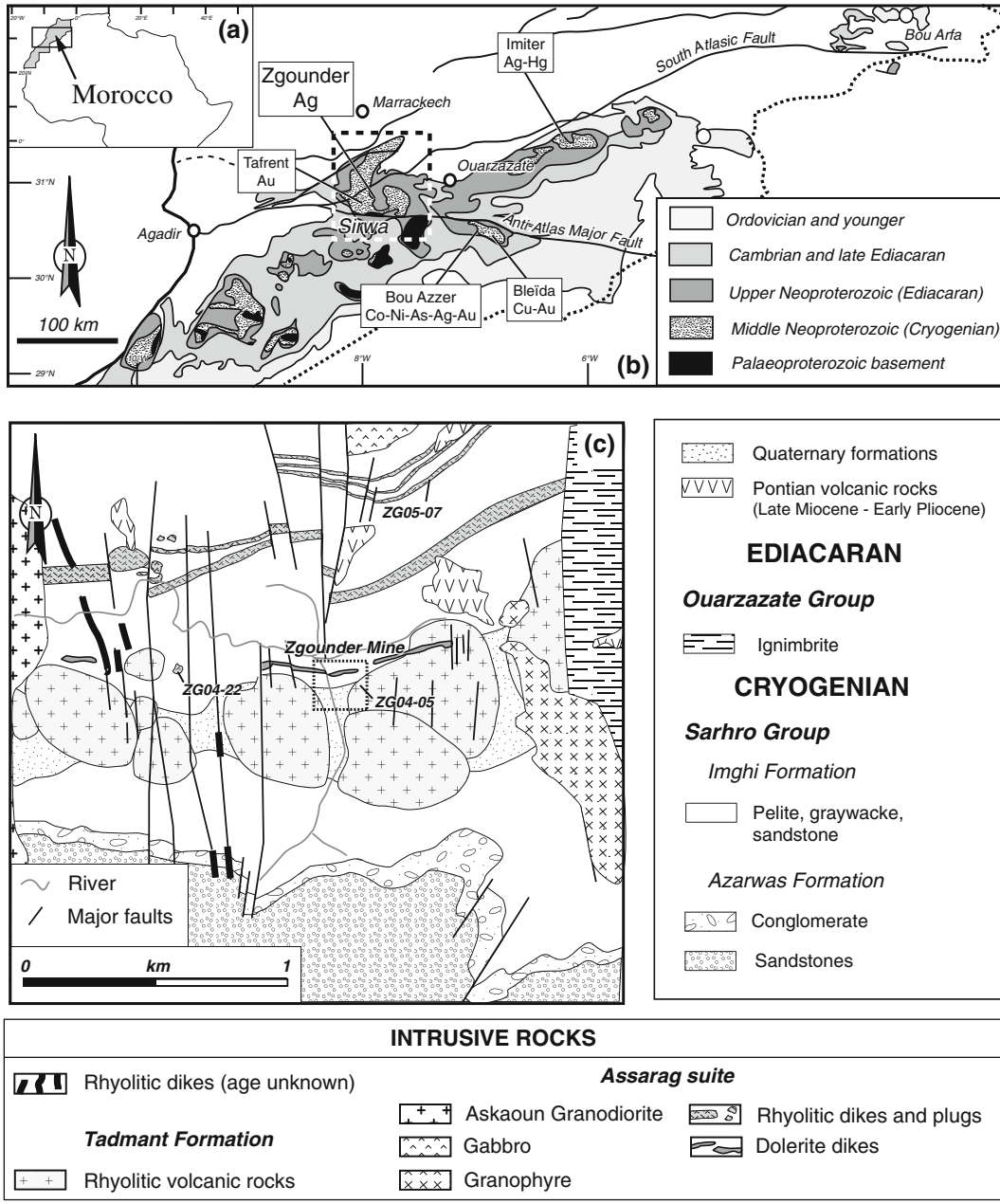

Fig. 1 **a** Localization of studied area. **b** Localization of the Zgounder Ag–Hg deposit in the Anti-Atlas Mountains. Other major mining camps are also shown. **c** Geological map of the Zgounder district. Modified from Demange (1977), Choubert et al. (1980), new field mapping (this work). Nomenclature of geological groups and formations from Thomas et al. (2002)

mineralization (Levresse 2001). Similar Ar/Ar ages of 547 ± 10 Ma and U/Pb ages at 550 ± 3 Ma, respectively from muscovite and rhyolite dikes related to the Ag mineralization, attest to the late Ediacaran age of the epithermal Ag event at Imiter (Levresse 2001; Fig. 1b). At the Zgounder deposit, only one reliable age has been obtained on the Tadmant rhyolite (606 ± 6 Ma;

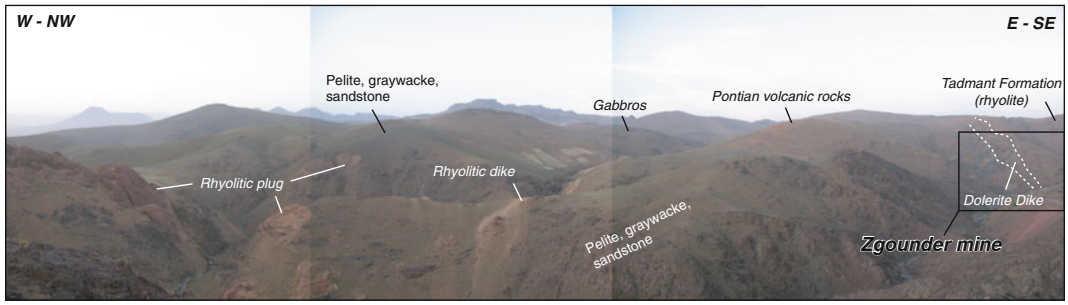

Fig. 2 Geologic panorama of the Zgounder area

Minerals	Stage I : Fe-As	Stage II : Zn-Pb-Cu-Ag-Hg
Arsenopyrite		
Pyrite		
Chalcopyrite		
Native silver		
Sphalerite		
Galena		
Marcasite		
Acanthite / Polybasite		
Tetraedrite / Tennantite		
Pyrrhotite		
Quartz		
Biotite		
Tourmaline		
Calcite		
Chlorite		
Albite		
Siderite		

Fig. 3 Paragenetic sequence of the Zgounder deposit (modified from Essarraj et al. 1998; Marcoux and Wadjinny 2005)

Thomas et al. 2002). However, 20 km northwest of the Zgounder mine, the Askaoun Granodiorite, which belongs to the Assarag Suite (Fig. 1c), has a U/Pb zircon age of 558±2Ma (Toummite et al. 2013) similar to that of the neighbouring Imourkhssen Granite (561±3Ma) and of the Taouzzakt Granodiorite at Imiter (572 ± 5 Ma; Levresse 2001). A 550 Ma Pb isotope model age on galena has been reported for Zgounder (Marcoux and Wadjinny 2005), which reinforces the temporal link between the two deposits. Moreover, previously unknown intrusive bodies have been identified during our last mapping campaign, among them rhyolitic dikes and plugs (Figs. 1c and 2) characterized by strong hydrothermal alteration, suggesting that these intrusions are candidates for an epithermal magmatic event related to the Ag mineralization. Mafic magmatic intrusions are also reported in the Zgounder area (Choubert et al. 1980), including a gabbro massif to the north and several E-W-trending dolerite dikes close to the Zgounder deposit.

2 Felsic Magmatism at Zgounder

New geological mapping of the diverse intrusive bodies in the Zgounder district yields some improvements to the geological map (Fig. 1) Particularly evident are the E-W-trending

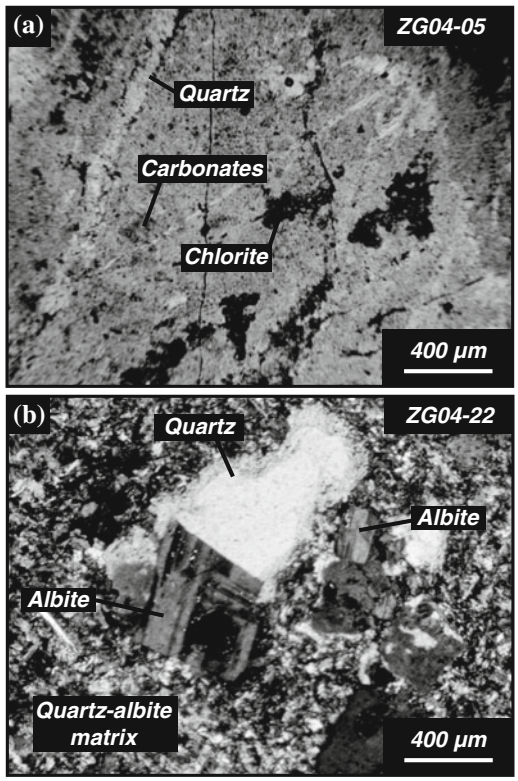

Fig. 4 Photomicrographs of altered rhyolites. **a** Rhyolite sample ZG04-05 from Tadmant Formation, showing significant silicification, chloritization, and carbonatization. **b** ZG04-22 of hypabyssal volcanic plug from Assarag suite showing strong albitization of feldspar, and zoned euhedral albite in matrix

Tadmant rhyolitic plugs that form the spine of the area between the Askaoun Granodiorite to the west and the Ouarzazate volcano-sedimentary group to the east. One sample from the Tadmant Formation (ZG04-05) has been collected at the mine site for dating. This sample has a microcrystalline porphyritic texture and consists mainly of quartz and K-feldspar. Alteration is dominated by patchy chloritization, carbonatization, slight albitization, and strong sericitization of feldspar (Fig. 4a). Whole-rock analysis (Table 1) points to a high-K, calc-alkaline petrologic character with an anomalous Ag concentration (64 ppm), linked to the proximity of the epithermal mineralization.

The other subvolcanic formations that crop out in the Zgounder area belong to the Assarag suite (Thomas et al. 2002). We selected two samples, one from the E-W-trending rhyolitic dikes in the northern part of the district (sample ZG05-07), and another from a small albitic rhyolite plug (ZG04-22) in the central part of the district (Fig. 1c). Both samples display a microcrystalline porphyritic texture and are chiefly composed of quartz, K-feldspar, and/or albite. Sample ZG05-07 appears less hydrothermally altered, even though significant chloritization and sericitization can be observed on thin section. In sample ZG04-22, hydrothermal alteration is dominated by pervasive albitization (Fig. 4b). K-feldspars are strongly altered to albite; numerous albite microlaths have crystallized inside a devitrified matrix. A high alkali character ($Na_2O + K_2O = 10$ %) appears in the chemical analysis (Table 1), together with low contents in Cu (33 ppm), Pb (11 ppm), and Zn (29 ppm). In the outcrop, the albitized rhyolite is cut by albite-chlorite veins linked to the Ag paragenetic stage (Fig. 3).

3 U/Pb Analytical Techniques

Zircons from the three selected samples were extracted from the 50–200 and 200–315 µm size fractions by use of heavy liquids and a magnetic separator. Euhedral to sub-euhedral zircon crystals were handpicked and mounted in epoxy resin with grains of the 91500 zircon standard, and then polished. All grains were imaged in cathodoluminescence (CL) using a Philips XL30 SEM and in back-scattered electron (BSE) mode with a Hitachi 2500 SEM, to examine internal textures. Elemental compositions of zircon grains were obtained using CAMECA SX 100 and CAMECA SX50 electron microprobes at the Université de Lorraine in Nancy (France). Accelerating voltage was 15 kV and beam current 10 nA. For determination of rare earth elements (REE), zircons were analyzed with a CAMECA IMS 3f ion microprobe at CRPG-CNRS in Nancy. The O_2^- primary ion beam was accelerated at 10 kV with an intensity of 20 nA. Counting times were 10 s for each mass during 16 cycles. For further information on analytical procedure, see Martin et al. (2008). Instrumental fractionation was

Table 1 Whole-rock analysis (ICP-OES and ICP-MS) of samples ZG04-05, ZG04-22, and ZG05-07

	ZG04-05	ZG04-22	ZG05-07
%			
SiO_2	74.3	74.6	75.5
Al_2O_3	13.1	15.0	14.3
Fe_2O_3	2.2	<D.L.	1.1
MnO	<D.L.	<D.L.	0.01
MgO	<D.L.	<D.L.	0.32
CaO	0.16	<D.L.	0.17
Na_2O	2.1	6.3	4.9
K_2O	7.3	3.7	2.5
TiO_2	0.14	< D.L.	0.08
P_2O_5	0.03	< D.L.	0.03
LOI	0.6	0.28	1.01
ppm			
Ag*	64	1	<D.L.
As	2.7	6.2	3.2
Ba	940	632	437
Be	3.8	2.8	1.5
Co	0.3	<D.L.	1.8
Cs	1.9	0.4	2.1
Cu	<D.L.	34	8
Ga	35.65	16.72	19.71
Ge	1.95	1.12	0.99
Ho	2.37	2.39	0.30
In	0.2	<D.L.	<D.L.
Mo	0.9	2.0	<D.L.
Ni	<D.L.	<D.L.	3.55
Pb	30	12	2
Rb	219	99	85
Sb	1.0	1.7	0.5
Sn	5.2	3.3	0.8
Sr	63	75	55
V	<D.L.	<D.L.	1.2
W	1.0	1.1	0.9
Y	65.5	67.5	9.3
Zn	45	29	23
Th	16.8	30.4	7.6
U	3.1	15.5	3.9
Nb	32.7	61.6	9.3
Ta	2.74	6.75	0.84
Zr	404	189	60

(continued)

Table 1 (continued)

	ZG04-05	ZG04-22	ZG05-07
Hf	11.42	10.27	2.48
La	61.6	2.8	22.7
Ce	131.5	9.3	42.4
Pr	15.5	1.7	5.0
Nd	60.5	8.5	17.7
Sm	12.9	4.4	3.2
Eu	1.72	0.38	0.74
Gd	11.89	6.02	2.18
Tb	1.96	1.38	0.32
Dy	11.94	10.47	1.70
Er	6.86	8.00	0.85
Tm	1.03	1.38	0.13
Yb	6.76	10.12	0.90
Lu	1.02	1.57	0.14

Abbreviation: <*D.L.* below detection limit

corrected using the 91500 zircon standard (REE concentration from Sano et al. 2002).

For U–Pb analysis, zircon grains were analyzed with the CAMECA IMS 1270 ion microprobe at CRPG-CNRS in Nancy (complete description of the analytical procedure is given in Deloule et al. 2002). Instrumental fractionation was corrected using the 91500 zircon standard (age 1062.4 ± 0.4 Ma; Wiedenbeck et al. 1995). Because of high U contents (i.e. >0.5 % U) in some analyzed zircons, problems with the calibration of U–Pb ratios may be expected (Rayner et al. 2005). As a consequence, for U-rich zircons only Pb/Pb ages were used for age interpretation because the $^{207}Pb/^{206}Pb$ age is independent of inter-element fractionation effects. Inverse and normal Concordia diagrams were produced using the Isoplot/Ex program of Ludwig (2004).

4 Zircon Morphology and Internal Structures

Sample ZG04-05: Zircons are 50–200 µm in diameter, light-pink colored, and have mainly euhedral to subeuhedral, and prismatic to acicular habits; several grains represent fragments of larger crystals. CL images display regular, fine-scale magmatic zoning with no inherited cores (Fig. 5). Fractures and mineral inclusions can be very abundant in some grains.

Sample ZG04-22: Zircon crystals range in size from 50 to 200 µm, and are brownish-red and generally have euhedral prismatic shapes (Fig. 6a). In CL images, zircon grains appear darker than the epoxy resin, suggesting that these zircons contain high U concentrations and/or are partially to highly metamict (e.g., Koshek 1993; Nasdala et al. 2002). Only one inherited core has

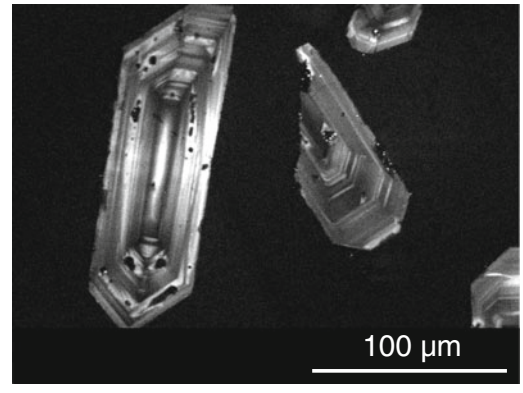

Fig. 5 Cathodoluminescence (CL) image of zircons from sample ZG04-05

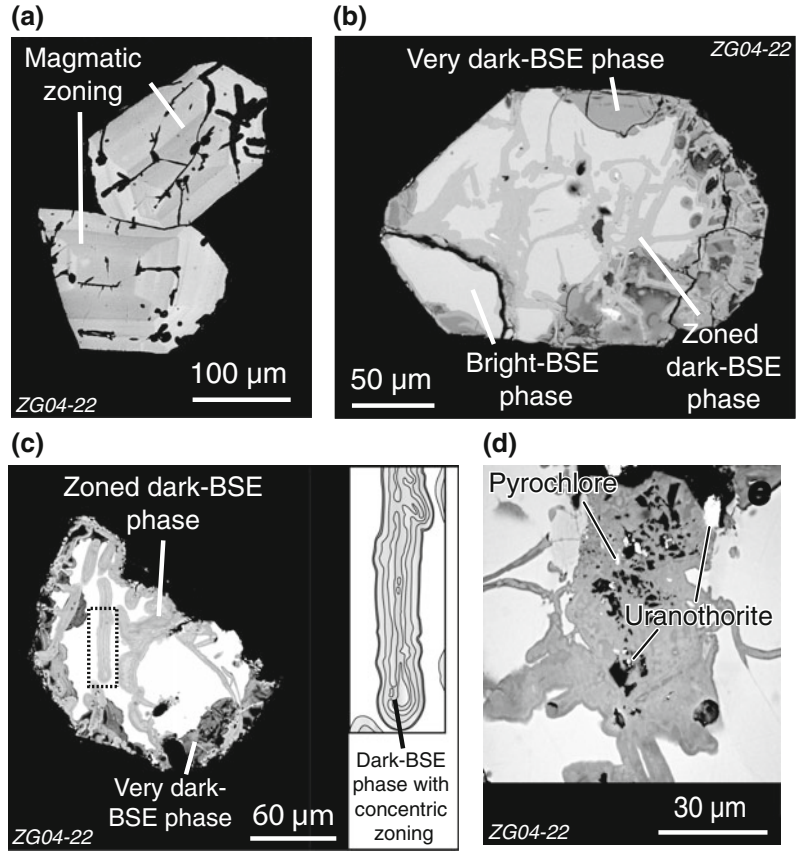

Fig. 6 Back-scattered electron (BSE) images of zircon from sample ZG04-22. **a** Bright-BSE phase exhibits oscillatory zoning typical of magmatic zircon. **b** Grain with dark and bright BSE phases; dark-BSE phase is divided into zoned dark-BSE and very dark-BSE phases. This latter phase is interpreted as a low-temperature alteration of metamict zircon; zoned dark-BSE phase follows cracks inferred to be high-temperature alteration related to albitization. **c** Zoned dark-BSE phase cuts bright-BSE zone along discontinuities and displays lobate and concentric zoning (*inset* on *right* shows details). **d** Close-up of zoned dark-BSE phase; several solid inclusions and micrometer-sized pores are indicative of volume change during dissolution-reprecipitation

been observed; in CL images it shows growth zoning typical of igneous zircon.

Sample ZG05-07: This sample contains only a few euhedral to subeuhedral, acicular to prismatic grains that generally exhibit oscillatory zoning. Grain sizes range from 50 to 300 µm. Some crystals are interpreted to be inherited zircon, which may be mantled by low-CL emission overgrowths (Fig. 7a). Locally, on CL images, fine-scale oscillatory zoning changes outward towards a homogeneous, low-CL emission zone (Fig. 7b). This growth pattern may reflect increasing U concentrations in zircon, from core to rim, possibly related to progressive enrichment of this element during differentiation of the rhyolitic melt.

BSE imaging of ZG04-22 and ZG05-07: BSE imaging distinguishes two major types of textures in the zircon grains (Figs. 6a–d and 7a–c). First, some domains exhibit oscillatory zoning or growth zoning (Fig. 6a) typical of igneous zircon (Corfu et al. 2003). Because these domains display the highest BSE intensities, they are termed here the *bright-BSE phase*. Second, other domains have low to very low BSE intensities (Figs. 6 and 7). These *dark-BSE phases* are typically developed in response to the circulation of hydrothermal fluids (Corfu et al. 2003; Rayner et al. 2005; Hay and

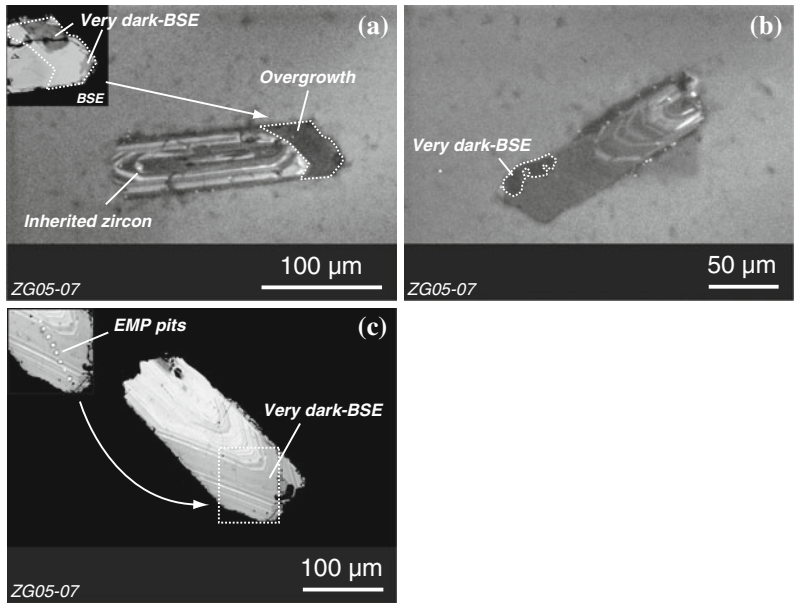

Fig. 7 SEM images of zircon from sample ZG05-07. **a** CL image of inherited zircon with dark U-rich overgrowth (i.e. Low-CL emission zone); *inset* in *upper left* shows BSE image of overgrowth with very dark-BSE phase overprint. **b** CL image of zircon with a low-CL emission rim; note slight alteration (very dark-BSE phase) at edge of low-CL emission rim. **c** BSE image of altered zircon. Very dark-BSE phase follows U-rich zones. Primary magmatic growth zoning is still visible; *inset* (*upper left*) corresponds to BSE image after EMP analysis; note strong pitting of very dark-BSE phase due to high hydrous concentration

Dempster 2009; Kusiak et al. 2009). Such dark-BSE phases in zircons from the Zgounder area can be subdivided into two categories:

(1) dark BSE phases characterized by lobate morphology and displaying concentric zoning (zoned dark-BSE phase; Fig. 6c). This type develops along former cracks and completely obliterates the original oscillatory zoning (Fig. 6a), and is generally small (5–40 µm wide). Detailed images of well-developed domains reveal a complex, spongy, and micro-porous texture (Fig. 6d). Altered domains are characterized by the presence of uranothorite, yttropyrochlore, apatite, calcite, quartz, phengite, and micron-sized pores typical of newly-crystallized hydrothermal zircon. These features are generally indicative of an aggressive attack by a hydrothermal fluid and related dissolution-reprecipitation processes (Tomasheck et al. 2003; Geisler et al. 2007; Kusiak et al. 2009; Nasdala et al. 2010);

(2) very dark-BSE phases can be distinguished by an extremely low BSE intensity. This feature generally occurs at the edges of zircon crystals and grows either progressively towards the center of grains or parallel to primary oscillatory zoning (Figs. 6b, c, and 7c). Such alteration is limited to the low CL emission area that represents U-rich domains (Fig. 7a, b). These alteration patterns are typical of low-temperature, altered metamict zircon that results from a diffusion-reaction process (Corfu et al. 2003; Rayner et al. 2005; Geisler et al. 2007; Kusiak et al. 2009).

5 Geochemistry of Magmatic and Hydrothermal Zircons

Magmatic zircon has stoichiometric compositions (ZrO_2 60–66.2 wt%; SiO_2 31.1–33.1 wt%; HfO_2 0.5–2.5 wt%; Table 2). Uranium and thorium concentrations vary significantly, from low values in sample ZG05-07 (UO_2 < 0.3–1.4 wt%; ThO_2 < 0.17–0.35 wt%), to extremely high U

Table 2 EMP analyses (wt% oxide) of zircon from samples ZG04-22 and ZG05-07

Sample	N°	ZrO_2	SiO_2	HfO_2	Y_2O_3	ThO_2	UO_2	P_2O_5	K_2O	CaO	FeO	Na_2O	Al_2O_3	MgO	MnO	Dy_2O_3	Yb_2O_3	Total	Comment
CAMECA SX 100																			
D.L.		*0.17*	*0.05*	*0.29*	–	*0.17*	*0.34*	*0.02*	*0.05*	*0.06*	*0.40*	*0.08*	*0.04*	*0.04*	*0.27*	*0.62*	*0.77*		
ZG04-22	118	63.11	31.11	–**	N/A	0.35	1.28	0.70	–	–	–	–	–	–	–	–	–	96.54	Bright–BSE
Zr17	119	61.61	31.51	1.75	N/A	0.52	1.34	0.51	–	–	–	–	–	0.06	–	–	0.77	98.07	
	120	61.31	31.30	1.62	N/A	0.53	2.04	0.36	–	–	–	–	–	0.07	–	–	–	97.22	
	121	53.84	28.24	–**	N/A	0.71	2.14	0.42	0.12	1.97	–	–	–	0.07	–	–	–	87.50	Zoned dark–BSE
	122	54.15	28.24	1.33	N/A	0.77	2.24	0.39	0.10	1.79	–	0.09	–	0.23	0.28	–	–	89.62	
	123	54.13	28.10	0.76	N/A	0.78	2.64	0.35	0.08	2.08	–	0.11	–	0.08	0.54	–	–	89.64	
	124	54.24	28.70	–	N/A	0.97	2.28	0.35	0.21	1.55	–	–	–	0.33	0.34	–	0.78	89.73	
	125	60.08	31.16	–**	N/A	1.01	2.85	0.37	–	–	–	–	–	0.04	–	–	–	95.51	Bright–BSE
	126	54.25	27.35	1.55	N/A	0.69	2.20	0.34	0.27	1.49	0.59	0.16	0.13	–	0.52	0.74	1.16	91.43	Zoned dark–BSE
	127	57.51	28.89	–	N/A	0.32	1.56	0.39	0.12	0.74	–	–	–	0.05	–	–	–	89.58	
D.L.		*0.16*	*0.05*	*0.21*	–	*0.17*	*0.37*	–	*0.05*	*0.06*	*0.38*	*0.08*	*0.04*	*0.04*	*0.27*	*0.60*	*0.76*		
ZG05-07	1	63.68	32.00	1.02	N/A	–	–	N/A	0.08	0.09	–	0.13	–	0.02	–	–	–	97.02	Bright–BSE
Zr4	2	65.49	33.29	2.45	N/A	–	–	N/A	–	–	–	–	–	0.12	–	–	–	101.35	
	3	65.93	32.99	1.23	N/A	–	–	N/A	–	–	–	–	–	0.04	–	–	–	100.19	
	4	65.67	32.78	0.87	N/A	–	–	N/A	–	–	–	0.10	–	0.20	–	–	–	99.62	
	5	63.61	32.11	1.14	N/A	–	–	N/A	–	–	–	–	0.15	0.10	–	–	–	97.10	
	6	56.24	28.26	0.63	N/A	–	0.55	N/A	–	0.34	1.71	0.13	0.53	0.28	–	–	–	88.66	Deep dark–BSE
	7	65.36	32.39	1.21	N/A	–	–	N/A	–	–	–	–	–	0.57	–	–	–	99.54	Bright–BSE
	8	63.99	31.97	1.55	N/A	–	–	N/A	–	0.07	–	–	0.30	0.07	–	–	–	97.96	
	9	60.15	29.93	1.13	N/A	–	0.46	N/A	0.28	0.26	0.65	0.19	0.27	0.30	–	–	–	93.62	Deep dark–BSE
	10	55.52	28.58	1.43	N/A	0.24	1.10	N/A	–	0.48	1.16	–	0.66	3.49	–	–	–	92.65	
	11	49.74	26.61	1.18	N/A	0.27	0.59	N/A	0.15	0.46	4.63	–	0.90	0.37	–	–	–	84.89	
	12	52.96	28.18	1.45	N/A	–	0.45	N/A	0.29	0.42	0.96	–	0.75	0.22	–	–	–	85.68	
	13	51.21	28.27	1.29	N/A	–	0.53	N/A	0.40	0.44	1.38	–	0.79	0.47	–	–	–	84.79	
	14	51.62	29.50	–**	N/A	0.28	0.83	N/A	0.23	0.43	1.06	–	0.78	0.11	–	–	–	84.84	
	15	49.69	29.11	1.29	N/A	0.35	0.92	N/A	–	0.43	1.39	–	0.96	0.09	–	–	–	84.23	
	16	55.74	27.69	0.93	N/A	0.29	0.67	N/A	–	0.31	1.60	–	0.60	0.35	–	–	–	88.19	
	17	53.36	28.53	–**	N/A	0.26	0.64	N/A	–	0.43	1.72	–	0.62	0.23	–	–	–	85.78	

(continued)

Table 2 (continued)

Sample	N°	ZrO_2	SiO_2	HfO_2	Y_2O_3	ThO_2	UO_2	P_2O_5	K_2O	CaO	FeO	Na_2O	Al_2O_3	MgO	MnO	Dy_2O_3	Yb_2O_3	Total	Comment
ZG05-07	35	65.33	31.30	1.64	N/A	–	1.38	N/A	–	–	–	–	0.04	0.09	–	–	–	99.77	Bright–BSE
Zr11	36	64.08	32.01	–**	N/A	–	0.94	N/A	–	–	–	–	–	0.05	–	–	–	97.08	
	37	64.28	32.50	–**	N/A	0.25	1.24	N/A	–	–	–	–	–	0.05	–	–	–	98.32	
	38	62.78	31.97	0.56	N/A	0.32	1.11	N/A	–	–	–	–	–	–	–	–	–	96.73	
	39	62.48	32.46	1.59	N/A	0.38	1.33	N/A	–	–	–	–	–	0.57	–	–	–	98.80	
	40	63.85	32.12	0.58	N/A	0.24	1.21	N/A	–	–	–	–	–	0.08	–	–	–	98.08	
	41	60.54	29.56	–**	N/A	0.18	0.87	N/A	–	0.20	0.54	–	–	–	–	–	–	91.89	Deep dark–BSE
	42	62.34	31.67	1.34	N/A	–	0.32	N/A	–	–	0.80	–	0.11	0.14	–	–	–	96.73	Bright–BSE
	44	62.41	32.08	0.47	N/A	–	0.60	N/A	–	–	–	–	–	0.90	–	–	–	96.46	
	45	64.08	32.13	1.45	N/A	–	1.11	N/A	–	–	–	–	–	0.77	–	–	–	99.53	
	46	62.89	31.97	1.37	N/A	–	0.75	N/A	–	–	–	–	–	0.16	–	–	–	97.14	
	47	65.70	32.23	0.52	N/A	–	–	N/A	–	–	–	–	–	0.17	–	–	–	98.62	
	48	65.36	32.32	1.01	N/A	–	0.42	N/A	–	–	–	–	–	0.12	–	–	–	99.23	
	49	63.96	32.60	1.47	N/A	–	–	N/A	–	–	–	–	–	0.28	–	–	–	98.31	
	50	65.01	32.68	1.42	N/A	–	–	N/A	–	–	–	–	–	–	–	–	–	99.10	
	51	64.95	33.11	1.80	N/A	–	0.39	N/A	–	–	–	–	–	–	–	–	–	100.25	
	52	64.91	32.89	0.55	N/A	–	0.42	N/A	–	–	–	–	–	0.09	–	–	–	98.85	
	53	65.42	32.59	0.80	N/A	–	0.37	N/A	–	–	–	–	–	–	–	–	–	99.18	
	54	66.17	32.77	1.43	N/A	–	–	N/A	–	–	–	–	–	0.09	–	–	–	100.46	
	56	65.69	32.75	1.10	N/A	–	–	N/A	–	–	–	–	0.05	0.88	–	–	–	100.47	
	57	65.07	32.66	0.44	N/A	–	–	N/A	–	–	–	–	0.09	0.19	–	–	–	98.45	
	58	64.55	32.84	–**	N/A	–	–	N/A	–	–	–	–	–	0.22	–	–	–	97.61	

(continued)

Table 2 (continued)

Sample	N°	ZrO_2	SiO_2	HfO_2	Y_2O_3	ThO_2	UO_2	P_2O_5	K_2O	CaO	FeO	Na_2O	Al_2O_3	MgO	MnO	Dy_2O_3	Yb_2O_3	Total	Comment
D.L.		*0.32*	*0.06*	*0.17*	*0.21*	*0.32*	*0.42*	*0.07*	*0.08*	*0.07*	*0.19*	*0.22*	*0.05*	*0.05*	*0.19*	–	*0.78*		
ZG05-07	10	65.18	31.23	1.11	–	0.33	–	0.61	–	–	–	–	0.08	–	–	N/A	–	98.53	Bright–BSE
Zr5	11	65.00	30.58	1.05	–	–	–	0.58	–	0.10	0.26	–	0.06	–	–	N/A	–	97.63	
	12	58.16	27.16	1.24	0.92	–	0.60	2.33	0.09	0.14	1.54	–	0.26	0.05	–	N/A	–	92.47	Deep dark–BSE
	13	53.94	24.34	1.04	2.02	–	0.57	3.67	0.16	0.31	1.79	–	0.39	–	–	N/A	–	88.22	
	14	51.11	22.77	1.13	2.11	0.37	0.79	4.14	–	0.34	2.06	–	0.42	–	–	N/A	–	85.23	
	15	46.67	20.11	1.33	2.69	–	0.74	5.69	–	0.71	2.30	–	0.59	–	–	N/A	–	80.83	
ZG05-07	16	65.37	31.56	1.00	–	–	0.18	0.35	–	–	–	–	–	–	–	N/A	–	98.46	Bright–BSE
Zr11	17	63.66	31.20	1.74	–	0.40	1.22	0.53	–	–	–	–	–	–	–	N/A	–	98.75	

Abbreviation: *D.L.* detection limit in wt%; "-" below detection limit, **Analytical problem suspected for these analyses

concentrations in sample ZG04-22 (UO_2 1.28–2.85 wt%; ThO_2 0.35–1.01 wt%). Light REE (LREE) are low (e.g., La $\leq$ 0.1 ppm), whereas heavy REE (HREE) show high concentrations (e.g., Yb > 6400 ppm; Table 3). REE patterns of the magmatic phase (Fig. 8) increase steeply from La to Lu ($Lu_N/Gd_N > 39$; $Sm_N/La_N > 200$), and show a strong positive Ce anomaly (Ce/Ce* > 123) and negative Eu anomaly (Eu/Eu* < 0.03; Fig. 10). This distinctive REE signature is characteristic of zircons that have crystallized from a strongly fractionated (large negative Eu anomaly) and oxidized (large positive Ce anomaly) silicate melt (Hoskin and Schaltegger 2003; Hoskin 2005; Pelleter et al. 2007; Pelleter et al. 2008; Pettke et al. 2005).

5.1 Hydrothermal Domains in Zircons

Due to a relatively large ion spot (ca. 25 µm) and small grain sizes of zircon, only a few REE analyses were acquired on the hydrothermal domains. Also, some analyses yield a mixed signature between bright- and dark-BSE zones, and thus are not meaningful. Zoned dark-BSE phases are characterized by low ZrO_2 and SiO_2 concentrations (Table 2). An electron microprobe profile across (Fig. 9) clearly shows a drop of ZrO_2 and SiO_2 contents from magmatic to hydrothermal domains (i.e., ~63.1 to ~54.1 wt% ZrO_2 and ~31.5 to ~28.2 wt% SiO_2). In addition, hydrothermal areas can be significantly enriched in non-essential elements (Table 2) such as CaO (0.7–2.1 wt%), MnO (up to 0.54 wt%), K_2O (0.08–0.27 wt%), MgO (0.05–0.33 wt%), FeO (up to 0.59 wt%), Na_2O (up to 0.16 wt%), and Al_2O_3 (up to 0.13 wt%). Significant gains of such elements have been reported in previous studies of experimentally altered metamict zircon (Geisler et al. 2003a) and natural samples (Geisler et al. 2003b; Rayner et al. 2005; Kusiak et al. 2009; Nasdala et al. 2010). Highly altered domains in zircon are also characterized by low analytical total (i.e., 87.5–94 wt%; Table 2), which could reflect relatively high concentrations of hydrous species (Caruba and Iacconi 1983; Woodhead et al. 1991; Geisler et al. 2003a) and/or the presence of nanometer-sized pores (Nasdala et al. 2009). Hydrothermal domains display high HREE concentrations (up to 8508 ppm for Yb) and relatively high LREE contents (La 29 and 142 ppm). REE patterns (Fig. 8) show flat profiles ($Lu_N/Gd_N < 13$; $Sm_N/La_N < 47$) with moderately low Eu negative anomalies (Eu/Eu* $\geq$ 0.3) and small cerium positive anomalies (Ce/Ce* 2.1 and 3.6). This REE signature suggests that hydrothermal phases crystallized in the presence of a hot and reduced hydrothermal fluid (Pelleter et al. 2007). The difference between magmatic and hydrothermal domains in zircons appears clearly in a Ce/Ce* versus Eu/Eu* diagram (Fig. 10). Analyses that plot on a mixing hyperbola defined the magmatic and hydrothermal end members.

Very dark-BSE domains display low to very low ZrO_2 and SiO_2 concentrations (46.7–60.2 and 20.1–29.9 wt%, respectively; Table 2). Uranium content varies from 0.46 to 1.10 wt% UO_2 and thorium is up to 0.37 wt% ThO_2. Non-essential elements including FeO (0.65–4.63 wt%), MgO (0.05–3.5 wt%), Al_2O_3 (0.26–0.96 wt%), CaO (0.14–0.71 wt%), and K_2O (up to 0.4 wt%) are strongly incorporated into the zircon structure. Yttrium and phosphorous can be highly enriched (up to 2.7 and 5.7 wt%, respectively; Table 2) and correlate with the lowest SiO_2 and ZrO_2 concentrations. These chemical signatures differ from those of the zoned dark-BSE domains.

6 U–Pb Results

Sample ZG04-05: Sixteen in situ SIMS U–Pb analyses were performed (Table 4). On the inverse Concordia diagram (Tera and Wasserburg 1972) most analyses are discordant (Fig. 11). Dispersion along the $^{207}Pb/^{206}Pb$ axis underlines the incorporation of common lead during crystallization of zircon, whereas dispersion along the $^{238}U/^{206}Pb$ axis is most likely related to large Pb loss during later hydrothermal events. As a consequence, nearly all of the discordant analyses were rejected for age calculation. The only concordant analysis yields a $^{238}U/^{206}Pb$ age at 617 ± 6 Ma. A mixing line between the three

Table 3 REE data on zircons from sample ZG04-22

Name of REE analysis	Contents (ppm)											Ce*/Ce	Eu*/Eu	Domain
	La	Ce	Pr	Nd	Sm	Eu	Gd	Dy	Er	Yb	Lu			
ZG22-8b	<d.l.	111	<d.l.	3	13	0.3	175	2013	3180	6487	1005	>270	0.01	Bright-BSE
ZG22-11	<d.l.	83	0.2	6	16	0.3	211	2152	4139	6409	1067	>150	0.01	Bright-BSE
ZG22-12	0.1	87	0.3	8	20	0.7	220	2235	3842	6491	1084	123	0.03	Bright-BSE
ZG22-2	142	1119	116	1034	313	69	909	4240	5154	6989	1446	2.1	0.59	Zoned dark-BSE
ZG22-14	29	537	47	854	263	32	781	4328	5559	8508	1453	3.6	0.31	Zoned dark-BSE
ZG22-1	2	101	1	19	18	3	200	1883	3535	5888	1077	15.8	0.10	Mixed
ZG22-1b	5	112	3	27	21	3	164	1293	2285	3594	628	6.8	0.14	Mixed

Note Relative analytical errors are ca. 35–40 % for La, 15–20 % for Ce, 30–35 % for Pr, 20–25 % for Nd and Sm, 25–30 % for Eu, 15–20 % for Gd, and 8–14 % for Dy to Lu; *<d.l.* below detection limit (0.1 ppm); Ce and Eu anomalies were calculated in this manner: $Ce/Ce^* = Ce_N/(sqrt(La_N \times Pr_N))$ and $Eu/Eu^* = Eu_N/(sqrt(Sm_N \times Gd_N)$; Chrondrite normalizing values from McDonough and Sun (1995)

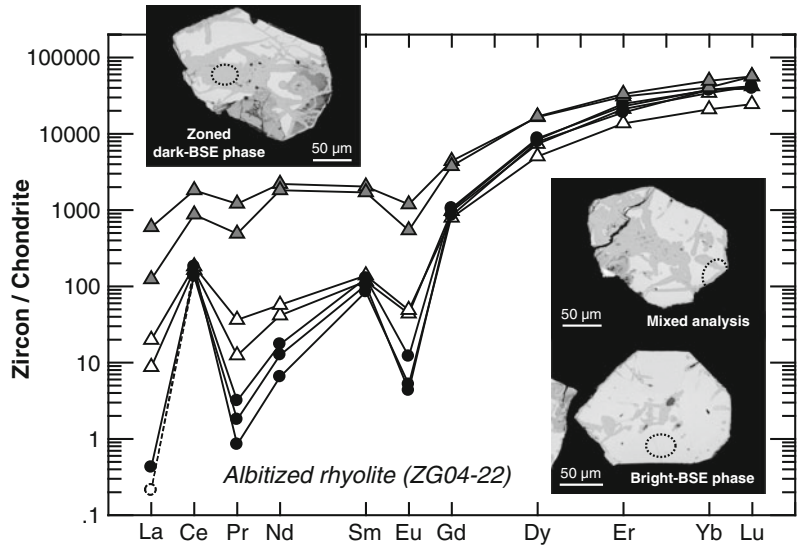

Fig. 8 Chondrite-normalized REE patterns of zircons from sample ZG04-22. *Grey triangle* represents zoned dark-BSE phase (hydrothermal domain); *filled black circle* corresponds to bright-BSE phase (igneous domain); *open triangle* represents mixed analyses of two domains. Chondrite data from Sun and McDonough (1989)

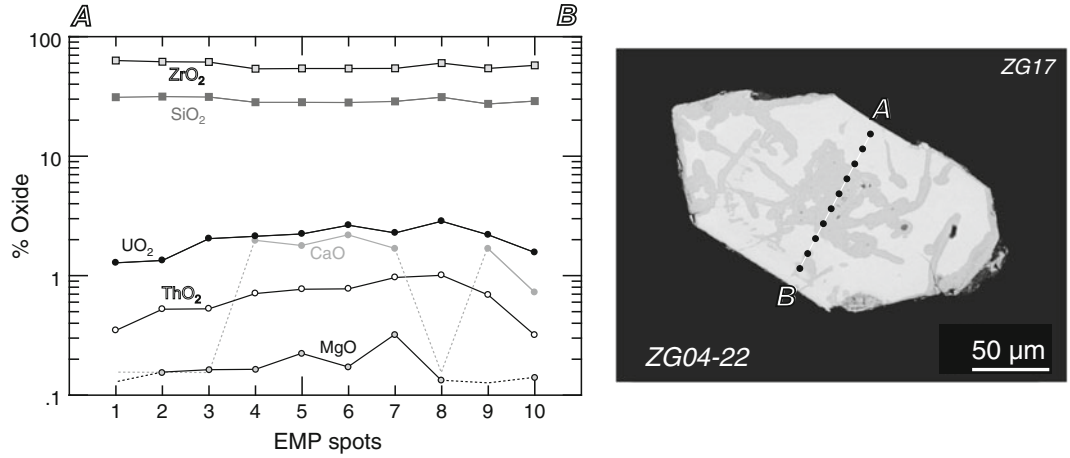

Fig. 9 EMP traverse of zircon from sample ZG04-22 (*left*); section line of traverse (*right* BSE image) is across bright- and dark-BSE phases. Latter phase has low Zr and Si concentrations, and displays strong enrichment in Ca as a non-essential element

zircon analyses and the common Pb composition at 600 Ma (i.e., $^{207}Pb/^{206}Pb = 0.8774$) is plotted on Fig. 6. A lower intercept age at 610 ± 7 Ma (MSWD = 1.9) and a mean $^{238}U/^{206}Pb$ age of 610 ± 7 Ma (MSWD = 1.7, $n = 3$) were calculated. This age (i.e. 610 ± 7 Ma) is similar to the age of 606 ± 6 Ma reported for the Tadmant rhyolite by Thomas et al. (2002).

Sample ZG05-07: Only three analyses of zircon from this sample gave reliable data (Table 5). Among these analyses, one point is concordant yielding a $^{207}Pb/^{206}Pb$ age at 576 ± 10.5 Ma.

Sample ZG04-22: The two analyses obtained on the inherited zircon crystal are concordant to subconcordant (Fig. 12a). These data yield two

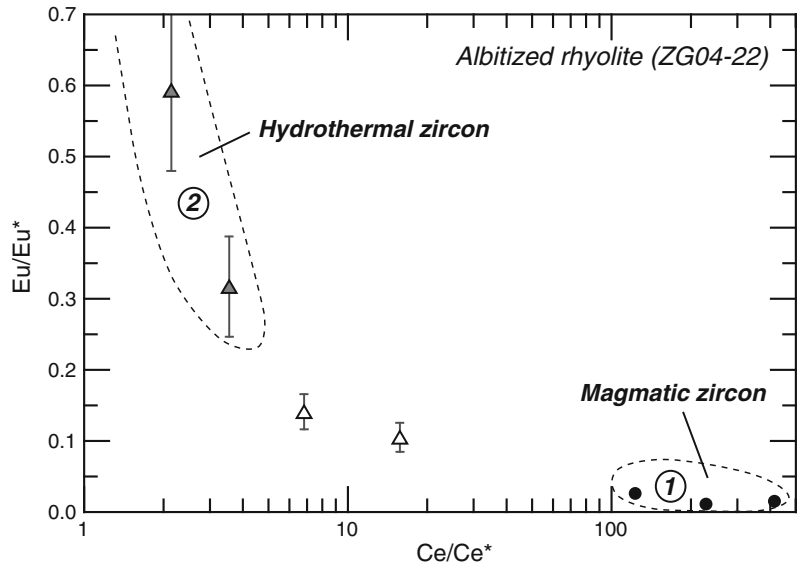

Fig. 10 Plot of europium anomaly (Eu/Eu*) versus cerium anomaly (Ce/Ce*) for zircon from sample ZG04-22. *1* Magmatic zircon field. *2* Hydrothermal zircon field. Legend as in Fig. 8

$^{206}Pb/^{238}U$ ages at 819 ± 7 and 815 ± 7 Ma for core and rim; respectively (Table 5).

SIMS analyses performed on bright- and dark-BSE phases show strongly discordant $^{207}Pb/^{235}U$, $^{206}Pb/^{238}U$, and $^{207}Pb/^{206}Pb$ ages. In Fig. 12a, most of the data display reverse discordance, which is a common, but not general, feature of U-rich zircon (Williams and Hergt 2000; Nasdala et al. 2002; Geisler et al. 2003b; Rayner et al. 2005). Three explanations can account for such apparent reversely discordant data: (1) a strong uranium depletion during recent events (Romer 2003; Nasdala et al. 2010), (2) U and Pb fractionation due to decomposition of zircon in oxides (i.e., $ZrSiO_4 \rightarrow ZrO_2 + SiO_2$) during annealing processes (Nasdala et al. 2002), and (3) analytical problems during calibration of U–Pb ratios in relation with high U contents in analyzed grain compared to zircon standards (Black et al. 1991; Rayner et al. 2005). Even if the two first processes occurred, the differences in U and Th concentrations (i.e., matrices) between the standard zircon and the U-rich analyzed zircons make it impossible to reliably calibrate for the U–Pb fractionation. This problem would explain most of the observed reverse discordance. As a consequence, only $^{207}Pb/^{206}Pb$ ages were used for age calculation, because Pb ratios are not affected. However, use of Pb/Pb ages implies that zircons did not lose Pb. A probable disturbance of the U–Pb system may have occurred during Late Miocene–Early Pliocene volcanism (8–5 Ma), but its effect on the $^{207}Pb/^{206}Pb$ ratio can be considered negligible (see below). An opening of U–Pb system is also possible during the Variscan or Alpine orogenesis. However, since the Sirwa window was not significantly overprinted thermally (>300 °C) during these events (Thomas et al. 2002), we assume that $^{207}Pb/^{206}Pb$ ages provide a good estimate of crystallization ages.

Analyses performed on magmatic zircons (bright-BSE phases) from sample ZG04-22 are plotted in a Concordia diagram and are scattered along a Discordia line that yields an upper intercept age at 576 ± 27 Ma and a lower intercept age at 6 ± 97 Ma (Fig. 12b). This lower intercept may be related to a slight opening of the U–Pb system during the Cenozoic magmatic event. The upper intercept age is in good agreement with the calculated mean $^{207}Pb/^{206}Pb$ age of 578 ± 4 Ma (n = 10; MSWD = 2). This age is similar to the $^{207}Pb/^{206}Pb$ age of 576 ± 11 Ma for sample ZG05-07 (Table 2). Therefore, we consider that the age of 578 ± 4 Ma corresponds to the age of emplacement of rhyolitic dikes and plugs of the Assarag suite in the Zgounder area.

Table 4 U–Pb isotopic data for zircons from sample ZG04-05

Name of U–Pb analysis	Contents (ppm)				Measured	% Pbc	Corrected ratios						Ages (Ma)					
	Pb	U	Th	Th/U	$^{204}Pb/^{206}Pb$		$^{207}Pb/^{206}Pb$	±	$^{206}Pb/^{238}U$	±	$^{207}Pb/^{235}U$	±	$^{206}Pb/^{238}U$	±	$^{207}Pb/^{235}U$	±	$^{206}Pb/^{207}Pb$	±
ZG0405																		
ZG0405-1	53	767	488	0.64	0.00067	3.06	0.0572	0.0165	0.0800	0.0013	0.6317	0.0147	496.3	7.8	497.1	9.1	1040.5	22.5
ZG0405-3	11	134	65	0.49	0.00063	1.12	0.0583	0.0271	0.0958	0.0011	0.7695	0.0227	589.8	6.6	579.5	13.0	539.5	54.3
ZG0405-4	21	321	229	0.71	0.00082	1.95	0.0568	0.0409	0.0779	0.0023	0.6105	0.0308	483.8	13.8	483.9	19.2	638.2	74.7
ZG0405-5	12	151	82	0.54	0.00259	4.83	0.0570	0.0735	0.0902	0.0019	0.7089	0.0542	556.8	11.2	544.1	31.7	10.0	149.8
ZG0405-6	23	288	246	0.85	0.00037	1.06	0.0590	0.0135	0.0929	0.0013	0.7558	0.0147	572.9	7.7	571.6	8.5	688.4	24.4
ZG0405-7	68	890	742	0.83	0.00102	1.95	0.0588	0.0063	0.0888	0.0014	0.7196	0.0122	548.4	8.3	550.5	7.2	600.4	11.8
ZG0405-8	13	158	75	0.48	0.00215	3.83	0.0597	0.0706	0.0992	0.0019	0.8160	0.0598	609.6	11.2	605.8	32.9	592.1	139.2
ZG0405-10	15	187	104	0.56	0.00176	2.70	0.0596	0.0368	0.0940	0.0010	0.7729	0.0296	579.2	5.8	581.4	16.8	444.1	77.6
ZG0405-11	17	202	146	0.72	0.00009	0.16	0.0612	0.0076	0.0980	0.0017	0.8274	0.0157	602.9	10.0	612.2	8.7	646.7	14.9
ZG0405-12	26	316	213	0.67	0.00286	5.08	0.0596	0.0690	0.0970	0.0015	0.7973	0.0565	596.8	9.1	595.3	31.4	589.7	137.0
ZG0405-13	27	332	250	0.75	0.00017	0.30	0.0596	0.0076	0.0955	0.0021	0.7847	0.0184	588.2	12.4	588.2	10.4	588.1	15.1
ZG0405-15	16	192	111	0.58	0.00209	3.05	0.0613	0.0829	0.0961	0.0011	0.8118	0.0680	591.2	6.8	603.5	37.4	649.7	168.6
ZG0405-16	11	139	87	0.63	0.00114	1.52	0.0517	0.0203	0.0949	0.0009	0.6764	0.0150	584.7	5.1	524.6	9.1	271.0	45.8
ZG0405-18	33	393	308	0.78	0.00017	0.14	0.0596	0.0062	0.0983	0.0009	0.8077	0.0089	604.6	5.2	601.2	5.0	588.0	13.4
ZG0405-19	19	223	149	0.67	0.00023	0.11	0.0598	0.0082	0.1005	0.0009	0.8288	0.0103	617.3	5.5	612.9	5.7	596.8	17.6
ZG0405-20	11	131	67	0.51	0.00069	0.67	0.0576	0.0173	0.0959	0.0009	0.7615	0.0151	590.3	5.4	574.9	8.7	514.2	37.6

Note %Pbc is the percent of common lead in the ^{206}Pb intensity as determined by measured ^{204}Pb concentrations

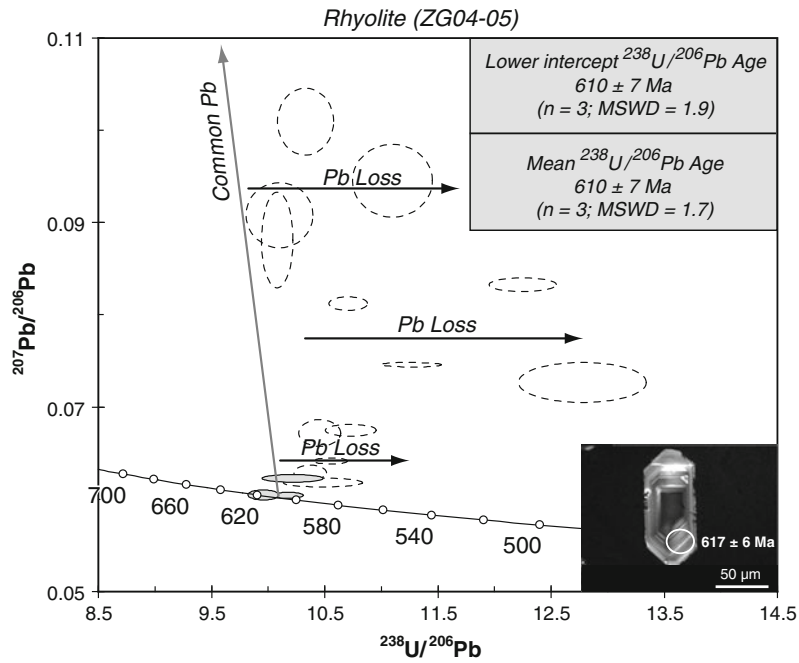

Fig. 11 Inverse Concordia plot for zircon data from rhyolite sample ZG04-05. Most analyses are characterized by common Pb contribution and significant Pb loss. CL image (*lower right*) represents concordant zircon

Hydrothermal domains in zircon crystals (dark-BSE phases) yield less-reliable age data on one sample (ZG04-22; Fig. 12c). Data are scattered along a Discordia line characterized by an upper intercept age at 560 ± 21 Ma and a lower intercept age at 21 ± 120 Ma (Fig. 12c). The 560 ± 21 Ma age is in agreement with the calculated mean $^{207}Pb/^{206}Pb$ age of 564 ± 15 Ma (n = 7; MSWD = 6.6). This less precisely defined $^{207}Pb/^{206}Pb$ age and the large dispersion of $^{207}Pb/^{206}Pb$ ages may reflect analytical spots that overlap hydrothermal domains, inclusions, and/or magmatic zones. However, the 564 ± 15 Ma age matches, within error, the 578 ± 4 Ma age determined on the bright-BSE phases of the same sample.

7 Timing of Magmatic/Hydrothermal Events in the Zgounder District

One inherited zircon has been identified during this study. It provides an age of ca. 818 Ma, which has not been mentioned in previous studies (Thomas et al. 2002). However, ages at 880 Ma were recorded for old detrital zircons from the Saghro turbidites (Liégeois et al. 2006). According to geodynamic reconstructions (e.g., Thomas et al. 2002, 2004; Gasquet et al. 2005, 2008), this age of ca. 818 Ma might be related to ocean opening during the break-up of the Mesoproterozoic supercontinent Rodinia. It attests to reworking of the Neoproterozoic crust during the Pan-African orogeny.

We have determined two distinct late Neoproterozoic magmatic ages in the Zgounder area. The first, 610 ± 7 Ma, was obtained on the rhyolitic domes (sample ZG04-05) from the Tadmant Formation, and is similar to the age of 606 ± 6 Ma reported by Thomas et al. (2002) for the same formation. The second age was obtained for zircons from the rhyolitic hypabyssal dikes and plugs (samples ZG04-22 and ZG05-07). For these samples, the $^{207}Pb/^{206}Pb$ ages were used to calculate a mean age of 578 ± 4 Ma. Similar U–Pb ages were proposed by Thomas et al. (2002) for the Tourcht Diorite (579 ± 7 Ma), a rhyolite from the Tikhfist Formation (571 ± 8 Ma), the Aguins member (577 ± 8 Ma), and the Tilsakht Granite (579 ± 7 Ma) emplaced in the Sirwa massif.

Table 5 U–Pb isotopic data for zircons from samples ZG04-22 and ZG05-07

Name of U–Pb analysis	Contents (ppm)				Measured $^{204}Pb/^{206}Pb$	% Pbc	Corrected ratios						Ages (Ma)						Discordance	Phase analyzed
	Pb	U	Th	Th/U			$^{207}Pb/^{206}Pb$	±	$^{206}Pb/^{238}U$	±	$^{207}Pb/^{235}U$	±	$^{206}Pb/^{238}U$	±	$^{207}Pb/^{235}U$	±	$^{206}Pb/^{207}Pb$	±		
ZG0422																				
ZG0422-1	1515	13318	5883	0.44	0.00002	0.03	0.0594	0.0014	0.1324	0.0012	1.0847	0.0096	801.3	6.6	745.9	4.6	583.2	2.9	27	Bright-BSE
ZG0422-2	1009	8811	3186	0.36	0.00001	0.02	0.0592	0.0019	0.1333	0.0012	1.0886	0.0099	806.4	6.7	747.8	4.8	576.3	4.1	29	
ZG0422-3	1057	8533	3219	0.38	0.00009	0.15	0.0592	0.0040	0.1441	0.0013	1.1757	0.0114	868.0	7.1	789.3	5.3	572.9	8.1	34	
ZG0422-4	1320	11756	4752	0.40	0.00003	0.06	0.0594	0.0021	0.1307	0.0012	1.0697	0.0097	791.8	6.6	738.6	4.7	580.4	4.3	27	
ZG0422-5	939	8234	3054	0.37	0.00006	0.10	0.0595	0.0026	0.1327	0.0012	1.0882	0.0102	803.1	6.8	747.6	4.9	585.1	5.4	27	
ZG0422-6	2274	14659	7388	0.50	0.00001	0.00	0.0595	0.0019	0.1806	0.0017	1.4808	0.0139	1070.0	9.1	922.6	5.7	584.8	4.0	45	
ZG0422-7	2032	15996	7476	0.47	0.00005	0.07	0.0592	0.0024	0.1478	0.0013	1.2064	0.0113	888.8	7.5	803.5	5.2	573.9	5.2	35	
ZG0422-8	1315	11636	6458	0.56	0.00007	0.08	0.0594	0.0032	0.1315	0.0012	1.0770	0.0103	796.4	6.8	742.2	5.0	582.0	7.0	27	
ZG0422-9	800	7803	2765	0.35	0.00025	0.44	0.0590	0.0055	0.1193	0.0010	0.9706	0.0101	726.6	6.0	688.7	5.2	566.9	10.8	22	
ZG0422-14	1348	10887	3705	0.34	0.00001	0.00	0.0591	0.0012	0.1441	0.0014	1.1743	0.0111	868.0	7.6	788.7	5.2	570.4	2.8	34	
ZG0422-10	1124	12162	5402	0.44	0.00008	0.14	0.0589	0.0026	0.1076	0.0011	0.8735	0.0090	658.6	6.2	637.5	4.8	563.5	5.2	14	Zoned dark-BSE
ZG0422-11	938	11834	5147	0.43	0.00017	0.31	0.0595	0.0025	0.0922	0.0009	0.7567	0.0076	568.7	5.3	572.1	4.4	585.6	5.0	−3	
ZG0422-12	785	8786	5939	0.68	0.00956	17.08	0.0579	0.0379	0.1040	0.0011	0.8303	0.0327	638.1	6.5	613.8	18.0	526.0	76.0	18	
ZG0422-13	1664	17389	6645	0.38	0.00298	4.69	0.0585	0.0160	0.1113	0.0010	0.8983	0.0167	680.5	6.1	650.8	8.9	549.0	34.6	19	
ZG0422-15	1744	15813	6581	0.42	0.00012	0.20	0.0591	0.0026	0.1284	0.0012	1.0454	0.0102	778.6	6.9	726.6	5.1	569.4	5.6	27	
ZG0422-16	1605	17282	9033	0.52	0.00006	0.06	0.0585	0.0020	0.1081	0.0010	0.8719	0.0085	661.7	6.0	636.6	4.6	548.7	4.3	17	
ZG0422-17	1071	20861	10869	0.52	0.00021	0.30	0.0581	0.0051	0.0598	0.0011	0.4790	0.0089	374.3	6.5	397.4	6.1	534.3	11.0	-43	
ZG0422-18	19	162	171	1.06	0.00029	0.21	0.0649	0.0098	0.1355	0.0012	1.2136	0.0163	819.4	7.0	806.9	7.4	772.5	20.5	6	inh. core
ZG0422-19	38	325	172	0.53	0.00011	0.03	0.0668	0.0045	0.1348	0.0013	1.2419	0.0128	815.1	7.1	819.7	5.8	832.4	9.4	-2	inh. core
ZG0507																				
ZG0507-1	924	10092	2502	0.25	0.00026	0.25	0.0593	0.0034	0.1065	0.0013	0.8708	0.0112	652.7	7.7	636.0	6.1	577.3	7.3	12	Bright-BSE
ZG0507-2	626	6828	1362	0.20	0.00017	0.02	0.0594	0.0016	0.1067	0.0013	0.8740	0.0110	653.8	7.8	637.8	6.0	581.4	3.5	11	
ZG0507-3	56	700	71	0.10	0.00009	0.13	0.0592	0.0049	0.0937	0.0021	0.7655	0.0178	577.4	12.5	577.2	10.2	576.2	10.5	0	

Note %Pbc is the percent of common lead in the ^{206}Pb intensity as determined by measured ^{204}Pb concentrations; Discordance: difference between the ^{204}Pb-corrected $^{206}Pb/^{238}U$ and $^{207}Pb/^{206}Pb$ ages; *inh. core* inherited core

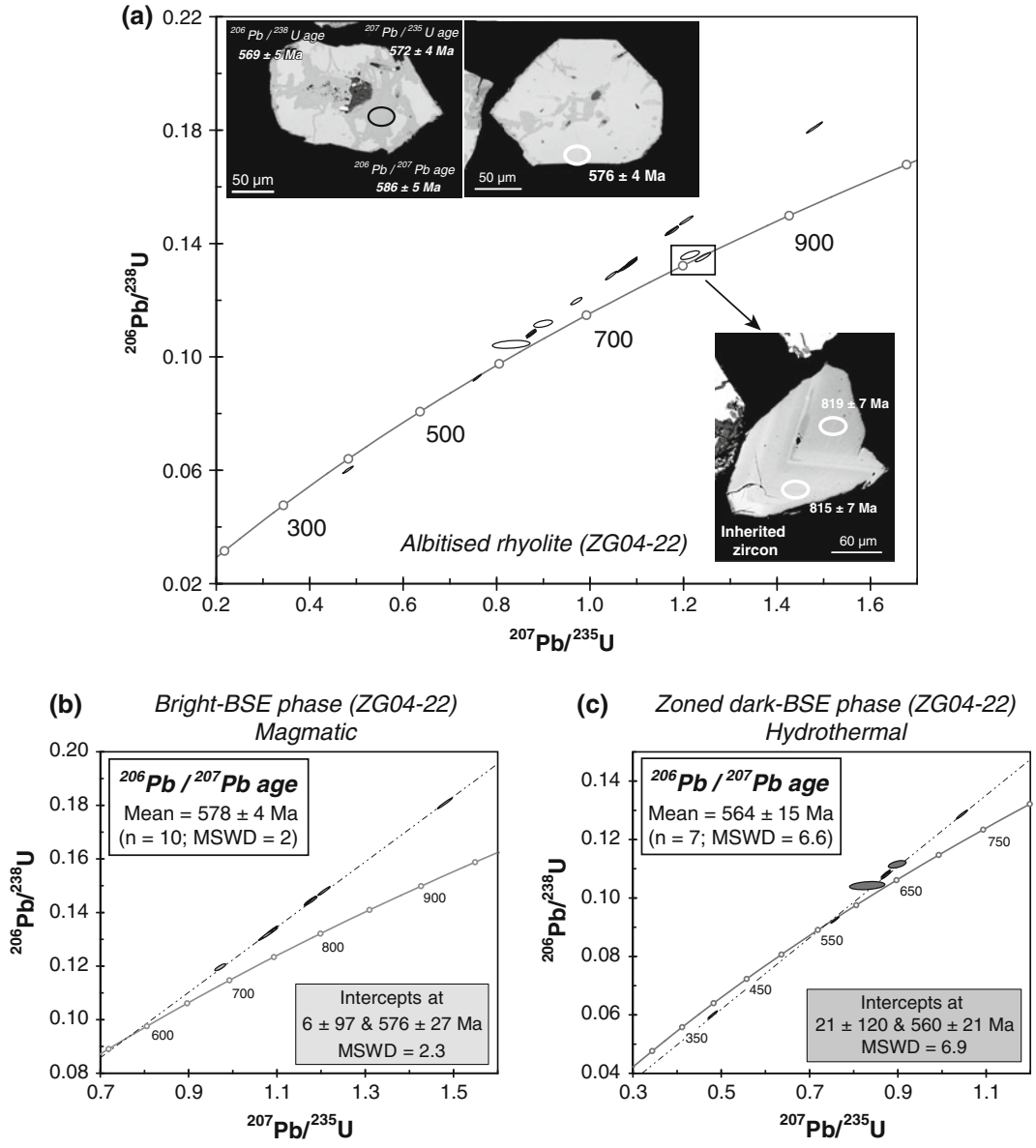

Fig. 12 **a** Concordia plot for zircon data from rhyolite sample ZG04-22. CL images show analyzed zircon crystals or domains: dark-BSE phase, bright-BSE phase, and inherited zircon. **b** Concordia plot for bright-BSE/magmatic phase. **c** Concordia plot for dark-BSE/hydrothermal phase

These geochronological results clearly demonstrate the existence of at least two periods of magmatic activity in the Zgounder district of the Sirwa window during the late Neoproterozoic.

Hydrothermal domains are well documented by precise textural and chemical analyses of zircons from the rhyolitic volcanic rocks in the district (Pelleter et al. 2008). Due to a high content of uranium in the original zircons (up to 2.9 %) and to subsequent pervasive hydrothermal alteration, in situ U/Pb dating of the hydrothermal domains has proved difficult (large dispersion of data, Pb loss, few concordant points). The best U/Pb age we have obtained on hydrothermal domains

(564 ± 15 Ma) is less precise, but significantly younger than, the age of the rhyolitic plugs and dikes (578 ± 4 Ma), notwithstanding the larger analytical uncertainty of the former. Whether this age for the hydrothermal domains represents a dissolution-reprecipitation or a diffusion-reaction process remains an open question, considering the few analyses available. The first hypothesis implies that the measured age records effects of the alteration. The diffusion-reaction process reflects a mixing between a crystallization age and a multistage alteration, which can affect metamict zircons until recent time (heritage), making such data meaningless. Considering the similarity between the alteration paragenesis of the rhyolitic plugs (albitization, chloritization, hydrothermal zircon containing apatite, calcite, quartz, and phengites; this study) and the albite-chlorite veins associated with formation of the Ag paragenetic stage (Essarraj et al. 1998; Marcoux and Wadjinny 2005), it seems reasonable to correlate the two events. Other arguments are geological (spatial association of the epithermal Zgounder Ag–Hg deposit with major rhyolitic volcanism), structural (E-W strike of mineralized fractures and rhyolitic dike; Fig. 1), and geochemical (depositional temperature of 400–500 °C for early paragenetic stage deduced from fluid inclusions, suggesting a magmatic influence; Marcoux and Wadjinny 2005). Additionally, the Pb isotope model age of 550 Ma proposed by Marcoux and Wadjinny (2005) for the ore deposit fits well with the Neoproterozoic age of the whole magmatic sequence in the Zgounder district. We therefore consider the U/Pb age of 564 ± 15 Ma obtained on hydrothermal zircons from sample ZG04-22 (this study) as recording a dissolution-reprecipitation process, thus representing the best estimate, with a large error range, of this alteration process. This interpretation does not preclude the possibility of later remobilization during the Hercynian and/or Alpine orogenies leading to perturbations of the U/Pb geochronometer (particularly the $^{207}Pb/^{206}Pb$ ratio). Indirect dating of the Zgounder Ag mineralization using hydrothermally altered zircon therefore does not provide a robust age. However, these new U/Pb data support the conclusions of Smeykal (1972), Choubert et al. (1980), and Marcoux and Wadjinny (2005) linking the genesis of this deposit to the late Neoproterozoic magmatic event in the Anti-Atlas Mountains. Consequently, these authors ruled out the Triassic age proposed by Essarraj et al. (1998) and Essarraj et al. (2005) for the deposition of most of the Ag–Hg mineralization at Zgounder. Precise dating of the Ag–Hg paragenetic stage would provide an ultimate answer to this controversy.

8 Conclusions

Strongly altered U-rich zircons were selected to determine in situ U–Pb ages of the multistage rhyolitic intrusions associated with the Ag–Hg Zgounder deposit in the Sirwa window of the Anti-Atlas, Morocco. This highly differentiated magmatism is linked to pervasive hydrothermal alteration (albitization and chloritization) probably genetically related to the Ag–Hg mineralization. Based on morphological features, internal microstructures, and chemical characteristics, two types of zircon representing two stages of magmatic and hydrothermal evolutions are characterized. Geochronological data acquired by in situ SIMS analysis records four geological events:

(1) the ca. 815 Ma age reflects inheritance and illustrates reworking of the Neoproterozoic crust during the Pan-African (~885–555 Ma) orogenic cycle;

(2) the 610 ± 7 Ma, and (3) 578 ± 4 Ma ages correspond to emplacement-crystallization of the multistage rhyolitic intrusions, which record a large magmatic input into the upper crust of the Pan-African chain during the late Neoproterozoic; and

(4) a less-precise age at 564 ± 15 Ma obtained on hydrothermally altered domains can be related to dissolution-reprecipitation of magmatic zones. Presently, this age is the best estimate for the timing of albitization/mineralization in the Zgounder Ag–Hg deposit.

Late Neoproterozoic magmatism dated at 620–550 Ma is well documented in the Zgounder district and neighboring areas (Askaoun and Ida ou Illoun batholith; Thomas et al. 2002; Toummite et al. 2013 this study). This time period

brackets also the previous ages obtained for magmatic-hydrothermal evolution in the Imiter Ag–Hg deposit (Levresse 2001; Cheilletz et al. 2002; Levresse et al. this volume). These two major precious-metal deposits, situated 200 km apart, highlight the importance of the late Neoproterozoic epithermal silver-rich metallogenic belt in the Anti-Atlas (Cheilletz et al. 2002; Gasquet et al. 2005; Marcoux and Wadjinny 2005). Within the Zgounder district, additional field work is necessary to better characterize the structural controls on the Ag–Hg mineralization. In fact, it has been demonstrated at Imiter that normal faulting associated with the development of a passive continental margin during the Precambrian/Cambrian transition in the Anti-Atlas was a fundamental parameter for controlling magmatism and related mineralization.

Similar tectonic control might exist in the Zgounder district that thus could be used for a better strategy in mineral exploration programs. In this context, we emphasize the importance of E-W and conjugate veins and rhyolitic dikes, E-W development of the Azarwas Conglomerate that reflects an old normal fault, and lastly the presence south of the district of an E-W continental-scale structure, the Anti-Atlas Major Fault.

Acknowledgments This study was supported by two scientific cooperative grants awarded to A.C. and D.G. by the French Ministry of Industry (# 03 2 24 00 03 and # 00 01 324) and the Office National des Hydrocarbures et des Mines (Morocco). We would like to thank M. Champenois, D. Mangin, and C. Rollion-Bard for use of the Cameca IMS1270 and IMS 3F facilities at CRPG-CNRS in Nancy, and Johann Ravaux and Alain Kholer for access to the Hitachi 2500 SEM and CAMECA SX100 and SX50 electron microprobe facilities at Université de Lorraine in Nancy. We gratefully thank Mohammed Bouabdellah and John Slack for their constructive comments which helped us to improve the manuscript.

References

Black LP, Kinny PD, Sheraton JW (1991) The difficulties of dating mafic dykes: an Antarctic example. Contrib Mineral Petrol 109:183–194

Caruba R, Iacconi P (1983) Les zircons des pegmatites de Narssarssuk (Groenland): l'eau et les groupements OH dans les zircons metamictes. Chem Geol 38:75–92

Cheilletz A, Levresse G, Gasquet D, Azizi Samir MR, Zyadi R, Archibald DA (2002) The Imiter epithermal deposit (Morocco): new petrographic, microtectonic and geochronological data. Importance of the Precambrian-Cambrian transition for major precious metals deposits in the Anti-Atlas. Mineral Deposita 37:772–781

Choubert G, Faure-Muret A, El-Rzima A (1980) L'alignement de volcans rhyolitiques du Précambrien de Zgounder (région de Taliwine). Mines Géol Energie 43:115–117

Corfu F, Hanchar JM, Hoskin PWO, Kinny P (2003) Atlas of zircon textures. In: Hanchar JM, Hoskin PWO (eds) Zircon. Rev Mineral Geochem 53:469–500

Deloule E, Alexandrov P, Cheilletz A, Laumonier B, Barbey P (2002) In situ U-Pb zircon ages for Early Ordovician magmatism in the eastern Pyrenees, France: the Canigou orthogneisses. Intern Jour Earth Sci (Geolog Rundschau) 91:398–405

Demange M (1977) Le cadre géologique du gisement argentifère de Zgounder (Massif du Siroua, Anti-Atlas, Maroc). Note Serv Géol Maroc 267:105–122

Essarraj S, Boiron MC, Cathelineau M, Banks DA, El Boukhari A, Chouhaidi Y (1998) Brines related to Ag deposition in the Zgounder silver deposit (Anti-Atlas, Morocco). Eur J Mineral 10:1201–1214

Essarraj S, Boiron MC, Cathelineau M, Banks DA, Benharref M (2005) Penetration of surface-evaporated brines into the Proterozoic basement and deposition of Co and Ag at Bou Azzer (Morocco): evidence from fluid inclusions. J Afr Earth Sci 41:25–39

Gasquet D, Levresse G, Cheilletz A, Azizi-Samir MR, Mouttaqi A (2005) Contribution to a geodynamic reconstruction of the Anti-Atlas (Morocco) during Pan-African times with the emphasis on inversion tectonics and metallogenic activity at the Precambrian-Cambrian transition. Precamb Res 140:157–182

Gasquet D, Ennih N, Liégeois JP, Soulaimani A, Michard A (2008) The Pan-African belt. In: Michard A, Saddiqui O, Chalouan A, Frizon de Lamotte D (eds) Continental evolution: the geology of Morocco. Springer, Berlin, pp 33–64

Geisler T, Pidgeon RT, Kurtz R, Van Bronswijk W, Schleicher H (2003a) Experimental hydrothermal alteration of partially metamict zircon. Amer Mineral 88:1496–1513

Geisler T, Rashwan AA, Rahn MKW, Poller U, Zwingmann H, Pidgeon RT, Schleicher H, Tomaschek F (2003b) Low-temperature hydrothermal alteration of natural metamict zircons from the Eastern Desert, Egypt. Mineral Mag 67:485–508

Geisler T, Schaltegger U, Tomaschek F (2007) Re-equilibration of zircon in aqueous fluids and melts. Elements 3:43–50

Hay DC, Dempster TJ (2009) Zircon behaviour during low-temperature metamorphism. J Petrol 50:571–589

Hoskin PWO, Schaltegger U (2003) The composition of zircon and igneous and metamorphic petrogenesis. In:

Hanchar JM, Hoskin PWO (eds) Zircon. Rev Mineral Geochem 53:27–62

Hoskin PWO (2005) Trace-element composition of hydrothermal zircon and the alteration of Hadean zircon from the Jack Hills, Australia. Geochim Cosmochim Acta 69:637–648

Koshek G (1993) Origin and significance of the SEM cathodoluminescence from zircon. J Microsc 171:223–232

Kusiak MA, Dunkley DJ, Slaby E, Martin H, Budzyn B (2009) Sensitive high-resolution ion microprobe analysis of zircon reequilibrated by late magmatic fluids in a hybridized pluton. Geology 37:1063–1066

Levresse G (2001) Contribution à l'établissement d'un modèle génétique des gisements d'Imiter (Ag–Hg) Bou Madine (Pb–Zn–Cu–Au) et Bou Azzer (Co–Ni–As–Au–Ag) dans l'Anti-Atlas marocain. Unpubl PhD Thesis, INPL, Nancy, France, 191 pp

Liégeois JP, Fekkak A, Bruguier O, Errami E, Ennih N (2006) The Lower Ediacaran (630–610 Ma) Saghro group: an orogenic transpressive basin development during the early metacratonic evolution of the Anti-Atlas (Morocco). IGCP485 4th meeting, Algiers, Abstr. Vol. 57

Ludwig KR (2004) Users manual for ISOPLOT/EX, version3.1. A geochronological toolkit for Microsoft Excel. Berkeley Geochronology Center, Berkeley, California, Spec Publ 4, 73 pp

Marcoux E, Wadjinny A (2005) Le gisement Ag-Hg de Zgounder (Jebel Siroua, Anti-Atlas, Maroc): un épithermal néoprotérozoïque de type Imiter. Comptes Rendus Geosci 337:1439–1446

McDonough WF, Sun SS (1995) The composition of the Earth. Chem Geol 120:223–253

Martin LAJ, Duchene S, Deloule E, Vanderhaeghe O (2008) Mobility of trace elements and oxygen in zircon during metamorphism: consequences for geochemical tracing. Earth Planet Sci Lett 267:161–174

Nasdala L, Lengauer CL, Hanchar JM, Kronz A, Wirth R, Blanc P, Kennedy AK, Seydoux-Guillaume AM (2002) Annealing radiation damage and the recovery of cathodoluminescence. Chem Geol 191:121–140

Nasdala L et al (2009) The phenomenon of deficient electron microprobe totals in radiation-damaged and altered zircon. Geochim Cosmochim Acta 73:1637–1650

Nasdala L, Hanchar JM, Rhede D, Kennedy AK, Váczi T (2010) Retention of uranium in complexly altered zircon: an example from Bancroft, Ontario. Chem Geol 269:290–300

Pelleter E, Cheilletz A, Gasquet D, Mouttaqi A, Annich M, El Hakour A, Deloule E, Féraud G (2007) Hydrothermal zircons: a tool for ion microprobe U-Pb dating of gold mineralisation (Tamlalt-Menhouhou gold deposit Morocco). Chem Geol 245:135–161

Pelleter E, Cheilletz A, Gasquet D, Mouttaqi A, Annich A, Deloule E (2008) Hydrothermal zircons: a tool for ion microprobe U-Pb dating of ore mineralisation in polyphase deposits. 18th Annual VM Goldschmidt Conf, Vancouver, Canada. Geochim Cosmochim Acta 72:A733–A733

Pettke T, Audetat A, Shaltegger U, Heinrich CA (2005) Magmatic-to-hydrothermal crystallisation in the W-Sn mineralized Mole Granite (NSW, Australia) Part II: evolving zircon and thorite trace element chemistry. Chem Geol 220:191–213

Petruk W (1975) Mineralogy and geology of the Zgounder silver deposit in Morocco. Can Mineral 13:43–54

Popov AG, Millar G, Belhaj O, Sermat R, Fettouhi A (1989) Gisement argentifère de Zgounder: étude des minéralisations et des roches encaissantes porteuses de sulfures. Unpubl BRPM Report, 15 pp

Rayner N, Stern RA, Carr SD (2005) Grain-scale variations in trace element composition of fluid-altered zircon, Acasta Gneiss Complex, northwestern Canada. Contrib Mineral Petrol 148:721–734

Romer RL (2003) Alpha-recoil in U-Pb geochronology: effective sample size matters. Contrib Mineral Petrol 145:481–491

Sano Y, Terada K, Fukuoka T (2002) High mass resolution ion microprobe analysis of rare earth elements in silicate glass, apatite and zircon: lack of matrix dependency. Chem Geol 184:217–230

Smeykal S (1972) Traits géologiques et métallogéniques du gîte argentifère de Zgounder. Mines Géo 36:33–42

Tera F, Wasserburg GJ (1972) U-Th-Pb systematics in three Apollo basalts and problem of the initial Pb in lunar rocks. Earth Planet Sci Lett 14:281–304

Thomas RJ, Chevallier LP, Gresse PG, Harmer RE, Eglington BM, Armstrong RA, De Beer CH, Martini JEJ, De kock GS, Macey PH, Ingram BA (2002) Precambrian evolution of the Sirwa window, Anti-Atlas orogen, Morocco. Precamb Res 118:1–57

Thomas RJ, Fekkak A, Ennih N, Errami E, Loughlin SC, Gresse PG, Chevallier LP, Liégeois JP (2004) A new lithostratigraphic framework for the Anti-Atlas orogen, Morocco. J Afr Earth Sci 39:217–226

Tomasheck F, Kennedy AK, Villa IM, Lagos M, Ballhaus C (2003) Zircons from Syros, Cyclades, Greece —recrystallisation and mobilization of zircon during high-pressure metamorphism. J Petrol 44:1977–2002

Toummite A, Liegeois JP, Gasquet D, Bruguier O, Beraaouz EH, Ikenne M (2013) Field, geochemistry and Sr-Nd isotopes of the Pan-African granitoids from the Tifnoute Valley (Sirwa, Anti-Atlas, Morocco): a post-collisional event in a metacratonic setting. Mineral Petrol 107:739–763

Wiedenbeck M, Alle P, Corfu F, Griffin WL, Meier M, Oberli F, Von Quadt A, Roddick JC, Spiegel W (1995) Three natural zircon standards for U-Th-Pb, Lu-Hf, trace element and REE analyses. Geostand Newslett 19:1–23

Williams IS, Hergt JM (2000) U-Pb dating of Tasmanian dolerites: a cautionary tale of SHRIMP analysis of high U zircon. In: Woodhead JD, Hergt JM, Noble WP (eds) Beyond 2000: new frontiers in isotopes geoscience, Lorne 2000, Abstracts Proceedings. University of Melbourne, Australia, pp 185–188

Woodhead JA, Rossman GR, Thomas AP (1991) Hydrous species in zircon. Amer Mineral 76:1533–1546

Edough-Cap de Fer Polymetallic District, Northeast Algeria: II. Metallogenic Evolution of a Late Miocene Metamorphic Core Complex in the Alpine Maghrebide Belt

C. Marignac, D.E. Aïssa, A. Cheilletz and D. Gasquet

Abstract

During the late Oligocene-early Miocene, three main hydrothermal events formed polymetallic deposits of the Edoug-Cap de Fer in the Edough massif of the Alpine Maghrebide belt. At ca. 17 Ma, the Karézas As (löllingite)-F (fluorite)-W (scheelite) deposit formed at a depth of ca. 2 km and temperatures of ca. 450–500 °C, from mixing between magmatic-hydrothermal hypersaline fluids issued from a concealed rare-metal granite and several metamorphic fluids derived from the metamorphic core complex. Slightly later, at ca. 16 Ma, the intrusion of microgranites produced high-enthalpy, liquid-dominated geothermal fields at the basement-Kabylian flysch boundary, with Numidian flysch acting as an impermeable lid and host for "mesothermal" polymetallic vein fields (Aïn Barbar, Mellaha, Saf-Saf). Temperatures as high as ca. 350–375 °C were attained in the deep parts of the Aïn Barbar field, at depths of ca. 1.3–1.5 km, accompanied by massive input of sodium that formed metasomatic plagioclase-rich hornfels (Chaïba domain); higher in the Cretaceous flysch aquifer, influx of hydrothermal fluids (300–270 °C) produced hydrothermal metamorphic assemblages of quartz-chlorite, calcite- chlorite, wairakite-chlorite, and epidote. The source of these hot fluids was a basement of the Edough type, in which heat advection was likely related to emplacement of a

C. Marignac (✉) · A. Cheilletz
Laboratoire Géoressources, UMR-CNRS 7359,
Ecole Des Mines de Nancy, Campus ARTEM,
54042 CS14234 Nancy Cedex, France
e-mail: christian.marignac@univ-lorraine.fr

D.E. Aïssa
Laboratoire de métallogénie,
FSTGAT-USTHB-Algiers, BP32 El Alia, 1600
Alger, Algeria

D. Gasquet
Laboratoire EDYTEM UMR-CNRS 5204, Bâtiment
"Pôle Montagne", Université de Savoie, Campus
Technolac, 73 376 Le-Bourget-du-Lac, France

M. Bouabdellah and J.F. Slack (eds.), *Mineral Deposits of North Africa*,
Mineral Resource Reviews, DOI 10.1007/978-3-319-31733-5_6

granite batholith at depth. Concomitant with the paleogeothermal circulations, fault activity created N170° E-trending fracture zones that progressively channeled fluid flow, with the development of propylitically altered linear zones and ore precipitation (Zn–Pb–Cu) at temperatures between 330 and 285 °C. At ca. 15 Ma, renewed magmatic activity (subvolcanic rhyolite dikes) was associated with the generation of new and shallow (ca. 800 m depth) geothermal fields, wherein convected surficial fluids (meteoric and possibly seawater) formed "epithermal" deposits including polymetallic quartz veins, quartz-stibnite metasomatic deposits in marble, and quartz-arsenopyrite-gold showings, at mostly lower temperatures of 300–250 °C. Excepting the Karézas skarn, for which a magmatic origin of the tungsten is likely, the metals deposited by the different hydrothermal systems were mainly sourced in rocks of the metamorphic core complex and its tectonically emplaced cover of Cretaceous flysch. Only a minor contribution of metals came from the magmatic rocks, as shown by lead isotope data for the Aïn Barbar area. In particular, amphibolite of the Marble Complex in the Edough sequence may have been a major source of copper and the epithermal antimony (and gold?). The Edough-Cap de Fer district is directly linked to the evolution of the Edough metamorphic core complex. Although metallogenic activity began after the end of ductile deformation, metamorphic fluids derived from the core complex seem to have played a key role in the first stages of the hydrothermal circulation and related mineralization (Karézas W skarn, mesothermal polymetallic veins). However, the role of the late Miocene magmatism, induced by collisional processes through slab break-off and/or lithospheric delamination, was of equal importance in the genesis of the Edough-Cap de Fer metallic deposits, being the source of the heat advection responsible for hydrothermal convection during the meso- and epithermal mineralization. Finally, it appears that the transition from extension (related to opening of the Algerian-Provençal oceanic basin) to transpression (when the collision resumed), at the end of the Miocene, was the ultimate control on the mineralizing events in the Edough metamorphic core complex.

Keywords

Edough · Metamorphic core complex · Alpine · Tungsten skarn · Polymetallic vein · Aïn barbar · Paleogeothermal field · Cu–Zn–Pb · Epithermal · As–Sb–Au

1 Introduction

The recognition in the late 1970s of metamorphic core complexes (Monastero et al. 2005, and references therein) led rapidly to the recognition of their role in the genesis of diverse base and precious metals vein deposits, mainly of the epithermal type (e.g., Spencer and Welty 1986; Doblas et al. 1988; Beaudouin et al. 1991; Howard 2003; Machev et al. 2005). In the majority of described

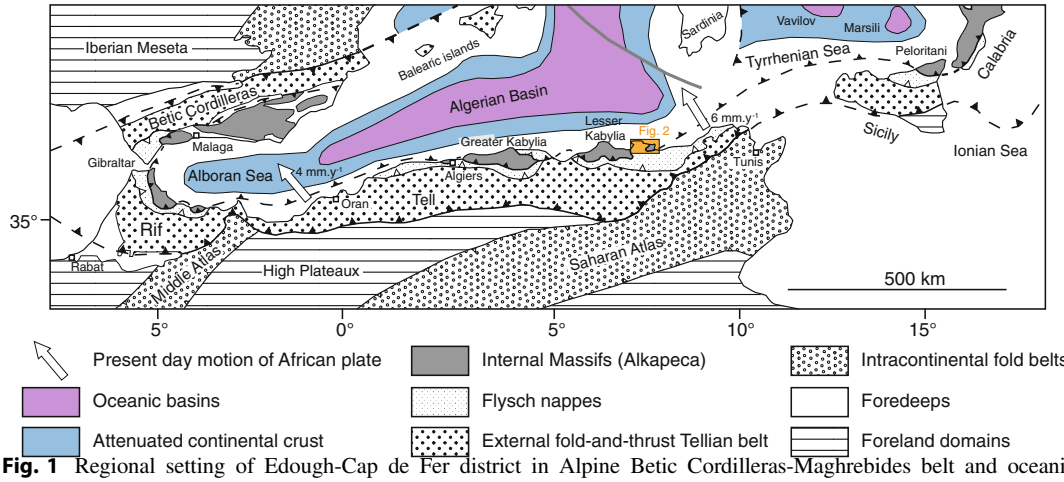

Fig. 1 Regional setting of Edough-Cap de Fer district in Alpine Betic Cordilleras-Maghrebides belt and oceanic Western Mediterranean basins (adapted from Michard et al. 2006). *Box* shows area of Fig. 2

metamorphic core complexes, mineralization is coeval with detachment tectonics and associated metamorphism, which together allow fluid transfer of both shallow fluids in the upper plate and deep fluids in the lower plate of the complex, and their mixing at favorable sites (e.g., Beaudouin et al. 1991; Costagliola et al. 1999; Holk and Taylor 2007). Synchronous with the ductile tectonics, high-enthalpy geothermal systems may evolve in the upper plate of metamorphic core complexes (e.g., Monastero et al. 2005). There are, however, a few examples of mineralized core complexes in which the mineralizing processes, although controlled by the geometry of the complex and presence of favorable depositional sites created by extensional events, are clearly post-kinematic, in which fluid circulations are dependent on other thermal controls in addition to the high temperature gradients generated by formation of the core complex (e.g., Marchev et al. 2005; Gilg et al. 2006).

Several Alpine metamorphic core complexes are known in the Maghrebide belt, where they appear as the internal crystalline massifs that occur from the Rif to the Calabria (Fig. 1). Alpine ore fields, mainly of the epithermal type (e.g., Glaçon 1971), are present in some of these complexes, but appear to be later than the main detachment tectonics; their possible relationships with the hosting core complex were not studied. In eastern Algeria, the Edough-Cap de Fer massif is one of these metal-endowed complexes (Aïssa et al. 1995), displaying a variety of mineralization styles including W–(Sn)-skarns, polymetallic Cu–Zn–Pb vein systems, and Sb–As–(Au) veins and replacements (Aïssa et al. 1999). In this paper, we describe the main mineralized systems of the Edough-Cap de Fer district and discuss time relationships of exhumation of the core complex with associated tectonic, magmatic, and hydrothermal events.

2 Geological Background

The Edough-Cap de Fer area is part of the internal zone of the Betic-Maghrebide belt (Durand-Delga 1969) (Fig. 1) that makes up the westernmost extension of the Alpine chains of the Tethys (Dercourt et al. 1986). The belt resulted from the Eocene to Miocene collision between the African (Gondwanan) plate and the European plate (e.g., Jolivet and Faccenna 2000), with an intervening northern microplate exposed in a series of crystalline upper nappes, the internal massifs, which comprise a pre-Mesozoic basement and a Mesozoic- Cenozoic cover, both being affected by Alpine metamorphism. These massifs were thrust southward onto the Tellian nappes, a fold-and-thrust belt with southward vergence that originated

from the former passive margin of the African plate (e.g., Piqué et al. 2002; Frizon de Lamotte et al. 2000, 2006). Interleaved between the internal massifs and the Tellian nappes is an elongated flysch belt that extends from the Rif to Calabria. This flysch belt comprises a complex of Mesozoic nappes (Kabylian flysch), former cover of an elongated oceanic Tethysian tract (Durand-Delga et al. 2000), and the Numidian flysch (Late Oligocene-Burdigalian), deposited on the African margin during opening of the Algeria-Provence oceanic margin (Thomas et al. 2010) and incorporated into the nappe pile at the end of the Burdigalian (Bouillin 1979; Sami et al. 2010).

The Edough-Cap de Fer area in eastern Algeria (Fig. 1) consists of an inlier of crystalline basement, the Edough massif, which forms an antiformal dome that was uplifted from under a complex of nappes outcropping to the west, with mainly the Numidian nappe, overlying a complex of Kabylian flysch outcropping as small inliers particularly within the Aïn Barbar antiform (Fig. 2). The Edough massif comprises a stack of crystalline rocks (paragneiss, amphibolite,

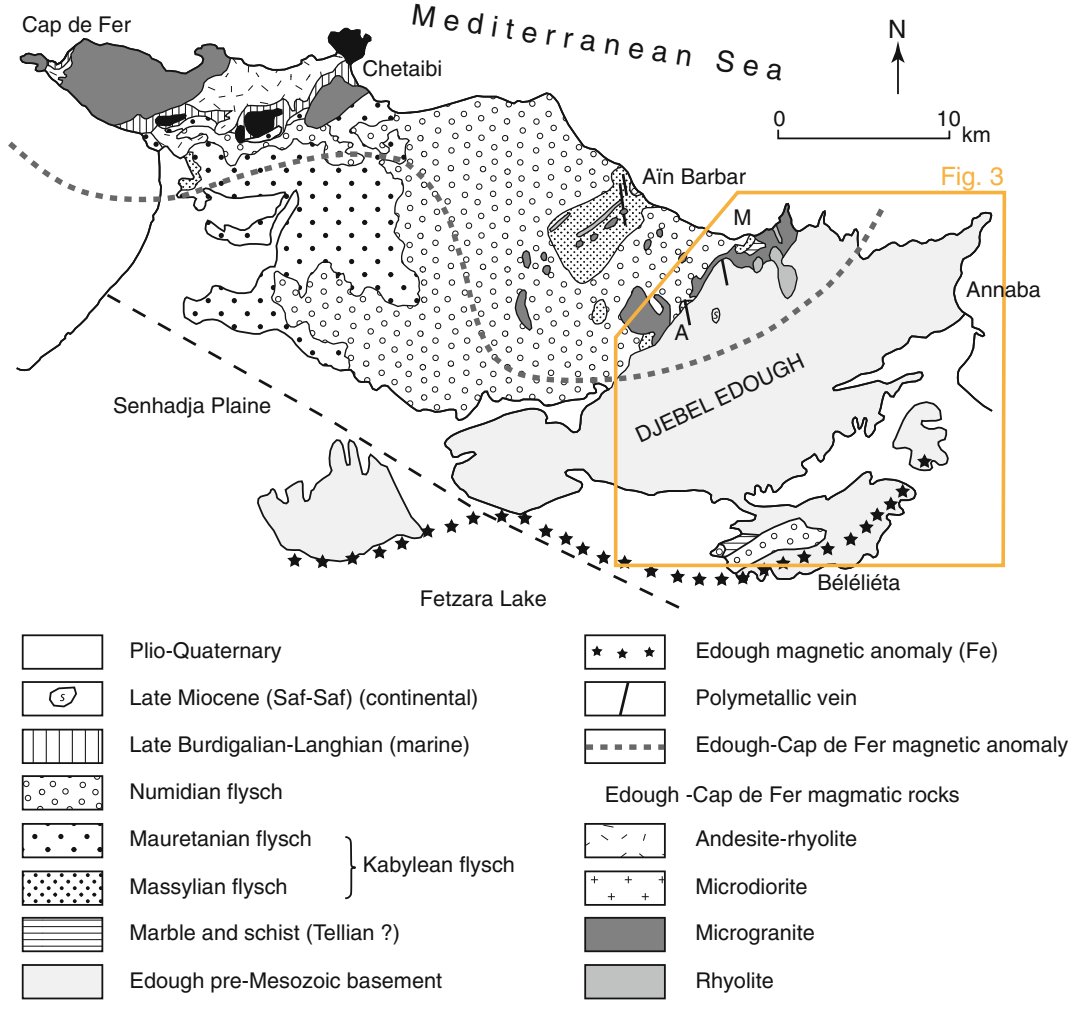

Fig. 2 Geology of Edough-Cap de Fer district (modified from Hilly 1962 and Marignac 1985). *Box* shows area of Fig. 3

marble, micaschist), which evolved as a metamorphic core complex during the late Oligocene-early Miocene (Brunel et al. 1988; Caby and Hammor 1992) and was overthrust by the flysch nappes during the late Burdigalian.

2.1 The Edough Metamorphic Core Complex

The Edough crystalline basement is a folded tectonic pile comprising three units (Ilavsky and Snopkova 1987; Gleizes et al. 1988) (Fig. 3). The Seraidi Gneiss Unit (SGU) is made of monotonous high-grade paragneiss (metagreywacke; Aïssa 1996; Hadj Zobir and Mocek 2012), intercalated with tourmaline-bearing leucogneiss. The Marble Complex Unit (MCU) comprises high-grade marble, micaschist, and amphibolite, and includes the large Kef Lakhal (Voile Noire) massif (Ahmed-Said and Leake 1992). The Alternance Series Unit (ASU) is a medium-grade metapelitic unit with numerous intercalations of marble and feldspathic quartzite in graphitic-andalusite-micaschist; acritarches having Ordovician to Silurian ages occur in some of these metaquartzite units (Ilavsky and Snopkova 1987).

The Edough crystalline basement was constructed in two main tectono-metamorphic stages (Aïssa 1996; Aïssa et al. 1998a). During the first stage, the MCU was tectonically imbricated with the SGU, forming isoclinally pinched synclines within the gneiss (Fig. 3b), under medium pressure metamorphic conditions (M2 kyanite); the main schistosity (S2) was coeval with isoclinal F2 meso-scale folds. During the second stage, the ASU was superposed onto the resulting complex along a ductile detachment fault (Fig. 3b), under amphibolite facies conditions (low pressure-high temperature gradient, M3 metamorphic event),

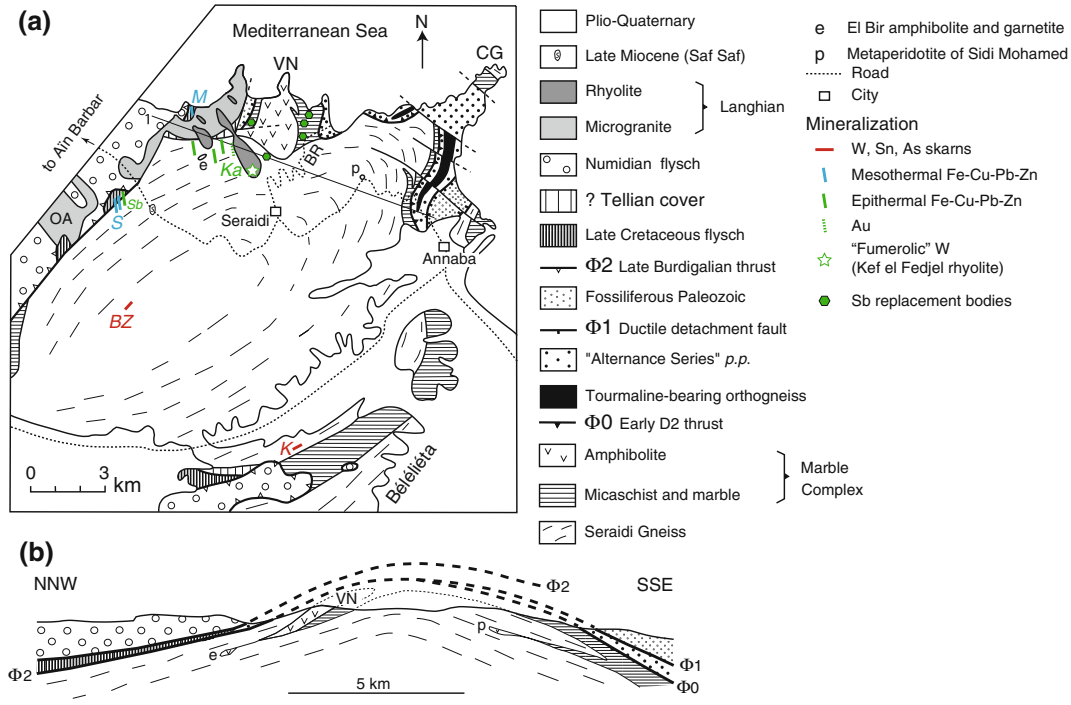

Fig. 3 The Edough massif. **a** Geologic map (modified from Aïssa 1998a). **b** Interpretative cross section of the Edough antiform; Miocene intrusions are omitted for simplicity; some features (El Bir and Sidi Mohammed ultramafic bodies) are projected onto the section plane. Abbreviations for localities: *BR* Beach Road; *BZ* Bou Zizi; *CG* Cap de Garde; *OA* Oued el Aneb microgranite; *VN* Kef Lakhal. Abbreviations for mineral deposits and showings: *K* Karézas; *Ka* Koudiet el Harrach; *Ke* Kef el Fedjel; *M* Mellaha cove; *S* Saf-Saf

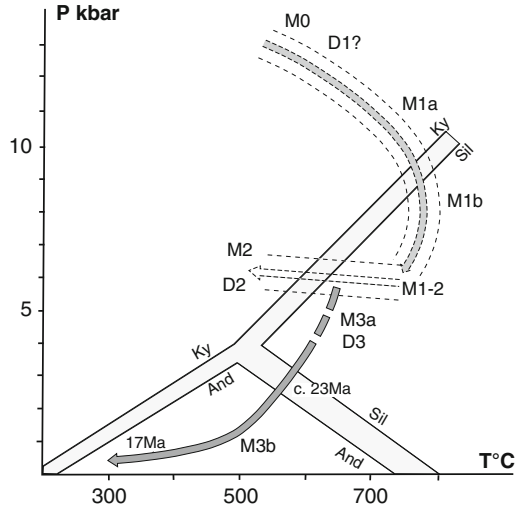

Fig. 4 Reconstruction of Edough P-T-t paths (modified from Aïssa 1989). Abbreviations: *M0* high-pressure (eclogite) relics in Kef Lakhal amphibolite; *D1* hypothetical early deformation stage; *M1a*, *b* high-pressure granulite-facies metamorphism and partial melting; *M1–2* nearly isobaric retrogression (porphyroblastic muscovite); *M2*, *D2* barrovian metamorphism and isoclinal deformation (Alpine?); *M3a*, *D3* peak low pressure-high temperature metamorphism and detachment tectonics (Edough metamorphic core complex); *M3b* post-kinematic andalusite blastesis, beginning of the Edough exhumation. Stability boundaries for kyanite (*Ky*), sillimanite (*Sil*), and andalusite (*And*) are shown

including formation of a S3 flat schistosity and sillimanite-bearing C/S structures within the gneiss (Brunel et al. 1988). Prior to these stages, the MCU and SGU rocks experienced high T and P metamorphic events, only known presently by mineral relicts (Aïssa 1996) (Fig. 4). The younger high temperature event is dated as late Miocene (Monié et al. 1992), which is when the Edough massif was a metamorphic core complex with extension occurring in the northwest direction (present-day coordinates) (Caby and Hammor 1992). The Edough metamorphic core complex is noteworthy for the very limited development of the upper plate, in contrast to true core complexes that have extended upper plates made of fault-bounded blocks. The Edough upper plate was likely truncated by late Burdigalian overthrusting of the flysch nappes a few million years after the end of ductile deformation.

At the northern termination of the Edough dome, a penetrative network of leucocratic veins within the Seraidi gneisses are clearly late-kinematic (D3) in origin, coeval with the deformation associated with extension in the metamorphic core complex. Owing to these veins, the Seraidi gneisses are described as "diatexites" (e.g., Hadj Zobir and Mocek 2012), although these rocks are not the result of in situ partial melting. It is most likely that the granitic melts that formed during this veining derived from an anatectic domain at depth, and that the leucocratic veins form a peri-anatectic network of leucosomes. One of these veins has a U–Pb zircon age of 17.84 ± 0.12 Ma, i.e., late Burdigalian (Bruguier et al. 2009). Small (several 100 m) leucogranite bodies and tourmaline-muscovite pegmatite swarms are equally abundant. The leucogranites are late kinematic but the pegmatites post-date all deformation and are associated with the formation of post-kinematic andalusite porphyroblasts. A 17.0 ± 0.3 Ma ^{39}Ar–^{40}Ar age was obtained on muscovite from such a pegmatite at Bouzizi (Fig. 8a). This Burdiagalian/Langhian boundary age is slightly younger than the age of the peri-anatectic leucosomes, hence the Edough leucogranite-pegmatite complex may be considered a late expression of the same anatectic event and thus also represents a peri-anatectic complex.

2.2 The Edough-Cap de Fer Magmatic District

A large magnetic anomaly underlines the area of the Cap de Fer to Edough massif. This anomaly is currently interpreted as indicating the presence at depth of a large magmatic body (Vila 1980), the surface expression of which comprises the Cap de Fer, Aïn Barbar, and Edough intrusive complexes (Fig. 2). These felsic magmatic rocks were emplaced in two stages in the basement and its tectonic cover over a very short time interval comprised between ca. 15–ca. 16 Ma (Marignac

et al. 2015, and references therein). The main stage is mainly subvolcanic and comprises the subvolcanic intrusions from the Edough massif and Aïn Barbar areas (microgranite), and the subvolcanic-volcanic complex of the Cap de Fer (microdiorite to microgranite and associated andesite-rhyolite), all with a well constrained age close to 16 Ma (Burdigalian to Langhian boundary; K–Ar, stratigraphy). The second stage consists of a few rhyolite dikes and domes (Aïn Barbar, Edough) of early Langhian age (ca. 15 Ma, K–Ar).

2.3 Metallogeny

Despite the presence of pervasive hydrothermal alteration in the Cap de Fer complex, no significant mineralization is known there, with the notable exception of an unstudied iron ore body that was mined from the end of the 19th Century (hence the "Cap de Fer" name). All of the known mineralization and occurrences are restricted to the polymetallic Fe–Cu–Pb–Zn vein system of the Aïn Barba inlier and the Edough massif. In the latter setting various pre-Alpine mineralizations are documented, together with a series of Alpine mineralizations including the Karézas skarns (As–W), polymetallic vein systems of Saf-Saf and Mellaha Cove (Cu–Pb–Zn), and a group of epithermal W–Au–Sb occurrences (Fig. 3). The pre-Alpine mineralizations were described by Aïssa et al. (1998a), Henni et al. (2002), and Henni and Aïssa (2007), and are not discussed further in the present study.

3 The Karézas Skarn

The Karézas skarn is located on the northern side of the Béléliéta massif, 12 km southeast of Annaba (Figs. 3 and 5). This skarn was mined initially, from 1928, for As (as löllingite) and later, beginning in 1949, for scheelite. Due to processing difficulties, mining ceased in 1953, after the extraction of only 25 kt of ore @ 0.97 % WO_3, i.e. ~192 t W. Host rocks are monotonous Seraidi gneisses, with a uniform NE-SW foliation and consistent 50° SE dip. Sillimanite-bearing C/S structures (D3 deformation) are abundant.

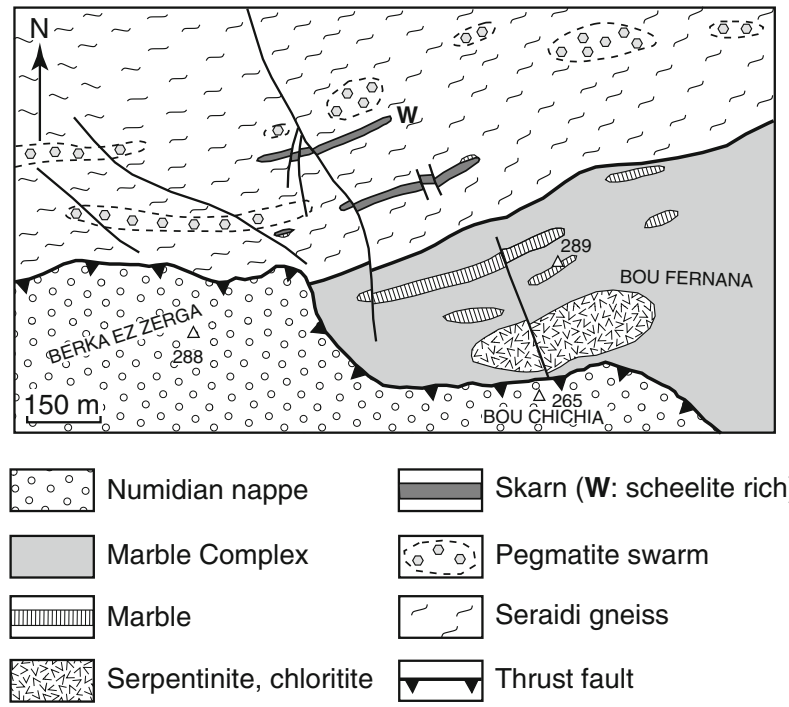

Fig. 5 Geologic map of part of Béléliéta massif the showing setting of tungsten skarn and numerous pegmatite swarms, which are roughly coincident with gneissic foliation. Redrawn from Aïssa et al. (1998a)

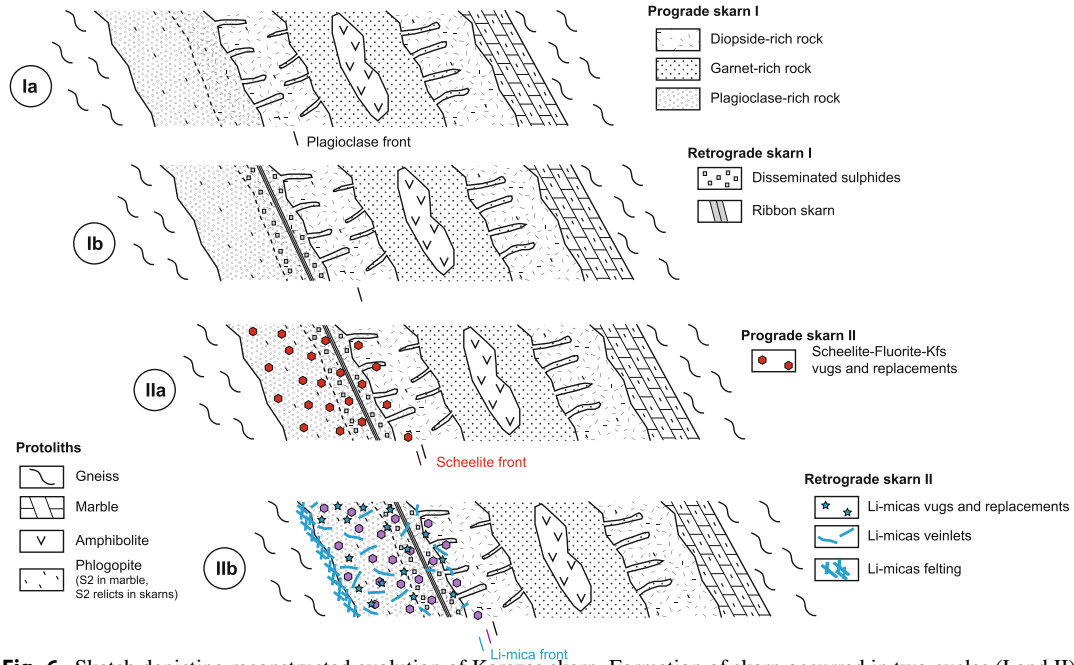

Fig. 6 Sketch depicting reconstructed evolution of Karezas skarn. Formation of skarn occurred in two cycles (I and II) and four sub-stages (Ia, Ib, IIa, IIb). See text for explanation

Magmatic rocks are represented by local small lenses of aplite and leucogranite, which are affected by the C/S structures, and by swarms of pegmatite lenses that post-date the ductile shearing. Pegmatite swarms are approximately parallel to the gneissic foliation, but lack any particular relationship with the mineralization (Fig. 5). The pegmatites are quartzo-feldspathic and contain tourmaline and muscovite.

The deposit consists of two lenticular skarn bodies parallel to the foliation of the host gneiss ("strata-bound" skarns). The northern lens, the only minable body, extends ~700 m along strike and is known at depths down to −135 m, with a variable thickness of 1–4 m. Tungsten grades are 0.7–1.5 % WO_3. Most of the contained tungsten remains to be mined. In addition, gold is present in some samples, suggesting that the skarn may have a gold potential. Unfortunately, outcrops in the ore area are scarce, and the old underground workings are foundered and inaccessible. Based on very limited field observations and mainly on numerous samples from the old mine dumps, a reconstruction of skarn protoliths and recognition of a two-stage evolution of the skarn system are proposed (Fig. 6).

3.1 Skarn Protoliths

The skarn formed at a marble-gneiss boundary and affected both lithologies. The marble consists of a more or less annealed, calcite-diopside-phlogopite assemblage in which the phlogopite defines the foliation. A garnetite is part of the protolith package (see below). In addition, a small outcrop of amphibolite (likely the "diorite" of Caillère and Kraut 1947) was observed in the middle of the skarn exposure. Both the garnetite and amphibolite are lithologically identical to those in the large Kef Lakhal massif, which suggests that the Karézas skarn was overprinted on a tectonically emplaced lens of the MCU (within the SGU), in the same way as the El Bir tectonic amphibolite-garnetite lens in the northern Edough (Fig. 3b).

3.2 One Skarn, Two Cycles

Two cycles of skarn formation are recognized at Karézas. Each cycle consists of a succession of prograde and retrograde stages *sensu* Einaudi et al. (1981), i.e., a succession of early anhydrous and late hydrous (±S) assemblages, respectively. Cycle I formed a classical prograde substage (Ia) of zoned plagioclase-garnet- and clinopyroxene- rich skarn, with plagioclase-rich rock occurring on the footwall (partly replacing the gneiss) and the clinopyroxenite on the hangingwall (developed in the marble). A retrograde substage (Ib) contains sulphides (pyrrhotite, chalcopyrite, cubanite) and ferro-actinolitic amphibole, developed at the expense of the clinopyroxene (Fig. 6). A distinct clinopyroxene- plagioclase subzone, locally organized into alternating microbands, formed at the plagioclase rock-clinopyroxenite contact and is the main host for substage Ib. This subzone may have been controlled by a ribboned cataclastic band that affected the Ia minerals. Pyrrhotite, the first mineral of substage Ib, commonly forms thin parallel ribbons that are deformed by small folds. Chalcopyrite deposition is coeval with replacement of Ia clinopyroxene by ferro-actinolite, along microcracks or in patches. Thus, substage Ib was controlled by a deformational event that overprinted the Ia skarn, likely correlated with the presence, along the footwall, of a mylonitic band; related porphyroclastic clinopyroxene was affected only by the second-cycle mineralization. The Cycle I skarn, and in particular the retrograde substage Ib, lacks tungsten enrichment, in strong contrast with most tungsten skarns worldwide (e.g., Einaudi et al. 1981).

The second cycle, localized on the footwall of the skarn, is superimposed on the first cycle assemblages (Fig. 6). Cycle II consists of replacement patches, anastomosing veinlets, and fillings of microvugs. Prograde substage IIa is characterized by quartz, fluorite, scheelite-1, apatite, and minor K-feldspar. The retrograde substage IIb is multiphase, with (1) a quartz-mica-scheelite-2-apatite-allanite- löllingite assemblage, (2) simultaneous transformation of löllingite into arsenopyrite and scheelite into wolframite, and (3) late development of a native bismuth-bismuthinite-tetradymite-(rare native gold) association. The hydrothermal micas are of two types, "pink" and "green," the former being mainly associated with allanite and scheelite-2 and the latter with löllingite and forming monomineralic "micacites." The scheelite (10 μm to 1 cm) is devoid of detectable molybdenum, thus strongly contrasting with the scheelite from classical prograde skarns worldwide (Einaudi et al. 1981). Overall, the Cycle II skarn of Karézas is much akin to "greisenized skarns" and "skarns-greisens" as defined by Kwak (1987). A very late stage of mineralization, consisting of chlorite-clinozoisite-calcite-pyrite, is widespread in the skarn and is likely related to the "mesothermal" stage of the northern Edough massif.

3.3 Skarn Mineralogy

Clinopyroxene: The clinopyroxenite is an aggregate of large (several mm to several cm) prisms of a ferrosalitic clinopyroxene. No zoning of crystals is apparent at the 100-μm scale, but the Fe/(Fe + Mg) ratio (Fe number: Fe#) varies along strike of the clinopyroxene prisms, and displays oscillatory zoning with Fe# varying between 0.75 and 0.9.

Garnet: The garnetite comprises euhedral to subhedral crystals of the grossular-andradite solid solution, typically having a micro-vuggy appearance. The anisotropic crystals exhibit in SEM-BSE (backscattered electron) images a complex zoning, including sector zoning and a delicate, micron-scale, oscillatory growth zoning with grossular-rich cores and andradite-rich rims (Fig. 7). In several samples, the grossular-andradite garnets appear superimposed on an older garnetite, also composed of subhedral to anhedral crystal aggregates, but these are distinctly isotropic and dominated by the pyrope-almandine-(spessartine) solid solution. The latter are compositionally identical to garnets in the garnetites associated with the Kef Lakhal amphibolites, and for this reason, the isotropic garnetite is considered to be inherited from the early metamorphic events in the Edough massif and a protolith for the grossular-andradite skarn.

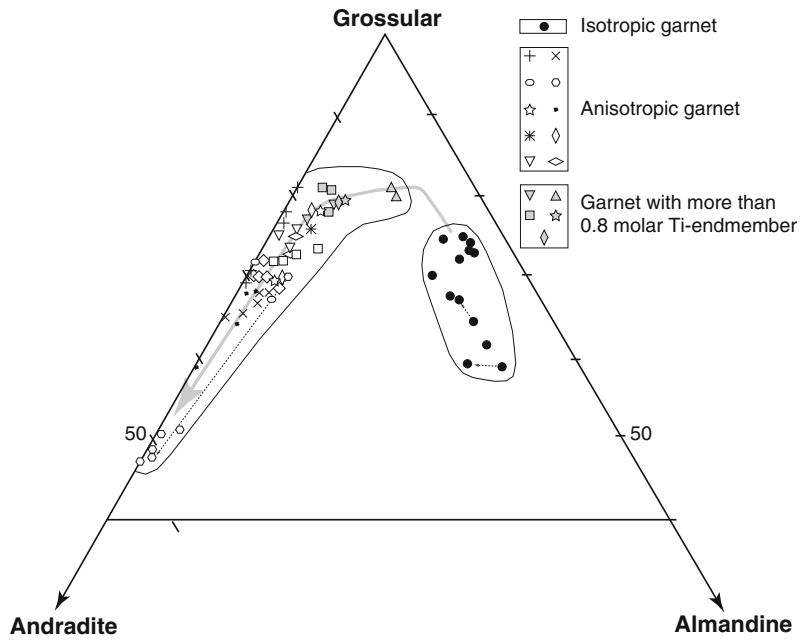

Fig. 7 Composition of Karezas skarn garnets, plotted in the grossular (Ca)-andradite (Fe^{3+})-almandine (Fe^{2+}) ternary. For non-isotropic garnets, each *symbol* represents a single crystal

The isotropic garnetite to skarn boundary is outlined by a thin rim of garnet having intermediate compositions between the pyralspite and grossular end-members and Ti-enrichment (>0.8 mol% Ti end-member, up to 3.0 mol%; Fig. 7).

Micas: Green and pink micas have different compositions (Table 1). The green mica is close to the siderophyllite end-member with a mean Fe# of 0.81, and displays a limited fluorine content (mean F 1.26 wt%), with very minor Rb and Cl. Compared to the green mica, the pink mica is more magnesian, with a mean Fe# of 0.51, and F-rich (mean F 4.94 wt%, up to 6.26 wt%), and contains slightly more Rb and distinctly less Cl. Li_2O was estimated using the F content as a proxy (Tischendorff et al. 1997). The pink micas have significant contents of Li_2O (~2.7–4.0 wt%) and are close to zinnwaldite in composition, whereas the green mica may be considered a lithian siderophyllite.

Löllingite and arsenopyrite: The substage IIb löllingite has a near- constant composition characterized by the systematic presence of minor sulphur, yielding a mean structural formula of $Fe_{0.99}As_{1.88}S_{0.12}$. The arsenopyrite is enriched in arsenic, with a mean of As content of 35.5 apfu (35.1–37.0 apfu As), and a mean structural formula of $Fe_{0.99}As_{1.07}S_{0.93}$.

3.4 Age of the Skarn

$^{39}Ar/^{40}Ar$ dating of two micas obtained in this study from the same sample (Fig. 8b) yields ages of 16.8 ± 0.4 Ma for the pink mica and 17.0 ± 0.5 Ma for the associated green mica. These two ages are the same, within analytical uncertainty, hence the two micas are considered coeval. The mean ago for the two dates of 17.0 ± 0.2 Ma may be taken as the age of substage IIb at Karézas, i.e., late Burdigalian.

3.5 Fluid Inclusion Study

Although fluid inclusions (FIs) are observed in Cycle I clinopyroxene and amphibole (apparently primary in the latter), they typically decrepitate upon heating, except for a very limited number of small (10–20 μm) FIs, commonly with negative crystal shapes. Only Th measurements were possible, and most FIs homogenized to the vapor phase, yielding temperatures of 390–410 °C in

Table 1 Representative analyses of Karézas micas

	Pink micas				Green micas			
	KZ7-12				KZ89-8B			
	8	1	4	110	114	111	17	15
SiO_2	36.95	37.17	39.11	37.13	33.82	33.85	33.54	34.07
TiO_2	0.84	0.82	0.6	0.64	0.04	0.00	0.08	0.05
Al_2O_3	16.26	17.07	14.68	17.77	17.71	16.49	17.18	16.72
FeO	18.82	18.49	16.81	17.97	31.11	31.27	31.11	31.77
MnO	0.18	0.16	0.00	0.27	0.30	0.3	0.23	0.24
MgO	10.11	9.58	11.27	10.48	3.91	4.47	3.79	4.18
Na_2O	0.21	0.23	0.18	0.11	0.23	0.12	0.17	0.16
K_2O	9.53	9.46	9.53	9.42	8.91	8.91	9.00	8.84
Rb_2O	n.a.	n.a.	n.a.	0.17	0.14	0.14	0.03	0.08
Li_2O*	2.67	2.87	3.21	4.01	0.31	0.48	0.58	0.68
F	4.23	4.46	4.85	5.74	0.84	1.16	1.34	1.51
Cl	0.12	0.14	0.01	n.a	n.a	n.a.	n.a.	n.a
H_2O*	1.99	1.91	1.75	1.25	3.35	3.18	3.09	3.03
Total**	100.13	100.48	99.96	102.7	100.3	99.88	99.57	100.7
Si	2.77	2.77	2.89	2.69	2.7	2.72	2.7	2.72
Al^{iv}	1.23	1.23	1.11	1.31	1.3	1.27	1.3	1.28
Ti	0.05	0.05	0.03	0.03	0.00	0.00	0.00	0.00
Al^{vi}	0.21	0.26	0.17	0.21	0.37	0.29	0.33	0.29
Fe	1.18	1.15	1.04	1.09	2.08	2.1	2.1	2.12
Mn	0.01	0.01	0.00	0.02	0.02	0.02	0.02	0.02
Mg	1.13	1.06	1.24	1.13	0.47	0.54	0.46	0.5
Na	0.03	0.03	0.03	0.02	0.04	0.02	0.03	0.02
K	0.91	0.9	0.90	0.87	0.91	0.91	0.93	0.9
Rb	n.a.	n.a.	n.a.	0.01	0.01	0.01	0.00	0.00
Li*	0.81	0.86	0.95	1.17	0.1	0.16	0.19	0.22
F	1.00	1.05	1.14	1.32	0.21	0.30	0.34	0.38
Fe #	0.51	0.52	0.46	0.49	0.82	0.80	0.82	0.81

Owing to high MgO contents (>6 wt%: pink micas), or SiO_2 contents (<34 wt% green micas), LiO_2 was estimated using F wt% as a proxy: $Li_2O^* = 0.395 \times F^{1.326}$ (Tischendorf et al. 1997). "Total" includes F correction to oxygen, and an estimated H_2O content calculated on the basis of OH

clinopyroxene and 380–440 °C in amphibole. A few other FIs homogenized to the liquid phase (400 and 410 °C in one clinopyroxene, 350–470 °C in three amphiboles). Mean values of Th (V) and Th(L) are very similar for FIs hosted in the clinopyroxene (ca. 405 °C) and amphibole (ca. 420 °C). The following fluid inclusion results are restricted to Cycle II minerals, for which more than 230 measurements were obtained.

Petrography: FIs occur in quartz, fluorite, and scheelite. Two varieties of quartz hosts were studied: Qm, forming disseminated millimeter-sized patches and Qv, forming veinlets, both of early substage IIb. In addition, FIs were studied in quartz (Qp) from a pegmatite in a nearby late pegmatite swarm. In total, seven types of FIs were observed and could be studied (nomenclature from Boiron et al. 2003): (1) Vc, two-phase

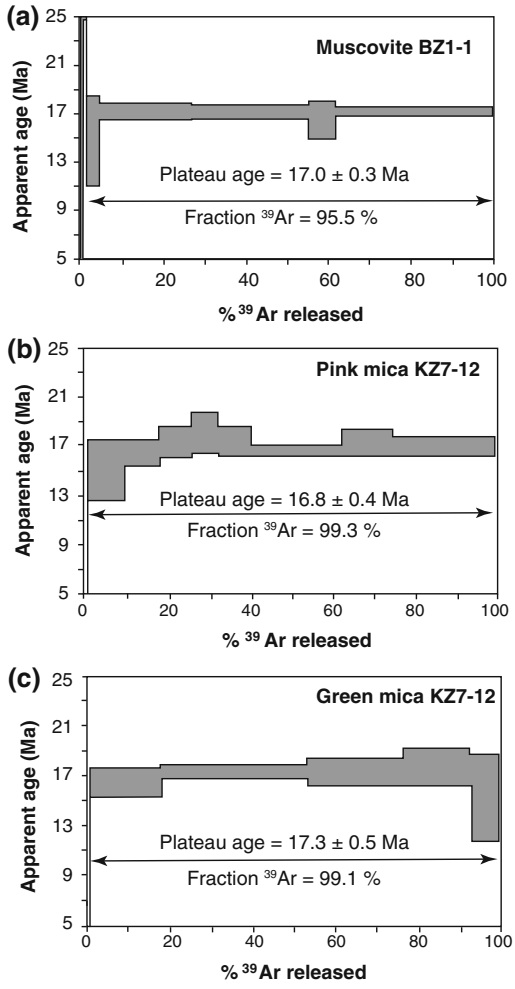

Fig. 8 $^{39}Ar/^{40}Ar$ evidence of a late Burdigalian magmatic event in Edough massif (from Aïssa et al. 1998a). **a** Age data for muscovite from post-tectonic tourmaline-bearing pegmatite (Bouzizi swarm). **b** Age data for Karézas hydrothermal pink mica. **c** Age data for Karézas hydrothermal green mica

(at room temperature) FIs with only volatiles (CO_2 predominant), and homogenization to the vapor phase; (2) Vc-w, two- to three-phase (at room temperature) volatile-bearing FIs with vapor volumic ratio (Rv) $\geq$ 50 %, and final homogenization to the vapor (volatile) phase; (3) Vc-wSn, same as Vc-w, but containing solid phases, in number n (n = 1 to 5); (4) Lw-(c), two-phase FIs with Rv < 30 %, and homogenization to the liquid phase, the presence of volatiles being recorded by appearance of clathrates during the freezing experiments, or by Raman microspectrometry; (5) Lw-(c)Sn, same as Lw-(c), but containing solid phases, in number n (n = 1–4); (6) Lw, two-phase aqueous FIs that homogenize to the liquid phase; and (7) LwSn, same as Lw, but containing solid phases, in number n (n = 1–4). All of the above types of FIs are not found in all of the minerals (Table 2). The daughter minerals, identified by SEM-EDS on opened inclusions, comprise halite, sylvite, possibly antarcticite ($CaCl_2 \cdot 6H_2O$), calcite, dolomite, zircon, and scheelite. In addition, unidentified birefringent daughter minerals and an opaque mineral with smooth faces (in one FI identified as graphite), are also present. All of the solid-bearing FIs appear to have trapped hypersaline fluids (see below).

Within the skarn minerals, hypersaline FIs may be interpreted as primary inclusions: these either follow growth zones in euhedral to subhedral crystals, or are organized in isolated clusters (mainly in quartz). In a given zone or cluster, vapor-dominated Vc-wSn and liquid-dominated LwSn FIs typically co-exist, and consequently define "fluid inclusion assemblages" (Goldstein and Reynolds 1994, in Bodnar 2003). The Vc-w inclusions are uniformly found alone and are organized into short planes, which are systematically internal in the host crystals, nowhere being observed to cross crystal boundaries, and on this basis are interpreted as pseudo-secondary inclusions, as defined by Roedder (1984). The Lw inclusions are systematically organized in typical planes of secondary FIs that cut crystal boundaries. A relative chronology may therefore be deduced for these skarn FIs: paragenetically first are the hypersaline inclusions, followed by the Vc-w, and finally the Lw. In contrast, within quartz Qp of the external pegmatite, all FIs are secondary and organized into fluid inclusion planes (FIPs).

Microthermometry: Results of the microthermometric measurements are summarized in Table 3. The volatile phase is far from being pure CO_2, as indicated by the range in Tm CO_2, from −57 to −76. The nature of this volatile phase could not be determined in most FIs by Raman microprobe, because either the host mineral is

Table 2 Major characteristics of FI types in host minerals from Karézas skarn

Mineral	Types present	Size (μm)	Abundance	n	Solid phases
Quartz Qm	Vc-w	10–100	Common		
	Vc-wSn	10–100	Common	1–3	Hl, Syl, unknown 2-refringent
	Lw-(c)Sn	10–100	Common	1	sporadic black speck: Gr?
	Lw	10–100	Rare		
	LwSn	10–100	Common	1–4	Hl, Syl, Anc?,Cal, Zrn
Quartz Qv	Vc-w	10–70	Common		
	Vc-wSn	10–70	Common	1–2	Zrn? and Hl or smooth opaque: Gr?
	Lw-(c)Sn	10–70	Rare	1–2	Zrn? and smooth opaque: Gr?
	Lw	10–70	Common		
	LwSn	10–70	Common	1–2	Zrn? and Hl or smooth opaque: Gr?
Fluorite	Vc-w	10–80	Common		
	Vc-wSn	10–80	Common	2–5	Hl and Sch + Syl, Anc?, Cal, phyllite
	Lw-(c)Sn	10–80	Rare	1	Hl
	LwSn	10–80	Common	2–5	Hl and Sch + Syl, Anc?, Cal, phyllite
Scheelite	Vc-w	10–100	Common		
	Vc-wSn	10–100	Rare	2	Hl, Syl
	Lw-(c)Sn	10–100	Rare	4	Hl, Syl, 2 unknown 2-refringent
	LwSn	10–100	Common	2	Hl, Syl
	Lw	10–100	Common		
Quartz Qp	Vc-w	10–70	Common		
	Lw	10–70	Common		
	LwSn	10–70	Common	1–2	Hl, Syl

Abbreviations: *Anc* antarcticite; *Cal* calcite; *Dol* dolomite; *Gr* graphite; *Hl* halite; *Sch* scheelite; *Syl* sylvite; *Zrn* zircon

fluorescent under the laser beam (fluorite and scheelite hosts) or the presence of graphite in the volatile phase (bubble) blurred the Raman signal (quartz host). This graphite may either be present initially (as observed in LwSn FIs in Qm, or Vc-wSn FIs in fluorite), or be produced under the laser beam by the reaction $CO_2 + CH_4 = 2C + 2H_2O$. Finally, only three V-type inclusions from Qm quartz could be measured, yielding compositions rich in CH_4 and N_2; these two volatiles amount to 40–50 vol.% of the total, with either CH_4 predominant or mixed CH_4–N_2 compositions (Table 4). Given the Tm CO_2 values (Table 3), these conclusions may be extended to all of the volatile-bearing FIs from Karézas. In addition, a few Raman spectra demonstrate the presence of H_2S in the Vc-w inclusions, from either fluorite or quartz Qm hosts. Most included solids are daughter minerals, disappearing before bulk homogenization during the heating experiments, i.e., homogeneous hypersaline fluids were trapped. This result is true even for most birefringent daughter minerals, in particular those contained in fluorite (identified as scheelite) and those contained in scheelite-2. In the latter host mineral, the melting temperature of the birefringent daughter is close to the bulk homogenization temperature (400 vs. 416 °C), meaning that trapping of the fluid is close to saturation in this mineral (the expected situation if the birefringent crystal is scheelite, which is indeed likely although not demon-

Table 3 Summary of microthermometric measurements for Karézas FIs

Type	Rv	$TmCO_2$	T "e"	Tm ice	Tm hhl	Tm clt	$ThCO_2$	Th	Tm hl	Tm syl
Quartz Qm										
Vc-w	0.7/0.8	–57/–61	–25/–48	–5.2/–8		2/9.3	5/13 (V)	309/506		
Vc-wSn	0.5	–57/–76	–29/–48	–22/–30		–7/4	10/18 (V)	417/532	146/257	119/175
Lw-(c)Sn	0.35/0.5		–67.5*	–39*				415*		
Lw	0.35/0.5		–52/–31	–17/–25	–5.3*			389/396		
LwSn	0.35/0.5		–34/–57	–40/–16				399/543	239/311	161*
Quartz Qv										
Vc-w	0.8/0.9	–57/–62	–25/–49	–6/–9		4/9	0.5/7 (V)	325/535		
Vc-wSn	0.8/0.9	–69/–58	–34/–42			1/6		386/476		
Lw-(c)Sn			–26*	–18*		–4.2/–2.1		372/386		
Lw	0.1/0.45		–68*	–19/–6				317/550		
LwSn	0.1/0.45		–45/–68	–33/–27				302/479	158/175	
Fluorite										
Vc-w	0.9/1	–57/–59	–22*	–1*		9*	1/3 (V)	372/502		
Vc-wSn	0.9/1	–58/–59	–34/–37	–32/–26		–15/–8	11/21 (V)	369/526	154/287	165*
Lw-(c)Sn		–60*		–25*		5.6*		423*	404*	
LwSn			–26/–53	–42/–30				419/427	259*	165*
Scheelite 2										
Vc-w	0.7/0.9	-57/-65	–44*	–40*	–2.4	5/9	6* (V)	310/397		
Vc-wSn	0.7/0.9	-57/-68	–34/–46	–26/–16		1/3		402/423		
Lw-[c]			–38*	–14.6*				352*		
Lw-(c)Sn	0.1/0.45		–26/–44	–13.8/–9.6		–5.2/–2.5		379/411	279*	110*
Lw	0.1/0.45		–34/–38	–16/–4	–22/–30			334/378		
LwSn	0.1/0.45		–36/–43	–31/–25				329/416	112/316	

(continued)

Table 3 (continued)

Type	Rv	$TmCO_2$	T "e"	Tm ice	Tm hhl	Tm clt	$ThCO_2$	Th	Tm hl	Tm syl
Quartz Qp										
Vc-w	0.8/0.9	–56.7/–62.4				8.9/11.3	8.5/18.4 (V)	341/357		
Lw			–22	–6.2/–3.5				276/316		
LwSn			–37/–54	–41/–28.5				336/370	106/239	140*

Abbreviations: *Rv* volumetric ratio of vapor or volatile phase; *Tm* CO_2 melting temperature of "CO_2" ice; *T "e"* first melting temperature of water ice, a proxy for eutectic temperature Te; *Tm ice* melting temperature of water ice; *Tm hh* hydrohalite melting temperature; *Tm clt* clathrate melting temperature; *Th*CO_2 homogenization temperature of volatile phase (V into the vapor phase); *Th* global homogenization temperature; *Tm hl* halite melting temperature; *Tm syl* sylvite melting temperature. Temperature range is indicated, excepted where only one measurement was possible (*). In one FI of the Lw-(c)Sn type in scheelite, melting temperatures of 58 and 124 °C were also obtained for two separate birefringent crystals

Table 4 Composition of volatile phase obtained by Raman microspectrometry in three inclusions from Qm quartz at Karézas

Type	Numéro	ZCO_2	ZCH_4	ZN_2
Vc-w	Kz7-13B1/3	57.1	24.8	18.1
Vc-wSn	Kz26-2	49.9	36.5	21.6
Vc-wSn	Kz7-13B1/1	50.0	50.0	0.0

strated). The aqueous phase of most FI types (except in quartz Qp) contains dissolved divalent cations, as shown by the first melting temperatures of ice, which are as low as −48 to −68 °C. The latter temperature could reflect the presence of abundant lithium, as the eutectic temperature in the LiCl–H_2O system is −77 °C (e.g., Dubois et al. 2010). The bulk Th values are elevated for all Karézas skarn FIs, most being ≥ 350 °C, with a distinct trend in which vapor-dominated FIs display higher Th than liquid FIs, and the same for daughter mineral-bearing FIs of each family relative to the less-saline ones (Fig. 9). By contrast, the FIs from the external quartz Qp have significantly lower Th values.

3.6 Fluid Compositional Trends and Fluid Evolution

The bulk salinity (expressed as wt% equiv NaCl) was estimated in the Vc-w inclusions using the temperatures of clathrate melting and "CO_2" homogenization (Diamond 1992). Compositions of the hypersaline and aqueous FIs were estimated using the $CaCl_2$–NaCl–H_2O model system (Bodnar 2003, and references therein), which yields both a bulk salinity estimate and an estimation of the Ca/(Ca + Na) atomic ratio (Ca number = Ca#). The "Na" component deduced from the model system must be, for many analyzed hypersaline FIs, a Na + K component, as

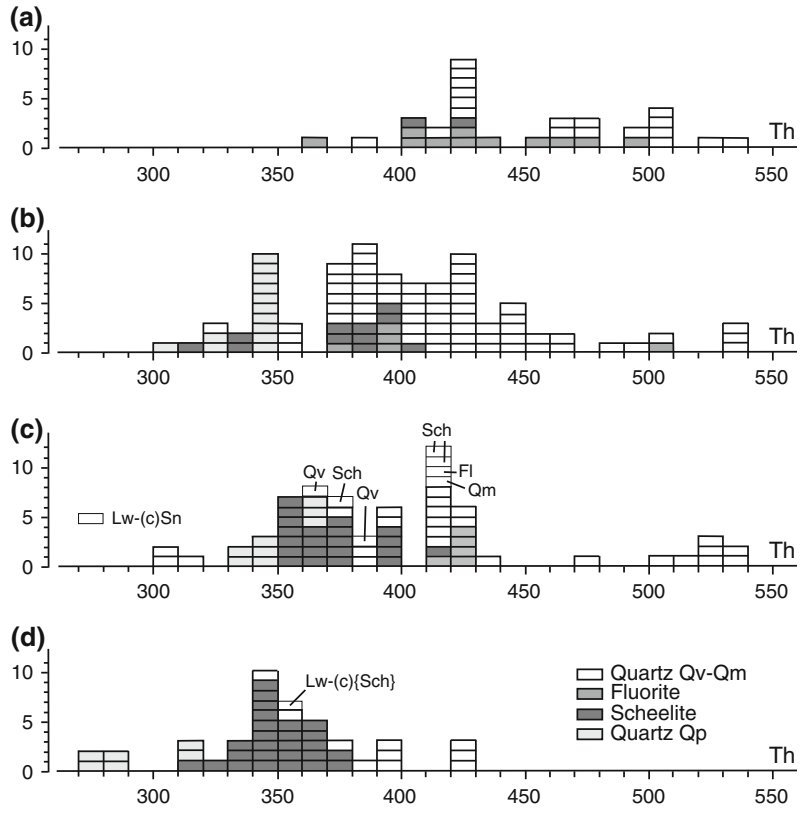

Fig. 9 Histograms of homogenization temperatures for the different families of fluid inclusions in Cycle II minerals from Karézas skarn. **a** Vc-wSn; **b** Vc-w; **c**, LwSn; **d** Lw

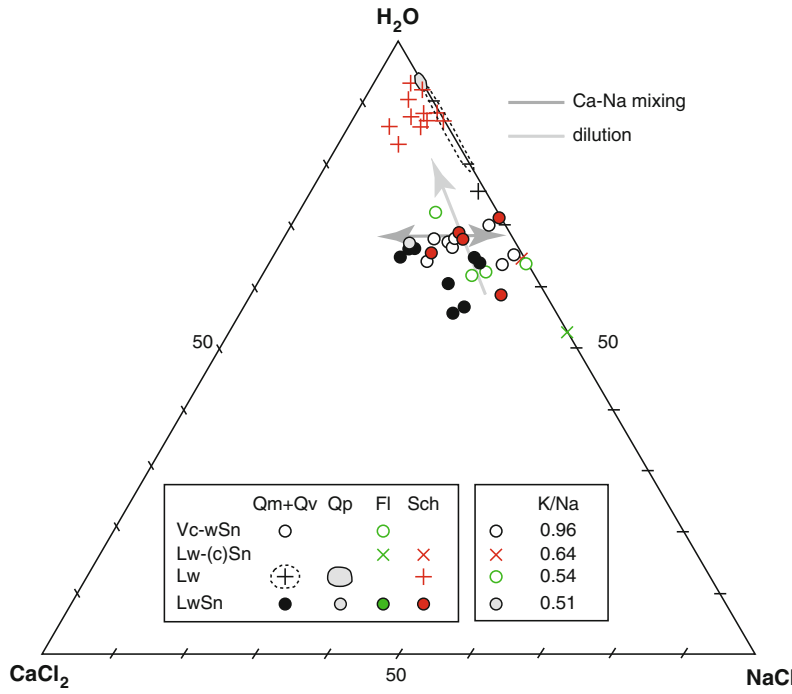

Fig. 10 Estimated compositions of hypersaline and aqueous fluid inclusions from Karézas in the H_2O–NaCl–$CaCl_2$ diagram (Bodnar 2003 and references therein)

shown by the presence of sylvite among the daughter minerals. A few K/Na ratios can be estimated using the KCl–NaCl–H_2O model system (Bodnar 2003 and references therein), and are rather high, varying from 0.96 (Vc-wSn in quartz Qm) to 0.51 (LwSn in quartz Qp), with intermediate values occurring in fluorite (0.54 in Vc-wSn) and scheelite-2 (0.64 in Lw-(c)Sn). For a given type of FI, and in each host mineral, the Ca# varies between very low values (close to pure "sodic" compositions, i.e., <0.05) and a maximum value of 0.58. The mean Ca# is similar for most Vc-wSn and LwSn inclusions, from 0.19 to 0.23. The Lw FIs from scheelite-2 display a similar mean Ca# of 0.23. As shown in Fig. 10, these variations are attributed to (1) mixing between a pure NaCl (±KCl) component and a component dominated by $CaCl_2$ (with Ca# 0.6), and (2) dilution by a low-salinity aqueous component. Because the hydrohalite is systematically observed to melt before the ice in the Lw inclusions from scheelite-2, their salinity in the $CaCl_2$–NaCl–H_2O model system (Table 3) is rather low (Fig. 10).

In the Th-bulk salinity diagram (Fig. 11a), the Karézas FIs display three distinct trends. The first includes all of the hypersaline FIs, with no difference found between the volatile-rich and purely aqueous ones; the second trend includes all aqueous Lw FIs; the third comprises the Vc-w FIs. These three trends have the same two characteristics: (1) a salinity decrease correlated to a decrease in Th, and (2) the more-saline and higher-Th FIs are hosted in the skarn quartz (Qm and Qv) and the less-saline and lower-Th FIs are in the pegmatite quartz (Qp), whereas the fluorite- and scheelite-2-hosted FIs have intermediate values of salinity and Th. Similar trends are observed for the volatile components where the melting temperature of the "CO_2" ice is taken as a proxy for the more or less significant proportion of a $CH_4 + N_2$ component in the volatile phase (Fig. 11b). There is one trend for the Vc-wSn FIs and another trend for the Vc-w, each trend showing a decrease in $TmCO_2$, i.e., in the $CH_4 + N_2$ content, as Th decreases. These trends correspond to the three successive trapping episodes identified for the fluid inclusions, i.e., a

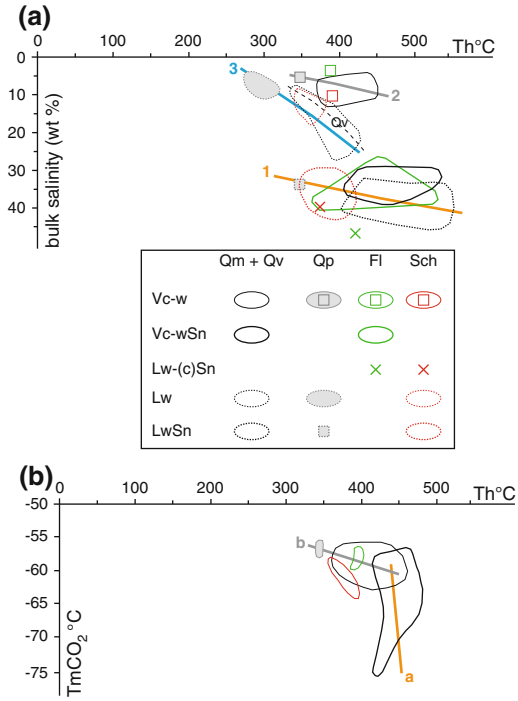

Fig. 11 Fluid evolution in Karézas skarn (Cycle II). **a** Th-bulk salinity diagram (salinity as NaCl equiv wt%); **b** Th-Tmclath diagram relating the volatile composition to temperature of homogenization. Explanations in the text

first "hypersaline" trend for the primary hypersaline FIs, then a "volatile-rich" trend for the pseudo-secondary Vc-w inclusions, and finally an "aqueous" trend for the secondary Lw FIs. Together, these record complex mixing processes involving different end-member fluids, occurring at different times.

"Hypersaline" trends: Coexistence of the hypersaline aqueous LwSn FIs with the vapor-dominated Vc-wSn could suggest that both FI types may be the result of an unmixing process. This model is, however, undermined by the very high salinities of the Vc-wSn inclusions, which are similar to those of the LwSn inclusions. The hypersaline vapor-dominated Vc-wSn FIs follow in Fig. 11a, a trend that systematically parallels the LwSn trend. It is therefore possible to interpret the Vc-wSn FIs as the result of a mixing process between brines of the LwSn type and a volatile-rich, low-density component, i.e., salinity of the Vc-wSn is inherited from the mixed brine. The LwSn trend may record the mixing between a very saline end member possibly represented by LwSn FIs in the skarn quartz (Qm and Qv), and a slightly less-saline end member represented by LwSn FIs in the quartz Qp, the latter being characterized by a high Ca#, in contrast to the former (Fig. 10). Being trapped in FIPs within the pegmatite quartz far from the Karézas skarn proper, these Ca-rich brines are interpreted as being representative of the "regional" fluids, which equilibrated with the basement rocks.

"Aqueous" trend: Data for the Lw fluids testify to the mixing between a rather saline and Ca-rich fluid and a low-salinity fluid without calcium (Figs. 10 and 11a). The latter is found in FIs in the skarn minerals, whereas the former is preserved in the external pegmatite quartz.

3.7 Reconstructing the Karézas P-T-t Path

A series of isochores were constructed (Fig. 12), using data from Bodnar (2003) for the aqueous inclusions, including the hypersaline LwSn, and from Bowers and Helgeson (1983) for the Vc-w inclusions. Only a few external data constrain the P-T-t path of the Karézas skarn. First, the retrograde path of the M3 regional metamorphism was independently estimated (Fig. 4) and may be used as a reference frame in Fig. 12. Second, the löllingite to arsenopyrite transformation, likely following the reaction Lol + Po + S_2 = Apy (using substage Ib pyrrhotite) provides an independent thermometer. Knowing the arsenopyrite composition, and using an ideal solid solution model for the sulphur content in löllingite, the experimental data of Kretschmar and Scott (1976) for the pure end members yield a temperature estimate of 420 ± 30 °C. The pressure effect on the equilibrium temperature (Sharp et al. 1985) can be neglected at the low pressure inferred for the skarn formation (see below). Third, a pressure estimate at the time of retrograde substage Ib may be obtained using the Al-in-amphibole barometer of Schmidt (1992) and the ∑Al content of the retrograde amphibole

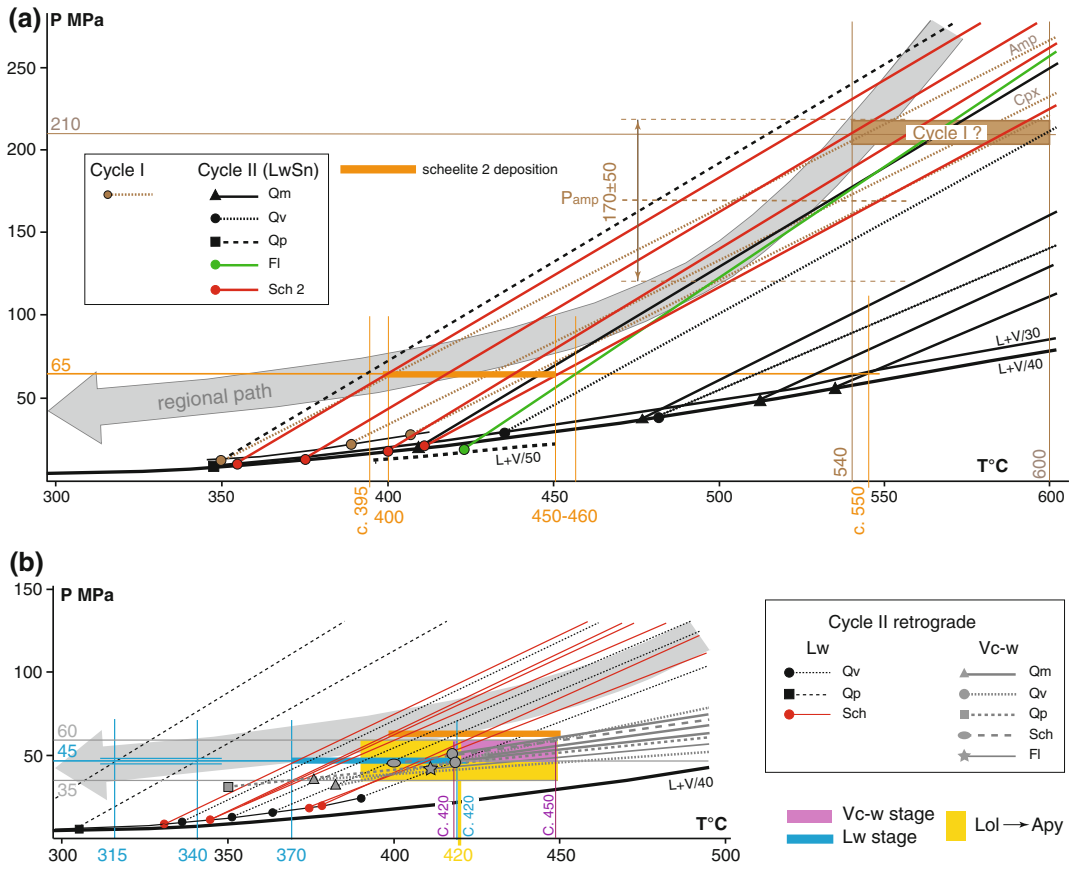

Fig. 12 Estimation of P-T conditions of Karézas skarn formation. **a** *Cycle I* and scheelite deposition during substage IIA of *Cycle II*; **b** Substage IIB of *Cycle II*. See text for discussion

in the skarn. With ∑Al between 1.03 and 1.10 apfu, a mean pressure estimate of 170 ± 50 MPa is thus obtained.

P and T conditions for Cycle I: In the absence of salinity data, no isochore can be drawn with confidence, but assuming skarn I-forming fluids have a salinity of 20 wt% equiv NaCl or more (not unrealistic in such environments), hypothetical isochores may be drawn for the Ib clinopyroxene and the Ib amphibole (Fig. 12a). Only the lowest Th isochore (for retrograde amphibole) intersect the regional M3 P-T-t trend, at a pressure of ca. 210 MPa for a temperature of ca. 540 °C; this pressure is consistent with the Al-in-amphibole geobarometer, although only in the upper part of the confidence interval of the latter (Fig. 12a). It would correspond (with density of 2.7 for the crustal rocks) to a depth of ca. 8 km. The clinopyroxene isochores, on the other hand, are a poor match with the regional trend, and instead suggest anomalously high trapping temperatures, up to 600 °C or more, at the 210 MPa pressure. This condition would remain true even if the skarn I-forming fluids were far more saline than 20 wt% equiv NaCl. We therefore conclude that the Cycle I skarn developed by a thermal anomaly that was superimposed on the regional P-T-t trend, and thus was coeval with the partial melting at the end of the M3 event (syn- to post-transition of sillimanite to andalusite) and the peri-anatectic leucogranites and pegmatites. The pegmatite swarms in the Karézas area imply proximity to a concealed late Miocene anatectic domain,

hence the barren Cycle I skarn could be viewed as peri-anatectic in setting and origin.

P and T conditions for Cycle II: In order to reconstruct the P-T conditions at the time of Cycle II skarn formation, it is necessary to consider the fluids that were trapped in the Qp quartz under the regional conditions, i.e., on the M3 P-T-t path. This evaluation must be done successively for each of the three trends shown in Fig. 11 (hypersaline, volatile-rich, and aqueous).

"Hypersaline" trend: Intersection of a representative isochore for LwSn FIs within quartz Qp with the regional path yields estimated trapping conditions of ca. 395 °C and ca. 65 MPa (Fig. 12a). The pressure must be interpreted as lithostatic, i.e., a depth of ca. 2.4 km for skarn formation. Under this ca. 65 MPa regional pressure, the most saline brines circulated and mixed with the regional brines, at temperatures that decrease from ca. 550 to ca. 400 °C, during which scheelite-2 deposition occurred in the temperature range of 450–400 °C.

Aqueous trend: Isochores for Lw inclusions in quartz Qp intersect the regional P-T-t path at ca. 45 MPa, for temperatures between 340 and 315 °C (Fig. 12b), at a depth of ca. 1.7 km (i.e., ca. 700 m of exhumation). Under this regional pressure, the residual brines in the skarn system were cooled and diluted from ca. 420 to ca. 370 °C.

"Volatile-rich" trend: The Vc-w trapping conditions may be constrained in two ways. First, being slightly later paragenetically than the main growth stage of the scheelite in which they are contained, these pseudo-secondary FIs likely were trapped at pressures equal or lower to those of the main stage of scheelite deposition. Second, given that the Raman spectra of some Vc-w inclusions indicate the presence of H_2S, it is probable that the circulation of fluids of this trend was linked to an increase in sulphur activity during the löllingite transformation to arsenopyrite, i.e., at the estimated temperature of 420 ± 30 °C. The latter constraint is met for a large range of trapping pressures, between ca. 60 and ca. 35 MPa (Fig. 12b). However, this range must be enlarged to ca. 60–ca. 45 MPa in order to ensure that the Vc-w FIs were trapped before the Lw FIs, as is observed; in that case, the trapping temperatures were ca. 450–ca. 420 °C and thus consistent with the estimated löllingite to arsenopyrite transition temperature (but in the higher part of the temperature range of the confidence interval). These pressures are less than the scheelite-2 trapping pressure, which satisfies the constraint of Vc-w FIs being later than scheelite-2. It may be seen in Fig. 12b that the estimated trapping temperatures of Vc-w are higher than scheelite-2 (450–420 vs. 450–400 °C). Consequently, we conclude that the skarn environment experienced a temperature increase after scheelite-2 deposition.

4 "Mesothermal" Polymetallic Deposits

Three significant polymetallic vein systems are known in the Edough-Cap de Fer district: Aïn Barbar, Mellaha Cove, and Saf-Saf (Figs. 2 and 3). Each has concentrations of Cu, Zn, and Pb, but significant mining in recent times has only taken place at Aïn Barbar. The Mellaha occurrence was the site of old artisanal mining; the Saf-Saf deposit was found by drilling and underground exploration.

The three vein systems share common characteristics. First, all are located close to the interface between the Edough crystalline basement (inferred at Aïn Barbar) and the tectonic cover of Cretaceous flysch. Veins are hosted either within the flysch (which acted as a reservoir for the hydrothermal fluids) or in the basement, where the flysch thickness is greatly reduced (Saf-Saf). Second, all veins are spatially associated with coeval microgranite bodies that are cut by intrusions at the basement-flysch interface (Mellaha and Saf-Saf laccoliths) or that protrude as blind dikes in the flysch cover (Aïn Barbar). Third, the veins formed under the impermeable lid of the Numidian flysch nappe (with self-sealing alterations of silicification and/or chloritization), with thicknesses of ∼1200 m. Therefore, fluid pressures were mainly lithostatic ($\geq$ 33 MPa), except where local fracturing of the impermeable lid allowed transient shifts towards hydrostatic pressure, as documented at Aïn Barbar (Marignac et al.

2015). Fourth, all of the veins strike N170°–N150° E and share an evolution dominated by hydraulic fracturing (brecciation, crack-sealing). Fifth, they display the same paragenetic succession, involving two stages of mineralization. An earlier "mesothermal" stage (Lindgren 1933) with accompanying propylitic alteration (chlorite, epidote) is characterized by the successive deposition of (1) sphalerite and galena, and (2) chalcopyrite ± Bi-sulphides, the sphalerite displaying the so-called "chalcopyrite disease" (Barton 1978). Following a paragenetic gap, an epithermal stage formed comb quartz in veins and the succession of quartz-chlorite-adularia-base metal sulphides (Mellaha, Saf-Saf), and chalcedonic quartz-Sb-rich arsenopyrite ± stibnite (Saf-Saf).

Aïn Barbar: This deposit is described in detail in a companion paper (Marignac et al. 2015) and is only briefly summarized here. At ca. 16 Ma, during intrusions of microgranites, a high-enthalpy, liquid-dominated geothermal system was active in the Cretaceous flysch reservoir. Temperatures as high as ca. 350–375 °C were attained in the deep parts of the system, at a depth of ca. 2 km, accompanied by a massive input of sodium that formed metasomatic plagioclase-rich hornfels (Chaïba domain); higher in the Cretaceous flysch aquifer, invasion of hydrothermal fluids (300–270 °C) was associated with hydrothermal metamorphism that produced quartz-chlorite, calcite-chlorite, wairakite-chlorite, and epidote alteration zones. Concomitant with the paleogeothermal circulations, faulting created N170° E fracture zones that progressively channelled fluid flow, with the development of linear propylitic zones and precipitation of Zn–Pb–Cu sulphides at temperatures of 330–285 °C. Ore deposition during this mesothermal stage resulted from anisothermal mixing of two fluids, one relatively hot and moderately saline (~7 wt% equiv NaCl) and the other colder and of low salinity (0.5 wt% equiv NaCl). At ca. 15 Ma, renewed magmatic activity (subvolcanic rhyolite dikes) produced a new and shallower (ca. 800 m depth) geothermal system, in which the convective circulation of surficially derived fluids formed the epithermal veins, at temperatures between 300 and 250 °C.

Mellaha cove: At Mellaha cove, a small inlier of Senonian flysch uplifted from beneath the Numidian flysch, on the western limb of the Edough anticline (Fig. 2), exhibits the same zoning pattern of hydrothermal alteration as at Aïn Barbar, except for the plagioclase-rich hornfels (Fig. 13). A garnet (grossularite) zone formed along the shallow westward-dipping contact of a microgranite body. An epidote zone cuts the garnet zone in the mineralized area, in which the garnet is altered to chlorite and amphibole. Within the veins, a quartz-adularia assemblage is a late feature. Thus, like at Aïn Barbar, a vein-related alteration seems to have overprinted an earlier paleogeothermal alteration (Fig. 14).

Saf-Saf: In the Saf-Saf area (Fig. 3), two main chalcedonic quartz-Sb-rich arsenopyrite ± stibnite veins are recognized, plus numerous (up to 20) secondary veins. As demonstrated by exploration drilling, the veins have a mean dip of 65° E and extend to depths of more than 150 m. The veins are hosted mainly by the gneissic basement.

5 Epithermal Showings

In addition to the epithermal mineralization that overprints the mesothermal polymetallic veins, a group of separate epithermal showings occurs in the Edough massif. These showings are all hosted by basement rocks in a small area in the NE of the massif, where there also are concentrations of the Langhian magmatic intrusions (Fig. 3). Four styles of epithermal showings are recognized: (1) "fumerolic" tungsten, (2) polymetallic quartz veins, (3) stibnite veins and replacements, and (4) arsenopyrite-gold quartz veins. All of the veins display the characteristic attributes of epithermal vein systems of the adularia-sericite (low sulphidation) class, as defined by Heald et al. (1986) and Sillitoe (1993).

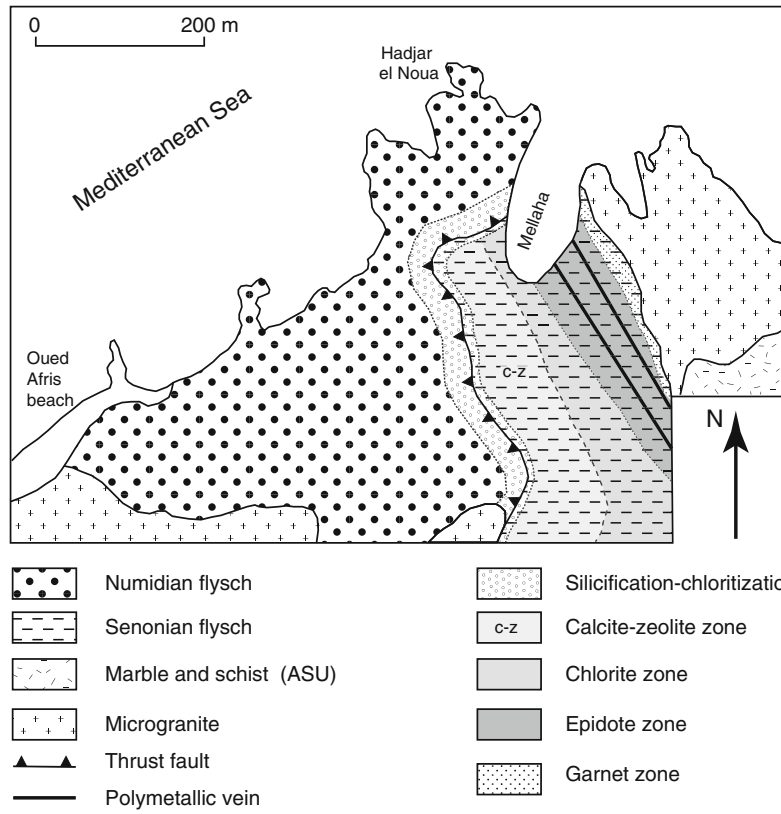

Fig. 13 Geologic map of the Mellaha cove area (from Aïssa et al. 1998a)

5.1 "Fumerolic" Tungsten

The Kef el Fedjel tungsten showing is hosted within a subvolcanic rhyolite plug that branches from a N170° E dike (Fig. 3). This rhyolite belongs to the peraluminous K- and F-rich group of late rhyolites of early Langhian age in the Edough massif. In addition to F (mean 0.4 wt%) and Li (mean 92 ppm), the rhyolites are enriched in rare metals (mean 19 ppm W, 100 ppm Sn, 12 ppm U), relative to typical rhyolite. The devitrified rhyolite contains either veinlets or "miarolitic" vugs filled with a quartz-topaz-fluorite-adularia-scheelite-(tourmaline- zircon) assemblage. Topaz and scheelite are the earliest paragenetically, followed by quartz and fluorite. These late minerals host aqueous FIs of low (1.4 wt% equiv NaCl, in quartz) to very low ($\leq$ 0.5 wt% equiv NaCl, in fluorite) salinity, that show a range homogenization temperatures from 270–250 °C in quartz to 245–160 °C in fluorite.

5.2 Polymetallic Veins

A series of uneconomic, polymetallic quartz veins are widespread in the northern part of the Edough massif (Fig. 3). These veins are hosted in rhyolite, micaschist, gneiss, and amphibolite, and trend N0° to N150° E. Conspicuous wall-rock alteration is absent, although white micas are disseminated in wall rocks up to a few meter from the veins. The polymetallic quartz veins exhibit the same two-stage evolution as their counterparts in the mesothermal deposits, and may be considered equivalent. Paragenetically first is a microcrystalline quartz-base metal sulphide-(adularia- phengitic-illite) assemblage, and second, following a faulting event, a chalcedonic quartz-pyrite- arsenopyrite-marcasite--fluorite-chlorite assemblage, with typical comb and crack-seal features. Within the amphibolite-hosted veins, tennantite is associated with chalcopyrite, and boulangerite occurs as microcracks in galena.

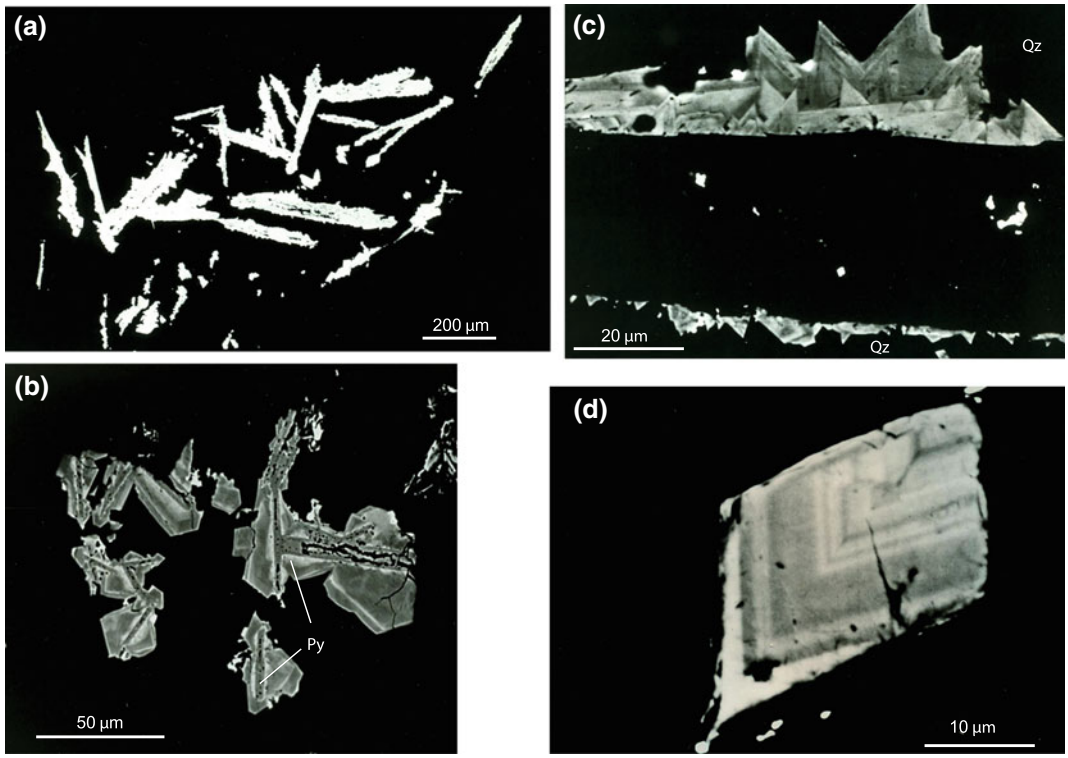

Fig. 14 SEM backscattered electron images of gold-bearing arsenopyrite from Koudiat El Harrach gold occurrence. **a** Pyrite laths (likely pseudomorphs after pyrrhotite), with arsenopyrite overgrowths, in quartz matrix (*black*). **b**, **c** Zoned arsenopyrite overgrowths. **d** Detail of zoning in arsenopyrite. Abbreviations: *Qz* quartz; *Py* pyrite

5.3 Stibnite Mineralization

Several stibnite showings are widespread in rocks of the Marble Complex surrounding the Kef Lakhal amphibolite (Fig. 3). These showings occur mainly in the marbles, forming veins, stockworks, and replacements, either discordant or strata-bound in lenses and disseminations (Toubal 1984; Aïssa 1996). For several meters surrounding the ore bodies, the marble is silicified, expressed first as replacements along calcite cleavage and microcracks and last as nearly total replacements (by microcrystalline quartz) close to the ore. The siliceous mineralized bodies display a three-stage depositional history including the formation of: (1) mosaic quartz and rare sulphides (pyrrhotite and base-metal sulphides); (2) chalcedony microspherulites, with interspersed antimony minerals including acicular prisms of stibnite that replace earlier berthierite, relics of which are common within the stibnite, and a series of rare sulphosalts (füloppite, zinkenite, stephanite, freibergite); and (3) microcrystalline quartz recrystallized from the chalcedony microspherules, concomitantly with replacement of the stibnite prisms by pyrite and/or marcasite and skeletal arsenopyrite. Thus, the stibnite mineralization was interspersed between the two epithermal episodes recorded in the late polymetallic quartz veins. Fluid inclusion studies (Aïssa 1996; Aïssa et al. 1998a) show the anisothermal mixing of a hot and moderately saline La fluid (ca. 300 °C; up to 5.1 wt% equiv NaCl) with a slightly cooler and less saline Lb fluid (ca. 250 °C; 1.4 wt% equiv NaCl). The FIs typically contain several birefringent solids (heterogeneous trapping), including kaolinite and anhydrite. The temperature decrease associated

with the mixing event is considered the main cause of stibnite deposition (e.g., Belhaj 1992), implying that La was the Sb-transporting fluid. During the late (post-chalcedony) stage, only the Lb fluid was involved in hydrothermal circulation, including much lower temperatures, down to 140–150 °C.

5.4 The Koudiet El Harrach Gold Showing

At the westernmost end of the Kef Lakhal amphibolite massif, two vertical quartz veins, striking N10° to N170° E, located at the contact of the Kef el Fedjel rhyolite plug with the surrounding gneiss, are the host for gold (Fig. 3) (Aïssa et al. 1998b). Gold is only found as invisible grains within arsenopyrite. For a width of ca. 20 cm along the margins of the veins, the surrounding gneiss is intensely brecciated and altered (silicification, chloritization, sericitization, and kaolinization) and contains numerous quartz-adularia-fluorite veinlets. The quartz filling of the veins was multi-stage. It began with a stibnite episode (comb quartz and microcrystalline quartz containing acicular stibnite and relicts of berthierite). Fracture-related reopening of the veins was followed by deposition of comb chalcedonic quartz containing small microinclusions of cubic fluorite that were trapped at the end of its growth, then by barren massive quartz including ghosts of a bladed mineral that may have been anhydrite. A third episode of fracturing and brecciating was followed by deposition of microcrystalline quartz with sulphides, including gold-bearing arsenopyrite. The arsenopyrite is euhedral and uniformly rims elongate blades of a dissolved mineral, replaced by As-bearing marcasite (Fig. 16). Relicts of pyrrhotite (X_{FeS} 0.905) and pyrite suggest that these blades are former pyrrhotite. The arsenopyrite is zoned and shows rhythmic variations of the (As + Sb)/S ratio; compositions are uniformly sulphur-rich, ranging from $Fe_{0.987}As_{0.886}$ $Sb_{0.010}$ $S_{1.117}$ to $Fe_{1.004}$ $As_{0.974}$ $Sb_{0.016}$ $S_{1.006}$. A mean gold content of 600 ppm was measured in the arsenopyrite using a CAMECA SX50 electron microprobe, under experimental conditions (20 kV, 30 nA, 30 s counting time) that yielded a detection level of 400 ppm; the maximum observed gold content is 1700 ppm. Ion microprobe images confirm the incorporation of gold in the arsenopyrite crystal structure and show that the gold is preferentially concentrated in the As-rich growth zones (Aïssa et al. 1999).

Measurable FIs in quartz from the Koudiet el Harrach showing were only found in the chalcedonic quartz that preceded the gold mineralizing event. These are aqueous two-phase FIs that display evidence of mixing between two fluids of different salinities, LI ($\geq$ 2.2 wt% equiv NaCl), and LII (0.5 wt% equiv NaCl), under decreasing temperatures with time from ca. 270 °C down to ca. 210 °C, but with several inverse trends suggesting to thermal recharges of the hydrothermal system. Leaching of the nearby rhyolite is the likely source of the fluorine in the microinclusions of fluorite in the quartz.

6 Discussion

6.1 The Karézas Skarn: Role of a Concealed Rare-Metal Granite

Origin of the Karézas fluids: During mineralizing stage IIB, three components were involved in the Karézas hydrothermal fluid: a volatile-rich component, and two brines, one of regional distribution, the other local and specific to the skarn. The volatile component is rich in CO_2, methane, and nitrogen, and therefore likely results from the devolatilization of a carbon-rich rock. The Seraidi gneisses that host the Karézas skarn are typically poor in graphite, but graphitic metapelites are abundant in the tectonically overlying Alternance Series Unit (ASU). The regional brine has a Na/Ca ratio of ~0.7, and cannot have equibrated solely with the rather sodic Seraidi Gneiss (mean Na/Ca 6.8). In order to yield the Ca content observed in the FIs, a contribution from mafic rocks is required (e.g., Bucher and Stober 2010), such as the massive amphibolites in the

Marble Complex Unit. The "local" brine, on the other hand, has a low Ca# and high K/Na ratio: it thus shares characteristics of a "magmatic" fluid, i.e., one that equilibrated with a granitic magma (Aïssa et al. 2001). It thus may be concluded that the "hypersaline" trend reflects mixing between a magmatic-hydrothermal end member and two metamorphic fluids, one (the calcic brine) derived from the host-rock gneiss (and more distal amphibolites), the other (the C–O–H–N fluid) from the overlying ASU graphitic rocks. We suggest that this mixing process was the cause of the scheelite precipitation (Fig. 11a). The presence of nitrogen in the volatile component of the mixed fluids evidently facilitated scheelite precipitation, as demonstrated by Gibert et al. (1992).

Presence at depth of a rare-metal granite (RMG): The granite that generated the W-rich magmatic brine is concealed, but its nature may be further constrained by considering the chemistry of the skarn minerals. Given the abundance of fluorine and lithium (fluorite, zinnwaldite), this granite is likely a member of the RMG class (e.g., Linnen and Cuney 2005). Another late Miocene RMG is known in the internal zone of the Maghrebide belt (Filfila granite; Bouabsa et al. 2010). Indeed, emplacement of peraluminous leucogranites and/or RMG intrusions immediately following the end of ductile detachment seems typical of Mediterranean metamorphic core complexes, being documented for instance in the Betic Cordillera (Esteban et al. 2008), the Alpi Apuane in the Apennines (Larderello Li-granite; Puxeddu 1984; Cathelineau et al. 1994), and Turkey (Okay and Samir 2000). For such granites, the solidus temperature is usually low, down to 700 or even 650 °C at low pressures (e.g., Pichavant et al. 1987; Aksyuk and Konyshev 2011), which should be the temperature of the pristine magmatic fluid (prior to mixing with external fluids). Using the pressure-salinity diagram for the H_2O–NaCl system (Atkinson 2002), the emplacement depth of the concealed parent granite may be constrained to ca. 2.6 km (70 MPa), for a solidus temperature between 650 °C (i.e., ~4 % F in the melt) and 700 °C (i.e., ~1 % F in the melt), if the high-salinity skarn-forming magmatic brine resulted from phase unmixing ("second boiling") in the granite cupola. The top of the concealed intrusion may therefore lie only ~200 m below the skarn, estimated formed at ca. 2.4 km depth (see above). This cupola would therefore be too deep to have been reached by the mine workings (–135 m).

Subsequent evolution: The Vc-w fluids are typical C–H–O–N fluids, and consequently may also be interpreted as fluids of metamorphic origin, derived from devolatilized graphitic metapelites. Given continuity of the Vc-w fluids with the volatile component of the "hypersaline" trend (Fig. 12b), they may be envisaged as paragenetically late representatives of the same metamorphic fluids that issued from the ASU, circulating at a time when magmatic brines were no longer present in the skarn environment. In the same way, it may be proposed that for the late "aqueous" stage, the Ca-rich fluid is a late representative of those involved in skarn formation, whereas the low-salinity fluid is typical of those of more external derivation that circulated within the basement of the Edough massif.

Necessity of a new magmatic episode: Theoretical models suggest that a temperature of ca. 350–400 °C cannot be sustained in a fluid circulating above an intrusion having a diameter of a few kilometers (realistic if the Filfila granite is taken as a reference; Bouabsa et al. 2010) for more than ~20 kyr (e.g., Cathles 1977; Norton and Cathles 1979). Such temperatures were likely maintained in the Karézas skarn, but because it was exhumed from ca. 2.4 to ca. 1.7 km, this difference in depth would require an unrealistic exhumation rate of ~37 mm yr^{-1}. Conversely, at a reasonable estimated exhumation rate of ca. 1 mm yr^{-1} (Fig. 16), a time span on the order of 700 kyr would have elapsed between the scheelite-2 mineralizing event (ca. 2.4 km) and the late sulphidation episode (ca. 1.7 km), i.e., this episode would be of earliest Langhian age. We therefore conclude that a new magmatic heat advection event occurred in the Karézas area at the latter time, thus explaining the temperature increase recorded in the FIs (Fig. 15). As no new influx of magmatic fluid

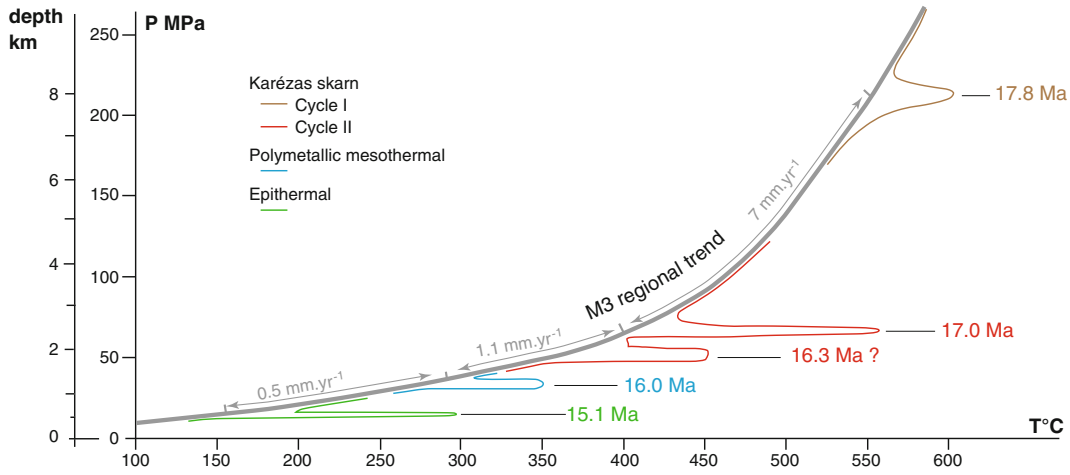

Fig. 15 Reconstructed P-T-t path of Edough Massif during late Burdigalian-early Langhian exhumation. The M3 trend is from Fig. 4

is observed in the skarn environment, this inferred intrusion must be deeper than the concealed RMG.

6.2 Mesothermal Stage: Role of the Basement

In the Aïn Barbar paleogeothermal system, sodium metasomatism resulted from invasion of the reservoir by fluids that had equilibrated with the sodic Edough gneiss. Moreover, lead isotope systematics suggest that the Edough basement (both gneiss and amphibolite) contributed significantly to the metal budget of the polymetallic veins (Marignac et al. 2015). Therefore, the Lw regional fluid that existed during the final stage of Karézas skarn evolution is the best candidate to represent at Aïn Barbar both the early metasomatizing fluid and the hot and saline component of the mineralizing fluids. Confined to the basement until the earliest Langhian, these fluids would have been mobilized by the intrusion of a concealed granite batholith at depth (Marignac et al. 2015). A large granite massif of Langhian age is known in Lesser Kabylia (Bougaroun massif; Bouillin 1979; Fourcade et al. 2001), which is a possible model for the granite batholith inferred in the Edough-Cap de Fer area.

6.3 Epithermal Stage: Shallow Meteoric Water-Dominated Hydrothermal Systems

The group of late veins formed at very shallow depths and under temperatures below 300 °C and low salinity ($\leq$5–7 wt% equiv NaCl). Spatially associated alteration zones are mainly cryptic and characterized by chlorite, adularia, and phengitic illite; sulphides are disseminated. This group of veins is best classified as a member of the low sulphidation type of epithermal system (Heald et al. 1986; Sillitoe 1993).

Paleodepth: The Aïn Barbar epithermal veins were deposited beneath a Numidian cover of no more than 700 m, under predominantly hydrostatic pressure, with episodic boiling having occurred when the fluid temperature was close to 300 °C. On the one hand, the lack of evidence for boiling in the Edough veins, where temperature reached ca. 300 °C (although mostly $\leq$270 °C), indicates that hydrostatic pressure was uniformly $\geq$7 MPa, i.e., the deposits formed at no less than 700 m depth. On the other hand, owing to the subvolcanic setting of the Edough rhyolites, the formational depth could not have been much greater: a paleodepth of ca. 800 m is arbitrarily used in Figs. 15 and 16.

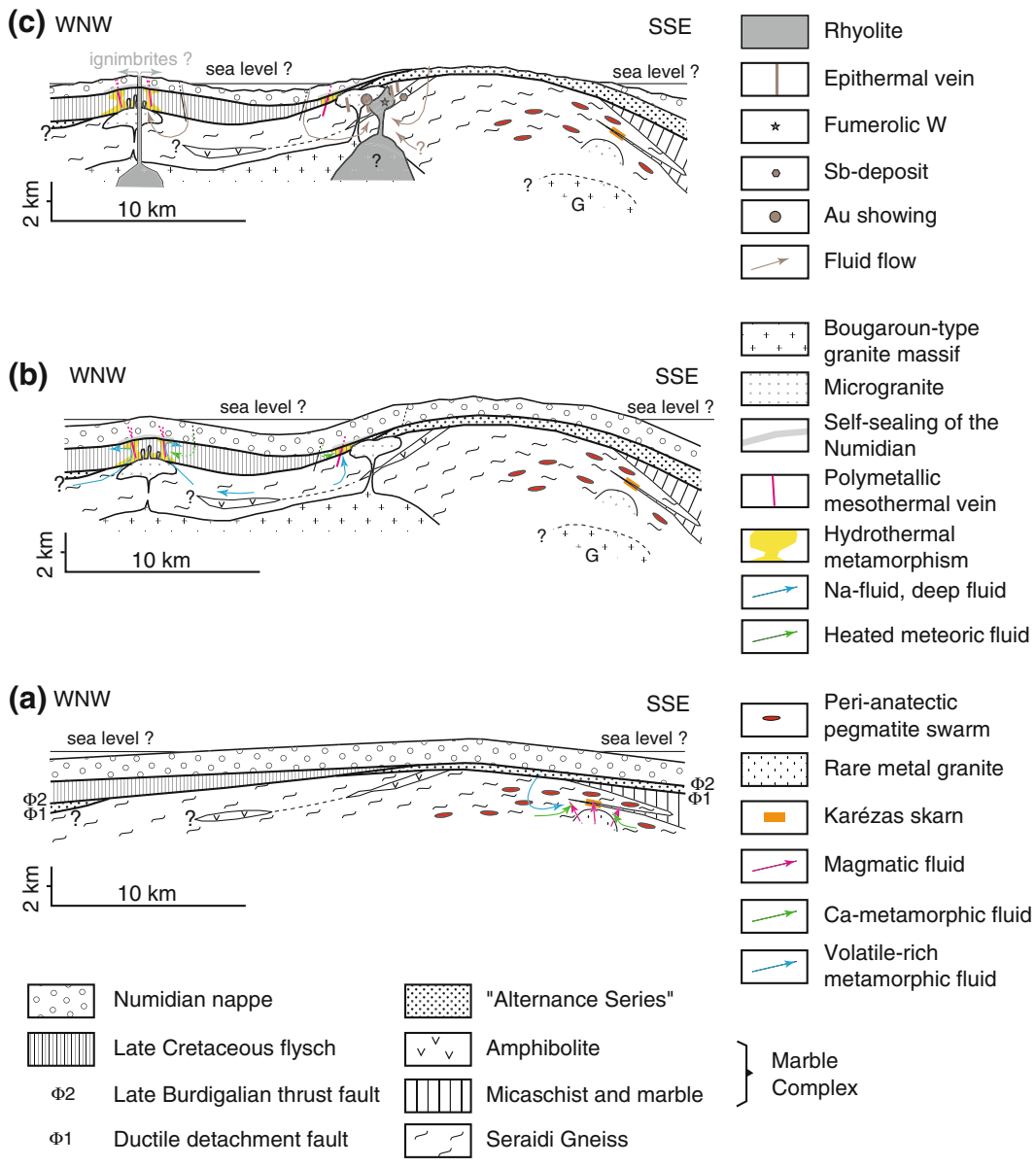

Fig. 16 Proposed three stages in late post-kinematic exhumation of Edough-Cap de Fer and associated mineralizing systems. During this time period (ca. 17–15 Ma), elevation of the paleosurface above sea-level likely remained moderate, as suggested by preservation of marine sediments of Burdigalian-Langhian age to west in Cap de Fer area (Hilly 1962). Hypothetical persistence of amphibolite or Alternance Series units are shown to explain their involvement in metal budget of mesothermal and epithermal deposits. **a** Burdigalian/Langhian boundary (ca. 17 Ma): intrusion of rare-metal granite and mixing of magmatic-hydrothermal and metamorphic fluids to form Karézas W-As-skarn; **b** Earliest Langhian (ca. 16 Ma): progressive emplacement of large granite batholith at depth modifies the fluid circulation regime; owing to related emplacement of high-level microgranite bodies, Cretaceous flysch reservoirs are invaded by hydrothermal fluids and mesothermal polymetallic vein deposits form in resulting paleogeothermal systems; G: possible precursor of granite batholith at ca. 16.3 Ma (see text); **c** Early Langhian (ca. 15 Ma): renewal of magmatic activity (subvolcanic rhyolites, ignimbrites?) promote active convection of surficial fluids (meteoric and possibly sea water) and formation of low-sulphidation epithermal deposits

Nature of the fluids: Two fluids were involved in mineralization of all of the studied epithermal deposits. The first fluid is characterized by a very low salinity (≤ 0.5 wt% equiv NaCl) and is best interpreted as meteoric water. As seen in Fig. 16c, the northern Edough epithermal deposits formed under a residual Numidian cover, whereas to the northeast basement denudation is likely, thus having allowed continuous recharge of the hydrothermal systems by meteoric water. The second fluid is of low salinity (up to ~ 5 wt% equiv NaCl); its origin is difficult to ascertain in the absence of isotopic data. This fluid could also be of meteoric origin, but exchanged with the reservoir rocks, or was a last remnant of the deep fluids involved in forming the mesothermal deposits. The presence in some of the Edough deposits of anhydrite remnants suggests that seawater could have been involved in the epithermal systems. Occurrence of the former Langhian Sea to the north of the east Algerian internal massifs is known from sedimentary rocks (Bouillin 1979; Hilly 1962), and, as suggested in Fig. 16c, this sea could well have surrounded the emergent highlands (Aïn Barbar and Edough antiforms).

Source of heat: The first stage in the evolution of the fumerolic scheelite showing of Kef el Fedjel is characterized by topaz, a high temperature mineral. The epithermal stage closely followed rhyolite emplacement in the early Langhian. The ca. 250 °C and higher temperatures that characterize the epithermal stage are far higher than expected for the very shallow depth inferred for their formation. Moreover, numerous indications exist of heat recharge during evolution of the hydrothermal systems. With respect to the mesothermal deposits, a sustained source of heat is necessary, and could not have been provided by the known rhyolite bodies, thus implying the existence at depth of larger magmatic reservoirs beneath both the northeast Edough and Aïn Barbar massifs (Fig. 16c).

Source of metals: Lead isotope data for the Aïn Barbar epithermal stage (Marignac et al. 2015) show that the Edough basement was a main source of the metals, a conclusion that apply to the Edough deposits given their similarities. Concerning the antimony deposits, two facts in particular suggest that the Kef Lakhal amphibolite was the source of this metal. First, these deposits are located close to the amphibolite massif (Fig. 3). Second, although Sb is usually absent from the polymetallic veins, the only polymetallic vein that cuts the amphibolite is found to display a Sb-bearing mineral (boulangerite).

7 Synthesis and Conclusions

The Edough-Cap de Fer massif was an active metamorphic core complex during the early Miocene, and its formation was coeval with opening of the Algerian oceanic basin. Ductile deformation in the complex had ceased before the late Burdigalian, when a return to compressive conditions resulted in emplacement of the Numidian flysch nappe with its sole of Cretaceous Kabylian flysch. This event was followed, in the very early Langhian, by folding that produced broad, SW-NE antiforms and synforms of the resulting tectonic pile, under a transpressive compressive regime linked to the Africa-Europa convergence, which is still active today.

During this change in global tectonic conditions, three magmatic events successively impacted the progressively exhuming Edough-Cap de Fer massif. These events, from the latest Burdigalian to the early Langhian, were ultimately driven by lithospheric delamination (Roure et al. 2012) or slab break-off and partial melting in the mantle, and by resulting heat advection and partial melting in the continental crust (Maury et al. 2000). When the deep parts of a metamorphic core complex undergo decompression, partial melting occurs (e.g., Norlander et al. 2002), resulting in migmatization and migration of granitic melts overlapping with deformation (e.g., Vanderhaeghe 1999). As heat is advected with the migrating melts, a feed-back relation promotes amplification of the thermal anomaly and its transfer (together with the pervasive melt migration) towards more and more shallow levels in the crust (Brown and Solar 1999). Such events occurred in the Edough

massif in the latest Burdigalian, accompanied by the emplacement of late- to post-kinematic leucocratic intrusions (leucosomes, leucogranites, pegmatites) within the Edough gneisses, forming a broad, peri-anatectic swarm. During the end of this event, at the Burdigalian/Langhian boundary, a highly fractionated granite was emplaced at shallow depth. In the earliest Langhian (ca. 16 Ma), mixing/mingling of mantle-derived and crustal melts led to the intrusion of the Edough-Cap de Fer I-type suite of dioritic, granodioritic, and granitic magmas, all of which were associated with the emplacement of a large concealed batholith. Finally, in the early Langhian (ca. 15 Ma), new batches of highly evolved granitic magma were emplaced under subvolcanic conditions, forming the Edough and Aïn Barbar rhyolites.

Four hydrothermal events were produced by these magmatic events in the Edough-Cap de Fer massif. As seen in Fig. 15, the late thermal history of the massif is marked by exhumation along a high temperature-low pressure path and punctuated by thermal pulses of magmatic origin (heat advection in uppermost crust), plus hydrothermal convection and the formation of a series of metallic deposits at progressively decreasing temperatures and depths. The estimated exhumation rates for the Burdigalian/Langhian boundary and early Langhian times in the Edough massif (1.1 mm yr^{-1}; Fig. 15) are consistent with those inferred for other peri-Mediterranean metamorphic core complexes during the post-kinematic stage, such as the Alpi Apuane in Italy (0.5 mm yr^{-1} in the Larderello system; Cathelineau et al. 1994; 0.7 mm yr^{-1}: Fellin et al. 2007), and the Aspromonte in Calabria (0.9 mm yr^{-1}; Heymes et al. 2010). The first hydrothermal event took place in the latest Burdigalian (ca. 17.8 Ma), when barren skarns were associated in the Edough gneisses with the percolation of peri-anatectic melts. Slightly later, at the Burdigalian to Langhian boundary (ca. 17 Ma), a second event produced scheelite-bearing skarn, superimposed on a barren skarn, associated with intrusion of a Li–F-rich granite. The third event was related to emplacement in the earliest Langhian of microgranites and the formation of mesothermal polymetallic veins (Cu–Zn–Pb) by high enthalpy paleogeothermal systems located in the Cretaceous flysch reservoirs; at this time, the role of the Numidian flysch nappe as an impermeable lid was decisive in maintaining very high temperatures (up to 350 °C) at a relatively shallow depth (ca. 1500 m). Finally, in the early Langhian (ca. 15 Ma), the fourth event produced epithermal systems associated with the late rhyolite intrusions.

The contribution of surficial fluids to the hydrothermal circulation and mineralization increased progressively, from none in the beginning to apparently 100 % at the end. These fluids were mainly of meteoric derivation, but a contribution of Langhian seawater is possible during the epithermal stage. The mineralizing fluids that formed the Karézas skarn were magmatic-hydrothermal and issued from a rare-metal granite; mixing of these fluids with volatile-bearing metamorphic fluids derived from the metamorphic core complex promoted the scheelite mineralization (Fig. 16a). Later, sodic to sodic-calcic brines evolved from fluid-gneiss interaction during the high-temperature metamorphism and were mobilized owing to emplacement of the Langhian granite batholith and related subvolcanic intrusions. These brines eventually invaded the Cretaceous flysch reservoirs and created high-enthalpy, liquid- dominated geothermal systems, products of the Aïn Barbar paleogeothermal field being the best exposed (Fig. 16b). Coupled with the inception of brittle faulting and progressive involvement of meteoric water, these systems were the site of mesothermal polymetallic lode formation. Finally, due to erosion of the impermeable Numidian cap during the exhumation process and emplacement of the late rhyolite bodies in the early Langhian, circulation of heated meteoric water (and possibly seawater) created the epithermal deposits, the deep fluid contribution having been likely (nearly) exhausted by that time (Fig. 16c).

Except for the Karézas skarn, for which a magmatic origin of the tungsten is likely, the metals concentrated by the different hydrothermal systems were mainly sourced in rocks of the metamorphic core complex and its tectonic cover of Cretaceous flysch. By contrast, only a minor

contribution came from the magma, as suggested by the lead isotope data for the Aïn Barbar deposit. Amphibolites of the Marble Complex in the Edough massif may have been a major copper source and the source of the epithermal antimony (and gold?).

From the preceding results, it appears that mineralization in the Edough-Cap de Fer metallic district is directly linked to the evolution of the metamorphic core complex, although not during the ductile detachment tectonics. In contrast to metamorphic core complexes such as Valhalla in British Columbia, which is linked genetically to syn-metamorphic base-metal veins in the brittle-fractured upper plate (Beaudouin et al. 1991), the Edough mineralization formed in the lower plate. This mineralization also occurred during the exhumation process, but followed the cessation of ductile tectonics as in the Rhodope core complex where Pb–Zn veins (Maidan ore field) are similarly hosted in high-grade rocks of the lower plate and are essentially synchronous with uplift of a post-extensional dome (Marchev et al. 2005; Rhormeyer et al. 2013). In the Edough case, however, the metamorphic fluids derived from the core complex seem to have played a key role during the first stages of hydrothermal circulation and related mineralization (Karézas skarn, mesothermal polymetallic veins). In addition, there evidently was a contribution from the high-grade metamorphic rocks of the lower plate to the metal budget of the hydrothermal systems, as shown for the Aïn Barbar deposit (Marignac et al. 2015).

The role of the late Miocene magmatism induced by collisional processes through slab break-off and/or lithospheric delamination (Maury et al. 2000) was of equal importance in the genesis of the Edough-Cap de Fer mineralization. This magmatism was the locus of the heat advection responsible for the hydrothermal convection cells that formed the meso- and epithermal stages. Also, it appears that the transition from extension (related to opening of the Algerian-Provençal oceanic basin) to transpression at the end of the Miocene, when the collision resumed, was the ultimate control on the sequence of mineralizing events in the Edough metamorphic core complex.

Finally, we suggest that the metal potential of the Edough-Cap de Fer district remains under explored. Given the structure of the basement, the existence of other skarns of the Karézas type is thus possible. Moreover, the concealed RMG of Karézas is a possible Ta resource. Other polymetallic ore fields of the Aïn-Barbar type may be concealed under the Numidian flysch cover between the Edough massif and the Cap de Fer (Fig. 2); extensions of the known deposits at depth or under the Mediterranean Sea are also possible. The gold potential of the Edough massif is similarly worth re-evaluating: on the one hand, the gold content of the Karézas skarn should be assessed; and on the other hand, the possible existence of epithermal gold veins should be considered in the northern part of the massif.

Acknowledgements John Slack is warmly thanked for his careful editing work and improvement to the manuscript.

References

Ahmed-Saïd Y, Leake RE (1992) The composition and origin of Kef Lahal amphibolites and associated amphibolite and olivine-rich enclaves, Edough, Annba, NE Algeria. Min Mag 56:459–468

Aïssa DE (1996) Etude géologique, géochimique et métallogénique du massif de l'Edough (Annaba, NE Algérie). Unpubl Thèse Doctorat Etat, USTHB, Alger, Algeria, 500 pp

Aïssa DE, Cheilletz A, Gasquet D, Marignac C (1995) Alpine metamorphic core complexes and metallogenesis: the Edough case (NE Algeria). In: Pašava J, Kříbek B, Žák K (eds) Mineral deposits: from their origin to their environmental impacts. In: Proceedings of 3rd Biennial SGA Meeting, Prague. A.A. Balkema, Rotterdam, pp 23–26

Aïssa DE, Marignac C, Cheilletz A, Gasquet D (1998a) Géologie et métallogénie sommaire du massif de l'Edough (NE Algérie). Mémoires Serv Géol Algérie 9:7–55

Aïssa DE, Marignac C, Cheilletz A, Boiron M-C (1998b) L'indice à arsénopyrite aurifère du Koudiet El Harrach (Edough, Annaba). Bull Serv Géol Algérie 13:3–20

Aïssa DE, Marignac C, Cheilletz A, Gasquet D (1999) Le skarn à scheelite de Karezas (Annaba, Nord-Est Algérie): un skarn polycyclique d'âge burdigalien. Bull Serv Géol Algérie 10:3–53

Aïssa DE, Cheilletz A, Marignac C (2001) Magmatic fluids and skarn mineralization: the Burdigalian As-W skarn at Karézas (Edough massif, NE Algeria). In: Piestrzyñski A (ed) Mineral deposits at the beginning of the 21st Century. In: Proceedings of 6th Biennial SGA Meeting, Krakow, A.A. Balkema, Rotterdam, pp 877–880

Aksyuk AM, Konyshev AA (2011) Experimental study of melting of the Voznesenska biotite and Li-F granites. Vestn Otd Nauk Zemle 3:NZ6002, doi:10.2205/2011NZ000132

Atkinson AB (2002) A model for the PTX properties of H_2O-NaCl. Unpublished MS Thesis, Virginia Polytechnic Institute, Blacksburg, Virginia, USA, 124 pp

Barton PB Jr (1978) Some ore textures involving sphalerite from the Futurobe mine, Akita Prefecture, Japan. Min Geol 28:293–300

Beaudouin G, Taylor BE, Sangster DF (1991) Silver-lead-zinc veins, metamorphic core complexes, and hydrologic regimes during crustal extension. Geology 19:1217–1220

Belhaj O (1992) Les gisements d'antimoine du massif du Tazekka (Maroc oriental): minéralogie, fluides hydrothermaux et conditions de formation. Unpublished Doctoral Thesis, Toulouse 3 University, Toulouse, France, 396 pp

Bodnar RJ (2003) Introduction to aqueous-electrolyte fluid inclusions. In: Samson I, Anderson M, Marshall D (eds) Fluid inclusions: analysis and interpretation. Mineral Assoc Canada, Short Course Notes 32:81–99

Boiron M-C, Cathelineau M, Banks DA, Fourcade S, Vallance J (2003) Mixing of metamorphic and surficial fluids during the uplift of the Hercynian upper crust: consequences for gold deposition. Chem Geol 194:119–142

Bouabsa L, Marignac C, Chabbi R, Cuney M (2010) The Filfila (NE Algeria) topaz-bearing granites and their rare metal minerals: petrologic and metallogenic implications. J Afr Earth Sci 56:107–113

Bouillin J-P (1979) La transversale de Collo et El-Milia (Petite Kabylie): une région-clef pour l'interprétation alpine de la chaîne littorale d'Algérie. Mémoire Soc Geol France 57:84 pp

Bowers TS, Helgeson HC (1983) Calculation of the thermodynamics and geochemical consequences of non-ideal mixing in the system H_2O-CO_2-NaCl on phase relations in geological systems: equation of state for H_2O-CO_2-NaCl fluids at high pressures and temperatures. Geochim Cosmochim Acta 47:1247–1275

Brown M, Solar GS (1999) The mechanism of ascent and emplacement of granite magma during transpression: a syntectonic granite paradigm. Tectonophys 312:1–33

Bruguier O, Hammor D, Bosch D, Caby R (2009) Miocene incorporation of peridotite into the Hercynian basement of the Maghrebides (Edough massif, NE Algeria): implications for the geodynamic evolution of the Western Mediterranean. Chem Geol 261:172–184

Brunel M, Hammor D, Misseri M, Gleizes G, Bouleton J (1988) Cisaillements synmétamorphiques avec transport vers le Nord-Ouest dans le massif cristallin de l'Edough (Est Algérien). C R Acad Sci Paris 306 (II):1039–1045

Bucher K, Stober I (2010) Fluids in the upper continental crust. Geofluids 10:241–253

Caby R, Hammor D (1992) Le massif cristallin de l'Edough (Algérie): un "metamorphic core complex" d'âge Miocène dans les Maghrébides. C R Acad Sci Paris 314:829–835

Caillère S, Kraut F (1947) Sur une zone tungstifère d'origine métamorphique dans le massif de Béléliéta (Algérie). C R Acad Sci Paris 225:129–131

Cathelineau M, Marignac C, Boiron MC, Gianelli G, Puxeddu M (1994) Evidence for Li-rich brines and early magmatic fluid-rock interaction in the Larderello geothermal system. Geochim Cosmochim Acta 58:1083–1099

Cathles L (1977) An analysis of the cooling of intrusives by ground-water convection which includes boiling. Econ Geol 72:804–826

Costagliola P, Benvenuti M, Maineri C, Lattanzi P, Ruggieri G (1999) Fluid circulation in the Apuane Alps core complex: evidence from extension veins in the Carrara marble. Mineral Mag 63:111

Dercourt J, Zonenshain LP, Ricou LE, Kazmin VG, Le Pichon X, Knipper AL, Grandjacquet C, Sbortshikov IM, Geyssant J, Lepvrier C, Pechersky DH, Boulin J, Sibuet J-C, Savostin LA, Sorokhtin O, Westphal W, Bazhenov ML, Lauer JP, Biju-Duval B (1986) Geological evolution of the Tethys belt from the Atlantic to the Pamirs since the Lias. Tectonophys 123:241–315

Diamond LW (1992) Stability of CO_2 clathrate hydrate +CO_2 liquid+CO_2 vapor+aqueous KCl-NaCl solutions: experimental determination and application to salinity estimates of fluid inclusions. Geochim Cosmochim Acta 56:273–280

Doblas M, Oyarzun R, Lunar R, Mayor N, Martinez J (1988) Detachment faulting and late Paleozoic epithermal Ag-base metal mineralization in the Spanish central system. Geology 16:800–803

Dubois M, Monnin C, Castelain T, Coquinot Y, Gouy S, Gauthier A, Goffé B (2010) Investigation of the H_2O-NaCl-LiCl system: a synthetic fluid inclusion study and thermodynamic modelling from -50° to +100°C and up to 12 mol/kg. Econ Geol 105:329–338

Durand-Delga M (1969) Mise au point sur la structure Nord-Est de la Berbérie. Bull Serv Carte Géol Algérie 39:89–131

Durand-Delga M, Rossi P, Olivier P, Puglisi D (2000) Situation structurale et nature ophiolitique de roches basiques jurassiques associées aux flyschs maghrébins du Rif (Maroc) et de Sicile. C R Acad Sci Paris, Sci Terre Planètes/Earth Planet Sci 331:29–38

Einaudi MT, Meinert LD, Newberry RJ (1981) Skarn deposits. In: Skinner BJ (ed) Economic geology 75th anniversary volume, 1905–1980. Economic Geology Publishing Co, El Paso, pp 317–391

Esteban JJ, Cuevas J, Vegas N, Tubia JM (2008) Deformation and kinematics in a melt-bearing shear zone from the western Betic Cordilleras (southern Spain). J Struct Geol 30:380–393

Fellin MG, Reiners PW, Brandon MT, Wüthrich E, Balestrieri ML, Molli G (2007) Thermochronologic evidence for the exhumational history of the Alpi Apuane metamorphic core complex, northern Apennines, Italy. Tectonics, vol 26. doi:10.1029/2006TC002085

Fourcade S, Capdevila R, Ouabadi A, Matineau F (2001) The origin and geodynamic significance of the Alpine cordierite-bearing granitoids of northern Algeria: a combined petrological, mineralogical and isotopic O, H, Sr, Nd study. Lithos 57:187–216

Frizon de Lamotte D, Saint-Bezar B, Bracene R, Mercier E (2000) The two main steps of the Atlas building and geodynamics of the western Mediterranean. Tectonics 19:740–761

Gibert F, Moine B, Schott J, Dandurand J-L (1992) Modeling of the transport and deposition of tungsten in the scheelite-bearing calc-silicate gneisses of the Montagne Noire, France. Contrib Mineral Petrol 112:371–384

Gilg HA, Boni M, Balassone G, Allen CR, Banks D, Moore F (2006) Marble-hosted sulfide ores in the Angouran Zn-(Pb-Ag) deposit, NW Iran: interaction of sedimentary brine with a metamorphic core complex. Min Dep 41:1–16

Glaçon J (1971) Les gîtes minéraux liés au magmatisme tertiaire en Algérie du Nord. Colloque E Raguin. Les roches plutoniques dans leurs rapports avec les gîtes minéraux. Masson, Paris, pp 214–224

Gleizes G, Bouloton J, Bossière G, Collomb P (1988) Données lithologiques et pétrostructurales nouvelles sur le massif cristallophyllien de l'Edough (Est Algérien). C R Acad Sci Paris 306(II):1001–1008

Hadj Zobir S, Mocek B (2012) Determination of the source rocks for the diatexites from the Edough massif, Annaba, NE Algeria. J Afr Earth Sci 69:26–33

Heald P, Foley NK, Hayba DO (1986) Comparative anatomy of volcanic-hosted epithermal deposits; acid-sulfate and adularia-sericite types. Econ Geol 82:1–26

Henni B, Aïssa DE (2007) Géologie et géochimie des formations ferrifères de l'Edough (Annaba, NE algérien). Bull Serv Géol Algérie 18:297–314

Henni B, Guy B, Aïssa DE, Garcia D (2002) Les anciens gisements et indices de magnétite de Berrahal et ses environs, massif de l'Edough (NE algérien): environnement géologique et données pétrographiques. Bull Serv Géol Algérie 13:33–48

Heymes T, Monié P, Arnaud N, Pêcher A, Bouillin JP, Compagnoni R (2010) Alpine tectonics in the Calabrian-Peloritan belt (southern Italy): new $^{40}Ar/^{39}Ar$ data in the Aspromonte Massif area. Lithos 114:451–472

Hilly J (1962) Etude géologique du massif de l'Edough et du Cap de Fer (est Constantinois). Publ Serv Géol Algérie (nouv sér) 19:1–408

Holk GH, Taylor HP Jr (2007) $^{18}O/^{16}O$ evidence for contrasting hydrothermal regimes involving magmatic and meteoric-hydrothermal waters at the Valhalla metamorphic core complex, British Columbia. Econ Geol 102:1063–1078

Howard KA (2003) Crustal structure in the Elko-Carlin region, Nevada, during Eocene gold mineralization: Ruby-East Humboldt metamorphic core complex as a guide to the deep crust. Econ Geol 98:249–268

Ilavsky J, Snopkova P (1987) Découverte d'Acritarches paléozoïques dans les terrains métamorphiques de l'Edough (Willaya d'Annaba, Algérie). C R Acad Sci Paris 305:881–884

Jolivet L, Faccenna C (2000) Mediterranean extension and the Africa-Eurasia collision. Tectonics 19:1095–1106

Kretschmar U, Scott SD (1976) Phase relations involving arsenopyrite in the system Fe-As-S and their application. Can Miner 14:364–386

Kwak TAP (1987) W-Sn skarn deposits and related metamorphic skarns and granitoids. Elsevier Sci Publ B.V, Amsterdam 449 pp

Lindgren W (1933) Mineral deposits, 4th edn. McGraw-Hill, New York 930 pp

Linnen RL, Cuney M (2005) Granite-related rare-element deposits and experimental constraints on Ta-Nb-W-Sn-Zr-Hf mineralization. In: Linnen RL, Samson IM (eds) Rare-element geochemistry and mineral deposits. Geological Association of Canada. Short Course Notes 17:45–67

Marchev P, Kaiser-Rhormeier M, Heinrich C, Ovtcharova M, von Quadt A, Raicheva R (2005) Hydrothermal ore deposits related to post-orogenic extensional magmatism and core complex formation: the Rhodope massif of Bulgaria and Greece. Ore Geol Rev 27:53–89

Marignac C (1985) Les minéralisations filoniennes d'Aïn Barbar (Algérie): un exemple d'hydrothermalisme lié à l'activité géothermique alpine en Afrique du Nord. Unpubl Thesis Doctorat Etat, INPL-Nancy: 2 vol, p. 1163

Marignac C, Aïssa DE, Cheilletz A, Gasquet D (2015) Edough-Cap de Fer polymetallic district, northeast Algeria: I. The late Miocene paleogeothermal system of Aïn Barbar and its Cu-Zn-Pb vein mineralization. In: Bouabdellah M, Slack JF (eds) Mineral deposits of North Africa. Springer, Berlin

Maury RC, Fourcade S, Coulon C, El Azzouzi M, Bellon H, Coutelle A, Ouabadi A, Semroud B, Megartzsi M, Cotton J, Belanteur O, Louni-Hacini A, Piqué A, Capdevila R, Hernandez J, Réhault JP (2000) Post-collisional Neogene magmatism of the Mediterranean Maghreb margin: a consequence of slab break-off. C R Acad Sci Paris 331:159–173

Michard A, Negro F, Saddiqi O, Bouybaouene ML, Chalouan A, Montigny R;, Goffé B (2006) Pressure-temperature-time constraints on the Maghrebide mountain building: evidence from the Rif-Betic transect (Morocco, Spain), Algerian correlations, and geodynamic implications. Comptes Rendus Géoscience 338:92–114

Monastero FC, Katzenstein AM, Miller JS, Unruh JR, Adams MC, Richards-Dinger K (2005) The Coso geothermal field: a nascent metamorphic core complex. Geol Soc Am Bull 117:1534–1553

Monié P, Montigny R, Maluski H (1992) Age Burdigalien de la tectonique ductile extensive dans le massif de l'Edough (Kabylies, Algérie). Données radiométriques $^{39}Ar/^{40}Ar$. Bull Soc Géol France 163:571–584

Norlander BH, Whitney DL, Teyssier C, Vanderhaeghe O (2002) Partial melting and decompression of the Thor-Odin dome, Shuswap metamorphic core complex, Canadian Cordillera. Lithos 61:103–125

Norton D, Cathles LM (1979) Thermal aspects of ore deposition. In: Barnes HL (ed) Geochemistry of hydrothermal ore deposits, 2nd edn. Wiley, New York, pp 568–610

Okay AI, Samir M (2000) Coeval plutonism and metamorphism in a latest Oligocene metamorphic core complex in northwest Turkey. Geol Mag 137:495–516

Pichavant M, Boher M, Stenger JF, Aïssa M, Charoy B (1987) Relations de phase des granites de Beauvoir à 1 et 3 kb, en conditions de saturation en H_2O. Géologie France 2–3:77–86

Piqué A, Tricart P, Guiraud R, Laville E, Bouaziz S, Amrhar M, Ait Ouali R (2002) The Mesozoic-Cenozoic Atlas belt (North Africa): an overview. Geodinam Acta 15:185–208

Puxeddu E (1984) Structure and late Cenozoic evolution of the upper lithosphere in southwest Tuscany (Italy). Tectonophys 101:357–382

Rhormeyer MK, von Quadt A, Driesner T, Heinrich CA, Handler R, Ovtcharova M, Ivanov Z, Petrov P, Sarov ST, Peytcheva I (2013) Post-orogenic extension and hydrothermal ore formation: high-precision geochronology of the central Rhodopian metamorphic core complex (Bulgaria-Greece). Econ Geol 108:691–718

Roedder E (1984) Fluid inclusions. Min Soc Am Rev Mineral 12:646 pp

Roure F, Casero P, Addoum B (2012) Alpine inversion of the North African margin and delamination of its continental lithosphere. Tectonics 31:TC3006. doi:10.1029/2011TC0022989

Sami R, Soussi M, Kamel B, Lattrache Kmar BI, Stow D, Sami K, Mourad B (2010) Stratigraphy, sedimentology and structure of the Numidian Flysch thrust belt in northern Tunisia. J AFR EARTH SCI 57:109–126

Schmidt MW (1992) Amphibole composition in tonalite as a function of pressure: an experimental calibration of the Al-in-hornblende barometer. Contrib Mineral Petrol 110:304–310

Sharp ZD, Essene EJ, Kelly WC (1985) A re-examination of the arsenopyrite geothermometer: pressure considerations and applications to natural assemblages. Can Mineral 23:517–534

Sillitoe RH (1993) Epithermal models: genetic tpes, geometrical controls and shallow features. In: Kirkham RV, Sinclair WD, Thorpe RI, Duke JM (eds) Mineral deposit modeling, Geol Assoc Canada Spec Paper 40:403–418

Spencer JE, Welty JW (1986) Possible control of base- and precious-metal mineralization associated with Tertiary detachment faults in the lower Colorado River trough, Arizona and California. Geology 14:195–198

Thomas MFH, Bodin S, Redfern J, Irving DHB (2010) A constrained African craton source for the Cenozoic Numidian flysch: implications for the palaeogeography of the western Mediterranean basin. Earth Sci Rev 101:1–23

Tischendorff G, Gottesmann B, Förster H-J, Trumbull RB (1997) On Li-bearing micas: estimating Li from electron microprobe analyses and an improved diagram for graphical representation. Min Mag 61:809–834

Toubal A (1984) Contribution à l'étude des minéralisations antimonifères du Nord-Est algérien: une province métallogénique hétérochrone. Unpublished Doct 3rd Cycle, UPMC (Paris 6 Univ), Paris, France, 141 pp

Vanderhaeghe O (1999) Pervasive melt migration from migmatites to leucogranites in the Shuswap metamorphic core complex, Canada: control of regional deformation. Tectonophys 312:35–55

Vila JM (1980) La chaîne alpine d'Algérie orientale et des confins algéro-tunisiens. Unpubl Thèse Doctorat Etat, Université Paris VI, Paris, France, 663 pp

Skarn to Porphyry-Epithermal Transition in the Ouixane Fe District, Northeast Morocco: Interplay of Meteoric Water and Magmatic-Hydrothermal Fluids

Mohammed Bouabdellah, Raouf Jabrane, Daoud Margoum and Mohammed Sadequi

Abstract

The Ouixane Fe skarn district in the northeastern Alpine Rifan belt is the highest grade iron district in Morocco with past production of 65 Mt of ore at >50 % Fe and estimated remaining reserves of 30 Mt grading 58 % Fe. Overall, the district consists of three major deposits, distributed in a 6 × 6 km zone along the northeastern part of the Beni Bou Ifrour Massif. Mineralization occurs either within the 7.58 ± 0.03 Ma Ouixane post-collisional, hornblende-biotite quartz-diorite porphyry and related dike swarms, or more importantly at contacts of the porphyry with a ~1,500-m-thick sequence of Upper Jurassic-Lower Cretaceous turbiditic and volcaniclastic sedimentary rocks. Igneous rocks have high-K, calc-alkaline to shoshonitic affinities and REE patterns that are consistent with emplacement in a typical arc setting. Concordance between the age of mineralization, which is thought to have occurred at 7.04 ± 0.47 Ma, and the 7.58 ± 0.03 Ma crystallization age of the Ouixane quartz-diorite porphyry constitutes strong evidence for a genetic relationship between Ouixane magnetite skarn mineralization and Late Neogene magmatism. Structural controls were important in focusing fluids and localizing the emplacement of late mineralizing phases. The ore zones have undergone strong post-ore displacement along steeply dipping, predominantly thrust

M. Bouabdellah (✉) · D. Margoum
Département de Géologie, Faculté Des Sciences,
Université Mohammed Premier, B.P. 717 Avenue
Mohammed VI, 60000 Oujda, Morocco
e-mail: mbouabdellah2002@yahoo.fr

R. Jabrane
Faculté Des Sciences et Techniques,
Université Moulay Abdellah, B.P. 2202
Route d'Imouzzer Fès, Morocco

M. Sadequi
Arbensa, B.P. 135 Beni Chiker, 62302 Nador,
Morocco

M. Bouabdellah and J.F. Slack (eds.), *Mineral Deposits of North Africa*,
Mineral Resource Reviews, DOI 10.1007/978-3-319-31733-5_7

faults, with significant remobilization of ore. Initial skarn formation started with isochemical reconversion of the hot rocks to marbles and hornfels and evolved through time into metasomatic replacements of carbonate precursors by calc-silicate, oxide, and sulphide minerals. High-temperature, early prograde mineral assemblages are dominated by pyroxene ($Di_{95}Hd_5$–$Di_{46}Hd_{53}$; max johannsenite content of 3 mol%) and garnet ($Ad_{98}Gr_2$–$Ad_{40}Gr_{60}$), with minor magnetite, K-feldspar, plagioclase, titanite, and scapolite. Low-temperature hydrous retrograde assemblages formed by nearly the complete replacement of the preexisting anhydrous skarn assemblage involve various proportions of amphibole, biotite, chlorite, epidote, quartz, calcite, barite, and sulphides. High Fe grades are spatially related to retrograde skarn zones that developed from carbonate precursors. A later potassic ± phyllic ± propylitic alteration overprints the calc-silicate mineral assemblages. The resulting alteration halos are spatially associated with porphyry-type and epithermal-style mineralization. The skarn mineral compositions indicate emplacement under high f_{O2} conditions that shifted through time to a reduced environment. Such an evolutionary trend may record the temporal decrease of f_{O2} and corresponding increase of pH and f_{S2}. Epithermal sulphide-rich mineralization occurred at progressively lower pressures, shallower depths, and lower temperatures, relative to iron-rich skarn mineralization. Indeed, fluid inclusion data together with oxygen isotopic compositions are consistent with the involvement of early high-temperature (347–600 °C), low CO_2 (<0.05 mol%), NaCl–KCl boiled magmatic brines, that mixed outward with increasing components of cooler (300–125 °C) and dilute (up to 7 wt% NaCl equiv) fluids probably of meteoric origin, which re-equilibrated with the early magmatic fluids. Late epithermal sulphide-rich veins formed at temperatures of 250–125 °C and pressures of <100 bars, corresponding to shallow depths of «1 km. The shift from oxidized to reduced fluid conditions is attributed to a transition in magma evolution from high-K calc-alkaline to shoshonitic compositions.

1 Introduction

The Ouixane Fe skarn district described herein is part of the large Miocene-Pliocene-Quaternary metallogenic province that characterizes the entire Mediterranean basin (Koděra et al. 1998; Ciobanu and Cook 2004; Palinkas et al. 2013). This district has played a crucial role in Moroccan's mining history and economy since the 1900s, as the mined deposits were the largest iron ore producers of the country. The district covers a 6 × 6 km zone along the northeastern part of the Beni Bou Ifrour Massif, within the Alpine Rifan orogen (Fig. 1) south of the large Gourougou stratovolcano (Hernandez and Bellon 1985; EL Bakkali et al. 1998). The Ouixane district *sl* hosts three main Fe skarn deposits collectively termed the Ouixane Fe skarn district. From west to east, these deposits are Ouixane, Axara-Imnassen, and Setolazar-Bokoya (Fig. 1). A fourth sulphide-rich magnetite deposit known as Afra (500,000 t of ore at 45 % Fe; Jeannette

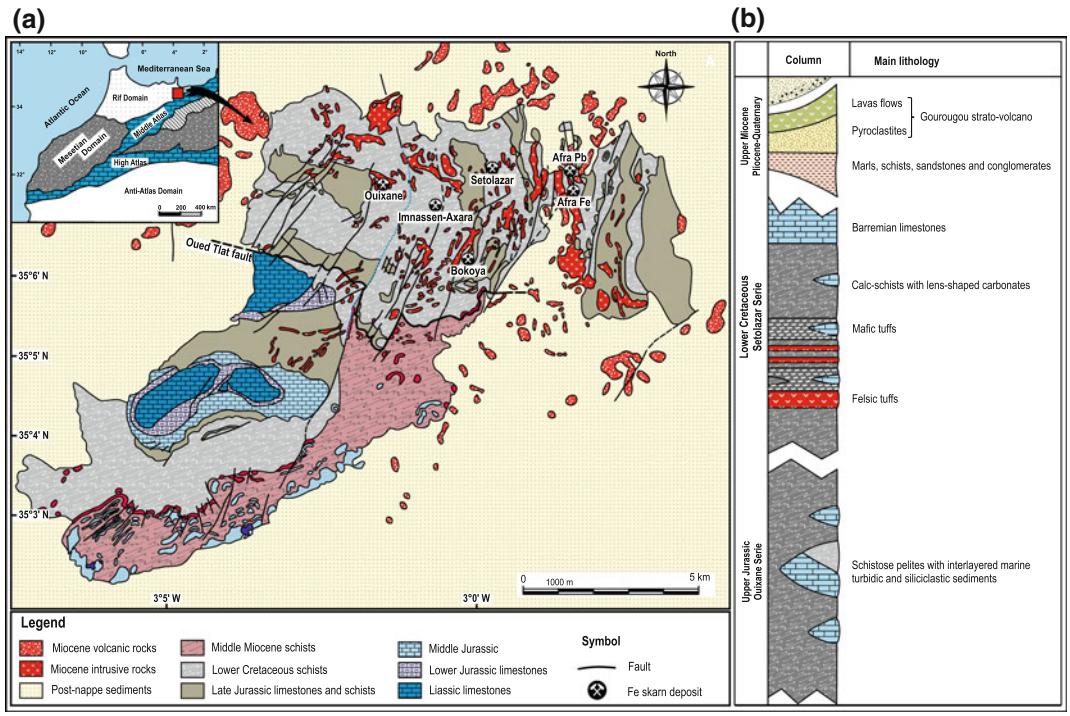

Fig. 1 **a** Surface geological map of Beni Bou Ifrour massif showing regional geology, lithostructural domains, major faults, and igneous occurrences together with historically mined Ouixane, Axara-Imnassen, Setolazar-Bokoya, and Afra iron skarn deposits (modified after Zeghanghane geological sheet, scale 1/50,000). Oued Tlat listric fault delineates the thrust contact between northern and southern blocks of the massif. Inset shows location of Beni Bou Ifrour massif within the framework of major tectonostratigraphic domains of Morocco. **b** Generalized stratigraphic column for the Beni Bou Ifrour massif showing main lithostratigraphic units (modified after Rhoden and Ereno 1962; Duflot et al. 1984)

1961) of less economic interest is also recognized (Fig. 1).

Discovered in 1905–1907 based on strong magnetic anomalies (Rhoden and Ereno 1962) and mined since 1914 by the Spanish mining companies CEMR (Compagnie Espagnole des Mines du Rif) and SAMS (Société Minière Anonyme de Sétolazar), the Ouixane open pit and underground mines produced from 1914 to 1967 approximately 65 Mt of ore at >50 % Fe (Rhoden and Ereno 1962; Duflot et al. 1984). In 1967, the mining license was transferred to the Moroccan government, which created the state SEFERIF Company and launched new exploitation and evaluation programs based on gravity, airborne magnetic, and seismic datasets. A mineral inventory estimated at the time of the closure of the district in 1978 reported inferred total reserves of 30 Mt at 58 % Fe and 4 % S (Anonymous 1985), positioning the district as the largest remaining iron resource of Morocco.

Economic orebodies are oriented N-S and occur exclusively within the Upper Jurassic-Lower Cretaceous shallow-marine turbiditic and volcaniclastic succession. These orebodies are spatially and genetically related to the post-collisional Ouixane quartz-diorite porphyry and related apophysis dated between 8.13 ± 0.20 and 7.58 ± 0.03 Ma (K/Ar and $^{40}Ar/^{39}Ar$ on biotite separates; EL Bakkali et al. 1998; EL Rhazi and Hayashi 2002; Duggen et al. 2005; Lebret 2014) (Fig. 1a). In spite of its great economic importance, the origin of the iron mineralization remains poorly constrained owing to the lack of reliable fluid inclusion, isotopic, and geochemical data, thereby limiting exploration efforts to areas adjacent to known prospects.

Earlier research into the metallogenic history of the district focused on individual deposits by documenting geological settings and mineralogical characteristics without attempting to correlate data between or among deposits. As a consequence, conflicting and contradictory models have been proposed (Heim 1934; Delizaur 1952; Rhoden and Ereno 1962; Viland 1977; Duflot et al. 1984; Kerchaoui 1985). Heim (1934) suggested a magmatic origin for the iron ore, whereas Rhoden and Ereno (1962) favored a pneumatolytic genesis. Based on the laminated geometry of the magnetite mineralization that parallels bedding, and the close spatial relationship between iron-rich orebodies and tuff deposition, Duflot et al. (1984) proposed an exhalative origin in which hydrothermal circulation was driven by magmatism, or a combined exhalative-sedimentary origin in which mineralization was overprinted by hydrothermal processes.

Recent mineralogical, structural, geochemical, and geochronological investigations (Viland 1977; Kerchaoui 1985; EL Rhazi and Hayashi 2002; Bouabdellah et al. 2012; Lebret 2014) have significantly improved our understanding of the origin of the Ouixane Fe skarn mineralization. Together, these studies suggest that metasomatic replacement processes and subsequent epithermal fluid circulation played a crucial role in ore formation, and as such Ouixane is described herein as a Fe skarn-type district.

The objective of this 30 year synthesis of field-, mineralogical-, and geochemical-data is to (1) re-examine the geological environment of the Ouixane district; (2) describe the mineralogy and alteration patterns of the different skarn types; and (3) summarize unpublished fluid inclusion data on paragenetically well-constrained skarn minerals, in order to discuss time-space relationships of the mineralization. Consideration of these combined data provides constraints on an integrated fluid evolution model for the genesis of the Ouixane skarn-type district including the composition and sources of the ore-forming fluids.

2 Geological Setting

The Beni Ifrour Massif that hosts in its northeastern termination (Fig. 1a) the Ouixane Fe skarn district is composed of two contrasting and tectonically superimposed domains referred to as the allochthonous Northern Block and the autochthonous Southern Block (Kerchaoui 1985, 1994) (Fig. 1). Both of these domains underwent a complex protracted evolution from the Early Jurassic to the present, involving subduction and post-collisional processes, and Neotectonic strike-slip faulting (Kerchaoui 1994).

The first mine workings were developed both on surface and underground in the Northern Block where major iron-rich orebodies have been mined (Fig. 1a) near the contact between Late Neogene to Quaternary post-collisional bimodal intrusive rocks and lava flows. No economic mineralization has been documented yet in the Southern Block. Previous descriptions of the regional geology and Fe skarn mineralization include Heim (1934), Jeannette and Hamel (1961), Rhoden and Ereno (1962), and Viland (1977). Extensive field, mineralogical, fluid inclusion, and isotope geochemical studies performed during the last three decades have greatly improved our understanding of the mine sequences (Duflot et al. 1984; Kerchaoui 1985, 1994; Jabrane 1993), the ore geochemistry (Jabrane 1993; EL Rhazi and Hayashi 2002; Bouabdellah et al. 2012; Lebret 2014), and the mineralogy and ages of mineralization (EL Rhazi and Hayashi 2002; Lebret 2014). Therefore, only a brief synopsis of the geological history of the Ouixane district is given below, complemented by observations by the authors and by unpublished geochemical data.

The regional geology of the Northern Block (Fig. 1) is stratigraphically correlated with the Ouixane and Setolazar series (Rhoden and Ereno 1962) and consists of a thick turbiditic siliciclastic package of Late Jurassic to Early Cretaceous rhythmically laminated sandstone, siltstone, shale, and pelite interlayered with

ash-flow tuffs (i.e., tuffite; Kerchaoui 1994) and lens-shaped carbonate bodies several meters in diameter. These rocks are cut by numerous granodioritic to dioritic intrusions, and by bimodal dike swarms and basaltic to rhyolitic lava flows of Late Neogene to Pliocene age (Hernandez and Bellon 1985; Kerchaoui 1994; EL Bakkali et al. 1998; Duggen et al. 2005).

The chaotic distribution of the lens-like carbonate bodies within the turbiditic matrix along with sedimentological, paleogeographical, and structural constraints led Kerchaoui (1985, 1994) to interpret the Northern Block as an olistostrome that was thrust to the south between 7.8 Ma (upper limit of mineralization age; see below) and the Messinian (Lebret 2014). Sedimentary facies changes and paleogeographic evidence suggest that the precursor siliciclastic sediments were derived from a northeasterly source and that thrusting was directed chiefly southward from sites ca. 110–130 km to the north (Lebret 2014).

Conversely, the Southern Block (Fig. 1a) is interpreted as the para-autochthon with exposed strata consisting of Lower to Middle Jurassic (Lias-Dogger) shallow marine carbonates and marls, Upper Jurassic (Callovian-Oxfordian, Kimmeridgian, Tithonian) black shale and sandstone with interlayered carbonates, and Cretaceous (Berriasian-Neocomian) schistose pelite with interbedded carbonates and marls. All of these strata are unconformably overlain by a thick sequence of Middle Miocene and younger gypsum-bearing argillaceous limestone, schistose pelite, and sandstone together with molasse-like and post-nappe sedimentary rocks (Viland 1977).

Overall, the host rocks and associated iron mineralization have experienced a protracted history of structural, metamorphic, and igneous events. Two groups of Neogene magmatic rocks are distinguished (1) an Upper Miocene to Lower Pliocene (8.2–4.8 Ma), Si–K-rich group; and (2) an Upper Miocene to Pleistocene (6.3–0.65 Ma) Si-poor, Na-rich group (Duggen et al. 2005). EL Bakkali et al. (1998) stressed that there is a consistent evolution of magma compositions from ca. 13.1–9.8 Ma calc-alkaline to alkaline (basaltic andesite and andesite, and rhyolite) compositions, through a discrete ca. 9.0–6.6 Ma high-K calc-alkaline (basaltic to rhyolitic lava flows and granodiorite) compositions, and ca. 7.0–5.4 Ma shoshonitic (K-enriched mafic to absarokite, shoshonite, latite and trachyte) compositions. These igneous rocks were interpreted to have been produced either by subduction-related processes (Coulon et al. 2002; Gutscher et al. 2002; Duggen et al. 2005) during the collision between the African and European plates, or alternatively in response to intraplate mantle processes (Comas et al. 1999; Platt et al. 2003; Duggen et al. 2005). Both models are consistent with extensional tectonics, melting, and a subsequently increased geothermal gradient and related fluid activity.

Regional metamorphism in the district is typically low grade with mineral assembalges indicating greenschist facies as attested by the widespread presence of chlorite and biotite in metapelites, and chlorite, epidote, and albite ± actinolite in metabasites. In addition to regional metamorphism, low-pressure, high-temperature contact metamorphism has been recorded in aureoles adjacent to large intrusions (i.e., Ouixane quartz-diorite porphyry), resulting in pervasive recrystallization and silicification of the host rocks and formation of porphyroblasts of biotite, andalusite, and cordierite. The peak metamorphic conditions attained temperatures of 520–580 °C and a mean lithostatic pressure of 600 bars (Jabrane 1993).

Structurally, the Upper Jurassic to Upper Miocene host rocks record the effects of three shortening deformational events (D_1, D_2, and D_3). The event D_1 event, of Oligocene age (Frizon de Lamotte 1982; Kerchaoui 1994), produced west-verging reverse faults. It is noteworthy that this early deformational event affected only the allochthonous terranes, leaving the autochthonous package undeformed.

The D_2 event involved predominantly the development of regional-scale, overturned, upright to isoclinal, west-vergent fold nappes with an axial planar cleavage accompanied by a north-south-trending, low-angle thrust fault system and associated splays that have been reactivated and displaced by NE-SW strike-slip faults. Gentle anticlinal structures were also generated. The

common spatial association between anticlinal and overturned fold structures led Kerchaoui (1994) to attribute this relationship to the surface expression of a flat, intra-crustal detachment zone at depth. Accordingly, we interpret the Oued Tlat fault (Fig. 1a), which heals the contact between the Northern and Southern Blocks as a listric fault that is rooted at depth, to a detachment structure dipping slightly to the north. The D_2 event is thought to have occurred during Middle Miocene time (Tortonian ~10 Ma), and was accompanied by low-pressure greenschist-facies metamorphism at ~8.2–7.3 Ma (Kerchaoui 1994) synchronously with emplacement of the nappes.

The late Neotectonic compressional D_3 event substantially modified the stratigraphic and structural architecture of the eastern part of the Rifan belt. This event is represented by the northeast plunging Jbel Bouzerib anticlinorium (Kerchaoui 1994), and at the regional scale, a series of major northeast-, east-west-, and northwest-trending, steeply dipping faults that offset all older structures. The most prominent characteristic of the D_3 event in terms of magmatism and skarn mineralization is that these later faults were important in controlling emplacement of the igneous bodies, spatially associated alteration zones, and related mineralizing fluids.

3 District Geology

3.1 Ouixane Deposit

With a total production of >60 Mt of magnetite concentrates from a remaining reserve of 3 Mt (Anonymous 1985), the Ouixane mine is considered the most productive of the district in accounting for more than 70 % of the extracted ore. Most of the mine production has come from a single, subcircular, ~1-km-long by 800-m-wide open pit slightly elongate in a mainly east-west direction (Figs. 2 and 3).

The lithologic succession is assigned to the monoclinal Ouixane series (Figs. 1b and 2) and consists of a 1,500-m-thick folded and metamorphosed succession of Upper Jurassic, rhythmically laminated siliciclastic turbidites, carbonates, and volcaniclastic rocks. All of these strata are intruded by a suite of Late Neogene shallow intrusives and dike swarms of various compositions (Fig. 2). The lower basal unit comprises a 600-m-thick Tithonian sequence of thinly bedded, fine- to medium-grained, silver-green schistose pelite conformably overlain by 300 m of flysch-like strata (Jeannette and Hamel 1961), composed of interlayered dark gray to black marine turbiditic and siliciclastic sedimentary rockss with abundant lens-shaped bodies of mostly pure limestone and lesser dolomitedispersed within the schistose pelitic matrix. The richest Fe mineralization is contained within this unit, being intimately associated spatially with the carbonate lithologies that have been overprinted by hydrothermal alteration, mineralization, and skarn formation. Transition to the upper unit is marked by a 250–400-m-thick, flat-lying, medium-bedded, massive carbonate platform unit (regional marker) referred to as the Ouixane Mount limestone (Fig. 2).

Most of the host rocks show a well developed axial planar schistosity (S_1) and associated folds with local crenulation cleavage (S_2). A number of northeast verging folds, thrust-fault ramps, and flat thrust faults are also present but display variable offsets of the folded beds. In addition to these brittle compressional structures, there are also northwest-striking Neogene faults, intrusions, dike swarms, and lava flows of diverse composition. The most prominent of these faults is the ENE-trending, postore Ouixane Fault that divides the deposit area into western and eastern structural blocks (Figs. 2 and 3). On the northeastern side of the Ouixane Fault, the Ouixane quartz-diorite porphyry is largely exposed, whereas the southwestern side (Fig. 3) is dominated by outcrops of the Upper Jurassic skarn-mineralized turbiditic to siliciclastic rocks. The Ouixane fault consists of a >4-km-long and 100–200-m-wide, NS-trending corridor of subparallel faults and associated splays, which have been reactivated and displaced by EW-trending strike-slip faults that typically show displacements of 10 m down to the north. Structurally,

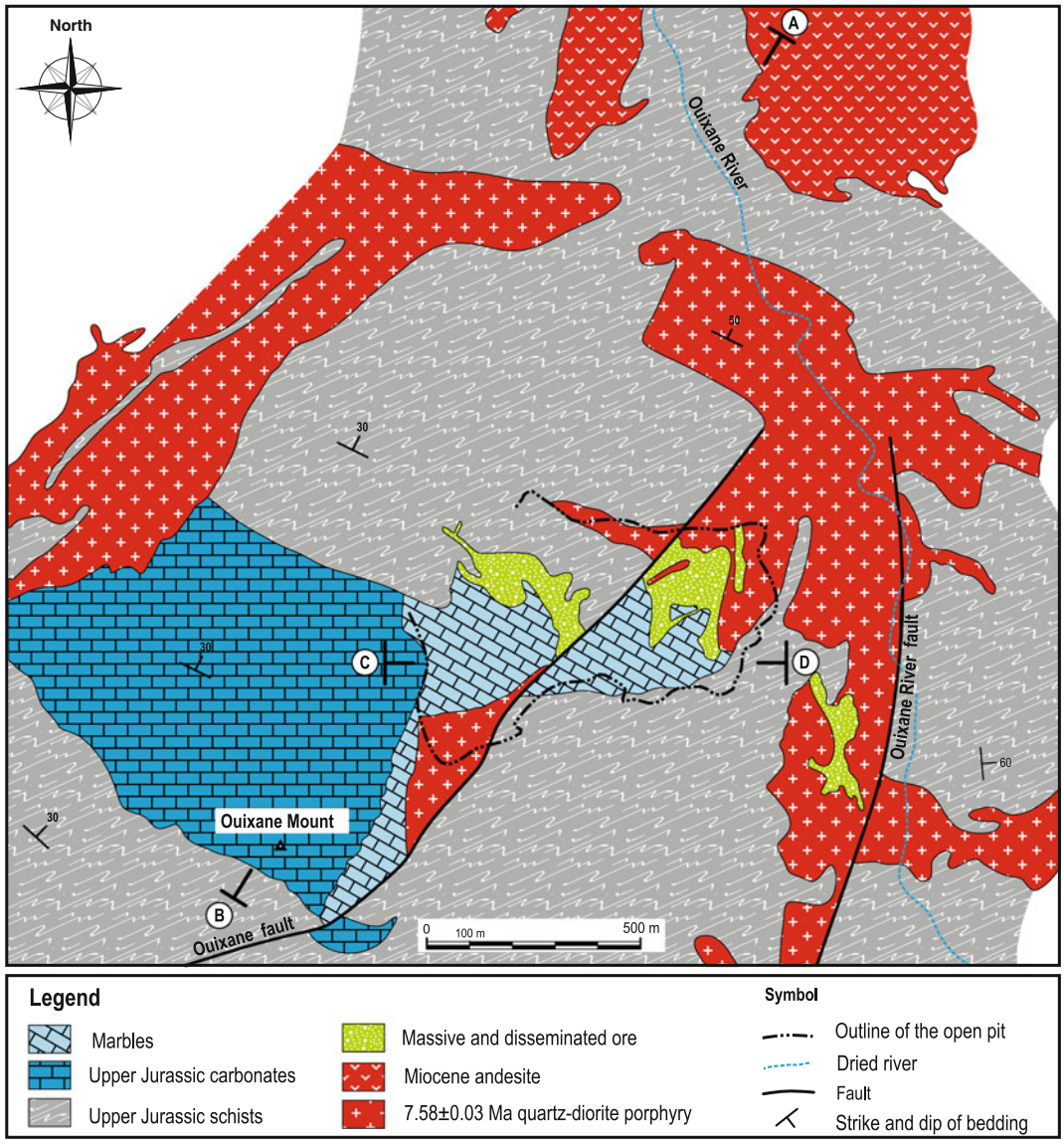

Fig. 2 Surface geological map of Ouixane deposit showing host-rock lithology, major faults, and Ouixane quartz-diorite porphyry intruding Upper Jurassic host rock strata (modified after Rhoden and Ereno 1962). Also shown is position of magnetite skarn mineralization along contact zone of the quartz-diorite porphyry. Section lines *A–B* and *C–D* indicate cross-sections presented in Fig. 4. Outline of open pit is shown for reference

the Ouixane Fault is interpreted as a tear fault for which emplacement coincided with the last movement of the Oued Tlat detachment fault (Kerchaoui 1994).

Widespread igneous rocks in the area are represented by a suite of granitic to dioritic stocks and associated aphyric to porphyritic dike swarms plus andesitic lava flows, all of which have of K-rich, calc-alkaline affinity (Jabrane 1993; Kerchaoui 1994; EL Bakkali et al. 1998; Duggen et al. 2005). Among these igneous rocks (Fig. 2), the Ouixane quartz-diorite porphyry covers a total area of 5 km^2 and is the most prominent both volumetrically (representing the

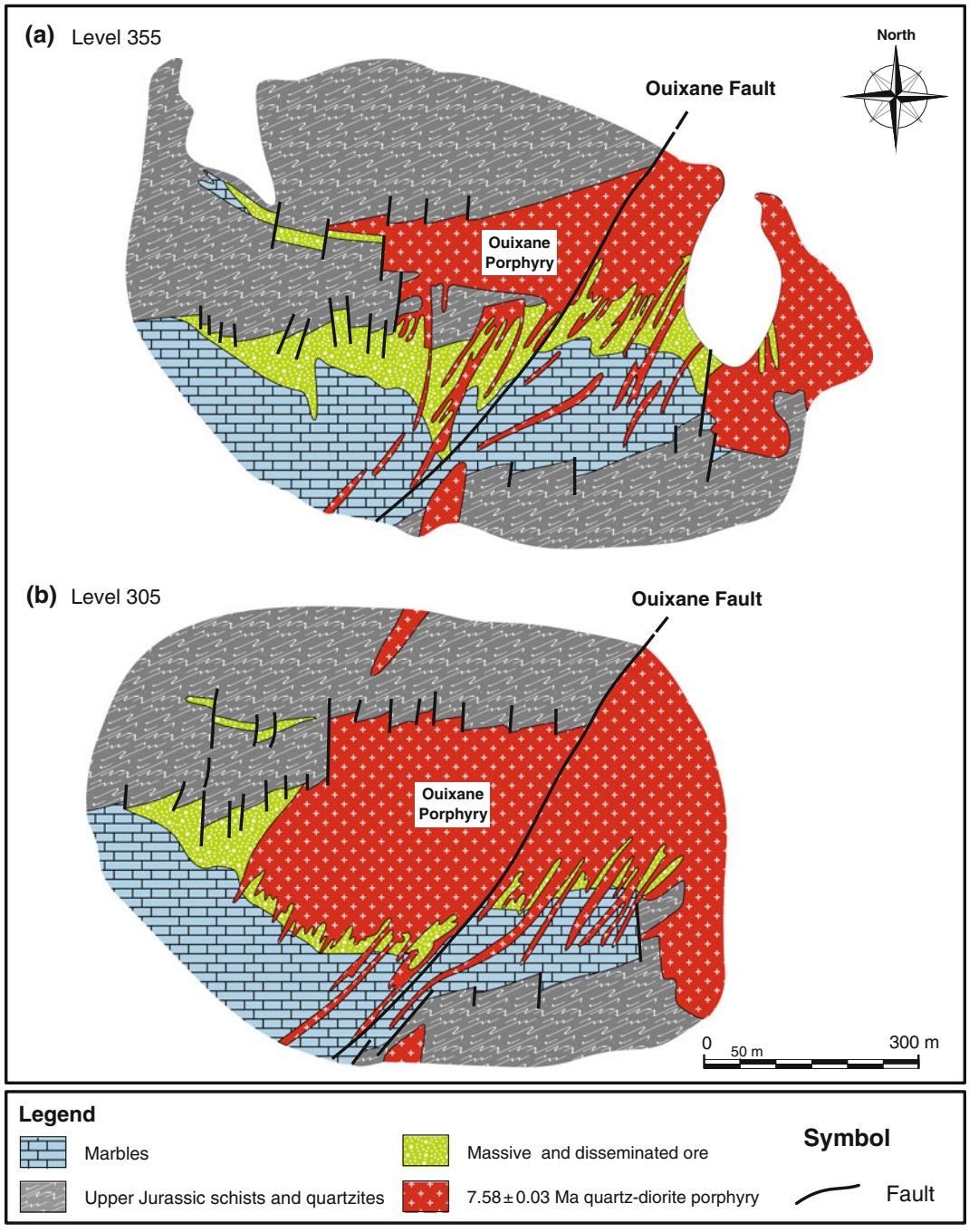

Fig. 3 Surface geological map of Ouixane open pit at levels 355 (**a**) and 305 (**b**) showing separation of the deposit by the Ouixane Fault into eastern and the western blocks (modified after Rhoden and Ereno 1962)

largest exposed intrusion in the area) and economically (because of its intimate relationship to skarn mineralization).

The Ouixane quartz-diorite porphyry is a light gray, medium-grained, equigranular to porphyritic intrusion that displays a laccolithic

geometry. Numerous spatially associated sills and dikes on its margins were emplaced within N-S- to NNE-striking fractures (Fig. 4). A 10 × 20 m apophysis of the stock is exposed on the southern margin of the open pit. Petrographically, the intrusion consists mainly of diorite (Duggen et al.

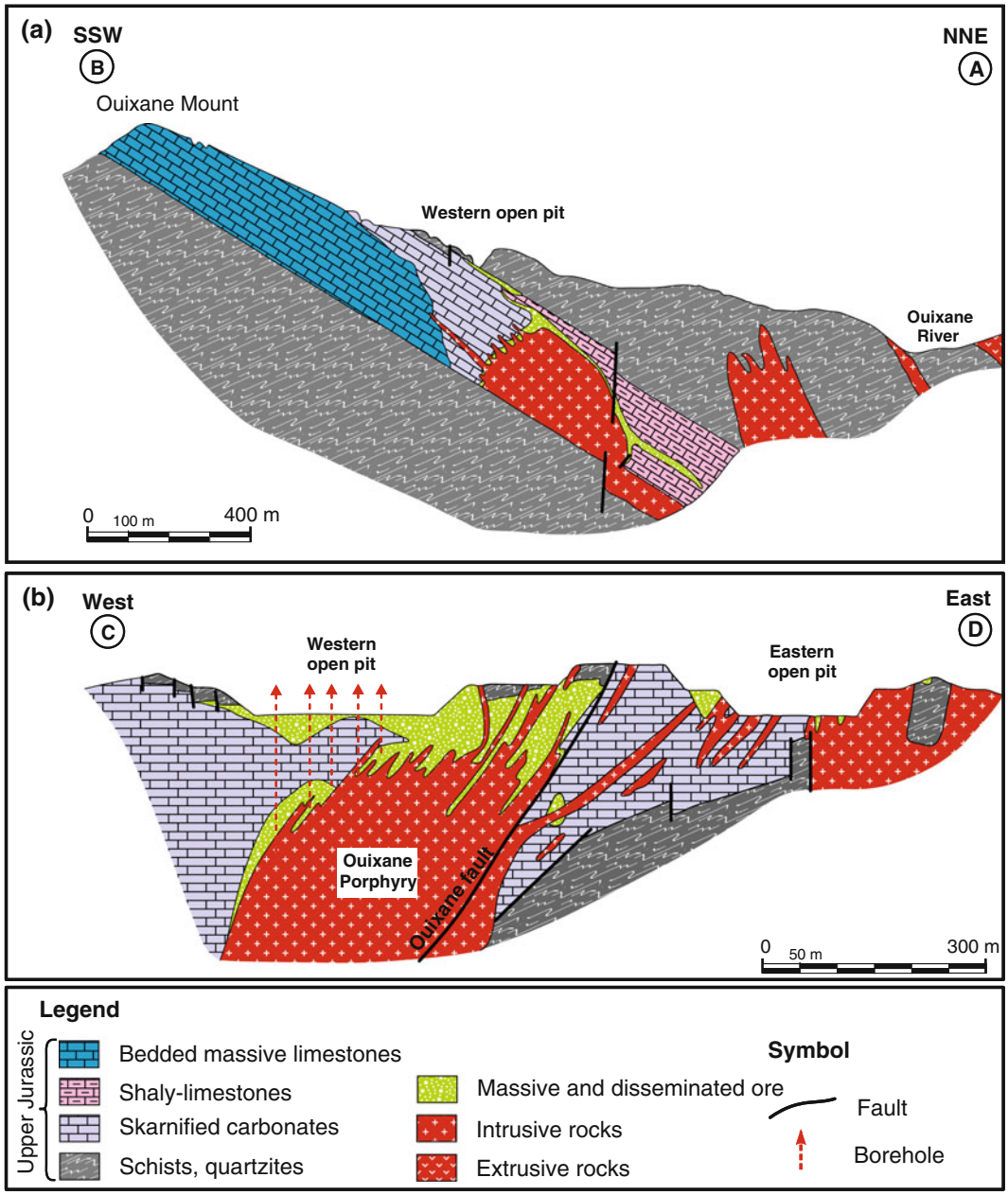

Fig. 4 **a** Generalized NNE-SSW cross section through Ouixane deposit showing western open pit and relationship between intrusive rocks and associated iron skarn mineralization (modified after Rhoden and Ereno 1962). **b** Generalized E-W cross section through open pit showing Ouixane quartz-diorite porphyry and relative positions of endoskarn, and proximal and exoskarns (modified after Rhoden and Ereno 1962). See Fig. 2 for positions of cross sections

2005; and present study) with lesser granodiorite (Viland 1977; EL Bakkali et al. 1998; Jabrane 1993). In this contribution, we collectively refer these intrusions as quartz diorite; the high silica and K contents allowed previous authors (Viland 1977; Jabrane 1993; EL Bakkali et al. 1998) to classify these rocks as granodiorite as secondary in origin, being related to the intensive hydrothermal alteration that accompanied the skarn mineralization. Mineralogically, the Ouixane diorite-quartz porphyry consists essentially of plagioclase (40–50 %, $An_{34–65}$), K-feldspar (20–25 %, $Or_{80–85}$), quartz (10–15 %), actinolitic hornblende (10–15 %), and coarse-grained biotite (10 %, annite-X_{Fe} = 0.38 and Al^{IV} = 2.4; Jabrane 1993) as major rock-forming minerals, accompanied by accessory titanite (1 %), apatite (1 %), zircon (<1 %), pyrite (2 %), and magnetite (1 %). The presence of primary titanite together with magnetite, combined with the absence of ilmenite, indicates that the intrusion crystallized from a relatively oxidized, I-type magma. Alteration minerals include epidote, sericite, prehnite, and chlorite.

$^{39}Ar/^{40}Ar$ dating of biotite separates yield a well-constrained plateau age of 7.58 ± 0.03 Ma (Duggen et al. 2005), consistent with the time span determined by Kerchaoui (1994) and EL Bakkali et al. (1998). Duggen et al. (2005) also reported a $(^{87}Sr/^{86}Sr)_{initial}$ ratio of 0.709675 and negative ε_{Nd} value of −5.1 for the Ouixane quartz-diorite porphyry. The K-rich, calk-alkaline affinity and REE patterns exhibited by these rocks are consistent with a primitive arc-related magmatic system that formed from a mantle source, modified by older subduction (EL Bakkali et al. 1998).

Emplacement of the Ouixane porphyritic intrusion produced an extensive thermal contact-metamorphic aureole and metasomatized the surrounding volcano-sedimentary units. Close to the Ouixane porphyry, thermal contact metamorphism converted the host sedimentary rocks into quartz, K-feldspar, muscovite, biotite, chlorite, andalusite, and cordierite hornfels; quartzite; and calcite or dolomite marble composed of various proportions of calcite, dolomite, orthoclase ($Or_{81}Ab_{19}$), muscovite (phengite, Si/Al^{IV} = 3.47, MgO = 1.26 wt%, FeO = 1.11 wt%), biotite (X_{Fe} = 0.472; TiO_2 = 3 wt%), chlorite, tremolite, diopside, forsterite ($Fo_{94}Fa_6$), and spinel. Calculated peak-metamorphic P-T conditions have been estimated at 600 bars and 550 ± 30 °C (Jabrane 1993). Metasomatic metamorphism resulted in extensive replacement of the reactive calcareous protoliths by calc-silicate minerals and iron oxides (see below).

The andesitic lava flow that crops out in the northern part of the Ouixane deposit (Fig. 2) is mineralogically and geochemically similar to the Ouixane quartz-diorite porphyry and therefore is considered to be comagmatic with it. Andesite lava flows are generally black to dark green and contain phlogopite or hornblende phenocrysts in an aphanitic groundmass composed of plagioclase, phlogopite, olivine, carbonate minerals, quartz, and apatite.

4 Axara-Imnassen Deposit

The Axara deposit was mined in several open pits aligned mainly N-S for 4 km and dispersed over a ~6 km^2 area, approximately 2–3 km southeast of the Ouixane deposit (Fig. 1). Historic production of the mine totaled >10 Mt of ore with a present remaining reserve of 5 Mt grading 57 % Fe and 4.4 % S. Overall, the mine is made up of an en echelon array of magnetite-bearing orebodies of various sizes referred to, from north to south, as Creston 1-2-6-7-3-5, and Sidi Chakroune (Duflot et al. 1984; Fig. 5). Among these, the Axara open pit from, which the Creston 3 and 5 orebodies were exploited, is by far the largest having an average strike length of 300 m and mean depth of 100 m (Fig. 6a, b). The underground Imnassen orebody (15.5 Mt at a grade of 57 % Fe) represents the extension at depth of the Axara subsurface mineralization; the latter is displaced to the west by a major flat listric detachment fault known as the Iberkanen Fault (Fig. 7).

Lithologic units in the vicinity of the Axara open pit consist of a monoclinal 500–600-m-thick succession of Lower Cretaceous (Neocomian) sedimentary rocks. These strata,

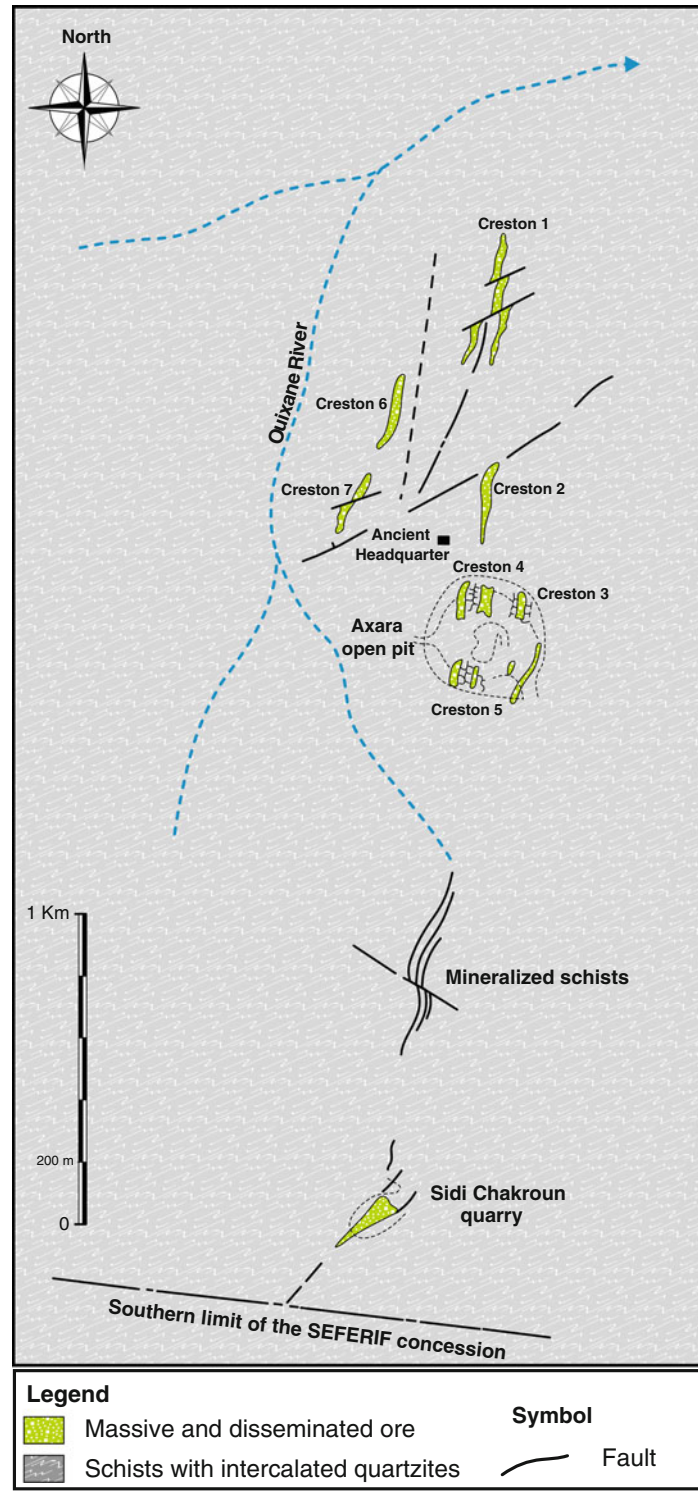

Fig. 5 Spatial distribution of major exploited magnetite-rich orebodies (red pattern) composing the Axara deposit (modified after Duflot et al. 1984). *Numbers* refer to main exploited orebodies

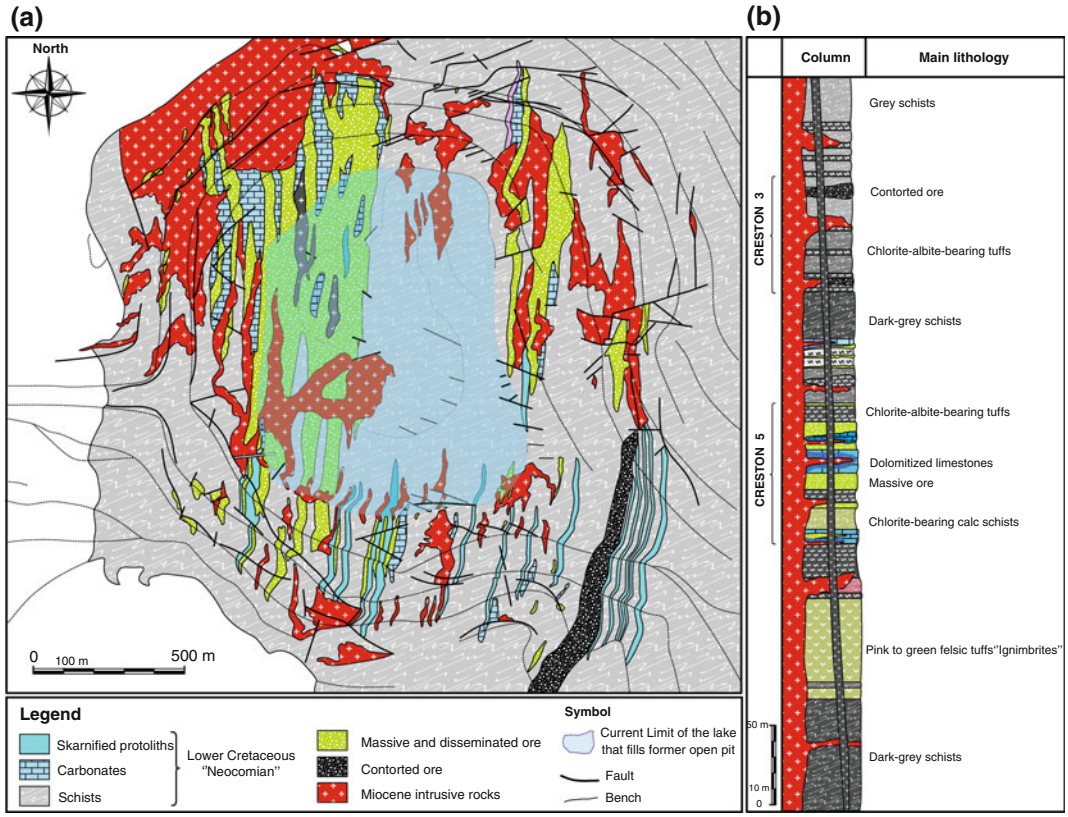

Fig. 6 **a** Surface geological map of Axara deposit showing main host-rock lithologies, major faults, and igneous occurrences with emphasis on relationships among intrusions, carbonate protoliths, and magnetite skarn orebodies. Also indicated are broadly elliptical, vertical zones of endoskarn and exoskarn developed between porphyritic intrusions and carbonate host rocks, and outline of lake (modified after Duflot et al. 1984). **b** Idealized stratigraphic column for Axara deposit based on core logging and field mapping by Duflot et al. (1984), complemented by observations of the authors

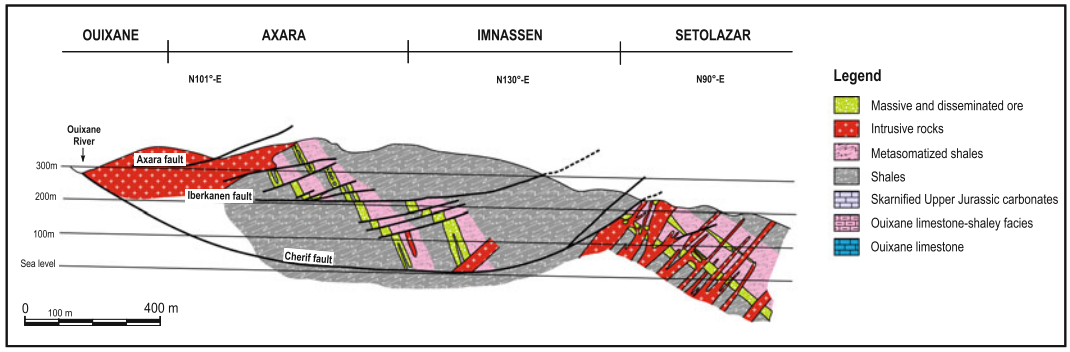

Fig. 7 Geologic cross section through the Ouixane district between Ouixane and Setolazar deposits along an approximately NW-SE transect showing geometry and position of Axara, Imnassen, and Setolazar orebodies relative to stratigraphy, intrusions, skarn, and listric detachment faults. Cross section is drawn based on geological investigations, exploration drill holes, and underground mine developments

which dip 60–70° E, comprise rhythmically laminated, schistose pelites with thin- to medium-bedded sandstone, calcareous siltstone, carbonate, and more importantly felsic to mafic ash-flow tuffs (Fig. 6). Carbonate rocks occur either as thinly to medium-sized bedded strata or as meter-sized, lens-like bodies dispersed within the pelitic matrix. The mean thickness of the carbonate lenses is 40 m. The lower basal unit is a succession of thinly bedded, fine- to medium-grained, silver-green schistose pelite ("schistes argentés") conformably overlain by a 80-m-thick sequence of grayish-green to pink, lithic-vitric, mafic to felsic pyroclastic rocks. Transition to the upper unit is marked by a ~100-m-thick, medium-bedded succession of carbonates with intercalated calcschist and andesitic tuff, which in turn is capped by an uppermost, >200-m-thick flysch-like sequence (i.e., Creston 3, 5; Fig. 6b). All of these units have undergone contact metamorphism and subsequent metasomatism during emplacement of the Late Neogene shallow stocks, dike swarms, and lava flows.

Ash-flow tuffs (tuffites of Kerchaoui 1994) are widespread in the mine area making up nearly 40 vol.% of exposed rocks. With a total aggregate thickness of >80 m, the ash-flow tuff succession (Fig. 6) comprises basal, greenish-gray to pink, fine-grained, stratified "ignimbritic" tuffs overlain by mafic andesitic tuffs. The tuffaceous rocks dated at 9.4 ± 0.4 Ma by Kerchaoui (1994) are not laterally extensive mainly because of erosion and more importantly faulting. The basal rhyolitic tuff sequence, which represents the early products of pyroclastic activity, consists of a 40-m-thick succession of crystal-rich to aphyric, eutaxitic-textured lapilli tuffs containing abundant broken subhedral crystals of embayed quartz and plagioclase, with minor K-feldspar and biotite pseudomorphed by white mica and chlorite. Irregular pumiceous clasts, randomly oriented shards, and lenticular fiamme are also common within an ash-rich foliated matrix of flattened vitroclasts. In most outcrops, the tuffaceous succession is pervasively propylitically altered to abundant illite/montmorillonite, chlorite, epidote, and sericite, with minor calcite replacing feldspar, mafic phenocrysts, and the groundmass. We interpret these rhyolitic lapilli tuffs as ignimbrite deposits that experienced a high degree of welding. If so, these pyroclastic rocks may constitute the missing evidence that supports the caldera structure model proposed by EL Bakkali et al. (1998) for the Ouixane mineralization. Iron mineralization is confined within silicified units and is closely associated with tuffs. This association led Duflot et al. (1984) to interpret the Axara mineralization as an epithermal or exhalative system in which hydrothermal circulation was driven by magmatism. However, this interpretation should be taken with care, because the iron mineralization formed by replacive and not exhalative processes (Bouabdellah et al. 2012; and the present study). The rhyolitic tuffaceous unit is overlain and interlayered with a 40-m-thick, grayish-green, lithic-vitric andesite composed of plagioclase (15 vol.% Ab_{67}), alkali feldspar (3 %), and quartz (2 %) fragments in a glassy matrix (65 %). Pyroxene (2 %), hornblende (1 %), biotite (1 %), and magnetite (5 %) occur as accessory xenocrysts.

Numerous intrusions plus dike swarm, sills, and basaltic lava flows of Late Neogene to Pliocene age occur in the deposit area (Figs. 6 and 7). Those intrusions that are adjacent to the skarns and/or are considered relevant to their formation consist petrographically of magnetite-series quartz-diorite and an associated dike swarm of aplite and microdiorite. Several narrow (<25 m-wide) subvolcanic basalt dikes and basaltic-andesite pyroxene- to biotite-phyric dikes are also present.

The host rocks have been deformed by ductile and brittle structures including a series of west-vergent, N-S to NNE-striking folds, thrust faults, and a penetrative axial-planar schistosity (S_1) paralleling S_0. Brittle structures are typified by listric faults, of which the most prominent is the Iberkanen Fault (Fig. 7) that produced a displacement of the upper part of the Axara orebody 100 m down to the west. The later brittle event gave rise to NS- to NE- and to a lesser extent, E-NE- to E-SE-trending subvertical faults with both sinistral to dextral motions (Duflot et al. 1984).

5 Setolazar-Bokoya Deposit

Of the three deposits that compose the Ouixane district, the Setolazar-Bokoya ore is economically the least attractive both in term of tonnage (13 Mt) and grade (35–55 % Fe), and more importantly because of a high sulphide contents (mainly pyrite-pyrrhotite) reaching concentrations as high as 20 % (average 4 %). In addition to sulphur, the Setolazar-Bokkoya ore is characterized by anomalous concentrations of deleterious elements such silica (up to 20 % SiO_2) that lower the market value of the produced iron ore.

The stratigraphic succession in the deposit area consists of a 150 m of rhythmically laminated, shallow-marine turbiditic and siliciclastic sedimentary rocks interlayered with calcareous siltstone, limestone, and felsic tuffs, all of which are intruded by a suite of Late Neogene alkali and calc-alkaline intrusions, sills, and dikes (Fig. 8).

The lowermost part of the lithostratigraphic column comprises a monoclinal, N-S-dipping package of finely laminated keratophyre tuffs containing quartz, sericite, and chlorite. Randomly oriented shards and fiamme are also common within an ash-rich foliated matrix of

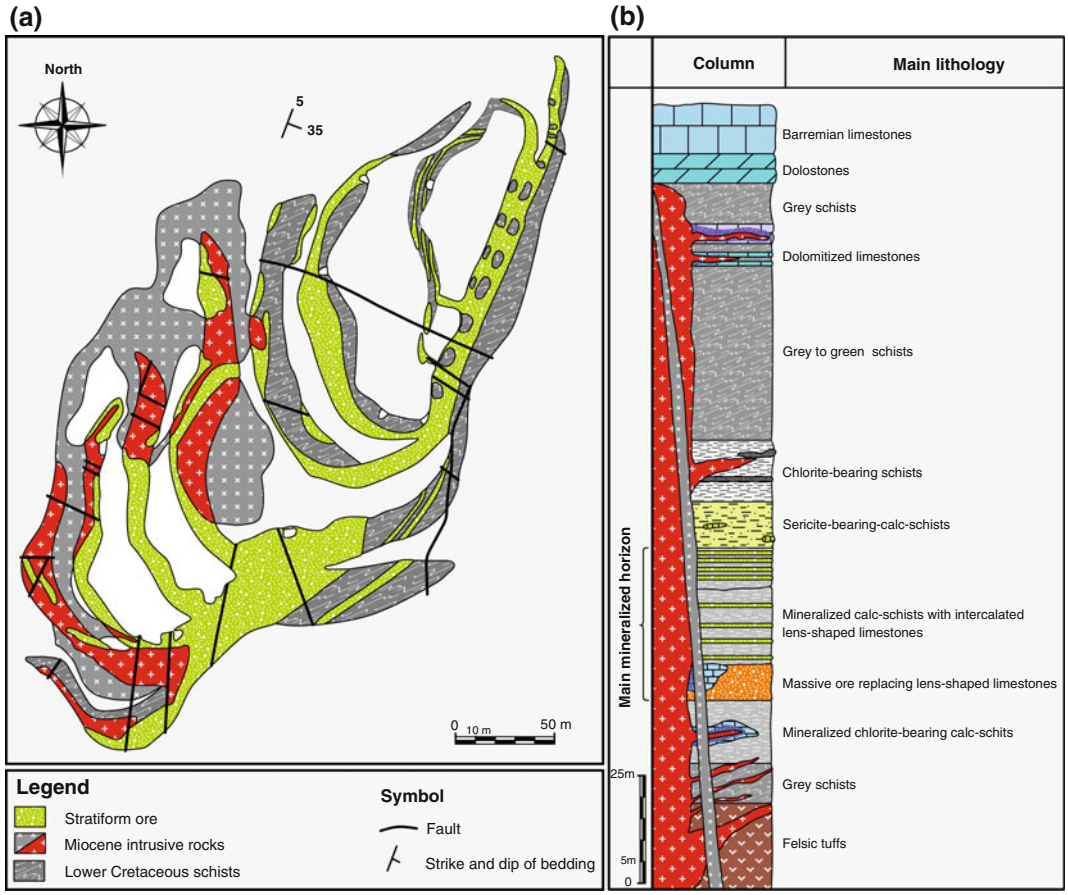

Fig. 8 **a** Surface geological map of Bokoya deposit showing main host-rock lithologies, major faults, and igneous occurrences with emphasis on relationships among intrusions, carbonate protoliths, and Fe-skarn mineralization. **b** Idealized stratigraphic column for Bokoya deposit based on core logging and field mapping by Duflot et al. (1984), complemented by authors' observations

flattened vitroclasts. All of the extracted iron mineralization occurs near the top of these keratophyre tuffs, and with a ~50-m-thick, finely bedded succession of calcareous, phyllitic-bearing schistose pelite interlayered with barren gray schistose pelite (Fig. 8). The uppermost part of the stratigraphic host rock unit is capped by the ~50-m-thick, unmetamorphosed massive limestone stratigraphic marker of Barremian age (Fig. 8b). Igneous rocks of alkali to calc-alkaline affinity (Lebret 2014) include granodioritic to dioritic intrusions and dikes, plagioclase-porphyritic dikes, rhyolite dikes, and late andesitic to basaltic lava flows and dikes.

Initial ductile deformation (D_1) of the host rocks produced kilometer-scale, west-plunging, N-S-trending F_1 folds. These folds have an axial-planar schistosity (S_1) parallel to bedding (S_0) that dips 30–40° to the east. Later deformation (D_2) folded the turbiditic and siliciclastic sequences into meter-scale, E-NE-plunging, NE-striking F_2 folds having a locally developed S_2 cleavage inclined on S_{0-1}. Brittle structures are represented by major N-S- and NNW-striking sub-vertical to steeply dipping faults. A late set of minor strike-slip faults with subordinate, low-amplitude displacements is also recognized. It is noteworthy that the higher grade Fe orebodies are confined to intensely folded and fractured rocks at the intersection of the major N-S- and NNW-trending faults.

6 Afra Deposit

Discovered in 1906, the Afra deposit was operated from 1932 to 1941 and 1947 to 1959 by the European and North African Mines Ltd. and Compania Maroqui de las Minas de Afra, respectively, having produced ~500,000 t of magnetite concentrates. An additional 6500 t of lead concentrate was recovered from the northern part of the deposit (Jeannette 1961; Fig. 9). With such low production, the Afra deposit is considered economically the least productive of all deposits in the Ouixane district. Afra includes two deposits: Afra Pb to the north and Afra Fe to the south (Fig. 1). The magnetite ± sulphide-rich orebodies, or minas, which were exploited along three zones (Zones C and M and level 104; Fig. 9), consist of en echelon, massive, lens-shaped accumulations straddling the faulted contact between the Upper Jurassic and Lower Jurassic formations. The Upper Jurassic formation consists of a folded and low- to medium-grade, flysch-like sequence of Tithonian age composed of green schistose pelite with intercalated quartzite and pyrite-bearing blue limestone, tectonically (thrust) overlain by Lower Cretaceous (Neocomian) Aptychus-bearing schist, marl, and limestone (Fig. 9). Several swarms of NE- and E-W-trending, fine-grained, porphyritic dikes of microdioritic composition intrude the Jurassic-Cretaceous host rocks, which in turn are dissected by a series of N-S-, E-W-, and WNW-striking faults.

The magnetite-hematite skarn mineralization is overprinted by a later fracture-controlled sulphide mineral assemblage (Afra Pb deposit; Fig. 1). This assemblage is accompanied by various proportions of quartz, calcite, Fe-carbonate (siderite, ankerite), braunite, lamellar hematite, barite, quartz, and local chalcedony-opal. The Pb-rich mineralized structures form narrow (0.5–1 m, rarely up to 3 m thick), linear stockworks, veinlets, or veins that strike predominantly E-W, dip 60° N, and extend up to 500 m along strike and 65 m down dip, enclosed either within the Jurassic-Cretaceous sedimentary rocks or the microdioritic dike swarm (Jeannette 1961). Sulphide minerals consist mostly of galena with subordinate sphalerite, chalcopyrite, and pyrite.

7 Skarn Distribution, Mineralogy, Textures, and Paragenesis

In the Ouixane Fe-skarn district, mined orebodies are spatially restricted to the eastern margin of the northern allochthonous terrane (Fig. 1) where

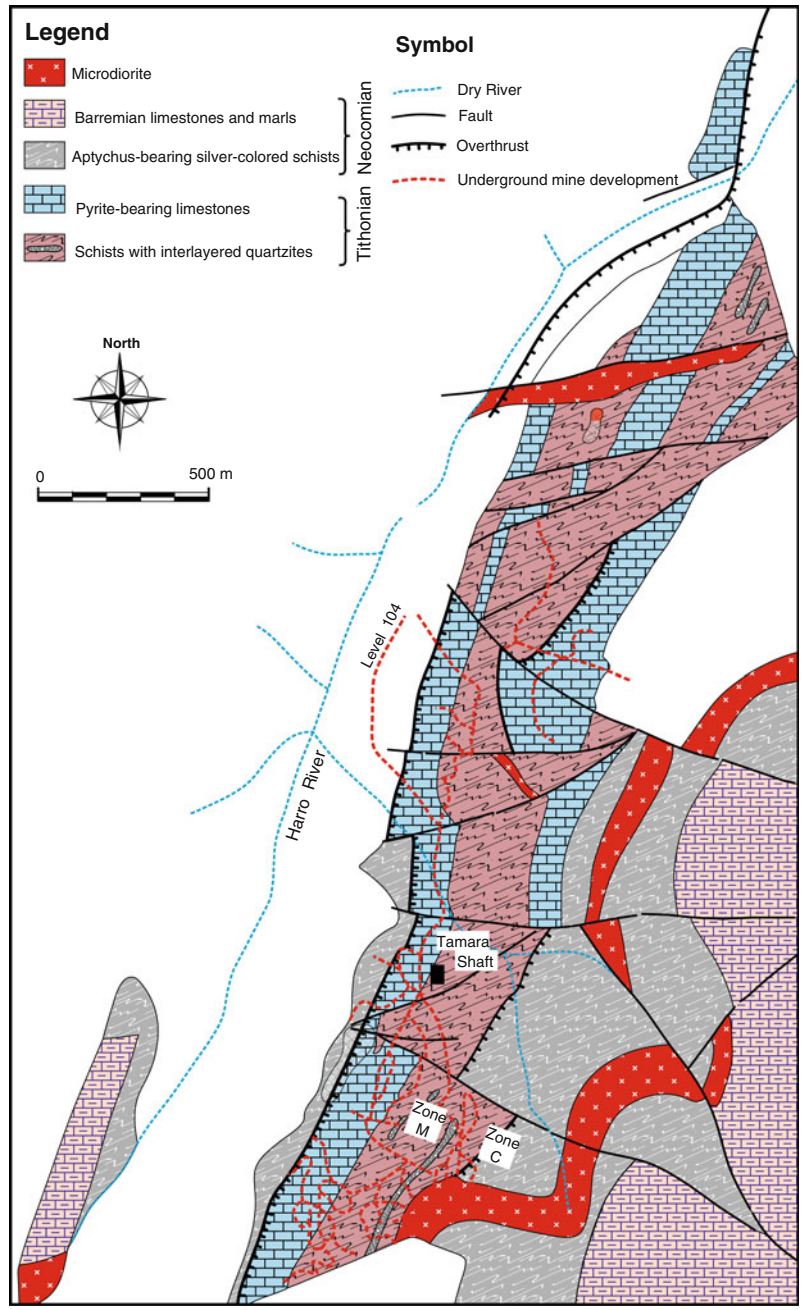

Fig. 9 Surface geological map of Afra deposit (modified after Jeannette 1961) showing main host-rock lithology, major faults, and igneous occurrences with emphasis on relationships among intrusions, carbonate protoliths, and underground mine exposures (*dashed lines*)

apophyses of the Ouixane quartz-diorite porphyry intrude the shallow-marine, turbiditic and siliciclastic, carbonate-rich lithologic sequence. Higher grade orebodies are confined to extensively altered carbonate rocks above or adjacent to, the 7.58 ± 0.03 Ma Ouixane quartz-diorite porphyry and related intrusions.

8 Replacement versus Open-Space Filling Mineralization

Based on stratigraphic position, geometry of ore deposits, and style of mineralization, two main contrasting types of mineralization are

distinguished: (1) prograde to retrograde metasomatic replacement, and (2) open-space filling. Most of the skarn deposits formed by replacement of carbonate rocks and therefore have important stratigraphic and lithologic controls on their distribution. Indeed, replacement mineralization, which accounts for more than 90 % of the extracted ore in the Ouixane district, occurs either as centimeter- to decimeter-thick, rhythmically interlayered laminae of magnetite-hematite and barren host rock; this style of mineralization defines the stratiform ore (i.e., Axara and Setolozar deposits; Fig. 1). Discordant, irregular and lenticular orebodies define stratabound massive ore (i.e., Ouixane deposit; Fig. 2). The stratiform/stratabound ratio is primarily determined by the initial geometry along with porosity and permeability of the carbonate precursor.

Particularly striking is the wavy laminated, lens-like mottled ore locally referred to as contorted ore (Fig. 7). This style of mineralization is interpreted to have resulted from the replacement of initial bioturbated contorted bedding, related to soft-sediment deformation of preexistent carbonate precursors. The geometry of the mineralized massive lenses appears therefore to be controlled by preferential replacement of specific lithologic units or stratigraphic contacts. Conversely, open-space filling mineralization—of only minor economic interest—occurs either in veins, stockworks, or breccias matrices.

9 Prograde and Retrograde Hydrothermal Alteration, Textures, and Mineral Paragenesis

Skarn mineralization and associated hydrothermal alteration are developed in three settings (Fig. 4). These include (1) the Ouixane hornblende-biotite quartz-diorite porphyry and associated satellites defining the endoskarns, (2) along contacts of the intrusions with the carbonate rocks defining the proximal skarns, and (3) more importantly hundreds of meters away from the contact zones defining the exoskarns. Exoskarn is typically massive, unzoned, extends laterally along the bedding, and grades outward to calc-silicate marble and marble. Endoskarn is developed at the intrusion-carbonate contact, or more commonly within the intrusions along faults and fractures filled with plagioclase, epidote, and pyroxene ± titanite ± apatite ± magnetite.

Paragenetic studies in the Ouixane district show that skarn evolution occurred in four stages (isochemical, skarn calc-silicate, potassic-phyllic-propylitic, and supergene).

Initial skarn formation started with isochemical conversion of carbonate, shale, and sandstone lithologies to marbles and hornfels along the intrusive contacts. Evolution as a consequence of the opening of the system promoted metasomatic replacement of the protoliths by calc-silicate, oxide, and sulphide minerals. Overall, the Fe skarn mineralization took place over a wide range of temperatures during three successive stages: isochemical, prograde metasomatic, and retrograde metasomatic. Distribution of the skarn alteration zones lacks symmetric zoning due to the effects of later intense shearing. The initial isochemical stage resulted in the development of a 300–400-m-wide thermal aureole composed of quartz, K-feldspar, muscovite, biotite, chlorite, andalusite, and cordierite hornfels, quartzite, and marble.

The metasomatic process included two main skarn-forming stages and related ore formation. Of these, the early stage was dominated by an anhydrous calc-silicate mineral assemblage and represents the prograde stage; the later metasomatic event deposited hydrous rock-forming minerals and therefore is referred to as the retrograde stage. The earlier prograde skarn alteration consists predominantly of clinopyroxene (diopside-hedenbergite series) and garnet (grossularite-andradite series), with an overall clinopyroxene/garnet ratio of approximately 2:1. Clinopyroxene, the earliest calc-silicate mineral that precipitated due to interaction of calcareous host rock with ore-bearing metasomatic fluids, shows wide compositional variations ranging from $Di_{95}Hd_5$ to $Di_{46}Hd_{53}$ with a maximum johannsenite content of 3 %. Garnet is mainly andraditic with compositions ranging from nearly

pure andradite ($Ad_{98}Gr_2$) to $Ad_{40}Gr_{60}$ accompanied by a mean spessartine content of <3 % (Jabrane 1993; EL Rhazi and Hayashi 2002; Lebret 2014). These compositions are in agreement with those characterizing Fe-skarn deposits worldwide (e.g., Meinert 1998). Most of the Ouixane garnets are isotropic, although some display anisotropy with sector and oscillatory zoning. The optically isotropic zones are Fe-rich and Al-poor, whereas the anisotropic zones are Al-rich and Fe-poor (EL Rhazi and Hayashi 2002).

Conversely, the retrograde lower-temperature hydrous skarn stage resulted in nearly complete replacement of the prograde garnet-pyroxene mineralogy by massive magnetite, amphibole (ferropargasite-ferroactinolite), phlogopite, chlorite (brusvigite-chamosite), epidote (35 % pistachite), calcite, quartz, and barite. Mineralizing metasomatic fluids were channelized along fractures, stratigraphic contacts, and permeable horizons forming the iron rich mineralization. It is noteworthy that high iron grades are spatially related to the retrograde skarn assemblages.

In addition to the prograde and retrograde events, later potassic followed by propylitic and phyllic alteration overprinting the magmatic-hydrothermal skarn stages. The resulting mineral assemblages have composition similar to those recorded for the retrograde skarn, occurring as patches or scattered fracture fillings within or close to the intrusive bodies. The potassic assemblage consists of quartz-K-feldspar (orthoclase, adularia), and biotite with minor plagioclase (oligoclase), amphibole, epidote, chlorite, and calcite. The later propylitic (chlorite-epidote-carbonate) and phyllic (quartz-sericite-carbonate-sulphide) assemblages extend kilometers away from the major skarns; these constitute the equivalent of porphyry-epithermal-style mineralization expressed in the form of extensive but generally low-grade Pb–Zn–Ba veins (i.e., Pb-rich Afra deposit). The post-skarn hydrothermal alterations and related porphyry-epithermal occurrences are asymmetrically zoned around the Ouixane quartz-diorite porphyry. Sericite from the epidote skarn has a K–Ar age of 7.04 ± 0.22 Ma (EL Rhazi and Hayashi 2002).

A distinctive albite-scapolite alteration (i.e., Na–Cl metasomatism) zone is also developed within the intrusive rocks that host part of the Ouixane ore (Jabrane 1993). Scapolite (marialite-meionite series) is white and compositionally a Na-rich variety (mean composition 74 mol% marialite; Jabrane 1993). Associated phases are actinolite, tourmaline, apatite, chlorite, albite, and calcite. It is noteworthy that scapolite is a common mineral in Fe–Cu and Au skarns (Pan 1998), particularly those related to shoshonitic series igneous rocks (e.g., Forster et al. 2004; Soloviev 2011). Based on the presence of this magma type in the region, more attention should paid to the Neogene post-collisional magmatism of the Ouixane area, because all of the geochemical ingredients are present there to suggest potential of the area for hosting undiscovered porphyry and Fe–Cu and Au skarn deposits.

9.1 Ore Mineralogy

Typically, most of the economic iron orebodies in the district are spatially related to prograde and retrograde metasomatic stages. Iron mineralization commonly forms either interlayered, cm- to dm-thick magnetite-bearing laminae that replace compositionally contrasting rocks (mainly calcareous beds and barren host rocks), massive lens-shaped orebodies up to 30 m thick and >50 m long dispersed within schistose pelite, or as matrices to breccias. Subordinate disseminations, contiguous patches, and crosscutting veins and veinlets of magnetite are also present.

Despite the extensive segmentation of the orebodies by post-mineralization strike-slip faults (Fig. 7), the original morphology of the orebodies as lensoid and tabular zones in both plan and vertical sections are still recognizable. The N-S to NNE strikes and ca. 45° E dips of the orebodies reflect control by the dominant E-W-striking Iberkanen listric fault (Fig. 7). Surface mineralization consists of jasperoidal "gossan" (earthy hematite, goethite) that was mined historically as a pigment for the paint

industry. This secondary ore grades at depth into primary magnetite-rich mineralization.

Ore mineralogy consists of various proportions of magnetite and hematite (total 95 %) with minor to trace quantities of sulphides (<5 %). Magnetite is by far the main ore mineral, displaying a large range of textures varying from disseminated crystals of diverse size dispersed within the host rocks, to clusters, massive aggregates, or stratiform cm- to dm-sized bedded laminae parallel to primary stratification, giving rise to a rhythmically banded zebra texture. Also present are ribbon, mossy, mottled, nodular, spotted, and orbicular textures, together with fluid-assisted brecciated and deformational textures (see Ciobanu and Cook 2004). Magnetite is also found as fillings of stockworks and veins as well as anhedral inclusions within pyroxene, garnet, and amphibole. The magnetite has very low concentrations of Cr_2O_3, TiO_2, and V_2O_5 (Lebret 2014; present study), which are typical of magnetite occurring in skarn or low-grade metamorphic rocks (Dupuis and Beaudoin 2011).

The later "porphyry-epithermal" fracture-controlled sulphide assemblage consists principally of pyrite and pyrrhotite with subordinate amounts of galena, sphalerite, and chalcopyrite. Locally (i.e., Pb-rich Afra deposit; Fig. 9), galena-rich mineralization forms subeconomic concentrations. Gangue minerals include various proportions of quartz, calcite, Fe-carbonate (siderite, ankerite), lamellar hematite, barite, quartz, and local chalcedony-opal.

Supergene processes include martitization of magnetite, replacement of chalcopyrite by covellite, and pyrite/pyrrhotite by goethite. Dendritic manganese oxides are present in the outermost parts of the alteration halo.

10 Fluid Inclusion and Oxygen Isotopic Data

Microthermometric measurements have been performed on selected fluid inclusions hosted both in quartz from the Ouixane quartz-diorite intrusion adjacent to the skarn contact and in a range of paragenetically well-constrained prograde and retrograde skarn minerals including garnet, clinopyroxene, quartz, scapolite, apatite, calcite, plagioclase, and chlorite (Jabrane 1993; EL Rhazi and Hayashi 2002; Bouabdellah unpublished data). Overall, data from these fluid inclusions show a wide range of liquid-vapor-solid ratios, homogenization temperatures, and salinities. Identified daughter minerals, based on crystal habits, physical properties, and color, consist principally of halite and sylvite ± magnetite ± hematite; the two iron oxides are interpreted as captive minerals because they occur only locally and display variable phase ratios, and more importantly do not dissolve upon heating (see Shepherd et al. 1985). Traces of CO_2 were only detected in a very few inclusions by Raman spectroscopy, but on freezing neither solidification of CO_2 nor nucleation of a clathrate was observed. The low eutectic temperatures in the range of −70 to −45 °C indicate the presence of other dissolved salts, in addition to NaCl ± KCl, likely as divalent cations such as $CaCl_2$, $MgCl_2$, $FeCl_2$, and $LiCl_2$ (Crawford 1981; Davis et al. 1990).

Fluid inclusions within quartz from the granodiorite exhibit the highest temperatures and corresponding salinities from 307 to 600 °C and 49 to 73 wt% NaCl equiv, respectively (EL Rhazi and Hayashi 2002). Clinopyroxene- and garnet-hosted fluid inclusions from the early anhydrous skarn stage typically homogenize between 347 to 530 °C and 480 to ~600 °C, respectively, with calculated salinities ranging from 25 to 55 wt% NaCl + KCl equiv and 55–65 wt% equiv NaCl + KCl (Jabrane 1993; EL Rhazi and Hayashi 2002). Mean fluid pressure at this temperature range is estimated at 600 bars (Jabrane 1993), which corresponds to a maximum depth of 6 km if a hydrostatic regime is assumed or ~2 km for a lithostatic system (rock density =2.7 g/cm^3).

In contrast, fluid inclusions in quartz and calcite associated with the late retrograde alteration stage homogenize from 250 to 125 °C. These fluid inclusions lack daughter minerals and average 7 wt% NaCl equiv. Homogenization temperatures and related salinities from scapolite, apatite, and quartz cover a large range from 215

to 450 °C, and 20 to 45 wt% NaCl equiv, respectively (Jabrane 1993). Considered paragenetically, there is an overall trend of decreasing temperatures, pressures, and salinities from the early to later stages of mineralization.

Oxygen isotopic compositions of clinopyroxene and garnet from the prograde skarn stage are tightly clustered with $\delta^{18}O$ values ranging from 8.3 to 9.7 and 9.5 to 12.8 ‰, respectively (EL Rhazi and Hayashi 2002). Conversely, data for magnetite span a wide range of ~12 ‰ with $\delta^{18}O$ values oscillating from −2.9 to 9.2 ‰, partially overlapping the isotopic compositions of clinopyroxene.

11 Discussion

11.1 Relationship to Late Neogene Intrusions and Redox Conditions

The close spatial relationship between the iron-rich orebodies and the Ouixane quartz-diorite porphyry constitutes permissive evidence for a magmatic-hydrothermal and contact-metasomatic origin for the iron mineralization. Moreover, the uniform composition of calc-silicate and ore mineralogy throughout the ore field indicates that the genesis of all of the deposits of the district reflects the interplay of different stages of magmatic-hydrothermal activity during emplacement of a single, high-level, granitoid magma of high-K, calc-alkaline and shoshonitic affinity. Indeed, the age of mineralization (7.04 ± 0.47 Ma based on K/Ar and Ar/Ar dating of skarn epidote and phlogopite; EL Rhazi and Hayashi 2002) coincides within 2σ error with the K/Ar and Ar/Ar ages of the Ouixane quartz-diorite porphyry (7.58 ± 0.03 Ma; Duggen et al. 2005), thus providing strong evidence for a genetic relationship between the iron mineralization and the Late Neogene Ouixane intrusion. The presence of ribbon skarn textures and fine-grained chilled margins are consistent with a skarn system that developed in a relatively shallow setting (e.g., above cupolas of high-level granites; Kwak 1986). Skarn formation was probably related to fluids derived from the Ouixane quartz-diorite porphyry that migrated vertically and laterally within permeable calcareous units. Structural controls were also important in focusing fluids and localizing the emplacement of late mineralizing phases.

Skarn mineralogy and the calcic and andraditic compositions of garnet and pyroxene from the prograde stage suggest that the magnetite orebodies formed under relatively oxidized conditions. The widespread occurrence of epidote is also consistent with oxidizing conditions (e.g., Kwak 1994). Both endoskarn and exoskarn, which formed at relatively low temperatures (<500 °C), lack olivine and wollastonite, and contain extremely andradite rich-garnet (Ad > 40 mol%). Such features are also common worldwide among Phanerozoic Fe-skarn deposits associated with dioritic intrusions (Einaudi et al. 1981; Einaudi 1982).

The predominance of sulphides (i.e., mostly pyrite and pyrrhotite with subordinate galena, sphalerite, and chalcopyrite) late in the paragenetic sequence (Fig. 10) indicates that this late retrograde sulphide stage formed under relatively reduced (pyrite-pyrrhotite f_{O2} buffer) and much cooler (ca. 160–360 °C) conditions, in contrast to the high- temperature and strongly oxidized conditions that prevailed during the earlier prograde stage. Such a paragenetic trend may record the decrease through time of f_{O2} and corresponding increase of pH and f_{S2}. Increased sulphur fugacity is mostly a consequence of sulphur degassing from the magma body. Accordingly, we propose that the prograde stage of the Ouixane magnetite mineralization formed initially under relatively shallow oxidizing conditions, which evolved through time during the retrograde stage towards more reducing conditions.

11.2 Sources of Ore Fluids and Ore Depositional Processes

The wide variations both in observed temperature (~600–125 °C) and salinity (7–73 wt% NaCl equiv) are suggestive of the involvement of multiple distinct fluids and/or ore-forming

processes in the genesis of the Ouixane Fe skarn deposits. Overall, the bulk composition of the mineralizing fluids can be modeled in the H_2O–NaCl–KCl ± $FeCl_2$ ± $CaCl_2$ ± $MgCl_2$ ± $LiCl_2$ system. These fluid compositions are similar to those characterizing skarn mineralizing systems worldwide (Einaudi et al. 1981). The systematic paragenetic trend of decreasing temperature, pressure, and salinity through time is consistent with the study of Soloviev (2011) in which a contact diffusion-metasomatic mechanism prevailed during the early prograde skarn stage, in contrast to an infiltration process that predominated during late prograde skarn formation.

11.3 Evidence for Fluid Immiscibility "Boiling"

The early mineralizing fluids associated with the prograde skarn stage are high-temperature (347–600 °C), low CO_2 (<0.05 mol%), NaCl–KCl brines with total salinities ranging from 25 to 65 wt% NaCl + KCl equiv. Later fluids associated with the retrograde stage exhibit much lower temperatures (300–125 °C) and salinities (up to 7 wt% NaCl equiv). This evolutionary trend of decreasing temperatures and salinities through time suggests the involvement of late cooler and dilute fluids, probably of meteoric origin, which mixed and equilibrated with the early magmatic-hydrothermal fluids. High-temperature and high-salinity fluids may be produced either by the dissolution of ancient evaporites or by phase separation from boiling magmas at relatively low pressures (<0.3 kb; Burnham 1979). The first hypothesis can be discarded because there are no outcropping evaporates intercalated within the Upper Jurassic-Lower Cretaceous host rock sequence.

The high salinities (up to 70 wt% NaCl + KCl equiv) recorded during the early skarn stage are attributed to the involvement of a magmatic fluid component that experienced phase separation (i.e., fluid immiscibility or boiling; Bodnar 1995) from the crystallizing Ouixane quartz-dioritic parental magma. In this regard, it is well documented that emplacement of volatile-rich magmas at shallow levels, as is the case for the Ouixane intrusion that crystallized at 0.8–2.7 kb (Jabrane 1993), promotes the direct exsolution of metalliferous, highly saline aqueous fluids (e.g., Richards 1995). In such an environment, the first fluids to exsolve will have moderate salinities (6–8 wt% NaCl equiv; Bodnar 1995). As crystallization proceeds, chlorine becomes concentrated in the melt, such that those fluids which continue to exsolve have successively higher salinities.

In the Ouixane district, the presence of captured magnetite and hematite crystals in fluid inclusions reflects the high iron content of the early mineralizing fluids. This high iron content is consistent with an extremely high salinity, based on the likely aqueous transport of iron by one or more chloride complexes. Geochemical evidence for high chloride activity in the early mineralizing fluids is attested by occurrence of the scapolite-albite alteration halo (i.e., Na–Cl metasomatism) developed within the Ouixane quartz-diorite porphyry. Therefore, we attribute the Na–Cl metasomatism that generated the albite-scapolite alteration to brines that exsolved from the cooling quartz-dioritic melt. Rapid ascent to a depth of ~2 km (~600 bars assuming lithostatic pressure; Jabrane 1993) caused this melt to intersect its solvus at a temperature of 560–600 °C, which coincides with the temperatures determined from fluid inclusions hosted in the prograde clinopyroxene and garnet, producing condensates of a high-salinity fluid (~49 wt% NaCl equiv) from a lower-density vapor, as modeled by Zhu et al. (2015). The resulting early brines were highly oxidized as suggested by the bulk mineralogical constraint (i.e., pervasive crystallization of magnetite). Furthermore, calculated $\delta^{18}O_{fluid}$ compositions for garnet and clinopyroxene (+5.4 to +8.9 ‰ V-SMOW) further support the involvement of a magmatically derived fluid source during the earlier stages of skarn mineralization. Similarly, lead isotope data (discussed below) are consistent with the derivation of lead—and by inference other ore-forming metals—from the crystallizing Ouixane granitic magma.

Involvement of metamorphic fluids seems unlikely, however, because the regional metamorphism recorded in the Ouixane district only attained a low grade (greenschist facies), and consequently the metamorphic temperatures were not high enough to mobilize sufficient high-temperature metamorphic pore fluids like those that prevailed during the earlier stages of skarn mineralization (Taylor 1997). The boiling process accompanied by a drop in temperature and/or pressure of the hydrothermal fluids may have triggered magnetite precipitation during stage I.

11.4 Fluid Mixing

The large range of ~12 ‰ in $\delta^{18}O$ values for magnetite is consistent with mixing of variable proportions of different fluids and/or a wide range of physiochemical conditions such as temperature, pH, and f_{O2} under which the different mineral assemblages of the Ouixane district precipitated. Low $\delta^{18}O_{magnetite}$ values from 1 to 4 ‰ (EL Rhazi and Hayashi 2002) are suggestive of an igneous origin through the direct crystallization of Fe-oxide-dominated melts (Naslund et al. 2002; Chen et al. 2010). Accordingly, we propose that part of the magnetite mineralization in the district related to oxide stage I records the emplacement of oxidized melts that commingled with a quartz-diorite melt.

The gradual trend of cooling and decreasing pressure and salinity together with fluid compositional changes (from H_2O–NaCl–KCl to H_2O–NaCl–$CaCl_2 \pm MgCl_2$) can be interpreted as resulting from one or more of the following processes: (1) incursion of meteoric water and its mixing with a magmatic fluid-dominated component, (2) addition of basinal fluids from the enclosing sedimentary host rocks, and/or (3) release of $CaCl_2$ during calc-silicate precipitation and skarn formation (Kwak and Tan 1981). Such trends have been documented in many porphyry and skarns systems (e.g., Roedder 1984; Lai et al. 2007).

In the Ouixane district, high iron grades are spatially related to retrograde skarn assemblages suggesting that the bulk of magnetite precipitated at lower temperatures and pressures, compared to the first pulse of Fe-oxides that occurred during the earlier stages of skarn mineralization (i.e., oxide stage I). It therefore seems that mixing of magmatic-dominated fluids emanating from the crystallizing quartz-diorite porphyry, with surficially derived, cooler fluids was the main ore depositional process that triggered iron deposition. The coexistence of Fe-rich epidote and magnetite (EL Rhazi and Hayashi 2002) indicates temperatures lower than 600 °C and pressures at 1 kb P_{H2O} (Liou 1973). Particularly striking is the fact that the main stage of iron mineralization (i.e., retrograde oxide substage II; Fig. 10) coincides with development of fluid inclusions devoid of saline daughter minerals. This observation suggests, in agreement with the statements of Lai et al. (2007), that the bulk of the Ouixane iron skarn mineralization occurred when the hydrothermal system was diluted by cool external fluids.

Fluid mixing and associated extensive fluid-wall-rock interaction processes are also supported by oxygen isotope constraints. Indeed, the heavy $\delta^{18}O$ values reflect the involvement of increasing amounts of externally derived dilute fluids (i.e., sedimentary formation water) that equilibrated with the sedimentary host rocks in a predominantly closed and rock-buffered system under increasing water/rock ratios.

A further decrease in temperature, pressure, and salinity resulted in deposition of "porphyry-epithermal" fracture-controlled, sulphide-rich assemblages of stage III that coincide spatially with the potassic-phyllic-propylitic alteration zones. The presence of vuggy quartz together with lattice-bladed calcite replaced by quartz (Bouabdellah et al. 2012), and crustiform-colloform textures, constitutes the most diagnostic features (Sillitoe 1993) that suggest deposition of the later sulphide-rich mineralization occurred under epithermal conditions. Moreover, fluid inclusion data (Jabrane 1993; EL Rhazi and Hayashi 2002; Bouabdellah unpublished data) indicate that the sulphide-rich epithermal veins formed from lower salinity (<15 wt% NaCl equiv) fluids at temperatures of

250–120 °C and pressures of <100 bars, corresponding to depths below 1 km.

11.5 Source(s) of Metals

Lead isotope compositions of galena ore ($^{206}Pb/^{204}Pb$ = 18.764–18.787, $^{207}Pb/^{204}Pb$ = 15.661–15.669, $^{208}Pb/^{204}Pb$ = 38.850–38.958; Lebret 2014) are characterized by relatively homogenous values that are broadly comparable with the Pb isotope ratios of the Ouixane intrusion ($^{206}Pb/^{204}Pb$ = 18.789, $^{207}Pb/^{204}Pb$ = 15.650, $^{208}Pb/^{204}Pb$ = 38.822; Lebret 2014). Significantly, the ore leads are isotopically distinct from those of contemporaneous basalts ($^{206}Pb/^{204}Pb$ = 18.831–19.139, $^{207}Pb/^{204}Pb$ = 15.602–15.643, $^{208}Pb/^{204}Pb$ = 38.703–39.012; Duggen et al. 2005). Accordingly, we suggest that most of the lead and, by inference other ore-forming metals, were derived mainly from the crystallizing Ouixane granitic magma.

12 Conclusions

Based on microthermometric measurements and isotopic-geochemical data discussed above, it is apparent that the overall mineralogy of the Ouixane magmatic-hydrothermal system shifted through time from early deep-seated, magmatic, H_2O–NaCl–KCl ± $FeCl_2$ fluids to surficial, non-magmatic, H_2O–NaCl–$CaCl_2$ ± $FeCl_2$ fluids. These fluids deposited, with advancing paragenetic sequence, high-temperature (400–500 °C) iron oxides (magnetite-hematite) of stage I, followed at decreasing temperatures, pressures, and salinities magnetite-hematite of stage II, and finally at the lowest temperatures (125 °C) under epithermal conditions sulphides and carbonate-barite assemblages due to mixing with external dilute fluids. Ascending boiled fluids may have been focused along regional brittle fault structures to upper crustal levels, flowing laterally within permeable calcareous units and subsequently mixing with downward percolating surficial waters, resulting in deposition of the Fe-skarn and associated sulphide mineralization.

References

Anonymous (1985) Les gisements de fer du Rif Oriental (Nador): synthèse géologique et évaluation des réserves. Société d'exploitation mines du Rif (SEFERIF), Rabat, 69 pp

Bodnar RJ (1995) Fluid inclusion evidence for a magmatic source for metals in porphyry copper deposits. In: Thompson JFH (ed) Magmas, fluids and ore deposits. Mineralogical Association of Canada, short course series, vol 23, pp 139–152

Bouabdellah M, Lebret N, Marcoux E, Sadequi M (2012) Les mines des Beni Bou Ifrour-Ouixane (Rif Oriental): un district ferrugineux néogène de type skarn. Nouveaux guides géologiques miniers Maroc, Notes Mémoires Service Géologique Maroc 9:357–362

Burnham CW (1979) Magmas and hydrothermal fluids. In: Barnes HL (ed) Geochemistry of hydrothermal ore deposits, 2nd edn. Wiley, New York, pp 71–136

Chen H, Clark AH, Kyser TK (2010) The Marcona magnetite deposit, Ica, south-central Peru: a product of hydrous, iron oxide-rich melts. Econ Geol 105:1441–1456

Ciobanu CL, Cook NJ (2004) Skarn textures and a case study: the Ocna de Fier-Dognecea orefield, Banat, Romania. Ore Geol Rev 24:315–370

Comas MC, Platt JP, Soto JI, Watts AB (1999) The origin and tectonic history of the Alboran basin. Proc Ocean Drill Program, Sci Results 161:555–580

Coulon C, Megartsi M, Fourcade S, Maury RC, Bellon H, Louni-Hacini A, Cotton J, Coutelle A, Hermitte D (2002) Post-collisional transition from calc-alkaline to alkaline volcanism during the Neogene in Oranie (Algeria): magmatic expression of a slab breakoff. Lithos 62:87–110

Crawford LM (1981) Phase equilibria in aqueous fluid inclusions. In: Hollister LS, Crawford ML (eds) Fluid inclusions: applications to petrology. Mineral Association Canada, short course handbook, vol 6, pp 75–100

Davis DW, Lowenstein TK, Spencer RJ (1990) Melting behavior of fluid inclusions in laboratory grown halite crystals in the systems NaCl-H_2O, NaCl-KCl-H_2O, NaCl-$MgCl_2$-H_2O and NaCl-$CaCl_2$-H_2O. Geochim Cosmochim Acta 54:591–601

Delizaur J (1952) Gîtes de fer des Kelaia. XIX Congr Géol Inter, Alger, Livret-guide 7, série Maroc, pp 24–27

Duflot H, Jezequel P, Roman Bernal A (1984) Le gisement de fer de Nador (zone rifaine, Maroc): nouvelles observations géologiques. Unpubl Rept, Sec d'études géologiques et minières, option géologie minière, Ecole Mines de Paris, France, 101 pp

Duggen S, Hoernle K, Van Den Bogaard P, Garbe-Schönberg D (2005) Post-collisional transition from subduction- to intraplate-type magmatism in the westernmost Mediterranean: evidence for continental-edge delamination of subcontinental lithosphere. J Petrol 46:1155–1201

Dupuis C, Beaudoin G (2011) Discriminant diagrams for iron oxide trace element fingerprinting of mineral deposit types. Miner Deposita 46:319–335

Einaudi MT (1982) Descriptions of skarns associated with porphyry copper plutons. In: Titley SR (ed) Advances in geology of the porphyry copper deposits, southwestern North America. University Arizona Press, Tucson, pp 139–183

Einaudi MT, Meinert LD, Newberry RJ (1981) Skarn deposits. Economic Geology 75th Anniversary Volume, pp 317–391

EL Bakkali S, Gourgaud A, Bourdier JL, Bellon H, Gundogdu N (1998) Post-collision Neogene volcanism of the eastern Rif (Morocco): magmatic evolution through time. Lithos 45:523–543

EL Rhazi M, Hayashi K (2002) Mineralogy, geochemistry, and age constraints on the Beni Bou Ifrour skarn type magnetite deposit, northeastern Morocco. Resour Geol 52:25–39

Forster DB, Seccombe PK, Phillips D (2004) Control on skarn mineralization and alteration at the Acadia deposits, New South Wales, Australia. Econ Geol 99:761–788

Frizon de Lamotte D (1982) Contribution à l'étude de l'évolution structurale du Rif Oriental (Maroc). Notes Mémoires Service Géologique Maroc 314:241–304

Gutscher MA, Malod J, Rehault J-P, Contrucci I, Klingelhoefer F, Mendes-Victor L, Spakman W (2002) Evidence for active subduction beneath Gibraltar. Geology 30:1071–1074

Heim A (1934) The iron ores of minas del Rif, Spanish Morocco. Econ Geol 29:294–300

Hernandez J, Bellon H (1985) Chronologie K-Ar du volcanisme miocène du Rif oriental (Maroc): implications tectoniques et magmatologiques. Revue Géologie Dynamique Géograph Physique 26(2):85–94

Jabrane R (1993) Etudes génétiques de la minéralisation en fer de Nador (Maroc nord oriental). Unpublished Ph.D. Thesis, Université Libre Bruxelles, Belgium, 566 pp

Jeannette A (1961) Les ressources minérales du Rif nord-oriental. Mines Géologie 14:17–45

Jeannette A, Hamel C (1961) Présentation géologique et structurale du Rif Oriental. Mines Géologie 14:7–16

Kerchaoui S (1985) Etude géologique et structurale du massif des Beni Bou Ifrour (Rif oriental, Maroc). Unpublished Ph.D. Thesis, Université Paris XI, Paris, 193 pp

Kerchaoui S (1994) Pétrologie, géochimie et âges des roches magmatiques, leur place dans l'évolution structurale du massif des Beni Bou Ifrour et du Rif oriental, Maroc. Unpublished Ph.D. Thesis, Université Laval, Québec, Canada, 296 pp

Koděra P, Rankin AH, Lexa J (1998) Evolution of fluids responsible for iron skarn mineralisation: an example from the Vyhne-Klokoč deposit, western Carpathians, Slovakia. Mineral Petrol 64:119–147

Kwak TAP (1986) Fluid inclusions in skarns (carbonate replacement deposits). J Metamorph Geol 4:363–384

Kwak TAP (1994) Hydrothermal alteration in carbonate replacement deposits. Geol Assoc Canada, Short Course Notes 11:381–402

Kwak TAP, Tan TH (1981) The importance of $CaCl_2$ in fluid composition trends—evidence from the King Island (Dolphin) skarn deposit. Econ Geol 76:955–960

Lai J, Chi G, Peng S, Shao Y, Yang B (2007) Fluid evolution in the formation of the Fenghuangshan Cu-Fe-Au deposit, Tongling, Anhui, China. Econ Geol 102:949–970

Lebret N (2014) Contexte structural et métallogénique des skarns à magnetite des Beni Bou Ifrour (Rif Oriental, Maroc): apports à l'évolution géodynamique de la Méditerranée occidentale. Unpublished Ph.D. Thesis, Université d'Orléans, France, 477 pp

Liou JG (1973) Synthesis and stability relations of epidote $Ca_2Al_2FeSi_3O_{12}(OH)$. J Petrol 14:381–413

Meinert LD (1998) Skarns and skarn deposits. Geosci Canada 19:145–162

Naslund HR, Henriquez F, Nyström JO, Vivallo W, Dobbs FM (2002) Magnetic iron ores and associated mineralization: examples from the Chilean High Andes and Coastal Cordillera. In: Porter TM (ed) Hydrothermal iron oxide copper-gold & related deposits: a global perspective. Porter Geoscience Consultancy Publishing, Adelaide, vol 2, pp 207–228

Palinkaš SS, Palinkaš LA, Renac C, Spangenberg JE, Lüders V, Molnar F, Maliqi G (2013) Metallogenic model of the Trepcă Pb-Zn-Ag skarn deposit, Kosovo: evidence from fluid inclusions, rare earth elements, and stable isotope data. Econ Geol 108:135–162

Pan Y (1998) Scapolite in skarn deposits: petrological and geochemical significance. In: Lentz DR (ed) Mineralized intrusion-related skarn systems. Mineralogical Association of Canada, Short Course Series, vol 26, pp 169–209

Platt JP, Whitehouse MJ, Kelly SP, Carter A, Hollick L (2003) Simultaneous extension exhumation across the Alboran basin: implications for the causes of late orogenic extension. Geology 31:251–254

Rhoden HN, Ereno J (1962) Magnetite ores of northern Morocco. Inst Min Metall Trans 71:B629–B661

Richards JP (1995) Alkalic-type epithermal gold deposits—a review. In: Thompson JFH (ed) Magmas, fluids, and ore deposits. Mineralogical Association of Canada, short course series, vol 23, pp 367–400

Roedder E (1984) Fluid inclusions. Rev Mineral 12: 644

Shepherd TJ, Rankin AH, Alderton DHM (1985) A practical guide to fluid inclusion studies. Blackie and Son, London 235 pp

Sillitoe RH (1993) Epithermal models: genetic types, geometrical controls and shallow features. In: Kirkham RV, Sinclair WD, Thorpe RI, Duke JM

(eds) Mineral deposit modeling. Geological Association of Canada. Special paper, vol 40, pp 403–417

Soloviev SG (2011) Geology, mineralization, fluid inclusion characteristics of the Kensu W-Mo skarn and Mo-W-Cu-Au alkali porphyry deposit, Tien Shan, Kyrgyzstan. Econ Geol 106:193–222

Taylor HP Jr (1997) Oxygen and hydrogen isotope relationships in hydrothermal mineral deposits. In: Barnes HL (ed) Geochemistry of hydrothermal ore deposits. Wiley, New York, pp 229–302

Viland JC (1977) Les roches éruptives et métamorphiques associées, d'âge néogène, de la zone nord des Beni Bou Ifrour. Notes Mémoires Service Géologique Maroc 37(267):27–84

Zhu JJ, Hu R, Richards JR, Bi X, Zhong H (2015) Genesis and magmatic-hydrothermal evolution of the Yangla skarn Cu deposit, southwest China. Econ Geol 110:631–652

Part III
Hydrothermal Vein-Type Deposits

The Bou Azzer Co–Ni–Fe–As (±Au ± Ag) District of Central Anti-Atlas (Morocco): A Long-Lived Late Hercynian to Triassic Magmatic-Hydrothermal to Low-Sulphidation Epithermal System

Mohammed Bouabdellah, Lhou Maacha, Gilles Levresse and Omar Saddiqi

Abstract

The Neoproterozoic Bou Azzer Co–Ni–Fe–As(±Au ± Ag) district in the Central Anti-Atlas Mountains of southern Morocco hosts the only mine in the world where Co is produced as a primary commodity directly from Co- and As-bearing arsenide minerals. The district has a mean annual production of 100,000 t of ore at an average grade of ~1 % Co, 1 % Ni, 3–42 g/t Ag, and 3–4 g/t Au. Major orebodies are developed either within serpentinite or more importantly along the contact between serpentinite and quartz-diorite rocks. Field and textural relationships record three hydrothermal stages characterized by mineral assemblages of pre-arsenide auriferous stage I, (Co, Ni, Fe)-arsenide and sulpharsenide stage II, and sulphide-sulphosalt ± Au ± Ag epithermal stage III; one postore supergene stage IV is characterized by secondary Co minerals (erythrine, roselite,

M. Bouabdellah (✉)
Faculté des Sciences, Département de Géologie, Université Mohammed Premier, Avenue Mohammed VI, B.P. 717, 60000 Oujda, Morocco
e-mail: mbouabdellah2002@yahoo.fr

L. Maacha
Managem Group, Twin Center, Tour A, Angle Boulevards Zerktouni et Al Massira Al Khadra, B.P. 5199, 20000 Casablanca, Morocco

G. Levresse
Programa de Geofluidos, Centro de Geociencias UNAM-Campus Juriquilla, AP 1-253, CP 76230 Juriquilla, Querétaro, Mexico

O. Saddiqi
Laboratoire Géosciences, Faculté des Sciences, Université Hassan II Aîn Chock, B.P. 5366, 20100 Maârif, Casablanca, Morocco

M. Bouabdellah and J.F. Slack (eds.), *Mineral Deposits of North Africa*, Mineral Resource Reviews, DOI 10.1007/978-3-319-31733-5_8

talmessite). Ore mineralogy is dominated by diarsenide, triarsenide, and sulpharsenide minerals, accompanied by various generations of intergrown calcite, dolomite, and quartz. Gold- and silver-bearing assemblages mainly comprise native gold and electrum, polybasite, proustite, xanthoconite, argyrodite, stromeyerite, and freibergite. Similarity of structural orientations of the veins that formed during the three stages suggests a common mechanism of ore formation. Available radiometric dating shows highly discordant ages for the Bou Azzer Co–Ni–Fe–As(±Au ± Ag) deposits that range from Neoproterozoic to Late Triassic. A maximum age constraint indicates that all of the mineralized structures are younger than emplacement of the trachytic sills dated at ~530 Ma, thus precluding a Precambrian age for the mineralization. Fluid inclusion data indicate consistent trend towards lower temperatures and salinities with advancing paragenetic sequence. In this regard, calculated P-T trapping conditions decrease from 1.6 to >2 kbars and 320 to 400 °C during the early pre-arsenide auriferous stage I, to 880–1400 bars and <200 °C during the (Co, Ni, Fe)-arsenide and sulpharsenide stage II, and finally to pressures as low as ~650 bars and temperatures in the range of 150–200 °C during the sulphide-sulphosalt ± Au ± Ag epithermal stage III. Stable isotope compositions (i.e., O, H, S) are consistent with derivation of the mineralizing fluids either from magmatic, metamorphic, or meteoric sources or a mixture of all of these fluid sources. Magmatic and/or magmatic-hydrothermal models propose that crystallizing magmas provided the fluids, ore and gangue components, and thermal energy to drive fluid flow that carried and deposited the metals including gold. In both metamorphic and meteoric models, metals were derived from the serpentinites and enclosing metasedimentary rocks, transported to shallower levels, and then deposited along dilatant faults.

1 Introduction

Cobalt, a corrosion- and water-resistant, high-strength alloy, is mined from diverse types of mineral deposits including orthomagmatic sulphide deposits (e.g., Noril'sk, Russia; Sudbury, Canada; Lightfoot et al. 2001; Marakushev et al. 2002; Ripley et al. 2002), strata-bound deposits (e.g., Central African Copper belt of Democratic Republic Congo and Zambia; Smith 2001), lateritic deposits (New Caledonia, Cuba, Australia; Elias 2002; Jacques et al. 2002), volcanogenic sulphide deposits, and the so-called intriguing five-element (Ni–Co–Ag–As–Bi) hydrothermal vein-type deposits to which the Bou Azzer district belongs (Fig. 1). Due to its unique properties allowing its use in many industrial applications, the demand for cobalt is unlikely to decrease in the near future (Hawkins 2006). However, most cobalt is not produced directly from cobalt ores, but rather is recovered as a by-product from nickel and copper ores. The Bou Azzer district in the Central Anti-Atlas of Morocco (Figs. 1 and 2) hosts the only mine in the world where Co is produced as a primary commodity directly from Co- and As-bearing arsenide minerals.

Mined since antiquity and well-described in the literature (Leblanc 1975, and references herein), the Bou Azzer district has produced more than

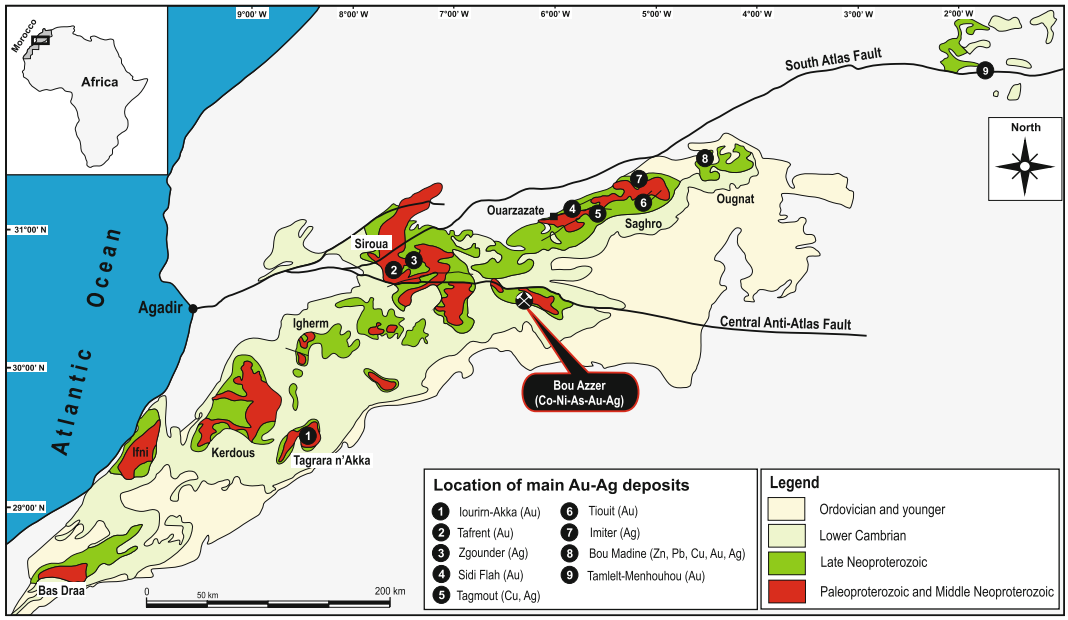

Fig. 1 Location of the Bou Azzer Co–As–Fe–Ni (±Ag ± Au) district with respect to the Anti-Atlas system and other nearby Au–Ag deposits. *Inset* shows location of Bou Azzer district with respect to the Anti-Atlas orogen and African continent

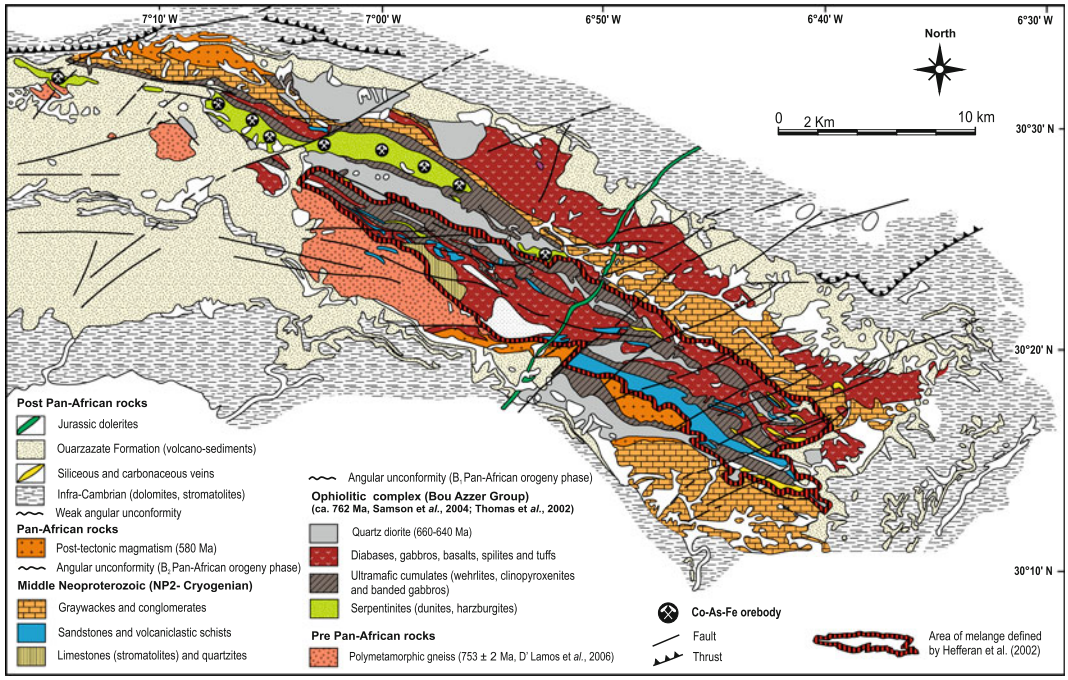

Fig. 2 Surface geological map of the Bou Azzer area showing regional geology, main lithologic-structural units of the Bou Azzer ophiolitic complex, major faults, and spatial distribution of main historically mined Co–As–Fe–Ni(±Ag ± Au) orebodies, projected to surface (adapted and modified after Bousquet et al. 2008)

55,000 t of cobalt (Leblanc and Billaud 1982) and contains more than one hundred Co–Ni–Fe-arsenide ± Au ± Ag orebodies distributed along Hercynian reactivated major Paleoproterozoic Eburnian (~2.1–2.0 Ga) and Neoproterozoic Pan-African (~560–550 Ma) faults, contributing as much as ~2 % of the world's cobalt production (U.S. Geological Survey 2013). In addition to Co, sub-economic gold and silver concentrations are also recovered as by products, with total production of these two metals ranging from 2 to 13 t (Leblanc and Billaud 1982; Buisson and Leblanc 1987). Mean annual production currently is about 100,000 t of ore at an average grade of ~1 % Co, 1 % Ni, and 3–4 g/t Au.

Despite its great economic importance coupled with numerous recent investigations of the district, there is still great debate about key issues related to the genesis of the Bou Azzer mineralization, such as sources of heat and metal components, origin of the ore fluids, mechanism (s) of ore deposition, and age of mineralization. The present contribution aims to review the published and unpublished literature, and provide a summary of these data and previous genetic models. Finally, we synthesize this information into a new model for the origin of the Bou Azzer mineralization, integrated into the most recent genetic framework for five-element (Ni–Co–Ag–As–Bi) hydrothermal vein-type deposits.

2 Economic and Historical Perspectives

Since the discovery of arsenide-rich outcrops in the 1920s, the Bou Azzer district has grown to become one of the largest Co–Ni–Fe–As (±Au ± Ag) mining districts worldwide, and more importantly the only mine known where Co is produced as a primary commodity. This discovery dates back to medieval times, during which the indigenous Berber population identified the benefits of secondary Co-arsenide minerals (e.g., erythrite) as an insecticide and mouse poison. In addition to Co, Ni, and As, exploration during the 20th Century has led to the discovery of accessory gold and silver as byproducts of mining the Co arsenide and sulphide ores (Jouravsky 1949, 1952; Buisson and Leblanc 1987; and references therein).

\After an initial stage of artisanal production (1929–1932) from surface outcrops, industrial exploitation of the arsenide-bearing orebodies started in 1934 under the auspices of Société Minière de Bou Gaffer (SMAG) that focused

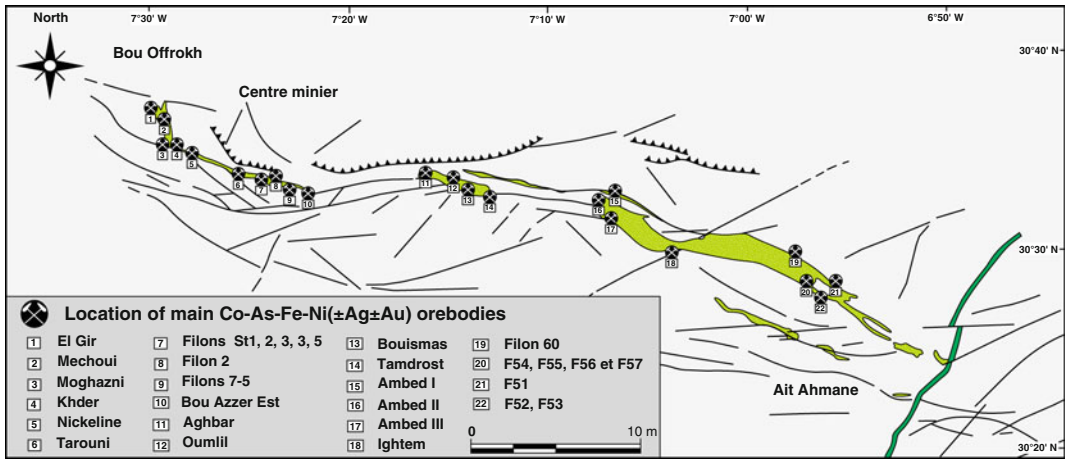

Fig. 3 Distribution of major Co–As–Fe–Ni(± Ag ± Au) orebodies (previously and presently mined), projected to surface and their relationships to serpentinite occurrences (shown in *green*) and major fault systems. Note that serpentinite occurrences and related orebodies are elongate parallel to the main WNW-ESE-trending fault system, and are cut by Jurassic mafic dike swarms. Numbers 1–22 refer to locations of orebodies mentioned in text

mining activities on veins 7, 5, and 2 of the Central Bou Azzer orebodies and the Ightem orebodies to the east (Fig. 3). Following a short interruption due to World War II, the Penàrroya mining society, encouraged by high prices of Co at that time, purchased the assets and implemented a new treatment plant. As a result, an extensive exploration for new deposits was launched based on the assumption that Co–Ni mineralization is hydrothermal in origin and Hercynian in age. From 1958 onward, mining in the district shifted to Compagnie de Tifnoute Tirhanimine (CTT), a subsidiary of Managemgroup, which is the current operator in charge of the Bou Azzer mines.

The major period of cobalt mining ended with closure of underground 7 and 5 mines in 1967 and the Aghbar mine in 1970 due to depleted reserves and decreased ore grades with depth. From 1969 to 1971, the Russian consulting company Technoexport carried out a major exploration program along strike from the Bou Azzer district, resulting in the discoveries of the Taghouni, Bou Azzer East, and Tamdrost orebodies (Fig. 3). Concomitantly, geologic investigations conducted by the French Bureau de Recherches Géologiques et Minières (BRGM) found additional orebodies, namely Bouismas and Aït Ahmane. Following a brief interruption in 1983, continued exploration of the underexplored areas discovered in 1987 the concealed Mechoui orebody (Fig. 3). As a consequence, two new hydrometallurgical plants were built in 1995 and 1998 for the treatment of Co-oxides and arsenides. A third new plant has been installed for the treatment of cobalt derivates resulting in high added values of precious metals (Ag, Au). Current annual production in the district is 2,500 t of Co, 10,000 t of As, 300 t of Ni, and 250 kg of Au (Managemgroup unpublished data).

3 District Geological Setting

The Bou Azzer Co–Ni–Fe–As(±Au ± Ag) mining district occurs within the saddle-shaped Bou Azzer-El Graara Precambrian inlier of the central part of the Pan-African (ca. 750–540 Ma) Anti-Atlas orogen (Figs. 2 and 3). The district has been extensively studied over the last few decades resulting in the release of a wealth of geological, mineralogical, and geochemical data, in hundreds of research papers, theses, geological maps at different scales, and unpublished mining company reports. The regional and local geological descriptions presented here draw extensively from the pioneering work of Leblanc (1975, 1986) together with recent studies of Hefferan et al. (2000), Thomas et al. (2002, 2004), Walsh et al. (2002), Inglis et al. (2004, 2005), Gasquet et al. (2005), Soulaimani et al. (2006), El Hadi et al. (2010), and Blein et al. (2014). Accordingly, only a summary of major conclusions relevant to the present synthesis is given below.

Bou Azzer stratigraphy (Fig. 2) comprises a complex succession of Proterozoic crustal rock units exposed within a series of tectonic blocks surrounded by late Ediacaran to Cambrian rocks (Leblanc 1975; Saquaque et al. 1989). These tectonic blocks have been interpreted to represent dismembered parts of a subduction zone (Leblanc 1981; Saquaque et al. 1989; Hefferan et al. 2002) where a volcanic arc, ophiolite, and continental platform have been distinguished (Saquaque et al. 1989). The end of subduction and the beginning of obduction of the Bou Azzer ophiolite onto the northern margin of the West African craton occurred at 655–635 Ma (El Hadi et al. 2010) in response to oblique sinistral transpression along a northward-dipping subduction zone (Saquaque et al. 1989; Hefferan et al. 2000). The oldest rocks exposed in the Bou Azzer district consist of Neoproterozoic orthogneiss, metagabbro, and schist (i.e., Oumlill granite dated at 741 ± 9 Ma; El Hadi et al. 2010), unconformably overlain by the Cryogenic Bou Azzer Group.

The 60-km-long, 4- to 5-km-thick Bou Azzer ophiolite (Figs. 2 and 3) consists of a succession of mafic-ultramafic bodies, structurally from the base to the top, of serpentinized, chromite-bearing harburgites and dunites, layered gabbros dated at 697 ± 8 Ma (SHRIMP U–Pb on zircon; El Hadi et al. 2010), sheeted dike swarms, and submarine pillow lavas (spilite and keratophyre) locally

capped by pelitic schist, red chert, sandstone, and limestone. Several syn- to post-kinematic, high-K calc-alkaline, subduction-related diorite-tonalite stocks (655–635 ± 5 Ma) intruded the ophiolitic sequence at the end of subduction and the beginning of exhumation-obduction (Inglis et al. 2005; El Hadi et al. 2010). To the north of the Bou Azzer district, the mafic-ultramafic succession is bounded by a tectonic sliver <300 m wide composed of a blueschist-facies metamorphic assemblage suggesting maximum pressure conditions of 5–6 kbar and temperatures of 400–600 °C (Hefferan et al. 2002; Bousquet et al. 2008). Younger, post-collisional igneous rocks including the Bleida granodiorite dated at 579.4 ± 1.2 and 578.5 ± 1.2 Ma (U–Pb on zircon; Inglis et al. 2004) constrain the cessation of principal Pan-African deformation to before ca. 580 Ma.

The ophiolitic complex is unconformably overlain by weakly metamorphosed, late-orogenic molasses of the Tiddline Formation made of a succession of siltstone and conglomerate. These strata are interpreted to have been deposited in small syn-orogenic basins (Hefferan et al. 1992), which in turn are successively overlain by a thick sequence of late Neoproterozoic (586 ± 20 to 563 ± 10 Ma; U/Pb on monozircon: Mifdal and Peucat 1985) dacitic to rhyolitic ignimbrites and andesitic tuffs intercalated with red beds. Stratigraphically above this sequence are thick (~1000 m) late Ediacaran to Early Cambrian shallow marine carbonates and purple shales with intercalations of siltstones, evaporates, and graywackes, intruded by rare sills of syenite and trachyte dated at 533 ± 2 Ma (U/Pb on monozircon: Levresse 2001; Gasquet et al. 2005; D'Lemos et al. 2006).

The tectonic evolution of the Bou Azzer district is complex due to the superposition of tectonic structures developed both in response to ophiolite emplacement and a late-collisional stage of Hercynian age. Resulting structures are represented by SW-directed thrusts and crustal stacks, folds and associated cleavage, and greenschist facies metamorphism dated at ~663–650 Ma (Thomas et al. 2002; Inglis et al. 2004). Reactivation of the major Eburnian and Pan-African faults during the Hercynian orogeny triggered the injection of felsic dike swarms at 470–400 Ma (Huch 1988), and the development of two hydrothermal stages at 356 ± 20 to 300 Ma (Leblanc 1975; Levresse 2001) and 240 ± 10 to 218 ± 8 Ma (i.e., Late Triassic, Ledent 1960; Levresse 2001). The Hercynian deformation events resulted in uplift of the Precambrian basement, development of regional-scale doming and basin topography (Soulaimani et al. 1997; Caritg et al. 2004), and injection of serpentinites within the overlying strata (Leblanc 1975). However, the timing of this Hercynian deformation remains poorly constrained.

4 Mineralogy, Alteration, Textures, and Paragenesis

4.1 Arsenide Mineralization

Over 100 Co–Ni–Fe-arsenide(±Au ± Ag) deposits of different sizes and morphologies are scattered through the WNW-ESE-trending Neoproterozoic Bou Azzer ophiolite, all of which are closely related spatially to serpentinite outcrops and adjacent quartz-diorite rocks. Twelve orebodies have been and/or are being mined underground. From east to the west, these are the Filon 7/5, Aghbar, Bouismass, Bou-Azzer Est, Tarouni, Agoudal, Agoudal Est, Ait Ahman, Filon II, Oumlil, Tamdrost, and Lakhder orebodies (Fig. 3). Mineralization in the district has been exploited to a depth of >300 m.

The Co–Ni–Fe-arsenide(±Au ± Ag) deposits are structurally controlled and consist of a complex system of trans-tensional, sub-vertical fault-jogs, flame-shaped orebodies, flat lensoidal and pocket-like masses, lodes, veins, veinlets, cemented breccias within veins, and fillings of en echelon tension gashes (Fig. 4). Locally, Co–Ni–Fe-arsenide mineralization may extend into serpentinite and quartz-diorite wall rocks for 10 m or more.

The bulk of the ores straddle the serpentinite-wall rock contacts. Larger, high-grade orebodies occur where major WNW- and ENE-trending faults intersect each other (i.e., "noeuds tectoniques"), and where veins are

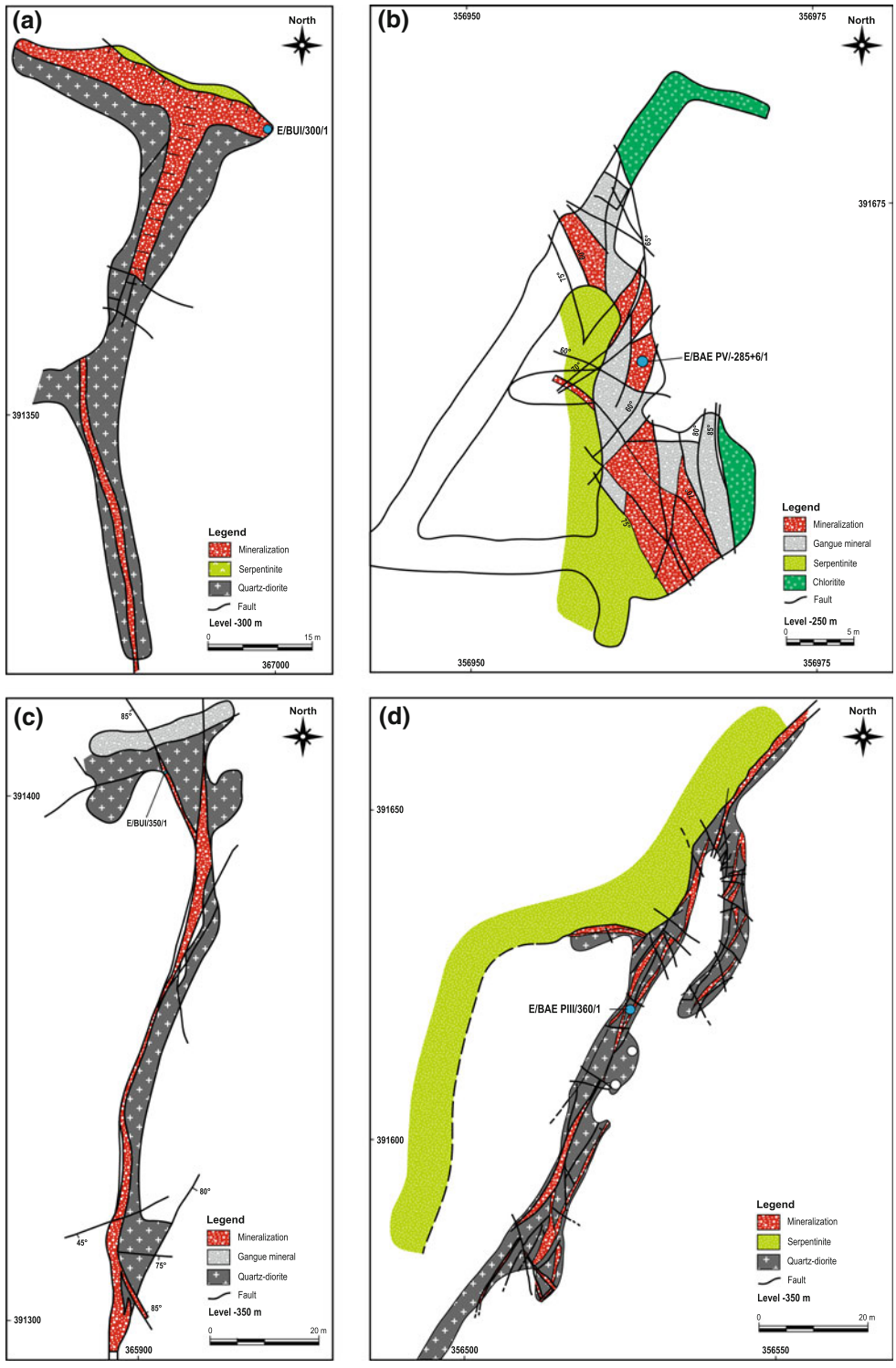

Fig. 4 Underground vertical geological cross sections through selected orebodies. **a**, **c** Bouismas orebody, levels −300 and −350 m. **b**, **d**. Bou Azzer East orebody, levels −250 and −350 m. Shown are host-rock lithology, dominant alteration styles, major faults, and mode of occurrence of Co–As–Fe–Ni(±Ag ± Au) mineralization with emphasis on relationships between quartz-diorite intrusions and spatially associated serpentinites

deflected or branch. Texturally, the veins display comb, cockade, laminated, breccia and crack and seal textures, consistent with frequent reopening and filling of open structures. In fact, the presence of crack-and-seal textures indicates that the trans-tensional veins formed as a result of many episodes of brecciation, fluid infiltration, and mineral precipitation. Replacement textures are rare.

Wall-rock alteration related to the arsenide mineralization is confined to the mineralized structures, and forms narrow (several centimeters to a meter or more in width) halos and stringers composed of strong chloritic, silicic, carbonate, and to a lesser extent, talc-rich assemblages surrounding the veins. Ore mineralogy is dominated by diarsenide, triarsenide, and sulpharsenide minerals accompanied by various generations of intergrown calcite, dolomite, and quartz.

4.2 Silver-Rich Mineralization

The silver-rich mineralization occurs along rodingitized tectonic contacts between serpentinite and quartz-diorite within the Filon 7-5, Oumlil, Aghbar, and Bouismas Co-bearing orebodies (Leblanc and Lbouabi 1988; and this study). Estimated average silver grades for mineralized rocks in the district, based on a new compilation here, are 0.05 to 45.15 g/t Ag, whereas average grades in ore range from 12.96 to 47.79 g/t Ag (Table 1). Calculated average grades show large variations among deposits (3.10–42.5 g/t) and even within a single deposit. The highest grades are recorded within the F7 vein (42.5 g/t Ag), Aghbar (30.01 g/t Ag), Oumlil (26.98 g/t Ag), and Bouismas (22.00 g/t Ag) orebodies (Table 1).

Mineralized structures are confined within a 4- to 5-m-thick mylonitic zone averaging 500–600 g/Ag (Leblanc and Lbouabi 1988; Essarraj et al. 2005), and consist of a branching network of crosscutting, en echelon, mm- to cm-scale veinlets. In addition to native silver containing up to 10 wt% Hg, Ag-bearing minerals that are intimately intergrown with sulphides, are represented by the sulphosalts polybasite, proustite, xanthoconite, argyrodite, stromeyerite, and freibergite. Sulphide minerals include chalcopyrite, chalcocite, bornite, digenite, molybdenite, sphalerite, and galena, locally accompanied by safflorite, löellingite, niccolite, brannerite, and gold (Jouravsky 1949 and references herein). Wall-rock alteration includes choritization, carbonatation, and epidotization. Significantly, the mineralized structures are spatially associated with strong K–(Na) metasomatism resulting in the development of adularia-albite veins.

4.3 Gold Mineralization

Gold in the district was first recognized by Jouravsky (1948) who described the occurrence of fine-grained (10–30 μm) inclusions in quartz.

Table 1 Summary of updated Au and Ag grades from the main orebodies of the polymetallic Bou Azzer Co–As–Fe–Ni(±Ag ± Au) district

District sector		Western sector			Central sector			Eastern sector		
Orebody		F7	Bou Azzer East	Tarouni	Oumlil	Aghbar	Bouismas	F51	F53	Agoudal
Au grade (g/t)	Orebody scale	3.42	8.47	5.55	8.67	4.76	7.69	12.1	2.16	5.58
	District scale	Au bulk grade: 0.02–12.1 g/t; Au grade in the ore: 2.87–48.70 g/t								
Ag grade (g/t)	Orebody scale	42.5	3.18	3.10	26.98	30.01	22.00	7.85	4.34	15.51
	District scale	Ag bulk grade: 0.05–45.15 g/t; Ag grade in the ore: 12.96–47.79 g/t								

Subsequently, a major gold rush occurred resulting in the discovery of new gold occurrences (Leblanc 1986; En-Naciri 1995a, b; El Ghorfi et al. 2009; this study). Most early mineralogical studies focused on Co ore (i.e., skutterudite) as the exclusive host for gold in the Bou Azzer district. In this respect, Leblanc (1986) and Buisson and Leblanc (1987) showed that gold contents in Co ore are randomly distributed, ranging from 1 to 100 g/t Au, with the highest grades (up to 100 g/t Au) contained in the skutterudite lattice. More importantly, En-Naciri et al. (1996) demonstrated that native gold is preferentially associated with skutterudite grains having [Ni/(Co + Fe + Ni)] ratios of 0.01–0.14; grains with higher [Ni/(Co + Fe + Ni)] ratios (>0.16) lack gold inclusions.

Contrary to the predictions of previous workers (Jouravsky 1948, 1952; Leblanc 1986; Buisson and Leblanc 1987; En-Naciri 1995a, b) who highlighted the exclusive relationship between gold and skutterudite, our mineralogical observations indicate that gold is widely distributed throughout the district and occurs in most of the mined orebodies, except Tarouni and Agoudal where its presence has not yet been detected. In addition to microscopic ("invisible") gold, visible free gold has been observed in the Ait Ahmane (F51 and F53 structures), Bou Azzer East, Aghbar, Oumlil, and Bouismas orebodies.

Estimated bulk gold grades for the Bou Azzer district, presented here for the first time, range from 0.02 to 12.1 g/t Au. Average grades in ore range from 2.87 to 48.70 g/t. Individual contributions of the major orebodies are reported in Table 1. The estimated grades vary greatly from deposit to deposit (2.16–12.1 g/t Au) and even within a single deposit. The highest gold grades are confined to the F51 (12.1 g/t Au), Oumlil (8.7 g/t Au), Bou Azzer East (8.5 g/t Au), and Bouismas (7.7 g/t Au) orebodies (Fig. 2). Most orebodies have less Au than Ag, with Au/Ag ratios ranging from 0.1 to 0.5. Conversely, the Bou Azzer East, Tarouni, and F51 vein orebodies have high Au/Ag ratios up to 2.7.

Gold occurs in carbonate-rich, quartz-arsenide-sulphide veins and proximal serpentinite wall rocks, and forms either submicroscopic inclusions within a variety of host minerals including chalcopyrite, molybdenite, chalcocite, cobaltite, safflorite, rammelsbergite, gersdorffite, niccolite, and annabergite, or visible "free" grains that infill fractures in sulphides (Fig. 5). Gold is also found along grain boundaries of adjacent sulphide minerals. Sulphide and native gold appear to be in textural equilibrium with the silicate gangue and other vein minerals with which they are intergrown.

Textural relationships suggest that gold deposition occurred during two major episodes, the earlier being of limited economic interest that predated the deposition of arsenide ore. Paragenetically late gold is intimately related, in time and space, to sulphides and sulphosalts. Microscopic observations show a positive correlation between Au grade and the abundance of sulphides. Metallurgical tests support of this observation, revealing that most of the recovered gold is bound in the sulphide minerals (Managemgroup confidential report).

Electron microprobe analyses performed on a selection of 16 Au-bearing minerals from the major mined orebodies of the district show highly variable Au and Ag contents from 6.14 to 89.04 wt%, and 8.04 to 80.16 wt%, respectively. Mercury is present in appreciable amounts, locally reaching up to 6.71 wt% due to inclusions of Au–Ag–Hg amalgam. However, Pd is present only at very low concentrations (0.01 ppm), close to the analytical limit detection.

The fineness of the analyzed grains, expressed as [Au/(Au + Ag)] × 1000, ranges from 72 to 898 allowing the distinction between three Au-bearing mineral species, specifically electrum, kustelite (Ag–Au alloy grading up 10–30 % Au), and native gold.

4.4 Paragenetic Sequence

Although no consistent paragenetic sequence can be defined owing to multiple overlapping pulses of mineralization, the sequence of mineral deposition shows three main stages of ore deposition (En-Naciri et al. 1997; Ahmed et al. 2009; Gervilla et al. 2012, this study). These three stages (Fig. 6) are distinguished on the basis of dominant

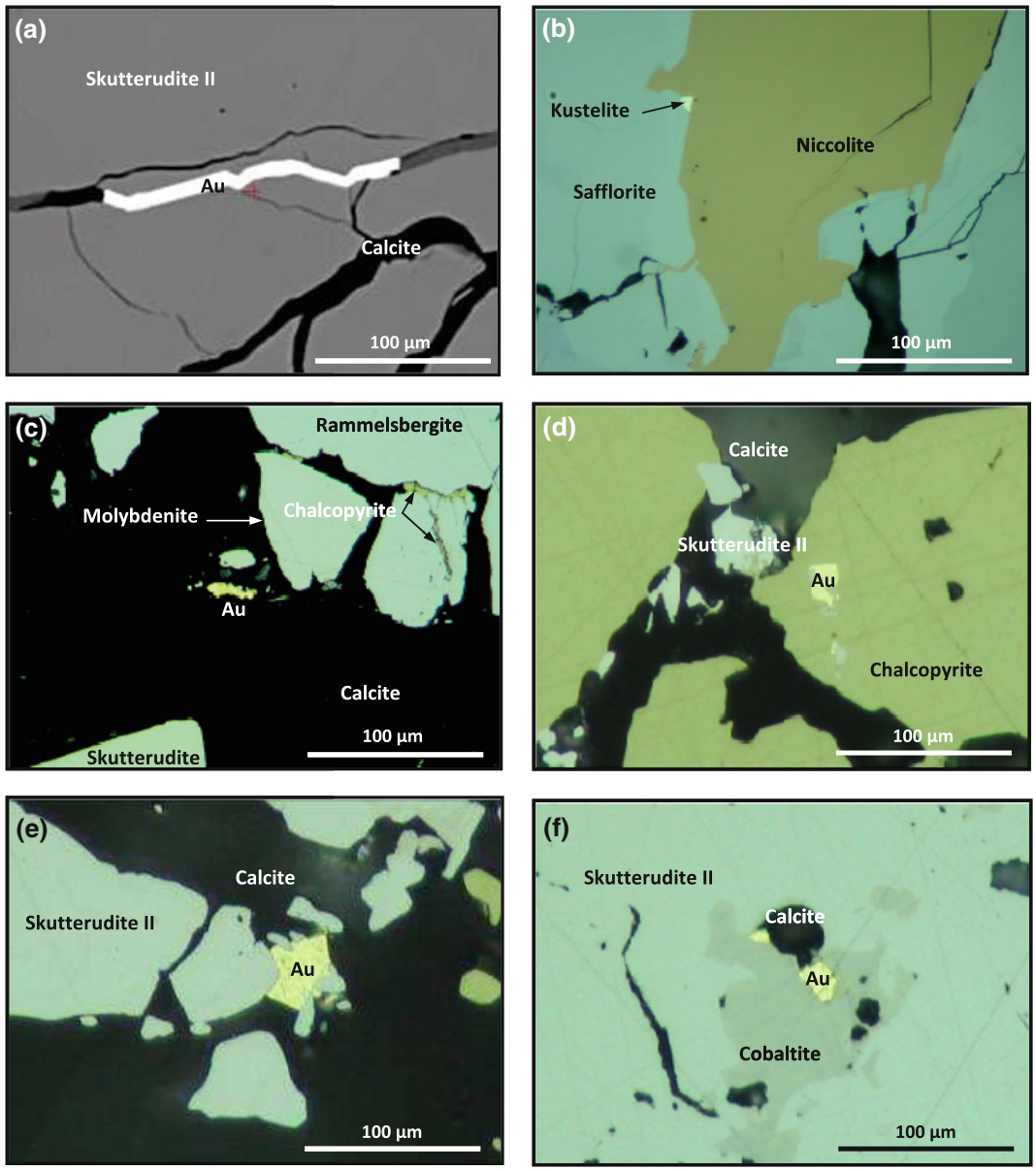

Fig. 5 Selected microphotographs illustrating textural features of gold-bearing assemblage (stage III) of Bou Azzer Co–As–Fe–Ni(±Ag ± Au) orebodies. **a** Gold (Au, *white*) filling cracks in strongly fractured skutterudite II. **b** Small kustelite grain (Au–Ag alloy, *yellowest*) at grain boundaries between safflorite and niccolite. **c** Breccia-textured ore with fragments of rammelsbergite, molybdenite, and skutterudite II cemented by calcite, which contains a gold inclusion. Note that chalcopyrite fills cracks in strongly fractured molybdenite. **d** Gold inclusion in chalcopyrite, associated with skutterudite II and calcite. **e** Brecciated skutterudite II cemented by calcite with gold grain intimately related to clasts of skutterudite II. **f** Native gold closely associated with skutterudite II at grain boundaries between cobaltite and calcite (**a** scanning electron microscope-backscattered electron image; **b**, **c**, **d**, **e**, **f**, plane-polarized reflected light microscope images)

minerals, grain size, and textural relationships; within each stage, several sub-stages are distinguished. The three mineralizing stages are separated by episodes of intense shearing and brecciation. Transitions between these episodes are marked by the overlap of mineral assemblages

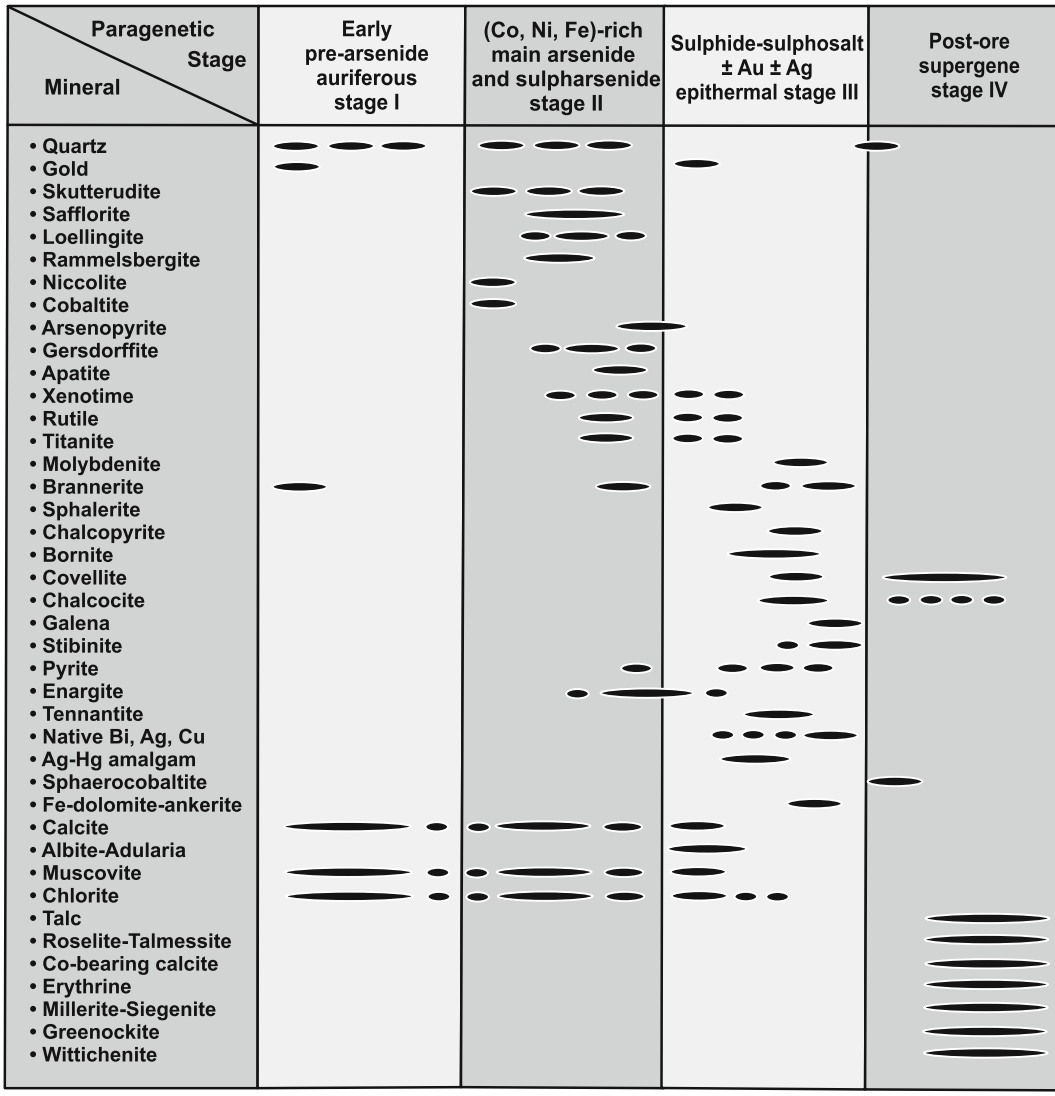

Fig. 6 Idealized paragenetic sequence for polymetallic Bou Azzer Co–As–Fe–Ni(±Ag ± Au) district

and a progressive decrease in As, coupled with a concomitant increase in S and Fe in later fluids (Ahmed et al. 2009; Gervilla et al. 2012). Such prograde geochemical trend may reflect the temporal evolution of a single, long-lived multistage hydrothermal system rather than the involvement of three chronologically separate hydrothermal events.

The early pre-arseniade auriferous stage comprises quartz, calcite, brannerite-1, and native gold. The subsequent stage (i.e., main Co–Ni–Fe-arsenide and sulpharsenide stage II), which accounts for most of the exploited ore at Bou Azzer district, consists of sequentially crystallized diarsenide (i.e., safflorite, löellingite, and rammelsbergite together with a complex series of rammelsbergite-safflorite-löllingite solid solutions), triarsenide (Ni–Fe-rich skutterudite), and sulpharsenide (arsenopyrite, gersdorffite) assemblages (En-Naciri et al. 1996; Dolansky 2007; Ahmed et al. 2009; Gervilla et al. 2012) that are spatially associated with distinctive, strong chloritic and locally silicic alteration envelopes. Conversely, stage III contains a

sulphide-sulphosalt ± Au ± Ag epithermal assemblage that occurs in calcite or quartz veins, or as late fillings within stage I and II veins. The ore mineralogy consists of sphalerite, galena, chalcopyrite, bornite, chalcocite, pyrite, pyrrhotite, molybdenite, and freibergite within a gangue of adularia and albite. Gold- and silver-bearing assemblages are dominated by native gold and electrum, and polybasite, proustite, xanthoconite, argyrodite, stromeyerite, and freibergite, respectively. Similarity of the structural orientation of the veins that formed during the three stages suggests a common mechanism of ore formation. The zinc, lead, and carbonate contents of the ore zones, together with the presence of adularia and Fe-poor nature of the sphalerite, combine to suggest that this late-stage mineralization has an affinity with low-sulphidation epithermal deposits (Sillitoe and Hedenquist 2003). Silicates (quartz, chlorite, muscovite, sodic and potassic feldspars) and carbonates (Fe-dolomite, ankerite, calcite, sphaerocobaltite ($CoCO_3$)) are by far the most dominant gangue minerals, followed by minor oxides (rutile, brannerite) and sparse phosphates (apatite, xenotime).

In addition to the three hypogene stages, a fourth supergene stage is well developed in the uppermost sulphide-rich part of the mineralized structures where oxidized ore zones extend as deep as 400 m. The resulting paragenesis consists of a series of secondary rare arsenides making the Bou Azzer district a unique and globally famous locality for some exotic mineral species like roselite, talmessite, and Co-bearing calcite.

4.5 Age of Mineralization

Numerous high-resolution isotopic decay systems (U/Pb, Pb–Pb, $^{40}Ar/^{39}Ar$, Re–Os, Sm–Nd) have been used to determine the timing of Bou Azzer mineralization, and to understand the duration and frequency of mineralizing events (Ledent 1960; En-Naciri et al. 1996, 1997; Levresse 2001; Dolansky 2007; Oberthür et al. 2009). However, the calculated radiometric ages are highly discordant and therefore not straight forward to interpret owing to the superimposition of several hydrothermal events. Overall, the obtained data yield ages from ca. 680 Ma synchronous of major metamorphic stages related to the Pan-African orogeny (Leblanc and Lbouabi 1988) to ca. 215 Ma (Ledent 1960; En-Naciri et al. 1996, 1997; Levresse 2001; Dolansky 2007; Oberthür et al. 2009), and therefore are broadly bracketed between the Neoproterozoic and Late Triassic. An even younger post-Triassic age has been proposed by Essarraj et al. (2005) based on the interpretation of chlorinity, cation (Na/Ca ca. 2.2) and halogen ratios (Cl/Br from 300 to 360).

Early introduction of mineralization during the Pan-African stage seems, however, inconsistent with field and textural relationships that show that ore infillings were not affected by late Pan-African deformation and subsequent metamorphism. More importantly, a maximum age constraint on the timing of mineralization in the district comes from crosscutting and offsetting relationships that indicate that all of the mineralized structures irrespective of their paragenetic position are younger than the emplacement of the trachytic sills dated at ~530 Ma (533 ± 2 Ma, Levresse 2001; 531±5 Ma, Gasquet et al. 2005). These ages thus preclude a Precambrian age for the Bou Azzer Co–Ni–Fe–As(± Au ± Ag) mineralization. In a follow-up study, Dolansky (2007) reported Re–Os brannerite ages of 383 ± 7 to 355 ± 10 Ma. More recently, Oberthür et al. (2009) presented brannerite U–Pb and carbonate Sm–Nd ages of 308 ± 31 Ma and 310 ± 5 Ma; respectively. Re–Os and Sm–Nd present comparable set of age determined directly on the mineralization which seems to be a more realistic age of the mineralization.

Owing to the fact that brannerite at Bou Azzer is intimately intergrown with arsenide minerals, it is reasonable to conclude that the brannerite formed synchronously with primary mineralization. Based on these textural relationships, the Re–Os data of Dolansky (2007), together with the U–Pb and Sm–Nd ages determined by Oberthür et al. (2009), suggest that hydrothermal activity and associated Co–Ni–Fe–As(±Au ± Ag) mineralization occurred between 380 and 310 Ma (i.e., end of the Hercynian orogeny and onset of

Central Atlantic rifting during the Permian-Triassic) consistent with radiometric age data of Levresse et al. (2001), Gasquet et al. (2004), and Pelleter et al. (2007). The younger ages of 240 ± 10 Ma (Ledent 1960) and 218 ± 8 Ma (Levresse 2001) may correspond to deposition of the paragenetically late, low-temperature sulphide-sulphosalt(±Au ± Ag) mineralization that occurs throughout the Central and Eastern Anti-Atlas (i.e., Imiter and Bou Madine deposits; Fig. 1). Interestingly, the inferred deposition of this type of mineralization fits within the time span of hydrothermal events dated at 250–210 Ma (Ghorbal et al. 2008; Saddiqi et al. 2009; Barbero et al. 2011) that affected most Hercynide domains of North Africa (Valenza et al. 2000; Cheilletz et al. 2010) and Western Europe (Johnson et al. 1996; Sánchez et al. 2006).

5 Fluid Inclusion Studies

Microthermometric measurements of fluid inclusions in ore-related quartz from the three main ore stages recognized throughout the district display wide ranges in homogenization temperatures and salinities, with T_h values from 190° to >400 °C and salinities from ca. 36 to ~51 wt percent NaCl + $CaCl_2$ equiv (Leblanc and Lbouabi 1988; En-Naciri 1995a, b; Lebedev et al. 1999; Essarraj et al. 2005; Dolansky 2007). The bulk composition of these highly saline fluids lies within a H_2O–NaCl–$CaCl_2$ ± $MgCl_2$ ± $CaBr_2$ ± CH_4 ± N_2 ± CO_2 ± ethane system (Dolansky 2007, and references therein), and is similar to that reported for Co- and As-rich vein and stratabound deposits worldwide (Marshall et al. 1993). Trapped solids include, in addition to halite (the sole recognized salt daughter mineral), sericite, phengite, and feldspars (En-Naciri 1995a, b; Robert 2005), molybdenite (Dolansky 2007), and barite (Lebedev et al. 1999).

A consistent trend is apparent towards lower temperatures and salinities with advancing paragenetic sequence (Dolansky 2007; present study). Indeed, fluid inclusions in paragenetically early quartz and calcite show significantly higher temperatures and salinities than those related to paragenetically younger stages. In this context, microthermometric measurements indicate that the early mineralizing fluids had mean temperatures of 320–400 °C and were dominantly NaCl-rich brines with total salinities of 43.5 to 52.5 wt% NaCl + $CaCl_2$ equiv.; fluids related to the succeeding main-stage Co–Ni–Fe arsenide mineralization homogenized at lower temperatures and salinities but were increasingly Ca-rich (36 to 45 wt% NaCl + $CaCl_2$ equiv.). Conversely, fluids from the latest stage (III) exhibit lower temperatures of 171–194 °C, and are more Ca-rich than paragenetically earlier fluids (total salinities of 39–40 wt% NaCl + $CaCl_2$ equiv., with 17.5–19.1 wt% NaCl, and 20.9–21.5 wt% $CaCl_2$ equiv.; Dolansky 2007). The fluid compositions evolved by a relative decrease in Na^+ and accompanying increase in Ca^{2+} with mineral deposition over time. Interestingly, calculated P-T trapping conditions decrease also from 1.6 to >2 kbars and 320–400 °C during the early stage, to 880–1400 bars and <200 °C during the stage II Co–Ni–Fe-arsenide mineralization, and finally to pressures as low as ~650 bars and temperatures in the range of 150–200 °C during stage III sulphide-sulphosalt Ag- and Au-rich sulphide-sulphosalt mineralization.

6 Isotope Geochemistry

Isotopic investigations, particularly the stable isotopes of O, H, and S, have been critically important in constraining the fluid sources and mechanism(s) of ore deposition in the Bou Azzer district.

Quartz and chlorite separates exhibit $\delta^{18}O$ and δD values that range from 11.5 to 17.0 ‰ and −62 to −30 ‰, respectively, consistent with derivation of the fluids from a primary magmatic source for the hydrothermal fluids (Dolansky 2007). Moreover, sulphur isotope compositions determined on a variety of sulphide minerals, mainly from sulphide-sulphosalt-rich stage III including pyrite, chalcopyrite, and sphalerite, display highly variable $\delta^{34}S$ values of −32.2 to 2.8 ‰ with a prominent peak at ca. 3 ‰ (Maacha et al. 1998; Levresse 2001; Dolansky 2007).

7 Genetic Model and Conclusions

Despite the great number of fluid inclusion and geochemical investigations carried out on the Bou Azzer deposits, several critical issues remain highly controversial including the source(s) of heat, ore fluids, cobalt, arsenic, and other components of the ore-forming system such as Cl and S, physicochemical controls on ore mineral deposition, and more importantly the age of mineralization.

Three conflicting genetic models have advocated the involvement of magmatic, metamorphic, or deeply circulating meteoric waters (En-Naciri et al. 1996; Leblanc and Lbouabi 1988; Essarraj et al. 2005; Dolansky 2007). Magmatic and/or magmatic-hydrothermal models propose that crystallizing magmas provided the fluids, ore and gangue components, and thermal energy to drive fluid flow that carried and deposited the metals including gold. In both metamorphic and meteoric models, metals were derived from the serpentinites and enclosing metasedimentary rocks, transported to shallower levels, and then deposited along dilatant faults.

Based on mineralogical observations and textural relationships, the paleohydrothermal history of the Bou Azzer ore-forming system comprised three main episodes, all of which were probably linked to the temporal evolution of the same, protracted, multiphase hydrothermal system that operated during a ~140 Ma time span from 380–240 Ma (Ledent 1960; En-Naciri et al. 1996, 1997; Levresse 2001; Dolansky 2007; Oberthür et al. 2009). Chronologic steps in the proposed paleohydrothermal evolution of the district are based on the distinct mineralogical and paragenetic stages shown in Fig. 6.

The first of these three episodes (stage I) was characterized by the formation of pre-arsenide auriferous quartz-carbonate veins and veinlets. Resulting structures are narrow, discontinuous, and invariably sealed, suggesting lithostatic pressures (Wagner et al. 2009). Microthermometric measurements show that the hydrothermal fluid responsible for this early gold-bearing stage corresponds to hot (320 to >400 °C), hypersaline (43.5–52.5 wt% NaCl + $CaCl_2$ equiv.) brines that were trapped at pressures of 1.6 to more than 2 kbars.

The subsequent main-stage arsenide ore (stage II) is by far the predominant mineralization style and economically the most important. It consists of dense, open-space structures, mostly veins, veinlets, and en echelon tension gash fillings, with ubiquitous vugs, all of which are indicative of hydrostatic conditions. Evidence for multiple reopenings of the veins suggests that the pressure shifted from lithostatic to hydrostatic conditions during ore deposition. Fluid inclusion data indicate that, relative to stage I, the circulating hydrothermal fluids homogenized at lower temperatures and lower salinities but were increasingly Ca-rich (36–45 wt% NaCl + $CaCl_2$ equiv.).

During the late sulphide-sulphosalt stage to which we link the Ag–Au mineralization (En-Naciri et al. 1996; Essarraj et al. 2005; El Ghorfi et al. 2006), the temperature and salinity ranges decreased to 171–194 °C and 39–40 wt% NaCl + $CaCl_2$ equiv., with 17.5–19.1 wt% NaCl, and 20.9–21.5 wt% $CaCl_2$ equiv., respectively (Dolansky 2007). Pressures were as low as ~650 bars, suggesting epithermal conditions.

Overall, fluid inclusion data document a systematic trend of decreasing temperatures and related salinities with advancing paragenetic sequence from early to late stages. More importantly, fluid compositions evolved by a relative decrease in Na^+ and a concomitant increase in Ca^{2+} over time. These systematic variations in temperature, salinity, and NaCl/(NaCl + $CaCl_2$) ratios are interpreted to reflect, in addition to differences in fluid sources, progressive and extensive interaction with evolved meteoric waters in a shallow hydrothermal system. The origin of the $CaCl_2$-rich fluid inclusions (up to 22 % in late stage; Dolansky 2007) remains the subject of ongoing debate, because Ca-rich fluids could be related to either sedimentary (Hunt et al. 2005) or igneous (Xue 2000) processes. In the case of Bou Azzer mineralization, $CaCl_2$-rich fluids may have evolved through extensive interaction of the hydrothermal fluids with serpentinite wall rocks.

The origin of the high salinities that characterize the Bou Azzer mineralizing fluids also

remains enigmatic and could be attributed to either upflow of boiling fluids or basinal brines, or mixtures of both. In this respect, calculated $\delta^{18}O_{fluid}$ and δD_{fluid} values of quartz and chlorite (Dolansky et al. 2007) plot within the range of $\delta^{18}O$ and δD values diagnostic of magmatic fluids (Taylor 1997). A contribution of metamorphic fluids remains possible though not confirmed yet.

The large spread in sulphur isotope data with $\delta^{34}S_{sulphide}$ values ranging from −32.3 to up to 10 ‰ are more difficult to interpret. Indeed, although the clustering of δ^{34} S values around 3 ‰ are consistent with sulphur being derived directly from a granitic magmatic source (e.g., Hoefs 2007) or through leaching of originally disseminated igneous sulphides, e.g., pyrite or pyrrhotite in volcanic or intrusive rocks, including serpentinites, the heavy and light signatures ($\delta^{34}S$ values up to 10 and −32.3 ‰; Dolansky 2007) could be interpreted as reflecting the involvement of an external sulphur source, such as biogenic sulphur, reduced seawater sulphate, and/or evaporite sulphate and/or W/R interaction, consistent with the highly saline Ca–Na-rich nature of the mineralizing fluids (Leblanc and Lbouabi 1988; En-Naciri 1995a, b; Lebedev et al. 1999; Essarraj et al. 2005; Dolansky 2007). Indeed, the relatively heavy $\delta^{34}S$ values (up to 10 ‰) indicate that the mineralizing fluids acquired some sulphur from evaporites along the fluid-flow path. Conversely, the low pyrite $\delta^{34}S$ values are interpreted to reflect biogenic reduction of seawater sulphate during early diagenesis. Interaction with more oxidized (higher f_{O2}) meteoric water may have caused exchange reactions, resulting in slightly higher $\delta^{34}S$ values (Figueiredo e Silva et al. 2013). The inverse trend of decreasing δD values with depth (Dolansky 2007) is interpreted to indicate greater contribution of cooler meteoric fluids during the later stages of hydrothermal activity.

Although the coexistence of primary fluid- and vapor-rich fluid inclusions could suggest that fluid boiling occurred in Bou Azzer district, the calculated chlorinity, cation (Na/Ca ratios ca. 2.2) and halogen ratios (Cl/Br ratios ranging from 300 to 360) favor, however, the involvement of deeply buried surface-evaporated mineralizing brines that exceeded halite saturation (Essarraj et al. 2005). Accordingly, the coexistence of liquid-vapor-halite cube and vapor-rich fluid inclusions is interpreted to represent two distinct fluids trapped synchronously during mineral deposition: a Na–Ca rich brine and a $CH_4 \pm N_2$-rich fluid.

Regionally, evaporite occurrences are recorded in late Proterozoic sequences (Chbani et al. 1999) and more importantly in the late Triassic and Early Jurassic (Olsen et al. 2000). Thus, the formation of the sedimentary-derived hot brines that circulated throughout the Bou Azzer host rocks could have occurred after the Late Proterozoic, or more likely after the late-Triassic which constitutes a major period of evaporite deposition. A late Triassic circulation for the mineralizing brines is supported by radiometric age data as discussed above (see age of mineralization section).

Considering the shallow level of emplacement of the third stage of mineralization and absence of very low-salinity fluids, it is concluded that fluid boiling occurred in the Bou Azzer district, and therefore may have constituted a possible mechanism for ore deposition. Further evidence for the involvement of fluid boiling comes from structural and mineralogical data that indicate a transition from a closed to an open vein system, and a concomitant change from lithostatic to hydrostatic conditions. Accordingly, the hot hypersaline brine is interpreted to be of magmatic origin as also suggested by oxygen, hydrogen, and some sulphur isotope data. The Au–Ag–Zn (–Pb–Cu) contents of the mineralization, and Fe-poor composition of the sphalerite, together with the presence of visible gold, and occurrence of Na–K (albite-adularia) metasomatism combine to suggest that this end-stage (i.e., stage III) mineralization has an affinity to intermediate to low sulphidation epithermal deposits.

The occurrence in fluid inclusions of CH_4 and/or N_2 (Lebedev et al. 1999; Essarraj et al. 2005; Dolansky 2007) is consistent with a reducing nature of the mineralizing fluids. Fluctuations in redox conditions therefore may have been major factors in controlling ore deposition.

The high chlorinity of the mineralizing fluids suggest that metals were transported as chloride-complexes (e.g., $CoCl_4^{2-}$) for conditions like those that characterize the Bou Azzer ore-forming system (i.e., acid to near-neutral pH, temperatures >200 °C, moderate to high chloride activity). Co(II)-bisulphide, hydroxide, or mixed chloride-hydroxide complexes are unimportant for these physicochemical conditions (Migdisov et al. 2011). Moreover, stable isotope compositions, together with fluid inclusion and crush-leach data, are consistent with mixing of magmatic fluids with hot Ca- and SO_4^{2-} bearing groundwaters of meteoric origin, as the most effective mechanism of ore deposition. In a such model, fluid mixing would have oxidized the fluid, increased overall pH, and decreased temperature and ligand activity, all of which would have destabilized Co–As ± Au ± Ag chloride complexes and triggered precipitation of Co and associated metals. Stage III mineralization, which constitutes the major gold-bearing assemblage, took place under relatively high fS_2 (gas) (or $aH_2S_{(aq)}$) conditions as suggested by the consistent decrease in As and concomitant increase in S and Fe in later fluids (Ahmed et al. 2009; Gervilla et al. 2012). Deposition of Au could have resulted either from an increase or decrease in pH, or a decrease in the activity of reduced sulphur. However, because much of the observed gold occurs along sulphide-sulphosalt boundaries or within crosscutting fractures (Fig. 4), it seems likely that a decrease in the activity of reduced sulphur may have constituted the major factor that caused gold deposition.

The positive correlation between the distribution of serpentinite outcrops and Co–Ni–Fe-arsenide orebodies suggests that Co and Ni were scavenged from serpentinized and rodingitized ultramafic protoliths (Leblanc and Billaud 1982). In support of this proposed origin, available geochemical data indicate that the Bou Azzer serpentinites are enriched in Ni and Co, relative to the other host rock lithologies, containing up to 2800 ppm Ni and ~176 ppm Co (Leblanc and Billaud 1982; Gahlan et al. 2006; Ahmed et al. 2009). If this serpentinite source of Ni and Co is accepted, the origin of As in the ores remains still uncertain. Several potential sources have been proposed, in addition to serpentinites, including, (1) Late Neoproterozoic igneous and volcano-sedimentary rock sequences, (2) Silurian organic-rich shales (Dolansky 2007), and more importantly, as we suggest here, the involvement of the Neoproterozoic organic-rich black shales of the Imiter Group that contain As contents up to 6180 ppm (Pašava 1994). The high As contents of these black shales, as documented worldwide (Large et al. 2011), could constitute the most viable As source, in addition to other metals like Co, Ni, Au, and Ag, for the Bou Azzer orebodies.

References

Ahmed AH, Arai S, Ikenne M (2009) Mineralogy and paragenesis of the Co–Ni arsenide ores of Bou Azzer, Anti-Atlas, Morocco. Econ Geol 104:249–266

Barbero L, Jabaloy A, Gómez-Ortiz D, Pérez-Peña JV, Rodríguez-Peces MJ, Tejero R, Estupiñan J, Azdimousa A, Vázquez M, Asebriy L (2011) Evidence for surface uplift of the Atlas Mountains and the surrounding peripheral plateaux: combining apatite fission-track results and geomorphic indicators in the Western Moroccan Meseta (coastal Variscan Paleozoic basement). Tectonophysics 502:90–104

Blein O, Baudin T, Chèvremont P, Soulaimani A, Admou H, Gasquet P, Cocherie A, Egal E, Youbi N, Razin P, Bouabdelli M, Gombert P (2014) Geochronological constraints on the polycyclic magmatism in the Bou Azzer-El Graara inlier (Central Anti-Atlas Morocco). J Afr Earth Sc 99:287–306

Bousquet R, Mamoun R, Saddiqi O, Goffé B, Möller A, Madi A (2008) Mélanges and ophiolites during the Pan-African orogeny: the case of the Bou Azzer ophiolite suite (Morocco). In: Ennih N, Liégeois JP (eds) The boundaries of the West African Craton. Geol Soc, London, pp 233–247

Buisson G, Leblanc M (1987) Gold in mantle peridotites from Upper Proterozoic ophiolites in Arabia, Mali and Morocco. Econ Geol 82:2091–2097

Caritg S, Burkhard M, Ducommun R, Helg U, Kopp L, Sue C (2004) Fold interference patterns in the late Palaeozoic Anti-Atlas belt of Morocco. Terra Nova 16:27–37

Chbani B, Beauchamp J, Algouti A, Zouhair A (1999) Un enregistrement sédimentaire éocambrien dans un bassin intracontinental en distension: le cycle conglomérats de base-unité calcaire-grès de Tikirt de Bou Azzer-El Graara (Anti-Atlas, Maroc). CR Acad Sci Paris 329:317–323

Cheilletz A, Gasquet D, Filali F, Archibald DA, Nespolo M (2010) A late Triassic $^{40}Ar/^{39}Ar$ age for the El Hammam high-REE fluorite deposit (Morocco): mineralization related to the Central Atlantic Magmatic Province? Miner Deposita 45:323–329

D'Lemos RS, Inglis JD, Samson SD (2006) A newly discovered orogenci event in Morocco: Neoproterozoic ages for supposed Eburnean basement of the Bou Azzer inlier. Anti Atlas Mt Precambr Res 147:65–78

Dolansky LM (2007) Controls on the genesis of hydrothermal cobalt mineralization: insights from the mineralogy and geochemistry of the Bou Azzer depsoits, Morocco. Unpublished Master thesis, McGill University, Montreal, Canada, 162 pp

El Ghorfi M, Oberthür T, Melcher F, Lüders V, El Boukhari A, Maacha L, Ziadi R, Baoutould H (2006) Gold-palladium mineralization at Bleida Far West, Bou Azzer-El Graara inlier, Anti-Atlas, Morocco. Miner Deposita 41:549–564

El Hadi H, Simancas JF, Martínez-Poyatos D, Azor A, Tahiri A, Montero P, Fanning CM, Bea F, González-Lodeiro F (2010) Structural and geochronological constraints on the evolution of the Bou Azzer Neoproterozoic ophiolite (Anti-Atlas, Morocco). Precambr Res 182:1–14

Elias M (2002) Nickel laterite deposits-geological overview, resources and exploitation: University of Tasmania. CODES Spec Publ 4:205–220

En-Naciri A (1995a) Contribution à l'étude du district à Co, As, (Ni, Au, Ag) de Bou Azzer, Anti-Atlas (Maroc). Données minéralogiques et géochimiques; étude des inclusions fluides. Unpublished Ph.D. thesis, Université d'Orléans, Orléans, France, 238 pp

En-Naciri A (1995b) Mineralized hydrothermal solution cavities in the Co-As Aït Ahmane mine (Bou Azzer, Morocco). Miner Deposita 30:75–77

En-Naciri A, Barbanson L, Touray J-C (1996) Minéralogie de l'or dans le district de Bou Azzer (Anti-Atlas, Maroc). Chronique de la Recherche Minière 524: 41–51

En-Naciri A, Barbanson L, Touray J-C (1997) Brine inclusions from the Co-As(Au) Bou Azzer district, Anti-Atlas Mountains, Morocco. Econ Geol 92: 360–367

Essarraj S, Boiron M-C, Cathelineau M, Banks DA, Benharref M (2005) Penetration of surface-evaporated brines into the Proterozoic basement and deposition of Co and Ag at Bou Azzer (Morocco): evidence from fluid inclusions. J Afr Earth Sc 41:25–39

Figueiredo e Silva RC, Hagemann S, Labato LM, Rosière CA, Banks DA, Davidson GJ, Vennemann T, Hergt J (2013) Hydrothermal fluid processes and evolution of the giant Serra Norte jaspilite-hosted iron ore deposits, Carajás mineral province, Brazil. Econ Geol 108: 739–779

Gahlan H, Arai S, Ahmed AH, Ishida Y, Abdel-Aziz YM, Rahimi A (2006) Origin of magnetite veins in serpentinite from the Late Proterozoic Bou-Azzer ophiolite, Anti-Atlas, Morocco: An implication for mobility of iron during serpentinization. J Afr Earth Sc 46:318–330

Gasquet D, Levresse G, Cheilletz A, Azizi Samir MR, Mouttaqi A (2005) Contribution to a geodynamic reconstruction of the Anti-Atlas (Morocco) during Pan-African times with the emphasis on inversion tectonics and metallogenic activity at the Precambrian-Cambrian transition. Precambr Res 140:157–182

Gervilla F, Fanlo I, Colás V, Subías I (2012) Mineral compositions and phase relations of Ni-Co-Fe arsenide ores from the Aghbar mine, Bou Azzer, Morocco. Can Mineral 50:447–470

Ghorbal B, Bertotti G, Foeken J, Andriessen P (2008) Unexpected Jurassic to Neogene vertical movements in 'stable' parts of NW Africa revealed by low temperature geochronology. Terra Nova 20:355–363

Hawkins, M (2006) Cobalt news. The Cobalt Development Institute. http://www.thecdi.com/cobaltnews.php

Hefferan KP, Karson JA, Saquaque A (1992) Proterozoic collisional basins in a Pan-African suture zone, Anti-Atlas Mountains, Morocco. Precambr Res 54:295–319

Hefferan K, Admou H, Karson J, Saquaque A (2000) Anti-Atlas (Morocco) role in Neoproterozoic Western Gondwana reconstruction. Precambr Res 103:89–96

Hefferan KP, Admou H, Hilal R, Karson JA, Saquaque A, Juteua T, Bohn MM, Samson SD, Kornprobst JM (2002) Proterozoic blueschist-bearing mélange in the Anti-Atlas Mountains, Morocco. Precambr Res 118:179194

Huch KM (1988) Die panafrikanische Khzama-Geosutur im zentralen Anti-Atlas. Petrographie, Geochemie und Geochrnologie des subduktionskomplexes der Tourtit-Ophiolithe und der Tachoukacht-Gneise sowie einiger Kollisionsgresteine im Nordosten des Sirwa-Kristallindoms. Verlag Schelzky and Jeep, 172 pp

Hunt JA, Baker T, Thorkelson DJ (2005) Regional-scale Proterozoic IOCG-mineralized breccia systems: examples from the Wernecke Mountains, Yukon, Canada. Miner Deposita 40:492–514

Inglis JD, MacLean JS, Samson SD, D'Lemos RS, Admou H, Hefferan K (2004) A precise U–Pb zircon age for the Bleida granodiorite, Anti-Atlas, Morocco: implications for the timing of deformation and terrane assembly in the eastern Anti-Atlas. J Afr Earth Sc 39:277–283

Inglis JD, D'Lemos RS, Samson SD, Admou H (2005) Geochronological constraints on Late Precambrian intrusion, metamorphism, and tectonism in the Anti-Atals Mountains. J Geol 113:439–450

Jacques AL, Jaireth S, Walshe JL (2002) Mineral systems of Australia: An overview of resources, settings and processes. Aust J Earth Sci 49:623–660

Johnson CA, Cardellach E, Tritlla Hanan BB (1996) Cierco Pb-Zn vein deposits: isotopic and fluid inclusion evdience for formation during the Mesozoic extension in the Pyrenees of Spain. Econ Geol 91:297–306

Jouravsky G (1949) L'or et l'argent dans la région minéralisée de Bou Azzer. Notes et Mém Serv Géol Maroc 74:193–207

Jouravsky G (1952) Cobalt et nickel. Notes et Mém. Serv. Géol. Maroc 87:87–101

Large RR, Bull SW, Maslennikov VV (2011) A carbonaceous sedimentary source-rock model for Carlin-type and orogenic gold deposits. Econ Geol 106:3313–350

Lebedev VI, Borovikov AA, Borisenko AS, Azizi R, Ishkov YM, Borisenko DA (1999) Physicochemical constraints of cobalt ore formation in the Bou Azzer deposit, Morocco. Dokl Erath Sci 368:985–988

Leblanc M (1975) Ophiolites précambriennes et gîtes arséniés de cobalt (Bou Azzer-Maroc). Unpublished Ph. D. thesis, Université de Paris VI, Paris, France, 367 pp

Leblanc M (1981) Ophiolites précambriennes et gîtes arséniés de cobalt (Bou Azzer-Maroc). Notes et Mém Serv Géol Maroc 280:306 pp

Leblanc M (1986) Co-Ni arsenide deposits, with accessory gold, in ultramafic rocks from Morocco. Can J Earth Sci 23:1592–1602

Leblanc M, Billaud P (1982) Cobalt arsenide orebodies related to an Upper Proterozoic ophiolite: Bou Azzer (Morocco). Econ Geol 77:162–175

Leblanc M, Lbouabi M (1988) Native silver mineralization along a rodingite tectonic contact between serpentinite and quartz diorite (Bou Azzer, Morocco). Econ Geol 83:1379–1391

Ledent D (1960) Age absolu d'une brannérite de Bou-Azzer (sud-Marocain). Comptes Rendus Académie des Sciences de Paris 250:1309–1311

Levresse G (2001) Contribution à l'établissement d'un modèle génétique des gisements d'Imiter (Ag-Hg), Bou Madine (Pb-Zn-Cu-Ag-Au) et Bou Azzer (Co-Ni-As-Ag-Au) dans l'Anti-Atlas marocain. Unpublished PhD Thesis, CRPG-CNRS, Nancy, France, 191 pp

Lightfoot PC, Keays RR, Doherty W (2001) Chemical evolution and origin of nickel sulfide mineralization in the Sudbury igneous complex, Ontario, Canada. Econ Geol 96:1855–1875

Maacha L, Azizi R, Bouchta R (1998) Gisements cobaltifères du district de Bou Azzer (Anti-Atlas): structure, minéralogie et conditions de genèse. Chron Rech Min 531–532:65–75

Marakushev AA, Paneyakh NA, Zotov IA (2002) Specific features of the formation of copper-nickel sulfide deposits in trap rocks: Evidence from Pechenga and Noril'sk regions. Dokl Earth Sci 383:129–133

Marshall DD, Diamond LW, Skippen GB (1993) Silver transport and deposition at cobalt, Ontario, Canada: fluid inclusion evidence. Econ Geol 88:837–854

Mifdal A, Peucat J-J (1985) Datations U–Pb et Rb-Sr du volcanisme acide de l'Anti-Atlas Marocain et du socle sous-jacent dans la région de Ouarzazate: apport au problème de la limite Précambrien-Cambrien. Sci Géol Bull 38(2):185–200

Migdisov AA, Zezin D, Williams-Jones AE (2011) An experimental study of Cobalt (II) complexation in Cl^- and H_2S-bearing hydrothermal solution. Geochim Cosmochim Acta 75(14):4065–4079

Oberthür T, Melcher F, Henjes-Kunst F, Gerdes A, Stein H, Zimmerman A, El Ghorfi M (2009) Hercynian age of the cobalt-nickel-arsenide-(gold) ores, Bou Azzer, Anti-Atlas, Morocco: Re–Os, Sm–Nd and U–Pb age determinations. Econ Geol 104:1065–1079

Olsen PE, Kent DV, Fowell SJ, Schlische RW, Withjack MO, LeTourneau PM (2000) Implications of a comparison of the stratigraphy and depositional environments of the Argana (Morocco) and Fundy (Nova Scotia, Canada) Permian-Jurassic basins. In: Oujidi M, Et-Touhami M (eds) Le Permien et le Trias du Maroc. Actes de la Première Réunion du Groupe Marocain du Permien et du Trias. Hilal Impression, Oujda (Maroc), pp 165–183

Pašava J (1994) Geochemistry and the role of anoxic sediments in the origin of the Imiter silver deposit in Morocco. Vestnik Ceského geologického ustavu 69:1–11

Pelleter E, Cheilletz A, Gasquet D, Mouttaqi A, Annich M, El Hakour A, Deloule E, Féraud G (2007) Hydrothermal zircons: A tool for ion microprobe U–Pb dating of gold mineralization (Tamlalt-Menhouhou gold deposit, Morocco). Chem Geol 245:135–161

Ripley EM, Li C, Shin D (2002) Paragenesis assimilation in the genesis of magmatic Ni-Cu-Co sulfide mineralization at Voisey's Bay, Labrador: $\delta^{34}S$, $\delta^{13}C$, and Se/S evidence. Econ Geol 97:1307–1318

Robert G (2005) Hydrothermal cobalt mineralization at Agoudal, Bou Azzer, Morocco. Unpublished B.Sc. thesis, McGill University, Montréal, Canada, 52p

Saddiqi O, El Haimer F-Z, Michard A, Barbarand J, Ruiz GMH, Mansour EM, Leturmy P, Frizon de Lamotte D (2009) Apatite fission-track analyses on basement granites from south-western Meseta, Morocco: paleogeographic implications and interpretations of AFT age discrepancies. Tectonophysics 475:29–37

Sánchez V, Corbella M, Fuenlabrada JM, Vindel E, Martin Crespo T (2006) Sr and Nd isotope data from the fluorspar district Asturias, northern Spain. J Geochem Explor 89:348–50

Saquaque A, Admou H, Karson J, Hefferan K, Reuber I (1989) Precambrian accretionary tectonics in the Bou Azzer-El Graara region, Anti-Atlas, Morocco. Geology 17:1107–1110

Sillitoe RH, Hedenquist JW (2003) Linkages between volcanotectonic settings, ore-fluid compositions, and epithermal precious metal deposits. Soc Econ Geol Spec Publ 10:315–343

Soulaimani A, Le Corre C, Farazdaq R (1997) Déformation hercynienne et relation socle/couverture dans le domaine du Bas-Drâa (Anti-Atlas occidental, Maroc). J Afr Earth Sc 24:271–284

Soulaimani A, Jaffal M, Maacha L, Kchikach A, Najine A, Saidi A (2006) Modélisation magnétique de la suture ophiolitique de Bou Azzer-El Graara (Anti-Atlas central, Moroc). Implications sur la reconstitution géodynamique panafricaine. CR Géosci 338:153–160

Smith CG (2001) Always the bridesmaid, never the bride: Cobalt geology and resources. Transactions of the Institution of Mining and Metallurgy 110:B 75–80

Taylor HP (1997) Oxygen and hydrogen isotope relationships in hydrothermal mineral deposits. In: Barnes HL (ed.) Geochemistry of hydrothermal ore deposits, 3rd ed. John Wiley & Sons, New York, 972 pp

Thomas RJ, Chevallier LP, Gresse PG, Harmer RE, Eglington BM, Armstrong RA, de Beer CH, Martini JEJ, de Kock GS, Macey PH, Ingram BA (2002) Precambrian evolution of the Siroua Window, Anti-Atlas Orogen, Morocco. Precambr Res 118:1–57

Thomas RJ, Fekkak A, Ennih N, Errami E, Loughlin SC, Gresse PG, Chevallier LC, Liégeois J-P (2004) A new lithostratigraphic framework for the Anti-Atlas Orogen, Morocco. J Afr Earth Sc 39:217–226

U.S. Geological Survey (2013) Mineral commodity summaries 2013. U.S. Geological Survey: 198 p

Valenza K, Moritz R, Mouttaqi A, Fontignie D, Sharp Z (2000) Vein and karst barite deposits in the western Jebilet of Morocco: fluid inclusion and isotope (S, O, Sr) evidence for regional fluid mixing related to Central Atlantic rifting. Econ Geol 95:587–606

Wagner T, Mlynarrczyk MSJ Williams-Jones AE, Boyce AJ (2009) Stable isotopes constraints on ore formation at the San Rafael tin-copper deposit, Southeast Peru. Econ Geol 104:223–248

Walsh GE, Aleinikoff JN, Benziane F, Yazidi A, Armstrong TR (2002) U–Pb zircon geochronology of the Paleoproterozoic Tagragra de Tata inlier and its Neoproterozoic cover, Western Anti-Atlas, Morocco. Precambr Res 117:1–20

Xue G (2000) Fluid inclusions with NaCl–$CaCl_2$–H_2O composition from the Cloncurry hydrothermal system, NW Queensland, Australia. Lithos 53:21–35

Edough-Cap de Fer Polymetallic District, Northeast Algeria: I. The Late Miocene Paleogeothermal System of Aïn Barbar and Its Cu–Zn–Pb Vein Mineralization

C. Marignac, D.E. Aïssa, E. Deloule, A. Cheilletz and D. Gasquet

Abstract

In northeast Algeria, the internal Edough massif of the Alpine Maghrebide belt, is an inlier of basement rocks under a cover of Cretaceous (Kabylian) and Cenozoic (Numidian) flysch nappes. During the late Oligocene-early Miocene, the Edough massif was an Oligo-Miocene metamorphic core complex involving the basement rocks (Pan-African gneiss, marble, amphibolite) and its Paleozoic cover. In a short time interval from latest Burdigalian to early Langhian (ca. 17–15 Ma), felsic intrusive rocks were emplaced in the basement and its tectonic cover under progressively shallower conditions (granite to rhyolite) that define the Edough-Cap de Fer magmatic district. At Aïn Barbar, during intrusion of microgranites at ca. 16 Ma, a high-enthalpy, liquid-dominated geothermal system was active in the Cretaceous flysch reservoir, with Oligo-Miocene Numidian flysch serving as an impermeable cap. Temperatures as high as ca. 350–375 °C were attained in the deep parts of the Aïn Barbar paleogeothermal field, at a depth of ca. 1.3–1.5 km. Input of massive amounts of sodium resulted in the formation of metasomatic plagioclase-rich hornfels (Chaïba domain),

C. Marignac (✉) · A. Cheilletz
Laboratoire Géoressources, UMR-CNRS 7359,
Ecole des Mines de Nancy, Campus ARTEM,
54042 CS14234 Nancy Cedex, France
e-mail: christian.marignac@univ-lorraine.fr

D.E. Aïssa
Laboratoire de métallogénie, FSTGAT-
USTHB-Algiers, BP32 El Alia, 1600 Alger, Algeria

E. Deloule
CRPG UMR-CNRS 7358 15 rue Notre-Dame des
Pauvres, 54500 Vandoeuvre-les-Nancy, France

D. Gasquet
Laboratoire EDYTEM UMR-CNRS 5204,
Bâtimen "Pôle Montagne", Université de Savoie,
Campus Technolac, 73 376 Le-Bourget-du-Lac,
France

M. Bouabdellah and J.F. Slack (eds.), *Mineral Deposits of North Africa*,
Mineral Resource Reviews, DOI 10.1007/978-3-319-31733-5_9

whereas higher in the Cretaceous flysch aquifer, invasion of hot fluids (300–270 °C) was associated with hydrothermal metamorphism (quartz-chlorite, calcite-chlorite, wairakite-chlorite, and epidote domains). The source of these hot fluids was a basement of the Edough type, in which advection of heat was likely related to emplacement of a granite batholith at depth. Concomitant with the paleogeothermal circulations, fault activity created N170° E fracture zones that progressively channelled fluid flow, with related development of linear propylitically altered zones and precipitation of Zn–Pb–Cu sulphides at temperatures between 330 and 285 °C. At ca. 15 Ma, renewed magmatic activity (subvolcanic rhyolite dikes) was associated with a new and shallower (ca. 800 m depth) geothermal system, involving the convective circulation of surficial fluids (meteoric and possibly seawater) at temperatures between 300 and 250 °C. Epithermal quartz and sulphides were deposited in the same vein systems as in the previous mineralization stage, but remained uneconomic. However, concomitant formation of massive adularia during alteration of the Chaïba rhyolite produced an economic K-feldspar body mined for ceramics.

Keywords
Edough · Alpine · Polymetallic vein · Aïn barbar · Paleogeothermal system · Cu–Zn–Pb · Epithermal mineralization · Adularia deposit

1 Introduction

In northern Africa, a number of Alpine metamorphic core complexes in the Maghrebide belt form internal crystalline massifs that are known from the Rif to the Calabria (Fig. 1). Alpine ore fields, mainly of the epithermal type (e.g., Glaçon 1971), occur within some of these core complexes, but appear to be later than the main detachment tectonics; their possible relationships with the host core complex were not examined until now. In eastern Algeria, the Edough-Cap de Fer massif is one of these metal-endowed core complexes (Aïssa et al. 1995), displaying a variety of mineralization styles including W-(Sn) skarns, polymetallic Cu–Zn–Pb vein systems, and Sb–As–(Au) veins and replacements (Marignac 1988a; Aïssa et al. 1998; Marignac et al. 2015).

Modern epithermal deposits are related to the activity of geothermal systems (Rowland and Symmons 2012, and references therein). In this paper, we address the Aïn Barbar polymetallic (Cu–Zn–Pb) vein system and its relationships to paleogeothermal activity in the Edough-Cap de Fer massif. A companion paper (Marignac et al. this volume) discusses time relationships among the Edough-Cap de Fer mineralization, exhumation of the core complex, and associated tectonic, magmatic, and hydrothermal events.

2 Geological Background

The Edough-Cap de Fer area, in eastern Algeria (Fig. 1), is part of the internal zone of the Betic-Maghrebide belt (Durand-Delga 1969) that forms the westernmost extension of the Alpine chain derived from the Tethyian realm (Dercourt et al. 1986). This belt resulted from the Eocene to Miocene collision between the African (Gondwanan) plate and the European plate (e.g., Jolivet and Faccenna 2000). An intervening northern microplate, presently exposed in a series of crystalline upper nappes, the internal massifs,

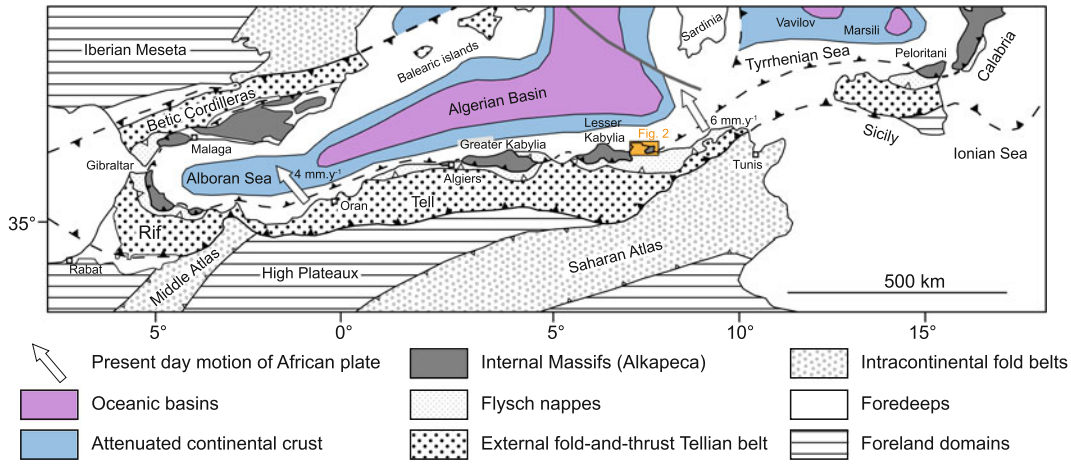

Fig. 1 Regional setting of Edough-Cap de Fer district in Alpine Betic Cordilleras-Maghrebides belt and oceanic Western Mediterranean basins (adapted from Michard et al. 2006). Box shows area of Fig. 2

formed from a pre-Mesozoic basement and Mesozoic-Cenozoic cover, and were affected by Alpine metamorphism. The internal massifs were subsequently thrust southwestward onto the Tellian nappes, a fold-and-thrust belt with southward vergence that was derived from the former passive margin of the African plate (e.g., Piqué et al. 2002; Frizon de Lamotte et al. 2000, 2006). Interleaved between the internal massifs and the Tellian nappes is an elongate flysch belt that extends from the Rif to Calabria. This belt comprises a complex of Mesozoic nappes (Kabylian flysch), former cover of an oceanic Tethysian tract (Durand-Delga et al. 2000), and Numidian flysch (Late Oligocene-Burdigalian), which was deposited on the African margin during opening of the Algeria-Provence oceanic basin (Thomas et al. 2010) and incorporated in the nappe at the end of the Burdigalian (Bouillin 1979; Sami et al. 2010).

The Edough-Cap de Fer area (Fig. 1) consists of an inlier of crystalline basement, the Edough massif, which forms an antiformal dome that was uplifted from under a complex of nappes that crop out to the west. The main Numidian nappe overlies a complex of Kabylian flysch outcropping as small inliers, particularly in the Aïn Barbar antiform (Fig. 2). The Edough massif comprises a stack of crystalline rocks (paragneiss, amphibolite, marble, and micaschist), which evolved as a metamorphic core complex during the late Oligocene-early Miocene (Brunel et al. 1988; Caby and Hammor 1992) and was overthrust by the flysch nappes during the late Burdigalian.

3 The Cap de Fer-Edough Magmatic District

A large magnetic anomaly underlines the Cap de Fer to Edough massif that is currently interpreted as a large magmatic body at depth (Vila 1980). The surface expression of this body is the Cap de Fer, Aïn Barbar, and Edough intrusive complexes (Fig. 2). The post-tectonic magmatism that formed these intrusions occurred in two stages during the late Miocene. The first stage was mainly subvolcanic and produced intrusions in the Edough massif and Aïn Barbar areas (microgranites), and the subvolcanic-volcanic complex of the Cap de Fer (microdiorite to microgranite and associated andesite-rhyolite). These rocks have been thoroughly studied petrographically and petrologically (Hilly 1962; Marignac 1985; Fougnot 1990; Ahmed-Saïd et al. 1993; Laouar et al. 2005), and their age is well constrained to be close to 16 Ma (Burdigalian to Langhian boundary) by whole-rock K/Ar dating (Bagdasarjan et al. 1973; Bellon

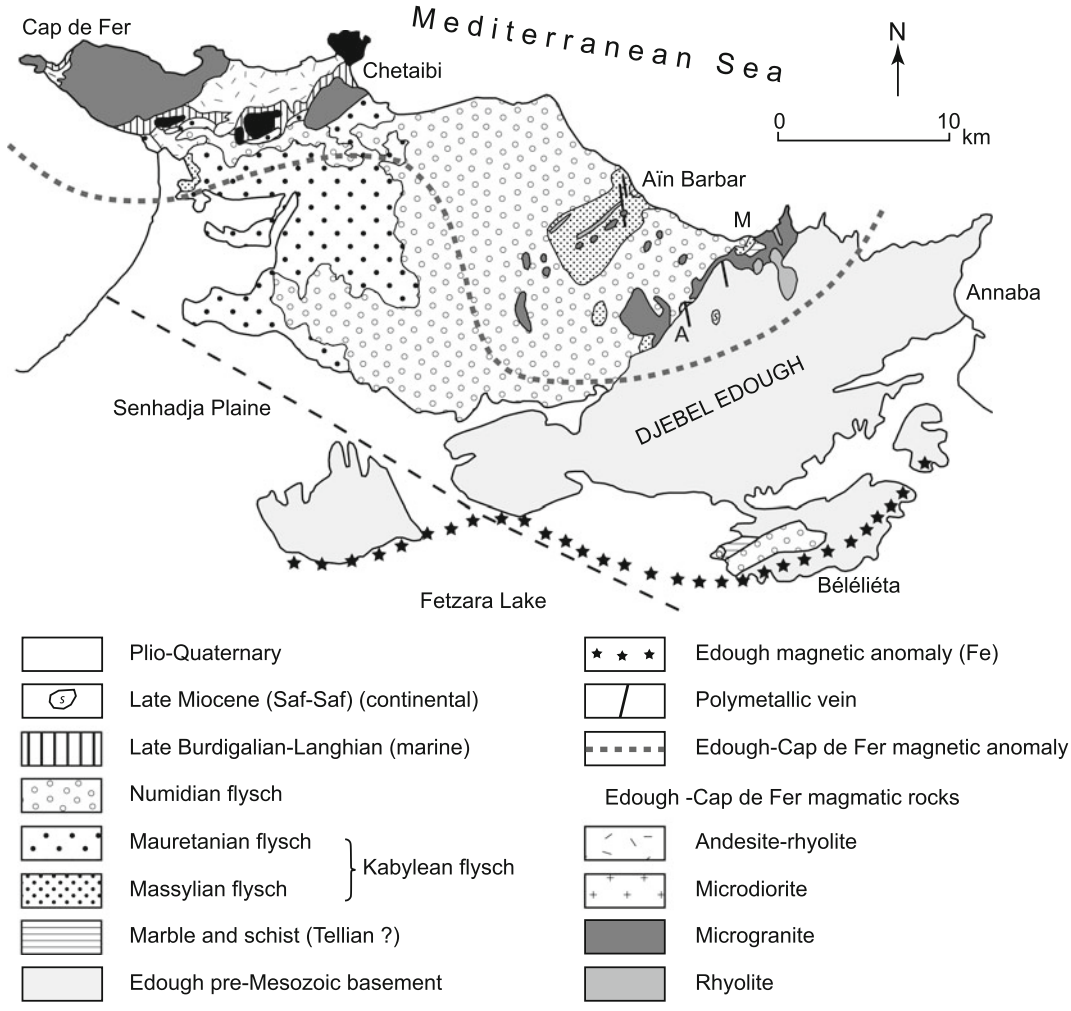

Fig. 2 Geology of Edough-Cap de Fer district (modified from Hilly 1962 and Marignac 1985)

1981; Marignac and Zimmermann 1983), although stratigraphic evidence indicates that the earlier basaltic rocks in the Cap de Fer massif were extruded during the late Burdigalian (Hilly 1962). Laouar et al. (2005) characterized these rocks as a high-K, calc-alkaline to shoshonitic series, and on the basis of Harker diagrams and stable isotope (O, S) data, interpreted them as a fractionated series of mantle derivation. Most analyses, however, are biased by intense hydrothermal alteration that affected the intrusions and lavas, including advanced propylitic (chlorite, epidote, calcite), potassic (adularia), and sericitic (quartz, sericite) alterations that occurred in all of the massifs (Marignac 1985; Fougnot 1990; Aïssa 1996; Laouar et al. 2005). The importance of these effects, although variable from one complex to another, is well seen in the Al-excess (Al–K–Na–2Ca) versus mafic charge (Fe + Mg + Ti) diagram (Debon and Le Fort 1983) that is highly sensitive even to small increments of alteration (Fig. 3). When these alteration effects are discarded, data for the early Langhian subvolcanic and volcanic rocks display a clear magmatic trend of the Cordilleran I-type (sensu Frost et al. 2001), ending with slightly peraluminous, highly fractionated rhyolites (Cap de Fer) and microgranites (Aïn Barbar). This trend is consistent with a mixing process between a mafic magma and a crustally derived magma

followed by fractional crystallization, as proposed by Maury et al. (2000) at the scale of the Maghrebide belt.

The second stage is represented by a few rhyolite dikes and domes (Aïn Barbar, Edough) that are significantly distinct from the preceding trend, being petrologically closer to evolved compositions of the "rare-metal granite" (RMG) type (Fig. 3). The Aïn Barbar dikes are 15.1 ± 0.1 Ma (whole-rock K–Ar age; Marignac and Zimmerman 1983), an early Langhian age that is significantly younger than the calc–alkaline series. Owing to the strong geochemical similarities of these two stages, a similar age is proposed for the Edough rhyolites.

4 Geological Setting of the Aïn Barbar Inlier

The Aïn Barbar inlier contains ~10 polymetallic veins (Fig. 4). Many of these veins were mined out in the 19th to early 20th Century (Abdallah, Ketterer, Merendet, Salah, Saint-Jean), or are

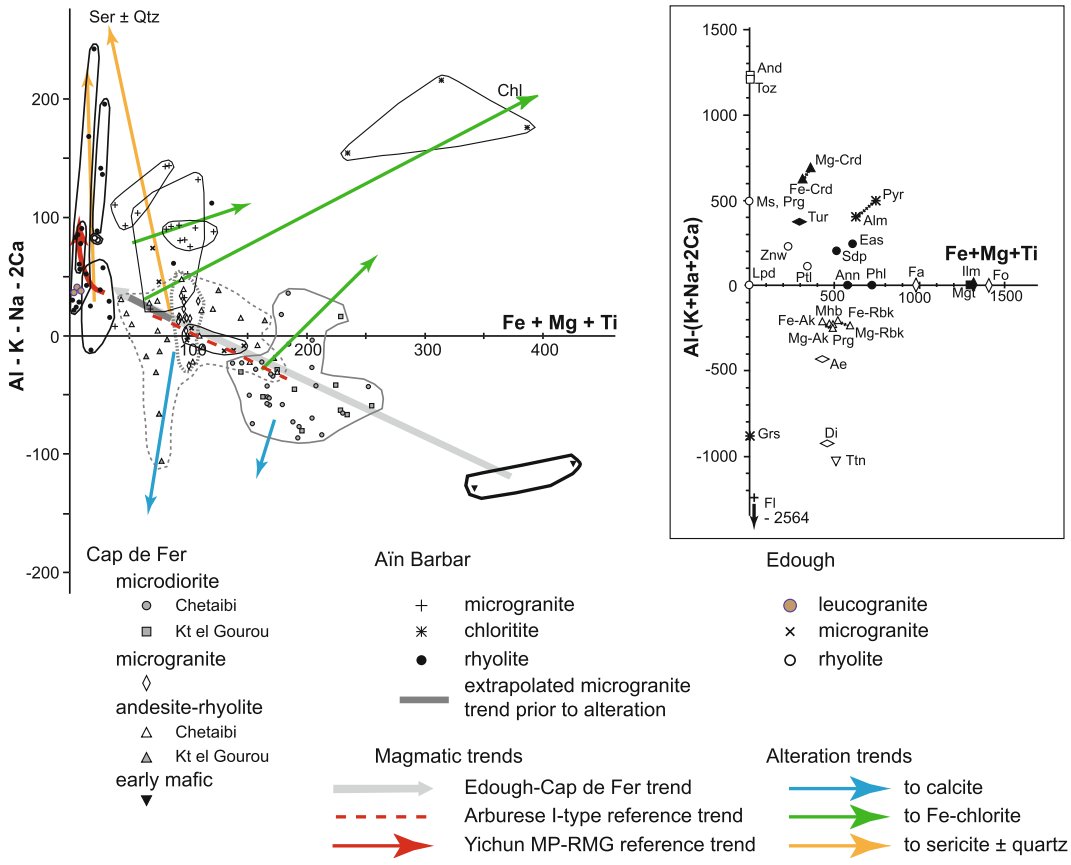

Fig. 3 Magmatic evolution trends of Edough-Cap de Fer magmatic district in (Al–Na–K–2Ca) versus (Fe + Mg + Ti) discrimination diagram of Debon and Le Fort (1983). Insert shows position of reference silicates in the diagram (IMA abbreviations; Whitney and Evans 2010). Data are from Marignac (1985), Fougnot (1990), and Laouar et al. (2005). Most analyses are grouped along a differentiation trend typical of a "Caledonian-style" I-type ("Arburese trend" shown as reference; data from Secchi et al. 1991), significantly excepting data for Edough leucogranites and late rhyolites, which follow a trend typical of the medium-P (MP) rare-metal granites (RMG) class (Linnen and Cuney 2005). Strong dispersion of the data from the magmatic trend is interpreted in terms of alteration, including chloritization, sericitization, and calcitization

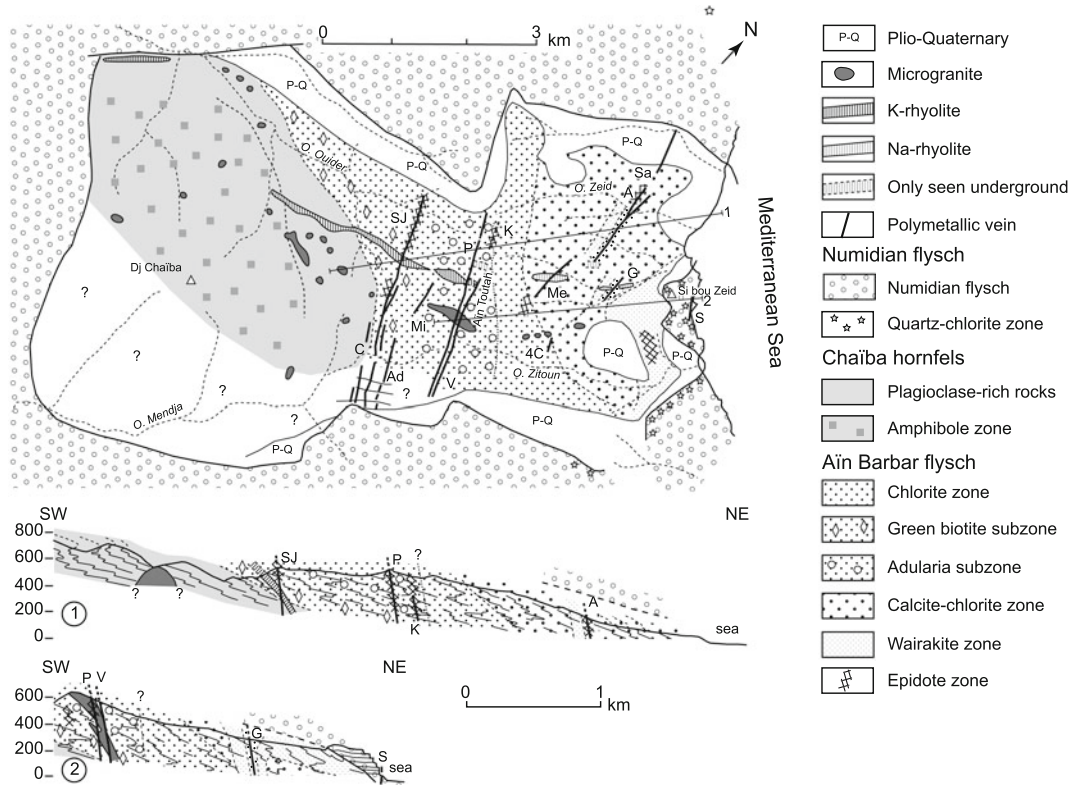

Fig. 4 Geologic map and interpretive cross sections (*1*, *2*) of Aïn Barbar inlier (modified after Marignac 1988b). Numidian limits are in part derived from photo-interpretation. Aïn Barbar flysch is considered part of an inverted limb of a nappe. Polymetallic veins: *A* Abaïd; *Ad* Abdallah; *C* Chaïba; *G* Gray; *K* Ketterer; *Me* Merendet; *Mi* Michaud; *P* Playfair; *4C* Four Roads ("Quatre Chemins"); *S* Sea ("Filon de la Mer"); *Sa* Salah; *SJ* Saint-Jean; *V* Victor

only known as ferruginous caps (e.g., Chaïba, "Quatre Chemins", Michaud). In recent times, only the Playfair, Victor, and Abaïd-Gray veins have been mined and allowed underground observations. Mining of these veins ceased in the mid-1990s. The main veins strike ~N170° E, with a strong eastward dip (Fig. 4). Principal ore minerals are sphalerite, galena, and chalcopyrite; average grades were rather high (Cu 3 %, Zn 4.3 %, Pb 1.4 %), with contained metals amounting to at least 125 kt Cu, 80 kt Zn, and 26 kt Pb (unpublished mined data). Silver was a by-product, concentrated in galena (mean 2000 ppm Ag) together with bismuth (mean 4,000 ppm Bi), and in chalcopyrite (mean 335 ppm Ag).

4.1 Sedimentary Formations

Owing to a NE-SE anticlinal arching, the Aïn Barbar inlier exposes a late Maestrichtian Massylian flysch under the tectonic Numidian flysch cover (Fig. 4). The latter is essentially undeformed and in outcrop displays an alternation of thick sandstone (up to 10 m) and thin (several 10 cm to a few meters) mudstone typical of the Kroumirie member of the Numidian sequence, as described in northeastern Tunisia (Sami et al. 2010, and references therein), in which the basal (more argillaceous) member was truncated during nappe emplacement. The original (pre-tectonic) thickness of this Kroumirie member is estimated to ~1200 m (Lahondere et al. 1979; Sami et al. 2010). The Aïn

Barbar flysch is a typical turbidite deposit, with three main facies: abyssal plain (argillaceous flysch), and two distal-lobe facies, a carbonate flysch (calcic clasts predominant), and silicate flysch (quartz-chlorite clasts more abundant than calcic clasts), the latter two having the potential to act as reservoir rocks (Marignac 1985). In contrast to the Numidian flysch, the Aïn Barbar Cretaceous flysch exhibits intense internal deformation at the meter scale, reflecting a subduction prism setting (Marignac 1985). In apparent continuity with these early deformations, the entire flysch deposit is isoclinally folding associated with an incipient schistosity, and displays very low-grade (illite-chlorite) metamorphism.

4.2 Magmatic Rocks

Swarms of small porphyritic microgranite intrusions are widespread throughout the inlier, most being only locally exposed owing to recent erosion. The Chaïba swarm (Fig. 4) could represent a larger intrusion, similar in size to those in the nearby Edough massif or the Cap de Fer (Fig. 2). However, most microgranite swarms are linear, and hence are dikes, as seen in underground workings (Fig. 4). Two groups of rhyolite dikes are recognized. In the Chaïba massif, there are two dikes (Oued Ouider, Chaïba) of high-K rhyolite that contain numerous enclaves, including silicified Numidian flysch; these dikes have a K–Ar age of 15.1 ± 0.1 Ma (Marignac and Zimmerman 1983). A second group of sodium-rich rhyolite dikes, largely unexposed, (Abaïd and Gray-Merendet-Playfair dikes), are slightly older and have the same age (16.0 ± 0.1 Ma) as the microgranites (Marignac and Zimmermann 1983).

5 Mineralization

Two main stages of mineralization (divisible in episodes) may be defined on the basis of textures and quartz abundance (Fig. 5). A first stage has predominantly breccia textures and minor quartz; it is the main mineralizing stage and is here classified as "mesothermal" (sensu Lindgren 1933). The second stage is characterized by an abundance of quartz, which gives the lodes their "vein" appearance, and by widespread open vug fillings; it includes a subordinate polymetallic (Pb, Zn, Cu) episode and a later arsenopyrite episode, and is here classified as "epithermal." All stages and episodes are separated by fracturing events and may be correlated at the scale of the vein field. The resulting lodes display complicated and highly variable patterns at the 10 cm scale (Fig. 6). Nevertheless, no significant variation in the paragenetic successions or in mineral compositions was found either along strike or down dip, within the Abaïd-Gray, Victor, and Playfair vein systems (the last being exposed from the 580 to the 260 m levels, i.e., more than 300 m vertically), in contrast with the classical low-sulphidation gold epithermal veins.

The mesothermal stage began with intense propylitic alteration in the vein wall rocks, accompanied by the development of matrix-supported and crackle breccias with a chlorite matrix. These breccias are elongate along the main vein direction, with the matrix-supported breccias occupying a more central position. Locally, an older propylitic event may be observed, having produced microfolded chlorite veinlets and an early crackle breccia reworked by the main propylitic event. Coeval with the chlorite breccias, swarms of epidote veinlets and linear (N160° E) epidotite bodies occur locally along strike (Fig. 4). Chlorite breccias and epidotite bodies were repeatedly reworked and served as the main focus for later hydrothermal fluid flow (Fig. 6). The first mineralizing episode deposited massive sphalerite and galena, within breccia bodies that overprint the chlorite breccia. The sphalerite is iron-rich (X_{FeS} 0.20–0.25). Massive hexagonal pyrrhotite is present locally (Salah, Merendet veins). A silicification episode formed both dissolution cavities at the expense of sphalerite and intense silicification of flysch breccia clasts and wall rocks (up to several 10 cm from veins). This episode was typically preceded by deposition of millimetre-size epidote prisms lining the cavity walls, and of quartz accompanied by a new generation of chlorite. Crack-seal textures are common within the veins.

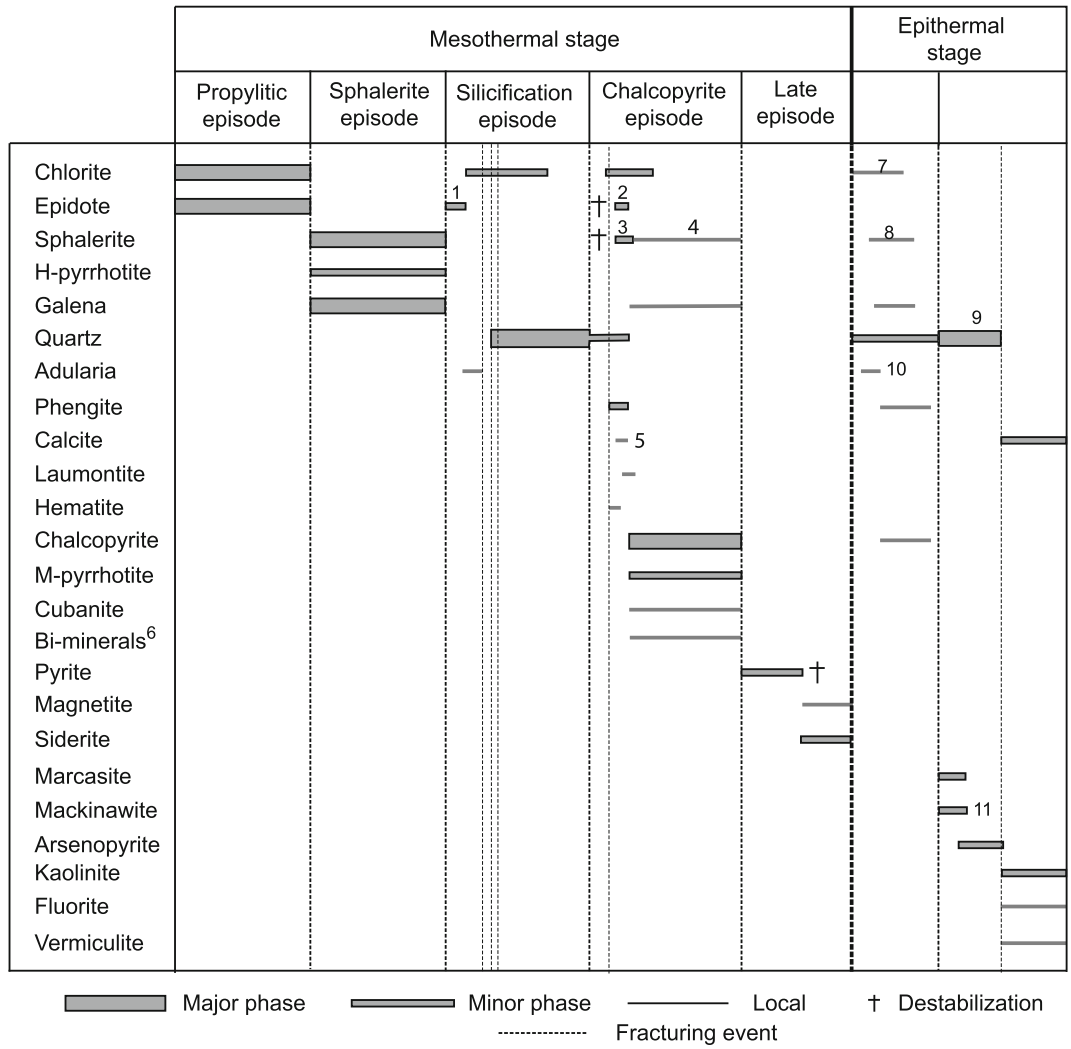

Fig. 5 Paragenetic succession in polymetallic veins of Aïn Barbar inlier (modified from Marignac 1976, 1988a). Minerals are listed in order of first appearance. *Notes*: *1* aluminous epidote (X_{Ps} 0.10–0.20); *2* ferriferous epidote ($X_{Ps} > 0.25$); *3* sphalerite reworking by chalcopyrite disease; *4* low-Fe epitaxial skeletal sphalerite "stars" in chalcopyrite; *5* calcite blades; *6* mainly bismuthinite, with minor cosalite and rare Pb–Bi–Te–S mineral inclusions in cosalite having composition close to aleksite member ($PbBi_2Te_2S_2$) of aleksite sulphosalt series (Moëlo et al. 2008); *7* Fe-rich chlorite; *8* Fe-rich sphalerite; *9* quartz typically exhibiting chalcedony-like radial fibrous habit, termed chalcedonic quartz (e.g., Marignac 1976); *10* Ba-rich adularia (up to $X_{Cls} \sim 0.1$); *11* mackinawite ± M-pyrrhotite inclusions in chalcopyrite resulting in sphalerite with chalcopyrite disease. Abbreviations: H-pyrrhotite, hexagonal pyrrhotite; M-pyrrhotite, monoclinic pyrrhotite

The chalcopyrite episode is complex. Chalcopyrite either fills quartz-chlorite-(rare adularia) cavities, as a continuation of the preceding episode, replaces part of the sphalerite breccias, or forms monomineralic breccias in the wall rocks, yielding a zoned lode with a sphalerite-rich core and chalcopyrite-rich rims; massive chalcopyrite, up to 20 cm thick, is present locally (Fig. 6). Chalcopyrite deposition was preceded by an event of coeval precipitation of hematite, phengite, iron-rich epidote (close to pistachite end-member), and bladed calcite, either within the vein system or wall rocks. Hematite is rare (only seen in Ketterer vein); the Fe-rich epidote is present as local veinlets, and overgrowths on older epidote. Phengite is ubiquitous in the

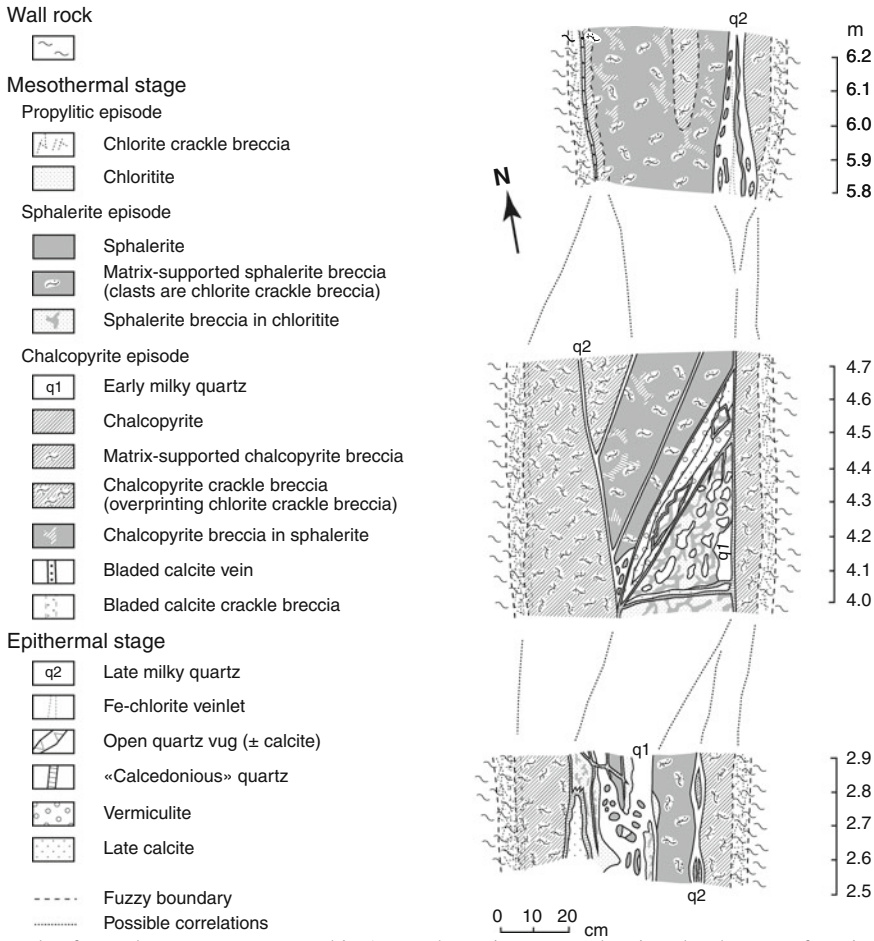

Fig. 6 Example of complex structures exposed in Aïn Barbar vein system, showing sketch maps of portions of Abaïd vein on 80 N level (observations of hanging wall in 1967). Horizontal distances are measured from the central shaft. Owing to different styles of mineralization with time and polyphase evolution, lateral textural variations in vein system are extreme and, because of observational gaps, correlations are mostly speculative

Playfair-Victor veins, and less common in the Abaïd-Gray veins; its appearance correlates with the partial dissolution of the preceding epidote and epidotite (formation of skeletal epidote may be the result). The widespread calcite blades are known to characterize boiling conditions (Browne 1978; Simmons and Browne 2000) leading to oxidizing conditions (Drummond and Ohmoto 1985), that are also recorded by the more local hematite and Fe-rich epidote. This transitional event occurred just prior to chalcopyrite deposition. Chalcopyrite uniformly contains subhedral laths of a monoclinic pyrrhotite and rare blades of cubanite, and in the Playfair-Victor vein system is associated with the deposition of bismuth minerals (mainly bismuthinite, with minor cosalite and a rare Pb–Bi–Te–S sulphosalt of the aleksite series). Chalcopyrite exhibits growth twinning, and contains minute inclusions of skeletal low-Fe sphalerite (X_{FeS} 0.11–0.18), which are interpreted to have been deposited epitaxially onto chalcopyrite faces, thus promoting the observed twinning (Marignac 1989). Concomitant with chalcopyrite replacement of the early sphalerite, the latter was partially dissolved and overgrown by a lower Fe-sphalerite rim (X_{FeS} 0.17–0.20, up to 0.22) at the chalcopyrite contact. Typical chalcopyrite disease (Barton 1978; Barton and Bethke 1987; Eldridge et al. 1988) associated with iron loss (diffusion zoning) developed within the sphalerite crystals. All of these features are evidence for an increase in fS_2 in the hydrothermal systems during

the chalcopyrite episode: in fact, the monoclinic pyrrhotite formed metastably under conditions where pyrite was theoretically stable (Marignac 1987, 1988a). This depositional environment explains why pyrite replacement of the monoclinic pyrrhotite was ubiquitous during the late episode of the mesothermal stage (Fig. 5), which in the Playfair and Victor veins ended with the dissolution-replacement of pyrite by siderite ± magnetite.

The epithermal stage began with a recurrence of base-metal mineralization (Fe-rich sphalerite, galena, chalcopyrite) associated with quartz deposition. Whereas the older mesothermal galena displays a cubo-octahedral habit and is silver- and bismuth-rich, the late galena is only cubic and has significant antimony (mean 700 ppm Sb). This latter episode is very minor, except in the Abaïd-Gray vein system, where "green hydrothermal quartzites" fill en-echelon N160° E tension joints and N170° E veins. These "quartzites" are an assemblage of microcrystalline quartz, Fe-rich chlorite-adularia (Ba-rich adularia, up to XCls ~0.1) and phengite, with base metal sulphides. The final episode was marked by the widespread development along the N170° E vein trend of a chalcedonic comb quartz (Fig. 6), associated with small euhedral crystals of arsenopyrite with glaucodot cores, and rims of alternating (oscillatory zoned) Sb-rich and As-rich bands (Marignac 1987, 1988a). At the very end of this episode, cavities were filled with kaolinite, Ca-vermiculite, calcite, and local fluorite (mainly in the Abaïd-Gray system). Late calcite veinlets are widespread.

6 Alteration of Magmatic Rocks

The microgranites and Abaïd-Gray rhyolites display a sequence of alteration corresponding to the paragenetic sequence in the ore veins, beginning with epidote-chlorite, followed by propylitic, quartz-chlorite-(albite), epidote-adularia, and ending with quartz-calcite-phengite ± chlorite. Within the Abaïd rhyolite, the propylitic episode transformed the rock into a chloritite (+apatite). Paragenetically very late quartz-adularia-kaolinite in microvugs is widespread in the Abaïd and Gray rhyolites, and in places within the microgranites; adularite bodies may be locally observed in the ryolites. The adularia is Ba-rich (up to XCls ~0.1). This late assemblage seems to correlate with the epithermal stage. The K-rich rhyolites are unaffected by the propylitic alteration, and contain as enclaves hydrothermally altered chlorite-epidote rocks derived from both the Aïn Barbar and Numidian flysch. The main alteration that affected these rhyolites is massive replacement of the matrix by adularia, which is correlated to the transformation of K-feldspar phenocrysts into an assemblage of chlorite-adularia ± Ti-oxide. The resulting rock is a feldspar ore containing reserves of ~7 Mt @ 9.5 wt% K_2O, which was mined for ceramics in the 1990s (SOFELD Spa 1999); mining ended in 2003, but may resume in the near future. Following this intense adularia alteration, a local greisen-forming event formed quartz-phengite or tourmaline-phengite assemblages. Fluorite-tourmaline veinlets are also present in wall rocks of the Chaïba rhyolite. As in the Abaïd-Gray rhyolites, late microvugs filled with quartz-adularia-kaolinite-apatite ± phengite are widespread. All of these features point to a correlation with the epithermal stage.

7 Hydrothermal Metamorphism

All of the Aïn Barbar flysch facies were affected by the development of hydrothermal mineral assemblages (Marignac 1985, 1988b) (Fig. 4). To the southwest of the inlier, in the Djebel Chaïba massif, plagioclase hornfels resulted from intense sodium metasomatism that affected distal facies of the Aïn Barbar flysch (Marignac 1988b). To the northeast, although apparently not transformed at the macroscopic scale, the flysch contains hydrothermal replacements and veinlets at the microscopic scale (cryptic alteration), except in the areas most transformed. The hydrothermal domain boundaries are roughly coincident with the lithological boundaries. A chlorite-quartz domain corresponds approximately to the silicate facies of the flysch, whereas a calcite-chlorite domain is more or less coincident with the

carbonate facies. A thin (<100 m thick) albite-"green biotite" subzone marks the transition to the hornfels, gently dipping to the northeast as shown by its presence in the Playfair underground workings at the 260 m level (Fig. 4, cross section 2). In the chlorite-quartz zone, a subzone characterized by adularia (more or less overprinted by phengite) is coincident with the Aïn Toutah vein systems. Close to the Numidian contact in the northeast of the inlier is a wairakite-plagioclase-chlorite domain in which a central zone has epidote as the main hydrothermal mineral (Fig. 4). Similarly, wairakite zones (although linear) also occur along the Abaïd and Gray veins, surrounded by a thin chloritized zone or by epidotite bodies (propylitic episode of the mesothermal stage), such as along the Playfair and Victor veins. Where observed, the basal beds of the Numidian flysch show evidence of hydrothermal alteration: the arenitic beds are strongly silicified, forming fine-grained quartzite; the intervening argillaceous beds are chloritized, forming replacements and numerous veinlets. Higher in the Numidian flysch, a similar alteration is developed around a set of poorly mineralized quartz veins known as the "Filon de la Mer" (Sea vein), along the coast (Fig. 4).

The Chaïba domain is characterized by mimetic replacement of the flysch minerals by fine-grained Na–Ca plagioclase (An_{30}). The resultant rock, although undeformed, exhibits an apparent "schistose" texture and numerous remnants of the original lithology trapped within the plagioclase crystals—mainly graphite-like particles. Within more internal parts of the domain is a banded facies characterized by alternations, at the centimeter to decimeter scale, of plagioclase-rich and amphibole ± clinopyroxene + plagioclase beds, the latter likely having evolved from former Ca-rich arenite beds. The clinopyroxene (salite with X_{Hd} 0.50–0.53) is systematically replaced by the amphibole (ferro-actinolitic hornblende with mean composition $(K_{0.06}Na_{0.14})\ Ca_{2.00}\ (Fe^{2+}_{2.70}Mg_{0.82}Mn_{0.02})\ (Fe^{3+}_{0.30}Al^{vi}_{0.16})\ [Si_{7.32}Al^{iv}_{0.68}O_{22}(OH)_2]$).

Several retrograde events affected the Chaïba hornfelses. First, the amphibole-plagioclase assemblage was replaced along plagioclase grain boundaries by a "vermiculite"-epidote assemblage, with concomitant "clearing" of the plagioclase (owing to oxidation of the graphite particles). The "vermiculite" is an interstratified chlorite-potassic saponite phase (Marignac 1985); the epidote is relatively iron-rich ($X_{Pst} > 0.20$). The vermiculite-epidote assemblage evolved into an epidote-adularia assemblage. Late calcite-chlorite veinlets are rare. Mass-balance calculations show that the hornfels zones were produced under near-constant Al and Ti contents, with a net gain of Na and Sr, and loss of all remaining elements, including trace base metals (Marignac 1985, 1988b). The hornfels domain is devoid of sulphides. In contrast, at the boundary with the quartz-chlorite domain, the "green biotite"-quartz-albite subzone typically contains abundant pyrrhotite, resulting from the transformation of the pyrite initially present in the flysch. The metasomatic Na front is thus coincident with the dissolution of older sulphides. In detail, the "green biotite" consists of interstratified biotite (Fe# 0.45) and chlorite (Fe# 0.54, Al^{iv} 1.35) (Marignac 1988b). Within this subzone, epidote and younger chlorite + adularia are late assemblages, widespread retrograde chlorite having grown at the expense of the "green biotite".

The quartz-chlorite domain is characterized by chlorite recrystallization and replacement of the flysch matrix and silicate clasts. Ti-oxide and albite are commonly associated, the latter mainly occurring in chlorite ± albite ± pyrrhotite veinlets. Early calcite-rich clasts are more or less completely silicified, suggesting that the silicate facies of the Aïn Barbar flysch is in part the result of hydrothermal alteration. Chloritization of an early illite likely developed according to the reaction illite + quartz + water + (Fe^{2+}, Mg^{2+}) = chlorite + H^+ + K^+ (Riverin and Hodgson 1980). Epidote may be present, in former calcite-rich beds, where pyrite is also found, evidently shielded by epidote. The adularia subzone, which resulted from the replacement of albite by adularia, is interpreted to have a sub-vertical boundary, paralleling the trend of the veins. The calcite-chlorite domain is characterized by a sparite-pyrite and recrystallization-replacement by chlorite at the intergranular scale. There is some evidence of an illite to chlorite transformation,

but most early illite altered to interstratified Ca-smectite-phengite. A Ca-smectite is the main hydrothermal mineral at the boundary with the wairakite zone.

The wairakite domain is poor in calcite and has a wairakite-plagioclase (An_{25} to An_{50})-chlorite assemblage. The wairakite is uniformly sodium-rich, with a mean formula $(Na_{0.06}Ca_{0.94})[Si_{3.99}Al_{2.01}Fe_{0.01}]\cdot 2H_2O$. Pyrrhotite occurs in place of pyrite, and locally a few base-metal sulphides may be present (chalcopyrite > sphalerite > galena). The wairakite appears as replacements and veinlets. In the core of the domain, epidote ($0.10 < XPst < 0.20$) is the main Ca-silicate: the arenite-rich laminae of the flysch are transformed into quartz-chlorite-epidote-wairakite assemblages, whereas the more pelitic laminae are pseudomorphed by an epidotite that preserves the schistose texture. Locally within the epidote subzone, microvugs fringed with epidote prisms are filled by bladed calcite and wairakite, together with minor phengite (wairakite being replaced by epistilbite). This assemblage, which owing to the bladed habit of the calcite testifies to boiling (Browne 1978), is reminiscent of the transient boiling episode inferred for the vein systems during the onset of chalcopyrite precipitation. A very similar vug filling of epidote-calcite-laumontite was observed at the 260 level of the Playfair vein (Marignac 1988b). A late epidote, occurring as veinlets or associated with adularia, is typically more iron-rich ($0.20 < X_{Pst} < 0.33$).

8 Tectonic Context of Hydrothermal Metamorphism and Mineralization

Concomitant with the beginning of the hydrothermal metamorphism, a tectonic event characterized by vertical shortening was pervasive in the reservoir rocks This tectonic event is recorded by microfolds of hydrothermal veinlets regardless of composition (chlorite, phengite, wairakite, epidote, and adularia in the flysch; plagioclase and amphibole in the hornfels), and by the development of pytgmatic syn-deformation veinlets. At the macroscopic scale, this event was responsible for low-angle shearing and mylonitization that may be seen in several places within the Aïn Barbar field, including the hydrothermally altered basal tectonic contact of the Numidian nappe, which was clearly reworked at that time (Marignac 1985). Early chlorite alteration zones within the Aïn Toutah micro-granite are equally affected by the shortening event, which formed stylolites that appear to be of very early Langhian age. Undeformed hydrothermal veins and veinlets are, however, everywhere present, thus showing that fluid circulation occurred after the end of the ductile deformation. In fact, insofar as the main metasomatic alteration zones are undeformed, the main hydrothermal event(s) must be considered post-kinematic for the extensional event. Following the late increments of ductile tectonics, more steeply dipping, brittle-ductile faults with a ~N170° E trend formed the first expression of what was to become the main Aïn Barbar vein system. These faults evolved from normal to transcurrent, N160° E shortening directions marked in particular by the epidotite bodies of the propylitic episode.

9 P-T Conditions of Mineralization

9.1 Estimates of Paleodepth at the Time of Ore Deposition

During the mesothermal stage, the confining pressure in the vein system may be estimated in two ways. First, we presume that in the very early Langhian, the Numidian flysch, which was emplaced during the late Burdigalian, was still uneroded. This is considered a realistic assumption, because not far to the west, in the Cap de Fer area, marine sediments of late Burdigalian and early Langhian age (Hilly 1962) testify to inboard moderate elevation above sea level (Fig. 2). On the other hand, as seen in Fig. 7a, the basal thrust contact was likely no more than ~100 m above the present-day erosional surface. This setting would yield, at the top of the Playfair vein, for instance, a paleodepth of ca. 1.3 km, or a 13 MPa hydrostatic pressure, during hydrothermal mineralization. Second,

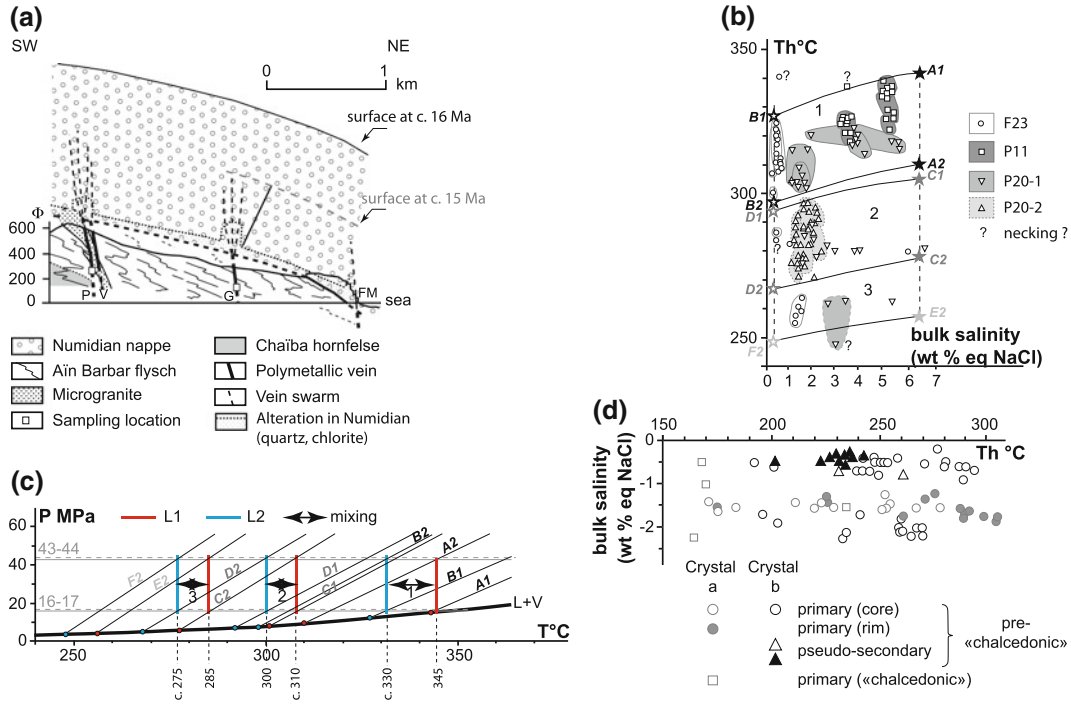

Fig. 7 P-T-X evolution in Aïn Barbar veins. **a** Estimation of paleodepth; **b** and **c**, Chalcopyrite episode of mesothermal stage; **b** Interpreted Th-bulk salinity diagram; **c** Isochores for selected inclusions from **b**, and interpretation in terms of fluctuating pressure; **d** epithermal stage: Th-salinity diagram (FI data from zoned comb quartz with core and chalcedonic fringe)

fluid inclusions (FIs) were observed in magmatic quartz of a Chaïba microgranite, located at the same potential paleodepth as the top of the Playfair vein (Fig. 7a). This microgranite is affected by a strong chlorite-adularia alteration focused along microcracks. The FIs are either aqueous or hypersaline three-phase (halite-bearing) liquid inclusions, indicative of a boiling event. Boiling conditions are estimated to have been ca. 350 °C and 130 MPa (Marignac 1988a), the latter pressure in excellent agreement with the preceding paleodepth estimate.

At the epithermal stage, chalcedonic quartz from the 80 m level of the Gray vein contains pseudo-secondary aqueous vapour FIs, recording a boiling event, which was evidently transient, since the vapour FIPs are overprinted by other pseudo-secondary, but two-phase, low-salinity aqueous FIs. Because the highest homogenization temperature measured in the aqueous FIs is 300 °C, the pressure could not have exceeded ~7 MPa in order to allow boiling at slightly higher temperatures, i.e., a paleodepth of ca. 0.7 km. This in turn suggests that the Numidian nappe cover was reduced from ca. 1200 m to no more than ca. 600 m (Fig. 7a).

9.2 P-T-X Conditions of Ore Deposition

In present-day active geothermal systems, silicate assemblages with quartz, chlorite, epidote, adularia, and phengite typically form at temperatures ≥250–280 °C (e.g., Browne 1978; Simmons and Browne 2000). Coeval precipitation of high-Fe sphalerite and hexagonal pyrrhotite, and development of the chalcopyrite disease in sphalerite, are also indications of relatively high temperatures of deposition, the latter implying a temperature increase beginning at the time of sphalerite precipitation (Barton and Bethke 1987; Eldridge et al. 1988). More precise sources of thermometric information are the fluid inclusions and the chlorite compositions.

Fluid inclusions are unfortunately rare within the Aïn Barbar ores. For the mesothermal stage, measurements were possible only in a few quartz crystals that grew just prior to chalcopyrite: the inclusions occur in numerous healed microcracks (fluid inclusion planes) that are considered pseudo-secondary (Marignac 1988a). Microthermometric results (Fig. 7b) suggest the mixing of fluids having different salinities, one a saline L1 fluid (≥ 7 wt% equiv NaCl) and the second a low-salinity L2 fluid (∼0.5 wt% equiv NaCl). Figure 7b may be interpreted using the modelling of such Th-salinity diagrams by Dubessy et al. (2003) to test various hypotheses of fluid mixing. Following the results of that study, it may be deduced that for Aïn Barbar (1) the mixing process was not isothermal, and that L1 was hotter than L2; (2) this mixing occurred in a reservoir at the temperature of the L2 fluid, allowing partial heat exchange between the reservoir and the mixed fluids; and (3) the pressure fluctuated between lithostatic and hydrostatic conditions. Concerning points (1) and (2), the argument is that the envelope of data points is a trapezoid, which is clearly the case for the points shown in the Fig. 7b, if it is taken in consideration that when fluid trapping was discontinuous, or when discrete pulses of fluids were mixed, or both, the data points will be also, and therefore a bulk envelope needs to be considered (Dubessy et al. 2003). Concerning point (3), a spread in Th at constant salinity, if not due to the necking-down phenomenon, is necessarily the result of pressure fluctuations for a specific event (e.g., specific mixing ratio between the two end-member fluids). At Aïn Barbar, necking of FIs is excluded as the main reason for the observed spread in Th at constant salinity, because the trend is typically represented by a combination of data points from distinct fluid inclusion planes that show a restricted dispersion of Th values (Fig. 7b). Pressure fluctuations between lithostatic and hydrostatic extremes are exactly what is expected for Aïn Barbar, owing to the numerous breccias of clearly hydraulic fracturing origin and the abundant crack-seal textures. The analyzed samples come from the 320–350 m levels of the Playfair vein, which as seen in Fig. 7a correspond to paleodepths of ca. 1.6–1.7 km, and pressures of 16–17 MPa (if hydrostatic) or 43–44 MPa (if lithostatic). However, the Th spread (Fig. 7b) is too great to allow modelling by a single anisothermal mixing event between L1 and L2. As shown in Fig. 7c, a series of mixing events must be considered, under an overall decrease in both the reservoir (or L2) and L1 temperatures, starting from ca. 345 °C (L1) and ca. 330 °C (L2), and apparently ending at ca. 285 °C (L1) and ca. 275 °C (L2). This temperature interval likely spans chalcopyrite deposition and the monoclinic-pyrrhotite to pyrite transformation, because the studied quartz crystals with their pseudo-secondary fluid inclusion planes are rimmed by overgrowths coeval with the late siderite.

For the epithermal stage, FIs from the chalcedonic quartz episode (Abaïd vein, at the 80 m level) equally support anisothermal fluid mixing under fluctuating pressure conditions (Fig. 7d), involving a low-salinity fluid (∼0.5 wt% equiv NaCl), very similar to the L2 end-member of the mesothermal stage and of likely meteoric origin, and a slightly more saline fluid (∼2.0 wt% equiv NaCl) of unknown origin. The formational temperatures were between 300 and 170 °C, and included several heat recharge events as recorded by the FIs (Fig. 7d).

9.3 Chlorite Geothermometry

The temperature dependence of chlorite compositions is well known (e.g., de Caritat et al. 1993, and references therein). Qualitatively, the contents of Fe + Mg and Al^{iv} increase, and Al^{vi} and octahedral vacancy decrease, when temperature increases. Numerous geothermometers, both empirical (e.g., Cathelineau and Nieva 1985; Cathelineau 1988; Zang and Fyfe 1995) and thermodynamically based (Bourdelle et al. 2013a; b), have been devised. In this work, a mean of two empirical thermometers (Cathelineau 1988; Zang and Fyfe 1995) appear to yield the most consistent results if the temperature of chalcopyrite deposition is taken as a reference (Fig. 8). Chlorite from the early propylitic

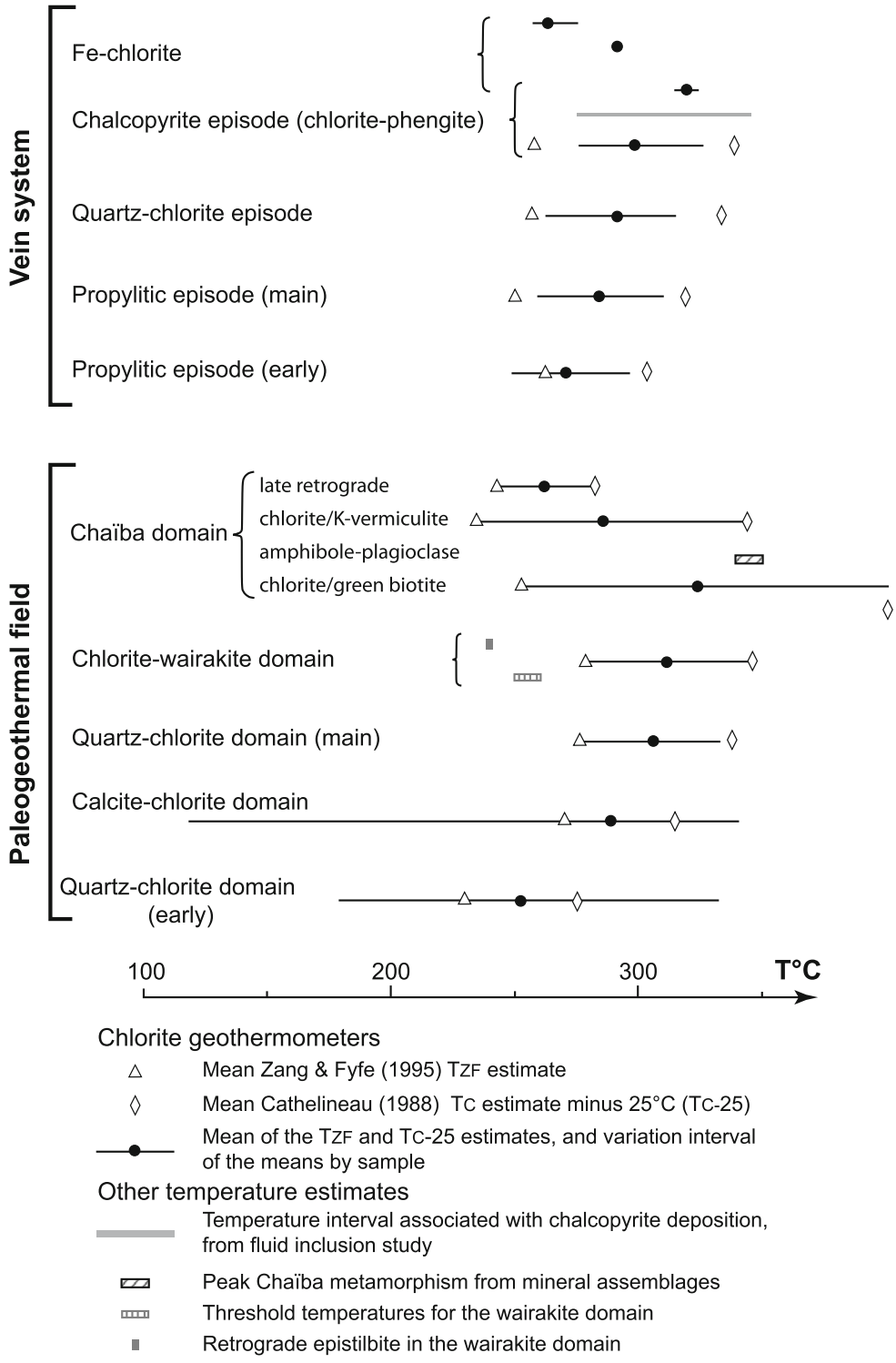

Fig. 8 Evolution of temperatures in Aïn Barbar paleogeothermal field and mesothermal mineralization based on chlorite geothermometry and other temperature estimates. Mean value obtained from two chlorite thermometers is used: Zang and Fyfe (1995), which underestimates, and Cathelineau (1988), which overestimates, the temperatures. For latter reference, lower confidence interval of estimated T is 25 °C

episode (deformed chlorite veinlets, first stage of chlorite breccia) has the lowest temperatures (ca. 270 °C). Starting from this early event, temperature continuously increased through ca. 280 °C (main propylitic episode) and ca. 290 °C (quartz-chlorite episode), up to ca. 300–320 °C during the chalcopyrite stage, and then decreased to ca. 260 °C when the late iron-rich chlorites formed. As expected from the chalcopyrite disease phenomenon, the sphalerite-galena-(hexagonal pyrrhotite) depositional temperature, which was likely close to the propylitic temperature (ca. 280 °C), appears lower than the chalcopyrite depositional temperature.

10 Temperature Estimates for the Hydrothermal Metamorphism

The peak amphibole + plagioclase assemblage within the Chaïba domain formed at low pressure (depth no more than ca. 2 km) under temperatures of ca. 340–350 °C, in the presence of a fluid with XH_2O of ca. 0.80 (Marignac 1985, 1988b). However, higher temperatures, up to 370–380 °C, must have been reached at an early stage in the core of the domain to allow the formation of clinopyroxene. The calcite-chlorite to chlorite-wairakite boundary corresponds to a decarbonation reaction of the type Al-bearing phyllite + calcite = wairakite + CO_2, where the phyllite may consist of illite, illite + chlorite, Ca-smectite, or even kaolinite (Marignac 1985). Relative to the calcite-chlorite domain, this reaction implies a temperature increase, but a decrease in XCO_2 of the fluid to less than ~0.05 is also necessary in order to stabilize wairakite (Marignac 1985). The characteristic abundance of Ca-smectite at the boundary with the calcite-chlorite domain is the result of the wairakite + CO_2 = Ca-smectite + calcite + quartz reaction. In the wairakite domain, both the stability of the quartz-wairakite assemblage and the absence of yugawaralite demonstrate that temperatures were higher than 250 °C (Zeng and Liou 1982); the presence of calcic plagioclase testifies to temperatures higher than 260 °C when $XH_2O \geq 0.95$ (Marignac 1985). The retrograde formation of epistilbite in the quartz-epidote-calcite-wairakite microvugs indicates, however, a ca. 240 °C temperature (if the pressure is considered hydrostatic, i.e., ca. 10 MPa), according to the data in Lo (1978) for the quartz + wairakite = epistilbite reaction.

Further insight into the temperature range may be obtained from chlorite geothermometry (Fig. 8). The temperature estimates continually increase from the chlorite-calcite domain (and early chlorites in the quartz-chlorite domain: deformed veinlets, interstitial neoformed chlorite) to the quartz-chlorite and chlorite-wairakite domain, starting from ca. 250–280 °C up to ca. 300 °C. The chlorite interstratified with the green biotite yields a temperature of ca. 330 °C (with a high dispersion). In the Chaïba domain, the chlorite interstratified with the retrograde K-vermiculite yields ca. 290 °C (with a high dispersion), whereas the late chlorite has distinctly lower temperatures, of ca. 260 °C.

11 Isotope Data

A few sulphur isotope values were obtained by Laouar et al. (2002) on pyrite, sphalerite, and chalcopyrite of unidentified origin from the Aïn Barbar ores. Reported $\delta^{34}S$ values are –10.8 to –9.6 ‰, interpreted here as indicating a significant sedimentary source for the sulphur. Lead isotope compositions were measured on representative sulphides from the mesothermal and epithermal stages (Table 1). The data range from rather un-radiogenic ($^{206}Pb/^{204}Pb$ 18.565, $^{207}Pb/^{204}Pb$ 15.541, $^{208}Pb/^{204}Pb$ 38.331) to much more radiogenic values ($^{206}Pb/^{204}$ 18.823, $^{207}Pb/^{204}Pb$ 15.741, $Pb^{208}Pb/^{204}Pb$ 39.119), overall defining three separate arrays (Fig. 9a). Lead isotope compositions are displaced towards more radiogenic $^{206}Pb/^{204}Pb$ values from the first mineralizing episode to the chalcopyrite episode, the epithermal stage yielding intermediate compositions.

Table 1 Lead isotope compositions of Aïn Barbar ores (from Nigretto 1992)

Mineral	Vein	Sample	$^{206}Pb/^{204}Pb$	$^{207}Pb/^{204}Pb$	$^{208}Pb/^{204}Pb$
			2σ	2σ	2σ
Mesothermal stage					
Galena	Gray	G11b	18.823	15.742	39.119
			0.009	0.012	0.028
	Playfair	P9-67 c	18.801	15.574	38.911
			0.005	0.003	0.008
	Victor	V12 b	18.740	15.586	38.661
			0.005	0.004	0.010
Sphalerite	Abaïd	A22 a	18.699	15.544	38.428
			0.004	0.003	0.008
	Playfair	P9-67 b	18.629	15.554	38.401
			0.004	0.010	0.028
	Victor	V12 a	18.640	15.494	38.271
			0.034	0.037	0.100
H-Pyrrhotite	Salah	Sa66 a	18.642	15.467	38.226
			0.020	0.029	0.078
Chalcopyrite	Abaïd	A24 b	18.786	15.608	38.696
			0.008	0.008	0.021
	Playfair	P9-67 e	18.705	15.518	38.468
			0.005	0.007	0.014
	Victor	V12 c	18.814	15.663	38.739
			0.012	0.010	0.029
Epithermal stage					
Galena	Abaïd	Ab80-2 b	18.868	15.700	38.967
			0.012	0.011	0.040
	Playfair	P14 d	18.795	15.680	38.969
			0.013	0.008	0.027
	Playfair	Pl300-J b	18.791	15.698	39.015
			0.008	0.008	0.017
Sphalerite	Abaïd	Ab80-2 a	18.655	15.541	38.605
			0.044	0.030	0.081
	Playfair	Pl300-J e	18.732	15.583	38.590
			0.010	0.007	0.022
	Victor	V4 c	18.739	15.614	38.666
			0.009	0.010	0.022
Chalcopyrite	Abaïd	Ab80-2 c	18.565	15.546	38.331
			0.053	0.052	0.097
	Playfair	Pl300-J c	18.652	15.497	38.427
			0.031	0.025	0.078

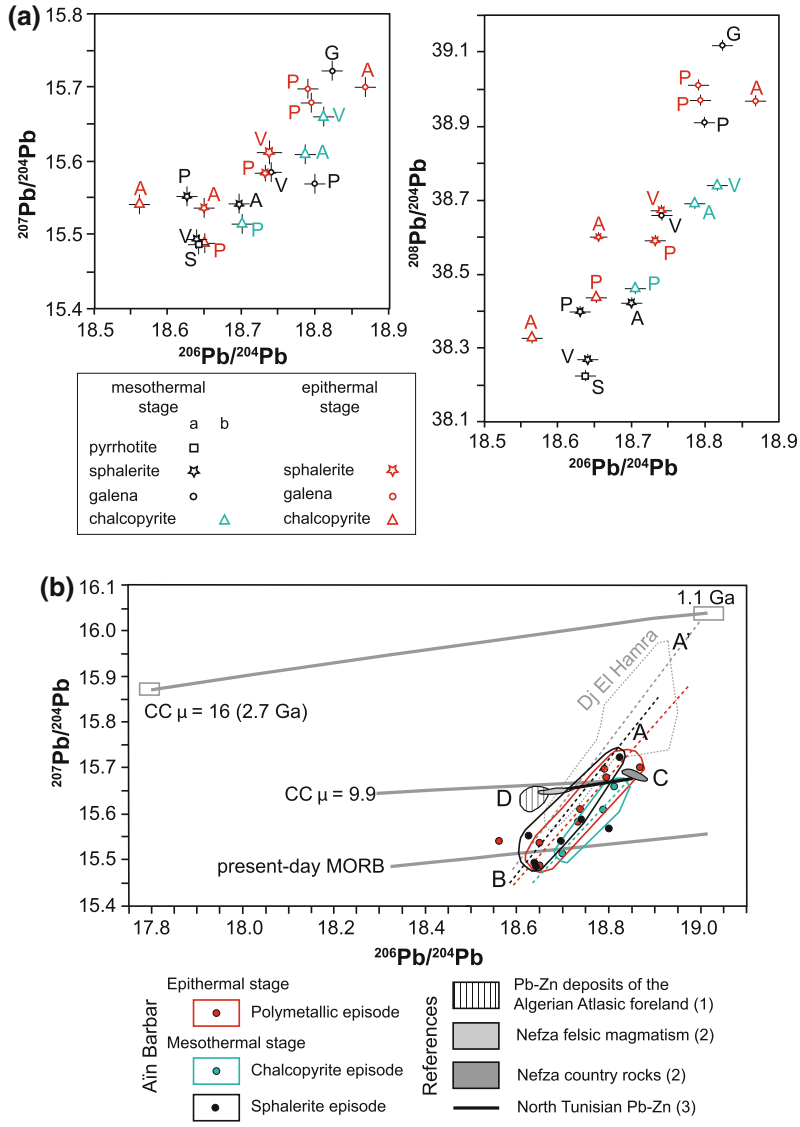

Fig. 9 Lead isotope compositions of selected sulphides from two main hydrothermal stages (**a**), and interpretation by four end-member model (**b**). Sources of data: *1* Touahri (1987); *2* Decrée et al. (2014); *3* Bouhlel et al. (2013); Charef (1986); Jemmali et al. (2011, 2013a, b). Abbreviations: *CC* continental crust; μ, $^{238}U/^{206}Pb$ ratio used in growth curves calculation (see text)

12 Aïn Barbar as a High-Enthalpy Liquid-Dominated Paleogeothermal System

The hydrothermal metamorphism in the Aïn Barbar inlier is typical of the so-called "telescoped low-pressure, low-temperature facies series" (Schiffman et al. 1984) that characterizes present-day (active) high-enthalpy geothermal fields hosted in sedimentary reservoirs, such as Cerro Prieto in Mexico (Bird et al. 1984; Schiffman et al. 1984), the Salton Sea in California (McDowell and Elders 1980), and Larderello in Italy (Cavaretta et al. 1982). In the Larderello system, actinolite and clinopyroxene are found below 1500 m depth (Cavaretta et al. 1982); actinolite occurs at 1100 m in the Salton Sea (McDowell and Elders 1980), similar to the estimated depths of formation for this mineral at Aïn Barbar (Fig. 7a). In the Salton Sea, amphibole appearance correlates with a textural change towards a hornfelsic texture (McDowell and Elders 1980), as at Aïn Barbar. These facts

represent compelling evidence for the existence of a high-enthalpy paleogeothermal system in the Aïn Barbar region at the beginning of the Langhian. Owing to the low-permeability cap of the Numidian (with additional self-sealing effects), this most likely was a blind system, and pressures were mostly lithostatic with the consequence that fluid circulations were chiefly in the liquid state (liquid-dominated system). In present-day geothermal fields, active polymetallic mineralization is observed both in sediment-hosted (Salton Sea; McKibben and Elders 1985) and volcanic-hosted (Broadlands-Ohaaki; Simmons and Browne 1997) settings, but these mineralizations are disseminated in veinlets or microvugs. Fossil high-enthalpy geothermal systems with significant polymetallic vein mineralization are equally rare, the Tayoltita deposit in Mexico (Conrad et al. 1992) being an example, although it is hosted in andesite. The Aïn Barbar sediment-hosted paleogeothermal system and its polymetallic lodes are therefore rather exceptional.

12.1 Architecture and Evolution of the Paleogeothermal System

The main hydrothermal domains are organized according to a concentric pattern, with a core formed by the Chaïba hornfels and outward quartz-chlorite and calcite-chlorite domains (Fig. 4), with boundaries roughly conforming to the mean bedding in the host flysch. The estimated temperatures more or less regularly decrease from the Chaïba core to the external calcite-chlorite domain (Fig. 8), with an apparent geothermal gradient of ca. 90 °C km^{-1}, based on the ~0.8 km distance between the top of the chlorite-calcite zone and the actinolite front in the Chaïba domain. Elevated gradients of ca. 100 °C km^{-1} are common in active geothermal systems associated with a granite intrusion at shallow depth, for instance at Larderello in Italy (Cathelineau et al. 1994) or Kakkonda in Japan (Ohtani et al. 2001). However, the chlorite-wairakite domain is excluded from this zoning because it (1) is rooted in linear zones lining the Abaïd-Gray vein system (Fig. 4), (2) overprints the chlorite-calcite domain, and (3) formed at a significantly higher temperature, the wairakite assemblages being prograde. This domain would thus record invasion of the chlorite-calcite domain reservoir by hydrothermal fluids derived from the Abaïd-Gray vein system. This interpretation points to a relationship between the hydrothermal metamorphism and development of the mineralized vein system. Such a model may be better appreciated by considering the chlorite crystal chemistry shown in Fig. 10. The data points are consistently organized in three arrays, grouping (1) early chlorite from the quartz-chlorite domain with those of the chlorite-calcite domain (array A), (2) chlorite from the chlorite-wairakite domain and the quartz-chlorite domain with those of the early propylitic episode (array B), and (3) chlorite of the mesothermal stage in the veins (array C). We attribute these three arrays as recording three steps of the evolution in the Aïn Barbar vein system. The first array represents the primary zoning, with a core in the Chaïba domain and an outward zone in the flysch reservoir(s). The second array records the influx into some parts of the reservoir by hydrothermal fluids issuing from the early vein systems, in which developed the early propylitic event. The present-day quartz-chlorite domain thus appears composite, with unevenly superimposition of the two first stages of mineralization. The third document the mesothermal stage, with fluid circulation apparently restricted to the vein system and its close vicinity, being responsible for the linear propylitic zones that fringe the veins at the map scale.

12.2 Mass Transfer in the Paleogeothermal System

Mass-balance calculations show that to transform the Aïn Barbar flysch into the Chaïba hornfels sodium (and strontium) must be added, whereas aluminium and titanium remain more or less constant and all the other elements are leached

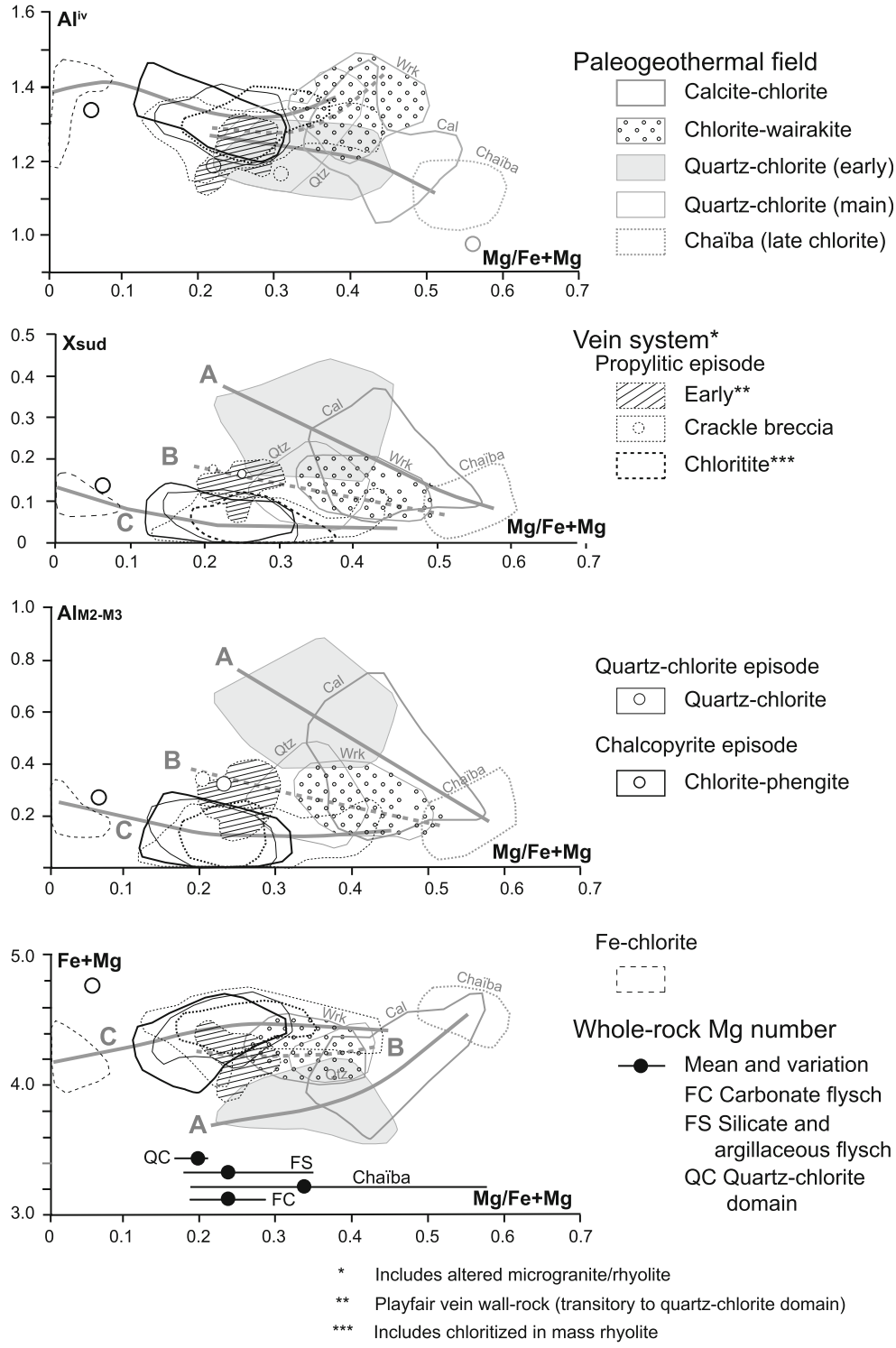

Fig. 10 Crystal chemistry of Aïn Barbar chlorites. Structural formulas were computed using sequential scheme of Vidal et al. (2001) to fit the theoretical formula $[(Fe, Mg, Al)_4^{M2-M3}(Fe, Mg, Al, \Diamond)^{M1}Al^{M4}]_6^{vi}[Si_2^{T1}(Si, Al)_2^{T2}]^{iv}O_{10}(0H)_8$, with four octahedral sites (M1 to 4) and two tetrahedral sites (T1 and T2), where ◇ is an octahedral vacancy equal to the sudoite molar fraction (X_{Sud}) in chlorite solid solution

(Marignac 1985, 1988b). The calcium extracted from the protolith of the hornfels could have contributed to the formation of abundant calcite spar in the calcite-chlorite domain. Chlorite formation at the expense of illite demands the addition of iron and magnesium, which could come from the leached Chaïba rocks. The Mg/Fe ratio of the chlorite-forming fluid was high: as shown in Fig. 10, the Mg# of the older hydrothermal chlorite is generally higher than that of the corresponding wall rocks of the different hydrothermal domains. There is, however, a tendency of decreasing chlorite Mg# with time, which culminates during the mesothermal stage of mineralization. This trend is tentatively correlated with the disappearance in the hornfels of the otherwise abundant diagenetic pyrite of the flysch, thus explaining the higher Mg# than the protolith (Fig. 10). Because minor base-metal sulphides occur in the chlorite-wairakite domain, it may also be suggested that base metals were leached from the Chaïba domain while the leached diagenetic pyrite provided the sulphur. Compared to the less-transformed carbonate flysch, the chlorite-wairakite domain is enriched in base metals (47 ppm vs. 23 ppm Cu, 230 ppm vs. 178 ppm Zn, and 42 ppm vs. 10 ppm Pb), whereas the Chaïba plagioclase-rich rocks are strongly depleted (10 ppm Cu, 27 ppm Zn, < 4 ppm Pb). On a constant titanium basis, it may be estimated that ∼20 ppm Cu was leached from the Chaïba domain; moreover, calculations show that between 200 and 350 kt Cu was extracted from the hornfels, i.e., a sufficient amount to provide the ca. 140 kt deposited within the Aïn Barbar veins (Marignac 1988b). Similar conclusions may be reached for the source of zinc and lead in the veins. In the active Salton Sea geothermal system, brines issued from a deep drill hole contain significant base metal contents, which have been attributed to the release of these metals from their host sediments "as the metamorphism proceeds" (Skinner et al. 1967), exactly as proposed here for the Aïn Barbar system.

12.3 Source of Metals: The Basement Connection

The massive sodium metasomatism that created the plagioclase-rich hornfels testifies to the invasion of the flysch reservoir by a Na–Sr-rich hydrothermal fluid having an elevated Na/Ca ratio. These characteristics would fit a fluid that had equilibrated with the plagioclase-rich gneisses in the underlying basement, which have a Na/Ca ratio of ∼6.8 (Aïssa 1996). The question then arises of a possible contribution from the basement to the metal budget of the Aïn Barbar vein system. Interpretation of the lead isotope data leads indeed to the conclusion that, as far as lead is concerned, the basement of the Edough massif did contribute to the Aïn Barbar mineralization. The Aïn Barbar lead isotope data are compared in Fig. 9b with those of a series of Pb–Zn deposits from the Tunisian internal zones (Numidian nappe domain), the Tellian fold-and-thrust belt, and the Sahara foreland. Those deposits show a spread of Pb-isotope values between "Neogene magmatic" (C) and "sedimentary host rock" (D) end-members, attributed here to a mixing trend between lead sources characteristic of a Variscan basement (Fig. 9b). The Aïn Barbar trends are distinctly oblique, involving end-member $^{207}Pb/^{204}Pb$ compositions, respectively less radiogenic (A) and more radiogenic (B), than the two end-members C and D (Fig. 9b).

However, the displacement between the separate mesothermal and epithermal trends for Aïn Barbar may be interpreted as reflecting exactly the same C-D trend as shown by the other deposits in North Africa and that for Aïn Barbar it is the chalcopyrite episode, which shows a greater influence of the sedimentary contribution. The A-B trend may be interpreted as a contribution from the underlying Edough basement. The B end-member represents the contribution of a highly radiogenic "J-type" lead (Russell and Farquhar 1960), and may be modelled by the Neoproterozoic (ca. 1 Ga) extraction of a J-type

lead evolved from an anomalously U-rich, Neoarchean continental crust (Fig. 9b). The Edough gneisses, which are likely Pan-African metagraywacke (Aïssa 1996), are good candidates for the source of such a J-type lead. The A end-member, on the other hand, is evidently derived from a mafic source, which may be the large amphibolite bodies in the Edough basement. An amphibolite contribution to the copper budget is consistent with this model. A further argument for an amphibolite contribution may be found in the sulphur isotope data of Laouar et al. (2002) for pyrrhotite from the Kef Lakhal (Voile Noire) massif, yielding mostly negative values ($\delta^{34}S$ –18 ‰ to +2.1 ‰) that are similar to those reported by the same authors for the Aïn Barbar sulphides.

12.4 The Problem of the Heat Source

The microgranite intrusions remain unaffected by the Chaïba metasomatism, but, in the external part of the Chaïba domain, where clinopyroxene or amphibole are generally absent, these minerals may be found a few meters around the microgranite bodies. Thus, Chaïba metasomatism (and by inference, the whole of the hydrothermal metamorphism) and microgranite intrusions were broadly coeval. However, rough calculations show that the visible microgranite intrusions were not sufficient to provide the required heat. Assuming a 10 % porosity (a current value in Cretaceous flysch of similar tectonic position in the Mediterranean Alpine belt; e.g., Czubek et al. 1982, Douvens and Diamantopoulos 1997), to warm 1 m^3 of reservoir rocks from an initial T0 to a final T1 temperature, we need a quantity of heat of $(0.9 \times 0.8 + 0.1 \times 4.18) \times (T1 - T0) \times 10^3$ kJ $= 1.1 \times (T1 - T0) \times 10^3$ kJ, adopting a rock Cp of 0.8 kJ kg^{-1} (Vorsteen and Schellschmidt 2003). For all the entire paleogeothermal field, T0 would have been no more than ca 50 °C (with geothermal gradients no more than 40 °C km^{-1}, which seems reasonable). It is convenient to model the heated Aïn Barbar aquifer as the assemblage of a Chaïba reservoir, with a volume of ca 9 km^3 ($5.5 \times 4 \times 0.4$ km) and a median temperature of 350 °C, and a flysch reservoir, with a volume of ca 11 km^3 ($4 \times 4 \times 0.7$ km) and a median temperature of 275 °C. Thus the total heat quantity required to warm the paleogeothermal reservoirs would amount to ca $9 \times 1.1 \times (350 - 50) \times 10^9 \times 10^3 + 11 \times 1.1 \times (275 - 50) \times 10^9 \times 10^3 = (3071 + 28{,}178) \times 10^{12} = 6 \times 10^{15}$ kJ. On the other hand, 1 m^3 of a granite magma heated at 800 °C and cooled down to an ambient reservoir temperature of ca 400 °C would deliver a heat quantity Q equal to $2400 \times \Delta H + 2400 \times Cp \times (800 - 400)$ kJ, with ΔH the latent heat of fusion (taken at 335 kJ kg^{-1}) and Cp = 1.05 kJ kg^{-1} (Heuze 1981), i.e., $Q = 756 \times 10^3 + 804 \times 10^3 = 1560 \times 10^3$ kJ, the granite density being taken at 2.4. It results that heating of the Aïn Barbar reservoirs would have required $\sim 2 \times 10^9$ m^3 (or 2 km^3) of granite intrusions. The volume of each of the 15 small bodies of the Chaïba massif may be estimated between ca 4×10^6 and 10×10^6 m^3 and the Playfair microgranite dike is no more than $\sim 25 \times 10^6$ m^3 (see Fig. 4), and thus the total volume of the visible bodies may not exceed ca 175×10^6 m^3, far less than the total required. Thus, the heat budget of the microgranite intrusions was not sufficient to warm the whole Aïn Barbar aquifer—not considering that water in the basement rocks would also had to be warmed. These intrusions are however likely to have been protruding from a larger body, similar in size to the sill-like microgranite intrusions of the western Edough massif (Fig. 2) that were emplaced at the basement-flysch nappe boundary (Fig. 11). With an observed areal occupancy up to ca 10 km^2 in the Edough and an estimated thickness of about 200 m, the volume of such a body (about 2 km^3) could be (just) sufficient to warm the paleogeothermal aquifers, not considering however the heating of the basement reservoir. However, once the heat contained in the intrusion was exhausted, whereas the reservoirs were warmed at the convenient temperature, it remained to sustain this temperature regime for some time, the duration of which is likely to be in the order of several kyr to several 10 s of kyr, given the observed succession of distinct hydrothermal events in the paleogeothermal field. Moreover,

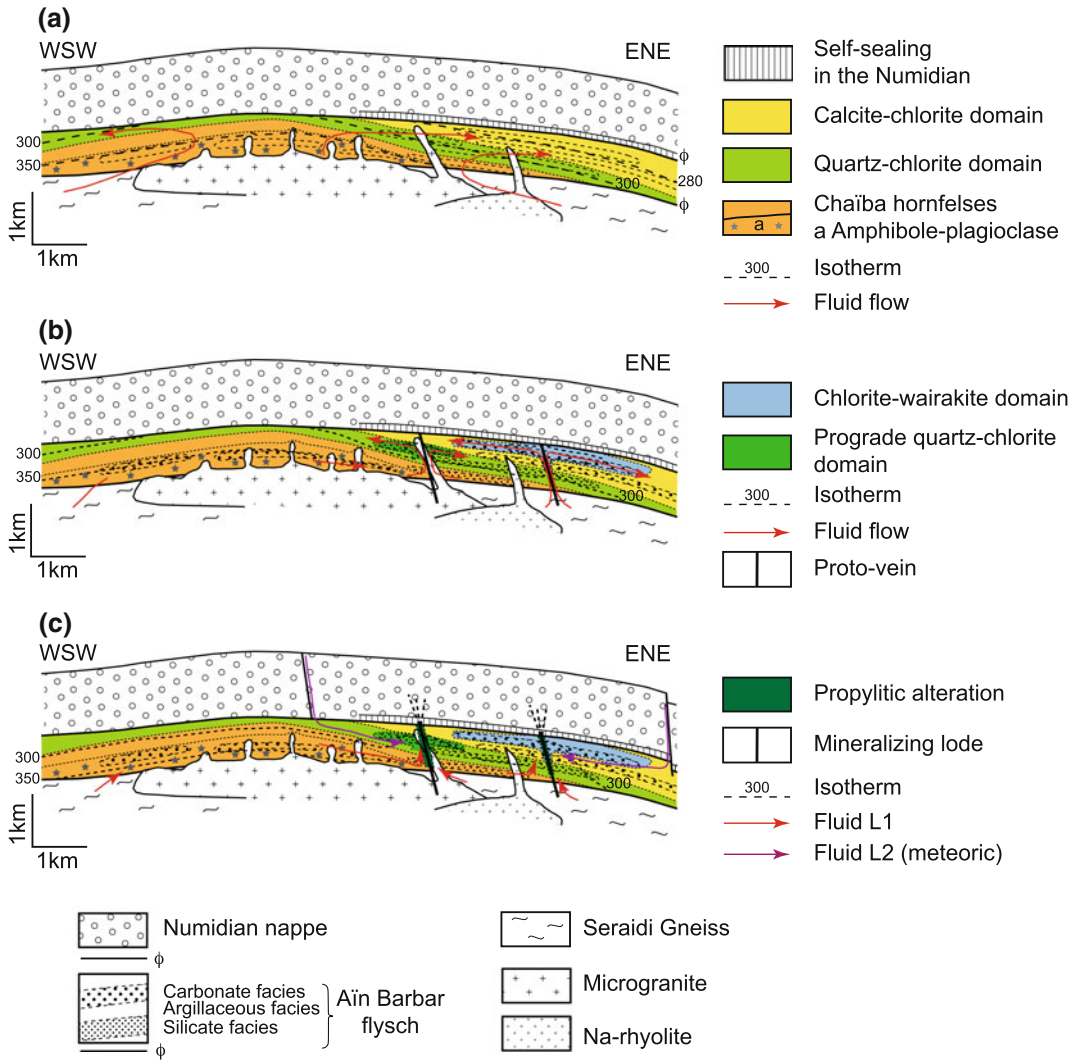

Fig. 11 Conceptual model of three-stage evolution of paleogeothermal, high-enthalpy, liquid-dominated Aïn Barbar field. **a** "Salton Sea" stage: deep "metamorphic" fluids contained in basement are mobilized by early Langhian intrusion of magmatic rocks, including a large microgranite body at basement-Cretaceous flysch boundary; large convection cells are established and flysch reservoirs are invaded by hot waters during origin of the hydrothermal metamorphism, under an impermeable Numidian flysch cap. **b** "Taupo" stage: as a consequence of both partial sealing in deepest aquifer (Chaïba hornfels) and formation of fracture zones ("proto-lodes"), plumes of deep and hot fluids are transferred into shallow aquifers, where small convection cells are established. Owing to control on wairakite deposition by XCO_2 (i.e., fluid-rock ratio in decarbonating rocks), boundary of calcite-chlorite domain is not coincident with an isotherm. **c** Mesothermal ("Tayoltita") stage: reservoirs being more or less sealed, circulation of deep fluids is now restricted to active faults that act as main channels and host the mineralized lodes; contemporaneously, surficial (meteoric) waters may invade shallow reservoirs and mix with deep fluids to promote mineralization

the life-time of such a small intrusion is short, less than 20 kyr for a ca 1 km thick sill-like body according to Michel et al. (2008). But, a first order approximation, based on the "conductive thermal shock" model, show that to attain a 250 °C temperature at ~1 km from the intrusion boundary (as is the case at Aïn Barbar), a time interval of ca 200 kyr would elapse (using a

thermal conductivity of 1.5 W m^{-1} K^{-1}; Vorsteen and Schellschmidt 2003). An additional source of heat is therefore a necessity. The presence of a large magmatic body emplaced at depth beneath the Aïn Barbar field is apparently testified by the conspicuous magnetic anomaly that underlies the Edough-Cap de Fer massif. To the west, in the Lesser Kabylia, a large granite batholith, the Bougaroun granite, with a suite of microgranite and rhyolite, was emplaced into the internal massif basement during the Langhian (Bouillin 1979; Fourcade et al. 2001). It is likely that a similar granite batholith was emplaced in the Edough-Cap de Fer area at ca. 16 Ma, and thus was ultimately responsible for the Aïn Barbar thermal anomaly.

13 Conclusions

The Aïn Barbar inlier exposes a fossil high-enthalpy geothermal system, which evolved in three stages. In the first stage, the Aïn Barbar flysch was invaded by hydrothermal fluids under an impermeable cover of Numidian flysch, yielding the Chaïba metasomatic plagioclase-rich rocks and the early quartz-chlorite and calcite-chlorite domains. During that stage, the paleogeothermal system was very similar to the present-day Salton Sea geothermal field. The hydrothermal fluids likely issued from the basement. At that time, a paleogeothermal gradient of $\sim$90 °C km^{-1} seems to have been established, and the thermal anomaly (T ≥ 350 °C) was confined to the deepest parts of the paleoaquifer (Fig. 11a). In the second stage, the thermal anomaly (T ≥ 300 °C) was transferred to higher levels, heat advection being linked to a plume of hot fluid that was channelled through the now active fracture zones, during the origin of the vein systems and expanding into the higher portions of the flysch reservoir (Fig. 11b). At that time, the Aïn Barbar geothermal system was similar to the modern Taupo systems in New Zealand (Rowland and Symmons 2012). During these first two stages, the paleogeothermal system evolved under the thick impermeable cap made by the self-sealed Numidian flysch, producing chloritized and silicified alteration zones. As a consequence of this sealing cap, pressure was close to lithostatic and the system was entirely liquid-dominated. In the third stage ucode Type="General_Pun">—the mesothermal stage in the vein systems—fluid flow was localized in narrow conduits corresponding to the high permeability zones associated with faulting, which was still active as part of a transtensional tectonic regime (Fig. 11c). The Aïn Barbar system may be compared to the paleohydrothermal system of the Tayoltita vein deposit in Mexico (Conrad et al. 1992). During this stage, active fracturing repeatedly opened fractures in the Numidian cap, yielding the nearly barren "Filon de la Mer" veins (Fig. 7a), and allowing the fluctuating pressures recorded by the FIs trapped during the chalcopyrite episode. Local boiling was possible under the hydrostatic conditions for fluids having temperatures ≥350 °C (Fig. 7c). However, as the temperature of the circulating fluids rapidly decreased, the geothermal system remained basically liquid-dominated. During this third stage, a heated meteoric fluid was involved in the paleogeothermal system. The temperature of the deep (hot, saline) fluid flowing through the vein system was lowered from 345 °C down to 285 °C during the chalcopyrite episode of the mesothermal stage, likely reflecting a similar temperature reduction in the Chaïba reservoir. It is therefore during this episode that the K-vermiculite retrograde assemblage was established in the Chaïba domain; this interpretation is consistent with the potassium input recorded in the vein system and coeval alteration (adularia, phengite) occurring within the microgranites and Na-rhyolites. Simultaneously, the temperature of the heated meteoric fluid, which likely exchanged heat with the highest parts of the geothermal reservoir, decreased from 330 to 275 °C. A general lowering of the temperature in the reservoirs is thus apparent during the mesothermal stage of the Aïn Barbar paleogeothermal field. At the end of this stage, the lower recorded temperature being $\sim$260° in the Chaïba domain and $\sim$240 °C in the wairakite domain, the paleogeothermal gradient was at most $\sim$20 °C km^{-1} within the reservoir.

In all of the hydrothermal domains (particularly Chaïba), there was a general evolutionary tendency from early lithologically controlled recrystallization and metasomatic replacement to later microfracture healing and sealing (Batzle and Simmons 1976), which overall seemingly records a progressive decrease in bulk rock permeability. However, the numerous veinlets and microvugs uniformly have the same mineralogy as the surrounding rocks at the centimeter scale, meaning that lithologic permeability was still controlling, at least in part, the fluid circulation. This evolution in permeability controls culminated with the mesothermal stage, when the channelling of fluid circulation in the restricted volume of the fracture zones correlates with the most intense alteration in the vein walls. A similar evolution is apparent for the Tayoltita paleogeothermal system that hosts significant polymetallic and/or precious-metal vein mineralization (Conrad et al. 1992).

Acknowledgments J. Slack is warmly thanked for his careful editing work and improvement of the manuscript. M. Pichavant and S. Barrat cheerfully helped for thermodynamic calculations.

References

Ahmed-Saïd Y, Leake BE, Rogers G (1993) The petrology, geochemistry and petrogenesis of the Edough igneous rocks, Annaba, NE Algeria. J Afr Earth Sci 17:111–123

Aïssa DE (1996) Etude géologique, géochimique et métallogénique du massif de l'Edough (Annaba, NE Algérie). Unpubl. Thèse Doctorat Etat, USTHB, Alger, Algeria, 500 pp

Aïssa DE, Cheilletz A, Gasquet D, Marignac C (1995) Alpine metamorphic core complexes and metallogenesis: the Edough case (NE Algeria). In: Pašava J, Kříbek B, Žák K (eds) Mineral deposits: from their origin to their environmental impacts, Proceed 3rd Biennial SGA Meeting. Prague, Balkema Rotterdam, pp 23–26

Aïssa DE, Marignac C, Cheilletz A, Gasquet D (1998) Géologie et métallogénie sommaire du massif de l'Edough (NE Algérie). Mémoire Service Géologique de l'Algérie 9:7–55

Bagdasarjan GP, Bajanik S, Vass D (1973) Age radiométrique du volcanisme néogène dans le Nord tunisien. Notes Serv Géol Tunisie 40:79–83

Barton PB Jr (1978) Some ore textures involving sphalerite from the Furutobe mine, Akita Prefecture, Japan. Mining Geol 28:293–300

Barton PB Jr, Bethke PM (1987) Chalcopyrite disease in sphalerite: pathology and epidemiology. Amer Mineral 72:451–467

Batzle ML, Simmons G (1976) Microfractures in rocks from two geothermal areas. Earth Planet Sci Lett 30:71–93

Bellon H (1981) Chronologie radiométrique K-Ar des manifestations magmatiques autour de la Méditerranée occidentale entre 33 et 1 Ma. In: Wezel FC (ed) Sedimentary basins of Mediterranean margins. Technoprint, Bologne, pp 341–360

Bird DK, Schiffman P, Elders WA, Williams AE, McDowell SD (1984) Calc-silicate mineralization in active geothermal systems. Econ Geol 79:671–695

Bouhlel S, Garnit H, Bejaoui J, Skaggs S (2013) Lead isotopes signatures of the MVT lead-zinc (± F) deposits across central-north Tunisia: evidence for the heterogeneity in uranium component of the underlying source rocks. In: Jonsson E et al. (eds), Mineral deposit research for a high-tech world, Proceedings of 12th Biennial SGA Meeting, Uppsala, Sweden, Geol Survey Sweden, v. 2, pp 612–615

Bouillin J-P (1979) La transversale de Collo et El-Milia (Petite Kabylie): une région-clef pour l'interprétation alpine de la chaîne littorale d'Algérie. Mémoire Soc Geol France 57, 84 pp

Bourdelle F, Parra T, Beyssa O, Chopin C, Vidal O (2013a) Clay minerals as geo-thermometer: a comparative study based on high spatial resolution analyses of illite and chlorite in Gulf Coast sandstones (Texas, U.S.A). Amer Mineral 98:914–926

Bourdelle F, Parra T, Chopin C, Beyssac O (2013b) A new chlorite geothermometer for diagenetic to low-grade conditions. Contrib Mineral Petrol 165:723–735

Browne PRL (1978) Hydrothermal alteration in active geothermal fields. Ann Rev Earth Planet Sci 6:229–250

Brunel M, Hammor D, Misseri M, Gleizes G, Bouleton J (1988) Cisaillements synmétamorphiques avec transport vers le Nord-Ouest dans le massif cristallin de l'Edough (Est Algérien). C R Acad Sci Paris 306 (II):1039–1045

Caby R, Hammor D (1992) Le massif cristallin de l'Edough (Algérie): un "metamorphic core complex" d'âge Miocène dans les Maghrébides. C R Acad Sci Paris 314:829–835

Cathelineau M (1988) Cation site occupancy in chlorites and illites as a function of temperature. Clay Miner 23:471–485

Cathelineau M, Nieva D (1985) A chlorite solid solution geothermometer: the Los Azufres (Mexico) geothermal system. Contrib Mineral Petrol 91:235–244

Cathelineau M, Marignac C, Boiron MC, Gianelli G, Puxeddu M (1994) Evidence for Li-rich brines and early magmatic fluid-rock interaction in the Larderello geothermal system. Geochim Cosmochim Acta 58:1083–1099

Cavaretta G, Gianelli G, Puxeddu M (1982) Formation of authigenic minerals and their use as indicators of the physicochemical parameters of the fluid in the Larderello-Travale geothermal field. Econ Geol 77:1071–1084

Charef A (1986) La nature et le rôle des phases fluids associées à la mineralisation Pb-Zn dans les formations carbonates et leurs consequences métallogéniques: étude des inclusions fluids et des isotopes (H, C, O, S, Pb) des gisements des Malines (France), Jebel Hallouf-Sidi Bou Aouane at Fedj-el-Adoum (Tunisie). Unpubl Thèse Doct Etat, Nancy, France, 291 pp

Conrad ME, Petersen U, O'Neil JR (1992) Evolution of an Au-Ag-producing hydrothermal system: the Tayoltita mine, Durango, Mexico. Econ Geol 87:1451–1474

Czubek JA, Buniak M, Loskiewicz J, Bogacz J, Dabrowski J, Lenda A, Zorski T (1982) Statistical and geostatistical characteristics of some formations in the Carpathian flysch. Ann Soc Geol Pol 52:305–333

de Caritat P, Hutcheon I, Walshe JL (1993) Chlorite geothermometry: a review. Clays Clay Minerals 41:219–239

Debon F, Le Fort P (1983) A chemical-mineralogical classification of common plutonic rocks and associations. Trans R Soc Edinburgh (Earth and Environ Sci) 73:135–149

Decrée S, Marignac C, Liégeois J-P, Yans J, Ben Abdallah R, Demaiffre D (2014) Miocene magmatic evolution in the Nefza district (northern Tunisia) and its relationship with the genesis of polymetallic mineralizations. Lithos 192–195:240–258

Dercourt J, Zonenshain LP, Ricou LE, Kazmin VG, Le Pichon X, Knipper AL, Grandjacquet C, Sbortshikov IM, Geyssant J, Lepvrier C, Pechersky DH, Boulin J, Sibuet J-C, Savostin LA, Sorokhtin O, Westphal W, Bazhenov ML, Lauer JP, Biju-Duval B (1986) Geological evolution of the Tethys belt from the Atlantic to the Pamirs since the Lias. Tectonophys 123:241–315

Douvens N, Diamantopoulos P (1997) Weathering profiles in rock units of Pindos and Ionian flyschs, Greece, and their importance in geotechnical works. In: Marinos et al. (eds) Engineering geology and the Environment, Balkema, Rotterdam, pp 97–102

Drummond SE, Ohmoto H (1985) Chemical evolution and mineral deposition in boiling hydrothermal systems. Econ Geol 80:126–147

Dubessy J, Derome D, Sausse J (2003) Numerical modelling of fluid mixing in the H2O-NaCl system: application to the North Carama U prospect (Australia). Chem Geol 194:25–39

Durand-Delga M (1969) Mise au point sur la structure Nord-Est de la Berbérie. Bull Serv Carte Géol Algérie 39:89–131

Durand-Delga M, Rossi P, Olivier P, Puglisi D (2000) Situation structurale et nature ophiolitique des roches basiques jurassiques associées aux flyschs maghrébins du Rif (Maroc) et de Sicile. C R Acad Sci Paris, Sci Terre Planètes/Earth Planet Sci 331:29–38

Eldridge CS, Bourcier WL, Ohmoto H, Barnes HL (1988) Hydrothermal inoculation and incubation of the chalcopyrite disease in sphalerite. Econ Geol 83:972–989

Fougnot J (1990) Le magmatisme néogène du littoral nord-constantinois. Unpubl, Thèse de Doctorat, INPL, Nancy, France 358 pp

Fourcade S, Capdevila R, Ouabadi A, Matineau F (2001) The origin and geodynamic significance of the Alpine cordierite-bearing granitoids of northern Algeria: a combined petrological, mineralogical and isotopic O, H, Sr, Nd study. Lithos 57:187–216

Frizon de Lamotte D, Saint-Bezar B, Bracene R, Mercier E (2000) The two main steps of the Atlas building and geodynamics of the western Mediterranean. Tectonics 19:740–761

Frizon de Lamotte D, Michard A, Saddiqi O (2006) Quelques développements récents sur la géodynamique du Maghreb (Some recent developments on the Maghreb geodynamics). Comptes Rendus Géoscience 338:1–10

Frost RF, Barnes CG, Collins WJ, Arculus RJ, Ellis DJ, Frost CD (2001) A geochemical classification for granitic rocks. J Petrol 42:2033–2048

Glaçon J (1971) Les gîtes minéraux liés au magmatisme tertiaire en Algérie du Nord. Colloque E Raguin. Les roches plutoniques dans leurs rapports avec les gîtes minéraux, Masson, Paris, pp 214–224

Heuze FE (1981) High-temperature mechanical, physical and thermal properties of granitic rocks—a review. Int J Rock Mechan Min Sci Geomech Abstr 20:3–10

Hilly J (1962) Etude géologique du massif de l'Edough et du Cap de Fer (Est Constantinois). Publ Serv Géol Algérie (nouv sér) 19, 408 pp

Jemmali N, Souissi F, Villa IM, Vennemann T (2011) Ore genesis of Pb-Zn deposits in the nappe zone of northern Tunisia: constraints from Pb-S-C-O isotopic systems. Ore Geol Rev 40:41–53

Jemmali N, Souissi F, Carranza EJM, Vennemann T (2013a) Sulfur and lead isotopes of Guern Halfaya and Bou Grine deposits (Domes zone, northern Tunisia): implications for sources of metal and timing of mineralization. Ore Geol Rev 54:17–28

Jemmali N, Souissi F, Carranza EJM, Bouabdellah M (2013b) Lead and sulphur isotope constraints on the genesis of the polymetallic mineralization at Oued Maden, Jebel Hallouf and Fedj Hassene carbonate-hosted Pb-Zn (As-Cu-Hg-Sb) deposits, northern Tunisia. J Geochem Expl 132:6–14

Jolivet L, Faccenna C (2000) Mediterranean extension and the Africa-Eurasia collision. Tectonics 19: 1095–1106

Lahondere JC, Feinberg H, Haq BU (1979) Datation des grès numidiens d'Algérie orientale: conséquences structurales. C R Acad Sci Paris 289 (D):383–386

Laouar R, Boyce AJ, Ahmed-Saïd Y, Ouabadi A, Fallick AE, Toubal A (2002) Stable isotope study of the igneous, metamorphic and mineralized rocks of the

Edough complex, Annaba, northeast Algeria. J Afr Earth Sci 35:271–283

Laouar R, Boyce AJ, Arafa M, Ouabadi A, Fallick AE (2005) Petrological, geochemical and stable isotope constraints on the genesis of the Miocene igneous rocks of Chetaibi and Cap de Fer (NE Algeria). J Afr Earth Sci 41:445–465

Lindgren W (1933) Mineral deposits, 4th edn. McGraw-Hill, New York 930 pp

Linnen R, Cuney M (2005) Granite-related rare-element deposits and experimental constraints on Ta-Nb-W-Sn-Zr-Hf mineralization. In Linnen R, Samson IM (eds) Rare-element geochemistry and mineral deposits, Geological Association of Canada (GAC) Short Course Notes 17:45–67

Lo HJ (1978) The stability of epistilbite and its bearing on the zeolite facies. Proc Geol Soc China (Formosa) 21:25–33

Marignac C (1976) Mise en évidence des successions paragénétiques dans les principaux filons minéralisés du district filonien d'Aïn Barbar (Willaya d'Annaba, Algérie). Science de la Terre Nancy XX:333–401

Marignac C (1985) Les minéralisations filoniennes d'Aïn Barbar (Algérie): un exemple d'hydrothermalisme lié à l'activité géothermique alpine en Afrique du Nord. Unpubl Thèse Doctorat Etat, INPL, Nancy, France, 2 vol, 1163 pp, 1 vol Annexes 176 pp

Marignac C (1987) Composition des phases minérales et évolution des phases fluides: le cas des filons polymétalliques d'Aïn Barbar (Algérie). Bull Minéralogie 111:183–206

Marignac C (1988a) P-T-X evolution of ore veins associated with paleogeothermal activity at Aïn Barbar (NE Constantinois, Algeria): reconstruction from fluid inclusion data. Bull Minéralogie 111:359–381

Marignac C (1988b) A case of ore deposition associated with geothermal activity: the polymetallic ore veins of Aïn Barbar (NE Constantinois, Algeria). Mineral Petrol 39:107–127

Marignac C (1989) Sphalerite stars in chalcopyrite: are they always the result of an unmixing process? Miner Deposita 24:176–182

Marignac C, Zimmermann JL (1983) Ages K-Ar de l'évènement hydrothermal et des minéralisations associées dans le district minéralisé miocène d'Aïn Barbar (Est Constantinois). Miner Deposita 18:457–467

Marignac C, Aïssa DE, Cheilletz A, Gasquet D (2015) Edough-Cap de Fer polymetallic district, northeast Algeria: II. Metallogenic evolution of a late Miocene metamorphic core complex in the Alpine Maghrebide belt. In: Bouabdellah M, Slack JF (eds) Mineral deposits of North Africa: Springer, Berlin-Heidelberg

Maury RC, Fourcade S, Coulon C, El Azzouzi M, Bellon H, Coutelle A, Ouabadi A, Semroud B, Megartsi M, Cotten J, Belanteur O, Louni-Hacini A, Piqué A, Capdevila R, Hernandez J, Réhault JP (2000) Post-collisional Neogene magmatism of teh Mediterranean Maghreb margin: a consequence of slab breakoff. Comptes Rendus Académie Sciences Paris 331:159–173

McDowell SD, Elders WA (1980) Authigenic layer silicates in borehole Elmore 1, Salton Sea geothermal field, California, U.S.A. Contrib Mineral Petrol 74:293–310

McKibben MA, Elders WA (1985) Fe-Zn-Cu-Pb mineralization in the Salton Sea geothermal system, Imperial Valley, California. Econ Geol 80:539–559

Michard A, Negro F, Saddiqi O, Bouybaouene ML, Chalouan A, Montigny R, Goffé B (2006) Pressure-temperature-time constraints on the Maghrebide mountain building: evidence from the Rif-Betic transect (Morocco, Spain), Algerian correlations, and geodynamic implications. Comptes Rendus Géoscience 338:92–114

Michel J, Baumgartner L, Putlitz B, Schaltegger U, Ovtcharova M (2008) Incremental growth of the Patagonian Torres del Paine laccolith over 90 k.y. Geology 36:459–462

Moëlo Y, Makovicky E, Mozgova N et al (2008) Sulfosalt systematics: a review. Report of the sulfosalt sub-committee of the IMA Commission on Ore Mineralogy. Eur J Mineral 20:7–46

Nigretto G (1992) Age et origine des minéralisations plomb-zinc d'Aïn-Barbar en Algérie. Unpubl DEA Memoire, CRPG Nancy 45 pp

Ohtani T, Nakano T, Nakashima Y, Muraoka H (2001) Three-dimensional shape analysis of miarolitic cavities and enclaves in the Kakkonda granite by X-ray computed tomography. J Struct Geol 23:1741–1751

Piqué A, Tricart P, Guiraud R, Laville E, Bouaziz S, Amrhar M, Ait Ouali R (2002) The Mesozoic-Cenozoic Atlas belt (North Africa): an overview. Geodinam Acta 15:185–208

Riverin G, Hodgson CJ (1980) Wall-rock alteration at the Millenbach Cu-Zn mine, Noranda, Quebec. Econ Geol 75:424–444

Rowland JV, Symmons SF (2012) Hydrologic, magmatic, and tectonic controls on hydrothermal flow, Taupo volcanic zone, New Zealand: implications for the formation of epithermal veins. Econ Geol 107:427–457

Russell RD, Farquhar RM (1960) Lead isotopes in geology. Interscience Publishers, New York-London 241 pp

Sami R, Soussi M, Kamel B, Lattrache Kmar BI, Stow D, Sami K, Mourad B (2010) Stratigraphy, sedimentology and structure of the Numidian flysch thrust belt in northern Tunisia. J Afr Earth Sci 57:109–126

Schiffman P, Elders WA, Williams AE, McDowell SD, Bird DK (1984) Active metasomatism in the Cerro Prieto geothermal system, Baja California, Mexico: a telescoped low-pressure, low-temperature metamorphic facies series. Geology 12:12–15

Secchi FA, Brotzu P, Callegari E (1991) The Arburese igneous complex (SW Sardinia, Italy)—an example of

dominant igneous fractionation leading to peraluminous cordierite-bearing leucogranites as residual melts. Chem Geol 92:213–249

Simmons SF, Browne PRL (1997) Saline fluid inclusions in sphalerite from the Broadlands-Ohaaki geothermal system: a coincidental trapping of fluids being boiled towards dryness. Econ Geol 92:485–489

Simmons SF, Browne PRL (2000) Hydrothermal minerals and precious metals in the Broadlands-Ohaaki geothermal system: implications for understanding low-sulfidation epithermal environments. Econ Geol 95:971–999

Skinner BJ, White DE, Rose HJ, Mays RE (1967) Sulfides associated with the Salton Sea geothermal brines. Econ Geol 62:316–330

SOFELD Spa (Société des feldspaths d'Algérie) (1999) Présentation du gisement de felsites de Aïn Barbar, Willaya Annaba., 13 pp

Thomas MFH, Bodin S, Redfern J, Irving DHB (2010) A constrained African craton source for the Cenozoic Numidian flysch: implications for the palaeogeography of the western Mediterranean basin. Earth-Sci Rev 101:1–23

Touahri B (1987) Géochimie et métallogénie des minéralisations à plomb et zinc du nord de l'Algérie. Unpubl PhD Thesis, Pierre et Marie Curie Univ, Paris, France, 380 pp

Vidal O, Parra T, Trotet A (2001) A thermodynamic model for Fe-Mg aluminous chlorite using data from phase equilibrium experiments and natural pelitic assemblages in the 100 °C to 600 °C, 1 to 25 kb range. Amer J Sci 301:557–592

Vila JM (1980) La chaîne alpine d'Algérie orientale et des confins algéro-tunisiens. Unpubl Thèse Doctorat Etat, Université Paris VI, Paris, France, 663 pp

Vorsteen H-D, Schellschmidt R (2003) Influence of temperature on thermal conductivity, thermal capacity and thermal diffusivity for different types of rocks. Phys Chem Earth 28:499–509

Whitney DL, Evans BW (2010) Abbreviations for names of rock-forming minerals. Amer Mineral 95:185–187

Zang W, Fyfe WS (1995) Chloritization of the hydrothermally altered bedrock at the Igarapé Bahia gold deposit, Carajás, Brazil. Miner Deposita 30:30–38

Zeng Y, Liou JG (1982) Experimental investigation of yugawaralite-wairakite equilibrium. Amer Mineral 67:937–943

Re/Os Age Determination, Lead and Sulphur Isotope Constraints on the Origin of the Bouskour Cu–Pb–Zn Vein-Type Deposit (Eastern Anti-Atlas, Morocco) and Its Relationship to Neoproterozoic Granitic Magmatism

Mohammed Bouabdellah, Lhou Maacha, Michel Jébrak and Mohammed Zouhair

Abstract

The newly re-evaluated Bouskour deposit is a large, polymetallic vein-type system in the Precambrian Sidi Flah-Bouskour inlier of the eastern Anti-Atlas orogen. Resources are >53 Mt at 0.8 % Cu, of which 21 Mt has a higher grade of 1.3 % Cu and 9 g/t Ag. Host rocks are assigned to the Ediacaran Ouarzazate Group, and consist of a succession of mafic-ultramafic to felsic igneous rocks, both intrusive and extrusive, with ages ranging from 570 ± 5 to 557 ± 5 Ma, partly intruding Cryogenian basalt and andesite. Among these igneous bodies, intrusive felsic rocks are by far the most abundant lithologies, consisting of three elongate, NW-SE-trending, calc-alkaline intrusions referred to as: (1) Bouskour Granodiorite, (2) Bouskour Granite dated at 570 ± 5 Ma, and (3) amphibole-bearing Bouskour Granodiorite. An extensive dike

M. Bouabdellah (✉)
Département de Géologie, Faculté des Sciences, Université Mohammed Premier, B.P. 717 Avenue Mohammed VI, 60000 Oujda, Morocco
e-mail: mbouabdellah2002@yahoo.fr

L. Maacha · M. Zouhair
Managem Group, Twin Center, Tour A, Angle Boulevard Zerktouni et al Massira al Khadra, 20000 B.P. 5199, Casablanca, Morocco

M. Jébrak
Department of Earth and Atmospheric Sciences, UQAM, 201 President Kennedy boulevard, CP 8888 Centre Ville, Montreal, QC H3C3P8, Canada

M. Bouabdellah and J.F. Slack (eds.), *Mineral Deposits of North Africa*, Mineral Resource Reviews, DOI 10.1007/978-3-319-31733-5_10

system of red to white aphanitic rhyolite locally known as the "Bouskour rhyolitic dike swarm" intruded all older units at 564 ± 7 to 562 ± 5 Ma. Cu–Pb–Zn sulphide mineralization produced an array of five transtensional, N-S and ENE- to NNW-trending vein systems referred to as "Filon Principal," "Filon Ouest," "Filon I," "Filon II," and "Filon Camra." The veins are up to 20 m wide and extend laterally from a few hundred meters to more than 10 km, spaced 50 to >1000 m apart, striking predominantly N160° E with steep dips (70° to ~90°). Characteristic are comb, cockade, laminated, breccia, and crack and seal textures, suggesting that episodic mechanisms were important in vein formation. Sulphide minerals consist predominantly of various proportions of chalcopyrite, bornite, galena, sphalerite, pyrite, and arsenopyrite, with subordinate tetrahedrite-tennantite, magnetite, cassiterite, and rutile. The hydrothermal alteration assemblage comprises sericite, epidote, chlorite, quartz, and carbonates (calcite, dolomite). Three successive stages of ore deposition are recognized. The earliest stage (I) is referred to as "Cu–Zn–(Fe–As–Co–Bi–Sn) stage" is followed by the main Cu–Pb–Zn sulphide stage (II), which accounts for most of the exploited sulphide ore at Bouskour. The latest stage (III) forms late fillings in calcite or quartz veins or within older stage I and II assemblages, and includes Au–Ag–Cu–(Zn–Pb) mineralization. New $^{187}Re/^{188}Os$ age dating of a single molybdenite crystal from stage II yields an age of 574.9 ± 2.4 Ma. This age coincides, within analytical uncertainty, with a SHRIMP U–Pb age on zircon from the Bouskour Granite. The age correspondence suggests a foremost role of granite-derived hydrothermal fluids in the genesis of this polymetallic vein system, consistent with sulphur and lead isotopic data. This timing of mineralization relates to the final, post-collision extensional stage of the Pan-African orogeny.

1 Introduction

The Bouskour deposit (lat 30°55′46.59″ N; long 6°18′4.86″ W) in southeastern Morocco (Fig. 1) is one of the most productive Cu–Pb–Zn ± Ag ± Au vein-type deposits of North Africa wherein mineralized structures are intimately associated with granitic intrusions of Neoproterozoic age. To date, no detailed geochronologic and isotopic geochemical studies have been performed on this deposit, except for a few reconnaissance surveys carried out during exploration and mine planning (Marcoux and Jébrak 2012; El Azmi et al. 2014). Accordingly, the origin of the deposit remains poorly understood and critical ore genetic constraints are lacking. The absence of precise age determination required previous workers to constrain the timing of mineralization by crosscutting relationships (Marcoux and Jébrak 2012; El Azmi et al. 2014).

In this contribution, we document and interpret the geologic history, mineralization, alteration, and paragenesis of the Bouskour deposit. More importantly we contribute, for the first time, a Re/Os molybdenite age together with sulphur and lead isotope data relevant to the age of mineralization and source(s) of sulphur and metals. Collectively, these results place new constraints on the origin and evolution of the Cu–Pb–Zn ± Ag ± Au mineralization and related implications

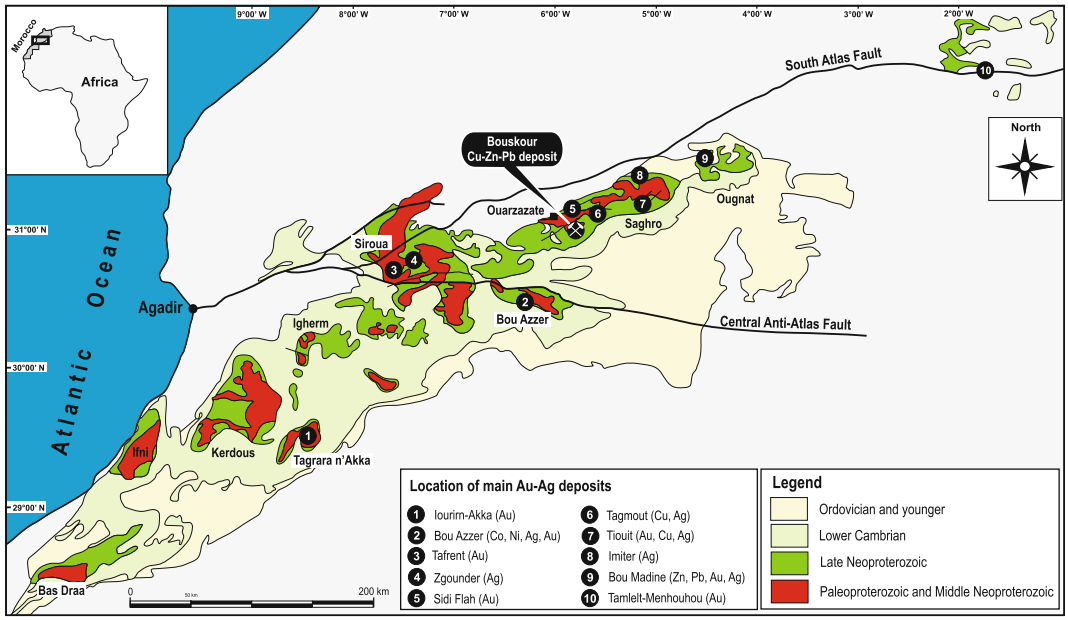

Fig. 1 Regional geologic setting of Anti-Atlas system in southern Morocco showing location of Bouskour Cu–Pb–Zn district, and regional-scale faults and their relationship to similar polymetallic mining camps

for understanding ore-forming processes with respect to Neoproterozoic magmatism.

2 Exploration History

Mining activity in the Bouskour district goes back to the medieval period. In recent times, mineralization in the district was re-discovered in the late 1940s by "la Société Minière de Jbel Sarhro" (Sosarhro), and since then has been mined intermittently for Cu–Ag, Pb, and Zn. During the French colonial period, between 1948 and 1950, upper parts of the main vein were exploited, yielding an estimated 10,000 t of ore extracted at an average grade of ~2 % Cu. After many years of closure and following regional aeromagnetic surveys, the "Bureau de Recherches et de Participation Minière" (BRPM, actual ONHYM), and "la Société des Mines de Bouskour" in conjunction with the former Soviet Union consulting group Technoexport conducted, between 1958 and 1977, a multidisciplinary regional exploration program. This program integrated geologic mapping and multi-element geochemical surveys that resulted in delineation of promising Cu–(Pb, Zn) targets.

In 1977, the Bouskour mine closed due to decreasing prices and ore grade with depth. At the time of the closure, remaining ore reserves were estimated at 0.43 Mt. Managemgroup, a subsidiary of ONA Holding, later purchased the assets and started an ambitious exploration program using surface mapping, geophysical surveys, mineralogical studies, and diamond drilling campaigns to reassess the mineral potential of the district. About 10,000 m of drilling (mostly diamond drill holes) were completed, providing an extensive database for geologic modeling and resource estimation. Subsequent resource estimates released by the mining company have delineated a global resource of >53 Mt at an average grade of 0.8 % Cu and 8 g/t Ag, of which 21 Mt has a higher grade of 1.3 % Cu (Maacha et al. 2011).

3 District Scale Geology

The Precambrian Sidi Flah-Bouskour inlier of the eastern Anti-Atlas orogen, which in its southern termination hosts the Bouskour Cu–Pb–Zn deposit (Fig. 1), is a Neoproterozoic basement massif located in the central part of the larger Saghro massif. The inlier consists of a succession of Cryogenian (middle Neoproterozoic; 850–630 Ma) to Ediacaran (late Neoproterozoic; 630–542 Ma) deformed and metamorphosed volcanic-sedimentary, volcanic, and intrusive rocks interpreted to have been emplaced either in a back-arc environment (Saquaque et al. 1992; Leblanc and Moussine-Pouchkine 1994; Bouougri and Saquaque 2004) or in an intra-continental basin synchronous with Pre-African rifting (Fekkak et al. 2003).

The resulting Neoproterozoic country rocks were heterogeneously deformed and metamorphosed during two Pan African events, B_1 and B_2, from about 760–550 Ma (Leblanc and Lancelot 1980; Saquaque et al. 1989; Walsh et al. 2002; Thomas et al. 2004; El Hadi et al. 2010). The B_1 event was collisional and gave rise to strong folding and ophiolite emplacement; B_2 caused moderate shortening and tliting. The metamorphic grade of the country rocks is middle to upper greenschist facies, reaching amphibolite facies in the vicinity of the intrusive rocks.

The geology of the Bouskour district has been summarized by Tixeront (1971), Clavel and Tixeront (1971), Ezzouhairi (1989, 1997, 2001), Ezzouhairi et al. (2008), and Walsh et al. (2008). The following description summarizes work by these authors supplemented by our own observations.

Exposed rock types are stratigraphically assigned to the middle to late Neoproterozoic Ouarzazate Supergroup, and are geodynamically related to the post-collision extensional stage of the Pan-African orogeny (Thomas et al. 2002; Walsh et al. 2012). The oldest rocks (Fig. 2), which constitute part of the Saghro Group (Gasquet et al. 2005; Benziane 2007) or the Sidi Flah Group (Fekkak et al. 2001, 2003), comprise a Cryogenian succession of turbiditic to flysch-like (Walsh et al. 2008) sequence of black shale, sandstone, siltstone, greywacke, tuff, limestone, jasper, and rare conglomerate; these strata are interbedded with, and overlain by, basaltic to andesitic flows and sills of the Sidi Flah-Bouskour metamorphic series (Walsh et al. 2008). The unconformably overlying Ediacaran Ouarzazate Group (Thomas et al. 2002) that hosts the Bouskour vein system comprises a wide spectrum of mafic-ultramafic to felsic igneous rocks, both intrusive and extrusive, having ages ranging from 570 ± 5 to 557 ± 5 Ma (Walsh et al. 2008, and references therein), partly intruding the Cryogenian basalts and andesites (Fig. 2). The mafic-ultramafic intrusions dated at 561 ± 2 Ma (TIMS U–Pb zircon geochronology; Chebbaa 1996) and 563 ± 5 Ma (SHRIMP U–Pb zircon; Walsh et al. 2008) consist of fine-grained olivine-gabbro and serpentinized peridotite (dunite, wherlite) (Ezzouhairi et al. 1998; Saquaque et al. 1992; Fekkak 2000; Thomas et al. 2002; and present study). The mafic volcanic rocks that host the southernmost part of the Bou Skour vein system (i.e., Amas central and Cobra orebodies; Fig. 3) are basaltic to andesitic in composition; felsic intrusions, flows and dikes which in turn host the northern orebodies (i.e., Anne-Marie, Chaigne, and Panthere; Fig. 3) are aphanitic to porphyritic dacite and rhyolite. Red rhyolitic rocks from the Bouskour area have a SHRIMP U–Pb zircon age of 564 ± 7 Ma (Walsh et al. 2008). Intrusive felsic rocks, which constitute the most abundant lithology in the district (Fig. 2), comprise three elongate, NW-SE-trending, calc-alkaline intrusions referred to as (1) Bouskour Granodiorite, (2) Bouskour Granite, and (3) Bouskour amphibole-bearing Granodiorite; the two first intrusions host approximately two thirds of the ore zones within the Bouskour vein system (Fig. 3). The Bouskour Granite, dated at 570 ± 5 Ma (SHRIMP U–Pb zircon; Walsh et al. 2012), forms an elongate, NW-SE-trending, multi-phase pluton that covers an area of 40 km^2 at surface (Fig. 2). Most Bouskour granitic rocks are granodiorite, but a few are monzogranite. The granodiorite is equigranular in the central part of the pluton, grading to a porphyritic amphibole-bearing granodiorite along the margins. Based on whole-rock

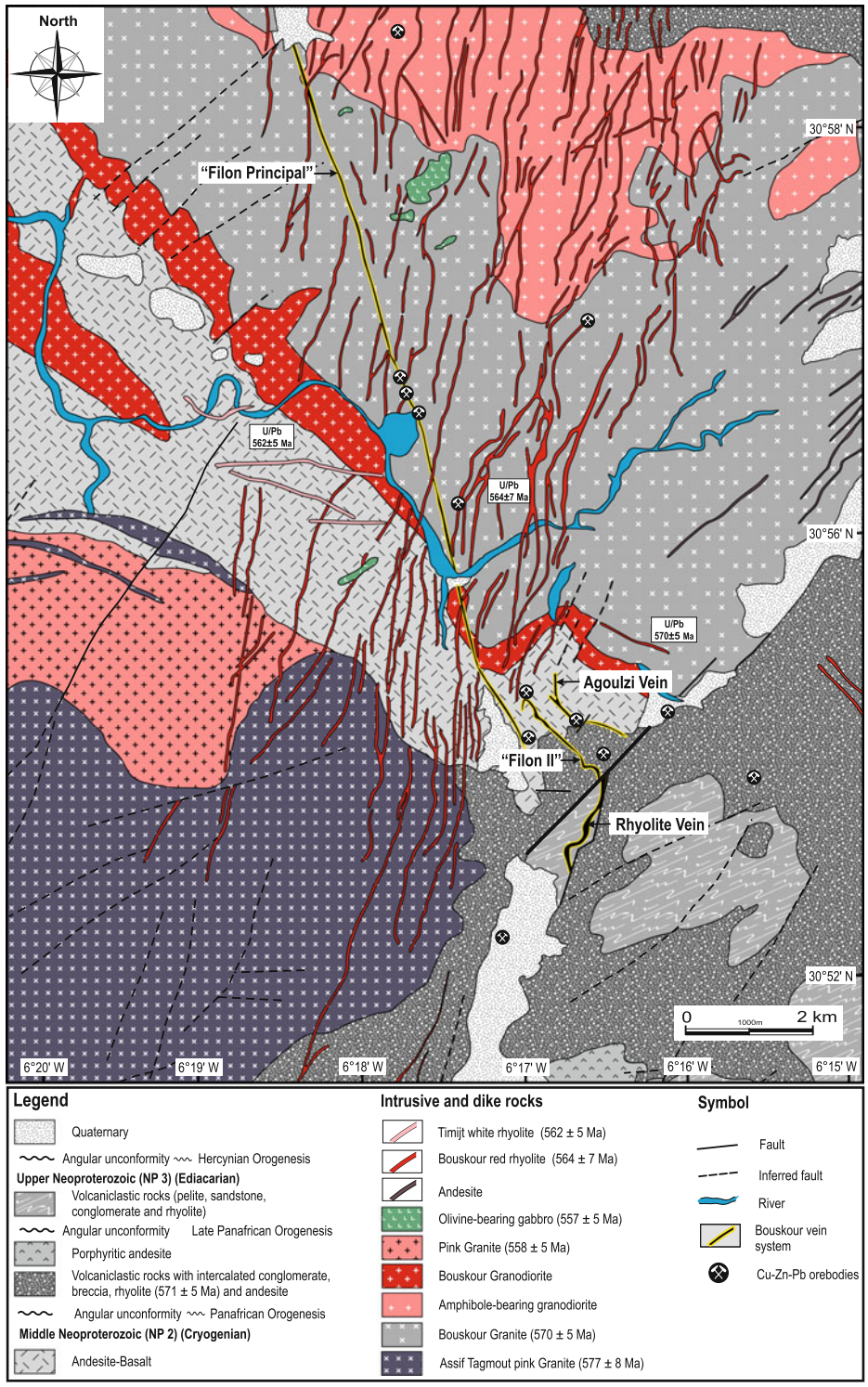

Fig. 2 Geological map of Bouskour Cu–Pb–Zn district (modified after Walsh et al. 2008) showing main lithostratigraphic units, extent of structures, and relative position of known vein-type orebodies and their relationships to late Neoproterozoic igneous rocks

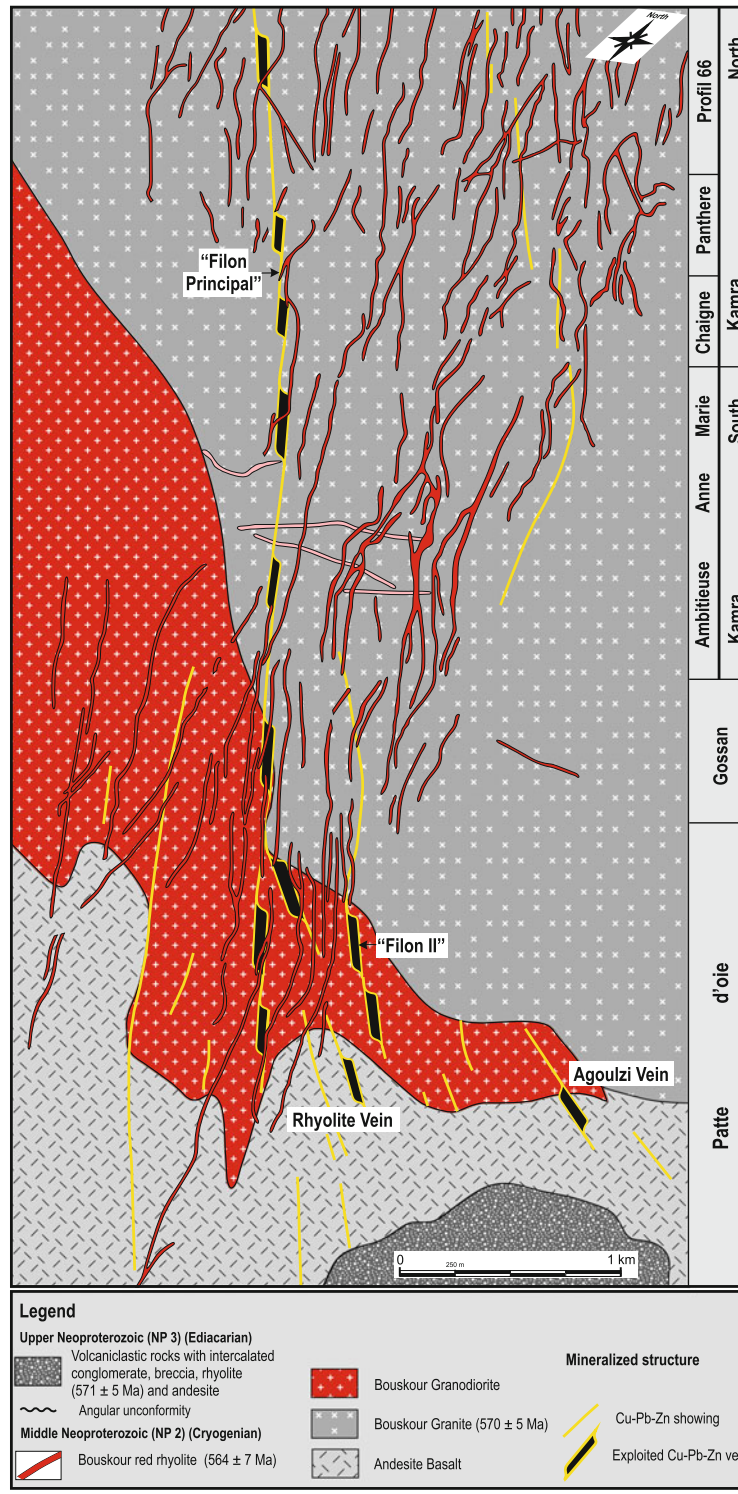

Fig. 3 Detailed geologic map of Bouskour district showing distribution of major economic veins and their spatial relationships to late Neoproterozoic igneous rocks, particularly rhyolitic dikes

and radiogenic isotope geochemistry, the Bouskour intrusion is a high-K, calc-alkaline granodiorite of island-arc affinity, having a mantle derivation with negligible crustal contamination (Ezzouhairi et al. 2008). Intrusion of the granodiorite produced a 300-m-wide contact metamorphic aureole of massive hornfels comprising biotite, cordierite, and andalusite.

During late Neoproterozoic time and prior to the Cambrian, a system of extensive (up to 25 km long), N-S-trending, 5-km-wide, red to white aphanitic rhyolitic dikes (564 ± 7 to 562 ± 5 Ma; Walsh et al. 2012) locally known as the "Bouskour rhyolitic dike swarm" intruded and cut all older units (Figs. 2 and 3).

4 Mineralogy, Alteration, and Paragenesis

Cu–Pb–Zn ± Ag ± Au sulphide mineralization consists of an array of transtensional N-S and ENE- to NNW-trending vein systems (Fig. 3). Five principal mineralized veins, referred to as "Filon Principal," "Filon Ouest," "Filon I," "Filon II," and "Filon Camra," together with two less-economic structures "Agoulzi Vein" and "Rhyolite Vein," have been exploited both from open pits and underground workings. The veins are up to 20 m wide and extend laterally from a few hundred meters up to more than 10 km, are spaced 50 to >1,000 m apart, and strike predominantly N160° E with steep dips (70° to ~90°). The veins display comb, cockade, laminated, breccia, and crack and seal textures, suggesting that episodic, multiple mechanisms were important in vein formation. Early precipitated minerals are cut, or are brecciated and cemented by the succeeding minerals. Overall, the textural features indicate that mineralization took place in open spaces.

The main vein "Filon Principal" is historically and economically the most important and accounts for more than 80 % of the total mineral resources of the district. This vein truncates all major igneous units including the Cryogenian andesite and the Ediacaran Bouskour Granite and Bouskour Granodiorite. The vein is >10 km long and varies from 0.5–20 m wide, dips steeply to the south, has a vertical extension of more than 150 m, and comprises a succession of strongly mineralized "dilational jogs" and barren segments. The economic ore zones, grading 1.5–3 % Cu (Clavel and Tixeront 1971), consist of seven mined orebodies, and include from north to south: "Profil 66," "Panthère," "Chaigne," "Anne-Marie," "Ambitieuse," "Gossan," and "Patte-d'Oie" (Fig. 3). The "Patte-d'Oie," ore zone is the most promising, where an intensive exploration program has been conducted by Managemgroup over the last past 5 years (2007–2012). A reconnaissance diamond drilling program has been carried out, resulting in the delineation of a new stockwork zone of Cu-rich mineralization at depths of 150–160 m.

Pervasive hydrothermal alteration has affected, to varying degrees, all country rocks particularly those adjacent to the mineralized structures. Alteration halos range from centimeter-wide selvages to 2-m-wide (up to 6 m) zones that envelope the veins. The alteration halos consist mainly of sericite, epidote, chlorite, quartz, and carbonates (calcite, dolomite), with variable amounts of sulphides (chalcopyrite, galena, sphalerite, pyrite); no vertical or lateral mineral and/or geochemical zoning is evident, although Tixeront (1971) reported vertical mineral zonation within the "Chaigne," "Panthère," and "Patte-d'Oie" veins. Electron microprobe analysis indicates that chlorite in the veins has an average composition of clinochlore with a structural formula ($Fe_{1.97}Mg_{2.69}Al_{1.26}$) $Si_{2.86}Al_{1.14}O_{10}$ $(OH, O)_8$ (Marocux and Jébrak 2012).

All of the mineralized veins display similar mineral assemblages but the relative proportions of base-metal sulphides relative to other minerals vary among the veins. Sulphide minerals are dominated by chalcopyrite, bornite, galena, sphalerite, pyrite, and arsenopyrite, accompanied by minor molybdenite with secondary covellite and chalcocite. Sulphosalts (tetrahedrite-tennantite) and oxides (magnetite, cassiterite, rutile) are also present. Non-sulphide gangue minerals, whose development relates to the

composition of the host rocks, consist predominantly of quartz where the mineralized veins cut the Bouskour Granite, and conversely calcite and dolomite where the veins traverse the andesite. An idealized sequence of mineral deposition, drawn from mineral assemblages and textural and crosscutting relationships, shows the existence of three successive stages of ore deposition, each of which is separated by episodes of intense shearing and brecciation.

The early stage referred to as "Cu–Zn–(Fe–As–Co–Bi–Sn) stage" comprises quartz, calcite, pyrite, arsenopyrite, sphalerite, chalcopyrite, bornite, covellite, digenite, chalcocite, tetrahedrite-tennantite ± rutile ± magnetite ± cassiterite. The subsequent stage (main Cu–Pb–Zn sulphide stage II) accounts for most of the exploited ore, and consists of sequentially deposited chalcopyrite, sphalerite, galena, bornite, covellite, digenite, chalcocite, and tetrahedrite-tennantite ± molybdenite; this paragenesis is spatially associated with a distinctive, strong chloritic and locally silicic alteration zone. The latest stage (III), referred to as Zn–Pb–(Cu) sulphide ± Au ± Ag stage, occurs in calcite or quartz veins or as late fillings within the older stage I and II assemblages.

In addition to the three hypogene stages, a post-ore supergene stage (IV) is well developed in the uppermost sulphide-rich part of the mineralized structures, where oxidized zones extend more than 110 m deep. The mineral assemblage of this supergene stage consist of varying amounts of goethite, hematite, lepidocrocite, malachite, azurite, chrysocolla, wulfenite, and autunite.

5 Sulphur and Lead Isotope Geochemistry and Re/Os Geochronology

A suite of representative sulphide (i.e., galena, pyrite, chalcopyrite) separates from the recently reworked Filon II, Agoulzi Vein, and Rhyolite Vein orebodies (Fig. 2) were analyzed for sulphur and lead isotope compositions (Table 1). Sulphur isotope analyses were carried out at the Environmental Isotope facilities of the University of Waterloo (Canada) using an Isochrom Continuous Flow Stable Isotope Ratio Mass Spectrometer GVI Micromass coupled to a Carlo Erba Elemental Analyzer CHNS-O EA1108. The data are reported as per mil (‰) deviations relative to the Canyon Diabolo troilite (CDT) standard. Analytical uncertainty (2σ) is ± 0.12 ‰. Lead isotopic compositions were determined on galena using a multi-collector–inductively coupled plasma–mass spectrometer (MC–ICP–MS) instrument (Micromass Isoprobe) operated in "solution mode" with an Aridus nebulizer system.

Re/Os analyses were performed on a single molybdenite separate from stage II of the "Patte-d'Oie" vein system. The sample was collected from drill core F2SC312 (X = 415422, Y = 434021, Z = 1550) at a depth of 623 m. Analyses were performed by J. Perello, Vice President of Antofagasta copper mining group.

The $\delta^{34}S$ values are all negative, ranging from −9.3 to −2.7 ‰ (avg −6.1 ± 2.6 ‰, $n = 9$), and show relatively little variation with respect to location in the deposit. These rather uniform $\delta^{34}S$ values are similar to but more negative than those that characterize igneous sulphur (−3 to +1 ‰; Hoefs 2009). The observed range in sulphur isotope compositions could be explained by the interaction of a magmatically derived ore fluid with an isotopically low end member (e.g., −9.3 ‰), such as that inferred for biogenic pyrite within the Cryogenian black shale country rocks. Alternatively, such low $\delta^{34}S$ values in the sulphides could record somewhat low temperatures of deposition, in the range of ∼150–200 °C (see Ohmoto and Goldhaber 1997). The more negative $\delta^{34}S$ values may also reflect boiling processes during mineralization (see Drummond and Ohmoto 1985). Indeed, it is well established that boiling will lead to a loss of H_2 and oxidation of the ore fluid, which ultimately results in lower $\delta^{34}S$ values in sulphides (e.g., Duuring et al. 2009; Kamvong and Zaw 2009). Based on these

Table 1 Sulphur and lead isotope compositions of sulphide separates from the Bouskour Cu–Pb–Zn deposit

Vein system	Sulphide	$\delta^{34}S$	$^{206}Pb/^{204}Pb$	$^{207}Pb/^{204}Pb$	$^{208}Pb/^{204}Pb$
Filon II	Pyrite	−3.1	–	–	–
Filon II	Pyrite	−2.7	–	–	–
Filon II_Level-140	Chalcopyrite	−6.6	–	–	–
Filon II_Level-140	Chalcopyrite	−6.3	–	–	–
Agoulzi	Galena	−9.2	–	–	–
Agoulzi	Galena	−3.3	–	–	–
Rhyolite	Chalcopyrite	−6.1	–	–	–
Rhyolite	Galena	−9.3	17.738	15.523	37.616
Rhyolite	Galena	−8.1	17.768	15.524	37.710
Rhyolite	Galena	–	17.883	15.526	37.619
Rhyolite	Galena	–	17.913	15.541	37.675
Rhyolite	Galena	–	17.946	15.537	37.614
Rhyolite	Galena	–	17.947	15.537	37.607
Rhyolite	Galena	–	17.950	15.538	37.619
Rhyolite	Galena	–	18.080	15.552	37.687

constraints, and notwithstanding the possible involvement of externally derived bacteriogenic sulphur, we attribute the limited spread in $\delta^{34}S$ values at Bouskour to a large-scale hydrothermal system with a homogeneous source of sulphur that was likely entirely of magmatic origin.

Lead isotope ratios for galena separates range from 17.785 to 18.113 for $^{206}Pb/^{204}Pb$, 15.521–15.552 for $^{207}Pb/^{204}Pb$, and 37.620–37.823 for $^{208}Pb/^{204}Pb$ (Table 1). These values plot between the orogene and mantle growth curves of Zartman and Doe (1981) (Fig. 4). Accordingly, we interpret the tight linear clustering of Pb isotope data as reflecting the mixing of lead from isotopically homogeneous mantle and various crustal reservoirs during leaching and fluid transport, as also suggested by the sulphur isotope data reported above.

A Re/Os molybdenite age determination yields a weighted average age of 574.9 ± 2.4 Ma (2-sigma). This age is broadly consistent, within analytical uncertainty, with the 570 ± 5 Ma SHRIMP U–Pb zircon age for the Bouskour Granite reported by Walsh et al. (2012).

6 Discussion

The conclusions drawn herein are based on geological and mineralogical information on the vein systems, on limited sulphur and lead isotope data, and more importantly on one Re/Os molybdenite age determination. In the absence of reliable fluid inclusion and additional geochronological constraints on mineralization, our interpretations thus could change when new data become available.

Earlier studies (Clavel and Tixeront 1971; Tixeront 1971) classified the Bouskour deposits as a typical zoned vein system whose genesis is directly related to emplacement of the Bouskour granitic complex. More recently, Marcoux and Jébrak (2012) and El Azmi et al. (2014) have argued that the veins should be considered part of a porphyry copper system. However, several lines of evidence obtained from the current study are inconsistent with such a model: (1) there is no zoned distribution of alteration assemblages or sulphide minerals (i.e., bornite, chalcopyrite, pyrite) as is commonly described for typical

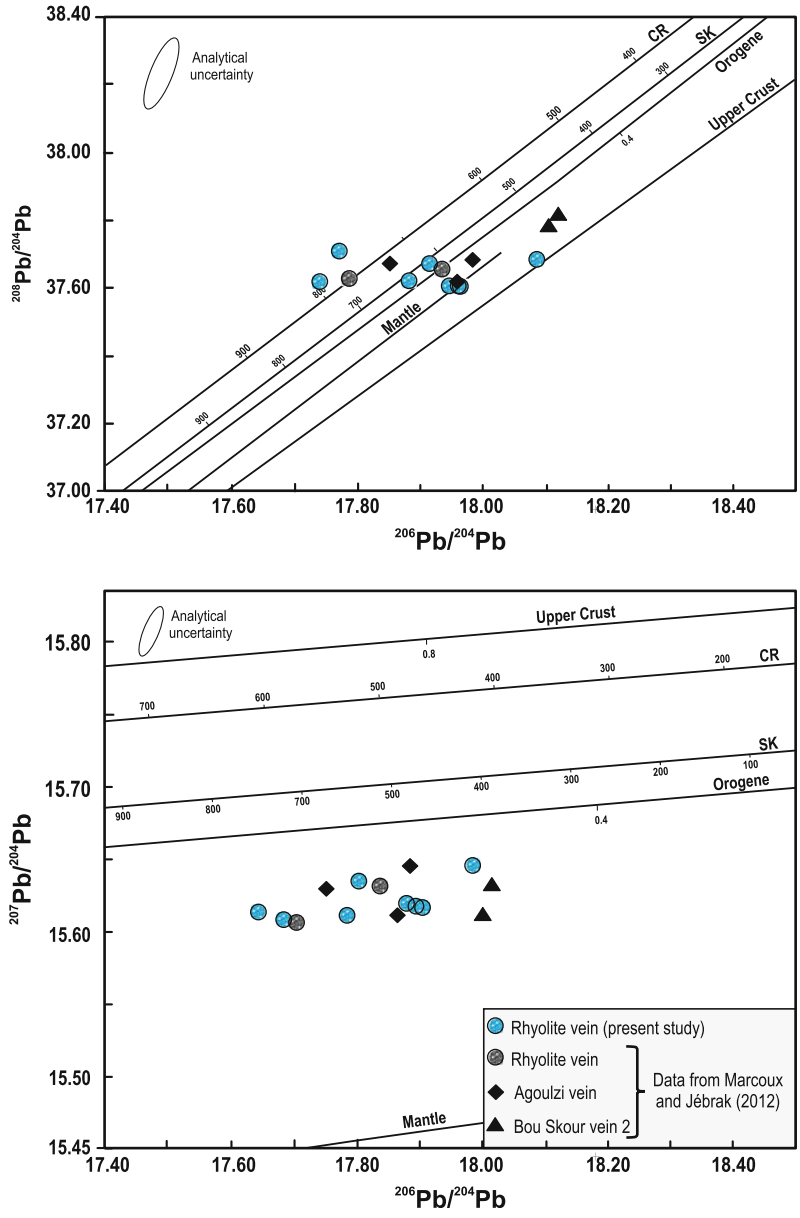

Fig. 4 Lead isotopic compositions of galena ores from the Rhyolite vein system of the Bouskour Cu–Pb–Zn deposit, plotted on **a** $^{208}Pb/^{204}Pb$ versus $^{206}Pb/^{204}Pb$ and **b** $^{207}Pb/^{204}Pb$ versus $^{206}Pb/^{204}Pb$ diagrams. Evolution curves of Stacey and Kramers (1975) and Cumming and Richards (1975), labelled SK and CR, respectively; along with the evolution curves for Upper Crust, Mantle and Orogene from Zartman and Doe (1981), are shown for reference

porphyry Cu deposits; (2) alteration mineral assemblages that are diagnostic of porphyry Cu deposits (i.e., potassic, phyllic, propylitic) predate the bulk of the vein sulphide minerals; (3) areas having high Cu contents are correlated with zones of weak potassic alteration (<2 % K_2O; Marcoux and Jébrak 2012), which is the inverse of that displayed in typical porphyry Cu systems; (4) the bulk of Bouskour ores do not occur within vein stockwork structures, instead being hosted by a transcrustal, kilometer-long megastructure; (5) anhydrite that characterizes porphyry Cu systems is absent in the veins; and (6) the presence of a Sn–Fe–As–Co mineral paragenesis in the veins, although uncommon, is absent in porphyry Cu systems. Collectively, these lines of evidence argue against a purely porphyry Cu model for the Bouskour vein

mineralization, pointing instead to a classical granite-related polymetallic vein system. Paragenetic studies indicate that the paleohydrothermal history of the ore-forming vein system comprised three main contrasting hydrothermal events. However, it is unclear whether these events are genetically related to the protracted evolution of a single mineralizing fluid, or alternatively to three separate hydrothermal episodes.

The earliest of the three stages referred to as the "Cu–As–(Sn) stage" exhibits a stockwork of Cu-rich mineralization having an assemblage of ore minerals (pyrite, arsenopyrite, chalcopyrite, sphalerite, galena, tetrahedrite-tennantite), cassiterite, stannite, native bismuth and Bi-sulphosalt, and alteration assemblages similar to those commonly reported for volcanic-hosted massive sulphide (VHMS) deposits. Accordingly, we interpret this early type of mineralization, which is confined exclusively to the Cryogenian andesites, as representing the stockwork zone of a possibly hidden VHMS system that existed on or beneath the Cryogenian seafloor.

The second Cu–Pb–Zn stage of mineralization, which is by far predominant and economically the most important, is epigenetic, structurally controlled, and consists of open-space fillings of brittle structures that were likely open to the surface. Structural constraints based on geometry of the mineralized vein systems led Clavel and Tixeront (1971) to favor an Hercynian age for the Cu–Pb–Zn sulphide mineralization. This inferred age is in accord with the time span of mineralizing hydrothermal events dated at 250 to 210 ± 10 Ma (Ghorbal et al. 2008; Sebti et al. 2009; Barbero et al. 2011) that affected most Hercynide domains of North Africa (Valenza et al. 2000; Cheilletz et al. 2010) and Western Europe (Sánchez et al. 2006). However, crosscutting relationships indicate that the mineralized structures cut the 570 ± 5 Bouskour Granite but in turn do not transgress overlying 558 ± 4 Ma upper Neoproterozoic strata, thereby bracketing the mineralization between 570 ± 5 and 558 ± 4 Ma. More interestingly, the Re/Os molybdenite age of 574.9 ± 2.4 Ma (2-sigma) reported here is similar, within analytical uncertainty, to the 570 ± 5 Ma SHRIMP U–Pb zircon age reported for the Bouskour Granite (Walsh et al. 2012). This new Re–Os molybdenite age provides strong evidence for contemporaneity between emplacement of the Bouskour Granite and the spatially associated Cu–Pb–Zn sulphide mineralization. Accordingly, a genetic relationship between mineralization and the Bouskour Granite is therefore indicated. These relationships thus suggest that the bulk of Bouskour Cu–Pb–Zn mineralization, veining, and alteration occurred late in the tectonic history of the Bouskour area, towards the end of the latest phase of Pan-African deformation, contemporaneously or immediately after emplacement of the 570 ± 5 Ma Bouskour Granite, as also suggested by the sulphur and lead isotope data discussed above. Moreover, the trend of Pb isotope data (Fig. 4) together with the presence of abundant mafic and ultramafic igneous rocks in the footwall succession, suggests derivation of the galena-hosted lead from sources in both the deep crust and mantle, although a contribution of lead from the middle crust (orogene) cannot be ruled out.

Owing to the absence of reliable fluid inclusion data, the main stage of copper deposition is estimated to have occurred at temperatures of 200–400 °C based on the common occurrence of "chalcopyrite disease" in sphalerite grains (Barton and Bethke 1987). This interval of temperatures matches those bracketed between 260 and 305°C based on equilibrium temperatures inferred from chlorite geothermometry (Marcoux and Jébrak 2012).

Sulphur together with lead isotope compositions indicate that the hydrothermal fluids were predominantly magmatic although the involvement of meteoric water remains possible. However, the data are insufficient to confidently define relative proportions of magmatic fluid and meteoric water in the mineralizing process. Exsolution of magmatic SO_2 could have produced a shallow crustal fluid reservoir enriched in SO_2 or SO, either through condensation into meteoric water or through the disproportionation of the magmatic gas phase (see Rye 1993).

Indeed, it is well documented that in shallow crustal environments like the one inferred here for Bouskour ore deposition, exsolution of hydrothermal fluids from a crystallizing magma can release large volumes of gases, including oxidizing components such as $SO_{2(g)}$, acidic components such as $HCl_{(g)}$, and smaller volumes of dense, saline brines (Bodnar et al. 1985). The occurrence of acidic fluid conditions during emplacement of the copper mineralization at Bouskour is supported by the coexistence of illite-chlorite alteration assemblages (see Hedenquist and Browne 1989; Bove et al. 2002).

The paragenetically late third stage (III) characterized by base-metal ± Ag ± Au ± copper sulphide mineralization remains enigmatic and its emplacement is poorly constrained due to the lack of reliable geochemical data. Further studies are thus required to adequately characterize this stage. However, when considered regionally, stage III could be correlative with the Hercynian auriferous base-metal stage that typifies the metal deposits of the Anti-Atlas system (e.g., Bou Azzer and Bou Madine deposits described in this volume).

References

Barbero L, Jabaloy A, Gómez-Ortiz D, Pérez-Peña JV, Rodríguez-Peces MJ, Tejero R, Estupiñan J, Azdimousa A, Vázquez M, Asebriy L (2011) Evidence for surface uplift of the Atlas Mountains and the surrounding peripheral plateaux: combining apatite fission-track results and geomorphic indicators in the western Moroccan Meseta (coastal Variscan Paleozoic basement). Tectonophys 502:90–104

Barton PB Jr, Bethke PM (1987) Chalcopyrite disease in sphalerite: pathology and epidemiology. Am Mineral 72:451–467

Benziane F (2007) Lithostratigraphie et évolution géodynamique de l'Anti-Atlas (Maroc) du Paléoprotérozoïque au Néoprotérozoïque: exemple de la boutonnière de Tagragra da Tata et du Jbel Saghro. Unpublished Ph.D. Thesis, Haute Savoie University CISM, Chambéry, France, 320 pp

Bodnar RJ, Burnham CW, Sterner SM (1985) Synthetic fluid inclusions in natural quartz. III. Determination of phase equilibrium properties in the system H_2O-NaCl to 1000°C and 1500 bars. Geochim Cosmochim Acta 49:186l–1873

Bouougri EH, Saquaque A (2004) Lithostratigraphic framework and correlation of the Neoproterozoic northern West African craton passive margin sequence (Siroua, Zenaga, Bouazzer-Elgraara inliers, Central Anti-Atlas, Morocco): an integrated approach. J Afr Earth Sci 39:227–238

Bove DJ, Eberl DD, McCarty DK (2002) Characterization and modeling of illite crystal particles and growth mechanisms in a zoned hydrothermal deposit, Lake City, Colorado. Am Mineral 87:1546–1556

Chebbaa B (1996) Métallogénie du cuivre associé aux roches volcaniques d'âge Précambrien II supérieur dans l'Anti-Atlas marocain. Unpublished Ph.D. Thesis, University Lausanne, Switzerland, 235 pp

Cheilletz A, Gasquet D, Filali F, Archibald DA, Nespolo M (2010) A Late Triassic $^{40}Ar/^{39}Ar$ age for the El Hammam high-REE fluorite deposit (Morocco): mineralization related to the Central Atlantic Magmatic Province? Miner Deposita 45:323–329

Clavel M, Tixeront M (1971) Une gîte de cuivre filonien, hydrothermal intraplutonique: Bou Skour (Anti-Atlas, Maroc). Notes Mémoires Service Géologiques Maroc 31(237):203–228

Cumming GL, Richards JR (1975) Ore lead isotope ratios in a continuously changing Earth. Earth Planet Sci Lett 28:155–171

Drummond SE, Ohmoto H (1985) Chemical evolution and mineral deposition in boiling hydrothermal systems. Econ Geol 80:126–147

Duuring P, McKinley BSM, Dickinson JM, Diakow LJ, Kim YS, Creaser RA (2009) Examining potential genetic links between Jurassic porphyry Cu-Au±Mo and epithermal Au±Ag mineralization in the Toodggone district of north-central British Columbia. Miner Deposita 44:463–490

EL Azmi D, Aissa M, Ouguir H, Mahdoudi ML, El Azmi M, Ouadjo A, Zouhair M (2014) Magmatic context of Bou Skour copper deposit (eastern Anti-Atlas, Morocco): petrogrography, geochemistry and alterations. J Afr Earth Sci 97:40–55

El Hadi H, Simancas JF, Martínez-Poyatos D, Azor A, Tahiri A, Montero P, Fanning CM, Bea F, González-Lodeiro F (2010) Structural and geochronological constraints on the evolution of the Bou Azzer Neoproterozoic ophiolite (Anti-Atlas, Morocco). Precambr Res 182:1–14

Ezzouhairi H (1989) Etude pétrographique, géochimique et structurale des formations plutoniques du Précambrien II de la boutonnière de Bou Skour (Saghro occidental, Anti Atlas, Maroc). Unpublished Doct 3ème cycle, Cadi Ayyad University, Marrakech, Morocco, 210 pp

Ezzouhairi H (1997) Magmatisme et tectonique de l'arc précambrien de Bou Skour(Saghro occidental, Anti Atlas, Maroc). Comunic Instituto Geologico Mineiro Portugal 83:47–52

Ezzouhairi H (2001) Le magmatisme post-collisionnel panafricain (tardi à post-orogénique) des régions d'Aghbalou, Sidi Flah Bouskour et Oued Imini

(Ouarzazate, Anti-Atlas central, Maroc). Lithostratigraphie, géochimie, pétrogenèse et contexte géodynamique. Unpublished Ph.D. thesis, Chouaïb Doukkali University, El Jadida, Morocco, 210 pp

Ezzouhairi H, Ribeiro ML, Ferreira P, Ait Ayad N, Charif A, Ramos JMF (1998) Magmatisme précambrien de la région d'Aghbalou-Oued Imini (Anti-Atlas central du Maroc): nature géochimique et quelques aspects significatifs. Comunic Instituto Geologico Mineiro Portugal 84:178–181

Ezzouhairi H, Ribeiro ML, Ait Ayad N, Moreira ME, Charif A, Ramos JMF, De Oliveira DPS, Coke C (2008) The magmatic evolution of the Moroccan outboard of the West African Craton between the Late Neoproterozoic and the Early Palaeozoic. In Ennih N, Liégeois J-P (eds) The boundaries of the West African Craton. Geological Society, Special Publication, vol 297, pp 329–343

Fekkak A (2000) Les groupes du Néoprotérozoïque inférieur de Sidi Flah, Kelaat Mgouna et Tiboulkhirine (Saghro, Anti-Atlas, Maroc): témoins d'un rift intracontinental pré-panafricain. Unpublished Ph.D. Thesis, Moulay Ismail University, Meknès, Morocco, 265 pp

Fekkak A, Pouclet A, Ouguir H, Ouazzani H, Badra L Gasquet D (2001) Géochimie et signification géotectonique des volcanites du Cryogénien inférieur du Saghro (Anti-Atlas oriental, Maroc). Geodin Acta 14:373–385

Fekkak A, Pouclet A, Benharref M (2003) The Middle Neoproterozoic Sidi Flah group (Anti Atlas, Morocco): synrift deposition in a panafricain continent/ocean transition zone. J Afr Earth Sci 37:73–87

Gasquet D, Levresse G, Cheilletz A, Azizi Samir MR, Mouttaqi A (2005) Contribution to a geodynamic reconstruction of the Anti-Atlas (Morocco) during Pan-African times with the emphasis on inversion tectonics and metallogenic activity at the Precambrian-Cambrian transition. Precambr Res 140:157–182

Ghorbal B, Bertotti G, Foeken J, Andriessen P (2008) Unexpected Jurassic to Neogene vertical movements in 'stable' parts of NW Africa revealed by low temperature geochronology. Terra Nova 20:355–363

Hedenquist JW, Browne RPL (1989) The evolution of the Waiotapu geothermal system, New Zealand, based on the chemical and isotopic composition of its fluids, minerals, and rocks. Geochim Cosmochim Acta 53:2235–2257

Hoefs J (2009) Stable isotope geochemistry, 6th edn. Springer, Berlin, 285 pp

Kamvong T, Zaw K (2009) The origin and evolution of skarn-forming fluids from the Phu Lon deposit, northern Loei Fold Belt, Thailand: evidence from fluid inclusion and sulfur isotope studies. J Asian Earth Sci 34:624–633

Leblanc M, Lancelot Y (1980) Interprétation géodynamique du domaine pan-africain (Précambrien terminal) de l'Anti-Atlas (Maroc) à partir de données géologiques et géochronologiques. Canad J Earth Sci 17:142–155

Leblanc M, Moussine-Pouchkine A (1994) Sedimentary and volcanic evolution of a Neoproterozoic continental margin (Belida, Anti-Atlas, Morocco). Precambr Res 70:25–44

Maacha L, Ouadjou A, Azmi M, Zouhair M, Saquaque A, Alansari A, Soulaimani A (2011) Bouskour copper and silver mine (J Saghro inlier, eastern Anti-Atlas). Notes Mémoires Service Géologique Maroc 564:59–64

Marcoux E, Jébrak M (2012) Le projet à cuivre de Bou Skour. Unpubl confidential report, Managemgroup, 105 pp

Ohmoto H, Goldhaber MB (1997) Sulfur and carbon isotopes. In: Barnes HL (ed) Geochemistry of hydrothermal ore deposits, 3rd edn. John Wiley and Sons, New York, pp 517–611

Rye RO (1993) The evolution of magmatic fluids in the epithermal environment: the stable isotope perspective. Econ Geol 88:733–753

Sánchez V, Corbella M, Fuenlabrada JM, Vindel E, Martín Crespo T (2006) Sr and Nd isotope data from the fluorspar district Asturias, Northern Spain. J Geochem Explor 89:348–350

Saquaque A, Admou H, Karson J, Hefferan K, Reuber I (1989) Precambrian accretionary tectonics in the Bou Azzer-El Graara region, Anti-Atlas, Morocco. Geology 17:1107–1110

Saquaque A, Benharref M, Abia H, Mrini Z, Reuber I, Karson JA (1992) Evidence for a Panafrican volcanic arc and wrench fault tectonics in the Jbel Saghro, Anti-Atlas, Morocco. Geologische Rundschau 81 (1):1–13

Sebti S, Saddiqi O, El Haimer FH, Michard A, Ruiz G, Bousquet R, Baidder L, Frizon de Lamotte D (2009) Vertical movements at the fringe of the West African Craton: first fission track datings from the Anti-Atlas Precambrian basement, Morocco. C. R. Geosci 341:71–77

Stacey JS, Kramers JC (1975) Approximation of terrestrial lead isotope evolution by a two-stage model. Earth Planet Sci Lett 26:207–221

Thomas RJ, Chevallier LP, Gresse PG, Harmer RE, Eglington BM, Armstrong RA, de Beer CH, Martini JEJ, de Kock GS, Macey PH, Ingram BA (2002) Precambrian evolution of the Siroua window, Anti-Atlas orogen, Morocco. Precambr Res 118:1–57

Thomas RJ, Fekkak A, Ennih N, Errami E, Loughlin SC, Gresse PG, Chevallier LC, Liégeois J-P (2004) A new lithostratigraphic framework for the Anti-Atlas orogen, Morocco. J Afr Earth Sci 39:217–226

Tixeront M (1971) Les formations précambriennes de la région minéralisée en cuivre de Bou Skour (Anti-Atlas marocain). Notes Mémoires Service Géologique Maroc 31(237):181–202

Valenza K, Moritz R, Mouttaqi A, Fontignie D, Sharp Z (2000) Vein and karst barite deposits in the western Jebilet of Morocco: fluid inclusion and isotope (S, O, Sr) evidence for regional fluid mixing related to Central Atlantic rifting. Econ Geol 95:587–606

Walsh GE, Aleinikoff JN, Benziane F, Yazidi A, Armstrong TR (2002) U–Pb zircon geochronology of the Paleoproterozoic Tagragra de Tata inlier and its Neoproterozoic cover, western Anti-Atlas, Morocco. Precambr Res 117:1–20

Walsh GJ, Benziane F, Burton WC, El Fahssi A, Yazidi A, Yazidi M, Saadane A, Aleinikoff JN, Ejjaouani H, Harrison RW, Stone BD, Kalai M (2008) Carte géologique au 1/50 000, Feuille Bouskour. Notes et Mémoires Service Géologique Maroc 469, 131 pp

Walsh GJ, Benziane F, Aleinikoff JN, Harrison RW, Yazidi A, Burton WC, Quick JE, Saadane A (2012) Neoproterozoic tectonic evolution of the Jebel Saghro and Bou Azzer-El Graara inliers, eastern and central Anti-Atlas, Morocco. Precambr Res 216–219:23–62

Zartman RE, Doe BR (1981) Plumbotectonics–the model. Tectonophys 75:35–162

Geology, Fluid Inclusions, and Geochemistry of the Aouli Sulphide ± Fluorite ± Barite Vein Deposit (Upper Moulouya District, Morocco) and Its Relationships to Pangean Rifting and Opening of the Tethys and Central Atlantic Oceans

Mohammed Bouabdellah and Daoud Margoum

Abstract

The Aouli Pb–Zn ± F ± Ba deposit in the upper Moulouya district of central Morocco consists of an array of multi-kilometer, transtensional, sub-vertical veins grouped into four main systems referred to as Aouli, Ansegmir, Sidi Said, and Sidi Ayad. Collectively, these veins produced ~10 Mt of ore at a grade of 5 % Pb. Host rocks are a succession of folded and low- to medium-grade metasedimentary and minor metavolcanic rocks of Cambro-Ordovician age locally intruded by the multiphase ca. ~330–319 Ma Aouli batholith. The veins occur either within the Aouli granitic intrusion (i.e., Ansgemir), Cambro-Ordovician schistose pelites (i.e., Aouli, Sidi Said), or both (i.e., Sidi Ayad). Overall, the orebodies exhibit very low Zn/Pb ratios, and contain 150–600 g/t Ag and 200–700 g/t Bi. Hydrothermal alteration is weakly to moderately developed in the vicinity and surrounding the veins, and is dominated by intense silicification coupled with minor sericitization, both types being superimposed on regional propylitic alteration. The sulphide mineralization consists principally of varying proportions of galena and sphalerite, and to a much lesser extent chalcopyrite and pyrite. Gangue minerals include multiple generations of quartz and paragenetically later fluorite and barite. Combined fluid inclusion data together with stable and radiogenic isotopic constraints indicate that the Aouli vein-type sulphide ± fluorite ± barite mineralization formed during the Permian-Jurassic contemporaneously with Pangean rifting and subsequent opening of the Tethys and Central

M. Bouabdellah (✉) · D. Margoum
Département de Géologie, Faculté des Sciences,
Université Mohammed Premier, Avenue
Mohammed VI, B.P. 717, 60000 Oujda, Morocco
e-mail: mbouabdellah2002@yahoo.fr

M. Bouabdellah and J.F. Slack (eds.), *Mineral Deposits of North Africa*,
Mineral Resource Reviews, DOI 10.1007/978-3-319-31733-5_11

Atlantic oceans. Mixing at the basement-cover interface of an ascending, deep-seated fluid that equilibrated with Hercynian crystalline basement rocks, and formation and/or meteoric water, is proposed to have triggered ore deposition.

1 Introduction

The Hercynian (Variscan) Aouli inlier of the upper Moulouya district (Fig. 1) and its unconformably overlying Mesozoic-Cenozoic strata host some of the largest Pb–Zn ± F ± Ba deposits of Morocco with a cumulative production in excess of 31 Mt of ore at an average grade of ~4.5 % Pb (Annich and Rahhali 2002; Rahhali 2002a, b). This district is unique in containing a wide variety of mineralization styles including (Fig. 2): (1) vein-type (i.e., Aouli deposit described herein; 9.6 Mt at 5 % Pb), (2) stratiform diagenetic type (i.e., Zeida deposit; 16 Mt at 3 % Pb); and (3) stratabound Mississippi Valley-type (MVT) (i.e., Mibladen deposit; 6.5 Mt at 5 % Pb). Although comparative studies exist (Bouladon 1956; Emberger 1965a, b, c; Duthou et al. 1976; Jébrak et al. 1998), the genetic relationships among these three deposit types remain poorly constrained owing to the lack of detailed geochronological and geochemical data. Based specifically on differences in geological environment, alteration mineral assemblages, and textures, we interpret these different deposit types as being genetically unrelated. Indeed, the Zeida deposit exhibits many diagnostic features typical of so-called sandstone-hosted Pb deposits that contrast greatly with those of the epigenetic Mibladen MVT mineralization. Conversely, the Aouli vein deposit belongs to the large family of hydrothermal vein-type deposits or "filon péri--plutonique de départ acide" of Routhier (1963, 1980) that are spatially but not genetically related to granitoid intrusions and associated apophyses (Wolff et al. 2015, and references herein)

The Aouli district was discovered in the 1920s and had many periods of intermittent mining. From 1926 to 1983, the district produced more than 9.6 Mt of ore at an average grade of 5 % Pb. The mines closed in 1988, but exploration in the area is continuing by "la Compagnie Minière de Touissit" which recently carried out a program of diamond drilling. Remaining reserves, estimated at the time of closure of the mines, are ~3 Mt at 3.4 % Pb (Rahhali 2001). Underground workings are currently inaccessible but outcrops of the mineralization are well exposed.

The present contribution aims to: (1) review and update the geological environment of the Aouli Pb–Zn ± Ba ± F vein mineralization; (2) present newly acquired microthermometric measurements and consequently reinterpret existing data for rare earth elements and yttrium (REY) and isotope in order to constrain the chemistry of the mineralizing fluids; and (3) discuss the evolution of the mineralizing system and its implications for understanding ore-forming processes with respect to basin setting, associated magmatism, and geodynamic evolution.

2 Geologic Setting

The stratigraphy of the Aouli orefield consists of a succession of greenschist- to amphibolite-facies metasedimentary and minor metavolcanic rocks of lower Paleozoic age and unconformably overlying Mesozoic to Cenozoic strata (Emberger 1965a, b, c; Fig. 1). The lower Paleozoic sequence, locally intruded by the hydrothermally altered multiphase Aouli batholith, consists of up to 3800 m of Cambro-Ordovician pelite, shale, greywacke, and siltstone interlayered with minor tuff, mudstone, and metabasalt (i.e., amphibolite; Ouali et al. 2000).

The Aouli batholith forms a large (15 km × 25 km) elongate, ENE-trending, multiphase, syn- to post-orogenic Hercynian intrusion (Fig. 1).

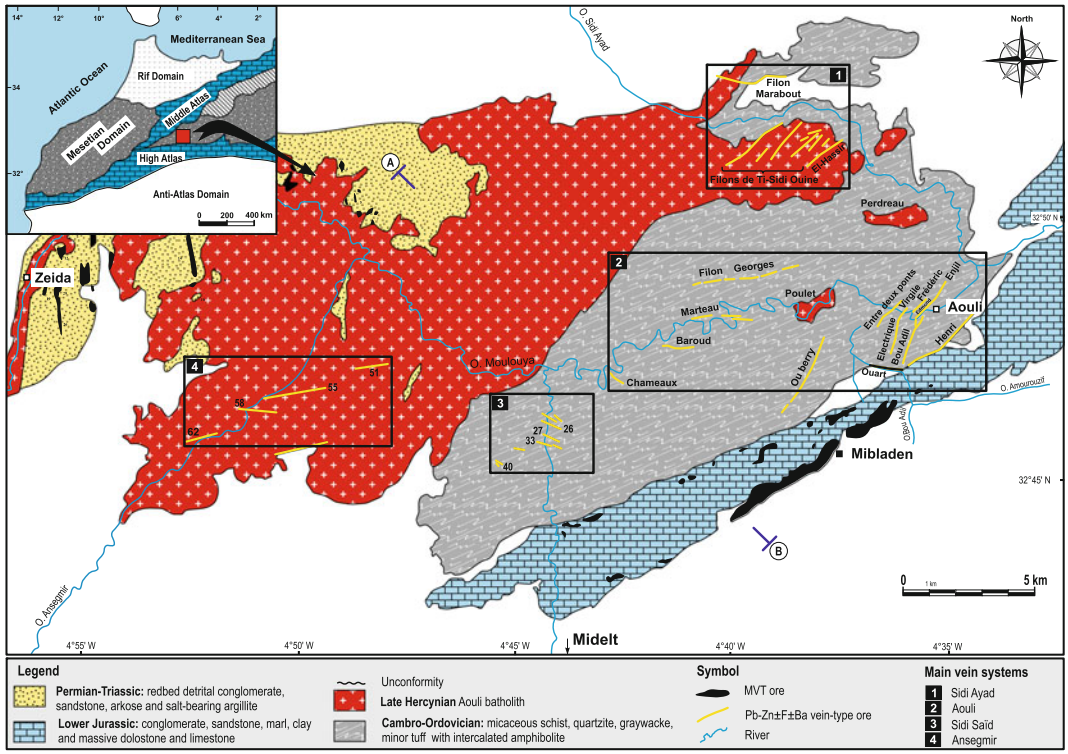

Fig. 1 Generalized geologic map of upper Moulouya district showing regional geology, major faults, and location of historically mined Aouli, Mibladen, and Zeida base-metal ± fluorite ± barite deposits (modified after Emberger 1965b). Inset shows district within major tectonostratigraphic domains of Morocco. Outlined boxes refer to main base-metal sulphide ± fluorite ± barite vein systems of Aouli district. Section line *A–B* indicates cross-section presented in Fig. 2

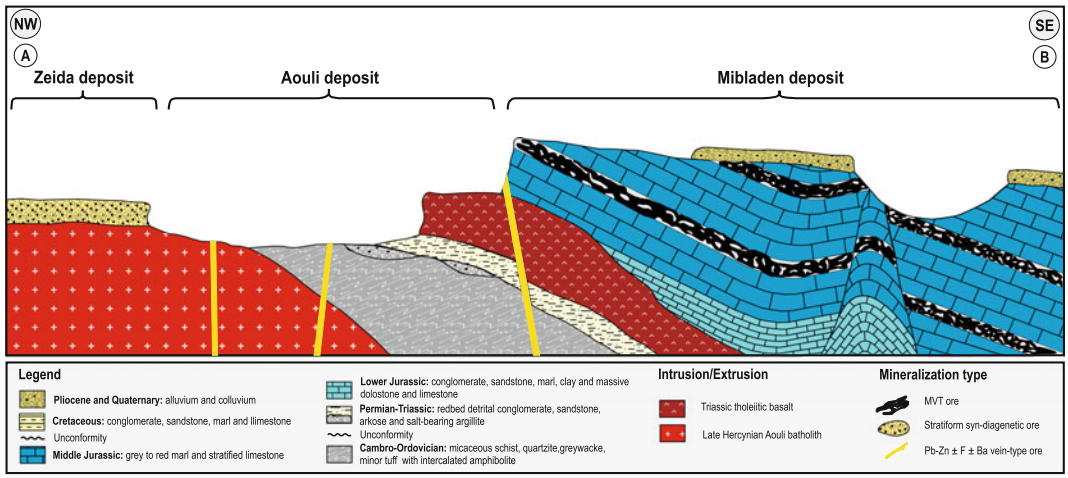

Fig. 2 Idealized longitudinal NW-SE cross section through upper Moulouya district showing spatial distribution of historically mined Aouli, Zeida, and Mibladen base-metal sulphide ± fluorite ± barite deposits, and their relationship to stratigraphy and fault systems (modified after Emberger 1965b). See Fig. 1 for position of cross section

Based on whole-rock geochemistry, radiometric ages, and crosscutting relationships, the Aouli batholith is subdivided into three major mappable units: (1) El Hassir apophysis, (2) Aouli-Bou Mia (Aolui *ss*) intrusion, and (3) Poulet-Perdreaux intrusions. Radiometric ages indicate that the El Hassir apophysis, dated at 347–328 Ma (Oukemeni 1993; Oukemeni and Bourne 1994; Oukemeni et al. 1995; Dahire 2004), was emplaced before the 329–319 Ma Aouli *ss* intrusion (Oukemini 1993; Oukemeni and Bourne 1994; Oukemeni et al. 1995), which in turn preceded the 308–281 Ma Poulet-Perdreaux leucogranite (Tisserant 1977; Clauer et al. 1980). Following emplacement, the Aouli batholith was intruded by an undated, northeast-trending dike swarm of microgranite, aplite, and pegmatite, and by Triassic dolerite-diabase sills (Fig. 1). Pervasive hydrothermal alteration affected, to varying degrees, the Aouli batholith resulting in the formation of microcline, albite, chlorite, and greisen-type assemblages in all granitic units.

Regional metamorphic grade of the stratified rocks ranges from greenschist to amphibolite. Conversely, intrusion of the Aouli batholith gave rise to contact metamorphic mineral assemblages (i.e., cordierite, andalusite, chlorite, muscovite, and biotite ± sillimanite ± garnet), which record peak thermal conditions of 400–550 °C and pressures of less than 3 kbar, corresponding to emplacement depths ranging from 4 to 7 km (Filali 1996; Dahire 2004).

Unconformably overlying the Paleozoic package is a ~400–500-m-thick sequence of Permian-Triassic redbed sedimentary rocks including basal conglomerate, sandstone, arkose, and gypsiferous to salt-bearing argillite interbedded with tholeiitic basalt sills and lava flows, followed by up to 1000 m of Jurassic-Cretaceous shallow marine carbonates and marls. Locally covering these strata are Plio-Quaternary (ca. 14.6–0.5 Ma) alkaline basaltic lava flows (Harmand and Cantagrel 1984; Duggen et al. 2009; Wittig et al. 2010).

The tectonic structures resulting from both the Variscan and Atlasic orogenies are dominated by a succession of tight to isoclinal folds with fracture cleavage or flow schistosity, along with a series of dominant E-W-trending and sub-ordinate ENE-WSW, NW-SE and WNW-ESE multiple kilometre-scale faults. Structural analysis indicates that these faults are characterized by an early compressional shearing overprinted by several late extensional events (Jébrak et al. 1998).

3 Alteration, Mineralogy, and Paragenesis

In the mining area the Pb–Zn ± fluorite ± barite mineralization consists of a complex system of transtensional, sub-vertical veins (Fig. 1), veinlets, and en echelon tension-gash fillings. These mineralized structures occur principally within the Aouli granitic intrusion and surrounding Cambro-Ordovician country rocks, or along the contact of the Paleozoic rocks and unconformably overlying Triassic to Liassic sedimentary cover. Locally, some mineralized veins branch into the Triassic-Liassic strata (Fig. 2). It is noteworthy that most mineralized veins occur along regional fault zones, display similar morphologic and textural features, and exhibit sharp margins with host rocks.

Four Pb–Zn ± fluorite ± barite vein systems, referred to as Sidi Ayad, Aouli, Sidi Said, and Ansegmir, have been exploited both from open pits and underground workings (Fig. 1). The Aouli and to a lesser extent Sidi Ayad vein sets are historically and economically the most important; the Georges, Henry, Engil, and Marabout are by far the most productive, accounting for more than 90 % of extracted Pb–Zn ore in the district.

The veins are confined to crustal-scale faults and occur principally as ENE-WSW-, WNW-ESE-, and to a lesser extent E-W-trending, transtensional brittle structures. Surface exposures are over a strike length of as much as 10 km or more. Veins are spaced 50 to >1000 m apart, dip sub-vertically, are up to 40 m wide (i.e., George vein), and are continuous for several hundred meters down plunge. Most, if not all, of the exploited veins are displaced by second-order faults and thus are fragmented into a succession of one or more orebodies and less mineralized barren segments. The orebodies exhibit very low

Zn/Pb ratios from 0.004 to 0.006, and contain 150–600 g/t Ag and 200–700 g/t Bi. Most veins show a pronounced vertical metal zonation, with Ag and Bi contents increasing systematically with depth from 150 and 200 g/t to 300–600 and 400–700 g/t, respectively (Naji 2004). Characteristic are banded structures and symmetrical mineral zoning expressed from the margin toward the vein center, consisting of quartz + barite, quartz + barite + fluorite, quartz + galena, quartz + sphalerite, and quartz + galena + sphalerite + silver minerals. Early precipitated minerals are variably eroded, cut, or brecciated and then cemented by subsequent phases (i.e., drusy or comb-textured quartz, locally barite and fluorite). Vuggy, cockade, and crustiform textures surrounding clasts of wall rock and post-mineral faults are common, suggesting that multiple episodic mechanisms were important during transtensional vein formation. The pinch-and-swell geometry shown by most of the Aouli veins may be explained following the model of Wise (2005), in which mineralization formed in local dilatant zones along anastomosing faults (i.e., Aouli and Ahmourou faults). Hydrothermal alteration is weakly to moderately developed near the veins, decreases outward sharply, and within a few centimeters to several meters of the veins is dominated by intense silicification coupled with minor sericitization, both types having been superimposed on regional propylitic alteration.

Exploited veins display generally similar mineral assemblages dominated by various proportions of quartz, galena, sphalerite, chalcopyrite, and pyrite. Fluorite and barite occur locally, although their relative abundances compared to other minerals vary from one vein to another. Geochemical data indicate that the Aouli fluorite has high total REY contents ranging from 250 to 662 ppm, distinctive positive Eu and Y anomalies, and relative enrichment of middle REE resulting in "hump-shaped" patterns (Margoum et al. 2015), consistent with typical fluorite compositions determined for "Mesozoic" fluorite-barite vein deposits of Central and Western Europe (Wolff et al. 2015).

The sequence of mineral deposition comprises four successive stages of Pb–Zn ± F ± Ba mineralization, two of which (stages I and II) are of economic importance. The earliest stage (I) consists of fine-grained Ag-rich galena, sphalerite, and pyrite in a gangue of amorphous silica (chalcedony). The second stage (II), referred to as the "main-ore stage," is economically the most valuable, accounting for more than 90 % of total Pb–Zn resources; the assemblage consists of coarse-grained galena in addition to sphalerite and sucrosic quartz. The third stage (III) comprises a sulphide-quartz-fluorite-barite assemblage, in which galena is scarce and the major gangue minerals are variably coloured fluorite and massive white to pink barite. The fourth stage (IV), referred to as the "late-ore cuboctahedral stage," consists of variably coloured, centimeter-sized, cubes of galena and fluorite crystals, accompanied by tabular white to pink barite (i.e., crested barite or barite roses) and drusy quartz that line vugs.

The post-ore supergene stage (IV) resulted from the oxidation of primary sulphides. This stage comprises minor amounts of cerussite, malachite, azurite, and Fe- and Mn-oxides.

4 Age of Mineralization

No radiometric age is available for the Aouli sulphide ± fluorite ± barite veins. As a result, combined geological field observations and cross-cutting relationships have been used to bracket the relative timing of mineralization. The veins are structurally controlled and cut both the dominant regional S_{2-3} foliation and the late Hercynian (ca. 347–319 Ma) Aouli granitic intrusion. Moreover, the sulphide ± fluorite ± barite mineralization extends upward into the Triassic red beds and Liassic carbonates. Together, these relationships indicate that the Aouli sulphide ± fluorite ± barite veins formed late in the tectonic history of the district, toward the end of the latest phase of the Hercynian orogeny and the onset of Tethys and Central Atlantic opening

during Triassic-Jurassic. Thus, the inferred timing for Aouli vein mineralization is constrained between the Permian and the Jurassic. This inferred time interval fits within the span of hydrothermal events dated by apatite fission track techniques at 250–210 Ma (Ghorbal et al. 2008; Saddiqi et al. 2009; Barbero et al. 2011) that affected most Hercynide domains of North Africa, and agrees with radiometric ages obtained for the similar polymetallic Tighza vein (280–275 Ma; Watanabe 2002; Marcoux et al. 2015; Rossi et al. 2016), the El Hammam REE-fluorite vein (205 ± 1 Ma; Cheilletz et al. 2010; Bouabdellah et al. 2010), and the vein and karst barite deposits in the Western Meseta of Morocco (220–155 Ma; Valenza et al. 2000), as well as for most late Paleozoic to Mesozoic Pb–Zn ± F ± Ba vein deposits in Central and Western Europe (Meyer et al. 2000; Sánchez et al. 2006; Wolff et al. 2015).

5 Fluid-Inclusion Microthermometry

Fluid inclusions were studied in ore-related quartz from the four main vein systems that constitute the Aouli district. The fluid inclusions are classified as primary, pseudosecondary, or secondary according to the criteria of Roedder (1984).

Based on the number of observable phases present at room temperature, all inclusions are two-phase (liquid + vapor), with relatively uniform vapor/liquid ratios of about 0.15. No daughter phases, clathrates, or visual evidence of CO_2 have been recorded. Microthermometric measurements, presented here for the first time, were performed exclusively on liquid-rich inclusions that homogenized by disappearance of the vapor bubble. Data are summarized in Table 1 and plotted in Figs. 3, 4, and 5.

Homogenization temperatures (T_h) of primary and pseudosecondary inclusions range from 62 to 205 °C (n = 129) and show a roughly bimodal distribution (Fig. 3A), with a prominent major peak at ~120–140 °C and a subordinate minor peak at 110–120 °C. Similarly, there is a wide spread of final ice melting temperatures of −21.7 to −10.3 (n = 79), reflecting variable fluid salinities. Assuming that the trapped liquid consists of water and dissolved salts, calculated salinities range between 16 and 24 wt% NaCl equiv. The distribution of calculated salinities defines a main peak at 22–23 wt% NaCl equiv and a weakly defined peak at 18 wt% NaCl equiv (Fig. 3b). These microthermometric data match the range of T_h and salinity values recorded for the associated paragenetically late fluorite (Fig. 4; Margoum et al. 2015). All of these observations indicate that the ore-related quartz and late fluorite were deposited by the same hydrothermal system.

Significantly, fluid inclusions in quartz from the Ansegmir vein system have the highest salinities (21–23 wt% NaCl equiv), whereas those from the Aouli vein system exhibit the lowest salinities with an average of 17 wt% NaCl equiv. Intermediate salinities of 19 and 20 wt% NaCl equiv are recorded in quartz-hosted inclusions from the Sidi Ayad and Sidi Said vein systems; respectively (Fig. 5). These spatial microthermometric trends are similar to those described by Margoum et al. (2015) for paragenetically late fluorite mineralization in the district.

5.1 Oxygen, Sulphur, Lead, and Strontium Isotope Geochemistry

The isotopic data discussed hereafter draw extensively from Jébrak et al. (1998), Naji (2004), and Margoum et al. (2015).

Quartz separates from the Henri and Engill veins have highly variable $\delta^{18}O$ values from +13.9 to +28.9 ‰ (avg = + 18.8 ± 3.8 ‰, n = 14); most values cluster between +15 and +20 ‰ (Naji 2004). Barite separates show $\delta^{34}S$ ratios of +11 to +13.4 ‰, similar to those of Permian-Triassic seawater sulphate (Margoum et al. 2015). Jébrak et al. (1998) reported two $\delta^{34}S$ values for galena of −9 and 1.5 ‰, and Pb isotopic compositions that plot in a tight linear array above the evolution curve of Stacey and Kramers (1975), with fairly uniform $^{206}Pb/^{204}Pb$ (18.110–

Table 1 Summary of microthermometric data for fluid inclusions hosted in ore-related quartz from different vein systems of Aouli sulphide ± fluorite ± barite district

Vein system	T_e					$T_{m(ice)}$					$T_{m(hh)}$					T_h					Salinity				
	n	Min	Max	Avg.	Std. Dev	*n*	Min	Max	Avg.	Std. Dev	*n*	Min	Max	Avg.	Std. Dev	*n*	Min	Max	Avg.	Std. Dev	*n*	Min	Max	Avg.	Std. Dev
Aouli	37	−80	−44	−60	9.7	12	−16.5	−10.3	−13.2	2.0	3	−20.1	−18.2	−19.4	1.0	45	62	205	137	25.7	9	15.9	17.6	16.6	0.56
Sidi Ayad	23	−59	−45	−52	4.1	23	−19.4	−15.4	−16.8	0.9	10	−21.5	19.7	−16.4	12.7	34	79	130	108	12.4	23	19.1	22.2	20.2	0.71
Sidi Said	17	−77	−49	−66	8.4	19	−21.7	14.7	−15.1	7.8	–	–	–	–	–	16	125	163	143	12.0	16	17.7	23.8	19.3	1.91
Ansegmir	31	−90	71	−69	27.3	31	−20.7	−19	−19.9	0.5	14	−25.5	−22.3	−24	0.8	34	125	164	138	8.5	31	21.9	23.2	22.6	0.33

Abbreviation: *Avg*. average; *n* number of measurements; *Max* maximum; *Min* minimum; *Std. Dev* standard deviation

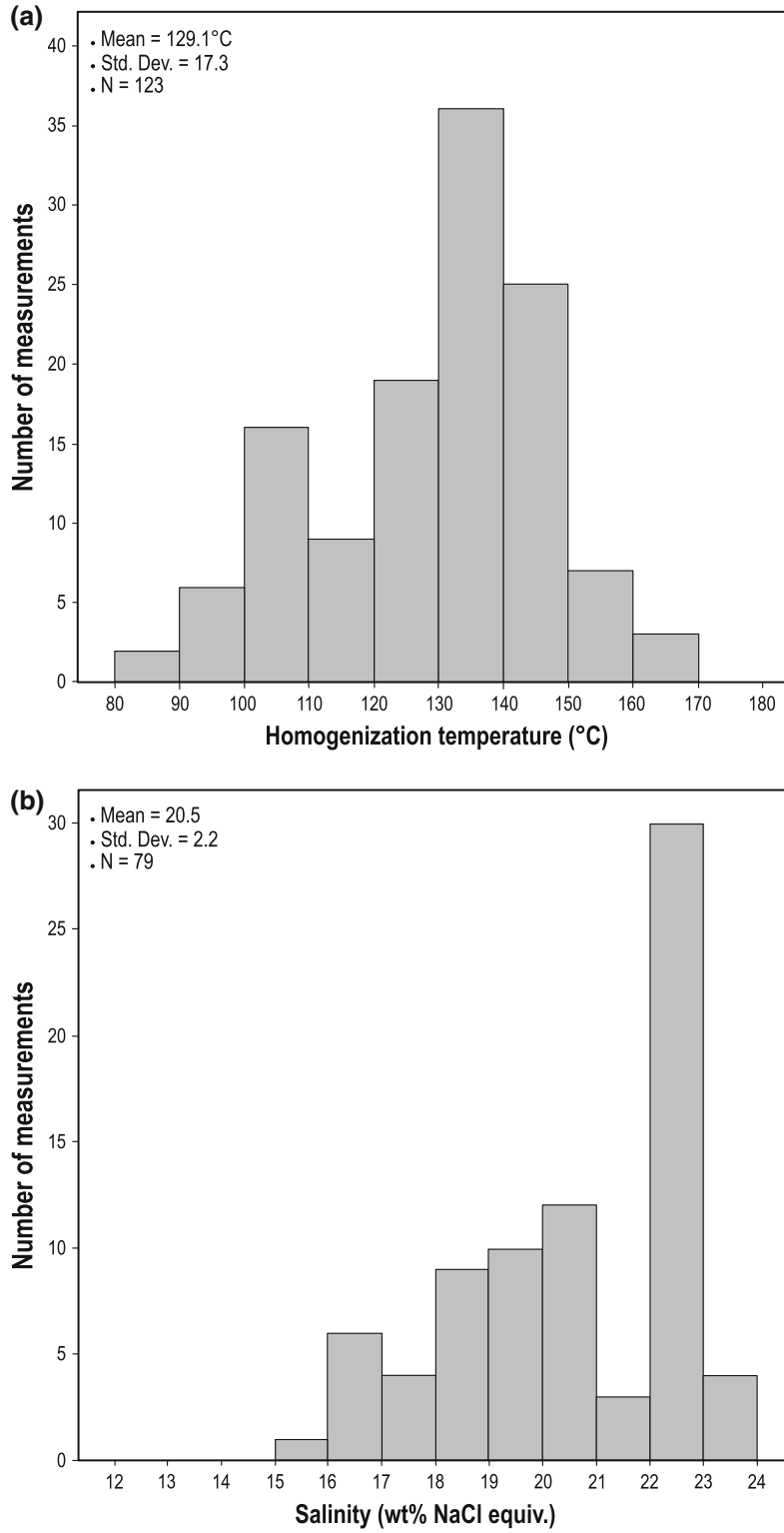

Fig. 3 Cumulative histograms of homogenization temperatures (**a**) and salinities (**b**) for ore-related fluid inclusions in quartz from main vein systems of Aouli base metal sulphide ± fluorite ± barite district

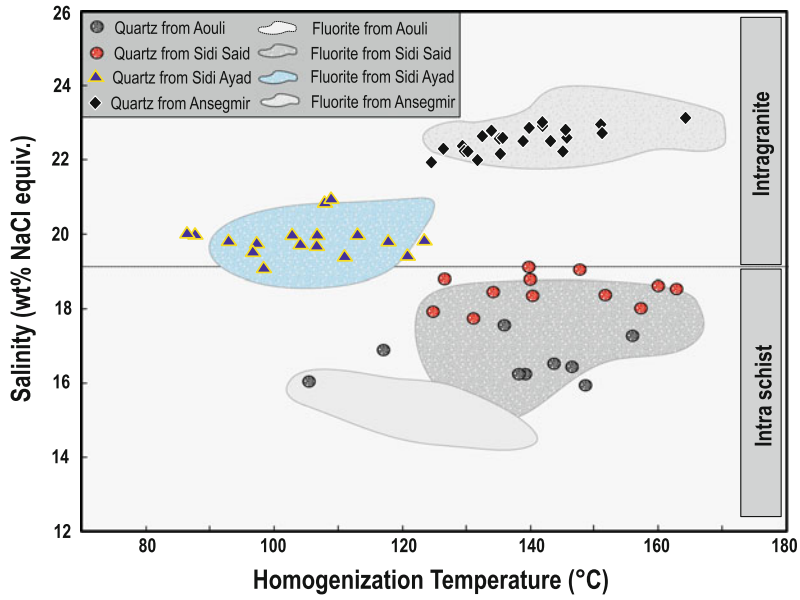

Fig. 4 Homogenization temperature (T_h) versus salinity plot of primary and pseudosecondary fluid inclusions hosted in ore-related quartz from main vein systems of Aouli base metal sulphide ± fluorite ± barite district. Shown for comparison are fields that define ranges of microthermometric values for paragenetically late fluorite from the different vein systems of this district (data from Margoum et al. 2015)

18.246), $^{207}Pb/^{204}Pb$ (15.601–15.630), and $^{208}Pb/^{204}Pb$ (38.370–38.530) ratios. These Pb isotopic compositions are slightly more radiogenic than those for K-feldspar separates from the Aouli granite that have $^{206}Pb/^{204}Pb$, $^{207}Pb/^{204}Pb$, and $^{208}Pb/^{204}Pb$ ratios of 17.943–18.083, 15.511–15.585, and 37.784–38.147, respectively (Duthou et al. 1976; Jébrak et al. 1998).

The strontium isotopic composition of paragenetically late fluorite ($^{87}Sr/^{86}Sr$ = 0.710155–0.712293) and barite (0.710215–0.701401) overlap partially or wholly with those reported for Triassic arkoses and Liassic dolomitized limestones (0.707867–0.708140) and are more radiogenic than coeval Cambro-Ordovician and Triassic-Early Jurassic seawater sulphate, with the Late Variscan granite displaying the highest $^{87}Sr/^{86}Sr$ ratios of 0.718510 ± 0.00002 (Margoum et al. 2015).

6 Discussion

6.1 Physico-Chemical Conditions and Sources of Ore Fluids

Microthermometric data from ore-related quartz show wide ranges in homogenization temperatures and related salinities, the former ranging from 62 to 205 °C and the latter from ca. 16–24 wt% NaCl equiv (Fig. 4). Owing to low first-melting temperatures of the fluid inclusions (Table 1) that plot well below that of pure NaCl–H_2O and NaCl–KCl–H_2O systems (Crawford 1981), the bulk composition of these saline fluids approximate the H_2O–NaCl–$CaCl_2$ ± $BaCl_2$ ± $MgCl_2$ ± KCl system, with NaCl/(NaCl + $CaCl_2$) ratios varying widely from 0.1 to 1.0 (Fig. 6). Moreover, the similarity of fluid compositions in ore-related quartz and paragenetically late fluorite (Margoum et al. 2015) suggests homogeneity of the parent mineralizing fluid and that these two genetically related minerals precipitated from the same hydrothermal system.

No genetic connection exists between the Aouli sulphide ± fluorite ± barite mineralization and the spatially associated late Hercynian to Permian intrusions as inferred from structural, REY, and isotopic constraints (Margoum et al. 2015). If this interpretation is correct, the saline Na–Ca–Mg–K-bearing mineralizing fluids were derived from a basinal source, thereby supporting a model in which basin-derived brines and subsequent fluid-rock reactions at high fluid/rock ratios (Margoum et al. 2015) were the main factors that controlled the distribution of the

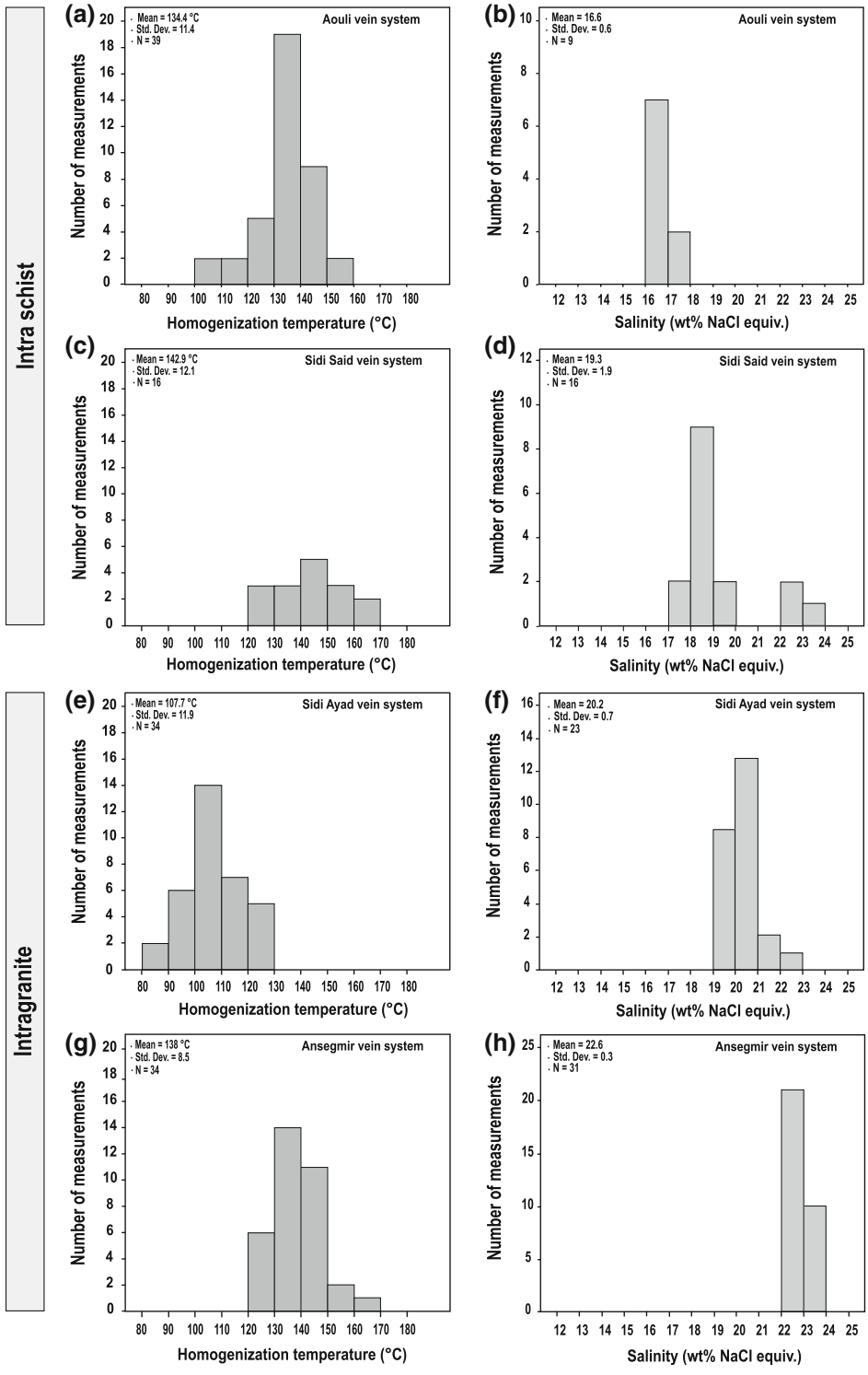

Fig. 5 Histograms summarizing ore-related quartz-hosted fluid inclusion homogenization temperatures (**a**, **c**, **e**, **g**) and related calculated salinities (**b**, **d**, **f**, **h**) for different vein systems of Aouli base metal sulphide ± fluorite ± barite district

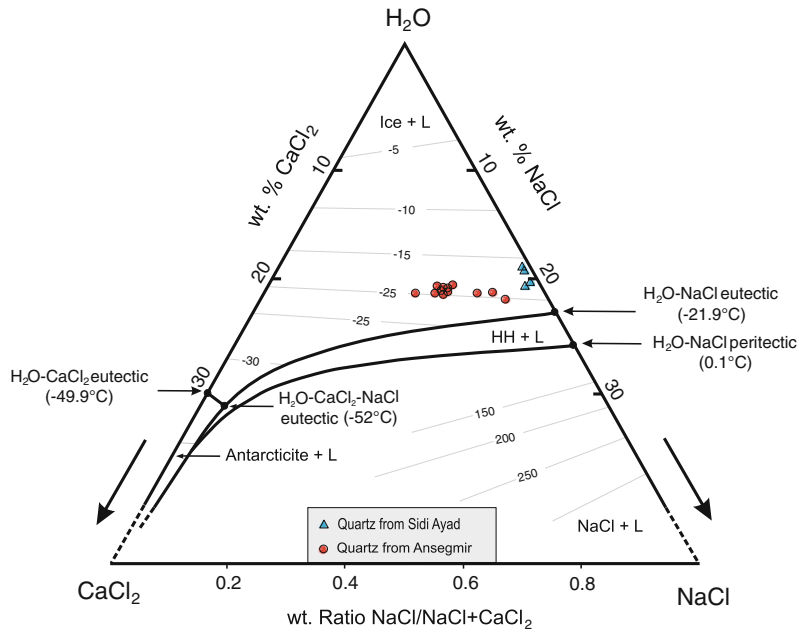

Fig. 6 Ternary plot of Oakes et al. (1990) showing distribution of H_2O–NaCl–$CaCl_2$ ratios of primary fluid inclusions hosted in ore-related quartz from Ansegmir and Sidi Ayad vein systems of Aouli base metal sulphide ± fluorite ± barite district

sulphide ± fluorite ± barite vein mineralization. Indeed, calculated $\delta^{18}O_{H2O}$ values of the ore-forming fluids, using the quartz-H_2O fractionation factor of Zheng (1993) and mean homogenization temperatures of 130 °C based on fluid inclusion data, average 0.3 ± 3.8 ‰ further indicating evolution from a predominant seawater source. From textural evidence (i.e., hydrothermal brecciation) and pressure estimates, it is inferred that the Aouli Pb–Zn ± F ± Ba mineralization occurred at relatively shallow depths (270 and 540 bars, corresponding to depths of 1–2 km under lithostatic conditions; Margoum et al. 2015).

6.2 Ore Depositional Processes

As stressed above, microthermometric data for fluid inclusions from the different vein systems show significant differences for ore-related quartz in term of homogenization temperature, salinity, and major components. In this regard, quartz-hosted inclusions from the Ansegmir vein system, entirely enclosed in granite, exhibit the highest salinities and $CaCl_2$ contents, whereas those from the Aouli vein system have the lowest salinities and $CaCl_2$ contents (Figs. 5 and 6). These fluid characteristics could reflect either temporal evolution of a single hydrothermal system or chronologically distinct hydrothermal events. However, similarity of mineral assemblages within the different vein systems, coupled with the presence of oscillatory zoning in the paragenetically late fluorite (Margoum et al. 2015), argue for episodic fluctuation in fluid composition rather than separate mineralizing events. Thermally induced re-equilibration and subsequent cooling cannot explain these variations, as fluid inclusion data indicate similar temperature ranges for all of the veins. The large spread in fluid characteristics is therefore best interpreted in terms of fluid mixing. Indeed, the linear trend of data shown by the salinity versus vein system plot (Fig. 7) suggests a binary mixing line representing fluid mixing and fluid-rock reactions between two distinct brine types. It appears, therefore, that deposition of the Aouli sulphide ± fluorite ± barite mineralization was likely triggered by fluid mixing.

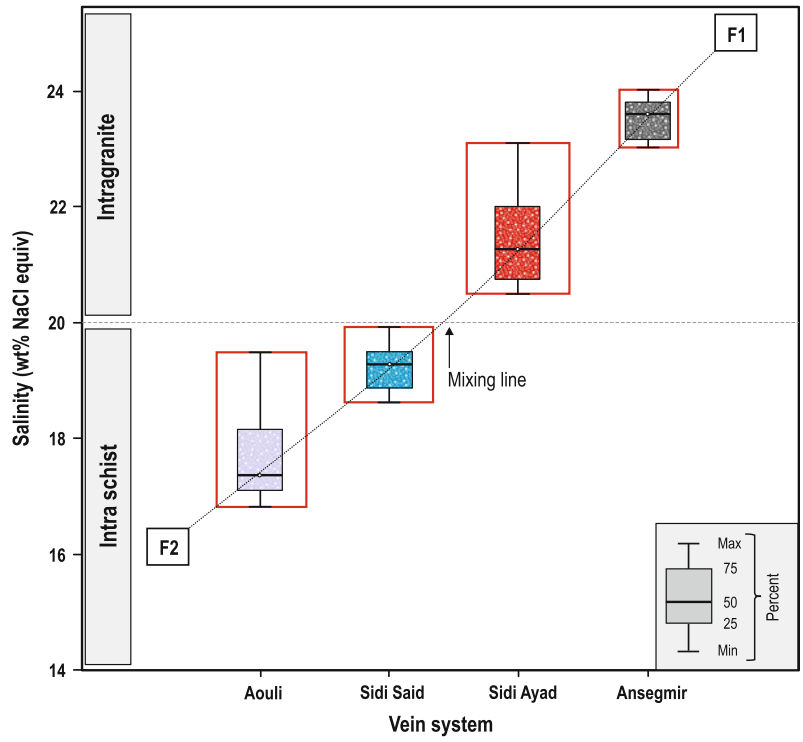

Fig. 7 Plot showing distribution of salinity data as a function of different base-metal sulphide ± fluorite ± barite vein systems of Aouli district. *Line* drawn through data (*boxes*) is interpreted to represent binary mixing involving two fluid end-members *F1* and *F2* (see text for discussion)

6.3 Controls on Fluid Flow, Fluid-Rock Interaction, and Metal Sources

The spatial distribution of the structurally controlled Aouli veins and their intimate relationships to major ENE (Atlantic dominance) and EW (Tethyan dominance) faults (Ellouz et al. 2003) suggest that these brittle structures were the major pathways that focused fluid flow from the basement upward into the overlying Cambro-Ordovician to Liassic host rocks. During fluid migration, extensive chemical interaction between the heated basinal brines and host rocks occurred, as inferred from data for fluid inclusions, REYs, and isotopes (Margoum et al. 2015; present study).

The Ca enrichment of the mineralizing fluids shown by microthermometric measurements (Fig. 6) may be attributed to either albitization of plagioclase, decarbonation and leaching of carbonate strata, and/or dissolution of the Triassic evaporites, or a combination of all these processes. Further evidence for extensive fluid/rock reactions comes from S and Sr isotope values that suggest mixing at or near the site of deposition, between a deep-seated, ascending, seawater-derived brine that equilibrated with late Hercynian crystalline basement rocks at a depth of at least 5–7 km, and Permian to Triassic stagnant formation waters and/or meteoric waters (Margoum et al. 2015). The recorded $\delta^{34}S$ values of −9 to 1 ‰ (Jébrak et al. 1998) are interpreted to reflect fluid circulation through late Hercynian granitic basement rocks and/or incorporation of sulphur from early diagenetic pyrite dispersed within the Cambro-Ordovician schists. Similarly, the lead isotope compositions of galena separates, some of which plot close to those of the granitic K-feldspars (Jébrak et al. 1998), further indicate chemical interaction with the late Hercynian granitic basement rocks and/or Rb-rich siliciclastic sedimentary rocks (i.e., Triassic evaporite-bearing clastics), thus implying that these rocks were the main source of Pb in the Aouli deposit.

6.4 Proposed Genetic Model

Paleogeographic reconstructions indicate that the overburden in the Upper Moulouya district never exceeded 2 km (Beauchamp et al. 1996; Ellouz et al. 2003). The maximum burial temperature is thus restricted to <85 °C, assuming a mean geothermal gradient of 30 °C/km and a surface temperature of 25 °C. These burial temperatures are substantially lower than the mean fluid-inclusion temperatures of 135 °C recorded during ore deposition, considering lithostatic pressure conditions. Anomalously high temperatures for such depths in the range of 80–170 °C (Table 1) require either an abnormally high geothermal gradient or over-pressured fluids that were expelled from the deepest levels of the nearby sedimentary basin(s).

The difficulty in delineating the age of mineralization in the Aouli district relates to the well-documented record of multiple and repetitive openings and reopenings of the veins. As a consequence, different superimposed styles of mineralization related to chronologically distinct mineralizing epochs could occur within one single vein system. In this regard, structural relationships together with K–Ar and Ar–Ar ages on mica, as well as apatite fission track ages (Valenza et al. 2000; Watanabe 2002; Ghorbal et al. 2008; Saddiqi et al. 2009; Cheilletz et al. 2010; Barbero et al. 2011; Marcoux et al. 2015; Rossi et al. 2016), constrain the timing of Aouli sulphide ± fluorite ± barite mineralization to the Permian-Jurassic time span, coincident with the early stages of Pangean rifting and subsequent rift- and post-rift stages of the Triassic opening of the Tethys Ocean and the Jurassic to Cretaceous opening of the Central Atlantic Ocean (Muttoni et al. 2003; Martins et al. 2008). Regionally, this time span fits within the post-Variscan "Mesozoic" hydrothermal period recognized throughout Central and Western Europe (Wolff et al. 2015).

From a geodynamic perspective, the Permian-Jurassic coincides with the emplacement of lamprophyre dikes (Bouabdellah et al. 2010) and Triassic dolerite-diabase sills and lava flows (Fig. 1) resulting in high heat flow and consequently an increased geothermal gradient and related fluid activity. Inferred crustal thinning and a high geothermal gradient could have promoted small-scale convection cells that acted as the heat source and driving mechanism to move the mineralizing fluids toward shallower depths. In this respect, hydrological modelling by Staude et al. (2009) has shown that extension can release, through decompression of over-pressured rocks and/or heating, sufficient amounts of fluids (ca. 10^{-3}–10^{-4} km^3 fluid per km^2) to form an economic metal deposit.

In conclusion, combined fluid inclusion and isotope geochemical data support a fluid-flow model involving deep basement circulation of migrating basinal brines that interacted extensively with Cambro-Ordovician siliciclastic rocks and the late Hercynian granitic crystalline basement. Fluid mixing at the basement-cover interface of an ascending deep-seated fluid and formation and/or meteoric waters seems the most likely mechanism to have triggered Aouli sulphide ± fluorite ± barite deposition, coincident with Pangean rifting and subsequent opening of the Tethys and Central Atlantic oceans during Permian-Jurassic time.

References

Annich M, Rahhali M (2002) Gisement de plomb de Zeida. In: Barodi E-B, Watanabe Y, Mouttaqi A, Annich M (eds) Méthodes et techniques d'exploration minière et principaux gisements au Maroc. Projet JICA/BRPM, Rabat, Morocco, pp 179–183

Barbero L, Jabaloy A, Gómez-Ortiz D, Pérez-Peña JV, Rodríguez-Peces MJ, Tejero R, Estupiñan J, Azdimousa A, Vázquez M, Asebriy L (2011) Evidence for surface uplift of the Atlas Mountains and the surrounding peripheral plateaux: combining apatite fission-track results and geomorphic indicators in the western Moroccan Meseta (coastal Variscan Paleozoic basement). Tectonophys 502:90–104

Beauchamp W, Barazangi M, Demnati A, El Alji M (1996) Intracontinental rifting and inversion: Missour Basin and Atlas Mountains, Morocco. AAPG Bull 80:1459–1482

Bouabdellah M, Banks D, Klügel A (2010) Comment on A Late Triassic $^{40}Ar/^{39}Ar$ age for the El Hammam high-REE fluorite deposit (Morocco): mineralization related to the Central Atlantic magmatic province? Mineral Deposita 45:729–731

Bouladon J (1956) Les filons d'Aouli et les gîtes de substitution de Mibladen, deux formes d'une même minéralisation dans la région de Midelt (Maroc). In: Proceed 20th Internat Geol Congress, Mexico City, vol 13, pp 43–63

Cheilletz A, Gasquet D, Filali F, Archibald DA, Nespolo M (2010) A Late Triassic $^{40}Ar/^{39}Ar$ age for the El Hammam high-REE fluorite deposit (Morocco): mineralization related to the central Atlantic magmatic province? Miner Deposita 45:323–329

Clauer N, Jeannette D, Tisserant D (1980) Datation isotopique des cristallisations successives du socle cristallin et cristallophyllien de la haute Moulouya (Maroc hercynien). Geol Rundsch 68:63–83

Crawford ML (1981) Phase equilibria in aqueous fluid inclusions. In: Hollister LS, Crawford ML (eds) Fluid inclusions: applications to petrology. Mineral Assoc Canada Short Course Handbook, vol 6, pp 75–100

Dahire M (2004) Le complexe plutonique de la Haute Moulouya (Meseta oriental, Maroc): evolution pétrologique et structurale. Unpubl PhD Thesis, Mohamed Ben Abdellah University, Fès, Morocco, 322 pp

Duggen S, Hoernle K, Hauff F, Klügel A, Bouabdellah M, Thirlwall MF (2009) Flow of Canary mantle plume material through a subcontinental lithospheric corridor beneath Africa to the Mediterranean. Geology 37:283–286

Duthou JL, Emberger A, Lasserre M (1976) Résultats graphiques et interpretation des mesures isotopiques de plomb de galène et de minéraux oxydés du Maroc. Mem Ser Soc Géol France 7:221–226

Ellouz N, Patriat M, Gaulier JM, Bouatmani R, Saboundji S (2003) From rifting to Alpine inversion: Mesozoic and Cenozoic subsidence history of some Moroccan basins. Sedimen Geol 156:185–212

Emberger A (1965a) Caractères polygénétiques des minéralisations plombifères de la Haute Moulouya (gisements d'Aouli, Mibladen et Zeïda, Maroc). Comptes Rendus Acad Sci Paris t 260. Groupe 9:3433–3436

Emberger A (1965b) Éléments pour une synthèse métallogénique du district plombifère de la Haute Moulouya. Notes Mém Serv géol Maroc 181:235–238

Emberger A (1965c) Introduction à l'étude des minéralisations plombifères de la Haute-Moulouya. Notes Mém Serv géol Maroc 181:167–174

Filali F (1996) Étude pétro-structurale de l'encaissant métamorphique de la boutonnière d'Aouli-Mibladen (Haute Moulouya, Maroc): conséquences sur la géodynamique hercynienne au Maroc. Unpubl PhD thesis, Muséum National d'Histoire Naturelle, Paris, France, 174 pp

Ghorbal B, Bertotti G, Foeken J, Andriessen P (2008) Unexpected Jurassic to Neogene vertical movements in 'stable' parts of NW Africa revealed by low temperature geochronology. Terra Nova 20:355–363

Harmand C, Cantagrel JM (1984) Le volcanisme alcalin Tertiaire et Quaternaire du Moyen Atlas (Maroc): chronologie K/Ar et cadre géodynamique. J Afr Earth Sci 2:51–55

Jébrak M, Marcoux E, Nasloubi M, Zahraoui M (1998) From sandstone- to carbonate-hosted stratabound deposits: an isotope study of galena in the upper-Molulouya district (Morocco). Miner Deposita 33:406–415

Marcoux E, Nerci K, Branquet Y, Ramboz C, Ruffet G, Peucat J-J, Stevenson R, Jebrak M (2015) Late-Hercynian Intrusion gold-related gold deposits: an integrated model on the Tighza polymetallic district, central Morocco. Jour African Earth Sci 107:65–88

Margoum D, Bouabdellah M, Klügel A, Castorina F, Cuney M, Jébrak M, Cardellach E (2015) Central Atlantic rifting and/or Tethys opening as fertilizer agents for the genesis of the Aouli REE-rich fluorite-barite vein system (upper Moulouya district, Morocco): evidence from REE, fluid inclusions, sulfur, and strontium isotopes. J Afr Earth Sci 108:22–39

Martins LT, Madeira J, Youbi N, Munhá J, Mata J, Kerrich R (2008) Rift-related magmatism of the central Atlantic magmatic province in Algarve, southern Portugal. Lithos 101:102–124

Meyer M, Brockamp O, Clauer N, Renk A, Zuther M (2000) Further evidence for a Jurassic mineralizing event in central Europe: K–Ar dating of hydrothermal alteration and fluid inclusion systematics in wall rocks of the Käfersteige fluorite vein deposit in the northern Black Forest, Germany. Mineral Deposita 35:754–761

Muttoni G, Kent DV, Garzanti E, Brack P, Abrahamsen N, Gaetani M (2003) Early Permian Pangea 'B' to Late Permian Pangea 'A'. Earth Planet Sci Lett 215:379–394

Naji M (2004) Les minéralisations plombo-barytiques du district de la Haute Moulouya. Contexte géologique, contrôle tectonique et modèle de mise en place: gisements d'Aoul-Mibladen-Zeida. Unpubl PhD Thesis, Mohammed V University, Rabat, Morocco, 218 pp

Oakes CS, Bodnar RJ, Simonson JM (1990) The system $NaCl–CaCl_2–H_2O$. I. The vapor-saturated ice liquidus. Geochim Cosmochim Acta 54:603–610

Ouali H, Briand B, Bouchardon JL, El Maâtaoui M (2000) Mise en évidence d'un volcanisme alcalin intraplaque d'âge Acadien dans la Meseta nord-occidentale (Maroc). Comptes Rendus Acad Sci Paris 330:611–616

Oukemeni D (1993) Géochimie, géochronologie (U–Pb) du pluton d'Aouli et comparaisons géochimiques avec d'autres granitoïdes hercyniens du Maroc par analyse discriminante. Unpubl PhD Thesis, Université du Québec à Montréal, Canada, 141 pp

Oukemeni D, Bourne JH (1994) Étude géochimique des granitoïdes du pluton d'Aouli, Haute Moulouya, Maroc. J Afr Earth Sci 17:429–443

Oukemeni D, Bourne JH, Krogh TE (1995) Géochronologie U-Pb sur zircon du pluton d'Aoul, Haute Moulouya, Maroc. Bull Soc Géol France 166:15–21

Rahhali M (2001) Les potentialités actuelles des gisements plombifères d'Aouli-Mibladen (Haute Moulouya). Unpubl Rept BRPM, DE/DO/Dépt ZN, 16 pp

Rahhali M (2002a) Gisements stratiformes de Mibladen. In: Barodi E-B, Watanabe Y, Mouttaqi A, Annich M (eds) Méthodes et techniques d'exploration minière et principaux gisements au Maroc. Projet JICA/BRPM, pp 166–170

Rahhali M (2002b) Gisements filoniens d'Aouli. In: Barodi E-B, Watanabe Y, Mouttaqi A, Annich M (eds) Méthodes et techniques d'exploration minière et principaux gisements au Maroc. Projet JICA/BRPM, pp 171–173

Roedder E (1984) Fluid inclusions. Rev Miner 12:1–644

Rossi M et al (2016) The polymetallic (W–Au and Pb–Zn–Ag) Tighza district (Central Morocco): ages of magmatic and hydrothermal events. In: M. Bouabdellah and Slack JF (eds) Mineral Deposits of North Africa. doi:10.1007/978-3-319-31733-5_3

Routhier P (1963) Les gisements métallifères. Paris, Masson, Géologie et principes de recherches, p 1282

Routhier P (1980) Où sont les métaux pour l'avenir? Les provinces métalliques. Essai de métallogénie globale. BRGM Mémoire No. 105, 410 pp

Saddiqi O, El Haimer F-Z, Michard A, Barbarand J, Ruiz GMH, Mansour EM, Leturmy P, Frizon de Lamotte D (2009) Apatite fission-track analyses on basement granites from south-western Meseta, Morocco: paleogeographic implications and interpretations of AFT age discrepancies. Tectonophys 475:29–37

Sánchez V, Corbella M, Fuenlabrada JM, Vindel E, Martín-Crespo T (2006) Sr and Nd isotope data from the fluorspar district Asturias, northern Spain. J Geochem Explor 89:348–350

Stacey JS, Kramers JC (1975) Approximation of terrestrial lead isotope evolution by a two-stage model. Earth Planet Sci Lett 26:207–221

Staude S, Bons PD, Markl G (2009) Hydrothermal vein formation by extension-driven dewatering of the middle crust: an example from SW Germany. Earth Planet Sci Lett 286:387–395

Tisserant D (1977) Les isotopes du strontium et l'histoire hercynienne du Maroc: étude de quelques massifs atlasiques et mésétiens. Unpubl PhD Thesis, Louis Pasteur University, Strasbourg, France, 103 pp

Valenza K, Moritz R, Mouttaqi A, Fontignie D, Sharp Z (2000) Vein and karst barite deposits in the western Jebilet of Morocco: fluid inclusion and isotope (S, O, Sr) evidence for regional fluid mixing related to central Atlantic rifting. Econ Geol 95:587–606

Watanabe Y (2002) $^{40}Ar/^{39}Ar$ geochronologic constraints on the timing of massive sulfide and vein-type Pb–Zn mineralization in the western Meseta of Morocco. Econ Geol 97:145–157

Wise JM (2005) Undulatory silver-rich polymetallic veins of the Castrovirreyna district, central Peru: fault growth and mineralization in a perturbed local stress field. Econ Geol 100:689–705

Wittig N, Pearson DG, Baker J, Duggen S, Hoernle K (2010) A major element, PGE and Re-Os isotope study of Middle Atlas (Morocco) peridotite xenoliths: evidence for coupled introduction of metasomatic sulphides and clinopyroxene. Lithos 115:15–26

Wolff R, Dunkl I, Kempe U, von Eynatten H (2015) The age of the latest thermal overprint of tin and polymetallic deposits in the Erzgebirge, Germany: constraints from fluorite (U–Th–Sm)/He thermochronology. Econ Geol 110:2025–2040

Zheng YF (1993) Calculation of oxygen isotope fractionation in anhydrous silicate minerals. Geochim Cosmochim Acta 57:1079–1091

Geology and Mineralogy of the El Hammam REE-Rich Fluorite Deposit (Central Morocco): A Product of Transtensional Pangean Rifting and Central Atlantic Opening

Mohammed Bouabdellah, Oussama Zemri, Michel Jébrak, Andreas Klügel, Gilles Levresse, Lhou Maacha, Abdelaziz Gaouzi and Mohamed Souiah

Abstract

The El Hammam REE-rich fluorite deposit in central Morocco constitutes the largest fluorite deposit in North Africa with an annual production of 110,000 t of fluorite concentrate at 98 % purity. Enclosing host rocks consist of a Silurian to Namurian succession of multiply folded and metamorphosed sedimentary and volcaniclastic rocks locally intruded by late Hercynian granitic stocks. A dike swarm of poorly dated, mostly ENE-striking, steeply south-dipping microgranite and tholeiitic dolerite-diabase intrude all of the supracrustal rocks. Structurally, the mineralized area is dissected by a NE-trending, prominent, crustal-scale strike-slip shear corridor locally known as the El Hammam shear zone along which most of the exploited orebodies occur. Mineralized structures consist predominantly of an array of

M. Bouabdellah (✉) · O. Zemri
Département de Géologie/Faculté des Sciences,
Université Mohammed Premier,
Avenue Mohammed VI, B.P. 717,
Oujda 60000, Morocco
e-mail: mbouabdellah2002@yahoo.fr

M. Jébrak
Department of Earth and Atmospheric Sciences,
Université du Québec à Montréal, CP 8888
Centre Ville, Montreal, Québec H3C3P8, Canada

A. Klügel
Universität Bremen, Fachbereich
Geowissenschaften, Postfach 33 04 40, 28334
Bremen, Germany

G. Levresse
Programa de Geofluidos, Centro de Geociencias
UNAM-Campus Juriquilla, AP 1-253, Querétaro
Mexico CP 76230, Mexico

L. Maacha · A. Gaouzi · M. Souiah
Managem Group, Twin Center, Tour A, Angle
Boulevards Zerktouni et Al Massira Al Khadra,
B.P. 5199, Casablanca 20000, Morocco

M. Bouabdellah and J.F. Slack (eds.), *Mineral Deposits of North Africa*,
Mineral Resource Reviews, DOI 10.1007/978-3-319-31733-5_12

three major, multi-kilometer-long, transtensional, mostly ENE-trending, subparallel, and steeply dipping veins referred to as the Moufrès-Bergamou, Tlatezma-Achemache, and Mizourza vein systems. The mineralogy of the veins is simple and consists of diversely colored fluorite, accompanied by variable amounts of calcite, quartz, and sulphides ± siderite ± adularia. Texturally, the veins display comb, cockade, laminated, breccia, and crack and seal textures suggesting that episodic, multiple, crack-seal processes were important during vein formation. Irrespective of location, paragenesis, and textural position within the mineralized vein structure, green fluorite is characterized by high total REY contents ranging on average from ~249–995 ppm, light REE enrichment, and distinctive positive Y anomalies with or without positive Eu anomalies. Associated pre-ore hydrothermal calcite is strongly REY enriched (average ΣREY = 1164–3192 ppm) and only has a distinctively positive Eu anomaly without a Y anomaly. Preliminary fluid inclusion data indicate that the ore-forming fluids correspond to evolved basin-derived, hot (92–176 °C), very saline (up to 33 wt% NaCl equiv), NaCl–$CaCl_2$–KCl–$MgCl_2$ ± $BaCl_2$ brines. Overall, REY compositions together with fluid inclusion constraints suggest a key role for hot basin-derived brines and fluid-rock interaction in the genesis of El Hammam REE-rich fluorite deposit. Formation of this deposit is probably related to Pangean rifting and subsequent Central Atlantic opening during Permian-Triassic time.

1 Introduction

Hercynian inliers throughout the Moroccan territory host numerous base metal-fluorite-barite veins mainly of post-Carboniferous to Early Cretaceous age (Bouabdellah et al. 2014). Most veins are within a Paleozoic succession of greenschist-facies sedimentary and volcaniclastic rocks locally intruded by multiphase (ca. 347–328 Ma) granitoid bodies. Among these, the El Hammam fluorite deposit located at 33°33′ N and 5°48′ W (Fig. 1) at the northeastern termination of the Khouribga-Oulmes anticlinorium is developed by the largest and sole operating fluorite mine in North Africa. Mining dates back to the 1930s and continues today, with annual production of 110,000 t of fluorite concentrate at 98 % purity.

The El Hammam district contains mostly ENE- to NW-striking, steeply dipping veins distributed over an area of 12 × 10 km (Fig. 2). Fluorite mineralization is typically poor in sulphides and quartz and shares attributes with Mississippi Valley Type (MVT) mineralization. Published geochronological data for the district are very limited (Cheilletz et al. 2010) and temporal links of fluorite mineralization to late Hercynian granitoids remains a matter of ongoing debate. In this contribution, we review the geological setting, present new LA-ICP-MS data and preliminary fluid inclusion microthermometric measurements, and based on these results discuss the time-space relationships between the fluorite mineralization and associated late Hercynian granitoids.

The present contribution is part of an ongoing PhD study by the second author and as a result the conclusions drawn herein are based on limited REY and microthermometric data, hence our interpretations could change when new exhaustive data become available.

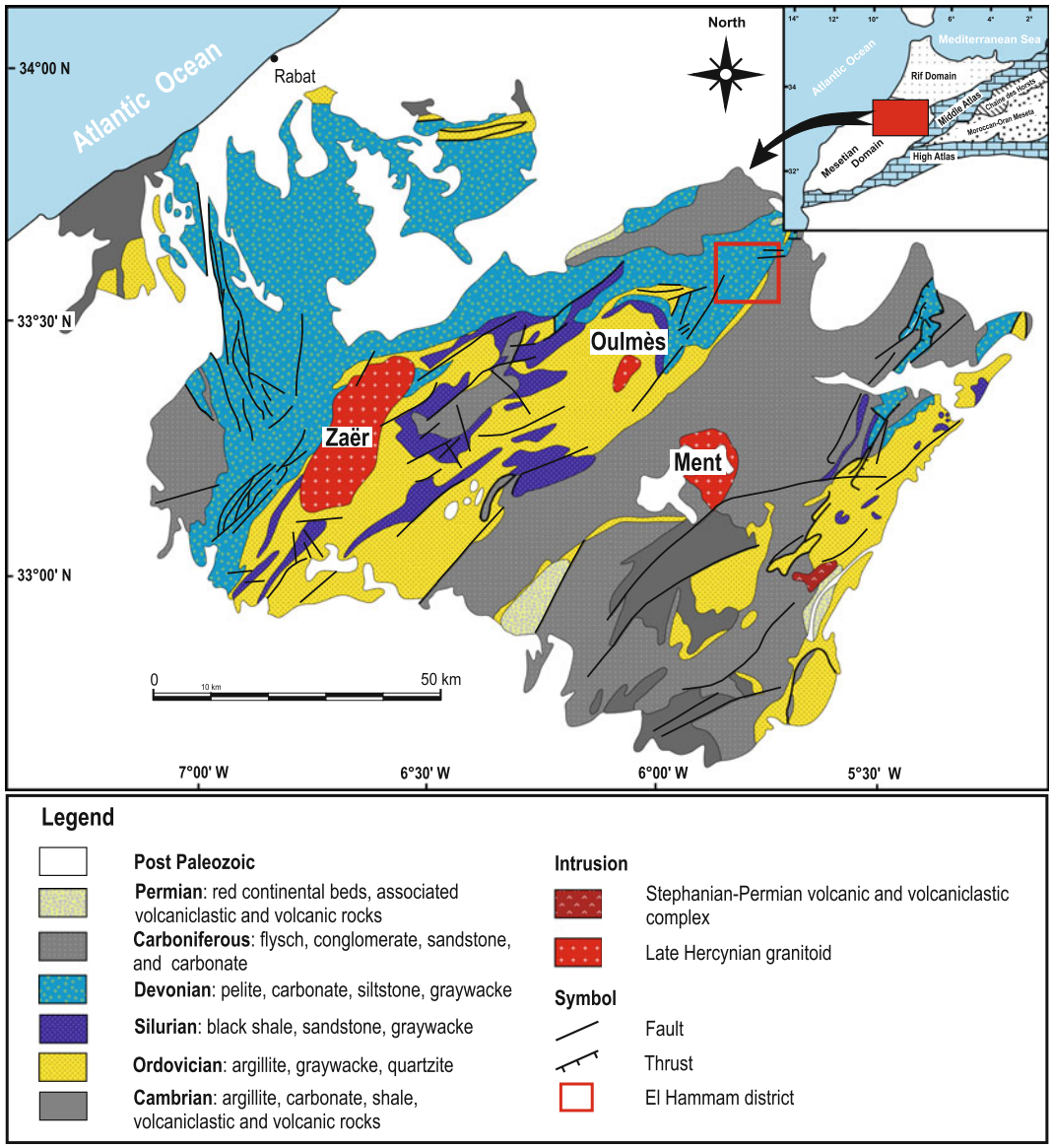

Fig. 1 Generalized geological map of Variscan domain in central Morocco showing regional geology, major tectonostratigraphic units, associated faults, and salient late Hercynian granitoids (modified after Agard 1966). *Inset* shows location of El Hammam high-REE fluorite district within framework of major tectonostratigraphic units of central Morocco

2 Mining and Exploration History

Fluorite mineralization in the El Hammam district was discovered by Barthoux in 1923 and subsequently explored by Termier (1936) and the Dubois brothers in 1941. From 1941 to 1951, during which Morocco was under French occupation, intensive exploration carried out by geologists of the Ministry of Energy and Mines and the Ugine Mining Company discovered several vein-type fluorite-calcite occurrences. Early in the 1960s, the Office National des Hydrocarbures et des Mines (ONHYM;

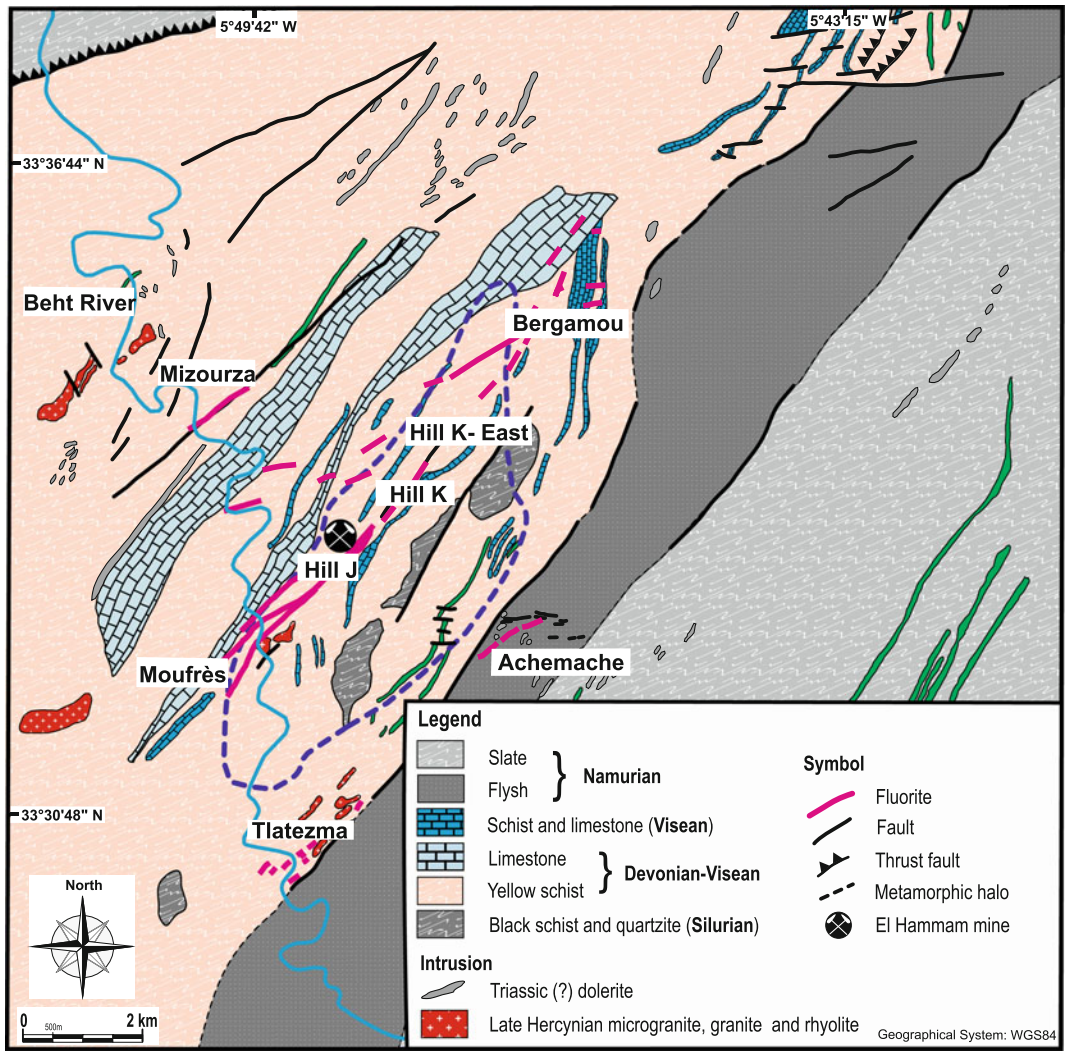

Fig. 2 Geological map of El Hammam district emphasizing spatial distribution of major REE-rich fluorite veins and relationships to stratigraphy, igneous rocks, fault systems, and metamorphism (modified after Agard 1966)

formerly BRPM) and the SAMINE Mining Company (a subsidiary of Managemgroup), concluded a joint venture and continued evaluation of the district with infill and step-out drilling and tunneling, which led to a production decision in 1973.

Most of the exploited veins are related to the prominent so-called Central Vein structure (Fig. 3) that has provided all fluorite production in the district. Due to declining fluorite production and depletion of reserves, the SAMINE Company in 2006 launched an intensive program of exploration and development drilling, which delineated additional mineral resources and reserves from a newly discovered set of fluorite-carbonate-quartz veins, namely the Tlatezma-Achemache and Mizourza veins (Fig. 2). To date, the El Hammam deposit has produced more than 10 Mt of fluorite concentrate at 98 % purity. Present reserves are estimated in the range of 8–10 Mt that should ensure a future mine life of at least a decade.

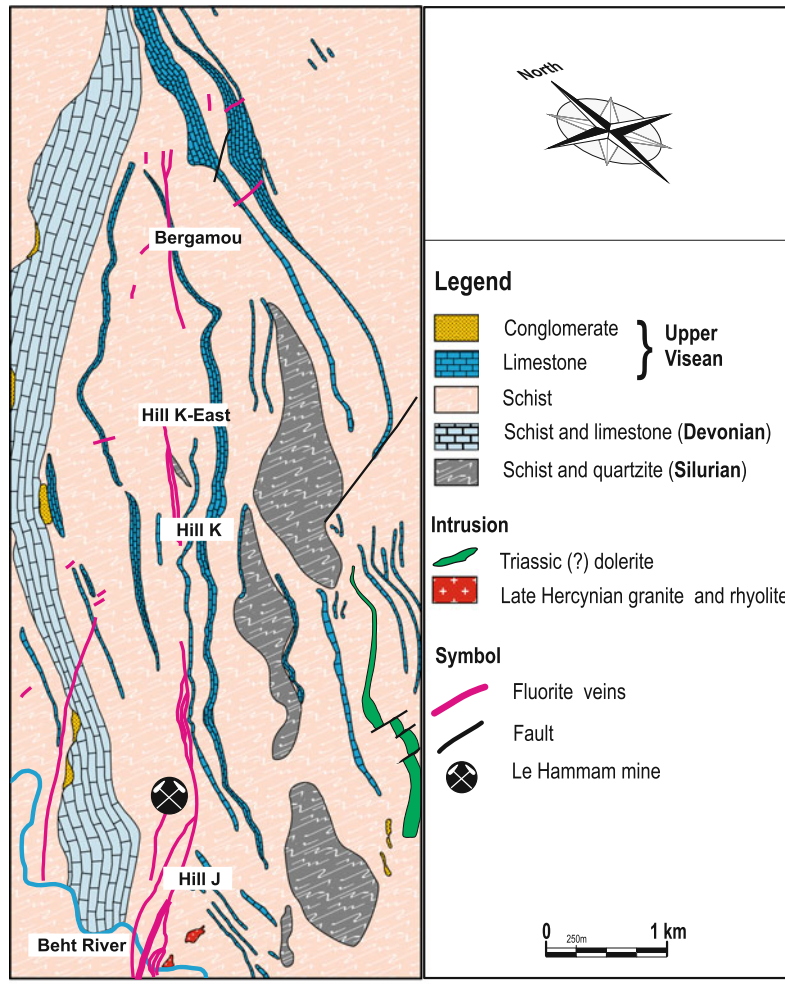

Fig. 3 Detailed geological map showing spatial distribution of named fluorite-bearing ore segments related to the major Central vein system and to late Hercynian granite apophysis

3 District Geology

The Central Massif of the Moroccan Meseta in which the El Hammam district occurs is a ~100-km-wide Hercynian belt of deformed and metamorphosed quartz-rich turbidites of Cambro-Ordovician to late Carboniferous age (Fig. 1). Its geological history is similar to those of terranes affected by the Variscan orogeny worldwide (Hoepffner et al. 2005). Indeed, the Central Massif corresponds to the southwestern-most segment of the Variscan belt of Europe (Michard et al. 2008) and was part of the extensive shallow marine platform that characterized the Variscan paleogeography of Europe, North America, and North Africa in early to late Paleozoic time (Moreno et al. 2008).

All stratigraphic units of the district were deformed into a series of eastward-vergent anticlines and synclines accompanied by thrust faults, mesoscopic folds and associated axial surface cleavage, and normal faults. All of these structures developed in response to the Eovariscan and Mesovariscan compressional stages during the Late Ordovician to Early Silurian (370–360 Ma) and the Late Devonian to early Carboniferous (330–320 Ma), followed by Late Variscan events in the Early Permian to Triassic (Hoepffner et al. 2005, 2006).

The generalized stratigraphic column comprises, from base to top, a succession of Silurian

to Visean-Namurian (early Carboniferous) sedimentary and volcaniclastic rocks locally intruded by minor stocks and dike swarms (Fig. 2). The Silurian comprises a >400-m-thick shallow-marine sequence of organic-rich, graptolite-bearing black shale and subordinate, continentally derived, quartz- and lithic-rich sandstone, greywacke, and siltstone. Overlying Devonian strata consist of rhythmically banded pelite, siltstone, and greywacke, and local trilobite- and *Tentaculite*-bearing platform carbonates. The transition to the overlying Visean-Namurian is marked by a map-scale unconformity. Overall, the Visean consists of a transgressive, interlayered sedimentary and volcanic succession dominated by pelite, quartz wacke, sandstone, calcareous greywacke with carbonate intercalations, and tholeiitic dolerite-diabase dike swarms attributed to the Upper Visean-Namurian (Jébrak 1984; Kharbouch 1994). The Namurian, which caps the stratigraphic column, consists of ~1000 m of basal conglomerate and flysch turbidites. During Namurain-Early Westphalian time, the shallow marine shelf emerged and the area was affected by the last stage of Hercynian deformation.

The main intrusive rocks are an aligned group of ENE-trending stocks and subvolcanic dikes assigned to the Upper Visean-Namurian. Very limited geochronological data are available for these igneous rocks. No large exposures of granitoid intrusions are known in the vicinity of El Hammam mine, but a buried granitic body has been inferred both by geophysical data (i.e., negative Bouguer anomaly gravity; Jébrak 1982) and a 16 km × 4 km surface thermal metamorphic aureole (Fig. 2), and was intersected at 200 m depth during exploration drilling. The outcropping fine-grained, peraluminous El Hammam intrusion dated at 243 ± 7 Ma (Jébrak 1984) corresponds to an apophysis of the hidden pluton, and is spatially and genetically related to contact metasomatic W-skarn mineralization (Sonnet and Verkaeren 1989). A swarm of mostly ENE-striking, steeply south-dipping microgranite and tholeiitic dolerite-diabase dikes attributed to the Upper Visean-Namurian (Jébrak 1984; Kharbouch 1994) intrudes all of the supracrustal rocks described above. A volumetrically less important group of ENE-trending lamprophyre dikes with contained vesicles "carbonatitic-like" crop out in the vicinity of the El Hammam mine along the Bergamou River (Jébrak 1985; Remmal et al. 1997; Izart et al. 2001a, b; Bouabdellah et al. 2010). Izart et al. (2001a, b) reported for these lamprophyre dikes a mean K/Ar age of 277 ± 4 Ma. Thermal metamorphism produced by the emplacement of the buried El Hammam pluton gave rise to the regional metamorphic aureole that consists predominantly of spotted-textured schists with porphyroblasts of cordierite, andalusite, chlorite, muscovite, and biotite (Sonnet 1981; Rahho 1996). These mineral assemblages indicate peak thermal conditions of <610 °C and an estimated pressure of ≤2.3 kb (Sonnet 1981).

During the Variscan orogeny, the geodynamic setting of the region was controlled by a transtensional-transpressive stress field related to opening and closing of the Devonian-Carbonifeous basin. Two main stages of late Hercynian deformation are recognized in the El Hammam area (Rahho 1996; Izart et al. 2001a, b). The first stage (D_1) is characterized by NE-SW-, ENE-WSW-, and E-W-trending isoclinal folds (P_1) and an associated axial planar foliation S_1 parallel to bedding. During the second stage (D_2), P_1 folds were refolded (P_2). The second foliation S_2 is axial planar to and crenulates the first-generation fabrics. K–Ar ages on muscovite separates suggest that peak low-grade greenschist-facies metamorphic conditions occurred at 290 ± 4 Ma (Huon 1985; Huon et al. 1988). Post-metamorphic, brittle strike-slip shears and related dextral to sinistral normal and reverse faults, transect both the Paleozoic and Permian strata. Of these, the NE-trending, steeply dipping, El Hammam Fault is the most prominent and hosts most of the exploited fluorite mineralization.

4 Fluorite Mineralization

Fluorite concentrations occur along a crustal-scale strike-slip shear corridor locally known as the El Hammam Shear Zone that resulted from a NW-SE compressive event (Tahiri et al. 1996). The mineralized structures consist of massive open-space fillings of an array of transtensional, mostly ENE-trending veins (Fig. 2). Three major, roughly continuous, sub-parallel and steeply dipping vein structures have been and/or are currently being mined both from open pits and underground workings: Moufrès-Bergamou (i.e., Central Vein), Tlatezma-Achemache, and Mizourza. The major veins extend laterally for as much as ~10 km along strike, dip sub-vertically, and vary in thickness from several cm up to 10 m. Known vertical extents of fluorite mineralization are greater than 700 m. The veins pinch and swell, and undulate along strike and down dip. Vein surfaces display a near-horizontal striation and evidence of dextral to sinistral strike-slip movement, as indicated by slickensides and dragging textures. The veins therefore formed as extensional shear fractures in a transtensional regime. Moreover, all of the mineralized structures are confined to the thermal metamorphic aureole centered on the buried El Hammam granitic intrusion that parallels the major El Hammam Fault (Fig. 2).

The Moufrès-Bergamou vein, locally known as the Central vein (Fig. 3), is historically and economically the most important accounting for nearly all of the extracted fluorite ore in the district. This vein strikes ENE, whereas in the central part of the mine deflections to WNW-ESE or even NW-SE trends are recorded. The vein extends laterally for almost 10 km along strike, truncates all lithostratigraphic units from Devonian pelite and limestone in the south to the Upper Visean pelite, greywacke, and carbonates in the north. For mining purposes, the Central vein is subdivided into four mineralized segments referred to as the Moufrès orebody to the SW, the Hills J, K, and K-East orebodies in the central part (i.e., Central vein *ss*), and the Bergamou orebody in the NE termination (Fig. 3).

Vein fillings are strongly banded indicating multiple dilatational and depositional events. Most vein margins are brecciated and cemented by drusy or comb-textured quartz, cubic fluorite, and calcite. Characteristic are comb, cockade, laminated, breccia, and crack and seal textures that suggest episodic mechanisms were important for vein formation. Wall-rock alteration surrounding the veins is generally subtle and produced hydrothermal clays, quartz, and carbonates. Well-developed cubic fluorite crystals are common as linings of vugs.

All of the veins display similar mineral assemblages dominated by fluorite with minor sulphides plus sparry calcite and quartz. The relative proportion of fluorite relative to other minerals varies among the veins. Overall, El Hammam fluorite is massive and typically greenish throughout the orebodies but locally displays a wide spectrum of colors ranging from purple to colorless through emerald blue; yellow and black varieties also exist. Sulphides, locally abundant, comprise variable amounts of pyrrhotite, galena, sphalerite, pyrite, and chalcopyrite. Barite occurs in places (i.e., Bergamou orebody; Figs. 2 and 3), either as massive aggregates or tabular white to pink crystals encrusting voids (i.e., crested barite or barite roses).

The sequence of mineral deposition shows four successive stages of hydrothermal mineralization (designated I to IV) of which II and III are of economic interest (Fig. 4). Stage I, referred to as "pre-ore brecciated stage," is barren and consists of brecciated fragments of host rocks up to several meters in diameter cemented by white to pink sparry calcite, and minor quartz and sulphides. Stage II is economically the most important and forms the major part of the exploited veins, accounting for more than 90 vol% of total fluorite resources. The mineral paragenesis consists of variably colored (i.e., black, purple, blue, emerald, and green) massive to centimeter-sized cubic fluorite; the greenish variety is the most abundant. Stage III comprises finely to coarsely banded, comb, crustiform, and brecciated yellow to colorless fluorite and barite accompanied by massive quartz-chalcedony, sulphides, and local siderite

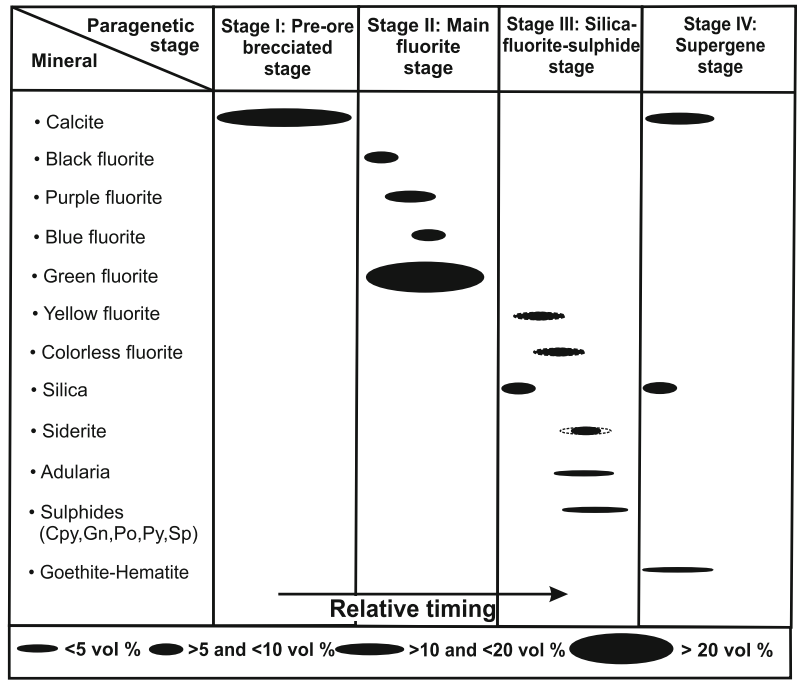

Fig. 4 Summary of the paragenetic sequence illustrating hydrothermal stages of El Hammam high-REE fluorite vein system. Width of bars is roughly proportional to intensity or volume of mineralizing event. Abbreviations for sulphide minerals: *Cpy* chalcopyrite; *Gn* galena; *Po* pyrrhotite; *Py* pyrite; *Sp* sphalerite

and adularia. The most abundant sulphides are pyrrhotite, galena, sphalerite, pyrite, and chalcopyrite. Post-ore supergene stage IV, resulting from the oxidation of primary sulphides, consists of minor cerussite, malachite, azurite, and Fe and Mn oxides.

5 REE and Trace Element Compositions

Overall, the El Hammam fluorite is characterized by high total REE and Y (ΣREYs) concentrations from 249 to 995 ppm (Table 1). Significant enrichment in the light REE (LREE) relative to the heavy REE (HREE) is present, resulting in steeply inclined chondrite-normalized REY patterns, especially between Y and Lu that reflect strong depletion in HREE (Fig. 5). The analyzed fluorite crystals also mostly exhibit negative Eu anomalies coupled with distinctively positive Y anomalies. Interestingly, pre-ore hydrothermal calcite separates have the highest total REY abundances ranging from 1164 to 3192 ppm, but with REYs less fractionated than in associated fluorite, as indicated by lower $(La/Yb)_{CN}$ and $(Sm/Yb)_{CN}$ ratios and hence flat REY patterns (Fig. 5, Table 1). Additionally, pre-ore hydrothermal calcite lacks Ce and Y anomalies, but does show prominent negative Eu anomalies. High field strength elements such as Nb, Ta, U, Th, Zr, and Hf are present in small amounts within this calcite, typically close to the detection limits; Sr and Rb concentrations range from ~10 to 158 ppm, and ~0.1 to 0.7 ppm, respectively (Table 1). Green fluorite separates from the Central vein *ss* (i.e., Hills J and K orebodies) show roughly similar in situ LA-ICP-MS trace elements concentrations irrespective of location and textural position within the vein. Compared to green fluorite and pre-ore hydrothermal calcite, whole-rock samples of the late Hercynian granite show substantially lower ΣREY concentrations (Table 1). The chondrite-normalized REY pattern of the El Hammam granite (Fig. 5) displays a weak fractionation and a large negative Eu anomaly, both of which are typical of highly fractionated, high-K, calc-alkaline A-type granites (Taylor 1982; Pérez-Soba and Villaseca 2010).

Table 1 LA-ICPMS trace-element compositions (ppm) of selected greenish fluorite and pre-ore hydrothermal calcite separates from Central vein *ss* of El Hammam REE-rich fluorite deposit

Orebody	Hill K			Hill J	Hill K		Hill J	Late Hercynian Granite
Sample no.	KGF1 (n = 4)	KGF2 (n = 5)	KGF3 (n = 4)	JGF1 (n = 3)	KCa1 (n = 7)	KCa2 (n = 4)	JCa1 (n = 3)	HG1 (n = 4)
Element (ppm)	Average and range	Average and range	Average and range	Average and range	Average and range	Average and range	Average and range	Average and range
Ca[a]	73.7 (73.7–73.7)	73.7 (73.7–73.7)	73.7 (73.7–73.7)	52.6 (52.6–52.6)	40 (40–40)	38.9 (38.8–39)	38.7 (38.7–38.8)	3.01 (0.82–6.47)
Rb	0.03 (0.006–0.11)	0.02 (0.01–0.04)	0.02 (0.01–0.03)	0.43 (0.22–0.73)	0.40 (0.17–0.63)	b.d.	b.d.	195 (98.8–233)
Sr	15.7 (9.8–24.1)	21.9 (18.1–33)	22.6 (18–28.2)	27.5 (16.9–44.7)	56.6 (44.8–77.7)	57.8 (46.9–66.9)	128 (107–158)	713 (6.65–2824)
Y	45.3 (20.9–78.7)	41.7 (26.5–58.3)	44.8 (38.8–54.8)	67.1 (57.5–82.2)	165 (44.8–287)	465 (62.8–1249)	470 (379–596)	15.7 (6.9–27.3)
Zr	0.002 (0.002–0.002)	0.003 (0.002–0.006)	0.003 (0.002–0.003)	0.003 (0.00–0.007)	0.08 (0.05–0.13)	b.d.	b.d.	188 (63.6–516)
Nb	0.000 (0.000–0.000)	0.00 (0.00–0.00)	0.002 (0.00–0.005)	0.0003 (−0.002–0.002)	0.003 (0.00–0.007)	b.d.	b.d.	45.4 (8.63–155)
Ba	0.9 (0.56–1.12)	0.83 (0.44–1.53)	0.86 (0.64–1.03)	1.4 (1.07–2.03)	1.83 (1.21–2.45)	3.25 (1.76–4.91)	0.95 (0.74–1.29)	550 (85.9–1897)
La	89.2 (30.7–197)	73.3 (27.4–232)	93.3 (56.4–149)	426 (303–530)	138 (15.88–385)	224 (15.8–712)	360 (287–469)	20.4 (2.66–62)
Ce	104.1 (40.6–211)	86.9 (42.4–220)	121 (83.5–175)	324 (248–434)	374 (43.5–1003)	660 (44.4–2115)	1083 (905–1397)	30.8 (10.8–68.3)
Pr	8.43 (4.24–15.4)	7.54 (4.1–15.5)	9.78 (7.08–13)	35.2 (21.1–58.3)	52.7 (5.98–143)	87.4 (6.48–269)	149 (124–192)	2.68 (0.79–4.8)
Nd	29 (19.1–48.2)	26.4 (15.2–45.4)	31.4 (23.3–40.3)	99 (60.3–156)	231 (26.5–643)	401 (26.6–1229)	587 (505–746)	8.98 (2.99–16.6)
Sm	4.37 (3.17–6.61)	3.8 (2.16–5.56)	3.89 (2.81–5.22)	12 (7.81–16.3)	52.9 (6.92–133)	124 (7.77–372)	144 (117–182)	1.92 (0.74–4.15)
Eu	1.54 (1.08–1.99)	1.52 (0.7–2.25)	1.22 (0.86–1.71)	8.95 (6.2–11.7)	22.9 (3.35–45.8)	36.3 (2.02–105)	53.9 (44.3–68.5)	0.32 (0.08–0.6)
Gd	4.48 (2.57–6.27)	3.88 (2.1–4.77)	3.85 (2.65–4.75)	10.7 (6.57–13.6)	44.5 (6.83–103)	129 (8.77–376)	125 (96.9–158)	1.94 (0.77–3.97)
Tb	0.49 (0.25–0.71)	0.38 (0.23–0.47)	0.44 (0.34–0.61)	1.28 (0.79–1.66)	6.43 (1.28–12.9)	20.2 (1.69–57.3)	19.1 (14.9–24.5)	0.36 (0.16–0.74)
Dy	2.51 (1.2–3.64)	1.97 (1.3–2.45)	2.40 (1.9–3.29)	7.28 (4.39–9.37)	39 (10.3–74)	109 (11.1–299)	108 (87.9–138)	2.39 (1.12–4.74)
Ho	0.38 (0.17–0.55)	0.31 (0.21–0.39)	0.38 (0.31–0.53)	1.15 (0.81–1.40)	6.92 (2.24–12.2)	17.9 (2.58–47.7)	18.4 (15.1–23)	0.52 (0.25–0.99)
Er	0.67 (0.3–0.98)	0.54 (0.41–0.7)	0.69 (0.56–0.94)	2.25 (1.53–3.03)	16.5 (7–26.6)	37.4 (7.97–95.5)	44.3 (37.9–54.6)	1.64 (0.82–2.96)
Tm	0.05 (0.02–0.07)	0.04 (0.03–0.05)	0.05 (0.04–0.07)	0.15 (0.12–0.22)	1.96 (1.13–3)	3.2 (1.19–7.06)	4.83 (4.39–5.69)	0.29 (0.15–0.5)
Yb	0.13 (0.05–0.21)	0.11 (0.06–0.18)	0.13 (0.1–0.2)	0.5 (0.25–0.83)	10.4 (4.75–17.4)	11.6 (6.54–20.4)	23.5 (21.6–26.1)	2.15 (1.12–3.64)

(continued)

Table 1 (continued)

Orebody	Hill K			Hill J	Hill K		Hill J	Late Hercynian Granite
Sample no.	KGF1 (n = 4)	KGF2 (n = 5)	KGF3 (n = 4)	JGF1 (n = 3)	KCa1 (n = 7)	KCa2 (n = 4)	JCa1 (n = 3)	HG1 (n = 4)
Element (ppm)	Average and range	Average and range	Average and range	Average and range	Average and range	Average and range	Average and range	Average and range
Lu	0.009 (0.01–0.02)	0.01 (0.004–0.01)	0.008 (0.006–0.014)	0.03 (0.01–0.06)	1.26 (0.47–2.11)	1.01 (0.69–1.46)	2.55 (2.26–2.82)	0.32 (0.17–0.53)
ΣREY	**291 (173–540)**	**249 (125–564)**	**313 (222–449)**	**995 (718–1319)**	**1164 (185–2837)**	**2325 (206–6955)**	**3192 (2642–4083)**	**90.4 (33.7–180)**
Hf	0.004 (0.002–0.007)	0.005 (0.001–0.014)	0.004 (0.003–0.006)	0.002 (0.00–0.007)	0.006 (−0.001–0.01)	b.d.	b.d.	4.18 (2.83–7.79)
Ta	0.00 (0.00–0.00)	0.00 (0.00–0.00)	0.00 (0.00–0.00)	0.0006 (0.00–0.002)	0.002 (0.00–0.003)	b.d.	b.d.	2.21 (1.67–3.22)
Th	0.02 (0.01–0.04)	0.15 (0.03–0.41)	0.08 (0.05–0.14)	0.02 (0.01–0.04)	0.16 (0.04–0.41)	0.01 (0.002–0.03)	0.03 (0.02–0.03)	8.1 (5.46–14.6)
U	0.002 (0.001–0.002)	0.002 (0.001–0.005)	0.002 (0.001–0.002)	0.012 (0.003–0.025)	0.02 (0.002–0.06)	0.001 (0.00–0.002)	0.006 (0.005–0.006)	9.38 (3.36–13.2)
Tb/La	0.01 (0.003–0.02)	0.01 (0.002–0.02)	0.005 (0.004–0.006)	0.003 (0.003–0.003)	0.06 (0.03–0.09)	0.09 (0.11–0.08)	0.053 (0.52–0.53)	0.05 (0.01–0.08)
Tb/Ca	0.01 (0.003–0.01)	0.005 (0.003–0.006)	0.006 (0.005–0.008)	0.02 (0.015–0.03)	0.16 (0.03–0.3)	0.52 (0.04–1.47)	0.49 (0.39–0.63)	0.15 (0.05–0.22)
$(La/Yb)_{CN}$	500 (408–691)	474 (308–914)	523 (417–528)	611 (460–881)	9.51 (2.4–15.9)	13.8 (1.73–25)	11 (9.55–12.9)	6.83 (1.7–12.2)
$(Sm/Yb)_{CN}$	38 (35.8–65.2)	35.7 (34–37.5)	30.46 (28.7–32.2)	26.8 (22–35.2)	5.65 (1.62–8.54)	11.8 (1.32–20.2)	6.79 (6.02–7.75)	0.99 (0.73–1.27)

Average whole-rock trace-element composition of El Hammam late Hercynian granite is listed for comparison
Abbreviations: *b.d.* below detection; *CN* chondrite; *Max* maximum; *Min* minimum; *n* number of analyses
[a]Internal standard, values expressed as wt% are assumed but not analyzed

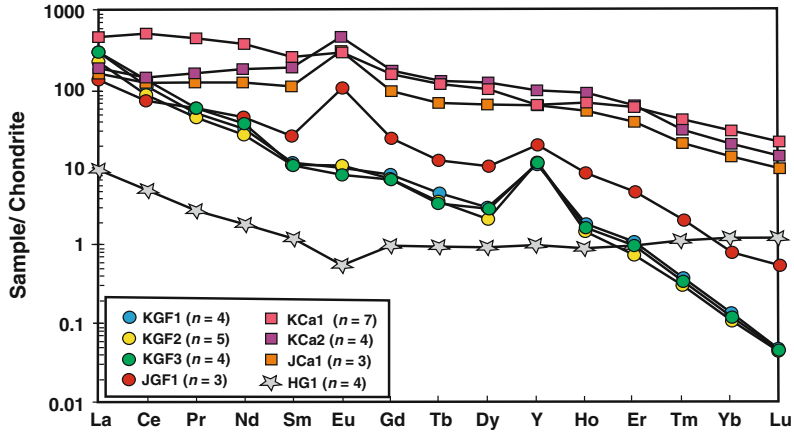

Fig. 5 Chondrite-normalized REY patterns of pre-ore hydrothermal calcite and greenish fluorite from El Hammam vein system, compared to that of spatially associated Late Hercynian granite. Data represent averages for calcite (JCa1, KCa2, KCa1) and fluorite (JGF1, KGF1-3); average granite data shown by *symbol* for HG1. Chondrite normalization values from McLennan (1989)

6 Fluid Inclusion Studies

A reconnaissance fluid inclusion survey has been conducted on selected samples of green fluorite from several parts of the Central vein. The fluid inclusions present are classified as primary, pseudosecondary, or secondary according to the criteria of Roedder (1984). Most occur either as trails of regular to irregularly-shaped inclusions (i.e., oval, rounded, or elongate) distributed along secondary fractures and cracks that cut the primary growth zones (i.e., pseudosecondary and secondary fluid inclusions), or rarely along growth zones (i.e., primary inclusions), or as scattered and isolated fluid inclusions exhibiting consistently regular cubic, tabular, elongate, or wedge-shaped, negative-crystal forms.

Based on the number of observable phases present at room temperature, two main types of fluid inclusions are recognized: (1) Type 1 NaCl-undersaturated, liquid-vapor (L + V) inclusions; and (2) Type 2 NaCl-saturated, liquid-vapor-halite (L + V + H) inclusions. Type 1 inclusions, by far the most abundant (>70–80 vol%), are ca. 50–100 µm in diameter, and exhibit rounded or negative crystal shapes with relatively uniform vapor/liquid ratios of about 0.2–0.3. Type 2 inclusions are up to 100 µm across, typically coexist with type 1 inclusions, are of similar size and shape, and occur along planar arrays cutting the host mineral.

Microthermometric data are summarized in Table 2. Fluid salinities were calculated only for three-phase (L + V + H) inclusions using $T_{m\ (NaCl)}$ values (Steele-MacInnis et al. 2012). The temperature of first melting ranged from −65 to −37 °C. Such low eutectic temperatures suggest the presence of other dissolved salts in addition to NaCl ± KCl, likely divalent chlorides (i.e., Mg^{2+}, Ca^{2+}; $Te_{(MgCl2)}$ = −35 °C, Dubois and Marignac 1997; $Te_{(CaCl2)}$ = −52 °C, Davis et al. 1990). Such compositions may be expected in view of the occurrence of intercalated carbonate strata within the El Hammam stratigraphic column. No clathrates and/or CO_2-rich inclusions were observed. Overall, homogenization temperatures ($T_{h\ (L-V)}$) range from 92.1 to 176.3 °C (avg = 140 ± 24 °C; n = 34). $T_{m(NaCl)}$ values vary from 127 to 157 °C (avg = 148 ± 10 °C; n = 18), indicating salinities in the range of 31.9–32.7 wt% NaCl equiv (avg = 32.5 ± 0.3 wt% NaCl, n = 18). These data are similar to those for the El Hammam ores reported previously by Yajima and Touray (1970) and Jébrak et al. (1988).

Table 2 Summary of microthermometric data for fluid inclusions hosted in greenish fluorite from the Central vein *ss* of El Hammam REE-rich fluorite deposit

Sample no.	Mineral/Fluid inlusion type	T_h	$T_{m(NaCl)}$	Salinity
F_1	F-1 fluorite (two-phase L + V)	123.5	–	–
		92.1	–	–
		102.1	–	–
		104.1	–	–
		118.5	–	–
		153.6	–	–
		149.2	–	–
		150.0	–	–
		125.2	–	–
		134.8	–	–
		108.9	–	–
		162.0	–	–
		154.4	–	–
		128.2	–	–
		153.0	–	–
		155.6	–	–
F2	F-2 fluorite (three-phase L + V + H)	156.7	149.4	32.5
		174.3	149.0	32.5
		167.3	149.4	32.5
		176.3	152.2	32.6
		169.1	148.7	32.5
		168.2	148.4	32.5
		173.8	156.3	32.7
		174.1	156.7	32.8
		169.0	154.8	32.7
		175.9	154.6	32.7
		170.1	155.8	32.7
		148.6	127.0	31.9
		145.8	128.2	31.9
		149.1	128.2	31.9
		167.6	149.2	32.5
		168.1	150.0	32.6
		165.6	150.5	32.6
		167.2	151.0	32.6

(continued)

Table 2 (continued)

Sample no.	Mineral/Fluid inlusion type	T_h	$T_{m(NaCl)}$	Salinity
C_7	Ca-1 calcite (three-phase L + V + H)	122	144	29.6
		139	112.9	28.4
		108	138.5	29.7
		218	155	29.9
		128.5	96.5	27.9
		116	97.7	27.9
		150.3	144.5	29.5
		151.2	145	29.5
		129	148.9	29.7
		151.2	166.2	30.2
C_9	Ca-1 calcite (three-phase L + V + H)	150	165	30.1
		121.9	149	29.9
		135.9	138.7	28.8
		106	146.9	30.3
		124.2	136	29
		122.3	136.9	29
		125	135.8	29
		124	140.6	29.3
		117.3	140.2	29.5
		120	138.8	29.3
		120.9	142	29.5
C_{12}	Ca-1 calcite (three-phase L + V + H)	119.5	141	29.5
		123.9	139.4	29.3
		123.2	141.5	29.4
		123.3	141.2	29.4
		124	140.6	29.3
		162.1	151	29.7
		168.5	152	29.7
		164	155	29.9
		166.4	142.8	29.4
		136.5	144	29.1
		124.5	139.9	29.3
		166	143	29.4
		133.6	144.5	29.2
C_{17}	Ca-1 calcite (three-phase L + V + H)	134.5	146.2	29.3
		120	158	30.6
		131	158.9	30.3
		128	149	29.7
		126	152	30
		140	142.8	28.9
		132.7	144.2	29.3

7 Discussion

The high REE contents of the El Hammam fluorite and related pre-ore hydrothermal calcite (up to 3192 ppm; Table 1) impose specific requirements in term of fluid source(s) and fluid-rock interactions. Indeed, unlike low-REE fluorite deposits that are genetically related to sedimentary basinal brines, the origin of REE-rich fluorite deposits remains controversial (e.g., Cheilletz et al. 2010; Bouabdellah et al. 2010).

Microthermometric data for fluid inclusions show wide ranges in homogenization temperatures with $T_{h(L-V)}$ and $T_{m(NaCl)}$ values varying from 92 to 173 °C, and salinities up to 33 wt% NaCl equiv. The salinity of the mineralizing fluids is made up of NaCl together with other salts, likely divalent cation (Ca, Mg, Ba) chlorides, as indicated by the low first-melting temperatures of the fluid inclusions. Thus, the bulk composition of these highly saline brines is represented by the H_2O–NaCl–$CaCl_2$–KCl–$MgCl_2 \pm BaCl_2$ system, which is similar to that of present-day oil-field brines, Mississippi Valley-type mineralizing fluids (Carpenter et al. 1974; Haynes and Kesler 1987; Leach and Sangster 1993) and fluids related to "peridiapiric" Pb–Zn ± F ± Ba ± Fe deposits of North Africa (Sheppard et al. 1996; Bouabdellah et al. 2014). From textural evidence (i.e., hydrothermal brecciation) and fluid inclusion pressure estimates, it is inferred that the El Hammam mineralization occurred at relatively shallow depths (<2 km; Sonnet and Verkaeren 1989; this study).

The origin of the high salinities in the fluid inclusions remains controversial and could reflect a variety of mechanisms, including: (1) evaporation of seawater or dissolution of evaporite minerals (primarily halite), or mixtures of both fluids in subsurface environments; (2) fluid immiscibility "boiling"; and (3) H_2O loss by preferential partitioning into hydrous minerals during retrograde metamorphism (Yardley and Graham 2002). In the El Hammam district, the last mechanism seems improbable because the peak metamorphic grade never exceeded lower greenschist facies (Huon et al. 1988). More importantly, definitive diagnostic evidence that supports fluid immiscibility (i.e., coexistence of CO_2-rich and H_2O-rich fluid inclusions having highly variable densities along the same growth planes, together with the presence of platy calcite (Simmons and Christenson 1994)) is lacking based on our limited microthermometric measurements. Given these constraints, it is therefore suggested that the occurrence of the hypersaline Na–Ca–K–Mg–Ba-bearing fluid compositions in the El Hammam fluorite indicates an evaporitic sedimentary source. Accordingly, it is concluded that the high REE contents of the El Hammam fluorite reflect the role of hot, basin-derived brines and subsequent fluid-rock interaction as the main factors that controlled the concentration and distribution of REE. Moreover, although the relative enrichment or depletion of individual elements varies for the greenish fluorite and pre-ore hydrothermal calcite, the resulting REY patterns are broadly similar (Fig. 6), suggesting a common origin for both minerals. The positive chondrite-normalized Eu anomaly shown by the El Hammam fluorite (Fig. 5) could indicate either: (1) deposition from high-temperature (>250 °C) reduced fluids where Eu^{2+} dominates over Eu^{3+} (Möller et al. 1994, 1997; Bau 1991), (2) inheritance from dissolved host-rock Eu at temperatures <250 °C, and/or (3) chemical complexation reactions or adsorption effects.

The presence of fluorite together with pre-ore hydrothermal calcite and sparse barite indicates that F^-, CO_3^{2-}, and SO_4^{2-} were probably the main complexing agents in the hydrothermal fluids. In this regard, thermodynamic calculations indicate that under hydrothermal conditions, and for temperatures similar to those that prevailed in the El Hammam REE-rich vein system (i.e., <250 °C), all of the REE are transported most efficiently as chloride and sulphate complexes and not as fluoride complexes (Migdisov and Williams-Jones 2007, 2008; Migdisov et al. 2009; Migdisov and Williams-Jones 2014). In the El Hammam district, the predominance of aqueous chloride, carbonate, and sulphate over fluoride within the hydrothermal fluids is suggested by: (1) occurrence of highly saline,

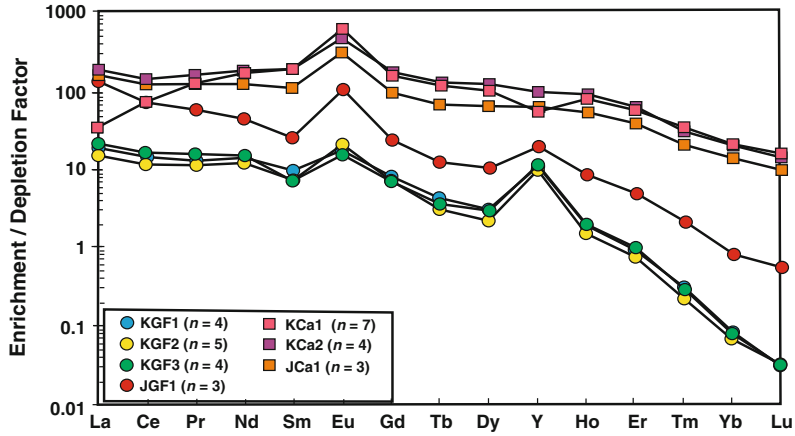

Fig. 6 Element enrichment or depletion factors for greenish fluorite and pre-ore hydrothermal calcite from El Hammam REE-rich fluorite vein system relative to late Hercynian granite. Factors are calculated (Gagnon et al. 2003) by dividing average concentration of an element in fluorite or calcite by its average concentration in the late Hercynian granite

Ca-rich brine in fluid inclusions (avg = 32.5 ± 8 wt% NaCl equiv, Table 2); (2) predominance of pre-ore hydrothermal calcite as the main gangue mineral; and (3) limited occurrence of barite. Accordingly, it is concluded that Cl^-, CO_3^{2-}, and to a much lesser extent SO_4^{2-} complexes were the main complexing agents that controlled the hydrothermal mobilization of REE. Sorption of REE onto mineral surfaces (e.g., Bau 1996) is likely to have played a minor, if any, role because of the large size of the Aouli fluorite crystals that offered only a small reactive surface area for sorption.

The large positive chondrite-normalized Y anomalies shown by the El Hammam fluorite (Fig. 5) are suggestive of Y-complexation, fluid interaction along the flow path, remobilization, and long-distance migration of the F-rich mineralizing fluid (see Bau and Dulski 1995; Wood 1990a, b; Sallet et al. 2005; Schwinn and Markl 2005; Schönenberger et al. 2008). During long migration toward the site of deposition, intensive, high-temperature (>250 °C) interaction of the mineralizing fluids with plagioclase-bearing rocks (i.e., greywacke and diabase-dolerite dikes) resulted in leaching of Eu, a process that may explain the prominent positive Eu anomalies. The high thermal regime required to maintain the positive Eu anomaly, however, contrasts with fluid inclusion data indicating that fluid temperatures for fluorite precipitation were substantially below 200 °C (Table 2). To overcome such kinetic constraints, we propose that the ore-forming fluids acquired REY characteristics during fluid-rock interaction at higher temperatures, within deeper parts of the adjacent sedimentary basin(s), and then migrated to the site of ore deposition prior to fluorite crystallization. Moreover, the positive Eu anomaly shown by the fluorite argues against inheritance of this Eu from the hidden granitic K-feldspar-rich intrusion, which lacks appreciable plagioclase and exhibits a negative Eu anomaly (Fig. 5). Consequently, host rocks that could have provided the required Eu for creating the positive Eu anomalies are the plagioclase-rich greywacke intercalated in the Silurian to Namurian succession, or more likely the intensely hydrothermally altered diabase-dolerite dikes that cut the metasedimentary host rocks (Figs. 2 and 3).

Fluorite-barite veins in the El Hammam district are confined mostly to ENE-trending faults in which brecciation and open space filling occurred repeatedly. Such intimate relationships to major tectonic structures (Fig. 1) suggest that ENE-trending brittle structures (Atlantic dominance; Ellouz et al. 2003) were the major pathways that focused fluid flow. Structural

constraints (Rahho 1996), coupled with $^{39}Ar/^{40}Ar$ ages on adularia (Cheilletz et al. 2010), indicate that the fluorite-barite mineralization occurred during the Permian-Triassic, coincident with Pangean rifting and later opening of the Central Atlantic Ocean (Muttoni et al. 2003; Martins et al. 2008). This interval of time fits within the Late Triassic-Early Jurassic period during which most mineralization of the Western Europe fluorite province formed (Sizaret et al. 2009). Subsequent crustal thinning and a related increased geothermal gradient could have resulted in the development of small-scale convection cells that acted as the source of heat to move the mineralizing fluids toward shallower depths where the fluorite-rich ores were deposited.

References

Agard J (1966) Données nouvelles sur le district fluorifère d'El Hammam-Berkamène (Maroc central). Rapport Service d'Etude Gîtes Minéraux 843, Rabat, Morocco, 25 pp

Barthoux JC (1923) Observations relatives à la genèse de certains gisements manganésifères. Comptes Rendus Acad Sci Paris 196:818–1821

Bau M (1991) Rare earth element mobility during hydrothermal and metamorphic fluid-rock interaction and the significance of the oxidation state of europium. Chem Geol 93:219–230

Bau M (1996) Controls on the fractionation of isovalent trace elements in magmatic and aqueous systems: evidence from Y/Ho, Zr/Hf and lanthanide tetrad effect. Contrib Miner Petrol 123:323–333

Bau M, Dulski P (1995) Comparative study of yttrium and rare-earth element behaviours in fluorine-rich hydrothermal fluids. Contrib Mineral Petrol 119:213–223

Bouabdellah M, Banks D, Klügel A (2010) Comment on "A Late Triassic $^{40}Ar/^{39}Ar$ age for the El Hammam high-REE fluorite deposit (Morocco): mineralization related to the Central Atlantic magmatic province? Mineral Deposita 45:729–731

Bouabdellah M, Castorina F, Bodnar RJ, Jébrak M, Prochaska W, Klügel A, Hoernle K (2014) Petroleum migration, fluid mixing, and halokinesis as the main ore-forming processes at the peridiapiric Jbel Tirremi fluorite-barite hydrothermal deposit, northeastern Morocco. Econ Geol 109:1223–1256

Carpenter AB, Trout ML, Pickett EE (1974) Preliminary report on the origin and chemical evolution of lead and zinc rich oil field brines in central Mississippi. Econ Geol 69:119–1206

Cheilletz A, Gasquet D, Filali F, Archibald DA, Nespolo M (2010) A Late Triassic $^{40}Ar/^{39}Ar$ age for the El Hammam high-REE fluorite deposit (Morocco): mineralization related to the Central Atlantic magmatic province? Mineral Deposita 45:323–329

Davis DW, Lowenstein TK, Spencer RJ (1990) Melting behavior of fluid inclusions in laboratory-grown halite crystals in the systems NaCl-H_2O, NaCl-KCl-H_2O, NaCl-$MgCl_2$-H_2O and NaCl-$CaCl_2$-H_2O. Geochim Cosmochim Acta 54:591–601

Dubois M, Marignac C (1997) The H_2O-NaCl-$MgCl_2$ ternary phase diagram with special application to fluid inclusion studies. Econ Geol 92:114–119

Ellouz N, Patriat M, Gaulier JM, Bouatmani R, Sabounji S (2003) From rifting to Alpine inversion: Mesozoic and Cenozoic subsidence history of some Moroccan basins. Sediment Geol 156:185–212

Gagnon JE, Samson IM, Fryer BJ, Williams-Jones AE (2003) Compositional heterogeneity in fluorite and the genesis of fluorite deposits: insights from LA-ICP-MS analysis. Can Mineral 41:365–382

Haynes FM, Kesler SE (1987) Chemical evolution of brines during Mississippi Valley-type mineralization: evidence from east Tennessee and Pine Point. Econ Geol 82:53–71

Hoepffner C, Soulaimani A, Piqué A (2005) The Moroccan Hercynides. J Afr Earth Sci 43:144–165

Hoepffner C, Houari MR, Bouabdelli M (2006) Tectonics of the North African Variscides (Morocco, western Algeria), an outline. In: Frizon de Lamotte D, Saddiqi O, Michard A (eds) Recent developments on the Maghreb geodynamics. Comptes Rendus Geosci 338, pp 25–40

Huon S (1985) Clivage ardoisier et réhomogénéisation isotopique dans des schistes paléozoiques du Maroc: etude microstructurale et isotopique, conséquences régionales. Unpubl Ph.D. Thesis, Université de Strasbourg, France, 124 pp

Huon S, Kfibler B, Hunziker J (1988) Identification de mélanges de micas blancs par diffraction des rayons X: application à des séries carbonatées faiblement métamorphisées. Schweiz Mineral Petrogr Mitt 68:185–202

Izart A, Tahiri A, El Boursoumi A, Vachard D, Saidi M, Chèvrement P, Berkhli M (2001a) Nouvelles données biostratigraphiques et sédimentologiques des formations carbonifères de la région de Bouqachmir (Maroc central): implications sur la paléogéographie des bassins carbonifères nord-mésétiens. Comptes Rendus Acad Sci Paris 332:169–175

Izart A, Chèvrement P, Tahiri A, El Boursoumi A, Thiéblemont D (2001b) Carte géologique du Maroc au 1/50 000, feuille de Bouqachmir. Notes Mém Serv Géol Maroc 411 bis, 60 pp

Jébrak M (1982) Les districts à fluorine su Maroc central. Bull BRGM II 2:211–221

Jébrak M (1984) Le district filonien à Pb-Zn Ag et carbonates du Jbel Aouam. Bull Minéral 108:487–498

Jébrak M (1985) Contribution à l'histoire naturelle des filons (F, Ba) du domaine varisque. Doc BRGM 99:1–473

Jébrak M, Touray JC, Giret P (1988) Geochemical characteristics and genesis of fluorite deposits of Morocco. In: Zachrisson E (ed) Proceed Seventh Quad IAGOD Symp, E. Schweizerbart'sche Verlagsbuchhandlung, Stuttgart, pp 287–295

Kharbouch F (1994) Les laves dévono-dinantiennes de la Meseta Marocaine: étude pétrogéochimique et implication géodynamique. Unpubl PhD Thesis, Université de Bretagne, France, 278 pp

Leach DL, Sangster DF (1993) Mississippi Valley-type lead-zinc deposits. In: Kirkham RV, Sinclair WD, Thorpe RI, Duke JM (eds) Mineral deposit modeling. Geol Assoc Canada Spec Paper 40, pp 289–314

Martins LT, Madeira J, Youbi N, Munhá Mata J, Kerrich R (2008) Rift-related magmatism of the Central Atlantic magmatic province in Algarve, southern Portugal. Lithos 101:102–124

McLennan SM (1989) Rare earth elements in sedimentary rocks: influence of provenance and sedimentary processes. In: Lipin BR, McKays GA (eds) Rare earth elements. Rev Mineral 21, pp 169–200

Michard A, Hoepffner C, Soulaimani A, Baidder L (2008) The Variscan belt. In: Michard A, Saddiqi O, Chalouan A, Frizon de Lamotte D (eds) Continental evolution: the geology of Morocco. Lecture Notes Earth Sci 116, Springer-Verlag, Berlin-Heidelberg, pp 65–132

Migdisov AA, Williams-Jones AE (2007) An experimental study of the solubility and speciation of neodymium (III) fluoride in F-bearing aqueous solutions. Geochim Cosmochim Acta 71:3056–3069

Migdisov AA, Williams-Jones AE (2008) A spectrophotometric study of Nd(III), Sm(III) and Er(III) complexation in sulfate-bearing solutions at elevated temperatures. Geochim Cosmochim Acta 72:5291–5303

Migdisov AA, Williams-Jones AE (2014) Hydrothermal transport and deposition of the rare earth elements by fluorine-bearing aqueous liquids. Miner Deposita 49:987–997

Migdisov AA, Williams-Jones AE, Wagner T (2009) An experimental study of the solubility and speciation of the rare earth elements (III) in fluoride- and chloride-bearing aqueous solutions at temperatures up to 300°C. Geochim Cosmochim Acta 73:7087–7109

Möller P, Giese U, Dulski P (1994) Behaviour of REE in alteration processes of granites. In: Seltman R, Kämpf H, Möller P (eds) Metallogeny of collisional orogens. Czech Geological Survey, Prague, pp 368–374

Möller P, Stober I, Dulski P (1997) Seltenerdelement-, Yttrium-Gehalte und Bleiisotope in Thermal- und Mineralwässern des Schwarzwaldes. Zeischrift Fachsektion Hydrogeol 3:118–131

Moreno C, Sáez R, González F, Almodóvar G, Toscano M, Playford G, Alansari A, Rziki S, Bajddi A (2008) Age and depositional environment of the Draa Sfar massive sulphide deposit, Morocco. Miner Deposita 43:891–911

Muttoni G, Kent DV, Garzanti E, Brack P, Abrahamsen N, Gaetani M (2003) Early Permian Pangea "B" to Late Permian Pangea "A". Earth Planet Sci Lett 215:379–394

Pérez-Soba C, Villaseca C (2010) Petrogenesis of highly fractionated I-type peraluminous granites: La Pedriza pluton (Spanish central system). Geol Acta 8:131–149

Rahho H (1996) Etude géologique du paléozoïque d'El Hammam: analyse de la fracturation et relation avec les structures minéralisées (Maroc central septentrional). Unpubl Doctorat 3ème cycle, Université Mohammed V, Rabat, Morocco, 219 pp

Remmal T, El Kamel F, Mohsine A (1997) Le bassin viséen de Mechraâ Ben Abbou (Meseta occidentale, Maroc): une structure sur décrochement N80 associée à un magmatisme tholéitique d'intraplaque. Géol Médit 24:225–239

Roedder E (1984) Fluid inclusions. Rev Mineral 12:1–644

Sallet R, Moritz R, Fontignie D (2005) The use of vein fluorite as probe for paleofluid REE and Sr–Nd isotope geochemistry: The Santa Catarina fluorite district, southern Brazil. Chem Geol 223:227–248

Schönenberger J, Köhler J, Markl G (2008) REE systematics of fluorides, calcite and siderite in peralkaline plutonic rocks from the Gardar province, South Greenland. Chem Geol 247:16–35

Schwinn G, Markl G (2005) REE systematics in hydrothermal fluorite. Chem Geol 216:225–248

Sheppard SMF, Charef A, Bouhlel S (1996) Diapirs and Zn-Pb mineralization: a general model based on Tunisian (N. Africa) and Gulf Coast (USA) deposits. In: Sangster DF (ed) Carbonate-hosted lead-zinc deposits. Society economic geologists special publication, vol 4. pp 230–243

Simmons SF, Christenson BW (1994) Origins of calcite in a boiling geothermal system. Am J Sci 294:361–400

Sizaret S, Marcoux E, Boyce A, Jébrak M, Stevenson R, Ellam R (2009) Isotopic (S, Sr, Sm/Nd, D, Pb) evidence for multiple sources in the Early Jurassic Chaillac F-Ba ore deposit (Indre, France). Bull Soc Géol France 180(2):83–94

Sonnet PM (1981) Les skarns à tungstène, étain et bore de la région d'El Hammam (Maroc central). Unpubl Ph. D. Thesis, Univ Catholique Louvain, Belgium, 347 pp

Sonnet PM, Verkaeren J (1989) Scheelite-malayaite and axinite bearing skarns from El Hammam, central Morocco. Econ Geol 84:575–590

Steele-MacInnis M, Lecumberri-Sanchez P, Bodnar RJ (2012) HOKIEFLINCS_H_2O-NaCl: a Microsoft Excel spreadsheet for interpreting microthermometric data from fluid inclusions based on the PVTX properties of H_2O-NaCl. Comput Geosci 49:334–337

Tahiri A, Aït brahim L, Saidi A (1996) Analyse de la fracturation tardi-hercynienne dans le bassin Permien de Bou Achouch: modèle de la réactivation des accidents hercyniens dans le Maroc central septentrional. In: Medina F (ed) Le Permien et le Trias du Maroc. Etat des connaissances, Ed Pumag, Marrakech, pp 99–112

Taylor RS (1982) Planetary science: a lunar perspective. Lunar and Planetary Inst, Houston, Texas, USA 502 pp

Termier H (1936) Etudes géologiques sur le Maroc central et le Moyen Atlas septentrional. Notes Mém Serv Mines Carte Géol Maroc 33, 1566 pp

Wood SA (1990a) The aqueous geochemistry of the rare-earth elements and yttrium. (1). Review of available low temperature data for inorganic complexes and the inorganic REE speciation of natural waters. Chem Geol 82:159–186

Wood SA (1990b) The aqueous geochemistry of the rare-earth elements and yttrium. (2). Theoretical predictions of speciation in hydrothermal solutions to 350°C at saturation water vapor pressure. Chem Geol 88:99–125

Yajima J, Touray JC (1970) Analyse thermométrique du gisement de fluorite d'El Hammam (Maroc) (d'après les études des inclusions fluides). Miner Deposita 5:23–28

Yardley BWD, Graham JT (2002) The origins of salinity in metamorphic fluids. Geofluids 2:249–256

Part IV

Orogenic and Granitoid-Hosted Gold ± Rare-Metal Deposits

A Review of Gold Mineralization in Mali

David M. Lawrence, James S. Lambert-Smith and Peter J. Treloar

Abstract

Economic gold mineralization in Mali is confined to two terranes of Birimian-aged (Paleoproterozoic) rocks in the south and south-west of the country. The West Mali gold belt, along the border with Senegal, hosts two world-class orogenic gold districts (>5 Moz of Au mined or in reserve): the Loulo-Gounkoto and Sadiola-Yatela complexes. This gold province is hosted within greenschist metamorphosed siliciclastic and carbonate sedimentary rocks along the eastern side of the Kédougou-Kéniéba inlier, with mineralization linked to higher-order shears and folds related to the Senegal-Mali Shear Zone. Gold deposits within the West Mali gold belt show many features typical of orogenic gold mineralization, such as geological setting (accretionary orogen), late-orogenic timing (strike-slip deformation; post peak metamorphism), structural paragenesis, and deposit geometry (steep, tabular ore bodies). However, alteration assemblages (tourmalinization, silica-carbonate, sericite-chlorite-biotite, calc-silicate) and ore fluid compositions (carbonic-rich and high-salinity aqueous-rich fluids) are highly variable along the belt. Fluid inclusion and stable isotope studies have shown that this variability is caused by multi-fluid sources, with magmatic, evaporitic and regional metamorphic fluids all likely contributing to gold mineralization within the region. Supergene enrichment of the orogenic gold lodes is economically important in the northern parts of the West Mali gold belt, involving karstification of mineralized limestones. In addition to orogenic gold deposits, other styles of gold mineralization have been reported within the Birimian crust of West Africa. The Morila gold deposit, in southern Mali,

D.M. Lawrence (✉)
Randgold Resources Ltd, Unity Chambers,
Halkett Street, St Helier, Jersey JE2 4WJ, UK
e-mail: David.Lawrence@randgold.com

J.S. Lambert-Smith · P.J. Treloar
School of Natural and Built Environments,
Kingston University, London KT1 2EE, UK

M. Bouabdellah and J.F. Slack (eds.), *Mineral Deposits of North Africa*,
Mineral Resource Reviews, DOI 10.1007/978-3-319-31733-5_13

is classified as a reduced intrusion-related gold system, in which strata-bound Au–As–Sb–Bi–(W–Te) mineralization formed early in the Eburnean orogenic cycle (syn-metamorphic) with spatial and genetic links to syn-orogenic granodiorites and leucogranites.

1 Introduction

Gold mining in Mali has a long and illustrious history, with artisanal workers having exploited the metal since pre-historic times. During the peak of the Malian Empire in the 14th century, alluvial placers along the Falémé River (which now marks the international border with Senegal) were mined extensively. This mining alerted European and Arab rulers to the mineral wealth of the region, and helped develop political, cultural, and trade links between western Sudan (as it was then known) and the rest of the world. Collapse of the Songhai Empire in the late 16th Century ended the region's dominance in the African and world gold trade.

Commercial gold mining in Mali commenced in the 1970s. The first industrial mine, Kalana, was discovered after a large exploration program by Société Nationale de Recherche et d'Exploitation Minière (SONAREM) (Boltrukevitch 1973). In the following decade, a United Nations assisted project known as the Syndicat Or (a joint venture between the Malian government and BRGM) carried out extensive soil geochemical surveys in the southern and western parts of Mali. This project led to the discovery of many of the country's largest gold deposits, including Gara (previously known as Loulo-0), Sadiola, and Syama (Dommanget et al. 1993; Kusnir 1999). In 1991, Mali relaxed its mining codes, which led to renewed foreign interest and began the recent boom in the country. In 2013, Mali exported 64 t of gold, and is currently Africa's third largest gold producer after South Africa and Ghana (Diarra and Holliday 2014).

2 Geological Setting

The geology of Mali is dominated by Neoproterozoic to Paleozoic sedimentary rocks of the Taoudeni basin (Villeneuve and Cornée 1994), which formed during extensional deformation of the West African Craton during the Neoproterozoic (Brooner et al. 1990). Paleoproterozoic (Birimian; 2.2–2.0 Ga) basement rocks crop out from beneath the Taoudeni cover sequences in the Sikasso region of southern Mali, and in two small windows in the semi-arid Kayes region in the southwest, close to the border with Senegal (Kayes and Kédougou--Kéniéba inliers) (Fig. 1a). Gold mineralization in Mali is restricted to these two Birimian terranes that are referred to here as the Mali South Goldfields and West Mali Gold Belt, respectively.

2.1 Mali South Goldfields

Gold mineralization in southern Mali is located within Birimian rocks of the Baoulé-Mossi domain, which also hosts the well-known Ghanaian gold provinces (e.g., Oberthür et al. 1994; Allibone et al. 2002a, b; Berge 2011), as well as gold mineralization throughout Burkina Faso (Klemd and Ott 1997; Klemd et al. 1997; Béziat et al. 2008) and eastern and central Côte d'Ivoire (Coulibaly et al. 2008; Kadio et al. 2010). The Birimian geology of southern Mali comprises three volcanic-sedimentary belts with adjacent sedimentary basins (Fig. 1b). From west to east, these are known as the Yanfolila-Kalana belt, the Bougouni belt, and the Syama belt. The adjacent basins, from west to east, are referred to as the Siguri basin

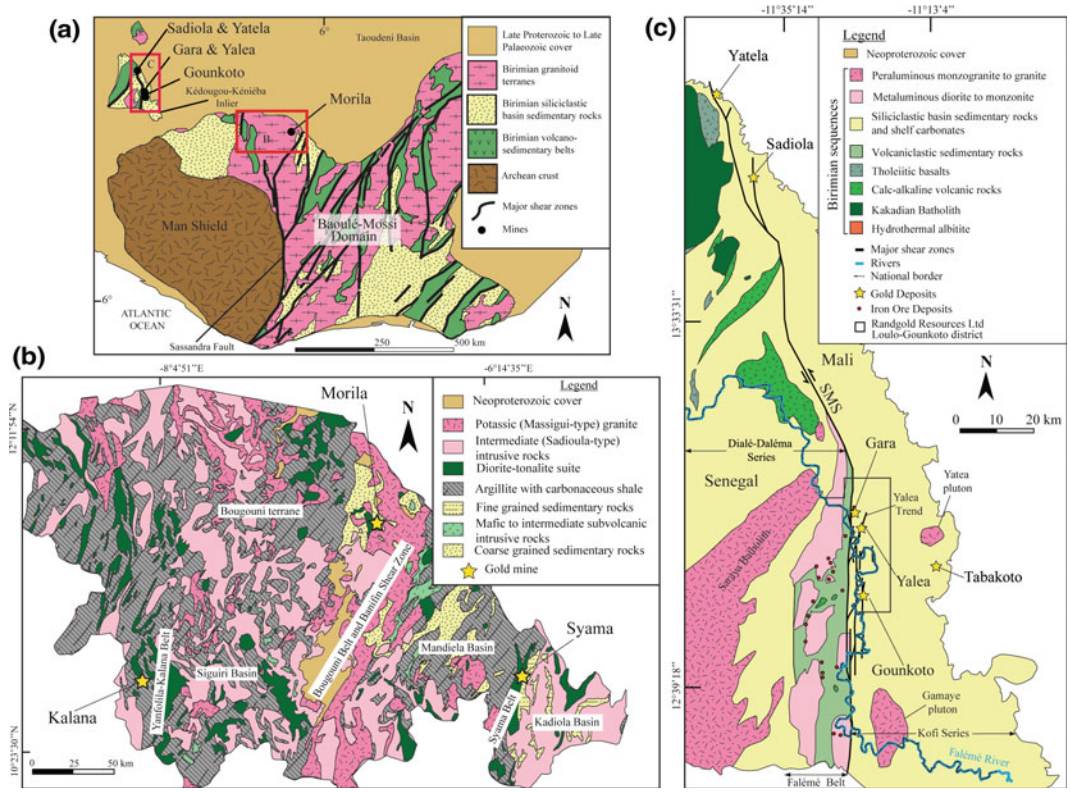

Fig. 1 Regional geologic maps of the Birimian terranes of Mali. **a** *Inset* of West African craton indicating locations of study areas (modified from Feybesse et al. 2006). **b** Detailed map of Mali South Goldfields, showing geology of northwestern part of Baoulé-Mossi domain. **c** Geologic map of eastern (Malian) part of Kédougou-Kéniéba inlier, showing locations of mines within the West Mali Gold Belt (modified from Lawrence et al. 2013a)

(located mainly in Guinea), the Mandiela basin, and the Kadiola basin. This area hosts some major gold deposits, including those exploited at the Morila, Kalana, and Syama mines (Milési et al. 1992; Olson et al. 1992; McFarlane et al. 2011).

Birimian rocks were deformed and metamorphosed during the Eburnean orogeny around 2.1–2.0 Ga. In southern Mali, three Eburnean deformational events have been identified (Liégeois et al. 1991). A first phase of isoclinal deformation (D1) was followed by a D2 phase of NW-SE compression recorded by a widespread, sub-vertical N- to NNE-trending schistosity (S2) and regional greenschist-amphibolite facies metamorphism. Major NNE-trending, sub-vertical, shear structures such as the Baniffin shear zone, which is located 30 km to the east of Morila, formed during a later transcurrent D3 event.

2.2 West Mali Gold Belt

Gold mineralization in western Mali is located along the eastern side of the Birimian Kédougou-Kéniéba inlier (KKI) (Fig. 1c). This inlier straddles the Mali-Senegal border; although the most productive and prospective region lies on the Malian side, and is referred to here as the West Mali Gold Belt. The gold belt extends for approximately 180 km and includes two

world-class gold districts (>10 Moz of Au), the Loulo-Gounkoto complex in the south and the Sadiola-Yatela district in the north, plus the smaller Tabakoto mine and several exploration projects such as the Fekola prospect south of Gounkoto.

The West Mali Gold Belt is hosted within Birimian sedimentary rocks of the Kofi Series (Fig. 1c). The sedimentary basin comprises a thrusted and folded sequence of quartz and feldspar wackes, mudstone, and limestone-marl sequences. In the southern part of the basin, these units are strongly albitized and tourmalinized. Tourmaline-bearing quartz-wackes at Loulo have detrital zircon ages of 2125 ± 27 to 2098 ± 11 Ma (Boher et al. 1992). The Kofi sedimentary rocks are intruded by a series of plutons of various generations and sizes. The largest intrusions are monzogranitic in composition and include the Gamaye pluton in the southern part of the basin, and the Yatea pluton north of the Tabakoto mine. Smaller, calc-alkaline, quartz-feldspar-phyric granodiorite stocks and finer-grained, mafic- to intermediate-composition dikes and sills, cut the sedimentary rocks in both the Loulo-Gounkoto and Sadiola-Yatela districts.

A polycyclic Eburnean deformational history, similar to that recorded in the Mali South Goldfields, is reported for the Kofi Series. The first deformational phase (D1) is a compressive event linked to the initial accretion of the Birimian terranes. D1 deformation is characterized by NNE-to NE-trending recumbent and overturned folds (F1), NW-verging thrusts, and axial planar schistosity (Milési et al. 1989, 1992; Ledru et al. 1991). Later deformation (D2–D3) is associated with transcurrent movement and formation of the regional-scale, N-S, Senegal-Mali Shear Zone (SMS; Bassot and Dommanget 1986). Gold deposits of the West Mali Gold Belt are confined to second- and higher-order structures on the eastern side of the SMS, in which mineralization was synchronous with D3 transtensional deformation (Lawrence et al. 2013a; Masurel et al. in press). Regional greenschist-facies metamorphism and associated plutonism are associated with both compressive and transcurrent phases of deformation. Minor hornblende-hornfels contact metamorphism is seen locally surrounding intrusive stocks at Sadiola.

3 Gold Mineralization Styles

The majority of gold deposits within the Birimian terranes of Mali, and the rest of West Africa, have been classified as orogenic gold mineralization (Milési et al. 1992; Olson et al. 1992; Lawrence et al. 2013a, b). Globally, orogenic gold lodes are shear-hosted deposits that developed along strike-slip fault systems linked to late-stage, non-orthogonal, orogenic crustal growth (Groves et al. 1998, 2000). They form over a range of crustal depths (<6 to >12 km; Groves et al. 1992), although the majority of deposits are hosted in greenschist-facies rocks (Bierlein and Crowe 2000). The general characteristics of orogenic gold deposits are summarized in Groves et al. (1998) and Ridley and Diamond (2000). Recently, a more complex Birimian gold metallogenesis has been recognised, with new styles of gold mineralization documented such as reduced intrusion-related gold systems and gold skarn deposits (McFarlane et al. 2011; Ouattara et al. 2014).

This review documents the genesis of both orogenic gold and reduced intrusion-relation gold mineralization in Mali, with emphasis on the country's four largest ore bodies: Loulo, Gounkoto, Sadiola, and Morila. Discussion of gold mineralization in the West Mali gold belt is a synthesis of three recent studies (Lawrence et al. 2013a, b; Masurel et al. in press). Synopsis of the Morila deposit in southern Mali relies on reports by Hammond et al. (2011) and McFarlane et al. (2011), together with data from two MSc theses by Quick (1999) and King (2012).

4 Orogenic Gold

4.1 Loulo-Gounkoto Complex

The Loulo-Gounkoto complex is one of the largest orogenic gold districts in West Africa. Three main deposits are known: Gara (current reserves of 1.5 Moz at 4.15 g/t), Yalea (reserves of 2.9 Moz at 5.82 g/t), and Gounkoto (reserves of 2.8 Moz at 5.1 g/t) (Randgold Resources Ltd 2014). The Gara ore body was discovered during

regional soil surveys by Syndicat Or in 1981. In 1992, Broken Hill Proprietary (BHP) Minerals entered into an option and share purchase agreement with Syndicat Or, and did work in the Loulo area until 1996 when Randgold Resources Ltd acquired BHP's Malian projects. Randgold carried out an intensive exploration program, which led to the discovery of the Yalea deposit in 1996/1997. In November 2005, the Loulo mine was officially opened. Gounkoto was added to Loulo's resource in 2009, discovered following an airborne electromagnetic survey of the region; mining commenced in 2011, 2 years after initial discovery. The Loulo-Gounkoto complex has produced over 3.5 Moz from both open pit and underground resources, and currently (2015) has a mining lifespan of 9 years at 660 Koz pa.

4.1.1 Yalea

The Yalea ore body is hosted along a third-order shear related to movement along the N-S-trending, brittle-ductile, Senegal-Mali Shear Zone (SMS). The SMS was initiated as a sinistral transpressional fault during the onset of D2 deformation. Higher-order structures that formed during D2 transpression include second-order, NNE-striking sinistral shears (P-shear geometry) such as those in the Yalea Trend. This extends for >20 km from the south of Yalea to the Loulo-2, Loulo-3, and Baboto satellite deposits. The Yalea ore body sits along a 2-km-long, N-S left-hand flexure of the Yalea Trend (known as the Yalea Shear), which formed during transtensional sinistral movement at the start of D3 deformation (Fig. 2).

The Yalea Shear is a 10–40-m-wide zone of strongly altered, brittle- to ductilely deformed rocks that dip 60° to the east at surface and steepen at depth. The footwall consists of argillaceous calcareous sandstone, with hydrothermal-tectonic breccias focused along footwall splays. Hanging-wall lithologies include arkosic arenite grading into arkosic wacke (Fig. 2). A carbonaceous dolomitic limestone caps the ore zone in the south of the deposit. Mineralization consists predominantly of disseminations that are confined to the matrix of hydrothermal and tectonic breccia units along the contact between the argillaceous and arkosic units (Fig. 3).

The alteration halo at Yalea extends 50–100 m into the wall rock and consists of two main components: (1) an early phase of albite-carbonate-quartz alteration that predates the main mineralization event (D2/early D3); and (2) a later syn-mineralization phase of phyllic alteration (D3) (Lawrence et al. 2013a). The first stage of alteration is divided spatially into two zones. An inner texturally destructive zone, located along the Yalea Shear, is carbonate rich and comprises an assemblage of albite-ankerite plus minor quartz, sericite, and pyrite. An outer zone occurs in mylonitic and brecciated footwall lithologies, with alteration becoming less intense and more albite-rich distal from the main shear. Altered zones generally have a pink or orange color due to the presence of fine-grained hematite. Sericite-chlorite alteration overprints the albite-ankerite-quartz alteration along the Yalea Shear. Alteration is confined to narrow (<5 cm) ductile shears, patchy replacements of hanging-wall limestones, interstitial phases in massive sulphide zones, and thin (<3 cm) green to black alteration envelopes surrounding auriferous sulphide stringers and veinlets (Lawrence et al. 2013a).

Disseminated ore assemblages at Yalea are dominated by arsenian pyrite and arsenopyrite, and locally by zones of abundant chalcopyrite. Paragenetic studies reveal a multi-stage ore development (Lawrence et al. 2013a; Fig. 4a). Arsenian pyrite (max. 3 wt% As) forms the first generation of auriferous sulphides and commonly contains euhedral inclusions and intergrowths of fine-grained arsenopyrite. Arsenian pyrite is post-dated by a generation of coarse-grained arsenopyrite that replaces, cuts, and/or forms pseudomorphs of early sulphides. A late phase of cross-cutting chalcopyrite is temporally associated with some gold remobilization. Gold is generally fine-grained (<10 μm); coarser particles up to 50 μm are spatially associated with arsenian pyrite. Gold fineness ranges from 920 to 990 (mean of 950).

4.1.2 Gara

The Gara deposit is 6 km NW of Yalea, adjacent to the Falémé River (Fig. 1c). Mineralization occurs over a strike length of 1.2 km. The

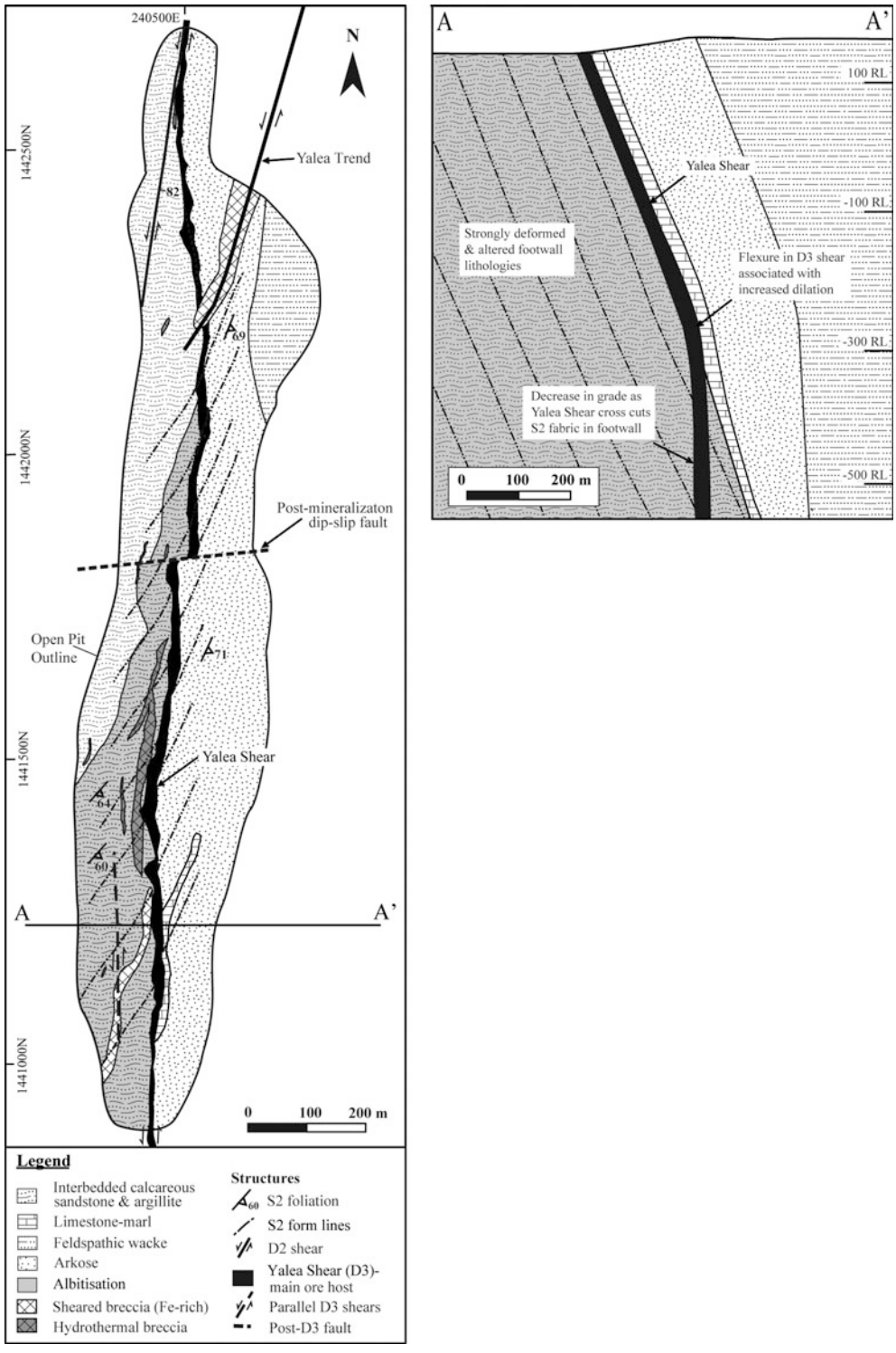

Fig. 2 Geological and structural plan map (*left*) and cross section (*right*) of Yalea gold deposit in Loulo district. Ore body is within a 2-km-long, N-S-trending, D3 structure known as the Yalea Shear, which forms a left-hand flexure in district-scale, NNE-trending, Yalea Trend

Fig. 3 Photograph of brittle-ductile deformation along Yalea Shear with gold mineralization hosted in dark matrix of pink albite-ankerite hydrothermal breccia (Lawrence et al. 2013a)

geometry of the ore body is controlled by macroscopic, SSW-plunging, upright F2 folds, related to transpressive D2 deformation along a series of second-order, NNE-trending shears linked to the SMS (Lawrence et al. 2013a; Fig. 5). Later extensional D3 deformation led to the formation of quartz-ankerite-tourmaline-pyrite-gold shear veins (Fig. 6). Minor amounts of disseminated sulphides surround these veins. The Gara stratigraphy consists of a tourmaline-altered quartz wacke (20–50 m thick), with mineralization being hosted in the most altered "tourmalinite" unit (5–20 m thick). Rocks immediately to the east and west of the ore body consist of carbonaceous limestone and marl, and argillaceous and calcareous sandstone (Fig. 5).

Gara is characterized by intense tourmaline alteration. Early studies at Gara (Milési et al. 1992; Dommanget et al. 1993) suggested that the boron-rich protolith to the tourmalinite had a submarine-exhalative origin. However, Lawrence et al. (2013a) has shown that tourmaline alteration is epigenetic and related to gold mineralization. Tourmaline growth shows a complex, multi-stage paragenesis (Lawrence et al. 2013a). The first generation (early D2) is the most pronounced and forms texturally destructive, cryptocrystalline (<10 μm) tourmaline that pervasively replaces the matrix of the quartz wacke host rock. The second generation of tourmaline growth (early D3) is synchronous with mineralization and forms acicular tourmaline grains (30–50 μm) confined to gold-bearing stockwork veins, commonly aligned perpendicular to vein walls. The last phase of tourmaline alteration (late D3) is a replacement of auriferous pyrite. The first tourmaline alteration event prepared the quartz wacke host for later stockwork vein formation and gold mineralization, by increasing the competency of the rock in relation to the surrounding wall rocks. During D2 and D3 deformations, this unit preferentially fractured, which facilitated fluid ingress (Lawrence et al. 2013a). Early D2 sodic alteration at Gara, analogous to the main alteration at Yalea, albeit with lower carbonate contents, occurs in more distal zones (up to 150 m from the ore body).

In contrast to Yalea, pyrite is the principal sulphide ore mineral at Gara (>95 % of total sulphides). Pyrite forms annealed aggregates and commonly displays minor Ni ± Co substitution (≤ 2 wt% Ni + Co). Trace sulphide assemblages include chalcopyrite, gersdorffite, pentlandite, Ni-bearing pyrrhotite, and arsenopyrite. Monazite, scheelite, and lesser amounts of xenotime are also present. Gold is associated with pyrite (95 %) or occurs as free gold in veins (5 %). Silver concentrations are lower than at Yalea, with gold fineness ranging from 988 to >998 (mean of 994). The ore and alteration paragenesis at Gara is summarized in Fig. 4b.

4.1.3 Gounkoto

The Gounkoto deposit is in the southern part of the mining district, approximately 30 km from Gara (Fig. 1c). The ore body is hosted along a 2-km-long, N-S-trending, third-order, transtensional sinistral structure; elevated grades are spatially associated with left-hand, NNW-trending dilational jogs that formed during late D3 deformation. Mineralogy is characterized by multiple overprinting hydrothermal events (Lawrence et al. 2013a). Strongly sheared semi-pelitic and carbonate rocks show evidence of (from oldest to youngest): (1) early albite-ankerite-quartz

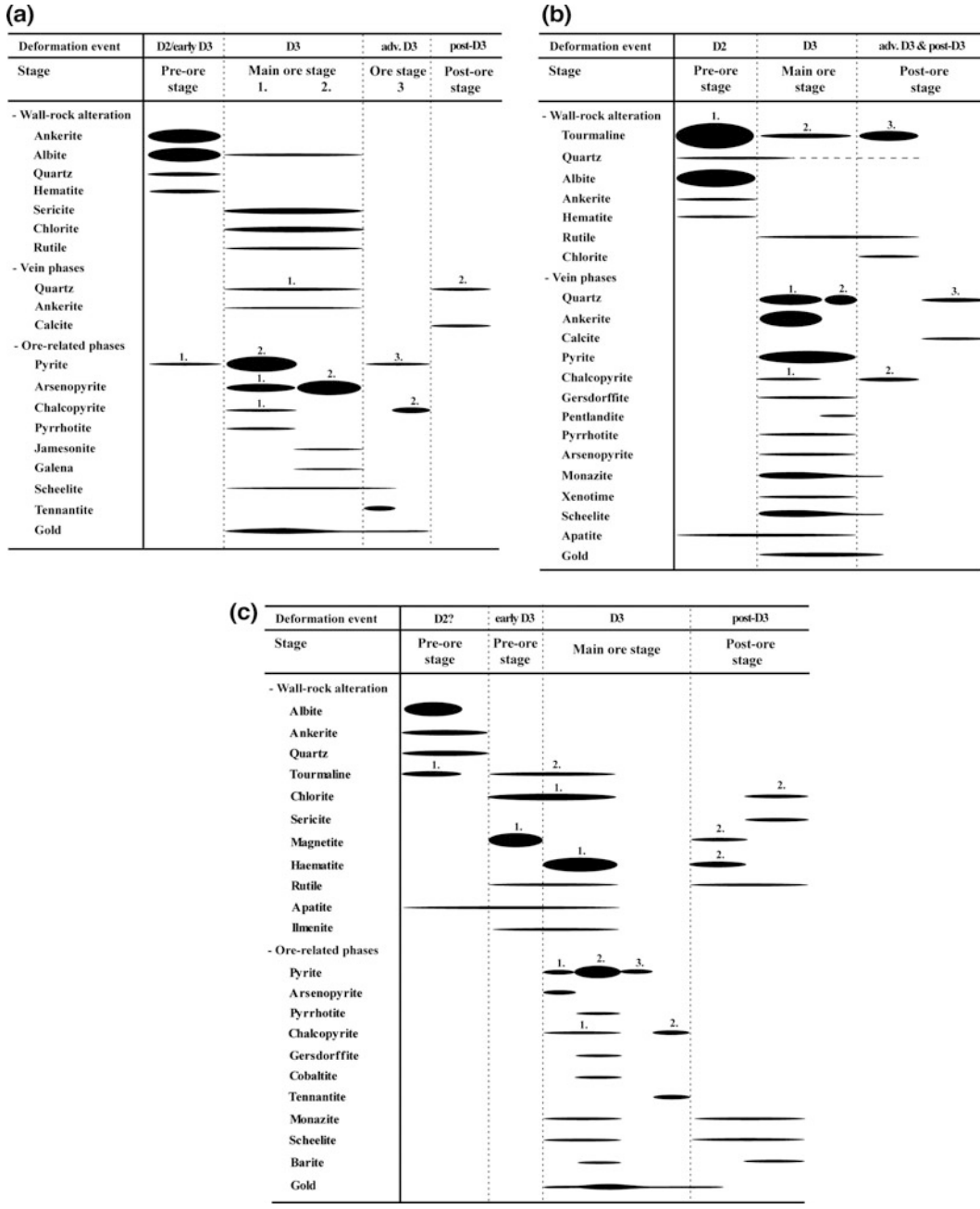

Fig. 4 Paragenesis of veins ore, and alteration zones for Yalea (**a**), Gara (**b**), and Gounkoto (main ore body; **c**). Data from Lawrence et al. (2013a)

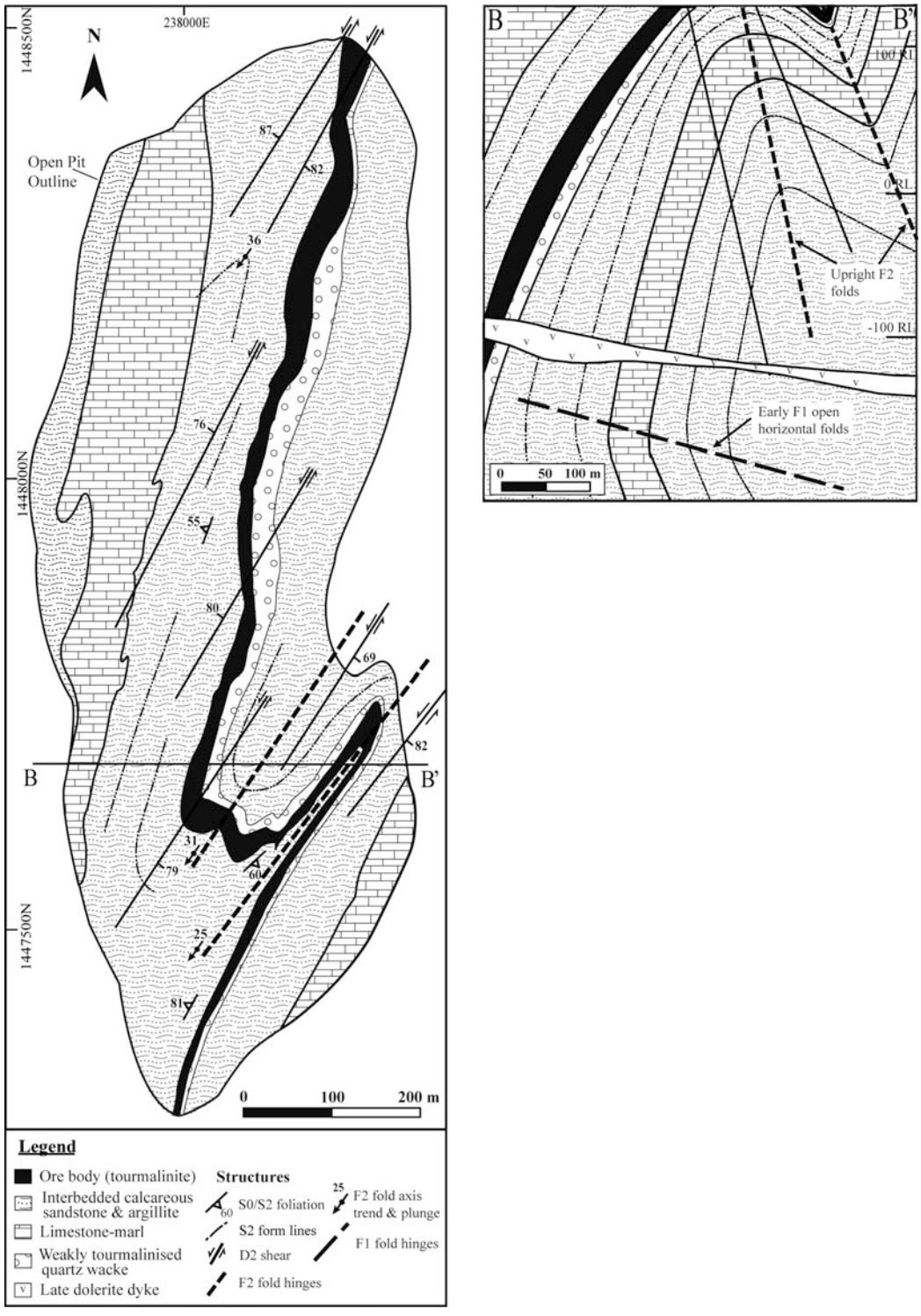

Fig. 5 Geological and structural plan map (*left*) and cross section (*right*) of Gara gold deposit in Loulo district, showing geometry of ore body and multi-phase development of folds

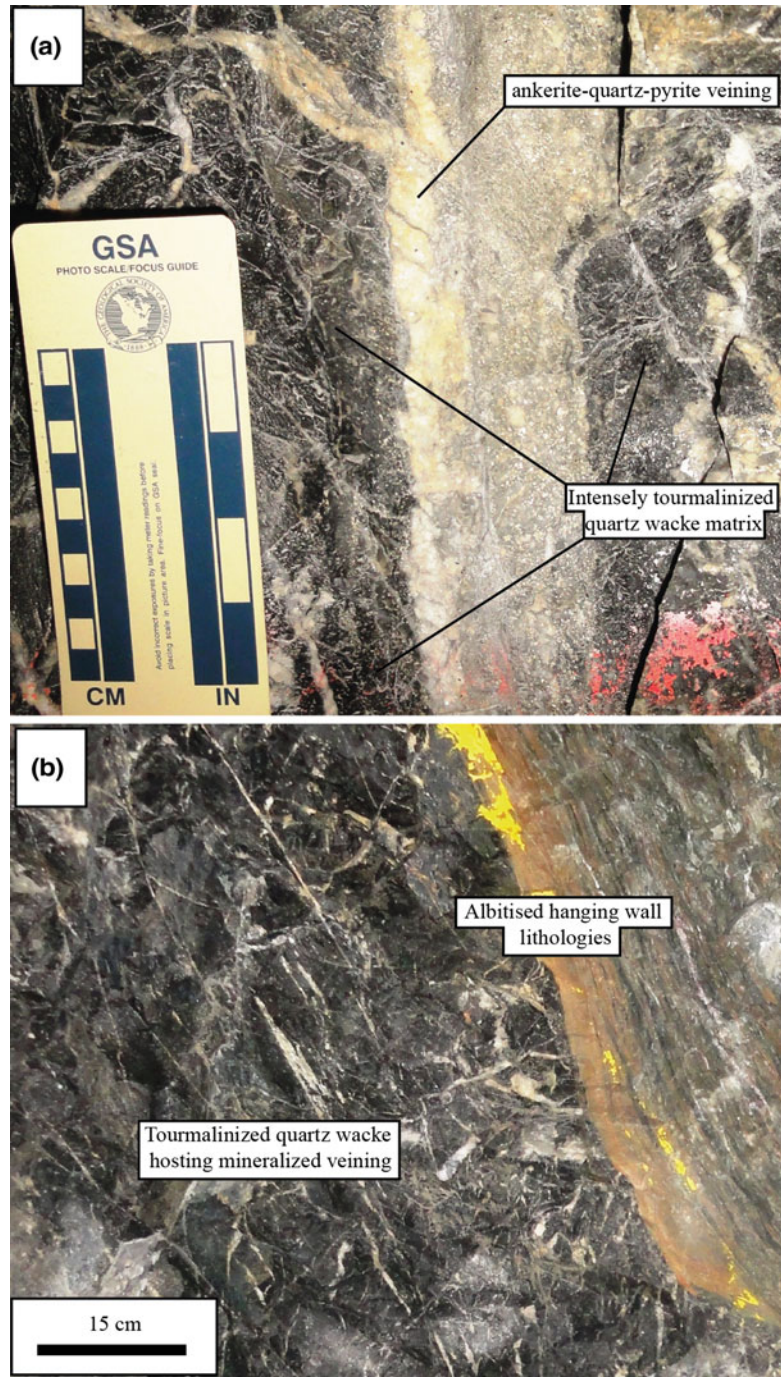

Fig. 6 Photographs of Gara ore showing dark tourmalinite host rocks cut by a stockwork of millimeter- to centimeter-scale quartz-gold-ankerite-pyrite veins

alteration, with an overlapping phase of subordinate tourmaline alteration; (2) magnetite-chlorite ± tourmaline alteration; (3) disseminated sulphide-Au mineralization; (4) replacement by magnetite and Au remobilization; and (5) minor replacement by hematite-sericite-chlorite (Fig. 4c). Ore minerals comprise pyrite and arsenian pyrite (≤ 2 wt% As), accompanied by minor to

trace amounts of chalcopyrite, arsenopyrite, pyrrhotite, tennantite, cobaltite, gersdorffite, scheelite, and monazite. Gold-bearing minerals consist of native gold (fineness > 980) and Au ± Ag tellurides including calaverite ($AuTe_2$), sylvanite (Ag, Au)Te_2, and petzite (Ag_3AuTe_2).

Hanging-wall mineralization at Gounkoto is disseminated within a 20-m-thick dolomitic limestone. These minor ores comprise nickeloan pyrite (max. 13 wt% Ni), Ni-rich cobaltite, clausthalite (PbSe), and chalcopyrite, with lesser galena, sphalerite, and other Ni-bearing sulphides. Gold is texturally associated with all major generations of sulphides.

4.1.4 Fluid Inclusion and Stable Isotope Data

Lawrence et al. (2013b) recently documented the petrography, geothermometry, and chemistry of fluid inclusion assemblages at the Gara and Yalea gold deposits. Four fluid inclusion types are recognized as being coeval with ore formation: (1) $CO_2 \pm N_2 \pm CH_4$ inclusions; (2) low-salinity H_2O–NaCl inclusions (≤ 10 wt% NaCl equiv.); (3) H_2O–CO_2–NaCl $\pm$ N_2 $\pm$ CH_4 inclusions; and (4) multi-phase H_2O–CO_2–NaCl–$FeCl_2$ $\pm$ CH_4 $\pm$ N_2 brines (Fig. 7). Type 4 inclusions contain daughter minerals, including NaCl, $FeCl_2$, Fe_2O_3, Fe_3O_4, and carbonates. All inclusion types are present within the Gara and Gounkoto ore bodies; however, hypersaline fluid inclusions are absent from Yalea.

Stable isotope data (Fouillac et al. 1993; Lawrence et al. 2013b) were used to determine the source of volatile ore-forming components (O, C, and S) at Loulo. Measured $\delta^{18}O_{quartz}$ values are remarkably homogenous (Fig. 8a) both for mineralized samples (+16.3 ± 0.3 ‰; $n = 20$) and barren quartz veins (+15.9 to +17.0 ‰; $n = 4$). Measured $\delta^{18}O_{carbonate}$ values for samples of mineralized veins and wall-rock alteration are more variable (15.9 ± 2.1 ‰; $n = 20$). In contrast, barren calcite veins display $\delta^{18}O$ values of +15.1 to +21.1 ‰ ($n = 5$) (Fig. 8b). Estimated $\delta^{18}O_{fluid}$ compositions for gold-bearing veins at Gara and Yalea range from +9 to +12 ‰. Carbonates associated with mineralization at Loulo show $\delta^{13}C$ values from −21.7 to −4.5 ‰ ($n = 20$) (Fig. 8c); barren calcite veins are isotopically heavier ($\delta^{13}C$ −2.0 to +3.8 ‰; $n = 5$), closely matching the values of the Kofi Series limestones (−2.9 to +1.3 ‰; $n = 6$). Auriferous sulphides display $\delta^{34}S$ values of +5.8 and +15.5 ‰ ($n = 27$) (Fig. 8d). Diagenetic pyrite from wall rock at Yalea has sulphur isotope compositions of +6.4 to +9.0 ‰ ($n = 2$).

4.1.5 Loulo-Gounkoto Ore Genetic Model

Ore bodies within the Loulo-Gounkoto district share many features typical of orogenic gold deposits such as a late-orogenic timing of mineralization, and strong regional and local structural controls on ore formation. Within this framework, Lawrence et al. (2013a, b) detailed two separate end-member styles of orogenic gold mineralization in the region (termed Gara- and Yalea-style) based on different ore and alteration mineralogy, and ore-fluid compositions. The Gara and Gounkoto deposits are characterized by: (1) predominance of pyrite; (2) distinct metal signatures enriched in Fe-REE-W and locally base metals (e.g., Gounkoto hanging-wall mineralization); (3) strong tourmaline alteration atypical of orogenic gold deposits (e.g., Groves et al. 1998); and (4) presence of brines in fluid inclusions. Conversely, Yalea-type deposits (Yalea and satellite ore bodies along the Yalea Trend) have a more typical Birimian orogenic gold ore mineralogy, wall-rock alteration, and ore fluid characteristics (cf. Milési et al. 1992; Allibone et al. 2002a, b; Béziat et al. 2008). These latter ore bodies: (1) are As-rich; (2) lack a REE-base metal enrichment; (3) have alteration assemblages dominated by quartz-carbonate-albite and sericite-chlorite (tourmaline-absent); and (4) lack brines in fluid inclusions.

Lawrence et al. (2013b) interpreted the various fluid inclusion assemblages as representing two distinct end-member fluids: (1) a high-temperature, high-salinity, CO_2-poor, aqueous fluid (~400 °C; ~45–55 wt% NaCl equiv.; X_{H2O} of 0.7–0.8; $X_{CO2} < 0.3$); and (2) a lower temperature, more dilute, aqueous-carbonic fluid (270–350 °C; <10 wt% NaCl equiv.). Partial mixing between these fluids

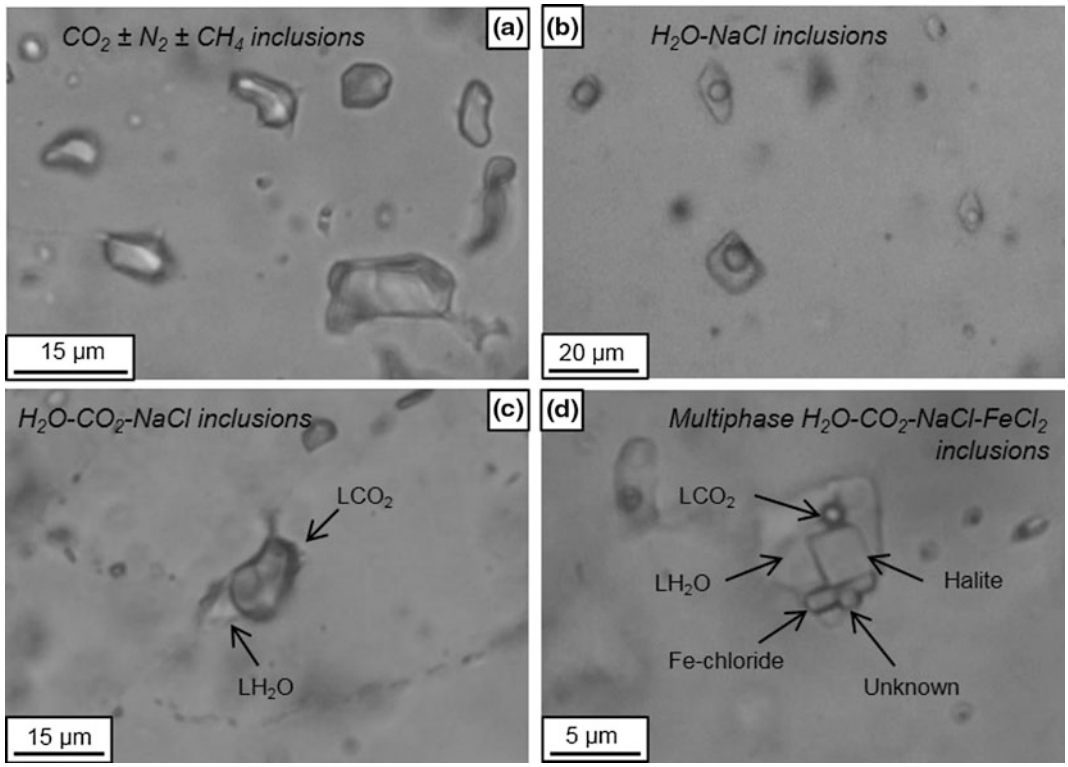

Fig. 7 Photomicrographs (taken at room temperature) of fluid inclusion types present in mineralized samples from Loulo district. **a** Single phase $CO_2 \pm N_2 \pm CH_4$ inclusions, **b** two-phase H_2O–NaCl inclusions, **c** rare H_2O–CO_2–NaCl inclusions, and **d** multi-phase, hyper-saline, H_2O–CO_2 inclusions with halite and Fe-chloride daughter minerals. *L* liquid phase; *V* vapor phase

during formation of the Gara-style ore bodies resulted in retrograde boiling ("salting out effect"; e.g., Anderson et al. 1992) and changes in the physicochemical state of both fluids, leading to precipitation of sulphide minerals and Au. At Yalea, the hypersaline fluid is absent and fluid inclusions contain two immiscible phases derived from the phase separation of a dilute, aqueous-carbonic fluid. Fluid immiscibility likely occurred in response to pressure-temperature fluctuations along the Yalea Shear and/or fluid-rock interaction with the hanging-wall carbonaceous limestone cap. The combination of microthermometric data and geothermometry based on ore and alteration assemblages indicates that mineralization occurred at mesozonal temperatures and pressures of 270–340 °C at 1.4–1.8 kbar (5.5–6 km) (Lawrence et al. 2013b).

The presence of a dilute aqueous-carbonic hydrothermal fluid is consistent with a metamorphic source for this fluid (e.g., Phillips and Powell 2010). Supporting evidence comes from stable isotope (O, C, and S) data that suggest devolatilization of a sedimentary sequence. Oxygen isotope values show $\delta^{18}O_{fluid}$ compositions between +9 to +12 ‰ that are similar to those of metamorphic fluids (cf. Ohmoto and Goldhaber 1997). Carbon isotope data for auriferous veins and hydrothermal alteration at Loulo fall on a tie line between ^{13}C-depleted organic carbon (−24.7 ± 6 ‰; Schidlowski et al. 1983) and inorganic carbonate minerals occurring in the host limestone (−2.9 to +1.3 ‰). On this basis, CO_2 is likely to have been sourced directly by the dissolution of carbonate-rich units in the host terrane during pro-grade metamorphism, and indirectly by fluid-rock interactions at the site of

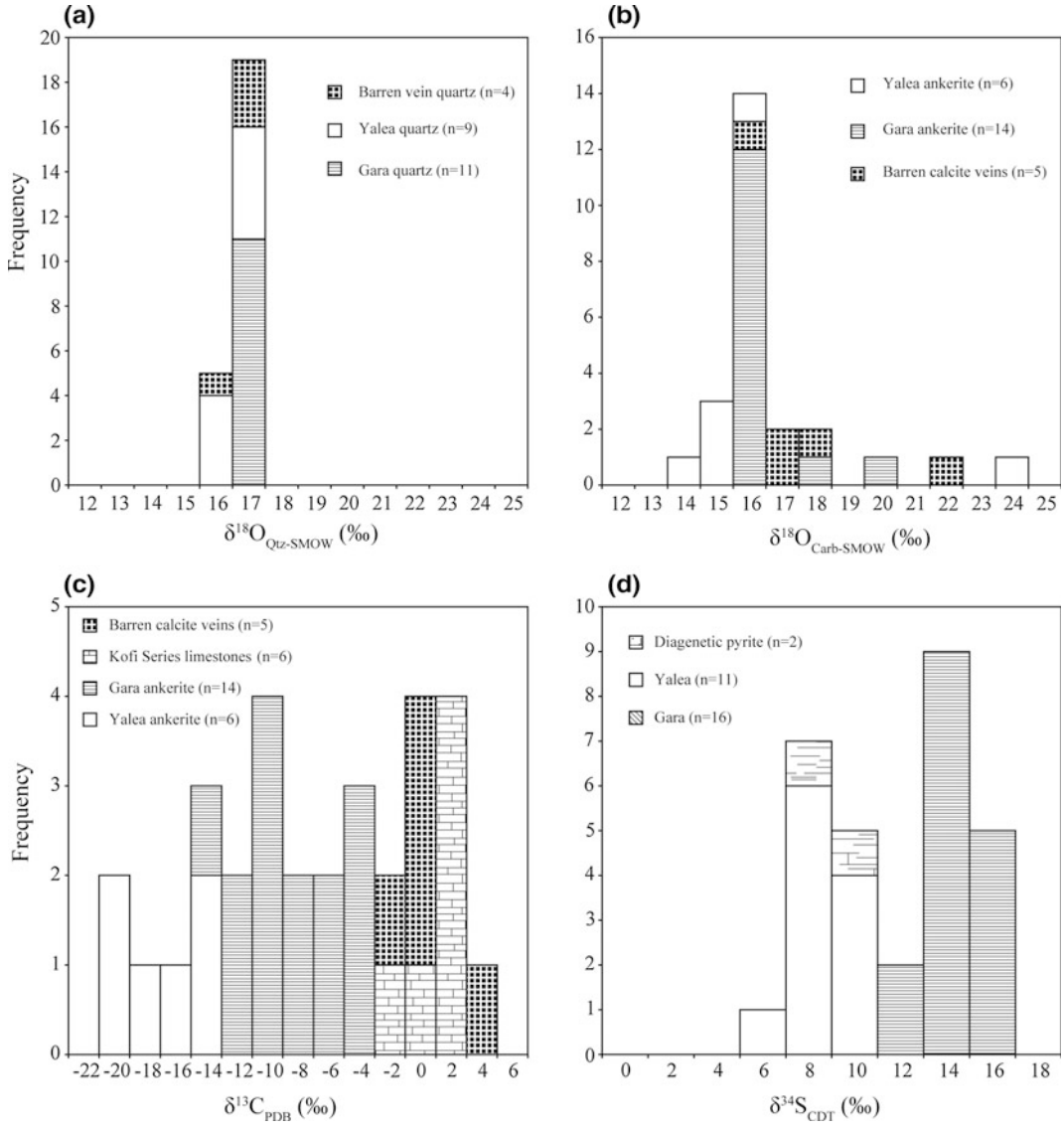

Fig. 8 Histograms showing $\delta^{18}O_{silicate}$, $\delta^{18}O_{carbonate}$, $\delta^{13}C_{carbonate}$, and $\delta^{34}S_{sulphide}$ stable isotope data for mineralized and non-mineralized rocks at Yalea and Gara (data compiled from Fouillac et al. 1993; Lawrence et al. 2013b; Lambert-Smith 2014)

ore formation. The $\delta^{34}S$ values of the ore sulphides (+5.8 to +15.5 ‰) broadly match limited $\delta^{34}S$ data for diagenetic pyrite in the Kofi Series (+6.4 to +9.0 ‰); this pattern suggests that sulphur was derived by the devolatilization of diagenetic pyrite in the host sedimentary terrane (cf. Tomkins 2010; Large et al. 2011; Gaboury 2013).

The hypersaline, aqueous-rich fluid inclusions present in the Gara-style deposits, together with the metal associations and intense tourmaline alteration, suggest that a magmatic fluid contributed to the Loulo ore-forming system (Lawrence et al. 2013a, b). However, the lack of a magmatic signature in the stable isotope dataset allows for a possible alternative fluid

origin in which brines were sourced from B-rich evaporite units within the Kofi Series. In this model, mixing of hypersaline fluids with regional, low-salinity, aqueous-carbonic metamorphic fluids led to the formation of atypical (Gara-style), tourmaline-rich, orogenic gold deposits in the Loulo district.

4.2 Sadiola

The Sadiola deposit is 120 km north of the Loulo-Gounkoto complex, in the northern part of the Kédougou-Kéniéba inlier (KKI) (Fig. 1c). The mine was officially opened in 1996 (and together with Yatela) is owned by Société des Mines d'Or du Mali (SEMOS), a joint venture between AngloGold Ashanti Limited, IAMGOLD Corporation, and the Malian government. Current probable reserves at Sadiola are 3.8 Moz of Au at an average grade of 2.1 g/t (IAMGOLD Corporation 2014).

4.2.1 Deposit Geology and Structure

The Kofi stratigraphy at Sadiola consists of a thick (>250 m) limestone-marl sequence that strikes N-S to NNW and dips 60–65° to the west, and is overlain by a hanging-wall unit composed of sandstone with interbedded siltstone and mudstone (Figs. 9 and 10). The contact between the two lithologic domains is structurally controlled by the mineralized brittle-ductile Sadiola Fracture Zone (SFZ), a splay off the Senegal-Mali Shear Zone (SMS). The SFZ is 10–50 m wide and consists of an anastomosing network of fractures and shears. Sedimentary rocks exposed in the Sadiola Hill open pit are cut by three successive generations of intrusions (Fig. 9), which include: (1) early diorite stocks, discontinuous dikes and sills, which were emplaced parallel to sub-parallel to bedding at the contact between carbonate and siliciclastic units; (2) sub-vertical, narrow (<5 m), NNE-trending, quartz-feldspar-phyric granodiorite dikes; and (3) a series of 1–2-m-wide, ENE-trending, dolerite dikes that cut the granodiorite dikes.

The Sadiola structural model proposed by Masurel et al. (in press) is similar to that outlined previously for the Loulo-Gounkoto district. Three main deformation events have been recorded. The first phase of deformation (D1) is associated with NNW-trending recumbent folding (F1) and the development of sub-horizontal, hinge-parallel, lineation. This event remains poorly constrained owing to poor exposure and reworking during later deformation. D2 deformation is linked to upright to inclined F2 folds that plunge gently (15–30°) to the SSW and have an axial-planar cleavage of 020°/75° E. NNE-trending thrusts, high-angle reverse faults, and quartz-feldspar-phyric dikes are spatially closely associated with these F2 folds. The N-S-trending SFZ is interpreted to have been initiated as a sinistral reverse fault during the latter part of D2.

D3 marks a switch from predominantly pure shear (folding and reverse faulting with minor strike-slip displacement during D2) to a simple-shear system. Fault geometries and kinematic indicators are consistent with NNW-SSE-directed shortening. Evidence for sinistral strike-slip movement is present in wall-rock limestones in close proximity to the SFZ, with steeply plunging parasitic folds showing pronounced S-shaped asymmetry. Mapping in the open pit has identified the occurrence of drag folds within the main structure, correlating with F2 folds and re-oriented along a N-S axis. Minor post-D3 brittle deformation is also present including late extensional quartz veins <30 cm wide and sub-vertical brittle faults 10 cm to >10 m in width (Fig. 9).

Structural data suggest that gold mineralization is confined to a single deformation event (D3) (Masurel et al. in press). The bulk of the ore is hosted within the SFZ and the deformed limestones in the adjacent footwall. Ore also occurs along the reactivated NNE-trending faults, although grades decrease with increasing distance from the SFZ. Mineralization is mainly present as zones of disseminated sulphides; minor sulphide veinlets and quartz-carbonate-sulphide ± biotite-tourmaline veins occur locally. A range of ductile to brittle ore textures are observed. Ductile shearing within the SFZ is commonly associated with gold grades of >10 g/t. Ductile textures are best observed in diorite dikes where fine-grained sulphides are consistently

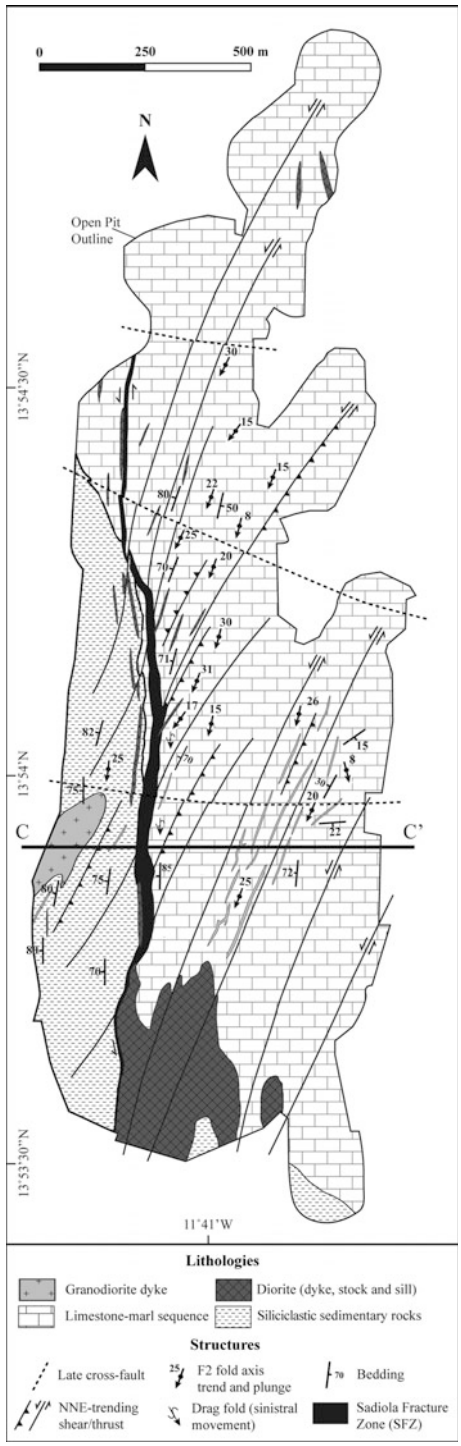

Fig. 9 Geological and structural map of Sadiola open pit (modified from Masurel et al. in press). Gold mineralization is largely confined to the Sadiola Fracture Zone. Cross section C–C′ is shown in Fig. 10

aligned parallel to the shear fabric. Brittle textures are well developed in the footwall limestones, characterized by randomly oriented dolomite stockworks and crackle breccias commonly sealed by sulphides. These hydrothermal-tectonic breccias form wide zones of low to medium grade mineralization (ca. 1 to 3 g/t Au).

4.2.2 Alteration and Mineralization

Masurel et al. (in press) reported a polyphase hydrothermal alteration history for the Sadiola deposit that involves an early calc-silicate phase followed by a potassic alteration stage (Fig. 11). The early high-temperature alteration is confined mainly to Ca-rich host rocks (limestone and mafic-intermediate dikes) and is represented by porphyroblastic actinolite and tremolite. This style of alteration is strongly developed within the SFZ and to a lesser extent along the NNE-trending faults. The calc-silicate alteration phase is overprinted by a later, syn-mineralization, potassic alteration stage, which contains a mineral assemblage dominated by biotite-(phlogopite), calcite-dolomite, and quartz, plus minor tourmaline (dravite), sericite, and microcline. The last stage of hydrothermal alteration recognized at Sadiola is associated with D5 normal reactivation of ore-hosting structures and the formation of numerous chlorite-calcite pyrite veins.

Ore sulphides related to the potassic alteration stage commonly form concentrations of 0.5 to 3 vol%. Paragenetic studies indicate a multi-stage ore development consisting of an early arsenopyrite-rich Au phase (Stage 1), and later Sb ± Au phases (Stages 2–3) (Fig. 11). Stage 2 comprises pyrrhotite + berthierite ($FeSb_2S_4$) + stibnite + native gold + aurostibite, whereas Stage 3 is characterized by native Sb + native Bi + Sb–Ni–Pb sulphosalts (e.g., gudmundite, ullmannite, jamesonite).

4.2.3 Sadiola Ore Genetic Model

Orogenic gold mineralization at Sadiola shows similar regional and local structural controls to that observed along the southern part of the Senegal-Mali Shear Zone (SMS). However in contrast to Loulo, ore and wall-rock alteration assemblages at Sadiola show distinctive features

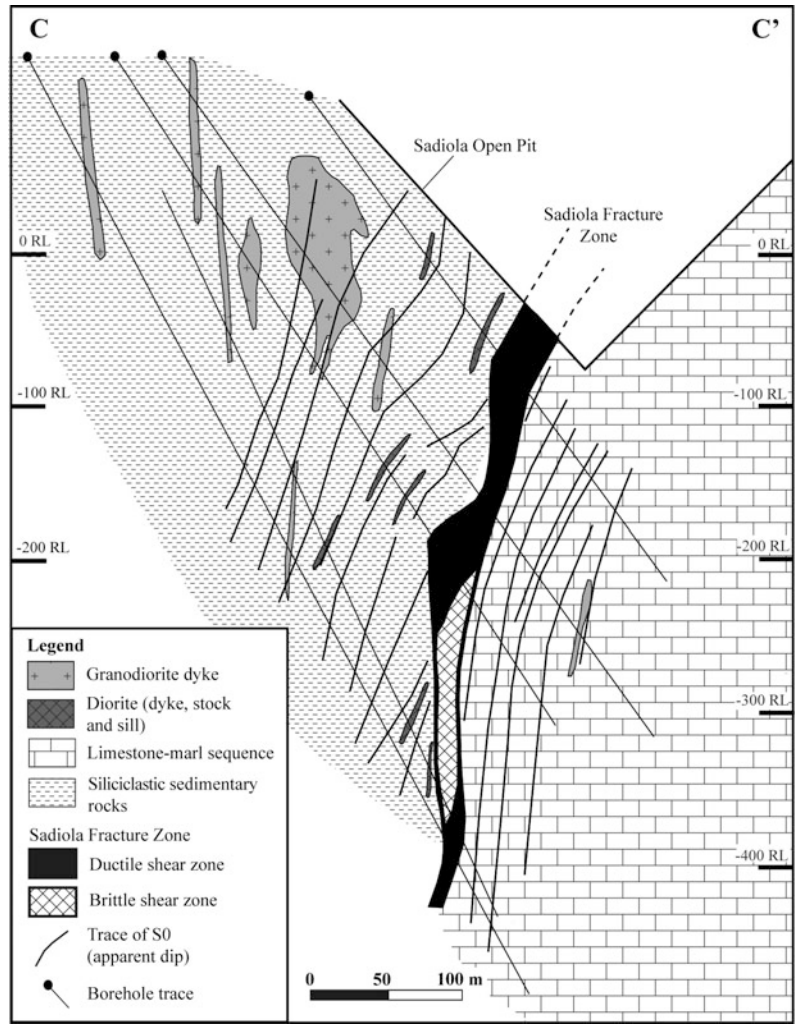

Fig. 10 Cross section through southern part of Sadiola ore body (cross section C–C′ on Fig. 9) showing geometry of Sadiola Fracture Zone (modified from Masurel et al. in press)

such as early high-temperature calc-silicate alteration, and later Au–Sb–Te–Bi mineralization typical of low temperature, epizonal (<6 km) orogenic gold deposits (cf. Groves et al. 1998). Combined field, mineralogical, geothermometric, and micro-textural data suggest that the multi-phase ore and alteration development at Sadiola reflects a hydrothermal cooling continuum in the temperature range of 400 to 260 °C, rather than representing contrasting mineralization styles at distinct crustal levels (Masurel et al. in press). Although rare, calc-silicate alteration has been reported in some amphibolite-hosted Precambrian orogenic gold deposits (McCuaig et al. 1993; Smith 1996), where the temperature of the mineralizing fluid was high enough to stabilize calc-silicate minerals in Ca-rich host rocks (McCuaig and Kerrich 1998). In contrast, the early ore and alteration paragenesis at Sadiola is in thermal disequilibrium with the greenschist-facies metamorphosed host rocks, hence the thermal gradient likely reflects the input of D3 Eburnean magmatism and related hydrothermal circulation in the region (Masurel et al. in press).

The Massawa orogenic gold deposit, located along the western (Senegalese) side of the Kédougou-Kéniéba inlier 80 km to the southwest of Sadiola, shares a similar deposit paragenesis albeit with the absence of calc-silicate alteration.

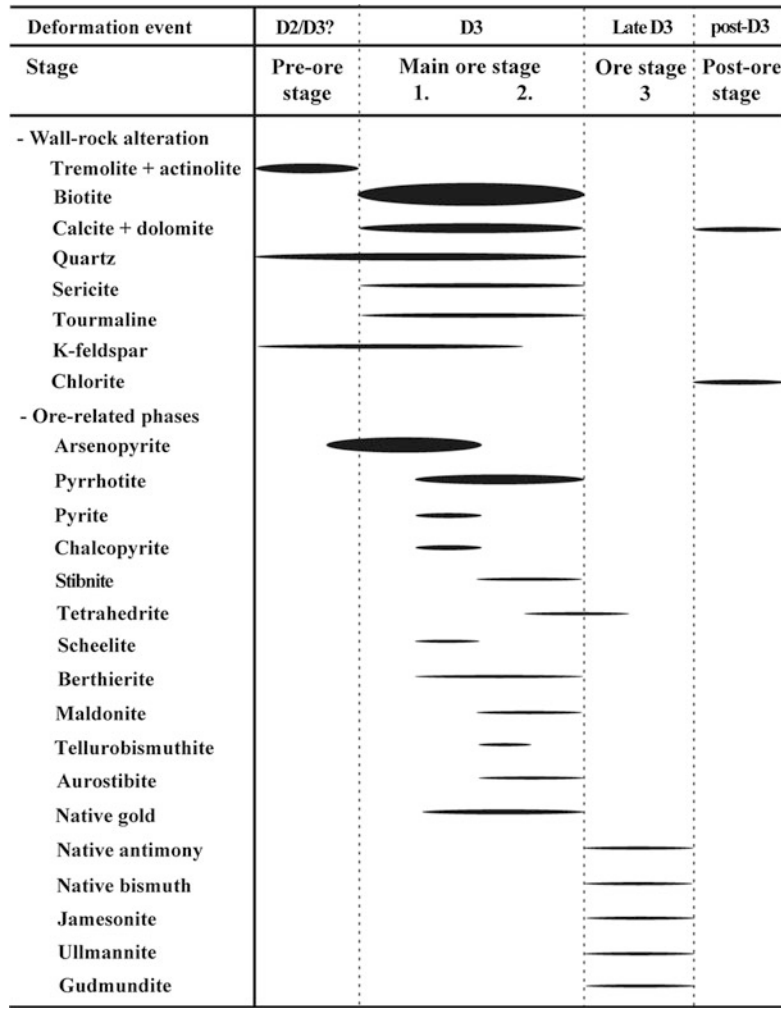

Fig. 11 Paragenesis of ore and alteration zones for the Sadiola deposit (modified from Masurel et al. in press)

The Massawa deposit is characterized by predominantly brittle deformation, widespread potassic alteration (mainly sericite) synchronous with disseminated arsenopyrite-pyrite mineralization, and a second phase of high-grade quartz-stibnite veins with coarse visible gold (Treloar et al. 2014a). Combined field relationships, fluid inclusion data, and stable isotope values suggest a magmatic fluid influence on gold mineralization in Massawa deposit, with ore formation occurring at epizonal depths (4–6 km) with a temperature-pressure range of 220–315 °C at 1–1.65 kbar (Treloar et al. 2014a).

4.3 Yatela

The Yatela gold mine is 25 km north of Sadiola, 50 km SSW of the regional capital of Kayes. Production began in 2001 by Société des Mines d'Or du Mali (SEMOS). The deposit geology comprises a Kofi limestone-marl package intruded by a dioritic pluton, both units being overlain by Upper Proterozoic Seroukoto sandstone of the Taoudeni basin. Primary gold mineralization is hosted in shear zones and localized along the lithologic contact between the limestone and diorite; spatially associated is disseminated pyrite

and an alteration assemblage of albite, sericite, and dolomite. Significantly, economic gold mineralization is supergene in origin and linked to karstic dissolution of the Kofi limestone (Hanssen et al. 2004). The weathering profile is characterized by deep troughs (maximum of 220 m) above the limestone, with infill sequences consisting of a basal unit composed of unconsolidated ferruginous, sandy, and locally clayey material, overlain by pisolithic gravels, laterite rubble, and fine-grained sands. The basal ferruginous layer represents the gold-enriched dissolution residue of the mineralized carbonate protolith (Hanssen et al. 2004).

5 Reduced Intrusion-Related Gold Systems

5.1 Morila

The multi-million ounce, world-class, Morila gold deposit is in southern Mali, 180 km south of Bamako and close to the town of Sanso (Fig. 1b). The mine has produced more than 7 Moz of gold at ~4.6 g/t since commissioning in 2000, and is predicted to produce a further estimated 267 Koz at 0.66 g/t from open pit extensions and stockpiles over the next few years (Randgold Resources Ltd 2014). Early exploration carried out by BUGECO in 1987 identified several large gold anomalies in soils. In 1992, BHP Minerals Mali acquired the rights to the area and carried out initial exploration drilling. Although this work returned encouraging results, BHP ceased exploration in Mali in 1996. Randgold Resources acquired BHP Minerals Mali and commenced detailed exploration of the Morila permit, which led to the discovery of the Morila deposit. In 2000, AngloGold Ashanti purchased 40 % of Morila with Randgold Resources retaining 40 % and the Government of Mali 20 %.

5.2 Deposit Geology and Structure

The Morila deposit is located within the Bougouni terrane that is characterized by a volcano-sedimentary sequence intruded by large granitoid batholiths and numerous smaller mafic to felsic bodies (Liégeois et al. 1991) (Fig. 1b). Deposit geology is characterized by a NW-trending package of turbiditic metasedimentary rocks bounded to the east and northeast by the Massigui Granite and to the southwest by the Doubalaokoro tonalite-trondjhemite-granite (TTG) suite (Fig. 12). The metasedimentary rocks comprise a 1-km-thick monotonous sequence of medium- to coarse-grained, moderately to poorly sorted, biotite-rich, feldspathic wacke. Subtle lithologic variations occur locally with interbeds composed of finer-grained meta-pelitic rocks and meta-basalts. Within the siliciclastic rocks, beds have sharp bases, grade upwards, and show pronounced soft-sediment deformation features typical of turbidite systems such as flame structures and load clasts (McFarlane et al. 2011). Sedimentary rocks in the vicinity of Morila have contact metamorphic assemblages typical of amphibolite-facies conditions, including abundant hornblende in the meta-basalts and cordierite and andalusite preserved in the more pelitic rocks.

Several intrusions are emplaced into the meta-sedimentary sequence of the Morila permit area (McFarlane et al. 2011). The oldest of these are thin (5–10 m), porphyritic mafic to intermediate-composition hypabyssal dikes for which geochemical data suggest a continental margin setting. These rocks are pre-orogenic and have U–Pb zircon ages of 2132 ± 4 to 2131 ± 5 Ma. Younger and more felsic, sub-alkaline, D2 intrusive bodies are represented by the Morila Tonalite (including quartz diorite) and the Doubalakorou suite of fine- to medium-grained biotite-rich granodiorite and coarser, foliated monzogranite; these intrusions yield U-Pb zircon crystallization ages of 2098 ± 4 to 2091 ± 4 Ma, respectively. Hornblende and cordierite-andalusite hornfels are concentrated around these D2 intrusive rocks. The Morila tonalite and Doubalakorou felsic rocks are post-dated (2075 ± 12 Ma; Armstrong 2003) by the Massigui leucogranite (post-D2 origin; D3?).

The Morila gold deposit is a flat-lying tabular body that dips gently to the east (0–30°) and

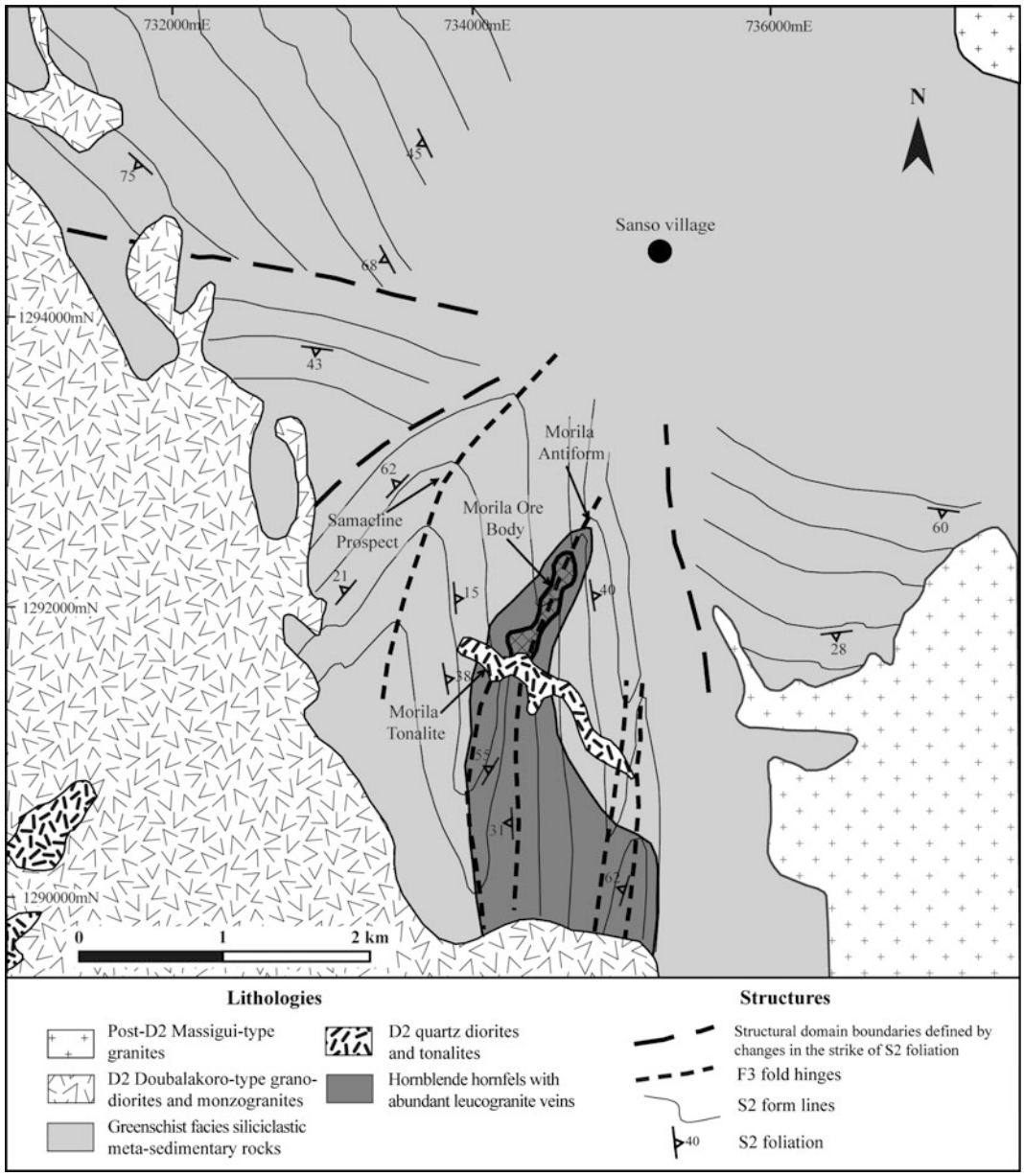

Fig. 12 Geological and structural map of Morila district. Main deposit and nearby Samacline prospect to northwest are located in hinge zones of upright F3 folds within domains of gently dipping S2 foliation. Hornblende-hornfels contact metamorphism is present in vicinity of Morila ore body, which extends southward towards Doubalakoro pluton (modified from King 2012)

varies in thickness from 25–160 m, with thicknesses increasing to the south and west close to contact with the Morila Tonalite (Fig. 13). A sub-parallel lode (Samocline prospect) is intersected at depth below the main deposit. The main ore body is truncated on its northern side by a steep fault (exposed on the northern wall of the Morila open pit) that is downthrown to the north. Displacement along this fault is likely to be significant because metasedimentary rocks to the

north show lower (greenschist facies) metamorphic grades and deep drilling has failed to intersect significant mineralization north of the fault. McFarlane et al. (2011) identified two stages of folding associated with D2 and post-D2 deformation: (1) recumbent F2 isoclinal folds that developed in a fold and thrust belt, accompanied by a strong S2 schistosity; and (2) more widespread, upright, open F3 N- to NNE-trending folds (Fig. 13). High-grade gold mineralization at Morila (avg grade > 10 g/t) is concentrated along the fold hinge of an F3 fold, known locally as the Morila antiform.

5.3 Alteration and Mineralization

King (2012) reported two main phases of hydrothermal alteration and associated gold mineralization at Morila. This interpretation is generally consistent with the results of both McFarlane et al. (2011) and Hammond et al. (2011), and builds on data presented by Quick (1999) (Fig. 14). Pervasive biotitization is synchronous with the penetrative S2 schistosity, and is spatially associated with millimeter- to centimetre-scale polymetallic (Au–Sb–Bi–Te) quartz veins having varying concentrations of hornblende, biotite, plagioclase, and fluorapatite. Sulphide assemblages consist of löllingite, pyrrhotite, and chalcopyrite. Free native gold (avg 940 fineness) is associated with scheelite, native bismuth, maldonite (Au_2Bi), aurostibite ($AuSb_2$), and tellurobismuthite (Bi_2Te_3). Au–Sb–Bi–Te mineralization is spatially and temporally associated with metasomatic zones that surround D2 granodiorite and quartz diorite intrusive stocks and associated dikes.

Following stage 1 mineralization, the Morila host rocks were pervasively albitized and sulphidized during post-D2 mineralization. This phase of gold mineralization is largely confined to the NE-trending fold hinge of the F3 Morila antiform, where gold was remobilized into high-grade ore shoots. Coarse-grained idioblastic arsenopyrite, which cuts earlier deformation

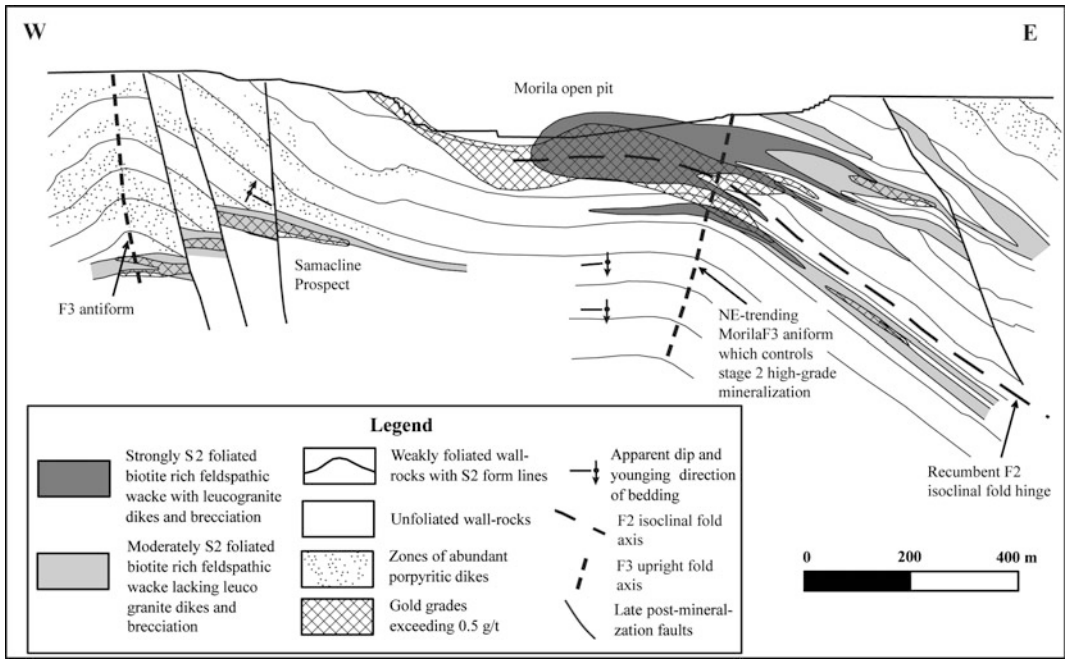

Fig. 13 Typical E-W cross section through the Morila deposit showing geometry of the ore body and multi-phase folds (modified from McFarlane et al. 2011)

fabrics, contains partially resorbed cores of löllingite with blebs of native gold (5–25 μm; fineness of 850) located along mineral boundaries. McFarlane et al. (2011) dated titanite associated with arsenopyrite that yielded a preliminary age for late-stage sulphidation of 2074 ± 14 Ma, which brackets mineralization as a whole to the interval 2098 ± 4 to 2074 ± 14 Ma. McFarlane et al. (2011) also identified a minor late vein stage containing chlorite-pyrite-quartz or quartz-plagioclase-apatite-tourmaline ± molybdenite ± beryl, accompanied by alteration selvages of cordierite, biotite, chlorite, and plagioclase.

5.4 Fluid Inclusion and Stable Isotope Data

Fluid inclusion and stable isotope investigations at Morila have been carried out by Quick (1999) and Hammond et al. (2011). Both studies identified similar fluid inclusion assemblages for both phases of mineralization. Two end-member fluids are distinguished, one a H_2O–NaCl ± N_2 ± CH_4 fluid characterized by high-temperatures (250–400 °C) and low to moderate salinities (0.5–8.0 wt % NaCl equivalent), and another a $CaCl_2$-bearing brine with low temperatures (100–200 °C) and higher salinities (20–32 wt% NaCl equivalent).

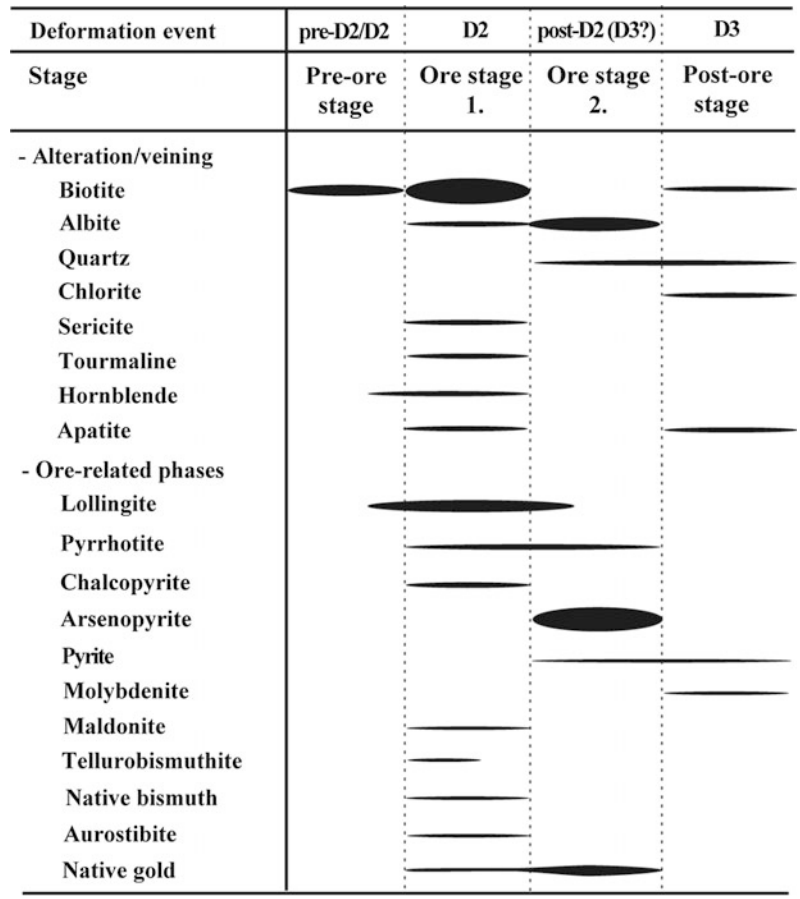

Fig. 14 Paragenesis of ore and alteration zones for the Morila deposit (data from McFarlane et al. 2011; King 2012)

Oxygen isotope data reported by Hammond et al. (2011) from quartz-biotite pairs indicate average $\delta^{18}O_{fluid}$ values of 9.8 ± 0.3 ‰ and 10.9 ± 0.3 ‰ for fluids that flowed through unmineralized and mineralized host rocks, respectively. Sulphur isotope data of Quick (1999) and Treloar et al. (2014b) show a unimodal distribution of $\delta^{34}S$ values between 2 and 5 ‰ for auriferous arsenopyrite from stage 2 mineralization.

5.5 Morila Ore Genetic Model

Morila is characterized by several features that are inconsistent with a conventional orogenic gold classification for the Birimian deposits. These include: (1) the sub-horizontal strata-bound ore geometry, which contrasts with the steeply dipping, tabular morphology typical of shear-hosted orogenic gold deposits (cf. Groves et al. 1998; Ridley and Diamond 2000); (2) the syn-metamorphic timing of gold mineralization (orogenic gold mineralization generally forms during post-peak metamorphism; Groves et al. 2000); and (3) the moderate salinity of the ore fluids, which is distinctly different from the low salinities (<10 wt% NaCl equiv.) and CO_2-rich nature of fluids that formed many Birimian gold deposits (excluding Gara) (e.g., Klemd et al. 1996; Schmidt Mumm et al. 1997).

The strata-bound geometry of the ore body appears to be lithologically controlled. Hammond et al. (2011) and McFarlane et al. (2011) reported higher Mg/(Mg + Fe) ratios in biotite and an increase in chalcophile elements (Cu, Ni, and Zn) in mineralized rocks compared to the immediate footwall and hanging-wall rocks, as well significantly elevated Cr contents in the ore zone from background levels of ~175 ppm to >300 ppm. Hammond et al. (2011) also noted decreases in the anorthite content of plagioclase from wall rocks to the mineralized zone ($An_{51–53}$ to An_{40}, respectively). McFarlane et al. (2011) postulated that mineralization is confined to deformed basaltic volcanic rocks. Although this model is inconsistent with the entire data set, the chemistry is in agreement with tuffaceous fallout from distal basaltic volcanic eruptions, which would have influenced the trace element chemistry of the host feldspathic wackes. Mafic tuffs will hydrate to smectite that is rheologically weak and thus will be more prone to slip during regional deformation, compared to lithologically different rocks above and below. In our interpretation, access to mineralizing fluids was thus preferentially concentrated along these rheologically weak, smectite-rich zones.

According to this model, stage 1 mineralization must have been initiated prior to contact metamorphism. This scenario is consistent with oxygen isotope geothermometry from Hammond et al. (2011), which shows an overlap in temperature estimates between unmineralized and mineralized rocks. The relative timing of metamorphism and stage 2 arsenopyrite mineralization remains enigmatic, however. McFarlane et al. (2011) dated late sulphidation at 2074 ± 14 Ma (U–Pb SHRIMP dating of tittanite), synchronous with emplacement of the post-D2 Massigui plutonic suite, with gold being remobilized into NE-plunging ore shoots as the tabular ore body was re-folded by F3 folds. If metamorphism predated stage 2 mineralization, as suggested by McFarlane et al. (2011), then equilibrium textures within the hornfelsic rocks necessarily would have been deformed during post-D2 folding in order to open grain boundary fractures to permit sufficient fluid access for gold dissolution and remobilization. In summary, the Morila model consists of Au–Sb–Bi–(W–Te) stage 1 mineralization, focussed by shearing along smectite-enhanced bedding surfaces, which produced the main tabular ore body. This mineralization was followed shortly by D2 hornfelsing and then development of stage 2 As–Au mineralization during post-D2 folding.

Fluid inclusion and isotopic compositions from both phases of mineralization suggest that the observed fluid inclusion assemblages formed by phase separation of a $NaCl–CaCl_2–H_2O–N_2–CH_4$ ore fluid of intermediate salinity (12–16 wt% NaCl equiv.). Oxygen isotope geothermometry from co-existing quartz-biotite pairs indicates a deep-seated fluid source with mineralization temperatures of 400–450 °C (Hammond et al. 2011).

Despite similar $\delta^{18}O_{fluid}$ ranges to that reported at Loulo (Lawrence et al. 2013a), Hammond et al. (2011) proposed a magmatic fluid source for gold mineralization at Morila. This interpretation is consistent with the ore genetic model established by McFarlane et al. (2011), which involves a reduced intrusion-related gold system (RIRGS) of gold mineralization at Morila. Using criteria set out by Hart (2007), Morila shows typical RIRGS characteristics, such as: (1) temporal and genetic association with reduced intrusive stocks and dikes that share geochemical and isotopic characteristics of magmatic processes suggested to enhance metal fertility in RIRGS (Sillitoe and Thompson 1998; Lang and Baker 2001); (2) deposition of native gold and rare tellurobisthmuthite in contact metasomatic zones; (3) the metal association of Au–As–Sb–Bi–(W–Te); and (4) hydrothermal alteration that includes albitization and K-metasomatism.

6 Conclusions

Gold deposits within the West Mali gold belt show many features typical of orogenic gold mineralization, such as geological setting, late-orogenic timing, structural paragenesis, and deposit geometry (cf. Groves et al. 1998; Ridley and Diamond 2000). However, ore fluid compositions, as well as mineralization and alteration assemblages, are highly variable along the belt and distinct sub-classes of orogenic gold mineralization are present (Lawrence et al. 2013a). Recent studies (Lawrence et al. 2013b; Lambert-Smith 2014; Masurel et al. in press) have shown that this variability is caused by multiple fluid sources within the Kofi Series (magmatic fluids, evaporite brines, and regional metamorphic fluids). Supergene enrichment of the orogenic gold lodes is economically important in the northern parts of the Gold Belt, involving karstification of mineralized limestones (Hanssen et al. 2004).

Recent studies at the Morila gold deposit, in the Mali South Goldfields, imply a more diverse Birimian gold metallogenesis. McFarlane et al. (2011) classified Morila as a reduced intrusion-related gold system, in which strata-bound gold mineralization formed early in the Eburnean orogenic cycle (syn-metamorphic) with spatial and genetic links to quartz-diorite, granodiorite, leucogranite, and apophyses of the D2 Doubalakoro pluton.

References

Allibone A, Teasdale J, Cameron G, Etheridge M, Uttley P, Soboh A, Appiah-Kubi J, Adanu A, Arthur R, Mamphey J, Odoom B, Zuta J, Tsikata A, Pataye F, Famiyeh S (2002a) Timing and structural controls on gold mineralization at the Bogoso gold mine, Ghana, West Africa. Econ Geol 97:949–969

Allibone A, McCuaig TC, Harris D, Etheridge M, Munroe S, Byrne D, Ammanor J, Gyapong W (2002b) Structural controls on gold mineralization at the Ashanti deposit, Obuasi, Ghana. Soc Econ Geologists Spec Publ 9:65–92

Anderson MR, Rankin AH, Spiro B (1992) Fluid mixing in the generation of mesothermal gold mineralisation in the Transvaal Sequence, Transvaal, South Africa. Eur J Mineral 4:933–948

Armstrong RA (2003) A geochronological investigation of the Morila gold mine, Mali. Canberra, Australian National Univ Research School Earth Sci, Precise Radiogenic Isotope Services (PRISE), p 25

Bassot JP, Dommanget A (1986) Mise en évidence d'un accident majeur affectant le Protérozoïque inférieur des confins sénégalo-maliens. Comptes Rendus Acad Sciences 302:1101–1106

Berge J (2011) Paleoproterozoic, turbidite-hosted, gold deposits of the Ashanti gold belt (Ghana, West Africa): comparative analysis of turbidite-hosted gold deposits and an updated genetic model. Ore Geol Rev 39:91–100

Béziat D, Dubois M, Debat P, Nikiéma S, Salvi S, Tollon F (2008) Gold metallogeny in the Birimian craton of Burkina Faso (West Africa). J African Earth Sci 50:215–233

Bierlein FP, Crowe DE (2000) Phanerzoic orogenic lode gold deposits. Rev Econ Geol 13:103–139

Boher M, Abouchami W, Michard A, Albarede F, Arndt NT (1992) Crustal growth in West Africa at 2.1 Ga. J Geophys Res 97(B):345–369

Boltrukevitch BN (1973) Notice explicative sur la carte des gisements et indices aurifères de la République du Mali. Unpubl Rep, SONAREM, Kati

Brooner G, Chauvel JJ, Trilboulet C (1990) Geochemistry and knowledge of banded-iron formations in the West African shield, an example. In: Chauvel JJ, Yuqi CH, El Shazly EM, Gross GA, Laajoki K, Markov MS, Rai KL, Stulchikov VA, Augusthithis SS

(eds) Ancient banded iron-formations (regional presentations). Theophrastus, Athens, p 462

Coulibaly Y, Boiron MC, Cathelineau M, Kouamelan AN (2008) Fluid immiscibility and gold deposition in the Birimian quartz veins of the Angovia deposit (Yaouré, Ivory Coast). J African Earth Sci 50:234–254

Diarra H, Holliday J (2014) Deep potential starts to emerge: new projects in Mali highlight deeper potential of Birimian belt. Mining Jour Nov 2014, 19–21

Dommanget A, Milési JP, Diallo M (1993) The Loulo gold and tourmaline-bearing deposit. Mineral Deposita 28:253–263

Feybesse J, Billa M, Guerrot C, Duguey E, Lescuyer J, Milési JP, Bouchot V (2006) The Paleoproterozoic Ghanaian province: geodynamic model and ore controls, including regional stress modelling. Precam Res 149:149–196

Fouillac AM, Dommanget A, Milési JP (1993) A carbon, oxygen, hydrogen and sulfur isotopic study of the gold mineralization at Loulo, Mali. Chem Geol 106:47–62

Gaboury D (2013) Does gold in orogenic deposits come from pyrite in deeply buried carbon-rich sediments? Insight from volatiles in fluid inclusions. Geology 41:1207–1210

Groves DI, Barley ME, Barnicoat AC, CassidY KF, Fare RJ, Hagemann SG, Ho SE, Hronsky JMA, Mikucki EJ, Mueller AG, McNaughton NJ, Perring CS, Ridley JR, Vearncombe JR (1992) Sub-greenschist to granulite-hosted Archean lode-gold deposits of the Yilgarn craton: a depositional continuum from deep sourced hydrothermal fluids in crustal-scale plumbing systems. Univer Western Australia Spec Publ 22:325–338

Groves DI, Goldfarb RJ, Gebre-Mariam M, Hagemann SG, Robert F (1998) Orogenic gold deposits: a proposed classification in the context of their crustal distribution and relationship to other gold deposit types. Ore Geol Rev 13:7–27

Groves DI, Goldfarb RJ, Knox-Robinson CM, Ojala J, Gardoll S, Yun GY, Holyland P (2000) Late-kinematic timing of orogenic gold deposits and significance for computer-based exploration techniques with emphasis on the Yilgarn Block, Western Australia. Ore Geol Rev 17:1–38

Hart CJR (2007) Reduced intrusion-related gold systems. In: Goodfellow WD (ed) Mineral deposits of Canada: a synthesis of major deposit types, district metallogeny, the evolution of geological provinces, and exploration methods. Geol Assoc Canada, Min Deposits Div, Spec Publ No. 5, pp 95–112

Hammond NQ, Robb L, Foya S, Ishiyama D (2011) Mineralogical, fluid inclusion and stable isotope characteristics of Birimian orogenic gold mineralization at the Morila mine, Mali, West Africa. Ore Geol Rev 39:218–229

Hanssen E, Kaisin J, Tessougue S (2004) The Yatela gold mine, western Mali: supergene enrichment of Lower Proterozoic gold mineralization in a surficial karst. CIM Ann Mtg, Edmonton, Conference Proceed

IAMGOLD Corporation (2014) Annual report. www.iamgold.com

Kadio E, Coulibaly ME, Kouamelan AN, Pothin KBK (2010) On the occurrence of gold mineralizations in southeastern Ivory Coast. Jour African Earth Sci 57:423–430

King K (2012) Geological, structural and mineralogical constraints on the evolution of the Morila gold deposit, south Mali, West Africa. Unpubl MSc Thesis, Kingston Univer, London, UK 170 pp

Klemd R, Ott S (1997) Compositional characteristics of fluid inclusions as exploration tool for Au-mineralization at Larafella, Burkina Faso. Jour Geochem Expl 59:251–258

Klemd R, Hünken U, Olesch M (1996) Fluid composition and source of Early Proterozoic lode gold deposits of the Birimian volcanic belt, West Africa. Intern Geol Rev 38:22–32

Klemd R, Oberthür T, Ouedrago A (1997) Gold-telluride mineralisation in the Birimian at Diabatou, Burkina Faso. J Afr Earth Sci 24:227–239

Kusnir I (1999) Gold in Mali. Acta Montan Slovaca 4:311–318

Lambert-Smith JS (2014) The geology, structure and metallogenesis of the world class Loulo-Bambadji Au district in Mali and Senegal, West Africa. Unpubl PhD Thesis, Kingston Univ, London, UK, 346 pp

Lang JR, Baker T (2001) Intrusion-related gold systems: the present level of understanding. Mineral Deposita 36:477–489

Large RR, Bull SW, Maslennikov VV (2011) A carbonaceous sedimentary source-rock model for Carlin-type and orogenic gold deposits. Econ Geol 106:331–358

Lawrence DM, Treloar PJ, Rankin AH, Harbidge P, Holliday J (2013a) The geology and mineralogy of the Loulo mining district, Mali, West Africa: evidence for two distinct styles of orogenic gold mineralization. Econ Geol 108:199–227

Lawrence DM, Treloar PJ, Rankin AH, Boyce A, Harbidge P (2013b) A fluid inclusion and stable isotope study at the Loulo mining district, Mali, West Africa: implications for multifluid sources in the generation of orogenic gold deposits. Econ Geol 108:229–257

Ledru P, Pons J, Milési JP, Feybesse JL, Johan V (1991) Transcurrent tectonics and polycyclic evolution in the Lower Proterozoic of Senegal-Mali. Precam Res 50:337–354

Liégeois JP, Claessens W, Camara D, Klerkx J (1991) Short-lived Eburnian orogeny in southern Mali: geology, tectonics, U-Pb and Rb-Sr geochronology. Precam Res 50:111–136

Masurel Q, Thébaud T, Miller J, Ulrich S, Hein KAA, Cameron G, Beziat D, Bruguier O (in press) Sadiola Hill: a world-class carbonate-hosted gold deposit in the Birimian terranes of Mali, West Africa. Econ Geol

McCuaig TC, Kerrich R (1998) P-T-t-deformation-fluid characteristics of lode gold deposits: evidence from alteration systematics. Ore Geol Rev 12:381–453

McCuaig TC, Kerrich R, Groves DI, Archer N (1993) The nature and dimension of regional and local gold-related hydrothermal alteration in tholeiitic metabasalts in the Norsemann goldfields: the missing link in a crustal continuum of gold deposits. Mineral Deposita 28:420–435

McFarlane C, Mavrogenes J, Lentz D, King K, Allibone A, Holcombe R (2011) Geology and intrusion-related affinity of the Morila gold mine, southeast Mali. Econ Geol 106:727–750

Meinert LD, Dipple GM, Nicolescu S (2005) World skarn deposits. Economic Geology 100th Ann Vol 299–335

Milési JP, Feybesse JL, Ledru P, Dommanget A, Ouedrago M, Marcoux E, Prost A, Vinchon C, Sylvain JP, Johan V, Tegyey M, Calvez JY, Lagny P (1989) West African gold deposits in their Lower Proterozoic lithostructural setting. Chron Recherche Minière 497:3–98

Milési JP, Ledru P, Feybesse J, Dommanget A, Marcoux E (1992) Early Proterozoic ore deposits and tectonics of the Birimian orogenic belt, West Africa. Precam Res 58:305–344

Oberthür T, Vetter U, Schmidt Mumm A, Weiser T, Amanor JA, Gyapong WA, Kumi R, Bleckinsop TG (1994) The Ashanti gold mine at Obuasi in Ghana. Geolog Jahrbuch D100:31–129

Ohmoto H, Goldhaber MB (1997) Sulphur and carbon isotopes. In: Barnes HL (ed) Geochemistry of hydrothermal ore deposits, 3rd edn. Willey, New York, pp 517–612

Olson SF, Diakite K, Ott L, Guindo A, Ford CRB, Winer N, Hanssen E, Lay N, Bradley R, Pohl D (1992) Regional setting, structure, and descriptive geology of the Middle Proterozoic Syama gold deposit, Mali, West Africa. Econ Geol 87:310–331

Ouattara Z, Coulibaly Y, Boiron MC, Lieben F (2014) Geology and ore localizations in the Bonikro gold deposit, Fettékro greenstone belt, Côte d'Ivoire. Soc Economic Geologists Keystone Conference, Abstracts

Phillips GN, Powell R (2010) Formation of gold deposits: a metamorphic devolatilization model. J Metamorph Geol 28:689–718

Quick R (1999) The Morila gold deposit, southern Mali, West Africa. Unpubl MSc Thesis, Leicester University, Leicester, UK

Randgold Resources Ltd (2014) Annual report. www.randgoldresources.com

Ridley JR, Diamond LW (2000) Fluid chemistry of orogenic lode gold deposits and implications for genetic models. Rev Econ Geol 13:141–162

Schidlowski M, Hayes JM, Kaplan IR (1983) Isotopic inferences of ancient biochemistries: carbon, sulphur, hydrogen and nitrogen. In: Schopf JW (ed) Earth's earliest biosphere: it's origin and evolution. Princeton University Press, New York, pp 149–186

Schmidt Mumm A, Oberthür T, Vetter U (1997) High CO_2 content of fluid inclusions in gold mineralizations in the Ashanti belt, Ghana: a new category of ore forming fluids. Mineral Deposita 32:107–118

Sillitoe RH, Thompson JFH (1998) Intrusion-related vein gold deposits: types, tectono-magmatic settings and the difficulties in distinction from orogenic gold deposits. Resour Geol 48:237–250

Smith DS (1996) Hydrothermal alteration at the Mineral Hill mine, Jardine, Montana; a lower amphibolite facies Archean lode gold deposit of probable syn-metamorphic origin. Econ Geol 91:723–750

Tomkins AG (2010) Windows of metamorphic sulfur liberation in the crust: implications for gold deposit genesis. Geochim Cosmochim Acta 74:3246–3259

Treloar PJ, Lawrence DM, Senghor D, Boyce A, Harbidge P (2014a) The Massawa gold deposit, eastern Senegal, West Africa: an orogenic gold deposit sourced from magmatically derived fluids? Geol Soc Spec Publ 393:135–160

Treloar PJ, Lawrence DM, Lambert-Smith J, Senghor D, Wiedenbeck M, Boyce A (2014b) West African orogenic gold deposits: do they fit the global paradigm? IMA 2014 Conference Johannesburg, Abstract Vol

Villeneuve M, Cornée JJ (1994) Structure, evolution and paleoceanography of the West African craton and bordering belts during the Neoproterozoic. Precam Res 69:307–326

Nature and Geodynamic Setting of Late Neoproterozoic Vein-Type Gold Mineralization in the Eastern Desert of Egypt: Mineralogical and Geochemical Constraints

K.I. Khalil, A.M. Moghazi and A.M. El Makky

Abstract

The vein-type gold mineralization in the Eastern Desert of Egypt consists of sulphide minerals in stockwork quartz veins with hydrothermal alteration zones. The veins cut Neoproterozoic rocks along contacts between granite intrusions and island arc metavolcano-sedimentary sequence and ophiolitic rocks. Mineralization shows a clear structural control and is thus classified as orogenic gold. A post-peak metamorphic origin for the deposition of gold, sulphides, and carbonate gangue in the veins is suggested on the basis of various observations, such as: (1) gold mineralization is confined to quartz-bearing shear zones that cut host metamorphic rocks; (2) many sulphide minerals such as pyrite and arsenopyrite in addition to native gold and carbonate occur in different generations and parageneses; several of the sulphide generations are formed as a result of sulphidization of pre-existing metamorphic rocks; and (3) the depositional temperature of the hydrothermal minerals is commonly less than 400 °C. Based on relationships to magmatism and geodynamic framework, the gold deposits formed during the post-collision stage ($\sim$640–590 Ma) of Neoproterozoic crustal evolution. Major and trace elements data for 848 gold-mineralized samples of host rocks and quartz veins are treated statistically utilizing multivariate methods including discriminant function and R-mode factor analyses. From the geochemical exploration point of view, the Au-mineralized alteration zones developed within granitoids and schists are the most

K.I. Khalil (✉) · A.M. Moghazi
Faculty of Science, Department of Geology,
Alexandria University, Moharam Bek,
Alexandria 21511, Egypt
e-mail: kebeid@yahoo.com

A.M. El Makky
Faculty of Education, Department of Biological
and Geological Sciences, Alexandria University,
Alexandria, Egypt

M. Bouabdellah and J.F. Slack (eds.), *Mineral Deposits of North Africa*,
Mineral Resource Reviews, DOI 10.1007/978-3-319-31733-5_14

promising for gold exploration, as well as the auriferous quartz veins. Moreover, the Zn–Cu association in the central part of the Eastern Desert and Pb in the southern part could be indicators for auriferous alteration zones, whereas the Ni–Cu–Pb–Zn association could be an indicator for the Au-sulphide quartz veins.

1 Introduction

The Arabian Nubian Shield (ANS) in eastern Africa records ~300 m.y. of orogenic evolution from intra-oceanic subduction, arc and back-arc magmatism (870–700 Ma), and terrane amalgamation (~800–650 Ma) to terminal collision between major fragments of East and West Gondwana, with attendant tectonic escape, strike-slip faulting, delamination, and extension (635–550 Ma) of the newly formed continental crust (Stern 1994; Johnson and Woldehaimanot 2003; Avigad and Gvirtzman 2009; Stern and Johnson 2010; Johnson et al. 2011; Moghazi et al. 2012). The ANS is thus the result of diverse and polyphase geodynamic events; its tectonic evolution can be divided into three major stages: (1) subduction (~850–635 Ma) during which island arc, volcano-sedimentary sequences and plutonic rocks formed; (2) continental orogenesis, transitional magmatism, tectonic escape, and extension (~635–590 Ma) resulting from continuing convergence between East and West Gondwana to form the East African orogen (Stern 1994); and (3) post-collision (590–540 Ma) characterized by the eruption and emplacement of increasingly alkaline "A-type" granite. The last two stages were accompanied by the development of sedimentary basins (Jarrar et al. 2003; Johnson 2003) and terminated with the intrusion of alkaline igneous rocks (Beyth et al. 1994; Eyal et al. 2010).

The Eastern Desert (ED) of Egypt (Fig. 1) represents the northern part of the ANS, which consists of late Neoproterozoic (850 − 550 Ma) crust representing an area of suturing between East and West Gondwana (Stern 1994; Johnson et al. 2011). Late Neoproterozoic mineralization within the ED is dominated by gold (e.g., Klemm et al. 2001; Amer et al. 2010; Gabr et al. 2010; Johnson et al. 2011), Ta Nb, W, rare earth elements (REE), U, and Sn (e.g. Abdalla and Mohamed 1999; Küster 2009; Lundmark et al. 2011). The ED has long been known as a mining region for gold since ancient times, with more than one hundred occurrences discovered and/or mined. Gold in the ED is present in different lithologies such as carbonated ultramafic rocks, gabbro-granite contacts, volcanic rocks and associated massive sulphide deposits, which are all characterized by multiple metal sources (e.g., Kusky and Ramadan 2002; Botros 2004; Zoheir 2008a, b, 2011; Gabr et al. 2010). However, the majority of gold deposits occur in quartz veins that crosscut greenschist/amphibolite facies metamorphic rocks in association with unmetamorphosed granitic intrusions. These quartz veins are mostly accompanied by abundant pyrite and arsenopyrite. The distribution of gold-bearing quartz veins is controlled by major faults (e.g., Loizenbauer and Neumayr 1996; Helmy et al. 2004; Zoheir 2008a; Zoheir 2011) mostly related to NW- or NNW-striking shear zones that generally reflect reactivated older accretionary sutures (e.g., Kusky and Ramadan 2002; Zoheir 2008a, b).

The genesis and timing of gold mineralization in Egypt is controversial. It is genetically connected either with (1) the post-collision granite in particular to its post-magmatic fluids (Hume 1937; Amin 1955; El Shazly 1957; El-Gaby et al. 1988); (2) hydrothermal activity induced by metamorphic processes (Hassaan and El Mezayen 1995), or by combined metamorphic-magmatic sources (Harraz 2000; Klemm et al. 2001; Botros 2004); or (3) hydrothermal processes, where the

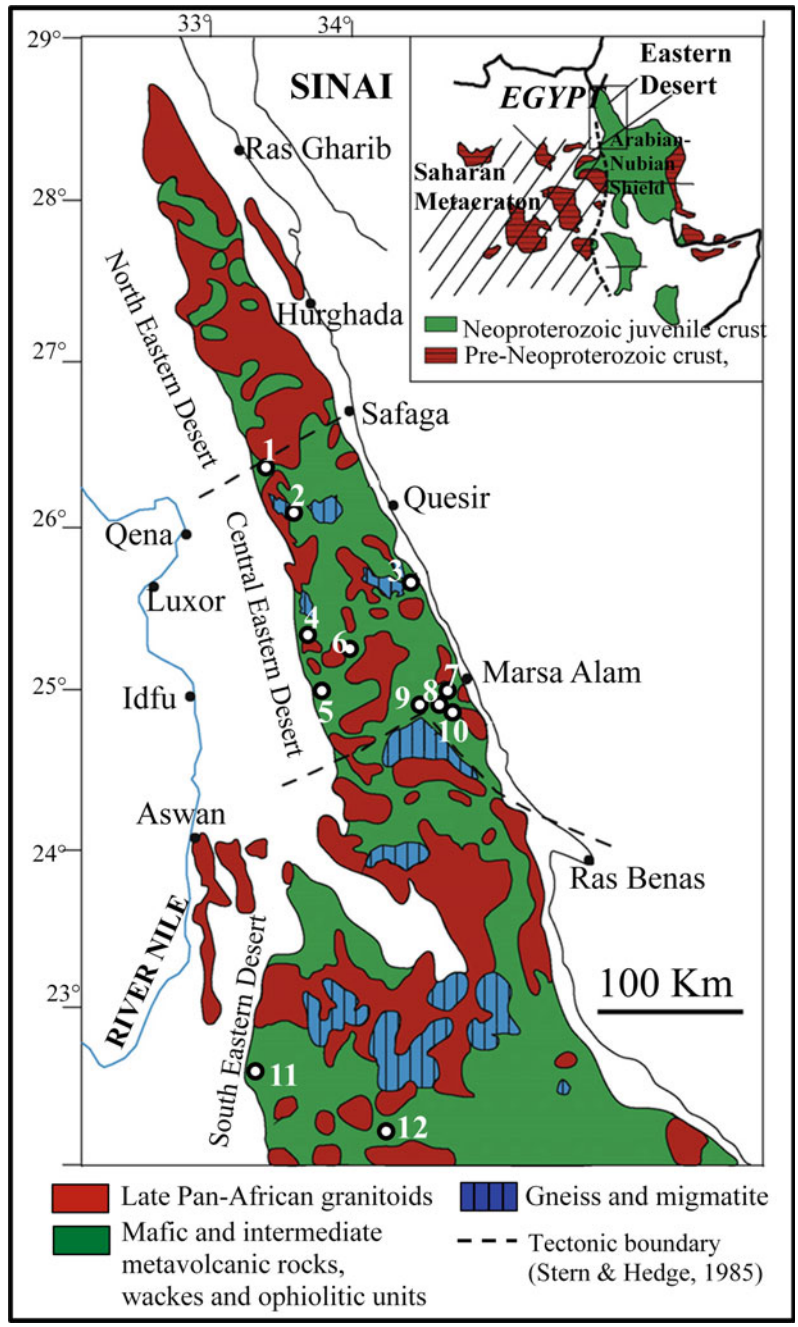

Fig. 1 **a** Simplified geological map of the Eastern Desert of Egypt showing locations of the studied gold deposits and occurrences. (*1*) Erediya, (*2*) EL Sid, (*3*) Umm Rus, (*4*) Barramiya, (*5*) Dungash, (*6*) Atud, (*7*) Sukari, (*8*) Kurdeman, (*9*) Hanglaliya, (*10*) Sabahia, (*11*) Umm Garayat, and (*12*) Umm Tuyur. Inset is geological sketch of NE Africa showing part of the Arabian–Nubian Shield (Liégeois and Stern 2010)

enrichment of gold is related to convective circulation of fluids through fractures. The granitic intrusions that occur at the contact with mafic or ultramafic rocks acted as a heat engine and promoted the fluid to migrate. These fluids leached gold from the country rocks to be re-deposited within the shear zone (Takla et al. 1989, 1990).

In this work, based on study of 12 selected gold deposits and occurrences (Fig. 1), we focus on the style of mineralization, petrography and

paragenetic sequences of ore minerals, and on geochemistry of the ore minerals. We use these data to construct a temporal framework for the genesis and tectonic setting of the gold mineralization. This integrated approach advances our understanding of how the gold mineralization is linked to tectono-magmatic evolution of the ANS.

2 General Geology and Petrography

2.1 Country Rocks

Country rocks of the gold ores in the study areas (Table 1) are Precambrian basement having different lithostratigraphic positions. These rocks can be categorized into three tectonic groups including ophiolitic rocks (serpentinites and talc-carbonates), island arc rocks (gabbro-diorite, meta-andesite, schists, and granodiorite), and post-collision rocks (monzogranite). These lithologies represent the main productive host basement rock types for gold within the ED of Egypt (Harraz 1991). Serpentinites are either metamorphosed dunite or harzburgite, and mainly comprise several serpentine minerals, with remnants of olivine, orthopyroxene, clinopyroxene, and chromian spinel in various proportions. The sheared varieties of serpentinites are transformed to a fine-grained mixture of talc and magnesite known as talc-carbonate rock. Gabbro-diorite rocks are coarse-grained and massive, and contain up to 50 vol.% euhedral to subhedral zoned plagioclase variably altered to sericite and epidote. Hornblende is the main mafic mineral, which locally contains remnants of augite. Meta-andesites consist primarily of glomerocrysts of plagioclase feldspar, hornblende, chlorite, opaque minerals, and accessory apatite with secondary quartz, sericite, and epidote set in a fine-grained groundmass displaying hyalopilitic texture. Plagioclase feldspar forms zoned and twinned subhedral crystals, affected by minor kaolinitization and sericitization. Hornblende displays alteration to chlorite and typically is accompanied by opaque minerals especially along cleavages and crystal borders. Opaque minerals and apatite occur as microphenocrysts or as inclusions in plagioclase and chlorite. Schists contain local porphyroblasts of garnet, quartz, and magnetite set in a fine-grained matrix composed of quartz, plagioclase, biotite, muscovite, and accessory magnetite. The main foliation is commonly defined by biotite, but in places also by muscovite. Granodiorite is either non-porphyritic or porphyritic, consisting mainly of plagioclase, quartz, K-feldspar, and biotite ± hornblende, with distinct shearing, brecciation, and hydrothermal alteration to sericite, kaolinite and Fe-oxides. Within the granodiorite, plagioclase is altered to sericite flakes oriented along cleavage planes or twining lamellae. Monzogranite consists essentially of K-feldspar, plagioclase, and quartz ± biotite; it contains two generations of plagioclase that are each commonly sericitized. Biotite is highly kinked due to deformation, and forms aggregates that contain different types of inclusions such as apatite, rutile, and zircon.

2.2 Quartz Veins and Alteration Zones

The gold mineralization in the study areas is confined to quartz veins occurring along brittle-ductile shear zones. Many of these veins were mined extensively since ancient time (Fig. 2a). Vein forms include ridge-like (Fig. 2b), en echelon (Fig. 2c), boudinag (Fig. 2d), and dense network (Fig. 2e).The quartz veins vary in thickness from few centimeters up to 6 m (El Sid gold mine), and extend along strike for more than 4 km. Geometric and textural features of the quartz veins indicate multistage opening and mineralization. Highly deformed and strongly altered rocks occur between bifurcating veins and/or within the quartz bodies (Fig. 2f). Generally, two main textural types of quartz are recognized: massive milky quartz and ribbon grey quartz (Fig. 2g). The massive veins consist of unstrained, polygonal, and tightly packed quartz crystals. At the contacts with wallrocks, quartz in the massive veins is relatively fine

Table 1 Characteristic features of the selected gold mineralization areas, Eastern Desert, Egypt

Au-occurrence	El Eradiya	El Sid	Um Rus	Barramiya	Atud
References	Arslan et al. (2001)	Harraz et al. (1992) and Khalil (1994)	Khalil (1994)	El-Bedawi et al.(1983) and Harraz and Khalil (in press)	Harraz and El Makky (1999a, b) and Helba et al. (2002)
Location	26° 22′ N–33° 25′ E	26° 00′ 17″ N–33° 35′ 42″ E	25° 27′ 56″ N–34° 34′ 47″ E	25° 04′ 26″ N–33° 47′ 27″ E	25° 00′ 10″ N–34° 24′ 10″ E
Host rocks	Older granite	Granitic rocks ⋙ serpentinite	Granodiorite ⋙ gabbro	Graphite-, actinolite schist + serpentinite ≫ granitoids	Diorite ⋙ metagabbro
Quartz veins					
Main strike	18–20° N	NE–SW	N–S ≫ N 30° E	E–W	NW–SE ≫ NE–SW
Dip			30° W & SW	–	42° SW ≫ 14–53° NW
Extention	About 1 km long	1000 m long	200 m long	1.2 km long	300 m long
Thickness	1 m	3–6 m	40 cm thikness	3 m	0.6–1.5
Sulphides association					
Quartz veins	py ⋙ asp + chp + sph + gn + cov	py + asp ⋙ pyr + chp + sph + gn + mr + alt	asp + py + mr ⋙ chp + gn + sph + pyr	py > asp ≫ pyr, chp, gn, sph, mr, tet	py > asp + minor chp, sph, pyr
Alteration zones	py	py + asp ⋙ pyr + chp + sph + gn + mr + alt	py + pyr + asp ⋙ chp + gn + sph + mr	py + asp ≫ mr, pyr	py > asp + minor chp, sph, pyr
Native gold					
Quartz veins	Rare free gold	Free gold	Free gold	Free gold	Free gold
Alteration zones	Rare free gold	Free gold	Free gold	Free gold	Free gold
Style of alteration	ser > car ⋙ alb, sulph, chl + silic	ser > chl > car > sulph + silic	ser > car > chl > sulph > epid + silic	car, ferru, ser, listv > talc, chl, + silic	ser > car > chl > sulph + silic
Temperature of formation					
Chlorite geotherm.	–	–	–	–	274–366 °C
Asp geotherm.	–	363–389 °C	415–480 °C	293–393 °C	–
Fluid inclusions	–	241–405 °C	–	–	–
Degree of metamorphism	Greenschist	Greenschist	Greenschist	Greenschist	Greenschist

Au-occurrence	Sukari	Dungash	Hangaliya	Kurdeman	Sabahia	Um Garayat	Um El Tuyor
References	Sharara (1999)	Helba et al. (2001) and Khalil et al. (2003)	Khalil and Helba (2000)	El-Makky et al. (2012)	Khalil et al. (2010)	Ivanov (1988) and El-Makky (2001)	El-Shimi (1996) and Zoheir (2008a, b)
Location	24° 56′ 50″ N–34° 42′ 27″ E	24° 57′ 25″ N–33° 52′ 35″ E	24° 51′ 22″ N–34° 39′ 30″ E	24° 52′ 04″ N–34° 41′ 16″ E	24° 50′ 55″ N–34° 44′ 45″ E	22° 22′ N–33° 25′ E	22° 18′ 15″ N–34° 38′ 00″ E
Host rocks	Granite	Meta-andesite ⋙ metapyroclastic	Granite ⋙ metagabbro-diorite	Meta-andesite ⋙ talc-carbonate	Meta-andesite ⋙ talc-carbonate	Meta-andesite	Schistosed metasediments

(continued)

Table 1 (continued)

Au-occurrence	Sukari	Dungash	Hangaliya	Kurdeman	Sabahia	Um Garayat	Um El Tuyor
Quartz veins							
Main strike	25–30° NE	ENE–WSW	ENE & NNE	310°	NE–SW	NW–NNE	NNW–NW
Dip	25–55° SE	65–85° NNW	65°SEE to vertical	Steeply SW	Almost vertical	60–80° SE	Subvertical
Extention	400 m long	1.5 km long	800 m long	60 m long	250 m long	about 4 km	–
Thickness	2.4 average	0.25–1.2 m	0.3–1.5 m	0.3 average	2–5 m	1.8 m	50–120 cm
Sulphides association							
Quartz veins	py > asp + few sph, chp, pyr, gn	py ⋙, chp, gn, pyr, sph, mr	few py > asp, chp, sph	minor py + rare chp	few py	py ⋙ chp + pyr + gn + cov + chalc + pr	asp > py + few chp, pyr, sph, gn
Alteration zones	py > asp + few sph, chp, pyr, gn	asp + py ⋙ chp, gn, pyr, gs	few py > asp, chp, sph	minor py + rare chp	few py	py ⋙ chp + pyr + gn + cov + chalc	asp > py + few chp, pyr, sph, gn
Native gold							
Quartz veins	Free gold	Free gold	Rare free gold	–	–	Free gold + Au tellurides	Free gold
Alteration zones	Free gold	Free gold	–	–	–	Free gold + Au tellurides	Free gold
Style of alteration	car > ser > alb > chl > sulph > listv + silic	ser > car > chl > sulph > listv + silic	ser > chl > sulph + silic	ser > car > chl + silic	ser > car > chl + silic	ser > car > pyroph > sulph ≫ kao > alb > chl > epid + silic	ser > car > chl > sulph + silic
Temperature of formation							
Chlorite geotherm.	–	307–325 °C	–	252–352 °C	288–312 °C	–	
Asp geotherm.	–	<300 °C	–	–	–	–	312–372 °C
n Fluid inclusions	262–370 °C	–	–	–	–	–	
Degree of metamorphism	Greenschist	Greenschist	Greenschist	Greenschist	Greenschist	Greenschist	Greenschist

Abbreviations *py* pyrite, *asp* arsenopyrite, *chp* chalcopyrite, *sph* sphalerite, *pyr* pyrrhotite, *gn* galena, *mr* marcasite, *cov* covellite, *chalc* chalcocite, *gs* gersdorffite, *alt* altite. *pr* proustite, *silic* silicification, *ser* sericitization, *car* carbonitization, *sulph* sulphidization, *chl* chloritization, *alb* albitization, *epid* epidotization, *pyroph* pyrophillitization, *kao* kaolinitizaion, *alun* alunitization, *talc* talcization, *listv* listvenitization, *ferru* ferrugination

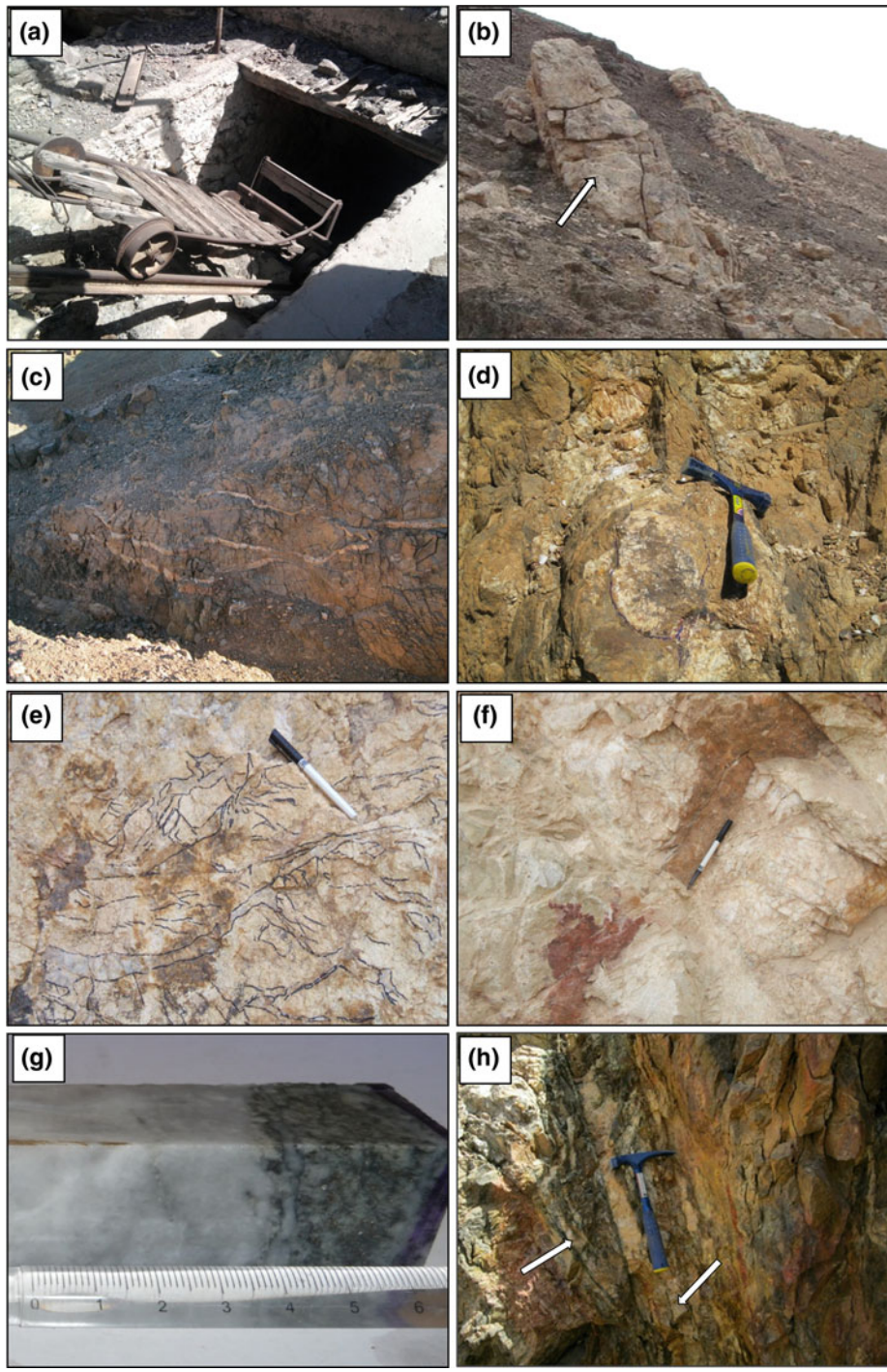

Fig. 2 Field photographs showing characteristic features of the gold-bearing quartz veins. **a** Old mine in the Fawakhir area; Au-bearing quartz vein was probably mined by the British during the 1950s; **b** parallel quartz veins (*arrow*) in the form of ridges, Sukari gold mine area; **c** sigmoidal en echelon quartz vein, Um Ud gold mine area; **d** boudinaged quartz vein along highly foliated and altered metavolcanic rocks, Dungash gold mine area; **e** dense and dendritic quartz veins hosted in altered granite, Sukari gold mine area; **f** wall rock xenoliths in quartz vein, Sukari gold mine area; **g** *grey* quartz rich in sulphides and wall rock materials (*right*), in contact with barren milky quartz, Um Garayat gold mine area; **h** quartz veins (*arrows*) are enveloped by haloes of alteration zones

grained and commonly forms sub-parallel, needle-shaped aggregates; the massive quartz veins are almost barren and consist of nearly pure quartz. Ribbon quartz veins comprise grey ribbons intermixed with wall rock constituents (e.g., sericite, chlorite, sulphides, carbonates). The ribbon-shaped quartz displays strong undulose extinction, seriate irregular grain boundaries, and sub-grain development. Contacts between the massive and ribbon quartz are generally sharp.

The gold-bearing quartz veins are surrounded by haloes of bleached rocks composed of mappable alteration zones (Fig. 2h). Mineralogical composition and intensity of these alteration zones depend largely on the host rock composition. Although the alteration patterns differ from one area to another, the following features can be generalized in the selected gold mining areas: (1) Thicknesses of the quartz veins generally show an inverse relation with those of the surrounding alteration zones. The presence of numerous corroded wallrock xenoliths and mineral relics within the quartz veins suggests that parts of the quartz veins are formed at the expense of pre-existing alteration zones; this pattern implies that silicification followed mineralization; (2) Based on textural analysis, the common alteration processes recognized can be arranged chronologically from chloritization to sericitization through sulphidization and carbonatization, and finally silicification. Kaolinitization, albitization, epidotization, alunitization, and listvinization are less common, (lisvanite forms when ultramafic rocks such as mantle peridotites are completely carbonated. It consists of quartz + carbonate ± talc ± Cr-mica); (3) The distribution of alteration minerals around the gold-quartz veins indicates that the amount of chlorite decreases whereas sericite, sulphides, and carbonates increase toward the veins. Based on the dominant hydrothermal alteration phases, a generalized spatial pattern of alteration zones can be mapped from outer chlorite–rich to inner carbonate–sulphides approaching the veins. Sericite is nearly a common alteration mineral within each of alteration zones; and (4) The alteration zones seem to be more or less symmetric around the veins, are parallel the foliation of the host rocks, and are modified where the veins cut the foliation.

3 Ore Mineralogy and Paragenesis

The opaque minerals within the deposits can be grouped into four assemblages: (1) magmatic, (2) metamorphic, (3) hydrothermal, and (4) weathering. Minerals of the magmatic assemblage are disseminated in the host rocks and may form relics in the altered rocks and the quartz veins. These magmatic minerals mainly are chromite, ilmenite, and magnetite ± pyrrhotite ± chalcopyrite ± gersdorffite. The chromite occurs chiefly in the serpentinite (e.g., Barramiya and El Sid gold mine deposits). Ilmenite ± magnetite is common in the metagabbro and meta-andesite (e.g., Um Rus, Atud, Dungash, Kurdeman, Sabahia, and Um Garayat gold deposit areas), whereas magnetite ± ilmenite is abundant in the granite (Fig. 3a) and the meta-andesite (e.g., El Sid, Um Rus, Sukari, Um Garayat, and Um El Tuyor gold deposits). However, primary pyrrhotite and chalcopyrite are confined to the serpentinite, metagabbro, and meta-andesite. Rare gersdorffite is recorded in the area of the Dungash gold deposit. During the metamorphic event, ilmenite typically altered to magnetite and rutile ± anatase. The rutile and anatase are also found along foliation planes of the wallrocks and as inclusions in the sulphide minerals (Fig. 3b). Graphite of metamorphic origin is widely distributed in some gold deposit areas (e.g., Barramiya, El Sid, and Um Garayat), and locally forms inclusions in the newly formed sulphide minerals (Fig. 3c).

Sulphides and native gold are products of the hydrothermal event. They are distributed within the quartz veins as well as in the altered wallrocks. Vein-hosted sulphides are spatially associated with carbonates and wallrock materials (Fig. 3d). Based on textural analysis, two types of hydrothermal sulphides are recognized: replacements and fracture-fillings. Sulphide minerals that formed by the sulphidation of pre-existing rocks include pyrite and arsenopyrite, subordinate pyrrhotite, sphalerite, chalcopyrite, and galena, and rare tetrahedrite.

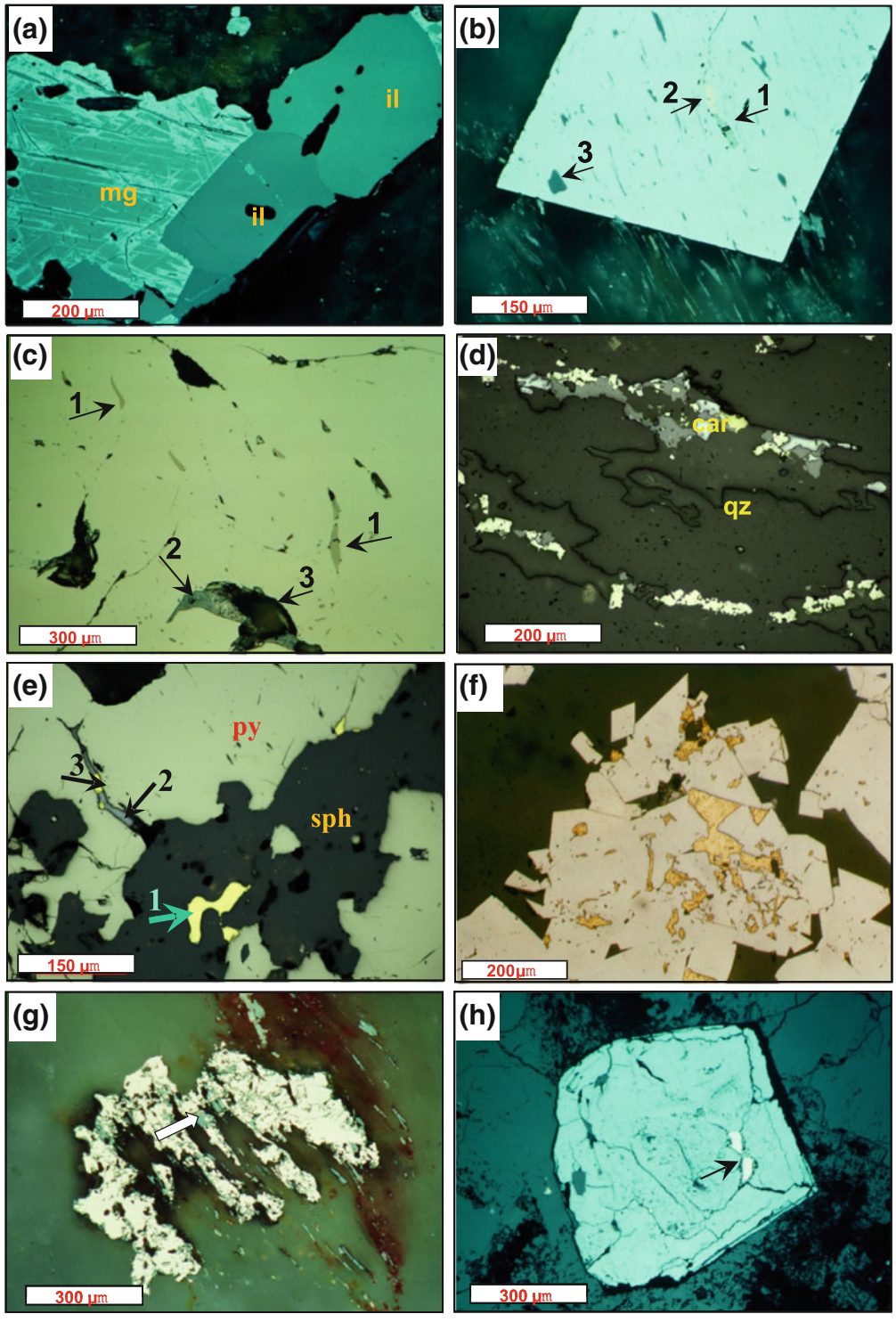
(a)
il
mg
il
200 μm
(b)
2
1
3
150 μm
(c)
1
1
2
3
300 μm
(d)
carb
qz
200 μm
(e)
py
3
2
sph
1
150 μm
(f)
200μm
(g)
300 μm
(h)
300 μm

Fig. 3 Textures and characteristic features of sulphides and native gold. **a** Ilmenite crystals (*il*) intergrown with magnetite (*mg*) that is partially martitized (El Sid gold mine); **b** idiomorphic coarse-grained arsenopyrite containing inherited parallel rutile needles (*pale grey*) that were originally contained in host rocks; other inclusions are pyrrhotite (*1*), native gold (*2*), and wall rock materials (*3*) (Um Rus gold mine); **c** coarse-grained pyrite with many relics of pyrrhotite (*1*), graphite (*2*), and wall rock materials (*3*), (El Sid gold mine); **d** sulphide-rich carbonate in association with sulphide-free quartz (Barramiya gold mine); **e** fracture filling sphalerite (*sph*), chalcopyrite (*1*), galena (*2*), and native gold (*3*) in pyrite (py), (Barramiya gold mine); **f** idiomorphic coarse-grained arsenopyrite containing abundant interstitial and fracture filling native gold (El Sid gold mine); **g** pervasive replacement of pyrite by silica due to silicification. Note that pyrite is slightly altered to goethite (*arrow*) (Dungash gold mine); **h** pseudomorphic replacement by goethite after sulphide in which relics are still preserved (*arrow*) (Um Rus gold mine). All photomicrographs were taken under reflected polarized light and oil immersion

Characteristic are different generations and parageneses of sulphides. Inclusions of native gold, graphite, rutile, and wallrock materials are common within pyrite (Fig. 3c) and arsenopyrite (Fig. 3b), and include relics of pyrrhotite and chalcopyrite (Fig. 3c, d). Elongated rutile inclusions typically occur parallel to the foliation of pre-existing wallrocks (Fig. 3b). The presence of pyrrhotite relics in other sulphide minerals, particularly pyrite and arsenopyrite, suggests their formation by the replacement of pre-existing pyrrhotite (Fig. 3b, c).

Fracture-filling sulphide minerals comprise mainly galena, sphalerite, and chalcopyrite in addition to native gold (Fig. 3e, f). Chalcopyrite commonly forms fine-grained blebs and rods within sphalerite. The fracture-filling sulphides and native gold typically are in pyrite (Fig. 3e) and arsenopyrite (Fig. 3f). Most sulphides in the quartz veins show features such as corrosion and replacement of borders indicating strong silicification (Fig. 3g). Sulphide minerals at or near the surface are weathered to goethite (Fig. 3h), lepidochrosite, and covellite; rutile, anatase, and ilmenite are converted into leucoxene. Very fine-grained native gold is present in the newly formed goethite/lepidochrosite. The generalized paragenetic sequence of minerals is illustrated in Fig. 4.

4 Geochemistry

Major and trace element data for 848 samples from gold-bearing host rocks and quartz veins in selected gold deposits (Fig. 1) have been processed statistically. The data processing includes multivariate methods of discriminant function analysis (DFA) and R-mode factor analysis (FA) utilizing the SPSS computer program (Norusis 1993). Using major elements as predictor variables, the distribution and geometric means of gold contents indicate that the granitoids (e.g., Sukari deposit) and schists (e.g., Um Tuyor deposit) are the most highly mineralized rocks, relative to serpentinite-talc-carbonate and meta-andesite (Dungash deposit). Generally, the gold contents of the host rocks increase as follows for the studied gold deposits and occurrences: Barramiya > Atud > Sukari > Um Tuyor ≥ Um Garayat > Hangaliya > Kurdeman > Dungash.

In terms of element associations, based on the factor analysis (Table 2 and Fig. 5) and significant factor scores (> +1 or < −1), achieved associations are: (1) [Cu–Zn–Au] in all host rock types (Factor 1), particularly in the central ED (Factor 1); (2) [Au–Pb] in all rock types (Factor 3) of the southern ED (Factor 2); and (3) [Ni–Co] as a general association and in the mineralized quartz veins [Cu–Pb–Zn, Factor 1] and [Co–Au–Ni, Factor 3]. For the discriminated quartz veins (Fig. 6), Ni and Co are predictor variables and differentiate the Au-rich, Au-intermediate and Au-poor vein groups (obtained by hierarchical agglomerative Q-mode cluster analysis) from the studied gold deposits. In the surficial environment, Zn, Cu, Pb, and Ni are relatively more mobile under oxidizing conditions, whereas Co is immobile (Moon et al. 2006). Consequently, in the host rocks within the auriferous alteration zones, the [Zn–Cu] association in the central ED and Pb in the southern ED may be used as indicators for

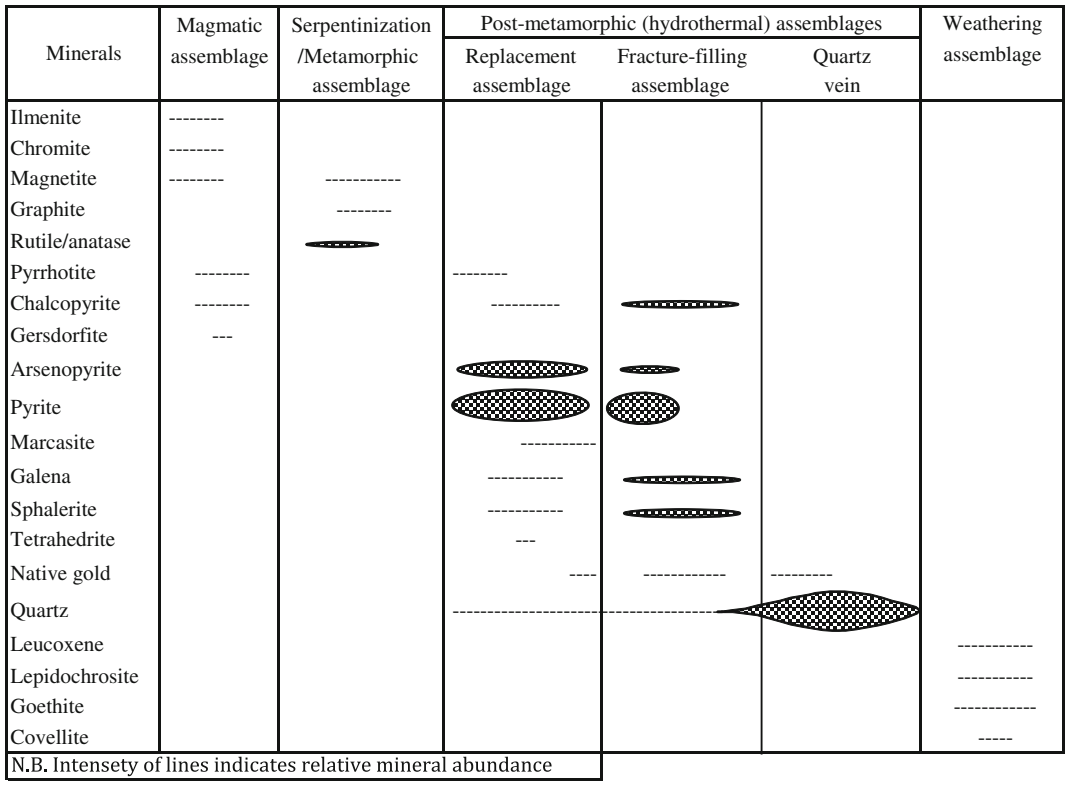

Fig. 4 Generalized paragenetic sequence of minerals in gold-mineralized zones of the study areas, Eastern Desert, Egypt

gold mineralization; in auriferous quartz veins, the [Ni–Cu–Pb–Zn] association can be utilized.

5 Discussion

The vein-type gold deposits of the ED have many similarities that permit a general concept of their genesis to be constructed. These deposits are related to shear zones that formed during the Neoproterozoic crustal evolution of the Arabian-Nubian Shield (e.g., Helmy et al. 2004; Zoheir 2008a, b). The shear zones cut sequences of metamorphosed ophiolitic and island arc volcanosedimentary rocks and/or occur along their contacts with I-type and post-collision, A-type granitoids (Table 1). Mineralized veins are surrounded by haloes of hydrothermal alteration zones characterized by sericitization, chloritization, carbonatization, sulphidation, and silicification. The veins formed below 400 °C except the Um Rus gold deposit, which formed at temperatures up to 480 °C (Table 1). These characteristics of the gold deposits in the ED share a number of features with orogenic-type gold deposits in terms of metamorphic, structural, and mineralogical aspects (e.g. Groves et al. 1998, 2003).

5.1 Age and Tectonic Setting of Gold Mineralization

The absolute age of gold mineralization in the ED of Egypt is unknown. Age determinations of the hydrothermal alteration have not been done and temporal, spatial, and genetic relationships of

Table 2 R-mode varimax rotated factor analysis (FA) for the Au-host rocks in some localities in the Eastern Desert, Egypt

Host rock	Locality	n	Factor 1	Factor 2	Factor 3	Cum. Var. %
Granitoids (granite, granodiorite and diorite)	H, B, At, Su	302	**Zn, Au, Cu**	Ni, Co	Pb, (Cu)	74.2
Metavolcanics (meta-andesite)	D, K, Ug	145	Ni, Co, (Cu)	**Au, Pb, Cu**	Zn, (Pb)	79.1
Serpentinite-talc-carbonates	B	89	**Au, Zn, Cu**	Co, Ni, -Pb		77.8
Schists	B, Ut	151	**Zn, Cu, Au**	Ni, Co, -Pb		68.3
All rock types in the central and southern Eastern Desert (ED)	D, H, K, B, At Su, Ug, Ut	687	**Cu, Zn, Au**	Ni, Co	**Pb, (Au)**	74.7
Central ED	B, D, K, At, Su, H	594	**Cu, Zn, Au**	Ni, Co	**Pb, (Au)**	76.4
Southern ED	Ug, Ut	93	Ni, Co, (Zn)	**Au, Pb**	Cu, Zn	81.2
Mineralized quartz veins	D, H, Su, Ug, Ut	48	Cu, Pb, Zn	-Ni, Au	**Co, (Au), (Ni)**	85.7

H Hangaliya, *B* Barramiya, *At* Atud, *Su* Sukari, *D* Dungash, *K* Kurdeman, *Ug* Um Garayat, *Ut* Um El Tuyor, *n* number of samples, *Cum. Var. %* cumulative variance percentage, loading of elements >0.4 as an absolute value, ( ) subsidiary variable, *Bold* Au-associated elements

various deposits to specific tectonic events are not well constrained. However, knowledge of the age of the gold-controlling structures and their relationship to tectonic evolution is critical for understanding the origin of mineralization episodes in the region. The distribution of orogenic gold deposits and occurrences in the ED shows a striking NW–SE alignment. Gold mineralization within these ore zones is close to NW–SE-trending shear zones and along NE–SW and approximately E–W-trending faults. This pattern confirms that NW–SE-trending structures played a major role in localizing mineralization and suggests possible temporal, spatial, and genetic relationships of orogenic gold deposits in the ED and the tectono-stratigraphic blocks that formed by regional stress regime prior to gold mineralization.

During the evolution of the ANS, subduction processes terminated with the emplacement of calc-alkaline, collisional I-type granitoids (670–635 Ma; Fleck et al. 1980; Stern and Hedge 1985). By ~635 Ma, the region was affected by oblique (transpressional) convergence of continental blocks that formed eastern and western Gondwana. North-trending shear and shortening zones developed in the southern ANS; NW-trending strike-slip shear zones of the Najd fault system predominated farther north (Moore 1979; Johnson et al. 2011). Convergence and transpression along the Najd fault system buckled the upper crust, causing structural highs with domes of gneisses overlain by ophiolitic rocks and volcano-sedimentary assemblages of island-arc activity (Neumayr et al. 1996a, b; Abdeen and Greiling 2005; Abdeen and Abdelghaffar 2011). Fowler and Osman (2001) described bedding, gneissosity, and complex mesoscopic folds within the high-grade metamorphic rocks exposed in the core of the gneiss dome in Wadi Um Had, and attributed these structures and metamorphism to the main collisional orogeny, and therefore to an age of ca. 640 Ma (Johnson et al. 2011). Following high-grade metamorphism, the region began to undergo orogenic collapse and NW–SE to NNW–SSE extension (Abdeen and Greiling 2005), resulting in subsidence and the development of

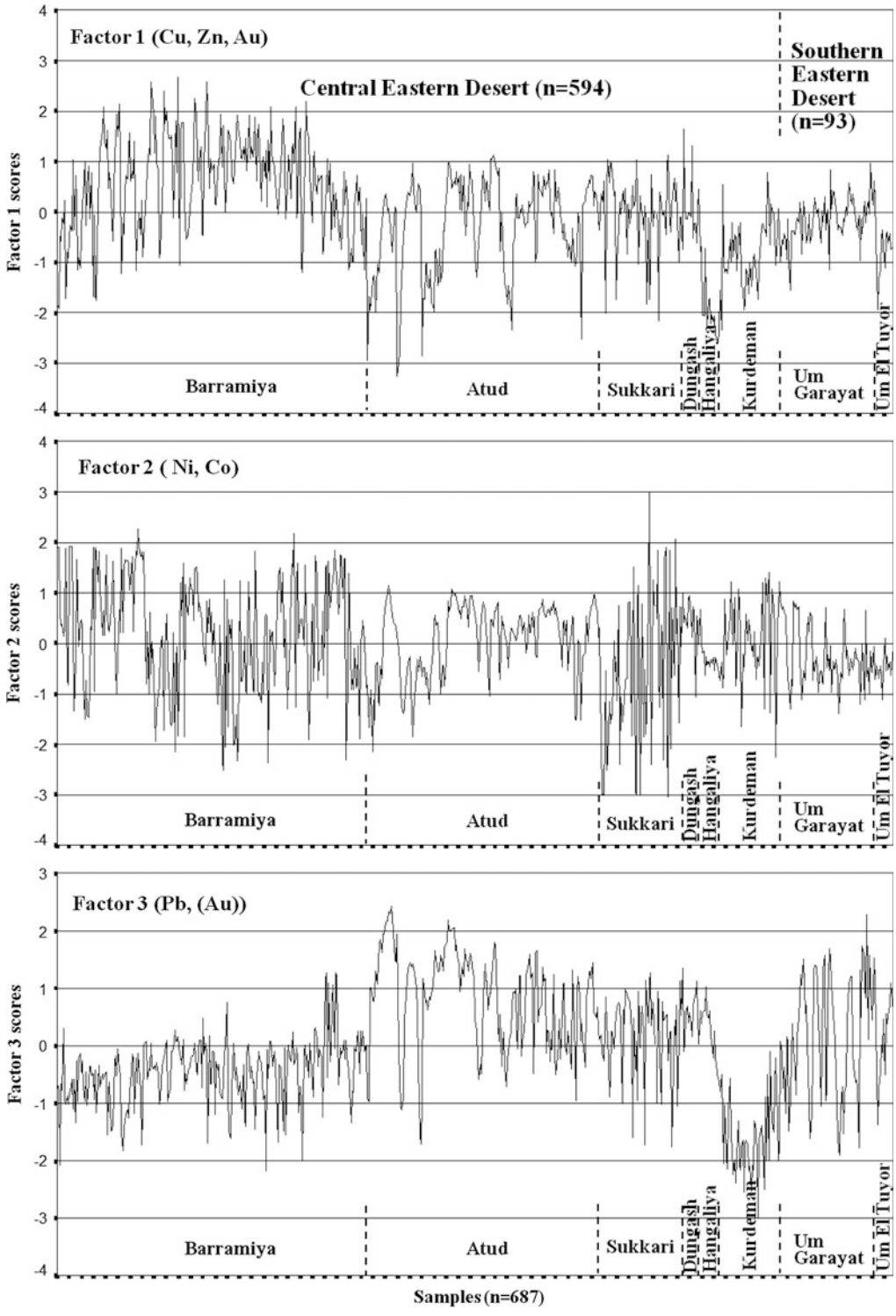

Fig. 5 *Factor 1*, *2*, and *3* scores for all gold-bearing host rock samples, Eastern Desert, Egypt. Factors are shown for eight gold deposits listed on x-axes

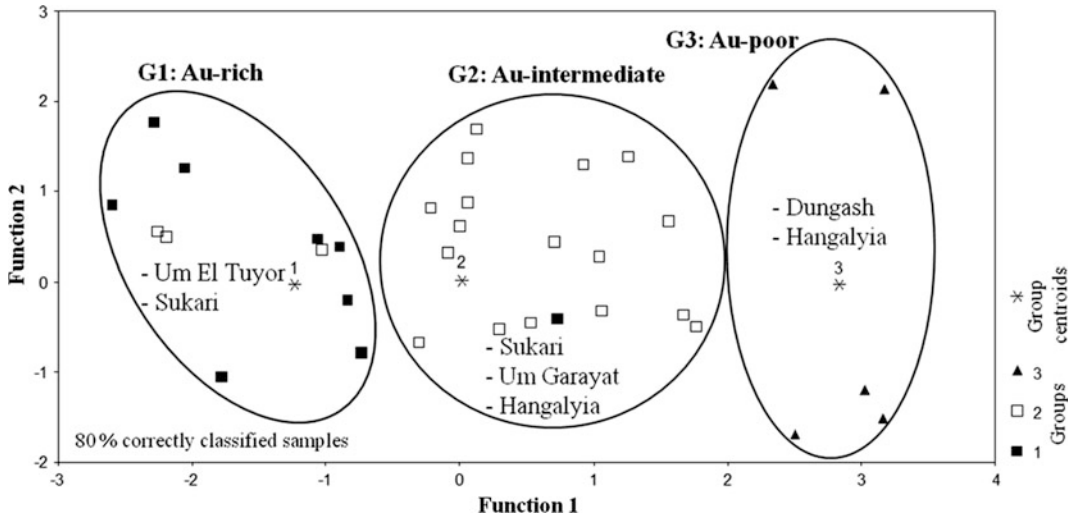

Fig. 6 Canonical discriminant function scores for the studied gold-quartz veins, Eastern Desert, Egypt

basins that became the site of deposition of the late Neoproterozoic (630–590 Ma) Dokhan Volcanics and the Hammamat Group.

Based on the present study and previous data from ore petrography, a post-peak metamorphic origin for deposition of gold, sulphides, and carbonates in the veins is proposed. This interpretation is informed by the following observations:

1. The disseminated sulphide mineralization is not confined to the quartz veins but also occurs in the adjacent altered wallrocks. Disseminated sulphides in the wallrocks do not appear restricted to a particular lithology but rather are spatially associated with shearing, fracturing, and foliation and occur in all lithological units close to the gold-quartz veins.
2. Occurrence of relics of wallrock materials within the sulphides and carbonates that are mineralized along pre-existing foliation planes (Fig. 4b, c). The mineralogical composition and texture of these relics are identical to those of the adjacent wallrocks.
3. Sulphides, gold, and carbonates occur in different generations and assemblages (Fig. 4), reflecting many stages of mineralization under a variety of conditions.
4. Replacement of wallrocks, including original textures, by sulphides and carbonates (Fig. 3b).
5. Some sulphides, particularly different generations of pyrite and arsenopyrite, are of secondary origin formed by replacement of pre-existing pyrrhotite due to the increase of sulphur fugacity. The abundance of pyrrhotite relics documents this suggestion (Fig. 3b, c). On the other hand, in the metamorphic model for the genesis of gold (Powell et al. 1991), pyrite is decomposed to release sulphur and form secondary pyrrhotite. The replacement of pyrite and arsenopyrite by pyrrhotite was not observed in any of the studied gold deposits in the ED.
6. The barren quartz veins represent multistage impulses with the main stage being probably the youngest in the paragenetic sequence. This quartz extensively replaced the wallrocks and associated sulphides (Fig. 3d, g); Intensity of the replacement depends on the composition of pre-existing minerals: silicates and carbonates in the wallrocks show extensive or even complete replacement, whereas sulphide minerals such as pyrite and arsenopyrite, in addition to native gold, were weakly affected by silicification.

5.2 Mineralization Model

If orogenic-type gold mineralization in the ED post-dates regional metamorphism and the development of major shear zones, the introduction of gold thus could be linked to the post-collisional tectonic setting of the ANS. The time period between 640 and 600 Ma would then represent the most important episode of gold mineralization in the ED of Egypt. Moreover, the widespread occurrence of orogenic gold of similar age in Saudi Arabia, Sudan, and Ethiopia (Johnson et al. 2011) suggests that this post-collisional stage played a major role in gold metallogeny of the ANS. During this stage, slab break-off following the cessation of subduction led to mantle upwelling and influx of hot asthenosphere, providing the heat supply that drove widespread magmatic and hydrothermal events, and possibly also the emplacement of younger granitoid intrusions. Worldwide, the formation of orogenic gold deposits reflects the passage of large volumes of hydrothermal fluids through permeable channelways in a brittle structural environment (e.g., Sibson et al. 1988; Goldfarb et al. 2005). Such fluids tend to have a common composition with low salinities and high CO_2 contents, and deposition that typically occurs at a temperature of approximately 350 °C and depths of 4–12 km (Goldfarb et al. 2001). Similarly, the fluids responsible for the gold precipitation mechanisms in the ED are thought to be a mixture of aqueous and carbonic fluids characterized by low salinities and alkaline to neutral pH (e.g., Harraz 2000; Zoheir 2008b).

Based on the mineralogical and geochemical data obtained in the present study, it is assumed that gold mineralization in the ED is of post-peak metamorphic origin. Regional metamorphism under greenschist to amphibolite facies conditions affected the ophiolites and island arc-related rocks within the ED. Tectonism and metamorphism have resulted in well-developed shear planes and foliation in the wallrocks. The formation of graphite (e.g., Barramiya, El Sid, and Um Garayat gold deposits), and ferritchromit from chromite, are related to the metamorphism. Rutile and anatase are metamorphic products probably after ilmenite and magnetite. The occurrence of rutile and anatase parallel to the foliation of metamorphic wallrocks indicates a syn-metamorphic origin. Sulphides, gold, and carbonates in the mineralized zones are relatively young, and are post-peak metamorphic as indicated by the presence of rutile and anatase inclusions (Fig. 3b). They are formed from hydrothermal fluids that circulated through the shear zones.

Alteration processes and associated gold mineralization in the ED are strongly related to elemental remobilization. Based on textural relationships, these processes can be arranged chronologically from chloritization, sericitization, carbonatization, sulphidation to silicification. We propose that the invading hydrothermal fluids were initially rich in H_2 and probably K, which led to the formation of chlorite at the expense of biotite ± amphibole, and sericite at the expense of feldspars. On progressive alteration, the chloritization and sericitization affected the pH of the fluids and consequently the degree of dissociation of H^+-containing complexes, which in turn affected the solubility of metals in the solution (Seward and Barnes 1997; Guilbert and Park 1986). Consumption of H^+ and increased pH of the fluids was accompanied by an increase in the CO_2/H_2O ratio and S content, which jointly promoted the formation of carbonates and sulphides. At a relatively high temperature (>250 °C), disseminated sulphides formed during replacement of pre-existing rocks. Many wallrock relics occur within the sulphide grains, some of which preserve the foliation trend of the pre-existing rocks. Some pyrite and arsenopyrite generations are of secondary origin, having formed by the replacement of pyrrhotite. With decreasing temperature, fracture-filling galena, sphalerite, and chalcopyrite were formed.

On a regional scale, native gold was first deposited during pyritization of pyrrhotite (e.g., Fig. 3b) because of increased sulphur fugacity. Gold was released during this replacement process; some of this gold was likely incorporated into pyrite and arsenopyrite, whereas most recrystallized as native gold inclusions within these two minerals (Fig. 3b). A second high concentration of gold distinguishes contacts of

the quartz vein ores to adjacent wallrocks. At these sites, gold transport was associated with CO_2-rich fluids and the deposition of carbonates; gold apparently precipitated in a native form that fills fractures in pyrite (Fig. 3e) and arsenopyrite (Fig. 3f). Finally, pre-existing native gold may have been concentrated by SiO_2-rich solutions that dissolved some previous minerals, including silicates in the wallrocks. Thus, in this case, chemically resistant minerals such as native gold, arsenopyrite, and pyrite were residually enriched. These minerals are not paragenetically associated with quartz, and only represent the last stable minerals within SiO_2-rich solutions, and consequently were concentrated in zones where SiO_2-rich solutions infiltrated.

6 Conclusions

1. Vein-type gold deposits in the ED of Egypt are distributed within different Pan-African rock types and seem to have developed late in the orogenic cycle of the Arabian Nubian Shield.
2. Rocks in the different study areas were affected by metamorphism up to amphibolite facies conditions, whereas the mineralization is the result of post-peak metamorphic hydrothermal conditions with a temperature of <400 °C. The hydrothermal fluids migrated along shear zones, fractures, and foliation of the metamorphosed wall rocks.
3. The majority of sulphides such as pyrite, arsenopyrite, sphalerite, galena, pyrrhotite, and chalcopyrite, as well as native gold, are of hydrothermal origin. Pyrite and arsenopyrite commonly display textures that indicate formation by the replacement of pre-existing pyrrhotite and chalcopyrite in wall rocks. In contrast, sphalerite, chalcopyrite, and galena commonly formed as fillings of fractures.
4. In the context of geochemical exploration, the [Zn–Cu] association in the central ED and Pb in the southern ED could be useful indicators for auriferous alteration zones. Alteration zones that developed in granitoids and schists are especially promising for the occurrence of gold. However, in the central and southern ED the [Ni–Cu–Pb–Zn] association could be used as a specific indicator for gold- and sulphide-bearing quartz veins.

References

Abdalla HM, Mohamed FH (1999) Mineralogical and geochemical investigation of emerald and beryl mineralisation, Pan-African Belt of Egypt: genetic and exploration aspects. J Afr Earth Sci 28:581–598

Abdeen MM, Abdelghaffar AA (2011) Syn- and post-accretionary structures in the Neoproterozoic central Allaqi-Heiani suture zone, southeastern Egypt. Precambr Res 185:95–108

Abdeen MM, Greiling RO (2005) A quantitative structural study of late Pan-African compressional deformation in the central Eastern Desert (Egypt) during Gondwana assembly. Gondwana Res 8:457–471

Amer R, Kusky TM, Ghulam A (2010) Lithological mapping in the central Eastern Desert of Egypt using ASTER data. J Afr Earth Sci 56:75–82

Amin MS (1955) Geological features of some mineral deposits in Egypt. Bull Inst Desert Egypt S I:208–239

Arslan AI, Khalil SO, El Sayed MM, Mohammed FH, El Deeb HM (2001) Contribution to the geochemistry of bedrocks and wallrock alterations, El Eradiya gold mine area, central Eastern Desert, Egypt. In: Proceedings 5th international conference geochemistry, vol II. Alexandria Univ, Alexandria, Egypt, pp 571–598

Avigad D, Gvirtzman Z (2009) Late Neoproterozoic rise and fall of the northern Arabian-Nubian shield: the role of lithospheric mantle delamination and subsequent thermal subsidence. Tectonophys 477:217–228

Beyth M, Stern RJ, Altherr R, Kroner A (1994) The Late Precambrian Timna igneous complex, southern Israel —evidence for comagmatic-type sanukitoid monzodiorite and alkali granite magma. Lithos 31:103–124

Botros NS (2004) A new classification of the gold deposits of Egypt. Ore Geol Rev 25:1–37

El Shazly EM (1957) Classification of Egyptian mineral deposits. Egypt J Geol 1:1–20

El-Bedawi MA, Hassan YM, Zaki ME, Arnous MM (1983) Results of prospecting-evaluation work carried out at Barramiya gold ore deposit (1979–1981). Geological Survey Egypt, internal report, 206 pp

El-Gaby S, List FK, Tehrani R (1988) Geology, evolution and metallogenesis of the Pan-African belt in Egypt. In: El-Gaby S, Greiling RO (eds) The Pan-African belt of northeast Africa and adjacent areas. Friedr, Vieweg Shon & Braunschweig/Wiesbaden, pp 17–68

El-Makky AM (2001) Trend surface analysis as an exploration guide in the environs of Um Garayat gold mine area, south Eastern Desert, Egypt. In: Abstracts 2nd international conference geology Africa, vol III-21. Assiut University Assiut, Egypt, pp 38–39

El-Makky AM, Khalil KI, Ibrahim IM (2012) Hydrothermal wall rock alteration at Kurdeman gold mine area, Eastern Desert, Egypt. Neus Jahrb Mineral Abh 189:75–95

El-Shimi KAM (1996) Geology, structure and exploration of gold mineralization in Wadi Allaqi area, SW Eastern Desert, Egypt. Ph.D. thesis, Ain Shams University, Cairo, Egypt. 326 pp

Eyal M, Litvinovsky B, Jahn BM, Zanvilevich A, Katzir Y (2010) Origin and evolution of post-collisional magmatism: coeval Neoproterozoic calc-alkaline and alkaline suites of the Sinai Peninsula. Chem Geol 269:153–179

Fleck RJ, Greenwood WR, Hadley DG, Anderson RE, Schmidt DL (1980) Rubidium-strontium geochronology and plate-tectonic evolution of the southern part of the Arabian Shield. U.S. Geol Survey Prof Paper 1131, 38 pp

Fowler TJ, Osman AF (2001) Gneiss-cored interference dome associated with two phases of late Pan-African thrusting in the central Eastern Desert, Egypt. Precambr Res 10817–43

Gabr S, Ghulam A, Kusky T (2010) Detecting areas of high-potential gold mineralization using ASTER data. Case study, Ore Deposit Rev doi:10.1016/j.oregeorev.2010.05.007

Goldfarb RJ, Groves DI, Gardoll S (2001) Orogenic gold and geologic time; a global synthesis. Ore Geol Rev 18:1–75

Goldfarb RJ, Baker T, Dubé B, Groves DI, Hart CJR, Gosselin P (2005) Distribution, character, and genesis of gold deposits in metamorphic terranes. In: Hedenquist JW, Thompson JFH, Goldfarb RJ, Richards JP (eds), Economic geology one hundredth anniversary volume, 1905–2005. Society Economic Geologists, Inc., Littleton, Colo, USA, pp 407–450

Groves DI, Goldfarb RJ, Gebre-Mariam M, Hagemann SG, Robert F (1998) Orogenic gold deposits: a proposed classification in the context of their crustal distribution and relationship to other gold deposit types. Ore Geol Rev 13:7–27

Groves DI, Goldfarb RJ, Robert F, Hart CJ (2003) Gold deposits in metamorphic belts; overview of current understanding, outstanding problems, future research, and exploration significance. Econ Geol 98:1–29

Guilbert JM, Park CF (1986) The geology of ore deposits. W.H. Freman and Company, New York, 985pp

Harraz HZ (1991) Lithochemical prospecting and genesis of gold deposit in the El Sukari gold mine, Eastern Desert, Egypt. Ph.D. thesis, Tanta University, Tanta, Egypt, 494 pp

Harraz HZ (2000) A genetic model for a mesothermal Au deposit: evidence from fluid inclusions and stable isotopic studies at El Sid gold mine, Eastern Desert, Egypt. J Afr Earth Sci 30:267–282

Harraz HZ, El Makky AM (1999a) Application of zoning of ore-associated elements to exploration for auriferous quartz vein deposits: a case study of Atud mine, Eastern Desert, Egypt. In: Proceedings 4th international conference geochemistry, vol I. Alexandria University, Alexandria, Egypt, pp 189–206

Harraz HZ, El Makky AM (1999b) Primary dispersion aureoles around auriferous quartz veins, Atud gold mine, central Eastern Desert, Egypt. In: Proceedings 4th internaional conference geochemistry, vol I. Alexandria University, Alexandria, Egypt, pp 207–223

Harraz HZ, Khalil KI (in press) Gold mineralization at the Barramiya mine area, Eastern Desert, Egypt: a mineralogical and genetic study. J Egypt Mineral

Harraz HZ, Hassanen MA, El Dahhar MA (1992) Fluid inclusions and stable isotopic studies of El Sid gold mine, Eastern Desert, Egypt. Egypt J Geol 36:323–343

Hassaan MM, El Mezayen AM (1995) Genesis of gold mineralization in the Eastern Desert of Egypt. Al Azhar Bull Sci 6:921–939

Helba HA, Khalil KI, Abdou NM (2001) Alteration patterns related to hydrothermal gold mineralization in meta-andesite at Dungash area, Eastern Desert, Egypt. Resour Geol 51:19–30

Helba HA, Khalil KI, El-Sayed MM (2002) A genetic concept on gold mineralization and its alteration zones at the Atud gold mine area, central Eastern Desert, Egypt. Bull Fac Sci Assiut Univ 31(I–F):89–109

Helmy HM, Kaindl R, Fritz H, Loizenbauer J (2004) The Sukari gold mine, Eastern Desert-Egypt: structural setting, mineralogy and fluid inclusion study. Miner Deposita 39:495–511

Hume WF (1937) Geology of Egypt: the minerals of economic values associated with the intrusive Precambrian igneous rocks. Ann Geol Survey Egypt 2–3:689–990

Ivanov TG (1988) Report of study of hydrothermal alterations in localities Um Garayat and Um Tundup, southeastern Desert, Egypt. United Nations Development Program Arab Republic Egypt. Geological Survey Egypt, internal report

Jarrar G, Stern RJ, Saffarini G, Al-Zubi H (2003) Late- and post-orogenic Neoproterozoic intrusions of Jordan: implications for crustal growth in the northernmost segment of the East African orogen. Precambr Res 123:295–320

Johnson PR (2003) Post-amalgamation basins of the NE Arabian Shield and implications for Neoproterozoic tectonism in the northern East African orogen. Precambr Res 123:321–337

Johnson PR, Woldehaimanot B (2003) Development of the Arabian–Nubian shield: perspectives on accretion and deformation in the northern East African orogen and the assembly of Gondwana. In: Yoshida M, Windley BF, Dasgupta S (eds), Proterozoic east Gondwana: supercontinent assembly and breakup, vol 206. Geological Society Special Publications, pp 290–325

Johnson PR, Andresen A, Collins AS, Fowler AR, Fritz H, Ghebrab W, KuskyT SR (2011) Late Cryogenian-Ediacaran history of the Arabian-Nubian Shield: a review of depositional, plutonic, structural, and tectonic event in the closing stages of the northern East African orogen. J Afr Earth Sci 61:167–232

Khalil KI (1994) Genetic studies of gold mineralization at some localities in the Eastern Desert, Egypt. Ph.D. thesis, Alexandria University, Alexandria, Egypt, 293 pp

Khalil KI, Helba A (2000) Gold mineralization and its alteration zones at the Hangalia gold mine area, Eastern Desert, Egypt. Egypt Mineral 12:65–92

Khalil KI, El-Sayed MM, Furnes H (2010) Mineralogy and implication of wall rock alteration in the Sabahia gold mine area, Eastern Desert, Egypt. World Acad Sci Eng Technol 71:1089–1102

Khalil KI, Helba HA, Mücke A (2003) Parageneses of gold mineralization at Dungash gold mine area, Eastern Desert, Egypt: a mineralogical study. J Afr Earth Sci 37:111–122

Klemm DD, Klemm R, Murr A (2001) Gold of the Pharaohs—6000 years of gold mining in Egypt and Nubia. J Afr Earth Sci 33:643–659

Kusky TM, Ramadan TM (2002) Structural controls on Neoproterozoic mineralization in the south Eastern Desert, Egypt: an integrated field, Landsat TM, and SIRC/X SAR approach. J Afr Earth Sci 35:107–121

Küster D (2009) Granitoid-hosted Ta mineralization in the Arabian-Nubian Shield: ore deposit types, tectono-metallogenic setting and petrogenetic framework. Ore Geol Rev 35:68–86

Liégeois JP, Stern RJ (2010) Sr–Nd isotopes and the geochemistry of granite-gneiss complexes from the Meatiq and Hafafit domes, Eastern Desert, Egypt: no evidence for pre-Neoproterozoic crust. J Afr Earth Sci 57:31–40

Loizenbauer J, Neumayr P (1996) Structural controls on the formation of the Fawakhir gold mine, EL Sid—Eastern Desert, Egypt: tectonic and fluid inclusion evidence. In: Proceedings geological survey Egypt centennial conference, pp 477–488

Lundmark AM, Andresen A, Hassan MA, Augland LE, Abu El-Rus MA, Baghdady GY (2011) Repeated magmatic pulses in the East African orogen of central Eastern Desert, Egypt: an old idea supported by new evidence. Gondwana Res 22:227–237

Moghazi AM, Ali KA, Wilde SA, Zhou Q, Andersen T, Andresen A, Abu El-Enen MM, Stern RJ (2012) Geochemistry, geochronology, and Sr–Nd isotopes of the late Neoproterozoic Wadi Kid volcano-sedimentary rocks, southern Sinai, Egypt: implications for tectonic setting and crustal evolution. Lithos 154:147–165

Moon CJ, Whateley MKG, Evans AM (2006) Introduction to mineral exploration, 2nd edn. Blackwell Publishing Ltd, Oxford 481 pp

Moore JM (1979) Tectonics of the Najd transcurrent fault system, Saudi Arabia. J Geol Soc 136:441–454

Neumayr P, Mogessie A, Hoinkes G, Puhl J (1996a) Geological setting of the Meatiq metamorphic core complex in the Eastern Desert of Egypt based on amphibolite geochemistry. J Afr Earth Sci 23:331–345

Neumayr P, Hoinkes G, Puhl J, Mogessie A (1996b) Polymetamorphism in the Meatiq basement complex (Eastern Desert, Egypt): P–T variations and implications for tectonic evolution. In: Geological survey Egypt, centennial symposium abstracts, pp 139–141

Norusis MJ (1993) Statistical package for the social sciences (SPSS for Windows), SPSS. Inc 444 N Michigan Avenue, 828 pp

Powell R, Will TM, Phillips GM (1991) Metamorphism in Archean greenstone belts: calculated fluid compositions and implications for gold mineralization. Metamorph Geol 9:141–150

Sharara NA (1999) Stable isotopes and fluid inclusions of the gold mineralization at El Sukari district, central Eastern Desert, Egypt: genetic constraints. In: Proceedings 4th international conference geochemistry. Alexander University, Alexandria, Egypt, pp 317–339

Seward TM, Barnes HL (1997) Metal transport by hydrothermal ore fluids. In: Barnes HL (ed) Geochemistry of hydrothermal ore deposits (3rd edn). Wiley, New York

Sibson RH, Robert F, Poulsen HK (1988) High angle reverse faults, fluid pressure cycling, and mesothermal gold-quartz deposits. Geology 16:551–555

Stern RJ (1994) Arc assembly and continental collision in the Neoproterozoic East African orogen: implications for the consolidation of Gondwanaland. Ann Rev Earth Planet Sci 22:319–351

Stern RJ, Hedge CE (1985) Geochronologic and isotopic constraints on Late Precambrian crustal evolution in the Eastern Desert of Egypt. Am J Sci 285:97–127

Stern RJ, Johnson PR (2010) Continental lithosphere of the Arabian Plate: a geologic, petrologic, and geophysical synthesis. Earth Sci Rev 101:29–67

Takla MA, El Dougdoug AA, Gad MA, Rasmy AH, El Tabbal HK (1989) Gold-bearing quartz veins in mafic and ultramafic rocks, Hutit and Um Tendba, south eastern Egypt. Ann Geol Surv Egypt 20:411–432

Takla MA, El Dougdoug AA, Rasmy AH, Gad MA, El Tabbal HK (1990) Origin of Umm El Eiga gold mineralization, south Eastern Desert, Egypt. Egypt Mineral 2:3–20

Zoheir BA (2008a) Structural controls, temperature-pressure conditions and fluid evolution of orogenic gold mineralization in Egypt: a case study from the Betam gold mine, south Eastern Desert. Miner Deposita 43:79–95

Zoheir BA (2008b) Characteristics and genesis of shear zone-related gold mineralization in Egypt: a case study from the Um El-Tuyor mine, south Eastern Desert. Ore Geol Rev 34:445–470

Zoheir BA (2011) Transpressional zones in ophiolitic mélange terranes: potential exploration targets for gold in the south Eastern Desert, Egypt. J Geochem Explor 111:23–38

The Hoggar Gold and Rare Metals Metallogenic Province of the Pan-African Tuareg Shield (Central Sahara, South Algeria): An Early Cambrian Echo of the Late Ediacaran Murzukian Event?

C. Marignac, D.E. Aïssa, L. Bouabsa, M. Kesraoui and S. Nedjari

Abstract

The Hoggar massif, a part of the Tuareg shield in the Trans-Saharan Pan-African orogen, is endowed in gold and rare metals (Sn, W, Ta, Be). Most of these metals are present at low levels compared to other Precambrian or collisional belts worldwide, but tantalum is concentrated in a series of evolved granitic cupolas, making the Hoggar a promising tantalum province. The Tuareg shield was built in three stages during the convergence of two cratonic masses, the West African Craton (WAC) to the west and the East Saharan craton to the east. The first stage (730–630 Ma; Cryogenian) involved the accretion of island and continental arcs to several cratons. The second stage (630–580 Ma, Ediacaran) was a collisional event, involving (1) northward escape of the Tuareg terranes between the two main cratons, along N-S mega-shear zones with up to 1000 km of lateral displacement; (2) emplacement of large high-K calc-alkaline (HKCA) linear batholiths resulting from mantle-crust interaction through linear lithospheric delamination along the mega-shear zones; and (3) concomitant high temperature-low pressure metamorphism. As a result, the small Eburnean cratons included in the Tuareg shield (In

C. Marignac (✉)
Laboratoire Géoressources, UMR-CNRS 7359,
Ecole des Mines de Nancy, Campus ARTEM,
CS14234, 54042 Nancy Cedex, France
e-mail: christian.marignac@univ-lorraine.fr

D.E. Aïssa · M. Kesraoui · S. Nedjari
Laboratoire de métallogénie,
FSTGAT- USTHB-Algiers, BP32 El Alia,
1600 Alger, Algeria

L. Bouabsa
Laboratoire Géodynamique et ressources naturelles,
Université Badji Mokhtar, Sidi Amar, BP12,
23000 Annaba, Algeria

M. Bouabdellah and J.F. Slack (eds.), *Mineral Deposits of North Africa*,
Mineral Resource Reviews, DOI 10.1007/978-3-319-31733-5_15

Ouzzal; Laouini-Azrou-n-Fad-Tefedest-Egere-Aleksod, or LATEA) were more or less reworked (metacratonization). The third stage (575–540 Ma, late Ediacaran) was limited to the eastern Hoggar province, and involved the intracratonic collision of terranes within the margin of the East Saharan metacraton (Murzukian event, Fezaa et al. 2010). Immediately following the Murzukian event (540–520 Ma, terminal Ediacaran-early Cambrian) was simultaneous reactivation of late (transtensional) mega-shear zones, intrusion of high-level granite plutons related to rare-metal mineralization, and inception of crustal-scale hydrothermal systems and gold mineralization. The granite plutons comprise a series of A-type granites that evolved towards F-rich (topaz-bearing) alaskites, and true peraluminous, F–Na–Li-rich rare-metal granites (RMGs), with evidence of mixing between the two lineages. However, only the RMG suites are associated with Sn–W quartz veins, whereas Ta-rich cupolas may be found either in the Taourirt lineage (Tim Mersoi and highly fractionated Rechla cupolas) or in the RMG suites (Ebelekan)—the rare-metal enrichment being, in any case, of magmatic origin. Emplacement of these late granites was controlled either by the mega-shear zones, as in the Iskel island arc terrane, or by secondary shears of various orientation (N10° E, N50° E, N140° E) that dissect the terranes, as in the LATEA metacraton. The quartz-gold deposits are of the "orogenic gold" class and display contrasting relationships with the shear-zone systems, from close spatial associations with mega-shear zones as in the shear-zone-hosted In Ouzzal deposits (Tirek-Amesmessa) and the Iskel showings, to the very distal association with the Raghane shear zone as in the Tiririne deposits, through the connexion with secondary N10° E shear zones of the In Abeggui deposits in the LATEA. In all of the deposits, the hosting quartz veins were plastically deformed prior to gold deposition, which was uniformly a very late event occurring under brittle conditions, typically during extension. Both gold lodes and RMGs were emplaced into evolving stress-strain fields, involving a rotation of the shortening direction ($\sigma 1$) from ca. N100° E to N30–40° E and finally close to N-S. In addition to rare-metal and gold mineralization, minor fracturing, magma emplacement, and hydrothermal activity are associated with these orientations in the entire Tuareg shield, far to the west of the locus of the Murzukian collision. We therefore conclude that the terminal Ediacaran-early Cambrian Hoggar gold and rare-metal province was controlled, at all scales, by the latest transtensional reactivation of Pan-African mega- and second-order shear zones, following and prolonging the late Ediacaran Murzukian event. Both magmatism and hydrothermal circulation were triggered by the heat flux associated with a renewal of linear lithospheric delamination processes that accompanied this reactivation. All of the known gold and rare metal deposits are hosted by metacratonic terranes with an indisputable Eburnean basement, whereas the juvenile terranes are either very poorly endowed (Iskel) or apparently barren. Although the connection with the gold mineralization seems likely, the reasons remain obscure. It may, however, be suggested that gold endowment is ultimately linked to an influx of mantle-derived CO_2 and the formation of ultra-high temperature granulites in the Eburnean lower crust.

Keywords
Tuareg shield · Eburnean · Neoproterozoic · Collisional orogen · Orogenic gold · Sn · W · Ta · Rare-metal granite · Mega-shear zone · Lithospheric delamination

1 Introduction

The Hoggar massif in southern Algeria is the main component of the Tuareg shield, which includes the Adrar des Iforas (Mali) and the Aïr (Niger) massifs (Fig. 1). This shield comprises a Pan-African collage of as many as 23 terranes, either juvenile or reworked from older Archaean or Paleoproterozoic terranes, or both (Black et al. 1994). Following the Pan-African events, the Tuareg shield was unconformably covered by sedimentary rocks of Paleozoic age (Saharan basin) that were eroded in two stages, first at the end of the Jurassic, and the second starting in the late Eocene (ca. 35 Ma), with an intervening recurrence of subsidence and sediment deposition (up to 3 km of Cretaceous and Eocene sediments, now totally eroded; Rougier et al. 2013). The final exhumation was coincident with Cenozoic volcanism, associated with a "Hoggar swell" (Rougier et al. 2013). The Tuareg shield (500,000 km^2) is presently a topographic high reaching 2400 m above sea level and surrounded by flat-lying Paleozoic sedimentary rocks of the Tassilis plateau.

The Hoggar massif has long been known for granite-related Sn and W mineralization. More recently, as a result of exploration carried out between 1969 and 1995 by the National Bureau of Mining and Geology of Algeria (ORGM), numerous gold deposits and occurrences have been discovered (Fig. 1). These gold deposits, all of the quartz-lode type, are hosted either in shear zones, granites, or (meta)sedimentary rocks (Aissa and Bedouhène 1988; Semiani et al. 2004). More than 100 rare-metal and 400 gold occurrences have been identified. Nevertheless, the total amount of gold known in the Hoggar part of the Tuareg shield (totalling between 120 and ≥200 t Au, according to various sources) is very low, compared to the endowment of other Precambrian shields worldwide (e.g., de Wit and Thiart 2005). In the same way, the ca. 23.5 kt of W present in the Hoggar (Mining Journal 2009) may be compared with the several 100 kt of W in the West European Variscan belt: indeed, a similar amount of about 30 kt is contained solely in the French Massif Central (Marignac and Cuney 1999). With several evolved cupolas reportedly having high Ta contents of ≥150 ppm (e.g., Ebelekan: Nedjari 2006; Rechla: Kesraoui 2005; Tim Mersoi: Abed 2009), the Hoggar may thus be considered a potential tantalum province.

In this paper, we review the main gold and rare-metal deposits and occurrences of the Hoggar metallogenic province, in order to (1) elucidate relationships with post-collisional events in the Tuareg shield, and (2) discuss the reasons for this apparently overall low metal endowment in the shield.

2 Geological Background: The Tuareg Shield

The Tuareg shield, part of the Trans-Saharan orogen, is a Pan-African collage of terranes that formed by the dissection of an Eburnean cratonized region (ca. 2 Ga, associated with formation of the Nuna supercontinent) during the dismembering of the Rodinia supercontinent in the Neoproterozoic. The resulting assemblage (part of the ephemeral Gondwana supercontinent) includes variably reworked (granitization, internal deformation) old cratonic fragments, which are characterized as "metacratons" (Abdelsalam et al. 2002; Liégeois et al. 2013), and juvenile Neoproterozoic terranes (oceanic and arc terranes, the latter locally with an older crust = continental

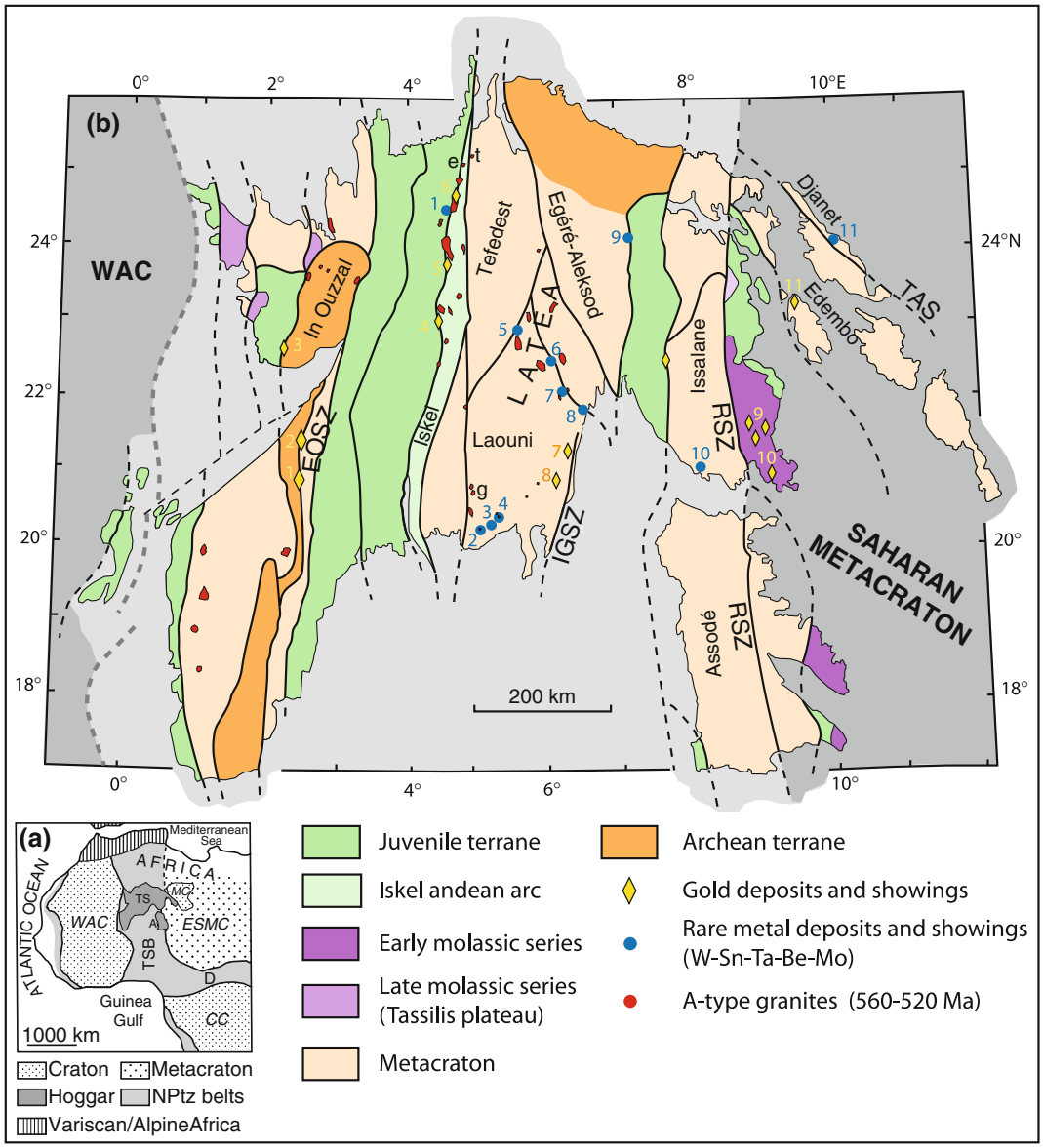

Fig. 1 Terrane architecture of the Targui shield and location of late granites, gold occurrences, and rare-metal mineralization. Terrane subdivisions after Black et al. (1994). *LATEA* is the acronym for the Laouni-Tefedest-Egéré-Aleksod-Arou-n-fad super-terrane. *WAC* Western African Craton; *EOSZ* East Ouzzal Shear Zone; *IGSZ* In Guezzam Shear Zone; *RSZ* Raghane Shear Zone; *TASZ* Tin Amali Shear Zone. Gold districts, deposits, and main showings (after Semiani et al. 2004): *1* Amesmessa; *2* Tirek; *3* In Hibaou; *4* Silet district; *5* Tin Felki (or Tekouyet) district; *6* Tesnou district; *7* In Abeggui district; *8* Tin Ezzerarine; *9* Tiririne district; *10* Hanane; *11* Tin Massaret-Tin Zekri. Rare metals deposits and main showings: *1* Tesnou (Sn–W); *2* Sedis (W)-Rechla; *3* Tamazaror (W-Sn); *4* Nahda (W–Be–Li); *5* Taessa (Sn–W); *6* In Tounine-Aheledj (W–Sn); *7* Tin Amzi-El Karoussa (W–Ta)-Alemeda (Sn–W–Ta); *8* Bachir (Sn–W); *9* Tin Akala (W); *10* Ebelekan (Sn–Ta); *11* Djilouet. Evolved plutons: *e* Egelé; *g* Guerrioun; *t* Tim Mersoi

arcs). Several of the terrane boundaries ended up as N-S mega-shear zones that are the main characteristic of the present-day shield. In particular are the two In Ouzzalian shear zones delineating the In Ouzzal metacraton, the 4° 50′ shear zone separating the Iskel island arc terrane from the Laouini-Azrou-n-Fad-Tefedest-Egere-Aleksod (LATEA) metacraton, and the Raghane (or 8° 30′) shear zone that is the western boundary of the Saharan metacraton (Liégeois et al. 2003) (Fig. 1). Along these mega-shear zones, lateral displacements of several hundred kilometers are registered, and up to 1000 km along the Raghane shear zone (Henry et al. 2009).

In the Tuareg shield, the Pan-African orogeny (750–580 Ma) was a two-stage process (Liégeois et al. 1994; Black et al. 1994; Liégeois et al. 1998; Caby 2003; Liégeois et al. 2003): (1) during the early Pan-African orogeny, from 750 to 660 Ma (Cryogenian), oceanic arcs were accreted onto microcratons and oceanic basins were created to the west, while in the east, oceanic and/or arc terranes were accreted to the margin of the East Saharan (meta)craton—the present-day Barghot and Aouzegueur terranes—starting there from the Tonian (ca. 900 Ma) (Henry et al. 2009); and (2) during the late Pan-African orogeny, from 660 to 580 Ma (Cryogenian-Ediacaran), these early collages were deformed between two giant cratonic masses, the 2 Ga Western African Craton (WAC) to the west, and the East Saharan metacraton to the east, resulting in northward escape of the Tuareg terranes along N-S mega-shear zones (Nouar et al. 2011; Liégeois et al. 2013). During that period, large high-K calc-alkaline (HKCA) batholiths were intruded along linear N-S zones paralleling the mega-shear zones, and extensive migmatization affected the metacratons (e.g., Assodé-Issalane terrane), related to linear lithospheric delamination along the submeridian mega-shear zones (Azzouni-Sekkal et al. 2003; Abdallah et al. 2007).

Starting at ca. 580 Ma, post-collisional stages of the Pan-African orogeny are marked in the western and central Hoggar by late movements along still-active mega-shear zones, under upper-crustal conditions. Other post-collisional events include the production of new HKCA granitoid melts, which evolved towards alkaline or even peralkaline (western part of Tuareg shield) magmatism (Liégeois et al. 1998; Azzouni-Sekkal et al. 2003). The latest activity along the mega-shear zones was transtensional and is dated as late Ediacaran to early Cambrian (540 Ma; Boullier et al. 1986) or slightly younger (520 Ma; Paquette et al. 1998). According to recent studies (Henry et al. 2009; Fezaa et al. 2010), these post-collisional events were the distal result of the formation, in the eastern Hoggar, of an intracontinental transpressive orogen driven by westward drift of the Murzuk craton (which is concealed under the large Mesozoic Murzuk basin, and revealed by geophysics, with a LAB at 250 km), a part of the East Saharan metacraton (Liégeois et al. 2013). During this late Ediacaran (575–540 Ma) Murzukian orogeny (Fezaa et al. 2010), the eastern margin of the Saharan metacraton was reactivated, and the Edembo and Djanet terranes collided along the dextral Tin Amali shear zone (TASZ). As for the main Pan-African events, a large syn- to post-kinematic HKCA batholith was emplaced in the Djanet terrane and extensive migmatization affected the Edembo terrane, both driven by linear delamination along the terrane boundary (Liégeois et al. 2013). The NW-SE shear zones separating the eastern Hoggar terranes (TASZ, Edembo-Aouzegueur boundary) merged with the Raghane SZ, which as a consequence was reactivated on its northern part, causing the deformation and the metamorphism of the Pan-African molassic basin of the Tiririne Group (Henry et al. 2009 and references therein).

2.1 The East Hoggar and Central Hoggar Metacratons

The reworked cratonic areas comprise (Fig. 1) the Kidal, In Ouzzal and Iforas terranes to the west; the LATEA super-terrane to the centre (dissected by the Pan-African shearing into the separate terranes of Laouni, Tefedest, Egéré-Aleksod and Azrou-n-Fad); and the Assodé-Issalane terrane to the east.

The In Ouzzal terrane (Ouzegane et al. 2003): The In Ouzzal granulitic unit (IOGU) is separated

from the Kidal terrane to the west by the sinistral West Ouzzal Shear Zone and from the Paleoproterozoic Tin Zaouatène terrane to the east by the dextral East Ouzzal Shear Zone (EOSZ). The In Ouzzal terrane is apparently the less transformed metacraton of the Tuareg shield, being only affected by the two bounding shear zones and a limited number of internal ductile to (mainly) brittle fault zones, with in addition the intrusion of post-collisional granites. The terrane is made of Archean felsic orthogneiss and subordinate supracrustals of various lithologies, that were affected by the ca. 2 Ga Eburnean HT-granulitic event (up to 1000 °C and 1.1 GPa). The Archean gneisses define two groups, with TTG gneiss older than 3 Ga and subalkaline gneiss dated at 2.6 Ga. They are cut by Eburnean cordierite-bearing monzogranite gneiss. Metasedimentary rocks define small synformal belts within the orthogneiss and comprise metapelites, marbles, quartzites (sometimes magnetite-rich) and aluminomagnesian granulites, with scarce stratiform mafic and ultramafic rocks (metacumulates).

The EOSZ (Attoum 1983) is a 1000-km-long mylonite belt, 1.5–3 km wide, with a central ultramylonite belt no more than 50 m wide on the IOGU side, containing discontinuous quartz veins that are stretched all along (see below). Marble beds from the In Ouzzal synclines are still recognisable as boudinaged lenses parallelising the mylonite foliation. Retrogressive metamorphism occurred concurrently with deformation and resulted in rehydration of earlier metamorphic rocks under low-grade conditions (biotite-chlorite-actinolite-carbonate paragenesis). Syn-kinematic mafic bodies (mainly, gabbros) are intrusive into the mylonite, and stable isotope (O, C) studies showed that the early CO_2-rich fluids percolating the shear-zone were of mantle derivation (Marignac et al. 1996). Thus, the EOSZ is of lithospheric scale.

The LATEA super-terrane (Black et al. 1994; Peucat et al. 2003; Liégeois et al. 2003): All the terranes that constitute the LATEA metacraton contain a basement of Archean (Egéré-Aleksod and Azrou-n-Fad terranes: Peucat et al. 2003) or Paleoproterozoic (Tefedest and Laouni terranes) gneiss affected by the Eburnean event (granulite facies) (Ouzegane et al. 2001). Paleoproproterozoic supracrustal sequences are of shelf facies, including quartzite, BIF, marble, calc-silicate gneiss and amphibolite, or metagraywacke. The Pan-African reworking (metacratonisation) includes (1) the thrusting of Neoproterozoic volcano-sedimentary terrains of oceanic or insular arc affinities, with ophiolites or eclogitic facies in some units; and (2) a new metamorphic event, under the greenschist- to amphibolite-facies conditions of a HT-LP metamorphism. The Laouni terrane is particularized by the numerous late- to post-kinematic high-level granite plutons that were emplaced from 580 to ca. 520 Ma (Cheilletz et al. 1992; Azzouni-Sekkal et al. 2003).

The Issalane-Assodé terrane (Bertrand et al. 1978; Liégeois et al. 1994): The Assodé-Issalane metacraton was initially part of the LATEA super-terrane (Liégeois et al. 2013), with the same Paleoproterozoic basement and supracrustal sequences. It was however far more strongly reworked by the late HT-LP metamorphic event, with pervasive migmatisation and injection of large bodies of late-kinematic leucocratic Renatt granites, issued from the partial melting of the middle crust, and dated at ca. 600 Ma (in Fezaa et al. 2010). According to Cottin et al. (1998), the source of the Renatt-type granite melts is made of Archean granulites with 3.1–2.5 Ga model ages (i.e., very similar in age to the In Ouzzal gneisses).

2.2 The Young (Juvenile) Terranes

Two young terranes (Iskel and Aouzegueur) are the host for significant gold deposits.

The Iskel terrane (Caby 2003): The Iskel terrane is likely of the Andean-type margin, and was accreted onto the LATEA craton during the late Pan-African event (presently the 4° 50′ megashear zone). It comprises an old shelf series, the basement of which remains unknown, which was affected by a first tectono-thermal event resulting in isoclinal recumbent folds and low-grade metamorphism, and the intrusion of giant HKCA batholiths at ca. 870 Ma (e.g., Tin Tekadiouit batholith). Post-dating these events, Neoproterozoic rocks (pelitic series and calc-alkaline

andesites and rhyodacites), were in turn folded (N-S upright folds) and metamorphosed into the greenschist facies. This second tectono-thermal event was coeval with the retrogression of the mylonites in the N-S mega-shear zones bordering the terrane and the HKCA granitoids (chlorite, calcite, and epidote), affected by a N-S schistosity. In the adjacent In Tedeini terrane to the west, the HKCA Immezzarene batholith, intrusive into Neoproterozoic siliciclastic low-grade rocks, is syn-kinematic with the dextral ductile 4° 13′ shear zone at the western boundary of the Iskel terrane, and dated at 583 ± 7 Ma (Bertrand et al. 1986), the likely age of the second tectono-thermal event in the Iskel terrane.

Like in the adjacent Laouni terrane, there are numerous (≥20) high-level HKCA granite plutons evolving towards alkaline magmatism, the so-called "Taourirt granites" (Azzouni-Sekkal and Boissonnas 1993; Azzouni-Sekkal 1995; Azzouni-Sekkal et al. 2003). They were dated at ca. 540 to *ca.* 520 Ma (Cheilletz et al. 1992), and their emplacement was mainly controlled by the late dextral re-activation of the 4° 13′ shear zone (Azzouni-Sekkal and Boissonnas 1993; Azzouni-Sekkal et al. 2003) with a ca N50° E shortening direction. The 523 ± 1 Ma Tioueine pluton is considered coeval with the latest increments of the dextral activity of the 4° 13′ shear zone (Paquette et al. 1998).

Aouzegueur (*Hoggar*: Bertrand et al. 1978; Caby and Andreopoulos-Renaud 1987) *and Barghot* (*Aïr:* Liégeois et al. 1994) *terranes:* The Aouzegueur and Barghot terranes were docked to the Saharan metacraton at an early Pan-African stage (Abdelsalam et al. 2002). They comprise an Eburnean basement, including juvenile granitic orthogneisses dated at 1.92 Ga (Nouar et al. 2011), and a complex of three superposed slices (platform, ophiolitic and arc units) emplaced during the early Pan-African event.

Following the early Pan-African event, a thick (up to 8,000 m) Neoproterozoic molassic sequence of immature siliclastic sediments (Tiririne Group) was unconformably laid upon the erased Barghot/Aouzegueur collage (the Proche-Ténéré terrane of Liégeois et al. 1994). In the Hoggar, the Tiririne Group was folded into a linear fold belt during the Murzukian event, in response to the reactivation of the dextral Raghane shear zone, simultaneously retrogressed into the greenschist facies. Deformation and metamorphism of the Tiririne Group increase from south to north. South from 22° 30′, the folds are very faint (dome and basins), without schistosity, and the metamorphism is of the uppermost greenschist facies. Numerous intrusions of a bi-modal magmatism are widespread in the Tiririne Group, with in particular swarms of N40° E–50° E vertical diabase dikes.

The age of the Tiririne Group is poorly constrained between ca 600 and ca 550 Ma. We have observed the unconformable resting of the Tiririne series onto the ultramylonites of the Raghane shear zone, inactive only since ca. 600 Ma (Liégeois et al. 1994; Henry et al. 2009). On the other hand, the Tiririne Group is overprinted by granitic plutons dated (Rb/Sr) at ca. 550 Ma (Henry et al. 2009). A significantly older age (>660 Ma) proposed by Bertrand et al. (1978) must be rejected.

2.3 The Saharan Metacraton

The Edembo and Djanet terranes are part of the Saharan metacraton, as defined by Abdelsalam et al. (2002). Recent work (Fezaa et al. 2010) has shown that the Djanet and Edembo terranes represent an intracontinental transpressive orogen affecting the margin of the Saharan metacraton at ca. 575–ca. 555 Ma. In this context, the Djanet terrane would represent the reactivated border of the craton (metacratonic margin), whereas the Edembo terrane would have suffered lithospheric delamination (guided by the Tin Amali shear zone) and intense migmatization (Fezaa et al. 2010).

The Djanet terrane (Fezaa et al. 2010): The Djanet terrane is unconformably covered to the east by the Paleozoic sedimentary rocks of the Tassilis plateau. The terrane consists in a metasedimentary clastic series of greenschist facies (Djanet Group) and a suite of granite intrusions, beginning with the giant syn-to late-kinematic HKCA Djanet batholith (571 ± 16 Ma) and ending with evolved sub-circular leucogranites of Taourirt affinity

(Oulebsir 2009), of which the Djilouet pluton displays a core of Li-muscovite-topaz granite with magmatic columbo-tantalite and cassiterite. The Djanet Group was coeval with the Tiririne Group, to which it is otherwise very similar (Liégeois et al. 2013).

3 Gold Deposits and Occurrences

All of the gold deposits and occurrences known in the Tuareg shield are of the quartz lode type. Gold deposits are found mainly in five terranes: In Ouzzal, Iskel, LATEA, Aouzegueur, and Edembo

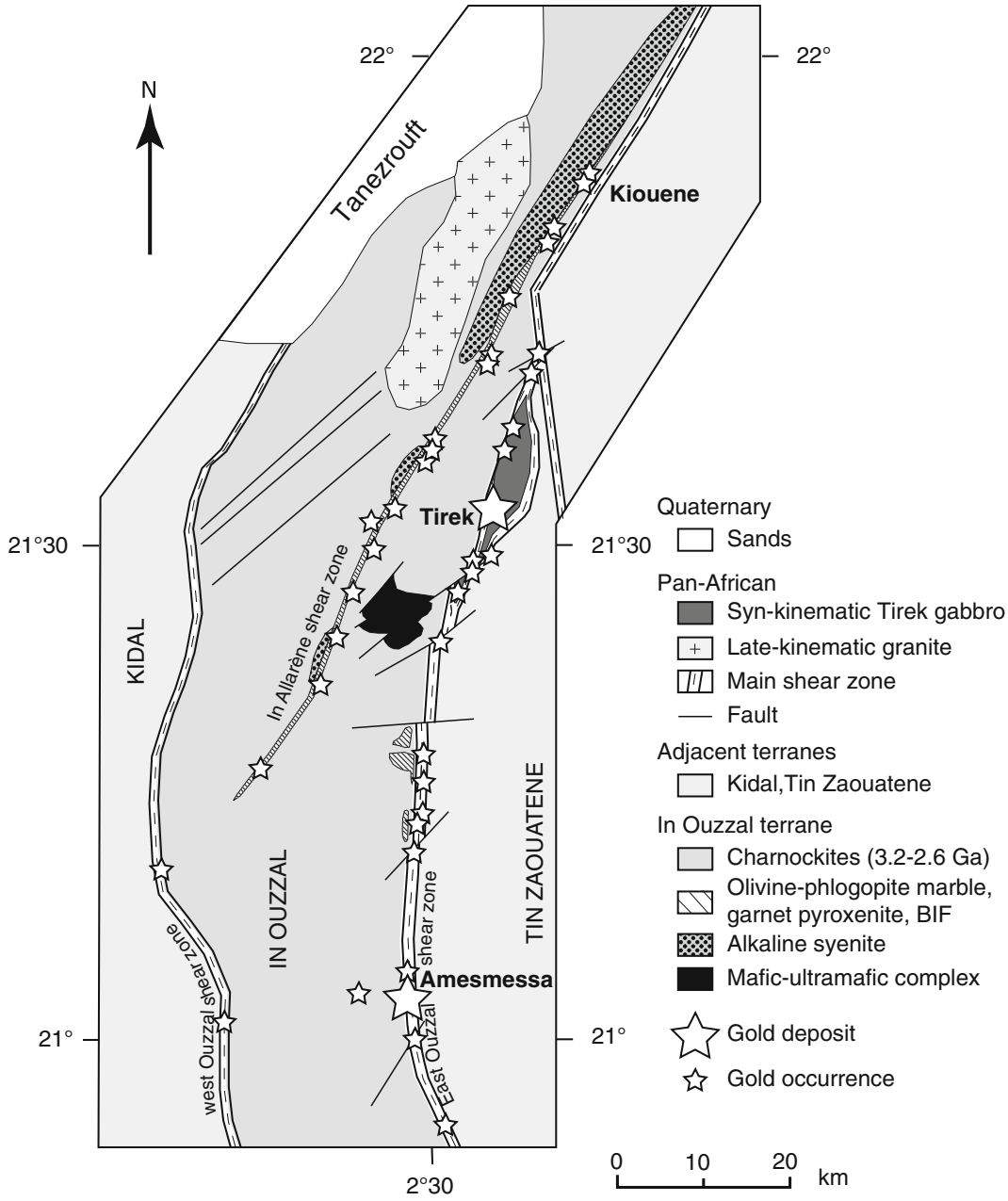

Fig. 2 Gold deposits in the In Ouzzal terrane (from Semiani et al. 2004)

(Fig. 1). However, according to ORGM unpublished data (cited by Ferkous and Monié 2002), three districts concentrate most of the gold reserves (120–200 t Au) until now documented in the Hoggar part of the Tuareg shield. To the west, the Tirek-Amesmessa district (nos. 1–2 in Fig. 1) is hosted by the EOSZ that contains ~75 t of gold, including the small (less than 2% of total) Kiouène deposit (see Fig. 2); a possible total of ca. 120 t of gold was assessed by ORGM. In the center, the Silet and Tekouyet (or Tin Felki) districts (nos. 4–5 in Fig. 1), with no more than 3–9 t of gold, are hosted chiefly in granite batholiths of the Iskel terrane. Within the Laouni terrane of the LATEA, the Neoproterozoic volcanosedimentary-hosted In Abeggui deposit contains ~10 t gold. To the east, the Tiririne district (no. 8 in Fig. 1), with about 8–30 t of gold (depending upon sources, 24 t being the most commonly tonnage proposed), is mainly within the Tiririne Group of the Aouzegueur terrane.

3.1 In Ouzzal Deposits: The Tirek-Amesmessa District

The Tirek-Amesmessa district (Fig. 2), hosted by the EOSZ, contains more than 100 minor gold occurrences along 70 km between the two main deposits of Tirek (to the north) and Amesmessa (to the south). With 44 and 18 t of gold, respectively, the Amesmessa and Tirek deposits contain half the gold concentrated along the EOSZ. The mean gold grade in the two main deposits is 18 g/t, but with a great variability (0.5–500 g/t). In addition, a gold halo is developed within the alteration envelope (beresite, see below) of the quartz lodes, with contents varying from 1 ppb to 15 ppm (ORGM, unpublished data). This district is by far the best studied of all within the Hoggar province, being well described in several publications (e.g., Ferkous and Leblanc 1995; Semiani 1995; Marignac et al. 1996; Ferkous and Monié 2002; and references therein).

Alteration and mineralization (Ferkous and Leblanc 1995; Marignac et al. 1996): The mineralized part of the EOSZ is characterized by a 20-m-wide alteration zone in the center of the ultramylonite belt, with a quartz-pyrite-sericite (phengite)-Fe-dolomite association (the so-called beresite) that overprints the mylonite foliation. Branching on the main N-S beresite belt, lesser N10° E- to N40° E-trending beresite belts also cut the mylonite foliation for lengths varying from 100 to 300 m.

The mineralized quartz veins trend either N-S along the beresite belt (type-I quartz veins: Amesmessa) or N30–40° E offsetting faults (type-II quartz veins: Tirek). The latter are only gold-rich where crossing the ultramylonite belt, the richest being hosted by the Tirek syn-kinematic gabbro, whereas the former are only gold-rich where associated with either syn-kinematic mafic intrusions or boudinaged marbles. This strong lithological control on the location of rich ore shoots is likely related to a kind of pH effect on gold deposition (Marignac et al. 1996). The gold-bearing veins are organized in dense swarms of subvertical veins (several 100 m in length, up to 1000 m), which are commonly irregular or boudinaged (lens-shaped veins), with thicknesses varying from a few centimeters to up to 3 m (Fig. 4). These veins extend downdip to 450 m, but show a decreasing gold content with depth.

Both beresite and type I veins (pyrite-bearing) were first mylonitized, then brecciated, during very late increments of N-S dextral shearing along the EOSZ. The type II veins likely filled late tensional joints along the shortening direction associated with the dextral shearing. In contrast to type I veins, the type II veins only experienced brittle deformation that accompanied a later stage of reactivation of the N40–50° E structures, as dextral cataclastic faults offsetting the earlier N-S shear zone. This brittle deformation is equally recorded in the type I veins.

The gold mineralizing stage post-dated these events and was apparently coeval with extensional conditions (Marignac et al. 1996). First, Fe-poor sphalerite (type I veins) or pyrite (type II veins), then galena and native gold, were successively deposited in a network of anastomosing veinlets that developed along intergranular joints in mylonitic and/or cataclastic quartz. Gold and galena deposition were strictly contemporaneous as demonstrated by textural relationships

(Marignac et al. 1996). The ore association includes minor chalcopyrite (Tirek), rare native bismuth and bismuthinite, and very rare hessite (Ag_2Te) and altaite (PbTe). Native gold has a quite constant fineness (around 740) and systematically contains appreciable bismuth (avg 0.4 wt%).

P-T-t evolution (Marignac et al. 1996): The P-T-t evolution of the EOSZ was reconstructed using mineral and fluid inclusion data. Early hydrothermal stages (pyrite-bearing beresite alteration, formation of type I and II quartz veins) that span ductile to brittle conditions, occurred at 500–300 MPa and 500–300 °C, and involved the circulation of aqueous-carbonic fluids. Ferkous and Monié (2002) provided similar estimates, of 400–500 °C and 400 MPa, down to 260–350 °C and 250 MPa. However, no gold mineralization was associated with these typical mesozonal events (sensu Gebre-Mariam et al. 1995). Rare gold grains are included in the earlier pyrite, but they were clearly introduced during the gold stage. Following a pressure drop related to the inception of extensional faulting, the mineralizing stage was characterized by the percolation through the EOSZ of hot (400–350 °C), Ca-rich brines. Gold deposition occurred at a depth of ca. 5 km, due to cooling (down to ca. 200 °C) and mixing of these brines with a cold, low-salinity water infiltrated downwards from the surface along the EOSZ.

Source of ore-forming fluids and metals (Marignac et al. 1996): Stable isotope data indicate that the late Ca-rich brines percolating through the EOSZ were of basinal derivation. These brines are interpreted as having originated in the (now eroded) late Pan-African molasse basins and then infiltrated deeply into the In Ouzzal basement.

Lead isotope data (Fig. 3) are thought to demonstrate that lead—and by inference the coeval gold—was leached from the Archean granulitic gneiss in the In Ouzzal terrane. Any contribution from the nearby Paleoproterozoic Tin Zaouatène terrane seems precluded, since the array of Tirek and Amesmessa data in Fig. 3 is best interpreted as a mixing line beween Archean gneiss compositions. In addition, lead isotope compositions for galena from gold barren quartz veins in the Tin Zaouatène terrane are clearly distinct from the In Ouzzal deposits (Fig. 3). The

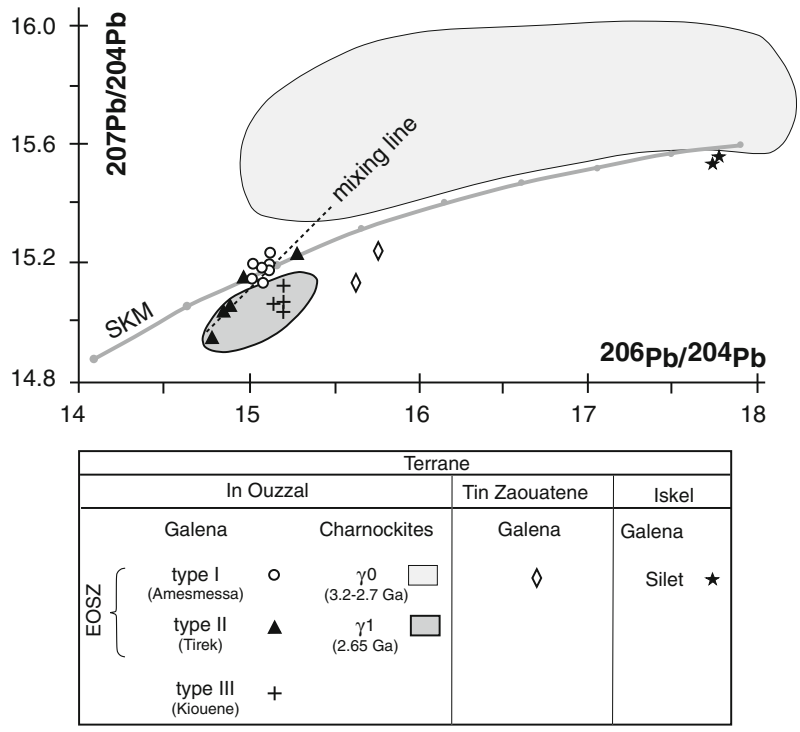

Fig. 3 Lead isotope data for In Ouzzal (Tirek, Amesmessa, Kiouène) and Iskel (Silet) gold deposits (from Semiani 1995). The lead isotope data for the Archean In Ouzzal granulitic orthogneisses are plotted for reference (γ0 TTG, γ1 subalkaline gneisses). Data for galena from barren quartz veins, located 2.5 km east of EOSZ in Tin Zaouatene Paleoproterozoic terrane (see Fig. 2), are plotted for comparison. SKM is Stacey and Kramers (1975) evolution curve for mantle

In Ouzzal gneiss has a mean gold content of about 3 ppb (Marignac et al. 1996), which is elevated compared to rocks of equivalent felsic granulite terranes worldwide (e.g., <1 ppb in Yangtze craton in China; Gao et al. 1992). Unpublished ORGM ICP-MS analyses from the In Ouzzal Archean rocks yield gold concentrations between 2 and 9 ppb, which are consistent with the previous data. Ferkous and Leblanc (1995) measured a relatively high gold content of 23 ppb for an Archean gneiss (sample 21, their Table 1), but as the sample location is unclear—it could have come from nearby the EOSZ—this elevated content could as well represent a gold halo of the mineralization, since Ferkous and Leblanc (1995) reported similar high values (10–30 ppb Au) in all rock types within the ultramylonite belt. In the Archean enderbitic and charnockitic gneisses, the most plausible host mineral for the gold is magnetite, which is known to concentrate gold in magmatic rocks (Bornhost and Rose 1986), but direct evidence for this hypothesis is as yet absent.

Timing of the gold event: U/Pb dating of single zircons from the Tirek syn-kinematic gabbro yielded three distinctive age peaks, at 630, 610, and 535 Ma (Marignac et al. 1996). Whereas the oldest age of 630 Ma clearly records the timing of deep ductile shearing and syn-kinematic emplacement of the gabbro in the EOSZ (see section II above), the younger ages likely record hydrothermal imprints. This interpretation is confirmed by $^{40}Ar/^{39}Ar$ age of 611 Ma (Ferkous and Monié 2002) for phengite from the Amesmessa beresite, very close to the 610 Ma U/Pb age. This is likely the age of the late-kinematic hydrothermal alteration along the ultramylonite belt in the EOSZ. These authors also obtained a 525 ± 5 Ma resetting age in syn-kinematic biotite from the ultramylonites at Amesmessa, again close to the 535 Ma U/Pb age. Given the high temperature of more than 350 °C for the Ca-rich brines that percolated the EOSZ during the gold mineralizing stage, as compared to the low closure temperature of biotite (ca. 300 °C), it may be safely concluded that this ca. 530 Ma age records the gold mineralizing event.

A genetic model: Given all of the previous data, the favored model by Marignac et al. (1996) proposes that gold was leached from the In Ouzzal felsic granulites by Ca-rich brines and channeled towards the EOSZ (or the In Allarène shear zone) along the numerous, late Pan-African NE-SW fault zones. A fluid inclusion study in and around some of these late NE-SW faults demonstrated that early Eburnean carbonic inclusions within the Archean gneiss were removed and replaced by hot Ca-rich brine inclusions (Coulibaly 1994). In the most permeable zones (represented by cataclastic quartz in the reactivated major shear zones), these gold-bearing fluids encountered cold,

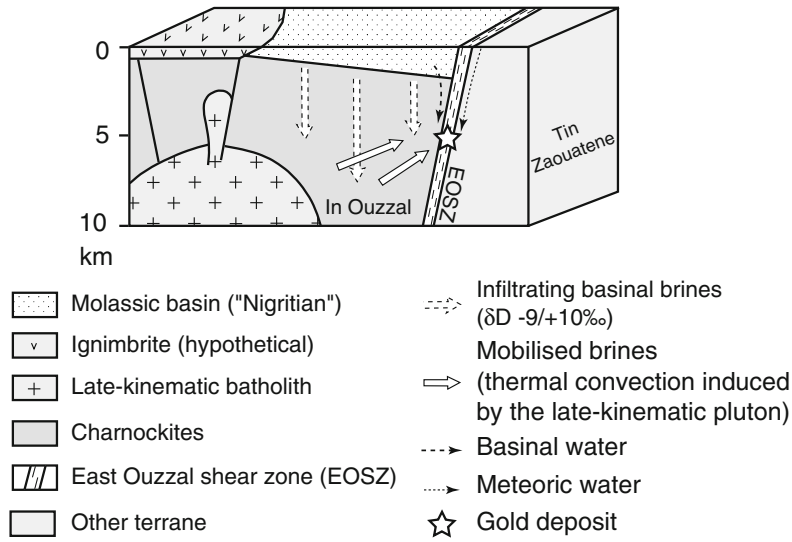

Fig. 4 Genetic model for East In Ouzzal Shear Zone-hosted gold deposits (from Marignac et al. 1996)

downgoing, low-salinity fluids and "reactive" rocks, and as a result deposited gold at ca. 200 °C. This interpretation is at variance with the model of Ferkous and Monié (2002) in which the older, deep-seated CO_2-rich fluids played the key role in gold transport and deposition.

It is known that in the northern part of the In Ouzzal terrane and in the Adrar des Iforas to the south, voluminous granite plutons were intruded at 540–530 Ma (e.g., Fabre 1988). Therefore, the Ca-rich brines are thought to have been heated and mobilized by the coeval intrusion of a late Pan-African concealed batholith (Fig. 4).

3.2 The Iskel Deposits (Semiani et al. 2004)

In the Iskel terrane, two contrasting styles of gold deposits are observed: the Silet and Tin Felki lode systems and the Tesnou lode swarms (Fig. 5). At present, the main gold resources are in the Silet and Tin Felki districts. Gold contents vary from 0.5 to 36 g t^{-1}; in the southern district, the Tekouyat deposit has 2.1 t gold @ 15 g t^{-1}. A gold halo (ca. 100 ppb) is developed up to 10 m from the veins.

The Silet and Tin Felki (Tekouyat) districts (Semiani et al. 2004): All known deposits are hosted in the large N-S-trending Tin-Tekadiouit batholith (Fig. 5). Although quartz veins are present throughout the batholith, including a giant system several tens of kilometers long and 4–8 km wide that parallels the In Tedeini-Iskel terrane boundary (the so-called 4° 13′ shear zone), these quartz veins only contain gold where mylonitic/cataclastic corridors several kilometers long, in a 50° E direction, branch onto the terrane boundary. The mineralized quartz veins are generally parallel to the early N50° E mylonitic foliation, and some are boudinaged. Others strike N-S. The early Q1 quartz was thoroughly deformed under ductile conditions, but where mineralized with gold, was systematically reworked under brittle conditions (brecciation, cataclasis), yielding Q2 saccharoidal, microcrystalline quartz. This quartz texture is the main criterion for identifying mineralized veins from barren ones, the latter being uniformly undeformed. A broad propylitic alteration is developed in the cataclastic band, involving chloritization of ferromagnesian minerals in the host granite. A few centimeters from the mineralized quartz veins, chloritization is overprinted by a quartz-sericite-pyrite-carbonate alteration ("beresite") or in places (at Tekouyat) a greisen-style alteration.

The mineralization developed according to the same paragenetic succession as in the In Ouzzal deposits, first with pyrite and chalcopyrite, then coeval deposition of galena and gold. Galena is a characteristic mineral of the Silet and Tekouyat districts; gold contents correlate with galena abundance. Bulk analyses of the ore show the systematic presence of bismuth. Compared to the In Ouzzal deposit, however, sphalerite is typically absent.

Lead isotope analyses of two galena samples from the Silet district (Timgaouine deposit) yield a 950 Ma model age (Fig. 3) that is only slightly older than the 870 Ma age of the Tin Tekadiouit batholith hosting the gold mineralization. These data are consistent with the leaching of lead and gold from the juvenile crust of the Pan-African Iskel arc.

The Tesnou district (Chaouche 2008): In the Tesnou district, gold deposits and showings are dispersed (Fig. 5) but display the same kind of tectonic and hydrothermal controls: (1) localization in broad linear zones of quartz veins, along both the In Tedeini-Iskel (4° 13′) and Iskel-LATEA (4° 50′) boundaries; (2) spatial association with a regional propylitic alteration; (3) overprinting of early Q1 quartz (plastically deformed) by a more or less cataclastic microcrystalline Q2 quartz; and (4) development of quartz-muscovite-carbonate alteration along the veins. The cataclastic Q2 quartz exerts a permeability control by focussing the subsequent fluid flow, and providing a trap for ore deposition. This cataclastic event may therefore be seen as a "mechanical preparation (or maturation)" of the quartz vein before inception of the mineralizing process. The locations of the mineralized quartz vein showings are further controlled by (1) proximity of mafic magmatic enclaves from granites of the Tin Tekadiouit family, diorite for

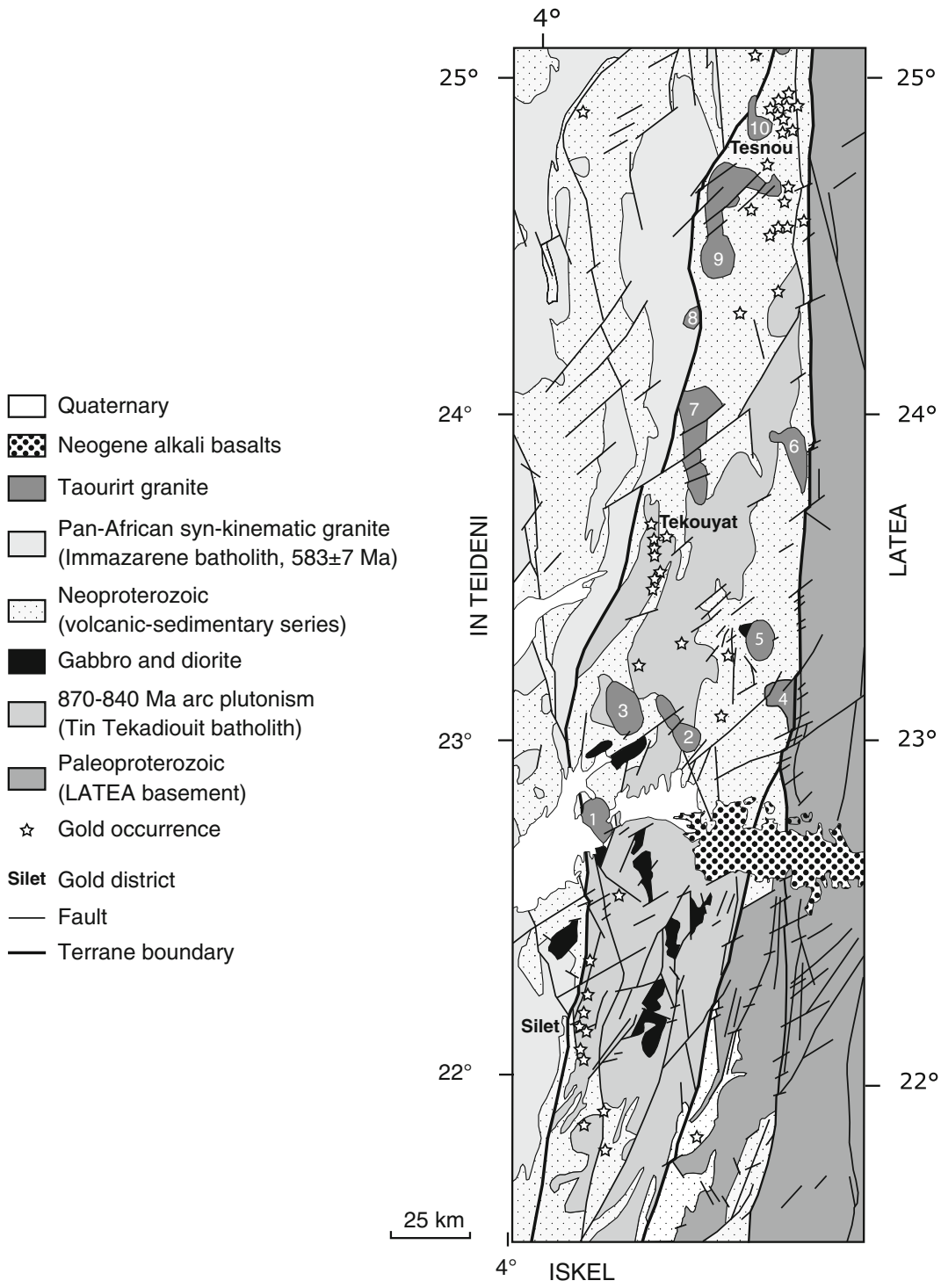

Fig. 5 Geological setting of Iskel gold occurrences (from Semiani et al. 2004). Note close relationships between gold occurrences and both Iskel-In Tedeini boundary and Taourirt granites. Key to numbered Taourirt granites (Azzouni-Sekkal 1995): *1* Tioueine; *2* Taharait-n-Abror; *3* Tin Erit; *4* Teg Orak; *5* Tihaliouine; *6* Tan Ataram and Tikertine; *7* Isseddienne and Imehellatène; *8* Ait Oklan; *9* Tin Ezzour, Tesnou and Tin Akkor; *10* Sildrar

instance as host for the Assouf Mellene veins; and (2) proximity of zoned Taourirt felsic plutons (Tesnou, Seldrar). Tourmaline is most common in gold-bearing veins, whereas actinolite-bearing quartz veins are uniformly barren. The mineral assemblage is generally simple: quartz-tourmaline-muscovite-(sericite)-pyrite-gold (electrum). As in the southern and central districts, sphalerite is not documented in the Tesnou district. Native gold grains (5–100 μm) occur in microcracks and are uniformly a very late phase. Tourmaline formed in two stages, a first generation of radiating ("en rosette") grains, which are brecciated and sealed by a second generation with which gold is preferentially associated (likely a semi-conductor effect: Y. Fuchs 2009, personal communication).

3.3 The LATEA (Laouni) Deposits: In Abeggui District

The In Abeggui deposit, discovered in 1971, contains about 10 t gold @ 3.59 g/t (1.1 t @ 7 g/t); 0.6 t of gold was mined in 2005. Another significant showing is Tin Ezzerarine (Fig. 6). The location of known gold occurrences is evidently controlled by the Neoproterozoic belts (Fig. 6). The Neoproterozoic formations include a volcanosedimentary sequence (bi-modal volcanism) that was deformed (N-S upright folds) and metamorphosed (low-grade LP-HT) and a rhyodacite ignimbrite sequence that is unconformably overlain by early Paleozoic strata of the Tassilis plateau (Serguine et al. 1974, in Boutrika 2006).

Geological setting of the In Abeggui district: At the regional scale, two sets of fractures are dominant (N10° E and N50° E) and may be interpreted as conjugate shears with a N30° E shortening (σ1) direction. In particular, the In Abeggui district appears to be located in a dextral relay of a set of N10° E dextral faults (Fig. 6). These faults are the northern termination of the In Guezzam normal fault that presently marks the boundary with the Paleozoic Tin Serririne basin (syncline). However, the In Guezzam fault is older, and likely was coeval with emplacement of the late Pan-African In Telloukh granite (a biotite-amphibole syenogranite); the latter is cut by Precambrian diorite dikes that record dextral activity on the In Guezzam fault (Henry et al. 2007).

At In Abeggui, a large biotite granite pluton is intrusive into the Neoproterozoic series (Fig. 7). Numerous gabbro-diorite bodies were mapped throughout the granite by Alexandrov (1973: in Boutrika 2006) and may be interpreted as coeval with the felsic magma (mingling process). The mineralized veins are mainly hosted in the largest of these bodies, which is dissected by a N10° E dextral ductile shear zone (Fig. 7). The mafic rocks are pervasively retrogressed into a serpentine-chlorite-actinolite-epidote-calcite-sericite-albite-magnetite assemblage.

Late Pan-African stress pattern in the In Abeggui district: Numerous mafic and felsic dikes cut both the biotite granite and the gabbro-diorite massif, as well as the N10° E shear zone. The mafic dikes (diorite and diabase) are older. The felsic dikes comprise fine-grained granite and microgranite, and pink aplo-pegmatite and aplite, the latter being locally topaz-bearing. The felsic dikes are particularly abundant within the gabbro-diorite massif, and toward the eastern margin of the biotite granite pluton, and encompassing the known gold deposits area (Fig. 7). As revealed by the detailed mapping by the SONAREM teams, the dikes are segmented along strike. This may be interpreted as intrusion along tectonic joints (set of conjugate virtual shears and the related tension joints), allowing the recognition of the (local) shortening (σ1) direction. The main pattern is the same as the regional one, i.e., N10° E and N50° E conjugate shears and related N30° E shortening (Fig. 7). However, in the mineralized area, these directions are distinctly rotated: this may tentatively be interpreted as a local perturbation of the regional stress field, induced by a concealed pluton at the origin of the felsic dike magmatism.

Gold mineralization: Gold is hosted mainly in swarms of quartz-tourmaline veins and lodes within the gabbro-diorite massif (Fig. 8a). The steep veins and lodes range in length from a few meters to about 100 m, with variable thicknesses (1–3 cm to 5–6 m); gold was found by drilling to

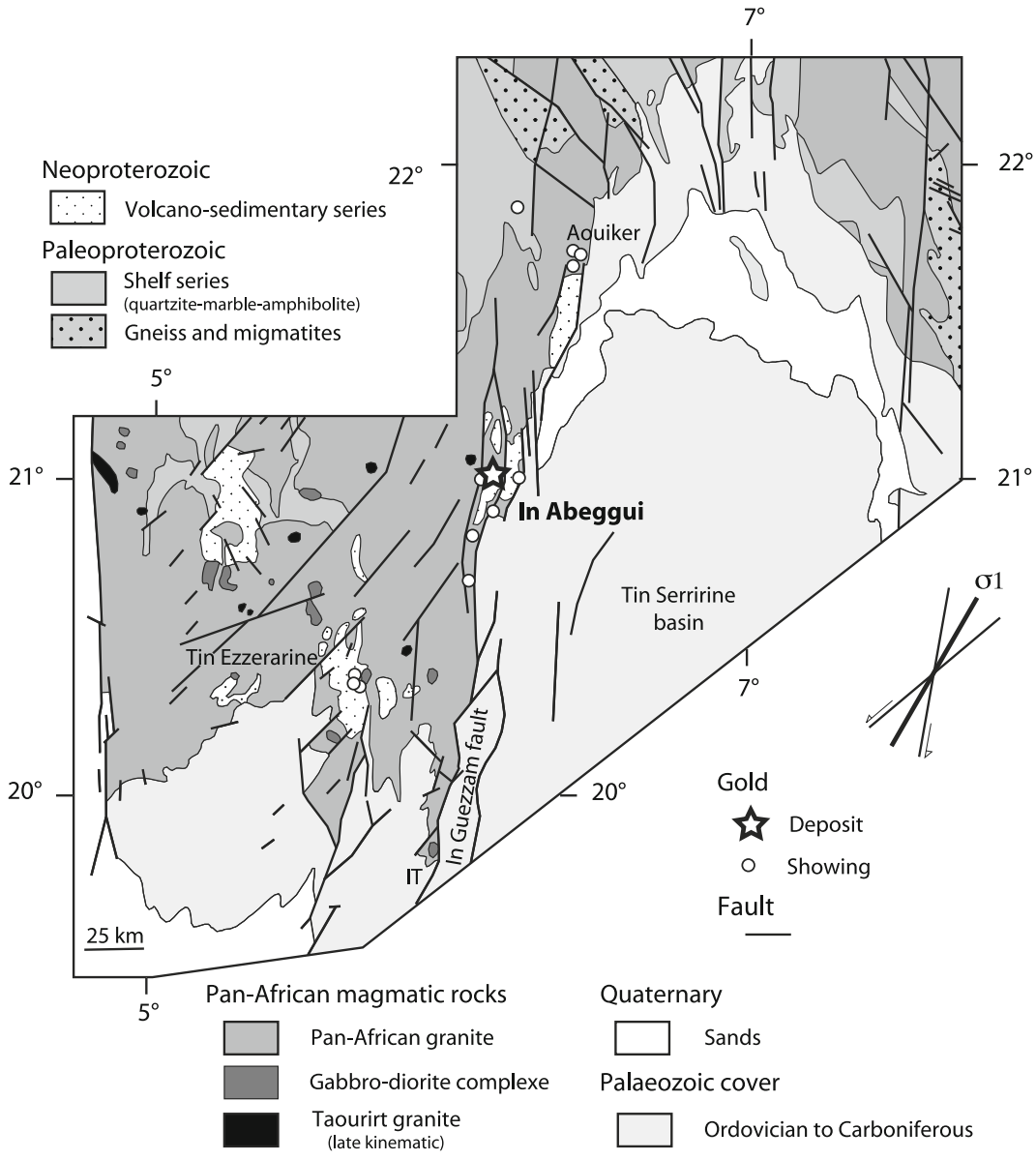

Fig. 6 Regional setting of In Abeggui and Tin Ezzerarine gold districts in Laouni (LATEA) terrane (from Semiani et al. 2004). Note spatial relationships between gold occurrences and Neoproterozoic "basins." In Abeggui district is located in dextral relay (N30° E shortening direction) of a regional set of N10° E shear zones (In Guezzam fault); *IT* In Telloukh Pan-African granite

depths of 200 m (Boutrika 2006). Several centimetres wide away from the veins, the mafic rocks are transformed into a chlorite-calcite-sericite assemblage. The vein orientations are consistent with the regional stress pattern, with N10° E and N50° E directions interpreted as conjugate shears, and N30° E directions interpreted as tension joints (main shortening, or σ1, direction) (Fig. 8a). Along strike, changes of the main stress directions are evident (Fig. 8b). Such changes may reflect the same perturbation of the regional stress field as for the felsic dikes, i.e., the anticlockwise rotation of σ1 southwards is consistent with the anticlockwise rotation observed in the dike patterns (Fig. 7).

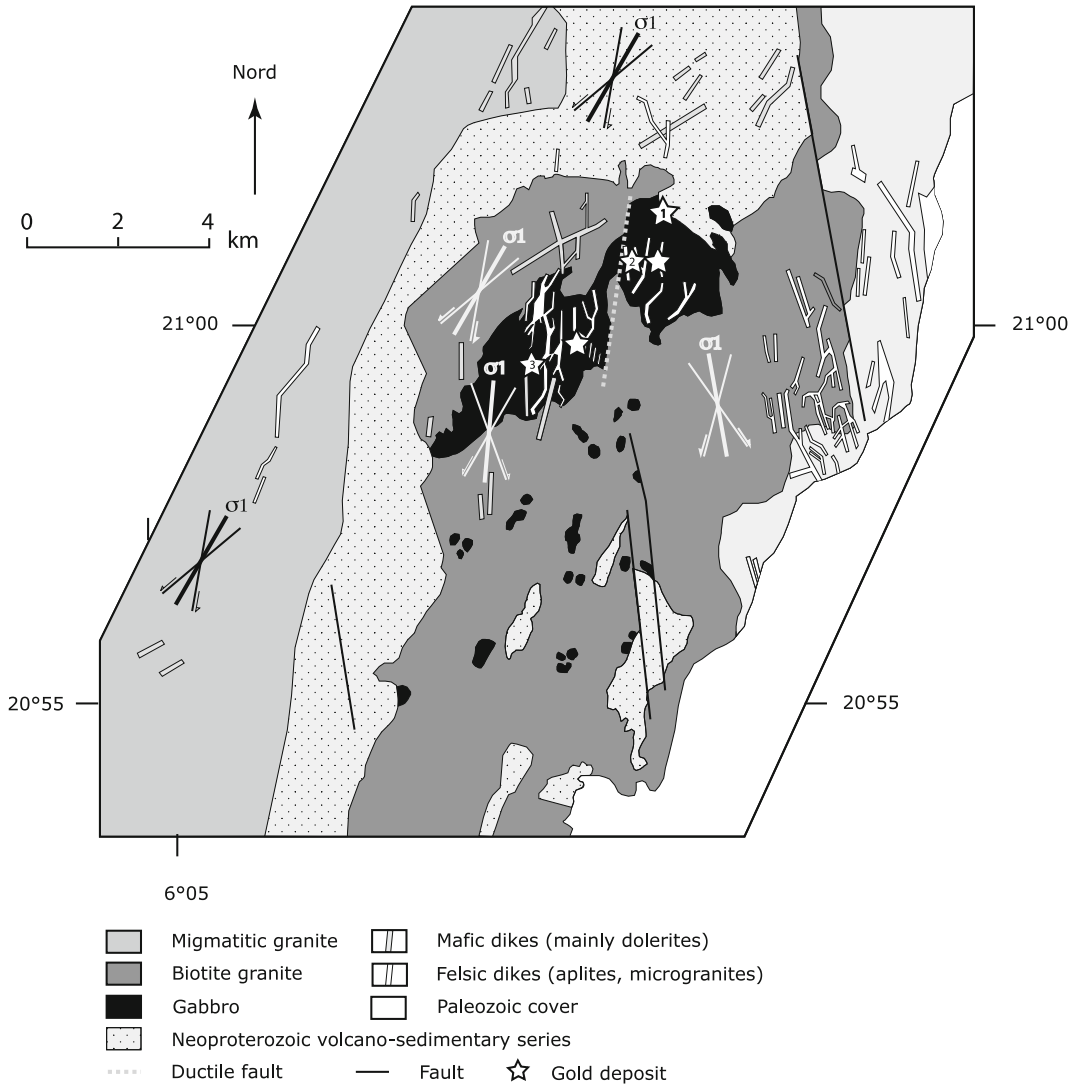

Fig. 7 Geological setting of In Abeggui gold district (from Alexandrov 1973, in Boutrika 2006). *1* In Abeggui deposit; *2*, *3* Unnamed gold showings illustrated in Fig. 8. Orientations of segmented mafic and felsic dikes are used to reconstruct the main stress (σ1) and associated shear directions (see text for details)

A second style of gold mineralization is represented by swarms of quartz-tourmaline veinlets and veins within some N10° N topaz-bearing aplite dikes that locally cut earlier quartz veins (Fig. 8c). These veins and veinlets fill tension joints (N30° E) and have associated pervasive wall-rock alteration, the aplites being transformed into a quartz-tourmaline-sericite-pyrite assemblage ("greisen"). Topaz ± cassiterite ± molybdenite ± wolframite are common in the greisen, and in the veins as well, representing among the earliest minerals (Alexandrov 1973, in Boutrika 2006). The quartz-filled joints extend beyond the aplite into the surrounding mafic rocks, with the same pattern (N10° E, N30° E, N50° E) as elsewhere in the In Abeggui district (Fig. 8c). However, these are commonly thinner, less numerous, and poorer in gold, terminating as barren quartz-tourmaline stringers with thin chloritized borders. The ore assemblage in both styles of mineralization is simple, with pyrite-arsenopyrite-pyrrhotite-(chalcopyrite)-gold-native

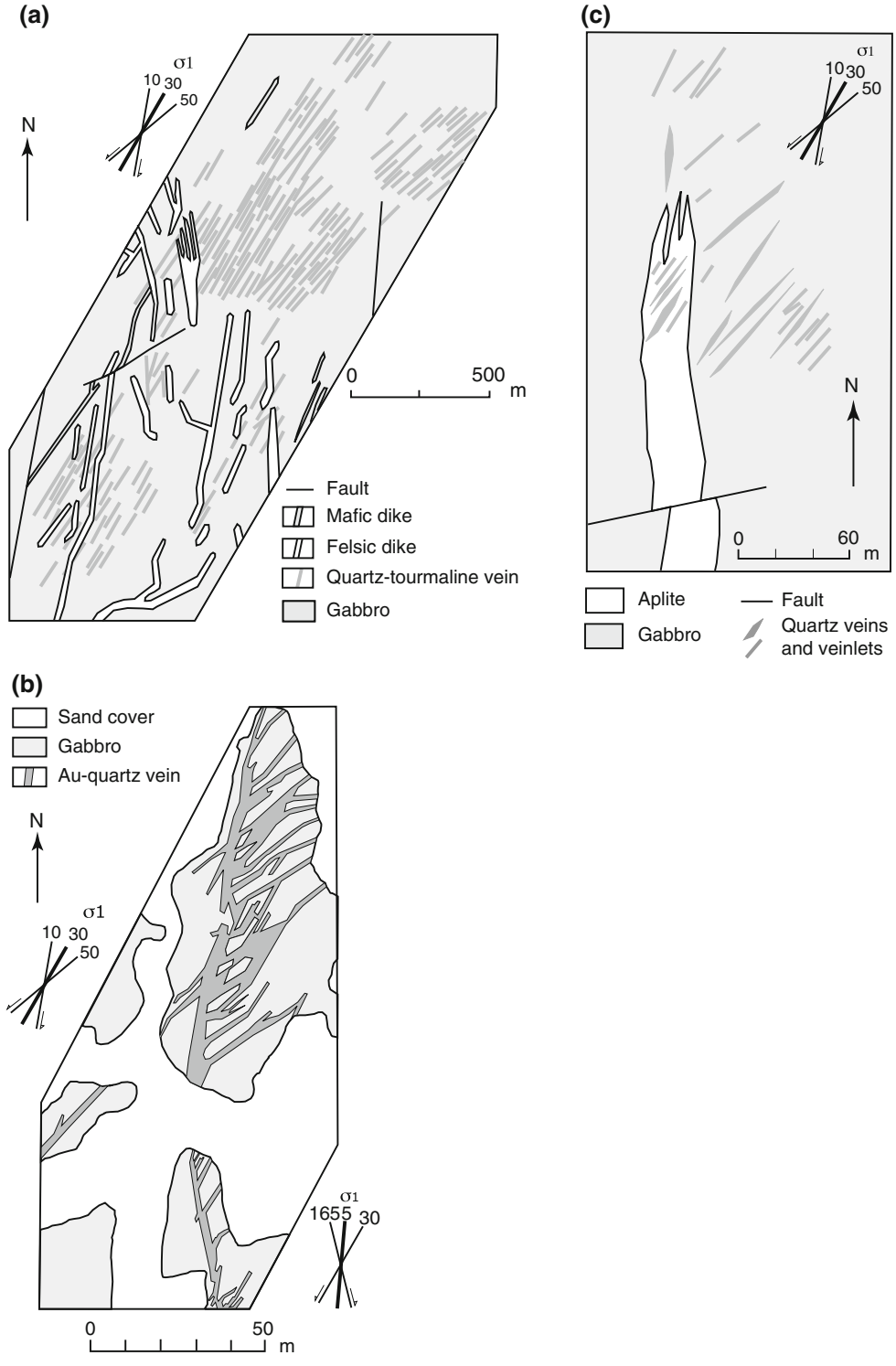

Fig. 8 Detailed field relationships in In Abeggui district between quartz-tourmaline ± gold vein systems and felsic dike systems (from Boutrika 2006), and their interpreted main stress (σ1)-shear relationships. **a** In Abeggui deposit (1 in Fig. 7). **b** Central part (2 in Fig. 7), this gold-bearing lode overprints N10° E ductile shear zone (not shown); complex vein system is organized according to two sets of conjugate shear fractures, the northernmost having associated N30° E shortening (σ1) direction, the southernmost one a N5° E shortening (σ1) direction. **c** Southwest part (3 in Fig. 7)

bismuth and rare galena. As in the other Hoggar deposits, gold is paragenetically late, deposited in close spatial association with native bismuth in microcracks in quartz, tourmaline, and earlier pyrite (Boutrika 2006).

From the above data the quartz vein systems at In Abeggui are interpreted to be coeval with a granitic magmatism. Given the topaz occurrences in the aplite, this magmatism is related to the rare-metal granite event (see below), dated at ca. 520 Ma (Cheilletz et al. 1992). Based on the similar sulphide and gold paragenesis in all of vein systems, a single gold mineralizing event is suggested, occurring late in the history of the vein systems. Moreover, because the same sequence is observed at Tin Ezzerarine, this gold event appears to be regional in scope.

Mineralizing fluids: A reconnaissance fluid inclusion (FI) study was conducted by Aissa et al. (2012) on quartz from the Tin Ezzerarine field and in comb quartz from the second stage tension veins in the aplite dikes from In Abeggui. In the cores of the latter quartz, melt inclusions occur locally, indicating that quartz growth began during the late magmatic stage. The fluid inclusions within these quartz crystals are dominantly volatile-rich (with a significant non-CO_2 component, judging by low melting temperature of the carbonic ice, down to −61.5 °C), or moderate- to low-salinity aqueous-rich (3–11 wt% equiv NaCl), both having high bulk homogenization temperatures of 360–520 °C. The volatile-rich FIs display evidence for both dilution by a low-salinity aqueous phase and density changes (transition from liquid- to vapor-rich FIs), the latter likely recording an exhumation process. The same types of FIs are found at Tin Ezzerarine, but the bulk homogenization temperatures are significantly lower, between 260 and 400 °C. A possible interpretation of these preliminary data is that volatile-rich fluids of regional metamorphic origin progressively mixed with an aqueous fluid while exhumation was proceeding (Aissa et al. 2012). In the gold deposits of the West European Variscan belt in Limousin, France, a similar event of mixing between metamorphic and surficial fluids is demonstrated to have been the cause for gold deposition (Boiron et al. 2003). The same conclusion is likely at In Abeggui, where, however, the highest temperatures of homogenization and presence of melt inclusions in the cores of some quartz crystals, suggest that magmatic-hydrothermal fluids could have been involved at the beginning of the event, being possibly linked to the early deposition of wolframite. This hypothesis is reinforced by the observation in the Abeggui quartz of rare three-phase, halite-bearing FIs that could record the mixing of a magmatically derived brine with the volatile-rich fluids (Aissa et al. 2012).

3.4 Gold Deposits in the Aouzegueur (Proche Ténéré) Terrane

Gold mineralization within the Aouzegueur terrane is also of the quartz-lode type. Mineralized veins there occur either in the "unfolded" part of the Tiririne molassic belt south of 22° 30′ (Tiririne district), or in the basement (Hanane) (Fig. 9a). The Tiririne district is the northernmost of a series of quartz fields, named Tiririne I (=Tiririne district), II, and III (close to the Mali border; not shown on Fig. 9). The Tiririne II and III are only slightly enriched in gold, Tiririne III being the poorer. As a whole, the Tiririne province contains about 1000 quartz veins, most being either barren or weakly mineralized (ca. 1 g t^{-1} gold).

The Tiririne district (Talbi 1984): The Tiririne district, having a documented resource of ~8 t gold @ 17 g t^{-1} (possibly as much as ca. 30 t; Semiani et al. 2004, written communication), comprises up to 400 quartz veins, some mineralized, some barren, which may be grouped into three fields. All display the same features (Talbi 1984; Aïssa and Bedouhène 1988): (1) quartz-chlorite-pyrite alteration along the veins; (2) veins varying from 0.3 to 1.5 m thick and 500–3000 m long; (3) similar ore mineralogy, dominated by pyrite, in some cases with scheelite and, in mineralized veins, native gold (the later being systematically late); and (4) presence of rafts of cataclastic wall rocks within the veins. Mean gold contents are highly variable, from 1 to 44 g/t.

Our field observations in the south Tiririne subdistrict (close to the old SONAREM base) show that the quartz-vein system comprises two

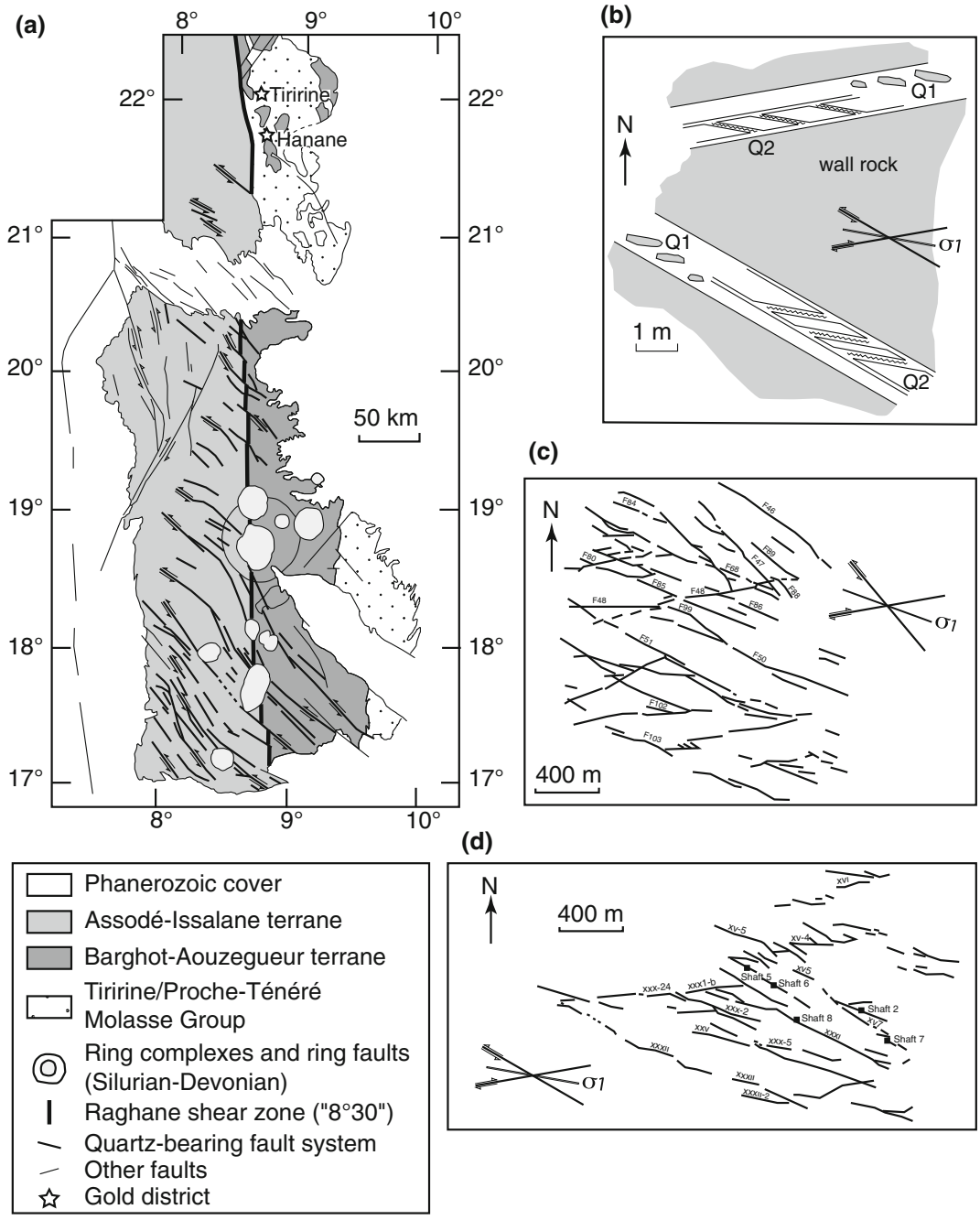

Fig. 9 Eastern Hoggar gold deposits. **a** Regional setting (from Liégeois et al. 1994; and Semiani et al. 2004). **b** Field relationships of quartz veins in south Tiririne district and interpreted main stress (σ1)-shear pattern. **c**, **d** Maps of gold-bearing vein quartz swarms of Tiririne district (**c** north Tiririne; **d** central Tiririne) (from Aïssa and Bedouhène 1988). *Q1*, *Q2* two quartz generations (see text)

sets of simultaneously opened conjugate shear fractures trending ca. N130° E and ca. N80° E, with a N110° E shortening (σ1) direction (Fig. 9b). This pattern holds for the entire Tririne district, as shown in Fig. 9c, d.

The quartz veins have a protracted history. Initial opening and filling produced veins with internal rafts of wall rocks (a few centimeters to meters in size) and deposition of a first generation of comb Q1 quartz (crystals to 10 cm or larger). Q1 quartz was reworked by several episodes of opening and shearing (striated walls). Up to 50 volume percent of comb Q2 quartz was added to the initial veins, mainly by opening of N100° E–110° E tension joints (Fig. 9b). The Q1 and Q2 quartz generations were reworked by a strong recrystallization event, which formed large quartz vugs, practically sealed (Q3), leaving only remnants of the initial quartz textures. Detailed observations show that a progressive rotation of the shortening direction is recorded within the quartz veins, from 110° E to N40° E (Fig. 10a). The latest events that affected the Tririne veins were small discrete normal faults (N50–60° E, 30–40° SE) and a new episode of dissolution-recrystallization, at the origin of microvugs of a Q4 quartz (Fig. 10b). Gold deposition, being currently observed to coat the small Q4 quartz, is the final event of this protracted history.

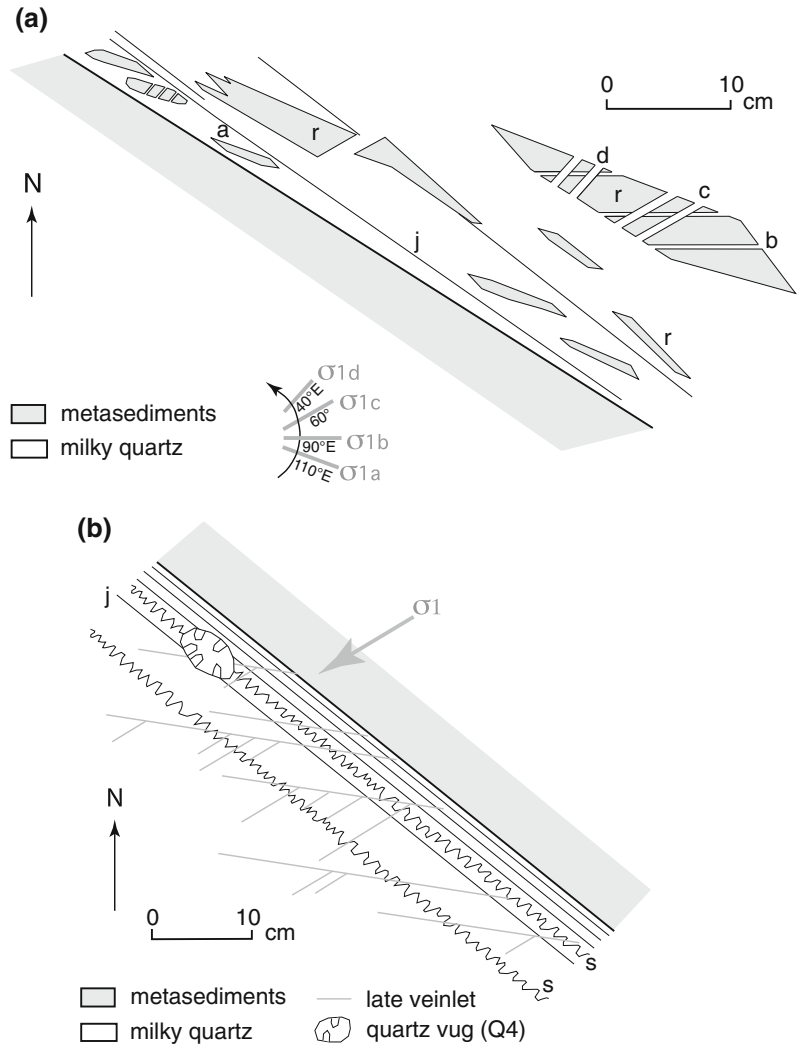

Fig. 10 Examples of features that record progressive σ1 rotation from N110° E towards N30° E in the south Tririne field. **a** Detail in border of N130° E quartz vein: early N130° E joints (j, Q2 event) are transformed into stylolites (s) under à N60° E shortening (σ1) direction, and a new set of cracks with N80° E (shear) and N60° E (tension) directions are produced. **b** Example of time-dependent changes in shortening (σ1) direction within country-rock rafts inherited from early (Q1) stage; j: early N120–130° E joints (Q2 event); quartz vein was repeatedly opened along tension joints, the younger obliterating the older, allowing reconstruction of an anticlockwise rotation for main stress orientation; σ1a, b, c, d: successive positions of the main stress as recorded by the tension veinlets

Hanane deposit: The poorly known Hanane deposit (1.9 t gold), 50 km south of the Tiririne 1 district, is hosted in a granodiorite pluton that was emplaced at 582 ± 3 Ma (Nouar et al. 2011) in orthogneisses of the Paleoproterozoic basement. Gold-bearing quartz veins are located along the boundaries of mafic dikes that cut the granite massif. These dikes are likely coeval with the late diabase dikes in the Tiririne Group. The ore mineralogy of the Hanane veins and the alteration envelopes are identical to those of the Tiririne district. It is thus likely that at Hanane, gold deposition was coeval with formation of the Tiririne lodes.

Timing: In the Aïr massif of Niger, Liégeois et al. (1994) reported that the Assodé, Barghot and Aouzegueur terranes were "sliced by NW-SE to NNW-SSE-trending sigmoidal sinistral wrench faults" hosting large quartz veins. These veins aggregate ca. 10,000 km of cumulate length, but are mostly barren, as are most of those in the Tiririne III field, which clearly is the northern continuation of the Aïr quartz vein system. Yet, in the vicinity of the Raghane shear zone, the quartz veins are reported to be slighltly gold bearing. The quartz lodes of the Tiririne district, being hosted by the same conjugate sets of dextral and sinistral faults as the giant Aïr quartz vein system, may consequently be considered part of this system.

In the Aïr massif, the hydrothermal event that formed the giant quartz vein system may be dated. The faults that host the quartz veins are later than the RSZ and the late granite intrusions (ca. 600 Ma), being consequently either a late Pan-African or a younger feature. On the other hand, some quartz veins in the south of the Aïr are overprinted by swarms of E-W-trending rhyolite dikes that are dated at 529 ± 11 Ma (U/Pb, zircon); and U/Pb dating of zircons in the Paleoproterozoic Azan gneiss in the vicinity of the veins yields a lower intercept of 524 ± 7 Ma, interpreted as the age of the hydrothermal disturbance (Liégeois et al. 1994). Thus, the giant quartz vein system, including the Tiririne veins, was coeval with the terminal stages of the Pan-African orogeny.

On the other hand, the N130° E dextral faults that host part of the giant quartz-vein system may be compared with the direction of the dextral shear zones that separate the Aouzegueur, Edembo, and Djanet terranes and were active during the late Ediacarian Murzukian event. Significantly, the shortening direction that characterizes the quartz-lode system seems identical to the main shortening direction of the Murzukian collision. It may thus be proposed that the giant Aïr-Tiririne quartz-vein system evolved at the very end of the Murzukian event, from changing boundary conditions (σ1) of N110° E to N40° E, as recorded in the Tiririne vein swarms. Formation of the host structures for the (later) gold mineralization would then be a direct consequence of the Murzukian event.

3.5 Gold in the Edembo Terrane

The Tin Zekri and Tin Massaret gold deposits (Fig. 1) contain 3.8 t of gold @15 g t^{-1} and 2 t of gold @ 8 g t^{-1}, respectively (unpublished ORGM data). The gold-bearing quartz veins are hosted in a granodiorite (likely, a dike of the Tin Amali system, dated at 558 ± 6 Ma; Fezaa et al. 2010) intrusive into Pan-African migmatites. The mineral association is simple, comprising pyrite, marcasite, sphalerite, galena, and sparse chalcopyrite and native bismuth. Native gold is late in the paragenesis. These deposits are reportedly very similar to the Hanane gold deposit.

4 W–Sn–Ta–Li–Be Mineralization

Rare-metal mineralization in the Hoggar part of the Tuareg shield is spatially associated with evolved Li–F-granites that are members of the latest stage of Pan-African felsic magmatism, together with Taourirt granites, at ca. 539–523 Ma (Cheilletz et al. 1992; Paquette et al. 1998; Azzouni-Sekkal et al. 2003 and references therein). Of the ca. 100 rare-metal occurrences (Sn–W–Ta–Li–Be) that were prospected by the ORGM in the Hoggar shield, only about ten are of economic interest. These occur mainly within the LATEA super-terrane (Fig. 1), especially in the southern Laouni terrane, the few exceptions

being Tesnou and Egele (Iskel terrane), Ebelekan (Issalane terrane), and Djilouet (Djanet terrane). In addition, the Ait Oklan Taourirt granite in the Iskel terrane is the host for a fluorite deposit amounting to 225 kt of fluorite, with a mean 30 wt% CaF_2.

The rare-metal deposits are associated with albite–topaz granite (RMG) or microgranite (RMmG) that form small elliptical stocks or dikes emplaced in, or close to, larger peraluminous leucogranite complexes that intrude coarse-grained biotite granite. These evolved granites are made of albite, quartz, Li–mica (mainly zinnwaldite), subordinate K–feldspar, and topaz with accessory columbite–tantalite, wolframoixiolite, wodginite, U–Hf–zircon, Th–uraninite, and Ta–rutile (Kesraoui et al. 2000; Nedjari et al. 2001). Cassiterite or wolframite, where present, is restricted to miarolitic cavities. The accessory minerals occur mostly as inclusions in micas.

The economic and sub-economic deposits can be subdivided into (1) classical Sn–W-quartz (±greisen) type, associated with essentially all known mineralized intrusions shown on Fig. 1, the only exception being at present Ebelekan; (2) disseminated cupola type (Tin Amzi, Ebelekan, and Rechla); and (3) Be-pegmatite bodies, known at Guerioun (containing large euhedral beryl crystals up to 20 cm), Nahda, and Rechla (Kesraoui 2005; Sarni 2012; Hamis et al. 2012).

4.1 Peri-intrusive Sn–W-Quartz Veins and Endogreisens (Bouabsa 1987)

The peri-intrusive or endogranitic Sn–W quartz veins contain an estimated total of ca. 37.0 (ORGM) or 23.5 (Mining Journal 2009) kt W and 5400 t Sn. Tungsten grades range between 0.32 % WO_3 (El Karoussa) and 1.5 % WO_3 (Nahda); Sn grades vary from 0.21 % (Hanana) to 0.75 % (El Karoussa) (ORGM data, in Sarni 2012). The deposits and showings can be subdivided into (1) Sn–(W) veinlets in the core of fissure greisens, and (2) W–(Sn) quartz veins with more or less intensively greisenised wall rocks. Where not endogranitic, the Laouni deposits are generally hosted in high-grade gneisses of the Laouni basement, typically migmatitic (the "granito-gneiss" on ORGM maps). In the Djanet terrane, the deposits are spatially associated with late, evolved, Taourirt-like cupolas, the main quartz-wolframite vein systems and associated cassiterite stockwork being related to the Djilouet pluton (Oulebsir 2009). Cassiterite showings are spatially associated with the evolved Taourirt granite of Tesnou, in the Iskel terrane (Azzouni-Sekkal 1995).

Cassiterite-bearing veinlets in fissure greisens: The best example of this type is the Alemeda field (Fig. 11). Fissure greisens there are

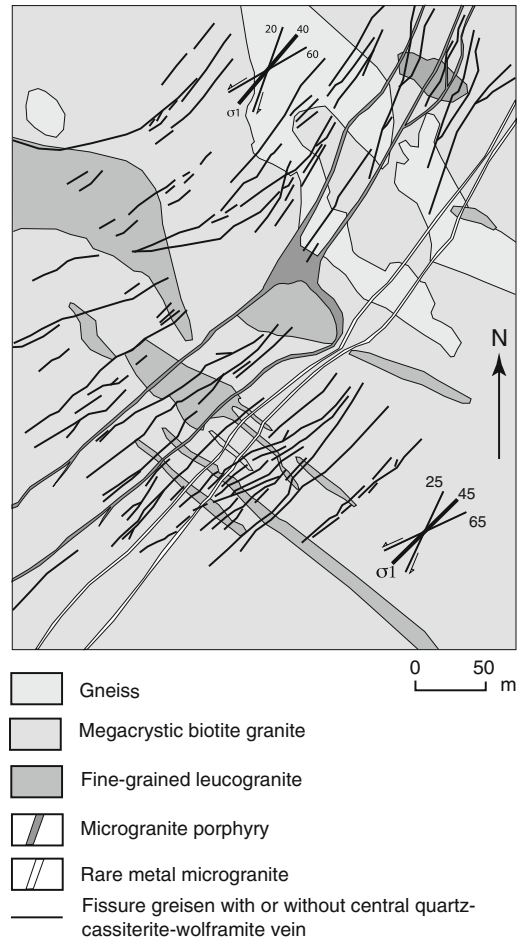

Fig. 11 Alemeda fissure greisen field (from EREM 1973–1976, modified in Bouabsa 1987)

coarse-grained, quartz-fluorite-mica (protolithionite and Li-muscovite) rocks, up to 1 m thick, which overprint a set of albite-topaz rare-metal microgranite dikes. Cassiterite (with minor wolframite) is present in quartz-mica veinlets parallel to the greisens, or as disseminations along greisen-wall rock boundaries.

In the detailed map by the EREM teams, the vertical fissure greisens and the late albite-topaz rare-metal microgranites (RMmG) display segmented patterns that are readily interpreted as reflecting a common shortening direction (σ1) at N40° E–45° E, accompanied by conjugate strike-slip fault directions at N20° E–25° E and N60–65° E (Fig. 11).

Quartz-wolframite-(cassiterite) veins: Quartz-wolframite-(cassiterite) veins are organized in fields that are in general spatially associated with stocks or dikes of RMG or RMmG (Fig. 12). Most are in a periplutonic position, with a few exceptions (Tamazaror, Hanana, Hananere). The mineralized veins occur as swarms with typically one or several prominent lodes (up to 100 m in length and depth and 0.3–0.6 m in thickness), as for instance in the In Tounine field (Fig. 12a). Country rocks are either gneiss, migmatite, and synkinematic granite of the Laouni terrane (e.g., Tin Amzi and El Karoussa, Fig. 12a, b), micaschist of the Neoproterozoic cover (e.g., Tamazaror, Fig. 12d), or older late Pan-African granite (e.g., In Tounine, Fig. 12c).

Greisenized wall rocks are the rule and systematically show F-enrichment, expressed as either secondary topaz (developed in RMG or RMmG) or fluorite (more common as fluorite patches at the expense of primary plagioclase in gneiss, migmatite, and granite). Li-mica (zinnwaldite) may be the predominant mineral, locally accompanied by significant Sn enrichment (e.g., Tin Amzi).

Wolframite is the main ore mineral in the quartz veins. It is paragenetically early, forming comb prisms, typically microfractured and sealed by later quartz in crack-seal veinlets. Cassiterite may be a late phase, as at Tin Amzi, where it is associated with late topaz in microvugs and microcracks. Wolframite compositions are extremely variable, at the deposit as well as the regional scale: the deposits may be grouped into "hubnerite-rich" (70–80 % Hnb; Tin Teganet, Rechla, Tamazaror), "intermediate" (25–40 mol % Hbn; El Karoussa, Alemeda, Bachir, Nahda), and "ferberite-rich" (10–20 mol% Hbn; Tekehermet, Taheleg, Ahelleg, Djilouet) (Chalal 2002; Oulebsir 2009; Sarni 2012).

4.2 Disseminated Rare-Metal Mineralization (Kesraoui and Nedjari 2002; Kesraoui 2005)

Within the Iskel terrane, notable Zr, Y, Nb, and Ta (up to 114 ppm) enrichments are documented in the evolved Egelé Taourirt pluton (Abed 2009). In the Tefedest terrane, the Tim Mersoi albite-topaz granite contains about 160 ppm Ta, residing in columbo-tantalite (Abed 2009). Most disseminated rare-metal mineralization, however, is hosted in evolved cupolas of highly differentiated Li–F granite massifs in the Laouni and Issalane (Ebelekan) terranes. Nb and Ta minerals are mainly disseminated and included in magmatic groundmass minerals; within the Alemeda RMmG dikes, Ta-rich wolframoixiolite is found in late-magmatic albite (Chalal and Marignac 1997). The main occurrences are at Tin Amzi, Ebelekan, and Rechla. The Ebelekan cupola hosts 9800 t Ta_2O_5 @ an average grade of 200 ppm, whereas up to 210 ppm Ta is documented in the Rechla cupola, which is also enriched in Be (Kesraoui 2005; Kesraoui and Marignac 2010).

The Tin Amzi cupola: This concealed cupola, revealed by drilling in the Tin Amzi quartz-wolframite field, consists of two encased intrusions (Kesraoui et al. 2000; Kesraoui and Nedjari 2002) (Fig. 13a). A first intrusion of fine-grained topaz-Fe-zinnwaldite I leucogranite progressively evolves upwards into a topaz-Fe-zinnwaldite II greisen. Near the top of the cupola, zinnwaldite II is transformed into an assemblage of muscovite and Mn-siderite, testifying to the involvement of CO_2-bearing fluids, which also are observed in associated quartz-hosted fluid inclusions. The second stage intrusion is a topaz-Li-muscovite leucogranite. Several

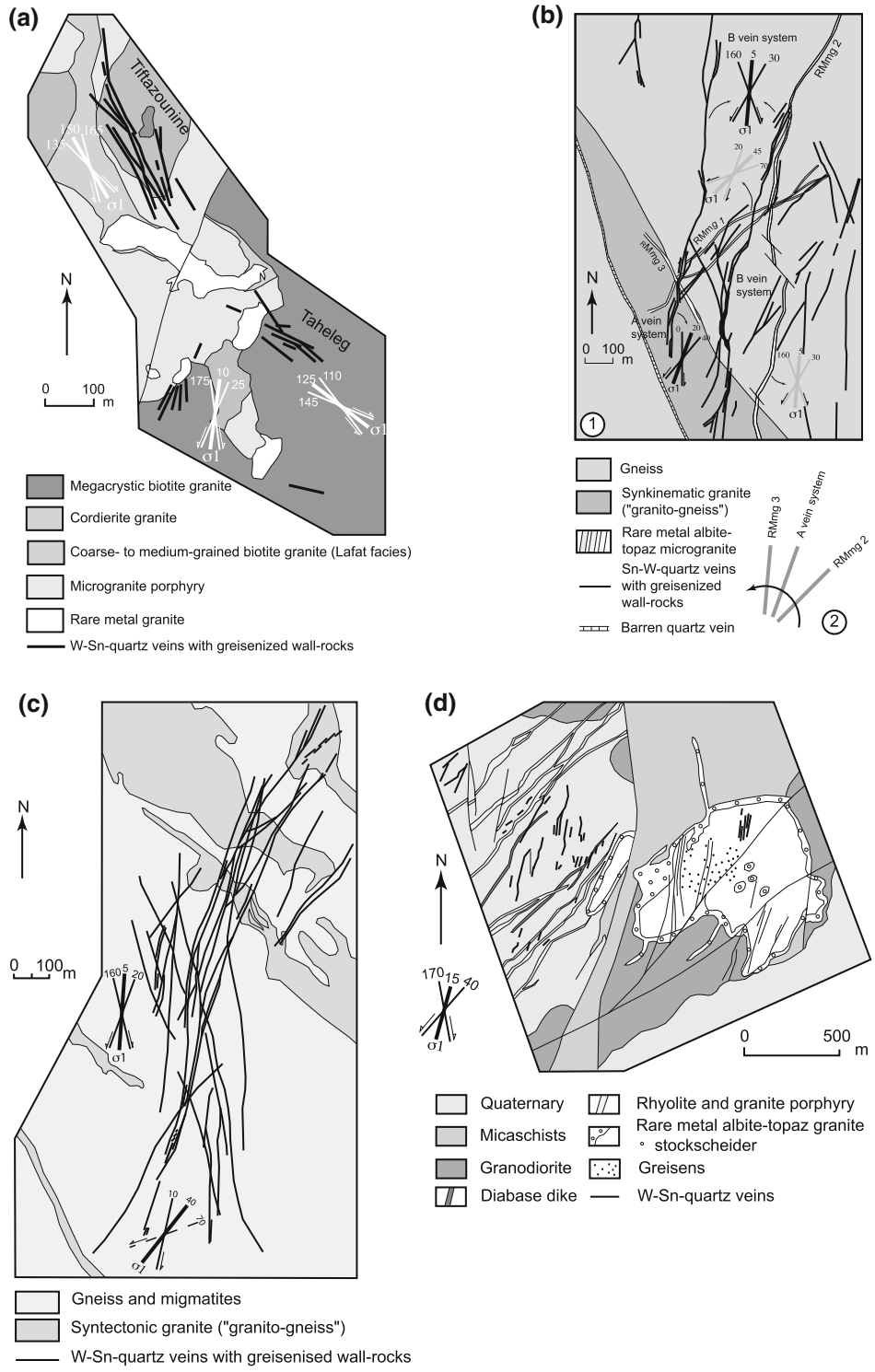

Fig. 12 Examples of Sn–W-quartz vein fields in central Hoggar (LATEA terrane); **a**, **b**, **c** from EREM maps as modified in Bouabsa (1987); **d** from SONAREM (1971), as modified in Chalal (2002). **a** In Tounine; **b** El Karoussa (1, Field relationships, 2, Interpreted relationships among stress patterns); **c** Tin Amzi; **d** Tamazaror

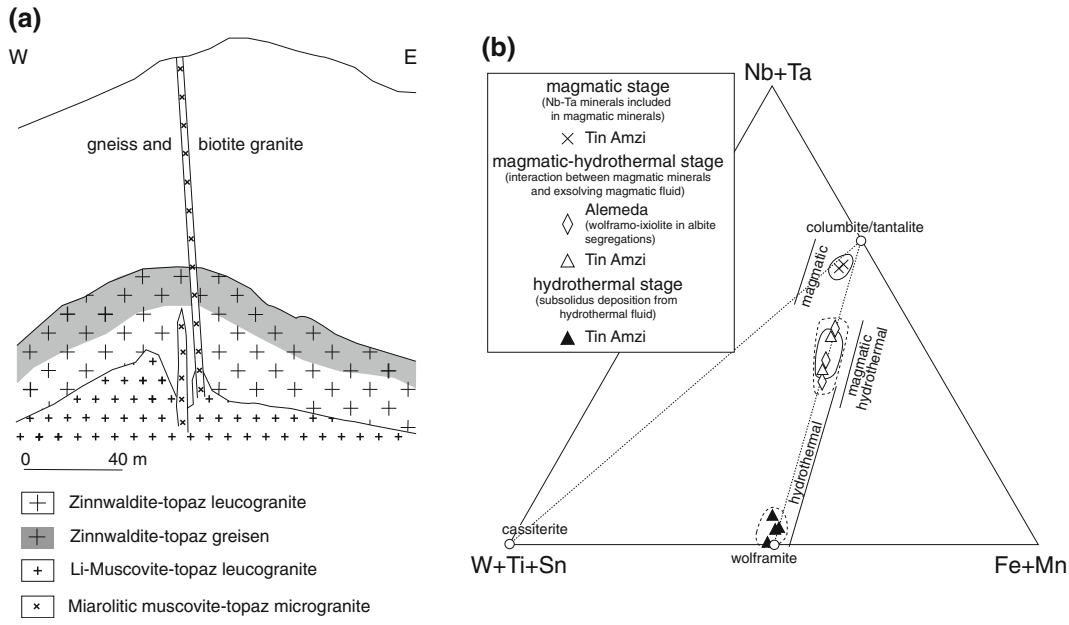

Fig. 13 Rare-metal disseminations in concealed Tin Amzi cupola of a Hoggar RMG. **a** Cross section of cupola (from Kesraoui 2005); **b** compositions of rare-metal minerals in the Nb + Ta, Fe + Mn, W + Ti + Sn ternary, and their interpreted origins in context of the magmatic to hydrothermal transition (from Marignac et al. 2001)

microgranite dikes, rooted in the leucogranite cupola, are spotted with miarolitic patches (3–5 mm) that contain quartz, albite, K-feldspar, Li-muscovite, arsenopyrite, Ta-cassiterite, and minor wolframoixiolite and wolframite.

Paralleling petrographic variations, a succession of rare metal minerals is observed (Kesraoui et al. 2000). In the topaz-zinnwaldite leucogranite, magmatic wolframoixiolite is contained in Fe-zinnwaldite I, whereas Fe-zinnwaldite II encloses euhedral crystals of wolframoixiolite with lower contents of Sn and Ti, but higher W. At the top of the cupola, correlatively to the transformation of Fe-zinnwaldite II to muscovite, inclusions of wolframoixiolites are resorbed by a Nb- and Ta-rich wolframite (Fig. 13b). A similar evolution is recorded in the topaz-Li-muscovite leucogranite cupola (columbite-tantalite, then wolframoixiolite, then wolframite).

These evolutions are interpreted as recording the transition from a magmatic Ta-dominated stage of mineralization to a hydrothermal W-dominated stage during crystallization of the rare metal granite melts and the W-enrichment of exsolved magmatic fluids (Marignac et al. 2001) (Fig. 13b).

4.3 Emplacement Conditions of the Hoggar RMG

Fluid inclusions were studied in magmatic quartz and topaz from the Hanana RMG cupola and an Alemeda RMmG dike (Bouabsa et al. 2012). Two main types of FIs were observed: (1) dense, CO_2-rich (with up to 28 % CH_4 and minor N_2), and displaying evidence of dilution by a water component; and (2) aqueous liquid of low to intermediate salinity (2–11 wt eq % NaCl). The latter type of FI is interpreted as magmatic-hydrothermal fluid, displaying evidence of anisothermal mixing (ca. 600–ca. 400 °C) with the former type, which is interpreted as external metamorphic fluids. The mixing occurred within the intrusions, due to hydraulic fracturing that allowed invasion of the cupolas by the external fluids, under pressures fluctuating between

supra-lithostatic (ca. 200 MPa) and lithostatic (ca. 150 MPa) conditions, at a depth of ca. 5 km (Bouabsa et al. 2012).

5 Discussion and Conclusions

5.1 Genetic Relationships Between Evolved Granites and Rare-Metal Mineralization

The magmatic nature of the Ta enrichment in the evolved RMG cupolas is beyond doubt. At first glance, a direct link between the evolved RMG and the Sn–W mineralization seems equally obvious. At Tin-Amzi and Alemeda, selective extraction of W by the Li–F-rich magmatic fluids unmixed from the Li–F-rich melts and their progressive interaction with the cupola and the dikes at Tin Amzi, were described above (Fig. 13b). At El Karoussa, centimeter-wide veinlets containing early topaz and late cassiterite (with Nb–Ta oxide inclusions) (Bouabsa 1987) are likely expressions of late-magmatic fluids. The presence of massive F–Li-rich greisens at Alemeda and the Na (albitization) and F (topaz, fluorite)-metasomatism, up to a few tens of meters thick, observed in the vicinity of the In Tounine and Aheledj plutons (Bouabsa 1987), testify to the interaction of exsolved magmatic fluids with surrounding host rocks.

The strict parallelism between the regional strain patterns associated with either RMmG emplacement or the mineralized quartz-vein systems (Figs. 11 and 12b–d) is considered strong evidence for a close temporal relationship between the two events. Particularly compelling is the observation that RMG emplacement likely interfered with the regional stress pattern responsible for the quartz-hosting fracture systems, as was the case for the In Tounine plutons (Fig. 12a).

However, as evidenced by the FI studies, there was very early interaction between the magmatic-hydrothermal fluids and high-temperature, externally derived fluids (volatile-rich), and as suggested in particular by the Tin Amzi concealed cupola, these mixed fluids could have been responsible for the tungsten mineralization. Given the absence of graphite in the high-grade gneisses of the granitic wall rocks, involvement of CO_2–CH_4–(N_2) fluids, as documented by Bouabsa et al. (2012), implies that distal supra-crustal Paleoproterozoic shelf (carbonate-rich) metasediments contributed components to the metamorphic fluids that invaded the cupolas. The ultimate implication is that large-scale crustal hydrothermal systems were established around the RMG plutons, at the inception of the rare-metal hydrothermal mineralization.

5.2 Evolved Taourirt Granites or Rare-Metal Granites or Both?

Based mainly on data from the Iskel terrane, Azzouni-Sekkal et al. (2003) suggested that the rare-metal plutons are late products of the differenciation trend of the Taourirt magmatism. In contrast, based on evidence from the Laouni terrane, Bouabsa (1987) pointed to seemingly significant geochemical differences, the rare-metal associated granites being distinctly enriched in Li, Sn, and W, and far more peraluminous. Figure 14 plots data for both Taourirt and the rare-metal-associated granites in terms of the Al-excess (Al–K–Na–2Ca, in millications) versus mafic components (Fe + Mg + Ti, in millications) of Debon and Le Fort (1988), which reveals several facts:

(1) The Taourirt GI to GII sequence, as defined by Azzouni-Sekkal et al. (2003) in the Silet district of the Iskel terrane (GI = biotite-amphibole monzogranites; GIIa = biotite ± amphibole monzo- to syenogranites; GIIb = albite-protolithionite/zinnwaldite ± topaz alaskites), follows a typical A-type differentiation trend, ending with F-enriched, low-P, mildly peraluminous granite, very similar to the low-P RMG class of Linnen and Cuney (2008). The peraluminous lepidolite granite of the Rechla cupola, which is Ta-rich although being a member of the low-P class (Kesraoui 2005), appears to result from an extreme fractionation process along the same trend.

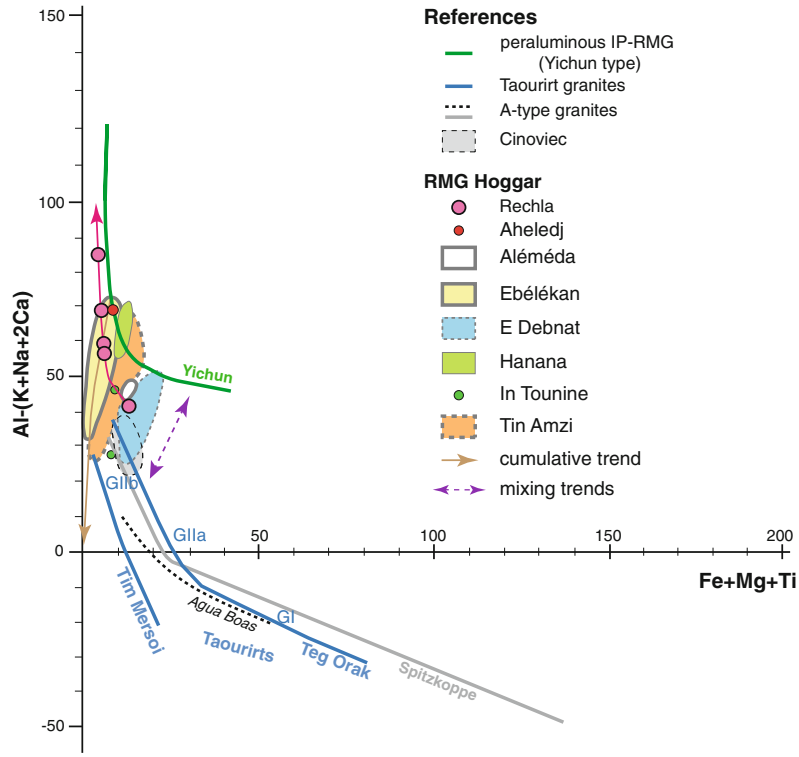

Fig. 14 Compositional relationships between magmatic trends of Taourirt and RMG lineages within Hoggar plutons, in terms of Al–(K + Na + 2Ca) versus (Fe + Ti + Mg) plot of Debon and Le Fort (1988)

(2) By contrast, the Ebelekan Li-rich and peraluminous cupola, which is also Ta-rich, is typically a member of the medium-P RMG class of Linnen and Cuney (2008), plotting on the Yichun (MP-RMG) differentiation trend. More precisely, the Ebelekan data follow a trend starting from the Yichun curve and pointing to the origin (where feldspars plot), which is typical of a cumulative effect involving albite in a combined Bagnold effect/filter-press process (Marignac et al. 2009).

(3) Several other rare-metal-associated plutons of the Laouni terrane, such as Hanana and Aheledj (members of the Tamanrasset group of evolved Taourirt granites according to Azzouni-Sekkal et al. 2003), similarly plot on the Yichun trend, meaning that they belong to the RMG, not the Taourirt, class of granites.

(4) Other plutons of the Tamanrasset group (such as E Debnat, Tin Amzi, In Tounine, Alemeda) plot in an intermediate position between the typical Taourirt trend and the Yichun-type trend. This may readily be explained by a mixing process between the two types of magma, the Tin-Amzi evolved granite being a particular example of this mixing process. Shown in Fig. 15 are results of a preliminary modelling of the mixing process based on the (rather heterogeneous) REE data, suggesting that a reasonable mixing model produces the Tin-Amzi evolved granite by a combination of ca. 20 % of a GIIb-type Taourirt melt and ca. 80 % of an evolved medium-P RMG-type Ebelekan melt. Consideration of other trace elements, including U and Th (not shown), supports the proposed mixing process. In Fig. 16, a speculative model is presented for the Taourirt-RMG relationships at a crustal scale.

We therefore conclude that in the Tuareg shield, the RMG are of two types. Some are evolved Taourirt granites of the GIIb class according to Azzouni-Sekkal et al. (2003), such as the zinnwaldite Tim Mersoi granite, and the far more fractionated lepidolite granite of Rechla. Most of the RMG, however, represent mildly fractionated peraluminous granites of the Yichun

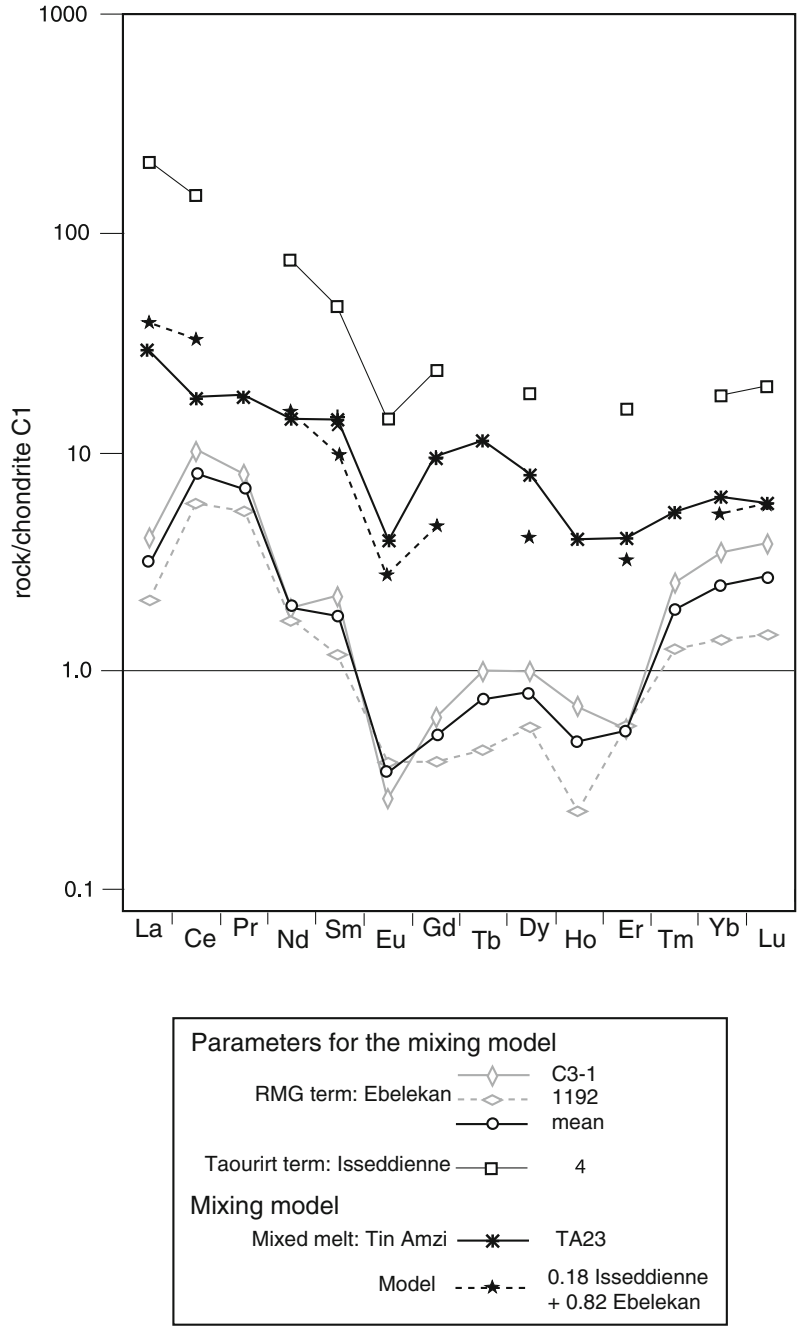

Fig. 15 Geochemical modeling of mixing of rare earth elements between evolved Taourirt magmas and "pure" members of the Yichun RMG trend, applied to In Tounine granite

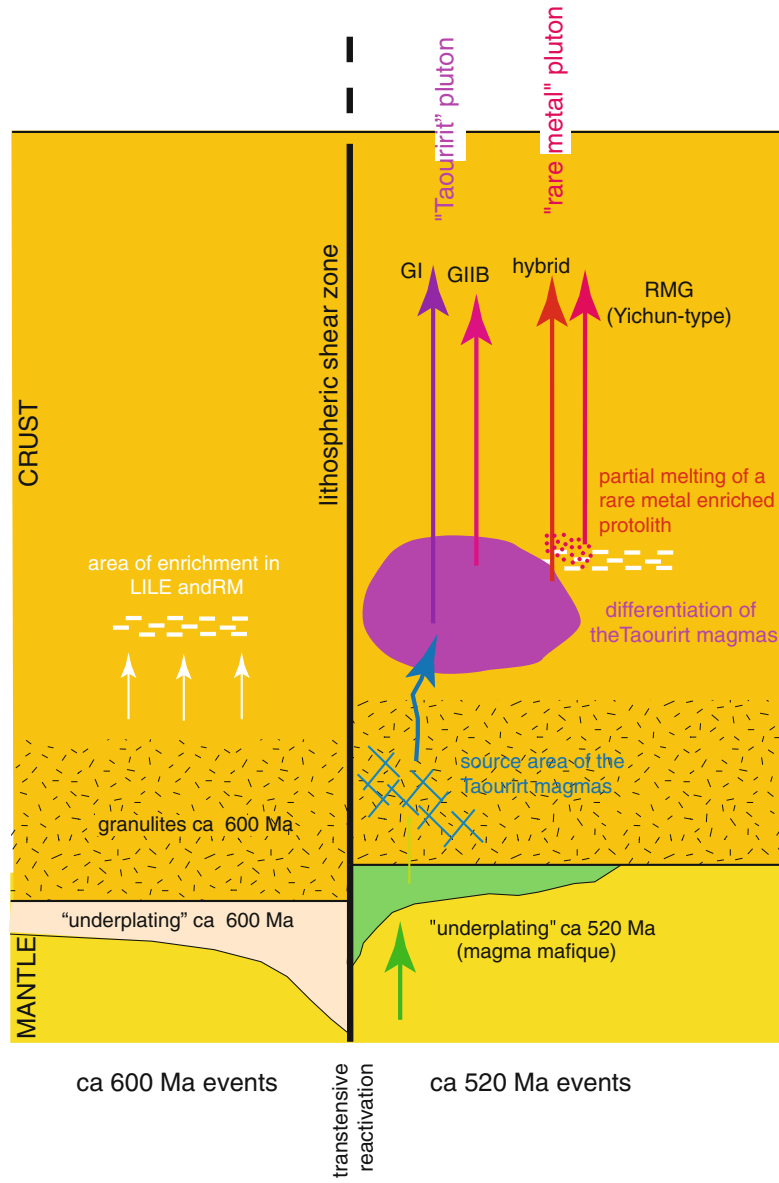

Fig. 16 Conceptual model of relationships between evolved Taourirt magmas, RMG melts and the evolution of the Tuareg crust during latest Ediacaran-Early Cambrian time

trend, such as Ebelekan, or result from mixing processes at depth between the two granite lineages (Taourirt- and Yichun-trends), with a clear predominance of the Yichun-trend magmas. Finally, it is remarkable that near all of the known RMG of direct or mixed Yichun-trend lineage are located within the Laouni terrane of the LATEA super-terrane, the exception being the Ebelekan cupola in the Issalane-Assodé terrane; the latter, however, is now considered akin to the LATEA super-terrane (Liégeois et al. 2013). To generate RMG magmas, Cuney and Barbey (2014, and references therein) propose a mechanism involving granulite-facies metamorphism in relation to "carbonic waves" in the deep continental crust. The F-, LILE- and rare-metal-rich fluids liberated by the breakdown of biotite (well known as a major host for Li, F, and rare metals) may ascend in the crust and promote partial melting at higher levels, generating potential RMG melts. This process is

greatly facilitated by the existence of crustal-scale shear zones that allow the focusing of fluids and the transfer of melts. Pan-African granulitization is not documented in the Tuareg shield. Yet, within the Issalane-Asmodé terrane the Renatt granite is very reminiscent of the Variscan Velay granite in the French part of the West European Variscan belt, itself the middle crustal expression of a major heating event (Barbey et al. 2014 and references therein). Although the time gap between the Renatt magmatism (ca. 600 Ma) and the Taourirt-RMG event (ca. 520 Ma) is too long to permit a direct genetic link, an intermediate sequestration in micas of the middle crust of the F and rare elements liberated by the granulite-facies metamorphism at ca. 600 Ma, is a distinct possibility: these enriched micas would then serve as protoliths for the generation of RMG melts during the latest thermal events in the Tuareg shield (Fig. 16). Such an explanation could be valid for the Ebelekan RMG, generated in the Issalane-Asmodé terrane. Application to the Laouni terrane would, however, require that similar phenomena (e.g., granulite-facies metamorphism in the lowermost crust and Renatt-like intrusion at higher levels) occurred within this terrane, which at present, although likely, remains speculative.

5.3 Hoggar Gold Endowment: An Eburnean Connection?

Most of the Hoggar gold is contained within the In Ouzzal terrane (at least 60–90 t Au in Tirek and Amesmessa), the remainder being in the Neoproterozoic-hosted deposits (at least 15–25 t Au). The least gold endowment (a maximum of 3–9 t Au) is in the Iskel terrane, which is relatively young; the lead isotope model ages of a Silet galena (950 Ma; Semiani 1995) are only slightly older than the emplacement age of the host batholith, whereas the Sm–Nd model ages obtained on the Taourirt granites span the interval 1.7–1.2 Ga (Azzouni-Sekkal et al. 2003). Compared to the ca. 2 Ga event, the Iskel terrane therefore is truly a young (apparently juvenile) terrane. By contrast, the better endowment is in the Archean In Ouzzal terrane, the less-transformed of all the Tuareg metacratons, where an Eburnean (ca. 2 Ga) event is well documented (Ouzegane et al. 2003). Within the LATEA super-terrane, Archean remnants are known in outcrops of the northern part, whereas Sm–Nd model ages of 3.1–2.5 Ga (similar to the In Ouzzal ages) have been reported for Neoproterozoic mafic intrusions of the Laouni terrane (Cottin et al. 1998); an Eburnean event (ca. 1.9 Ga) is documented everywhere within the super-terrane (Ouzegane et al. 2001; Peucat et al. 2003). Similarly, the Aouzegueur terrane is underlain by an Eburnean basement (Nouar et al. 2011), as is the nearby Barghot terrane, and in the Djanet terrane a 2-Ga Sm–Nd model age is present for the Djanet HKCA batholith (Fezaa et al. 2010). It therefore may be proposed that, in the Hoggar, the ultimate source of gold was from the Eburnean cratons: the In Ouzzal gneiss contains a mean of 3 ppb gold, which is elevated for a felsic granulite terrane (Marignac et al. 1996). We speculate that this gold specialization resulted from the ultra-high temperature granulite event during the Eburnean (Ouzegane et al. 2003), possibly related to a strong mantle-crust interaction (CO_2 influx) that characterizes this event.

It remains that the gold endowment of the Tuareg shield is low. This situation may be in part an appearance, owing to insufficient exploration of the shield. It is also possible that a part (possibly, the largest) of the initially concentrated gold has been eroded—in which case paleoplacers in the Paleozoic Tassili sequence could be promising. It is, however, very likely that the Tuareg shield was never more endowed than presently observed. Nonetheless, it seems clear that favorable conditions were established in the latest Ediacaran-early Cambrian in numerous parts of the Tuareg shield, hence the paucity of potentially fertile rocks (such as thick sequences of basalt or metalliferous black shale rich in diagenetic pyrite) could have been factors that limited the endowment of gold in this region.

5.4 Gold and Rare Metals: Correlated Distal Consequences of the Murzukian Event

A striking feature of the Hoggar metallic province is that gold and rare-metal mineralization were coeval phenomena, occurring at the very end of the Pan-African orogeny. All of the gold deposits are coeval and formed at ca. 530–520 Ma, i.e., at the time of the RMG emplacement. Dating is direct (Tirek-Amesmessa; Marignac et al. 1996; Tiririne quartz swarms; Liégeois et al. 1994), or indirect (in the Iskel and LATEA deposits, which are temporaly linked to Taourirt plutons; Boutrika 2006; Chaouche 2008). At the late collisional stage and at the scale of the entire Tuareg shield, the stress/strain fields experienced a transitory episode with a ca. E-W shortening direction (σ1) interspersed between two episodes having a ca. N45° E shortening direction. This history is well documented by the detailed studies in the In Ouzzal, Iskel, and Aouzegueur (Tiririne) areas, as described above. Within the Adrar des Iforas massif, a late brittle deformational regime with a N105° E-trending shortening direction and conjugate dextral N60° E-trending and sinistral N150° E-trending strike-slip faults was dated at ca. 545 Ma (Boullier et al. 1986), whereas in the Tin Zaouatène terrane, close to the EOSZ, the metasomatized wall rocks of an extensional E-W quartz vein contain phengite that has a $^{40}Ar/^{39}Ar$ age of 576 Ma (Ferkous and Monié 2002). It therefore seems likely that this "E-W" event was coeval with the 575–555 Ma Murzukian event (Fezaa et al. 2010). In this context, it must be noted that sets of brittle dextral N90° E and sinistral N120° E faults (i.e., similar to the early sets in the Tiririne field) are known to overprint both the Raghane fault zone and the Yvonne granodiorite (595 ± 3 Ma) in the Issalane terrane (Nouar et al. 2011).

This "E-W" event was operative during the generation of some of the gold-hosting quartz systems, such as in the Tiririne (main quartz swarms) or the Iskel and In Ouzzal (dextral N50° E faults overprinting the mega-shear zones) fields. However, with the progressive return to NE-SW and finally N-S shortening directions, and the concomitant transtensive reactivation of the mega-shear zones, both the protracted emplacement of the Taourirt and RMG plutons and the gold and Sn–W mineralizing events occurred at ca. 530–520 Ma. Similar rotation of the stress field at the end of the Pan-African collisions is documented in other segments of the Trans-Saharan Pan-African belt, where this rotation is attributed to complex interactions between the Congo and East Saharan cratons, the latter acting as an indenter and providing the ultimate control of far-field tectonic conditions (Tairou et al. 2007).

Azzouni-Sekkal et al. (2003) explained the generation of the giant linear HKCA batholith by mantle-crust interaction along linear lithospheric delamination zones that were promoted by late collisional reactivation of the submeridian mega-shear zones. As the youngest of these HKCA batholiths is ca. 580 Ma, Abdallah et al. (2007) argued that this age marks the end of the post-collisional events and that the Taourirt province (ca. 540–ca. 520 Ma) must therefore be considered anorogenic. However, the discovery of the Murzukian orogenic event (Fezaa et al. 2010) demonstrates that the eastern Hoggar at least was still subjected to collisional and post-collisional processes, including linear delamination and HKCA batholith emplacement, along the Tin Amali shear zone at the Djanet-Edembo boundary and by reactivation of the Raghan mega-shear zone. The late Ediacaran Murzukian event ended at ca. 555–550 Ma, which is the age of the late plutons in the Djanet terrane (Fezaa et al. 2010) and along the northern (reactivated) section of the Raghane shear zone (Henry et al. 2009). The Taourirt-RMG event immediately post-dated the Murzukian event in the Djanet terrane: the Djilouet pluton (an evolved GIIb Taourirt; Oulebsir 2009) overprinted an E-W mylonite zone, but experienced plastic deformation at the magmatic-subsolidus transition (Oulebsir 2009, written communication) indicating that it indeed had a late-kinematic emplacement. In the same way, reactivation of the central Hoggar mega-shear zones occurred as late as 520 Ma in association with Taourirt granite emplacement (Paquette et al. 1998). It may thus be proposed that a recurrence of the linear delamination process of Azzouni-Sekkal et al. (2003) was active as a late

"echo" of the Murzukian event, although at a more limited time and space scale than at the end of the Pan-African event proper (ca. 610–ca. 580 Ma), thus explaining the generation of the Taourir-RMG and related metallogenic provinces (Fig. 16).

The Ediacaran-Early Cambrian Hoggar gold and rare metal province appears to have been controlled at all scales by the latest transtensional reactivation of the Pan-African mega- and second-order shear zones. This reactivation followed the late Ediacaran Murzukian event (Fezaa et al. 2010), and was related to the heat flux associated with linear lithospheric delamination processes, which were responsible for the late magmatic events (Taourirt and RMG plutons) and associated hydrothermal circulation and mineralization in the Tuareg shield.

Acknowledgments John Slack is warmly thanked for his considerable editing work and improvement of the initial manuscript. The authors wish to thank ORGM (National Bureau of Mining and Geology of Algeria) for logistical assistance and for providing geologic data.

References

Abdallah N, Liégeois J-P, De Waele B, Fezaa N, Ouabadi A (2007) The Temaguessine Fe-cordierite orbicular granite (central Hoggar, Algeria): U-Pb SHRIMP age, petrology, origin and geodynamical consequences for the late Pan-African magmatism of the Tuareg shield. J Afr Earth Sci 49:153–178

Abdelsalam MG, Liégeois J-P, Stern JR (2002) The Saharan metacraton. J Afr Earth Sci 34:119–136

Abed A (2009) Les granites de l'Egelé et de Tim Mersoi (Hoggar): pétrographie, minéralogie, géochimie et considérations métallogéniques. Unpubl Magister Thesis, USTHB-Alger, Algeria, 104 pp

Attoum A (1983) Etude géologique et structurale des mylonites Panafricaines et des minéralisations associées dans le secteur de Tirek, Hoggar, Algérie. Unpubl Doct 3ème cycle, Univ Montpellier, France, 98 pp

Aissa DE, Bedouhène N (1988) Les minéralisations aurifères d'Algérie nord-orientale et du Hoggar: essai d'approche sur leur métallogénie. Publ Serv Géol Tunisie, Tunis, Tunisia, pp 429–442

Aissa DE, Boutrika R, Guessoum N, Marignac C (2012) Late Pan-African gold mineralization in the Laouni terrane (central Hoggar, Algeria): is it linked to late felsic magmatism. Proceed Geofluids VII-Internat Conf IFP Energies Nouvelles, June 6–8, 2012, Rueil-Malmaison, France

Azzouni-Sekkal A (1995) Pétrologie et géochimie des granites de type "Taourirt": un exemple de province magmatique de transition entre les régimes orogéniques et anorogéniques au pan-africain (Hoggar, Algérie). Mém Serv Géol Algérie 7:1–288

Azzouni-Sekkal A, Boissonnas J (1993) Une province magmatique de transition du calco-alcalin à l'alcalin: les granitoïdes pan-africains à structure annulaire de la chaîne pharusienne du Hoggar (Algérie). Bull Soc Géol France 164:597–608

Azzouni-Sekkal A, Liégeois J-P, Bechiri-Benmerzoug F, Belaidi-Zinet S, Bonin B (2003) The "Taourirt" magmatic province, a marker of the closing stage of the Pan-African orogeny in the Tuareg Shield: review of available data and Sr-Nd evidence. J Afr Earth Sci 37:331–350

Barbey P, Villaros A, Marignac C, Montel J-M (2014) Multiphase melting-, magma emplacement and P-T-time path in late-collisional context: the Velay example (Massif Central, France). Bull Soc Geol France Bull Soc Geol Fr 186:93–116

Bertrand J-M, Caby R, Ducrot J, Lancelot J, Moussine-Puchkine A, Saadallah A (1978) The late Pan-African intracontinental linear fold belt of the eastern Hoggar (central Sahara, Algeria): geology, structural development, U/Pb geochronology, tectonic implication for the Hoggar shield. Precamb Res 7:349–376

Bertrand J-M, Meriem D, Lapique F, Michard A, Dautel D, Gravelle M (1986) Nouvelles données radiométriques sur l'âge de la tectonique pan-africaine dans le rameau oriental de la chaîne pharusienne (région de Timgaouine, Hoggar, Algérie). C R Acad Sci Paris 302(II):437–440

Black R, Latouche L, Liégeois J-P, Caby R, Bertrand JM (1994) Pan-African displaced terranes in the Targui shield (central Sahara). Geology 22:641–644

Boiron M-C, Cathelineau M, Banks D, Fourcade S, Vallance J (2003) Mixing of metamorphic and surficial fluids during the uplift of the Hercynian upper crust: consequences for gold deposition. Chem Geol 194:119–141

Bornhost TJ, Rose WI Jr (1986) Partitioning of gold in young calc-alkalic volcanic rocks from Guatemala. J Geol 94:412–418

Bouabsa L (1987) Intrusions granitiques à albite-topaze: minéralistions stanno-wolframifères et altérations hydrothermales associées, l'exemple du Hoggar central, Algérie. Unpubl PhD Thesis, Univ. Nancy, France, 113 pp

Bouabsa L, Marignac C, Bouguebrine J, Boiron MC (2012) Transition magmatique-hydrothermale et interactions avec les fluides externes dans les systèmes granitiques: l'exemple des granites à métaux rares (RMG) du Hoggar central. Proc 2ème Conf Intern Geol Sahara. Oujda, Morocco, pp 63–69

Boullier A-M, Liégeois J-P, Black R, Fabre J, Sauvage M, Bertrand J-M (1986) Late Pan-African tectonics marking the transition from subduction-related calc-alkaline magmatism to within-plate alkaline

granitoids (Adrar des Iforas, Mali). Tectonophys 132:233–246

Boutrika R (2006) Le gisement d'or d'In Abeggui dans le terrane de Laouni. Unpubl Magister Thesis, USTHB, Alger, Algeria, 152 pp

Caby R (2003) Terrane assembly and geodynamic evolution of central-western Hoggar: a synthesis. J Afr Earth Sci 37:133–159

Caby R, Andreopoulos-Renaud U (1987) Le Hoggar central, bloc cratonisé à 730 Ma dans la chaîne pan-africaine du continent africain. Precamb Res 36:335–344

Chalal Y (2002) Magmatisme panafricain à albite-topaze, minéralisations Sn-W-Nb-Ta et fluides associés dans le terrane de Laouni (Hoggar central, Algérie). Unpubl Doct Etat, USTHB (Alger), Algeria 229 pp

Chalal Y, Marignac C (1997) Découverte de wolframoix-iolite dans les microgranites à albite-topaze d'Aléméda (Hoggar central, Algérie): implications métallogéniques. Bull Serv Géol Algérie 8:71–79

Chaouche I (2008) Apport de la minéralogie des tourmalines à la métallogénie de l'or. Exemple des indices du terrane d'Iskel (Hoggar occidental). Unpubl Magister Thesis, USTHB-Alger, Algeria, 90 pp

Cheilletz A, Bertrand JM, Charoy B, Moulahoum O, Bouabsa L, Farrar E, Zimmerman JL, Dautel D, Archibald D, Boullier AM (1992) Géochimie et géochronologie Rb–Sr, K-Ar et 40Ar/39Ar des complexes granitiques pan-africains de la région de Tamanrasset (Algérie): relations avec les minéralisations Sn-W associées et l'évolution tectonique du Hoggar central. Bull Soc Géol France 163:733–750

Cottin J-Y, Lorand J-P, Agrinier P, Bodinier J-L, Liégeois J-P (1998) Isotopic (O, Sr, Nd) and trace element geochemistry of the Laouni layered intrusions (Pan-African belt, Hoggar, Algeria): evidence for post-collisional continental tholeiitic magmatism variably contaminated by continental crust. Lithos 45:197–222

Coulibaly Y (1994) Caractéristiques physico-chimiques des fluides des granulites de haute pression d'Ihouahouène (In Ouzzal, Algérie). Unpubl DEA Memoir, INPL-Nancy, France 85 pp

Cuney M, Barbey P (2014) Uranium, rare metals-, and granulite-facies metamorphism. Geosci Frontiers 6:1–17

de Wit M, Thiart C (2005) Metallogenic fingerprints of Archaean cratons. In: McDonald I, Boyce A, Butler IB, Herrington RJ, Polya DA (eds) Mineral deposits and Earth evolution. Geol Soc London Spec Publ 248:59–70

Debon F, Le Fort P (1988) A cationic classification of common plutonic rocks and their magmatic associations: principle, method, applications. Bull Mineral 111:493–510

Fabre J (1988) Les séries paléozoïques d'Afrique: une approche. J Afr Earth Sci 7:1–40

Ferkous K, Leblanc M (1995) Gold mineralization in the west Hoggar shear zone, Algeria. Min Deposita 30:211–224

Ferkous K, Monie P (2002) Neoproterozoic shearing and auriferous hydrothermalism along the lithospheris N-S East In Ouzzal shear zone (western Hoggar, Algeria, North Africa). J Afr Earth Sci 35:399–415

Fezaa N, Liégeois J-P, Abdallah N, Cherfouh EH, De Waele B, Bruguier O, Ouabadi A (2010) Late Ediacaran geological evolution (575–555 Ma) of the Djanet terrane, eastern Hoggar, Algeria, evidence for a Mursukian intracontinental episode. Precamb Res 180:299–327

Gao S, Zhang B-R, Luo T-C, Li Z-J, Xie Q-L, Gu X-M, Zhang H-F, Ouyang J-P, Wang D-P, Gao C-L (1992) Chemical composition of the continental crust in the Qinling orogenic belt and its adjacent North China and Yangtze cratons. Geochim Cosmochim Acta 56:3933–3950

Gebre-Mariam M, Hagemann SG, Groves DI (1995) A classification scheme for epigenetic Archaean lode-gold deposits. Min Deposita 30:408–410

Hamis A, Marignac C, Kesraoui M, Fuchs Y, Ollier N, Rossano S (2012) L'indice de beryl émeraude du complexe granitique de Guérioun (Hoggar, Algérie). Proc 2ème Conf Intern Geol Sahara. Oujda, Morocco, pp 78–81

Henry B, Bayou B, Derder MEM, Djellit H, Ouabadi A, Khaldi A, Hemmi A (2007) Late Panafrican evolution of the main Hoggar fault zones: implications of magnetic fabric study in the In Telloukh pluton (Tin Serririne basin, Algeria). J Afr Earth Sci 49:211–221

Henry B, Liégeois J-P, Nouar O, Derder MEM, Bayou B, Bruguier O, Ouabadi A, Belhai D, Amenna M, Hemmi A, Ayache M (2009) Repeated granitoid intrusions during the Neoproterozoic along the western boundary of the Saharan metacraton, eastern Hoggar, Tuareg shield, Algeria: an AMS and U-Pb zircon age study. Tectonophys 474:417–434

Kesraoui M (2005) Nature et evolutions compares de granites à métaux rares dans le Hoggar central (Algérie) à travers la pétrographie, la cristallochimie des micas et des minéraux à Ta, Nb, Sn. Unpubl Doct Etat, USTHB-Alger, Algeria, W et la géochimie 257 pp

Kesraoui M, Marignac C (2010) Liquides résiduels et évolution magmatique-hydrothermale des granites à métaux rares: l'exemple des "pegmatites" à quartz-zinnwaldite de la coupole de Rechla (Hoggar, Algérie). 22ème Réun Sci Terre, Octobre 2010, Bordeaux, France, (Société Géologique de France, 77 rue Claude-bernard, 05 Paris)

Kesraoui M, Nedjari S (2002) Contrasting evolution of low-P rare metal granites from two different terranes in the Hoggar area, Algeria. J Afr Earth Sci 34:247–257

Kesraoui M, Marignac C, Verkaeren J (2000) L'évolution tardi-magmatique des granites à métaux rares: l'exemple de la coupole de Tin-Amzi (Hoggar, Algérie). Bull Serv Géol Algérie 11:195–216

Liégeois J-P, Black R, Navez J, Latouche L (1994) Early and late Pan-African orogenies in the Aïr assembly of terranes (Tuareg shield, Niger). Precamb Res 65:59–88

Liégeois J-P, Navez J, Hertogen J, Black R (1998) Contrasting origin of post-collisional high-K calc-alkaline and shoshonitic versus alkaline and peralkaline granitoids: the use of sliding normalization. Lithos 45:1–28

Liégeois J-P, Latouche L, Boughrara M, Navez J, Guiraud M (2003) The LATEA metacraton (central Hoggar, Tuareg shield, Algeria): behaviour of an old passive margin during the Pan-African orogeny. J Afr Earth Sci 37:161–190

Liégeois J-P, Abbelsalam MG, Ennih N, Ouabadi A (2013) Metacraton: nature, genesis and behavior. Gondwana Res 23:220–237

Linnen RL, Cuney M (2008) Granite-related rare-element deposits and experimental constraints on Ta-Nb-W-Sn-Zr-Hf mineralization. In: Linnen RL, Samson IM (eds) Rare-element geochemistry and mineral deposits. Geol Assoc Canada Short Course Notes 17:45–67

Marignac C, Cuney M (1999) Ore deposits of the French Massif Central: insight into the metallogenesis of the Variscan collision belt. Min Dep 34:472–504

Marignac C, Semiani A, Fourcade S, Boiron M-C, Joron J-L, Kienast J-R, Peucat J-J (1996) Metallogenesis of the late Pan-African gold-bearing east Ouzzal shear zone (Hoggar, Algeria). J Metam Geol 14:783–801

Marignac C, Belkasmi M, Chalal Y, Kesraoui M (2001) W-Nb-Ta oxides as markers of the magmatic to hydrothermal transition condition in rare-metal granites. In: Piestrzynski A (ed) Mineral deposits at the beginning of the 21st century. Proceed IIIrd Biennial SGA Meeting, Krakow, Poland, Balkema, Rotterdam, pp 441–444

Marignac C, Cuney M, Kesraoui M, Bouabsa L (2009) Differentiation-dedifferentiation processes in the rare metal granite (RMG) lineages. In: Williams P et al (eds) Smart science for exploration and mining. Proceed Xth Biennial SGA Meeting, Townsville, Australia, pp 991–994

Nedjari S (2006) Pétrographie, géochimie et mineralogie du massif d'Ebelekan (Hoggar central, Algérie). Minéralisations associées à tantale, nobium et étain. Cristallochimie des micas et des niobo-tantalates. Unpubl Magister Thesis, USTHB-Alger, Algeria, 211 pp

Nouar O, Henry B, Liégeois J-P, Derder MEM, Bayou B, Bruguier O, Ouabadi A, Amenna M, Hemmi A, Ayache M (2011) Eburnean and Pan-African granitoids and the Raghane mega-shear zone evolution: image analysis, U-Pb zircon age and AMS study in the Arokam Ténéré (Tuareg shield, Algeria). J Afr Earth Sci 60:133–152

Nedjari S, Kesraoui M, Marignac C, Aissa DE (2001) Le massif d'Ebelekan: un granite à tantale dans le sud-est du Hoggar central (Algérie). Bull Serv Géol Algérie 11:15–47

Oulebsir F (2009) Pétrographie, géochimie et minéralisations à Sn-W associées du massif de Djilouet (Djanet, Hoggar oriental). Unpubl Magister Thesis, USTHB-Alger, Algeria, 78 pp

Ouzegane K, Bendaoud A, Kienast J-R, Touret JLR (2001) Pressure-temperature-fluid evolution in Eburnean metabasites and metapelites from Tamanrasset (Hoggar, Algeria). J Geol 108:247–263

Ouzegane K, Kiénast J-R, Bendaoud A, Drareni A (2003) A review of Archean and Paleoproterozoic evolution of the In Ouzzal granulitic terrane (western Hoggar, Algeria). J Afr Earth Sci 37:207–227

Paquette J-L, Caby R, Djouadi MT, Bouchez J-L (1998) U-Pb dating of the end of the Pan-African orogeny in the Tuareg shield: the post-collisional syn-shear Tioueine pluton (western Hoggar, Algeria). Lithos 45:245–253

Peucat J-J, Drareni A, Latouche L, Deloule E, Vidal P (2003) U-Pb zircon (TIMS and SIMS) and Sm-Nd whole-rock geochronology of the Gour Oumelalen granulitic basement, Hoggar massif, Tuareg shield, Algeria. J Afr Earth Sci 37:229–339

Rougier S, Missenard Y, Gautheron C, Barbarand J, Zeyen H, Pinna R, Liégeois J-P, Bonin B, Ouabadi A, El-Messaoud Derder M, Frizon de Lamotte D (2013) Eocene exhumation of the Tuareg shield (Sahara Desert, Africa). Geology 41:615–618

Sarni Y (2012) Granites et pegmatites de la coupole de Nahda (Laouni, Hoggar central) et les minéralisations à métaux rares associiées. Unpubl Magister Thesis, USTHB-Alger, Algeria, 124 pp

Semiani A (1995) Métallogénie de la zone de cisaillement aurifère Est-Ouzzalienne: structure, pétrologie et géochimie des gisements d'or de Tirek-Amesmessa (Hoggar occidental, Algérie). Unpubl Doctoral Thesis, Rennes 1 Univ, France, 262 pp

Semiani A, Bellal M, Bennouh A (2004) La métallogénie de l'or liée à l'évolution de la chaîne Panafricaine du massif du Hoggar (Sud de l'Algérie): influence des socles anté-panafricains dans le processus de mise en place des minéralisations aurifères. Bull Serv Géol Algérie 15:107–133

Stacey JS, Kramers JD (1975) Approximation of terrestrial lead isotopic evolution by a two-stage model. Earth Planet Sci Lett 26:207–221

Tairou MS, Affaton P, Gélard J-P, Aïté R, Sabi BE (2007) Panafrican brittle deformation and palaeostress superposition in northern Togo (West Africa). CR Geosci 339:849–857

Talbi M (1984) Contribution à l'étude du gisement aurifère de Tiririne, Hoggar oriental. Unpubl Doct Thesis, Paris VI University, France, 220 pp

The Granitoid-Related Tiouit Gold Deposit, Saghro Inlier, Eastern Anti-Atlas (Morocco): Neoproterozoic Mineralization by a Polyphase Late-Magmatic to Hydrothermal System

M. Bouabdellah, F. Chekroun, A. Alansari and D. Margoum

Abstract

The Tiouit gold deposit occurs in the central part of the Precambrian Saghro inlier in the eastern Anti-Atlas orogen. It is the second-largest gold producer in Morocco with a total production of ca. 1 Mt of ore at an average grade of 7.9 g/t Au, 67 g/t Ag, and 0.45 % Cu. Host rocks consist of metamorphosed sedimentary, volcanic, and volcaniclastic rocks of the Neoproterozoic Ouarzazate Supergroup locally intruded by the syn- to post-tectonic, I-type, calc-alkaline Ikniwn Granodiorite and Isk-n-Alla Granite. Auriferous mineralization is restricted to the southwestern part of the hydrothermally altered 690 ± 57 Ma Tiouit granodiorite, forming discontinuous sulphide veins and disseminations that trend N-S to N10° E and dip 10°–30° E to SE. Four mineralized zones are recognized, referred to as North, Central, South, and Northeast. The veins are up to 6 m wide, averaging 1.5–2 m, and extend along strike 40–300 m. Silicified halos containing up to 2–3 % disseminated pyrite are common near the veins; the highest gold and sulphide concentrations are confined to veins that exhibit the largest pyrititic halos. Primary mineral assemblages consist of varying amounts of intergrown galena, sphalerite, chalcopyrite, pyrite,

M. Bouabdellah (✉) · D. Margoum
Département de Géologie, Faculté des Sciences,
Université Mohammed Premier,
B.P. 717 Avenue Mohammed VI,
60000 Oujda, Morocco
e-mail: mbouabdellah2002@yahoo.fr

F. Chekroun
Faculté des Sciences, Département de Géologie,
El Jadida, Morocco

A. Alansari
Faculté des Sciences Semlalia, Département de
Géologie, Université Cadi Ayyad, B.P. 2390,
Marrakech, Morocco

M. Bouabdellah and J.F. Slack (eds.), *Mineral Deposits of North Africa*,
Mineral Resource Reviews, DOI 10.1007/978-3-319-31733-5_16

electrum, and native gold, with subordinate arsenopyrite, argentite, sulphosalts (tetrahedrite-tennantite), and iron oxides plus quartz. Native gold occurs either as: (1) inclusions disseminated in sulphide grains, typically at boundaries between pyrite-chalcopyrite and arsenopyrite-galena-sphalerite-aikinite, interpreted to constitute the first generation of gold (Au-1); (2) anhedral fillings in pyrite, where gold (Au-2) is commonly accompanied by chalcopyrite; and (3) fillings of fractures in quartz ± chlorite ± hematite ± muscovite ± K-feldspar. Owing to the absence of radiometric age constraints, the inferred age for gold mineralization is attributed to emplacement and subsequent crystallization of the Ikniwn Granite. Mineralogical, textural, and geochemical data together with fluid inclusion measurements are consistent with phase separation of an H_2O-rich fluid containing dissolved CO_2, which ultimately exsolved an early high-salinity aqueous fluid from the Tiouit granitic magma. This early, high-salinity and CO_2-rich fluid progressively evolved and mixed with larger volumes of colder, oxygenated, and more acidic solutions resulting in the precipitation of the Tiouit auriferous and base-metal mineralization.

1 Introduction

The Precambrian Anti-Atlas system of southern Morocco hosts a number of gold occurrences, two of which at the Akka and Tiouit deposits (Fig. 1) are of economic interest. The Tiouit deposit (longitude 4° 47′ 29″ West; latitude 31° 9′ 52″ North) described herein is spatially and genetically associated with pervasively metamorphosed, arc-related granodiorite (ca. 690 ± 57 Ma), and as such has been classified as an intrusion-related gold deposit.

Discovered in the 1940s and exploited intermittently from 1950 to 1996 by several mining companies (COMANSOUR from 1950–1959, Canadian West Field Minerals Ltd from 1959–1964, SODECAT from 1982–2000), the Tiouit deposit is the second largest gold producer in Morocco with a total production approximating 1 Mt of ore at an average grade of 7.9, 67 g/t Ag, and 0.45 % Cu (Alansari and Sagon 1997). During 2011–2012, Canadian KEFI Minerals and Moroccan Roche Invest SARL acquired the property including treatment of mine tailings. In this regard, approximately 720,000 tonnes of tailings were generated during the lifetime of the mine, of which an estimated 460,000 tonnes contain 3–4 g/t Au and 20–30 g/t Ag (www.kefi-minerals.com/…/exclusivity_over_tiouit).

The Tiouit deposit lies within a segment of the eastern Anti-Atlas system along the central part of the Saghro inlier (Fig. 1). Gold ores are spatially associated with sulphide minerals in flat-lying quartz veins within hydrothermally altered, arc-related, syn- to post-collisional, I-type granodiorite, and share many attributes typical of intrusion-related gold deposits worldwide (e.g., Lang and Baker 2001; Groves et al. 2003). Mineralizing fluids ascended from unknown sources at depth and flowed through fractured older igneous host rocks, depositing quartz, gold, and associated minerals and causing extensive metasomatic alteration of country rocks and wall rocks.

The aim of the present contribution is to update the geological setting of the deposit and reexamine previously published geochemical data (Alansari 1997; Alansari and Sagon 1997; Chaker 1997; Jettane et al. 1999; Jettane 2001; Benchekroun and Jettane 2004; Alansari et al.

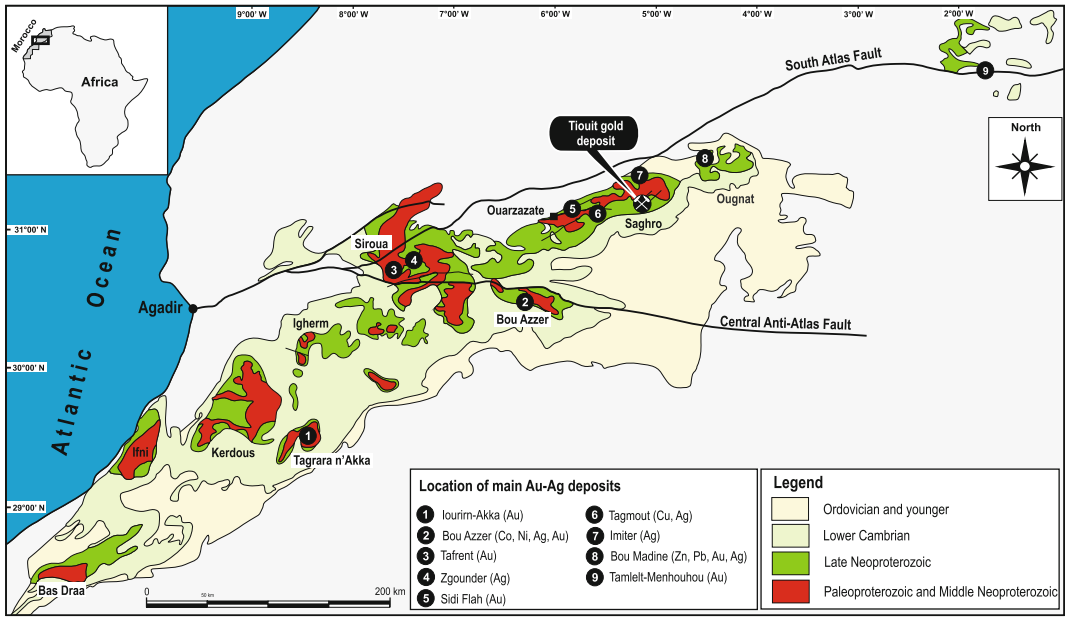

Fig. 1 Location of the Tiouit gold deposit with respect to the local Anti-Atlas system and nearly Au–Ag-bearing deposits. *Inset* shows location of Tiouit district with respect to the Anti-Atlas and African continent

2011), in the context of improved geologic understanding (Walsh et al. 2012) since publication of these earlier studies.

2 Geologic Setting

The stratigraphic sequence that hosts the Tiouit deposit consists of a succession of metamorphosed sedimentary, volcanic, and volcaniclastic rocks of the Neoproterozoic Ouarzazate Supergroup (BGS 1999a, b; Hawkins et al. 2001; Thomas et al. 2002) locally intruded by two suites of calc-alkaline plutons (Fig. 2), and numerous minor intrusions including dikes, sills, and volcanic plugs of varying composition (O'Connor 2010). Dominant intrusive rocks comprise the Ikniwn granodiorite (i.e., Bardouz suite) and the Isk-n-Alla granite (Tangourt suite) that pre- and post-date, respectively, deposition of the Ouarzazate Supergroup.

The oldest metasedimentary rocks assigned to the Middle to Upper Precambrian III (MEM 1975) Mansour and Imlas Groups. These Groups include a series of andesitic to dacitic volcanic rocks overlain by thickly bedded and coarse-grained conglomerate, sandstone, siltstone with significant rhyolitic tuff, and rhyolitic ignimbrite (O'Connor 2010). Overall, the intrusive rocks predate the Cambrian but are locally cut by a dolerite-diabase dike swarm of Triassic-Early Jurassic age (Sebai et al. 1991). The intrusions lack evidence of deformation; contacts with the enclosing metasedimentary host rocks are sharp. No precise temperature estimates have been published for the peak metamorphism in the area of low grade greenschist facies, but due to the widespread occurrence of albite, muscovite, chlorite, and epidote in mafic lithologies, it is unlikely that peak temperatures were in excess of 300 °C. Conversely, thermal metamorphism produced during emplacement of the hydrothermally altered Ikniwn Granodiorite and Isk-n-Alla Granite produced a metamorphic halo up to 1.5 km from the contact, consisting mainly of cordierite, andalusite, chlorite, and muscovite ± biotite. The predominant brittle structures are represented by a NNW-SSE-trending fault system offset by WNW-ESE faults.

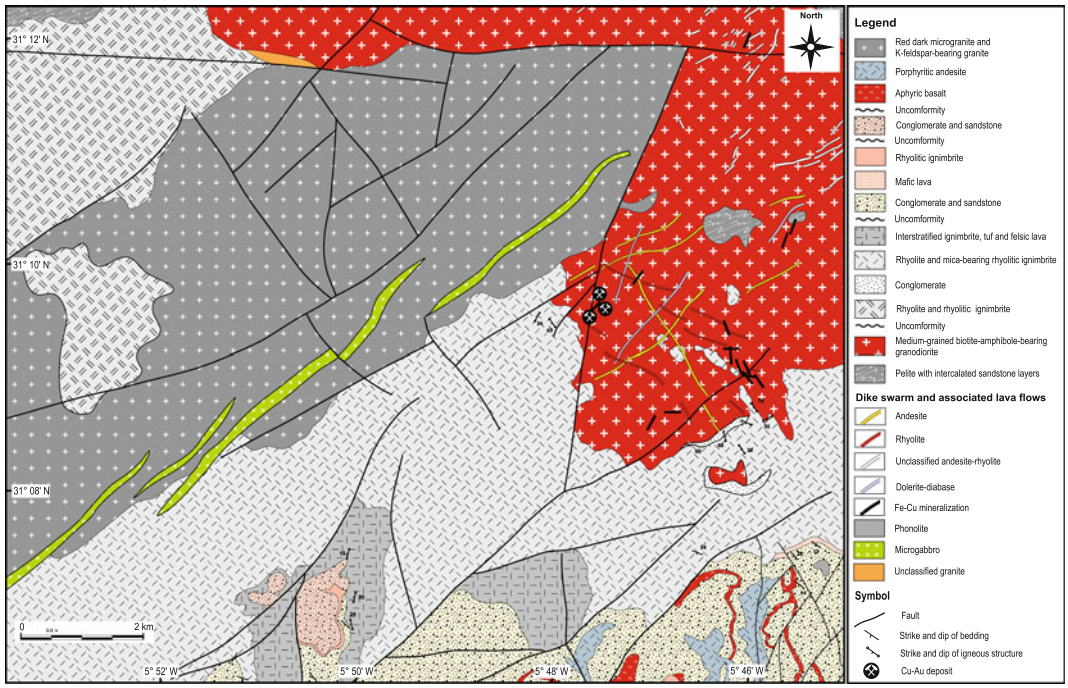

Fig. 2 Geological map of the Tiouit district (modified after geological map of Tiouit at a scale of 1:50,000; Hawkins et al. 2001) showing the main lithostratigraphic units, extent of structures, and relative position of known vein-type orebodies and their relationships to the 690 ± 57 Ma Ikniwn Granodiorite and 566 ± 20 Ma Isk-n-Alla Granite

The Tiouit goldfield covers an area of 6 km^2 and is restricted to the southwestern part of the hydrothermally altered Ikniwn intrusion referred hereafter as the Tiouit granodiorite (Fig. 2). The Tiouit granodiorite, which hosts the gold deposits and occurrences, has been dated broadly at 690 ± 57 Ma by the Laser Ablation-Plasma Ionisation Multicollector Mass Spectrometer (LA-PIMMS) method on zircons (O'Connor 2010). The intrusion is an E-W elongate, 9 × 9 km coarse-grained quartz monzonite to granodiorite composed predominantly of K-feldspar, quartz, plagioclase, and hornblende ± pyroxene ± biotite. Accessory minerals include titanite, apatite, zircon, rutile, monazite, pyrite, and Fe–Ti oxides. Mineralogically and geochemically, the intrusion is classified as I-type (i.e., formed from magma derived from an igneous protolith) calc-alkaline granite emplaced in an intracontinental volcanic arc and a syn- to post-collisional tectonic setting (Alansari 1997; Alansari and Sagon 1997; Chaker 1997). The presence of ilmenite and scarcity of magnetite suggest that the intrusion solidified at least partly under reducing conditions. Numerous closely-spaced, NE- and NNW-trending quartz-feldspar-porphyry (i.e., dacite-rhyolite and porphyritic microgranite), intermediate-composition to mafic dike swarms cut the Tiouit granodiorite, its metamorphic aureole, and surrounding country rocks. A large NE-SW-trending dolerite dike swarm of Triassic-Early Jurassic age (Sebai et al. 1991) cuts the Tiouit district. This dike forms the northeastern termination of the 300-km-long Great Dyke of Foum-Zguid (e.g., Leblanc 1973).

The Isk-n-Alla intrusion (ca. 566 ± 20 Ma, U-Pb zircon age; O'Connor 2010) occurs as an post-collisional, NW-SE-trending, elliptical-shaped, shallow-crustal body of calc-alkaline composition (Fig. 2). Contact with the adjacent Ikniwn Granite is covered Quaternary alluvium,

and is inferred to be largely faulted. The primary mineral assemblage is dominated by quartz, K-feldspar, plagioclase, pyroxene, and hornblende, with rare biotite and accessory apatite + zircon ± cassiterite ± beryl.

3 Mineralogy, Alteration, and Paragenesis

The auriferous Tiouit mineralization is structurally controlled and consists of numerous discontinuous, flat-lying sulphide veins and disseminations distributed over an area of 3 × 2 km (Figs. 3 and 4). All of the veins lie within the southwestern part of the hydrothermally altered Tiouit granodiorite, 9 km from the contact with the younger Isk-n-Alla Granite. Silicified halos containing up to 2–3 % disseminated pyrite are common within the granodiorite that hosts the veins; the highest gold and sulphide concentrations occur in veins having the largest pyrite halos. Four different mineralized zones, referred to as North, Central, South, and Northeast, are recognized (Fig. 3). The veins are up to 6 m wide, averaging 1.5–2 m, and extend along strike from 40 to 300 m (Alansari et al. 2011). Veins are spaced 50 cm to 2 m apart,

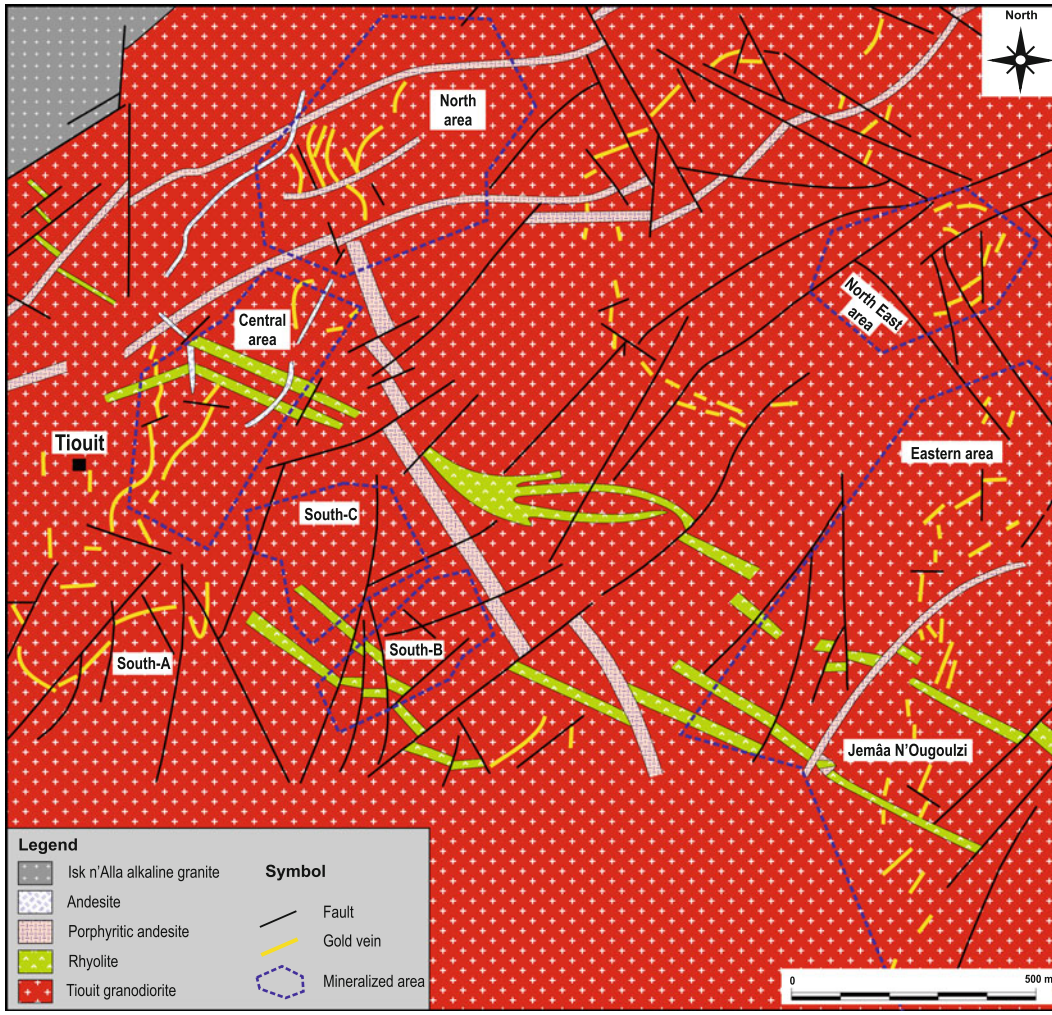

Fig. 3 Detailed mine-scale geology of the Tiouit deposit

strike roughly N-S to N10° E, and dip 10° to 30° E to SE. Locally, some veins form conjugate pairs and en echelon, tension-gash structures. The veins exhibit pinch and swell structures with the highest ore grades encountered in zones of maximum swell (Fig. 4).

All of the veins display more or less similar mineral assemblages dominated by varying amounts of intergrown galena, sphalerite, chalcopyrite, pyrite, electrum, and native gold. Minor consistuents are arsenopyrite and argentite, sulfosalts (tetrahedrite-tennantite), and iron oxides plus quartz; relative proportions of sulphide relative to iron oxides and quartz vary from one mineralized structure to another. Arsenopyrite is found only in Au- and Ag-rich veins. Pyrrhotite occurs as fine-grained inclusions within sulphide grains. The primary Fe-oxides include magnetite and possibly hematite. Supergene oxidation has resulted in the development of geothite, digenite, and covellite. In addition of quartz and Fe-oxides, other gangue minerals, in order of decreasing abundance, include sericite (muscovite), chlorite, carbonates (dolomite), epidote, and rutile.

Based on several studies (Chaker 1997; Alansari 1997; Alansari and Sagon 1997), native gold occurs either as: (1) inclusions disseminated in sulphide grains, typically at boundaries between pyrite-chalcopyrite and arsenopyrite-galena-sphalerite-aikinite, interpreted to constitute the first generation of gold (Au-1); (2) anhedral fillings in pyrite, where gold is commonly accompanied by chalcopyrite; and (3) fillings of fractures in quartz ± chlorite ± hematite ± muscovite ± K-feldspar (Au-2). This last type of gold has a distinctly more Ag-rich composition (i.e., Ag 41 wt%) compared to Au-1 that averages ~23 wt% Ag (Alansari et al. 2011), and is attributed to the second generation of gold (Au-2).

Gold associated with sulphides accounts for the highest grades in the deposit. Grain sizes of the gold are typically 5–30 μm and may reach 110 μm × 20 μm. Electron microprobe analyses indicate that the gold grains contain 47–71 and 26–34 wt% Ag. These compositions correspond to fineness values in the range of 639–732 (Chaker 1997).

Wall-rock alteration is well developed around the ore veins and to different extents throughout the Tiouit granodiorite. This alteration resulted in the development of a series of overlapping halos, which are defined by dominant mineralogy. In this context, four distinct hydrothermal stages are recognized (Chaker 1997; Alansari and Sagon 1997; present study) including: (1) late magmatic to early hydrothermal K-feldspar-biotite-hematite ± pyrite ± magnetite (K-silicate stage); (2) main hydrothermal propylitic chlorite-epidote-hematite; (3) late phyllic muscovite (phengite)-quartz-pyrite; and (4) supergene postore. Locally, an advanced argillic halo characterized by alunite with variable amounts of kaolinite, illite, and smectite ± montmorillonite has been recognized (Chaker 1997). Furthermore, the preferential concentration of disseminated sulphides and gold-bearing veins within intensely silicified, sericitized, and biotitized alteration zones suggests that the hydrothermal fluid discharge was strongly focused near the contacts of the Ikniwn Granodiorite and the Isk-n-Alla Granite.

The earliest stage of hydrothermal alteration (Stage I) is considered to have a potassic alteration assemblage recorded by pervasive development of K-feldspar and biotite ± hematite ± chlorite ± epidote ± sericite ± albite. This alteration is marked by reddening of feldspars during hematite crystallization in microfractures. The pink-red colour of most samples of the Tiouit granite is due to this alteration event. Coexistence of magnetite and hematite indicates that the alteration occurred close to the hematite-magnetite redox buffer (Wones 1981, 1989; Budd and Skirrow 2007). The second alteration (Stage II) is recognized as a propylitic assemblage that forms the outermost parts of the alteration halos surrounding the gold mineralization. This mineral assemblage consists mainly of disseminations and aggregates, with a local network of fine veinlets and fracture fillings of chlorite ± epidote ± muscovite ± hematite that are intimately associated with pyrite. Chlorite

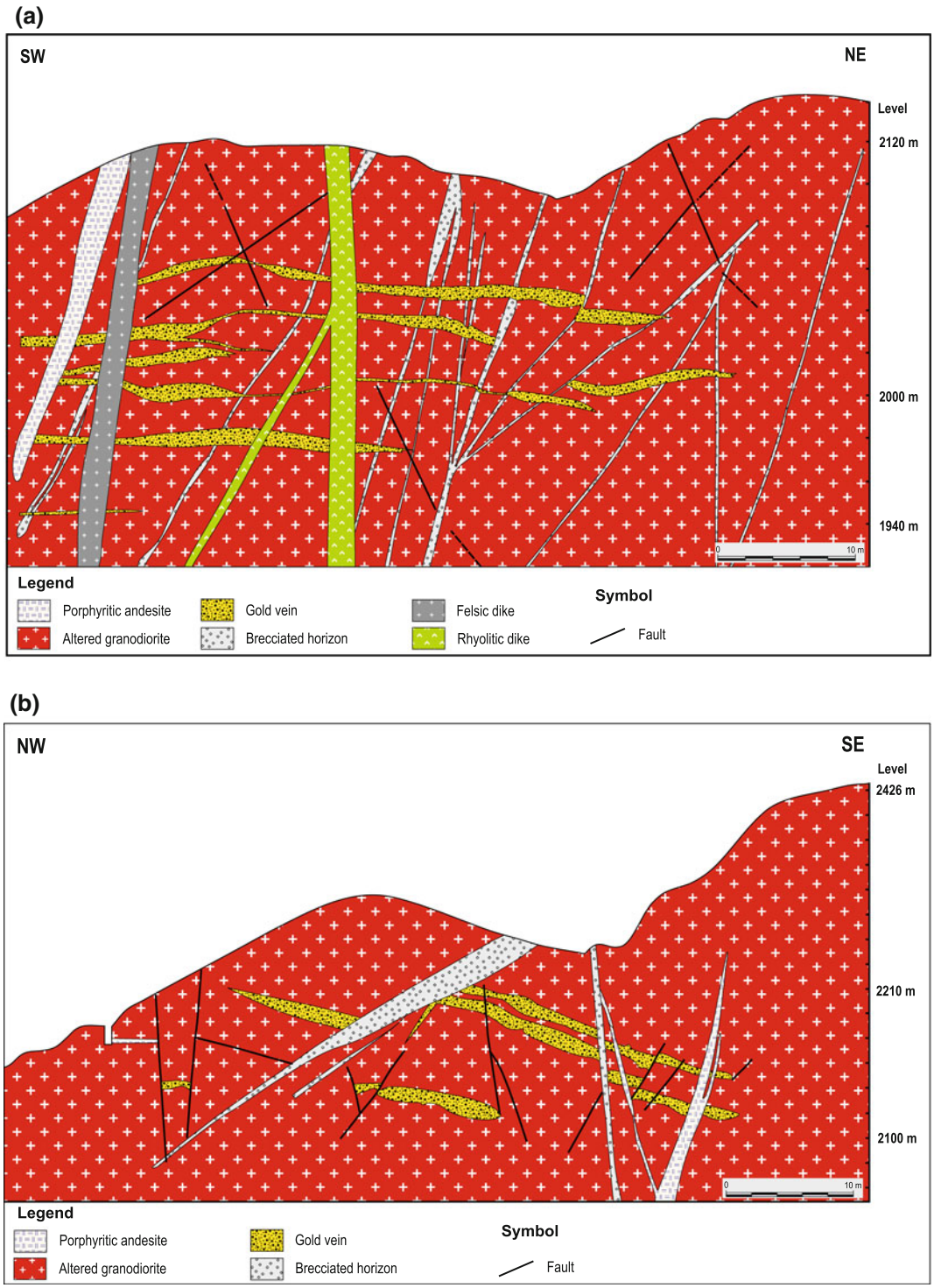

Fig. 4 Cross sections through the main mineralized areas of the Tiouit deposit showing distribution of auriferous flat-lying ore lenses in the host granodiorite and related rocks (modified after Chaker 1997)

shows a wide spectrum of compositions ranging from ripidolite to pycnochlorite to brunsvigite (Chaker 1997). Application of chlorite geothermometry (Cathelineau and Nieva 1985) indicates temperatures of equilibration in the range of 308–330 °C, consistent with data from fluid inclusions, as discussed below. The propylitic alteration assemblage is gradually replaced by a sericitic or phyllic assemblage in some parts of the Tiouit intrusion where chlorite is only preserved locally. This sericitic alteration (Stage III) is much more intense and texturally destructive than the potassic and porphyritic assemblages, and consists of muscovite (phengite)-quartz-pyrite ± hematite ± chlorite ± epidote ± albite ± carbonate. Most of the Tiouit gold and base-metal mineralization is associated with Stage II and III alteration assemblages.

The sequence of mineral deposition shows four successive stages of mineralization, two of which (Stages II and III) are related to gold mineralization. Stage I, referred to as the "Fe-As-ore stage," is the oldest and is devoid of economically recoverable gold. The mineral paragenesis consists of pyrite, arsenopyrite, and magnetite ± pyrrhotite ± enargite. Conversely, Stage II is economically the most important and therefore labelled the "sulphide-gold-bearing stage," consisting of galena, sphalerite, chalcopyrite, pyrite, arsenopyrite, tetrahedrite-tennantite, electrum (Au-1) ± aikinite ± bismuthinite. Stage II mineralization dominates bulk ore contents to the vein including high Cu and Au grades. We estimate that at least 80 % of the Au and Cu in the deposit were introduced during Stage II. Following deposition of this stage, Stage III is also auriferous, dominated by hematite and electrum (Au-2).

The post-ore supergene mineral assemblage (Stage IV) resulted from the oxidation of primary sulphides. This assemblage is of minor significance to the total metal endowment of the deposit, and consists of minor amounts of cerussite, bornite, digenite, chalcocite, covellite, malachite, azurite, Cu-sulphates, and Fe- and Mn-oxides.

4 Discussion

The 690 ± 57 Ma Ikniwn Granite that hosts the Tiouit gold deposit was emplaced as a syn- to post-tectonic, calc-alkaline, I-type intrusion within a Neoproterozoic, arc-like setting as suggested by petrogenetic and geochronologic data. Field relationships together with paragenetic studies show that this intrusion was subjected to at least two structurally controlled auriferous mineralizing events (i.e., Stages II and III). Owing to the lack of reliable radiometric age dating, combined geological field observations and cross-cutting relationships were used to bracket the timing of mineralization. In this respect, the age of mineralization is broadly constrained by the ca. 690 ± 57 Ma Ikniwn Granite that hosts the gold mineralization and the ca. 563 Ma (Walsh et al. 2008) rhyolitic dike swarm that cuts the mineralized structures (Fig. 3). Accordingly, the inferred age for gold mineralization appears to be intimately related to emplacement and subsequent crystallization of the Ikniwn Granite. The strong spatial and temporal association of the Tiouit mineralization with this granitic intrusion, the occurrence of the mineralized structures as sulphide-bearing veins and related alteration assemblages, and their metal association and sulphide content, are all similar to those described elsewhere for porphyry systems (Sillitoe 2010), and intrusion-related Au deposits (Lang and Baker 2001; Groves et al. 2003). More importantly, local occurrence of alunite in the advanced argillic alteration halo (Chaker 1997) is compatible with a high sulphidation epithermal system and resembles the steam-heated zones of advanced argillic alteration that characterize hot-spring-type Ag–Au deposits.

Fluid inclusion data from various generations of ore-related quartz show wide ranges in homogenization temperatures and salinities, with T_h values ranging from 150 to ~380 °C and salinities from ca. ~0 to 63 wt% NaCl equiv (Chaker 1997; Jettane 2001). These wide variations suggest that the Tiouit gold mineralization

resulted from the circulation of multiple fluids and/or ore-forming processes. In this respect, the bulk compositions of the ore fluids lie within H_2O–NaCl–CO_2, CO_2–(CH_4), and H_2O–NaCl ± $CaCl_2$ end-members. The high salinities (i.e., up to 63 wt% NaCl equiv) and high temperatures (i.e., up to 380 °C) exhibited by some fluid inclusions suggest that the hydrothermal fluids exsolved from a magmatic source, probably genetically related to the crystallizing history of the Tiouit granodiorite. Indeed, the coexistence of CO_2-rich and CO_2-free aqueous fluid inclusions (Chaker 1997) constitutes additional evidence for phase separation of an H_2O-rich fluid containing dissolved CO_2, which ultimately exsolved an early high-salinity aqueous fluid from the Tiouit granitic magma. This early, high-salinity and CO_2-rich fluid progressively evolved and deposited, at relatively high temperature, the Au-1 mineralization. It is well documented that fluids exsolved from felsic magmas containing hornblende, as in the case of the Tiouit intrusion, are enriched in KCl relative to NaCl (Burnham and Ohmoto 1980), consistent with the early pervasive K-alteration that affected the Tiouit intrusion. Moreover, the large spread in homogenization temperatures and salinities for the late H_2O–NaCl ± $CaCl_2$ fluid may have been caused by the influx of progressively larger volumes of colder, oxygenated, and more acidic solutions that interacted extensively with the granodiorite, resulting in the leaching of Ca from magmatic plagioclase, overprinting of the early K-rich magmatic-related mineral assemblages, and subsequent deposition of Au-2 within fractures in the hydrothermally altered rocks.

It has been shown experimentally that the solubility of gold depends of the stability of the chloride and/or sulphur-bearing complexes, with the latter being predominant under reducing conditions at near-neutral pH and relatively low temperatures (Seward and Barnes 1997; Williams-Jones et al. 2009). Due to the high chlorinity of the early mineralizing fluid that deposited Au-1 in the Tiouit deposit, it is suggested here that gold was transported as chloride complexes in a hot, saline, acidic, and oxidized fluid having a high KCl/NaCl ratio. Decreasing temperatures with advancing paragenetic sequence would have favored the transport of gold mainly as $Au(HS)^{2-}$. In this case, gold precipitated during phyllic alteration or was transported to outer zones (see Gammons and Williams-Jones 1997). The coexistence of K-feldspar and sericite in the wall-rock alteration assemblage that prevailed during the second stage of mineralization records a near-neutral pH (ca. 5 at 300 °C). Under such neutral conditions, gold-chloride complexes ($AuCl^{2-}$) are ineffective in transporting gold (Williams-Jones et al. 2009). Indeed, quantitative fluid modelling (Benchekroun and Jettane 2004) has shown that at the Tiouit deposit a significant amount of Au-2 (i.e., 3 mg deposited from one 1 kg of mineralizing solution equivalent to 43 % of total gold deposited) was transported as bisulphide complexes ($(HAu(HS)_2^0$, $AuHS^0$ and $Au(HS)^{2-}$) and deposited as a result of a decrease in both H_2S activity and oxygen fugacity (f_{O2}), produced by the alteration of pyrrhotite to pyrite. Moreover, the occurrence of pyrrhotite as small inclusions within pyrite and chalcopyrite, and of associated hydrothermal magnetite, indicates that the Tiouit deposit formed at low f_{O2} conditions near or above the pyrrhotite + pyrite + magnetite buffer.

Based on the microthermometric and geochemical data discussed above, it becomes apparent that the overall mineralogy of the late-magmatic-hydrothermal system at Tiouit evolved through time. This evolution includes a change from CO_2-rich to H_2O-rich ore-forming fluids that resulted in the precipitation, with advancing paragenetic sequence, of Au-1 related to stage II at relatively high temperatures, and of Au-bearing sulphide veins and disseminations (i.e., Au-2) of stage III at lower temperatures. This decrease in temperature may indicate cooling and dilution during fluid mixing, owing to the influx of progressively larger volumes of cooler, and possibly meteoric, fluids that overprinted the early magmatic-related mineral assemblages.

References

Alansari A (1997) La mine d'or de Tiouit: un exemple de veines aurifères mésothermales associées à une granodiorite d'âge protérozoïque supérieur (Massif Panafricain du Jbel Saghro, Anti-Atlas, Maroc). Unpublished Ph.D. Thesis, Université Cadi Ayyad, Faculté des Sciences Semlalia, Marrakech, Morocco, 284 pp

Alansari A, Sagon JP (1997) Le gisement de Tiouit (Jebel Saghro, Anti-Atlas, Maroc): un système mésothermal polyphasé à sulfures-or et hématite-or dans une granodiorite potassique d'âge Protérozoïque. Chron Recherche Minière 527:3–25

Alansari A, Mouguina M, Maacha M (2011) Le gisement de Tiouit à Au-Cu-Ag (Massif néoprotérozoïque du J. Saghro). In: Mouttaqi A, Rjimati EC, Maacha L, Michard A, Soulaimani A, Ibouh H (eds) Les principales mines du Maroc. Notes et Mémoires du Service Géologique du Maroc, vol 564, pp 53–57

Benchekroun F, Jettane A (2004) Fluid inclusions and quantitative model for gold precipitation in the Tiouit deposit (Anti-Atlas, Morocco). J Afr Earth Sci 39:295–300

BGS (1999a) Premier rapport intermédiaire, aout 1999. Feuilles de Tilemsoun et Laayoune Dra. British Geological Survey Technical report, WC/99/30C

BGS (1999b) Premier rapport intermédiaire, aout 1999. Feuilles d'Anzi, Had-n-Tahala, Bge Youssef B, Tachfine et Tanalt. British Geological Survey Technical report, WC/99/31C

Budd AR, Skirrow RG (2007) The nature and origin of gold deposits of the Tarcoola goldfield and implications for the Central Gawler gold province, South Australia. Econ Geol 102:1541–1563

Burnham CW, Ohmoto H (1980) Late-stage processes of felsic magmatism. Min Geol Spec Issue 8:1–11

Cathelineau M, Nieva D (1985) A chlorite solid solution geothermometer. The Los Azufres (Mexico) geothermal system: Contrib. Mineral Petrol 91:235–244

Chaker M (1997) Géochimie et métallogénie de la mine d'or de Tiouit, Anti-Atlas oriental (Sud du Maroc). Unpublished Ph.D. Thesis, Université de Chicoutimi, Chicoutimi, Québec, Canada, 276 pp

Gammons CH, Williams-Jones AE (1997) Chemical mobility of gold in the porphyry-epithermal environment. Econ Geol 92:45–59

Groves DI, Goldfarb RJ, Robert F, Hart CJR (2003) Gold Deposits in metamorphic belts: overview of current understanding, outstanding problems, future research, and exploration significance. Econ Geol 98:1–29

Hawkins MP, Beddoe-Stephens B, Gillespie MR, Loughlin S, Barron HF, Barnes RP, Powell JH, Waters CN, Williams M (2001) Carte géologique du Maroc au1/50 000, feuille Tiwit. Notes Mémoires Service Géologique Maroc, 404 pp

Jettane A (2001) Le gisement aurifère de Tiouit (Anti-Atlas oriental, Maroc) approche quantitative et modélisation du dépôt de l'or. Unpublished Ph.D. Thesis, Université Dhar El Mehraz de Fès, Fès, Morocco, 175 pp

Jettane A, Boutaleb M, Farazdaq H, Jabrane R (1999) Les événements thermiques polycycliques à sulfures-or et hématite-or du gisement de Tiouit (Anti-Atlas, Maroc). Chron Recherche Minière 536–537:65–78

Lang JR, Baker T (2001) Intrusion-related gold systems: the present level of understanding. Miner Deposita 36:477–489

Leblanc M (1973) Tectonique du Précambrien-II de Bou Azzer-El Graara (Anti-Atlas Central). Notes Mémoires Service Géologique Maroc 33:59–81

MEM (Ministère de l'Energie et des Mines) (1975) Carte géologique du Maroc: Jbel Saghro-Dades. Echelle 1/200,000

O'Connor EA (2010) Geology of the Drâa, Kerdous, and Boulmane Districts, Anti-Atlas, Morocco. Technical Report IR/10/072. British Geological Survey, Nottingham, 310 pp

Sebai A, Féraud G, Bertrand H, Hanes J (1991) $^{40}Ar/^{39}Ar$ dating and geochemistry of tholeiitic magmatism related to the early opening of Central Atlantic rift. Earth Planet Sci Lett 104:455–472

Seward TM, Barnes HL (1997) Metal transport by hydrothermal ore fluids. In: Barnes HL (ed) Geochemistry of hydrothermal ore deposits, 3rd edn. Wiley, New York, pp 435–486

Sillitoe RH (2010) Porphyry copper systems. Econ Geol 105:3–41

Thomas RJ, Chevallier LC, Gresse PG, Harmer RE, Elington BM, Armstrong RA, De Beer CH, Martini JEJ, De Kock GS, Macey P, Ingram B (2002) Precambrian evolution of the Sirwa Window, Anti-Atlas Orogen, Morocco. Precambr Res 118:1–57

Walsh GJ, Benziane F, Burton WC, El Fahssi A, Yazidi A, Yazidi M, Saadane A, Aleinikoff JN, Ejjaouani H, Harrison RW, Stone BD, Kalai M (2008) Carte géologique au 1/50 000, Feuille Bouskour. Notes Mémoires Service Géologique Maroc 469:131

Walsh GJ, Benziane F, Aleinikoff JN, Harrison RW, Yazidi A, Burton WC, Quick JE, Saadane A (2012) Neoproterozoic tectonic evolution of the Jebel Saghro and Bou Azzer-El Graara inliers, eastern and central Anti-Atlas, Morocco. Precambr Res 216–219:23–62

Williams-Jones AE, Bowell RJ, Migdisov AA (2009) Gold in solution. Elements 5:281–287

Wones DR (1981) Mafic silicates as indicators of intensive variables in granitic magmas. Min Geol 31:191–212

Wones DR (1989) Significance of the assemblage titanite + magnetite + quartz in granitic rocks. Am Mineral 74:744–749

Part V

Volcanic-Hosted Massive Sulphide Deposits

Volcanogenic Massive Sulphide–Oxide Gold Deposits of the Nubian Shield in Northeast Africa

C. Tucker Barrie, Mohamed Abu Fatima Abdalla and R. Daniel Hamer

Abstract

The 0.85–0.55 Ga Arabian-Nubian Shield of northeast Africa comprises an assemblage of volcanic arc and sub-arc strata that are fertile for volcanogenic massive sulphide (VMS) and overlying oxide gold deposits. At least fifty VMS deposits are known in the Nubian Shield west of the Red Sea, many of which are clustered in districts. The most important districts, including Ariab in NE Sudan, Bisha in western Eritrea, and Asmara in eastern Eritrea, have seen significant exploration and development recently. The Ariab VMS–oxide gold district contains over 20 oxide gold deposits that have been mined since 1991 (>2 Moz Au recovered), with several having large Cu–Au (+ Zn + Ag) sulphide resources below the oxide gold resources, including Hadal Awatib East (67.8 Mt), Hassai South (42.1 Mt), and Hadayamet (8.4 Mt). The Hadal Awatib East VMS resource comprises only one third of a giant sulphide lens that extends for more than 3.1 km continuously along strike, making it among the most extensive VMS deposits known globally: only Kidd Creek, Ontario (3.1 km to depth), and Neves Corvo, Portugal (3.4 km length), are comparable in size. Mining began in 2011 in the Bisha VMS district, following the discovery of five deposits with resources of >70 Mt. The main Bisha VMS–oxide gold deposit was discovered in 2003 when the first drill program tested a large hematite gossan that extended along strike for over 300 m. Subsequent discoveries at Harena, Bisha Northwest, Hambok, and Yakob Dewar have added significantly to the resource base.

C.T. Barrie (✉)
CTBA Geoconsultants, 12 Burnham Road, Ottawa
K1S 0J8, Canada
e-mail: barriect@sympatico.ca

M.A.F. Abdalla
Ariab Mining Co., P.O. Box 3250, Khartoum, Sudan

R.D. Hamer
CST Minerals Lady Annie Pty. Ltd., P.O. Box 2029,
Mount Isa, QLD 4825, Australia

M. Bouabdellah and J.F. Slack (eds.), *Mineral Deposits of North Africa*,
Mineral Resource Reviews, DOI 10.1007/978-3-319-31733-5_17

In the Asmara district, VMS deposits and occurrences were known for decades at Adi Nefas, Debarwa, and Emba Derho; however, exploration in the past decade has significantly increased known resources, particularly at Emba Derho (85 Mt). Many of the VMS deposits in the Nubian Shield have been subjected to strong, near-surface oxidation and supergene processes, probably since the early Tertiary, during a period of rapid uplift and concomitant deflation associated with opening of the Red Sea. This secondary alteration has produced unusual profiles consisting of horizontally stratified, gold-bearing oxide above supergene copper, and primary Cu–Zn–Au–Ag massive sulphides below. At Hadal Awatib East, Hassai South, and Bisha, a 10-fold enrichment in gold exists from primary VMS to oxide gold, and a 3.5-fold enrichment in copper from primary massive sulphide to the supergene zone. Above the redox front, the deposits are commonly surrounded by an incomplete halo of secondary copper oxide. The significant, near-surface gold and copper enrichments make these deposits particularly attractive targets for mineral exploration and development.

1 Introduction

The Arabian–Nubian Shield is a large, predominantly Neoproterozoic crustal block that hosts a variety of mineral deposit types, including orogenic gold deposits (e.g., Sukari, Egypt–15.3 Moz Au, Centamin Resources website; Maha el Dahb, Saudi Arabia >2 Moz Au, Ma'adan Gold website; Lega Dembe, Ethiopia 2.5 Moz Au, Orecorp website; Tulu Kapi, Ethiopia, 2.0 Moz Au, Nyota website); and volcanogenic massive sulphide (VMS)–oxide gold deposits. Since the discovery in 2003 of the high-grade Bisha VMS–oxide gold deposit, there has been a substantial increase in exploration and development of this deposit type in the Nubian Shield, with numerous discoveries, and a growing inventory of potentially mineable resources, in Egypt, Sudan, Eritrea, and Ethiopia. This contribution focuses on the geology and mineralization of VMS–oxide gold deposits within the Nubian Shield, and particularly on recently discovered deposits and resources in three major districts: Ariab in NE Sudan, Bisha in western Eritrea, and Asmara in eastern Eritrea.

2 Regional Geological Setting: The Neoproterozoic Nubian Shield

The ~0.85–0.55 Ga Nubian Shield (>3 × 10^6 km^2) underlies parts of Egypt, Sudan, Eritrea, Ethiopia, Somaliland, and Kenya (Fig. 1). It comprises gneissic, granitic, and volcanosedimentary rocks west of the Red Sea, which constitutes the western half of the Arabian-Nubian Shield that was divided by the opening of the Red Sea in the early Miocene. In broad terms, the Nubian Shield comprises a series of lithotectonic blocks and/or accreted arc terranes that broadly young from west to east, and that were intruded and sutured by younger, calc-alkalic to mildly alkaline, granitoid plutons from 600–525 Ma during the Pan-African orogeny (e.g., Stern 1994).

The Nubian Shield represents the northern sector of the East African orogen, in which supracrustal and mid-crustal rocks of similar age extend intermittently to the south into Mozambique, and to southern Madagascar (Stern 1994). Lead and neodymium isotope studies in the northern half of the Nubian Shield indicate that most of the contained Neoproterozoic rocks were

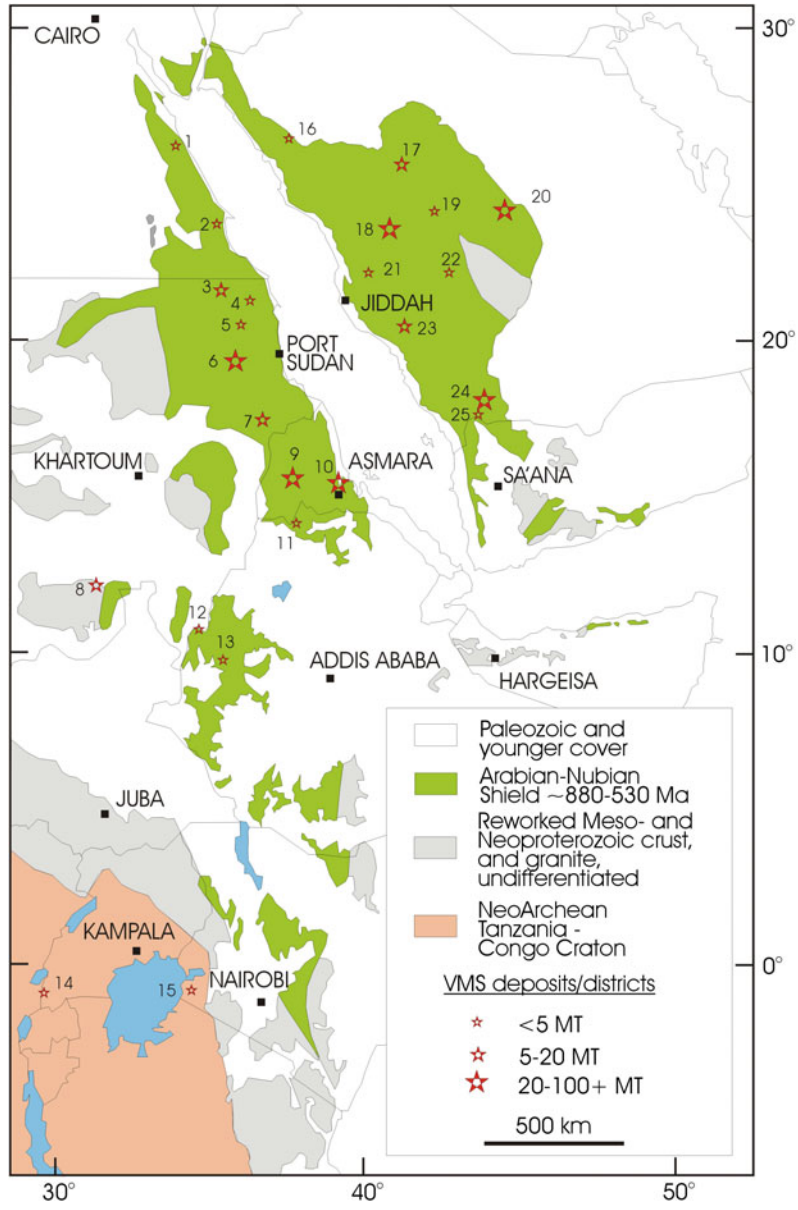

Fig. 1 Location of VMS deposits or districts in the Arabian–Nubian shield, and bordering areas. *Egypt*: *1* Hamama and Abu Marawat; *2* Um Samuiki. *Sudan*: *3* Hamissana district (Uar, Hamissana, Onib, Tbon, Eigiet, and Adarmo deposits); *4* Gebiet; *5* Serakoit; *6* Ariab (Hassai) district (see Fig. 2); *7* Eyob district (Tohamyam, Abu Samar, Eyob, Derudeb, and Tagoteb deposits); *8* NE Nuba Mountains (~1100 Ma, external to ANS) Tumluk, Jabal, Fayo, and Agbash deposits. *Eritrea: 9* Bisha district (see Fig. 3); *10* Asmara district (see Fig. 4). *Ethiopia*: *11* Tarakimti, *12* Abetselo, Azale, and Akendayu; *13* Tulu Boli and Wankey. *Uganda*: *14* Kilembe (external to ANS). *Kenya*: *15* Macalder (external to ANS). *Saudi Arabia*: *16* Ash Shizm; *17* Nuqrah, Nuqrah North, Nuqrah South, An Nimahr; *18* Jabal Sayid, Umm Ad Damar; *19* As Safra; *20* Ar Ridaniya, Khnaiguiyah, Al Amar, Umm Ash Shalahib; *21* Shayban, Jabal Baydan; *22* Shaib Lamisah; *23* Shaab Al Taare, Wadi Bidah, Gehab, Rabathan, Jadmar, Al Hajar; *24* Al Masane; *25* Kutam. See Tadasse et al. (2003), Ogola (2006), Owor et al. (2007), Barrie et al. (2007), Johnson et al. (2011)

derived either from a Neoproterozoic mantle directly, or from Paleo—or Mesoproterozoic lower crustal rocks (e.g., Egypt and Western Sudan areas; Stacey et al. 1982; Hargrove et al. 2006). Few radiogenic isotope studies have been carried out in the southern half in Ethiopia and Kenya, but it appears that much of these areas is underlain by relatively juvenile crust that is distinct from the Neoarchean to Mesoproterozoic rocks of the Tanzania-Congo craton to the west (Johnson et al. 2011; Stern et al. 2012). Strata of the Nubian Shield record the breakup of the supercontinent Rodinia, and particularly the formation of Gondwana through the closure of the Mozambique Ocean and the amalgamation of numerous island arcs at 800–650 Ma (Stern 1994). Attempts to divide the Nubian Shield into sub-terranes based on stratigraphy, age relationships, and lithotectonic boundaries (e.g., Kröner et al. 1987; Berhe 1990; Stern 1994; Teklay 1997; Drury and de Sousa Filho 1998) have been hampered by the limited number of high-precision, U–Pb, zircon age determinations, particularly for volcanic and sedimentary strata. These efforts are summarized in Johnson et al. (2011).

At least fifty VMS deposits are known in the Nubian Shield (Fig. 1; Table 1). Although there are several different types, most of the deposits have host rocks with a significant felsic component and barite (e.g., bimodal-felsic or bimodal-siliciclastic; Barrie and Hannington 1999), consistent with formation in evolved volcanic arc and back-arc settings. Because of the periodically arid or tropical environment, many of the VMS deposits have been subjected to near-surface oxidation and supergene enrichment, with the result that gold and copper are relatively enriched at shallow depths, thus making them favorable targets for exploration from an economic standpoint.

3 Ariab VMS–Oxide Gold District

The Ariab VMS–oxide gold district is located in NE Sudan, ~120 km east of the Nile River and ~170 km WSW of Port Sudan (Fig. 1, Tables 1 and 2). The main part of the district has dimensions of 40 km E-W × 20 km N-S, but has notable outlying deposits to the east and south. Production has come from 22 oxide gold surface mines, with most having massive sulphide identified below. Several of the VMS–oxide gold deposits are very large (e.g., likely >25 Mt massive sulphide), including Hadal Awatib, Hassai South, Adassedakh, and Taliaderut. This section focuses on the giant Hadal Awatib VMS–oxide gold system, and the large and well-documented Hassai South system.

The district is underlain by transitional tholeiitic to calc-alkalic volcanic strata and fine-grained siliciclastic rocks, that overlie and are cut by syn- to post-tectonic mafic to felsic intrusions (Fig. 2a: Abu Fatima 2006). One basement granitic intrusion has a U–Pb zircon age of 890 ± 3.7 Ma (Deschamps et al. 2004). Lead isotope data for eight mineral separates (five galenas, one cerrusite, one anglesite, one altaite) from seven deposits and one stratiform barite occurrence yield a model regression age of 702 ± 15 Ma (Barrie 2008).

Archeological evidence exists in the district for gold and copper production during Pharoanic, Roman, and pre-Islamic times. However, large-scale mineral exploitation did not begin until 1991 by COMINCOR, a partnership between the BRGM and the Sudanese government (later the Ariab Mining Co.). Oxide gold production from 22 deposits recovered over 2.0 Moz Au by 2012, with initial resources of 2.7 Moz Au (Table 2). Production for individual oxide gold deposits ranged from 4,240 oz Au at 4.2 g/t Au at Baderuk North, to 631,000 oz Au at 13.7 g/t Au at Hadal Awatib West. Significant production of gold continues from stockpiles, reprocessing of tailings, and from the Kamoeb vein gold deposit. As of 2012, the total resources (measured, indicated, and inferred) of oxide gold and gold mineralized tailings were 1.80 Moz Au at an average grade of 2.58 g/t Au (Bosc et al. 2012).

3.1 The Giant Hadal Awatib VMS–Oxide Gold System

Hadal Awatib is located in the northern part of the Ariab mining district (Fig. 1). In its entirety, the Hadal Awatib massive sulphide orebody is a

Table 1 Grade–tonnage data for VMS deposits in the Nubian Shield 2014

	Min class	Ore type	Tonnes × 10^6	Grade in wt%		Grade in g/t	
				Cu	Zn	Au	Ag
Ariab District, NE Sudan							
Hassai South[a]	Indicated	Sulfide	26.5	1.38	0.33	1.57	–
	Inferred	Sulfide	15.6	1.03	0.21	1.31	–
Hatal Awatib East[a]	Indicated	Sulfide	54.3	0.99	0.81	1.13	–
	Inferred	Sulfide	13.5	1.23	0.53	1.08	–
Hadayamet[a]	Inferred	Sulfide	8.4	0.93	1.97	1.05	–
Bisha District, W. Eritrea							
Bisha[b]	Mined in 2011–2013	Oxide	4.68	0	0	6.03	20
		Supergene	0.77	3.9	0	0.6	27
	Indicated	Oxide	0.41	0	0	6.8	21
		Supergene	7.46	3.68	0	0.6	27
		Sulfide	21.07	1.05	5.87	0.7	47
	Inferred	Oxide	0.03	0	0	7.3	39
		Supergene	0.01	7.23	0	0.1	10
		Sulfide	1.3	0.8	4.5	0.5	36
Bisha NW[b]	Indicated	Supergene	1.02	1.47	0	0.2	10
		Sulfide	2.53	1.04	1.08	0.3	13
	Inferred	Oxide	0.5	0	0	3.7	18
		Supergene	0.1	0.8	0	3.7	19
		Sulfide	0.1	0.9	0.9	2.9	15
Hambok[b]	Indicated	Sulfide	6.86	1.14	1.86	0.2	10
	Inferred	Oxide	0.02	0	0	1.5	17
		Sulfide	0.002	0.9	0.2	0.2	8
Harena[b]	Indicated	Oxide	0.07	0	0	5.5	14
		Sulfide	1.8	0.65	3.91	0.6	23
	Inferred	Oxide	0.02	0	0	5.9	8
		Sulfide	0.35	0.75	4.1	0.8	32
Asmara District, E. Eritrea							
Emba Derho[c]	Meas. and Indicated	Oxide	1.74	0.07	0.04	1.06	4.3
		Cu supergene	1.64	0.94	0.38	0.17	12.2
		Cu-rich sulfide	49.8	0.83	0.93	0.17	7.7
		Zn-rich sulfide	16.8	0.14	2.80	0.31	9.9
	Inferred	Cu-rich sulfide	13.28	0.87	0.89	0.25	10.0
		Zn-rich sulfide	1.77	0.20	1.94	0.39	11.0

(continued)

Table 1 (continued)

	Min class	Ore type	Tonnes × 10^6	Grade in wt%		Grade in g/t	
				Cu	Zn	Au	Ag
Adi Nefas[c]	Indicated	Sulfide	1.841	1.78	10.05	3.31	115
Debarwa[c]	Meas. and Indicated	Oxide	0.371	0.06	0.04	1.47	6
		Transition	0.720	0.08	0.05	2.85	27
		Supergene	1.389	5.15	0.07	1.40	33
		Cu-rich sulfide	0.774	2.34	3.92	1.30	29
		Zn-rich sulfide	0.058	0.36	3.05	1.24	22
	Inferred	Oxide	0.239	0.10	0.10	1.10	5
		Transition	0.138	0.10	0.05	1.40	22
		Supergene	0.144	2.70	0.10	0.60	31
		Cu-rich sulfide	0.154	1.20	3.60	2.60	41
		Zn-rich sulfide	0.006	0.40	3.30	1.10	21
Adi Rassi[c]	Inferred	Sulfide-surface	14.94	0.54	–	0.30	1.5
		Sulfide-UG	0.84	0.67	–	0.89	1.5
Kodatu[d]	Inferred	Oxide	0.99	–	–	1.24	1.61
Harvest District, N. Ethiopia							
Terakimti[e]	Indicated	Oxide	0.29	0.06	0.02	2.55	10.5
		Sulfide	1.84	2.2	1.65	1.06	17.5
	Inferred	Oxide	0.39	0.13	0.07	4.77	7.2
		Sulfide	2.583	1.09	1.42	0.96	20.6
		UG sulfide	0.94	0.69	2.92	0.84	15.2
Hamama District, SE Egypt							
Hamama[f]	Inferred	Surface-mixed	1.636	0.7	1.37	2.11	34.01
		UG-mixed	1.243	0.85	0.87	1.27	23.14

[a]Bosc et al. (2012). Note that 15 other deposits in the district were mined for oxide gold, and most have undefined sulfide resources below
[b]Gribble et al. (2014), and Nevsun Resources Annual Reports. Measured reserves included within indicated and inferred resources. Initial resources before mining given in Barrie et al. (2007)
[c]Senet (2013)
[d]Thomas and Martin (2013)
[e]Archibald et al. (2014)
[f]Valliant and Salmon (2012)

continuous sulphide accumulation that extends for over 3.1 km along strike, from the western extent of the Pipe deposit to the eastern extent of the East CD deposit, and perhaps farther to the west as outlined by airborne geophysical anomalies. More than 1 Moz Au have been recovered from oxide gold ore to date. Copper-zinc-gold sulphide resources have been calculated for the East AB, Link, and East CD areas, representing perhaps 1/3 of the total sulphide resource, and total 68.8 Mt at 1.22 % Cu, 0.74 % Zn, and 1.10 g/t Au (Bosc et al. 2012; Table 2). Considering the nature of host rocks and large size, the Hadal Awatib VMS–oxide gold system is classified as a bimodal-siliciclastic sub-type of VMS deposit. Significantly, it is among the most extensive VMS deposits in the world (Kidd Creek, Ontario total length 3.1 + km to depth: P. Calloway, pers.

Table 2 Pre-production resources in 1991 for Ariab VMS—Oxide Gold District, NE Sudan[a]

Oxide Gold	kg Au	oz Au
Hadal Awatib West	16,161	570,936
Hadal Awatib East	14,595	515,612
Hadayamet	12,012	424,360
Hassai South	7,080	250,122
Oderuk	6,978	246,519
Talaiderut	3,538	124,990
Adassedakh	3,046	107,609
Hadal Awatib North and Pipe	2,706	95,598
Baderuk North	2,110	74,542
Shulai	1,745	61,647
Dimdim 4,5	1,446	51,084
Yonim	1,283	45,326
Metadip1	1,200	42,394
Tagateb	1,055	37,271
Onor	753	26,602
Hassai North	570	20,137
Ganeat	503	17,770
Abderahman	277	9,786
Megzoub	214	7,560
Hamim South	150	5,299
Baderuk North	132	4,663
Hamim North	40	1,413
Total	77,594	2,741,241
Vein Gold		
Kamoeb	15,000	529,920

[a]From Abu Fatima (2006)

comm., 2014; Neves Corvo: 3.45 km: Rosa et al. 2008).

The Hadal Awatib VMS–oxide gold deposits comprise a series of seven open pit mines developed on a single, giant VMS system (Fig. 2b). Host rocks include: (1) footwall silicified and sericitized, massive rhyolite and rhyolite breccia (C2 rhyolite); (2) chloritized basalt–andesite flows, tuffs, and agglomerates; and (3) hanging wall felsic tuff, intermediate to felsic volcaniclastic rocks, and fine-grained siliciclastic rocks (Fig. 2b). The deposit and host rocks have been folded along WNW-ESE-trending and NNE-SSW-trending axes, with the hanging wall rocks extending to the north. Chloritic footwall rocks form the core of the principal WNW-ESE anticline; massive sulphide zones generally dip 65°–90° to the north.

The deposit comprises three horizontally stratified zones, with oxide gold occurring to 80–120 m depth, supergene copper from ~100–130 m depth, and primary (unoxidized) massive sulphide below. Massive and semi-massive sulphides form 10–100-m-thick accumulations, interspersed with chloritic tuffaceous partings that commonly have stringer pyrite–chalcopyrite mineralization. The primary sulphide minerals are pyrite, chalcopyrite, and sphalerite (low iron), with minor galena; tennantite, hessite, cobaltite, and electrum are sparse. Supergene sulphides comprise pyrite, chalcopyrite, covellite, and chalcocite. Locally, oxide gold ore is termed "SBR" for silica-barite rock; however,

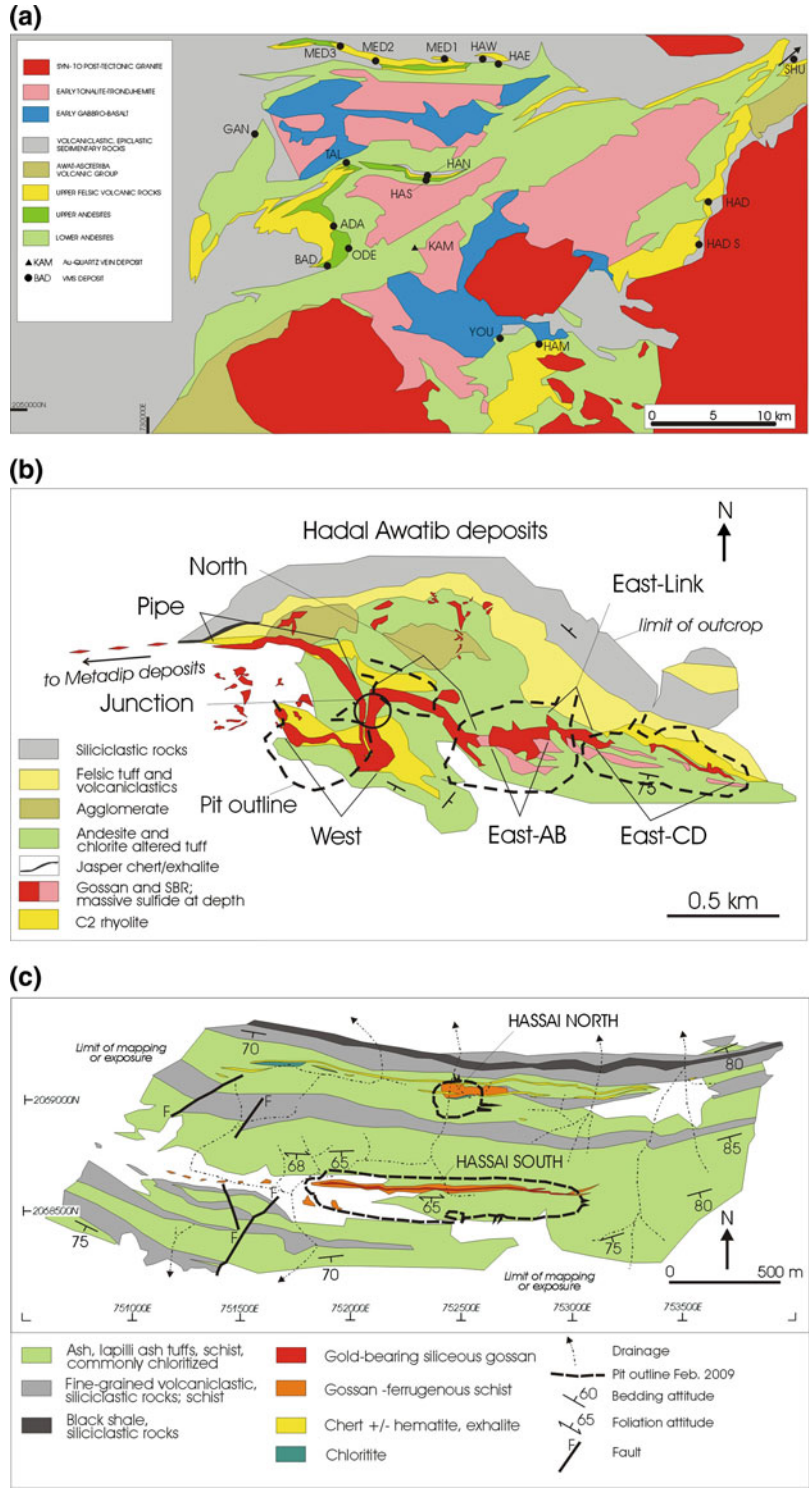

Fig. 2 Simplified geology of the Ariab VMS–oxide gold district, northeastern Sudan, and representative deposits. **a** Ariab district lithologic map showing deposits (simplified after Abu Fatima 2006; Barrie 2008). *ADA* Adassedakh; *BAD* Baderuk; *GAN* Ganeat; *HAD* Hadayamet, H. West; *HAD S* Hadayamet South; *HAE* Hadal Awatib East; *HAM* Hamin South and North; *HAW* Hadal Awatib West; *KAM* Kamoeb quartz-gold vein system; *MED2* Metadip 2; *MED3* Metadip 3; *TAL* Taladeirut; *HAS* Hassai South; *ODE* Oderuk; *SHU* Shulai; *YOU* Younim. Other exploited deposits outside map area: Dimdim 4, 5; Rukab 2, Umashar, Onor (70 km to south). **b** Geology of Hadal Awatib area. Note continuous strike length of Hadal Awatib massive sulphide lens is 3.1 + km, extending intermittently to west along the Metadip EM anomaly trend. It is among the most extensive VMS deposits known globally, comparable to Kidd Creek, Ontario (3.1 + km to depth), and Neves Corvo, Portugal (3.4 + km length). *SBR* "silica barite rock" equivalent to kaolinite quartz sulfate rock. **c** Geology of the Hassai South and Hassai North area

because most of this ore contains little barite, the term oxide gold ore is used here. The sub-horizontal contacts between ore types are transitional over a scale of meters to tens of meters, and oxidized ore commonly occurs along fractures and faults that cut supergene sulphides, and supergene copper enrichment at the margins of primary massive sulphide lenses below. In addition, there is Zn-Cu zonation in the primary massive sulphide.

3.2 Hassai South VMS–Oxide Gold System

Hassai South is located near the center of the Ariab VMS–oxide gold mining district (Fig. 1). Initial oxide gold resources were calculated at 250,000 oz Au with an average grade of 7.0 g/t Au (Table 2). Mining extended to a vertical depth of 100 m, with the oxide zone varying between 4 and 35 m in thickness. Beneath the oxide gold zone, 42.1 Mt of Cu–Zn–Au (+Ag) massive sulphide has been outlined to a depth of 500 m; the deposit is open at depth (Table 1). The supergene and primary, massive sulphide comprise a single, large lens 5–35 m thick with minor chloritic partings that dips 60°–70° to the south (Fig. 2c). Host strata consist of chloritic volcaniclastic and siliciclastic rocks (chlorite-quartz ± sericite ± carbonate ± iron oxide ± pyrite ± epidote ± incipient garnet) that have been foliated and are now phyllite and schist. Also present are minor lapilli tuffs; primary crystals in the tuffs have not been observed. Offsets of thin diorite dikes exposed in the pit walls mark minor cross-faults oriented N-S with small displacements of 10 cm–1 m.

The deposit lies on the south-dipping southern limb of an E-W-trending and south-dipping anticline. The smaller Hassai North oxide gold deposit (Table 2) is 1 km to the north. Rock fabrics are planar and dip 60°–70° to the south with a predominant E-W strike. Late brittle faults oriented NE and NNE in the area northwest of Hassai North have tens of meters of displacement on the horizontal plane. The Hassai South orebody does not appear to be affected significantly by late brittle faults, and is continuous along its entire 1.2 km strike length.

The mineralogy of the Hassai South VMS–oxide gold system has been well-studied (Recoche 1989; Barrie and Kjarsgaard 2010) and 66 ore and gangue minerals have been identified. The oxide gold zone ("SBR"—silica barite rock) has: native gold, electrum, anglesite, cerrusite, smithsonite, calaverite, petzite, tellurides of lead, silver and bismuth, chalcocite, tenorite, malachite, azurite chrysocolla, native copper; and gangue minerals of kaolinite, gypsum, anhydrite, barite, jarosite, chalcedony, iron-titanium oxides, epidote, chlorite, and sericite. Selected ore minerals in the primary and supergene massive sulphide are pyrite, chalcopyrite, sphalerite, marcasite, galena, clausthalite, tetrahedrite, tennantite, friebergite, arsenopyrite, polybasite, anglesite, altaite, tetradymite, tellurobismuthite, hessite, petzite, calaverite, electrum gold, cobaltite, magnetite, pyrrhotite, molybdenite, bismuthinite, mackinawite, bornite, covellite, digenite, cubanite, enargite, and several others.

There are numerous significant stockpiles and gold-bearing tailings. As of 2012, the total resources (measured, indicated, and inferred for oxide gold and tailings in the Ariab district) were 1.80 Moz Au at an average grade of 2.58 g/t Au (Bosc et al. 2012).

4 Bisha VMS–Oxide Gold District

The Bisha deposit, within Neoproterozoic strata of the western Nakfa terrane in western Eritrea (Figs. 1 and 3; Table 1), was discovered in 2003 after an initial six-drill-hole program intersected substantial oxide gold above massive sulphides. Further discoveries at Bisha Northwest, Harena, Hambok, and Yakob Dewar followed soon after. Considering the initial global resources identified at Bisha (39.0 Mt; Barrie et al. 2007) and Hambok (40.7 Mt; Giroux and Barrie 2009), and particularly the high precious and base metal grades at Bisha, the economic viability of the district was favorable, and enabled it to be fast-tracked into production, which commenced in 2011. This section focuses on the main Bisha

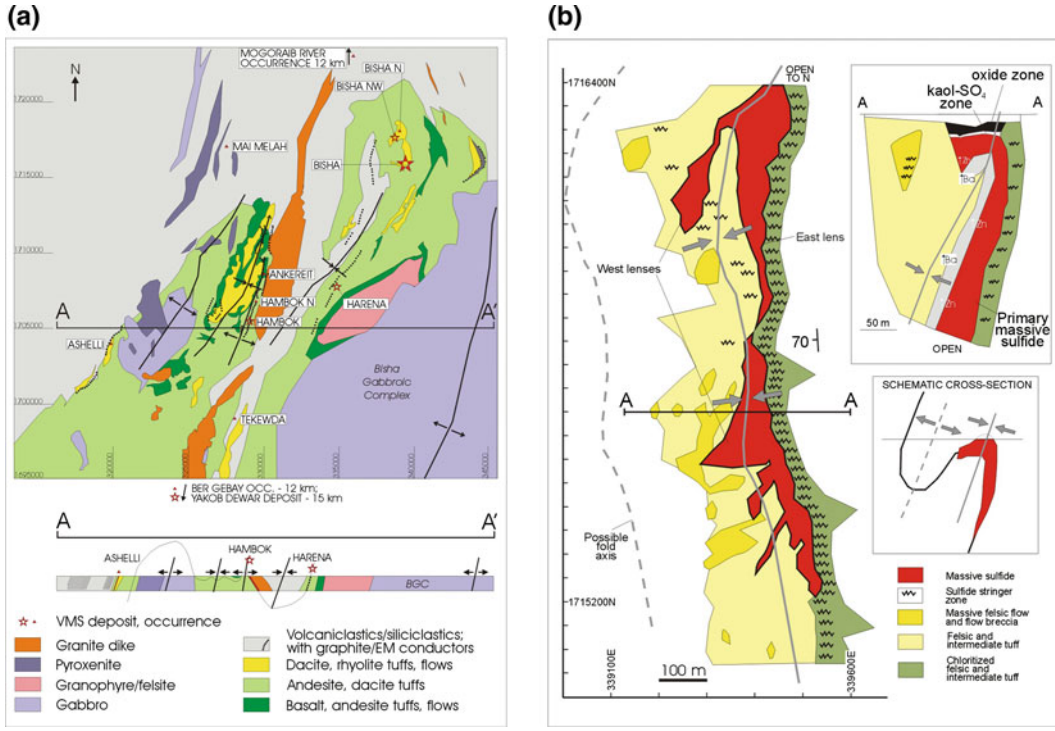

Fig. 3 **a** Geology of the Bisha VMS district, western Eritrea. **b** Bisha main deposit. Plan map (*left*) and cross sections (*right*). Modified after Barrie et al. (2007) and Gribble et al. (2014)

VMS–oxide gold deposit, as it has been the focus of most studies, and is well-exposed by mining through upper oxide and supergene zones.

In Eritrea, the Neoproterozoic rocks have been divided into four terranes on the basis of distinct stratigraphic and structural characteristics, including the Barka terrane to the far west (predominantly amphibolite-grade, metasedimentary rocks and mafic gneisses), the Hagar terrane to the north (principally mafic metavolcanic rocks including ophiolite-like assemblages), the Nakfa terrane (granitoid-greenstone belts and syn- to post-tectonic granitic intrusions), and the Arig terrane to the east (granitoid intrusions and metasedimentary rocks) (Berhe 1990; Teklay 1997; Drury and de Sousa Filho 1998). Mapping of the Hagar and Barka terranes in northwest Eritrea indicate consistent west-over-east thrust faulting, particularly near the terrane boundaries (Drury and de Sousa Filho 1998). Nearly all of the metavolcanic and metasedimentary rocks of the Nakfa terrane strike N-S (±25°). There is a significant volume of syn- to post-tectonic granite between the western and eastern segments of this terrane which host the Bisha and Asmara VMS–oxide gold districts, respectively.

The geology of the Bisha region (Fig. 3a) is dominated by the Bisha Gabbroic Complex (BGC), a large (275 km^2), partly layered intrusion consisting of cumulate gabbroic rocks, with lesser gabbro-norite, pyroxenite, and ferroan gabbro containing up to 8 vol% Fe–Ti oxides. Overlying the BGC, the stratigraphic section comprises, from base to top: (1) minor shallow-water carbonates, quartzite, and psammite; (2) intermediate-composition and felsic lapilli and ash-crystal lapilli tuffs; (3) mafic tuffs, amygdaloidal mafic flows, and hyaloclastite; and (4) thick units of fine-grained siliciclastic rocks. Volcanic rocks constitute ~75 % of the stratigraphic section between the deposit and the BGC, and ~25 % up-section from the Bisha deposit several kilometers to the southwest and

west. The volcanic and sedimentary strata are at prehnite-pumpellyite to mid-greenschist facies metamorphic grade, which generally increases toward the BGC. North-trending felsic dikes cut all strata.

The strata that host the Bisha deposit are commonly foliated, showing phyllic, schistose, and locally gneissic penetrative fabrics. East and southeast of Bisha, the BGC forms the core of a north-plunging anticline. The more competent BGC probably acted as a buttress to the Bisha host stratigraphy during west-over-east thrusting and amalgamation of the Neoproterozoic arc terranes in this region. A more detailed accounting of the structural geology is given in Barrie et al. (2007).

4.1 The Bisha VMS–Oxide Gold Deposit

Host rocks to the Bisha deposit are principally felsic and intermediate-composition lapilli, ash, and crystal-ash tuffs that are variably altered. Several of the units have distinctive mafic and felsic fragments and can be correlated for up to 250 m. Felsic dikes, up to 5 m thick, occur in drill core but comprise <5 % of the footwall and hanging wall rocks. These dikes have as much as 25 % phenocrysts of feldspar, quartz, and biotite, and are generally fine-grained. Within the structural hanging wall to the west, massive felsic flows and flow breccias are present with thicknesses up to 60 m.

The Bisha VMS–oxide gold deposit is effectively a single sheet of massive and semi-massive sulphide up to 70 m thick that has been folded and partly overturned along a north-trending, steeply west-dipping, axis (Fig. 3). The eastern lens is on the eastern limb of the fold; the western lenses (north and south) are on the opposing western fold limb. The east and west lenses are separated from each other due to erosion and surficial oxidation; however, massive sulphide is locally continuous over the fold nose, and oxidized material links them for several hundred meters in the central part of the deposit. Sulphide stringer veins are ubiquitous in chloritic felsic and intermediate-composition tuffs along the stratigraphic footwall to the eastern lens. Prior to mining, the surface expression of the northern half of the Bisha deposit was manifested as prominent hematite-goethite-quartz gossans up to 25 m wide and 2 m thick, extending N-S for tens to hundreds of meters.

The eastern sulphide lens is a nearly continuous sheet 1.2 km long that faces west and dips 65°–70° to the west. Evidence for a westerly facing direction is as follows: (1) primary (e.g., below the oxidized zone) massive sulphide is generally enriched in Zn to the west, reflecting the common enrichment of zinc at the tops of massive sulphide lenses, relative to the bases (e.g., Sato et al. 1974); (2) strong chlorite alteration and sulphide stringer mineralization in felsic tuffs are ubiquitous and strong to the east, and much less abundant west of the primary sulphide in the eastern lens at depth; and (3) high barium contents are much more common in tuffs west of the primary sulphide of the eastern lens at depth. The deepest drill holes in the southern half of the eastern lens intersect layered massive sulphide with high zinc contents and Zn/Cu ratios over two separate 5–10 m intervals, suggesting the presence of stacked massive sulphide lenses in this area (Barrie et al. 2007).

4.2 Mineralogy

Four principal ore types can be clearly delineated as spatially distinct zones or volumes of rock. From the surface downward, these are: (1) hematite-goethite-quartz oxide zone, or gossan, from ~0 to 30 m depth (Fig. 4); (2) kaolinite-quartz-sulphate zone at ~25–35 m depth (Fig. 4); (3) chalcocite-dominant supergene sulphide (~30–65 m); (4) primary massive sulphide (~65 to >450 m). The gossan can be subdivided into brecciated and semi-massive types; however, the mineralogy and metal contents of these two types are nearly identical. Additional resources are present as chalcocite-cemented alluvium and saprolite at the fringes of the deposit, particularly on the western, downslope side. The following mineralogical descriptions are paraphrased from Barrie et al. (2007).

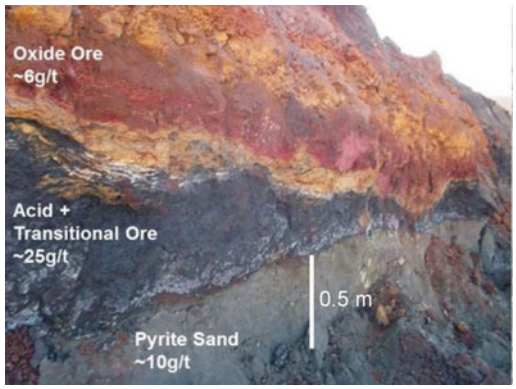

Fig. 4 Photograph of oxide gold–supergene copper transition in Bisha Main pit with typical gold grades indicated; see text for discussion. From Nevsun.com website (published with permission)

4.3 Oxide Zone

Hematite-goethite-quartz oxide zone: The hematite-goethite-quartz oxide zone, or gossan, comprises a massive, dense hematite-goethite-dominant assemblage, with hematite being more abundant near the surface. Gold and silver are the principal metals of value. Principal ore minerals are native gold, argentiferous gold, and pyargarite. The gangue includes iron oxides, quartz, and other silica polymorphs including chalcedony and minor (2–5 vol%) opaline chalcedony; kaolinite, jarosite, gypsum, barite, and calcite; and accessory (1–2 vol%) to trace (<1 vol %) amounts of alunite, cerrusite, anglesite, and native copper. All primary sulphides have been destroyed, although void space after pyrite crystals is present locally. Multiple generations of botryoidal iron oxides and lesser carbonate and sulphate minerals fill void space. Native gold is common as coatings of botryoidal or recrystallized hematite and goethite.

Kaolinite-quartz-sulphate zone: This zone is similar to the "SBR" or oxide gold zones described above for the Ariab VMS–oxide gold district. At Bisha, the kaolinite-quartz sulphate zone has a characteristic leached appearance, with white to cream-colored, aphanitic to fine-grained kaolinite (±illite)-gypsum-alunite encasing fine- to medium-grained quartz. The rocks are commonly slippery or soapy to the touch, due to abundance of aphanitic to fine-grained kaolinite, interpreted as highly altered and leached tuffaceous material. On average, this zone contains more than 13 ppm Au and more than 170 ppm Ag, and thus constitutes a very important component of the oxide zone resource. It also contains the highest proportion of lead among the four zones, which principally resides in sulphate and carbonate minerals. Ore minerals include chalcocite, chlorargyrite, and native gold; additional gangue minerals are siderite, calcite, gypsum, hematite, and goethite, with minor to trace manganese oxide, arsenopyrite, and unusual carbonates and sulphates including Zn-Pb–Mn siderite, cerrusite, barian anglesite, barian magnesite (norsethite?), and beudantite, a lead-arsenic hydrated sulphate that generally occurs in oxidized zones above VMS deposits. Malachite, azurite, and brochantite are notably absent in this zone (as well as in the gossan and supergene zones), despite the presence of carbonate and copper.

Supergene sulphide and transition zones: Supergene sulphide ore typically consists of medium- to coarse-grained massive sulphide enriched in secondary copper minerals. It is more granular, with local cavities and vugs, and has a darker gray appearance, than primary massive sulphide. The darker coloring is due to a high proportion of dark gray, commonly sooty chalcocite. The granular and vuggy textures reflect the partial to complete dissolution of sphalerite, galena, and pyrite, and the minor recrystallization or reprecipitation of iron sulphides (Fig. 4). Supergene sulphide greatly enriched in chalcocite has a characteristic steel blue-gray color and contains over 25 vol% Cu over tens of meters locally. Ore minerals include the aforementioned sulphides, as well as minor bornite, digenite, and covellite, and minor to trace enargite, tetrahedrite, and tennantite; gangue constituents are iron sulphides (marcasite, secondary pyrite and pyrrhotite), quartz, chlorite, and kaolinite, and minor to trace amounts of jarosite, barite, siderite, and calcite. Chalcocite is more abundant at higher levels, whereas digenite,

covellite, and bornite are more common approaching the primary sulphides below.

Primary massive sulphide zone: Beneath the effects of oxidization and supergene enrichment, primary massive sulphide is present. Most occurs in the eastern lens, where fine- and medium-grained massive sulphide locally dislays probable primary depositional layering. The massive sulphide contains most of the Zn resources in the deposit, as sphalerite has been partially to completely removed in the overlying secondary ore types. Principal ore minerals are a typical VMS assemblage, including pyrite, sphalerite, chalcopyrite, minor galena and pyrrhotite, and accessory arsenopyrite, tetrahedrite, tennantite, and enargite. Gangue minerals are quartz, chlorite, sericite-muscovite, clays, siderite, and ferroan carbonate, and minor to trace arsenopyrite, barite, and carbonates. Magnetite is notably absent. Sphalerite-rich massive sulphide has up 22.0 wt% Zn over tens of meters. Sphalerite is generally inclusion-free, but some contains very small chalcopyrite blebs aligned along crystallographic axes (i.e., chalcopyrite disease). Electron microprobe analyses indicate that the sphalerite has low to moderate iron contents, averaging 3.96 wt% Fe, or 6.8 mol% FeS.

5 Asmara VMS District

The Asmara district comprises a series of VMS deposits within Neoproterozoic rocks of the eastern Nakfa Terrane in eastern Eritrea (Figs. 1 and 5a; Table 1) in close proximity to the capital, Asmara. These include the main deposits of Debarwa, Emba Derho, and Adi Nefas; others are Adi Rassi and Kodadu. The Debarwa VMS deposit (Fig. 5d) was mined briefly in the 1980s; operations ceased due only to military conflict during Eritrea's prolonged struggle for independence from Ethiopia. The surface gossans at Emba Derho (Fig. 5b) were the focus of numerous drill programs both pre- and post-Eritrean Independence in 1993. However, after the cessation of renewed hostilities between Eritrea and Ethiopia following the 1998–2000 border conflict and the discovery of the Bisha VMS–oxide gold deposit in western Eritrea in 2003, systematic exploration of the Asmara district gathered pace, first by Sub-Sahara Resources NL and then Sunridge Gold Corporation.

At the time of writing, Sunridge Gold Corporation has signed an agreement with the Eritrean Government to establish the Asmara Mining Share Company, in order to develop the VMS deposits of the Asmara district. This project now awaits securing of the necessary finances and likely will proceed in due course.

It should be noted that with the exception of Debarwa, the Asmara VMS deposits lack oxide gold-enriched profiles of a magnitude like those developed above the VMS deposits of the Bisha and Ariab districts. One of the major factors to consider here is proximity of the Asmara district deposits to the pre-Miocene peneplain that extended across large areas of northeast Africa and the Arabian Peninsula. Although there has been considerable (>2 km) post-Miocene uplift in the Asmara area, erosion and deflation of the land surface since the Miocene have been minimal. Much of the Hamassien Plateau surrounding Asmara still retains a shallow, unconformable cover of Miocene tholeiitic basalts that were emplaced during initial opening of the Red Sea. Pre-Miocene, lateritized, Neoproterozoic basement rocks are exposed beneath the basalts in several locations. In other words, compared to the oxide profiles developed over the VMS deposits of the Bisha and Ariab districts, those of the Asmara district are, at least in part, of much older lineage and developed over an extended time frame and under different conditions.

5.1 Debarwa VMS Deposit

The Debarwa VMS deposit is situated 25 km SSW of Asmara in a sequence of bimodal, submarine, low-K tholeiitic basaltic and rhyolitic volcanic rocks together with minor exhalites. Surface gossans extend for 1.2 km in a NNE-SSW orientation and are sub-parallel to the regional strike and structural grain of the local stratigraphy. The host rocks are felsic volcanics although mafic rocks occur in the immediate

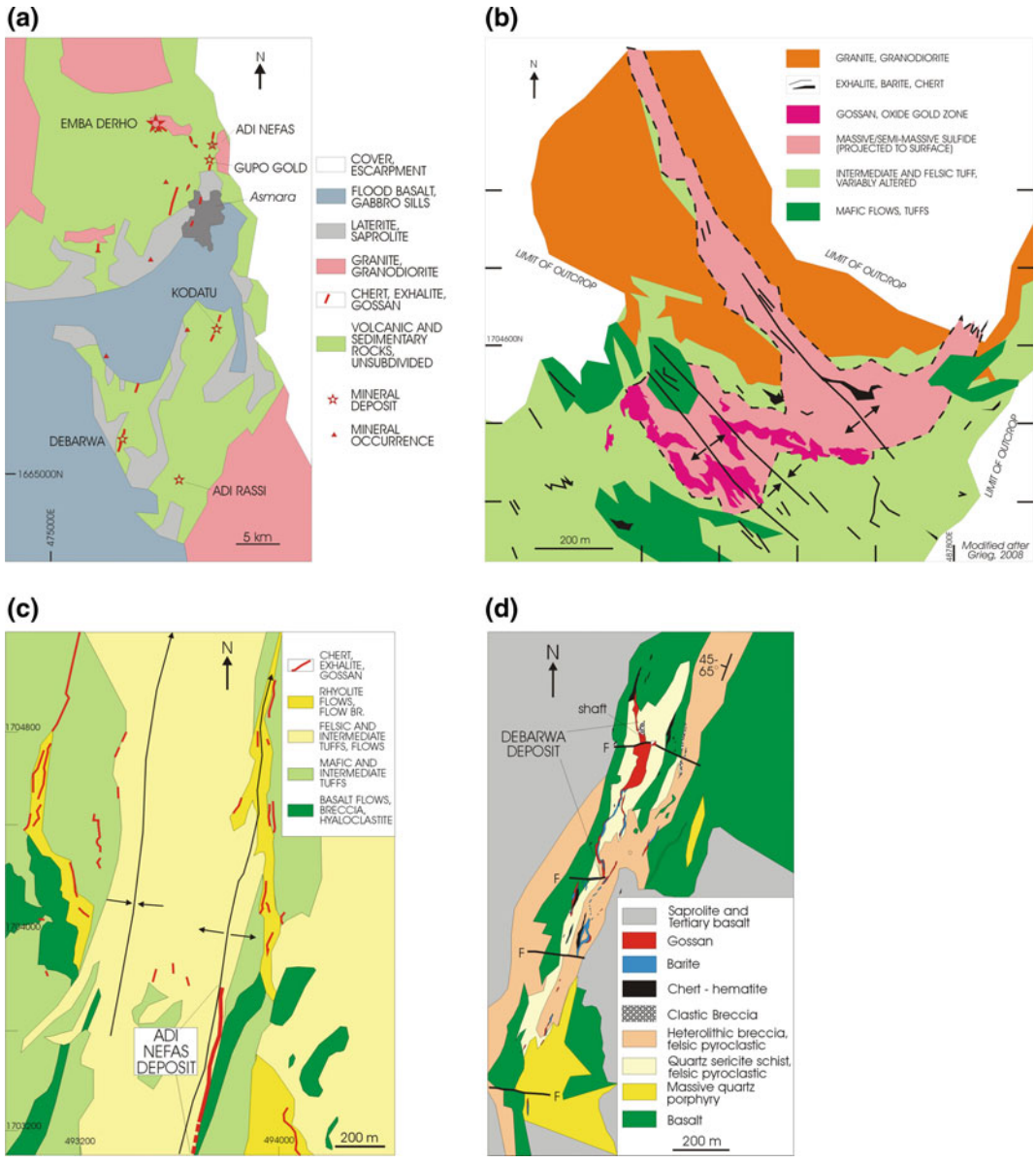

Fig. 5 Geology of Asmara VMS district, Eritrea. **a** Simplified district geology. **b** Geology of Emba Derho deposit and vicinity, modified after Greig (2008); internal report for Sunridge Gold). **c** Geology of Adi Nefas deposit area, modified after Zebremariam (2007), internal report for Sunridge Gold). **d** Geology of Debarwa deposit and vicinity, modified after Senet (2014) and Sunridge Gold Internal reports

footwall. This sequence is overturned and dips west at moderately steep angles. Two lenses of massive sulphides are known at depth. The larger, forming the Debarwa Main Zone, extends for 830 m and dips 50–60° W. A second lens, the Debarwa South Zone, is 285 m long and dips 35–45° W in the north and steepens to 60° W in the south. The latter zone is less thick, lower in grade, and not as continuous as the Debarwa Main Zone, for which sulphide mineralization has been intersected by drilling to 250 m below the surface.

The Debarwa deposit is vertically zoned and comprises oxide, transition, supergene, and primary

zones. The oxide zone extends from the surface gossan to 65 m depth and consists of iron oxides, silica, jarosite, and barite. This zone is severely depleted in base metals and moderately enriched in precious metals, relative to the primary sulphides. The transition zone is highly enriched in precious metals and extends to 80 m below surface. A zone of supergene enrichment occurs below this zone, containing significantly elevated copper grades and digenite, chalcocite, tenanite, covellite, and bornite; this zone extends to 110 m depth. Copper grades in the primary sulphides are 2–4 wt% and gold grades are typically <1 g/t.

5.2 Emba Derho

The Emba Derho VMS deposit is 15 km north of Asmara within metavolcanic and metasedimentary rocks of the Neoproterozoic, eastern Nakfa terrane that are cut by granitoid plutons (Fig. 5b). Surface gossans at Emba Derho have been known since at least the 1970s when the Ethiopian Geological Survey drilled the first six drill holes. During the next three decades a succession of mining and mineral exploration companies, including majors like Phelps Dodge, drilled beneath the main outcrops of gossan. Although considerable systematic exploration including detailed mapping, surface geochemistry, and multi-disciplinary geophysical surveys were carried out and numerous drill intersections returned significant results, no company was able to delineate a continuous body that could constitute an economic resource. In 2006, however, Sunridge Gold Corporation conducted a gravity survey that identified a promising anomaly offset several hundred meters to the northeast of the gossans. Drill hole ED-012-D, which targeted the core of this anomaly, intersected 203 m of massive sulphides grading 1.77 % Zn and 0.41 % Cu. The subsequent drill program eventually delineated a resource totaling 85 Mt in oxide, supergene, Cu-rich sulphide and Zn-rich sulphide zones (Table 1).

The footwall succession at Emba Derho comprises a sequence of quartz-phyric rhyolite flows, flow breccias, and felsic fragmental tuffs.

Fig. 6 Photograph of Debarwa drill core DEB-019 20–30 m showing "DSO" direct shipping ore, consisting of massive chalcocite (>35 % Cu) from supergene copper zone. Diameter of core is 7 cm

These volcanic rocks are locally altered to sericite-chlorite schists. The mineralized zone consists of a series of stacked layers of semi-massive and massive sulphides, interbedded with tuffaceous volcaniclastic rocks, flows, and a single barite layer. Multiple phases of post-tectonic felsic dikes 1–5 m thick cut this succession and are likely related to a major granitoid intrusion that partly truncates the mineralization in the northeast. The hangingwall sequence is dominated by pillow basalts and breccias with epidote-silica alteration zones. Several Mn-rich siliceous exhalite units and a pyroxenite sill occur immediately above the massive sulphides (Fig. 6).

The deposit is zoned and comprises a minor oxide zone up to 30 m thick that overlies a Zn-poor, Cu-rich supergene zone. At surface, the gossans extend over an area 800 m × 220 m and show at least two phases of folding. They form a 'W' shape open to the NW and folded about NW-trending fold axes. The supergene zone consists predominantly of pyrite, together with interstitial covellite and digenite, and minor bornite. Beneath this, the primary sulphides comprise both Zn-rich (pyrite and sphalerite) and Cu-rich zones (pyrite, pyrrhotite, chalcopyrite, and magnetite) that constitute the bulk of the resource.

5.3 Adi Nefas VMS Deposit

Adi Nefas is approximately 10 km NNE of Asmara. Unlike the other Asmara VMS deposits, it contains high-grade Zn zones. The host rocks consist of a bimodal sequence of volcanic rocks,

including epidotized pillow basalts intruded by later quartz porphyry sills and dikes, overlain by tuffaceous volcaniclastic sedimentary rocks together with magnetite-silica exhalite units. The VMS lens occurs on the eastern limb of a north-plunging, west-verging antiform and extends for 700 m. The Gupo gold deposit, 1.5 km to the north, appears to lie on the same stratigraphic horizon although it is clearly a later vein structure.

Adi Nefas is also zoned and comprises an oxide zone with modest enrichment in gold and depletion in base metals that extends to approximately 20 m below surface. The immediately underlying supergene zone contains elevated Cu down to 40 m depth. The primary sulphide zone is enriched in Zn and contains minor quantities of Cu, Au, and Ag.

6 Other VMS–Oxide Gold Districts in the African–Nubian Shield

6.1 Harvest District, Northern Ethiopia

A series of VMS gossans occur 140 km SSW of Debarwa in the Harvest district of northern Ethiopia. These gossans are hosted within a sequence of basaltic and felsic volcanic rocks, together with minor exhalites, and intruded by quartz-phyric porphyries. The most advanced deposit, Terakimti, comprises an 800-m-long gossan having elevated gold and silver values. Drilling beneath the gossan has intersected up to four stacked mineralized lenses containing elevated Cu, Au, Ag, and Zn.

6.2 Hamama District, Egypt

The Hamama VMS deposit occurs in the Eastern Desert of Egypt between the River Nile and the Red Sea within the Abu Marawat Concession. The main VMS horizon extends for 3 km. Elevated gold and silver values have been returned from the gossans over a strike length of 650 m; anomalous Zn and Au contents have been interested by drilling beneath the gossan.

6.3 Derudeb, Northeastern Sudan

During 2011–12, two of us (MAF and RDH) were involved in an exploration program to the east of a known VMS deposit at Derudeb in northeastern Sudan. This work identified significant airborne VTEM anomalies coincident with previously unreported gossans and associated gold-bearing oxides, along more than 3 km of strike in a remote area of rugged mountains along the Sudanese-Eritrean border. Although exploration work here remains at a preliminary stage, this area may prove to contain another VMS district and serves to highlight the mineral endowment and resource potential of this region.

7 Discussion

Metal distribution among the ore types: Many of the VMS–oxide gold deposits within the Nubian shield are classic examples of metallic enrichment in supergene and oxide zones above VMS deposits in weathered terrane. Zinc, Cd, and In, elements that reside in sphalerite, are nearly completely stripped from the three upper zones. Copper is enriched threefold in the supergene zone, relative to the hypogene massive sulphide zone, but is nearly completely removed from the upper two zones. In complimentary fashion, Au and Pb are significantly enriched in the upper two zones. At Bisha, for example, Au is enriched by factors of 8.3× and 18.6× in the oxide and kaolinite-quartz-sulphate zones, respectively, and Pb is enriched 2.6× and 6.5× for these two zones, respectively, compared to the primary massive sulphide. Manganese is depleted 80–90 % in the supergene and gossan zones relative to the hypogene zone.

7.1 Development of Oxide Gold and Supergene Copper Zones

There are significant enrichments of copper in the supergene sulphide zone, and of Pb, Au, and Ag in the kaolinite-quartz-sulphate and oxide zones, compared to the primary massive sulphide. These enrichments reflect: (1) fixation of oxidation products as insoluble minerals at or above the oxidation boundary; (2) reprecipitation of metal ions in a slightly reducing environment due to the change of electron potential; and (3) replacement of a sulphide by another sulphide under reduced conditions but with slightly higher electron potential to prevent the formation of native metals. Near the oxidized upper part of the water table, Cu^{2+} reacts with sulphur or hydrogen sulphide to form covellite (CuS) or chalcocite (Cu_2S), depending on the abundance of Cu and the redox potential. If there is excess copper under more oxidizing conditions, chalcocite predominates, as covellite takes on extra Cu^{2+}. For downward-migrating, Cu-saturated fluids, chalcocite generally forms above covellite under slightly oxidized conditions; this pattern is common at the Bisha, Hassai South, and Hadal Awatib East deposits. Pyrite plays a dual role in that (1) it acts as a host for Cu deposition as its Fe ions are replaced by Cu ions, and (2) its relatively high solubility in oxidizing environments frees sulphur to groundwaters, which lowers the groundwater pH and leads to the dissolution of chalcopyrite and other base-metal sulphides.

One dimensional, physiochemical fluid flow models have been developed for porphyry copper deposits that simulate supergene copper enrichment in an oxidizing, near-surface environment (Auge and Brimhall 1989). Using reasonable assumptions for porosity and Darcy fluid flow from the surface downward (e.g., rain water percolation), Auge and Brimhall (1989) found that bornite formed at the expense of chalcocite and covellite in the supergene blanket zone just below the groundwater table after ~6000 years, coincident with the formation of kaolinite after feldspars. Redox-controlled reactions were used almost exclusively and simulated the copper profile very closely, indicating that other processes for copper deposition, including kinetic and microbial reactions (e.g., Sillitoe et al. 1996) are probably second order effects. At the Bisha, Hassai South, and Hadal Awatib East deposits, supergene processes may have been operative over very long time periods, as warm arid/tropical conditions in these areas have existed for millions of years, evidenced by the presence of thick laterites [laterites form in a climatic regime where there are seasonal wet-dry periods] and saprolitic soils below mid-Oligocene flood basalts.

Zinc sulphide is significantly more soluble than lead and copper sulphides in the oxidized, low-pH ground-water environment and is more likely to be removed from the deposit area by ground water transport, unless sequestered by carbonate to form smithsonite. Although unusual Zn-Pb–Fe carbonate and sulphate minerals are present in the kaolinite-quartz- sulphate and oxide zones at Bisha and in the Hassai district, the overall carbonate and Zn contents are low and evidence for significant fixation of soluble Zn (and Cu) by carbonate is absent. It would appear that Zn has largely been removed from the oxidized upper zones of the deposit over time. In contrast, lead and barium form the relatively stable sulphates anglesite and barite, respectively, and are enriched in the kaolinite-quartz-sulphate and oxide zones.

Gold enrichment in the hematite-goethite gossan is common in weathered and oxidized ore deposits (e.g., at Bisha, Hassai South, Hadal Awatib East). In this environment, gold enrichment is believed to form by weathering, where the gold is derived from decomposition of auriferous sulphides (pyrite in particular), by a combination of chemical, residual, and mechanical processes. In this respect, the post-Miocene uplift and rapid deflation in the region, under a seasonal, wet-dry climatic regime, creates the opportunity to develop significantly enriched gold and copper oxide (and supergene copper) profiles above primary VMS sulphide deposits. Gold and silver can be transported as either chloride or aqueous sulphur complexes at low temperatures under oxidizing, low-pH conditions and precipitated as native metals with iron

oxides. Low-pH conditions are indicated by occurrence of a jarosite and goethite assemblage, which is stable only at pH 1–2.5 under oxidizing conditions, provided that potassium and sulphur are present (Alpers and Brimhall 1989).

Acknowledgments We have benefitted from discussions with colleagues Charlie Grieg, Remi Bosc, David Daoud, Alasdair Smith, Jean-Jacques Kachrillo, Amanuel Arafine, Bill Nielsen, Mike Hopley, Cliff Davis, Oqubatsion Zebremariam, and Sabrina Woldu. This paper was reviewed by DF Sangster and JF Slack.

References

Abu Fatima M (2006) Metallogenic genesis and geotectonic evolution of the polymetallic massive sulphides and the associated gold deposits at Ariab-Arbaat Belt, Red Sea Hills, NE Sudan. Unpubl Ph.D. thesis, Université Henri Poincaré, Nancy, France, 340 pp

Ague JJ, Brimhall GH (1989) Geochemical modeling of steady state fluid flow and chemical reaction during supergene enrichment of porphyry fluid flow and chemical reaction during supergene enrichment of porphyry. Econ Geol 84:506–528

Archibald SM, Martin C, Thomas DG (2014) NI43-101 technical report on a mineral resource estimate at the Terakimti Prospect, Harvest Property (centred at 38° 21′E, 14°19′N). Unpubl Report for Tigray Resources Inc., Tigray National Region, Ethiopia 207 pp

Barrie CT (2008) Lead isotope analysis of the Ariab and Nuba Mountains areas. Unpubl Internal Report for La Mancha Resources, Sudan 22 pp

Barrie CT, Hannington MD (1999) Volcanic-associated massive sulfide deposits: processes and examples in modern and ancient settings: introduction. Rev Econ Geol 8:1–11

Barrie CT, Kjarsgaard I (2010) Hadal Awatib East petrography and mineral chemistry report—internal report for La Mancha Resources Inc., 21 p

Barrie CT, Nielsen FW, Aussant C (2007) The Bisha volcanic-associated massive sulfide deposit, Western Eritrea. Econ Geol 102:717–738

Berhe S (1990) Ophiolites in northeast and east Africa: implications for Proterozoic crustal growth. J Geol Soc 147:41–57

Bosc R, Tamlyn N, Kachrillo JJ (2012) The Hassai mine project—-VMS resources update. Red Sea State, Sudan. NI 43-101 Technical Rept prepared for La Mancha Resources Inc., 227 pp

Deschamps Y, Lescuyer JL, Guerrot C, Osman AA (2004) Lower Neoproterozoic age of the Ariab volcanogenic massive sulphide mineralization, Red Sea Hills, Sudan: 20th College of African Geology. France, BRGM, Orléans, p 133

Drury SA, de Sousa Filho CR (1998) Neoproterozoic terrane assemblages in Eritrea: review and prospects. J African Earth Sci 27:331–348

Greig C (2008) Structural geology of the Bisha and Bisha NW deposits, Western Eritrea. Internal report for Nevsun Resources, 60 p

Giroux GH, Barrie CT (2009) Hambok deposit, Mogoraib Exploration License, Gash-Barka district, western Eritrea. 43-101 Technical Rept and Preliminary Resource Assessment, Report for Sanu Resources Ltd., 107 pp

Gribble P, Melnyk J, Munro P (2014) Bisha mine Eritrea Africa, NI 43-101 technical report for Nevsun Resources Ltd., 328 pp

Hargrove US, Stern RJ, Kimura JI, Manton WI, Johnson PR (2006) How juvenile is the Arabian-Nubian shield? Evidence from Nd isotopes and pre-Neoproterozoic inherited zircon in the Bi'r Umq suture zone, Saudi Arabia. Earth Planet Sci Lett 252:308–326

Johnson PR, Andresen A, Collins AS, Fowler AR, Fritz H, Ghebreab W, Kusky T, Stern RJ (2011) Late Cryogenian-Ediacaran history of the Arabian-Nubian shield: a review of depositional, plutonic, structural, and tectonic events in the closing stages of the northern East African orogen. J African Earth Sci 61:167–232

Kröner A, Greiling R, Reischmann T, Hussein IM, Stern RJ, Durr S, Kruger J, Zimmer M (1987) Pan-African crustal evolution in the Nubian segment of northeast Africa. In: Fuchs K, Froidevaux C (eds) Proterozoic lithospheric evolution, AGU Geodynamics Series 17:235–258

Ogola JS (2006) Mineralization in the Migori greenstone belt, Macalder, western Kenya. Geological J 22:25–44

Owor M, Hartwig T, Muwanga A, Zachmann D, Pohl W (2007) Impact of tailings from the Kilembe copper mining district on Lake George, Uganda. Environmental Geol 51:1065–1075

Recoche G (1989) Les concentrations aurifères supergènes liées aux minéralisations sulfurées polymétalliques de la ceinture volcano-sédimentaire d'Áriab-Arbaat. BRGM, Orléans, France, Rept 226, 318 pp

Rosa CJP, McPhie J, Relvas JMRS, Pereira Z, Oliveira T, Pacheco N (2008) Facies analyses and volcanic setting of the giant Neves Corvo massive sulfide deposit, Iberian Pyrite Belt, Portugal. Miner Deposita 43:449–466

Sato T, Tanijmra S, Ohtagaki T (1974) Geology and ore deposits of the Hokuroko district, Akita Prefecture. In: Ishihara S, Kanehira K, Sasaki A., Sato T, Shimaziki Y (eds) Geology of the Kuroko Deposits: Society of mineralogy and geology of Japan, Special Issue 6:11–18

Senet, 2014, Asmara Project Feasibility Study. Unpubl Report for Sunridge Gold Corp., 373 pp

Sillitoe RH, Folk RL, Saric N (1996) Bacteria as mediators of copper sulfide enrichment during weathering. Science 272:1153–1155

Stacey JS, Doe BR, Roberts RJ, Delevaux MH (1982) A lead isotope study of mineralization in the Saudi Arabian Shield. Contrib Mineral Petrol 74:175–188

Stern R (1994) Neoproterozoic (900–550 Ma) arc assembly and continental collision in the Proterozoic East African orogen: implications for the consolidation of Gondwanaland. Ann Rev Earth Planet Sci 22:319–351

Stern RJ, Ali KA, Abdelsalam MG, Wilde SA, Zhou Q (2012) U-Pb zircon geochronology of the eastern part of the southern Ethiopian Shield. Precamb Res 206–207:159–167

Tadasse S, Milesi J-P, Deschamps Y (2003) Geology and mineral potential of Ethiopia: a note on geology and mineral map of Ethiopia. J African Earth Sci 36:273–313

Teklay M (1997) Petrology, geochemistry and geochronology of Neoproterozoic magmatic arc rocks from Eritrea: implications for crustal evolution in the southern Nubian Shield. Eritrea Dept Mines Memoir 1, 125 pp

Thomas DG, Martin CJ (2013) NI 43-101 independent technical report–The Kodatu deposit. East Africa, for Sunridge Gold Corp, Eritrea, p 111

Valliant WW, Salmon B (2012) Technical report on the Abu Marawat concession, Egypt, for Alexander Nubia International Inc., 112 pp

Zebremariam O (2007) Geological map of the Adi Nefas Area (unpublished report for Sunridge Gold Corp.), 40 p

Geologic, Hydrothermal, and Geochemical Relationships Between Bimodal Magmatism and Massive Sulphide Mineralization in the Central Jebilet-Guemassa Province (Western Moroccan Hercynides)

Mohammed Bouabdellah, Mohammed Hibti, Lhou Maacha, Mohammed Zouhair and Francisco Velasco

Abstract

The Jebilet-Guemassa volcanic-hosted massive sulphide (VHMS) province comprises four sheet-like, polymetallic deposits. These are referred to as Kettara (>20 Mt at 0.6 % Cu with traces of Pb and Zn), Hajar (~20 Mt at 10.5 % Zn, 3.2 % Pb, 0.6 % Cu, and 60 g/t Ag), Draa Sfar (~11 Mt at 5.9 % Zn, 2.2 % Pb, and 0.3 % Cu), and Koudiat Aicha (3–5 Mt at 3 % Zn, 1 % Pb, and 0.6 % Cu), which collectively total >80 Mt of Pb–Zn–Cu ore. Host rocks consist predominantly of variably altered, mafic to felsic, submarine volcanic and tuffaceous volcaniclastic rocks within the metasedimentary Visean Sarhlef Series composed of black argillite with interbedded carbonate, siltstone, and sandstone. Hydrothermal alteration is distinctly asymmetric, occurring regionally in rocks of the stratigraphic

M. Bouabdellah (✉)
Département de Géologie, Faculté des Sciences,
Université Mohammed Premier,
Avenue Mohammed VI, B.P. 717,
60000 Oujda, Morocco
e-mail: mbouabdellah2002@yahoo.fr

M. Hibti
Département de Géologie/Faculté des Sciences
Semlalia, B.P. 2390, 40000 Marrakech, Morocco

L. Maacha · M. Zouhair
Managemgroup, Twin Center, Tour a, Angle
Boulevards Zerktouni et al Massira al Khadra,
B.P. 5199, 20000 Casablanca, Morocco

F. Velasco
Departamento de Mineralogía y Petrología,
Facultad de Ciencia y Tecnología,
Universidad del País Vasco, Apdo. 644,
E-48080 Bilbao, Spain

M. Bouabdellah and J.F. Slack (eds.), *Mineral Deposits of North Africa*,
Mineral Resource Reviews, DOI 10.1007/978-3-319-31733-5_18

footwall, immediate footwall, and hanging wall. In order of decreasing abundance, alteration assemblages consist of varying proportions of sericite, chlorite, quartz, carbonates (calcite, siderite, ankerite, and dolomite), talc, and epidote, with minor albite and tremolite-actinolite. These assemblages were controlled mainly by temperature and pH of the hydrothermal fluids. Mass-balance calculations indicate that hydrothermal alteration of the footwall rocks was accompanied by pervasive leaching of K_2O, Na_2O, and CaO, moderate loss of SiO_2, and addition of FeO, MgO, and MnO under a high-temperature (>150 °C) regime and high water/rock ratios (>10). In contrast, sericite- and calcite-rich alteration of hanging wall rocks involved lower temperatures (<150 °C) and water-rock ratios of <5. Sulphide ores are dominated by pyrrhotite with variable proportions of sphalerite, chalcopyrite, galena, and pyrite ± tetrahedrite ± arsenopyrite ± marcasite ± bismuthinite ± cassiterite ± stannite ± cobaltite ± cubanite ± electrum. Overall, the ore and host rocks were strongly deformed, foliated, and mylonitized under greenschist-facies metamorphic conditions. Lithogeochemistry, alteration mineralogy, mineral chemistry, fluid inclusion data, and stable and radiogenic isotope constraints indicate that the Jebilet-Guemassa VHMS deposits formed in the Upper Visean (~330 Ma) from an evolving hydrothermal system that was initiated by regional-scale convection of magmatic-hydrothermal fluids and ambient seawater. Compared to classical VHMS systems, the Jebilet-Guemassa deposits possess a number of distinctive attributes that set them apart. These include (1) a banded sheet-like morphology, (2) predominance of pyrrhotite (up to 90 vol.%) over pyrite, (2) lack of well-developed stockwork zones, (4) absence of barite, (5) high Zn/Cu ratio, and (6) volumetrically minor igneous rocks.

1 Introduction

The Variscan Jebilet-Guemassa volcanic-hosted massive sulphide (VHMS) province, ~30 km northwest and approximately the same distance southwest of Marrakech, is host to the largest and best-documented example of a bimodal ultramafic-felsic VHMS deposit in northern Africa (Fig. 1). Overall, the province contains four major mineable deposits (Kettara, Hajar, Draa Sfar, and Koudiat Aicha described herewith) together with a number of smaller prospects (i.e., Khwadra). Past production and current reserves total more than 80 Mt to a depth of ~1,000 m, with average grades of 4.5 % Zn, 1.2 % Pb, and 0.6 % Cu. In addition to base metal and Cu, Co, Au, and Ag are being recovered profitably as by-products.

All of the mined deposits were first detected using airborne electromagnetic surveys and subsequent intensive drilling in an area dominated by a thick sequence of Pliocene-Quaternary alluvium, and a large number of well-exposed surficial gossans. Ongoing drilling in areas adjacent to the known ore deposits has delineated substantial new reserves below the present level of mining. In the 1970s, mining was focused exclusively on the recovery of pyrrhotite for sulphur to supply the Maroc Chimie power plant for the treatment of phosphates and the production of phosphoric acid and its by-products. Interestingly, the recent discovery of gold

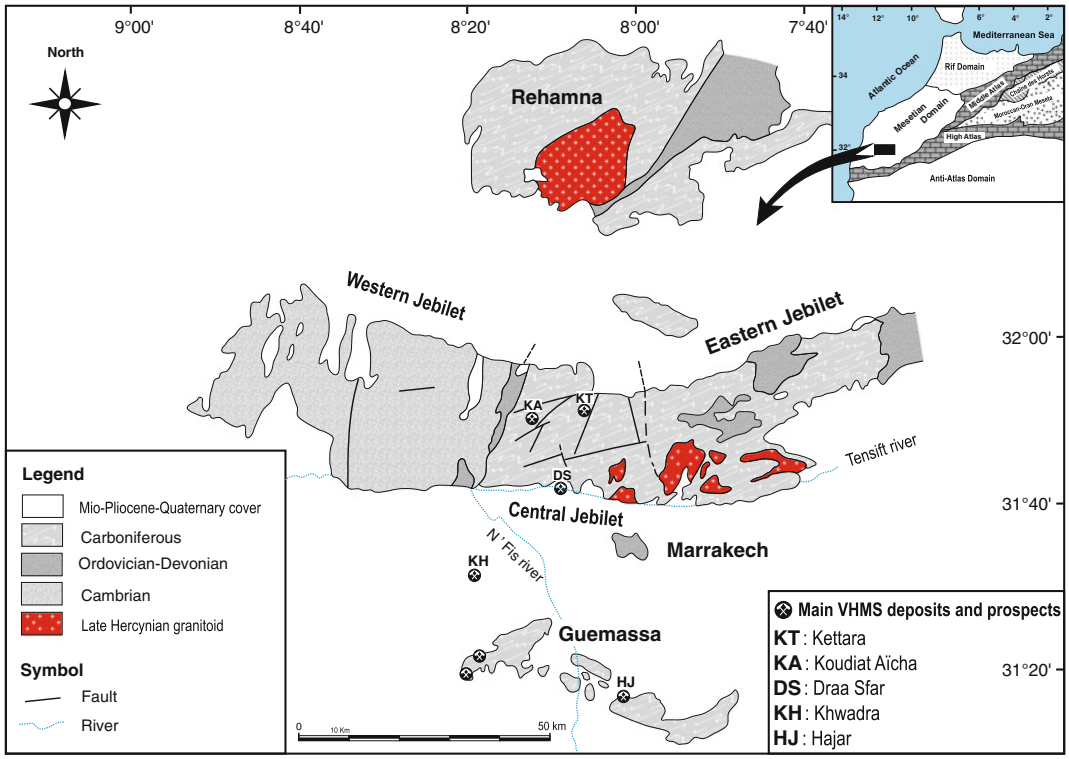

Fig. 1 Regional geologic setting of the Hercynian Rehamna, Jebilet, and Guemassa Massifs of the western Moroccan Meseta domain and locations of mined VHMS deposits of Kettara, Koudiat Aicha, Draa Sfar and Hajar (modified from Huvelin 1977). *Inset* shows location of the Central Jebilet-Guemassa VHMS province within the framework of major tectonostratigraphic domains of northern Morocco (Piqué and Michard 1989)

associated with sulphide mineralization at Draa Sfar (Rziki 2012) has renewed economic interest in these VHMS deposits and raised the question of the relationship between gold mineralization and the associated massive sulphides.

Stratigraphically, the enclosing host rocks are part of the metasedimentary Visean Sarhlef Series (Huvelin 1977; Bordonaro 1983; Playford et al. 2008; Moreno et al. 2008), a prominent tectonostratigraphic unit of the Central Jebilet, bounded to the east by the Marrakech Shear Zone (Lagarde and Choukroune 1982) and to the west by the NNE–SSW dextral, thrust-wrench shear zone (Le Corre and Bouloton 1987) (Fig. 1). The Guemassa metasedimentary rocks immediately south of the Central Jebilet are stratigraphically correlated with the Sarhlef Series based on similar characteristics and lithologies. Overall, the Visean metasedimentary rocks are intruded by a wide spectrum of syntectonic igneous rocks having compositions that range from an ultramafic-granitoid association and peraluminous granodiorites emplaced ca. 330 Ma, cut by younger (ca. 300 Ma) leucogranitic dikes (Essaifi et al. 2013) (Fig. 2). Massive to semi-massive sulphide mineralization occurs at the interface between late Visean footwall bimodal intrusions, lava flows, high-silica rhyolite and tuffaceous volcaniclastic rocks and overlying hanging wall black argillite interbedded with siltstone and sandstone. Although mostly exposed, the stratigraphy and structure of the Jebilet-Guemassa VHMS province have been largely refined from detailed mineralogical and geochemical underground mining studies and extensive diamond drilling over the past two decades (Essaifi et al. 2004; Belkabir et al. 2008; Marcoux et al. 2008; Moreno et al. 2008; Lotfi et al. 2008; Sáez et al. 2011). Proposed

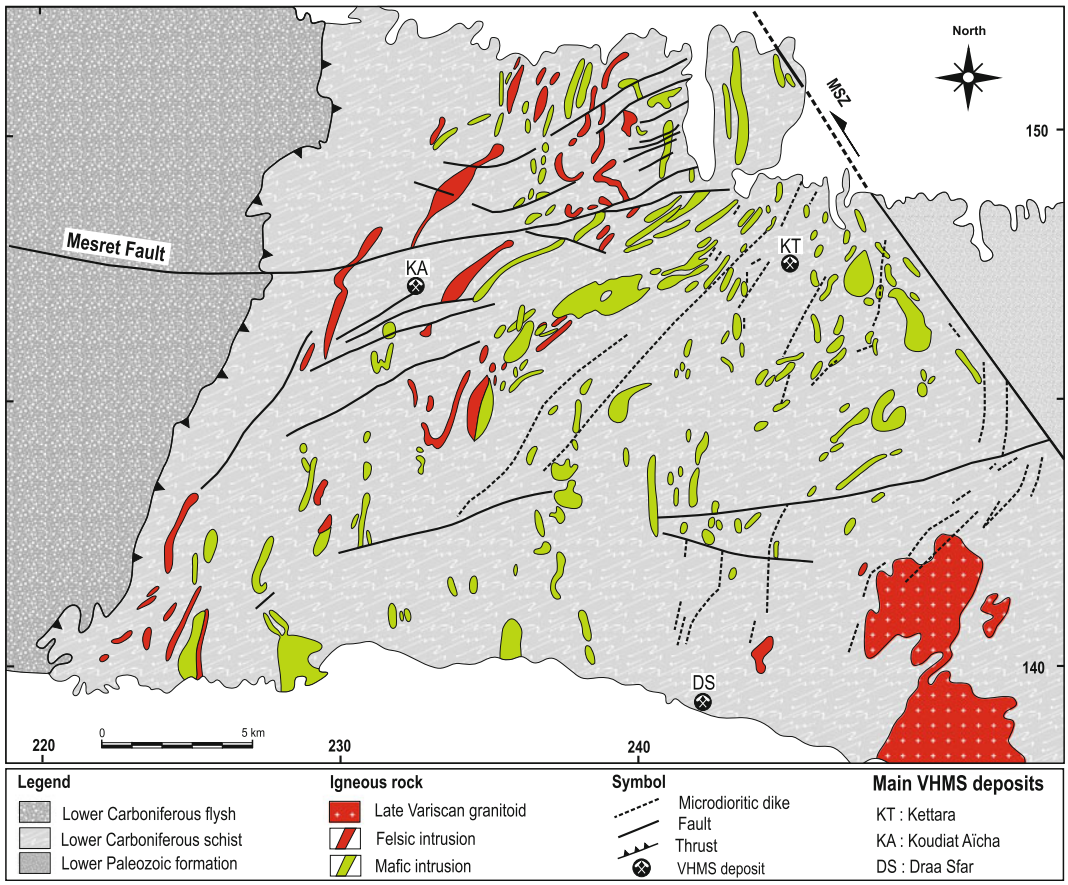

Fig. 2 Geologic setting of the Central Jebilet showing distribution of schistose pelite Sarhlef Series, locations of main VHMS ore deposits, and outcrops of bimodal igneous rocks (modified after Huvelin 1977). Abbreviation: *MSZ* Marrakech Shear Zone

paleogeographic models for the Jebilet Massif are divergent, ranging from extensional horst and graben sub-basins (Felenc et al. 1986; Beauchamp and Izart 1987), through foreland-type basins bounded by shear zones (Bouabdelli and Piqué 1996), to transtensional pull-apart basins delimited by strike-slip faults (Hoepffner et al. 2005).

The present contribution aims to: (1) review, and eventually reinterpret, the geological environment, mineral characteristics, and geochemistry of hydrothermal alteration of the investigated VHMS deposits; (2) document the spatial and temporal relationships among magmatism, alteration, mineralization, and deformation; (3) complement the existing isotopic geochemical database by integrating results of new unpublished analyses; and (4) propose a preliminary genetic model for exploration geologists searching for similar hidden deposits elsewhere in the North Africa Hercynides.

2 District Geology

2.1 Stratigraphy

The Sarhlef Series (Fig. 2), which hosts all of the exploited VHMS deposits described herein, is classically subdivided into Lower and Upper Members of late Visean (Asbian) to early Serpukhovian age (ca. ~331 Ma; Late Mississippian) (Moreno et al. 2008). This Series consists

of a >1,000-m-thick succession of metamorphosed schistose and lower greenschist-facies marine black shale, sandstone, and bimodal tuffs of the Lower Member, which grade upward into the proximal Upper Member composed of black shale, siltstone, and sandstone punctuated by minor intercalations (<10 % of surface outcrops) of felsic and ulramafic-mafic igneous bodies and associated volcaniclastic strata largely of dacitic to rhyolitic compositions. Paleogeographic reconstructions suggest that the Sarhlef Series was deposited in a tectonically driven, pull-apart marine basin (Moreno et al. 2008) under rapid sedimentation rates of 19–27 cm/ka (Sáez et al. 2011). During the Namurian and Westphalian, the marine basins closed (Piqué and Michard 1989).

Since their deposition, all host rocks to the VHMS deposits were affected by the major Variscan orogeny (i.e., Pennsylvian; Piqué and Michard 1989). This event produced a wide variety of tectonic structures including folds and associated schistosity, multidirectional faulting, shear zones, and thrusts. Regional metamorphism, developed contemporaneously with ductile deformation during Late Carboniferous crustal shortening (Hoepffner et al. 2005; Michard et al. 2010), ranges from low-grade greenschist to amphibolite facies. Conversely, thermal metamorphism produced by emplacement of the bimodal suite and late Hercynian intrusions, gave rise to a regionally developed metamorphic aureole that consists predominantly of hornblende- and pyroxene-hornfels, and spotted-textured schists with porphyroblasts of cordierite, andalusite, chlorite, muscovite, and biotite ± sillimanite ± garnet (Bouloton 1992). Structural and metamorphic mineral assemblages indicate pressures of 2.2 kb, corresponding to batholith emplacement depths of less than 8 km (Bouloton 1992).

3 Magmatism

Syntectonic Visean to late Variscan igneous activity (Fig. 2) resulted in development of a series of (1) a bimodal ultramafic to granitoid suite; and (2) peraluminous granodiorites emplaced ca. 330 Ma, intruded by leucogranites ca. 300 Ma (Bordonaro et al. 1979; Aarab and Beauchamp 1987; Mrini et al. 1992; Essaifi et al. 2003, 2013, and references therein). Based on whole-rock and isotopic geochemistry, Essaifi et al. (2013) interpreted the bimodal association of Central Jebilet as recording the cessation of continental subduction, slab-breakoff, asthenospheric upwelling, and development of strike-slip faulting.

The cordierite-bearing granodioritic intrusions are confined to the Marrakech shear zone whereas the bimodal suite is restricted to the Central Jebilet domain (Figs. 1 and 2). Mafic-ultramafic end-members of the bimodal suite, expressed as a series of stock- or sill-like layered intrusions of 303 ± 8 Ma olivine to quartzgabbros and peridotites locally intruded by 279 ± 7 Ma dolerite-diabase dikes (JICA 2003), belong to the tholeiitic series. The granitic end-member mainly comprises metaluminous to weakly peraluminous intrusions that show characteristics of A_2-type granites (Essaifi et al. 2013). Volumetrically insignificant quartz-diorite bodies occur at the gabbro-granitoid contacts. More importantly, numerous quartz-porphyritic to quartz-feldspar-porphyritic to aphyric rhyodacites-rhyolites and associated volcaniclastic rocks emplaced 350 ± 9 to 270 ± 7 Ma (JICA 2003), are intercalated within the schistose pelites of the Sarhlef Series (Bordonaro et al. 1979, and references therein). This large time interval indicates that bimodal magmatic activity predated and postdated sulphide mineralization which occurred at ca. 331 Ma.

The rhyolite-rhyodacite rocks include massive, flow-banded, flow-brecciated, pyroclastic, and volcaniclastic types. Most of these rocks form synvolcanic sills and crypto-domes with well-defined autoclastic breccias, autobrecciated and peperitic margins, and flow banding (Zouhry 1998; Hibti 2001; Belkabir et al. 2008). Occurrence of peperitic margins on the crypto-domes indicates intrusion while the enclosing volcano-sedimentary succession was still wet and unconsolidated. The resedimented autoclastic breccias most likely formed in response to oversteepening of dome margins during or

shortly after eruption through the sea floor (Doyle 2001; McPhie and Allen 2003). Volcaniclastic rocks occur as laminated tuff, lapilli tuff, lapillistone, and angular, block-rich (blocks up to 50 cm) tuff breccias. Thin (<1 mm to 1–2 cm) units of crystal tuff and local crystal-lithic tuff (<10 % felsic lapilli) are intercalated with the host black shales (Zouhry 1998; Belkabir et al. 2008).

The cordierite-bearing granodiorites form two main intrusions, the eastern and central Jebilet plutons (Figs. 1 and 2). These plutons are composed mainly of porphyritic biotite ± cordierite-bearing granodiorite, although modal compositions suggest monzogranitic to tonalitic compositions. Triassic microdiorite dikes postdate the Variscan deformation and cut both the bimodal igneous bodies and the granodioritic plutons.

4 Mine Site Geology

4.1 Kettara Deposit

Having a well-developed outcropping gossan, the Kettara deposit was the first mined in the Jebilet-Guemassa province, as its exploitation dates to 1930s when the deposit was exploited for iron oxides and hydroxides used in the manufacture of paint pigments. In the 1970s, the Moroccan government carried out underground mining for pyrrhotite production in an attempt to ensure a regular sulphur supply for the newly opened "Maroc Chimie" plant devoted to the treatment of phosphates and production of phosphoric acid and its by-products. The grill metallurgical method used at that time to extract sulphur from pyrrhotite resulted in the corrosion of the iron infrastructure and consequently the closure of the mine in 1982. Past production and geological resources are estimated at >20 Mt of massive pyrrhotite averaging 0.6 % Cu, with traces of Pb and Zn (Huvelin 1977).

The footwall rocks (Fig. 3) consist of a succession of schistose quartz-sericite pelites intercalated with sandstones. Similarly, the hanging wall rocks are composed of fine-grained banded metapelites with intercalated arenites and felsic metatuffs, locally intruded by bimodal rhyolitic to gabbroic sills.

Because the entire stratigraphic sequence dips steeply, the extent of alteration and mineralization along the original strike length of the orebody is best observed in a vertical cross section (Fig. 3). Drilling and underground development indicate that the massive sulphide orebody forms a single, strongly folded, NE–SW-trending lens, parallel to the hinges of major F_1 fold structures, with a narrow alteration envelope extending down-plunge to a depth of at least 250 m. The mineralized structure is about 100 m wide and has a horizontal strike length of nearly 1.5 km. From surface, mineralization extends at least 400 m vertically. The strike of the orebody is concordant with the host rocks and associated foliation. No underlying stockwork sulphide zone has been observed beneath the massive lens, although locally a dense network of irregular quartz-chalcopyrite veinlets has been documented (Bernard et al. 1988). Major sulphide minerals include pyrrhotite (up to 99 vol.%) accompanied by minor chalcopyrite, pyrite, and glaucodot. Sphalerite and galena are present only in accessory amounts.

4.2 Draa Sfar Deposit

With a total production and geological resources estimated at ~11 Mt averaging 5.9 % Zn, 2.2 % Pb, and 0.3 % Cu (Dagbert and Harfi 2004), Draa Sfar, which went into production by the end of 2004, represents the last operating mine in the Jebilet-Guemassa VHMS province.

Enclosing host rocks consist of schistose, low-grade metamorphosed Asbian black shale (Moreno et al. 2008) intercalated with sandstone and subordinate bimodal volcanic and volcaniclastic rocks (Huvelin 1977; Bordonaro et al. 1979) (Fig. 4). The detailed lithostratigraphic succession compiled from underground geologic mapping and examination of 25 km of diamond drilled cores comprises, from base to top: (1) footwall coherent rhyodacitic flows and domes, associated with in situ and transported autoclastic deposits, lappilli tuff, lappillistone, and

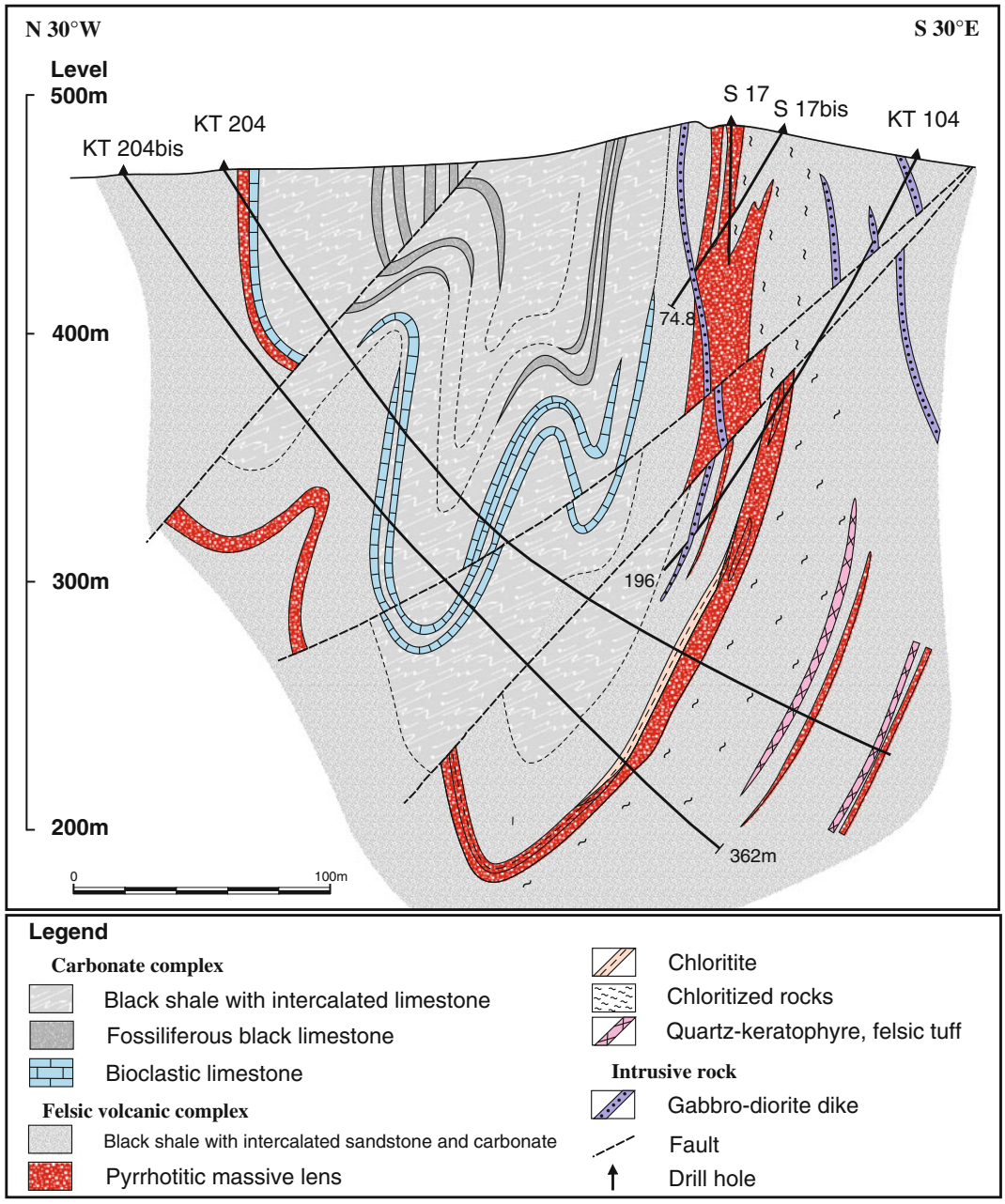

Fig. 3 NW–SE vertical cross section through the Kettara massive sulphide deposit showing distribution of different lithologies including bimodal igneous rocks and associated folded orebodies. Locations of main drill holes are indicated

tuff breccia with intercalations of Asbian black shale (Moreno et al. 2008), siltstone and thinly bedded to laminated sandstone (Belkabir et al. 2008); (2) massive sulphide lenses interfingered with siltstone and sandstone; and (3) hanging wall rocks consisting predominantly of a 20–80-m-thick succession of carbonaceous argillite and minor siltstone locally intruded by a large gabbro sill. Aphanitic basalt, together with porphyritic melanogabbro to doleritic dikes, occur

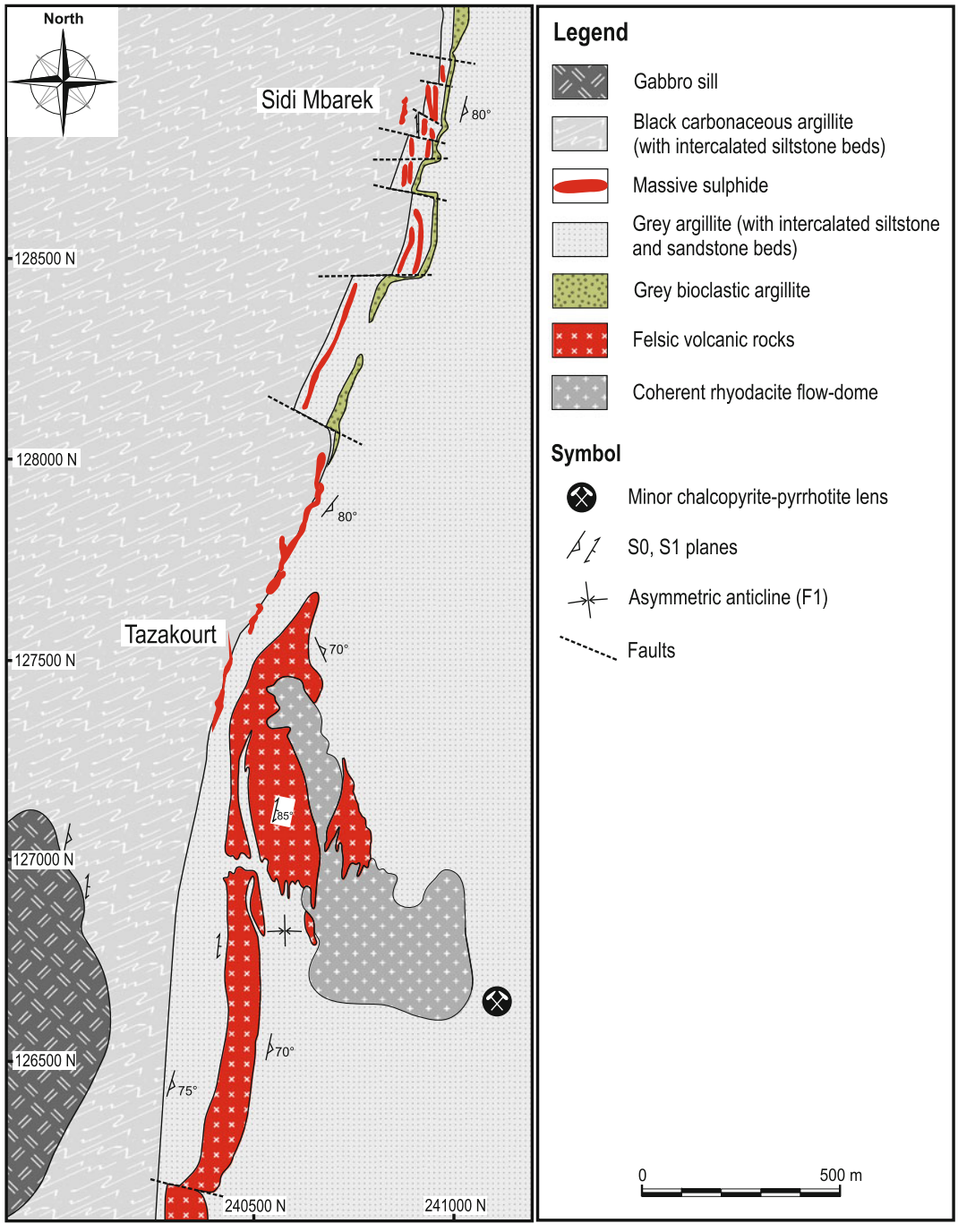

Fig. 4 Geological map of the Draa Sfar deposit projected onto the surface showing location of major massive sulphide lenses, namely Tazakourt and Sidi M'barek sheet-like orebodies and their relationships to faults and main lithologies including bimodal igneous rocks

within the footwall rhyodacite-volcaniclastic and argillite-siltstone units (Ben Aissi et al. 2005; Belkabir et al. 2008, Ben Aissi 2008; Rziki 2012).

Pyrrhotite-dominant mineralization forms two main sheet-like, subvertical and sub parallel, stratabound massive to semi-massive sulphide orebodies (Fig. 4). Located on both sides of the Tensift River, the Sidi M'Barek orebody occurs on the north and the Tazakourt orebody to the south, distributed along the western limb of a large, N-plunging, F_1 anticline (Bernard et al. 1988; Belkabir et al. 2008). Both orebodies appear to be localizedby synvolcanic structures. In surface outcrop, the identified orebodies are capped by well-developed gossans. A third mineralized structure called the Central orebody has recently been delineated. In this review, some new terms, such as the Northern (i.e., formerly Sidi M'Barek), Central, and Southern (i.e., formerly Tazakourt) orebodies (Fig. 5), are used to describe the three mineralized zones as presently understood. Each of the three identified orebodies is stratigraphically underlain by a well developed, discordant stockwork/stringer zone, and can be divided into upper sphalerite-rich ore and lower chalcopyrite-rich ore. This conclusion differs from that of Marcoux et al. (2008), who did not describe this vertical zoning.

Overall, the orebodies are intensely sheared, boudinaged, overturned to the west and plunge steeply to the east. Primary morphology has been obliterated. Accordingly, our interpretation is that the Southern and Central orebodies initially formed a single lens that was subsequently dismembered into two separate lenses and displaced from each other (Fig. 5). Macroscopically, the

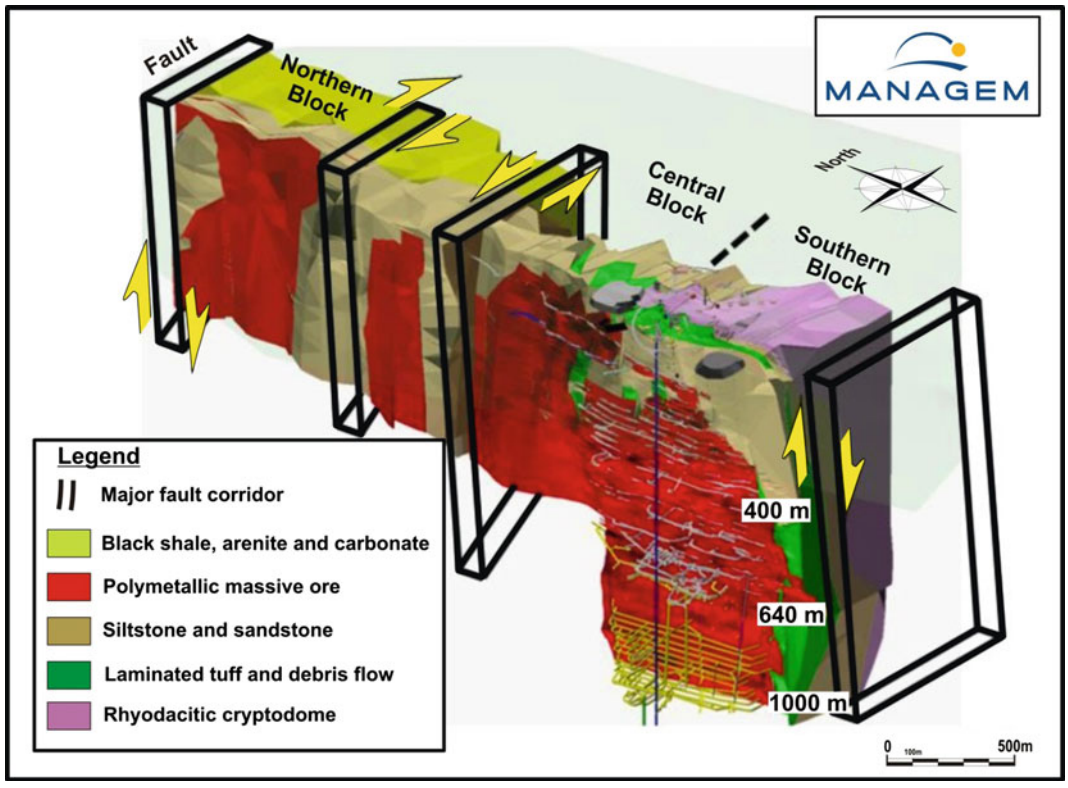

Fig. 5 Three dimensional view of the Draa Sfar deposit looking downdip to the east, illustrating segmentation of the initially single massive lens and relationship between main elements of the orebody. Brittle faults have cut and displaced various ore lenses

strongly deformed orebodies exhibit pinch and swell structures.

The South orebody forms a Zn-rich, N–S-trending, elongate sheet-like structure extending for more than 1 km along strike. According to updated estimates released in December, 2010, by "Compagnie Minière de Guemassa" (CMG), this orebody totals 7.19 Mt at average grades of 5.7 % Zn, 2 % Pb, and 0.3 % Cu (Rziki 2012). In contrast, the North orebody consists of two sub-parallel, elongate, Zn- and Cu-rich sulphide lenses (Fig. 4). The Cu-rich lens is interpreted to represent the stockwork-stringer zone for the stratigraphically overlying Zn-rich lens. It consists of irregular veinlets of chalcopyrite-quartz less than 1 m to several m wide, within pervasively chloritized and/or silicified and brecciated host rocks. The stockwork zones display distinct zoning of alteration with a core of massive silica surrounded by an intermediate silica-sericite zone, and by an outer zone of chlorite-pyrite-silica-sericite ± biotite (Ben Aissi 2008; Ben Aissi et al. 2005; Rziki 2012). Proven and probable reserves of the North orebody are estimated at 1.44 Mt averaging 4.3 % Zn, 0.8 % Pb, and 0.5 % Cu for the Zn-rich lens, and 0.64 Mt at 0.2 % Zn, 0.1 % Pb, and 0.9 % Cu for the Cu-rich stockwork lens.

The Central orebody forms a massive tabular to lenticular E–W-trending mineralized structure dipping to the east. Krigeage and 3D gridding estimates indicate geologic resources of 1.36 Mt averaging 2.9 % Zn, 0.3 % Pb, and 0.5 % Cu (Dagbert and Harfi 2004). The striking economic characteristic of the Central orebody resides in its high gold contents that reach up to 100 g/t.

Whatever the mineralized structure considered, three main ore types are recognized in the Draa Sfar deposit: massive, banded, and brecciated. Pyrrhotite, sphalerite, chalcopyrite, tetrahadrite, and galena are the main sulphide minerals, together with rare pyrite and marcasite (1–3 vol.% sulphides) and accessory to trace amounts of cobaltite, arsenopyrite, laitakarite ($Bi_4(Se,S)_3$), magnetite, native bismuth, and paraguanajuatite (Bi_2S_3) (Marcoux et al. 2008). Non-sulphide gangue minerals include quartz, sericite, carbonate, and chlorite.

4.3 Koudiat Aicha Deposit

The Koudiat Aicha deposit represents the smallest mined orebody of the Jebilet-Guemassa VHMS province. Total proven and probable resources are 3–5 Mt with average grades of 3 % Zn, 1 % Pb, and 0.6 % Cu (Lotfi et al. 2010). The deposit was discovered in 1963 based on a strong airborne electromagnetic anomaly in an area dominated by sparse outcrop and numerous well-developed gossans.

Enclosing host rocks (Fig. 6) consist of a succession of schistose, low-grade metamorphosed, rhythmically banded siliciclastic sediments (80 %) with intercalated igneous rocks (20 %). The footwall (i.e., basal lower unit) comprises Asbian black shale with interbedded sandstone and siltstone (Moreno et al. 2008), whereas the hanging wall consists of sandy limestone alternating with sandy and silty beds, locally with disseminated pyrrhotite. Igneous rocks are several massive gabbroic bodies intruded as sills at various stratigraphic levels including both the hanging wall and footwall rocks. Minor (<2 %) rhyodacitic lava flows together with pyroclastic tuffs, felsic to intermediate volcaniclastic lapilli tuffs, and lapillistones have also been documented (Lotfi et al. 2008).

Orebodies occur at transitions between black shale and siltstone in the footwall and more permeable tuffaceous units in the immediate hanging wall. The principal massive to semi-massive sulphide orebodies extend from the surface to at least 500 m and consist of three N-S-trending, sheet-like, sub-vertical, and sub-parallel, intensely sheared paraconcordant lenses, up to several hundred meters in length, 50–100 m wide, and 20–25 m thick (Fig. 6). The present shape of the orebodies is controlled by a regional F_1 anticlinal megastructure and associated schistosity (Lotfi et al. 2008, 2010), but the original lens-shaped geometry is largely retained.

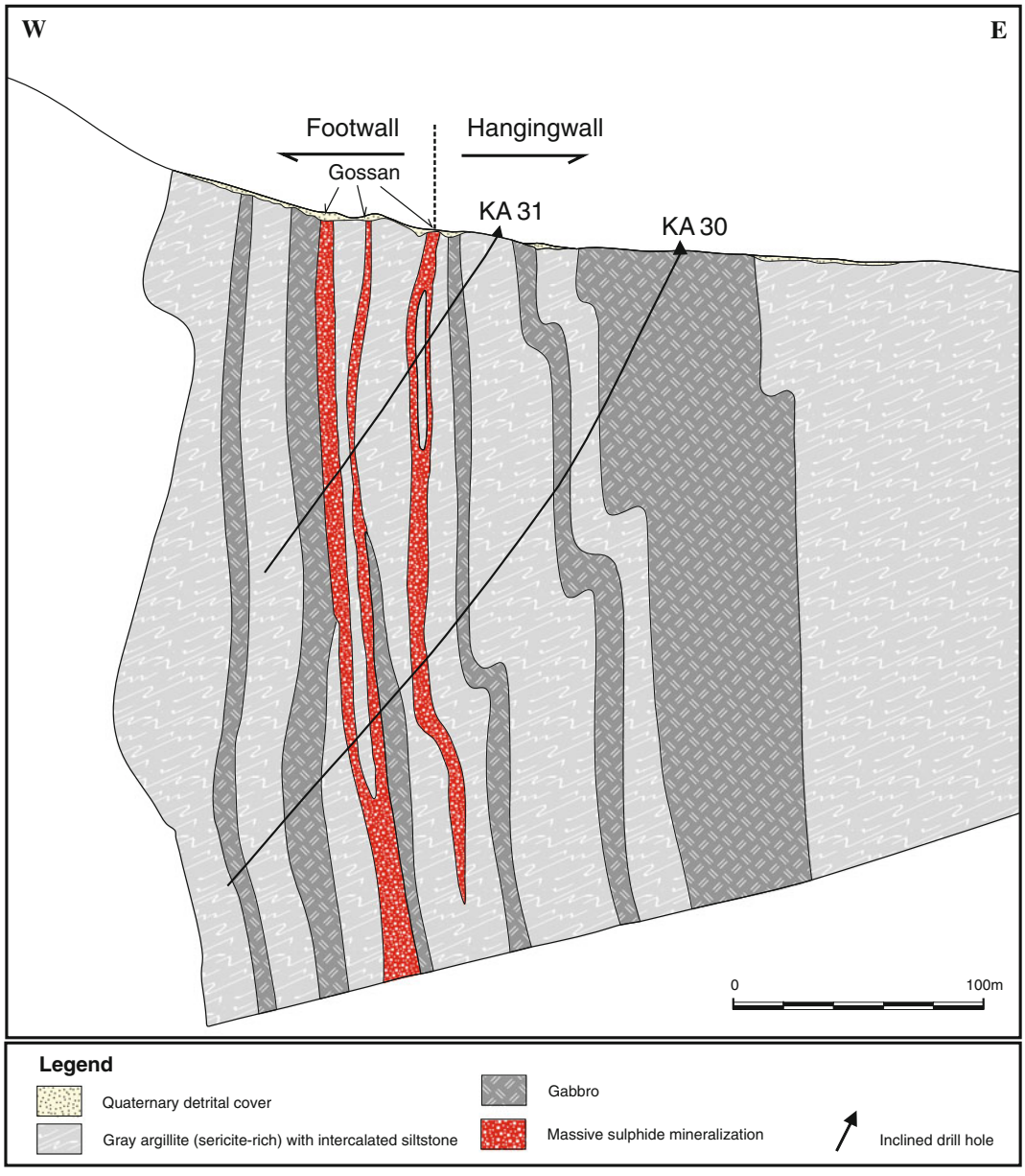

Fig. 6 E–W vertical cross section through the Koudiat Aicha deposit showing distribution of rock types, and the sheeted massive sulphide orebodies and their relationship to the gabbroic occurrences. Also indicated are the main drill holes from which extensions of the orebodies have been delineated

Four main ore types are recognized: massive pyrrhotite ore, banded ore, Cu-rich massive sulphides and related stringer mineralization, and barren, rhythmically banded pyrrhotite interpreted to represent synsedimentary sulphide deposition (Ben Aissi 2008; Lotfi et al. 2008, 2010). However, inferred syngenetic relationships between black shales and massive sulphides are commonly obliterated by intense shearing.

Individual orebodies display a strong vertical metal zonation that consists, from base to top of Cu-rich to Zn–Pb-rich orebodies. In contrast,

overall metal contents are consistently uniform between levels indicating little or no lateral zonation. Silver, Au, and Sn are concentrated at the top of the sulphide lenses and in adjacent hanging wall rocks (Lotfi et al. 2010). Monoclinic pyrrhotite (up to 95 vol.%), sphalerite (7–8 wt% Fe), galena, and chalcopyrite are the main ore minerals, together with stannite, arsenopyrite, and pyrite. Non-sulphide gangue constituents include quartz, siderite, calcite, chlorite, and sericite.

4.4 Hajar Deposit

Unlike the Kettara, Koudiat Aicha, and Dra Sfar deposits, Hajar is located within the Guemassa lithostructural domain, 30 km south of Marrakech city (Fig. 1). This deposit was discovered in 1968 following airborne geophysical surveys that delineated a strong electromagnetic anomaly centered on what became, in 1988, the Hajar orebody. From 1988 onward, mining of the Hajar deposit has produced ~20 Mt of ore at average grades of 10.5 % Zn, 3.2 % Pb, 0.6 % Cu, and 60 g/t Ag (Eddebi et al. 1998).

The lithostratigraphic succession drawn from underground geologic mapping and drill core logs comprises, from base to top: (1) footwall massive rhyodacitic flows interpreted to represent a proximal vent facies, overlain by andesitic tuff, rhyodacitic fragmental rocks, laminated tuff, and debris flows interbedded with tuffaceous rhyolite; (2) a 120 m-thick massive sulphide lenses intercalated with siltstone and sandstone; and (3) hanging wall rocks consisting predominantly of a succession of black shale interbedded with arenite and carbonates toward the top of the succession. The main volcanic and volcaniclastic rock types are quartz- to quartz-plagioclase porphyritic to aphyric, tholeiitic high silica (>70 wt % SiO_2) dacite and rhyolite. Footwall and hanging wall rocks are pervasively altered to chlorite, sericite, carbonate, albite, and epidote, with minor sphene and leucoxene.

Drilling and underground development have identified three major elongated massive lenses referred to as the Main, Eastern, and Western orebodies, each of which with an underlying well-developed stockwork/stringer zone (Fig. 7). From surface, mineralization extends at least 400 m vertically. In cross-section, the main orebody forms a folded lens that plunges steeply to the northeast; the strike is slightly discordant with the enclosing host rocks, suggesting that the current geometry is due to structural modification (Fig. 7). As a result, primary textures and mineral zonation—if originally present—have been largely obliterated by folding and/or translation of the sulphide mass during deformation. At the 520 m level (Fig. 8), massive sulphide mineralization is about 120 m wide, extends for an almost continuous strike length of 200 m horizontally, and is dislocated into three segments. The eastern segment is pyrrhotite-rich, whereas the western segment is pyrite-rich. The pyrite-pyrrhotite-rich central segment is stratigraphically underlain by a discordant stockwork zone (Fig. 8). This stockwork extends at least 100 m beneath the base of the central segment and displays a distinct zoning of alteration minerals (Zouhry 1998; Hibti 2001). Much of the ore occurs within felsic volcanic rocks, principally fragmental (primary volcanic breccias or autoclastic) to epiclastic strata.

The sulphide orebodies are mainly composed of pyrrhotite (70–90 vol.%), chalcopyrite, galena, pyrite, and arsenopyrite together with bismuth, cubanite, marcasite, costibite, molybdenite, magnetite and glaucodot. Hematite, rutile, and leucoxene are secondary minerals.

5 Hydrothermal Alteration

Due to the Variscan orogenic overprints, distinguishing regional alteration during low-grade greenschist-facies metamorphism from alteration that formed from hydrothermal solutions is challenging because both processes have produced similar mineral assemblages. Overall, four types of widespread hydrothermal alteration are recognized, including chloritization, silicification, sericitization, and talc-carbonate ± tremolite-actinolite ± epidote ± albite alteration. The resulting alteration zones are developed

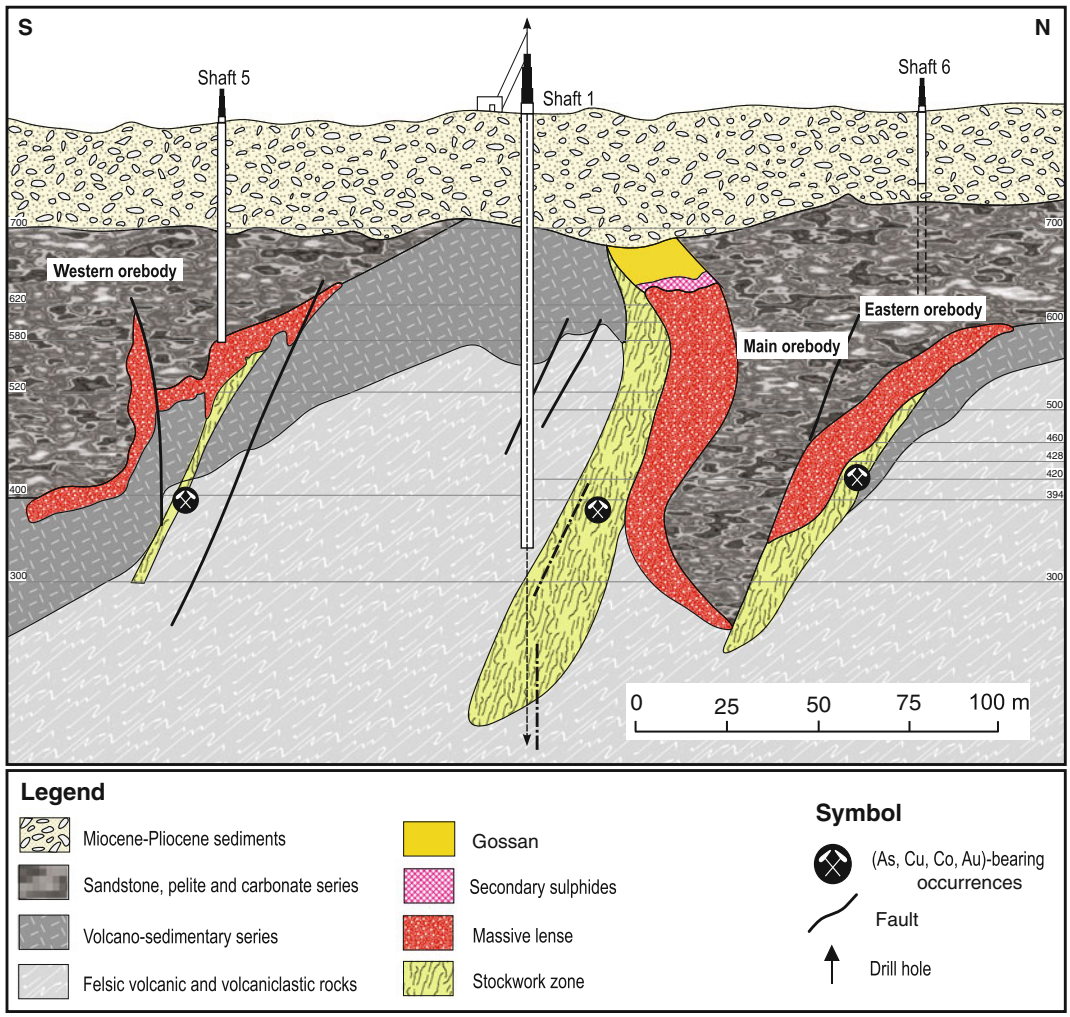

Fig. 7 NE–SW longitudinal cross-section through the Hajar deposit illustrating the distribution of different rock types, the location of the massive sulphide lenses and their relationships to the felsic volcanic and volcaniclastic occurrences. Locations of the main drill holes are also indicated

within and immediately surrounding the ores, both on hanging wall and footwall sides. Sericitization alteration manifested by pervasive development of coarse-grained phlogopite and illite has been described at the Hajar deposit (Zouhry 1998; Watanabe 2002). However, $^{40}Ar/^{39}Ar$ ages of 300.9 ± 2.6 Ma on biotite and 305.4 ± 4.8 Ma on illite (Watanabe 2002) are clearly younger that the likely age for VHMS mineralization (Asbian ~330 Ma; Moreno et al. 2008, and references therein), suggesting that this potassic hydrothermal event is related to the emplacement of late Hercynian leucogranite.

The chlorite ± sericite halos are very extensive and occur along the entire length of the investigated deposits to a depth exceeding 200 m below the orebodies. In general, these alteration zones are fairly weak compared to the texturally destructive alteration within the orebodies and related feeder zones (Zouhry 1998; Hibti 2001; Ben Aissi et al. 2005). Indeed, at Hajar and Draa Sfar where a well-developed stockwork/stringer

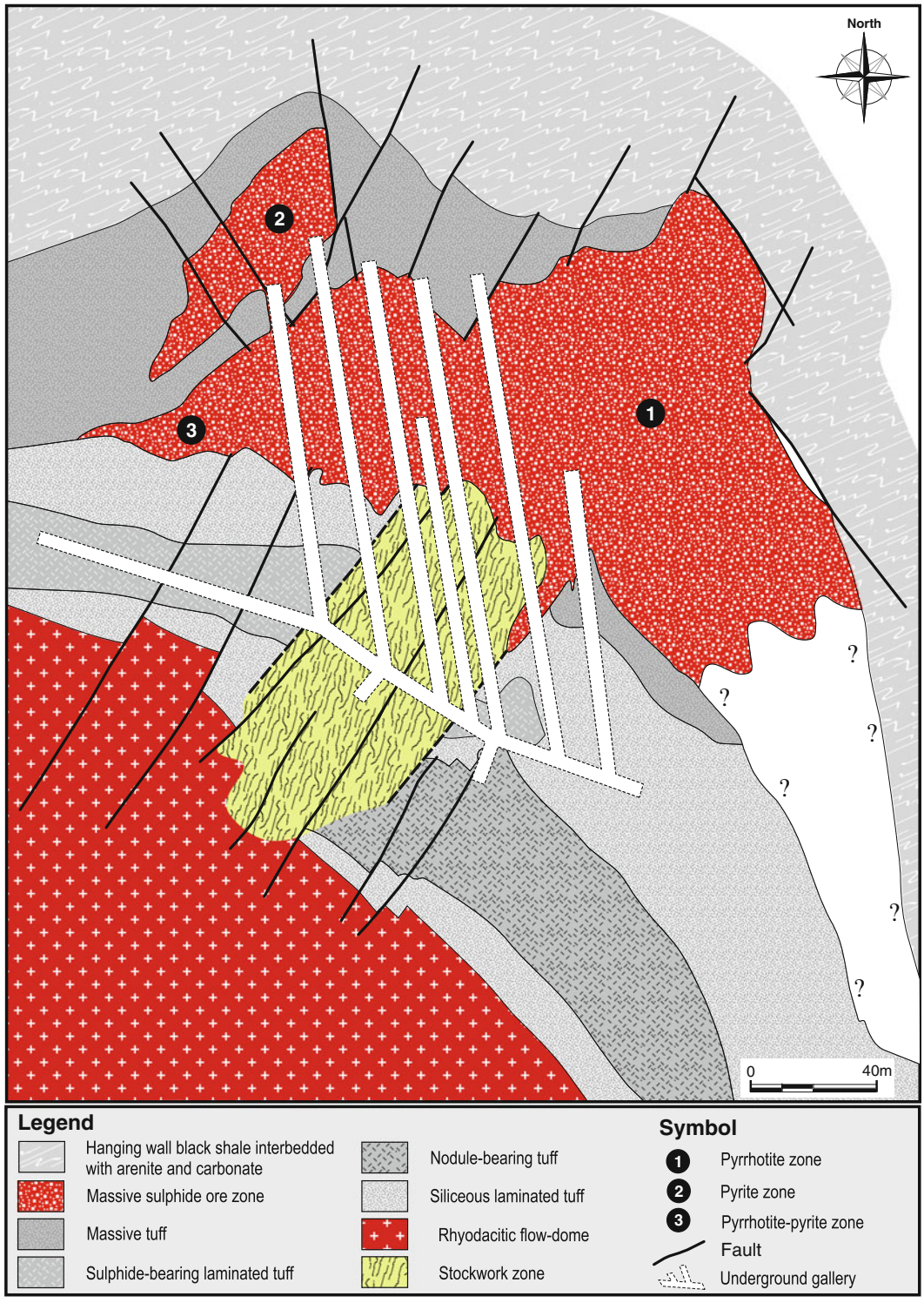

Fig. 8 Level 520 longitudinal section of the Hajar mine showing location of the massive and stockwork ore zones and their relationship to felsic volcanic and volcaniclastic rocks. Mine galleries are also indicated (modified from Zouhry 1998)

vein system is preserved, the alteration forms a zoned pipe with a core of massive silica surrounded by an intermediate silica-sericite zone, and by an outer zone of chlorite-pyrite-silica-sericite ± biotite (Zouhry 1998; Rziki 2012). This zoned alteration pattern probably reflects fluid/rock interactions controlled by decreasing temperature with distance from the center of the hydrothermal upflow zones. In this respect, Schardt et al. (2001) have shown that alteration mineral zoning depends primarily on variations in temperatures, pH, redox state, and fluid/rock ratio as hydrothermal fluids move outward from the center to edges of the alteration system.

The hanging wall alteration zone extends 200 m directly above the orebodies. Resulting mineral assemblages are similar but generally of less intensity than in the footwall alteration zone, comprising a sericite zone where white mica predominates over chlorite. Talc-carbonate ± tremolite-actinolite alteration is commonly developed in mafic-ultramafic igneous protoliths (Koudiat Aicha deposit), but also can be found as thin patches in the chlorite- or sericite-bearing zones close to ore, irrespective of the mineralogy of the spatially associated igneous rocks. Moreover, our observations indicate that the carbonate-bearing alteration zones form by infilling porosity and selective replacement of various components of the volcanic and volcaniclastic rocks (i.e., filling vesicles and replacing or rimming glass shards and feldspar phenocrysts), rather than by direct precipitation on the sea floor. Silicification predominates where felsic protoliths (rhyolite and associated epiclastic rocks) constitute the main host rocks. Three texturally distinct types of silicification are recognized in the study area: pervasive, patchy, and vein-textured. Most types are spatially associated with stringer ore. In general, silicification is the earliest alteration and is followed by chloritization. Later thin quartz ± sulphide ± carbonate veins and veinlets cut all alteration types and mineralization, and are attributed to fracturing and fluid movement during the waning stage of the hydrothermal system.

Mass balance calculations indicate that hydrothermal alteration of the footwall host rocks was accompanied by pervasive leaching of K_2O, Na_2O, and CaO, moderate loss of SiO_2, and precipitation of FeO, MgO, and MnO under a high-temperature regime (>150 °C) and high water/rock ratios (>10). Conversely, sericite- and calcite-rich alteration of hanging wall rocks involved lower temperatures (<150 °C) and atomic water-rock ratios (W/R) <5 (Marcoux et al. 2008; Zouhry 1998; Ben Aissi 2008; Lotfi et al. 2010; Rziki 2012).

6 Mineralogy and Mineral Chemistry

All of the mined deposits have similar mineral assemblages dominated by monoclinic pyrrhotite, sphalerite (10–12 mol% FeS), galena, chalcopyrite, and to a lesser extent pyrite (up to 10 %), together with minor tetrahedrite, arsenopyrite, and marcasite. Relative proportions of sulphide minerals vary among the deposits. Also present are accessory to trace amounts of Bi–Se phases such as laitakarite ($Bi_4(Se,S)_3$), together with native bismuth, bismuthinite, paraguanajuatite (Bi_2S_3), cassiterite, stannite, cobaltite, cubanite, and electrum (Hibti 2001; Marcoux et al. 2008; Lotfi et al. 2008). Major non-sulphide gangue constituents include chlorite, sericite-muscovite, quartz, Fe-rich to Mg-rich carbonates (calcite, siderite, ankerite, and dolomite), epidote, and tremolite-actinolite plus minor talc and ilmenite. These phases are intimately associated with the sulphides. Barite is absent from the deposits of the Jebilet-Guemassa VHMS province.

Chlorite, which is by far the most abundant alteration mineral, shows a wide spectrum of compositions ranging from ripidolite to sheridanite (Zouhry 1998; Marcoux et al. 2008; Ben Aissi 2008; Ben Aissi et al. 2005; Rziki 2012). These compositional variations correlate with a systematic decrease in Fe/(Fe + Mg) ratios laterally and vertically away from mineralization, reflecting therefore spatial and temporal

relationships with massive sulphide mineralization. Indeed, within the stockwork and distal alteration zones, syn-mineralization chlorite is predominantly Fe-rich ripidolite with a minor amount of Mg, whereas within the orebodies, chlorite has sheridanite-ripidolite to clinochlore compositions with Fe/(Fe + Mg) < 0.4, reflecting strong Mg-metasomatism during the hydrothermal emplacement of sulphides. In agreement with Roth et al. (1999), such a geochemical trend may have resulted from downward widespread circulation of seawater through the enclosing host rocks. Zones of massive sheridanite-ripidolite to clinochlore were probably dominated by the influx of seawater, whereas sericite-rich alteration zones may represent areas where ascending hydrothermal fluids were dominant.

Application of chlorite geothermometry (Cathelineau and Nieva 1985) indicates temperatures of equilibration in the range of 308–330 °C (Zouhry 1998; Hibti 2001; Rziki 2012). Distal chlorite shows lower temperature of formation of about 250 °C. At the Koudiat Aicha deposit, the calculated equilibrium temperatures are significantly lower, ranging from 261 to 286 °C (Ben Aissi et al. 2005).

Fine-grained white micas are phengitic with a larger muscovite than celadonite component (mean Al^{VI} = 1.5). The Fe/(Fe + Mg) ratios are lower but generally mimic those of associated chlorite. Most of the white micas have high contents of fluorine (avg ca. 1 wt% F). Fine-grained sericite has compositions that plot between the muscovite and celadonite end-members, with a net celadonite enrichment occurring toward mineralization.

7 Sulphide Deformation, Metamorphism, and Primary Depositional Features

Recent detailed mapping and structural analysis indicate that the massive sulphide orebodies and associated hydrothermal alteration zones have experienced at least two episodes of Variscan deformation and greenschist-facies metamorphism. The net discordance between the strikes of the intensely sheared and recrystallized orebodies and their enclosing host suggests that the present geometry of the orebodies was acquired during deformation. As a result, and with few exceptions, primary textures and mineral zonation have been largely obliterated, resulting in recrystallization, annealing, development of polygonal 120° triple junctions, remobilization of ductile phases and development of mylonitic microfabrics and tectonic banding (i.e., stretching and flow of pyrrhotite and chalcopyrite; Marcoux et al. 2008), pressure solution, piercement and pinch-and-swell structures (Hibti 2001; Lotfi et al. 2008; Belkabir et al. 2008; Marcoux et al. 2008; Ben Aissi 2008; Rziki 2012; this study). All of these structural and textural features are indicative of deformation and metamorphic recrystallization. In addition to brittle deformation, microscopic observations suggest that the ores were affected by late brittle faulting that displaced the main orebodies up to 50 m (Marcoux et al. 2008).

8 Fluid Inclusion Microthermometry

Microthermometric measurements performed on quartz-hosted fluid inclusions from the quartz-sulphide veins in the stockwork zone of the Hajar deposit (Zouhry 1998) show wide ranges in homogenization temperatures from 200 to 340 °C, with an overall mean of 274 ± 33 °C (n = 178). Measured salinities vary within a narrow range of 4–7 wt% NaCl equivalent, averaging ca. 6 wt% NaCl equivalent. These temperatures and salinities fall within the range of microthermometric values typical of VHMS deposits worldwide (e.g., Large 1992), and to the exit temperatures of fluids venting at many modern sea-floor hydrothermal sites (Von Damm, 1990). The melting temperature of the CO_2 varies between −60.5 and −54.7 °C,

indicating that an additional component such as CH_4 or N_2 is present. In this respect, Zouhry (1998) reported CH_4 contents up to 7 mol% for fluid inclusions from the Hajar deposit. The occurrence of CH_4 and/or N_2 is consistent with a reduced nature of the mineralizing fluids.

More importantly, the coexistence of CO_2-rich ± CH_4 ± N_2 fluid inclusions with CO_2-free, aqueous fluid inclusions, either along single growth zones or in proximity, constitutes strong evidence that all of the inclusions were trapped coevally and that the ore-forming fluid resulted from phase separation (boiling) including trapping of the fluid on the limbs of the H_2O and CO_2 solvus (Hendel and Hollister 1981). Therefore, a pressure correction is not necessary and the measured homogenization temperatures equal the trapping temperatures. It is thus concluded that the Jebilet-Guemassa sulphide mineralization occurred at a mean temperature of 274 ± 33 °C. This fluid inclusion temperature estimate is in good agreement with those predicted from vitrinite reflectance measurements (280–360 °C; Moreno et al. 2008) and chlorite geothermometry (308–330 °C; Zouhry 1998; Ben Aissi 2008; Lotfi et al. 2010; Rziki 2012).

9 Isotope Geochemistry

9.1 Sulphur, Hydrogen, and Oxygen Isotopes

Sulphur isotope compositions of sulphides (pyrrhotite, galena, sphalerite, pyrite, and chalcopyrite) from the major deposits (i.e., Draa Sfar, Hajar, Koudiat Aicha) and Khwadra prospect of the Central Jebilet-Guemassa VHMS province show a wide range of $\delta^{34}S$ values from −13 to 4.95 ‰, with the lowest ratios determined for samples from Koudiat Aicha and Khwadra (Ouguir 1987; Haimer 1988; Zouhry 1998; JICA 2003; Marcoux et al. 2008). A cumulative frequency plot shows three main groupings, with two major peaks at −10 ± 3 and 2 ± 2 ‰, together with a minor peak at −5 ± 1 ‰ (Fig. 9).

Overall, these sulphur isotope compositions are within the range of values commonly reported for VHMS deposits worldwide. Ninety percent of the data from the central Jebilet-Guemassa VHMS province fall between −1.0 and 1.0 ‰. Because of the self-buffering effect of the massive sulphides, the original

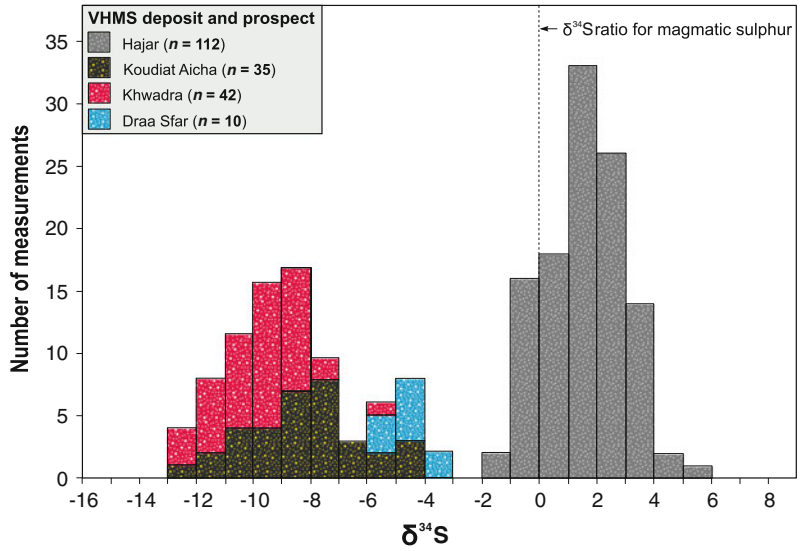

Fig. 9 Frequency distribution of $\delta^{34}S$ values for paragenetically different sulphide separates from the major deposits (i.e., Draa Sfar, Hajar, Koudiat Aicha) and Khwadra prospect of the Central Jebilet-Guemassa VHMS district. Compiled data are from Ouguir (1987), Haimer (1988), Zouhry (1998), JICA (2003), and Marcoux et al. (2008)

isotopic values in the massive ores tend to be preserved during metamorphic recrystallization, and during local pressure solution associated with annealing (cf. Hannington et al. 1999). Moreover, the equilibrium temperatures determined from coexisting sulphide pairs indicate isotopic disequilibrium, suggesting that the $\delta^{34}S$ values were controlled largely by kinetic effects rather than equilibrium fractionation as commonly inferred for modern sea-floor mineralization.

The large spread in sulphur isotope values is more difficult to interpret. Although the clustering of δ^{34} S values around 2 ± 2 ‰ is consistent with sulphur being derived from a magmatic source (−3 to +1 ‰; Hoefs 2009), the light isotopic signatures ($\delta^{34}S$ to −12 ‰) are attributed to partial bacteriogenic reduction of seawater sulphate along the fluid-flow path. Disproportionation of magmatic SO_2 may also explain negative $\delta^{34}S$ values of as low as −14 ‰ recorded by some sulphides (Arribas 1995). More importantly, the negative $\delta^{34}S$ values could also be achieved through boiling as implied by fluid inclusion data. In this respect, Drummond and Ohmoto (1985) suggested that boiling will lead to a loss of H_2 and the oxidation of the ore fluid, and in the more oxidized ore fluid, the ratio H_2S/SO_4^{2-} will decrease dramatically, leading to more negative $\delta^{34}S$ values in sulphides (e.g., Duuring et al. 2009; Kamvong and Zaw 2009). In conclusion, it appears that most of the recorded $\delta^{34}S$ values in the Central Jebilet-Guemassa VHMS province are consistent with a magmatic origin of the sulphur through boiling processes, although the involvement of biogenically reduced sulphur along the fluid-flow path cannot be excluded.

10 Lead Isotopes

Lead isotope compositions determined on galena separates from the Hajar deposit show homogenous isotopic ratios ranging from 18.165 to 18.205 for $^{206}Pb/^{204}Pb$, 15.631 to 15.661 for $^{207}Pb/^{204}Pb$, and 38.285 to 38.419 for $^{208}Pb/^{204}Pb$ (Zouhry 1998). Conversely, data for sulphide separates from the Draa Sfar deposit are highly variable with $^{206}Pb/^{204}Pb$ ratios ranging from 18.262 to 19.010, $^{207}Pb/^{204}Pb$ ratios from 15.630 to 15.701, and $^{208}Pb/^{204}Pb$ ratios from 38.293 to 39.702 (Marcoux et al. 2008) (Fig. 10). Collectively, the isotopic compositions from Draa Sfar delineate two partly overlapping groups; one defined by mixed Zn–Pb-rich ore forms the less radiogenic end-member. The second group of mixed Cu-rich samples are mostly more radiogenic. Overall, the Pb isotope compositions plot above the average crustal Pb growth curve of Stacey and Kramers (1975), and for some samples above the upper crustal model curve of Zartman and Doe (1981).

It is noteworthy that the lead isotopic compositions for galena separates from the Hajar deposit and those for mixed Zn–Pb ore from Draa Sfar plot either within, close to, or overlap partially the field for VHMS deposits of the Iberian Pyritic Belt. In contrast, lead isotopic compositions for Draa Sfar Cu-rich ores are uniformly more radiogenic. These differences in Pb isotope ratios for the Draa Sfar deposit may record a different lead source reservoir for the Zn–Pb ores relative to the Cu-rich ores, and/or different ages of mineralization for the two ore types.

The broad linear arrays of data in the $^{207}Pb/^{204}Pb$ versus $^{206}Pb/^{204}Pb$ and $^{208}Pb/^{204}Pb$ versus $^{206}Pb/^{204}Pb$ diagrams (Fig. 10) suggest a mixing of Pb from two contrasting end-members: (1) a radiogenic reservoir with $^{207}Pb/^{204}Pb$ ratios up to 15.701, and (2) a less radiogenic component. However, due to the absence of whole-rock Pb isotopic data for the host rocks to the deposit, identification of the source reservoirs involved in the mineralizing process is difficult to assess. Nevertheless, the close spatial association of the Jebilet-Guemassa base-metal ores with subvolcanic intrusions suggests that some of the metals present in these deposits were derived either directly from degassing magmas, or were leached from the underlying volcanic and volcaniclastic pile.

Moreover, the distribution of the galena Pb isotope compositions, plotting between the upper crustal and orogen model curves of Zartman and

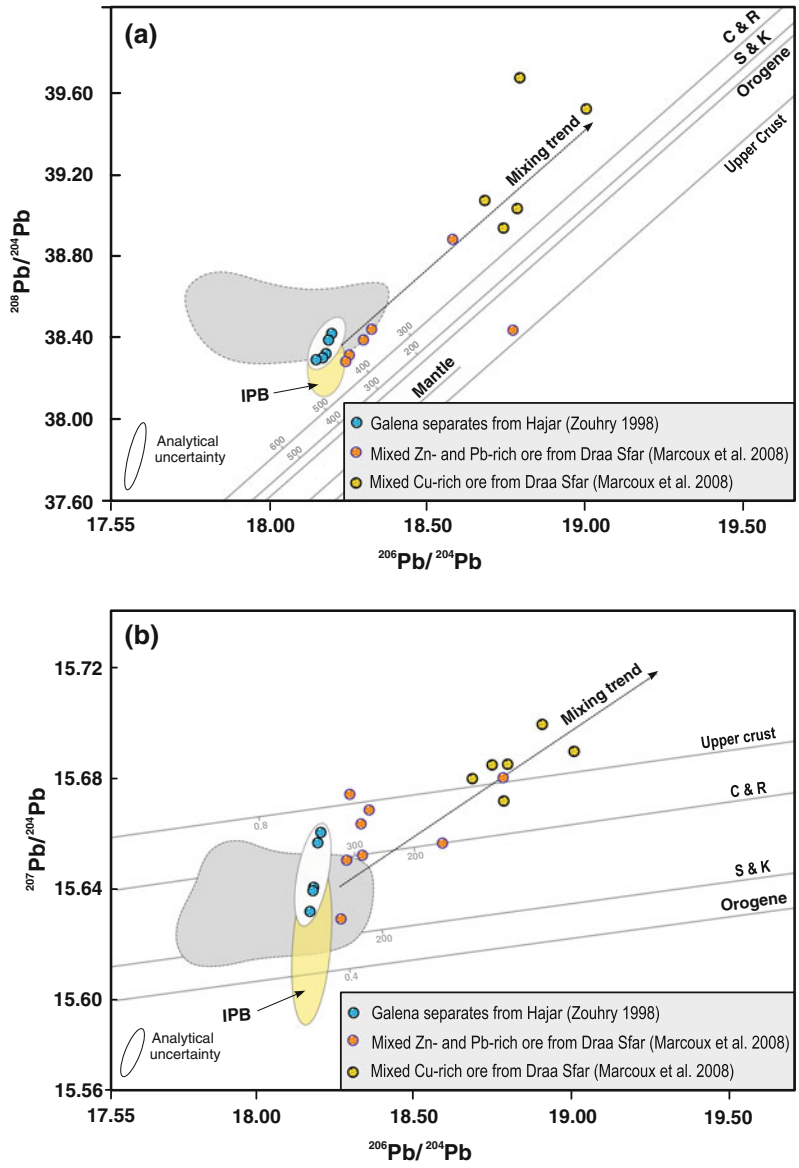

Fig. 10 Lead isotopic compositions of galena separates and mixed Zn- and Cu-rich ores from Hajar and Draa Sfar deposits of Jebilet-Guemassa VHMS district, plotted on **a** $^{208}Pb/^{204}Pb$ versus $^{206}Pb/^{204}Pb$ and **b** $^{207}Pb/^{204}Pb$ versus $^{206}Pb/^{204}Pb$ diagrams. Lead isotope data from Hajar and Draa Sfar are from Zouhry (1998) and Marcoux et al. (2008); respectively. Evolution curves of Stacey and Kramers (1975) and Cumming and Richards (1975) are labeled S & K and C & R, respectively; evolution curves for Upper Crust and Orogene (Zartman and Doe 1981) are shown for reference. Yellow field defines isotopic compositions for VHMS deposits of the Iberian Pyrite Belt (IPB). Grey field shows range of whole-rock lead isotopic compositions for Visean rhyodacite and schist from the eastern Meseta (Bouabdellah et al. 2015)

Doe (1981), suggests that the radiogenic end-member inherited its signature from the upper crustal lead reservoir, whereas the less radiogenic component reflects the extraction of lead from the orogen lead reservoir, with the latter being a product of the mixing of various leads during orogenic events. It is noteworthy that these Pb isotope compositions exclude any major component from a juvenile mantle-derived lead reservoir. Moreover, the plot of isotopic compositions of the Zn–Pb sulphide separates within the field of isotopic compositions defined for Visean rhyodacite and associated schistose pelite (Bouabdellah et al. 2015) indicates that a quantitatively significant proportion of the Pb, and by inference other metals, could have been derived from leaching from these local host rocks.

In contrast, the more radiogenic end-member may correspond to an upper crustal source represented by the terrigenous sediments within the stratigraphic sequence, or an unidentified source.

Another possibility is that the radiogenic end-member represents externally derived Pb that was incorporated into the sulphides during regional metamorphic recrystallization and fluid-rock reactions.

11 Genetic Model

The Central Jebilet-Guemassa VHMS deposits possess a number of attributes that set them apart from most classical VHMS deposits, but are commonly cited as the closest analog to those of the Iberian Pyrite Belt (Carvalho et al. 1999). These attributes include (1) banded sheet-like morphology, (2) predominance of pyrrhotite (up to 90 vol.%) over pyrite, (2) lack of well-developed stockwork zones, (4) absence of barite, (5) high Zn/Cu ratio, and (6) volumetrically minor igneous rocks. In certain respects, the Central Jebilet-Guemassa deposits have some of the diagnostic features of a SEDEX deposit, and thus may represent a hybrid type between VHMS and SEDEX deposits, developed within a marine to submarine volcanic and volcaniclastic succession. Most authors agree that the massive sulphide ores of the Central Jebilet-Guemassa province formed by replacement of the hosting unlithified wet mud at or just below the sediment-water interface, within sea-floor depressions or small grabens adjacent to fault-controlled hydrothermal vents (e.g., Moreno et al. 2008).

Geologic data together with fluid inclusion microthermometry and isotope data discussed above indicate a close relationship between igneous rock emplacement, district-scale alteration, seawater circulation, and massive sulphide mineralization. Based on these relationships, and in the context of the marine environment of the host volcanic and volcaniclastic rocks, and the associated exhalative units, we interpret the genesis of the Jebilet-Guemassa VHMS deposits as resulting from the interplay, to various degrees, of magmatic-hydrothermal fluids and ambient seawater. In our model, Upper Visean magmatism acted as the direct source of volatiles and metals, and as a heat engine during seawater convection, causing additional metals to be leached from the enclosing host rocks and contributing to the ore-forming fluid. More specifically, we suggest that the district VHMS mineralization resulted from mixing of a high-temperature (~350 °C) magmatic-hydrothermal fluid with a low-temperature, seawater-derived fluid under varying water/rock ratios. The syndepositional faults beneath the Jebilet-Guemassa deposits, fractured and glassy igneous rocks along with the porosity and permeability of the rhyolitic dome margins and associated volcaniclastic units, allowed infiltration of seawater that mixed with high-temperature, magmatically-derived fluid. Interaction of hydrothermal fluids with the host rocks is compatible with the linear array of Pb isotope data (Fig. 10) that suggests mixing of Pb, and by inference associated metals, which were leached from footwall rhyodacites and associated siliciclastic rocks and overlying terrigenous sediments.

Input of magmatic fluids could have occurred during the early stages of the hydrothermal system, probably as a result of exsolution from crystallizing Upper Visean igneous bodies. This interpretation is accord with the coexistence of CO_2-rich ± CH_4 ± N_2 fluid inclusions with CO_2-free, aqueous fluid inclusions (Zouhry 1998), suggestive of phase separation and boiling. Additional evidence for the involvement of magmatic fluid and for metal input into the hydrothermal system derives from the calculated $\delta^{18}O_{fluid}$ (11.5–17.0 ‰) and δD_{fluid} values (−62 to −30 ‰) (Lotfi et al. 2010) that are consistent with a magmatic-derived fluid (e.g., Taylor 1997). The presence of abundant sericite in the ore bodies and in surrounding alteration zones suggests that the upwelling hydrothermal fluid was mildly acidic, with pH values of 4.5–5.0 (see Doyle and Huston 1999).

Sulphur isotope data suggest that the sulphide sulphur was derived from a combination of predominantly deep-seated igneous sources through boiling processes, and a variable proportion of bacterially reduced sulphur along the fluid-flow path, with the convective mineralizing fluids being channelized through the most permeable volcanic and volcaniclastic strata beneath the Jebilet-Guemassa VHMS deposits.

During the later evolutionary stages, the system became largely open to the influx of large amounts of ambient seawater. Indeed, the lower salinities within the fluid inclusions (Zouhry 1998) that are close to that of normal seawater (3.5 wt% NaCl equiv.) are suggestive of modified seawater-dominated hydrothermal fluids. In agreement with Lydon (1988), the development of Mg-bearing chlorite in the footwall alteration zones of the Jebilet-Guemassa deposits is further evidences for entrainment of seawater into the hydrothermal system.

Predominance of pyrrhotite over pyrite (virtually absent), and the lack of magnetite at the temperature ranges recorded by fluid inclusion data (250–350 °C) are both indicative of low sulfur and oxygen fugacities (i.e., $\log fS_2 < 10^{-10}$ and $\log fO_2 < 10^{-35}$; Barton 1984) during alteration and associated sulphide mineralization (Lotfi et al. 2010; and present study). Decreasing temperatures in conjunction with increasing pH appear therefore to be major factors in controlling ore deposition within the mineralized structures.

In summary, we propose that deposition of the Jebilet-Guemassa massive sulphide ores occurred in response to mixing of ambient seawater-derived fluid with an early-stage, magmatic-hydrothermal fluid component. Fluid-rock reactions also could have played a crucial role in leaching additional amounts of Pb, Zn, Cu and associated cations from the traversed aquifers.The Upper Visean magmatism and associated high heat flow related to lithospheric extension drove hydrothermal fluids, including seawater convection and dewatering of the host black shale, resulting in upflow of deep-seated magmatic-hydrothermal fluids along major structural discontinuities, focusing of fluid flow, and sulphide deposition upon mixing with seawater.

References

Aarab EL, Beauchamp J (1987) Le magmatisme Carbonifère pré-orogénique des Jebilet centrales (Maroc), précisions stratigraphiques et sédimentologiques: implications géodynamiques. CR Acad Sci Paris Sér II 304:169–175

Arribas A Jr (1995) Characteristics of high-sulfidation epithermal deposits and their relation to magmatic fluids. Mineral Assoc Canada Short Course Ser 23:419–454

Barton PB Jr (1984) Redox reactions in hydrothermal fluids. In: Henley RW, Truesdall AH, Barton PB Jr (eds) Fluid-mineral equilibria in hydrothermal systems. Rev Econ Geol 1:99–113

Beauchamp J, Izart A (1987) Early Carboniferous basins of the Atlas-Meseta domain (Morocco): sedimentary model and geodynamic evolution. Geology 15:797–800

Belkabir A, Gibson H, Marcoux E, Lentz D, Rziki S (2008) Geology and wall-rock alteration at the Hercynian Draa Sfar Zn–Pb–Cu deposit, Morocco. Ore Geol Rev 33:280–306

Ben Aissi L (2008) Contribution à l'étude gîtologique des amas sulfurés polymétalliques de Draa Sfar et de Koudiat Aicha: comparaison avec les gisements de Benslimane et de Kettara, Jebilet Centrales, Maroc hercynien. Unpubl PhD Thesis, Cadi Ayyad Univer, Marrakech, 353 pp

Ben Aissi L, El Boukhari A, Hibti M, Elharfi M, Maacha L, Zinbi Y (2005) Altération hydrothermale et déformation ductile des roches volcaniques acides associées au gisement sulfuré de Draa Sfar (Jebilet Centrales, Maroc). Est Geol 61:147–160

Bernard AJ, Maier OW, Mellal A (1988) Aperçu sur les amas sulfurés massifs des Hercynides marocaines. Miner Deposita 13:104–114

Bordonaro M (1983) Tectonique et pétrographie du district à pyrrhotine de Kettara (Paléozoïque des Jebilet, Maroc). Unpubl PhD thesis, Louis Pasteur Univ, Starsbourg, 132 pp

Bordonaro M, Gaillet JL, Michard A (1979) Le géosynclinal Carbonifère sud-mésétien dans les Jebilet (Maroc): une corrélation avec la province pyriteuse du sud de l'Espagne. CR Acad Sci Paris Sér D 288:1371–1374

Bouabdellah M, Niedermann S, Velasco F (2015) The Touissit-Bou Beker Mississippi Valley-type district of northeastern Morocco: relationships to the Messinian salinity crisis, Late Neogene-Quaternary alkaline magmatism, and buoyancy-driven fluid convection. Econ Geol 110:1455–1484

Bouabdelli M, Piqué A (1996) Du bassin sur décrochement au basin d'avant-pays: dynamique du bassin d'Azrou-Khénifra (Maroc hercynien central). J Afr Earth Sci 23:213–224

Bouloton J (1992) Mise en evidence de cordiérite héritée des terrains traversés dans le pluton granitique des Oulad Ouaslam (Jebilet, Maroc). Can J Earth Sci 29:658–668

Carvalho D, Barriga FJAS, Munhá J (1999) Bimodal siliciclastic systems–the case of the Iberiuan Pyrite Belt. In: Barrie CT, Hannington MD (eds) Volcanic-associated massive sulfide deposits: processes and examples in modern and ancient settings. Rev Econ Geol 8:375–408

Cathelineau M, Nieva D (1985) A chlorite solid solution geothermometer: the Los Azufres (Mexico) geothermal system. Contr Mineral Petrol 91:235–244

Cumming GL, Richards JR (1975) Ore lead isotope ratios in a continuously changing Earth. Earth Planet Sci Lett 28:155–171

Dagbert M, Harfi M (2004) Resource estimation for the Draa Sfar South polymetallic deposit. Expl Mining Geol 11:99–112

Doyle MG (2001) Volcanic influences on hydrothermal and diagenetic alteration: evidence from the Highway-Reward deposit: Mount Windsor subprovince, Australia. Econ Geol 94:825–843

Doyle MG, Huston DL (1999) The subsea-floor replacement origin for the Ordovician Highway-Reward volcanic-associated massive sulfide deposit, Mount Windsor Subprovince, Australia. Econ Geol 94:825–884

Drummond SE, Ohmoto H (1985) Chemical evolution and mineral deposition in boiling hydrothermal systems. Econ Geol 80:126–147

Duuring P, McKinley BSM, Dickinson JM, Diakow LJ, Kim YS, Creaser RA (2009) Examining potential genetic links between Jurassic porphyry Cu–Au ± Mo and epithermal Au ± Ag mineralization in the Toodggone district of north-central British Columbia. Miner Deposita 44:463–490

Eddebi A, Saquaque A, Kersit M, Chbihi A (1998) L'amas sulfuré de Hajar (Guemassa, Maroc). Chron Rech Min 531–532:45–54

Essaifi A, Potrel A, Capdevila R, Lagarde JL (2003) Datation U-Pb: âge de mise en place du magmatisme bimodal des Jebilet Centrales (chaîne Varisque, Maroc). CR Acad Sci Paris Sér D 335:193–203

Essaifi A, Capdevila R, Fourcade S, Lagarde JL, Ballèvre M, Marignac C (2004) Hydrothermal alteration, fluid flow and volume change in shear zones: the layered mafic-ultramafic Kettara intrusion (Jebilet Massif, Variscan belt, Morocco). J Meta Geol 22:25–43

Essaifi A, Samson S, Goodenough K (2013) Geochemical and Sr-Nd isotopic constraints on the petrogenesis and geodynamic significance of the Jebilet magmatism (Variscan belt, Morocco). Geol Mag 1–26

Felenc J, Fournier M, Hmeurras M (1986) Contrôles géologiques des amas à pyrrhotine des Jebilet et Guemassa. Définition des guides de recherche. Rapport Bureau de Recherches Géologiques et Minières 86:54 p

Haimer J (1988) Contribution à l'étude de l'environnement volcanosédimentaire et minerai de Douar Lahjar (Guemassa, Maroc): lithologie, paléovolcanisme, géochimie, métallogénie. Unpubl MSc Thesis, Ecole Nationale Supérieure de Géologie, Nancy, France, 151 pp

Hannington MD, Poulsen KH, Thompson JFH, Sillitoe RH (1999) Volcanogenic gold and epithermal-style mineralization in the VMS environment. Rev Econ Geol 8:325–356

Hendel EM, Hollister LS (1981) An empirical solvus for CO_2–H_2O–2.6 wt.% salt. Geochim Cosmochim Acta 45:225–228

Hibti M (2001) Les amas sulfurés des Guemassa et des Jebilet (Meseta sud-occidentale, Maroc): témoins de l'hydrothermalisme précoce dans le bassin mesetien. Unpubl PhD Thesis, Cadi Ayyad University, Marrakech, Morocco, 318 pp

Hoefs J (2009) Stable isotope geochemistry, 6th edn. Springer, Berlin-Heidelberg, 285 p

Hoepffner C, Soulaimani A, Piqué A (2005) The Moroccan Hercynides. J Afr Earth Sci 43:144–165

Huvelin P (1977) Étude géologique et gitologique du massif hercynien des Jebilet (Maroc occidental). Notes Mém Serv Géol Maroc 37:7–22

JICA [Japan International Cooperation Agency] (2003) Report on the mineral exploration in Marrakech-Tekna area: Kingdom of Morocco. Phase 1. Japan Inter Cooperation Agency, 247 pp

Kamvong T, Zaw K (2009) The origin and evolution of skarn-forming fluids from the Phu Lon deposit, northern Loei fold belt, Thailand: evidence from fluid inclusion and sulfur isotope studies. J Asian Earth Sci 34:624–633

Lagarde JL, Choukroune P (1982) Cisaillement ductile et granitoïdes syntectoniques: l'exemple du massif hercynien des Jebilet (Maroc). Bull Soc Géol France 24:299–307

Large RR (1992) Australian volcanic-hosted massive sulfide deposits: features, styles, and genetic models. Econ Geol 87:471–510

Le Corre CL, Bouloton J (1987) Un modèle de "structure en fleur" associant décrochement et convergence: les Jebilets centro-occidentales (Maroc Hercynien). CR Acad Sci Paris 304(II):751–755

Lotfi F, Belkabir A, Brown AC, Marcoux E, Brunet S, Maacha L (2008) Geology and mineralogy of the Hercynian Koudiat Aïcha polymetallic (Zn, Pb, Cu) massive sulfide deposit, central Jebilet, Morocco. Explor Mining Geol 14:145–162

Lotfi F, Belkabir A, Brunet S, Brown AC, Marcoux E (2010) Lithogeochemical, mineralogical analyses, and oxygen-hydrogen isotopes of the Hercynian Koudiat Aïcha massive sulphide deposit, Morocco. J Afr Earth Sci 56:150–166

Lydon JW (1988) Volcanogenic massive sulphide deposits, Part 2: genetic models. Geosci Can Reprint Ser 3:155–182

Marcoux E, Belkabir A, Gibson H, Lentz D (2008) The Draa Sfar ore deposit (Jebilet, Morocco): an example of pyrrhotite dominant-polymetallic VHMS in Hercynian terranes. Ore Geol Rev 33:307–328

McPhie J, Allen RL (2003) Submarine, silicic, syn-eruptive pyroclastic units in the Mount Read Volcanics, western Tasmania: influence of vent setting and proximity on lithofacies characteristics. In: White JDL, Smellie JL, Clague DA (eds) Explosive subaqueous volcanism. Am Geophys Union, Geophys Monogr Washington, D.C. 140:245–258

Michard A, Soulaimani A, Hopffner C, Ounaimi H, Baidder L, Rjimati EC, Saddiqi O (2010) The South-Western branch of the Variscan Belt: evidence from Morocco. Tectonophys 492:1–24

Moreno C, Sáez R, González F, Almodóvar G, Tosano M, Playford G, Alansari A, Rziki S, Bajddi A (2008) Age and depositional environment of the Draa Sfar massive sulphide deposit, Morocco. Miner Deposita 43:891–911

Mrini Z, Rafi A, Duthou JL, Vidal P (1992) Chronologie Rb-Sr des granitoïdes hercyniens du Maroc: conséquences. Bull Soc Géol France 163:281–291

Ouguir H (1987) Étude métallogénique, conditions physicochimiques et géochimie isotopique de soufre de la minéralisation sulfurée: gîte de Douar Lahjar (Guemassa, Maroc). Unpubl MSc Thesis, Institut National Polytechnique de Lorraine, Nancy, France, 44 pp

Piqué A, Michard A (1989) Moroccan Hercynides. A synopsis. The Paleozoic sedimentary and tectonic evolution at the northern margin of West Africa. Am J Sci 29:286–330

Playford G, González F, Moreno C, Alansari A (2008) Palynostratigraphy of the Sarhlef Series (Mississippian); Jebilet Massif, Morocco. Micropaleo 54:89–124

Roth T, Thompson JFH, Barrett T (1999) The precious metal-rich Eskay Creek deposit, northwestern British Columbia. In: Barrie CT, Hannington MD (eds) Volcanic-associated massive sulfide deposits: processes and examples in modern and ancient settings. Rev Econ Geol 8:357–373

Rziki S (2012) Le gisement polymétallique de Draa Sfar: compilation et modélisation tridimentionnelle géologique et géophysique et perspectives de développement (Massif Hercynien des Jebilet Centrales, Maroc). Unpubl PhD Thesis, Cadi Ayyad Univ, Marrakech, Morocco, 294 pp

Sáez R, Moreno C, González F, Almodóvar G (2011) Black shales and massive sulfide deposits: causal or casual relationships? Insights from Rammelsberg, Tharsis, and Draa Sfar. Miner Deposita 46:585–614

Schardt C, Cooke DR, Gemmell JB, Large RR (2001) Geochemical modeling of the zoned footwall alteration pipe, Hellyer volcanic-hosted massive sulfide deposit, western Tasmania. Econ Geol 96:1037–1054

Stacey JS, Kramers JC (1975) Approximation of terrestrial lead isotope evolution by a two-stage model. Earth Planet Sci Lett 26:207–221

Taylor HP Jr (1997) Oxygen and hydrogen isotope relationships in hydrothermal mineral deposits. In: Barnes HL (ed) Geochemistry of hydrothermal ore deposits, 3rd edn. Wiley, New York, pp 229–302

Von Damm KL (1990) Seafloor hydrothermal activity: black smoker chemistry and chimneys. Ann Rev Earth Planet Sci 18:173–204

Watanabe Y (2002) $^{40}Ar/^{39}Ar$ geochronologic constraints on the timing of massive sulfide and vein-type Pb–Zn mineralization in the western Meseta of Morocco. Econ Geol 97:145–157

Zartman RE, Doe BR (1981) Plumbotectonics–the model. Tectonophys 75:35–162

Zouhry S (1998) Étude métallogénique d'un amas sulfuré viséen à Zn-Pb-Cu: cas de Hajar, Guemassa, Maroc. Unpubl PhD Thesis, École Polytechnique de Montréal, Canada, 352 pp

Part VI

Mississippi Valley-Type and SEDEX Deposits

Geology, Geochemistry, and Current Genetic Models for Major Mississippi Valley-Type Pb–Zn Deposits of Morocco

Mohammed Bouabdellah and Donald F. Sangster

Abstract

Morocco has been for the past two centuries one of the top ten Pb–Zn producers with two thirds of base-metal production derived from three major Mississippi Valley-type districts (Touissit-Bou Beker, Upper Moulouya, and Jbel Bou Dahar). Collectively, these districts have produced more than 100 Mt of ore at an average grade of ~3 wt% Zn and 4 wt% Pb. At the present time, none of the three districts is active. Economic orebodies are hosted by a succession of Lower to Middle Jurassic unmetamorphosed, platform carbonate rocks. The epigenetic and stratabound sulphide deposits occur as open-space fillings and metasomatic replacements of carbonate. Mineralization that fills open spaces (i.e., veins, interconnected cavities, solution-collapse breccias) accounts for most of the higher grade orebodies. Overall, the mineral paragenesis consists principally of variable proportions of sphalerite and galena, accompanied by different generations of saddle dolomite (Touissit-Bou Beker), calcite (Jbel Bou Dahar), or barite (Mibladen). In all of the districts, paleogeographic reconstructions indicate that the orebodies are located above basement topographic highs against which the Triassic and Early Jurassic formations pinch out. Regionally, ENE–WSW- and E–W-trending faults appear to have been a critical factor in ore genesis, having provided

M. Bouabdellah (✉)
Département de Géologie, Faculté des Sciences,
Université Mohammed Premier,
Avenue Mohammed VI, B.P. 717,
60000 Oujda, Morocco
e-mail: mbouabdellah2002@yahoo.fr

D.F. Sangster
Geological Survey of Canada, 601 Booth Street,
Ottawa, ON K1A 0E8, Canada

D.F. Sangster
Geological Survey of Canada, 2290 Relin Way,
North Gower, ON K0A 2T0, Canada

M. Bouabdellah and J.F. Slack (eds.), *Mineral Deposits of North Africa*,
Mineral Resource Reviews, DOI 10.1007/978-3-319-31733-5_19

favorable fluid channels for metal-bearing brines into permeable host rocks and dissolution structures. The geometry of the orebodies that parallel the major alpine faults, coupled with lead isotopic constraints, suggest that the MVT mineralizing event occurred during midle Tertiary time (i.e., Cretaceous to Miocene) coincident with closing stages of the Alpine orogeny in the Atlasic orogenic belt. Alpine mineralization is thought to have been promoted by the mixing of older, high-temperature, rock-buffered, dense brines stored within the Paleozoic basement, and a downwelling, cooler fluid probably of meteoric origin. The resulting mixed brines were centered mainly on the basement high structure and its flanks, then flowed laterally away from the basement high and giving rise to the lower grade mineralization of the distal prospects. Fluid migration towards the ore districts could have been achieved either by a gravity-driven system (Touissit-Bou Beker, Mibladen, and Jbel Bou Dahar) or sediment compaction in the foredeep (Jbel Bou Dahar), or a combination of both. An alternative buoyancy-driven fluid convection model is proposed for the Touissit-Bou Beker MVT mineralization.

1 Introduction

The Mesozoic to Cenozoic intra-continental Atlas system of Northwest Africa extends over a distance of 2000 km along strike from the Moroccan passive Atlantic continental margin to the Tunisian Mediterranean coast (Fig. 1). This system contains one of the most fertile Pb–Zn ± F ± Ba Tethyan-Atlantic metallogenic provinces as it is host to >1,000 Mississippi Valley-type (MVT) occurrences and deposits that range from small uneconomic showings to major districts of great size and productivity. This large province has been a world lead-zinc producer for at least 200 years, with an overall total production exceeding 20 Mt of combined Pb + Zn.

The Atlas system *ss* comprising the High and Middle Atlas in Morocco, the Saharian Atlas and Aurès Mountains in Algeria, and the Tunisian Atlas in Tunisia (Fig. 1) is attributed to the inversion of Jurassic rift or transtensional basins as a consequence of continental convergence between Africa and Europe during Cenozoic time (Jacobshagen et al. 1988; Beauchamp et al. 1996; Frizon de Lamotte et al. 2009). According to Leach et al. (2010), this interval of time included microplate assimilation that affected the western margin of North America and Africa-Eurasia and constitutes a favorable period worldwide during which approximately 36 % of dated MVT deposits formed.

In the Atlas system, economic Pb–Zn ± F ± Ba orebodies are enclosed within unmetamorphosed, flat-lying Mesozoic to Cenozoic shallow-water carbonate platform strata. These strata experienced multiple overlapping episodes of dolomitization, dissolution (i.e., karstification), and uplift during the Mesozoic breakup of the Pangean continental shelf of West Africa. There are no known Precambrian or Paleozoic examples of such orebodies. Among the major lithostratigraphic reservoirs, only three contain significant MVT mineralization, and all of these were important paleoaquifers during much of the evolution of the Atlas orogen. Indeed, more than 90 % of the exploited deposits and prospects occur within Lower and Middle Jurassic carbonates and, to a lesser extent, Triassic dolostones. Major deposits are concentrated in six separate mining camps, including in Morocco the word-class and historically important Touissit-Bou Beker district (>100 Mt at 4 wt% Pb, 3.5 wt% Zn, <1 wt% Cu, 120 g/t Ag; Bouabdellah et al. 2012, 2015), the Upper

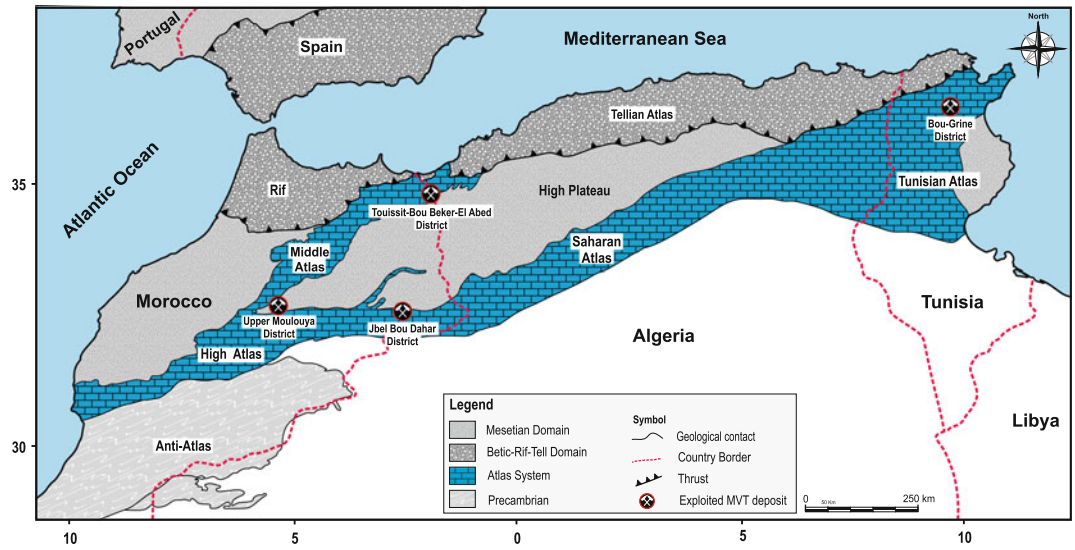

Fig. 1 Structural map of northwestern Africa and southern Iberia illustrating main lithostructural domains and spatial distribution of major Maghrebian (i.e., Moroccan, Algerian, and Tunisian) MVT districts within the Atlas system

Moulouya district (>30 Mt at 4 wt% Pb), and the Jbel Bou Dahar district (>30 Mt at 4 wt% Pb, 4 wt% Zn), the El Abed district in Algeria that constitutes the eastern termination of the Moroccan Touissit-Bou Beker district, and the Bou-Grine district and related deposits of the diapir zone in Tunisia (Fig. 1).

Extensive field, mineralogical, fluid inclusion, and isotopic studies during the last three decades have greatly improved our understanding of the genesis of MVT deposits in northwest Africa. However, in spite of abundant available geological, mineralogical, and geochemical data (Rajlich 1983; Dupuy and Touray 1986; Makhoukhi 1993; Bouabdellah 1994; Bouabdellah et al. 2012, 2015), the basic questions of genesis remain controversial with proposed models ranging from syngenetic to epigenetic. The lack of minerals suitable for radiometric age dating, together with the omnipresence of post-ore oxidizing events, have left the age of Pb–Zn mineralization as the subject of ongoing debate, and therefore any robust genetic model open to controversy.

The purpose of this paper is to (1) combine information on the most productive and best-studied MVT districts of Morocco for which production and reserve data are available; (2) review individual geological environments for these historically important base metal deposits; and (3) discuss the current new fluid inclusion and isotopic data, and proposed ore deposit models.

2 Touissit-Bou Beker District

The Touissit-Bou Beker district of northeastern Morocco and adjacent western Algeria (Fig. 2) is one of the top ten MVT districts in the world with a total production, over 75 years of mining activity, that exceeds 5 Mt of Pb + Zn. Production started in 1926 and ended in 2002 due to exhaustion of ore, decrease of ore grades with depth, and collapse of lead prices. Since 2002, however, limited-scale open-pit and associated subsurface artisanal mining is producing >10,000 t/years of ore averaging 6 % Pb.

The district (Fig. 2) is located within the northeastern part of "la Chaîne des Horsts" Atlasic belt, and covers an elongate, ENE-trending area of 64 km^2. Among the five mines that constitute the district, four are in Morocco (Mekta, Beddiane, Touissit, and Bou Beker) and one is in adjacent Algeria (El Abed).

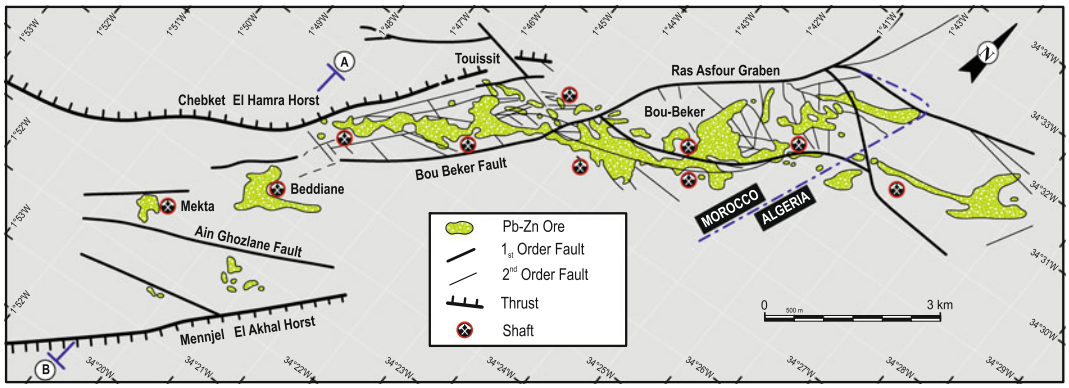

Fig. 2 Structural setting of Touissit-Bou Beker district showing exploited MVT orebodies projected to surface. Note that orebodies are elongate parallel to the main NE–SW fault system. Section line *A–B* indicates cross-section presented in Fig. 3

The Moroccan deposits, which occur in a primary envelope of Pb + Zn mineralization defined by a cutoff grade of 3 % Pb + Zn, differ from most MVT deposits owing to the dominance of lead over zinc, and locally (i.e., Beddiane deposit) to elevated concentrations of Cu (~1 %) and Ag (120 g/t). All of the exploited deposits are confined to a graben structure locally known as the Missouine graben (Fig. 2). Exploited higher grade lead-zinc orebodies are restricted to the Aalenian-Bajocian dolomite aquifer; making this tectonostratigraphic unit one of the most promising for MVT exploration in Morocco.

The summaries presented hereafter draw extensively from the recently published papers of Bouabdellah et al. (2012, 2015) as these constitute the most exhaustive and comprehensive descriptions published on this district.

2.1 Mining History

Discovered in 1926 and mined underground until 1973, the Bou Beker and Touissit deposits, the first operating underground mines in the district, were exploited by the European companies "la Société des Mines de Zellidja" and "la Compagnie Royale Asturienne des Mines," respectively. Between 1970 and 1980, widespread and intensive grid drilling along strike in the Missouine graben resulted in the discovery of the exceptionally high-grade Beddiane and Mekta deposits at depths of 110–180 m, respectively (Fig. 3). Calculated mean Pb grade for both deposits exceeded 10 % and locally reached 18 % (i.e., Hassi Msidira orebody; Bouabdellah et al. 2012). In 1980, the multinational "Compagnie Minière de Touissit" purchased the assets and began working the Mekta and Beddiane deposits.

2.2 Geological Setting

The geology of the Touissit-Bou Beker district has been well described by numerous investigations (Voirin 1965; Samson 1973; Touahri 1991; Rajlich 1983; Dupuy and Touray; 1986; Makhoukhi 1993; Bouabdellah 1994; Torbi and Gélard 1994; Ajaji et al. 1998; Aboutahir 1999; Bouabdellah et al. 1996a, b, 1999, 2001, 2012, 2015). Only a summary of the main conclusions relevant to the present study are given below.

Overall, the district stratigraphy consists of a Paleozoic basement unconformably overlain by a series of tabular and unmetamorphosed Meso-Cenozoic to Quaternary terranes (Fig. 4a, b). The Paleozoic rocks consist of weakly metamorphosed, Ordovician pelitic schists (Torbi 1996) locally intruded by porphyritic Visean rhyodacite. Unconformably overlying the Paleozoic basement is a thin lithostratigraphic unit made of a succession of basal

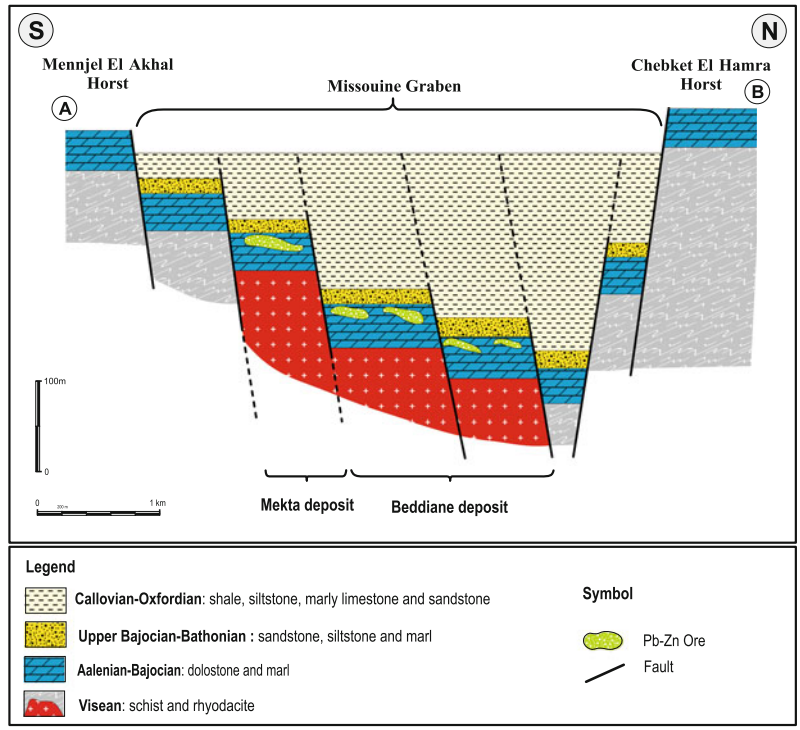

Fig. 3 Generalized N–S cross-section through Missouine graben showing position, at variable depths, of Mekta and Beddiane orebodies (see Fig. 2) relative to stratigraphy and facies units, and horst and graben structures with Middle to Upper Jurassic sedimentary infill

conglomerate and fine-grained limestone attributed to the Early Jurassic (Sinemurian-Carixian?). Paleogeographic reconstructions show that the Pb–Zn orebodies are located above an isolated topographically high carbonate platform of Paleozoic age known as the "Mole of Touissit" or "Touissit Shelf" (Samson 1973), against which the Triassic and Middle Jurassic formations pinch out (Fig. 5). The Aalenian-Bajocian (Middle Jurassic) carbonate sequence, which hosts nearly all economic deposits of the Touissit-Bou Beker district, rests either directly on the Paleozoic basement or conformably overlies the Early Jurassic unit. It consists of a succession of interbedded grey to brown, medium- to coarse-grained dolostone with thin (0.1 up to 1 m) layers of marl and clay, indicating a shallow sub- to intertidal, low-energy depositional environment. The 10–20-m-thick "Toit Jaune" unit constitutes the hangingwall rocks for the MVT mineralization and unconformably overlies the Aalenian-Bajocian dolostones (Fig. 4a, b). This unit consists primarily of a succession of yellow sandstone and silty shale interlayered with argillaceous carbonate, grading upward into a Bathonian regional stratigraphic marker made of a condensed succession (up to 2 m) of clay-rich siltstone and ammonite-bearing silty limestone with intercalated ferruginous oolitic beds. Overlying the Bathonian is a regionally developed organic-rich black shale up to 100 m thick that formed the "cap rock" during Pb–Zn mineralization. The host rocks are dissected by a series of faults, which regionally trend ENE–WSW and E–W, with a subordinate set that strikes NNW–SSE (Fig. 4). These fault structures appear to have played a critical role in ore genesis as they provided favorable fluid channels for MVT mineralization.

2.3 Alteration

Dolomitization is the principal type of wall-rock alteration. Two major stages have been distinguished based on petrographic, sedimentological, and isotopic (C, O, Sr) data (Bouabdellah 1994; Aboutahir 1999; Bouabdellah et al. 2012). Specifically, these are (1) regionally extensive, pre-ore diagenetic replacement dolomitization that

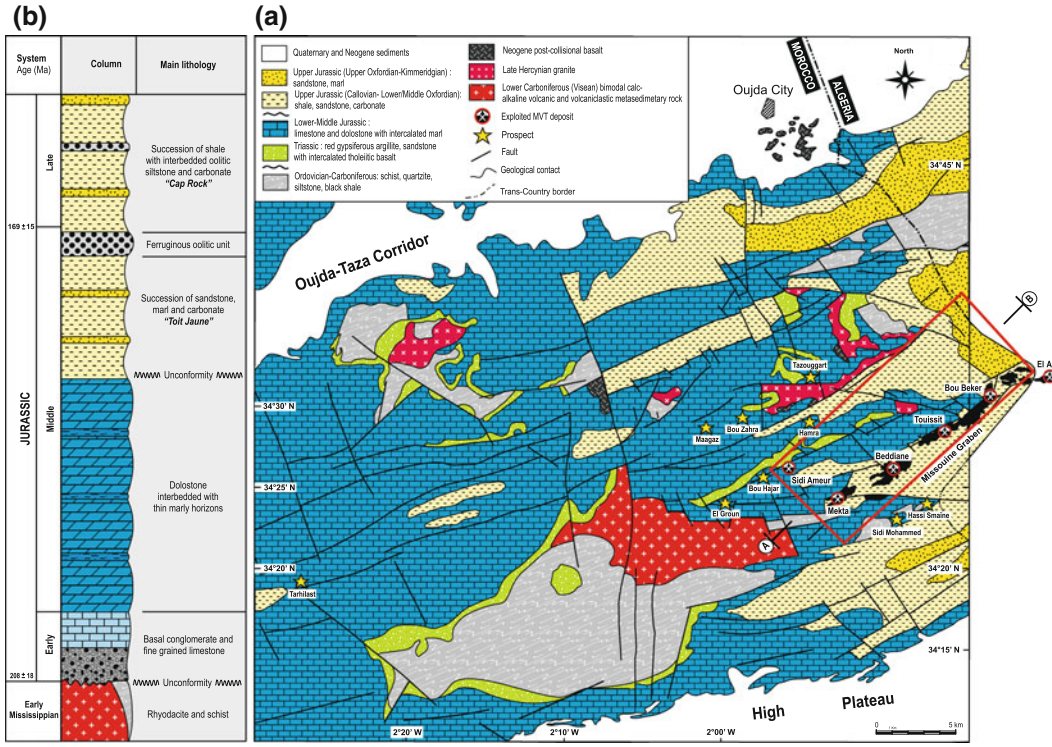

Fig. 4 **a** Geologic map of Touissit-Bou Beker district showing regional geology, major faults, distribution of ore-bearing dolostone, and associated MVT deposits (projected to surface). Regional geology simplified from Voirin (1965), Samson (1973), Owodenko (1976), Valin and Rakus (1979), and Bouabdellah et al. (2012, 2015). *Red rectangle* shows the location of the Touissit-Bou Beker district. **b** Generalized stratigraphic column for the Touissit-Bou Beker district showing main lithostratigraphic units. Section line *A–B* indicates cross-section presented in Fig. 5

forms 70 vol.% of the dolostone; and (2) epigenetic, ore-related, vug- and fracture-filling saddle dolomite cement.

The replacement dolomite pre-dates mineralization and significantly enhanced the porosity and permeability of the precursor limestones. In contrast, the ore-related hydrothermal sparry dolomite forms halos around the deposits and extends at least 100 m above the Aalenian-Bajocian dolostone host rocks into the overlying Upper Bajocian-Callovian-Oxfordian lithologies, and laterally for more than 10 km beyond the orebodies. Coexistence of the two types of dolomite led to the development diagnostic structures and textures that are commonly described in MVT environments elsewhere, such as saddle dolomite-cemented crackle, mosaic, and rubble breccias, and rock-matrix ("trash") breccias, zebra dolomite, and snow-on-roof texture (Bouabdellah et al. 2012).

Unlike dolomitization, silicification is weakly developed and is restricted to random, patchy-distributed occurrences of needle-like quartz crystals several centimetres long disseminated within the Aalenian-Bajocian dolostones.

2.4 Mineralization

The Pb–Zn deposits of the Touissit-Bou Beker district are epigenetic and stratabound. Sulphide mineralization consists principally of open-space fillings and metasomatic replacements of carbonate. Mineralization that fills open spaces (i.e.,

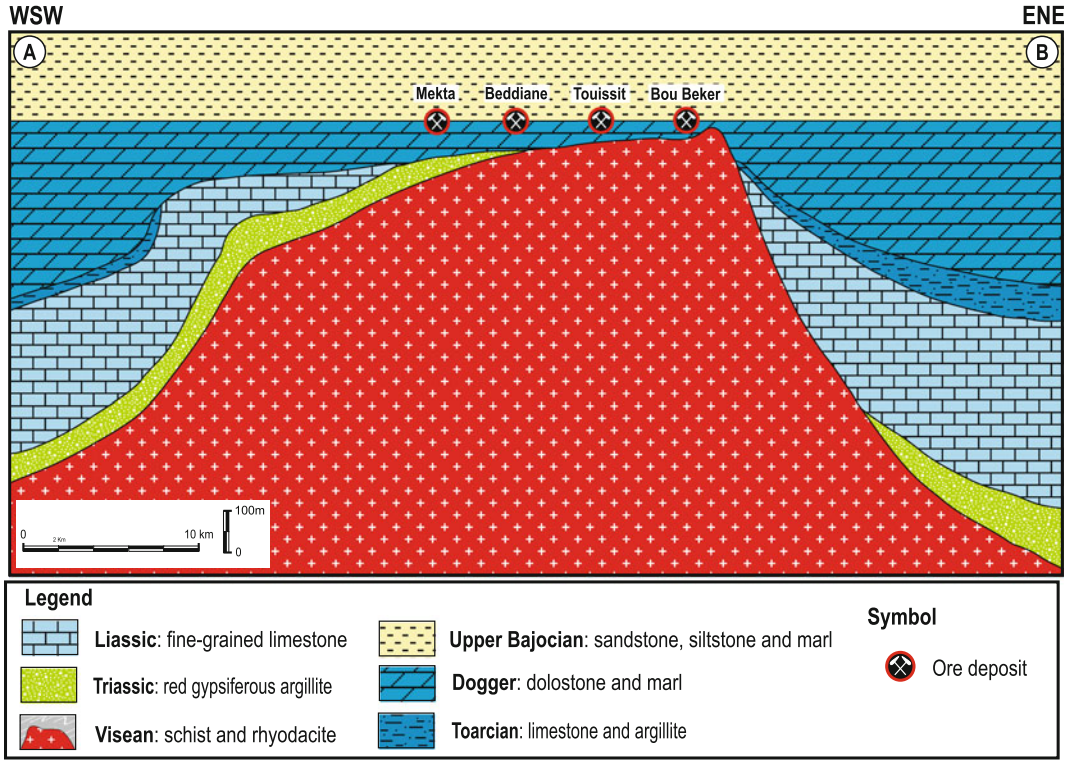

Fig. 5 Longitudinal ENE–WSW cross section through "Touissit Shelf" showing spatial distribution of main deposits of Touissit-Bou Beker district. Also illustrated is pinch-out of Triassic and overlying Liassic strata against "Touissit Shelf."

veins, interconnected cavities, or solution-collapse breccias) accounts for most of the high-grade orebodies (>80 % of extracted ore). These orebodies occur at various stratigraphic levels within the Aalenian-Bajocian (Middle Jurassic) strata, especially within the upper ten meters of the D_2 dolostone close to the upper Bajocian "Toit Jaune," and may extend for 10 m or more into the overlying Callovian-Oxfordian rocks (Fig. 4b). Uneconomic amounts of sulphides occur as veins (<1 m thick) within the Visean rhyodacitic basement. The mineralogy of the deposits is very simple, comprising sphalerite and galena, with minor pyrite-marcasite, and sparse chalcopyrite ± sulphosalts (i.e., tetrahedrite), accompanied by different generations of hydrothermal dolomite.

Field observations, together with mineralogical and textural relationships show that ore deposition occurred in three major stages, progressing from Zn-rich stage I to Pb-rich stage II and finally to a cuboctahedral stage III (Bouabdellah et al. 2012, 2015). Supergene mineral assemblages are extensively developed with oxidized ore zones extending as deep as 120 m, and account for nearly 60 % of the extracted ore. The transition from stage I to stage II mineralization is marked by the development of an intermediate Pb–Zn paragenesis in which mixed, co-genetic, fine-grained galena and sphalerite are intimately intergrown. Further evidence for the progressive evolution of the mineralizing fluid, from the Zn-rich to the Pb-rich ore stage, is shown by the presence of distinct metal zoning both vertically and laterally. Indeed, there is gradual decrease in Zn/Pb ratios from the east to the west and upward from the lower part to the uppermost part of the Aalenian-Bajocian dolomitic host rocks, with Zn/Pb ratios approaching unity in the case of

the Bou Beker and Touissit deposits (Bouabdellah et al. 2012).

The geometry of the orebodies that parallel the Atlasic ENE–WSW- and E–W-trending faults (Voirin 1965; Torbi and Gélard 1994; Jébrak et al. 1998) coupled with Pb–Pb geochronological data (Bouabdellah et al. 2012) suggest that the MVT mineralizing event occurred during the Miocene over a time span of <10 m.y., coincident with that recently proposed for the formation of carbonate-hosted Pb–Zn deposits in Tunisia (Jemmali et al. 2013).

2.5 Fluid Inclusion Thermometry

Microthermometric data performed on several generations of sphalerite and dolomite that span the paragenetic sequence (Dupy and Touray 1986; Makhoukhi et al. 2003; Aboutahir 1999; Bouabdellah et al. 2012) indicate that the ore-forming fluids correspond to evolved H_2O–NaCl–$CaCl_2$–KCl–$MgCl_2$ ± hydrocarbons hot (100 ± 20 °C) saline brines (>20 wt% NaCl equiv) of basin derivation. Calculated ore fluid pressures in the range of 150–200 bars (Makhoukhi et al. 2003) suggest depths of less than 1 km for ore deposition.

The high salinities and related high Ca/Na ratios of the ore-forming fluids imply that the predominant source of the ore-forming brine was seawater, although a contribution from halite dissolution to the total salt budget cannot be ruled out. Offset of fluid inclusion Na–Cl–Br leachate compositions away from the array for evaporated seawater was interpreted by Bouabdellah et al. (2012) to reflect dolomitization processes and fluid–rock interactions.

2.6 Stable Isotopes

Hundreds of carbon and oxygen isotope analyses were performed on several generations of replacement dolostones and ore-related hydrothermal dolomite cements (Bouabdellah 1994; Aboutahir 1999; Bouabdellah et al. 2012). Calculated $\delta^{18}O_{H2O}$ values of 3 ± 2 ‰ for the ore-forming fluids are consistent with several different sources, including connate waters, meteoric waters with long residence times in detrital rocks, and organically-derived (Sheppard 1986) and/or metamorphic waters. The absence of metamorphism of the Touissit-Bou Beker deposits excludes dehydration water as the ore fluid source. Organically-derived waters released from the organic-rich dolomitic host rocks and the unconformably overlying Bathonian black shales probably existed in the Touissit-Bou Beker deposits, but the low abundances of N_2, H_2S, and short-chain hydrocarbons within the fluid inclusions hosted in ore-related hydrothermal dolomite and sphalerite (Bouabdellah et al. 2012) suggest that organically-derived water was no more than a minor constituent. Furthermore, the high salinities of the fluid inclusions rule out meteoric water as the principal source of the ore-forming fluid, although meteoric water could have been a minor component. Alternatively, the Cl/Br and Na/Br molar ratios of the mineralizing fluids suggest that the source of the ore-forming brine was seawater that had evaporated beyond the point of halite saturation. Concurrently, the clustering of $\delta^{13}C$ values for all dolomite types at 0 ± 2 ‰, the typical value for Aalenian-Bajocian marine carbonate, implies that the dolomite carbon was inherited from the locally replaced limestone precursor.

In contrast to the uniform $\delta^{18}O$ and $\delta^{13}C$ values, sulphur isotope values for sulphide minerals display a wide range from −8.6 to + 12.9 ‰ (Bouabdellah et al. 2015). These values show distinct spatial (lateral and vertical) and temporal variations, expressed by an overall progressive decrease of $\delta^{34}S$ with (1) advancing paragenetic sequence toward younger sulfides (from stage I to stage III), (2) upward stratigraphic position (i.e., from base to top of the stratigraphic section), (3) towards the most distal parts of the deposits (i.e., surrounding prospects), and (4) within single grains (i.e., colloform-textured sphalerite) from the core toward the rim of analyzed sulphides. The resulting temporal shift from positive to negative $\delta^{34}S$ values may be interpreted as resulting from isotopic fractionation during inorganic (TSR) and/or bacteriogenic (BSR) reduction of seawater sulphate or porewater sulphate, at different rates of

sulphate availability (open versus closed reservoirs with respect to sulphate) (e.g., Basuki et al. 2008; Vikre et al. 2011). Mixing processes involving several sulphur sources having different $\delta^{34}S_{\Sigma S}$ values also can be invoked. Furthermore, the consistent decrease of $\delta^{34}S$ values both through space (i.e., towards higher stratigraphic position and more distal prospects) and time (i.e., with advancing paragenetic stage) is interpreted to reflect the entrainment of increasing amounts of surface fluid, possibly of meteoric origin, as this process would have resulted in oxidation of the fluids and shifting of $\delta^{34}S$ to lower values (Bouabdellah et al. 2015).

2.7 Radiogenic Isotopes

The $^{87}Sr/^{86}Sr$ ratios of replacement dolostones are similar to those of ore-related hydrothermal dolomites ranging from 0.70746 to 0.70833, and from 0.70769 to 0.70828, respectively, but are different from the ratios of the Visean rhyodacite (0.71849–0.72167) (Bouabdellah 1994; Bouabdellah et al. 2012). These $^{87}Sr/^{86}Sr$ ratios are higher than those for Aalenian-Bajocian seawater (0.70705–0.70735; Jenkyns et al. 2002). The negative correlation between $\delta^{18}O$ and $^{87}Sr/^{86}Sr$ isotopic ratios (Bouabdellah et al. 2012) suggests a link to deep circulation of the mineralizing fluids, probably at elevated temperatures, and as a consequence the input of radiogenic strontium from the underlying Visean rhyodacites, although the major source of dissolved strontium in the dolomitizing fluids was marine Aalenian-Bajocian carbonates.

Moreover, the lead isotope compositions of galena plot in a tight cluster above the evolution curve of Stacey and Kramers (1975), showing uniform $^{206}Pb/^{204}Pb$, $^{207}Pb/^{204}Pb$, and $^{208}Pb/^{204}Pb$ ratios ranging from 18.31 to 18.37, 15.61 to 15.66, and 38.45 to 38.62, respectively (Bouabdellah et al. 2012, 2015). Conversely, country rock samples display heterogeneous isotopic composition, with $^{206}Pb/^{204}Pb$ (17.76–18.49), $^{207}Pb/^{204}Pb$ (15.61–15.70), and $^{208}Pb/^{204}Pb$ (37.76–39.55) ratios defining two broad overlapping arrays on uranogenic and thorogenic plots (Bouabdellah et al. 2015). The tight linear clustering of Pb isotope data for galena from the ores, across the paragenetic sequence throughout the district, together with the overall tendency for the galena data to disperse along the Paleozoic, and more importantly the Mesozoic, sedimentary host-rock trends, led Bouabdellah et al. (2015) to conclude that Pb, and by inference other metals in the Touissit-Bou Beker district, were derived through the mixing of at least two main source-rock reservoirs characterized by contrasting Pb isotope compositions. The mineralizing process involved a large hydrothermal system that leached metals from the basement Visean rhyodacites and associated siliciclastic rocks, and more importantly from the overlying, multi-cycle, Triassic to Jurassic sediments including the "Toit Jaune" Pb-rich Bathonian sandstones.

2.8 Noble Gas Isotopes

Helium isotopic data for fluid inclusions show highly variable $^{3}He/^{4}He$ ratios ranging from completely radiogenic values of ~ 0.003 R_A to a maximum of 0.514 R_A (Bouabdellah et al. 2015). More interestingly, the distribution of $^{3}He/^{4}He$ ratios displays a distinct temporal and compositional trend including an overall decrease of $^{3}He/^{4}He$ ratios with advancing paragenetic sequence, consistent with the geochemical lowering trend exhibited by sulphur isotopic compositions. Overall, the highly variable $^{3}He/^{4}He$ ratios reflect variable degrees of mixing between mantle and crustal He along the flow path. The high concentration of ^{4}He, with a maximum of 38×10^{-8} cm^3/g (Bouabdellah et al. 2015), reflects prolonged residence times of the metalliferous brines within the basement host rocks prior to mineralization (Kendrick et al. 2002a, b). Long residence times of the resulting hot brines at such depths allowed them to equilibrate with the enclosing host rocks and attain high salinities, and as a consequence scavenge more metals.

Calculated contributions of the mantle-derived ^{4}He component involved in the paragenetically early Zn-rich, and succeeding Pb-rich main stages (i.e., $^{3}He/^{4}He$ ratios of ~ 0.15–0.51 R_A) are in the range of ~ 3–8 % for the

mineralizing fluids. This important finding led Bouabdellah et al. (2015) to conclude that the Late Neogene-Quaternary alkali basalts, which have ages coincident with the age of mineralization, could have contributed to the genesis of the Touissit-Bou Beker MVT mineralization by providing the necessary heat to drive fluid convection. The influence of mantle-derived He in the ore fluids decreased with time, consistent with the lowering of $\delta^{34}S$ values with advancing paragenetic sequence.

2.9 Ore Genesis

Conventional MVT genetic models including (1) episodic over-pressuring of compaction-driven fluids (Sharp 1978; Cathles and Smith 1983), (2) gravity-driven flow (e.g., Garven 1995; Bethke 1986), or (3) tectonically-driven "squeezing" flow (Oliver 1986) cannot satisfactorily account for Pb–Zn–Ag ore deposition in the Touissit-Bou Beker district (Bouabdellah et al. 2015). Of these, the widely accepted gravity-driven fluid model as a reliable driving force for fluid flow in this district may be possible (Bouabdellah et al. 2012), but seems unsupported by paleogeographic and paleoclimatic constraints. Indeed, this model assumes —even though not always clearly expressed—the existence of (1) a recharge zone that is permanently fueled by high rates of rainfall, and of (2) rapidly uplifted mountains as an efficient hydraulic head to create the high fluid flow velocities required to generate a fluid flow system efficient enough to form an economic deposit (Ge and Garven 1992; Appold and Garven 1999). However, paleogeographic and paleoclimatic reconstructions indicate that at the time of Pb–Zn mineralization in the Touissit-Bou Beker district (i.e., Late Neogene), Morocco and similarly the entire southwestern Mediterranean area, were under the influence of arid conditions (Fauquette et al. 2006). Moreover, structural data indicate that the later uplift stage, which took place during Messinian-Tortonian time (Frizon de Lamotte et al. 2009) contemporaneously with the emplacement of the Pb–Zn mineralization, did not exceed 1500 m. Based on these constraints, it is concluded that the gravity-driven fluid model would not have been efficienct enough to form ore deposits of the of sizes of those in the Touissit-Bou Beker district. An alternative model involving a genetic link among extensional tectonics, Neogene-Quaternary mafic magmatism, the Messinian salinity crisis, brine migration, and fluid mixing is therefore proposed for the Touissit-Bou Beker deposits (Bouabdellah et al. 2015).

The structurally controlled emplacement of the orebodies that parallel the Alpine ENE–WSW- and E–W-trending faults (Voirin 1965; Rajlich 1983; Torbi and Gélard 1994; Jébrak et al. 1998), coupled with lead isotopic constraints (Bouabdellah et al. 2012), suggest that the MVT mineralizing event occurred during the Miocene over a time span of 10 m.y. This inferred time period coincided with the emplacement of (1) Neogene to Quaternary calc-alkaline to alkaline basaltic magmatism (Duggen et al. 2005; Lustrino and Wilson 2007), and (2) a drastic paleoclimatic event at 5.96–5.33 Ma referred to as the Messinian salinity crisis (Hsü et al. 1973; Krijgsman et al. 1999). Indeed, the elevated $^{3}He/^{4}He$ ratios for fluid inclusions ($\sim$0.15–0.51 R_A; Bouabdellah et al. 2015) are consistent with the involvement of $\sim$3–8 % mantle-derived He, thus providing strong support for the contribution of mantle-derived volatiles and heat to the Touissit-Bou Beker mineralizing system. This addition of heat to the upper crust also may have promoted a long-lived convective hydrothermal system, consistent with the homogeneity of the galena Pb isotopic compositions and the formation of huge volumes of dolomitized rocks, which requires long-term fluid convection to provide a sufficient volume of dolomitizing fluids (Gomez-Rivas et al. 2014). The role of the Neogene-Quaternary basaltic magmatism was probably limited to providing the heat necessary to promote deep buoyancy driven, free convection and creating fluid conduits for focusing of the mineralizing hydrothermal brines into the permeable Aalenian-Bajocian ore-bearing dolostones.

The new model of Bouabdellah et al. (2015) also involves elevated heat flow and subsequent increased geothermal gradient initiated buoyancy-driven fluid convection of downward-flowing Messinian

seawater. This fluid convection ultimately promoted the mobilization of older, high-temperature, rock-buffered, dense brines stored within the Paleozoic basement, and the formation of base-metal-bearing chloride complexes. Mixing of Messinian seawater and basement-derived hydrothermal brines triggered the deposition of Pb- and Zn-rich stage I and II mineralization. The resulting mixed brines were mainly centered on the "Touissit Shelf" and its flanks, and then flowed laterally away from the basement high, giving rise to the lower grade mineralization of the distal prospects. The predominance of a high heat flow regime centered on a positive palaeographic structure (i.e., basement high) and more importantly the availability of appropriate sulphur nutrients (i.e., "fertile" vs. biogenic sulphur), may have been the critical ore controls that governed the size of the ore deposits.

3 Upper Moulouya District

The Upper Moulouya district of central Morocco (Fig. 6) constitutes the second largest producer of Pb in Morocco with a combined tonnage (production + reserves) of >31 Mt of ore at an average grade of ~4.5 wt% Pb (Annich and Rahhali 2002; Rahhali 2002). The mining district extends over a strike length of 40 km (east to west) and is 15 km wide (north to south), covering a total area of ~600 km^2. More than 100 Pb–Zn occurrences, ranging from small uneconomic showings to major deposits, have been delineated, three of which Aouli (9.6 Mt ore at 5 % Pb), Zeida (16 Mt at 3 % Pb), and Mibladen (6.5 Mt at 5 % Pb), are of economic interest (Fig. 7). Among these three deposits, only Mibladen is interpreted to belong to the MVT class (Jébrak et al. 1998; Naji 2004). At the present time, all of mines of the Upper Moulouya district are closed.

The village of Mibladen is famous as the source for most of the world's finest specimens of vanadinite (Jahn et al. 2003; Praszkier 2013). The Mibladen mining camp sensu stricto corresponds to an ENE-trending elongate area that extends for about 10 km (Fig. 8). Total production has been about 6.5 Mt of ore at 5 % Pb (Annich and Rahhali 2002; Rahhali 2002), accounting for approximately 30 % of Moroccan Pb production.

3.1 Mining History

Lead mining in the Upper Moulouya district has a long history with artisanal miners exploiting metals, particularly silver, since prehistoric and Medieval times (Emberger 1965). During the XII and the XIV Centuries, some deposits were mined by the Almohade Dynasty. In more recent times, mineral resources of the Mibladen area were re-discovered in the early 1920s and shortly thereafter were mined in open pits that produced lead concentrates. Between the 1920s and 1950s, mines of the district were owned and exploited by French mining companies, namely "la Société Penàrroya" and "la Société des Mines d'Aouli." The end of the 1950s and the beginning of 1960s marked the turning point in the district as an extensive exploration program was carried out to identify hidden deposits (Emberger 1965; Felenc and Lenoble 1965). Between 1968 and 1973, all of deposits were reevaluated during regional mapping (1:50,000 scale) and geochemical soil sampling, by a joint venture between the ONHYM "Office National des Hydrocarbures et des Mines" (formerly BRPM), the Ministry of Mines and Energy, and the Aouli Mining Company. The major period of lead mining ended with the closure in 1976 of the underground Mibladen mine.

3.2 District Geology Setting

The stratigraphy of the Upper Moulouya district consists of a succession of metamorphosed greenschist- to amphibolite-facies lower Paleozoic metasedimentary, volcaniclastic, and volcanic rocks, and unconformably overlying Mesozoic and Cenozoic strata (Emberger 1965; Fig. 6). The lower Paleozoic sequence comprises up to

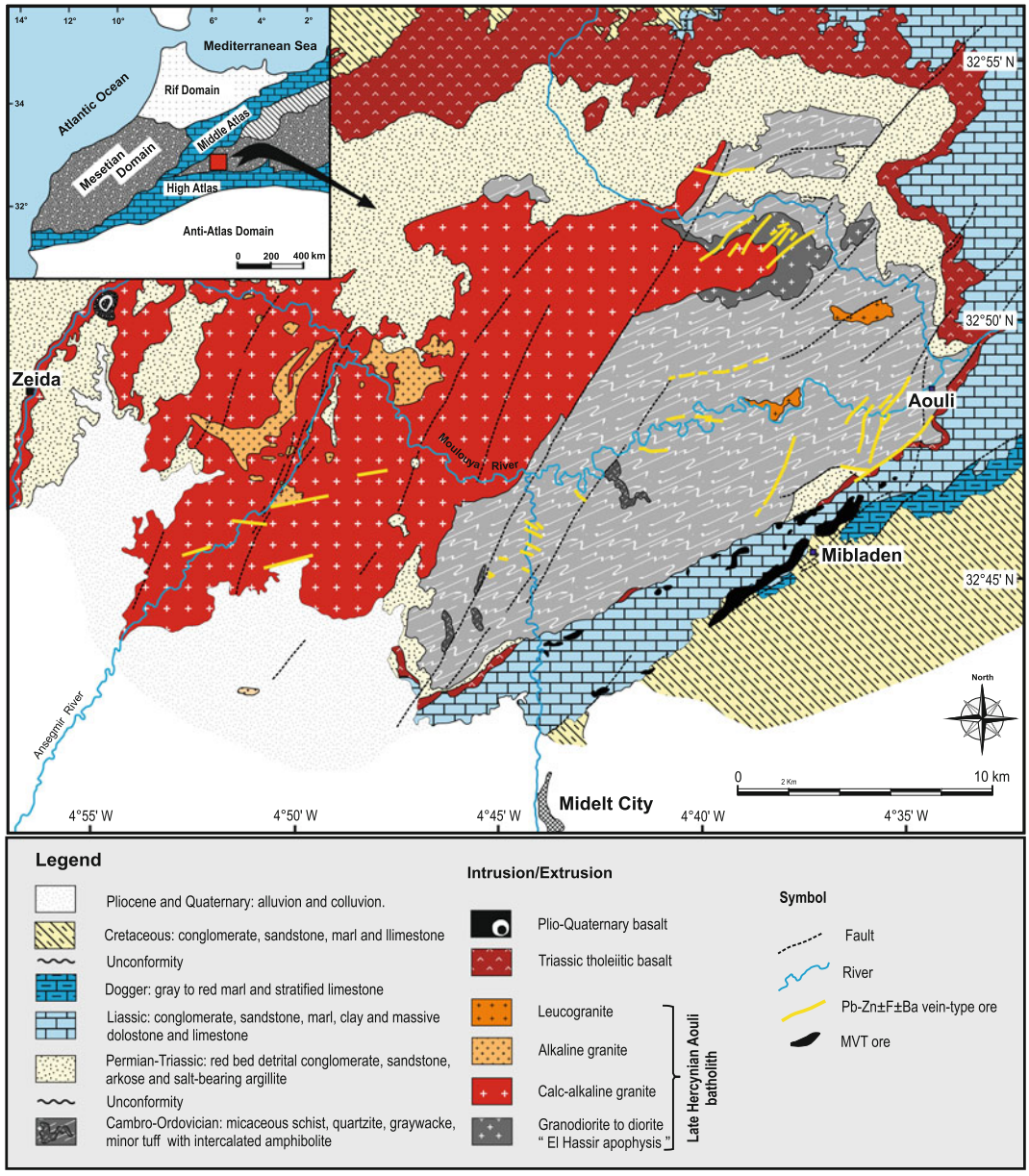

Fig. 6 Generalized geologic map of Upper Moulouya district showing regional geology, major faults, and location of historically mined Aouli, Mibladen, and Zeida base-metal ± fluorite ± barite deposits (modified after Emberger 1965). Inset shows Upper Moulouya district within framework of major tectonostratigraphic domains of northern Morocco

3,800 m of Cambro-Ordovician metasedimentary turbiditic flysch (Vauchez 1976; Filali et al. 1999) with intercalated mafic amphibolites. These rocks are locally intruded by the hydrothermally altered, multiphase, 347–281 ± 2 Ma alkaline to calc-alkaline Aouli granitoid batholith (Oukemini et al. 1995; Dahire 2004)

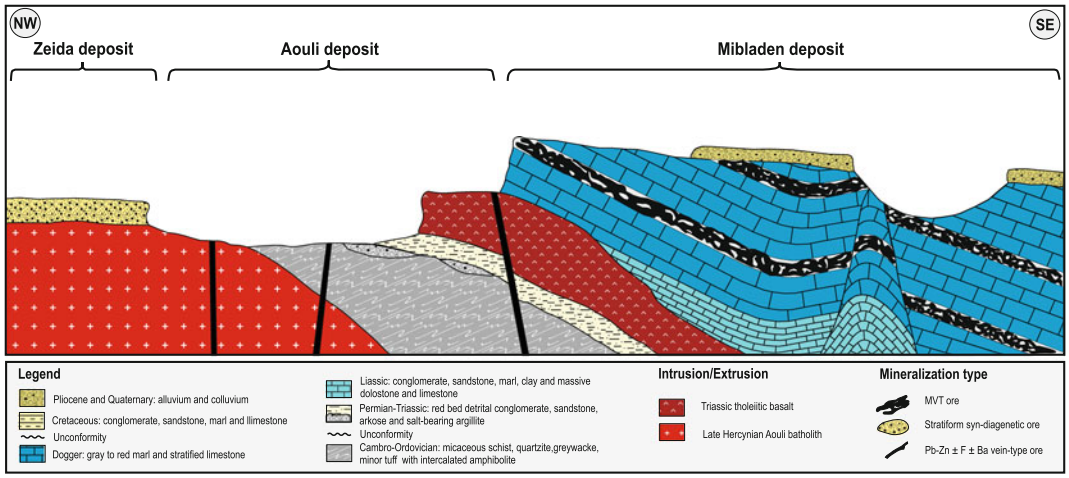

Fig. 7 Idealized longitudinal NW–SE cross section through Upper Moulouya district showing spatial distribution of Aouli, Zeida, and Mibladen base-metal ± fluorite ± barite deposits and their relationship to stratigraphy and fault systems (modified after Emberger 1965)

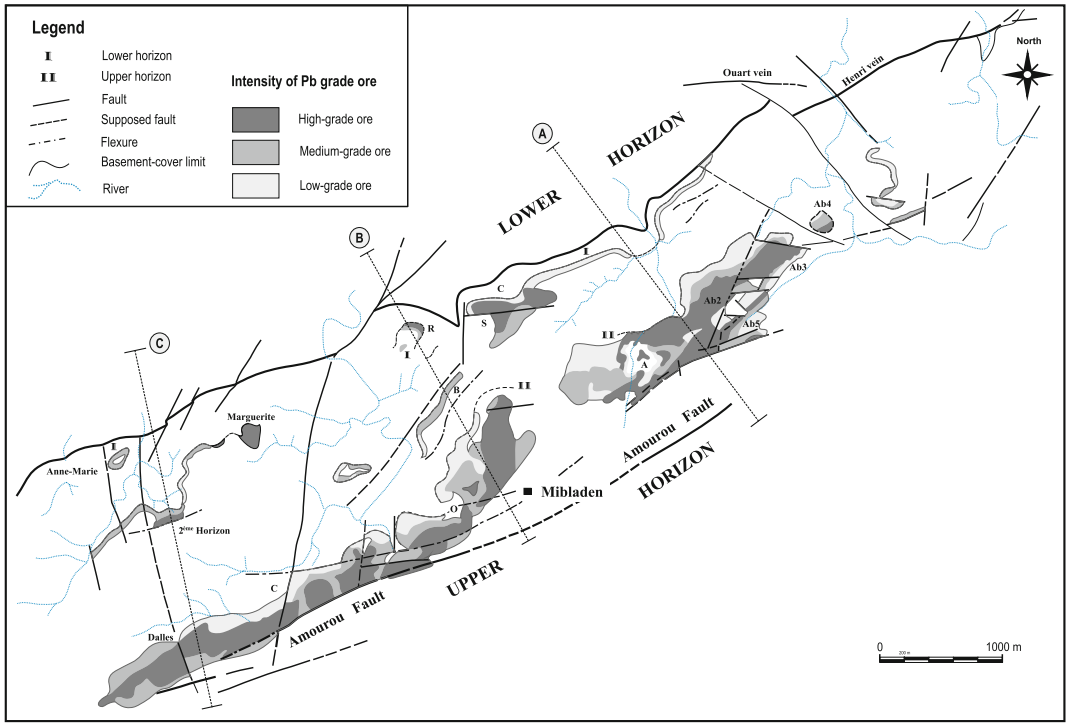

Fig. 8 Structural setting of Mibladen deposit with exploited MVT orebodies and contours of Pb grades projected to surface. Note that orebodies are elongate parallel to main fault system. Section lines *A*, *B*, and *C* refer to cross sections shown in Fig. 10. Modified from Felenc and Lenoble (1965)

From Triassic to Early Jurassic times the Upper Moulouya district experienced the influence of both the continental Atlantic and Tethys rifting processes (Ellouz et al. 2003; Ouarhache et al. 2012). This rifting resulted in the formation of syn- and post-rift, fault-controlled basins (i.e., horst and graben structures) that developed on a topographically high "shelf" during the major Triassic-Early Jurassic marine transgression (Ouarhache et al. 2012).

The syn-rift series consists of a thick (up to 1,000 m) succession of Permian to Triassic continental to fluvio-lacustrine red-bed sedimentary rocks with two main intercalated Central Atlantic Magmatic Province (CAMP) tholeiitic basaltic flows ca. 210 ± 2.1 to 196 ± 1.2 Ma ($^{40}Ar/^{39}Ar$; Fiechtner et al. 1992). The overlying, post-rift, Liassic to Dogger (Early-Middle Jurassic), shallow-water marine carbonates were deposited on a carbonate platform in a rapidly subsiding basin (Fedan et al. 1989). These strata are unconformably overlain by Cretaceous to Cenomanien shallow-marine carbonates, sandstones, marls, and shales, with intercalated units of lagoonar evaporites followed by up to 1,500 m of Miocene-Pliocene continental detrital sediments, locally intruded by ca. 14.6–0.5 Ma alkaline basaltic lava flows (Harmand and Cantagrel 1984; Duggen et al. 2009; Wittig et al. 2010).

It is noteworthy that the Domerian (Early Jurassic) dolomitized carbonates that host nearly all the economic occurrences of the Mibladen deposit experienced several episodes of karstification due to subaerial emergence of short duration in an active tensional tectonic regime (Dagallier and Macaudiere 1987). The Quaternary strata are made of alluvium and coluvium (Felenc and Lenoble 1965) and cap the lithostratigraphic column. Atlasic (Late Miocene) tectonic structures are dominated by a series of E–W-trending and subordinate ENE–WSW, NW–SE, and WNW–ESE kilometre-scale faults.

3.3 Alteration

Dolomitization and, to a lesser extent, silicification are the two main types of wall-rock alteration that affected the Domerian carbonate host rocks. Of these, the most pronounced alteration is expressed by regional, multi-stage, pre-ore and stratigraphically controlled diagenetic dolomite. Unlike this dolomitization, silicification is only weakly developed, being confined to centimeter-wide zones adjacent to the mineralized structures.

Pre-ore dolomitization forms massive replacements of the host rock carbonate but with most sedimentary fabrics such as bedding still preserved. This dolomitization prepared the host rocks for later MVT mineralization by increasing the initial porosity and permeability, and the competency of the precursor limestones. Unlike in the Touissit-Bou Beker district, ore-related hydrothermal dolomitization in the Upper Moulouya district is virtually absent.

3.4 Mineralization

The Mibladen Pb–Ba deposit extends over a wide stratigraphic interval within Triassic to Cretaceous strata. However, high-grade orebodies are exclusively confined to the Domerian (Early Jurassic) dolomitized carbonates. Mineralized structures are best developed in proximity to the major ENE-trending faults, namely the Aouli fault to the north and the Amourou fault to the south (Fig. 8). Overall, the sulphide-barite mineralization is clearly epigenetic and strata-bound, and occurs as massive fillings of horizontal and vertical karsts, veins, and of vuggy porosity related to dissolution of the host rocks infillings; to a lesser extent, this mineralization also forms metasomatic replacements (Fig. 9). The massive development of the orebodies within the upper 10 m of the Domerian

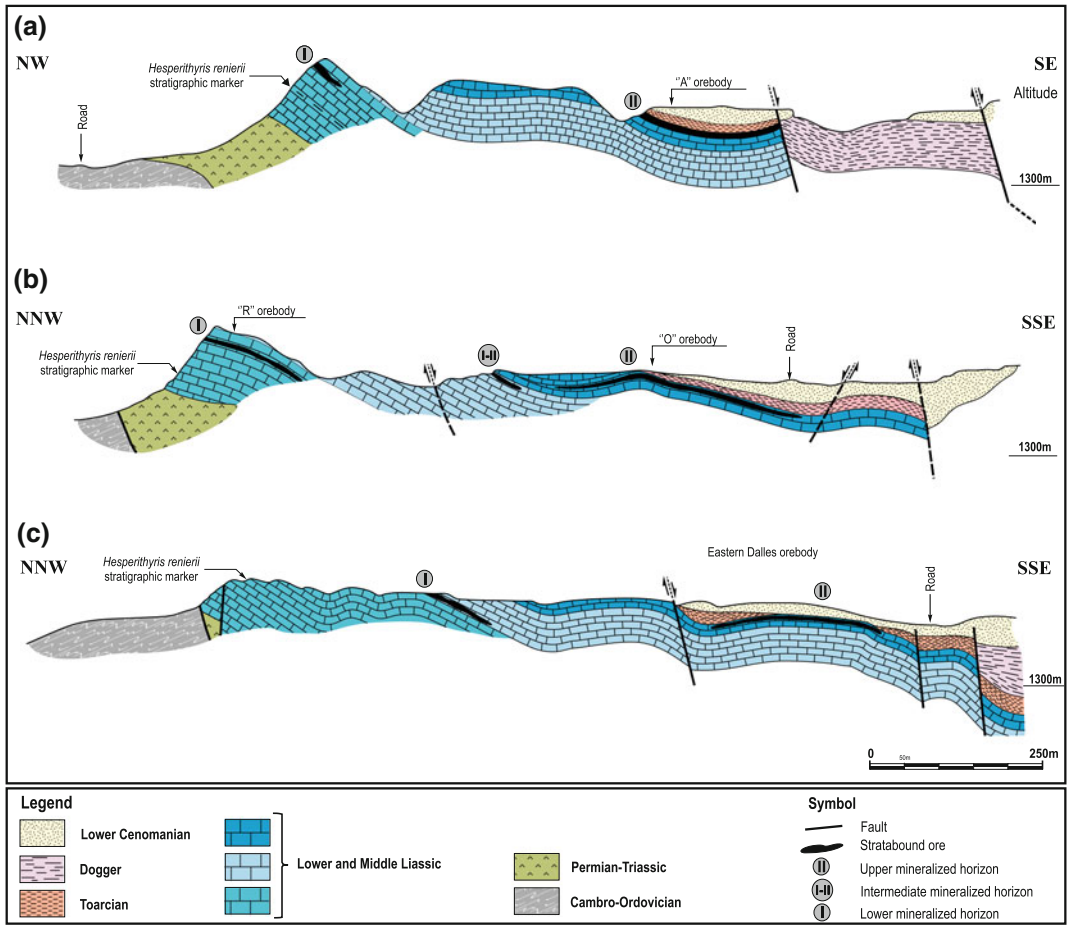

Fig. 9 Geological cross sections through Mibladen deposit in Upper Moulouya district illustrating morphology of MVT orebodies and post-Domerian age for mineralization. See Fig. 9 for locations of section lines. Modified after Agard and Du Dresnay (1965)

carbonates, near the Domerian-Toarcian unconformity, suggests that most of the dissolution structures, including early breccias and karst cavities, formed during periods of subaerial emergence. The higher grade, strata-bound orebodies are distributed along two main, sub-parallel, ENE-trending stratigraphic levels, locally referred to as upper and lower horizons (i.e., "Faisceau Supérieur" and "Faisceau inférieur," respectively; Felenc and Lenoble 1965) (Fig. 8).

Unlike the open-space filling galena that accounts for at least 90 % of the exploited ore, the metasomatic mineralization consists of less-economic, disseminated and/or grainy clusters of galena crystals that replace the dolomitized host rocks and associated sedimentary structures, giving rise to a stratiform style of mineralization.

3.5 Ore Mineralogy and Paragenesis

The mineralogy of the Mibladen deposit has among the simplest mineral assemblages ever documented for an MVT district. It consists mostly of galena, with minor amounts of pyrite and chalcopyrite. Sphalerite is virtually absent. Non-sulphide minerals are represented by barite with minor quartz. The unusual characteristic of

the Mibladen mineralogy results in the major predominance of lead over zinc with a Pb/Zn ratio of 10:1, and more importantly the development of an impressive supergene paragenesis from which some of the world's finest vanadinite, wulfenite, and cerussite specimens have been collected.

The sequence of mineral deposition shows three successive and overlapping stages of mineralization, two of which (Stages I and II) are of economic interest. Stage I, referred to as "main-stage ore," is the earliest and economically the most important, accounting for at least 80 vol.% of the total galena-barite resources. This stage comprises galena (Ga-1) and barite (Ba-1) accompanied by minor pyrite and chalcopyrite. Paragenetically later stage II mineralization, referred to as the "cuboctahedral stage," consists of centimeter-sized cubic to octahedral galena crystals (Ga-2) with white to pink crested barite (Ba-2) lining vugs.

Post-ore supergene Stage III resulting from the oxidation of hypogene sulphides consists of a rich secondary assemblage of vanadinite, wulfenite, cerussite, aragonite, calcite, quartz, gypsum, manganese oxides (coronadite, cryptomelane, and hollandite; Jahn et al. 2003), mottramite (PbCu$(VO_4)(OH)$), paralaurionite (PbCl(OH)), and phosgenite ($Pb_2CO_3Cl_2$) (Praszkier 2013).

3.6 Age of Mineralization

As debated for MVT deposits worldwide, the age of the Mibladen Pb mineralization has been, and still is, a source of ongoing controversy. Early debates focused on the question of whether the mineralization is syngenetic or epigenetic, and consequently occurred before or after the onset of the Atlasic orogeny in the Late Miocene. The lack of suitable minerals for radiometric dating along with the omnipresence of post-ore oxidizing events of unknown timing leave the age of hypogene mineralization uncertain.

Combined geological field observations and cross-cutting relationships have been used to estimate the relative timing of mineralization. Paragenetic studies show the presence of two distinct stages of mineralization, both of which are epigenetic and structurally controlled and formed after lithification and dissolution of the Domerian dolomitic host rocks. Thus, the deposition of these two stages post-dates the Early Jurassic (i.e., Domerian). More importantly, the $\delta^{34}S$ values of barite range from 17.1 to 18.1 ‰ (Table 1) and plot within the compositional interval for Cretaceous seawater, with an average range of 15–20 ‰ (Claypool et al. 1980; Kampschulte and Strauss 2004). These sulphur isotope data suggest that sulphur in the barite was derived from coeval seawater sulphate, either directly from the Cretaceous ocean or by the dissolution of Cretaceous marine evaporates. If so, this would place a maximum age of ~100 Ma for the Pb mineralization. However, based on the fault geometry and siting of economic orebodies within the Mibladen deposit, it is inferred that the ENE-, E–W-, and NW-trending fault zones acted as major fluid conduits for MVT mineralizing fluids. These fault systems are interpreted to have been reactivated during Neogene time, by tectonic inversion of preexisting Jurassic normal faults in response to NW–SE- and N–S-directed compressional events (Naji 2004).

Based on these constraints and the strong similarities in mineral assemblages and the nature and conditions of the mineralizing fluids with the Touissit-Bou Beker mineralization described above, it is concluded that the Mibladen MVT mineralization formed during the Late Miocene during the same time period in which the Touissit-Bou Beker mineralization formed. The same arguments and conclusions were reached previously by Jébrak et al. (1998).

3.7 Fluid Inclusion Microthermometry

At the Mibladen deposit, the only suitable mineral for fluid inclusions studies is barite. However, this is a questionable host mineral for microthermometric measurements due to its soft nature and tendency to stretch or leak during heating (e.g., Ulrich and Bodnar 1988).

Table 1 Sulphur and lead isotopic compositions of galena and barite separates from Mibladen (Upper Moulouya) and Jbel Bou Dahar (Eastern High Atlas) MVT deposits

Deposit/District	Mineral separate	$\delta^{34}S$	$^{206}Pb/^{204}Pb$	$^{208}Pb/^{204}Pb$
Mibladen	Galena	−20.5	18.268	38.484
Mibladen	Galena	−22.2	–	–
Mibladen	Galena	−19.7	–	–
Mibladen	Galena	−24.6	–	–
Mibladen	Galena	−21.9	–	–
Mibladen	Galena	−24.6	–	–
Mibladen	Galena	−23.2	18.250	38.413
Mibladen	Galena	−22.1	–	–
Mibladen	Galena	−23.4	–	–
Mibladen	Galena	−23.3	18.282	38.548
Mibladen	Barite	17.7	–	–
Mibladen	Barite	17.9	–	–
Mibladen	Barite	17.1	–	–
Mibladen	Barite	16.8	–	–
Mibladen	Barite	16.8	–	–
Mibladen	Barite	16.3	–	–
Mibladen	Barite	18.1	–	–
Jbel Bou Dahar	Galena	–	18.205	38.376
Jbel Bou Dahar	Galena	–	18.189	38.442
Jbel Bou Dahar	Galena	–	18.191	38.378
Jbel Bou Dahar	Galena	–	18.111	38.380

However, Kontak and Sangster (2005) challenged this statement and noted that, by careful examination, reliable fluid inclusion data can be extracted from barite. Being aware of such constraints, we carried out a series of microthermometric measurements on selected barite samples. The two-phase aqueous inclusions were overheated by up to 100 °C and then the T_h value was remeasured. Statistical treatment of the obtained data was applied and all of the abnormal temperatures (not on a Gaussian curve) were therefore not used. Accordingly, we think that the wide ranges of homogenization temperatures may be considered reliable and not related to stretching phenomena.

Altogether, the measured T_h values display homogenization temperatures of ~120°–~190 °C and salinities of ca. 14–24 wt% NaCl equiv (Table 2; Fig. 10). These wide ranges in both temperature and salinity fall within the ranges for present-day oil-field brines and ancient Mississippi Valley-type mineralizing fluids (Carpenter et al. 1974; Haynes and Kesler 1987; Leach and Sangster 1993), and are similar to the values obtained for MVT deposits worldwide (Leach et al. 2010; and references herein).

3.8 Sulphur and Lead Isotopes

Sulphur isotope compositions for galena separates that span the main stages of ore mineralization are all negative with $\delta^{34}S$ values of −24.6 ‰ to −19.7 (mean = −22.5, σ = 1.6 ‰; n = 10; Table 1). These sulphur isotopic compositions are among the lightest $\delta^{34}S$ values ever recorded for North African MVTs, and are similar to those reported for the Austrian MVT deposits in Bleiberg (Kucha et al. 2010). Overall, these $\delta^{34}S$ values are substantially lower than the range of $\delta^{34}S$ that characterizes Jurassic-Cretaceous seawater sulphate (~10–23 ‰; Claypool et al. 1980; Kampschulte

Table 2 Summary of microthermometric data (homogenization temperatures and salinities) for fluid inclusions in barite from Mibladen deposit in the Upper Moulouya district

Mineral	T_e					$T_{m(ice)}$					T_h					Salinity				
	n	Min	Max	Avg.	Std. Dev	n	Min	Max	Avg.	Std. Dev	n	Min	Max	Avg.	Std. Dev	n	Min	Max	Avg.	Std. Dev
Barite	38	−80	−45	−61	9	34	−21	−10	−14	3	51	122	199	170	20	34	14	23	18	2

Abbreviation: *Avg.* average; *n* number of measurements; *Max* maximum; *Min* minimum; *Std. Dev* standard deviation

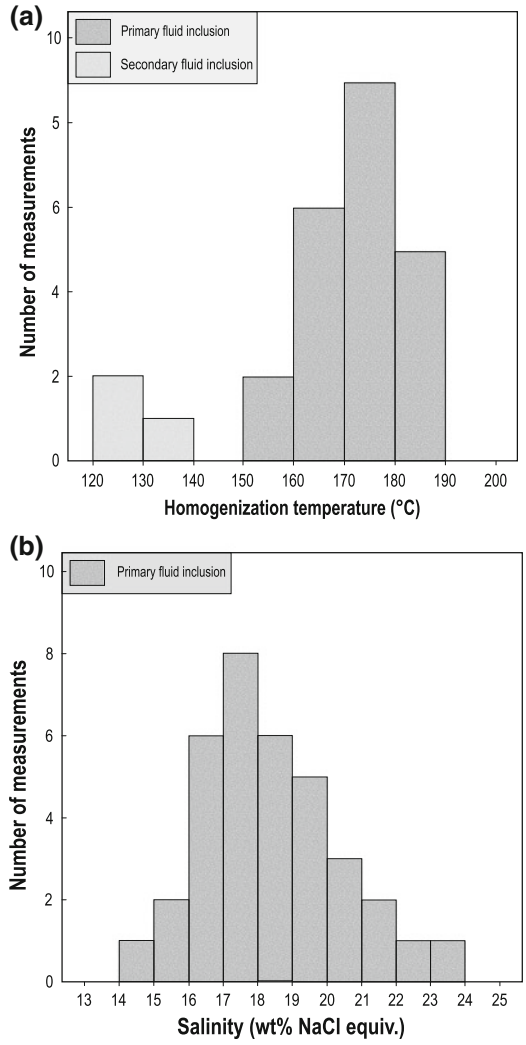

Fig. 10 Histograms of salinity (**a**) and homogenization temperature (**b**) for fluid inclusions in barite from Mibladen deposit in Upper Moulouya district

and Strauss 2004). Conversely, the sulphur isotope compositions of the paragenetically late barite, which range from 16.3 to 18.1 ‰ (mean = 17.2, σ = 0.7 ‰, *n* = 7; Table 1), are similar to Cretaceous seawater sulphate values (~10–22 ‰; Claypool et al. 1980; Kampschulte and Strauss 2004). This comparison suggests that sulphur in the barite was derived from coeval seawater sulphate either directly from the Cretaceous ocean or from dissolved marine evaporates. The underlying Triassic evaporates that potentially could have acted as the source of sulphur are not considered here because of the discrepancy between the sulphur isotopic compositions of these evaporates (mean $\delta^{34}S$ 13.7 ± 0.7 ‰; Bouabdellah et al. 2012) and values recorded for the barite (i.e., mean $\delta^{34}S$ 17.2 ± 0.7 ‰).

The strongly negative $\delta^{34}S$ values that characterize the Mibladen galena ore are indicative of bacteriogenic reduction of seawater sulphate (BSR) or of pore seawater in a system open to sulphate (e.g., Basuki et al. 2008; Vikre et al. 2011). Calculated $\Delta_{SO4\text{-galena}}$ values that are significantly greater than 20 ‰ exclude thermochemical sulphate reduction (TSR) as the main ore depositional process, thus leaving BSR as the most viable process responsible for the extremely low $\delta^{34}S$ values. Oil-window thermal maturation and degradation of organic matter dispersed within the Jurassic carbonates could have played a direct role in BSR and/or acted indirectly as a reductant for sulphate by releasing the H_2S component required for metal precipitation. Bacterial activity therefore may have been fed by hydrocarbon brines and sulphate remobilized from Cretaceous evaporites. The very low $\delta^{34}S$ values could also reflect reduced sulphur derived from diagenetic framboidal pyrite contained within the Jurassic sedimentary succession. However, the very low abundance of pyrite in the host strata of the Mibladen area makes this possibility unlikely.

Conversely, lead isotopic compositions of galena separates from the Mibladen deposit plot in a tight cluster above the evolution curve of Stacey and Kramers (1975) and show relatively uniform $^{206}Pb/^{204}Pb$, $^{207}Pb/^{204}Pb$, and $^{208}Pb/^{204}Pb$ ratios from 18.250 to 18.282, 15.607 to 15.645, and 38.413 to 38.548; respectively (Fig. 11). These isotopic compositions are roughly consistent with the range of Pb-isotopic ratios presented by Duthou et al. (1976) and Jébrak et al. (1998). Moreover, similarity in lead isotopic compositions for K-feldspar mineral separates from the Aouli intrusion (Jébrak et al. 1998) and the galena ore strongly suggest that the

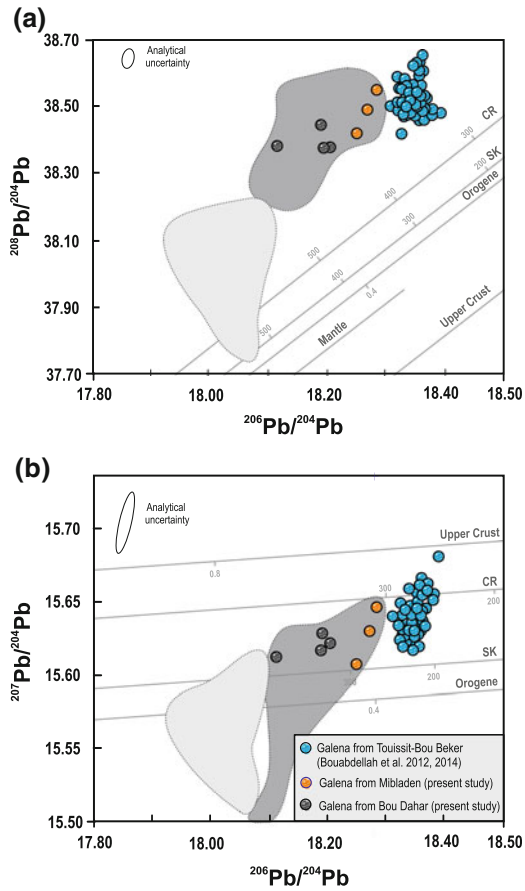

Fig. 11 Lead isotopic compositions of galena separates from Mibladen and Jbel Bou Dahar MVT districts compared to those from Touissit-Bou Beker district (Bouabdellah et al. 2015). **a** $^{208}Pb/^{204}Pb$ versus $^{206}Pb/^{204}Pb$; **b** $^{207}Pb/^{204}Pb$ versus $^{206}Pb/^{204}Pb$. Evolution curves of Stacey and Kramers (1975) and Cumming and Richards (1975) are labeled S and K and C and R, respectively; evolution curves for Upper Crust and Orogene (Zartman and Doe 1981) are shown for reference. Dark grey field defines galena isotopic compositions for Aouli-Mibladen district. Light grey field shows range of K-feldspar lead isotopic compositions for Late Hercynian granite from the Upper Moulouya district (Vitrac et al. 1981; Jébrak et al. 1998)

Late Hercynian granitoids were the main lead source, involving the leaching of K-feldspars, with possibly minor amounts of lead being derived from the Triassic arkoses. Compared to the ore lead isotope data for Touissit-Bou Beker, the Mibladen galena separates exhibit less radiogenic compositions (Fig. 11).

3.9 Proposed Genetic Model

Because no radiometric age for the emplacement of the Mibladen mineralization is available, the following proposed genetic model is only a first attempt toward the development of a more robust model.

Combining field relationships together with the petrographic and geochemical data presented above, it appears that the Mibladen MVT orebodies formed in mid-Tertiary time in response to large-scale crustal processes triggered by the Atlasic orogeny. Moreover, the fact that economic MVT mineralization is restricted to the Domerian carbonates strongly suggests that this formation constituted the main regional aquifer for the Mibladen mineralizing brines.

In addition to stratigraphy, the main ore controls include paleogeography (i.e., basement high and associated sedimentary pinchouts), brecciation and karstification (i.e., cavity filling mineralization), alteration (i.e., extensive dolomitization with subordinate silicification), and more importantly faulting. Indeed, the intimate relationship between the ENE- and WNW-trending faults and orebodies provides strong evidence that these faults were the major pathways that focused fluid flow. Compared to the Touissit-Bou Beker district, the Mibladen mineralization shares many empirical attributes that are common to the two districts. There are, however, a few differences that set the Mibladen district apart. These include (1) occurrence of barite as the principal gangue mineral rather than saddle dolomite, and (2) very high Pb/Zn ratios with sphalerite being virtually absent.

Data for fluid inclusions together with sulphur and lead isotopes indicate that the ore fluids were moderately hot (>100 °C) basin-derived brines that scavenged lead and associated metals from the underlying Late Hercynian granitoids and their overlying clastic rock derivates. The large quantities of both barite and the very low-$\delta^{34}S_{sulphide}$ values in the Mibladen deposit suggest, as also proposed by Hitzman and Beaty (1996) for the Irish deposits, a continuous resupply of marine sulphate and bacteriogenetically reduced sulphide to the site of

mineralization. This model indicates that there must have been communication with either a large reservoir of sulphate-rich formation water or with the Jurassic-Cretaceous Ocean.

The wide discrepancy between $\delta^{34}S$ values of galena and barite rules out the single model as the possible depositional mechanism for the Mibladen deposit. Instead, these data point to fluid mixing of at least two incompatible fluid reservoirs, as also suggested by coexistence of intergrown sulphides and barite. Similarly, the negative correlation between sulphur and lead isotope compositions (Jébrak et al. 1998) is interpreted to represent fluid mixing between two end-members: (1) a deep-seated, basement-equilibrated hydrothermal fluid; and (2) a surficial formation and/or meteoric water. The absence of extensive silicification in the wall rocks, which may reflect suppression of silica saturation by fluid mixing and dilution (Plumlee et al. 1994), coupled with the lack of evidence for fluid immiscibility indicates that an abrupt temperature decrease did not occur during fluid mixing. Moreover, the development of pervasive dissolution and replacement textures indicates acidic fluid conditions. This scenario requires a second depositional mechanism. Indeed, neutralization of the deep-seated fluid by reaction with the Domerian carbonate host rocks would have decreased metal solubilities, ultimately leading to development of the replacement-style mineralization. The reduced sulphur required for precipitation of the sulphides derived principally by BSR of aqueous sulphate. During the subsequent deposition of late barite, the oxidation state of the mineralizing fluid must have shifted towards more oxidizing conditions.

In order to maintain an efficient downward deep circulation of the mineralizing fluids, an uplift episode is required to provide the necessary hydrologic head for fluid movement. As mineralization is inferred to have occurred during Mid-Tertiary time that coincides with major uplift of the Atlas belt, we propose a gravity-driven flow model in which fluids recharged in the Atlas migrated through the Domerian aquifer along deep-seated ENE-trending faults. This fluid migration thereby drove the high salinity, mineralizing brines toward the edges of the basin where deposition of sulphides occurred, by fluid mixing with sulphur derived by BSR. In our model, downward-flowing and oxidized, SO_4^{2-} and Cl^--rich ground waters mixed with the deeper reduced H_2S-rich saline waters to form H_2SO_4. Barite precipitated where Ba^{2+} in the reduced fluid reacted with SO_4^{2-} that was generated in the mixing zone, thus explaining the abundance of barite in the late stages of ore formation.

4 Jbel Bou Dahar District

The Jbel Bou Dahar plateau (32°18′0″ N, 3°18′0′′ E) is located within the eastern part of the High Atlas Mountains. More than 20 economic Pb–Zn prospects and deposits are distributed along the margins of the Lower Jurassic reef carbonate platform, particularly its southern flank (Fig. 12). From 1961 to 1965, the district has produced about 100,000 t of Pb and 20,000 t of Zn (Agard et Du Dresnay 1965). At the present time, widespread exploration continues in the district focusing on productive targets.

4.1 District Geology

The present-day high-relief Jbel Bou Dahar plateau forms an elongate, ENE-trending, reefal structure 40 km × 15 km in size that encompasses a total area of ~600 km^2 (Fig. 12). The geologic setting of this plateau has been described in numerous papers (Agard and Dresnay Du 1965; Dresnay Du 1979; Evans and Kendall 1977; Warme 1988; Crevello 1990; Kenter and Campbell 1991; Blomeier and Reijmer 2002; Merino-Tomé et al. 2012; Rddad and Bouhlel 2016), from which the following summary has been inspired.

The core of the carbonate platform, which is exposed in the northern part of the reefal structure (i.e., Sebbab-Kébir inlier, Fig. 12), consists of a succession of greenschist-facies Cambro-Ordovician to Silurian metasedimentary and volcaniclastic rocks made dominantly of quartzite and schist. Unconformably overlying the

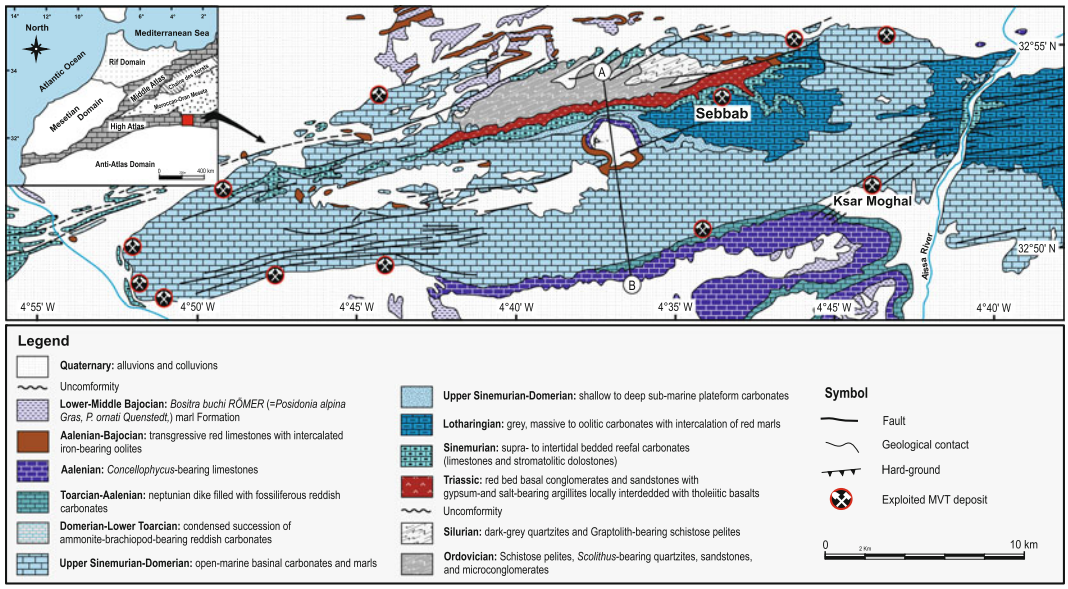

Fig. 12 Geological map of Jbel Bou Dahar early Mesozoic annular reefal complex emphasizing regional geology, main tectonic structures, and stratigraphic distribution of major MVT deposits. Line *A*–*B* indicates cross section shown in Fig. 13. Modified after Agard and Du Dresnay (1965)

metasedimentary Paleozoic package is a ~400–500 m sequence of Triassic sedimentary rocks consisting of red-bed siltstone and gypsiferous to salt-bearing argillite locally interbedded with CAMP tholeiitic basalts. During Early and Middle Liassic times, the lower Paleozoic formed a topographic high on which the Jbel Bou Dahar reef and lagoon were built, incompletely separated from the open sea by a barrier reef that developed to the south (Fig. 13). Strata of the Jbel Bou Dahar reef undergo a series of facies changes from an offshore basinal shale and limestone facies, through the undolomitized reef, to a back-reef facies having abundant porosity.

The reef deposits consist of unmetamorphosed, massive, coral-algal- and bivalve-bearing Pleinsbachian, flat-lying, thickly-bedded carbonate mudstone, skeletal wackestone, skeletal pelletal packstone, laminated carbonate mudstone, and calcareous clay. The sequence attains a maximum thickness of 175 m at the axis of the barrier and thins both south and north, forming a lens-like bank of sediment. Platform growth was initiated during the Sinemurian and ended at the Domerian (Upper Pliensbachian) and the Middle Toarcian (Crevello 1990; Blomeier and Reumer 1999). Toarcian shales and Aalenian lime mudstones progressively onlap the flanks of the Domerian platform and conformably overly the platform roof, recording an abrupt cessation of platform evolution at the Domerian-Toarcian transition (Crevello 1990; Campbell and Stafleu 1992). Dolomitization is restricted to the Sinemurian carbonates and is not observed in the Domerian rocks. During the Bajocian, the basin filled completely and became a continentally emergent structure by the Late Bajocian, or certainly by the Bathonian (Dresnay Du 1979).

The deformational history of the Jbel Bou Dahar plateau is divided into Hercynian (late Paleozoic) and Atlasic (Mesozoic to Tertiary) cycles. The predominant Atlasic fault structures form a consistent array, with many trending ENE–WSW, some larger and more continuous faults trending E–W, and a subsidiary set trending NNW–SSE. ENE- and E–W-trending faults probably played an important role in focusing the flow of ore-forming fluids, as suggested by

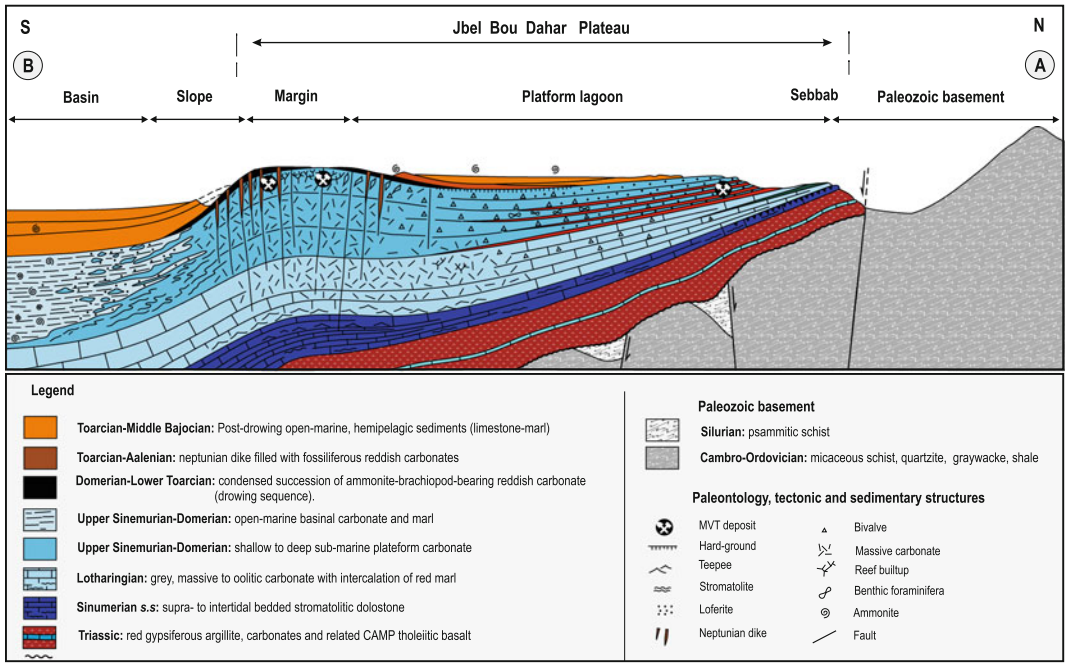

Fig. 13 N–S geological section along strike of Jbel Bou Dahar early Mesozoic carbonate platform showing spatial distribution of main lithofacies associations and MVT deposits; see Fig. 13 for location of section. Modified after Agard and Du Dresnay (1965)

proximity of these faults to the orebodies and by the general elongation of mineralized veins and ore zones in ENE and E–W directions (Fig. 12).

4.2 Alteration

The main wall-rock alteration in the Jbel Bou Dahar district is confined to patchy silicification and minor dolomitization. Although silicification could be interpreted as resulting from diagenetic alteration (Scheibner and Reumer 1999), the proximal location of the quartz alteration halo to the wall rocks of the mineralized structures suggests that this silicification is probably related to hydrothermal activity, and not to diagenesis. Dolomitization is weak or nonexistent. Unlike in the Touissit-Bou Beker and Upper Moulouya districts described above, neither pre-ore replacement nor ore-related hydrothermal dolomitization affected the Pliensbachian carbonate host rocks.

The most diagnostic feature of wall-rock alteration in the Jbel Bou Dahar district is intense veining and open-space filling by sparry calcite ± barite ± celestine typically developed immediately adjacent to the Pb–Zn orebodies. The white sparry calcite occurs as pre-, syn-, and post-ore massive fillings of veins, veinlets, karst cavities and related crackle and dissolution collapse-breccias, and echelon tension gashes intimately related to Pb–Zn mineralization. Of historical note, this sparry calcite was used by indigenous prospectors as a reliable guide to hidden Pb–Zn showings.

4.3 Mineralization

The district sulphide ± barite ± celestite deposits consist principally of galena and sphalerite with subordinate pyrite/marcasite and chalcopyrite. This mineralization is clearly epigenetic and predominantly stratabound, although local stratiform mineralization is also economically important (i.e., Sebbab deposit; Fig. 12). Economic sulphide mineralization may occur throughout all

the lithostratigraphic units, it is typically confined to the reef facies and/or to pinchouts of the Liassic strata against Paleozoic basement high (Fig. 13). Therefore, prominent ore controls are related to depositional pinchouts and configuration of the basement surface (i.e., presence of paleohigh structures).

Based on stratigraphic position, geometry of ore occurrences, and nature of the Pb–Zn deposits, two main styles of mineralization are distinguished: (1) open-space fillings, and (2) metasomatic replacements. Economic orebodies occur at various stratigraphic levels within the Lower to Middle Jurassic strata, from the Lotharingian to the Aalenian, with most of the higher-grade orebodies confined to the brecciated, Pliensbachian coarse sand to gravel, bioclastic bivalve-coral-algal packstones. Uneconomic mineralization that forms thin centimeter-thick veins may extend into the underlying Cambro-Ordovician schistose basement rocks.

Replacement mineralization occurs more commonly as interstitial sulphide disseminations of variable size and to a lesser extent as tabular lenses in which ore textures obliterate original sedimentary textures of the replaced Lotharingian oolitic reefal limestones and associated sub-reefal brecciated carbonates. Geometry of the sulphide masses appears to have been controlled by preferential replacement of specific carbonate units (i.e., bedded ooid, intraclast, and pisoid packstones to rudstones), and along stratigraphic contacts. The most representative example of this type of mineralization is shown by the Sebbab deposit (Fig. 12) and a large number of prospects exposed along the southern flank of the Jbel Bou Dahar reefal complex, where extensive and pervasive replacement of the carbonate host rocks is expressed by pseudomorphic remnants of bioclasts and faunal assemblages (Adil 2004).

At the Sebbab deposit, sulphide mineralization is distributed along two main, sub-parallel, ENE-trending levels, referred to as upper and lower horizons. These delineated mineralized zones, defined on the basis of the ~2 % Pb contour, follow the trend of the main extensional faults and are separated by undisturbed, massive, impermeable red marls. Irrespective of mineralized zone, Sebbab mineralization is characterized by fine-grained ore and locally the presence of dendritic sulphides.

Higher grade orebodies, accounting for more than 90 % of the extracted ore in the district, occur as massive fillings of fractures, veinlets, veins, karsts, and a variety of vuggy pore spaces, and as cements in solution collapse breccias related to post-lithification dissolution of brecciated Pliensbachian reefal carbonates. Locally, sulphide mineralization fills and cuts compactional stylolites. There is clear evidence that open-space deposition was accompanied by extensive dissolution and replacement of the Lower Jurassic carbonates.

Vein-type mineralization shows various morphologies ranging from planar centimeter- to kilometer-scale veins and veinlets, boudinage, and "en echelon" to sigmoidal arrays. Economic orebodies are confined to calcite-sulphide-barite veins localized along the intersection of E–W- and NE-trending fault arrays (i.e., "noeud tectoniques"). The most important of the structurally controlled veins is represented by the Ksar Moghal deposit (Fig. 12), from which 80,000 t of Pb concentrates have been produced (Agard and Du Dresnay 1965). In this deposit, two main vein sets, including the multi-kilometer, ENE-striking vein system and the E–W-trending vein array, are by far the dominant mineralizing structures. The exploited structures can be more than 1 km long, up to 4 m wide, and are mainly filled with galena, and form sub-vertical, WNW–ESE-striking brecciated major faults that dip steeply to the south and have vertical extents exceeding 150 m, without significant change in mineral assemblage.

4.4 Ore Mineralogy, Textures, and Paragenesis

The ore mineralogy is fairly simple and consists of variable amounts of sphalerite, galena, pyrite-marcasite, and chalcopyrite, accompanied by barite, celestite, and calcite as the main

gangue minerals. Sphalerite and galena are intimately intergrown, but display unequal proportions from deposit to deposit, and even within a single orebody. Common MVT ore textures include crackle breccias, collapse breccias, and impregnations.

The near surface of the exploited open pits and underground exposures contain numerous occurrences of oxidized ore. Oxidized zones extend to depths of at least 100 m below the present surface, and locally have economic concentrations of non-sulfide Zn-Pb ores referred to as "calamine ores." These calamine ores contain a mixture of supergene Zn (with minor Pb) carbonates (smithsonite), hydrated carbonates (hydrozincite), silicates (willemite) and hydrated silicates (hemimorphite, Zn clays) that cap the primary sulphide orebodies. Unlike most North African MVTs, this type of non-sulphide Zn ore deposits is largely confined to the central and eastern High Atlas Mountains (Goulet et al. 2014; present study). Such deposits are being extensively prospected by the mineral industry because (Sangster 2003): (1) environment impacts from mining are minimal owing to a characteristic lack of Pb, S, and other deleterious elements, (2) a potential for low-energy recovery of zinc, and (3) a generally higher in situ economic value (Borg 2002). According to our compilations, between 4,000 and 9,000 t of calamine ore are produced annually from the Jbel Bou Dahar district and adjacent deposits, at grades of 31–50 % Zn. Based on these estimates, a total of 220,000 to ~500,000 t of calamine ore have been produced since the 1970s when the CADETAF semi-private company in charge of selling the Pb–Zn ore from Jbel Bou Dahar, was created.

The sequence of mineral deposition shows the existence of five successive and overlapping stages of mineralization, almost all of which are of economic interest. These five stages are distinguished by megascopic and microscopic textural and cross-cutting relationships and mineral assemblages. Although an idealized paragenetic sequence is clearly identified throughout the district, there are variations in the abundance of minerals of particular stage from deposit to deposit, and even within the same deposit. Except for stage I that is barren, the rest of the paragenetic stages are of economic interest.

Stage I, the oldest hydrothermal stage, consists of pre-ore sparry calcite (Ca-1) and pyrite (Py-1), and is thought to record the earliest introduction of hydrothermal fluids into the district. Iron sulphides occur as fine disseminations of pyrite and marcasite dispersed within local host rocks, or as thin selvages coating rock porosity or clasts within breccias.

Stage II, referred to as the "main sulphide Pb–Zn stage ore," is economically the most important and accounts for more than 70 % of the Pb–Zn resources. The mineral paragenesis consists of variable proportions of galena and sphalerite with minor pyrite and chalcopyrite, accompanied by calcite (Ca-2) as the main gangue mineral.

Stage III is locally referred to as "Alquifoux" sulphide ore and constitutes for local miners the most attractive ore stage from which well-developed cubic and octahedral galena crystals (Gn-3) up to 12 cm across are being recovered. This stage matches the "cubo-octahedral stage" commonly described in MVTs worldwide (Bouabdellah et al. 2012).

Stage IV represents the late deposition of barite, celestite, and calcite (Ca-3), which are typically the last minerals deposited throughout the paragenesis, within the remaining open spaces near the Pb–Zn orebodies.

Stage V comprises later alteration, probably of supergene origin, of earlier stages that formed the most characteristic and commercially attractive mineral paragenesis in the district referred to as "calamine" or "non-sulphide Zn-Pb ore." This stage consists predominantly of an exotic mixture of smithsonite, hemimorphite, and hydrozincite together with calcite, and quartz. Calamine ores occur both as cavity fillings and as partial to massive replacements of host carbonates in the upper levels of the exploited orebodies. It seems that their genesis benefited from the interplay among weathering, uplift, and erosion and that there is no apparent relationship to the present water table (Goulet et al. 2014).

4.5 Fluid Inclusion Microthermometry

Microthermometric data from pre-ore hydrothermal calcite and various generations of sphalerite and barite display wide ranges in homogenization temperatures and related salinities, with T_h values ranging from <70° to 180 °C and salinities from ca. 15–26 wt percent NaCl equiv (Adil et al. 2004; Rddad and Bouhlel 2016). The similarity of fluid compositions in pre-ore hydrothermal calcite and sphalerite indicates homogeneity of the parent mineralizing fluid, and suggests that these two investigated minerals are genetically related and precipitated from the same hydrothermal system.

The measured Cl/Br and Na/Br molar ratios indicate that the mineralizing brines acquired high salinities and Ca/Na ratios through evaporation of seawater, and by subsequent dolomitization and fluid-rock interactions (Adil et al. 2004). Calculated fluid pressures in the range of 150–200 bars indicate depths of less than 1 km during ore deposition.

4.6 Sulphur and Lead Isotopes

Sulphur isotope compositions for various generations of sulphides from the Jbel Bou Dahar district show a wide range of $\delta^{34}S$ values from −1.2 to + 10.0 ‰ (Adil 2004). The highest values correspond to sulphides from the early Zn-rich stage I, whereas the lowest ratios are from the late cuboctahedral stage III. Secondary gypsum, interpreted to have resulted from supergene oxidation of preexisting sulphides, has $\delta^{34}S$ ratios of +4.5 to +9.6 ‰ (mean = 6.2 ‰, σ = 2.4 ‰, n = 4). Conversely, sulphur isotope compositions of the paragenetically late barite, with $\delta^{34}S$ values from 15.8 to 20.2 ‰ (mean = + 18.6 ‰, σ = 1.6 ‰, n = 7; Adil 2004), are within the range for Jurassic-Cretaceous seawater sulphate (∼10–23 ‰; Claypool et al. 1980; Kampschulte and Strauss 2004). This similarity suggests that the barite-hosted sulphur was derived from coeval seawater sulphate, either directly from the ocean or indirectly from leaching of marine evaporites. Celestite mineral separates exhibit the highest sulphur isotopic compositions with $\delta^{34}S$ values ranging from 16.3 to 27.5 ‰ (mean = 21.1 ‰, σ = 5 ‰, n = 5; Adil 2004).

Overall, the $\delta^{34}S$ values of sulphides (i.e., pyrite, sphalerite, and galena) are uniformly lower than the range of Jurassic seawater sulphate (∼10–23 ‰; Claypool et al. 1980; Kampschulte and Strauss 2004). More interestingly, the distribution of sulphur isotope compositions displays a general trend toward lower $\delta^{34}S_{sulphide}$ values with time (i.e., advancing paragenetic sequence) both at deposit and hand-sample scales. These large variations in sulphide $\delta^{34}S$ values from positive to negative are, therefore, interpreted to reflect isotopic fractionation during TSR and/or BSR of seawater sulphate or of pore seawater, at different rates of sulphate availability (open versus closed reservoirs with respect to sulphate) (Basuki et al. 2008; Vikre et al. 2011).

Indeed, the positive $\delta^{34}S_{sphalerite}$ values of the paragenetically early Zn-rich ore-stage (10–1 ‰; Adil 2004; Rddad and Bouhlel 2016) are consistent with rapid TSR of Mesozoic seawater sulphate or of dissolved pore-water sulphate. Conversely, the lower $\delta^{34}S_{galena}$ values of stages II and III (−1.2 to +7.8 ‰) fit within the range of values that record a system partially open to sulphate (Ohmoto et al. 2006; Basuki et al. 2008; Vikre et al. 2011).

Lead isotope compositions of galena performed in the course of the present study (Table 1; Fig. 11) plot in a tight cluster above the evolution curve of Stacey and Kramers (1975), with uniform $^{206}Pb/^{204}Pb$, $^{207}Pb/^{204}Pb$, and $^{208}Pb/^{204}Pb$ ratios from 18.111 to 18.205, 15.613 to 15.628, and 38.376 to 38.442, respectively. Compared to the Touissit and Mibladen Pb isotope compositions, the data for the Jbel Bou Dahar deposits fall precisely on the cluster of values shown by the Mibladen ore (Fig. 11), indicating again the derivation of Pb and by inference associated metals from a crustal source.

4.7 Age of Mineralization

The timing of MVT mineralization in the Jebel Bou Dahar district is poorly constrained because

of the lack of reliable geochronological data. Geological and paragenetic relationships indicate that the MVT deposits are clearly epigenetic and structurally controlled, and that the dolomitized host rocks were buried and lithified prior to the mineralizing event. Moreover, there is an intimate relationship between the ENE- and WSW-trending faults and the sites of MVT orebodies. Together, these relationships indicate that the Jbel Bou Dahar MVT mineralization formed as a result of hydrothermal processes initiated during deep burial by the compression and uplift during the Atlasic orogeny.

Textural relationships indicate that the mineralization post-dates compactional stylolites and therefore constrains the mineralizing event to after initial burial at about >600 m depth which occurred during the Cretaceous time. Consequently, a Cretaceous age (~100 Ma) can be used as a maximum time for mineralization. Furthermore, the strongly deformed nature of the ore suggests that the Jbel Bou Dahar mineralization took place shortly before, or during, the main pulse of the Atlasic orogeny, which is thought to have occurred in mid-Tertiary time (Frizon de Lamotte et al. 2009). Based on these constraints, it is thus concluded that the MVT mineralization in the Jbel Bou Dahar district occurred between the Cretaceous and Late Miocene, at the same time span during which the MVT deposits of the Touissit-Bou Beker and Mibladen districts formed.

4.8 Preliminary Genetic Model

Combined mineralogical, fluid inclusion, and geochemical data discussed above suggest that the Jbel Bou Dahar MVT deposits formed in mid- to late Tertiary time in response to large-scale crustal processes triggered by the Atalsic orogeny. The spatial link between the ENE- and WSW-trending faults and the sites of MVT orebodies implies that regional and local-scale faults played a crucial ore control by focusing fluid flow. Such spatial relationships and the occurrence of Pb–Zn mineralization in the Paleozoic basement rocks beneath the Liassic MVT host rocks (Adil 2004) requires an upward component of fluid flow (Fig. 14).

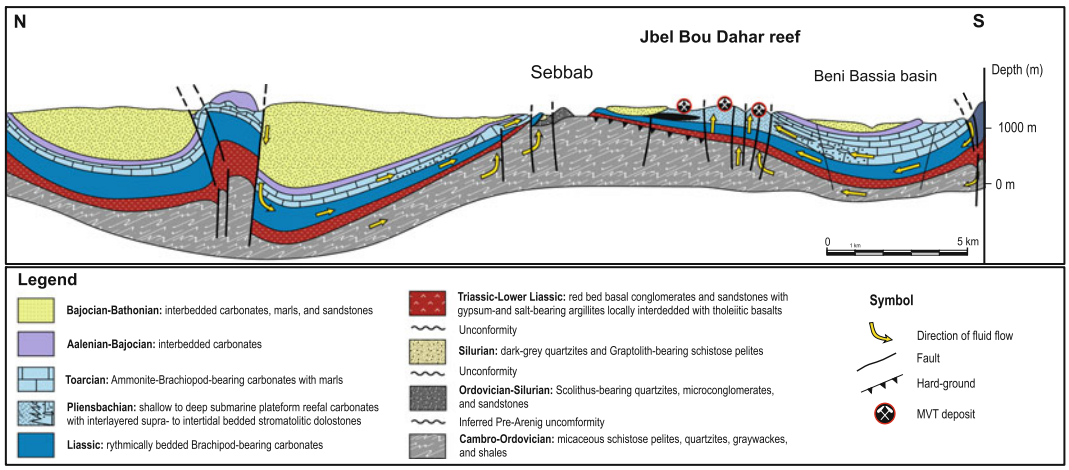

Fig. 14 N–S cross section illustrating compaction- and/or topographically driven fluid flow models for Jbel Bou Dahar hydrothermal fluids. Models invoke either (1) expulsion of hydrothermal fluids by compaction of sediments in depocenters, with sub-vertical faults acting as conduits for metal-bearing fluids under artesian conditions, or (2) transport of formation waters recharged in uplifted orogenic flank of Atlasic orogen, through early Mesozoic carbonate aquifer to Jbel Bou Dahar reef complex in mid-Tertiary time. Flow paths of fluids and waters are shown schematically by curved yellow arrows. Toarcian shales and Aalenian lime mudstones cap the early Liassic carbonate aquifer

The occurrence of mineralized veins within the Paleozoic basement rocks, and the unconformably overlying Aalenian-Bajocian marl and argillite cap rocks that likely forced ascending mineralizing brines to spread laterally to replace the more porous reefal facies of the Liassic strata, together indicate vertical fluid flow. This model is consistent with the vertical metal zoning that characterizes the Jbel Bou Dahar district. Similarly, the presence of sulphide orebodies within different lithologies, coupled with the succession of several episodes of brecciation, suggest that sulphide deposition was controlled largely by intrinsic characteristics of the host rocks, mainly permeability and porosity, and that the mineralizing fluids were introduced episodically.

Moreover, fluid inclusion data (Adil et al. 2004) indicate that multiple fluids were involved in forming the Jbel Bou Dahar deposits including saline formation brines, meteoric water, and mixed fluids. More interestingly, the linear distribution of homogenization temperatures and related salinities shown by Adil et al. (2004) is attribute to mixing and fluid-rock interaction between at least two distinct fluid types having contrasting salinities and Ca/(Ca + Mg) ratios: (1) an ascending warm (180 °C) and higher salinity (>25 wt% NaCl equiv), deep-seated, basement-equilibrated, metal-rich mineralizing fluid; and (2) a downward penetrating, cooler (70 °C), and lower salinity (16 wt% NaCl equiv), shallow, surface-derived formation water probably of meteoric origin.

Abundance of colloform-textured sulphides that infil vugs and veins constitutes additional evidence for fluid mixing. The fine-grained nature of the ore and local occurrence of dendritic forms of sulphides (i.e., Sebbab deposit) are indicative of rapid growth (e.g., Hitzman and Beaty 1996), which again is consistent with fluid mixing. Higher grade orebodies occur where pre-ore ground preparation provided sufficient porosity and permeability for fluid mixing. Consistent with the fluid inclusion data and textural relationships, the distribution of lead and sulphur isotope compositions suggests that metals and reduced sulphur did not travel together in the same brine, but mixed at the site of ore deposition. Moreover, the lowering of $\delta^{34}S$ values with advancing paragenetic sequence indicates that the Jbel Bou Dahar hydrothermal system, initially dominated by crustal fluids, became open at shallower levels to infiltration of increasing amounts of meteoric water, and to their mixing with the deep saline fluids. Cooling and dilution of a metal- and reduced sulphur-bearing fluid will not produce extensive sulphide replacement ore and dissolution of the host rocks (Plumlee et al. 1994), as observed in Jbel Bou Dahar district. From the standpoint of the source of lead, and by inference of associated metals, Pb isotope compositions indicate crustal sources via leaching of local Paleozoic basement rocks and derived siliciclastic country rocks.

Mineralization is thought to have taken place between the Cretaceous and mid-Tertiary time after maximum burial, as attested by the occurrence of sulphides cutting horizontal stylolites, coincident with maximum compression and rapid uplift during the Atlasic orogeny. This inferred depositional age for the Jbel Bou Dahar district which is consistent with the time span proposed by Rddad and Bouhlel (2016) coincides with the time interval proposed for the formation of the Touissit-Bou Beker and Mibladen MVT deposits. Accordingly, we suggest that the migration of the metaliferous basinal brines was initiated by a combination of basin subsidence and subsequent uplift during or immediately after the Atlasic orogeny. Although topographically driven fluid migration would have provided the main driving mechanism for the mineralizing fluids, rapid deposition of the thick post-Liassic carbonate and shale sequences in the neighboring depocenters (i.e., Beni Bassia basin; Fig. 14) could have provided compaction-driven fluids for generating the Jbel Bou Dahar ore-forming system.

5 Concluding Remarks

Major Moroccan MVT deposits share many similarities in term of geological environment, alteration, mineral paragenesis, and ore controls. Indeed, all of the three districts described herein (i.e., Touissit-Bou Beker, Mibladen, Jbel Bou

Dahar) are hosted by Jurassic shelf carbonate rocks unconformably overlain by an impermeable Upper Jurassic sequence that acted as aquitards, "cap rocks." Overall, the mineral paragenesis consists of variable proportions of sphalerite and galena, accompanied by lesser pyrite-marcasite and chalcopyrite ± sulphosalts (i.e., tetrahedrite). Non-sulphide gangue minerals include different generations of saddle dolomite (Touissit-Bou Beker), calcite (Jbel Bou Dahar), and barite (Mibladen).

Among several key factors that controlled the localization of the Pb–Zn ores, a crucial role in focusing fluid flow along the basement-cover interface involved the development of uplifted paleogeographic structures (basement highs) above which the economic Pb–Zn orebodies occur. The geometry of the orebodies that parallel the alpine ENE–WSW- and E–W-trending faults indicates that these deep-rooted structures allowed mineralizing fluids to recharge the basin, flow through aquifers and adjacent source rocks, replace the more porous carbonate rocks, and deposit metals into open spaces. Moreover, the presence of mineralized structures within the Paleozoic basement rocks, together with the presence of the overlying Upper Jurassic cap rocks that forced the ascending mineralizing brines to spread laterally along the Lower and Middle Jurassic aquifer, record both vertical and lateral fluid flow.

Fluid inclusion measurements, together with Na–Cl-Br leachate data, indicate that the ore-forming fluids correspond to evolved NaCl–$CaCl_2$–KCl–$MgCl_2$, basin-derived, hot (100 ± 20 °C), saline (>20 wt% NaCl equiv) brines. Calculated pressures for the ore fluids in the range of 150–200 bars suggest depths of less than 1 km for the Pb–Zn mineralization.

The absence of radiometric age constraints for ore formation constitutes the major obstacle to developing reliable genetic models. In this regard, field relationships together with Pb isotope data (Bouabdellah et al. 2012) indicate that the Moroccan MVT districts formed epigenetically during late Tertiary (Serravallian-Messinian) time, coincident with the major episode of Atlasic compression and uplift, and with the tectonic inversion of the Triassic-Jurassic basins in response to convergence of the African and Eurasian plates (Gieze and Jacobshagen 1992; Frizon de Lamotte et al. 2009). MVT mineralization is therefore interpreted to have resulted from the migration of deep metalliferous brines that were expelled either by (1) compaction of sediments in basin depocenters due to the rapid deposition of thick sequences of post-Liassic carbonate and shale (i.e., Jbel Bou Dahar district), or (2) a gravity-driven system (i.e., in all three districts) that provided the necessary hydrologic head for fluid movement, or (3) a combination of both processes. In the case of the Touissit-Bou Beker district, the main mineralizing event is attributed to the effects of extensional tectonics, Neogene-Quaternary mafic magmatism, and the Messinian salinity crisis (Bouabdellah et al. 2015). In this district, the associated elevated heat flow and subsequent increased geothermal gradient initiated buoyancy-driven fluid convection of downward-flowing Messinian seawater, which ultimately promoted the mobilization of older, high-temperature, rock-buffered basement brines stored within the Paleozoic basement, and the formation of base-metal-bearing chloride complexes. Mixing of Messinian seawater and basement-derived hydrothermal brines triggered deposition of the Pb- and Zn-rich ores (Bouabdellah et al. 2015).

References

Aboutahir N (1999) Pétrographie et géochimie des dolomites du district de Touissit-Bou Beker: hôte de la minéralisation de type de la Vallée du Mississippi (Maroc Nord-Oriental). Unpub PhD Thesis, Ecole Polytechnique, Montréal, Canada, 243 pp

Adil S (2004) Métallogenèse des gisements Pb–Zn de type Mississippi Valley de Jbel Bou Dahar (Haut Atlas Oriental, Maroc): apports des inclusions fluides et des isotopes de soufre. Unpub PhD Thesis, University Dhar El Mehraz, Fès, Morocco, 171 pp

Adil S, Bouabdellah M, Grandia F, Cardellach E, Canals A (2004) Caractérisation géochimique des fluides associés aux minéralisations Pb–Zn de Bou Dahar (Maroc). C R Geosci 336:1265–1272

Agard J, Du Dresnay R (1965) La région minéralisée du Jbel Bou Dahar, près de Beni Tajjit (Haut Atlas oriental): étude géologique et métallogénique. Notes Mem Serv Géol Maroc 181:135–166

Ajaji T, Weis D, Giret A, Bouabdellah M (1998) Coeval potassic and sodic calc-alkaline series in the post-collisional Hercynian Tanncherfi intrusive complex, northeastern Morocco: geochemical, isotopic and geochronological evidence. Lithos 45:371–393

Annich M, Rahhali M (2002) Gisement de plomb de Zeida. In: Barodi E-B, Watanabe Y, Mouttaqi A, Annich M (eds) Méthodes et techniques d'exploration minière et principaux gisements au Maroc. Projet JICA/BRPM, Bureau Recherche Participations Minières—BRPM, Rabat, pp 179–183

Appold MS, Garven G (1999) The hydrology of ore formation in the southeast Missouri district: numerical models of topography-driven fluid flow during the Ouachita orogeny. Econ Geol 94:913–935

Basuki NI, Taylor BE, Spooner ETC (2008) Sulfur isotope evidence for thermochemical reduction of dissolved sulfate in Mississippi Valley-type zinc-lead mineralization, Bongara area, northern Peru. Econ Geol 103:783–799

Beauchamp W, Barazangi M, Demnati A, El Alji M (1996) Intracontinental rifting and inversion: Missour Basin and Atlas Mountains, Morocco. AAPG Bull 80:1459–1482

Bethke CM (1986) Hydrologic constraints on the genesis of the Upper Mississippi Valley district from Illinois Basin brines. Econ Geol 81:233–249

Blomeier DPG, Reumer JJG (1999) Drowning of a Lower Jurassic carbonate paltform: Jbel Bou Dahar, High Atlas, Morocco. Facies 4:81–110

Blomeier DPG, Reijmer JJG (2002) Facies architecture of an Early Jurassic carbonate platform slope (Jbel Bou Dahar, High Atlas, Morocco). Jour Sed Research 72:462–475

Borg G (2002) The good, the bad, and the ugly—a maturity index for supergene non-sulfide zinc deposits [abs.]: Geol Soc America Abs Pgms 34:287

Bouabdellah M (1994) Métallogenèse d'un district de type Mississippi Valley, cas de Beddiane, district de Touissit-Bou Beker, Maroc. Unpub PhD Thesis, École Polytechnique, Montréal, Canada, 367 pp

Bouabdellah M, Héroux Y, Brown AC (1996a) Pétrographie et altération de la matière organique du gisement de plomb-zinc-cuivre de Beddiane, district de Touissit-Bou Beker, Maroc. Canad J Earth Sci 33:1363–1374

Bouabdellah M, Brown AC, Sangster DF (1996b) Mechanisms of formation of internal sediments at the Beddiane lead-zinc deposit, Touissit-Bou Beker mining district, northeastern Morocco. In: Sangster DF (ed) Carbonate-hosted lead-zinc deposits, society economic geologists, Spec Publ 4, pp 356–363

Bouabdellah M, Fontboté L, Haeberlin Y, Llinares L, Leach D, Spangenberg J (1999) Zoned sulphur isotope signatures at the Mississippi Valley-type Touissit-Bou Beker-El Abed district, Morocco, Algeria—evidence for thermochemical sulfate reduction and mixing of sulfur sources. In: Stanley C et al (eds) Mineral deposits: processes to processing, Fifth Bienn SGA Mtg and Fifth Quadrennial IAGOD Mtg, London, UK, 22–25 Aug 1999, pp 821–824

Bouabdellah M, Héroux Y, Chagnon A (2001) Zonation of organic matter reflectances and clay mineral assemblages around MVT deposits of Touissit-Bou Beker district, northeastern Morroco. In: Piestrzynski A, et al. (eds) Mineral deposits at the beginning of the 21st Century, 6th Bienn SGA Mtg, Krakow, Poland, 22–26 Aug 2001, pp 39–42

Bouabdellah M, Sangster DF, Leach DL, Brown AC, Johnson CA, Emsbo P (2012) Genesis of the Touissit-Bou Beker Mississippi Valley-type district (Morocco-Algeria) and its relationships to the Africa-Europe collision. Econ Geol 107:117–146

Bouabdellah M, Niedermann S, Velasco F (2015) The Touissit-Bou Beker Mississippi Valley-type district of northeastern Morocco: relationships to the Messinian salinity crisis, Late Neogene-Quaternary alkaline magmatism, and buoyancy-driven fluid convection. Econ Geol 110:1455–1484

Campbell AE, Stafleu J (1992) Seismic modeling of an early jurassic, drowned carbonate platform: Djebel Bou Dahar, High Atlas, Morocco. AAPG Bull 76:1760–1777

Carpenter AB, Trout ML, Pickett EE (1974) Preliminary report on the origin and chemical evolution of lead-and-zinc-rich oil field brines in central Mississippi. Econ Geol 69:1191–1206

Cathles LM, Smith AT (1983) Thermal constraints on the formation of Mississippi Valley-type lead-zinc deposits and their implications for episodic basin dewatering and deposit genesis. Econ Geol 78:983–1002

Crevello PD (1990) Stratigraphic evolution of Lower Jurassic carbonate platforms: record of rift tectonics and eustatsy, central and eastern High Atlas, Morocco. Unpubl PhD Thesis, Colorado School of Mines, Golden, Colorado, USA, 457 pp

Claypool GE, Holser WT, Kaplan TR, Sakai H, Zak I (1980) The age curves of sulfur and oxygen isotopes in marine sulfate and their mutual interpretations. Chem Geol 28:199–260

Cumming GL, Richards JR (1975) Ore lead isotope ratios in a continuously changing Earth. Earth Planet Sci Lett 28:155–171

Dagallier G, Macaudiere JM (1987) Contrôles tectoniques des concentrations Pb-Ba en milieu carbonaté de Mibladen (Maroc). Bull Soc Geol France 8:387–394

Dahire M (2004) Le complexe plutonique de la Haute Moulouya (Meseta oriental, Maroc): evolution pétrologique et structurale. Unpubl PhD Thesis, Mohamed Ben Abdellah University, Fès, Morocco, 322 pp

Dresnay Du R (1979) Sédiments jurassiques du domaine des chaines atlasiques du Maroc. Association des

Sédimentologistes Français (ASF) Spec Publ 1, pp 345–365

Duggen S, Hoernle K, van den Bogaard P, Garbe-Schönberg D (2005) Post collisional transition from subduction- to intraplate-type magmatism in the westernmost Mediterranean: evidence from continental-edge delamination of subcontinental lithosphere. J Petrol 46:1115–1201

Duggen S, Hoernle K, Hauff F, Klügel A, Bouabdellah M, Thirlwall MF (2009) Flow of Canary mantle plume material through a subcontinental lithospheric corridor beneath Africa to the Mediterranean. Geology 37:283–286

Dupuy JJ, Touray JC (1986) Multi-stage ore deposition at the Oued Mekta strata-bound lead deposit, Touissit-Bou Beker district, eastern Morocco. Econ Geol 81:1558–1561

Duthou JL, Emberger A, Lasserre M (1976) Résultats graphiques et interprétation de mesures isotopiques du plomb de galènes et des minéraux oxydés du Maroc. Soc Géol France 7:221–226

Ellouz N, Patriat M, Gaulier JM, Bouatmani R, Saboundji S (2003) From rifting to Alpine inversion: Mesozoic and Cenozoic subsidence history of some Moroccan basins. Sedimen Geol 156:185–212

Emberger A (1965) Eléments pour une synthèse métallogénique du district plombifère de la Haute Moulouya. Notes Mém Serv Géol Maroc 181:235–238

Evans I, Kendall CG (1977) An interpretation of the depositional setting of some deep-water Jurassic carbonates of the central High Atlas Mountains, Morocco. In: Cook HE, Enos P (eds) Deep-water carbonate environments, SEPM Spec Publ 25, pp 249–261

Fauquette S, Suc J-P, Bertini A, Popescu S-M, Warny S, Bachiri Taoufiq N, Perez Villa M-J, Chikhi H, Feddi N, Subally D, Clauzon G, Ferrier J (2006) How much did climate force the Messinian salinity crisis? Quantified climatic conditions from pollen records in the Mediterranean region. Palaeogeogr, Palaeoclimatol, Palaeoecol 238:281–301

Fedan B, Laville E, Mezgueldi AE (1989) Le bassin jurassique du Moyen Atlas (Maroc): exemple de bassin sur relais de décrochements. Bull Soc Géol France 5(6):1123–1136

Felenc R, Lenoble JP (1965) Le gîte de plomb de Mibladen. In: Colloque sur les gisements stratiformes de plomb, zinc et manganèse du Maroc. Notes Mem Serv Géol Maroc 181:185–204

Filali F, Guiraud M, Burg J-P (1999) Nouvelles données petro-structurales sur la boutonnière d'Aouli (Haute Moulouya): leurs conséquences sur la géodynamique hercynienne du Maroc. Bull Soc Géol France 4:435–450

Fiechtner L, Friedrichsen H, Hammerschmid K (1992) Geochemistry and geochronology of arly Mesozoic tholeiites from central Morococo. Geol Rundschau 81:45–62

Frizon de Lamotte D, Leturmy P, Missenard Y, Khomsi S, Ruiz G, Saddiqi O, Guillocheau F, Michard A (2009) Mesozoic and Cenozoic vertical movements in the Atlas system (Algeria, Morocco, Tunisia): an overview. Tectonophys 475:9–28

Garven G (1995) Continental-scale groundwater flow and geologic processes. Ann Review Earth Planet Sci 23:89–117

Ge S, Garven G (1992) Hydromechanical modeling of tectonically driven groundwater flow with application to the Arkoma foreland basin. J Geophys Res 97 (B6):9119–9144

Giese P, Jacobshagen V (1992) Inversion tectonics of intracontinental ranges: High and Middle Atlas, Morocco. Geol Rundschau 81:249–259

Gomez-Rivas E, Corbella M, Martín-Martín JD, Stafford SL, Teixell A, Bons PD, Griera A, Cardellach E (2014) Reactivity of dolomitizing fluids and Mg source evaluation of fault-controlled dolomitization at the Benicàssim outcrop analogue (Maestrat Basin, E Spain). Marine Petrol Geol 55:26–42

Goulet F, Charles N, Barbanson L, Branquet Y, Sizaret S, Annaciri A, Badra L, Chen Y (2014) Non-sulfide zinc deposits of the Moroccan High Atlas: multi-scale characterization and origin. Ore Geol Rev 56:115–140

Harmand C, Cantagrel JM (1984) Le volcanisme alcalin Tertiaire et Quaternaire du moyen Atlas (Maroc): chronologie K/Ar et cadre géodynamique. J Afr Earth Sci 2:51–55

Haynes FM, Kesler SS (1987) Chemical evolution of brines during Mississippi Valley-type mineralization: evidence from East Tennessee and Pine Point. Econ Geol 82:53–71

Hitzman MW, Beaty DW (1996) The Irish Zn-Pb orefield. In: Sangster DF (ed) Carbonate-hosted lead-zinc deposits. Soc Economic Geologists Spec Publ 4, pp 356–363

Hsü KJ, Cita MB, Ryan WBF (1973) The origin of the Mediterranean evaporites. Initial Repts Deep Sea Drilling Project 13:1203–1231

Jacobshagen VH, Gorler K, Giese P (1988) Geodynamic evolution of the Atlas system (Morocco). In: Jacobshagen VH (ed) The Atlas system of Morocco, Springer-Verlag, Berlin-Heidelberg-New York, Lecture Notes Earth Sci 15, pp 481–499

Jahn S, Bode R, Lyckberg P, Medenbach O, Lierl H-J (2003) Marokko-Land der Schönen Mineralien und fossilien. Bode Verlag GmbH, Salzhemmendorf, Germany 535 pp

Jébrak M, Marcoux E, Nasloubi M, Zahraoui M (1998) From sandstone- to carbonate-hosted stratabound deposits: an isotope study of galena in the Upper-Molulouya district (Morocco). Min Deposita 33:406–415

Jemmali N, Souissi F, Carranza EJM, Bouabdellah M (2013) Lead and sulfur isotope constraints on the genesis of the polymetallic mineralization at Oued

Maden, Jebel Hallouf and Fedj Hassene carbonate-hosted Pb–Zn (As–Cu–Hg–Sb) deposits, northern Tunisia. J Geochem Explor 132:6–14

Jenkyns HC, Jones CE, Grocke DR, Hesselbo SP, Parkinson DN (2002) Chemostratigraphy of the Jurassic system: applications, limitations and implications for palaeoceanography. J Geol Soc 159:351–378

Kampschulte A, Strauss H (2004) The sulfur isotope evolution of Phanerozoic seawater based on the analysis of structurally substituted sulfate in carbonates. Chem Geol 204:255–286

Kendrick MA, Burgess R, Leach DL, Pattrick RAD (2002a) Hydrothermal fluid origins in Mississippi Valley-type ore districts: combined noble gas (He, Ar, Kr) and halogen (Cl, Br, I) analysis of fluid inclusions from the Illinois-Kentucky fluorspar district Viburnum Trend and Tri-State districts, Midcontinent United States. Econ Geol 97:453–469

Kendrick MA, Burgess R, Pattrick RAD, Turner G (2002b) Hydrothermal fluid origins in a fluorite-rich Mississippi Valley-type district: combined noble gas (He, Ar, Kr) and halogen (Cl, Br, I) analysis of fluid inclusions from the South Pennine ore field, United Kingdom. Econ Geol 97:435–451

Kenter J, Campbell AE (1991) Sedimentation on a Lower Jurassic carbonate platform flank: geometry, sediment fabric and related depositional structures (Djebel Bou Dahar, High Atlas, Morocco). Sedimen Geol 72:1–34

Kontak DJ, Sangster DF (2005) Aqueous and liquid petroleum inclusions in barite from the Walton deposit, Nova Scotia, Canada: a Carboniferous, carbonate-hosted Ba–Pb–Zn–Cu–Ag deposit. Econ Geol 93:845–868

Krijgsman W, Langereis CG, Zachariasse WJ, Boccaletti M, Moratti G, Gelati R, Iaccarino S, Papani G, Villa G (1999) Late Neogene evolution of the Taza-Guercif basin (Rifian corridor, Morocco) and implications for the Messinian salinity crisis. Marine Geol 153:147–160

Kucha H, Schroll E, Raith JG, Halas S (2010) Microbial sphalerite formation in carbonate-hosted Zn-Pb ores, Bleiberg, Austria: micro- to nanotextural and sulfur isotope evidence. Econ Geol 105:1005–1023

Leach DL, Sangster DF (1993) Mississippi Valley-type lead-zinc deposits. In: Kirkham RV, Sinclair WD, Thorpe RI, Duke JM (eds) Mineral deposit modeling. Geol Assoc Can Spec Paper 40, pp 289–314

Leach DL, Bradley DC, Huston D, Pisarevsky SA, Taylor RD, Gardoll SJ (2010) Sediment-hosted lead-zinc deposits in Earth history. Econ Geol 105:593–625

Lustrino M, Wilson M (2007) The circum-Mediterranean anorogenic Cenozoic igneous province. Earth-Sci Rev 81:1–65

Makhoukhi S (1993) Le gisement de plomb de Beddiane (Maroc oriental): gîtologie et éléments de modélisation d'une minéralisation de type Mississippi Valley. Unpub PhD Thesis, École Normale Supérieure Paris, 124 pp

Makhoukhi S, Marignac Ch, Pironon J, Schmitt JM, Marrakchi C, Bouabdelli M, Bastoul A (2003) Aqueous and hydrocarbon inclusions in dolomite from Touissit-Bou Beker district, eastern Morocco: a Jurassic carbonate hosted Pb–Zn(Cu) deposit. J Geochem Explor 78–79:545–551

Merino-Tomé O, Della Porta G, Kenter JAM, Verwer K, Harris PM, Adams E-W, Playton T, Corrochano D (2012) Sequence development in an isolated carbonate platform (Lower Jurassic, Djebel Bou Dahar, High Atlas, Morocco): influence of tectonics, eustacy and carbonate production. Sedimentol 59:118–155

Naji M (2004) Les minéralisations plombo-barytiques du district de la Haute Moulouya. Contexte géologique, contrôle tectonique et modèle de mise en place: gisements d'Aoul-Mibladen-Zeida. Unpub PhD Thesis, Mohammed V University, Rabat, Morocco, 218 pp

Ohmoto H, Watanabe Y, Ikemi H, Poulson SR, Taylor BE (2006) Sulphur isotope evidence for an oxic Archaean atmosphere. Nature 442:908–911

Oliver J (1986) Fluids expelled tectonically from orogenic belts: their role in hydrocarbon migration and other geologic phenomena. Geology 14:99–102

Ouarhache D, Charrière A, Charlot-Prat F, El Wartiti M (2012) Chronologie et modalities du rifting triassico-liasique à la marge sud-ouest de la Téthys alpine (Moyen Atlas et Haute Moulouya, Maroc); corrélation avec le rifting Atlantique: simultanéité et diachronisme. Bull Soc Geol France 183:233–249

Oukemini D, Bourne J, Krogh TE (1995) Géochronologie U-Pb sur zircon du pluton d'Aouli, Haute Moulouya, Maroc. Bull Soc Geol France 166:15–21

Owodenko B (1976) Le bassin houiller de Jerada (Maroc oriental). Notes Mem Serv Géol Maroc 207, 147 pp

Plumlee GS, Leach DL, Hofstra AH, Landis GP, Rowan EL, Viets JG (1994) Chemical reaction path modeling of ore deposition in Mississippi Valley-type Pb–Zn deposits of the Ozark region, U.S. Mid-continent. Econ Geol 89:1361–1383

Praszkier T (2013) Mibladen, Morocco. Mineral Record 44:247–285

Rahhali M (2002) Gisements stratiformes de Mibladen. In: Barodi E-B, Watanabe Y, Mouttaqi A, Annich M (eds) Méthodes et techniques d'exploration minière et principaux gisements au Maroc. Projet JICA/BRPM, Bureau Recherche Participations Minières—BRPM, Rabat, pp 166–170

Rajlich P (1983) Geology of Oued Mekta, a Mississippi Valley-type deposit, Touissit-Bou Beker region, eastern Morocco. Econ Geol 78:1239–1254

Rddad L, Bouhlel S (2016) The Bou Dahar Jurassic carbonate-hosted Pb–Zn–Ba deposits (Oriental High Atlas, Morocco): fluid-inclusion and C–O–S–Pb isotope studies. Ore Geol Rev 72:1072–1087

Samson P (1973) Un gisement plombo-zincifère en milieu récifal: Touissit (Maroc oriental). Notes Mém Service Géol Maroc 242, 133 pp

Sangster DF (2003) A special issue devoted to nonsulfide zinc deposits: a new look. Econ Geol 98:683–684

Scheibner C, Reumer JJG (1999) Facies patterns within a Lower Jurassic upper slope to inner platform transect (Jbel Bou Dahar, Morocco). Facies 41:55–80

Sharp JM (1978) Energy and momentum transport model of the Ouachita basin and its possible impact on formation of economic mineral deposits. Econ Geol 73:1057–1068

Sheppard SMF (1986) Characterization and isotopic variations in natural waters. In: Valley JW, Taylor HP Jr, O'Neil JR (eds) Stable isotopes in high temperature geological processes. Mineral Soc Am Rev Mineral 16:165–184

Stacey JS, Kramers JC (1975) Approximation of terrestrial lead isotope evolution by a two-stage model. Earth Planet Sci Lett 26:207–221

Torbi A, Gélard JP (1994) Paléocontraintes enregistrées par la microfracturation, depuis l'Hercynien jusqu'à l'Actuel, dans les Monts du Sud-Est d'Oujda (Meseta orientale, Maroc). C R Acad Sci Paris 318:131–135

Torbi A (1996) Stratigraphie et évolution structurale paléozoïque d'un segment de la Meseta orientale marocaine (Monts du Sud-Est d'Oujda): rôle des décrochements dans la formation de l'olistostrome intraviséen et le plutonisme tardi-hercynien. Jour Afr Earth Sci 22:549–563

Touahri B (1991) Géochimie et métallogénie des minéralisations à Pb et Zn du nord de l'Algérie. Mémoire du Service Géologique d'Algérie No. 4, 260 pp

Ulrich MR, Bodnar RJ (1988) Systematics of stretching of fluid inclusions II: barite at 1 atm confining pressure. Econ Geol 83:1037–1046

Valin F, Rakus M (1979) Rapport concernant l'étude géologique du Paléozoique et de la couverture mésozoique dans les Monts d'Oujda. Unpub Rept, Service Géologique d'Oujda 60, 73 pp

Vauchez A (1976) Les déformations anté-triasiques dans la boutonnière d'Aouli-Mibladen. C R Acad Sci Paris 282:425–428

Vikre PG, Poulson SK, Koenig AE (2011) Derivation of S and Pb in Phanerozoic intrusion-related metal deposits from Neoproterozoic sedimentary pyrite, Great Basin, United States. Econ Geol 106:883–912

Vitrac AM, Albarede F, Allègre CJ (1981) Lead isotopic composition of Hercynian granitic K-feldspars constrains continental genesis. Nature 291:460–464

Voirin J (1965) Géologie du gisement plombo-zincifère de Bou Beker. In: Colloque sur les gîtes stratiformes de plomb, zinc et manganèse du Maroc 1962. Notes Mémoires Service Géologique Maroc 181:21–68

Warme JE (1988) Jurassic carbonate facies of the central and eastern High Atlas rift, Morocco. In: Jacobshagen V (ed) The Atlas system of Morocco, Springer-Verlag, Berlin-Heidelberg-New York, Lecture Notes Earth Sci 15, pp 169–199

Wittig N, Pearson DG, Baker J, Duggen S, Hoernle K (2010) A major element, PGE and Re-Os isotope study of Middle Atlas (Morocco) peridotite xenoliths: evidence for coupled introduction of metasomatic sulphides and clinopyroxene. Lithos 115:15–26

Zartman RE, Doe BR (1981) Plumbotectonics—the model. Tectonophys 75:35–162

Tectonomagmatic Context of Sedex Pb–Zn and Polymetallic Ore Deposits of the Nappe Zone Northern Tunisia, and Comparisons with MVT Deposits in the Region

Sophie Decrée, Christian Marignac, Riadh Abidi, Nejib Jemmali, Etienne Deloule and Fouad Souissi

Abstract

The Nefza region (Nappe Zone, northern Tunisia) is known both as a Late Miocene magmatic province and a base-metal district. In this region, small, post-nappe, continental extensional basins (Sidi Driss and

S. Decrée (✉)
Royal Belgian Institute of Natural Sciences,
rue Vautier 29, 1000 Brussels, Belgium
e-mail: sophie.decree@naturalsciences.be

C. Marignac
Géoressources Nancy (CNRS/Université de Lorraine) and Ecole Nationale Supérieure des Mines de Nancy, Campus Artem - CS 14 234, 92 rue Sergent Blandan, 54042 Nancy, France
e-mail: christian.marignac@univ-lorraine.fr

R. Abidi · F. Souissi
Faculté des Sciences de Tunis, Département de Géologie, Université de Tunis El Manar,
2092 El Manar, Tunisia
e-mail: abidi1riadh@yahoo.com

F. Souissi
e-mail: souissifoued2@gmail.com

N. Jemmali
Faculté des Sciences, Université de Gafsa,
Campus Universitaire Sidi Ahmed Zarroug,
2112 Gafsa, Tunisia
e-mail: nejib.jemmali@yahoo.fr

N. Jemmali · F. Souissi
Laboratoire des Matériaux Utiles, Institut National de Recherche et d'Analyse Physico-chimiques,
2026 Technopole de Sidi Thabet, Tunisia

E. Deloule
Centre de Recherches Pétrographiques et Géochimiques (CNRS), BP 20-54501,
Nancy, France
e-mail: deloule@crpg.cnrs-nancy.fr

M. Bouabdellah and J.F. Slack (eds.), *Mineral Deposits of North Africa*,
Mineral Resource Reviews, DOI 10.1007/978-3-319-31733-5_20

Douahria) host syndiagenetic Pb–Zn ore deposits that have been classified as Sediment-Hosted Massive Sulphide (SHMS)–Sedimentary-exhalative (Sedex). In addition to this mineralization, the Nappe zone contains other Pb–Zn and polymetallic deposits that show similarities both to the SHMS-Sedex and MVT deposits of the Dome and Graben zones, namely the "peri-diapiric" deposits of Jebel (Jb) el Hamra, Jalta, and Jebel Ghozlane. All of the Nappe Zone deposits share common characteristics, including: (1) age—the deposits formed between late collisional events (Late Tortonian) and inception of the Early Messinian extensional regime, in the context of the Alpine Maghrebide belt formation; (2) presence of pre-existing sulphates—these were likely the main source of sulphur for the sulphides; and (3) hydrothermal systems leading to their genesis—these testify to alternating influx of cold and warm fluids. The involvement of high temperature fluids are deduced from fluid inclusion studies (Th values of 140–240 °C), whereas the presence of distinctive sphalerite textures (microspherules and colloform textures) and sulphur isotopic compositions demonstrate in situ bacterial sulphate reduction, and consequently deposition at temperatures below 80 °C. These data constitute unifying characteristics for these mineralizations that are in contrast to the features of Pb–Zn(–fluorite) MVT deposits occurring in the Dome and Graben zones of Tunisia. The geodynamic context prevailing during the Late Miocene in the Nappe Zone is the underlying common factor that explains the diversity of ore deposits formed at that time in this region. Most deposits are located in the vicinity of shear zones and associated lineaments inherited from the Variscan orogeny. These deep structures were reactivated by transtensional processes during the Alpine orogeny and controlled post-collisional magmatism, circulation of hydrothermal fluids, and locations of related ore deposits and showings in the Nappe Zone.

1 Introduction

Northern Tunisia is part of the Alpine Maghrebide belt, which trends east-west for more than 2000 km from Morocco to eastern Algeria. This belt further stretches to the northeast, beginning in Tunisia, towards Sicily. It results from the Tertiary collision between northern Africa and a small Mesomediterranean plate, as part of the development of the Alpine chains (e.g., Piqué et al. 2002; Guerrera et al. 2005; Michard et al. 2006). The Maghrebides consist of (1) an Internal Zone, with basement nappes (Internal Massifs) derived from the Mesomediterranean plate, and a complex of flysch slices (or Flysch Zone) at their front, the two being thrust over (2) the Tellian nappes (or Tellian Zone), which in turn are thrust onto (3) the folded autochtonous units of the foreland (Tellian Atlas and Saharan Platform). The Tellian nappes represent the former passive margin of northern Africa, whereas the Tellian Atlas resulted from Eocene tectonic inversion of a Mesozoic rift system that formed parallel to the paleomargin (e.g., Masrouhi et al. 2008). In the northern part of Tunisia, the Internal Zone boundary is located south of the Galite Islands (Mascle et al. 2004). On land, the more internal units form part of the Tellian Zone

(or Nappe Zone). The Tellian Atlas comprises (1) an internal part, characterized by diapiric structures with Triassic cores; this internal part defines the Dome Zone, which is bordered to the southeast by the frontal Zaghouan fault (Fig. 1); and (2) an external domain, which was reworked by extension during the late Tertiary, corresponds to the present Graben Zone.

The northern Tunisian strata contain Pb–Zn–Ba–Sr–F and polymetallic deposits both in the Nappe Zone and the Tellian Atlas. Within the Dome Zone (and to a lesser extent in the Graben Zone), numerous peridiapiric Ba–Pb–Zn deposits are present (e.g., Rouvier et al. 1985; Orgeval 1994; Sheppard et al. 1996; Bouhlel 2005). A sub-province with CaF_2 deposits occurs

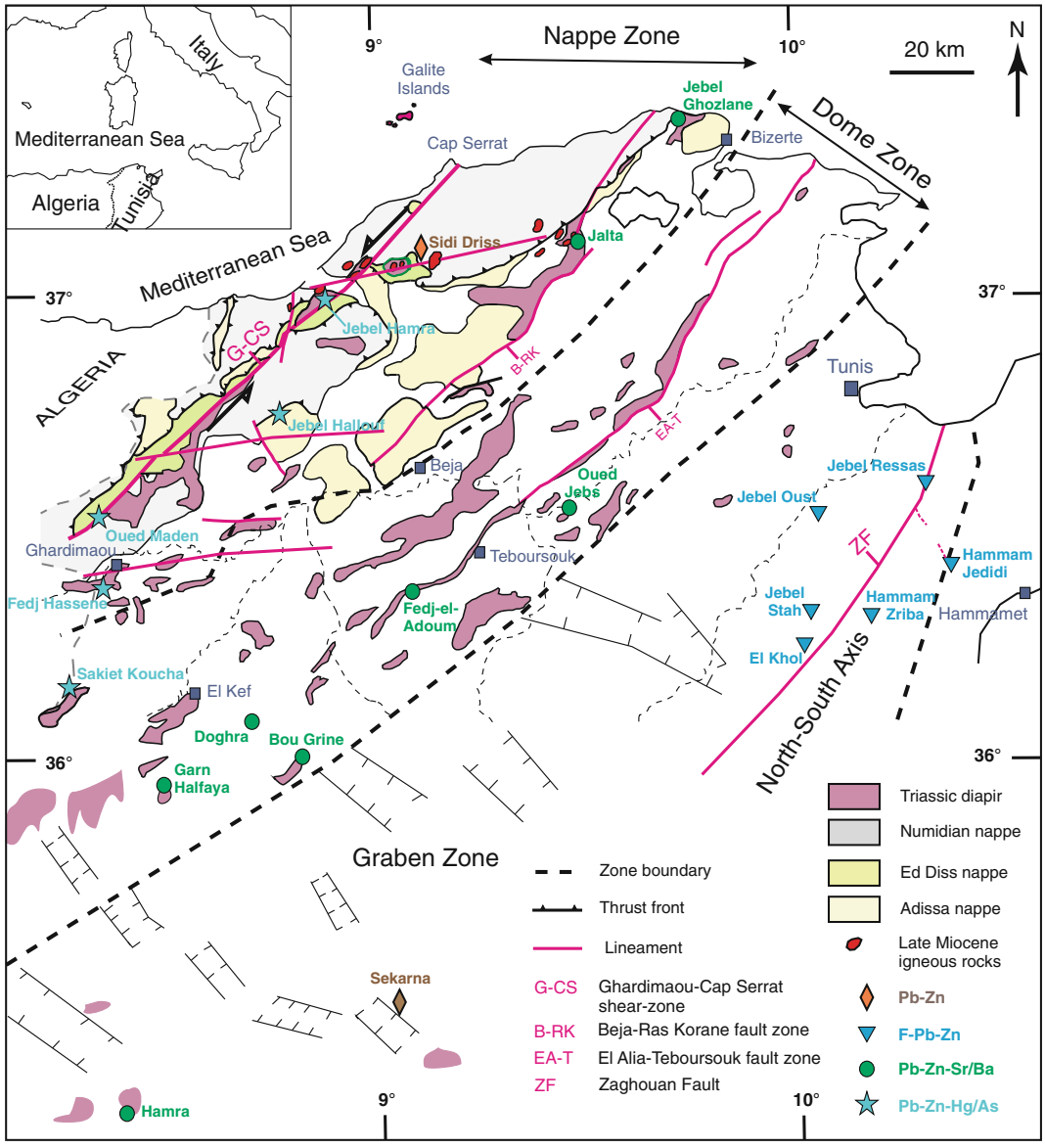

Fig. 1 Generalized tectonic and metallogenic map of central and northern Tunisia (adapted from Rouvier et al. 1985; Bouaziz et al. 2002; Bouhlel et al. 2013)

mainly along the Zaghouan fault (Souissi et al. 2013; Trabelsi et al. 2005). The diapirs, which are made of Triassic evaporitic lithologies, are exposed along major thrusts and anticlines (Perthuisot et al. 1999). Ore deposits of the Dome Zone have been interpreted either as being related to salt diapirism (Charef and Sheppard 1991; Orgeval 1994), or more often, as to MVT-type processes related to a Serravallian-Tortonian, gravity-driven fluid circulation event during late Alpine convergence (Rouvier et al. 1985; Bouhlel 2005).

Peridiapiric deposits also occur in the Nappe Zone (Jebel el Hamra, Abidi et al. 2010; Jb Ghozlane and Jalta, Jemmali et al. 2011b, 2013b, 2014). However, this zone is better known for containing a large variety of polymetallic deposits, among which several are present in the Nefza district. This district is characterized by the occurrence of late Tertiary mineral deposits, including the Tortonian Oued Belif iron oxide uranium (IOU) showing (Decrée et al. 2013), the Messinian Sidi Driss and Douahria Ba–Zn–Pb Sedex deposits (Decrée et al. 2008a), and the Pliocene iron deposit of Tamera (Decrée et al. 2008b). The two Sedex deposits are attributed to formation by thermally-driven circulating fluids related to Late Miocene magmatism and reactivation of shear zones during Messinian extension. These events (magmatism and reactivation of shear zones) are particularly well expressed in northern Tunisia (Decrée et al. 2008a). The Jebel el Hamra (Jb el Hamra hereafter) encompasses the Ba–Sr–Zn–Pb–Hg deposits of Aïn Allega, El Aguiba, and El Arja (Sainfeld 1952; Gharbi 1977; Abidi et al. 2010). These deposits were mined until the end of the 1970s. Aïn Allega produced 13,300 t of Pb and 9400 t of Zn (Abidi et al. 2011). At El Arja 370 t Hg were extracted from 1952 to 1975, with Hg grades of 0.08 to 1.5 wt% (Gharbi 1977). The Jalta mine, where the Pb–Zn mineralization is associated with the post-nappe Miocene series (Jemmali et al. 2014), has produced ~75,000 t of ore grading 59 % Pb. At Jebel Ghozlane, the mine produced ~6,680 t of Pb and 53,000 t of Zn.

The Nefza deposits, as well as the Jalta deposit, are spatially associated with a N80° E tectonic lineament. The latter deposit is linked to felsic and mafic magmatism of Tortonian to Messinian age (Talbi et al. 2005; Decrée et al. 2014 and references therein), and by geochemical haloes including As and Sb anomalies (Fig. 2). The Ghardimaou-Cap Serrat sinistral fault zone (Rouvier 1977), a major regional structure guiding Alpine tectonics at the tectonic plate scale (e.g., Piqué et al. 1998), also controlled the Tortonian to Messinian magmatism. This structure is similarly characterized by the same As and Sb geochemical haloes—and by Hg mineralization (Jb el Hamra, Abidi 2011; Oued Maden, Gharbi 1977). The presence of magmatism and mineralization is especially well expressed at the intersection of the Ghardimaou-Cap Serrat fault zone with N80° E lineaments (e.g., Jb el Hamra deposits and Ras Rajel rhyodacite subvolcanic intrusion).

In this paper, we address similarities and differences between the Nefza Sedex deposits and "peri-diapiric" deposits of the Nappe Zone, and other base-metal and polymetallic deposits of the Tellian Atlas.

2 Geological Setting

2.1 Regional Geology

In northern Tunisia, the Tellian Nappe Zone comprises three thrust sheets, which from base to top are the Adissa, Ed Diss, and Numidian (Fig. 2). The Adissa and Ed Diss thrust sheets, being up to 1500 m thick, are derived from the former passive margin of Africa, and consist of Late Cretaceous to Eocene limestone and marl (Rouvier 1977; Ould Bagga et al. 2006). The overlying Numidian thrust sheet, up to 1500 m thick, is made of Chattian to Early Burdigalian turbidites that were deposited in a narrow trench from present-day Morocco to Sicily, in the southern part of the Mesoditerranean domain prior to the final collision (Riahi et al. 2010). To the south of the Nappe Zone, the Dome Zone is characterized by a system of NE-SW "master faults" that are thought to have reactivated Hercynian lineaments (Melki et al. 2012)

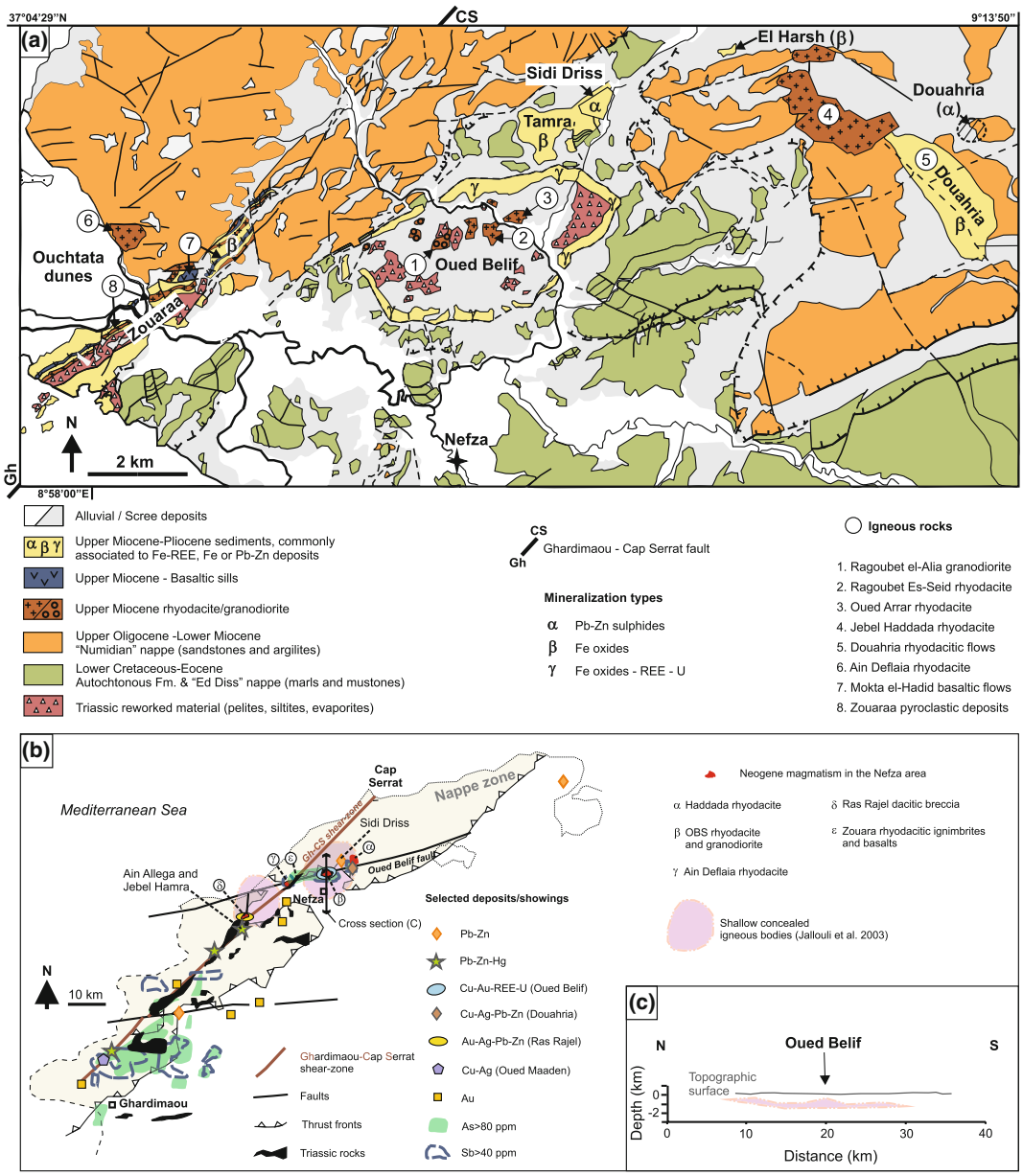

Fig. 2 **a** Geological sketch map of Nefza district (modified from Gottis and Sainfeld 1952; Batik 1980; Rouvier 1987, 1994; Decrée et al. 2014), showing locations of selected deposits/occurrences and igneous rocks. **b** Structural settings and mineralization in Nappe Zone (modified from Gharbi 1977; Albidon Limited 2004); locations of As and Sb anomalies are from Office National des Mines de Tunisie (modified from Decrée et al. 2013, 2014); Gh-CS is Ghardimaou-Cap Serrat shear zone. **c** Cross section illustrating shallow concealed igneous bodies beneath Oued Belif structure (modified from Jallouli et al. 2003)

(Fig. 1). These faults were active since the Mesozoic and localized numerous salt diapirs comprising Triassic material (Perthuisot et al. 1999). Afterward, they were inverted as thrust faults, during the Eocene and the Late Miocene. Structural lineaments inherited from the Variscan basement are also present within the Nappe Zone, the most prominent being the NE-SW

sinistral Ghardimaou-Cap Serrat fault zone (GCSFZ) (Rouvier 1977; Mamady 1998) and a series of N80° E lineaments that controlled both post-collisional magmatism and locations of most ore deposits and showings (Figs. 1 and 2). As shown in Fig. 2, Zn–Pb–Ba–Sr deposits and As anomalies occur along both trends, whereas REE and Sn–Sb occurrences/anomalies—as well as gold and related alteration zones (Albidon 2004)—are mostly controlled by the N80° E lineaments. However, the Hg deposits are restricted to the NE-SW trend of the GCSFZ.

The present-day structure of northern Tunisia is dominated by a fold-and-thrust belt that evolved starting in the latest Burdigalian in the Internal Zone and ending in the Late Tortonian at the Tellian front (Bouaziz et al. 2002). Within the Nappe Zone, the Numidian Nappe was emplaced first as part of the Internal Zone during the latest Burdigalian, and was then remobilized (as a gliding nappe on a reworked evaporate sole) and incorporated into the Tellian Zone during the Tortonian. The resulting nappe pile was then folded during the Late Tortonian (Khomsi et al. 2009). Short-lived returns to extensional conditions are recorded in the Late Tortonian-Early Messinian, and in the Pliocene (Bouaziz et al. 2002; Belguith et al. 2011), which promoted the formation of small continental basins in the Nappe Zone (e.g., Late Tortonian-Early Messinian Sidi Driss and Zouaraa basins, and Pliocene Tamra basin) (Fig. 2). The Africa-Europe convergence is still active (at the slow convergence rate of 0.5 cm $year^{-1}$) and the current plate boundary is thought to be still located at the front of the Tellian Zone (Jolivet et al. 2008).

Within the Dome Zone, the evaporitic diapirs are rooted in Triassic strata. The first extrusions occurred as soon as the Albian (e.g., Ben Slama et al. 2009). However, the main diapiric emplacement was coeval with the Atlasic inversion (Late Cretaceous to Paleocene), followed by reworking of the resulting bodies during the Late Miocene (Perthuisot et al. 1999). According to the most recent geophysical data, the Numidian nappe is pierced by Triassic salt diapirs that are rooted in the sole of the nappe, or more deeply. This setting testifies to a post-nappe stage of halokinesis in the region (Khomsi et al. 2009). The GCSFZ is marked by a line of antiforms that deform the nappe pile, including the Numidian nappe. The extrusion of Triassic rocks within the anticline cores is evidently part of this late (Tortonian) halokinesis stage (Fig. 1).

2.2 Miocene Tectonomagmatic Context of the Nefza Mining District

In the Nefza mining district, the entire nappe pile is cut by shallow-level, Late Serravallian-Messinian intrusive rocks (Fig. 2). The Jebel Haddada massif comprises a rhyodacitic dome, dated between 8.7 ± 0.15 and 8.2 ± 0.4 Ma (Bellon 1976; Faul and Foland 1981) and volcanic ash. The cordierite-bearing rhyodacite dome at Ain Deflaia has been variously dated at 12.3 ± 0.5 and 8.5 Ma (Bellon 1976; Rouvier 1977). However, because pyroclastic deposits related to the Ain Deflaia massif (Laridhi-Ouazaa 1988, 1989, 1996) fill the Zouaraa basin, the latter Late Tortonian age is favoured. In the same basin, transitional basalt sills outcropping at Mokta el-Hadid (Fig. 2) have been dated at 8.4 ± 0.4 Ma by Bellon (1976), and at 6.9 ± 0.3 and 6.4 ± 0.15 Ma by Rouvier (1977). Owing to the fact that these basalts were emplaced under extensional conditions (Mauduit 1978; Maury et al. 2000; Jallouli et al. 2003), the Messinian age must be preferred. The Oued Belif elliptical structure (Fig. 2) encloses the Ragoubet el-Alia granodiorite (12.9 ± 0.5 Ma; Badgasarian et al. 1972; Bellon 1976; Faul and Foland 1981). Because the ages of Bellon (1976) are uniformly too old, the Serravallian age for the granodiorite intrusion may thus be questioned.

Following a gravimetric survey, a very shallow concealed magmatic sill (0.5–1.5 km depth, 0.7–0.9 km thick, diameter ca. 20 km) has been recognized and may be the root or source of the Oued Belif intrusions (Jallouli et al. 2003). A similar sill is present further west, beneath the Ras Rajel dacitic plug (Jallouli et al. 2003) (Fig. 2). Small rhyolite dikelets derived from the Ras Rajel rhyodacite plug overprint a

matrix-supported dacitic breccia. The latter comprises angular Numidian clasts and a matrix of iron oxides and hydroxides that are reminiscent of the Oued Belif structure (Albidon 2004). In that case, the age of these small dikelets could be the same—ca. 9 Ma—as the Oued Belif rhyodacite (Decrée et al. 2013). Consequently, the Ras Rajel rhyodacite intrusion is likely Late Tortonian in age. In addition to the Numidian clasts, the rhyodacite body contains a variety of magmatic enclaves including fine-grained felsite, porphyritic felsite (with or without biotite), and coarse-grained granodiorite. This diversity of enclaves seems indicative of multistage magmatic activity. It is tempting to relate this pluton to the sill-like body described by Jallouli et al. (2003). By comparison with the Oued Belif structure, this intrusion could be as old as Serravallian.

Chemical compositions of the felsic rocks indicate the involvement of a metaluminous calc-alkaline magma (derived from a lithospheric enriched mantle source and contaminated by old crustal materials), mixed in variable proportions with melted continental crust (Decrée et al. 2014). The basalts, which are transitional between calc-alkaline and alkaline series, originated from an enriched mantle source at the lithosphere-asthenosphere boundary (Maury et al. 2000; Decrée et al. 2014). This magmatism was ultimately caused by partial melting of the North Africa sub-continental lithospheric mantle (SCLM; Maury et al. 2000) and is likely related to lithospheric delamination along reactivated deep-seated faults (Decrée et al. 2014). Shear zones and associated lineaments inherited from the Variscan orogeny were reactivated by transtensional processes during the Alpine orogeny (Piqué et al. 2002). Basalt dikes of mantle origin were also emplaced along these lineaments (e.g., Mokta el-Hadid basalts along the NE-SW Ghardimou-Cap Serrat Fault), suggesting that these fault zones are of lithospheric scale. In the Tell region of northern Tunisia, magma ascent was apparently facilitated due to a thinner lower crust (10 km vs. 20 km in central Tunisia; Jallouli and Mickus 2000) and a more proximal Moho (Mickus and Jallouli 1999). However, it cannot be ruled out that deep-seated intrusive felsic-mafic bodies were emplaced under the Tellian Atlas, following reactivation of the lineaments, as in the Nappe Zone. Hydrothermal activity is current along the Zaghouan Faults, as in the Nefza district, and along the Ghardimaou-Cap Serrat Fault (Gharbi 1977; Zouiten 1999; Charef et al. 2009).

2.3 Polymetallic Mineralization in the Nefza Mining District

The Oued Belif breccia (OBB) forms a $\sim 7 \times 3$ km elliptical ring with a WSW-ENE long axis, extending along the N80° E lineament and enclosing Triassic (diapiric) material and two generations of shallow felsic magmatism. This breccia is the host for iron oxide-uranium (gold) mineralization related to IOCG-type deposits (Decrée et al. 2013). The matrix-supported OBB comprises clasts of altered Triassic material and other rocks derived from the regional substrate. Fine-grained hematite is the main matrix mineral, accompanied by light REE (LREE) and U minerals. A multi-phase alteration episode (K-Fe-(Mg)-metasomatism) slightly predates the Fe-LREE-U mineralization. The alteration and mineralization are both related to very high-temperature fluid circulations (≥500–550 °C; Talbi et al. 1999). The major breccia-forming event (dated at 9.2 ± 0.25 Ma via K-Ar on K-feldspar) is coeval with mineralization and with emplacement of the Oued Belif rhyodacite intrusion, which could be related to a phreato-magmatic event (Mauduit 1978; Perthuisot 1978; Decrée et al. 2013).

Messinian Sedex Pb–Zn deposits of Sidi Driss and Douahria are hosted within small, post-nappe, continental to shallow open-marine extensional basins, currently controlled by NE-SW normal faults. These faults were inverted at the end of the Messinian period with the transformation of the basin into a broad synclinal depression. The Sedex deposits are described in a following section.

A second generation of small post-nappe continental extensional basins, characterized by

strong Fe-enrichment, has also been recognized. The Tamra Pliocene basin, unconformably overlying the Sidi Driss basin, is the host for iron mineralization in the form of a 50-m-thick succession of iron hydroxide-bearing sediments (Tamra Formation). Each mineralized sequence results from (1) sedimentation of iron-rich lateritic material, and (2) in situ pedogenetic reworking and iron concentration without evidence of a precursor hydrothermal event (Decrée et al. 2008b). A Late Pliocene low-temperature hydrothermal iron mineralization, accompanied by Mn, Sr, Ba, Zn, and Pb, is superimposed on this sedimentary iron concentration (Decrée et al. 2010; Moussi et al. 2011). This younger mineralization testifies to protracted hydrothermal activity in the Nefza area that is still active as shown by occurrence of present-day thermal springs (35–70 °C; Gharbi 1977; Zouiten 1999). In addition to the Tamra basin, other Fe-ore deposits occur in Miocene-Pliocene basins, in the vicinity of igneous rocks, as in the Douahria basin, at Mokta el-Hadid, in the Zouaraa basin, and at Jebel Harsh (Rouvier 1977; Negra 1987). Within the Douahria basin, the iron mineralization consists of pyroclastic deposits and volcanic ash strongly impregnated by iron oxides, which constitute the Douahria iron ore.

3 Sedex Pb–Zn Deposits of the Nefza Mining District

3.1 The Messinian Sedimentary Basins

The Sidi Driss Zn–Pb sulphide deposit was exploited for more than a century and the mine closed 30 years ago. The ore is now exhausted. Studies devoted to the geology and origin of the deposit have been conducted by Sainfeld (1952), Gottis and Sainfeld (1952), Stefanov and Ouchev (1972) (exploiting new exploratory drillings performed by the Tunisian National Mine Office (ONM) in the 1970s), Negra (1987), Dermech (1990), and Decrée et al. (2008a).

The small Sidi Driss-Tamra and Douahria basins unconformably overlie the eroded nappe pile. The Sidi Driss basin is presently a syncline (Stefanov and Ouchev 1972; Dermech 1990), containing longitudinal NE-SW faults that seemingly were active during sedimentation. Marl is the predominant rock type, with intercalations of conglomerate, supratidal limestone, and evaporite. According to Vassileff and Popov (1979) and Negra (1987), the Douahria basin is a small graben filled by a thick unit of marl with numerous volcaniclastic intercalations, all of which are impregnated by iron, overlain by argillite with thin interbeds of lenticular limestone towards the top.

The two basins display some similarities. First, sedimentation was mainly Messinian in age, although encompassing the Late Tortonian. The oldest sedimentary deposits comprise volcaniclastic strata derived from Tortonian subaerial rhyodacite intrusions and coeval felsic volcanic ash and tuffaceous beds. At Sidi Driss, anhydrite ghosts are numerous within the algal mats (Sainfeld 1952) that indicate an evaporitic (sabkha or saline) environment. These occurrences, together with the presence of lignite and cross stratifications in the upper strata of the basin, led Sainfeld (1952) to propose a Messinian age. Indeed, in the Douharia basin, argillites contain remnants of a mammalian Pikermi fauna dated from the latest Messinian (Roman and Solignac 1934; Jaeger 1977). An identical succession, from lagoonal (sabkha) facies, through lacustrine (with local shallow open-marine) facies, to continental deposits, was recently described in the Messinian Bizerte basin, unconformably below Pliocene sediments as in the Nefza basins (Harrab et al. 2013). This stratigraphy suggests a far larger extent of the Messinian deposits in northern Tunisia than could be documented owing to the paucity of outcrops. The significant post-Messinian erosion recorded by Harrab et al. (2013) would have removed most of the Messinian sediments, explaining the apparent lack of connection between the Mediterranean coast and the exposed parts of the Nefza Messinian basins.

Zn–Pb sulphide mineralization is found in limestones interpreted as marine in the two Nefza basins. At Sidi Driss, two mineralized layers are

recognized: (1) in a conglomeratic unit containing rounded limestone clasts derived from the Ed Diss unit ("mineralized layer 2" of Dermech 1990); and (2) a supratidal limestone of variable thickness, towards the top, made of alternating stromatolitic and micritic facies ("mineralized layer 1" of Dermech 1990). The Douahria Pb–Zn deposit occurs in a thin lenticular marine limestone in the Douahria basin, intercalated towards the base of the ferruginous unit unconformably above a sequence of fluviatile siliciclastic deposits.

3.2 The Sidi Driss and Douahria Pb–Zn Deposits

At Sidi Driss, the ore is stratabound and composed mainly of galena, sphalerite, and late Fe-sulphides (Decrée et al. 2008b). It is disseminated or banded (Fig. 3a, b) and formed in the host rock through dissolution/replacement or by infilling of voids. Zn–Pb–Fe sulphides are hosted either in early diagenetic Fe- and Mn-rich calcite (up 0.5 wt% Fe and 1.8 wt% Mn; Fig. 3c), resulting from a dedolomitization process involving ferromanganese rich-rich fluids, or in carbonate previously replaced by barite and/or celestite (Fig. 3d). Some sphalerite and galena layers display soft-sediment structures such as loadcasts (Fig. 3a), suggesting that the Pb–Zn ores are syn-diagenetic in origin. At Sidi Driss, carbonate-hosted mineralization is predominant, accompanied by lesser, although significant, barite-hosted sulphides. In contrast, at Douahria, celestite-hosted mineralization is by far the most important. In both Pb–Zn deposits, sphalerite is commonly enriched in Cd (up to 0.95 wt%) and has spherulitic textures (Fig. 3e), which being very similar to the "peloids" described by Kucha et al. (2010), are thus interpreted in the same way, i.e., as products of microbial activity. Sphalerite and galena display contrasting habits, the latter forming euhedral cubes and cuboctahedra (Fig. 3b). Alternation of galena and sphalerite deposition is systematic, although galena is typically the first sulphide in the paragenesis. Fe-sulphides (pyrite, marcasite) replace earlier carbonates and/or sulphides and fill voids. Finally, barite and Fe–Mn calcite fill the remaining voids.

Fluid inclusion (FI) study: Measurable FIs were only found in the late calcite (Fig. 3f). This late calcite fills galena-bordered vugs, and is cut by galena veinlets possibly related to the Pliocene hydrothermal event in the overlying Tamra basin (see above). The microthermometric study was performed at the Department of Earth and Environmental Sciences of the Katholieke Universiteit in Leuven (Laboratory of P. Muchez, using a Linkam THMSG 600 stage coupled to an Olympus BX60 microscope). Typical primary inclusions (7–50 µm), which are found along calcite growth zones (Fig. 3g), are two-phase with a gas-to-liquid volume ratio (Rv) between 5 and 20 %, and homogenize in the liquid state (Lw FI). Other FIs (4–30 µm) occurring in small isolated clusters (Fig. 3h) are also likely primary inclusions, and are equally of the Lw type with Rv varying from 5 to 15 %. Owing to the very small size of most FIs, only a limited number of measurements were possible. Whatever the inclusion type, the first ice melting temperature, T_{fm}, is between –21.4 and –21.7 °C, indicating that NaCl is the predominant salt component. The ice melting temperature varies from –14.6 to –8 °C, which, interpreted in the NaCl–H_2O model system (Bodnar 2003), yields moderate salinities of 18.3 to 11.7 wt% NaCl equiv. Such a variation in salinities may be explained by fluid mixing, involving a brine end-member (≥ca 20 wt% equiv NaCl) and a low-salinity end-member, the latter being most likely meteoric water. The brine could be hypersaline Messinian seawater (≥350 g l^{-1}: Vengosh et al. 2000; Flecker et al. 2002) or result from circulation through the salt-bearing evaporitic rocks constituting in part the nearby Oued Belif Triassic diapir. In any case, as no Na to Ca exchange occurred during brine evolution, the corresponding fluid circulation necessarily occurred over a relatively short distance.

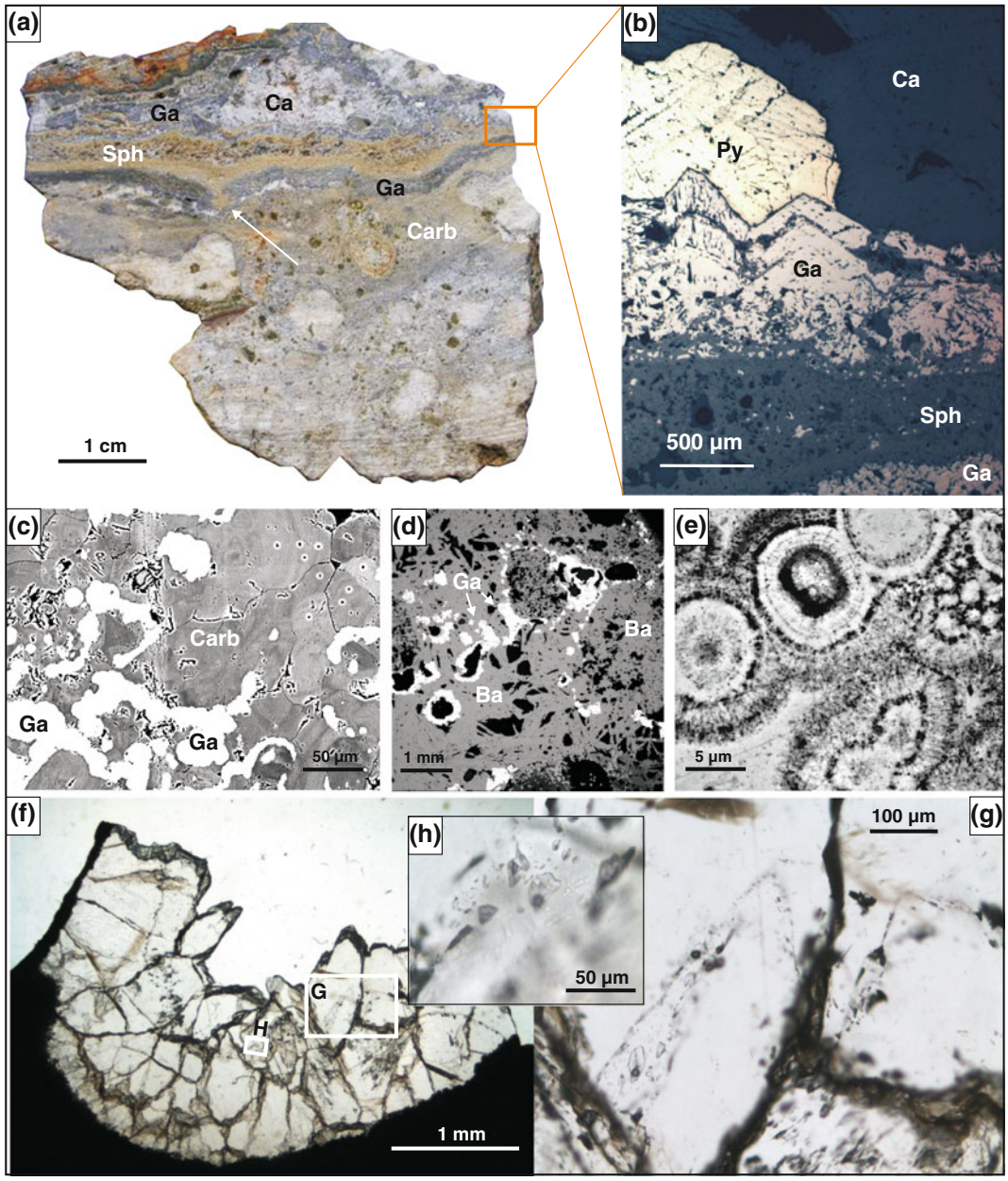

Fig. 3 Photographs and photomicrographs (**a**, **b**, **f**–**h**) and SEM backscattered electron images (**c**–**e**) of Pb–Zn ores from Sidi Driss and Douahria Sedex deposits (most are from Decrée et al. 2008a). **a** Alternating galena and sphalerite layers showing early soft-sediment deformation (loadcast indicated by *white arrow*) in texturally complex carbonate host rock; voids are filled with calcite. **b** Reflected light view of small zone illustrated in 3**a**: sphalerite layer is made up of coalesced spherules, whereas galena displays euhedral habit; remaining voids are filled with pyrite and calcite. **c** Recrystallized carbonate host rock showing zoned crystals (variations in Mn and/or Fe content), predating galena. **d** Galena replacing barite matrix (voids in *black*). **e** Sphalerite spherules; *darker bands* result from intergrowths of a silicate phase, probably kaolinite. **f** Late calcite infilling. **g** Primary fluid inclusions in late calcite infilling. **h** Other types of primary fluid inclusions (see text) in late calcite infilling. Abbreviations: *Ba* barite; *Ca* calcite; *Carb* carbonate (host rock); *Ga* galena; *Py* pyrite; *Sph* sphalerite

The bulk homogenization temperatures (Th) of the FIs are between 160 and 190 °C. Because there is no evidence of post-trapping modification, and considering the very shallow emplacement level of the mineralization, the Th values are considered to be close to the true trapping temperatures. No correlation exists between salinity and temperature variations. Despite the small number of measurements, it may tentatively be proposed that fluid mixing occurred outside of the Sidi Driss reservoir, the fluids being variously heated (on an overall trend of either heating or cooling) on a pathway to the reservoir.

Sulphur isotopes: All measurements of sulphur isotopes were performed in situ with an ion microprobe at Centre de Recherches Pétrographiques et Géochimiques–CRPG in Nancy (see Decrée et al. 2008a, for experimental conditions). Sulphur isotope data for sulphates define two populations. The first, characterized by $\delta^{34}S$ values between +21.5 and +24.4 ‰, corresponds to measurements of matrix celestite and barite (group A in Fig. 4). These values are in the range of Messinian evaporites (+20.7 to +24 ‰; Claypool et al. 1980; from +20.8 to +20.9 for Upper Miocene marine evaporitic sulphates; Kampschulte and Strauss 2004). The second population, which includes the late barite, has the highest $\delta^{34}S$ values (+40.7 to +57.0 ‰: group B). Considering only the sulphides, $\delta^{34}S$ values range from −30.3 to −2.0 ‰ for galena, and from −43.9 to 1.2 ‰ for sphalerite; Fe-sulphides display the maximum $\delta^{34}S$ variation, from −35.9 to +25.8 ‰ (Fig. 4). The sphalerite data are bimodal, consisting of a group 1 having very light $\delta^{34}S$ (≤−20 ‰) and group 2 with heavier values (Fig. 4). Owing to the inferred biogenic nature of the sphalerite, the reduced sulphur must derive from bacterially mediated reduction (BSR; Machel et al. 1995). Considering Messinian seawater or the early sulphates as the sulphur source, the sphalerite in group 1 would record a fractionation of −44 to −64 ‰, which is consistent with BSR processes (Machel et al. 1995). The isotopically heavier sulphur signature that characterizes the second group may be interpreted as reflecting Rayleigh fractionation, resulting from closure of the system. It has been shown by Filoche and Flinois (2007) that a rough negative correlation exists between Cd contents of the sphalerite and $\delta^{34}S$ values, which is expected in a closed system (i.e., progressive exhaustion of initial Cd contained in fluid). The galena commonly replaces sulphates, suggesting that the latter could have been a source of sulphur for galena. With few exceptions, the galena $\delta^{34}S$ values are heavier than ca. −10 ‰, implying the involvement of thermochemical sulphate reduction (TSR; Machel 2001). Because galena from the Sidi Driss and Douahria deposit commonly incorporates earlier sphalerite peloids, the few isotopically lighter $\delta^{34}S$ values measured for galena may result from a contribution of replaced sphalerite. Since sphalerite and galena are both typically replaced by marcasite, the preceding explanation may hold for the wide range of $\delta^{34}S$ values determined for marcasite (Fig. 4). On the other hand, largely positive $\delta^{34}S$ values observed for the late Fe-sulphide infillings could also record Rayleigh fractionation in a closed system, whereby the first sulphide precipitates (produced by TSR) are strongly enriched in ^{32}S and later "residual" sulphates are enriched in ^{34}S. The same fractionation process in a closed system can explain the isotopically heavy barite, following a major loss of light ^{32}S via the precipitation of Fe sulphides. As pointed out by Johnson et al. (2004, 2009), stratabound ("Sedex") barite deposits often present $\delta^{34}S$ values that are much higher than the contemporaneous marine sulphates. This is thought to reflect the contemporaneous reduction of marine sulphates by anaerobic oxidation of methane, which uses marine sulphate as an oxidant (Johnson et al. 2009). This process could be envisaged to explain the observed $\delta^{34}S$ enrichment observed for late sulphates at Sidi Driss and Douahria, compared to the ∼21 ‰ values of Upper Miocene marine evaporitic sulphates (Kampschulte and Strauss 2004).

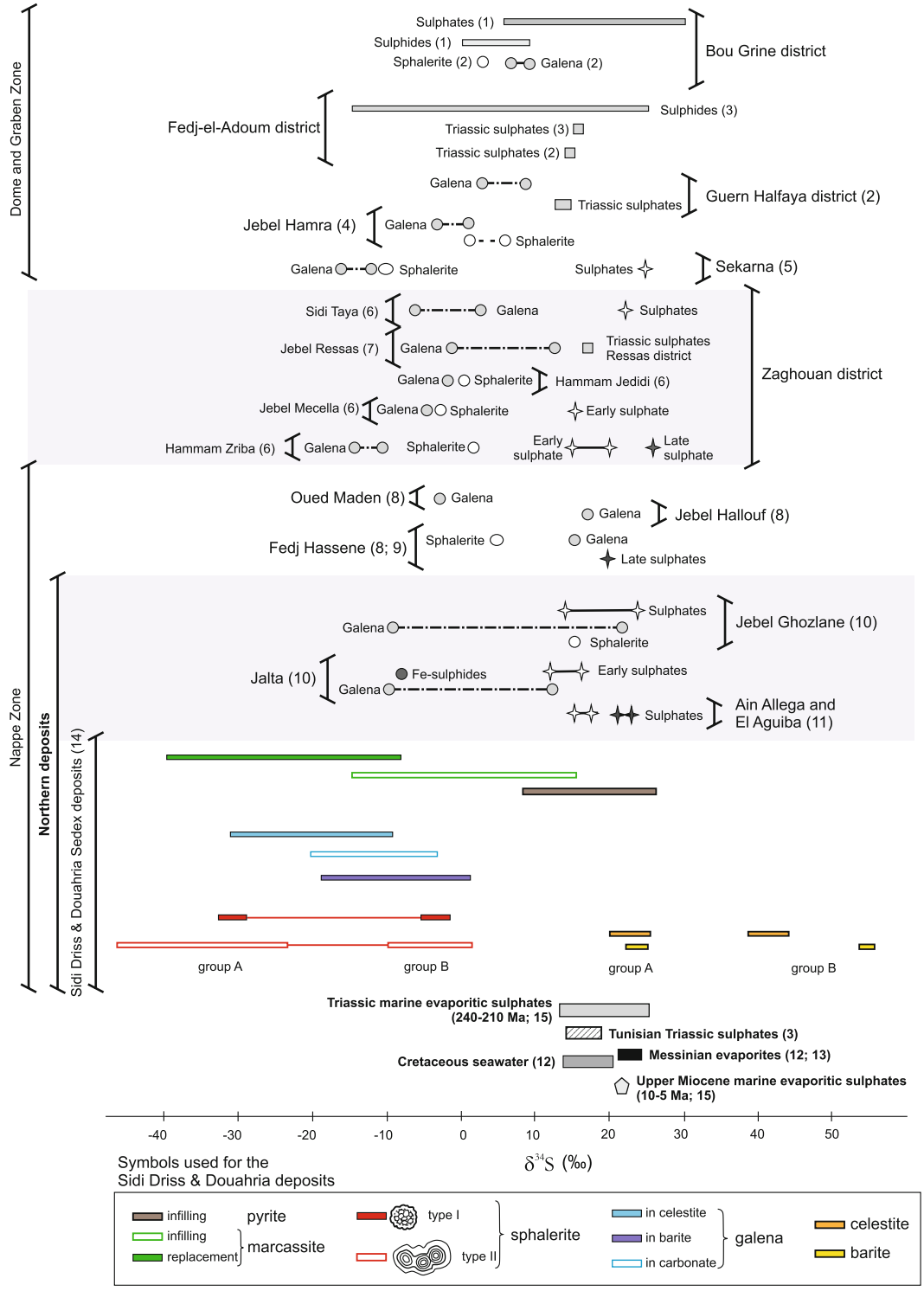

Fig. 4 Comparison of sulphur isotope values for ore deposits and occurrences in Tunisia. Data are from (*1*) Orgeval (1994), (*2*) Jemmali et al. (2013b), (*3*) Sheppard et al. (1996), (*4*) Bejaoui et al. (2013a), (*5*) Garnit et al. (2012), (*6*) Souissi et al. (2013), (*7*) Jemmali et al. (2011b), (*8*) Jemmali et al. (2013a), (*9*) Bejaoui et al. (2011), (*10*) Jemmali et al. (2011a), (*11*) Abidi et al. (2012), (*12*) Claypool et al. (1980), (*13*) Paytan et al. (1998), (*14*) Decrée et al. (2008a), (*15*) Kampschulte and Strauss (2004)

Lead isotopes: The lead isotopic compositions obtained on galena from the Sidi-Driss and Douahria deposits are variable: $15.670 < {}^{207}Pb/{}^{204}Pb < 15.674$; $18.772 < {}^{206}Pb/{}^{204}Pb < 18.812$; $38.848 < {}^{208}Pb/{}^{204}Pb < 38.888$ (Decrée et al. 2014). These values are intermediate between the Pb isotopic compositions of the sedimentary substrate and the local igneous rocks (Decrée et al. 2014), and suggest a mixing between these likely two lead sources.

3.3 The Sidi Driss and Douahria Genetic Model

Early celestite and barite and/or contemporaneous Messinian seawater are the most probable sulphur sources for the Pb–Zn sulphide deposits, as suggested by sulphur isotopic compositions. The likely involvement of Messinian seawater as a source of sulphur, the soft-sediment sedimentary structures within the sulphides, and early Fe–Mn enrichment of carbonates (implying early inception of hydrothermal circulation), collectively suggest that the Sidi Driss and Douahria Pb–Zn deposits formed during diagenesis of the host carbonate sediments. These aspects of the ore, together with the larger halo of the Fe–Mn carbonates compared to the base-metal sulphides and the Cd enrichment of sphalerite, support the assignment of these Pb–Zn ore deposits to the SHMS-Sedex type. Possible genetic analogs supporting this model include the stratabound and locally stratiform Pb–Zn deposits hosted in carbonate strata of the Irish orefield that are also attributed to predominantly Sedex-type mineralizing processes (Wilkinson 2014, and references therein).

The proposed Sedex Pb–Zn mineralization is attributed to thermally driven fluid circulation linked either to Messinian mafic magmatism and extensional conditions (Decrée et al. 2008a) and/or to the concealed igneous sill at shallow depth. In our model, this additional heat source enhanced and raised geothermal gradients, allowing the development of small, shallow, low-temperature convection cells. In that context, the structural discontinuities in the district (thrust sheet boundaries, magmatic contacts, and deformed plutons) likely served as the principal conduits (Decrée et al. 2008a).

4 Jb el Hamra Polymetallic (Ba–Sr–Zn–Pb–Hg) Deposits

The Jb el Hamra deposits have been described by Abidi (2011) and Abidi et al. (2010, 2012). A review is currently in preparation (Abidi et al. 2015). Accordingly, only a summary of the geology, mineralogy, and geochemistry of the deposits is given here.

4.1 Geological Setting

The three deposits of the small Jb el Hamra district are all hosted in Triassic rocks that form the antiformal core of the Jb el Hamra diapir (Fig. 1), close to the tectonic contact with Late Cretaceous marl (El Aguiba) or Paleocene black marl (Aïn Allega: Fig. 2, and El Arja). These deposits define two sub-districts, predominantly Hg-bearing to the west of the anticline (El Arja), and polymetallic (Ba–Sr–Zn–Pb) to the east (Aïn Allega and El Aguiba). The Jb el Hamra diapiric structure abuts to the north a (concealed) N100° E sinistral fault, which could be a splay of the Oued Belif N80° E lineament (Fig. 2).

The Triassic rocks in the extruded (diapiric) core of the antiform are representative of the "Transition Zone Formation" (TZF) that hosts Pb–Zn mineralization at a regional scale (Orgeval et al. 1986; Bouhlel 1993; Bouhlel et al. 2007). The TZF rocks within the Dome Zone diapirs are known to have formed during the first stage of halokinesis (Perthuisot 1978), which is Cretaceous in age. The "post-nappe stage of halokinesis," which is linked to Tortonian compression (Khomsi et al. 2009), corresponds here to reactivation of an older diapiric structure, rooted in the Triassic. This latter structure was likely guided by early reactivation of a NE-SW fault system in the pre-Mesozoic basement (the present-day GCSFZ). On the southeastern limb of the Jb el Hamra Triassic diapir, proximal

continental breccias and conglomerates are considered Late Tortonian to Early Messinian in age (Rouvier 1977), thus constraining the compressive deformation to Early to Middle Tortonian at the youngest.

4.2 Mineralization

Orebodies: The Triassic host rocks consist of alternating grey dolostone and stratiform (diagenetic) breccias, both of which are overprinted by zebra structures and mineralized breccias (Fig. 5a–d). Orebodies are stratabound, being 100–200 m long, up to 80 m wide, and having extensions at depth of less than ~100 m. The formation of zebra structures containing sulphates (mainly at El Aguiba) are followed paragenetically by dissolution breccias and associated veins hosting either sulphate or base-metal sulphide mineralization (Fig. 5c, d). At El Arja, the cinnabar mineralization is in breccias or spatially associated with crackle-breccias having a calcite matrix and, according to geochemical mapping (Gharbi 1977), is related to late NE-SW and NW-SE fracture systems.

Age of mineralization: The zebra structures are relatively flat (≤30° dip), regardless of the dip

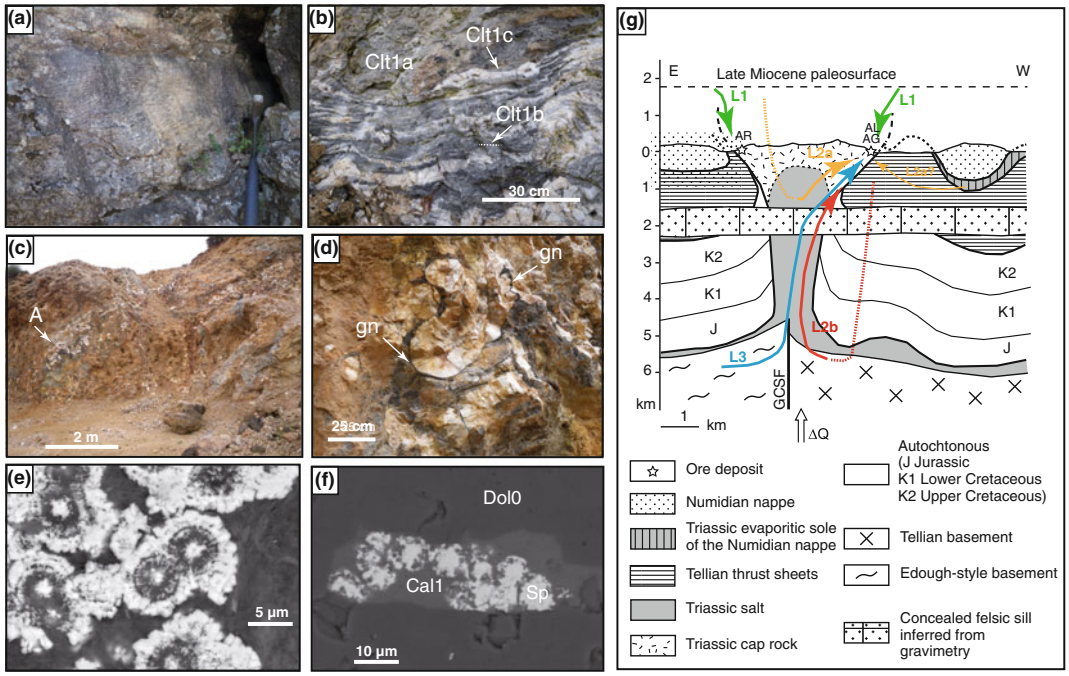

Fig. 5 Images of Jb el Hamra deposits including **a**–**d** field photographs, **e**, **f** SEM backscattered electron images, and **g** model for hydrothermal fluid circulation. **a** Zebra structure in Triassic dolostone at El Aguiba. **b** Zebra structure (*Clt1b*) obliterated by pseudo-zebra (*Clt1b*), both in matrix of *Clt1a* (celestite formed during stage IA, see text for further explanation). **c** Main zone at El Aguiba where concretions of celestite are present (*Cls1d*) (*arrow A*). **d** Detail of Fig. 5c showing concretic celestite (*Cls1d*) and late galena (*Gn*) as *black* stringers and disseminations (*arrows*). **e** Zoned sphalerite spherulites overprinting a siltite matrix (Aïn Allega, sample A10). **f** Sphalerite microspherules (*Sp*) in calcite lath (*Cal1*), interpreted as replaced anhydrite in a dolomitic matrix (*Dol0*) (Aïn Allega, sample AA22). **g** 2-D conceptual model for Jb el Hamra hydrothermal systems. Schematic cross section is for Late Tortonian time, prior to final exhumation and deposition of unconformably overlying Late Miocene continental sediments, based on Fig. 2 and seismological data from Khomsi et al. (2009). *L1, L2a, b, L3* fluid end-members and related trajectories; note that some fluid flow directions (L2 recharges, L1) are not in plane of section (see text for explanation). Abbreviations: *GCSF* Ghardimaou-Cap Serrat fault zone; *AL* Aïn Allega ore deposit; *AG* El Aguiba ore deposit; *AR* El Arja ore deposit; *ΔQ* heat advection

of the host rocks that typically is steep. Such flat structures are interpreted as tension joints resulting from hydraulic fracturing under a compressive or transtensional regime (e.g., Badoux et al. 2001; Nielsen et al. 1998; Lopez-Horgue et al. 2010); hence, these structures developed after—or more likely at the very end of—folding within the Jb el Hamra structure (i.e., not younger than Middle Tortonian, see above). On the other hand, close to the Aïn Allega deposit the Late Miocene breccias are rich in Triassic fragments, including celestite containing anhydrite remnants (Fainassi 2004). Combining these data, we thus infer that the beginning of the mineralizing process was late kinematic, i.e., Late Tortonian. At El Aguiba, however, a late stage of sulphate and galena deposition is spatially associated with contorted and subvertical E-W zones that are proposed as extension-related features, thus providing a link to the Late Tortonian-Early Messinian extensional event. It is therefore likely that the Jb el Hamra mineralizing systems were broadly coeval with those at Sidi Driss.

Paragenetic succession: Three principal stages of mineralization are superimposed on the TZF breccias. These include two stages (I, II) of alternating sulphate (IA, IIA) and sulphide (IB, IIB) deposition, and a final stage (III) of calcite ± marcasite ± As–Hg deposition. Each paragenetic stage is preceded by or associated with a tectono-hydrothermal event (hydraulic fracturing/brecciation). Relative importance of the different stages is, however, highly variable with respect to the Jb el Hamra. The sulphates are either Ba- or Sr-rich (Abidi et al. 2012), with a predominance of barite at Aïn Allega and celestite at El Aguiba. The main sulphide within stage IB is low-Fe sphalerite (≤0.16 wt% Fe) with variable Cd content (up to 0.43 wt%), and subordinate galena. Pyrite and marcasite are also part of the IB assemblage; rare occurrences suggest that these minerals postdate the base-metal sulphides. Sphalerite and galena form either replacements (of stage IA sulphates or dolostone in the Triassic breccias), or infillings of dissolution cavities. Replacement sphalerite mainly consists of coalescing microspherules (20–60 µm in diameter) (Fig. 5e). In some cases, microgranular sphalerite occurs within calcite laths, interpreted here as former anhydrite in the Triassic dolostone (Fig. 5f). Replacement galena is common as anhedral crystals (ca. µm to 30 µm), associated with sphalerite that seems to be overprinted. At Aïn Allega, the pervasive dissolution of the breccias formed cavities rimmed by replacement sulphides (alternating ribbons of botryoidal and banded sphalerite), which result both from coalescence of sphalerite microspherules, and granules, respectively. All of these features suggest a biomineralization origin for the sphalerite (cf. Kucha et al. 2010, and references therein). The banding is locally interrupted by more or less discontinuous, thin (a few tens of microns up to 250 µm) and asymmetric layers of galena. Corrosion textures suggest the replacement of the sphalerite by stage IIB galena.

Fluid inclusion data: Both primary and secondary FIs can be studied in celestite (stages I and II) and in late calcite. All are of the Lw type and yield similar microthermometric data. The trapped fluids are brines of variable salinity, resulting from a mixing process between a water-rich end-member (L1) and a series of saline end-members (L2) having variable Ca/Na ratios, from Na-rich (L2a) to Ca-rich (L2b). The Ca-rich fluid is attributed to Ca–Na exchange in a plagioclase-rich reservoir, whereas the Na-rich fluid resulted from halite dissolution. The Th values are variable, from 160 up to 230 °C, and are interpreted as recording isothermal mixing between the cooler L2 brines (200 ± 5 °C) and the hotter L1 diluted fluid (225 ± 5 °C, up to 245 ± 5 °C at El Arja), under fluctuating pressures (crack-seal mechanism) at an estimated depth of 1.8 ± 0.5 km. In addition, a few FI sets yield isothermal mixing trends, with Th values of ca. 140 °C. These data are thought to record rock-dominated fluid circulation and mixing at a temperature governed by the local reservoir.

Sulphur isotopes and sources of sulphur: Sulphur isotope measurements were performed in situ with an ion microprobe at CRPG in Nancy (see Decrée et al. 2008a, for experimental conditions). The $\delta^{34}S$ values of barite and celestite are ca. +16 ‰. A small group of celestite

samples has heavier values, up to +26.2 ‰. The $\delta^{34}S$ values for sphalerite range from +1.6 to +26.5 ‰. For galena, the data are bimodal and clearly distinguish the early stage IB galena (−28.4 to −14.8 ‰) from the late stage IIB galena (−6.9 to +8.2 ‰). The latter galena has systematically lower $\delta^{34}S$ values than the stage IA sphalerite that it replaces.

The sulphur isotopic composition of most of the Jb el Hamra sulphates (Fig. 4) is similar to that of Tethyan Triassic sulphate (including the Tunisian salt diapirs). This pattern indicates that these saline units are the likely source of the sulphur. The group of celestite samples that has heavier sulphur (up to +26.2 ‰) is thought to record Rayleigh fractionation. Given the observed textures, the sulphides have used sulphur from reduction of sulphate. This sulphate originates either from pre-existing sulphate crystals (as for the replacing sphalerite) or sulphate ions in solution. Deposition of the Jb el Hamra sphalerite by biomineralization must be due to BSR. However, the measured $\delta^{34}S$ compositions of this sphalerite, from +1.6 to +26.5 ‰, are inconsistent with the strong fractionation towards highly negative $\delta^{34}S$ associated with BSR ($\Delta^{34}S > -25$ ‰ in open systems; Machel et al. 1995), from a Triassic sulphate reservoir. This unexpected result may be explained using a "closed bacterial sulphate reduction process," as proposed by Bechtel et al. (1996) for the Bou Grine (Dome Zone) deposit. In contrast, the isotopically light sulphur of the stage IB galena was produced by BSR in an open system. The $\delta^{34}S$ values of the stage IIB galena are attributed to mixing between isotopically heavy sulphur recycled from the replaced sphalerite and a light end-member derived by TSR. Thus, the sulphide $\delta^{34}S$ data demonstrate that during mineralization (1) the mineralized cavities were alternatively closed and open; and (2) the temperatures fluctuated, allowing TSR and BSR to operate within the closed cavities, with T being most likely ≤80 °C (equivalent to ambient temperature in surrounding rocks). The paragenetic sequence, characterized by alternating sulphate (or carbonate) and sulphide stages, records the alternation of high-temperature fluid circulation with high fluid-rock ratios (sulphate or carbonate deposition) in an open system, and low-temperature fluid stagnation in a closed system (sulphide deposition).

Lead isotopes: Lead isotopes were measured in situ with an ion microprobe (at Centre de Recherches Pétrographiques et Géochimiques–CRPG in Nancy) on galena crystals. No significant differences exist in isotopic composition between the two galena generations. The lead isotope compositions are highly variable, with $^{207}Pb/^{204}Pb$ ratios ranging from 15.595 and 15.960, $^{206}Pb/^{204}Pb$ ratios from 18.673 to 18.985, and $^{208}Pb/^{204}Pb$ ratios from 38.330 to 39.396. These data display linear arrays in the $^{207}Pb/^{204}Pb$ versus $^{206}Pb/^{204}Pb$ and $^{208}Pb/^{204}Pb$ versus $^{206}Pb/^{204}Pb$ correlation diagrams (Fig. 7).

4.3 Genetic Model

Source of fluids: The fluids involved in the sulphate depositing systems are interpreted as a mixture of a low-salinity fluid (L1) and sodic- to sodic-calcic brines (L2a and b). The former fluid may have derived from the surface, as exchanged meteoric water or seawater. The L2a sodic brine must be sourced in Triassic salt, either within the core of the diapir or in the evaporitic sole of the nappe (at most a minor source) (Fig. 5g). The L2b Ca-rich brine is attributed to interaction between the L2a brine and a plagioclase-bearing rock (basement or felsic intrusive rocks). A third fluid end-member (L3) originating from an Edough-style basement must be invoked to explain part of the Pb isotopic signatures characterizing the mineralization at Jb el Hamra (see the discussion "Metal sources and connection with the basement" below).

Source of heat: Relatively high regional geothermal gradients are expected in collisional orogens. For example, gradients of 30–40 °C km^{-1} have been estimated for the west European Variscan fold-and-thrust belt during the late Carboniferous (Van Noten et al. 2011). Indeed, geothermal gradients in present-day central Tunisia range between 30 and 40 °C km^{-1}, with maximal values above 40 °C km^{-1} along major

crustal shear zones such as the Zaghouan fault (Ben Diah 1987). Similar heat flow may be expected along the Ghardimaou-Cap Serrat shear zone. In addition, within the study area, high transient geothermal gradients are likely to have been sustained by the Late Miocene magmatism (symbolized by heat advection ΔQ in Fig. 5g). On the other hand, given the likely development of biomineralization, the ambient temperature at ca. 2 km depth in the Jb el Hamra would have been 80 °C at most. Assuming an average 35 °C km^{-1} gradient during the Late Miocene, temperatures in the brine source would have been as high as 245–280 °C for L2b (at 7–8 km depth) or 105 °C for L2a (at 3 km depth) (Fig. 5g), and 280–320 °C, or 120 °C, respectively, if a higher temperature gradient of 40 °C km^{-1} is considered. Thus, temperatures up to 200 °C could easily have been attained for the mixed L2 brines, upon arrival at the site of mineralization. Steady-state circulation of such fluids may explain the transient heating to the 140 °C temperature inferred for the local reservoir rocks at the mineralization site. During the same stages, the hotter (≥220 °C) L1 fluid, such as the low-salinity variety can be explained by near-surface fluids heated by emplacement of the nearby Ras Rajel rhyodacite intrusion. Such fluids would likely have been channelled towards the mineralized sites along the E-W fault north of Jb el Hamra (Fig. 2).

5 The Jalta and Jebel Ghozlane Pb–Zn Deposits

In the northeastern part of the Nappe Zone (Fig. 1), other Pb–Zn deposits thought to be Upper Miocene in age are present at Jalta and Jebel Ghozlane (Jemmali 2011; Jemmali et al. 2011b, 2012, 2014).

The Jalta mine, where Pb–Zn mineralization is associated with post-nappe Miocene strata (Jemmali et al. 2014), has produced ~75,000 t of ore grading 59 % Pb. The enclosing basin is delimited by two major faults: the NE-SW Ras El Korane-Thibar fault in the northwest, and a N-S fault on the eastern side. In the northwestern part, the NE-SW-trending sinistral strike-slip faults constitute a mylonite zone, where Triassic strata —made of a chaotic breccia (shale, dolomitic limestone, and gypsum)—is in contact with Miocene to Pliocene continental sedimentary rocks. The latter comprise conglomerate (with altered basalt clasts), intercalated with lenticular dolomitic limestone, shale, and gypsum (Jemmali et al. 2014). The Triassic breccia has undergone advanced argillic hydrothermal alteration expressed as powdery white alunite, which is considered to have formed in a steam-heated environment (Jemmali et al. 2014). Dextral strike-slip faults that trend NW-SE with an extensional component represent other major structures. The mineralization occurs as infillings of voids, breccia cement, veins, stockworks, and disseminations at the contact between Triassic and Mio–Pliocene strata. Ore is hosted mainly by Triassic dolostone; minor deposits occur in Miocene conglomerate. Galena and sphalerite show banded or colloform textures or are disseminated in the matrix, and are associated with pyrite and barite. Jordanite is also present in the deposit.

The Jebel Ghozlane mine produced ~6,680 t of Pb and 53,000 t of Zn. Lead-zinc mineralization, hosted within Triassic dolostone and Lower Eocene dolomitic limestone, occurs as veins, dissemination, and breccia cement. The contact between these units reflects either NNE-SSW dextral strike-slip faults or thrust-sheet boundaries (Jemmali et al. 2012). The early stage of mineralization formed celestite, barite, dolomite, galena, and sphalerite, followed by disseminated galena and then late calcite. Sphalerite occurs as zoned crystals or spherulites and is seemingly partly replaced by the early celestite (Jemmali et al. 2012).

Fluid inclusion data: Fluid inclusions were studied in celestite from the Jebel Ghozlane deposit. The Th values vary from 160 and 180 °C and salinities from 15 to 22 wt% NaCl equiv. (Jemmali et al. 2013a, b). Homogenization of the gaseous CO_2-rich primary fluid inclusions into vapor phase supports low trapping pressures and hence formation of the Jebel Ghozlane deposit at relatively shallow depth, below 800 m under the

paleosurface (Jemmali et al. 2012). A mixing between saline fluids originating from basinal brines and a gaseous CO_2-rich fluid has been proposed (Jemmali et al. 2012).

Sulphur isotopes and sources of sulphur: The $\delta^{34}S$ values obtained on sulphates from both deposits (+12.2 to +16.2 ‰ at Jalta; +14.3 to +19.4 ‰ at Jebel Ghozlane; Fig. 4) are consistent with derivation of the sulphur from marine sulphate, possibly Triassic. The large range of $\delta^{34}S$ values for the sulphides (−10 to +12.5 ‰ at Jalta; −9.1 to +22.1 ‰ at Jebel Ghozlane) suggests sulphate reduction by BSR and/or TSR (Jemmali et al. 2011b). In terms of stable isotope data, the light $\delta^{13}C$ values of the late calcite suggest an organic source for part of the carbon, whereas the $\delta^{18}O$ values of +24.7 to +24.8 ‰ (Jemmali et al. 2011b) suggest buffering of the mineralizing fluids by the carbonate host rocks.

Lead isotopes: Both the Jalta and Jebel Ghozlane deposits display relatively homogeneous Pb isotope compositions ($^{206}Pb/^{204}Pb$ = 18.702–18.823, $^{207}Pb/^{204}Pb$ = 15.665–15.677, $^{208}Pb/^{204}Pb$ = 38.725–38.875). This pattern suggests a deep-seated source for the lead. Such source is also supported by the presence of jordanite [$Pb_{14}(As,Sb)_6S_{23}$] at Jalta (Jemmali et al. 2014). Indeed, in the Nappe Zone, As and Sb halos are closely linked to major shear zones, suggesting a deep source for these elements and accompanying Pb.

6 Discussion

Compared to other Pb–Zn deposits of Tunisia, the Nappe Zone deposits display several distinguishing characteristics, as outlined in the following comparison.

6.1 Paragenesis and Ore Texture

Regardless of deposit type, the Pb–Zn ores at Sidi Driss and Douahria, Jb el Hamra, Jalta, and Jebel Ghozlane share common features in terms of paragenesis and ore texture. Within all of these deposits, early stages of mineralization comprise sulphates (celestite and/or barite) that commonly replace carbonate strata. Zebra textures that formed during this stage may suggest a late-kinematic inception of the mineralizing events (as suggested at Jb el Hamra, see above). Later, the sulphates (and host carbonates) were replaced by sulphides. Sphalerite is most common as microspherules or granules a few microns in diameter that locally are coalesced to form ribbons and colloform/botryoidal concretions (Decrée et al. 2008a; Abidi et al. 2010; Jemmali et al. 2011b). These features are interpreted as products of biomineralization, and together with the characteristically low $\delta^{34}S$ values for the sulphides (e.g., −43.9 to +1.2 ‰ for the sphalerite at Sidi Driss and Douahria), point to the involvement of BSR as the sulphate reduction process, at least for some of the mineralization. Galena replaces host carbonates, sulphates, and sphalerite, or fills voids. It also forms disseminations and anhedral to euhedral crystals. Considering the fractionation in terms of $\delta^{34}S$ compositions of galena (e.g., $\delta^{34}S$ values heavier than ca. −10 ‰ at Sidi Driss and Douahria), it appears that its formation is mostly attributed to TSR. A late discrete hydrothermal event is observed in several of these deposits, expressed as As-rich galena (Sidi Driss, Jalta) or jordanite (Jb el Hamra, Jalta), resulting from the interaction of galena with an As-rich fluid. Late As-rich sulphide veins are also encountered in the Pliocene Tamra Fe deposit (Decrée et al. 2008b), suggesting that this event must be considered Pliocene in age.

6.2 Fluids and Temperature Fluctuations

Within the Nappe Zone deposits, FI data for the causative hydrothermal fluids display large salinity variations (Fig. 6a). Such variations are indicative of fluid mixing between a calcic ("basinal") brine and a less-saline fluid, likely derived from meteoric water (for instance at Jb el Hamra). Similar conclusions may be drawn for the deposits within the Dome (Graben) Zones (Fig. 6b, c), for which the lack of involvement of

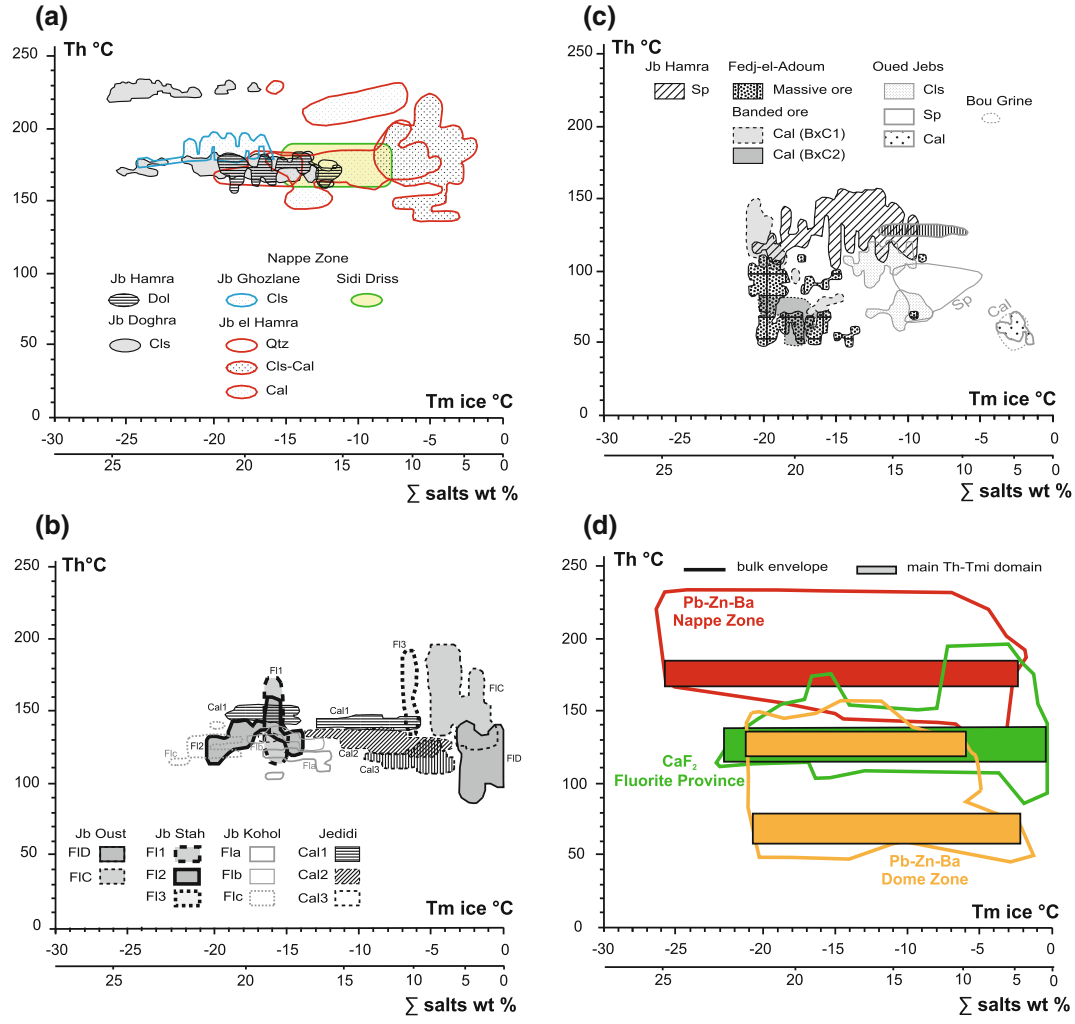

Fig. 6 Comparison of fluid inclusion data for deposits in Nappe Zone and Dome (Graben) Zones in terms of Th-Tmi/bulk salinity plots. Data are compiled from literature, using Tmi-salinity relationship of Steele-McInnis et al. (2011) where necessary. **a** Nappe Zone: Jb Ghozlane (Jemmali et al. 2012), Jb el Hamra (Abidi et al. 2015), Sidi-Driss (this study); comparable data: Jb Doghra (Souissi et al. 2007), Jb Hamra (Bejaoui et al. 2013a). **b** Fluorite province: Jb Kohol (Bejaoui et al. 2013b), Jb Oust (Souissi et al. 1997), Jb Stah (Souissi et al. 1998, 2010); calcite data from Jedidi (Charef et al. 2009). **c** Domes Zone (Pb–Zn–Ba): Bou Grine (Orgeval 1994, in Bejaoui et al. 2014), Fedj-el-Adoum (Charef and Sheppard 1991), Jb Hamra (Bejaoui et al. 2013a), Oued Jebs (Bejaoui et al. 2014). **d** Synthetic comparative diagram, showing both bulk envelopes of all data and main trends for each group from Figs. **a**, **b** and **c**. Abbreviations: *Cal* calcite; *Cls* celestie; *Dol* dolomite; *Fl* fluorite; *Qtz* quartz; *Sp* sphalerite

saline meteoric water is particularly evident for the contained fluorite deposits.

By comparison with the Dome Zone deposits, those of the Nappe Zone present two main differences. First, the temperatures recorded by FIs in the Nappe Zone deposits are higher overall. As seen in Fig. 6d, the homogenization temperatures delineate three sets of deposits, with Th values in the range of 140–240 °C, with a clear mode at 170–180 °C. Data for celestite from the Doghra deposit (Dome Zone) and early dolomite from the Jebel Hamra deposit (Graben Zone) also fall

within this predominant temperature range. In contrast are lower homogenization temperatures of 90–200 °C (mostly 120–140 °C) determined for MVT deposits of the Fluorite province, which are controlled by the crustal-scale Zaghouan Fault. Similar observations can be made for calcite from the Jedidi deposit (Charef et al. 2009). The Dome Zone Pb–Zn–Ba deposits display the larger range in homogenization temperatures, from less than 50–160 °C, and two main trends, one having the same 120–140 °C Th range as the fluorite deposits, and the other at lower temperatures of 60–80 °C. The highest temperatures recorded in the Dome (Graben) Zone deposits are compatible with heating of deeply sourced fluids under the 30–35 °C km^{-1} geothermal gradients recorded at the regional scale in central Tunisia (Ben Diah 1987). Where biomineralization textures are present in these deposits (e.g., Bou Grine), the associated gangue minerals contain low-Th FIs. On the second hand, the distinctive sphalerite textures and sulphur isotopic compositions demonstrate in situ BSR processes in the Nappe Zone deposits, and consequently low depositional temperatures, at less than 80 °C (i.e., lower Th range for the Dome Zone deposits). In contrast, TSR is the likely process for galena deposition, requiring temperatures above 150 °C, consistent with the FI data. Because textural relationships indicate alternating sphalerite and galena deposition, a cyclic behavior of the hydrothermal system is invoked, with alternating influx of relatively cold and warm fluids. Felsic (or mafic) magmatism was likely involved in heating the fluids, as illustrated for instance at Jb el Hamra. In this respect, the presence of concealed igneous bodies may be suspected in the Jalta and Jebel Ghozlane areas.

The Doghra celestite deposit in the Dome Zone and the Jebel Hamra Pb–Zn–Ba deposit in the Graben zone (Fig. 6a) remain enigmatic. Saline and pure gaseous volatile FIs coexist within the Doghra celestite. The latter type of FI, containing CO_2 and CH_4 (inferred from microthermometric measurements; Souissi et al. 2007), likely developed from over-maturation of a petroleum-bearing source rock. In the Jebel Hamra deposit, the high Th values are restricted to early saddle dolomite, typically deposited in zebra structures (Bejaoui et al. 2013a). The Th values of the sphalerite (110–152 °C; Bejaoui et al. 2013a) are in the range that characterizes deposits of the Dome (Graben) Zone (Fig. 6c).

6.3 Metal Sources and Connection with the Basement

For the Sedex deposits of the Nefza district (as for other mineralization type in the area), two main metal sources are proposed. According to the data of Decrée et al. (2013, 2014), one end-member source is the succession of sedimentary rocks within the Nappe Zone (C end-member in Fig. 7), whereas the second source includes the igneous rocks of the Nefza province (D end-member in Fig. 7). Figure 7 shows that many lead isotope compositions for the Zn–Pb deposits in northern Tunisia (from the Nappe and Dome zones), being spatially related to Neogene felsic rocks, or not, plot on a mixing trend between these two end-members, at near-constant $^{207}Pb/^{204}Pb$ values. This trend is also evident for the Jalta and Jebel Ghozlane deposits. Moreover, the D end-member coincides with the lead isotope composition of a series of deposits occurring in the Atlasic foreland in Algeria and Tunisia. Therefore, we propose that this end-member corresponds to the basement of the Atlasic foreland, from which originated (at least in part) the felsic magmas. Note also that the C–D line lies close to the evolution curve for Variscan crust, the likely basement present in the Atlasic foreland.

For the Jb el Hamra deposit, the lead isotope values define a linear array that is interpreted as a mixing trend between a highly radiogenic end-member A and a less radiogenic end-member B. Dispersion of the data around this mixing trend may reflect contributions from the sedimentary country rocks (end-member C) and the felsic igneous rocks (end-member D), similar to the scenario proposed for the Nefza Sedex deposits. Nevertheless, the A–B trend requires another source. End-member A represents the contribution of a highly radiogenic

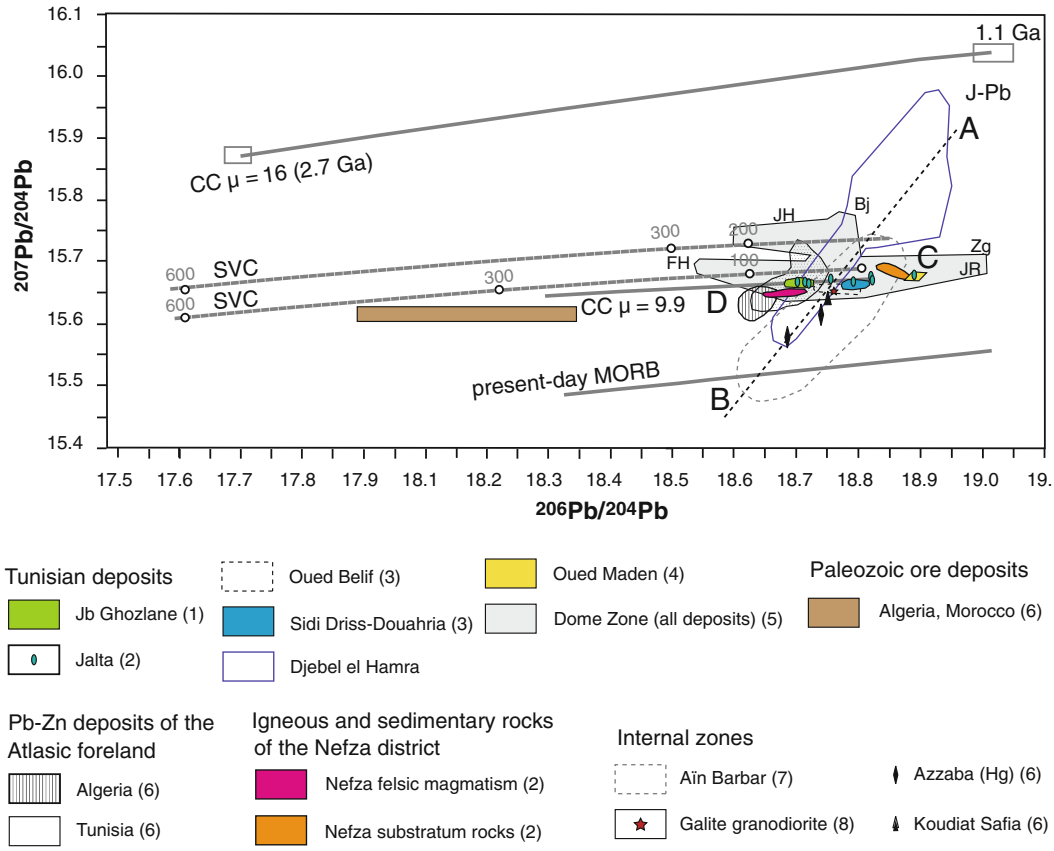

Fig. 7 Comparison of lead isotope data from northern Tunisia ore deposits (Jalta, Jb el Hamra, Jb Ghozlane, Sidi-Driss,) with other Pb–Zn–(F) deposits of Tunisia (Oued Maden, Dome Zone). Also shown are data for some Algerian Cenozoic deposits (Aïn Barbar, Azzaba, Koudiat Safia) and Paleozoic deposits (mainly VMS) from Algeria and Morocco. Abbreviations for Dome Zone deposits: *Bj* (Boujabeur), *FH* (Fedj-el-Adoum), *JH* (Jb Hamra), *JR* (Jb Ressas), *Zg* (Zaghouan); they are indicated as "end-members" of the Dome Zone deposits (*grey field* in the figure). Other abbreviations: *CC* Continental crust; *J-Pb* J-type lead; *SVC* evolution curves for South Variscan crust in Europe (Caron 1994; see text for explanation about evolution curves). *Line A–B* represents the basement of the "Edough style"; *C* and *D* represent sedimentary country rocks and felsic igneous rocks, respectively. Data are from: (*1*) Jemmali et al. (2012); (*2*) Jemmali et al. (2011a, b, 2014); (*3*) Decrée et al. 2013; (*4*) Jemmali et al. (2013b); (*5*) Bejaoui et al. (2013a), Jemmali et al. (2011a, 2013a), Skaggs (2010), Souissi et al. (2012, 2013); (*6*) Touahri (1987); (*7*) Marignac et al. (2016, this volume); and (*8*) Juteau et al. (1986). *Number suffixes* refer to data references

"J-type" lead (Russell and Farquhar 1960), and may be modelled by Neoproterozoic (ca. 1 Ga) extraction of a J-type lead that evolved from anomalously U-rich Neoarchean continental crust. End-member B is evidently related to a mafic source. Lead isotope data for many metal deposits occurring in the Internal Zone of nearby northeastern Algeria plot along the same trend. More particularly, at Aïn Barbar (Marignac et al. this volume), the lead source is found within the Edough Internal Massif, which contains Pan-African metagreywacke and huge amphibolite bodies; these rocks correspond to the A and B end-members, respectively (Marignac et al. this volume). One can therefore further interpret the A–B trend and propose that the source of metals for the Jb el Hamra deposit is mainly in a basement of the "Edough style." Involvement of this source is made possible through the juxtaposition —along the Ghardimaou-Cap Serrat main

fault—of an Internal Zone "Edough style" basement massif, to the west, with a Tellian Zone Variscan basement, to the east (Fig. 1). This proposed setting in turn implies the involvement of another fluid that evolved from this "Edough style" basement (L3 fluid), within the Jb el Hamra hydrothermal systems. In that context, control by the regional shear zones and lineaments on the hydrothermal plumbing systems is considered significant.

6.4 Sulphur Sources

At Sidi Driss and Douahria, $\delta^{34}S$ values of the sulphate matrix hosting the Sedex Pb–Zn mineralization are in the range of contemporaneous (Messinian) seawater (Fig. 4). Even if Messinian seawater is the most likely (or at least predominant) sulphur source for the deposits, a deeper source of sulphate (e.g., Triassic sulphates beneath the Oued Belif structure) must also be considered. In contrast, at Jb el Hamra, the $\delta^{34}S$ values of early barite and celestite are suggestive of a Triassic sulphate source, as is the case for Jalta and Jebel Ghozlane. All of these deposits are mainly hosted within—or located at the contact with—Triassic strata (Jemmali et al. 2011b). Yet, the immediate source of the sulphide sulphur is (mainly, if not wholly) the reduction of pre-existing sulphate. Such a derivation of sulphur from Triassic sulphate that hosts (or is near) the Pb–Zn mineralization is also compelling for many metal deposits in the Dome and Graben Zones (Fig. 4), as in the districts of Bou Grine, Fedj-el-Adoum, and Zaghouan. However, within these deposits the incorporation of earlier sulphate as an intermediate sulphur source is considered unlikely.

6.5 Age of Pb–Zn Mineralization

As described above, all of the metal deposits in the Tellian (Nappe) Zone formed at the turning point between late collisional events (Late Tortonian) and inception of the Early Messinian extensional regime. For some deposits (e.g., Jb el Hamra), mineralization encompassed both regimes. This setting is assigned also to the many Pb–Zn–(Cu–Sb–Hg–Ag–Au) deposits and showings located along, or in the vicinity of, the NE-SW Ghardimaou-Cap Serrat sinistral shear zone (e.g., Oued Maden, Jebel Hallouf, and Fedj Hassene), related to transtensional reactivation of the shear zones and faults during the last phase of the Alpine orogeny (Upper Miocene as suggested by Jemmali et al. 2013a).

Outside of the Nappe Zone, ages of the Pb–Zn–Ba–F deposits remain controversial. Owing to a systematic spatial association between the deposits and Triassic diapiric extrusions (Rouvier et al. 1985), one could relate the mineralization to the extrusion processes. In that case, the ore-forming fluids would be delivered onto or near the surface at the time of diapiric piercing, or close thereafter (Sheppard et al. 1996, and references therein). As diapiric salt extrusion is documented in Tunisia from the Albian (Ben Slama et al. 2009) to the Latest Cretaceous (Ben Mehrez et al. 2009); by this model the ore-forming event would have occurred no earlier than latest Cretaceous (or Early Paleocene). Another way to explain the relationship between the diapirs and the Pb–Zn–Ba–F deposits is to consider the latter as MVT mineralization that formed by typical post-collisional gravity-driven fluid flow (e.g., Leach et al. 2001, 2005). This model implies a Late Serravallian to Tortonian age for the Pb–Zn–Ba–F mineralization (Perthuisot and Rouvier 1996; Bouhlel 2005). Unfortunately, there is no direct published geological evidence for the age of these deposits. An indirect way, however, is to consider time-space relationships between the deposits and oil migration. On one hand, it has long been known that oil-bearing FIs occur in fluorite of nearly all Tunisian fluorite deposits. These occurrences are interpreted as reflecting coeval migration of oil and metal-bearing fluids (Bouhlel et al. 1988; Bejaoui et al. 2013b). On the other hand, several geochemical studies conducted on the Bou Grine Pb–Zn–Ba deposit point to the contemporaneity of sulphate reduction and oxidation of migrated oil, mediated by sulphate-reducing bacteria (Montacer et al. 1988; Bechtel et al. 1996, 1998).

Consequently, assuming this contemporaneity is valid, dating migration of the oil also dates (at least in part) ore formation. Three main oil-bearing units are present in northern and central Tunisia, namely the Fahdene (Albian), the Bahloul (Cenomanian-Turonian boundary), and the Bou Dabbous (Ypresian) Formations (e.g., El Eleuchi et al. 2002; Belhadj et al. 2015). The oldest could have been productive starting in the Paleocene, but peak oil migration did not occur before Early Miocene time. The two younger formations entered the oil window only in the Late Miocene, which is the likely timing for oil migration (Bedir et al. 2001; Racey et al. 2001). Indeed, Late Miocene sedimentary reservoirs contain oil in the Cap Bon area (Bedir and Khomsi 2015). Collectively, these data strongly support a Late Serravallian-Tortonian timing for the mineralizing events, as proposed earlier by Perthuisot and Rouvier (1996) and Bouhlel (2005). However, the possibility remains that the ore-forming processes were not unique to one time period. Indeed, within the similar Ba–Pb–Zn–F Aïn Kahla deposit of the Hodna Mountains in Algeria, Boutaleb (2000) demonstrated that formation of the stratabound barite (with Pb and Zn) was coeval with Triassic diapiric piercing (likely Late Cretaceous), although the fluorite (with characteristic oil-bearing FIs) formed later, after the Burdigalian (and prior to Early Pliocene). Clearly, more work is needed to definitely constrain the timing of Pb–Zn and polymetallic ore formation in the Dome (and Graben) Zones.

6.6 Geodynamic Context

The geodynamic context prevailing during the Late Miocene in the Tellian-Nappe zone is the unifying factor to the great diversity of deposit types (Sedex, MVT, IOU, etc.). Several key aspects of the mineralization, broadly interconnected, are dependent on the geodynamic context: (1) High geothermal gradients (≥35 °C km^{-1}, e.g., Jb el Hamra area) are expected in the late stages of collisional orogens and can contribute greatly to circulation of mineralizing hydrothermal fluids; (2) In the Nefza district and at Jb el Hamra, hydrothermal activity was modulated and reinforced by recurrent magmatism. In that way, the felsic igneous rocks were emplaced during the late Alpine compression/transtensional phase (some connected to concealed magmatic sills at very shallow depth; Fig. 2; Jallouli et al. 2003), while basaltic dikes were related to Messinian extension; these rocks also constitute potential metal sources for the mineralizing systems; (3) Post-collisional magmatism is specifically related to development of the Maghreb indenter that acted as a locked zone during the regional compression phase (Piqué et al. 2002), which induced lithospheric breaks. The Alpine orogeny is therefore responsible for the (transtensional) reactivation of deep shear zones and associated lineaments inherited from the Variscan orogeny (also possibly from the Pan-African orogeny; Piqué et al. 2002). These structures controlled both magmatism and hydrothermal fluid circulations within the Nappe Zone; (4) More locally, structural discontinuities induced by these events (e.g., thrust-sheet boundaries, igneous contacts, deformed diapirs) served as additional conduits for hydrothermal fluid circulation. These processes led to metal enrichment of the fluids through exchange with regional lithologies, including the basement rocks.

7 Conclusions

The synthesis presented here highlights the unity of Sedex and other Pb–Zn/polymetallic deposits in the Nappe Zone, namely the Jb el Hamra, Jalta, and Jebel Ghozlane deposits. All of these deposits formed within a narrow time span, ranging from the late collisional phase during the Late Tortonian, to the extensional regime during the Early Messinian. Relationships to hydrothermal circulation are expressed by FI data for alternating influx of high (>40 °C) and low (<80 °C) temperature fluids, the latter leading to typical bacterially mediated deposition of sphalerite microspherules through BSR. The main source of sulphur for the sulphides in these deposits is pre-existing sulphates. The contemporaneous

reduction of marine sulphates by anaerobic oxidation of methane, as described by Johnson et al. (2004, 2009) cannot be ruled out.

For the Sedex Pb–Zn deposits, sedimentary and igneous rocks of the province represent the two main metal sources involved in the mineralization. It is worth mentioning that the Pb isotopic arrays for most of the deposits within the Nappe and the Dome zones suggest the same mixing trend, even though these deposits are not associated spatially with Late Miocene igneous rocks. These arrays are close to the evolution curve for Variscan crust, which is the likely basement of the foreland and therefore a probable source of metals for the Pb–Zn mineralization. In the case of the southernmost MVT-type deposits, this basement and the overlying sedimentary formations would have been leached by gravity driven fluid circulation, coeval with development of the fold-and-thrust belt during the Langhian-Tortonian compression (Rouvier et al. 1985; Bouaziz et al. 2002; Bouhlel 2005).

Coeval with this compressional event, the deep shear zones and associated lineaments inherited from the Variscan orogeny were reactivated by transtensional processes (Piqué et al. 2002). A thinned lower crust and more proximal Moho (Mickus and Jallouli 1999; Jallouli and Mickus 2000) within the Nappe Zone, compared to the southernmost domains, favored the ascent of magmas and shallow-level emplacement, as well as the inception of high geothermal gradients along these crustal shear zones. Subsequently, thermally driven fluid circulations were enhanced in that area. It is also likely that such structures constituted an efficient plumbing system to transport metalliferous fluids from the basement, as demonstrated by the presence of many Pb–Zn–(Cu–Sb–Hg–Ag–Au) deposits and showings along or in the vicinity of the NE-SW Ghardimaou-Cap Serrat shear zone. At Jb el Hamra, the contribution of a more internal "Edough style" basement as another metal source was facilitated by the juxtaposition of this basement (to the west) and the Tellian Zone Variscan basement (to the east), along the Ghardimaou-Cap Serrat shear zone. Finally, these metalliferous high temperature fluids were affected by near-surface processes, being mixed with shallow, low-salinity low-temperature fluids, resulting in the diverse mineralization of the region.

Acknowledgments We especially thank all of the collaborators who have worked with us on research themes focused on ore deposits in northern Tunisia. The various Institutes and Ministries that have funded this research in Belgium, France, and Tunisia, are gratefully acknowledged. We also thank the mining companies that facilitated access to the mines for our studies. Finally, Mohammed Bouabdellah and John Slack are warmly thanked for their invitation to publish our works as a chapter of this book and their careful reviews of the manuscript.

References

Abidi R (2011) Etude minéralogique et paragénétique des minéralisations à Pb, Zn, (Sr, Ba) du district de Aïn Alllega-Kef Ressas (para-autochtone des Nefza, NW de la Tunisie). Unpubl PhD Thesis, Carthage University, Tunisia, 211 pp

Abidi R, Slim-Shimi N, Somarin A, Henchiri M (2010) Mineralogy and fluid inclusions study of carbonate-hosted Mississippi Valley-type Ain Allega Pb-Zn-Sr-Ba ore deposit, northern Tunisia. J Afr Earth Sci 57:262–272

Abidi R, Slim-Shimi N, Hatira N, Somarin A (2011) Genesis of celestite-bearing cap rock formation from the Ain Allega ore deposit (northern Tunisia): contributions from microthermometric studies. Bull Soc Géol France 182:427–435

Abidi R, Slim-Shimi N, Marignac C, Hatira N, Gasquet D, Renac C, Soumarin A, Gleeson S (2012) The origin of sulfate mineralization and the nature of the $BaSO_4$–$SrSO_4$ solid-solution series in the Ain Allega and El Aguiba ore deposits, northern Tunisia. Ore Geol Rev 48:165–179

Abidi R, Marignac C, Deloule E, Hibsch C, Gasquet D, Hatira N, Slim Shimi N (2015) The Jb el Hamra deposit (northern Tunisia): a diapir-hosted polymetallic (Ba-Sr-Pb-Zn-Hg) mineralization linked to Late Miocene magmatism. Submitted to Econ Geol

Albidon Limited (2004) Exploration report. http://www.albidon.com/documents/Nefza2.pdf

Badgasarian GP, Bajanik S, Vass D (1972) Age radiométrique du volcanisme néogène du Nord de la Tunisie. Notes Serv Géol Tunisie 40:79–85

Batik P (1980) Carte géologique de la Tunisie; feuille n° 11: Hédil. Service Géologique, Office National des Mines, scale 1:50,000; 1 sheet

Badoux V, Moritz R, Fontboté L (2001) The Mississippi Valley-type Zn-Pb deposit of San Vicente, Central Peru: an Andean syntectonic deposit. In: Piestrzynski et al. (eds) Mineral deposits at the beginning of the 21th Century. Proceed Joint 6th Biennial SGA-SEG Mtg, Krakow, Poland, pp 191–195

Bechtel A, Shieh Y-N, Pervaz M, Püttmann W (1996) Biodegradation of hydrocarbons and biogeochemical sulphur cycling in the salt dome environment: inferences from sulphur isotope and organic geochemical investigations of the Bahloul Formation at the Bou Grine Zn/Pb ore deposit, Tunisia. Geochim Cosmochim Acta 60:2833–2855

Bechtel A, Pervaz M, Püttmann W (1998) Role of organic matter and sulphate-reducing bacteria for metal sulphide precipitation in the Bahloul Formation at the Bou Grine Zn/Pb deposit (Tunisia). Chem Geol 144:1–21

Bedir M, Khomsi S (2015) Basin dynamics and sedimentary infilling of Miocene sandstone reservoir systems in eastern Tunisia African margin. EGU General Assembly, Vienna, 2015. http://adsabs.harvard.edu/abs/2015EGUGA.1715122B

Bedir M, Boukadi N, Tlig S, Ben Timzal F, Zitouni L, Alouani R, Slimane F, Bobier C, Zargouni F (2001) Subsurface Mesozoic basins in the central Atlas of Tunisia: tectonics, sequence deposit distribution, and hydrocarbon potential. AAPG Bull 85:885–907

Bejaoui J, Bouhlel S, Barca D, Braham A (2011) Le champ filonien à Zn-(Pb, Cu, As, Hg) du district minier de Fedj Hassène (nord-ouest de la Tunisie): minéralogie, éléments en traces, isotopes du soufre et inclusions fluides. Estud Geol 67:5–20

Bejaoui J, Bouhlel S, Cardellach E, Canals A, Perona J, Piqué A (2013a) Mineralization and fluid inclusion studies of the Aptian carbonate-hosted Pb Zn Ba ore deposits at Jebel Hamra, central Tunisia. J Geochem Explor 128:136–146

Bejaoui J, Bouhlel S, Barca D (2013b) Geology, mineralogy and fluid inclusions investigation of the fluorite deposit at Jebel Kohol, northeastern Tunisia. Period Mineral 82:217–237

Bejaoui J, Bouhlel S, Sellami A, Braham A (2014) Geology, mineralogy and fluid inclusion study of Oued Jebs Pb–Zn–Sr deposit: comparison with the Bou Grine deposit (diapirs zone, Tunisian Atlas). Arab J Geosci 7:2483–2497

Belguith Y, Geoffroy L, Rigane A, Gourmelen C, Ben Dhia H (2011) Neogene extensional deformation and related stress regimes in central Tunisia. Tectonophys 509:198–207

Belhadj A, Saidi M, Ben Jrad M, Soussi M, Riahi S, Bouazizi I, Saadani B (2015) The organic geochemistry of source-rocks, bitumens, asphalts and oil stains from northern Tunisia. In: 77th EAGE conference and exhibition 2015, source rocks and petroleum systems I. doi:10.3997/2214-4609.201413144

Ben Diah H (1987) The geothermal gradient map of central Tunisia: comparison with structural, gravimetric and petroleum data. Tectonophyscis 142:99–109

Ben Mehrez F, Kacem J, Dlala M (2009) Late Cretaceous synsedimentary diapirism of Bazina-Sidi Bou Krime Triassic evaporites (northern Tunisia): geodynamic implications. Comptes Rendus Geosci 341:78–84

Ben Slama M-M, Masrouhi A, Ghanni M, Ben Youssef M, Zargouni F (2009) Albian extrusion evidences of the Triassic salt and clues of the beginning of the Eocene Atlasic phase from the example of the Chitana-Ed Djebs structure (N Tunisia): implication in the North African Tethyan margin recorded events, comparisons. Comptes Rendus Geosci 341:547–556

Bellon N (1976) Séries magmatiques néogènes et quaternaires du pourtour de la Méditerranée occidentale comparées dans leur cadre géodynamique : implications géodynamiques. Unpubl PhD Thesis, Université Paris-Sud/Orsay, France, 363 pp

Bodnar RJ (2003) Introduction to aqueous-electrolyte fluid inclusions. In: Samson I, Anderson A, Marshall DD (eds) Fluid inclusions: analysis and Interpretation. Mineral Assoc Canada Short Course Notes, vol 32, pp 81–100

Bouaziz S, Barrier E, Soussi M, Turki MM, Zouari H (2002) Tectonic evolution of the northern African margin in Tunisia from paleostress data and sedimentary record. Tectonophysics 357:227–253

Bouhlel S (1993) Gîtologie, minéralogie et essai de modélisation des minéralisations à F-Ba-Sr-Pb-Zn-(S) associées aux carbonates (jurassiques et cretacés) et aux diapirs triasiques: gisements de Stah-Kohol. Zriba-Guebli, Bou Jaber et Fej Lahdoum (Tunisie Septentrionale). Unpubl PhD Thesis, Tunis University, Tunisia, 293 pp

Bouhlel S (2005) Carbonate-hosted Mississippi Valley-type Pb-Zn deposits in Tunisia (eastern Atlasic belts). In: Mao J, Bierlein FP (eds) Mineral deposit research: meeting the global challenge. Proceedings of 8th Biennial SGA Mtg, Beijing, China, pp 19–22

Bouhlel S, Fortuné JP, Guilhaumou N, Touray JC (1988) Les minéralisations stratiformes à F-Ba de Hammam Zriba, Jebel Guébli (Tunisie nord orientale): l'apport des études d'inclusions fluides à la modélisation génétique. Miner Deposita 23:166–173

Bouhlel S, Johnson CA, Leach DL (2007) The peridiapiric-type Pb–Zn deposit at Fedj El Adoum, Tunisia: geology, petrography, and stable isotopes. In: Andrew CJ et al. (eds) Digging deeper. Proceedings of 9th Biennial SGA Mtg, Dublin, Ireland, pp 323–325

Bouhlel S, Garnit H, Bejaoui J, Skaggs S (2013) Lead isotopes signatures of the MVT lead-zinc (±F) deposits across central-north Tunisia: evidence for the heterogeneity in uranium component of the underlying source rocks. In: Jonsson E et al. (Eds) Mineral deposit research for a high-tech world. Proceedings of 12th Biennial SGA Mtg, Uppsala, Sweden, pp 612–615

Boutaleb A (2000) Les minéralisations à Pb-Zn du Domaine sétifien-Hodna: gîtologie, pétrographie des dolomites, microthermométrie et implications métallogéniques. Unpubl Doctorat d'Etat, FSTGA-USTHB, Alger, Algeria 293 pp

Caron C (1994) Les minéralisations Pb-Zn associées au Paléozoïque inférieur d'Europe méridionale : traçage isotopique Pb-Pb des gîtes de l'Iglésiente (SW Sardaigne) et des Cévennes et évolution du socle encaissant par la géochronologie U-Pb, ^{40}Ar-^{39}Ar et

K-Ar. Unpubl PhD Thesis, University Montpellier II, France, 226 pp

Charef A, Sheppard SMF (1991) The diapir related Bou Grine Pb–Zn deposit (Tunisia): evidence for role of hot sedimentary basin brines. In: Pagel M, Leroy J (Eds) Source, transport and deposition of Metals. AA Balkema, Rotterdam, Proceed 25 Years SGA Anniv Mtg, Nancy, France, pp 269–272

Charef A, Guedes A, Noronha F, Sousa M (2009) Fossil and present-day hydrothermal fluids from north Tunisia: an example of a dynamic fluid evolution. Cadernos Lab Xeoloxico Laxe Coruña 34:43–58

Claypool G, Holser W, Kaplan I, Sakai H, Zak I (1980) The age curves of sulphur and oxygen isotopes in marine sulphate and their mutual interpretation. Chem Geol 28:199–260

Decrée S, Marignac C, De Putter T, Deloule E, Liégeois JP, Demaiffe D (2008a) Pb-Zn mineralization in a Miocene regional extensional context: the case of the Sidi Driss and the Douahria ore deposits (Nefza mining district, northern Tunisia). Ore Geol Rev 34:285–303

Decrée S, De Putter T, Yans J, Recourt P, Jamoussi F, Bruyère D, Dupuis C (2008b) Iron mineralization in Pliocene sediments of the Tamra iron mine (Nefza mining district, Tunisia): mixed influence of pedogenesis and hydrothermal alteration. Ore Geol Rev 33:397–410

Decrée S, Ruffet G, De Putter T, Baele JM, Recourt P, Yans J (2010) Mn oxides as efficient traps for metal pollutants in a Fe-Pb-Zn mine environment (Tamra iron mine, Nefza mining district, Tunisia). J Afr Earth Sci 57:249–261

Decrée S, Baele JM, De Putter T, Yans J, Clauer N, Dermech M, Aloui K, Marignac C (2013) The Oued Belif hematite-rich breccia (Nefza mining district, NW Tunisia): a potential candidate for a Miocene small-scale iron oxide copper gold (IOCG) deposit in northern Tunisia. Econ Geol 108:1425–1457

Decrée S, Marignac C, Liégeois JP, Yans J, Abdallah RB, Demaiffe D (2014) Miocene magmatic evolution in the Nefza district (northern Tunisia) and its relationship with the genesis of polymetallic mineralizations. Lithos 192:240–258

Dermech M (1990) Le complexe de l'Oued Belif–Sidi Driss (Tunisie septentrionale). Hydrothermalisme et métallogénie. Unpubl PhD Thesis, Paris VI University, France, 336 pp

El Eleuchi H, Saidi M, Fourati L, Ghenima R, Friha J, Hamouda F, Messaoudi F (2002) Northern Tunisia thrust belt: deformation model and hydrocarbon systems. AAPG Hedberg Conference, Palermo-Mondello, Italy, May 2002. AAPG Search and Discovery Article #9001

Fainassi B (2004) La bordure réactive du Trias salifère d'Aïn Allega (para-autochtone des Nefza, Tunisie septentrionale): pétrographie, minéralogie, distribution des minéralisations à Sr-Ba-Zn-Pb et comparaison avec d'autres structures de la zone des Dômes: Unpubl MSc Thesis, Faculté des Sciences, University of Carthage, Bizerte, Tunisia, 102 pp

Faul H, Foland K (1981) L'âge des rhyodacites de Nefza-Sedjenane. Notes Serv Géol Tunis n°46. Trav Géol Tun 14:47–49

Filoche C, Flinois JS (2007) Interférence de la réduction bactérienne des sulfates (BSR) et de la thermoréduction chimique (TSR) dans le cas d'une minéralisation sédimentaire de Zn–Pb (Sidi Driss, Tunisie): test par l'analyse isotopique du soufre par microsonde ionique. Unpublished Bachelor's thesis INPL-Nancy: 31 p

Flecker R, De Villiers S, Ellam RM (2002) Modelling the effect of evaporation on the salinity–87 Sr/86 Sr relationship in modern and ancient marginal-marine systems: the Mediterranean Messinian salinity crisis. Earth Planet Sci Lett 203:221–233

Garnit H, Bouhlel S, Barca D, Johnson CA, Chtara C (2012) Phosphorite-hosted zinc and lead mineralization in the Sekarna deposit (central Tunisia). Miner Deposita 47:545–562

Gharbi M (1977) Etude des minéralisations mercurifères de l'accident Ghardimaou-Cap Serrat (Tunisie du Nord-Ouest). Unpubl MSc Thesis, Ecole Nationale Supérieure Géologie Appliquée Prospection Minière Nancy, France, 131 pp

Gottis Ch, Sainfeld P (1952) Les gîtes métallifères tunisiens. XIXème Congrès Géologique International. Monographies régionales, 2e série, Tunisie n°2, 104 pp

Guerrera F, Martin-Martin M, Perrone V, Tramontana M (2005) Tectono-sedimentary evolution of the southern branch of the western Tethys (Maghrebian flysch basin and Lucanian ocean): consequences for western Mediterranean geodynamics. Terra Nova 17:358–367

Harrab S, Mannai-Tayech B, Rabhi M, Zargouni F (2013) Study of a Neogene basin dynamics: the "Bizerte basin", northeast Tunisia: relevance to the global Messinian salinity crisis. Comptes Rendus Geosci 345:251–261

Jaeger JJ (1977) Les rongeurs du Miocène moyen et supérieur du Maghreb. Palaeovertebr 8:1–166

Jallouli C, Mickus K (2000) Regional gravity analysis of the crustal structure of Tunisia. J Afr Earth Sci 30:53–78

Jallouli C, Mickus K, Turki MM, Rihane C (2003) Gravity and aeromagnetic constraints on the extent of Cenozoic rocks within the Nefza-Tabarka region, northwestern Tunisia. J Volcanol Geother Res 122:51–68

Jemmali N (2011) Le Trias du nord de la Tunisie et les minéralisations associées: minéralogie, géochimie (traces, isotopes O, C, S, Pb) et modèles génétiques. Unpubl PhD Thesis, Faculté des Sciences de Tunis, Université Tunis, Tunisia, 255 pp

Jemmali N, Souissi F, Vennemann TW, Carranza EJM (2011a) Genesis of the Jurassic carbonate-hosted Pb–Zn deposits of Jebel Ressas (north-eastern Tunisia):

evidence from mineralogy, petrography and trace metal contents and isotope (O, C, S, Pb) geochemistry. Resour Geol 61:367–383

Jemmali N, Souissi F, Villa IM, Vennemann TW (2011b) Ore genesis of Pb–Zn deposits in the Nappe zone of northern Tunisia: constraints from Pb–S–C–O isotopic systems. Ore Geol Rev 40:41–53

Jemmali N, Souissi F, Carranza EJM, Vennemann TW (2012) Mineralogical and geochemical constraints on the genesis of the carbonate-hosted Jebel Ghozlane Pb–Zn deposit (Nappe zone, northern Tunisia). Resour Geol 63:27–41

Jemmali N, Souissi F, Carranza EJM, Bouabdellah M (2013a) Lead and sulfur isotope constraints on the genesis of the polymetallic mineralization at Oued Maden, Jebel Hallouf and Fedj Hassene carbonate-hosted Pb–Zn (As–Cu–Hg–Sb) deposits, northern Tunisia. J Geochem Explor 132:6–14

Jemmali N, Souissi F, Carranza EJM, Vennemann TW (2013b) Sulfur and lead isotopes of Guern Halfaya and Bou Grine deposits (Domes zone, northern Tunisia): implications for sources of metals and timing of mineralization. Ore Geol Rev 54:17–28

Jemmali N, Souissi F, Carranza EJM, Vennemann TW, Bogdanov K (2014) Geochemical constraints on the genesis of the Pb–Zn deposit of Jalta (northern Tunisia): implications for timing of mineralization, sources of metals and relationship to the Neogene volcanism. Chem Erde-Geochem 74:601–613

Jolivet L, Augier R, Faccenna C, Rimmele G, Agard P, Robin C, Rossetti F, Crespo-Blanc A (2008) Subduction, convergence and the mode of backarc extension in the Mediterranean region. Bull Soc Géol France 179:525–550

Johnson CA, Kelley K, Leach DL (2004) Sulfur and oxygen isotopes in barite deposits of the Western Brooks Range, Alaska, and implications for the origin of the Red Dog Massive Sulfide Deposits. Econ Geol 99:1435–1448

Johnson CA, Emsbo P, Poole FG, Rye RO (2009) Sulfur- and oxygen-isotopes in sediment-hosted stratiform barite deposits. Geochim Cosmochim Acta 73:133–147

Juteau M, Michard A, Albarede F (1986) The Pb–Sr–Nd isotope geochemistry of some recent circum-Mediterranean granites. Contrib Mineral Petrol 92:331–340

Kampschulte A, Strauss H (2004) The sulfur isotopic evolution of Phanerozoic seawater based on the analysis of structurally substituted sulfate in carbonates. Chem Geol 204:255–286

Khomsi S, Soussi M, Mahersi C, Bedir M, Fakhfakh-Ben Jemina H, Riahi S, Bou Khalfa K (2009) New insights on the structural style of the subsurface of the Tell units in north-western Tunisia issued from seismic imaging: geodynamic implications. Comptes Rendus Géosci 341:347–356

Kucha H, Schroll E, Raith JG, Halas S (2010) Microbial sphalerite formation in carbonate-hosted Zn-Pb ores, Bleiberg, Austria: micro-to nanotextural and sulfur isotope evidence. Econ Geol 105:1005–1023

Laridhi Ouazaa N (1988) Premières descriptions pétrographiques de la série de pyroclastites du bassin sédimentaire mio-pliocène de l'oued Zouara (Nefza, Tunisie septentrionale). Comptes Rendus Acad Sci 307:2055–2060

Laridhi Ouazaa N (1989) Mise en évidence d'une identité minéralogique et géochimique entre la rhyodacite de Ain Deflaia et les pyroclastites du bassin sédimentaire de Oued Zouara (Nefza: Tunisie septentrionale). Comptes Rendus Acad Sci 309:1571–1576

Laridhi Ouazaa N (1996) Etude minéralogique et géologique des épisodes magmatiques mésozoïques et miocènes de la Tunisie. Unpubl PhD Thesis, Tunis University, Tunisia, 466 pp

Leach DL, Bradley DC, Lewchuk M, Symons DTA, Brannon J, de Marsily G (2001) Mississippi Valley-type lead-zinc deposits through geological time: implications from recent age-dating research. Miner Deposita 36:711–740

Leach DL, Sangster DF, Kelley KD, Large RR, Garven G, Allen CR, Gutzmer J, Walters S (2005) Sediment-hosted lead–zinc deposits: a global perspective. In: Hedenquist JW, Thompson JFH, Goldfarb RJ, Richards JP (eds) Economic Geology 100th Ann Vol 1905–2005. Soc Economic Geologists, Littleton, Colo, USA, pp 561–607

Lopez-Horgue MA, Iriarte E, Schroder S, Fernández--Mendiola PA, Caline B, Corneyllie H, Fremont J, Sudrie M, Zerti S (2010) Structurally controlled hydrothermal dolomites in Albian carbonates of the Asón valley, Basque Cantabrian Basin, Northern Spain. Mar Petrol Geol 27:1069–1092

Machel H (2001) Bacterial and thermochemical sulfate reduction in diagenetic settings — old and new insights. Sediment Geol 140:143–175

Machel H, Krouse H, Sassen R (1995) Products and distinguishing criteria of bacterial and thermochemical sulfate reduction. Appl Geochem 10:373–389

Mamady K (1998) Etude structurale de la région d 'Ain Allega (Nefza: Tunisie septentrionale). Diplôme d'étude approfondie. Unpubl MSc Thesis, Tunis University, Tunisia, 74 pp

Marignac C, Aïssa DE, Deloule E, Cheilletz A, Gasquet D (2016) The Edough-Cap de Fer polymetallic district, northeast Algeria: I. The late Miocene paleogeothermal system of Aïn Barbar and its Cu-Zn-Pb vein mineralization, this volume

Mascle G, Tricart P, Torelli L, Bouillin J-P, Compagnon R, Depardon S, Mascle J, Pecher A, Peis D, Rekhiss F, Rolfo F, Bellon H, Brocard G, Lapierre H, Monié P, Poupeau G (2004) Structure of the Sardinia channel: crustal thinning and late-orogenic extension in the Apenninic Maghrebian orogeny; results of the

Cyana submersible survey (SARCYA and SARTUCYA) in the western Mediterranean. Bull Soc Géol France 175:607–627

Masrouhi A, Ghanmi M, Ben Slama M-M, Ben Youssef M, Vila J-M, Zargouni F (2008) New tectono-sedimentary evidence constraining the timing of the positive tectonic inversion and the Eocene Atlasic phase in northern Tunisia: implication for the North African paleo-margin evolution. Comptes Rendus Geosci 340:771–778

Mauduit F (1978) Le volcanisme néogène de la Tunisie continentale. Unpubl PhD Thesis, Université de Paris Sud, France, 157 pp

Maury RC, Fourcade S, Coulon C, El Azzouzi M, Bellon H, Coutelle A, Ouabadi A, Semroud B, Megartsi M, Cotten J, Belanteur O, Louni-Hacini A, Piqué A, Capdevila R, Hernandez J, Réhault JP (2000) Post-collisional Neogene magmatism of the Mediterranean Maghreb margin: a consequence of slab breakoff. Comptes Rendus Acad Sci Paris 331:159–173

Melki F, Zargouni F, Chelbi MB, Bédir M, Zouaghi T (2012) Role of the NE-SW Hercynian master fault systems and associated lineaments on the structuring and evolution of the Mesozoic and Cenozoic basins of the Alpine margin, northern Tunisia. In: Shark E (ed) Tectonics-Recent Advances. doi:10.5772/50145

Michard A, Negro F, Saddiqi O, Bouybaouene ML, Chalouan A, Montigny R, Goffé B (2006) Pressure–temperature–time constraints on the Maghrebide mountain building: evidence from the Rif-Betic transect (Morocco, Spain), Algerian correlations, and geodynamic implications. Comptes Rendus Geosci 338:92–114

Mickus K, Jallouli C (1999) Crustal structure beneath the Tell and Atlas Mountains (Algeria and Tunisia) through the analysis of gravity data. Tectonophys 314:373–385

Montacer M, Disnar JR, Orgeval JJ, Trichet J (1988) Relationships between Zn-Pb ore and accumulation processes: example of the Bou Grine deposit (Tunisia). Organic Geochem 13:423–431

Moussi B, Medhioub M, Hatira N, Yans J, Hajjaji W, Rocha F, Labrincha JA, Jamoussi F (2011) Identification and use of white clayey deposits from the area of Tamra (northern Tunisia) as ceramic raw materials. Clay Min 46:165–175

Negra L (1987) Pétrologie, minéralogie et géochimie des minéralisations et des roches encaissantes des basins associés aux structures tectoniques et magmatiques de l'Oued Belif et du Jebel Haddada (nord des Nefza, Tunisie septentrionale). Unpubl PhD Thesis, Paris-Sud University, France, 223 pp

Nielsen P, Swennen R, Muchez P, Keppens E (1998) Origin of Dinantian zebra dolomites south of the Brabant-Wales Massif, Belgium. Sedimentology 45:727–743

Ould Bagga MA, Abdeljaouad D, Mercier E (2006) La « zone des nappes » de Tunisie: une marge méso-cénozoïque en blocs basculés modérément inversée (région de Taberka/Jendouba; Tunisie nord-occidentale). Bull Soc Géol France 177:145–154

Orgeval JJ (1994) Peridiapiric metal concentration: example of the Bougrine deposit (Tunisian Atlas). In: Fontboté L, Boni M (eds) Sediment-hosted Zn–Pb ores. Springer, Heidelberg, SGA Spec Publ 10, pp 354–389

Orgeval JJ, Giot D, Karoui J, Monthel J, Sahli R (1986) Le gisement de Zn-Pb de Bou Grine (Atlas tunisien): description et historique de la découverte. Chron Rech Minière 482:5–32

Paytan A, Kastner M, Campbell D, Thielmens M (1998) Sulfur isotopic composition of Cenozoic seawater sulphate. Science 282:1459–1462

Perthuisot V (1978) Dynamique et pétrogenèse des extrusions triasiques de Tunisie septentrionale: travaux du Laboratoire de Géologie, Presse Ecole Norm Sup Paris 12, France, 312 pp

Perthuisot V, Rouvier H (1996) Les dépôts Pb-Zn associés aux évaporites du Trias des diapirs du Maghreb oriental (Tunisie). In: 16ème Réunion des Sciences de la Terre, Orléans: Société Géologique France, p 158

Perthuisot V, Bouzenoune A, Hatira N, Henry B, Laatar E, Mansouri A, Rouvier H, Smati A, Thibieroz J (1999) Les diapirs du Maghreb oriental: part des déformations alpines et des structures initiales crétacées et éocènes dans les formes actuelles. Bull Soc Géol France 170:57–65

Piqué A, Ait Brahim L, El Azzouzi MH, Maury R, Bellon H, Semroud B, Laville E (1998) Le poinçon maghrébin: contraintes structurales et géochimiques. Comptes Rendus Acad Sci Paris 326:575–581

Piqué A, Tricart P, Guiraud R, Laville E, Bouaziz S, Amrhar M, Ait Ouali R (2002) The Mesozoic-Cenozoic Atlas belt (North Africa): an overview. Geodin Acta 15:185–208

Racey A, Bailey HW, Beckett D, Gallagher LT, Hampton MJ, McQuilken J (2001) The petroleum geology of the Early Eocene El Garia Formation, Hasdrubal field, offshore Tunisia. J Petrol Geol 24:29–53

Riahi S, Soussi M, Bou Khalfa K, Ben Ismail-Lattrache K, Stow D, Khomsi S, Bedir M (2010) Stratigraphy, sedimentology and structure of the Numidian flysch thrust belt in northern Tunisia. J Afr Earth Sci 57:109–126

Roman F, Solignac M (1934) Découverte d'un gisement de Mammifères pontiens à Douaria (Tunisie septentrionale). Comptes Rendus Acad Sci Paris 199:1649–1659

Rouvier H (1977) Géologie de l'extrême nord-Tunisien: tectoniques et paléogéographie superposées à l'extrémité orientale de la chaîne nord-Maghrebine. Unpubl PhD Thesis, Pierre et Marie Curie University, Paris, France, 215 pp

Rouvier H (1987) Carte géologique de la Tunisie; feuille n°10: Nefza. Service Géologique-Office National des Mines, scale 1: 50,000; 1 sheet

Rouvier H (1994) Notice explicative de la carte géologique de la Tunisie au 1/50000^{e} – Nefza, feuille

10. Office National des Mines, Direction de la Géologie 48 pp
Rouvier H, Perthuisot V, Mansouri A (1985) Pb-Zn deposits and salt-bearing diapirs in southern Europe and North Africa. Econ Geol 80:666–687
Russell RD, Farquhar RM (1960) Lead isotopes in geology. Interscience Publishers, New York 243 pp
Sainfeld P (1952) Les gîtes plombo-zincifères de Tunisie. Ann Mines Géol Tunisie 9, 285 pp
Sheppard S, Charef A, Boulhel S (1996) Diapirs and Pb-Zn mineralization: a general model based on Tunisian (N. Africa) and Gulf Coast (U.S.A.) deposits. In: Sangster D (Ed) Carbonate-hosted lead-zinc deposits. Soc Economic Geologists, Spec Publ 4, pp 230–243
Skaggs SA (2010) A lead isotope analysis of the provenance of defixiones (curse tablets) from Roman Carthage, Tunisia. Unpubl PhD Thesis, University of Georgia, USA, 132 pp
Steele-MacInnis M, Bodnar RJ, Naden J (2011) Numerical model to determine the composition of H_2O-NaCl-$CaCl_2$ fluid inclusions based on microthermometric and microanalytical data. Geochim Cosmochim Acta 75:21–40
Stefanov SH, Ouchev A (1972) Gisement plombo-zincifère de Sidi Driss. Rapport interne, Office National des Mines de Tunisie (Unpubl), Rapport géol avec estimation de réserves
Souissi F, Dandurand J-L, Fortuné J-P (1997) Thermal and chemical evolution of the fluids during fluorite deposition in the Province of Zaghouan (north-eastern Tunisia). Miner Deposita 32:257–270
Souissi F, Fortuné J-P, Sassi R (1998) Le gisement de type Mississippi Valley du Jebel Stah (Tunisie nord-orientale). Bull Soc Géol France 169:163–175
Souissi F, Sassi R, Dandurand JL, Bouhlel S, Hamda SB (2007) Fluid inclusion microthermometry and rare earth element distribution in the celestites of the Jebel Doghra ore deposit (Dome zone, northern Tunisia): towards a new genetic model. Bull Soc Géol France 178:459–471
Souissi F, Souissi R, Dandurand JL (2010) The Mississippi Valley-type fluorite ore at Jebel Stah (Zaghouan district, north-eastern Tunisia): contribution of REE and Sr isotope geochemistries to the genetic model. Ore Geol Rev 37:15–30
Souissi F, Dandurand JL, Souissi R (2012) The genesis of the Mississippi Valley-type fluorite ore at Jebel Stah (Zaghouan district, north-eastern Tunisia) constrained by thermal and chemical properties of fluids and REE and Sr isotope geochemistry. INTECH Open Access Publisher. http://cdn.intechopen.com/pdfs/36469/InTech-The_genesis_of_the_mississippi_valley_type_fluorite_ore_at_jebel_stah_zaghouan_district_north_eastern_tunisia_constrained_by_thermal_and_chemical_properties_of_fluids_and_ree_and_sr_isotope_geochemistry.pdf
Souissi F, Jemmali N, Souissi R, Dandurand JL (2013) REE and isotope (Sr, S, and Pb) geochemistry to constrain the genesis and timing of the F–(Ba–Pb–Zn) ores of the Zaghouan district (NE Tunisia). Ore Geol Rev 55:1–12
Talbi F, Slim-Shimi N, Tlig S, Zargouni F (1999) Nature, origine et evolution des fluids dans le district minier de la caldeira d'Oued Belif (Nefza, Tunisie septentrionale). Comptes Rendus Acad Sci Paris 328:153–160
Talbi F, Jaafari M, Tlig S (2005) Magmatisme néogène de la Tunisie septentrionale: pétrogenèse et événements géodynamiques. Rev Soc Geol España 18:241–252
Touahri B (1987) Géochimie et métallogénie des minéralisations à plomb et zinc du nord de l'Algérie. Unpubl PhD Thesis, Université Pierre Marie Curie (Paris 6), France, 380 pp
Trabelsi S, Bouri S, Gasmi M, Lahlou Mimi A, Inoubli N, Ben Dhia H (2005) Geological and hydrothermal outlines of the Tunisian fluorine province (north-eastern Tunisia). Proc World Geotherm Congress, Antalya, Turkey 3 pp
Van Noten K, Muchez P, Sintubin M (2011) Stress-state evolution of the brittle upper crust during compressional inversion as defined by successive quartz vein types (high-Ardenne slate belt, Germany). J Geol Soc London 168:407–422
Vengosh A, Gieskes J, Mahn C (2000) New evidence for the origin of hypersaline pore fluids in the Mediterranean basin. Chem Geol 163:287–298
Vassileff L, Popov A (1979) Formations minerales et zones métallogéniques de la Tunisie. Geol Acta 7:43–56
Wilkinson JJ (2014) Sediment-hosted zinc-lead mineralization: processes and perspectives. In: Scott SD (ed) Geochemistry of mineral deposits. Elsevier, Amsterdam, Treatise on Geochemistry vol 13, pp 219–249
Zouiten S (1999) Application de la géothermométrie chimique aux eaux des sources thermales du nord de la Tunisie. Unpubl PhD Thesis, Tunis II University, Tunisia, 197 pp

Part VII

Sediment-Hosted Iron and Manganese Deposits

The F'derik-Zouérate Iron District: Mesoarchean and Paleoproterozoic Iron Formation of the Tiris Complex, Islamic Republic of Mauritania

C.D. Taylor, C.A. Finn, E.D. Anderson, D.C. Bradley, M.Y. Joud, A. Taleb Mohamed and J.D. Horton

Abstract

High-grade hematitic iron ores (or HIF, containing 60–65 wt% Fe) have been mined in Mauritania since 1952 from Superior-type iron deposits of the F'derik-Zouérate district. Depletion of the high-grade ores in recent years has resulted in new exploration projects focused on lower-grade magnetite ores occurring in Algoma-type banded iron formation (or BIF, containing ca. 35 wt% Fe). Mauritania is the seventeenth largest iron producer in the world and currently has about 1.1 Gt of crude iron ore reserves. The main host for Algoma-type iron ore in the district is magnetite quartzite layers (formerly BIF) within Mesoarchean granulite-facies rocks of the Tiris Complex. Superior-type iron ores are restricted to the allochthonous Paleoproterozoic sequences of the Kediat

C.D. Taylor (✉) · E.D. Anderson · J.D. Horton
U.S. Geological Survey, Mineral Resources Program, Federal Center, MS-973, Box 25046, Denver, CO 80225, USA
e-mail: ctaylor@usgs.gov

C.A. Finn
U.S. Geological Survey, Crustal Imaging and Characterization Program, Federal Center, MS-964, Box 25046, Denver, CO 80225, USA

D.C. Bradley
U.S. Geological Survey (Emeritus), 11 Cold Brook Road, Randolph, NH 03593, USA

M.Y. Joud
Projet de Renforcement Institutionnel du Sector Minier (PRISM II), Ministere du Petrole, de l'Energie et des Mines de Mauritanie, BP 4530, Nouakchott, Mauritania

A. Taleb Mohamed
Ministere du Petrole, de l'Energie et des Mines de Mauritanie, Route de la plage rond-point Sabah, BP 4921, Nouakchott, Mauritania

M. Bouabdellah and J.F. Slack (eds.), *Mineral Deposits of North Africa*, Mineral Resource Reviews, DOI 10.1007/978-3-319-31733-5_21

Ijil and Guelb El Mhaoudat, which overlie the Tiris Complex. Paleoproterozoic BIF are present in the Sfariat belt that hosts at least three known iron occurrences, and at Guelb Zednes, all of which are interpreted as fragments of Superior-type BIF that were imbricated with, or allochthonously deposited on, the Mesoarchean-Paleoproterozoic suture zone during the Birimian orogeny. Prominent linear, high-amplitude magnetic anomalies associated with BIF are characteristic of the region. Paleoproterozoic rocks in the Kediat Ijil, a klippe of metasedimentary rocks including ferruginous chert capped by a distinctive conglomerate unit, and in the El Mhaoudat Range, produce very prominent, broad, high-amplitude magnetic anomalies that can be extended at least 150 km along strike projected beneath the Taoudeni Basin to depths of >2000 m. New petrographic, geochemical, and geochronologic data presented here elucidate several features of the iron deposits, their tectonic history, and possible processes of enrichment of BIF protore to HIF. The Zouérate district iron ores are remarkably pure, consisting almost wholly of hematite and quartz. Contents of all major elements other than iron and silica are well below global averages for hematitic iron ores; minor and trace element contents are similar to those of other deposits worldwide. However, Zouérate HIF shows a general depletion of REE, a positive Eu anomaly, and a preferential enrichment of HREE compared to LREE. U–Pb ages of detrital zircons in the Tazadit and Seyala Conglomerate Formations of the Kediat Ijil are consistent with their derivation from the Tiris Complex. This interpretation suggests a passive margin depositional environment on the northeastern edge of the Mesoarchean Rgueïbat Shield, unaffected by clastic input from early Birimian tectonic elements. In contrast, ages of detrital zircons from rocks faulted against the Mhaoudat Formation show depositional peaks consistent with input from Birimian and Neoproterozoic sources. These age data imply that tectonic emplacement of Guelb El Mhaoudat could have occurred as a result of Pan African orogenic events; such a Pan African record represents a previously unrecognized tectonic element in this part of the Rgueïbat Shield. Timing of enrichment of protore BIF to HIF is poorly constrained and may have resulted from multiple metamorphic-hydrothermal events from 2.83 to 1.6 Ga. Geochemical trends are consistent with interaction by a relatively high-temperature, oxidizing, and possibly alkaline fluid. A supergene weathering profile exists in the Zouérate district and began forming during uplift related to opening of the Atlantic Ocean at about 160 Ma, based on a new apatite fission track age. However, effects of this supergene enrichment are relatively minor, being superimposed on one or several metamorphic-hydrothermal events responsible for the transformation of BIF to HIF.

1 Introduction

Mauritania is the 12th largest exporter and 17th largest iron ore producer in the world and currently has about 1.1 Gt of crude iron ore reserves (Jorgenson 2012; Taib 2014). Production is mainly controlled by Société National Industrielle et Minière (SNIM), a parastatal company that is 78 % owned by the Mauritanian government. Iron ores account for about 43 % of the export earnings of the country (Taib 2014). Approximately 11 Mt of iron ore and concentrate (60 % direct-shipping ore, 40 % concentrate) per year are shipped from three mines hosted in Mesoarchean (Guelb el Rhein) to Paleoproterozoic (Guelb El Mhaoudat and TO14) rocks near Zouérate in the western Rgueïbat Shield (Fig. 1), to loading facilities on the Atlantic coast at Nouadhibou, via a 700-km-long railway constructed exclusively for this purpose. "Guelb" is the Arabic word for "hill."

Iron ore deposits are hosted in two types of iron formation. Banded iron formation (BIF) is a distinctive type of iron-rich sedimentary rock. Typical BIF consists of alternating layers of iron-poor shale or chert and nearly monomineralic Fe-oxide (magnetite and/or hematite), -carbonate, -silicate, or -sulphide minerals. BIF may have a clastic texture (referred to as granular iron formation or GIF) or a chemical sedimentary texture, and display banding on micro (mm), meso (cm), and/or macro scales (James 1954; Clout and Simonson 2005; Bekker et al. 2010). On a global basis, BIF occurs in rocks as old as 3.7 Ga, became abundant at 2.7 Ga (prior to the Great Oxygenation Event at ca. 2.4 Ga), and excluding Neoproterozoic glaciogenic Rapitan-type iron formations, is uncommon after about 1.8 Ga (Fig. 2; Cloud 1973; Bekker et al. 2010).

Algoma-type deposits tend to be smaller and globally contain the oldest BIF, preferentially occurring in Archean greenstone belts generally

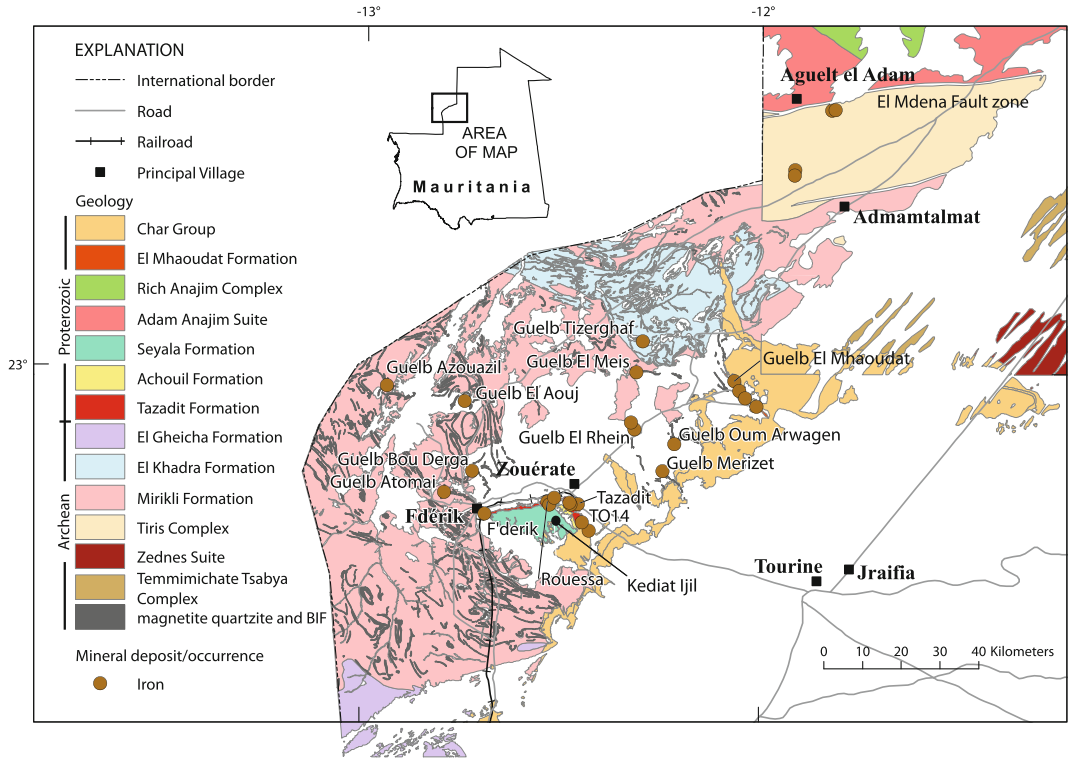

Fig. 1 Simplified geology of the Mesoarchean Tiris Complex showing Paleoproterozoic inselbergs of the Kediat Ijil and Guelb El Mhaoudat, and locations of producing iron mines, deposits, and occurrences mentioned in text

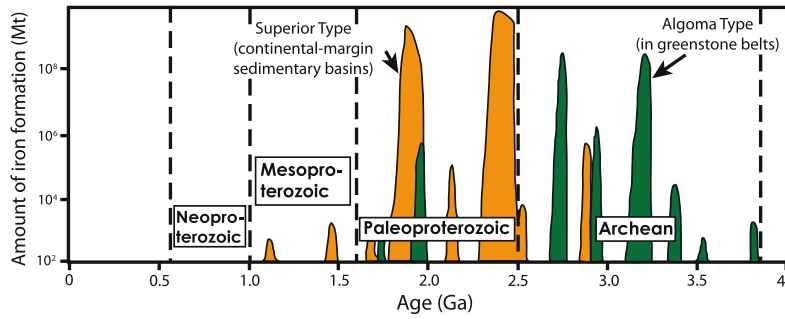

Fig. 2 Secular distribution of Algoma- and Superior-type iron formations on a global basis (modified from Beukes and Gutzmer 2008)

interlayered with volcanic and volcanogenic sedimentary rocks (e.g., Gross 1980). The Algoma-type deposits are commonly attributed to formation by hydrothermal-exhalative processes on the sea floor, as products of extensional tectonics at or near oceanic spreading centers. GIF is very rare within Algoma-type iron deposits. In the Tiris Complex, Algoma-type deposits are associated with narrow, sinuous exposures of >2.95 Ga BIF.

Superior-type BIF deposits are laterally extensive and include well-defined sequences thought to have formed as chemical sediments from Fe-rich oceans, episodically from the Paleoarchean to Paleoproterozoic (see Clout and Simonson 2005; Bekker et al. 2010). Older (>2.5 Ga) Superior-type BIF generally lacks associated GIF and is attributed to deposition in deep shelf to upper continental slope environments, whereas the younger deposits are generally regarded as part of passive margin sequences that formed on broad, sediment-starved continental shelves (Clout and Simonson 2005) and contain an abundance of GIF.

Regardless of origin and subsequent modification during diagenesis and metamorphism, most BIF has bulk iron contents in the range of 30–35 % Fe. Such rock, referred to as taconite in North America, can be profitably mined but requires beneficiation to produce an economic product containing ca. 65 % Fe. A more desirable, higher grade iron ore, referred to as martite-goethite, or high-grade hematite (HIF) ore, contains approximately 56–68 % Fe and is formed by a natural process that upgraded BIF protore to HIF, mainly by dissolution of silica and oxidation of magnetite. This process is thought to occur by a variety of mechanisms involving the leaching of BIF by hypogene-hydrothermal fluids, supergene waters, and variants or combinations thereof. The most recent models (see Powell et al. 1999; Morey 1999; Clout and Simonson 2005) call upon tectonically advancing foldbelts, adjacent to BIF-bearing successions, to provide the heated solutions capable of producing hematitic ores. Fluid inclusion evidence indicates that such fluids typically have temperatures between 200° and 400 °C and that the inferred highland areas produced by the tectonism can provide the hydraulic head needed to move the fluids into the iron deposits.

High-grade hematitic iron ores, containing 60–65 % Fe, have been mined in Mauritania since 1952 from Superior-type BIF in allochthonous Paleoproterozoic rocks of the F'derik-Zouérate district. Depletion of the high grade ores in recent years has resulted in new exploration projects focused on lower grade magnetite ores occurring within Mesoarchean Algoma-type BIF containing ca. 35 % Fe. Much of this lower grade iron ore occurs in the Tiris Complex, a Mesoarchean granite migmatite assemblage containing numerous units of highly magnetic magnetite quartzite (formerly chert-rich BIF), and paragneiss having mostly aluminous protoliths, together with minor mafic and Fe-rich marker units. The complex is metamorphosed to granulite facies conditions (O'Connor et al. 2005; Schofield and Gillespie 2007) and underlies the northeastern portion of the western Rgueïbat Shield (Fig. 1). Another of its main components, the Mirikli Formation, consists of quartzofeldspathic gneiss and minor mafic, calc-silicate, and Fe-rich marker units, which

have been migmatized and intruded by anatectic granites (O'Connor et al. 2005).

Although all of the iron production in Mauritania to date has come from the mines of the F'Derik-Zouérate district, significant potential exists in other regions of Mauritania for the discovery and exploitation of additional iron resources. Areas of active exploration, and documented iron occurrences and/or BIF include Mesoarchean rocks in the Tasiast-Tijirit and Amsaga terranes of the southwestern Rgueïbat Shield, and the Inchiri district around Akjoujt. Neoproterozoic rocks throughout the central and southern Mauritanides contain BIF, and large, low grade accumulations of Phanerozoic oolitic ironstone are present in the Mauritanian portions of the Taoudeni and Tindouf basins. The iron resource potential of these and other regions of Mauritania not discussed in this paper are documented in Taylor et al. (2015).

2 History of Iron Mining in the F'Derik-Zouérate Area

The history of iron mining in the F'Derik-Zouérate area has been summarized by several workers (Oksengorn 1973; Marot et al. 2003; O'Connor et al. 2005; Mining-technology.com 2012). The earliest apparent reference to iron in the region is in 1068 by Abou-Obeid-El Bekhri, who described a mountain called "Idrar en Ouzzal" in Berber, which translates as the mountain of iron; however, the iron deposits in the F'Derik area were probably known and worked in antiquity, and several have Berber names such as "El Hadid" meaning iron and "El Meiss" meaning magnet (Oksengorn 1973; O'Connor et al. 2005). Marot et al. (2003) commented that, since antiquity, the economic history of northern Mauritania has been dominated by Berber nomads and the Trans-Saharan trade. Since at least the 10th Century, the Trans-Saharan road of the West, from Morocco to the black kingdoms of sub-Saharan Africa, passed by the water wells of Tiris and Zemmour. These caravans transported copper (from Akjoujt), salt from the saltworks of Ijil, and especially gold from the Senegal River. By the 14th Century, accounts of travelers mention the "Iron Mountain" of the Zouérate area (Marot et al. 2003).

In 1900, the free Spanish convention on the sovereignty of Rio de Oro granted the saltworks of Ijil (and consequently the huge iron resources) to France, which was followed by the first geological expeditions in the region (Marot et al. 2003). The first modern reference to the iron deposits is a brief record in the Imperial Mineral Resources Bureau for 1922, which under Mauritania includes the statement (O'Connor et al. 2005, p. 336) "Iron ore is said to occur in the Tagant and Ijil districts where traces of native workings are reported to have been found. The ore is not now being worked." A further brief reference in 1933 records the use of iron ore in the construction of Fort Gouraud (F'Derik); the first geological studies in 1937 and 1939 identified iron ore in the Kediat Ijil (O'Connor et al. 2005).

Miferma (Mines de Fer de Mauritanie) was created in 1952 to exploit iron ore deposits in the Kediat Ijil (kediat is the Arabic word for "range"), a prominent range composed almost entirely of BIF protruding above the flat terrain of the underlying Tiris Complex. A mining center was constructed at Zouérate off the northeastern flank of the kediat, and was connected by railroad with port facilities at Nouadhibou on the Atlantic coast (Mining-technology.com 2012). Open-pit mining of direct-shipping hematite ore commenced in 1963 at the F'Derik, Rouessa, and Tazadit pits (Fig. 3).

As the high-grade, direct-shipping ore was being depleted, a crushing plant for lower grade ores was installed at Rouessa in 1973. Thereafter, the Algoma-type Guelb el Rhein magnetite deposit just to the NNE of Zouérate was developed (Fig. 1). Nationalization of the Miferma consortium in 1974–75 created SNIM (Société Nationale Industrielle et Minière). The Mauritanian government now owns 78 % of SNIM, and Arab financial and mining organizations own the balance.

Exploitation of new direct-shipping-grade ore discoveries began in 1991 at the TO14 deposit, a deep orebody located at the southeastern limit of

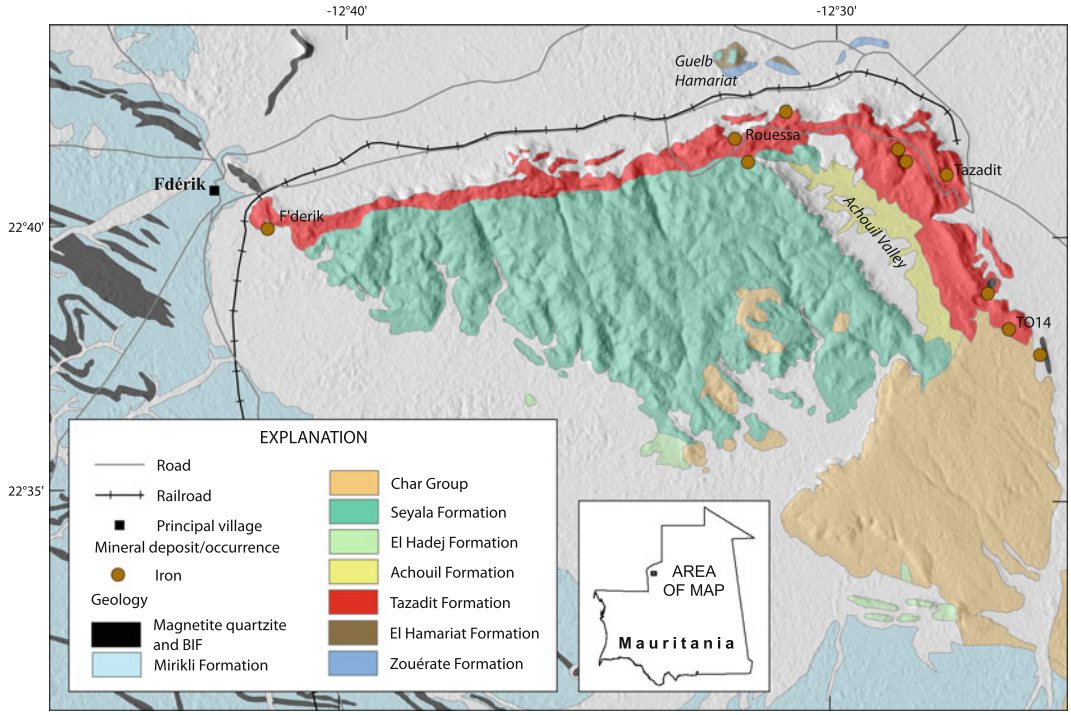

Fig. 3 Geology of Kediat Ijil and locations of major iron deposits mentioned in text

the Kediat Ijil and at Guelb El Mhaoudat, 50 km further east (Figs. 1 and 3). In the late 1990s, SNIM upgraded the terminal handling facilities at Nouadhibou, commissioning new tertiary and quaternary crushing and screening at the Point Central plant to maintain production at 12 Mt/y. A 960 t/h regrinding circuit at the Guelb el Rhein plant opened in November 2000 (Mining-technology.com 2012).

In 2001, SNIM formed a joint venture with Australia's Sphere Investments to study options for open-pit mining and beneficiation of the magnetite deposit at Guelb El Aouj. In March, 2008, Sphere Investments was granted a 30-year exploitation license on Guelb el Aouj, and was then acquired by Xstrata in 2010 together with projects at nearby Askaf, Tintekrate, and Bou Derga, and with Lebtheinia in the Tasiast-Tijirit terrane. ArcelorMittal entered into an agreement with SNIM to develop magnetite ores at Guelb Agareb, which may have iron resources of 1 Gt (Taib 2010). The Guelb el Aouj deposit has JORC-compliant measured, indicated, and inferred resources of 701 Mt of magnetite ore with an average grade of 36.3 % Fe (Mining Journal 2006; Sphere Minerals Ltd. 2012).

3 The Kediat Ijil Superior-Type Iron Deposits

The Kediat Ijil is a prominent range of hills trending E-W in a roughly triangular-shaped block between the towns of Zouérate and F'Derik (Fig. 3). The range is approximately 25 km long and 15 km wide at the widest point. As currently mapped (O'Connor et al. 2005), outcrop of the Kediat Ijil covers approximately 170 km^2. The entire inselberg is thought to consist of an allochthonous (or para-autochthonous) series of thrust nappes composed almost entirely of iron formation and associated sedimentary rocks of the Ijil Complex and overlying Seyala Conglomerate Formation (O'Connor et al. 2005). The Kediat Ijil, as well as Guelb El Mhaoudat to the northeast, were transported southwestward

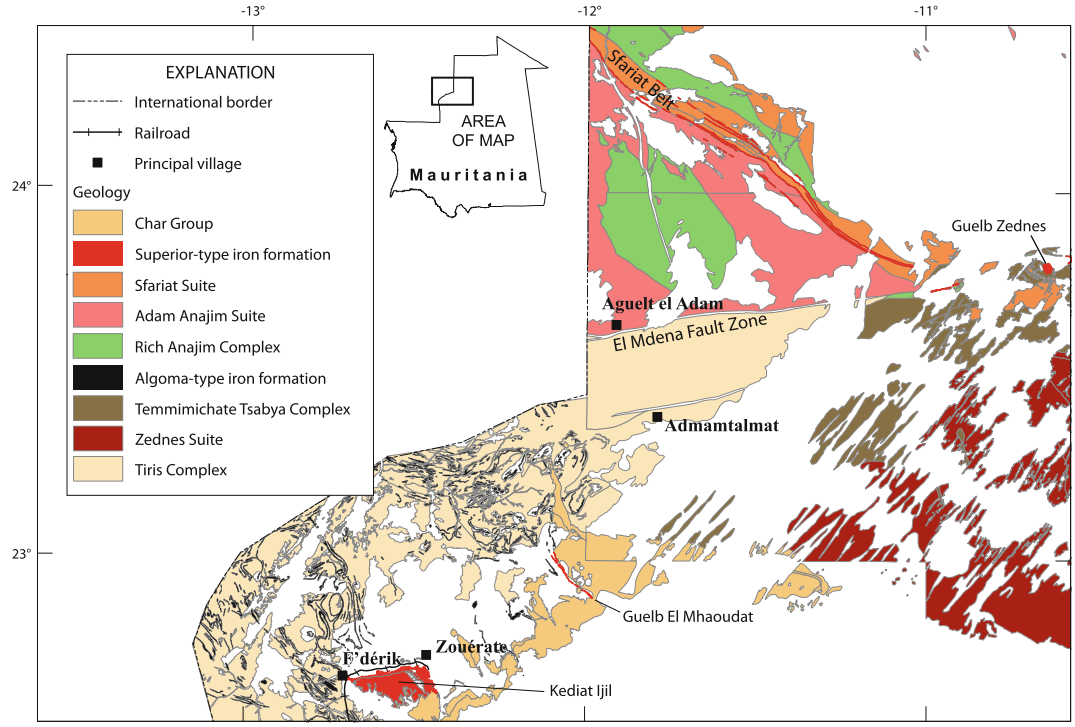

Fig. 4 Geology of northeastern margin of the Mesoarchean Rgueïbat Shield showing Paleoproterozoic suture zone marked by El Mdena Fault and locations of Kediat Ijil and Mhaoudat inselbergs southwest of the margin. Mesoarchean Algoma-type BIF is shown in *black*; Paleoproterozoic Superior-type BIF is in *red*

during the Birimian orogeny (2100–2000 Ma), and now lie approximately 130 km to the southwest of the Archean-Proterozoic suture zone marked by the El Mdena Fault (Figs. 4, 5 and 6; Schofield and Gillespie 2007). Although all attempts to directly date the Ijil Complex have failed, the shallow marine platformal nature of the associated sedimentary rocks, contrasting nature of the jasper-rich BIF of the Ijil Complex with the magnetite quartzite BIF of the Tiris Complex, and geologic relationships with other directly dated rock units, collectively suggest that the Ijil Complex is Paleoproterozoic. By this reasoning, the contained iron formation represents Superior-type BIF that was deposited on the northeastern passive margin of the Archean Rgueïbat Shield.

The Kediat Ijil consists of six lithostructural units that form a series of stacked thrust nappes overlying the Tiris Complex (Bronner and Chauvel 1979). The structurally uppermost unit is a breccia or conglomerate that is relatively undeformed, and is clearly younger than the other five units based on the presence of clasts composed of the underlying lithologies. Work in the area by the British Geological Survey (BGS) (O'Connor et al. 2005) redefined the Ijil Complex to include the lowermost five units, which have been given formational status, from base to top, as the Zouérate, El Hamariat, Tazadit, Achouil, and El Hadej formations (Fig. 5). The Ijil Complex comprises predominantly greenschist- to amphibolite-facies metasedimentary rocks including quartzite, ferruginous chert (BIF), micaceous quartzite, and mica-quartz schist. Igneous rocks and carbonate strata are minor components.

The lowest two lithostructural units, the Zouérate and overlying El Hamariat formations, are only exposed in outcrops at Guelb Hamariat and in several small inselbergs just to the north of the Kediat Ijil and west of Zouérate (Fig. 3). The Zouérate Formation consists of micaceous quartzite and mica schist overlain by a 50-m-thick,

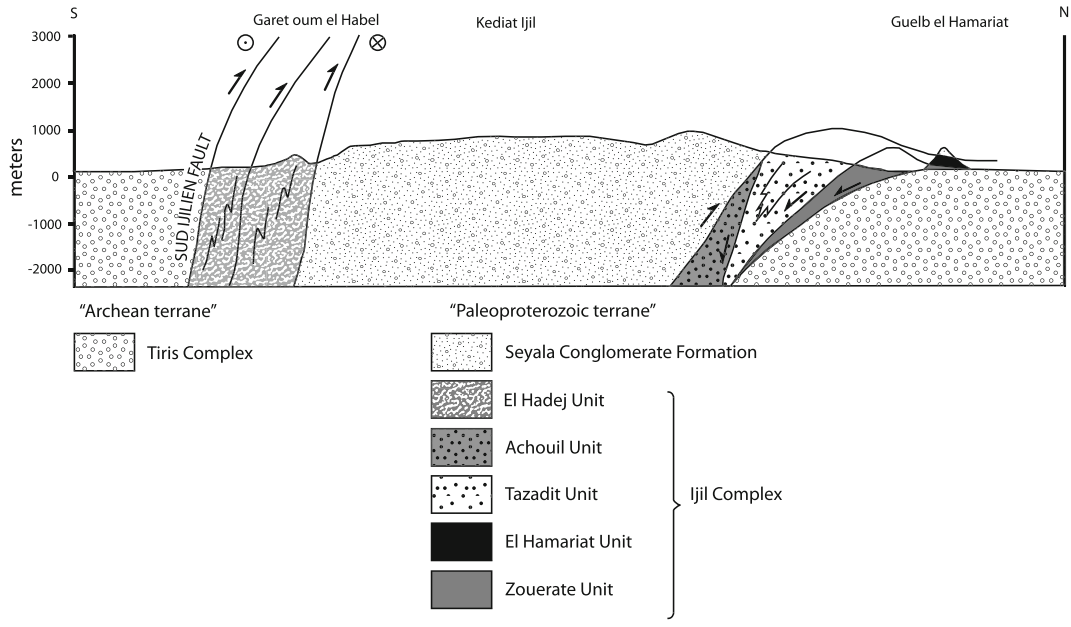

Fig. 5 Schematic cross section of Kediat Ijil showing possible allochthonous structural relationships with basement rocks of the Tiris Complex (modified from Schofield and Gillespie 2007)

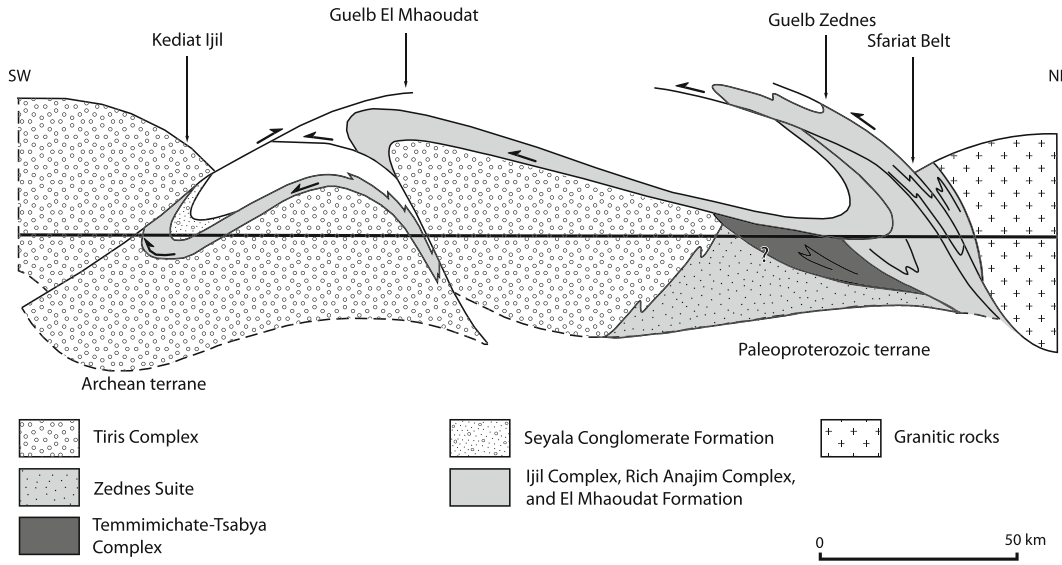

Fig. 6 Schematic cross section showing hypothetical Birimian thrust faulting of Paleoproterozoic Superior-type iron formation on northeastern margin of Mesoarchean Rgueïbat Shield (modified from Schofield and Gillespie 2007)

concordant sheet of metagabbroic rock, overlain by garnet-bearing muscovite-quartz schist. The metagabbro is the only igneous rock known within the Ijil Complex, and appears to have been emplaced prior to thrust stacking of the complex. Attempts to directly date the metagabbro have been unsuccessful (O'Connor et al. 2005). The El Hamariat Formation is composed primarily of

quartz-pebble metaconglomerate. Both formations dip moderately to the north and are juxtaposed along a north-dipping reverse fault (O'Connor et al. 2005; Schofield and Gillespie 2007).

The lowermost unit within the Kediat Ijil is also thought to be the Zouérate Formation although evidence of this relationship is entirely concealed by Cenozoic talus aprons and alluvial deposits (Schofield and Gillespie 2007). The Tazadit Formation and overlying nappes consisting of the Achouil, El Hadej, and Seyala Conglomerate formations structurally overlie the Tiris Complex basement, along a sole thrust that was described by Bronner and Chauvel (1979) as a very thick zone of crushed rock. USGS field examination of this locality (exploration trench) in October, 2007, was inconclusive owing to lack of exposure of the critical contact with the Tazadit Formation at the top of the trench. However, cataclastic and mylonitic textures were observed in rocks of the Tiris Complex in the lower portion of the trench.

The Tazadit Formation is the thickest and most voluminous unit of the Ijil Complex and, due to its high proportion of BIF, represents the protore as well as the host rock for the majority of HIF resources mined to date from the Kediat Ijil. This formation occurs along a narrow northern and eastern margin to the Kediat Ijil, roughly 1.6 km wide, trending mostly E-W and dipping steeply to the south. The formation wraps around and trends N-S at the eastern end of the inselberg, forming the crest of the range as well as the dramatic northern scarp (Figs. 3 and 7).

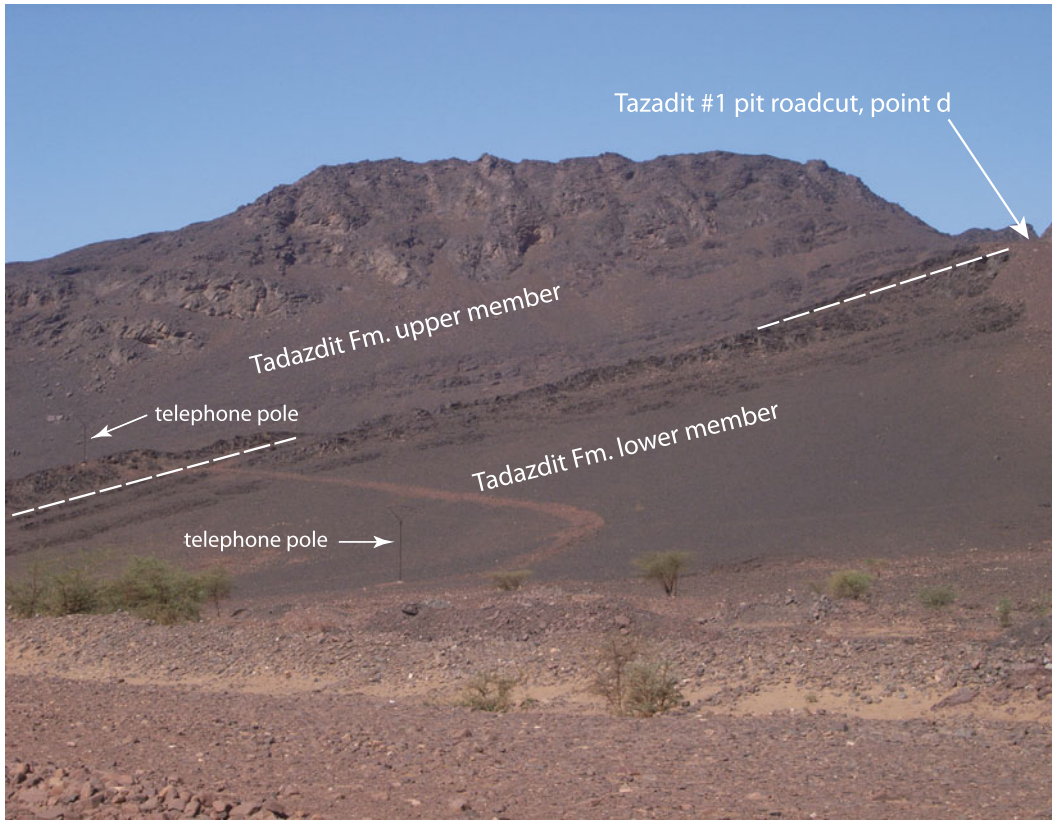

Fig. 7 View westward at eastern end of Kediat Ijil showing westward-dipping BIF of Tazadit Iron Formation (Ijil Complex). *Dashed line* marks contact between lower and upper members. *Arrow* shows location of point d in Fig. 8. Scale is shown by ca. 10-m-high telephone poles along the bulldozed track through *center* of photo. USGS photo

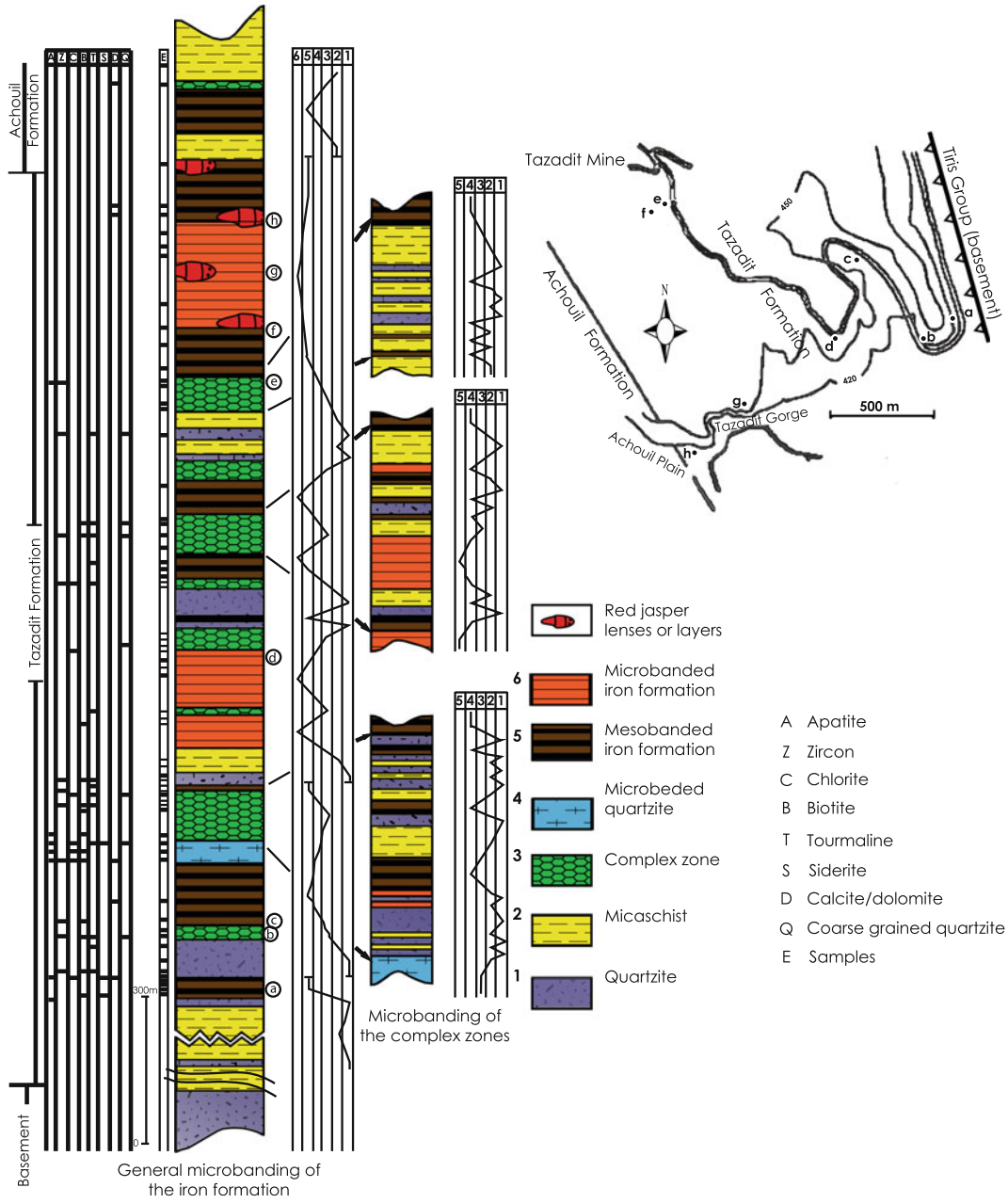

Fig. 8 Lithologic column and plan map of Tazadit Formation along road from Zouérate to Tazadit #1 mine (modified from Bronner and Chauvel 1979)

Petrographic and stratigraphic features of the Tazadit Formation are described in detail by Bronner and Chauvel (1979) based on examination of drill cores, thin sections, and excellent outcrops exposed in the roadcut between Zouérate and the Tazadit #1 iron mine (Fig. 8). The Tazadit mine road exposes a nearly continuous, 1000-m-thick sedimentary section composed of three repeating cycles of quartzite, mica schist, microbanded quartzite, mesobanded quartzite, mesobanded IF, and microbanded IF (Bronner and Chauvel 1979). Red jasper occurs in the

upper parts of each cycle. The lowermost two cycles are thinner than the uppermost cycle, which accounts for perhaps two thirds of the thickness of the Tazadit Formation (Fig. 8). Portions of the stratigraphy are repeated by folding and there are several "complex" zones in which some of the above rock types are intermixed and have reduced thicknesses (Bronner and Chauvel 1979). In practice, SNIM geologists divide the Tazadit Formation into: (1) a lower member consisting of the first two cycles described above and the lower portion of the third cycle, composed of quartzite, mica schist, and the lower portion of a microbanded IF unit; and (2) an upper member consisting of a higher proportion of meso- and microbanded BIF. A fault zone (near point d, Fig. 8) separates the two members and is shown in Fig. 9. On average, BIF units of the lower member contain ca. 30 % Fe, whereas upper member BIF units have ca. 38 % Fe (Szymon Oksengorn, oral commun, 2007). The upper member of the Tazadit Formation is therefore a better protore for the occurrence of HIF, and explains why most of the exploited mines in the Kediat Ijil are hosted within the upper member.

The Achouil Formation lies structurally above the Tazadit Formation and is exposed almost exclusively in the floor of the Achouil Valley that cuts through the northeastern portion of the Kediat Ijil (Fig. 3). The Achouil Formation contains an approximately 70-m-thick BIF unit near the base, but otherwise consists of fine-grained, muscovite-biotite ± garnet schist.

The El Hadej Formation is exposed in a series of small guelbs (inselbergs) just south of the southern margin of the Kediat Ijil (Fig. 3). The formation consists of conglomerate, quartzite, micaceous

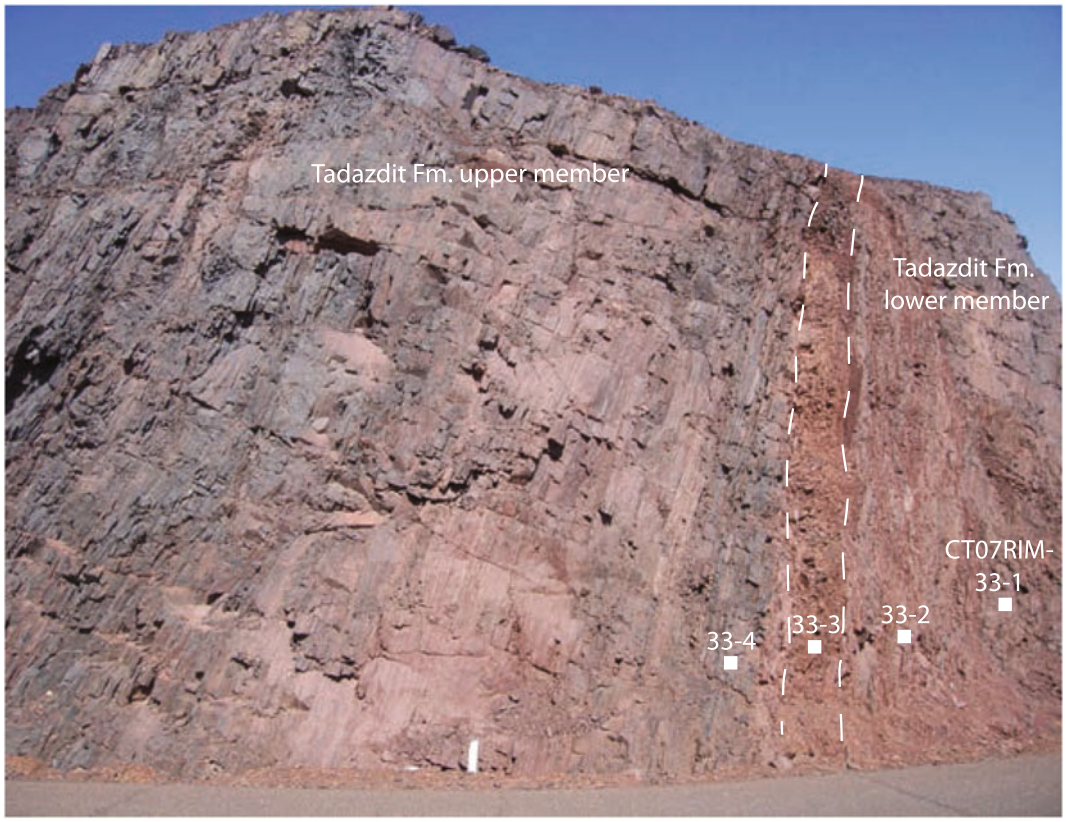

Fig. 9 Profile through section along road to Tazadit #1 pit, point d. Fault at right separates lower (*right*) and upper (*left*) members of Tazadit Formation. Locations of samples CT07RIM33-1 through -4 are shown. Width of fault zone is ca. 5 m. USGS photo

quartzite, mica schist, staurolite-bearing and garnetiferous mica schist, hornblende-bearing mica schist, dolostone, and ferruginous chert. Aeromagnetic data suggest that the boundary between the El Hadej Formation and the Tiris Complex takes the form of a steeply dipping tectonic contact along the southern margin of Garet Oum el Habel. The contact is also marked by abundant vein quartz (Bronner and Chauvel 1979; O'Connor et al. 2005).

The Seyala Conglomerate Formation, having an outcrop area of ca. 115 km^2, constitutes approximately 68 % of the main mass of the Kediat Ijil. It overlies the Ijil Complex along structural contacts with the Tazadit Formation (most of its northern margin), and with the Achouil Formation along the southwestern scarp of the Achouil Valley (northeastern margin). The contact of the Seyala Conglomerate Formation with the underlying El Hadej Formation in the southwestern and southern areas of the Kediat Ijil is obscured by Cenozoic talus and alluvial deposits, with the exception of the steeply dipping structural contact described above that may represent a north-verging back thrust (O'Connor et al. 2005).

The Seyala Conglomerate Formation comprises a heterogeneous assemblage of clastic rocks in which two major types of lithic clasts are recognized: rounded to oblate clasts of white to pale yellow quartzite, and angular clasts of BIF set in a dark, fine-grained matrix of iron oxide and silica (Fig. 10). The origin of the Seyala Conglomerate

Fig. 10 Conglomerate of Seyala Conglomerate Formation in outcrop east of Rouessa open pit. *Light* clasts are quartzite; *dark* matrix is a fine-grained mixture of iron oxides and silica. Note hammer point at upper left edge for scale. USGS photo

Formation has been the subject of debate. Early workers referred to it as the Ijil Breccia and suggested that this unit is essentially a tectonic melange (Bronner 1970; Bronner and Chauvel 1979). More recently, the BGS concluded that the formation is a sedimentary conglomerate, based primarily on the structural setting in which it occurs. The conglomerate is interpreted as a molasse deposit or olistostrome that was eroded from the hangingwall of the back thrust (O'Connor et al. 2005; Schofield and Gillespie 2007).

4 The Guelb El Mhaoudat Superior-Type Iron Formation

A second inselberg of BIF interpreted to consist of Paleoproterozoic Superior-type iron formation is located approximately 50 km to the northeast of the Kediat Ijil at Guelb El Mhaoudat. Guelb El Mhaoudat is a NW-SE-trending, sinuous ridge ca. 18 km long and less than 1 km (typically 300–600 m) wide, rising above the plain of Tiris Complex basement rocks to a height of approximately 250 m (Fig. 11). Similar to other major outcrop areas of Superior-type BIF in Mauritania, Guelb El Mhaoudat is regarded as an allochthonous (or parautochthonous) package of rocks that formerly occupied a more northeasterly position on the northeastern passive margin of the Mesoarchean Rgueïbat Shield, which was transported to its present location during the Birimian orogeny. However, in contrast to the relatively flat-lying Kediat Ijil and Guelb Zednes, Guelb El Mhaoudat is a steeply dipping succession interpreted to have been imbricated with the surrounding Tiris Complex during subsequent compression and thrusting, as were Superior-type BIF occurrences in the Sfariat belt to the north (Fig. 6; Schofield and Gillespie 2007).

The rock package at Guelb El Mhaoudat is similar to that at Kediat Ijil in that it consists mostly of ferruginous chert with lesser quartzite and mica schist. However, the entire Guelb has been mapped as a single unit: the El Mhaoudat Formation, which we suggest is misleading as it groups rock units of very different age. This formation is primarily micro- to mesobanded iron formation characterized by minor amounts of red jasper, hornblende, and carbonate minerals. Weakly ferruginous chert and quartzite containing minor tourmaline or garnet are the next most abundant lithologies, followed by fine-grained schist containing quartz, muscovite, and chlorite with variable amounts of iron oxide and tourmaline. Sedimentary facing indicators are sparse, although Bronner (1988) concluded that size grading of jasper clasts in quartzite beds indicates a younging direction to the southwest. The rock package dips steeply to the northeast, suggesting that it was overturned during imbrication and thrusting (O'Connor et al. 2005).

Structural interpretations imply that the El Mhaoudat Formation is bounded on the northeast and southwest by steeply northeast-dipping, sub-parallel fault zones (Bronner and Fourno 1992; O'Connor et al. 2005). Bronner (1988) described a contact consisting of a 10-m-wide zone of strongly sheared, recrystallized, and mylonitized chlorite-altered rock separating schist and quartzite of the Mhaoudat Formation from gneiss of the Tiris Complex. Our examination of the southwestern margin of Mhaoudat pit #2 confirms the presence of a steeply NE-dipping fault zone in greenschist and quartzite, grading into weakly ferruginous chert and chlorite-altered schist, and then to mesobanded BIF over a distance of approximately 10 m (Fig. 12). The El Mhaoudat Range disappears under Char Group sandstones to the southeast; based on audio-magnetotelluric (AMT) and aeromagnetic data, the range continues into the Taoudeni basement projected along strike for approximately 15 km (Fig. 13; Bronner and Chauvel 1979; Bronner and Fourno 1992; Finn and Anderson 2015). AMT data also suggest that the Mhaoudat Formation continues under regolith cover for an additional 6 km beyond the northwestern outcrop of the range. The steeply dipping eastern and western thrust faults merge about 10 km to the northwest of the northwestern extremity of the range, placing the northeastern part of the Archean Tiris Complex basement over Archean basement (Bronner and Fourno 1992).

In detail, the Guelb El Mhaoudat inselberg is broken into a series of shorter, relatively straight

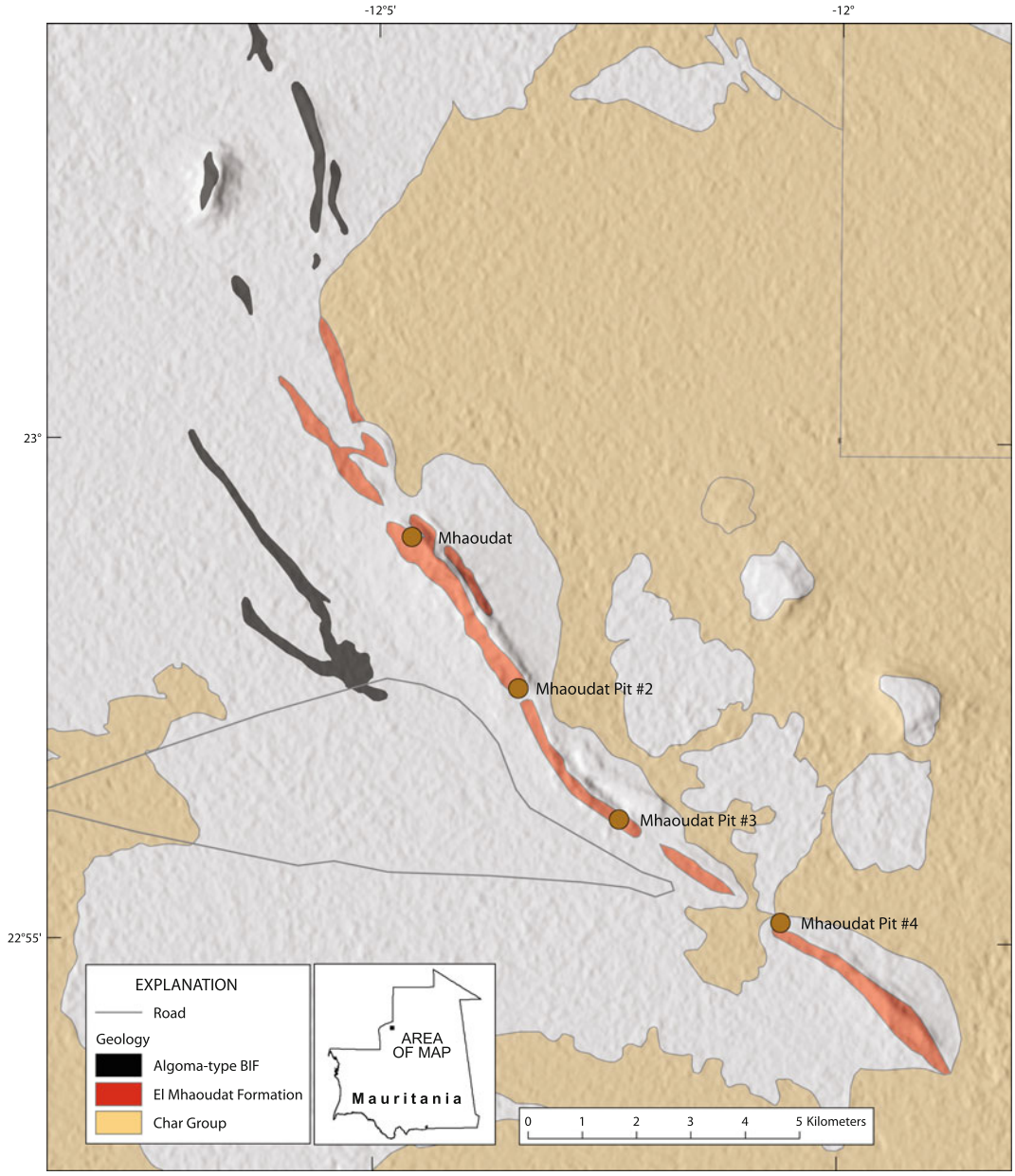

Fig. 11 Geology of Guelb El Mhaoudat showing locations of major open pit iron mines

segments of 2–4 km length that are separated by topographic gaps or passes (cols) through the range. Bronner (1988) and Bronner and Fourno (1992) noted that locations of the passes correspond to areas of thinning of the El Mhaoudat Formation and disappearance of red jasper in the ferruginous chert. Significantly, these passes are also the sites of upgrading of BIF to high-grade hematitic ore, and are the principal sites of iron mines throughout the range (Fig. 11). Thinning of the El Mhaoudat Formation and subsequent silica dissolution, oxidation, and upgrading of BIF at these locations was attributed by Bronner and Fourno (1992) to tensional tectonic forces

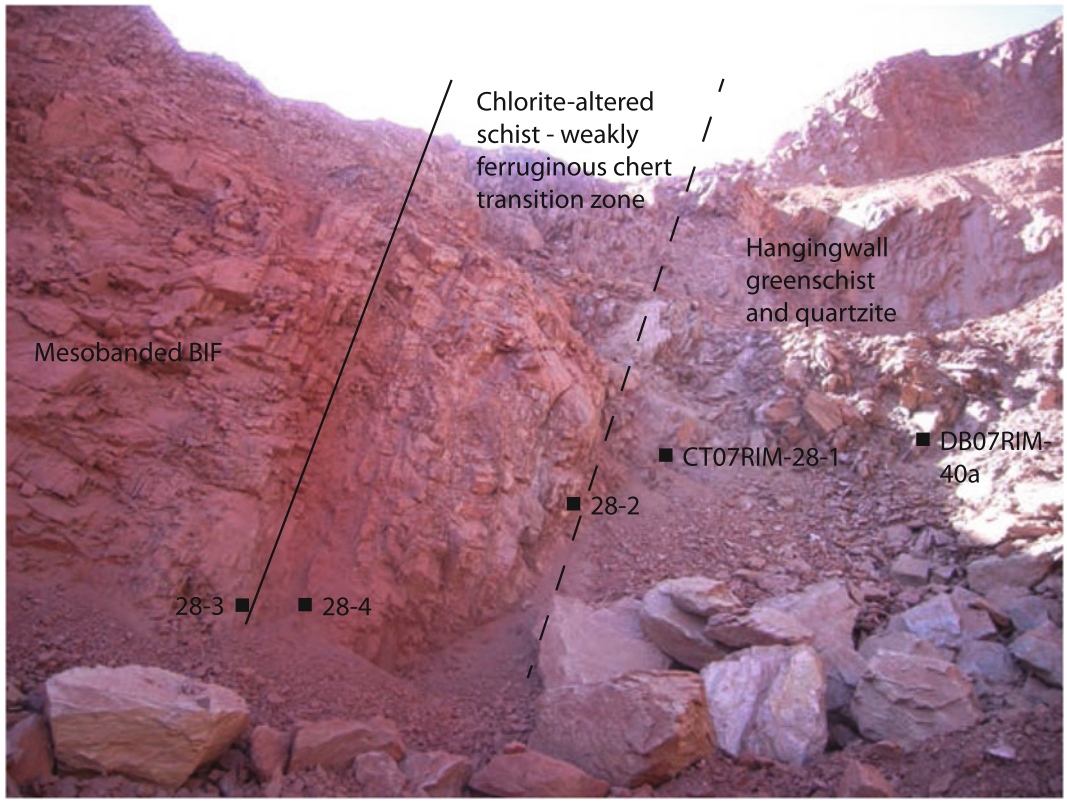

Fig. 12 View looking southeast at fault zone in southwestern wall of Mhaoudat #2 pit. Shown are locations of samples CT07RIM-28-1 through 28-4 and detrital zircon sample DB07RIM-40a. Width of fault zone is ca. 10 m. USGS photo

and metamorphism that formed kilometer-scale boudins. An AMT survey along four profiles across the range, supplemented by drillhole data, suggest that the eastern Mhaoudat thrust fault dips to the northeast at a relatively uniform attitude of 75°–85° along the length of the range (Bronner and Fourno 1992). However, the western thrust fault dips initially steeply but becomes progressively less steep and joins the eastern thrust at progressively greater depths along the length of the range, from northwest to southeast. The result is a steeply dipping lens of El Mhaoudat Formation that becomes deeper and wider along the range, until it disappears under the edge of the Taoudeni Basin at the southeast extremity of the range. Depth estimates of the magnetic data based on extended euler deconvolution (Phillips 2002) suggest that much of the covered extensions of the range lie at less than ~700 m depth (Fig. 14; Finn and Anderson 2015).

5 Sfariat Belt and Guelb Zednes

Additional areas having potential for Superior-type BIF in Mauritania are the Paleoproterozoic Sfariat belt approximately 180 km to the northeast of Zouérate and Guelb Zednes about 225 km east-northeast of Zouérate (Fig. 15). Four known iron occurrences there are hosted within imbricated slices or klippe of iron formation along the suture zone between Mesoarchean and Paleoproterozoic rocks of the Rgueïbat Shield. Three occurrences, Bouderga, Sfariat 1, and an unnamed occurrence are distributed along the NW-SE-trending Sfariat belt and are imbricated with Paleoproterozoic granitic rocks of the Adam

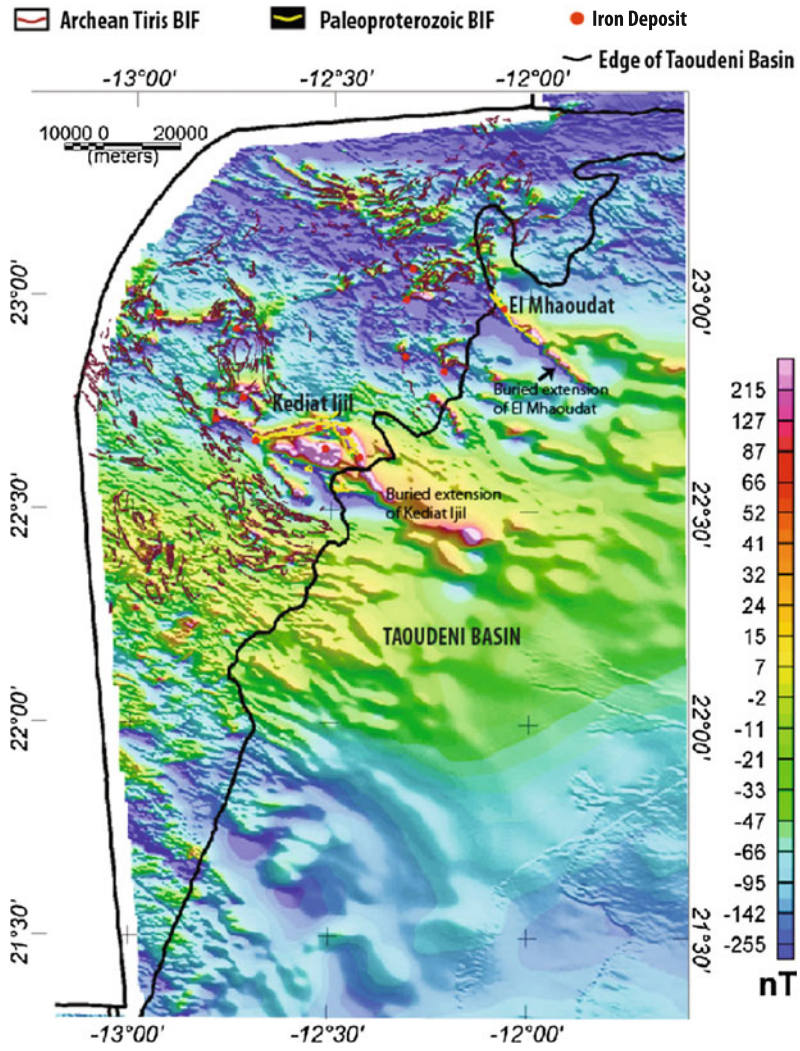

Fig. 13 Color-shaded relief image of reduced-to-pole magnetic data for Tiris Complex (from Finn and Anderson 2015) showing mapped BIF units and locations of iron deposits; see Fig. 16 for names of deposits. Note extension of both the Kediat Ijil and Guelb El Mhaoudat iron formations under margin of Taoudeni Basin

Anajim and Sfariat Suites, and volcanosedimentary rocks of the Rich Anajim Complex. Marot et al. (2003) described the Sfariat belt as a major zone of shearing and imbrication, ca. 175 km long and up to 13 km wide, which involves all of these constituent rock units. Mineral prospecting within the belt, primarily for gold, has focused on the magnetite quartzite layers of the Rich Anajim Complex.

The fourth iron occurrence is present at Guelb Zednes (Fig. 15). Guelb Zednes is a nearly flat-lying inselberg of the Rich Anajim Complex that rests unconformably on steeply inclined gneiss of the Mesoarchean Temmimichate Tsabya Complex. The Guelb rises about 160 m above the surrounding regolith plain and consists of gently southeast-dipping sedimentary rocks of the Guelb Zednes Formation (map unit RAgz; Lahondère et al. 2003). Like at the Kediat Ijil, the basal contact of the Guelb Zednes Formation with the underlying Mesoarchean basement is strongly sheared, suggesting that Guelb Zednes is an allochthonous klippe or tectonic inselberg. The distinguishing feature of the Guelb Zednes Formation is a more than 100-m-thick unit of magnetite-rich quartzite that forms the upper two thirds of the formation. The lower third is composed of quartz-mica-garnet-kyanite schist,

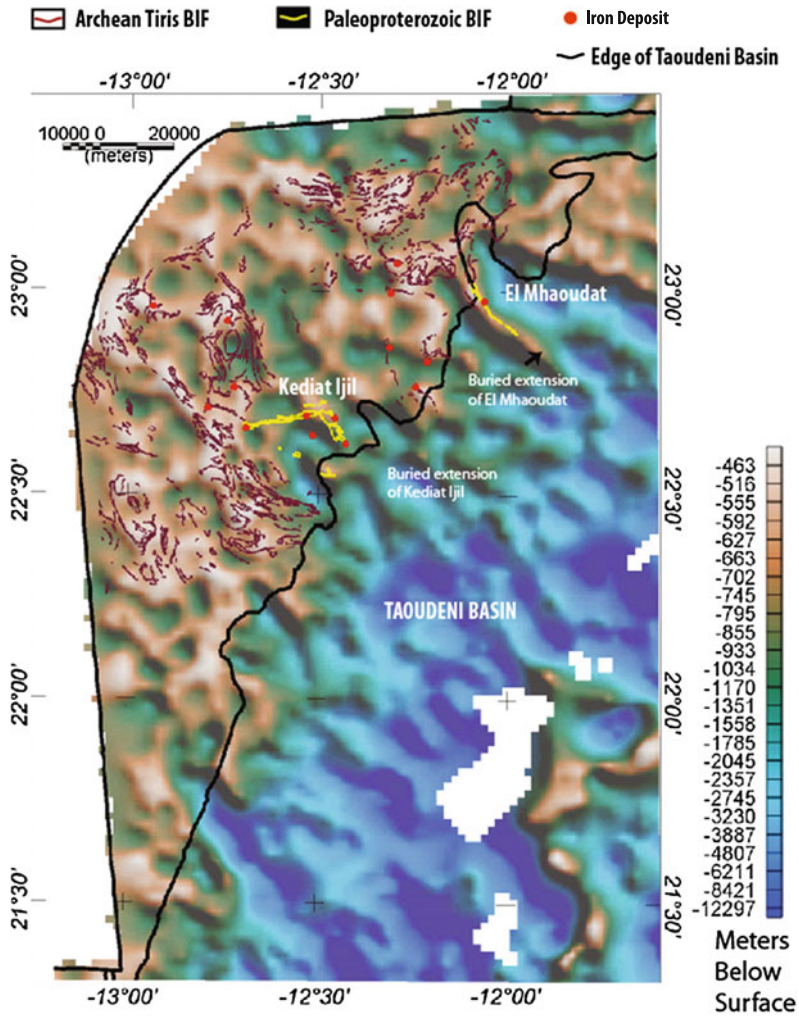

Fig. 14 Color-shaded relief image of gridded depth estimates using Extended Euler method from aeromagnetic data (Phillips 2002). Structural index of 1 and window size of 7 (1225 m) were used with mapped BIF units and locations of iron deposits (from Finn and Anderson 2015). See text for explanation and Fig. 16 for names of deposits

brecciated metagabbro, amphibolite, and metaconglomerate (Lahondère et al. 2003; Schofield and Gillespie 2007).

The Rich Anajim Complex is a metamorphosed early Birimian (>2150 Ma) group of primarily mafic metaigneous and metamorphosed volcanosedimentary rocks including metapyroxenite, amphibolite, dolomitic marble, magnetite quartzite, and migmatitic paragneiss. These rocks constitute broadly mapped areas on both sides of the Sfariat belt, in the southwestern portion of the Paleoproterozoic Rgueïbat Shield. The southern outcrop area lies wholly within the granitic rocks of the middle Birimian Adam Anajim Suite; the northern outcrop area is between the latest Birimian Sfariat belt and granitic rocks of the Gleibat Tenebdar Suite (Fig. 15).

The Rich Anajim Complex is divisible into lithostratigraphic packages consisting of gabbro and basalt thought to be of back-arc origin, a set of closely associated magnetite quartzite and marble, and a paragneiss suite derived from pelitic and calcareous sandstones. The magnetite quartzite (map unit RAqz; Lahondère et al. 2003) forms dark resistant ridges of highly variable length, with mapped outcrops nearly 70 km long. This magnetite quartzite is typically closely associated with impure dolomitic marble that reach thicknesses of several tens of meters but is laterally impersistent. The magnetite quartzite is generally fine grained,

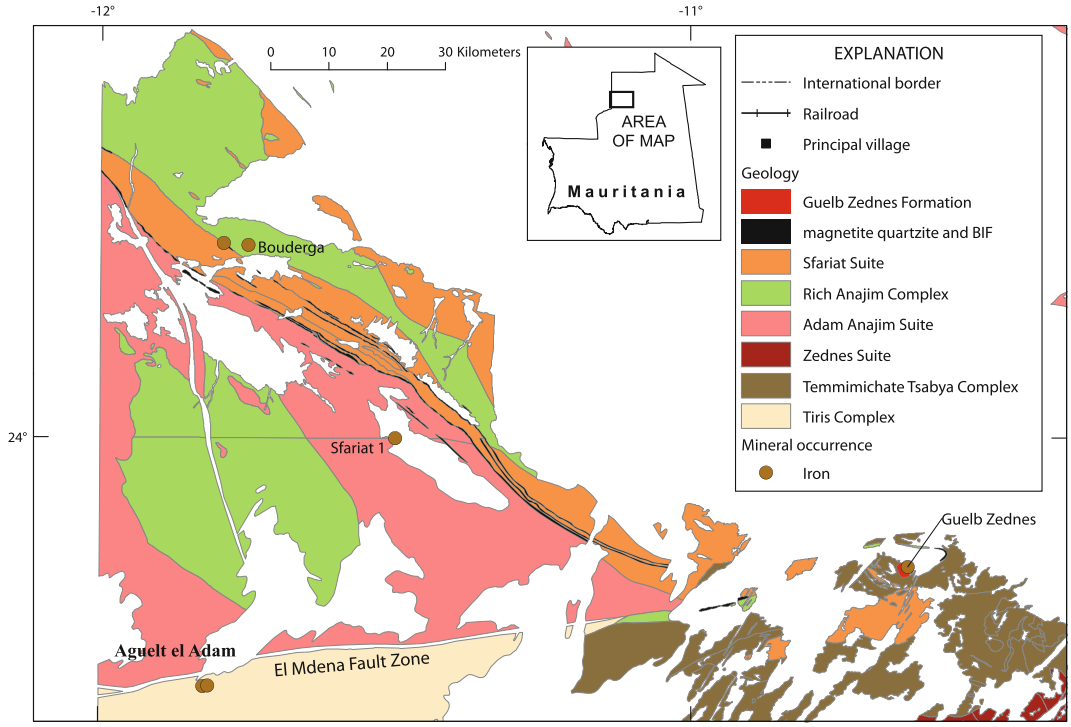

Fig. 15 Simplified geology of Sfariat belt and Guelb Zednes showing locations of Superior-type iron occurrences

but can have grain sizes of several centimeters. Chief constituents are quartz, hematite, and magnetite, accompanied by minor apatite and rare detrital zircon (Bronner 1992). The magnetite quartzite displays micro- to mesobanding (mm- to cm-scale), corresponding to variations in proportions of quartz compared to iron oxides. Iron contents of these BIF units range from 30 to 35 wt% Fe (Lahondère et al. 2003).

The latest Birimian (2020–2000 Ma) Sfariat Suite consists primarily of migmatitic granitoids, which are interpreted as products of anatectic melting of the older Rich Anajim supracrustal rocks (Lahondère et al. 2003). These granitoids crop out mainly between the magnetite quartzite ridges of the Rich Anajim Complex and consist of mylonitized corridors of penetratively deformed biotite-, garnet-, and cordierite-bearing granite and granodiorite. Foliation is generally subvertical and trends WNW, parallel to the magnetite quartzite ridges (Lahondère et al. 2003).

Marot et al. (2003) assigned a low potential for the discovery of economic iron deposits in the Sfariat belt, citing the generally low iron grades and insignificant thicknesses of the iron formation. However, Marot et al. (2003) mentioned previous descriptions by Sougy (1952) and Rocci (1957) of folded segments of iron formation within the Sfariat belt that reach thicknesses of 80 and 100 m, respectively, and noted that the magnetite-rich layer at Guelb Zednes is up to 130 m thick. Blanchot (1975) estimated that Guelb Zednes may contain ca. 300 Mt of low-grade iron ore in magnetite-hematite-quartzite iron formation.

Some uncertainty exists for the assignment of iron formation in the Sfariat belt to either Algoma or Superior type. Early workers (Sougy 1952, 1953; Rocci 1957) classified the iron formation as Algoma type based on an assumed Archean age of the surrounding granitic rocks. However, work by the Bureau de Recherches Géologiques et Minières (BRGM) has established an early Birimian age for the host supracrustal rocks of the Rich Anajim Complex (Lahondère et al. 2003). Marot et al. (2003)

assigned the iron formation to Algoma type based on observations during the BRGM field campaign. An Algoma-type classification is also consistent with the volcanosedimentary nature of the Rich Anajim Complex, which also may have a low potential for base-metal volcanogenic massive sulphide deposits (Taylor and Giles 2015). Consistent with an oceanic or perhaps back-arc tectonic environment for volcanosedimentary rocks of the Rich Anajim Complex, the geochemistry of the amphibolites and metagabbros in the Guelb Zednes Formation shows normal mid-ocean ridge to transitional basaltic signatures (Lahondère et al. 2003).

In contrast, Bronner (1992) and more recently Schofield et al. (2006) and Schofield and Gillespie (2007) assigned a Superior-type classification to the Sfariat belt iron formation. This different classification is based on descriptions of shallow marine calcareous, pelitic, and dolomitic protoliths of the Rich Anajim supracrustal sequence, and on correlation of the Sfariat belt iron formation to that of Guelb El Mhaoudat and Kediat Ijil. Schofield and Gillespie (2007) envisioned imbrication and tectonic transport of Birimian passive margin outliers as allochthonous inselbergs containing Superior-type iron formation, having been transported to their present position along the margin of the Mesoarchean Rgueïbat Shield and above the Tiris Complex to the southwest. For the purposes of the current summary, iron formations of the Sfariat belt and Guelb Zednes are considered permissive for being Superior-type BIF. However, more work is required to discern whether this interpretation is correct.

6 Algoma-Type Iron Deposits in the Tiris Complex

In the major iron-producing region around Zouérate, Algoma-type magnetite quartzite BIF is hosted in the Mesoarchean Tiris Complex. Although initially famous for the abundance of high-grade hematitic iron ores shipped from Superior-type deposits in the Kediat Ijil and Guelb El Mhaoudat, declining reserves of these HIF ensure that the future of iron mining in Mauritania will be dependent on successful exploitation of the abundant Algoma-type deposits. The Guelb El Rhein deposit, 25 km to the north of Kediat Ijil, currently supplies the bulk of magnetite ore produced in the district. However, plans to put the Guelb El Aouj and Askaf North deposits into production will provide additional magnetite ores for years to come.

The Tiris Complex of the central Rgueïbat Shield is well known for having high potential for magnetite iron resources. The Tiris Complex is a Mesoarchean granulite-facies terrane marked by the ubiquitous presence of Algoma-type iron formation. In general, the complex consists of granite domes and intervening keels of supracrustal rocks that together form linear belts showing tightly folded and steeply dipping fabrics. In addition to granite (ca. 70 vol.%), the overlying supracrustal rocks include aluminous cordierite- and biotite-bearing paragneiss, calc-silicate rocks, metamafic rocks, quartzite, and magnetite quartzite BIF (Schofield et al. 2012).

Geologic mapping in the Tiris Complex by the BGS (O'Connor et al. 2005) has divided this complex into three units defined as the El Gheicha, Mirikli, and El Khadra formations. Although correlation of the units is not precise, the TRla unit of the BRGM mapping equates to the El Khadra Formation, whereas the TRle unit of the BRGM (Lahondère et al. 2003) equates to the Mirikli and El Gheicha formations. BGS work (O'Connor et al. 2005) has further identified mappable units of Algoma-type iron formation (unit TRfe) that are ubiquitous throughout the Mirikli and El Khadra formations, but rare within the predominantly aluminous gneisses of the El Gheicha Formation. The El Khadra Formation is completely enclosed by the Mirikli Formation and is present in the northern part of the Tiris Complex. It is very similar to the Mirikli Formation, consisting of lithologically variable quartzofeldspathic and calc-silicate metasedimentary and metaigneous rocks, but is distinguished by a greater proportion of metasedimentary rocks and the widespread occurrence of BIF (Schofield et al. 2012).

A Rb–Sr whole-rock age of 2779 ± 84 Ma determined on the Mirikli Formation at Guelb El Rhein was reported by Vachette and Bronner (1975), which they interpreted as the age of migmatization of the country rocks. Recent work in the Tiris Complex suggests two main phases of intrusive activity at 2950–2870 and 2690–2650 Ma, involving the recycling of crustal material older than ca. 3250 Ma (Schofield et al. 2012). Thus, the supracrustal rocks of the Tiris Complex, including the contained Algoma-type BIF, can be no younger than about 2.95 Ga. Early tectonism, pre-dating the first intrusive episode, imparted a flat-lying, high-grade metamorphic fabric and recumbent folds (Schofield et al. 2012). Bronner (1992) suggested that this early isoclinal folding and thrust imbrication of a relatively small number of BIF units was responsible for their widespread distribution throughout the Tiris Complex.

The magnetite quartzite units are widespread and easily distinguished by linear, high amplitude aeromagnetic anomalies (Fig. 13) and by a tendency to form low ridges and guelbs. These strata vary in outcrop style from simple linear ridges that may be traced for up to several kilometers, to tightly and complexly folded units that form rugged ridges and peaks rising several hundred meters above the surrounding plains, fringed by broad talus aprons. Individual units are typically several meters thick but range from a few centimeters to 10 m thick (O'Connor et al. 2005). Economic deposits form where primary thicknesses of BIF units are doubled or tripled by thrust stacking or folding. Delineation of such targets can be accomplished by filtering of the aeromagnetic data, as displayed in Fig. 16 and explained in the section below. Numerous iron ore targets, both in outcrop and under shallow cover, remain to be explored.

Many occurrences of Algoma-type BIF in the Tiris Complex are listed in the Mauritanian National Mineral Deposits Database (Marsh and Anderson 2015). This database also contains information on the producing mine at Guelb El Rhein, and the deposit nearing production at Guelb El Aouj. Among the more important are occurrences at Guelb Azouazil, Guelb Bou Derga, and Guelb Atomai, which are generally referred to as the western guelbs, and at Guelb Merizet, Guelb Oum Arwagen, Guelb El Meis, and Guelb Tizerghaf, referred to collectively as the eastern guelbs. An additional four unnamed occurrences are ca. 60–75 km to the northeast of the Guelb Tizerghaf occurrence within undifferentiated rocks of the TRle unit (Fig. 1). All of these occurrences consist of layers or folded layers of magnetite quartzite BIF hosted in high-grade gneiss of the Tiris Complex (Marsh and Anderson 2015). Most occurrences are described as "petite gisements" (small occurrences), many of which have been mined by artisanal methods. The Guelb El Meis occurrence is perhaps the smallest. The most significant may be Guelb Oum Arwagen, located east of Guelb El Rhein approximately half way between Zouérate and Guelb El Mhaoudat. Descriptions in the Mauritanian National Mineral Deposits Database (Marsh and Anderson 2015) indicate that this occurrence may have been under consideration for development prior to the development of mines at Guelb El Mhaoudat, implying the presence of economic resources of iron. SNIM recently announced the discovery of an inferred resource of 830 Mt of magnetite ore at Guelb Tizerghaf based on 60,000 m of drilling (SNIM 2013).

The Guelb El Rhein deposit forms a prominent topographic feature ca. 25 km northeast of Zouérate. The deposit consists of a single layer of magnetite quartzite that has been deformed into a series of tight, kilometer-scale folds that form the crest and core of the guelb. Host rocks are migmatitic gneisses of the Mirikli Formation of the Tiris Complex. A structural interpretation by Bronner (1992) shows folding of the BIF into three stacked layers (Fig. 17). The folded layers form an approximately N-S-oriented synclinal structure that plunges gently and opens somewhat to the north. All three stacked layers are currently being mined at Guelb El Rhein in a series of open pits, within successively lower levels of the guelb.

Unlike the iron ore at Guelb El Mhaoudat and in the Kediat Ijil, the ore at Guelb El Rhein is relatively low grade and averages ca. 34–37 %

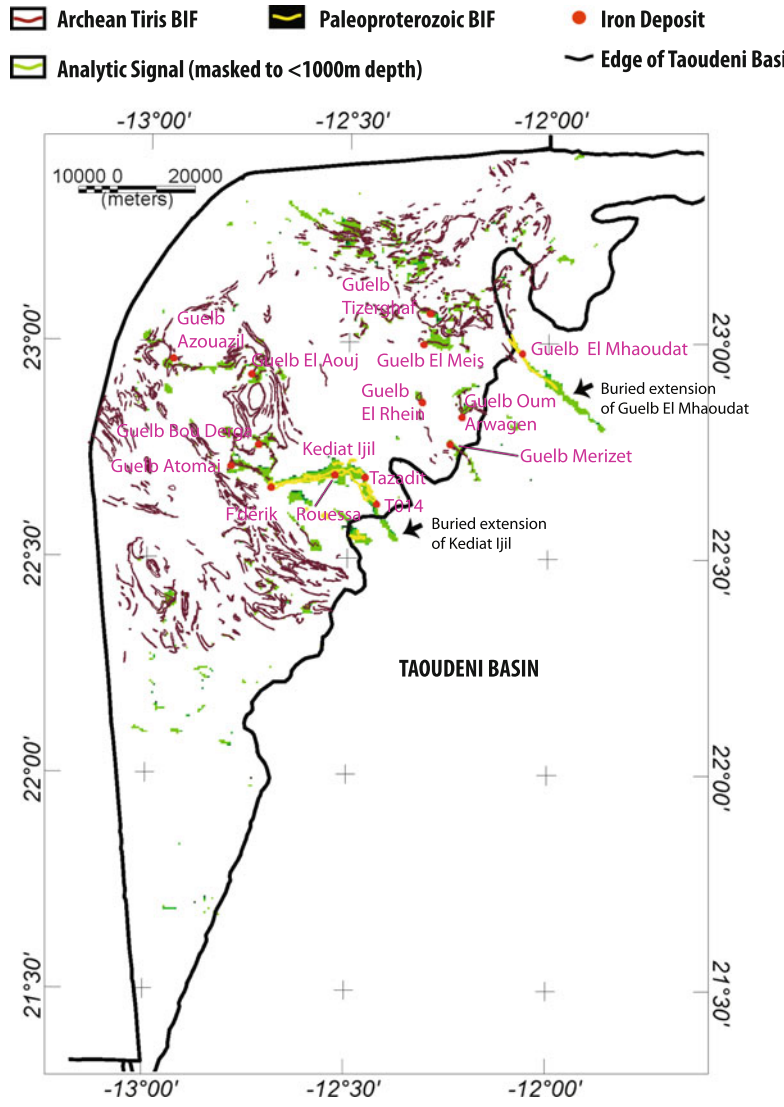

Fig. 16 Analytic signal (in nT/m) of total field magnetic data above 0.75 (areas enclosed by *green lines*) over regions where depth to magnetic basement (Fig. 14) is less than 1000 m, with mapped BIF units and locations of iron deposits. *Green* areas show new zones and extensions of mapped areas of BIF under cover. See text for explanation

Fe, and has not been upgraded by leaching or oxidation to produce hematitic ore. A surface oxidation profile is present and extends commonly 30–50 m below the present surface, and in places to depths as great as 200 m (Szymon Oksengorn, oral commun. 2007; Fig. 18). Hematite does form in the surface oxidation profile at the expense of magnetite; however, this process is detrimental to iron ore recovery because the oxidized surficial ores respond less well to magnetic separation processing. In general, iron formation at Guelb El Rhein is massive and unbanded, and consists of approximately equal proportions of relatively coarse-grained (3–5 mm), equant, quartz and magnetite. Accessories include amphibole and relict pyroxene, with rare sulphide minerals. Magnetite is separated from the gangue by crushing and grinding, followed by dry magnetic separation that produces a concentrate of 65 % Fe (O'Connor et al. 2005). Annual production of crude ore is approximately 10 Mt, resulting in yearly shipments of approximately 4 Mt of concentrate. Plans to install a second magnetic concentrator

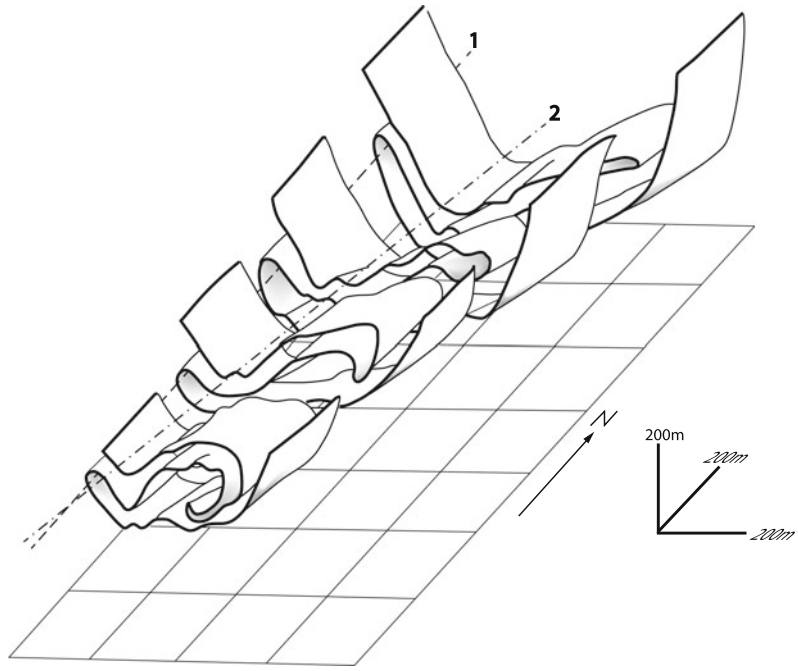

Fig. 17 Structural interpretation showing multiply folded geometry of quartz-magnetite iron formation at Guelb el Rhein (modified from Bronner et al. 1992)

facility at Guelb El Rhein are expected to double these numbers (Tecsult International Ltd. 2009; SNIM 2015).

The Guelb el Aouj deposit is located among the western guelbs approximately 35 km northwest of Zouérate (Fig. 1). It consists of three distinct ridges (East, Center, and West) of magnetite quartzite and associated rocks that rise to a height of approximately 200 m above the surrounding plain. Early attention was focused on the southern part of a tight isoclinal synform at El Aouj Center where BIF on the southwestern limb is 100–200 m thick along a strike length of 2.4 km. The southwest limb of the synform remains open at depth along its entire strike length. Additional ore-grade BIF is reported within the northeastern and northwestern limbs of the synform, which also remain open at depths greater than 50 m (O'Connor et al. 2005). Guelb el Aouj East also has a synclinal structure with magnetite quartzite exposed along a 4 km strike length of the thicker western limb. Guelb el Aouj West has significant outcrops of magnetite quartzite over 3 km of strike length, including favorable (thick) fold structures and high-amplitude, positive magnetic anomalies (Fig. 13; O'Connor et al. 2005).

Surface mapping and drill data show three main ore types at Guelb el Aouj: (1) massive, unlayered, and generally coarse grained; (2) well-layered and typically fine grained; and (3) an intermediate type consisting of both fine- and coarse-grained magnetite quartzite exhibiting discontinuous remnant layering. The magnetite quartzite ore has been oxidized to a depth of about 40 m, thus the weathered non-magnetic overburden is relatively thin. Other rock types associated closely with BIF at Guelb el Aouj Center are a basal (footwall) metagranite, magnetite-bearing quartzite, barren gray quartzite, and local magnetite-rich amphibole-garnet gneiss occurring in the center (hanging wall) of the synform. The southwest limb in places contains thin (<6 m thick) concordant bodies of granite within the main magnetite quartzite unit, particularly in its upper part. Two near-vertical basaltic dikes and one large, north-block-down normal fault cut the deposit. The presence of amphibolite and the range of magnetite-bearing

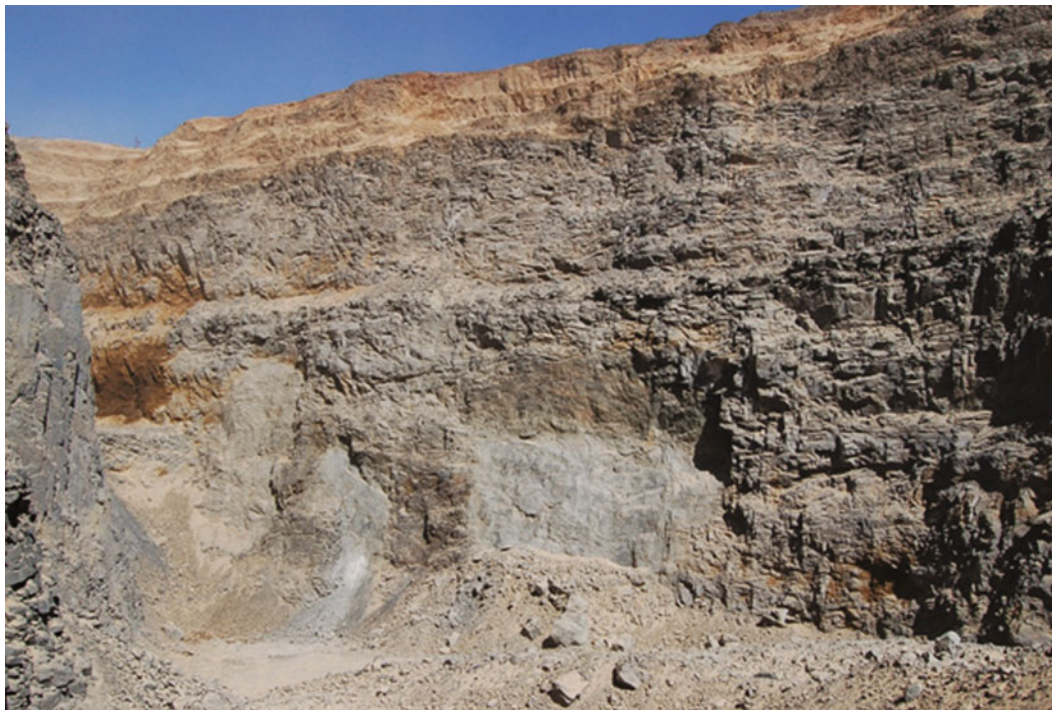

Fig. 18 Northeast wall of Guelb El Rhein open pit. Note prominent orange oxidized zone extending downward approximately 30–50 m from surface. Height of pit wall is ca. 200 m. USGS photo

and barren quartzite lithologies are fairly common features in the western Guelbs (O'Connor et al. 2005; Xstrata 2011a).

JORC-compliant reserves and resources were reported by Sphere Minerals in January, 2015 (Sphere Minerals Ltd. 2015). For Guelb el Aouj East, proven and probable reserves total 755 Mt at 35 % Fe. Total resources (measured + indicated + inferred) are 1870 Mt averaging 36 % Fe at a cut-off grade of 20 % Fe. Indicated and inferred resources are reported for Guelb el Aouj Center as 185 Mt and 615 Mt, respectively, averaging 34 % Fe and 35 % Fe, respectively, at a 20 % Fe cut-off grade (Sphere Minerals Ltd. 2015). As of mid-2009, Sphere Investments and SNIM planned to develop a new iron ore mine, beneficiation plant, and pelletizing plant to produce high-grade, direct-reduction pellets for export, based on ore in the three Guelb el Aouj magnetite deposits (Center, East, and West). Planned production, at that time, was 7 Mt/y of direct-reduction grade pellets (Mining Journal 2006). Two additional magnetite quartzite occurrences to the south of Guelb el Aouj, at Guelb Bou Derga (Fig. 1) and Tintekrate (Fig. 19), were under exploration by Sphere Investments and have inferred resources of 510 and 710 Mt, respectively, averaging 36 % Fe (Sphere Minerals Ltd. 2015). Sphere Investments Ltd. was acquired by Xstrata in 2010 including projects at nearby Askaf and Lebtheinia in the Tasiast-Tijirit terrane. As of December 2011, the Bankable Feasibility Study for Guelb el Aouj was under review by Xstrata (2011a). Recent reports mention drilling activity at Guelb Bou Derga and Tintekrate as well as continued evaluation of the Askaf project. The Askaf project is focused on a series of magnetite quartzite guelbs to the east and west of the track leading into F'Derik from the south, ca. 20–35 km south of F'Derik. Reported JORC-compliant measured + indicated + inferred resources in the Askaf project area are 405 Mt grading 36 % Fe including proven + probable reserves of 190 Mt

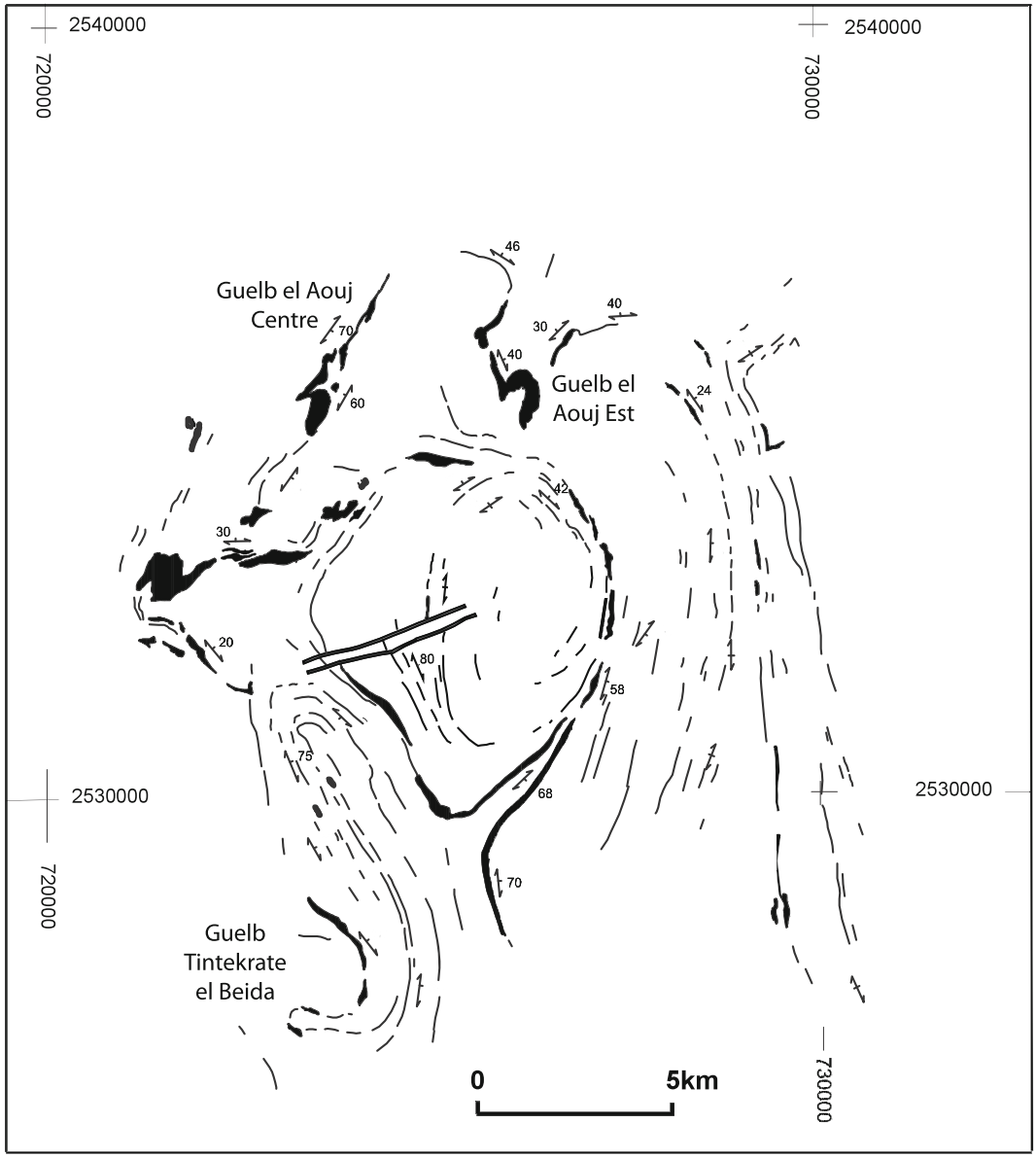

Fig. 19 Sketch map of Guelb el Aouj area showing major outcrops of Algoma-type iron formation (*thick lines*) and structural trends (*thin lines*). Location of Tintekrate el Beida iron occurrence is also indicated (modified from O'Connor et al. 2005)

at 35 % Fe at the Askaf North guelb. Askaf Centre and Askaf East have inferred resources of 95 Mt grading 36 % Fe and 70 Mt grading 35 % Fe, respectively (Xstrata 2011b; Sphere Minerals Ltd. 2015).

ArcelorMittal of Luxembourg also formed a partnership with SNIM in 2008 and was reportedly drilling for magnetite ore at Guelb Agareb, northeast of Zouérate and north of Guelb El Mhaoudat. Bronner (1992) described two guelbs, Agareb (East and West) as synformally folded, kilometer-scale, magnetite quartzite layers that are oriented approximately NE-SW within a minor range of hills called the Kedia Leghnem.

"Resources" of more than 1 Gt of magnetite quartzite may exist in this area (Taib 2010).

7 Geophysical Delineation of Banded Iron Formation

The main targets for iron exploration in Mauritania are banded iron formations. These rocks can be clearly identified in aeromagnetic data whether at the surface, or under sedimentary cover to depths of over 2 km. Radiometric data can also help delineate exposed BIF due to their relatively high thorium content (Finn and Anderson 2015). Magnetite BIF is very magnetic, having measured susceptibilities of nearly 1 SI (Finn and Anderson 2015), in some cases exceeding 2 SI (Clark 1997). Such high susceptibilites produce characteristic, short (10 s of km), narrow, wavy, high-amplitude (>500 nT-3000 nT) positive, reduced-to-the-pole (RTP) magnetic anomalies (Fig. 13; Finn and Anderson 2015). The Algoma-type BIFs act as structural markers within deformed, less-magnetic greenstone belts, and therefore can delineate folds. Estimates of depths to the top of the crystalline basement have been calculated from the magnetic data (Fig. 14; Finn and Anderson 2015). Reliability of these depth estimates are impacted by several factors including the window size used in the Euler depth calculations, accuracy of the flight elevation and topographic surfaces, and the flight line spacing. The window size must be small enough to capture features of interest, but not so large as to include multiple anomalies. After many trials, the window size that gave the largest number of good solutions is 1225 m. Good solutions may be obtained, but if the flight elevation and/or topographic surfaces are poorly known the depth estimates will be degraded. In the case of the Mauritania data, the topographic surface is poorly known in many places and flight elevations of the aeromagnetic data are probably good to within 25–50 m. For shallow sources, such as exposed rocks, depth estimates should equal zero, but the maximum depths that we calculated are generally 100–400 m too deep (Finn and Anderson 2015).

The most prominent high-amplitude magnetic highs over iron occurrences are associated with Paleoproterozoic thrust sheets and overlying Superior-type BIF, most notably at Kediat Ijil and Guelb El Mhaoudat and their extensions beneath the Taoudeni Basin (Fig. 13). The depth estimates suggest that large portions of the Paleoproterozoic rocks lie within ~700 m of the surface (Fig. 14). All of the remaining linear fabric on the RTP magnetic anomaly map relates to BIF within the Archean Tiris Complex (Fig. 13). There, iron concentrations occur where the magnetic anomalies display relatively high amplitudes, suggesting fairly thick sources.

In order to determine prospective regions for iron formation occurrence, we use the analytic signal data to identify anomalies that correspond to thick BIF. The amplitude of the 3-D analytic signal of the total magnetic field produces maxima over magnetic contacts regardless of the direction of magnetization, facilitating geologic interpretation of analytic signal amplitude compared to the original total field data or RTP magnetic field. By comparing the analytic signal and known iron occurrences, it was possible to develop a threshold for the analytic signal such that values greater than the threshold (which varied from region to region, but generally are >0.75 nT/m) are clearly associated spatially with relatively thick BIF units, thereby eliminating thinner, uneconomic BIF. We also masked these data to isolate anomalies whose sources are at depths of less than 1000 m (Fig. 16). The masked analytic signal data show that the Kediat Ijil and El Mhaoudat, and their buried extensions beneath the Taoudeni Basin, are favorable for the occurrence of magnetite iron formation. Some BIF of the Tiris Complex may also be thick enough to be economic (Fig. 16).

Susceptibilities of the hematite BIF are generally much lower than those of the magnetite BIF. If the hematitic, low-susceptibility portions of the BIF are extensive and thick, they would produce magnetic lows within the highs recorded by the magnetite BIF (Fig. 13). These lows are

not observed, however, suggesting that regions having demagnetized BIF are small relative to the line spacing of the magnetic survey (700 m).

8 Petrography and Geochemistry of Iron Formation in the Zouérate District

Thirty-one samples of iron formation and related host rocks were collected from the Zouérate district in October, 2007. Included are three samples of Algoma-type magnetite iron formation from the Mirikli Formation of the Tiris Complex, and 28 samples of Superior-type ferruginous chert, hematite iron formation, and associated host rocks from the El Mhaoudat Formation and the Tazadit and Seyala Conglomerate formations of the Kediat Ijil. The samples of Superior-type iron formation were collected mainly from a series of four profiles beginning in BIF protore and traversing into areas of high-grade hematite iron formation. Sampling profiles were designed for use in characterizing the petrography and geochemistry of the Superior-type BIF, and for providing information on possible mechanisms leading to formation of the high-grade hematite ores. Eighteen polished thin sections were examined for textural relationships accompanying increases in iron content.

The first profile of seven samples was collected from an area of active mining in the Guelb El Mhaoudat #2 pit. This profile extends 150 m from 5 m into greenschist and quartzite adjacent to the Mirikli Formation in the southwestern wall of the pit, across a faulted contact into BIF, and then into high-grade HIF of the El Mhaoudat Formation (Fig. 12). A second profile of six samples was collected from an area of active mining in the east wall of the Tazadit TO14 Sector 2 pit, extending 150 m from microbanded HIF of the Tazadit Formation 30 m below a paleoweathering surface on the iron formation at the southern margin of the pit, northwards into friable, high-grade HIF in the center of the pit. A third profile was collected across the contact between the lower and upper members of the Tazadit Formation along the mine road leading into the Tazadit #1 pit. This last profile sampled the classic outcrop described in detail by Bronner and Chauvel (1979) and serves as a type example of protore BIF of the Tazadit Formation. Five samples were collected: two from BIF and interbedded quartzite and muscovite schist in the upper 100 m of the lower member, one of altered muscovite schist in the faulted contact between the lower and upper members, and two of BIF of the upper member extending to 100 m west of the fault. A fourth profile was collected from a bench crossing the southwest wall of the Tazadit #1 pit about 100 m above the base of the pit. Here, five samples were collected from an approximately 100 m section of banded and brecciated HIF exhibiting marked changes in texture and coloration, from darker banded and brecciated HIF to pale orange HIF showing variable degrees of fabric-destructive alteration (Fig. 20). A sixth sample of well banded, unaltered, hematite-chert iron formation was collected 200 m east of the westernmost altered samples.

Other samples of Superior-type iron formation collected include one hematite-chert BIF from the Guelb El Mhaoudat #4 pit, a pair of samples from the Tazadit #1 pit overlook at the top of the north wall, representing supergene-enriched and normal banded HIF of the Tazadit Formation, and one sample of a thin HIF layer within the Seyala Conglomerate Formation just east of the Rouessa pit. Two samples of Algoma-type magnetite iron formation were collected from the Guelb El Rhein pit, one of massive, partially oxidized magnetite from the oxidized profile about 30 m below the present-day weathering surface, and a second of massive, unoxidized magnetite about 150 m above the base of the pit. A third sample of massive magnetite was collected from a 2-m-thick layer of iron formation in the Mirikli Formation, from the northeast side of the sole thrust fault exposed in the Guelb El Mhaoudat #3 pit.

Fig. 20 View of southwest wall of Tazadit #1 pit showing development of *orange*, fabric-destructive HIF in *darker colored*, well-layered protore BIF. Box shows location of Fig. 21j. USGS photo

9 Petrography of Mhaoudat and Tazadit Iron Formations

BIF protore is macroscopically characterized by bands of both quartz and hematite 1 mm–1 cm thick (Fig. 21a, b). Former chert bands are mostly massive aggregates of anhedral, interlocking, mosaic-textured quartz (Fig. 21c). Isolated grains of quartz are uncommon and grain boundaries are generally not etched or rimmed with other material. Iron oxides comprise varying proportions of massive, subhedral hematite-martite. Large grains and massive areas of hematite-martite display a fine, porous texture (Fig. 21d), which together with interstitial space are commonly filled with amorphous iron oxides. Rare to abundant patches of relict magnetite are ubiquitous. Some porous grains have a skeletal texture that may be incipient microplaty hematite, which may constitute 5–10 vol.% of the rock. None of the samples shows any macro- or microscopic evidence of being GIF.

BIF transitional to low-grade HIF ore shows a greater range of textures than either BIF protore or HIF. Macroscopically, these range from regularly banded hematite-chert iron formation (Fe = 46.9 wt%) with hematite bands 0.1–1 cm thick interbanded with 1- to 2-mm-thick recrystallized chert bands, to hydrothermally brecciated iron formation characterized by light orange colored areas of unbanded hematite-rich rock interspersed with darker zones in which banding is preserved (Fig. 21e; Fe = 52.0 wt%). The regularly banded IF consists of ~40 % quartz, which occurs either as massive bands and aggregates of anhedral interlocking mosaics or as anhedral grains that form the matrix to iron oxides. Rare reddish-brown, semi-translucent iron oxides are present and minor etching of

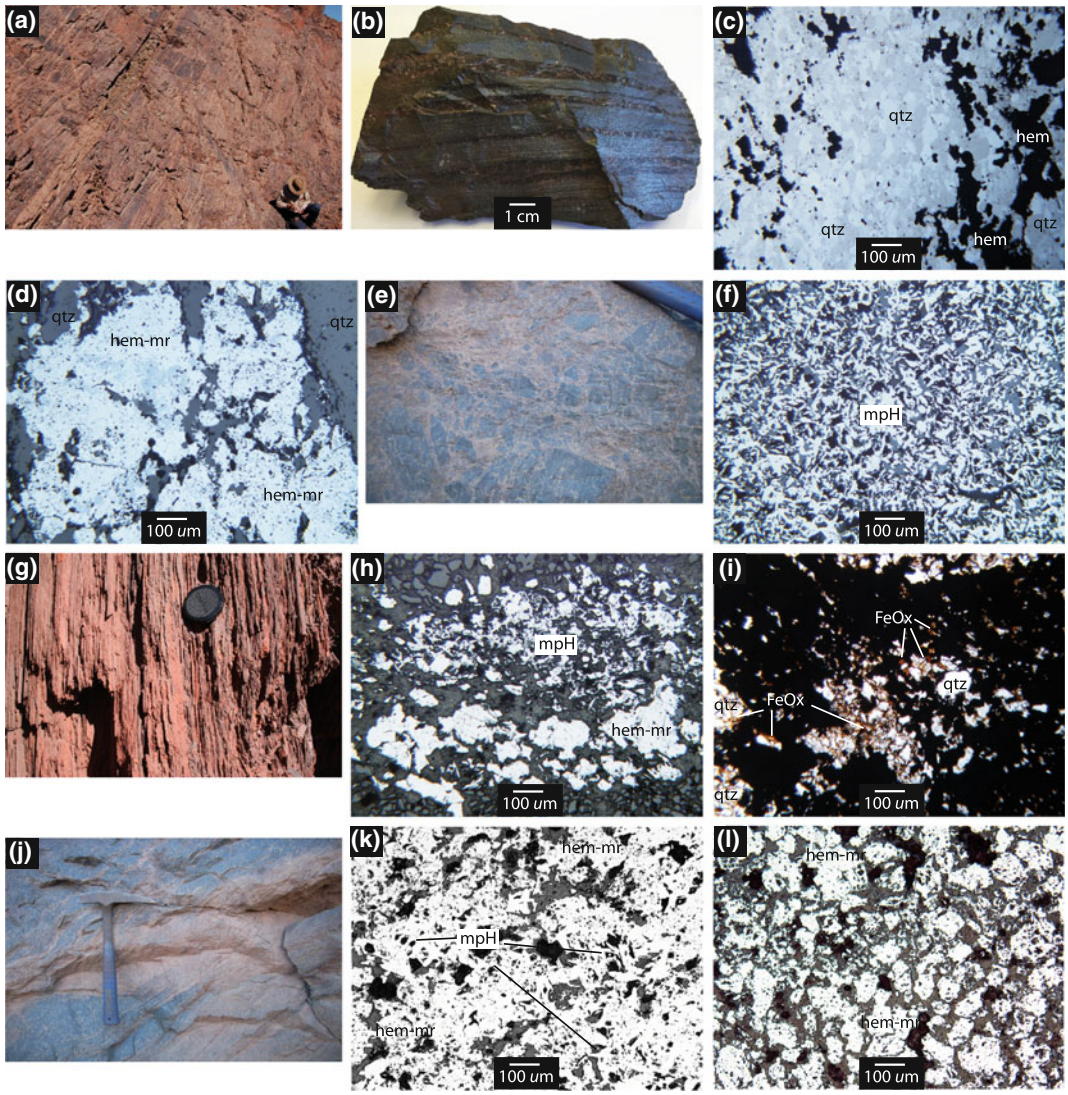

Fig. 21 **a** Micro- to mesobanded protore BIF of Tazadit Formation, upper member along Tazadit #1 pit roadcut. **b** Microbanded protore BIF. **c** Photomicrograph of sample CT07RIM-34-2, Tazadit #1 pit overlook, showing mosaic-textured quartz; plane-polarized transmitted light. **d** Photomicrograph of sample CT07RIM-34-2 showing subhedral hematite-martite with a fine, porous texture; plane-polarized reflected light. **e** Hydrothermally brecciated BIF transitional to HIF, Tazadit #1 pit; location of sample CT07RIM-36-1. **f** Photomicrograph of sample CT07RIM-36-1 showing development of microplaty hematite in orange hydrothermal breccia matrix; plane-polarized reflected light. **g** Outcrop photo of BIF transitional to HIF in supergene weathering profile at Tazadit #1 pit overlook; location of sample CT07RIM-34-1. **h** Photomicrograph of sample T07RIM-34-1 showing 1-mm-thick band of subhedral to anhedral hematite-martite and lesser euhedral to subhedral microplaty hematite; plane-polarized reflected light. **i** Photomicrograph of sample CT07RIM-34-1 showing etched and embayed quartz grains and amorphous, orange-brown iron oxides as matrix; plane-polarized transmitted light. **j** Tazadit #1 pit wall showing relict banding in darker IF (sample CT07RIM-36-2) and effects of fabric-destructive hydrothermal alteration in light orange HIF (sample CT07RIM-36-3). **k** Photomicrograph of sample CT07RIM-36-3 showing fabric-destructive anhedral hematite-martite and lesser euhedral to subhedral microplaty hematite; plane-polarized reflected light. **l** Photomicrograph of sample CT07RIM-36-5 showing relict banding in subhedral hematite-martite; plane-polarized reflected light. USGS photos

quartz grain boundaries is observed. Within hydrothermally brecciated IF, weakly persistent dark bands are gently folded and in places are broken and disrupted. Subhedral quartz (~30 %) forms individual grains in the matrix to semi-massive to massive hematite (Fig. 21f). There are minor areas of reddish-brown, semi-translucent iron-oxides distributed throughout. Quartz grain boundaries show minor to moderate etching and corrosion.

The regularly banded IF contains subhedral to slightly rounded hematite or semi-massive anhedral patches of hematite. Amorphous iron oxides occur throughout as a matrix and as fillings of porous areas within hematite. Rare relicts of magnetite are also present. The hydrothermally brecciated IF is composed mostly of semi-massive, subhedral intergrowths of microplaty hematite; macroscopically darker areas are nearly massive hematite that contains rare small inclusions of magnetite (<1–2 %). Domains having more interstitial quartz contain a higher percentage of subhedral to euhedral microplaty hematite (Fig. 21f).

A third sample of BIF transitional to low-grade HIF ore was collected from the supergene weathering profile within a few meters of the top of the Tazadit #1 pit at the overlook (Fig. 21g; Fe = 47.3 wt%). This sample consists of 1-mm-thick bands of subhedral to anhedral martite and lesser euhedral to subhedral microplaty hematite separated by 0.5- to 1.0-cm-thick bands of subhedral quartz grains. The martite-microplaty hematite has a goethite matrix. Martite grains locally contain inclusions of residual magnetite. Microplaty hematite constitutes ~25 % of the martite-microplaty hematite bands and is generally poorly formed. Euhedral microplaty hematite crystals occur in minor patches and grade into skeletal and embayed martite (Fig. 21h). Quartz bands are flecked with martite crystals, and quartz grains are strongly etched and corroded (Fig. 21i). The matrix appears to be mostly quartz and iron oxides (Fig. 22i).

High-grade iron formation samples generally show either complete fabric destruction or faint relict banding (Fig. 21j). Fabric destructive HIF in transmitted light has a uniformly dark color accentuated by slightly darker rounded patches 1–10 mm in size composed of hematite. The matrix constitutes ~2–3 % of the rock and comprises anhedral quartz and semi-translucent iron oxides. Quartz grains display irregular shapes with rounded edges and embayments. Hematite consists of ~60 % anhedral to subhedral, porous-textured martite and ~40 % subhedral to euhedral microplaty hematite that has equal or smaller grain sizes. The microplaty

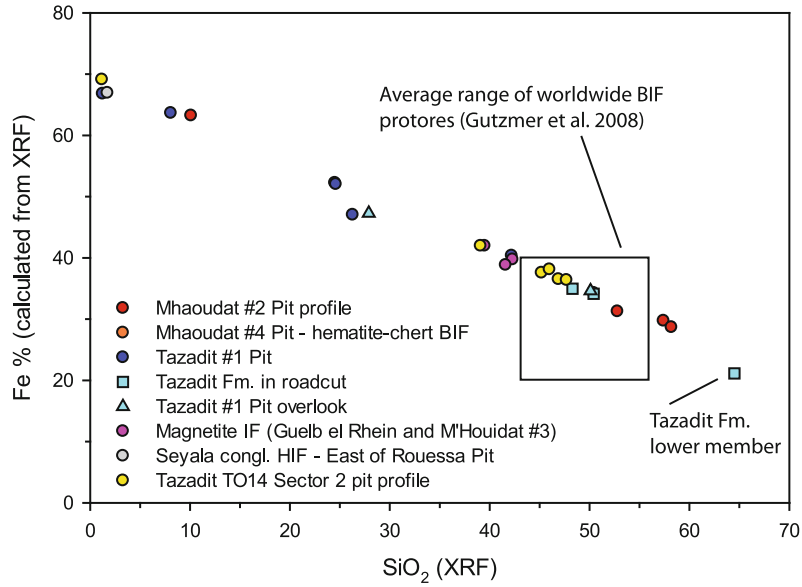

Fig. 22 Plot of SiO_2 versus iron content for Zouérate iron formation

hematite crystals lack the porous texture observed in martite. Relict magnetite is rarely present (Fig. 21k).

Relict banding in HIF is regularly spaced on a mm to cm scale. These rocks are ~95 % opaque minerals with ~5 % evenly distributed, very-fine-grained quartz and secondary iron oxides. Approximately 40 % of the opaque minerals consist of amorphous iron oxides as matrix to the hematite. About 90 % of the hematite forms rounded anhedral and irregularly-shaped grains with a pronounced porous texture; the remainder is microplaty hematite. No relict magnetite is observed (Fig. 21l).

Algoma-type magnetite iron formation from the Mhaoudat #3 pit was collected from a 1- to 2-m-thick band of magnetite quartzite iron formation 20–30 m from the thrust separating rocks of the Mhaoudat Formation from those of the Tiris Complex. Macroscopically, the Algoma-type iron formation has a moderate metamorphic foliation and displays a flattening and alignment of quartz and magnetite. In outcrop, the iron formation is strongly magnetic and consists of approximately 60 % quartz, 38 % magnetite-hematite, and a few percent secondary iron oxides (goethite).

Quartz is coarse grained and forms flattened aggregates exhibiting a granoblastic fabric without evidence of embayment or corrosion. Coarse-grained aggregates of hematite-magnetite consist of about 30 % clean, non-porous, magnetite contained within irregularly shaped anhedral hematite (martite). Both the magnetite and hematite-martite display irregular and anhedral grain boundaries. The hematite-martite grains have a pronounced fine, porous texture and contain large inclusions of secondary iron oxide.

In contrast, Algoma-type magnetite iron formation from the Guelb El Rhein pit consists of a massive, unoriented, coarse- to very coarse-grained mixture of 25–35 % hematite (martite)-magnetite, 65–75 % quartz, and up to 20 % orthopyroxene. In crossed-polars (transmitted light), the orthopyroxene exhibits second-order blue, green, yellow, and pink interference colors, suggesting that these grains are iron rich. In reflected light, a sample from well below the present-day surface oxidized zone contains only rounded subhedral to euhedral hematite-martite that is generally non-porous. Hematite-martite grains are surrounded by quartz and orthopyroxene, or form aggregates. In a second sample collected ca. 30 m below the present-day oxidized zone, hematite-magnetite forms euhedral to rounded, subhedral grains or large anhedral masses of hematite-martite, with magnetite showing distinct, crystal-shaped outlines. Enclaves of magnetite constitute approximately 30 % of the grains or grain aggregates and lack inclusions, whereas areas of hematite-martite display a fine porous texture.

10 Geochemistry of BIF

Geochemical data obtained on samples collected by the USGS during fieldwork in October, 2007, are presented in Table 1. All samples were analyzed at SGS Laboratories in Ontario, Canada. Concentrations of major elements were determined by X-ray fluorescence (XRF) using a Bruker S8 Tiger spectrometer, following preparation of standard glass disks by fusion of sample powders with a lithium metaborate-lithium tetraborate flux. The detection limits of the XRF analyses are 0.01 % for all major elements. Sample loss on ignition was determined by gravimetry.

Major, trace, and REE were measured by a combination of inductively coupled plasma-atomic emission spectrometry (ICP-AES) and inductively coupled plasma-mass spectrometry (ICP-MS). Powdered samples were decomposed using a sodium peroxide sinter at 450 °C and then leached with water and acidified with HNO_3. The ICP-AES analyses were conducted on a PerkinElmer Optima spectrometer; the ICP-MS analyses were done on a PerkinElmer Elan spectrometer. Precision and accuracy of the major and trace element determinations by XRF, ICP-AES, and ICP-MS were monitored using the georeference material GSP-2. Repeated analyses showed that precision was typically better than 5 % for elements occurring at concentrations significantly above their respective detection

Table 1 Geochemical data for representative samples of iron formation from the Zouérate district

Unit name and location	Mhaoudat Fm. Mhaoudat #2 pit		Tazadit Fm. TO14 sector 2 pit			Tazadit Fm. Tazadit #1 pit overlook		Tazadit Fm. Tazadit #1 pit			Seyala Fm. near Roussa pit	Mirikli Fm. Guelb El Rhein pit
Sample # (CTO7RIM-)	28–4	28–7	32–4	32–5	32–6	34–2	34–1	36–2	36–1	36–3	35–2	30–1
Lithology	Protore BIF	HIF	Protore BIF	Transitional BIF to HIF	HIF	Protore BIF	Transitional BIF to HIF	Protore BIF	Transitional BIF to HIF	HIF	HIF	Magnetite IF
Major elements (%)												
SiO_2	52.8	10.1	47.7	39.1	1.18	50.1	27.9	42.2	24.6	8.09	1.73	39.5
TiO_2	0.07	0.01	0.02	0.02	0.02	<0.01	0.08	<0.01	0.02	0.01	0.03	0.04
Al_2O_3	1.51	0.2	0.32	0.34	0.46	0.3	2.8	0.19	0.55	0.59	0.56	0.27
Fe_2O_3	44.7	90.4	52	60	98.8	49.5	67.6	57.7	74.4	91	95.7	60
Fe-calculated	31.3	63.2	36.4	42.0	69.1	34.6	47.3	40.4	52.0	63.6	66.9	42.0
FeO	0.03	0.03	0.88	0.36	0.66	1.14	0.14	0.07	0.07	0.04	0.07	22.3
MnO	0.02	0.12	<0.01	0.03	0.03	<0.01	0.01	<0.01	0.01	0.08	0.02	0.02
MgO	0.05	<0.01	0.03	0.04	<0.01	0.03	0.06	0.02	0.02	<0.01	0.07	1.33
CaO	0.03	0.02	0.03	0.02	<0.01	0.02	0.05	<0.01	0.01	<0.01	0.58	0.97
Na_2O	<0.01	<0.01	0.01	<0.01	<0.01	0.02	0.02	<0.01	0.01	<0.01	0.02	0.02
K_2O	<0.01	<0.01	<0.01	<0.01	<0.01	<0.01	0.09	<0.01	<0.01	<0.01	<0.01	<0.01
P_2O_5	0.05	0.08	0.02	0.02	0.03	0.07	0.06	<0.01	0.02	0.02	0.03	0.11
LOI	0.91	0.42	0.28	0.42	0.4	0.66	1.92	0.66	0.99	0.79	1.3	<0.01
Trace and REE (ppm)												
V	20	15	16	15	36	<5	25	<5	9	9	20	5
Co	2.9	2.1	2.7	1.7	4.5	0.9	1.9	1.5	1.7	1.8	1.8	0.7
Ni	<5	<5	<5	<5	<5	<5	6	<5	<5	<5	<5	<5
Cu	11	10	18	14	11	8	14	7	10	8	10	11
Zn	<5	<5	11	33	12	<5	<5	<5	9	<5	<5	<5
Rb	1	0.4	0.7	<0.2	0.3	0.4	6.4	0.3	0.2	0.2	0.3	0.6

(continued)

Table 1 (continued)

Unit name and location	Mhaoudat Fm. Mhaoudat #2 pit		Tazadit Fm. TO14 sector 2 pit			Tazadit Fm. Tazadit #1 pit overlook		Tazadit Fm. Tazadit #1 pit			Seyala Fm. near Roussa pit	Mirikli Fm. Guelb El Rhein pit
Sr	23	44.1	19.6	12.7	13.6	18	41	7.7	12.4	9.2	26	45.2
Ba	25.5	484	28.9	25	<0.5	25.3	36.1	5.9	7.9	169	82.2	8.4
Pb	<5	<5	23	34	35	<5	25	<5	14	<5	9	6
Y	3.8	17	7.9	2.5	2.5	4.6	11.1	1.1	2	2.4	2.1	2
Sc	<5	<5	<5	<5	<5	<5	<5	<5	<5	<5	<5	<5
Zr	14.8	4.3	2.6	2.9	4.1	5.3	19.3	1.8	2.9	2.9	7.8	1.3
Nb	1	<1	<1	<1	<1	<1	2	<1	<1	<1	<1	<1
Th	1.9	0.2	0.7	0.5	0.6	0.5	1.8	0.1	0.3	0.3	0.8	0.2
U	1.68	0.61	0.36	0.37	0.72	0.52	1.13	0.21	0.7	0.56	0.64	0.17
La	3.2	1.4	6.7	1.5	0.9	8.6	25.5	1.3	5	5.5	2.1	2.3
Ce	6.3	2.3	12.5	2.7	1.6	19.7	58.4	2	7.1	7.6	4.5	4.4
Pr	0.64	0.28	1.36	0.25	0.12	2.58	8.38	0.19	0.75	0.77	0.42	0.54
Nd	2.4	1.1	5.1	0.9	0.8	10.6	29.9	0.7	2.4	2.6	1.7	2.1
Sm	0.4	0.4	0.8	0.2	0.2	2.1	5.2	<0.1	0.3	0.4	0.3	0.4
Eu	0.16	0.24	0.51	0.11	0.13	0.56	1.38	0.07	0.23	0.21	0.1	0.19
Gd	0.51	0.95	1.01	0.28	0.29	2.07	3.63	0.11	0.33	0.3	0.31	0.32
Tb	0.06	0.19	0.15	<0.05	<0.05	0.28	0.48	<0.05	<0.05	<0.05	<0.05	<0.05
Dy	0.5	1.47	0.88	0.27	0.31	1.63	2.49	0.1	0.24	0.29	0.37	0.28
Ho	0.12	0.39	0.2	0.07	0.08	0.27	0.46	<0.05	<0.05	0.05	0.07	0.06
Er	0.32	1.27	0.59	0.22	0.29	0.51	1.27	0.07	0.14	0.2	0.19	0.16
Tm	<0.05	0.15	0.08	<0.05	<0.05	0.06	0.15	<0.05	<0.05	<0.05	<0.05	<0.05
Yb	0.3	0.9	0.5	0.2	0.3	0.3	1	0.1	0.2	0.2	0.2	0.2
Lu	0.05	0.13	0.09	0.06	0.06	0.08	0.17	<0.05	<0.05	<0.05	<0.05	<0.05

limits. Close agreement between the analytical data and the reference values suggests that the element determinations are also highly accurate. FeO was determined by digesting a 0.5 g sample using a mixture of sulphuric, hydrofluoric, and hydrochloric acids. The solution is titrated with potassium dichromate using a sodium diphenylanime sulphonate indicator. The lower limit of detection (LOD) for FeO is 0.01 % and analyses were deemed acceptable if recovery of FeO was ±15 % at five times the LOD, and if the calculated percent relative standard deviation of duplicate samples was no greater than 15 %.

In our geochemical comparison of BIF protores to high-grade HIF, we follow the methods and stated averages of Klein (2005) and Gutzmer et al. (2008). Although the range in total iron contents of our samples is nearly continuous from 21.1–69.1 wt% Fe, we have calculated the average composition of protore BIF from those samples having between 20 and 40 wt% Fe, and the average composition of high-grade HIF from those samples with iron content greater than 60 % Fe. Excluded is one sample of low-iron BIF from the lower member of the Tazadit Formation because the mineable iron deposits of the Kediat Ijil are all hosted within the upper member of this formation, whereas the lower member is generally not considered protore (Szymon Oksengorn, oral commun. 2007).

Overall, the geochemical data show the expected trend of increasing iron with concomitant decreasing silica that is characteristic worldwide of the transformation of BIF protore to high-grade HIF (Fig. 22; Gutzmer et al. 2008). BIF protore (n = 12; samples from profiles and locations described above) ranges from 28.7 to 40.3 wt% total Fe (avg = 34.1) and 42.2–58.2 wt% SiO_2 (avg = 49.6), whereas HIF (n = 5) ranges from 63.2–69.1 wt% total Fe (avg = 65.9) and 1.2–10.1 wt% SiO_2 (avg = 4.5). Al_2O_3 is uniformly low, averaging 0.5 wt% in both BIF protore and HIF, with a maximum of 1.5 wt% in BIF protore. The anomalously Al_2O_3-rich sample from the Tazadit pit overlook is from the supergene weathering profile. CaO and MgO contents are both quite low, from below detection up to generally 0.05 wt%, reflecting the near absence of carbonate minerals in both the protore and HIF. The only high-CaO exception is one sample of HIF from the Seyala Conglomerate Formation that was sampled in outcrop. Samples of Algoma-type magnetite iron formation from Guelb El Rhein show elevated CaO and MgO, probably due to the presence of minor pyroxene and amphibole. Data for samples from the Mhaoudat #2, Tazadit #1, and Tazadit TO14 Sector 2 pits show that manganese generally increases with increasing iron content. Similar to MnO, phosphorus increases with increasing iron content. Comparison of the major element oxide contents of BIF protores from the Zouérate district to those of average BIF protores worldwide shows that the Zouérate district BIF has uniformly lower average contents of all major oxides.

Comparison of Fe_2O_3 to FeO shows that nearly all of the iron in the iron formation samples is ferric. FeO content is <4.5 wt% in all samples of Superior-type iron formation and is <0.5 wt% in all but a few of the protore samples. In contrast, all three samples of Algoma-type magnetite iron formation have FeO contents of >4.5 wt%, ranging as high as 22.3 wt%.

Following the methods of Gutzmer et al. (2008) we normalized the major element, trace element, and REE contents of five samples of HIF from the Zouérate district to calculated average compositions of the protore BIF (n = 12). This approach is designed to elucidate element enrichments and depletions accompanying the transformation of BIF to HIF. Plots of data for major elements as oxides, transition metals, large ion lithophile elements (LILE), high field strength elements (HFSE), and rare earth elements (REE) are shown in Fig. 23. Average concentrations, maxima, minima, and standard deviations of oxides and elements in BIF and HIF are listed in Table 2.

Excluding data for one sample of Seyala Conglomerate Formation, all of the Zouérate HIF samples display a relatively consistent pattern of major element enrichments and depletions (Fig. 23a) similar to those of other HIF worldwide (e.g., Gutzmer et al. 2008). For example, SiO_2 shows a depletion factor ranging from 0.2 to 0.02, indicating that 80–98 % of all silica in

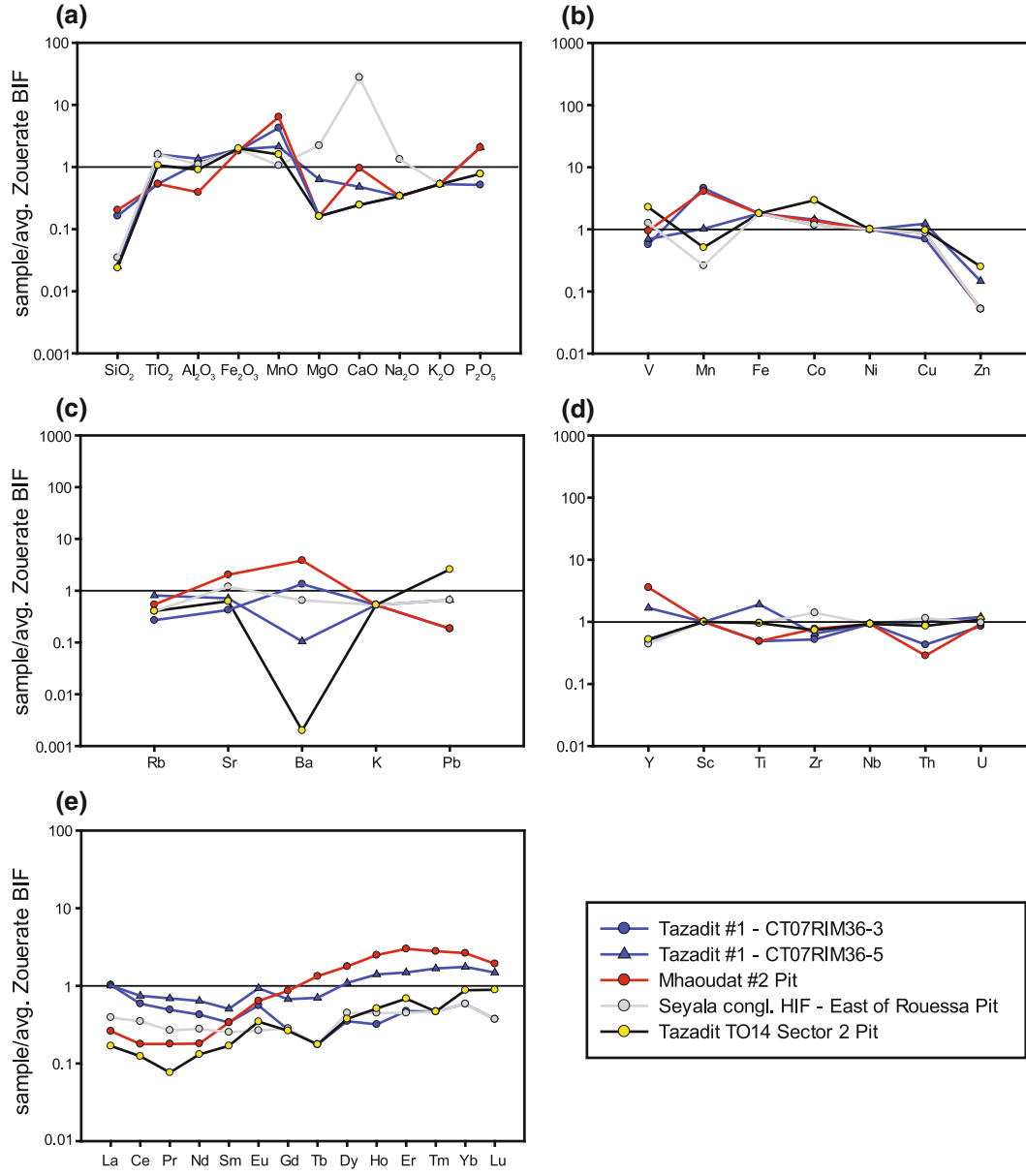

Fig. 23 Elemental concentrations of Zouérate HIF samples (n = 5) normalized to average values for Zouérate protore BIF (n = 12). **a** Major elements as oxides. **b** Transition metals. **c** LILEs. **d** HFSEs. **e** REEs

the protore BIF was leached during the transformation to HIF. Similarly, relative to BIF protore, Zouérate HIF exhibits depletions of MgO, CaO, Na_2O, and K_2O, each of which has concentrations at or only slightly above detection limits. As expected, total iron expressed as Fe_2O_3 ($Fe_2O_3^T$), shows an enrichment factor of 1.8–2.0, similar to examples elsewhere. In contrast, Zouérate HIF is variably enriched in MnO by a factor of one to over six. TiO_2, Al_2O_3, and P_2O_5 are all slightly enriched or depleted and have enrichment factors near unity, consistent with worldwide examples (cf. Gutzmer et al. 2008).

Concentrations of transition metals in all Zouérate iron formation samples are consistently low and result in nearly flat normalized patterns

Table 2 Average concentrations, maxima, minima, and standard deviations of whole-rock data for BIF and HIF from the Zouérate district

Major elements (%)	All BIF samples, n = 12				All HIF samples, n = 5			
	Avg.	Max.	Min.	Std. dev.	Avg.	Max.	Min.	Std. dev.
SiO_2	49.6	58.2	42.2	4.7	4.5	10.1	1.2	4.3
TiO_2	0.019	0.070	0.005	0.018	0.020	0.030	0.010	0.010
Al_2O_3	0.51	1.51	0.19	0.35	0.50	0.69	0.20	0.19
Fe_2O_3	49.6	57.7	41.0	4.9	94.3	98.8	90.4	3.5
Fe-calculated	34.7	40.4	28.7	3.5	65.9	69.1	63.2	2.5
FeO	0.99	4.42	0.03	1.48	0.17	0.66	0.03	0.27
MnO	0.019	0.070	0.005	0.025	0.058	0.120	0.020	0.041
MgO	0.032	0.050	0.020	0.009	0.021	0.070	0.005	0.028
CaO	0.021	0.040	0.005	0.011	0.124	0.580	0.005	0.255
Na_2O	0.015	0.050	0.005	0.013	0.008	0.020	0.005	0.007
K_2O	0.010	0.030	0.005	0.009	0.005	0.005	0.005	0.000
P_2O_5	0.039	0.080	0.005	0.024	0.048	0.080	0.020	0.029
LOI	0.57	1.01	0.28	0.26	0.80	1.30	0.40	0.40
Trace and REE (ppm)								
V	15.8	38.0	2.5	11.4	18.2	36.0	9.0	10.8
Co	1.5	2.9	0.9	0.7	2.5	4.5	1.8	1.1
Ni	2.5	2.5	2.5	0.0	2.5	2.5	2.5	0.0
Cu	11.4	18.0	7.0	3.1	10.6	14.0	8.0	2.2
Zn	47.9	529.0	2.5	151.5	5.3	12.0	2.5	4.2
Rb	0.74	1.40	0.30	0.34	0.36	0.60	0.20	0.15
Sr	21.7	33.5	7.7	8.2	21.7	44.1	9.2	14.0
Ba	126.1	972.0	5.9	269.2	149.7	484.0	0.3	198.5
Pb	13.6	32.0	2.5	10.5	11.6	35.0	2.5	13.5
Y	4.8	7.9	1.1	2.2	6.4	17.0	2.1	6.4
Sc	2.5	2.5	2.5	0.0	2.5	2.5	2.5	0.0
Zr	5.6	14.8	1.8	3.8	4.5	7.8	2.9	1.9
Nb	0.55	1.00	0.51	0.14	0.51	0.51	0.51	0.00
Th	0.70	1.90	0.10	0.49	0.52	0.80	0.20	0.26
U	0.66	1.68	0.21	0.40	0.66	0.79	0.56	0.09
La	5.4	21.9	1.1	5.9	3.1	5.5	0.9	2.2
Ce	12.9	64.3	2.0	17.7	5.1	9.6	1.6	3.4
Pr	1.57	8.57	0.19	2.38	0.53	1.08	0.12	0.39
Nd	6.1	33.9	0.7	9.4	2.0	3.9	0.8	1.3
Sm	1.19	6.90	0.05	1.92	0.38	0.60	0.20	0.15
Eu	0.38	1.58	0.03	0.43	0.21	0.35	0.10	0.10
Gd	1.10	4.87	0.11	1.34	0.52	0.95	0.29	0.31
Tb	0.14	0.55	0.03	0.16	0.07	0.19	0.03	0.07

(continued)

Table 2 (continued)

Major elements (%)	All BIF samples, n = 12				All HIF samples, n = 5			
	Avg.	Max.	Min.	Std. dev.	Avg.	Max.	Min.	Std. dev.
Dy	0.83	2.54	0.10	0.72	0.67	1.47	0.29	0.51
Ho	0.16	0.39	0.03	0.11	0.16	0.39	0.05	0.14
Er	0.42	0.79	0.07	0.22	0.52	1.27	0.19	0.46
Tm	0.05	0.09	0.03	0.03	0.06	0.15	0.03	0.06
Yb	0.34	0.60	0.10	0.18	0.44	0.90	0.20	0.30
Lu	0.07	0.10	0.03	0.02	0.07	0.13	0.03	0.05

(Fig. 23b). Cobalt is slightly enriched and V, Mn, and Cu are variably slightly enriched or depleted. The depleted Mn values are indicative of analytical inconsistencies between the XRF and ICP-MS methods. Uniformly strong depletion of Zn is an artifact of a single analysis of Tazadit Formation protore BIF having 529 ppm, which has greatly influenced the average.

Normalized patterns for LILE are also nearly flat and mostly show slight depletions (Fig. 23c). Exceptions are slight enrichments observed for Sr, Ba, and Pb particularly in the sample from the Mhaoudat #2 pit. In this sample, Sr and Ba are enriched by factors of 2.0 and 3.8, respectively, and Pb is depleted by a factor of 0.2. Barium is strongly depleted in two samples from the Tazadit #1 and TO14 Sector 2 pits. The general depletion of LILE elements in Zouérate HIF is in contrast to worldwide examples, which commonly show enrichments (Gutzmer et al. 2008).

HFSE concentrations are generally below 10 ppm for Y, Sc, Ti, Zr, and Nb, and below one ppm for Th and U. Only Y shows any significant variation, ranging from enrichments of 3.6 to depletions of 0.5 (Fig. 23d). Similar to global examples, these data indicate very slight differences in abundances of HFSE in BIF protores compared to HIF.

Most Zouérate iron formation has low total REE contents of 5 to ca. 20 ppm, although some samples have up to 144 ppm. According to Gutzmer et al. (2008), the majority of BIF protore globally displays REE patterns characterized by significant enrichment of heavy REE (HREE) and small, variable (negative) Eu anomalies. These HREE-enriched patterns are generally preserved during enrichment to HIF by hydrothermal, magmatic-hydrothermal, or supergene-modified hydrothermal processes. Inspection of the REE patterns of Zouérate HIF shows that with the exception of HREE in two samples, all REEs are variably depleted. Additionally, all Zouérate HIF show negatively sloped or U-shaped light REE (LREE), nearly flat to variable middle REE (MREE), and uniformly positively sloped HREE (Fig. 23e). These patterns are in contrast to examples elsewhere of supergene-enriched iron ores that show strong enrichment of the LREE. REE patterns of Zouérate HIF are most similar to those of HIF from the supergene-modified hydrothermal iron ores of the Carajás district in Brazil.

11 Geochronology of BIF

Several previous studies provide broad age constraints on the Algoma- and Superior-type iron deposits of the Zouérate district. Recent work in the Tiris Complex suggests two main phases of granitic intrusive activity at 2950–2870 and 2690–2650 Ma, involving the recycling of crustal material older than approximately 3250 Ma (Schofield et al. 2012). Because the supracrustal rocks of the Tiris Complex, including the Algoma-type BIF, are intruded by these granitic rocks, the iron deposits can be no younger than ca. 2.95 Ga. A Rb–Sr whole-rock age of 2779 ± 84 Ma determined on the Mirikli Formation at Guelb El Rhein has been interpreted as

the age of migmatization of the country rocks (Vachette and Bronner 1975).

Previous attempts to obtain geochronologic constraints on the Ijil Complex and Mhaoudat Formation, the host rocks for the Superior-type iron formation in the district, have been unsuccessful. Current models suggest that the Kediat Ijil as well as the Guelb El Mhaoudat are allochthonous klippen that were transported southwestward during the Birimian orogeny at ca. 2100–2000 Ma, from an original position on the passive margin of the Mesoarchean Rgueïbat Shield (Schofield and Gillespie 2007). This interpretation is based mainly on descriptions of shallow marine calcareous pelitic and dolomitic protoliths of the Rich Anajim supracrustal sequence and correlation of the Sfariat belt iron formation, hosted by the Rich Anajim supracrustal sequence, with supracrustal rocks at Guelb El Mhaoudat and Kediat Ijil (Bronner 1992; Schofield et al. 2006; Schofield and Gillespie 2007). Work by the BRGM has established an early Birimian (>2150 Ma) age for the supracrustal rocks of the Rich Anajim Complex (Lahondère et al. 2003), which if correct would establish a minimum age for the Superior-type BIF deposits of the Zouérate district, as well as for those in the Sfariat belt and at Guelb Zednes. We have also attempted to indirectly date the Superior-type BIF of the Zouérate district by U–Pb geochronology of detrital zircons and $^{40}Ar/^{39}Ar$ geochronology of metamorphic muscovite. Results of these studies are shown graphically in Figs. 24, 25, 26, 27 and 28 and are summarized below. Supporting data and more complete descriptions of the geochronological studies are presented in Bradley et al. (2015).

Sample DB07RIM46a is a quartzite from the Tazadit Formation collected for detrital zircon dating from the lower member along the roadcut to the Tazadit #1 pit. Among 120 zircons analyzed, only 31 pass the laser ablation-ICP-MS (LA-ICP-MS) filters. As described by Bradley et al. (2015), this filtering process culs potentially misleading analyses having age errors greater than 4 %, those having a probability of concordance of less than 0.15 as per Ludwig (1998), and those that yield fewer than 5 of 47 concordant scans. The resulting (screened) age distribution has maxima at 3294 and 2988 Ma (Fig. 24a); the unfiltered concordia plot shows clear evidence of young (Cenozoic or modern) lead loss (Fig. 24b). The youngest zircon age maximum of the Tazadit Formation, at 2988 Ma, is likely about a billion years older than the depositional age, because the geologic constraints favor deposition in the Paleoproterozoic (Pitfield et al. 2006). Sample RIM07DB46b, from the same outcrop, is a muscovite schist for which $^{40}Ar/^{39}Ar$ data on contained white mica are consistent with cooling of the rock below approximately 350 °C at ca. 1970 Ma (Fig. 24c).

Sample DB07RIM36a is Seyala Conglomerate collected from an outcrop east of the Rouessa pit. The rock consists of clasts of white quartzite (generally rounded) and iron formation (generally angular) within an argillaceous matrix (Fig. 10). Detrital zircons were analyzed in two sessions, one by secondary ion mass spectrometry (SIMS; in 2010, two mounts combined) and one by LA-ICP-MS (in 2012). Both sets of analyses included abundant discordant data, such that only 59 grains passed the filters (Bradley et al. 2015). The two datasets yield similar age distributions, which are here combined into a single probability plot, which shows maxima at 3094, 2988, and 2847 Ma (Fig. 25a). A few younger ages were determined, but none of these constitutes a population of three or more and hence all are ignored (see Dickinson and Gehrels 2009). The youngest robust age maximum, at 2847 Ma, is probably close to a billion years older than the depositional age as inferred from geologic constraints (Schofield and Gillespie 2007).

In an attempt to obtain geochronological constraints on tectonic emplacement of the Kediat Ijil over the Tiris Complex, sample DB07RIM45b was collected from a deformed pegmatite lens within the thrust zone. A white mica separate yields an integrated $^{40}Ar/^{39}Ar$ age of 2496 ± 8 Ma (Fig. 27). This age spectrum is difficult to evaluate, however. Internal complexity of the spectrum may record the presence of non-atmospheric trapped argon. One possible

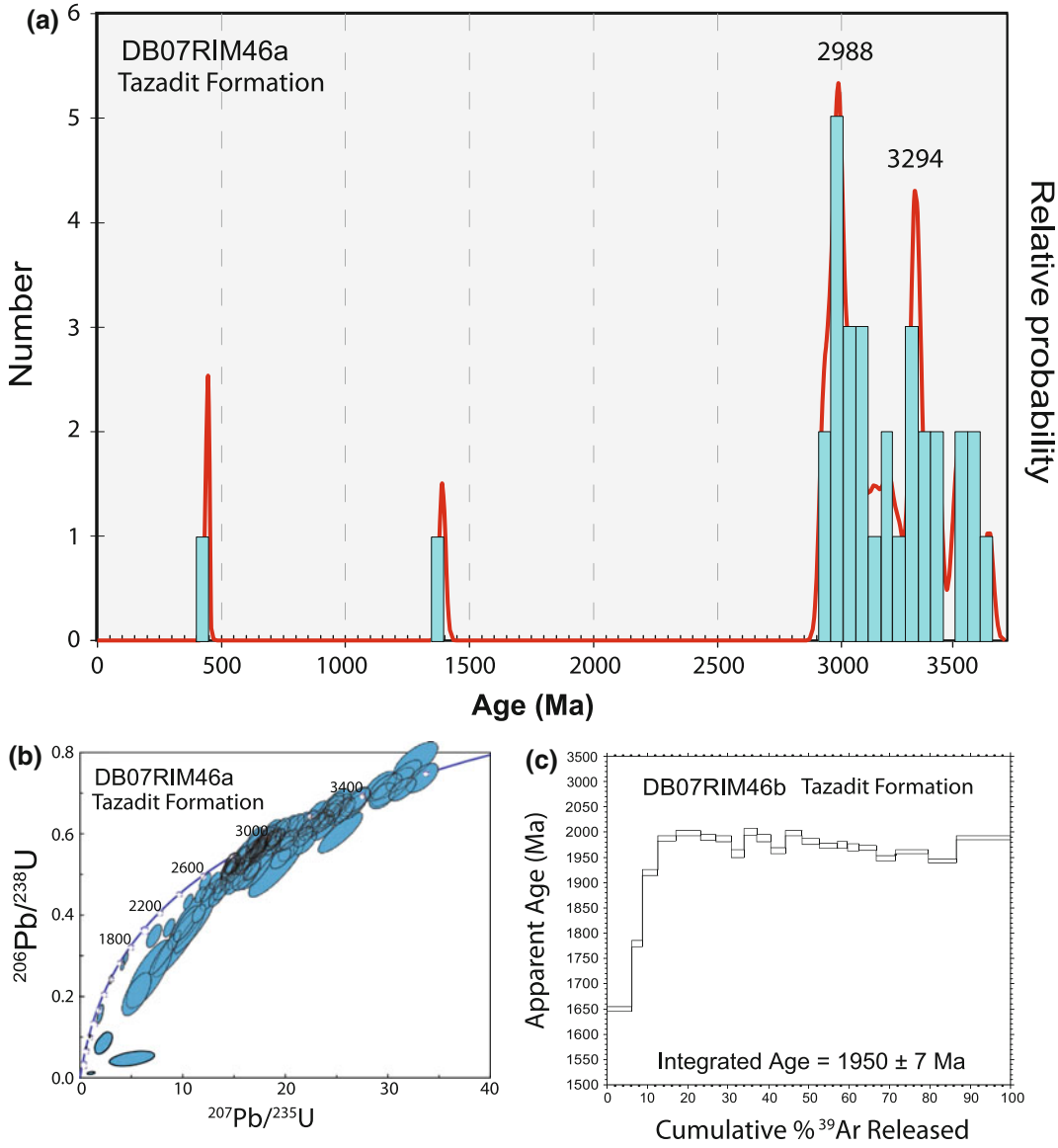

Fig. 24 U–Pb detrital zircon probability plot (**a**), unfiltered concordia plot (**b**), and $^{40}Ar/^{39}Ar$ age spectra (**c**) for samples DB07RIM46a and b from the Tazadit Formation

interpretation is that initial cooling occurred at approximately 2.8 Ga, followed by partial age resetting at ca. 1.6 Ga due to thermal overprinting.

Sample DB07RIM40a is a quartzite collected for detrital zircon dating from the supracrustal rocks in fault contact with the Mhaoudat Formation in the southwest wall of the Mhaoudat #2 pit. Previous mapping and interpretations suggest that these rocks are part of the Mirikli Formation of the Mesoarchean Tiris Complex. Among 120 zircons analyzed, 109 pass the LA-ICP-MS filters. In contrast to samples from the Tazadit Formation and Seyala Conglomerate Formation, the age distribution for this sample shows Paleoproterozoic maxima at 2127, 2012, and 1954 Ma, and a pronounced Neoproterozoic maximum at 579 Ma (Fig. 26). These unexpected results show that the dated rocks

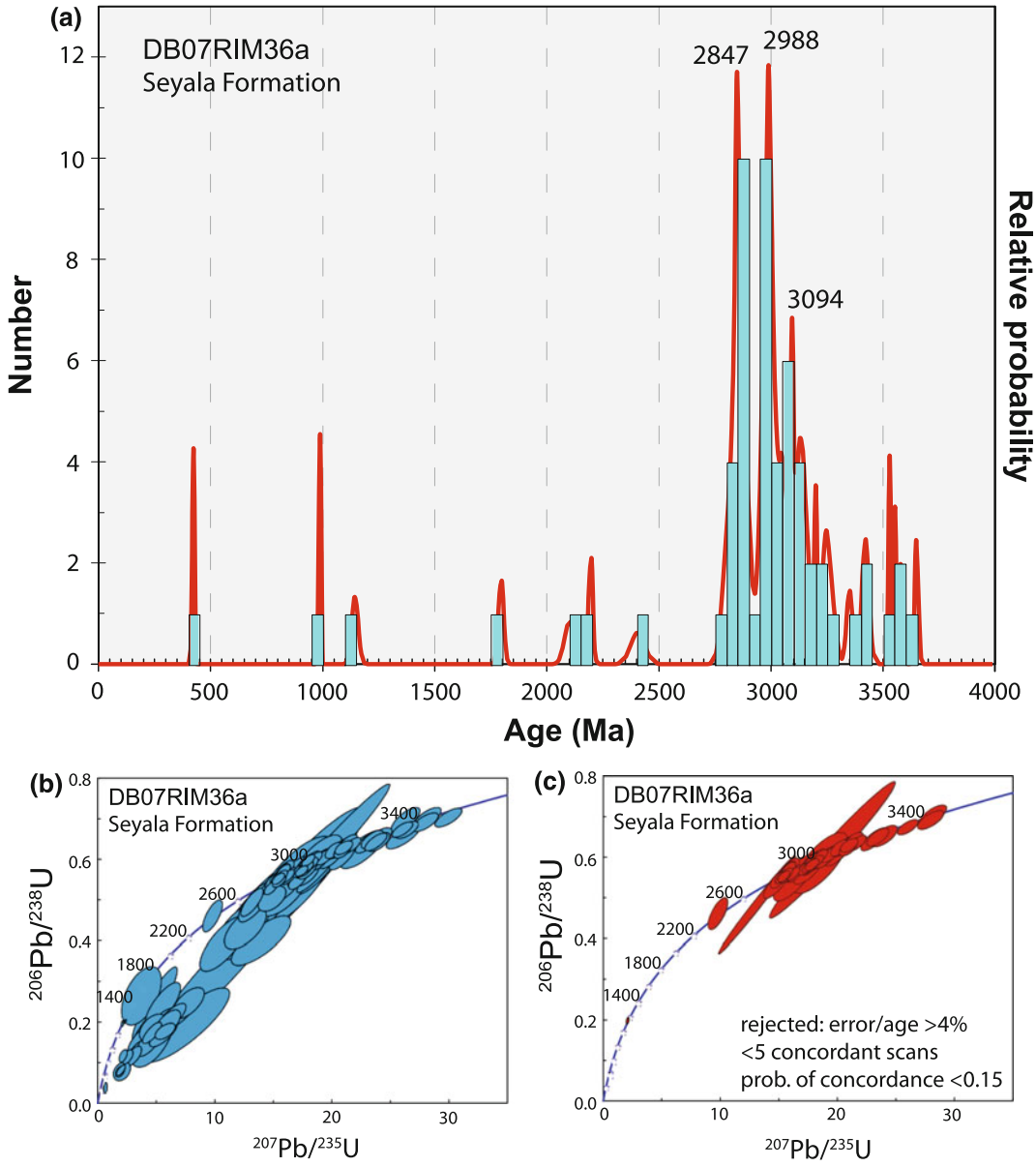

Fig. 25 U–Pb detrital zircon probability plot (**a**) and unfiltered and filtered concordia plots (**b**, **c**) for sample DB07RIM36a from the Seyala Conglomerate Formation

are not Mesoarchean, as per the previous model, nor Paleoproterozoic, a plausible alternative, but instead Neoproterozoic. Implications of these data are explored below in the Discussion.

Sample CT07RIM-27-1 was collected from a loose block of calcrete breccia that came from the weathered carapace of the Mhaoudat #4 pit. BIF from this pit has high contents of P_2O_5 (up to 14 wt%; Szymon Oksengorn, oral commun. 2007). Bradley et al. (2015) report a fission-track age of about 160 Ma on contained apatite (Fig. 28). These same apatite grains provide poorly resolved U–Pb ages that cluster around 2000–2100 and 600 Ma, similar to those obtained for the detrital

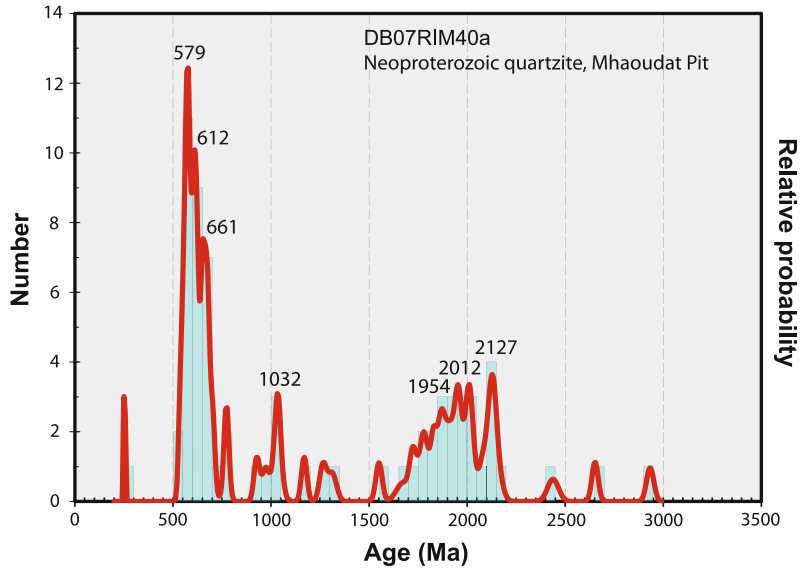

Fig. 26 U–Pb detrital zircon probability plot for sample DB07RIM40a from the Mhaoudat Formation

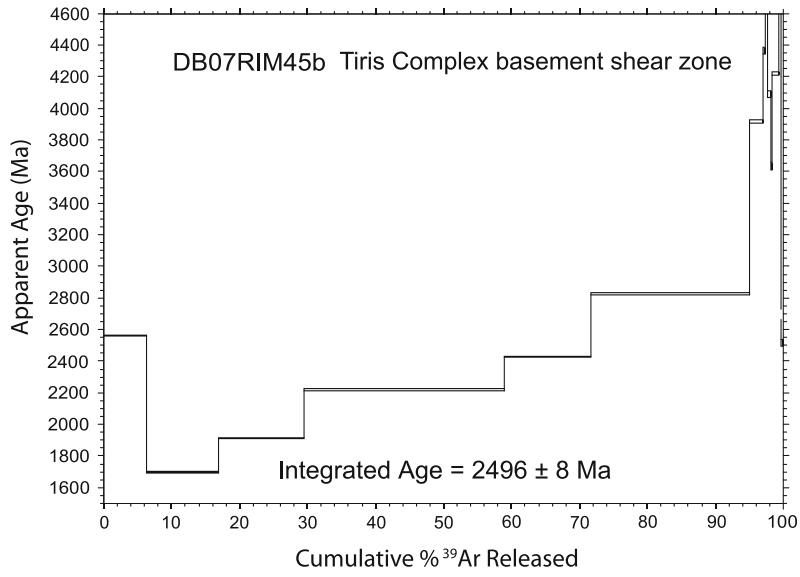

Fig. 27 $^{40}Ar/^{39}Ar$ age spectra for white mica sample DB07RIM45b from the Mirikli Formation

zircons from sample DB07RIM40a (Mhaoudat #2 pit). Accordingly, we interpret the apatite as being detrital and that this very young fission track age records exhumation below approximately 100 °C. At ca. 160 Ma, this part of Mauritania would have been on or near an uplifted rift shoulder related to opening of the central Atlantic Ocean, where seafloor spreading had begun about 25 m.y. earlier (Steiner et al. 1998).

12 Discussion

Our geochemical and petrographic data are consistent with the findings of previous studies (Bronner and Chauvel 1979; Bronner et al. 1992; Henry 1995) and demonstrate that iron formation of the Ijil Complex and Mhaoudat Formation are remarkably pure, consisting almost wholly of

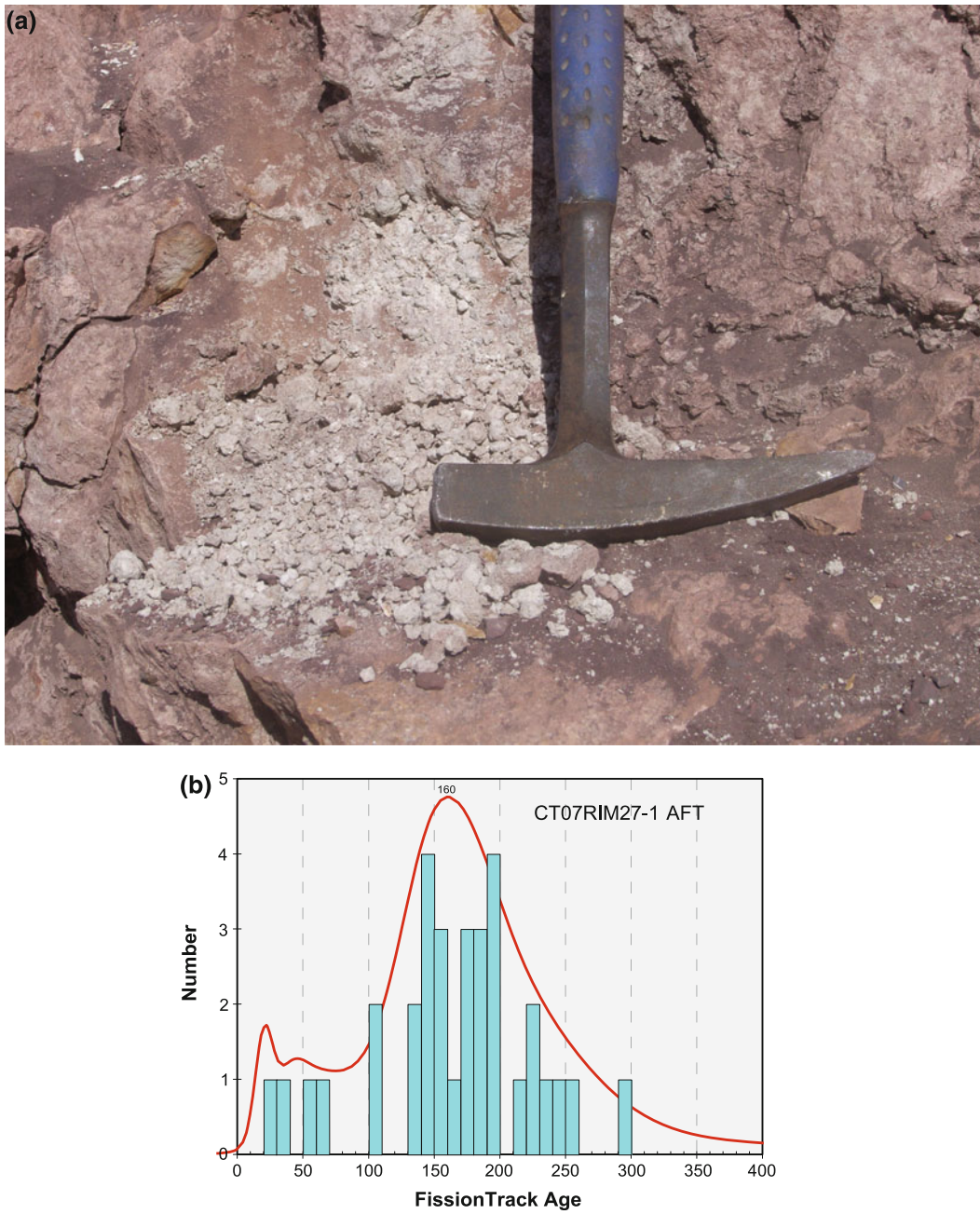

Fig. 28 Histogram of apatite fission track ages for calcrete breccia sample CT07RIM-27-1 from the Mhaoudat #4 pit

hematite and quartz. Comparisons show that contents of all major elements other than iron and silica are well below worldwide averages for iron formation. Texturally, our data indicate a complete absence of clastic features and show that the transformation of BIF protore to HIF proceeded from martitization of magnetite to the formation of subhedral and anhedral hematite followed by development of microplaty hematite. When normalized to BIF protore, Zouérate HIF displays enrichments and depletions similar to worldwide HIF with the exceptions that MnO is enriched to

a greater degree and LILE contents are generally depleted; Ba shows the most pronounced depletion. Similarly, and in contrast to worldwide patterns, Zouérate HIF exhibits a general depletion of REE and a positive Eu anomaly. Geochemical differences between iron formations of the the Ijil Complex and Mhaoudat Formation are slight: the Mhaoudat Formation has higher phosphorus, Sr, Ba, Y, and HREE, and lower alumina, Pb, Ti, and Th. Whether these differences are due to compositional variations in protore BIF or to a different process of enrichment to HIF is unknown.

Although our reconnaissance geochronological studies do not provide absolute ages for either the deposition of protore BIF or the timing of transformation to HIF, the new results do shed light on the geologic history of the region. Detrital zircon ages in samples from both the Tazadit Formation and Seyala Conglomerate Formation are consistent with derivation by erosion from the Mesoarchean Tiris Complex. This interpretation supports a passive-margin depositional environment on the northeastern edge of the Mesoarchean Rgueïbat Shield that was unaffected by clastic input related to early Birimian tectonic elements. Thus, the Ijil Complex was likely deposited sometime between the maximum depositional age of ca. 2.99 Ga and onset of the Birimian orogeny at ca. 2.15 Ga.

Our most surprising result is the new constraint on the age of metaclastic rocks at Guelb El Mhaoudat that are faulted against the iron formation (Fig. 12). The youngest age maximum in the detrital zircon population (Fig. 26) corresponds to the "Maximum Depositional Age" of Gehrels and Dickinson (2009). In this case, it is 579 Ma, which is late Neoproterozoic, or Ediacaran. The detrital zircon age distribution, showing major peaks at 661, 612, and 579 Ma and minor peaks at 2127, 2012, 1954, and 1032 Ma, is strikingly similar to patterns from the Mauritanide orogen and Taoudeni Basin, which Bradley et al. (2015) refer to as the Oujeft detrital zircon barcode. The Oujeft barcode was previously identified in nine samples from strata ranging in age from late Neoproterozoic to Ordovician by Bradley et al. (2015). The remote possibility of a sample-number mixup is discounted because the apatite fission-track sample, which is from regolith developed on the El Mhaoudat iron ore deposit, yields U–Pb apatite ages that are similar to the Mhaoudat detrital zircon ages. Some Archean and Paleoproterozoic igneous and metasedimentary rocks in Mauritania have yielded problematic Neoproterozoic U–Pb zircon ages, which appear to be the product of a Pan-African overprint. In the case of the sample from El Mhaoudat, the possibility of a Pan-African overprint on a significantly older rock can be ruled out because the detrital zircon age distribution yields *several* age peaks younger than ca. 2 Ga that are consistent with the well-defined Oujeft barcode. We therefore propose that the El Mhaoudat Formation is Paleoproterozoic and that it was juxtaposed against the dated Neoproterozoic rocks by faulting during Pan-African or younger tectonism. If true, these data reveal a previously unrecognized zone of Neoproterozoic or Paleozoic deformation in this part of the Rgueïbat Shield.

Most previous workers have not addressed the nature and timing of the transformation of protore BIF to HIF in the Zouérate district. Bronner et al. (1992) attributed HIF formation to the combined effects of silica removal during metamorphism followed by iron enrichment during supergene weathering. However, a plethora of age determinations suggests that multiple metamorphic events were responsible for the BIF to HIF transformation in this district. For example, Vachette and Bronner (1975) proposed migmatization of the Mirikli Formation at Guelb El Rhein at 2.78 Ga, and suggested that subsequent metamorphism or superimposed thermal disturbances affected the Ijil Complex at 2.2, 1.84, and 1.65 Ga, and the Tiris Complex at 1.8 and 1.72 Ga (see also Bronner and Chauvel 1979). Schofield and Gillespie (2007) cited U–Pb zircon and monazite ages from the Tiris Complex ranging from 2.83 to 2.45 Ga that record a protracted history of granite crystallization and metamorphism of the basement. Our limited geochronological work similarly suggests a possible metamorphic event in the Tiris Complex at about 2.8 Ga, followed by a disturbance at ca.

1.6 Ga. Our $^{40}Ar/^{39}Ar$ results from a sample of white mica from the Tazadit Formation indicate cooling of this rock below approximately 350 °C at about 1.97 Ga.

Geochemical data reported herein only provide minimal constraints on the nature of the fluid(s) responsible for upgrading of BIF protore to HIF. However, the observed MnO enrichment coupled with depletions in Ba and REE can be interpreted to suggest that the fluid had a relatively high temperature, was oxidizing, and possibly alkaline in order to mobilize these elements. Further constraints may be reflected in the observed enrichment of HREE over LREE in Zouérate HIF versus the inferred BIF protore. LREE-enriched profiles accompany enrichment of HIF in examples worldwide of supergene high-grade iron deposits, a characteristic that serves to differentiate deposits formed in this manner from those of hydrothermal and magmatic-hydrothermal origin (Gutzmer et al. 2008). In contrast, the observed concentrations of HREE in the Zouérate HIF (as well as the Carajás, Brazil, iron ores) may be a product of high-salinity hydrothermal fluids, which are known to effectively transport LREE over HREE (e.g., Humphris 1984; Williams-Jones et al. 2012). Nonetheless, our data clearly document a weathering profile in the Zouérate district that exhibits both textural as well as geochemical effects of supergene enrichment, coeval with uplift related to opening of the Atlantic Ocean at ca. 160 Ma, based on an apatite fission-track age. Such supergene enrichment may have had a relatively minor effect, however, being superimposed on one or several metamorphic-hydrothermal events responsible for the transformation of BIF to HIF in the district.

13 Conclusions

The F'derik-Zouérate district of Mauritania is a world-class iron ore district containing both Algoma- and Superior-type iron formations. Although the majority of iron production to date has come from the nearly exhausted Superior-type HIF deposits of the Kediat Ijil and Guelb El Mhaoudat, possible development of an underground mine at Tazadit #1 (Investec 2013; Taib 2014) could represent a new era of HIF mining in the district. Development of underground mines could also exploit HIF ores from subsurface continuations of both the Kediat Ijil and Guelb El Mhaoudat trends, as clearly shown in the aeromagnetic data. Recent exploration for, and development of, Algoma-type magnetite iron formation at Guelb El Rhein, Guelb el Aouj, and Guelb Agareb, among others, is poised to continue a steady supply of iron ores from Mauritania for many years to come.

Acknowledgments The authors wish to thank the management and geologic staff of SNIM in Zouérate, including Chief Geologist Mohamed Ould Woyssatt, Szymon Oksengorn, and Ghali Amar for their guided tour of, and permission to sample, the mines and roadcuts of the Kediat Ijil, Guelb El Mhaoudat, and Guelb El Rhein. PRISM regional coordinator Ahmed Salem Ben Mohamedou provided invaluable logistical assistance during our stay in Zouérate. DMG geologists Baydi Thiam, Sid-Ahmed Bouderballa, and Abdoullah Samoury provided able field assistance. USGS colleagues Stuart Giles and Samantha Pascarelli provided help in drafting figures, and Klaus Schulz and John Slack provided reviews that greatly improved this paper.

References

Bekker A, Slack JF, Planavsky N, Krapež B, Hofmann A, Konhauser KO, Rouxel OJ (2010) Iron formation: the sedimentary product of a complex interplay among mantle, tectonic, oceanic, and biospheric processes. Econ Geol 105:467–508

Beukes JB, Gutzmer J (2008) Origin and paleoenvironmental significance of major iron formations at the Archean-Paleoproterozoic boundary. Rev Econ Geol 15:5–48

Blanchot A (1975) Mineral plan of the Islamic Republic of Mauritania. BRGM Direction des Recherches Développement Minière, Orléans 554 pp

Bradley DC, O'Sullivan P, Cosca MA, Motts HA, Horton JD, Taylor CD, Beaudoin G, Lee GK, Ramezani J, Bradley DN, Jones JV, Bowring, S (2015) Synthesis of geological, structural, and geochronologic data. In: Taylor CD (ed) Second projet de renforcement institutionnel du secteur minier de la République Islamique de Mauritanie (PRISM-II). US Geol Survey Open-File Rept 2013–1280-A, 328 pp. http://dx.doi.org/10.3133/ofr20131280a/. [In English and French]

Bronner G (1970) Plissement, cisaillement, boudinage et laminage: mecanismes essentiels de la formation de la Breche d'Ijil (Precambrien de la Dorsale Reguibat, Fort-Gouraud, Mauritanie Septentrionale). Service Carte Geol, Alsace-Lorraine Bull 23:51–76

Bronner G (1988) La Chaîne de M'Haoudat (Mauritanie): géologie, architecture, minéralisations ferrifères riches associées. Rapp Inéd Société National Industrielle Minière, 33 pp

Bronner G (1992) Structure et évolution d'un craton archéen: la dorsale Rgueïbat occidentale (Mauritanie); tectonique et métallogénie des formations ferrifères. Thesis Doctoral, Univ Aix-Marseille III, Marseille, France, BRGM Doc 02212536, N° 201, 449 pp

Bronner G, Chauvel JJ (1979) Precambrian banded iron-formations of the Ijil Group (Kediat Ijil, Reguibat Shield, Mauritania). Econ Geol 74:77–94

Bronner G, Fourno JP (1992) Audio-magnetotelluric investigation of allochthonous iron formations in the Archaean Reguibat Shield (Mauritania): structural and mining implications. J Afr Earth Sci 15:341–351

Bronner G, Chauvel JJ, Triboulet C (1992) Les formations ferriferes du Precambrien de Mauritanie: origine et evolution des quartzites ferrugineux. Chronique Recherche Minière 508:3–27

Clark DA (1997) Magnetic petrophysics and magnetic petrology: aids to geological interpretation of magnetic surveys. AGSO J Aust Geol Geophys 17:83–103

Cloud P (1973) Paleoecological significance of the banded iron-formation. Econ Geol 68:1135–1110

Clout JMF, Simonson BM (2005) Precambrian iron formations and iron formation-hosted iron ore deposits. In: Hedenquist JW, Thompson JFH, Goldfarb RJ, Richards JP (eds) Economic geology 100th anniversary volume, 1905–2005. Society Economic Geologists, Inc, Littleton, CO, USA, pp 643–679

Finn CA, Anderson ED (2015) Synthesis of geophysical data. In: Taylor CD (ed) Second projet de renforcement institutionnel du secteur minier de la République Islamique de Mauritanie (PRISM-II). US Geol Survey Open-File Rept 2013–1280-B, 68 pp. http://dx.doi.org/10.3133/ofr20131280b/ (In English and French)

Gehrels GE, Dickinson WR (2009) Use of U–Pb ages of detrital zircons to infer maximum depositional ages of strata: a test against a Colorado Plateau Mesozoic database. Earth Planet Sci Lett 288:115–125

Gross GA (1980) A classification of iron-formation based on depositional environments. Can Min 18:215–222

Gutzmer J, Chisonga BC, Beukes NJ, Mukhopadhyay J (2008) The geochemistry of banded iron formation-hosted high-grade hematite-martite iron ore. Rev Econ Geol 15:157–183

Henry P (1995) Étude chimique et isotopique (Nd) de formations ferrifères (banded iron formations ou BIFs) du Craton ouest-africain. Bull Société Géologique France 166:3–13

Humphris SE (1984) The mobility of rare earth elements in the crust. In: Henderson P (ed) Rare earth element geochemistry. Elsevier, Amsterdam, pp 317–342

Investec (2013) Iron ore—Sector comment—700 mt gorilla missing in West Africa. 19 November 2013, 29 pp. http://www.kogiiron.com/IRM/Company/ShowPage.aspx/PDFs/1620-51002968/700mtgorillamissinginWestAfrica

James HL (1954) Sedimentary facies of iron-formation. Econ Geol 49:235–293

Jorgenson JD (2012) Iron ore: US Geol Survey, Mineral Commodity Summaries, January 2012, pp 84–85. http://minerals.usgs.gov/minerals/pubs/mcs/2012/mcs2012.pdf

Klein C (2005) Some Precambrian iron formations (BIFs) from around the world: their age, geologic setting, mineralogy, metamorphism, geochemistry, and origins. Am Mineral 90:1473–1499

Lahondère D, Thieblemont D, Goujou J-C, Roger J, Moussine-Pouchkine A, LeMetour J, Cocherie A, Guerrot C (2003) Notice explicative des cartes géologiques et gîtologiques à 1/200 000 et 1/500 000 du Nord de la Mauritanie. Ministère des Mines l'Industrie, Nouakchott, DMG, vol 1, 426 pp

Marot A, Stein G, Artigan D, Milési J-P (2003) Notice explicative des cartes géologiques et gîtologiques à 1/200 000 et 1/500 000 du Nord de la Mauritanie. Ministère Mines de l'Industrie, Nouakchott, DMG, Potentiel Minier, vol 2, 115 pp

Marsh EE, Anderson ED (2015) Database of mineral deposits in the Islamic Republic of Mauritania. In: Taylor CD (ed) Second projet de renforcement institutionnel du secteur minier de la République Islamique de Mauritanie (PRISM-II). US Geol Survey Open-File Rept 2013–1280-S, 9 pp. Access database. http://dx.doi.org/10.3133/ofr20131280s/. [In English and French]

Mining Journal (2006) Saudi backs Sphere. Min J 1

Mining-technology.com (2012) SNIM, Mauritania. http://www.mining-technology.com/projects/snim/

Morey GB (1999) High-grade iron ore deposits of the Mesabi Range, Minnesota—product of a continental-scale Proterozoic ground-water flow system. Econ Geol 94:133–142

O'Connor EA, Pitfield PEJ, Schofield DI, Coats S, Waters C, Powell J, Ford J, Clarke S, Gillespie M (2005) Notice explicative des cartes géologiques et gîtologiques à 1/200 000 et 1/500 000 du Nord-Ouest de la Mauritanie. Ministere des Mines de l'Industrie, Nouakchott 398 pp

Oksengorn S (1973) Les gisements de fer de la région de Zouérate (République de Mauritanie). Ind Min 55:338–351

Phillips JD (2002) Two-step processing for 3D magnetic source locations and structural indices using extended Euler or analytic signal methods. Soc Expl Geophysicists, 2002 Technical Pgm Expanded Abs 21:727–730

MCA Powell C, Oliver NHS, Li ZX, McD Martin, Ronaszeki J (1999) Synorogenic hydrothermal origin for giant Hamersley iron oxide ore bodies. Geology 27:175–178

Rocci G (1957) Formations métamorphiques et granitiques de la partie occidentale du pays Rgueïbat (Mauritanie

du Nord). Bull Direction Fédérale Mines Géologie. Afrique Occidentale Francaise, Dakar, no 21, 1308 pp

Schofield DI, Gillespie MR (2007) A tectonic interpretation of "Eburnian terrane" outliers in the Reguibat Shield, Mauritania. J Afr Earth Sci 49:179–186

Schofield DI, Horstwood MSA, Pitfield PEJ, Crowley QG, Wilkinson AF, Sidaty HCHO (2006) Timing and kinematics of Eburnean tectonics in the central Reguibat Shield, Mauritania. J Geol Soc 163:549–560

Schofield DI, Horstwood MSA, Pitfield PEJ, Gillespie MR, Darbyshire F, O'Connor EA, Abdouloye TB (2012) U–Pb dating and Sm–Nd isotopic analysis of granitic rocks from the Tiris Complex: new constraints on key events in the evolution of the Reguibat Shield, Mauritania. Precambr Res 204–205:1–11

SNIM (2013) Discovery of a new deposit of iron over 800 million metric tons in Tizerghaf (Zouerate), Press release 08 October 2013, 2 pp. http://www.snim.com/e/index.php/news-a-media/news/

SNIM (2015) Progress of Guelb2 project implementation, Press release 20 May 2015, 3 pp. http://www.snim.com/e/index.php/news-a-media/news/

Sougy J (1952) Rapport de Reconnaissance sur le Minerai de Fer des Sfariat (Mauritanie) Direction Fédérale Mines Géologie, Afrique Occidentale Francaise, Dakar, 25 ppSougy J (1953) Rapport géologique de fin de campagne 1951-1952 à Fort Trinquet (Mauritanie). Direction Fédérale Mines Géologie, Afrique Occidentale Francaise, Dakar 65 pp

Sphere Minerals Ltd. (2012) Annual report for the 12 month period ended 31 December 2012, 53 pp. http://www.asx.com.au/asxpdf/20130402/pdf/42f0fzh6mkfvdw.pdf

Sphere Minerals Ltd. (2015) Annual statement of mineral resources and ore reserves, ASX Release, 30 January 2015 9 pp. http://www.asx.com.au/asxpdf/20150130/pdf/42w84bwv9lnlvh.pdf

Steiner C, Hobson A, Favre P (1998) Mesozoic sequence of Fuerteventura (Canary Islands): witness of Early Jurassic sea-floor spreading in the Central Atlantic. Geol Soc Am Bull 110:1304–1317

Taib M (2010) The mineral industry of Mauritania. US Geol Survey 2008 Minerals Yearbook—Mauritania, 4 pp. http://minerals.usgs.gov/minerals/pubs/country/2008/myb3-2008-mr.pdf

Taib M (2014) The mineral industry of Mauritania. US Geol Survey 2012 Minerals Yearbook—Mauritania, 6 pp. http://minerals.usgs.gov/minerals/pubs/country/2012/myb3-2012-mr.pdf

Taylor CD, Giles SA (2015) Mineral potential for volcanogenic massive sulfide deposits in the Islamic Republic of Mauritania. In: Taylor CD (ed), Second projet de renforcement institutionnel du secteur minier de la République Islamique de Mauritanie (PRISM-II). US Geol Survey Open-File Rept 2013–1280-L, 70 pp. http://dx.doi.org/10.3133/ofr20131280l/ (In English and French)

Taylor CD, Finn CA, Anderson ED, Joud MY, Taleb MA, Horton JD (2015) Algoma-, Superior-, and oolitic-type iron deposits of the Islamic Republic of Mauritania. In: Taylor CD (ed) Second projet de renforcement institutionnel du secteur minier de la République Islamique de Mauritanie (PRISM-II). US Geol Survey Open-File Rept 2013–1280-O, 94 pp. http://dx.doi.org/10.3133/ofr20131280o/ (In English and French.)

Tecsult International Ltd. (2009) SNIM's Guelbs II Project, Mauritania—Environmental and Social Impact Assessment—Summary 05-17309, 41 pp. http://www.afdb.org/fileadmin/uploads/afdb/Documents/Environmental-and-Social-Assessments/SNIM_Guelb_PhaseII_EIES_ExecutiveSummary_English_Final_April24_2009.pdf

Vachette M, Bronner G (1975) Ages radiométriques Rb/Sr de 2,900 et 2,700 m.a. des series précambriennes de l'Amsaga et du Tiris, Dorsale Réguibat (Mauritanie). Trav Lab Sci Terre Marseille Série B 11:147–148

Williams-Jones AE, Migdisov AA, Samson IM (2012) Hydrothermal mobilization of the rare earth elements—a tale of "ceria" and "yttria". Elements 8:355–360

Xstrata (2011a) Mineral resources and ore reserves as at 31 December 2011, 48 pp. http://www.xstrata.com/content/assets/pdf/x_reserves_resources_201112.pdf

Xstrata (2011b) Hitting our stride, Xstrata investor seminar–part two, 6 December 2011, 60 pp. http://www.xstrata.com/investors/speechesandpresentations/2011/12/06/12/

The High-Grade Imini Manganese District—Karst-Hosted Deposits of Mn Oxides and Oxyhydroxides

Augustin Dekoninck, Rémi Leprêtre, Omar Saddiqi, Jocelyn Barbarand and Yans Johan

Abstract

For more than 80 years of mining the economically important Imini district has been the main producer of manganese in Morocco. Three stratabound manganiferous orebodies in the district are hosted in a 10-m-thick Cenomanian-Turonian dolostone that records the effects of laterally extensive dissolution and epigenetic processes. The predominance of pyrolusite, accompanied by minor amounts of hollandite group minerals (cryptomelane, hollandite *s.s.*, coronadite), lithiophorite, and romanechite, provide a high grade ore having more than 70 wt% MnO and low contents of SiO_2, Fe_2O_3, and P_2O_5. One metallogenic model suggests the main mineralization stage was related to a period of terrestrial exposure and weathering, leading to formation of an extensive karst system, following host rock deposition and dolomitization. This model envisages Mn mineralization prior to the deposition of Coniacian-Maastrichitan (Senonian) red beds, carbonates, and evaporites. A variety of data shows that the ore beds formed by epigenetic processes, in which Mn precipitation occurred with increasing pH and Eh. These physico-chemical conditions are linked to dolomite dissolution and the influx of oxygenated meteoric waters, probably in contact with deeper O_2-depleted meteoric groundwaters, and to surficial saline solutions and/or microbial

A. Dekoninck (✉) · Y. Johan
Département de Géologie, NaGRIDD,
Université de Namur, 61 rue de Bruxelles,
5000 Namur, Belgium
e-mail: Augustin.dekoninck@unamur.be

R. Leprêtre · J. Barbarand
GEOPS, Université Paris-Sud, CNRS,
Université Paris-Saclay, rue du Belvédère,
Bât. 504, 91405 Orsay, France

O. Saddiqi
Laboratoire Géosciences, Université Hassan II,
BP 5366, Maârif, Casablanca, Morocco

M. Bouabdellah and J.F. Slack (eds.), *Mineral Deposits of North Africa*,
Mineral Resource Reviews, DOI 10.1007/978-3-319-31733-5_22

activity. The Cenozoic construction of the Atlas Mountains probably remobilized or at least reworked previously formed manganese accumulations.

1 Introduction

The first evidence of black Mn-rich zones in Cenomanian-Turonian strata of the Imini district (Fig. 1a, b) was recorded in 1918, but mining did not begin until 1929 by "Société Anonyme Chérifienne d'Études Minières" (Gandini 2011; SACEM 2013). In 1957, annual production reached 18.1 % of the world market. After several decades of economic problems, annual production returned to 88 kt in 2013 (Lesavre 1975; SACEM 2013). Currently, the high grades of the ore and low contents of SiO_2 (avg 4.58 wt%), Fe_2O_3 (avg 0.09 wt%), and P_2O_5 (avg 0.11 wt%) (Table 1, Gutzmer et al. 2006; Dekoninck et al. 2016), allows the Imini district to produce a highly competitive product for the chemical industry with a concentrate of 74–92 wt% MnO_2, and for the steel industry with a lower concentration of 40–48 wt% MnO_2. The main economic markets for Imini manganese products are in South Africa and China, but negotiations are in progress to fulfill European and other Asian demands (SACEM 2013).

The unusual high grade of the manganese ore is due to the predominance of pyrolusite in two stratabound orebodies hosted in the lower part of a relatively thin succession of Cenomanian-Turonian carbonate strata (C_1 and C_2 in Fig. 1c). A third orebody above the host dolomite contains a greater proportion of hollandite group minerals, yielding lower Mn grade ore and higher contents of other metals (C_3 in Fig. 1c). Most previous contributions ascribed the manganese mineralization to a synsedimentary origin based on the laterally continuous and stratiform character of the

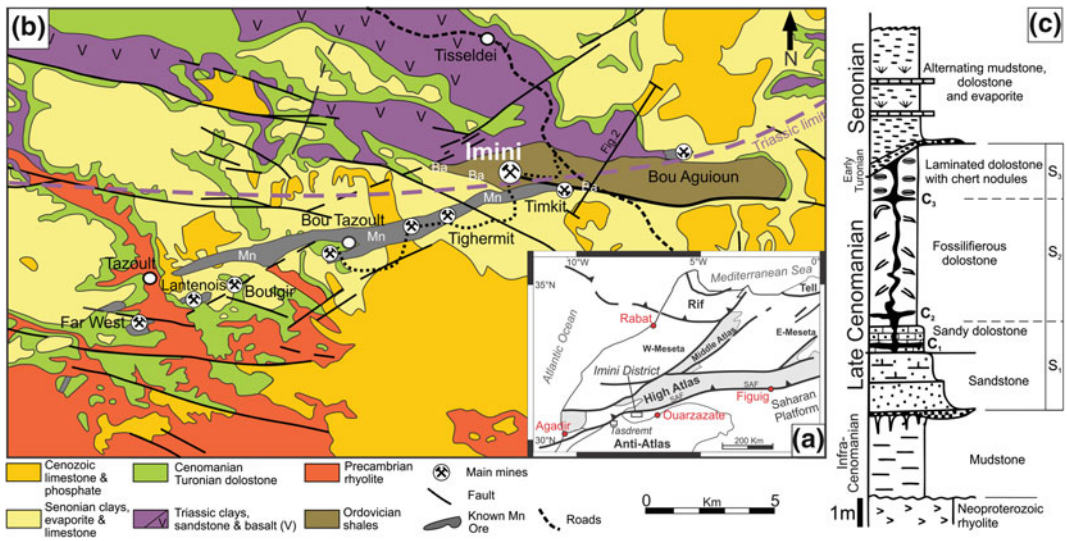

Fig. 1 **a** Location of Imini district, south of South Atlas Front (SAF). **b** Simplified geological map of Imini district showing distribution of Mn orebodies hosted in Cenomanian-Turonian dolostone (modified after Lalaoui et al. 1991). **c** Detailed stratigraphic column of Lantenois deposit showing three stratabound Mn levels (C_1, C_2, C_3; west of the district, modified after Gutzmer et al. 2006). Designation of three sedimentary systems (S_1, S_2, S_3) are from Rhalmi et al. (2000)

Table 1 Geochemistry of internal karst-fill sediments, manganese orebodies, and distal and proximal host rocks of the Imini district

Sample	IM20	IM26	IM43d	LAN58	LAN61	ECH98b	ECH102b	IM37	IM22	IM29	LAN51	IM41c	ECH101b	IM43m	LAN52	ECH76	ECH77	ECH79	ECH81	ECH85
Locality	Timkit		Lantenois			Bou Aggioun		Timkit			Lantenois	Far West	Bou Aggioun	Lantenois		Larba				Taouerda
Type	Proximal dolostone					C1		C1-C2	C2			C3	Stockwork	Breccia	Lt(2)	Distal dolostone				
SiO_2	5	0.88	2.62	8.59	0.75	4.62	2.75	3.59	0.99	0.49	26.74	2.67	7.72	3.16	7.31	0.35	0.35	0.37	0.67	0.58
TiO_2	0.03	0.02	0.03	0.03	0.02	0.03	0.05	0.03	0	0	0.29	0.02	0.1	0.04	0.1	0.01	0.01	0.01	0.01	0.01
Al_2O_3	0.8	0.31	0.56	0.86	0.43	1	1.33	1.39	0.34	1.39	5.71	0.78	2.17	0.76	1.98	0.17	0.17	0.19	0.24	0.17
Fe_2O_3	0.08	0.05	0.12	0.01	0.07	0.16	0.3	0.17	0.01	<0.01	2.4	0.04	0.59	0.58	0.75	0.03	<0.01	<0.01	<0.01	0.01
MnO	0.54	0.61	0.57	0.38	0.55	63.84	59.75	54.42	82.72	76.37	40.17	67.2	54.69	37.89	1.22	0.13	0.12	0.2	0.13	0.17
MgO	19.16	20.53	21.33	18.6	19.98	0.18	1.13	0.13	0.12	0.14	0.38	0.03	1.73	7.75	18.64	19.75	21.28	20.24	20.27	18.23
CaO	27.79	29.84	28.8	27.34	30.98	3.08	5.65	5.96	1.13	0.13	0.46	0.18	5.76	11.33	26.56	30.86	31	30.31	29.8	33.01
PbO	0	0	0.01	0.01	0.02	0.52	0.44	0.7	0.22	0.29	2.03	2.54	0.29	2.66	0.03	0	0	0	0	0
BaO	0.02	0	0.03	0.02	0.02	2.34	1.71	11.37	1.17	3.37	4.59	6.07	2.4	4.09	0.09	0	0	0	0	0
Na_2O	0.03	0.02	0	0.02	0.01	0.18	0.25	0.07	0.01	0.01	0.11	0.25	0.57	0.1	0.02	0.02	0.02	0.02	0.02	0.04
K_2O	0.24	0.06	0.03	0.26	0.05	4.88	4.61	0.43	0.16	0.25	1.79	1.04	2.22	0.96	0.37	0.02	0.01	0.02	0.02	0.02
P_2O_5	0.05	0.03	0.01	0.02	0.03	0.14	0.15	0.06	0.03	0.04	0.1	0.09	0.36	0.03	0.05	0.12	0.16	0.24	0.03	0.11
LOI	44.25	46.59	45.75	42.46	46.23	12.43	14.61	13.85	13.16	12.25	8.54	10.29	15.02	23.69	41.82	46.97	47	46.85	46.99	46.45
Total	98.08	99.05	99.94	98.67	99.22	90.65	90.67	80.22	98.79	91.1	86.81	82.69	91.03	86.4	98.92	98.52	100.2	98.53	98.27	98.9
FeO	<0.1	<0.1	<0.1	<0.1	<0.1	<0.1	<0.1	<0.1	<0.1	<0.1	<0.1	<0.1	0.1	<0.1	<0.1	<0.1	<0.1	<0.1	<0.1	<0.1

Samples were analyzed by Activation Laboratories (Ontario, Canada). Data for major elements were determined by fusion ICP-MS. "Distal" and "proximal" dolostones are defined by distance from known stratabound orebodies C_1-C_3.
Abbreviations: *IS Lt* (*no.*) internal sediment lithotype (no.); *N.A.* not analyzed

orebodies (Neltner 1933; Orcel 1942; Bouladon and Jouravsky 1952; Lesavre 1975; Pouit 1980; Force et al. 1986; Thein 1990; Lalaoui et al. 1991; Rhalmi et al. 1997). In contrast, Force et al. (1986) and Thein (1990) proposed a diagenetic origin controlled by meteoric waters and seawater. However, the absence of primary sedimentary Mn minerals such as rhodochrosite, the rather stratabound character of the orebodies, and their close spatial and genetic association with karst sediments in the enclosing dolostone, led Gutzmer et al. (2006) to support an epigenetic karst-hosted origin for the ore, by meteoric waters during post-Turonian diagenesis. Recent studies by Dekoninck et al. (2016) point out that the epigenetic formation of the Mn oxides occurred after dolomitization and late diagenesis. Mineralogical associations indicate that ore formation is clearly polyphase, following the first epigenetic mineralizing event in the karstic system. Cenozoic tectonic activity, due to the exhumation of the Atlas belt further north, probably remobilized and/or reworked the Mn ore (Leprêtre et al. 2015). The present chapter aims to provide an overview of the ore-forming processes, from host-rock deposition to manganese mineralization, based on field observations and petrography. Also considered here are new geochemical data acquired on distal and proximal host-rock dolostone, as well as on the orebodies.

2 Geological Setting

The Imini district lies in the western part of the Ouarzazate foreland basin, within the transition zone between two main structural domains: the Central High Atlas Mountains to the north and the Anti-Atlas Mountains to the south (Fig. 1a). Lower Mesozoic strata thicken northward and form a sedimentary wedge on the Anti-Atlas (Figs. 1b and 2; Zouhri et al. 2008). The Late Triassic red beds follow approximately a N70–80° E direction (purple dotted line in Fig. 1b). Manganese orebodies consist of weakly deformed, shallow marine carbonate rocks that were deposited during the Cenomanian and Turonian stages of the Late Cretaceous (Fig. 1b, c; Thein 1990; Gutzmer et al. 2006). The ore-bearing dolostone lies unconformably on Lower Cretaceous and Triassic red beds, folded Paleozoic schists to the north and east, and Precambrian volcanic rocks of the Anti-Atlas to the south (Figs. 1b and 2). The Anti-Atlas Mountains provided siliciclastic detritus into the Cenomanian-Turonian carbonate sediments (Rhalmi et al. 1997). The ~10-m-thick host succession (Fig. 1c) in the Imini district was dolomitized during diagenesis (Force et al. 1986). This succession is subdivided into three sedimentary facies: pink sandy dolostone (S_1, littoral margin) and white bioclastic dolostone (S_2, shallow lagoon), both of upper Cenomanian age, and cherty fossiliferous dolostone of lower Turonian age (S_3, tidal flat, Fig. 1c; Rhalmi et al. 2000). The Cenomanian transgression is recorded by flooding of the former fluviatile environment followed by shallowing upward of the platform during the Cenomanian-Turonian stage, and then by post-Turonian karstification (Thein 1990; Rhalmi et al. 2000). Rhalmi (1992) and Gutzmer et al. (2006) proposed that karst caves, which occur in the Cenomanian-Turonian dolostone, were filled by various sediments of Senonian (Coniacian-Maastrichtian) age that also cover the Cenomanian-Turonian sequence by up to 200 m of red argillaceous sandstone, clays, limestone, and evaporite (Fig. 2). Deposition of these terrestrial sediments, sourced from the Anti-Atlas Mountains, continued into the Paleocene (Rhalmi 1992; Saddiqi et al. 2011 and references therein). Sedimentation resumed during Eocene time with the deposition of fossiliferous shallow marine carbonate and clays, coeval with quiescent periods between the three main constructional stages of the High Atlas Mountains (Leprêtre et al. 2015): Late Eocene, Middle to Late Miocene, and post-Miocene. Cenomanian to Eocene sequence forms broad plateaus more or less titled and mildly folded, in contrast to the nearby South Atlas Front (SAF, Fig. 1a; Leprêtre et al. 2015). Paleozoic basement is exposed typically in valleys underlain by former anticlinal cores (Fig. 2). Older Neoproterozoic basement is

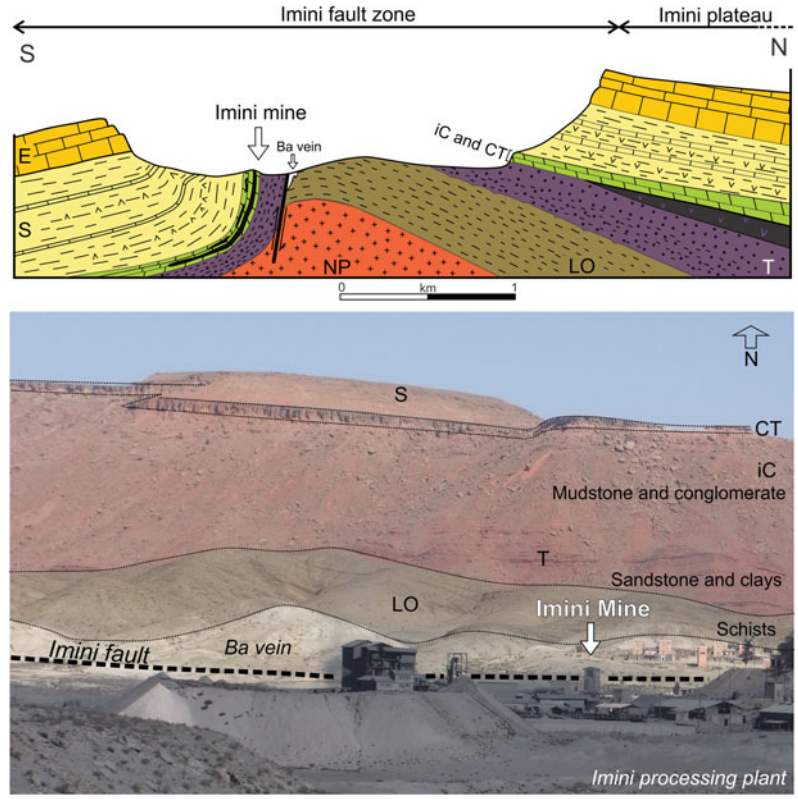

Fig. 2 Schematic cross section from Pouit (1964) (*above*) and field photograph (*below*) illustrating important attributes of the topography, geomorphology, and geology of Imini district. Legend corresponds to that in Fig. 1b. Abbreviations: *E* Eocene; *S* Senonian; *CT* Cenomanian-Turonian; *iC* infra-Cenomanian; *T* Triassic; *LO* Lower Ordovician; *NP* Neoproterozoic. *Black stratabound lenses* within Cenomanian-Turonian dolostone (*green*) represent Mn orebodies

exposed in deeper valleys or where Mesozoic-Cenozoic cover unconformably overlies directly on this basement (e.g., to the south in Fig. 1b). Mn-bearing Cenomanian-Turonian dolostone appears as resistant beds below Senonian sandstone (Fig. 2; Gutzmer et al. 2006).

Strata of the Imini district are affected by numerous faults mainly inherited from the Triassic-Jurassic rift system (Missenard et al. 2007) and reactivated during the Cenozoic inversion of the Atlas Mountains (Frizon de Lamotte et al. 2000). Structures that trend N90° E to N130° E, as well as N20–30° E to N45° E, are well represented in the Precambrian Anti-Atlas basement, and were reactivated during the Cenozoic (Leprêtre et al. 2015). The main structural feature of the district is the N90° E Imini anticline (Figs. 1b and 2) that corresponds to the Variscan trend of the Anti-Atlas Major Fault further south (Choubert 1963; Ennih et al. 2001; Ennih and Liégeois 2001; Gasquet et al. 2008). The Imini anticline was exhumed again during a late Atlasic (late ore post-Miocene) phase, at the same time as the related N90° E Imini Fault that hosts massive vein-type barite deposits (Fig. 2). Ore deposits are aligned along a N70° E direction, reflecting small-scale deformation and large folds. This direction is related to the first Eocene constructional phase of the Atlas Mountains, leading to strong deformation focused in a narrow Eocene Atlas belt with minor deformation on the borders (Leprêtre et al. 2015).

3 Distribution and Style of Mineralization

Manganese ores follow a WSW–ENE trend, forming a belt ~25 km long and 400–1000 m wide, similar to the N70° E orientation of Atlasic tectonic structures (Dekoninck et al. 2016) and the Cenomanian-Turonian paleoshoreline (Fig. 2, Gutzmer et al. 2006). The northern boundary of the ore zone is remarkably straight

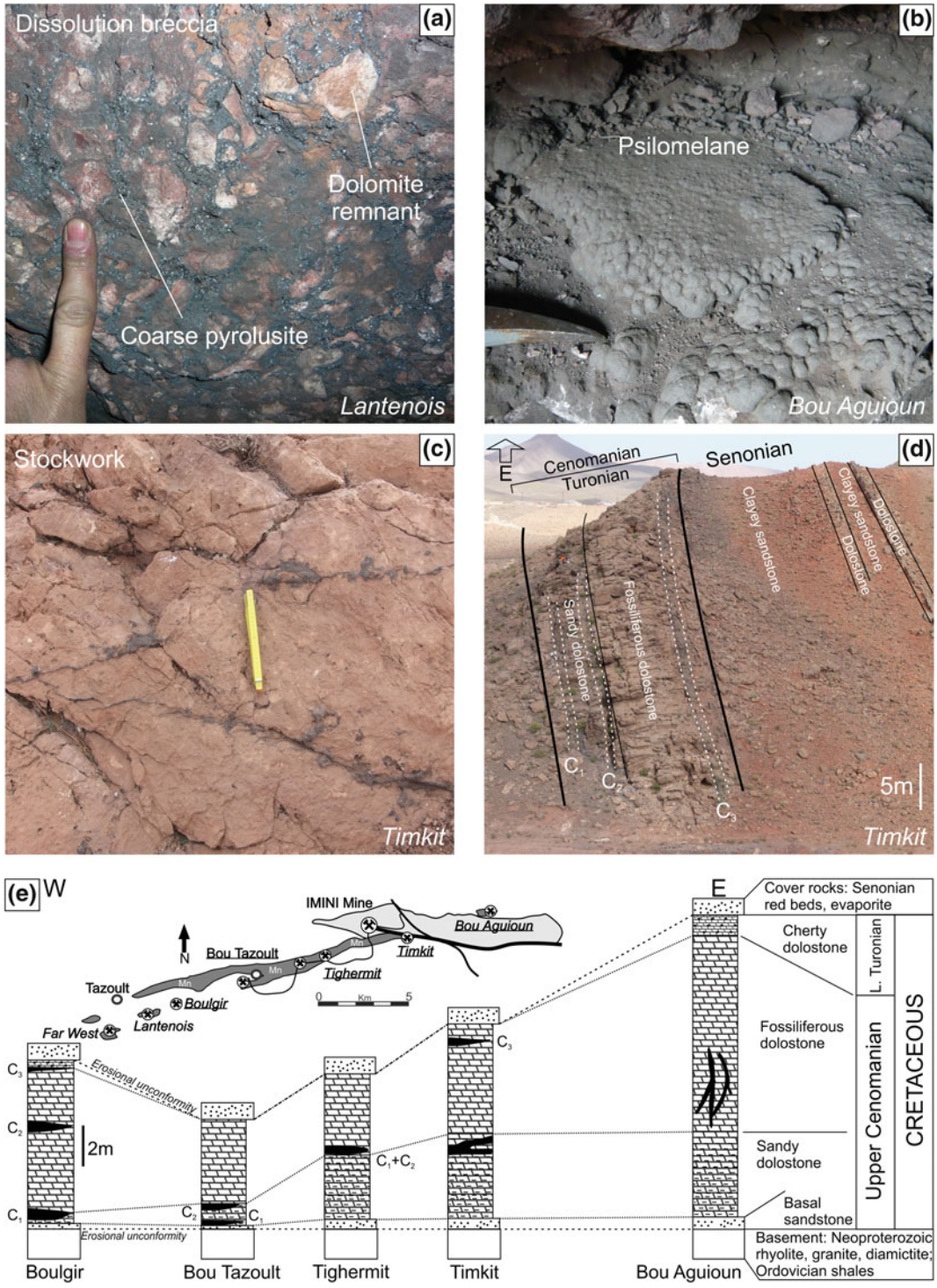
(a)
Dissolution breccia
Dolomite remnant
Coarse pyrolusite
Lantenois
(b)
Psilomelane
Bou Aguioun
(c)
Stockwork
Timkit
(d)
E
Cenomanian
Turonian
Senonian
Clayey sandstone
Dolostone
Clayey sandstone
Dolostone
Fossiliferous dolostone
Sandy dolostone
C1
C2
C3
5m
Timkit
(e) W
IMINI Mine
Bou Aguioun
N
Bou Tazoult
Timkit
Tighermit
Tazoult
Boulgir
Far West
Lantenois
0 Km 5
C3
C2
C1
2m
Erosional unconformity
C1+C2
Erosional unconformity
Boulgir
Bou Tazoult
Tighermit
Timkit
E
Bou Aguioun
Cover rocks: Senonian red beds, evaporite
Cherty dolostone
L. Turonian
Fossiliferous dolostone
Upper Cenomanian
CRETACEOUS
Sandy dolostone
Basal sandstone
Basement: Neoproterozoic rhyolite, granite, diamictite; Ordovician shales

◀ **Fig. 3** Main occurrences of manganese mineralization in host dolostone and distribution across the district. **a** Dissolution breccia mineralized and replaced by coarse pyrolusite. **b** Botryoidal psilomelane composed of hollandite group minerals in stratabound orebody of the Bou Aguioun mine; tip of hammer head (*lower left*) provides scale. **c** Stockwork veinlets composed of Mn oxides and oxyhydroxides within bioclastic dolostone (from Dekoninck et al. 2016). **d** Stratigraphic sequence of Cenomanian-Turonian and lower part of Senonian showing three stratabound orebodies (C_1, C_2, C_3) at Timkit. **e** Stratigraphic columns from west to east across the district showing stratabound but not stratiform character of Mn orebodies; *inset* shows plan view of Mn belt and locations of mines (modified after Gutzmer et al. 2006)

and is characterized by an iron-rich front, unlike the southern border (Bouladon and Jouravsky 1952; Pouit 1964; Lesavre 1975; Thein 1990). The peculiar feature of the Imini manganese ores is the occurrence of only Mn oxide (pyrolusite; Fig. 3a) and oxyhydroxide minerals (hollandite group minerals, lithiophorite, and romanechite; Fig. 3b). These minerals provide high concentrations of Mn and low Fe_2O_3 and SiO_2 (Table 1; Gutzmer et al. 2006; Dekoninck et al. 2016). The Mn oxide and oxyhydroxide minerals occur mainly as poorly consolidated, soft, and easily extracted material. Although manganese minerals form veinlets and stockwork (Fig. 3c) and breccia bodies that cut the host dolostone (Fig. 3a), economic Mn concentrations are

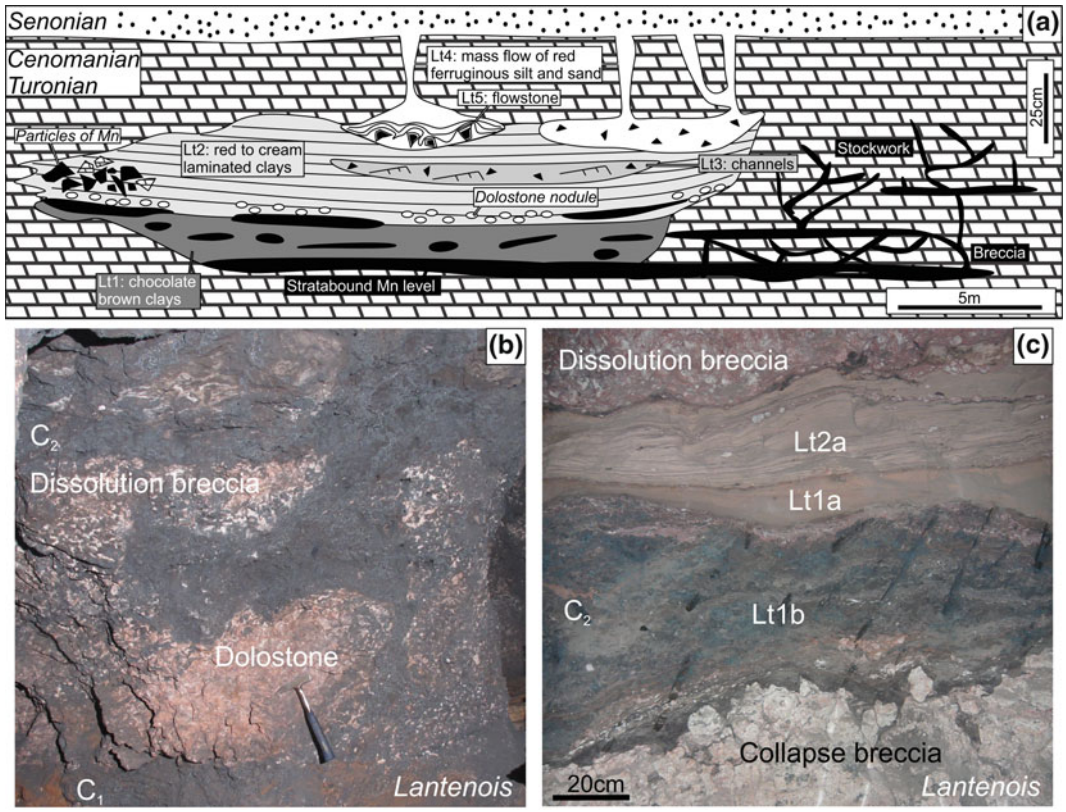

Fig. 4 Style of internal karst-fill sediments and associated manganese orebodies. **a** Sketch map illustrating relationship between manganese mineralization and different types of internal sediments in underground exposures (modified after Gutzmer et al. 2006). **b** Underground exposure of C_1 and C_2 mineralized level and relations to dissolution breccia and karst features. **c** Internal sediment lenses of lithotypes 1 (lt1) and 2 (lt2) enclosing C_2 orebody. Angular clasts of white dolostone record collapse of roof material that forms the collapse breccia shown at *bottom* of photograph

restricted to three stratabound orebodies, informally known from base to top, as C_1, C_2, and C_3 (Figs. 1c and 3d). Their spacing and stratigraphic position differ within the district, and as a result Gutzmer et al. (2006) described the orebodies as stratabound rather than stratiform (Fig. 3e). The orebodies may correspond to a network of subhorizontal epigenetic veinlets and lenses that formed in a karstic environment (Fig. 4a, b, c). C_1 and C_2 (1–2.5 m thick; Gebert 1989) form the most continuous and closely spaced layers, respectively located in the sandy dolostone (S_1) and the lowermost part of the main fossiliferous unit (S_2) (Figs. 1c and 3e). These two orebodies are both separated by laterally discontinuous sandstone lenses and contain a predominance (5–75 vol.%) of coarse-grained pyrolusite (Lesavre 1975), accounting for most of the manganese resources of the district. The third orebody (C_3) is less laterally continuous and thinner than C_1 and C_2, owing to its location at the boundary of the second and third sedimentary systems (S_2 and S_3), close to erosional unconformities (Fig. 3e). The C_3 orebody is composed mainly of hollandite group minerals (XMn_8O_{16} where X = Ba, Pb, or K), which locally are strongly enriched in Pb (Table 1; Gutzmer et al. 2006, Dekoninck et al. 2016). Brecciated zones reflect active dissolution of the host dolostone where mineralization formed. Collapse breccias in the district formed by physical collapse of roof materials, whereas dissolution breccias (or pseudobreccias) formed by chemical dissolution concurrent with stockwork mineralization (Fig. 4b, c). Stockworks and veinlets mainly occur in the footwall and hangingwall of karstic zones (Figs. 3c and 4a; Gutzmer et al. 2006).

4 Mineralogy and Petrology

Detailed studies of mineralogy and petrography have refined information about the ore petrology. Force et al. (1986), Thein (1990), and Rhalmi (1992) focused their observations on the host dolostone, whereas Gutzmer et al. (2006) and Dekoninck et al. (2016) studied the ore mineralogy and petrography.

4.1 Host Dolostone

Force et al. (1986) and Thein (1990) proposed a proximal saline environment for sedimentation of the Cenomanian-Turonian host dolostone. The only remains of such processes are quartz, feldspar, and accessory mineral relics, anhydrite ghosts (Fig. 5a; Rhalmi 1992; Dekoninck et al. 2016), and brachiopod shells and organism imprints (Fig. 5b; Rhalmi et al. 1997). Primary calcite or aragonite sediments were affected by widespread dolomitization in a mixing zone between meteoric and marine waters during early diagenesis, resulting in the formation of massive dolomite microspar that obscures original textures (Fig. 5c; Force et al. 1986; Rhalmi 1992; Rhalmi et al. 1997). Early dolomite was subsequently replaced by pseudosparitic dolomite rhombs (25–150 μm), mainly within the bioclastic dolostone, during dissolution by meteoric waters (Fig. 5c). Some dolomite rhombs have a thin rim of calcite, which may reflect dedolomitization or chemical zoning during growth (Gutzmer et al. 2006). Dolomitization enhanced the permeability of the host rock, creating porosity prior to the main stage of mineralization. Recent meteorically formed calcite and aragonite, and to a lesser extent coronadite and halite, filled fractures and remnant porosity of the dolostone during the end of ore formation (Fig. 5c; Dekoninck et al. 2016). Although only proximal dolostone contains disseminated Mn oxides and oxyhydroxides, both proximal and distal dolostones contain small bedding-parallel nodules composed of Fe oxides (goethite and hematite; Fig. 5d) associated with calcite.

4.2 Internal Karst-Fill Sediments

Gutzmer et al. (2006) suggested that the development of a karstic network in the Imini district is linked to proximity of a paleosurface to the Senonian strata, and to Cenozoic uplift of the Atlas Mountains. The caves are filled by five types of siliciclastic sediments called “lithotypes” (lt), which formed prior to, during, and after epigenetic manganese mineralization (Fig. 4a, c):

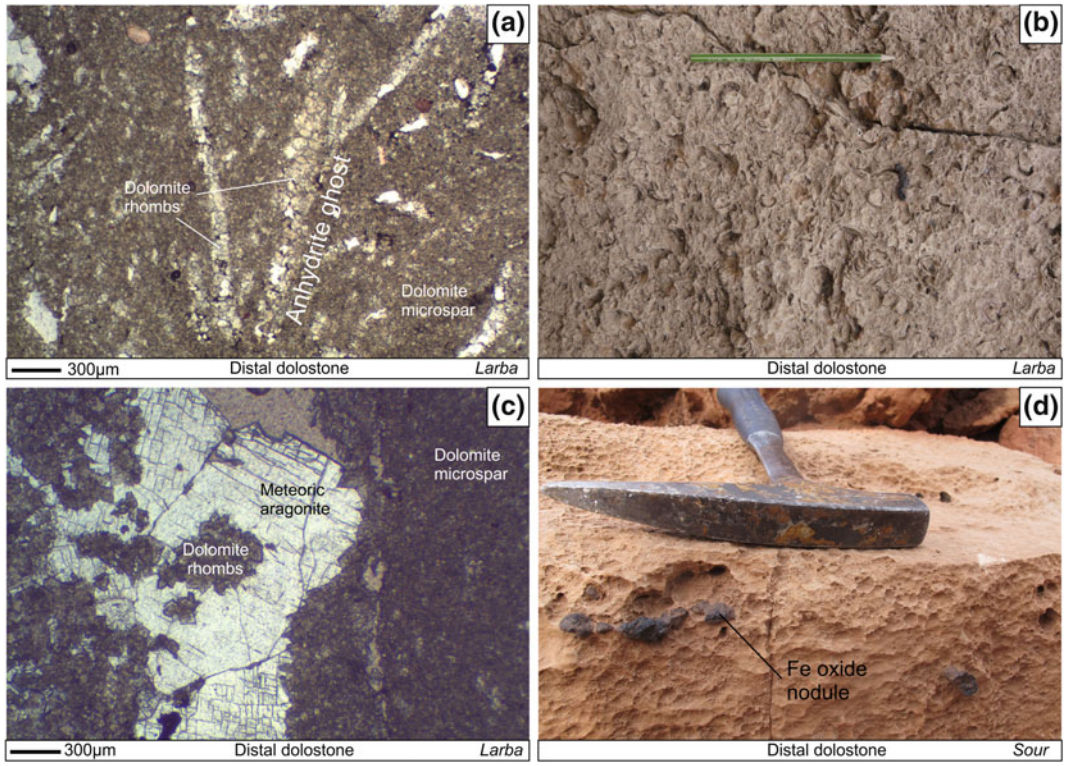

Fig. 5 Petrography of the host dolostone. **a** Photomicrograph (transmitted light) of anhydrite ghost (laths) filled by late meteoric dolomite rhombs within dolomite microspar matrix of a distal dolostone. Presence of former anhydrite suggests deposition in a saline environment. **b** Fossiliferous dolostone in distal Cenomanian-Turonian sequence. **c** Photomicrograph (transmitted light) of fine-grained, early diagenetic dolomite microspar, late meteoric diagenetic dolomite rhombs, and recent cement of coarse-grained aragonite, within distal dolostone. **d** Fe-oxide nodules with calcite in distal host dolostone

lt1 predates Mn ore deposition based on the replacement of chocolate brown clay by Mn oxides, lt2 overlies the main ore zone with red to cream laminated clay containing dolomite nodules at its base, lt3 and lt4 contain reworked grains of Mn ore indicating that they postdate the main ore deposition, lt5 is a recent flowstone encrusting dolostone fragments, marked by predominance of authigenic kaolinite with variable amounts of authigenic dolomite, quartz, Mn oxyhydroxides, and pyrolusite. Gutzmer et al. (2006) also considered that lt4 is the equivalent of the Senonian red beds. The occurrence of dolomite nodules in lt2 marks the stratigraphic limit of manganese mineralization that could represent a change in physicochemical conditions in the karst system. This level has been attributed to a pronounced change in climate, from humid and warm in the Upper Turonian, to arid and warm in the Senonian (Rhalmi 1992). Based on these relationships, Gutzmer et al. (2006) proposed a Senonian age for these sediments, probably 5 m.y. after the Turonian fall in sea level. This model is supported by the observation that the manganese ores were exposed along a pre-Senonian erosion surface.

4.3 Manganese Ore

The peculiar feature of the Imini orebodies is the occurrence of exclusively Mn oxides and oxyhydroxides in the form of pyrolusite (MnO_2), hollandite group minerals, romanechite [(Ba, $H_2O)Mn_5O_{10}$], and lithiophorite [(Al, Li) $MnO_2(OH)_2$]—minerals normally found in

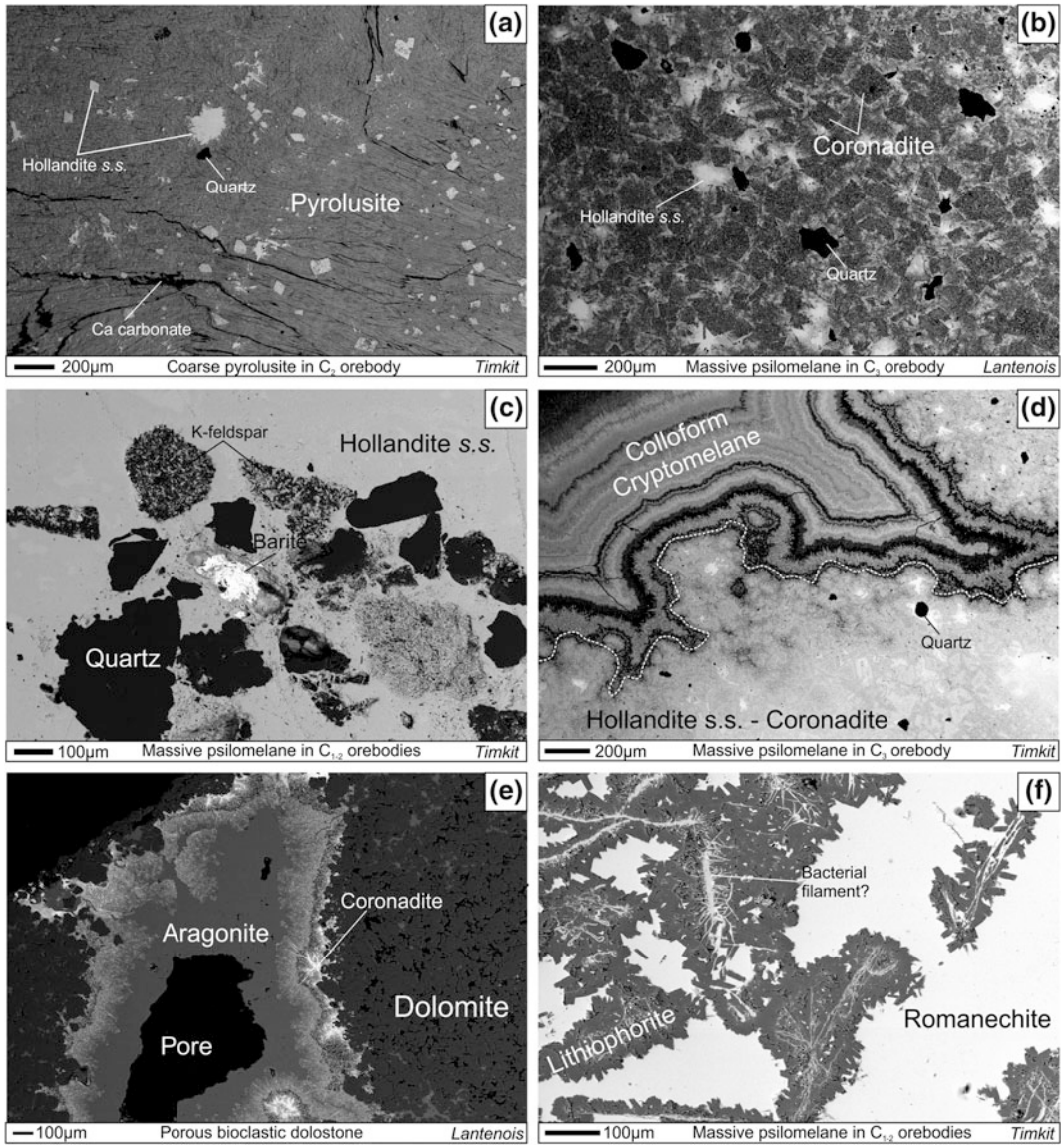

Fig. 6 Petrography of Mn ore zones by Scanning Electron Microscopy. **a** Coarse pyrolusite containing hollandite *s.s.* rhombs indicating that pyrolusite is paragenetically early; note late calcite or aragonite fills fractures in pyrolusite. **b** Coronadite replaces late diagenetic rhombs of dolomite. **c** Corrosion and replacement of quartz and feldspars by hollandite *s.s.*; barite formed at end of the paragenesis. **d** Colloform aggregates of cryptomelane grow on manganiferous matrix composed of dolomite rhombs that are replaced by hollandite *s.s.* and coronadite; this indicates that the colloform aggregates formed after Mn mineralization of the host epigenesist dolostone. **e** Recent coronadite followed by calcite or aragonite filling open space in host dolostone (Dekoninck et al. 2016); this image documents the role of porosity in ore precipitation. **f** Association of lithiophorite laths and romanechite; internal network of small filaments may reflect bacterial control on Mn mineralization (Dekoninck et al. 2016)

supergene manganese deposits (Dekoninck et al. 2016). Pyrolusite forms coarse prismatic crystals (Figs. 3a and 6a) and accounts for most of the mineralization present in stratabound lenses (Fig. 4b, c), cemented breccias (Fig. 3a), and stockworks (Fig. 3c). Pyrolusite crystalized

during early and late stages of mineralization (Fig. 6a). Hollandite group minerals display complete solid solutions between cryptomelane (KMn_8O_{16}), hollandite *s.s.* ($BaMn_8O_{16}$), and coronadite ($PbMn_8O_{16}$), all of which are commonly associated with pyrolusite in open spaces, but form hard levels in the C_3 orebody. These minerals replace both early dolomite microspar and late dolomite rhombs by epigenetic processes (Fig. 6b), supporting the premise that hollandite group minerals postdate dolomitization and late diagenesis. Quartz and feldspars are partly replaced by hollandite group minerals, indicating highly alkaline conditions for ore formation (Fig. 6c; Dekoninck et al. 2016). Colloform aggregates of hollandite group minerals (mainly cryptomelane) formed during brecciation stages after the replacement of the dolomite matrix by Mn oxides (Fig. 6d). Late coronadite is associated with a late calcite that fills porosity of the dolostone (Fig. 6e). Hence, the presence of hollandite group minerals shows that ore deposition is clearly polyphase, even after the first mineralization (Senonian in age; Gutzmer et al. 2006). Romanechite is uniformly associated with these minerals and forms fine-grained homogeneous masses (Fig. 6f). Barite is associated with Ba-rich romanechite and hollandite *s.s.* in the form of thin veinlets or small masses within Ba-rich manganese oxyhydroxides (Fig. 6c). Barite, rarely observed, formed at the end of the mineralizing sequence. Lithiophorite is disseminated as small inclusions or larger masses within the Ba-rich colloform Mn oxyhydroxides (Fig. 6f). Paragenesis of the Imini deposits is summarized in Fig. 7.

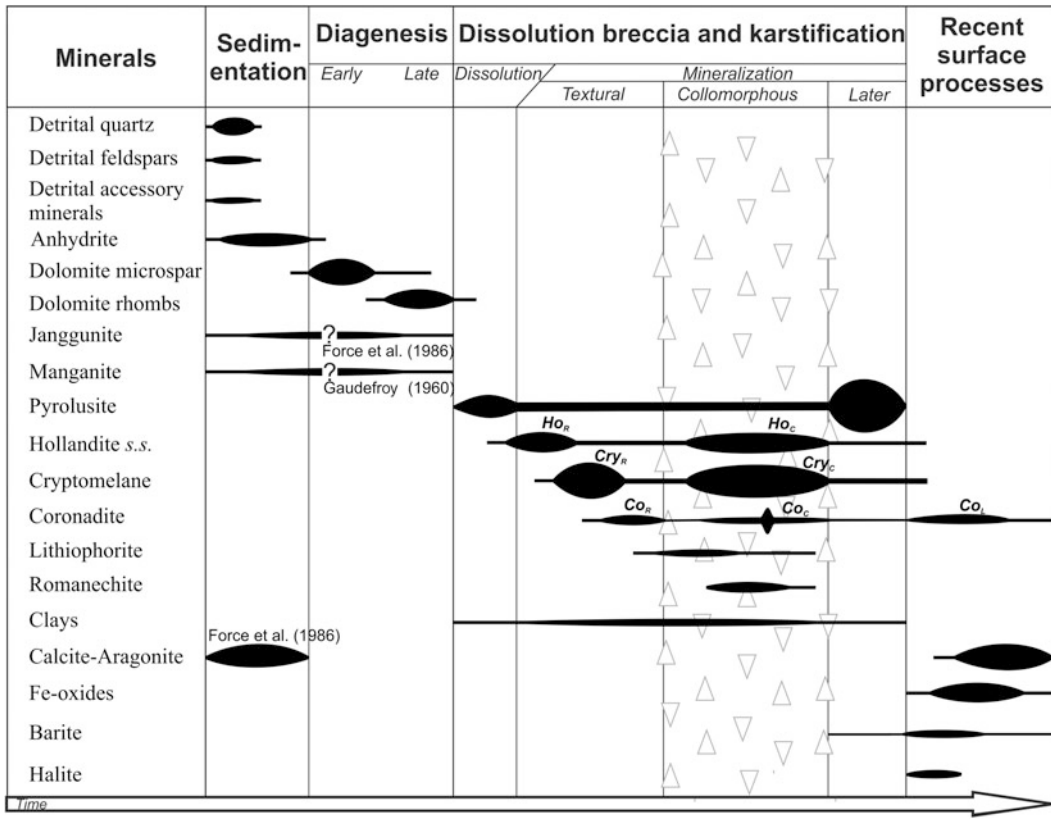

Fig. 7 Preliminary paragenetic sequence for Mn deposits of Imini district (Dekoninck et al. 2016) showing that manganese ore deposition was polyphase. Ho_R, replacement of dolomite by hollandite *s.s.*; Cry_R, replacement of dolomite by cryptomelane; Co_R replacement of dolomite by coronadite; Ho_C colloform hollandite *s.s.*; Cry_C colloform cryptomelane; Co_C colloform coronadite; Co_L late coronadite, *Triangle symbols*, main brecciation events

5 Geochemistry

5.1 Host Dolostone

The dolostone host to the Mn orebodies has a major element composition close to pure dolomite without significant detrital components (Table 1). Both distal and proximal dolostones display typical flat and depleted REE patterns of carbonate rocks (La_N/Yb_N 1.16–2.29, Table 2) with large negative Ce anomalies (Ce/Ce* 0.39–0.63, Fig. 8a; Piper 1974; Palmer 1985). The presence of Mn oxyhydroxides has a significant effect on the bulk compositions: (1) Mn concentrations of distal dolostone (0.12–0.2 wt% MnO) are characteristic of Phanerozoic dolostone (trace to 0.2 wt% MnO, Hill et al. 1967), whereas proximal dolostone has much higher MnO contents (0.38–0.61 wt% MnO; Table 1) due to the occurrence of finely dispersed Mn oxyhydroxides (Gutzmer et al. 2006); (2) higher REE contents in proximal than distal dolostone are controlled by the occurrence of dispersed Mn oxyhydroxides and clay assemblages (Fig. 8a). Iron contents are unusually low because Fe^{2+} is nearly absent compared to Fe^{3+}, and Mn/Fe ratios are systematically higher than 1.0 even in distal dolostone (4.72–13.6, Tables 1 and 3; Hill et al. 1967).

5.2 Internal Karst-Fill Sediments

Whilst internal karst-fill sediments have high SiO_2 concentrations compared to host dolostone, the molar ratios of immobile elements are similar (Table 3). This pattern suggests that most of the clay assemblages of lt1-2 represent the insoluble residue that was preserved during karstification. Dolomite is also an important mineral phase of authigenic origin in the internal sediments. Geochemical data for REE support this interpretation based on the presence of identical patterns in distal and proximal dolostones, as well as in the internal sediments (Fig. 8a; Gutzmer et al. 2006).

5.3 Manganese Ores

Ore samples were collected selectively from stratabound bodies, breccias, and stockworks. The most distinctive feature of the manganese ores of the Imini district is the high contents of MnO (typically >70 wt% MnO, Table 1), which is augmented by very low Fe_2O_3 (and SiO_2, Al_2O_3, TiO_2, and P_2O_5; Table 1) compared to other Mn deposits (<0.6 wt% Fe_2O_3; Table 1; e.g., Maynard 2014). The observed enrichments in Ba, Pb, and K, as well as Cu, Sr, and V, are related to the abundance of hollandite group minerals (Table 1), but not for other metals such as Zn, Ni, Co, As, Cr, Rb, La, and Ce that commonly are much higher than in other Mn deposits (Tables 2 and 3; Gutzmer et al. 2006). Using a discrimination plot proposed by Nicholson (1992), a high concentration of Pb (and Ba, Table 1) within the hollandite group minerals reflects a Mn-rich gossan in the Imini district (Fig. 8b). The low Mn/Fe ratios and correlation of Fe with detrital elements within the internal karst-fill sediments suggests that iron was geochemically decoupled from manganese and records weathering processes (Gutzmer et al. 2006; Table 3).

6 Metallogenic Models and Classification

Since 1929, the manganese deposits of the Imini district have been attributed to four different metallogenic models: (1) synsedimentary, (2) diagenetic, (3) hydrothermal, and (4) karst-hosted. We summarize below the main aspects of these models.

(1) Most workers have proposed a synsedimentary origin in order to explain the stratiform character of the orebodies (Neltner 1933; Orcel 1942; Bouladon and Jouravsky 1952; Lesavre 1975; Pouit 1980; Force et al. 1986; Thein 1990; Lalaoui et al. 1991; Rhalmi et al. 1997). The interbedded orebodies seem to occur between transitional facies of the dolomite host rock, and

Table 2 Data for rare earth elements (REE) normalized to average Post-Archean Australian Shale (PAAS; Taylor and McLennan 1985)

Sample	IM20	IM26	IM43d	LAN58	LAN61	ECH98b	ECH102b	IM37	IM22	IM29	LAN51	IM41c	ECH101b	IM43m	LAN52	ECH76	ECH77	ECH79	ECH81	ECH85
Locality	Timkit		Lantenois			Bou Aggioun		Timkit			Lantenois	Far West	Bou Aggioun	Lantenois		Larba				Taouerda
Type	Proximal dolostone					C1		C1-C2	C2			C3	Stockwork	Breccia	Lt(2)	Distal dolostone				
La	3	2	2	4	3	4	8	6	7	4	31	20	18	8	11	2	2	2	2	2
Ce	4	1	2	4	2	10	14	10	6	10	42	25	23	12	10	1	1	1	1	2
Pr	0.72	0.29	0.3	0.67	0.37	0.63	0.91	2.21	1.53	0.5	4.16	1.89	2.91	0.72	2.38	0.24	0.28	0.24	0.33	0.22
Nd	3.19	1.13	1.22	2.41	1.33	2.18	3.07	9.66	5.54	1.67	14.8	5.82	11.5	2.07	9.66	1	1.21	0.85	1.26	0.96
Sm	0.62	0.19	0.17	0.42	0.25	0.46	0.62	1.82	1.02	0.47	2.49	1.18	2.28	0.53	1.94	0.12	0.13	0.14	0.19	0.12
Eu	0.11	0.04	0.05	0.1	0.06	0.37	0.36	0.34	0.28	0.61	0.38	1.15	0.43	0.7	0.44	0.03	0.03	0.03	0.04	0.03
Gd	0.54	0.18	0.19	0.37	0.29	0.59	0.81	1.89	1.3	0.82	2.14	1.43	2.17	0.78	1.96	0.12	0.12	0.13	0.18	0.15
Tb	0.09	0.04	0.04	0.05	0.04	0.06	0.1	0.22	0.21	0.08	0.31	0.13	0.3	0.06	0.26	0.02	0.02	0.02	0.03	0.02
Dy	0.52	0.19	0.22	0.28	0.21	0.31	0.51	1.13	1.23	0.44	1.61	0.58	1.67	0.26	1.42	0.14	0.12	0.15	0.2	0.12
Ho	0.09	0.03	0.04	0.05	0.04	0.06	0.1	0.19	0.26	0.1	0.32	0.12	0.3	0.04	0.25	0.03	0.02	0.03	0.04	0.02
Er	0.23	0.07	0.11	0.16	0.13	0.18	0.28	0.45	0.71	0.28	0.92	0.34	0.77	0.13	0.55	0.08	0.06	0.1	0.09	0.07
Tm	0.03	0.01	0.02	0.02	0.02	0.03	0.05	0.05	0.09	0.04	0.14	0.05	0.1	0.02	0.07	0.01	0.01	0.02	0.01	0.01
Yb	0.2	0.07	0.13	0.14	0.12	0.21	0.34	0.29	0.57	0.23	0.9	0.33	0.64	0.16	0.5	0.08	0.07	0.12	0.09	0.07
Lu	0.03	0.02	0.02	0.02	0.02	0.04	0.07	0.05	0.09	0.04	0.16	0.05	0.1	0.02	0.07	0.01	0.01	0.02	0.01	0.01
Ce/Ce*	2.72	1.31	2.58	2.44	1.90	6.30	5.19	2.75	1.83	7.07	3.70	4.07	3.18	5.00	1.95	1.44	1.34	1.44	1.23	3.02

Determinations by fusion ICP-MS at Activation Laboratories (Ontario, Canada)

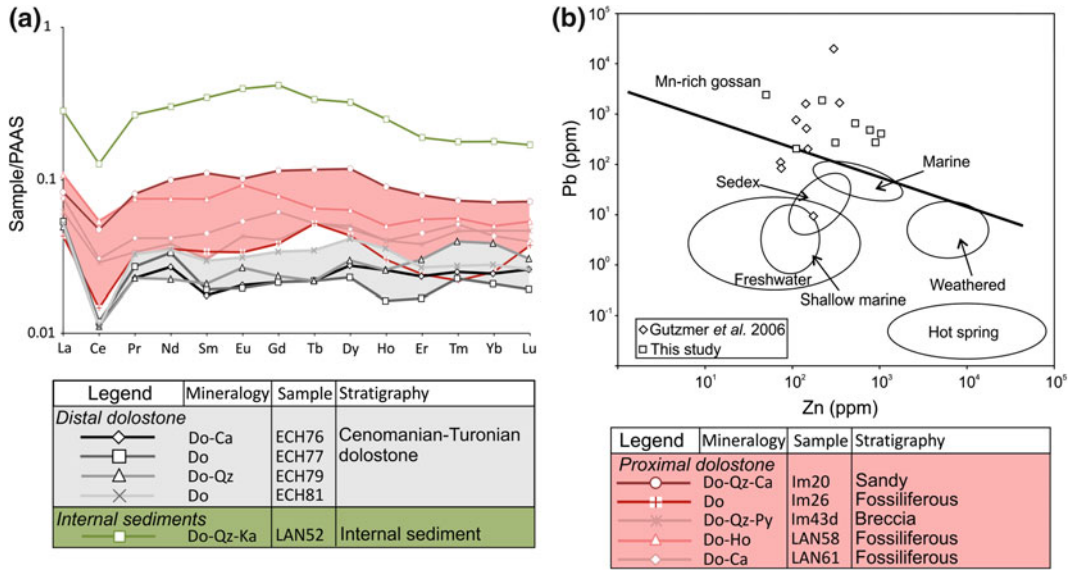

Fig. 8 Geochemistry of manganese orebodies of Imini district. **a** Rare earth element (REE) patterns of internal karst-fill sediments (*green*), and distal (*pink*) and proximal (*grey*) dolostones, normalized to average Post-Archean Australian Shale (PAAS) reference (Taylor and McLennan 1985). REE patterns of Cenomanian-Turonian dolostone are typical of Phanerozoic marine dolostone; conservation of the dolostone REE pattern for the internal sediments indicates that dolomite residues come from authigenic deposition during karstification. Proximal dolostone contains dispersed grains of Mn oxides. **b** Zn and Pb concentrations for manganese orebodies from Gutzmer et al. (2006) and this study plot mainly in Mn-rich gossan field on discrimination plot of Nicholson (1992). Abbreviations: *Do* dolomite; *Ca* calcite; *Qz* quartz; *Ka* kaolinite; *Py* pyrolusite; *Ho* hollandite *s.s*

have been linked to transgressional phases of the Cenomanian-Turonian paleoshoreline (Bouladon and Jouravsky 1952) or to marine paleocurrents (Pouit 1964; Lesavre 1975). The presence of Mn-dolomite below the cherty dolostone in the Aghbalou deposit (30 km SW of Imini) and of psilomelane interbedded in the dolostone (Lesavre 1975) or chert (Force et al. 1986) supports this synsedimentary model. Large regional halos of minor metals in the surrounding carbonates record a geochemical anomaly that could be related to remobilization of these metals and Mn in an anoxic deep ocean with deposition occurring near the coast where reducing metalliferous seawater mixed with oxidized groundwaters (Thein 1990).

(2) An alternative diagenetic model, proposed by Force et al. (1986) and revisited by Thein (1990), argues that the host rock became dolomitized in a mixing zone between CO_2-bearing fresh groundwater and Mg-bearing saline seawater. In this model, chert, hollandite group minerals, and calcite precipitated concurrently in the uppermost part of the meteoric zone. The first Mn-mineral janggunite subsequently formed hollandite group minerals followed by pyrolusite owing to increased oxidation (Fig. 7; Force et al. 1986). Two variants of the model have been proposed: (i) primary sedimentary manganese was modified by diagenesis, or (ii) Mn oxides precipitated in a ground-water mixing zone. A sedimentary origin for the Mn necessarily implies lower Pb and Ba (Table 1) contents and the existence of primary sedimentary Mn minerals (Force et al. 1986; Lalaoui et al. 1991). On the other hand, precipitation of Mn oxides during diagenesis requires the transport of reduced Mn, and the presence of other Mn oxide deposits at the same stratigraphic level in Cenomanian-Turonian dolostone that formed on the margin of anoxic seas (Force et al. 1986). Both synsedimentary and early diagenetic models need to be revisited because Mn oxides in the district form stratabound lenses rather than stratiform beds

Table 3 Trace element geochemistry of internal sediments, manganese orebodies, distal and proximal host rocks of Imini district

Sample	IM20	IM26	IM43d	LAN58	LAN61	ECH98b	ECH102b	IM37	IM22	IM29	LAN51	IM41c	ECH101b	IM43m	LAN52	ECH76	ECH77	ECH79	ECH81	ECH85	
Locality	Timkit		Lantenois			Bou Aggioun		Timkit			Lantenois	Far West	Bou Aggioun	Lantenois		Larba				Taouerda	
Type	Proximal dolostone					C1		C1-C2	C2			C3	Stockwork	Breccia	Lt(2)	Distal dolostone					
Mn/Fe	7	14	5	42	9	442	221	354	9159	/	19	1860	ECH101b	IM43m	LAN52	ECH76	ECH77	ECH79	ECH81	ECH85	
V	14	12	9	11	15	1469	874	1795	392	832	522	921	103	72	2	5	/	/	/	19	Chalcophile
Cu	20	< 10	20	20	10	1510	2170	830	1430	1930	1120	1550	1190	289	53	23	25	26	22	22	
Zn	<30	80	<30	<30	<30	770	1030	520	110	310	220	50	1500	690	110	<10	<10	<10	<10	<10	
Ni	<20	<20	<20	<20	<20	40	250	80	40	330	50	30	890	<30	60	140	180	260	260	<30	
Co	2	1	2	2	4	1120	2480	540	68	429	190	476	340	<20	<20	<20	<20	<20	<20	<20	
As	<5	<5	<5	<5	<5	443	230	80	39	153	72	66	1230	135	9	<1	<1	<1	<1	<1	
Cr	<20	20	30	30	<20	20	40	30	<20	60	110	20	222	49	6	<5	<5	<5	<5	<5	Immobile
Zr	13	2	14	16	4	17	13	12	7	8	208	12	30	30	40	<20	<20	<20	40	30	
Rb	6	2	5	4	<1	15	17	4	<1	<1	39	5	31	18	34	2	1	<1	3	1	Mobile
Sr	61	47	64	59	57	2577	3014	1091	423	449	1464	1912	19	4	14	<1	<1	<1	<1	<1	
La	3	2	2	4	3	4	8	6	7	4	31	20	2933	1545	53	47	50	55	45	125	REE
Ce	4	1	2	4	2	10	14	10	6	10	42	25	18	8	11	2	2	2	2	2	

V and Sr were analyzed by fusion ICP-MS methods and other elements by FUS-MS. Abbreviations: *IS Lt* (*no*.) internal sediment lithotype (no.); *N.A*. not analyzed

(Fig. 3e; Gutzmer et al. 2006), and because the Mn minerals clearly postdate dolomitization (Fig. 7; Dekoninck et al. 2016).

(3) Close to the Imini area, several epithermal Mn-rich veins that cut both Triassic and Cenomanian rocks have been attributed to a deep hydrothermal origin (Westerveld 1951; Pouit and Jouravsky 1960). However, such veins are small and local, and do not relate to the main mineralogy of the stratabound ores. We should rather expect enrichment in As–Cu–Mo–Pb–V–Zn within hydrothermal Mn deposits, which is not observed (Table 3, Fig. 8b; Nicholson 1992).

(4) Moret (1931) suggested a lateritic formation for the Imini deposits following the Cenomanian-Turonian transgression. However, Lesavre (1975) and Beaudoin et al. (1976) provided the first observations on the role of weathering processes in Mn ore concentration after the Cenomanian and Turonian. These authors noted that the host dolostone has preferentially undergone weathering and dissolution due to its permeable character (Fig. 4a, b, c). Nonetheless, it might be argued that these processes only affected the primary Mn concentrations and conserved original sedimentary morphology. The main issue is the low solubility of Mn^{4+} in meteoric waters (Lesavre 1975; Beaudoin et al. 1976). Geochemical data and petrographic observations obtained by Gutzmer et al. (2006), Dekoninck et al. (2016), and in this study indicate that a karst-hosted model, involving epigenetic processes of Mn deposition, is the best mechanism to explain Mn ores in the Imini district. The manganese ores are spatially associated with siliciclastic sediments that were washed into the cave system by meteoric waters and then transported and redistributed by ground waters (Fig. 4a). Evidence for this process is recorded by sedimentary textures and reworked grains of Mn oxides within internal karst-fill sediments (Fig. 4a), as well as by the dissolution and collapse breccias (Figs. 3a and 4b, c; Gutzmer et al. 2006). Distal dolostone contains only trace amounts of manganese and little insoluble siliciclastic components such as SiO_2 and Al_2O_3 (Table 1). Total dissolution of the host dolostone to form stratabound Mn orebodies, 1–2 m thick, would only lead to a few centimeters of in situ insoluble siliciclastic residue (Gutzmer et al. 2006). Recent observations in the district of Fe oxide nodules within distal and proximal host rocks (Fig. 5d; Dekoninck et al. 2016) suggest an authigenic source for the manganese. However the thickness and the amount of Fe nodules, which could host Mn, are not sufficient to provide the high Mn/Fe ratios and concentration in manganese present in the Imini orebodies (Tables 1 and 3). Therefore, both siliciclastic internal sediments and stratabound Mn oxides and oxyhydroxides must have been introduced from one or more external sources during in situ chemical and mechanical dissolution of the host dolostone (Gutzmer et al. 2006). The presence of compositionally different layers in the colloform cryptomelane supports this model (Fig. 6d; Dekoninck et al. 2016). Moreover, the occurrence of hollandite *s.s.* and coronadite provides large enrichments of Ba and Pb, which are very unusual in synsedimentary Mn deposits (Table 1, Fig. 8b; Nicholson 1992), as coronadite and lithiophorite are normally found in the weathering zones of hypogene manganese and lead deposits (Hewett 1971; De Villiers 1983). The proposed external input of manganese gives to the Imini deposits an unusual feature compared to other well-known karst-hosted Mn deposits, such as those in the Postmasburg manganese field of South Africa (Gutzmer and Beukes 1996).

7 Timing of Manganese Mineralization

The replacement of late diagenetic dolomite rhombs by hollandite group minerals (Fig. 6b) indicates that Mn mineralization occurred after dolomitization and late diagenesis, and therefore after the Turonian stage (Dekoninck et al. 2016). Dissolution of the host dolostone led to the formation of the stratabound manganese orebodies, within karstic pipes that are connected to the paleosurface and were infilled by epigenetic processes (Fig. 4a, b). Gutzmer et al. (2006) suggested that karstification occurred prior to,

and continued throughout, manganese oxide deposition by the early Senonian. However, attempts to accurately date the internal karst-fill sediments and their origin should be discussed. Age constraints are mainly based on the change in physicochemical conditions in lithotypes attributed to a climate change between the Upper Turonian and Senonian, as well as on the exposure of the manganese ores to a pre-Senonian erosion surface. Moreover, alignment of the orebodies along a N70° E direction might indicate a structural origin of the karstification. However, no tectonic phase is recorded during the Late Cretaceous, which thus argues for a later mineralization during building of the Atlas Mountains. During the Cenozoic exhumation of the Atlas Mountains (Leprêtre et al. 2015), mineralizing fluids could have percolated down through weak zones such as faults, permeable strata, or stratigraphic boundaries in the dolostone, and then reactivated mineral deposition or reworked the previously formed manganiferous orebodies as well as the karst features (Fig. 9). Alignment of orebodies in the district also might be controlled by the paleoshoreline of the Triassic red beds, having formed a stratigraphic trap for the Mn ore (Fig. 2). The enrichment in Fe minerals to the north and Mn minerals to the south may be explained by the flow of meteoric waters preferentially in this direction. Iron precipitates faster in O_2-rich environments than manganese (e.g., Maynard 2014), a process that might be responsible for the presence of pyrolusite to the north and psilomelane to the south (Lesavre 1975).

8 Fluid Composition and Potential Metal Sources

Manganese is a soluble element with a bivalent state in reduced and acidic environments (e.g., Hem 1963). Aqueous fluids at low temperature (<100 °C) can transport significant quantities of Mn, Ba, and Pb only if acidic, at low to moderate Eh, and sulphur-poor. The presence of appreciable sulphate or sulphide ions in fluids leads to the precipitation of barite and galena and, under alkaline conditions Ba and Pb form witherite and cerussite, respectively. However, these minerals

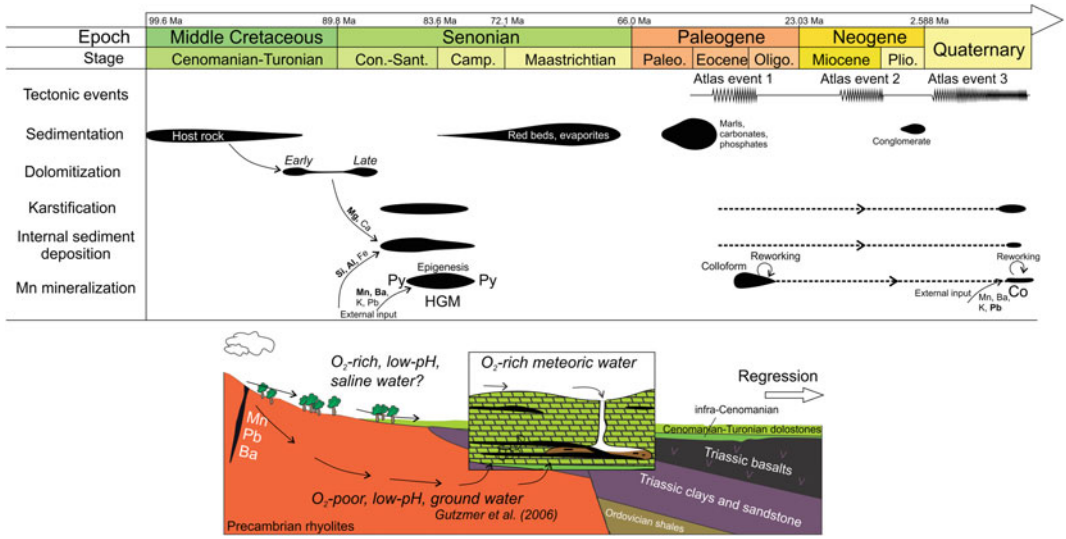

Fig. 9 Time-event chart and revisited metallogenic model for Imini district illustrating multistage character of ore deposition and likely tectonic control during the Cenozoic. See text for discussion on role of mineralizing fluids and potential metal sources. Abbreviations: *Py* pyrolusite; *HGM* hollandite group minerals; *Co* coronadite

are absent or scarce in the Imini orebodies. Higher temperatures or salt contents would have increased the capacity of the fluids to transport Mn, Ba, and Pb (e.g., Seward and Barnes 1997). Gutzmer et al. (2006) proposed that manganese orebodies in the karstic environment formed during a period of terrestrial exposure, in which the well-developed karst system corresponded to the mixing vadose zone between O_2-rich surficial waters and O_2-poor (and mildly acidic) low-temperature fluids derived from deeper sources (Fig. 9). In this model, the latter fluids ascended through basement rocks and leached metal cations. The laterally extensive cave system tended to form in the zone of a fluctuating ground water table. Fluctuations of this water table could be responsible for occurrence of the three epigenetic stratabound orebodies from C_1 to C_3. The presence of modern halite (Dekoninck et al. 2016) suggests that the Mn-bearing fluids also were saline and originated from surface input. Dissolution of the host dolostone could explain the precipitation and epigenetic replacement of Mn–Ba–Pb-rich oxyhydroxides and quartz by hollandite group minerals (Fig. 6c; Dekoninck et al. 2016). In addition, the Mn accumulation also could have been enhanced by bacterial filament formation, as observed in the romanechite-rich samples (Fig. 6f) and also in stromatolites from the upper part of the C_3 orebody (Lesavre 1975).

Voluminous volcanic rocks of the Anti-Atlas region may be the ultimate source rocks for the unusual metal assemblage in the manganese ores of the Imini district. These rocks constitute the Senonian hinterland to the south of the district, and contain several manganese, barite, and Pb-rich base-metal deposits (Neltner 1933; Orcel 1942; Westerveld 1951; Bouladon and Jouravsky 1952; Pouit and Jouravsky 1960; Pouit 1964, 1976; Lesavre 1975). Also important is the presence in the volcanic rocks of large amounts of K and Ba in K-feldspar, and base metals in mafic minerals (Gutzmer et al. 2006). An alternative source of the metals could also be the High Atlas Mountain to the north, where Triassic basalts are exposed (Moret 1931).

9 Other Manganese Deposits Hosted in Cenomanian-Turonian Dolostone

A small manganese deposit is situated at the Upper Souss River, near the village of Tasdremt, 100 km to the west of the Imini area (Fig. 1a). This deposit was mined from 1930 to the 1960s with reported grades of 39–56 wt% MnO, 4.8–6.9 wt% PbO, 5.1–7.2 wt% BaO, 0.5–1.1 wt% Fe_2O_3, and 6.9–26.3 wt% SiO_2, including some similarities to the manganese deposits at Imini (Bouladon and Meune 1951; Bouladon and Jouravsky 1952; Lesavre 1975). The Tasdremt deposit is hosted in Cenomanian-Turonian dolostone and separated from the basement by a few meters of red "infra-Cenomanian." Manganese oxides and oxyhydroxides are dominated by coronadite and hollandite *s.s.* (Lesavre 1975), which occur in two irregular layers ~0.2 and 0.6 m thick that replace some corals and other organisms. Pyrolusite constitutes a minor mineral in contrast to the Imini ores. The deposition of manganese at the Tasdremt deposit is considered to be synsedimentary (Thein 1990) or linked to dolomitization (Lesavre 1975). The Aghbalou deposit ca. 30 km southwest of Imini (precise location is not known) shows little enrichment of stratiform Mn and Fe below the cherty dolostone that corresponds to the C_3 orebody. This deposit produced only 5 kt of manganese at an average grade of 30 wt% MnO. Manganese there occurs as small needles of coronadite within the host dolostone (Lesavre 1975).

10 Conclusions

The Imini district is situated between the Cenozoic High Atlas Mountains to the north and the Precambrian Anti-Atlas Mountains to the south. For more than 80 years of mining activity it has been the main producer of manganese in Morocco because of its high grade (>70 wt% MnO) and low contents of SiO_2, Fe_2O_3, and P_2O_5. The ore is hosted in a ~10-m-thick, Cenomanian-Turonian sequence, mainly in three stratabound

levels composed only of Mn oxides and oxyhydroxides. The absence of significant amounts of MnO in distal dolostone and in primary minerals, as well as the close spatial relationship between internal sediments and ore beds, suggests an epigenetic, karst-filling deposition of manganese oxides in the Imini area. Ore deposition in the district occurred after host-rock formation and diagenesis, probably during post-Turonian karstification of the dolostone, followed by reactivation or/and reworking of the Mn minerals during Cenozoic uplift(s) of the Atlas Mountains. Formation of the orebodies implies neutralization of the host dolostone by fluids to provide the high pH and O_2-rich conditions necessary for manganese precipitation. The stratabound character of the ore is attributed here to preferential karstification and epigenetic processes, permeability, and lithological heterogeneities within the dolostone sequence. The main sources for manganese and related metals (Pb, Ba) in the Imini orebodies may be the Anti-Atlas basement or Triassic basalt of the High "Atlas" Mountains.

Acknowledgments We are grateful to the staff of the Imini mine and to Société Anonyme Chérifienne d'Etude Minière (SACEM) for hospitality, field authorizations, and guidance on sampling sites. We warmly thank Prof. A. Bernard of the Université Libre de Bruxelles for SEM images and analytical advice, as well as Y. Missenard and B. Saint-Bézar for helpful discussions on structural features of the Imini area.

References

Beaudoin B, Lesavre A, Pelissonnier H (1976) Action des eaux superficielles dans le gisement de manganese d'Imini (Maroc). Bull Société Géol France 18:95–100

Bouladon J, Jouravsky G (1952) Géologie des gites minéraux marocains: manganèse. Congrès Géol Intern, Alger, pp 44–80

Bouladon J, Meune M (1951) Le gisement de Tasdremt (Haut-Sous): un gîte sédimentaire de manganèse plombifère dans le Mésocrétacé transgressif. Notes Mémoires Service Géol Maroc 4:221–250

Choubert G (1963) Histoire géologique du domaine de l'Anti-Atlas. Notes Mémoires Service Géol Maroc, Rabat, pp 75–194

de Villiers JE (1983) The manganese deposits of Griqualand West, South Africa: some mineralogic aspects. Econ Geol 78:1108–1118

Dekoninck A, Bernard A, Barbarand J, Saint-Bezar B, Missenard Y, Leprêtre R, Saddiqi O, Yans J (2016) Detailed mineralogy and petrology of manganese oxyhydroxide deposits of the Imini district (Morocco). Miner Deposita 51:13–23

Ennih N, Liégeois JP (2001) The Moroccan Anti-Atlas: the West African craton passive margin with limited Pan-African activity: implications for the northern limit of the craton. Precamb Res 112:289–302

Ennih N, Laduron D, Greiling R, Errami E, de Wall H, Boutaleb M (2001) Superposition de la tectonique éburnéenne et panafricaine dans les granitoïdes de la bordure nord du craton ouest africain, boutonnière de Zenaga, Anti-Atlas central, Maroc. J Afr Earth Sci 32:677–693

Force ER, Back W, Spiker EC, Knauth LP (1986) A ground-water mixing model for the origin of the Imini manganese deposit (Cretaceous) of Morocco. Econ Geol 81:65–79

Frizon de Lamotte D, Saint Bezar B, Bracène R, Mercier E (2000) The two main steps of the Atlas building and geodynamics of the western Mediterranean. Tectonics 19:740–761

Gandini J (2011) Province de Ouarzazate—Les Mines: Ouarzazate au temps du protectorat. http://www.ouarzazate-1928-1956.com/les-mines/index.html. Accessed 21 Sept 2015

Gasquet D, Ennih N, Liégeois JP, Soulaimani A, Michard A (2008) The Pan-African belt. In: Michard A, Saddiqi O, Chalouan A, de Lamotte DF (eds) Continental evolution: the geology of Morocco. Springer, Berlin-Heidelberg, pp 33–64

Gaudefroy G (1960) Caractères distinctifs de la pyrolusite—ex manganite (application au minerai de l'Imini). Notes Service Géol Marocain 19:77–86

Gebert H (1989) Schichtgebundene Manganlagerstätten. F. Enke, Stuttgart 237 pp

Gutzmer J, Beukes NJ (1996) Karst-hosted fresh-water Paleoproterozoic manganese deposits, Postmasburg, South Africa. Econ Geol 91:1435–1454

Gutzmer J, Beukes NJ, Rhalmi M, Mukhopadhyay J (2006) Cretaceous karstic cave-fill manganese-lead-barium deposits of Imini, Morocco. Econ Geol 101:385–405

Hem JD (1963) Chemical equilibria and rates of manganese oxidation. U.S. Geol Survey Water-Supply Paper 1667-A, 64 pp

Hewett DF (1971) Coronadite; modes of occurrence and origin. Econ Geol 66:164–177

Hill TP, Werner MA, Horton MJ (1967) Chemical composition of sedimentary rocks in Colorado, Kansas, Montana, Nebraska, North Dakota, South Dakota, and Wyoming. U.S. Geol Survey Prof Paper 561, 241 pp

Lalaoui MD, Beauchamp J, Sagon JP (1991) Le gisement de manganèse de l'Imini (Maroc): un dépôt sur la ligne de rivage. Chronique Recherche Minière 502:23–36

Leprêtre R, Missenard Y, Saint-Bezar B, Barbarand J, Delpech G, Yans J, Dekoninck A, Saddiqi O (2015)

The three main steps of the Marrakech High Atlas building in Morocco: structural evidences from the southern foreland, Imini area. J Afr Earth Sci 109:177–194

Lesavre A (1975) Le gisement de manganèse d'Imini (Maroc). Unpubl PhD Thesis, Université Pierre et Marie Curie, Paris, 101 pp

Maynard JB (2014) Manganiferous sediments, rocks and ores. In: Mackenzie FT (Ed) Sediments, diagenesis and sedimentary rocks. Elsevier, Treatise on geochemistry, 2nd edn, vol 9. pp 327–349

Missenard Y, Taki Z, Frizon de Lamotte D, Benammi M, Hafid M, Leturmy P, Sébrier M (2007) Tectonic styles in the Marrakesh High Atlas (Morocco): the role of heritage and mechanical stratigraphy. J Afr Earth Sci 48:247–266

Moret L (1931) Les ressources minérales et les mines du Maroc français. Revue Géographie Alpine 18:261–302

Neltner L (1933) Le manganèse dans les possessions françaises. Les Ressources minérales de la France d'Outremer. Publications Bureau d'Etudes Géologiques Minières Coloniales (Paris) 2:81–144

Nicholson K (1992) Contrasting mineralogical-geochemical signatures of manganese oxides: guides to metallogenesis. Econ Geol 87:1253–1264

Orcel J (1942) La Coronadite et le minerai qui la renferme dans les gîtes de manganèse de l'Imini: Sud Marocain. Bull Société Française Minéralogie 65:73–111

Palmer MR (1985) Rare earth elements in foraminifera tests. Earth Planet Sci Lett 73:285–298

Piper DZ (1974) Rare earth elements in the sedimentary cycle: a summary. Chem Geol 14:285–304

Pouit G (1964) Les gîtes de manganèse marocains encaissés dans les Formations carbonatées: éléments pour une synthèse. Chronique Mines Recherche Minière 337:371–380

Pouit G (1976) La concentration de manganèse de l'Imini (Maroc) peut-elle être d'origine karstique ? Comptes Rendus Sommaire Société Géologique France 5:227–229

Pouit (1980) Manganèse. Notes et Mémoires du Service Géologique du Maroc, Rabat 13:61–67

Pouit G, Jouravsky G (1960) Présence de filons de manganèse d'âge post-triasique ou post-Cénomanien dans la région de l'Imini. Notes Mémoires Service Géologique Maroc 13:61–67

Rhalmi M (1992) Les systèmes sédimentaires cénomano-turoniens et sénoniens de la région manganésifère d'Imini (Haut-Atlas Central, Maroc) et leur évolution diagénétique. Unpubl PhD Thesis, Université Bourgogne, Dijon, France, 168 pp

Rhalmi M, Pascal A, Lang J (1997) Contrôle sédimentaire et diagénétique de la minéralisation manganésifère au cours du Crétacé Supérieur dans la région d'Imini (Haut-Atlas central, Maroc). Comptes Rendus Académie Sciences 323(2):213–220

Rhalmi M, Pascal A, Chellai E (2000) Lithobiostratigraphie, diagenèse et paléogéographie au Cénomanien supérieur-Turonien inférieur des bassins sud-atlasiques marocains. Géologie Alpine 76:135–149

SACEM (2013) Les mines de l'Imini (Rapport d'activité). Société Anonyme Chérifienne d'Etudes Minières, Casablanca 41 pp

Saddiqi O, Baidder L, Michard A (2011) Haut Atlas et Anti-Atlas, Circuit Oriental. Nouveaux Guides Géologiques Miniers Maroc. Notes Mémoires Service Géologique Maroc, Rabat, pp 11–75

Seward TM, Barnes HL (1997) Metal transport by hydrothermal ore fluids. In: Barnes HL (ed) Geochemistry of hydrothermal ore deposits. Wiley, New York, pp 435–486

Taylor SR, McLennan SM (1985) The continental crust: its composition and evolution. Blackwell, Oxford 312 pp

Thein J (1990) Paleogeography and geochemistry of the "Cenomano-Turonian" formations in the manganese district of Imini (Morocco) and their relation to ore deposition. Ore Geol Rev 5:257–291

Westerveld J (1951) Les gîtes de manganèse du domaine atlasique au Maroc français et leur classification géologique. Geologie Mijnbouw 2:25–52

Zouhri S, Kchikach A, Saddiqi O, Haïmer FZE, Baidder L, Michard A (2008) The Cretaceous-Tertiary Plateaus. In: Michard A, Saddiqi O, Chalouan A, de Lamotte DF (eds) Continental evolution: the geology of Morocco. Springer, Berlin-Heidelberg, pp 331–358